Serbian Tribology Society

**Faculty of Engineering
University of Kragujevac**

SERBIATRIB '17

15th International Conference on Tribology

17 – 19 May 2017, Kragujevac, Serbia

PROCEEDINGS

SERBIATRIB '17

Serbian Tribology Society

University of Kragujevac,
Faculty of Engineering

SERBIATRIB '17

15th International Conference on Tribology

17 – 19 May 2017, Kragujevac, Serbia

PROCEEDINGS

EDITOR: Slobodan Mitrović

SERBIATRIB '17

15th International Conference on Tribology – SERBIATRIB '17 PROCEEDINGS

Editor:	**Slobodan Mitrović**
	University of Kragujevac, Faculty of Engineering
Publisher:	**University of Kragujevac, Faculty of Engineering**
	Sestre Janjić 6, 34000 Kragujevac, Serbia
	Serbian Tribology Society
	Sestre Janjić 6, 34000 Kragujevac, Serbia
For the Publisher:	**Dobrica Milovanović**
	University of Kragujevac, Faculty of Engineering
Technical editor:	**Marko Pantić**
	University of Kragujevac, Faculty of Engineering
Printed by:	**InterPrint**
	Jurija Gagarina 12, 34000 Kragujevac, Serbia
Circulation:	150 copies

International Scientific Committee

President:

Miroslav Babić	University of Kragujevac (Serbia)

Members:

Aleksandar Marinković	University of Belgrade (Serbia)
Aleksandar Rac	Serbian Tribology Society (Serbia)
Aleksandar Vencl	University of Belgrade (Serbia)
Andrei Tudor	University Politehnica of Bucharest (Romania)
Bharat Bhushan	The Ohio State University (USA)
Branko Škorić	University of Novi Sad (Serbia)
Dušan Stamenković	University of Niš (Serbia)
Emilia Assenova	Society of Bulgarian Tribologists (Bulgaria)
Gordana Globočki Lakić	University of Banja Luka (Bosnia and Herzegovina)
Hakan Kaleli	Yildiz Technical University (Turkey)
Igor Budak	University of Novi Sad (Serbia)
J. Paulo Davim	University of Aveiro, Portugal
Konstantinos-Dionysios Bouzakis	Aristotle University of Thessaloniki (Greece)
Lorena Deleanu	University Dunarea de Jos of Galati (Romania)
Mara Kandeva	Technical University of Sofia (Bulgaria)
Mehmet Baki Karamis	Erciyes University (Turkey)
Michel Fillon	University of Poitiers (France)
Niculae Napoleon Antonescu	Petroleum-Gas University of Ploiesti (Romania)
Nikolai Myshkin	V.A. Belyi Metal-Polymer Research Institute of National Academy of Sciences of Belarus (Belarus)
Nikolaos M. Vaxevanidis	School of Pedagogical and Technological Education (Greece)
Pantelis G. Nikolakopoulos	University of Patras, Greece
Slobodan Mitrović	University of Kragujevac (Serbia)

Organising Committee

President:

Slobodan Mitrović	University of Kragujevac (Serbia)

Members:

Dragan Dzunić, Conference Secretary	University of Kragujevac (Serbia)
Marko Pantić, Technical Coordinator	University of Kragujevac (Serbia)
Fatima Zivić	University of Kragujevac (Serbia)
Blaža Stojanović	University of Kragujevac (Serbia)
Aleksandar Vencl	University of Belgrade (Serbia)

Preface

The International Conference on Tribology – SERBIATRIB, is traditionally organized by the Serbian Tribology Society every two years, since 1989. The previous conferences were held in Kragujevac (1989, 1991, 1993, 1999, 2005, 2007, 2011 and 2013), Herceg Novi (1995), Kopaonik (1997), Belgrade (2001, 2003, 2009 and 2015). This year the 15th International Conference on Tribology – SERBIATRIB '17 also takes place on May 17-19, 2017 in Kragujevac.

This Conference is organized by the University of Kragujevac, Faculty of Engineering and the Serbian Tribology Society (STS). Organizing Scientific Conferences, STS plays a significant role in helping engineers and researchers to introduce in the fundamentals of tribology and to present their experience, solutions and research results.

The scope of the 15th International Conference on Tribology – SERBIATRIB '17 embraces the state of art and future trends in tribology research and application. The following two aspects of tribology practice require special attention. Firstly, the requirement for higher productivity of machinery means that machines must operate under higher loads and at higher speeds and temperatures, and that is why finding the right solutions for tribological processes is extremely important. Secondly, the good tribology knowledge can greatly contribute to the saving of material and energy.

The Conference program generally includes the following topics: fundamentals of friction and wear; tribological properties of solid materials; surface engineering and coating tribology; lubricants and lubrication; tribotesting and tribosystem monitoring; tribology in machine elements; tribology in manufacturing processes; tribology in transportation engineering; design and calculation of tribocontacts; sealing tribology; biotribology; nano and microtribology and other topics related to tribology.

All together 96 papers of authors from 23 countries (Australia, Bangladesh, Belarus, Bosnia and Herzegovina, Bulgaria, China, Croatia, Czech Republic, Greece, India, Iraq, Italy, Mexico, Nigeria, Romania, Russia, Serbia, Slovakia, South Korea, Taiwan, Turkey, Ukraine and USA) are published in the Proceedings. Approximately 59 papers were submitted by the foreign authors and app. 37 papers by the Serbian authors.

All papers are classified into nine chapters:

- Plenary lectures (4)
- Tribology of Solid Materials (19)
- Surface Engineering and Coating Tribology (9)
- Tribology of Machine Elements (15)
- Tribology of Manufacturing Processes (11)
- Lubricants and Lubrication (12)
- Tribometry (15)
- Biotribology (8)
- Trenje, habanje i podmazivanje (3) – papers written in Serbian language

It was a great pleasure for us to organize this Conference and we hope that the Conference, bringing together specialists, research scientists and industrial technologists, and Proceedings will stimulate new ideas and concepts, promoting further advances in the field of tribology. The Editor would like to thank the Scientific and the Organizing Committee and all those who have helped in making the Conference better.

The Conference is financially supported by the Ministry of Education, Science and Technological Development, Republic of Serbia.

This Conference is dedicated to the late Professor Branko Ivković, who is the founder of the Tribology Society in our Balkan region and established our SERBIATRIB Conference from its beginning, previously YUTRIB. We hope we will be able to continue his great work in this area.

We wish to all participants a pleasant stay in Kragujevac and we are looking forward to seeing you all together at the 16th International Conference on Tribology – SERBIATRIB '19.

Kragujevac, May 2017   Editor
                                                       Prof. Dr Slobodan Mitrović

Dedicated to Tribology Guru Prof. Dr Branko Ivković

After 28 years long tradition, this SERBIATRIB 2017 is our first tribological conference that has been organized without Prof. Dr Branko Ivković. A year ago, in April 2016, our beloved and respected colleague, exceptional professor and tribologist suddenly passed away.

Professor Branko Ivković was born on November 10, 1931 in Kragujevac. He finished elementary and high school in Krgaujevac. Until 1954, he was engaged as technician in tool design in number of military industry institutions. He studied at the Faculty of Mechanical Engineering, Belgrade, and graduated in 1960, at the Department for general engineering with main subject Tool machines and industrial production. His part time academy carrier started in 1961 at the Faculty of Mechanical Engineering in Belgrade, Department in Kragujevac. In 1966 he was elected as the full time lecturer, than in 1968, for assistant professor, and finally he became full time professor in 1976.

He died on date very close to the celebration of the 50th anniversary of tribology. Namely, the government report on lubrication, friction and wear published on 9 March 1966, which was written by a committee chaired by Dr Jost, who coined the engineering subject named „tribology"within the report. Tribology was a missing multidisciplinary concept that was dealing with the interactive processes of surface in relative motion, with their scientific, technical and economic consequences. That new concept was adopted among many researchers in all parts of Yugoslavia, almost from its first appearance. Beside the whole series of scientific experts, like, Prof. Dr V. Solaja, Prof. Dr Vercon, Prof. Dr M. Nedeljković, Prof. Dr Zgaga, a special contribution to the dissemination of the tribological approach, and to the creation of the institutional framework for progress of tribology, certainly belongs to Prof. Dr B. Ivković, who defended one of the first tribological PhD thesis in 1970.

Already in 1971, thus only a few years after the introduction of the term tribology, on the Production Engineering Conference in Novi Sad, the group of Yugoslav authors had pointed to the necessity for stronger tribological research. Also, in early seventies, The Yugoslav Society for Fuels and Lubricants, on its traditional conference, was using the term tribology.

At that time, Laboratory for Metal Cutting of the Faculty of Mechanical Engineering in Kragujevac, with researchers gathered around Prof. Dr B. Ivković, was very convenient environment for accepting the tribology as a new approach. Namely, tribology was naturally implanted into very voluminous and diversified investigations in manufacturing processes. In the following years, very intensive growth of tribological research occurred. It was based on application of originally developed contact surface of radioactive activation method in different areas, like tribological processes on elements for motion guiding, elements for transmission of power and motion, tribological properties of coolants and lubrication, etc. Parallel to development of tribological research, the publication „Reports of Laboratory for metal cutting and Metal Cutting and Tribology ", with Prof. Dr B. Ivković as editor, was established in 1973.

The further development of tribology was supported by education at academic level. Namely, thanks to pioneering efforts of Prof. Ivković, tribology has incorporated to Study curriculum of the Production engineering in 1976. It was the seed of the many current tribology study subjects, from Basics of tribology to Nanotribology and Biotribology.

During seventies, the strong and worldwide recognized tribological school was formed, headed by Prof. Dr B. Ivković. That school took the role of center to which numerous tribologists and young tribological researchers had gravitated. Thus, in May of 1986 the first national tribological association was formed at the Faculty of Mechanical Engineering in Kragujevac. It was Yugoslav Committee for Tribology, seated at this faculty and with Prof. Dr B. Ivković as the president. The association had the goal to unite and improve tribological researches on territory of SFRJ Yugoslavia, by increasing the degree of information exchange among the research centers and ensuring the transfer of the existing knowledge into practice.

Already, in 1978 started the publishing one of the first specialized tribological journals „Tribology in Industry" edited by Prof. Dr B. Ivković. The members of editorial board were scientists from the country and abroad. Today, close to its thirtieth anniversary, the journal, with its four issues per year, has the recognized international character.

After the breakup of Yugoslavia, the group of scientists: Prof. Dr B. Ivković, Prof. Dr A. Rac, Prof. Dr M. Babić and Prof. Dr S. Tanasijević, started the procedure of founding The Yugoslav Society for Tribology that would continue all the activities of former Yugoslav Committee for Tribology. The founding assembly was held in the November of 1992, at the Faculty of Mechanical Engineering in Belgrade. Prof. Dr B. Ivković was elected for the president, and for vice-presidents Prof. Dr A. Rac and Prof. Dr M. Babić. Following the further disintegration of our country, the Serbian Tribology Society has been founded in 2007, as the successor of former national tribological associations.

With an increasing number of young scientists and researchers in the fundamental and boundary areas of tribology, the need for providing the new space for a presentation and exchange of obtained results was rising. Trying to meet that demand, Yugoslav Committee for Tribology decided to organize Yugoslav tribological conference YUTRIB, with participation of domestic and foreign scientists.

The first conference YUTRIB 1989 was organized by Prof. Ivković, and held in Kragujevac. The opening ceremony had a glorious character, with highest level representatives and spokesman of the government, republic, city, university and industry. Altogether, 79 papers were accepted for presentation in four sections, mostly from all republics of federal Yugoslavia. That conference was characterized by very significant number of participants from industry.

It was the starting point for 28 years long tradition of YUTRIB, i.e. SERBIATRIB conferences, which shared the numerous difficulties of the war and the transition years. All of them were smoothly overcome thanks to enormous stability, patience, diligence, dedication, persistence, and optimism of Prof. Ivković.

Prof. Dr B. Ivković was one of the very first scientists which recognized the necessity and the significant potential of regional tribological networking. Accordingly, in November 1993 the founding Assembly of Balkan Tribological Association in the form of BALKANTRIB 93 Round Table was held, at the University of Architecture in Sofia. The main purpose of Balkan Tribological Association is the integration and the support of tribology researches and education in the Balkans, considering the specificity, as whole, and of the different countries in it, in accordance with the status of International Council of Tribology and of the national tribology associations. This association ensures that Balkan conference on tribology BALKANTRIB is organized by host national society every three years.

These are only some of prof. Ivković's activities and contributions to the development of tribology science and technology. Prof. Dr Ivković was an outstanding professor, very fruitful and original researcher, leader, mentor and great entrepreneur devoted to the development of young associates, to dissemination of knowledge and networking of researchers on local, regional and worldwide levels.

Although he is not here, this SERBIATRIB 2017 conference, and almost everything regarding tribological research, education, knowledge transfer, publication and organization in our country, as well as international recognition of Serbian tribology school is his legacy.

President of Serbian Tribology Association

Prof. Dr Miroslav Babić

Contents

Surface Engineering and Coating Tribology

Tribology of Machine Elements

Tribology of Manufacturing Processes

Lubricants and Lubrication

Tribometry

Biotribology

Trenje, habanje i podmazivanje

Plenary Lectures

15th International Conference on Tribology – SERBIATRIB '17

17 – 19 May 2017, Kragujevac, Serbia

A CRITICAL REVIEW OF MEASURES FOR AN EFFECTIVE APPLICATION OF NANO-STRUCTURED COATINGS IN MILLING

G. SKORDARIS, K.-D. BOUZAKIS*, T. KOTSANIS, P. CHARALAMPOUS

Laboratory for Machine Tools and Manufacturing Engineering, Department of Mechanical Engineering, Aristotle University of Thessaloniki, Greece
*Corresponding author: bouzakis@eng.auth.gr

Abstract: The evolution of the coating deposition technologies led, among others, to the production of nano-structured coatings. Such coatings are often deposited on cutting tools since they contribute to an impressive enhancement of the coated tool life. Hereupon, attention has to be given for avoiding a rapid crack propagation due to a potential coating brittleness increase and for achieving a sufficient film adhesion. In this context, film residual stresses and structure may also affect the film adhesion. This paper introduces characteristic measures for an effective application of nano-structured PVD and diamond coatings on cemented carbide tools in milling. More specifically, the adhesion of PVD HPPMS nano-structured coatings can be improved via an appropriate adhesive interlayer. Besides, the coating brittleness can be restricted through the application of nano multi-layer film structures. Furthermore, for improving the diamond coated tool performance, the diamond film nano-structure may be interrupted by micro diamond layers. The introduction of successive nano- and micro-structured layers restricts the film brittleness since micro-structured layers are more deformable compared to nano-structured ones. Finally, the interfacial fatigue strength of diamond coatings is affected by the film residual stresses. Inclined impact tests supported by appropriate FEM simulations facilitate the quantitative adhesion characterization of such films.

Keywords: Nano-structured coatings, HPPMS PVD films, diamond films, adhesion, brittleness, wear.

1. INTRODUCTION

Nano-structured coatings constitute the majority of the tools applied in material removal processes due to their elevated hardness [1,2]. However, only the application of nanostructured coatings cannot guarantee an improved wear behavior of the coated tools. More specifically, certain properties such as the film adhesion to the substrate and the coating brittleness affect significantly the wear resistance of the coated tools. In the paper, characteristic measures to be undertaken for an effective application of nano-structured PVD and diamond coatings on cemented carbide tools in milling are presented. In this context, the usage of high power pulsed magnetron sputtering (HPPMS) as a PVD coating deposition technique has to be combined with the deposition of adhesive interlayers for exploiting the production of coatings characterized by enhanced mechanical properties and uniform film thickness [3,4,5,6]. The effectiveness of the adhesive nano-interlayers depends on the substrate surface's integrity and on the layer material [2,3]. Moreover, nano multi-layer PVD structures has to be applied for restricting the film brittleness [7,8]. Furthermore, diamond

coatings deposited on cemented carbide tools are characterized by high residual stresses in their structure mainly due to epitaxial crystal differences and thermal expansion coefficients mismatch of the diamond coating and its cemented- carbide substrate [9,10,11]. Multi-layered diamond coating systems, with successive nano- and micro-structured layers, can absorb a part of the residual stresses because of the more deformable micro-structured layers compared to nanocomposite ones. The latter coatings possess increased brittleness due to their large compressive stresses which deteriorates the cutting performance [11]. It is worth mentioning that a prevailing mechanical property affecting significantly the cutting performance of diamond coated cemented carbide inserts is the fatigue strength of the diamond coating-substrate interface. The interfacial fatigue strength is temperature-dependent and is affected by the film residual stresses [12]. Inclined impact test supported by appropriate FEM simulations facilitate the quantitative characterization of the films' adhesion [1,12].

2. PVD HPPMS COATINGS

2.1 Adhesive interlayers for improving the film adhesion

High Power Pulsed Magnetron Sputtering (HPPMS) process, compared to the standard dc sputtering techniques or cathodic arc, produces denser nanostructured coatings and free of droplets [3,4,5,6]. The goal of HPPMS technology is to achieve a plasma density exceeding conventional ones by roughly three orders of magnitude. Normal sputtering leads to a plasma density of 10^{16} m^{-3}, while HPPMS reaches 10^{19} m^{-3}. This is done by pulsing the power to the source with average amplitude of approximately 1 kW and peak power densities of about 0.4–0.5 MW per pulse, but at a low duty cycle of about 1–20 ms (see figure 1). In the developed hot and dense plasma area, the metallic atoms are highly ionized and subsequently deposited on the specimen surfaces with elevated kinetic.
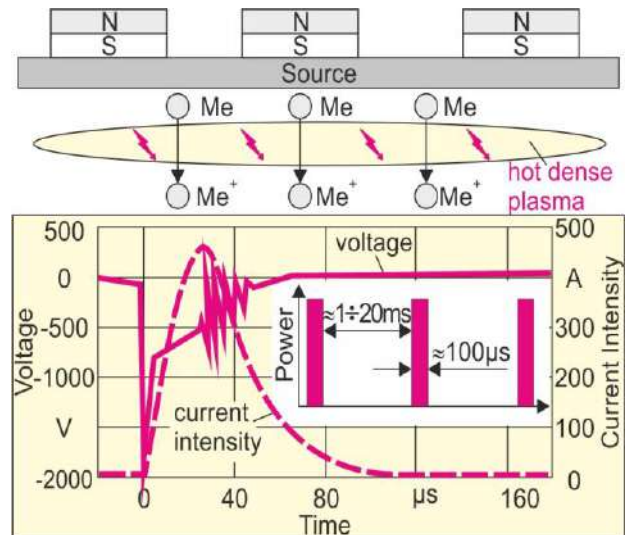
Figure 1. Plasma energy increase by HPPMS during PVD processes

The effectiveness of a coating deposited by HPPMS depends on the selection of an appropriate adhesive nano-interlayer, which immobilizes the WC carbides in reacting with high energy ions of the film material during their deposition on the substrate [4]. To evaluate the effect of different HPPMS deposited interlayers on the film adhesion, Rockwell HRC indentations and inclined impact tests were carried out on TiAlN coated inserts. No cracks or detachment signs appeared on the imprints of the coated insert with a Cr/CrN-nano-interlayer, indicating a good film adhesion (see figure 2a). However, inclined impact tests conducted on cemented carbide inserts with a Ti/TiN or W/WN nano-interlayer revealed the negative contribution of these materials on the adhesion. The related inclined impact test results are displayed in figure 2b. Moreover, milling investigations were carried out to examine the interlayer material effects on the coated tool wear behavior (see figure 2c). The results revealed that HPPMS techniques jointly with a Cr/CrN nano-interlayer lead to significant cutting performance improvement due to adhesion enhancement.

The film adhesion and consequently the tool life improvements of HPPMS coated tools with a graded Cr/CrN nano-interlayer depend on the roughness of the employed cemented carbide substrates and on the adhesive interlayer thickness.
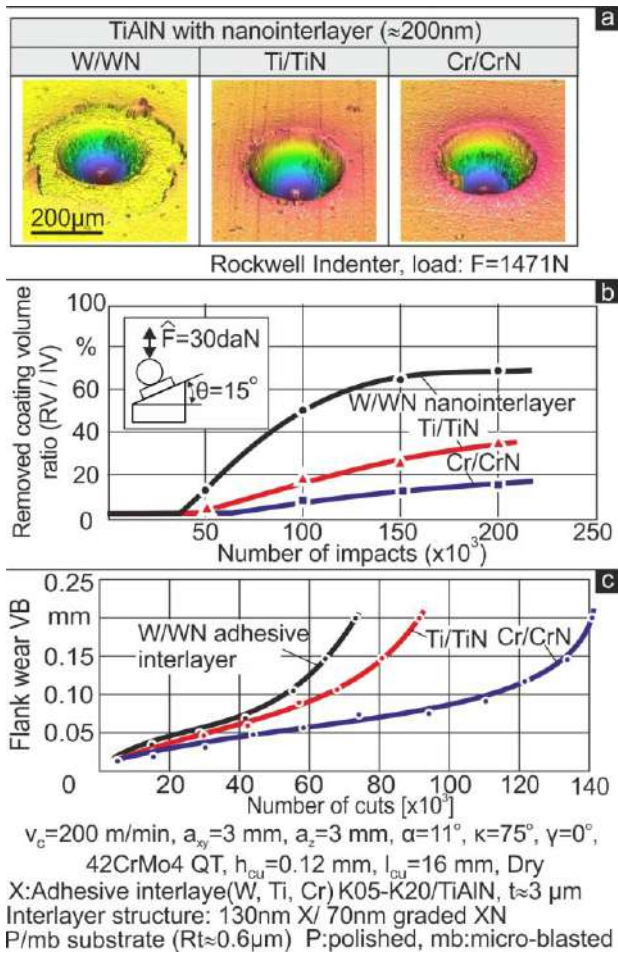
Figure 2. Effect of HPPMS nano-interlayers materials on the coating's adhesion characterized: (a) by Rockwell HRC indentations, (b) by inclined impact tests and (c) by cutting experiments

By inclined impact tests, significant adhesion quality differences were detected when different HPPMS graded Cr/CrN interlayer thickness are employed [3]. The removed film volume ratios (RVR) versus the number of impacts on inserts with various interlayers thicknesses were registered during the inclined impact tests. The corresponding results are exhibited in figure 3a. The TiAlN coated inserts with graded Cr/CrN interlayers of 200 nm withstand more effectively the repetitive oblique impact loads compared to the corresponding interlayers of 50 and 600 nm thicknesses. Furthermore, the wear resistance of HPPMS TiAlN coated inserts with graded Cr/CrN-interlayer of various thicknesses was tested in dry milling (see figure 3b). According to the obtained results, the coated inserts with graded Cr/CrN nano-interlayer thickness of 200 nm exhibit the best wear resistance, reaching a tool life of

approximately 140,000 cuts, at a flank wear VB of 0.2 mm. Moreover, coated inserts with 50 nm and 600 nm nano-interlayer managed to cut only ca. 100,000 and 90,000 times respectively, up to the flank wear of 0.2 mm.
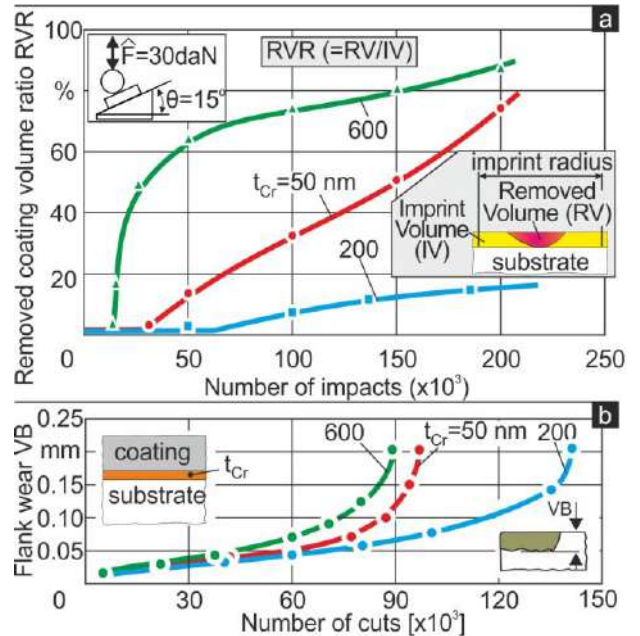
Figure 3. (a) Effect of interlayers' thickness on the removed film volume during the inclined impact test on HPPMS coated inserts (b) Flank wear development versus the number of cuts of HPPMS coated tools with different interlayer thickness
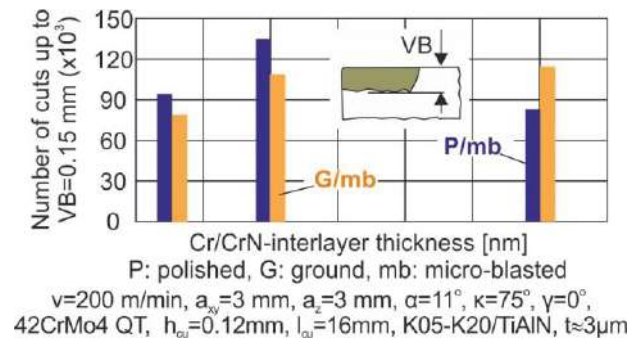
Figure 4. Number of cuts up to a flank wear of 0.15 mm for various HPPMS interlayers thickness and substrate treatments

Further milling investigations were conducted applying HPPMS TiAlN coated inserts with graded Cr/CrN-interlayer of various thicknesses and substrate mechanical treatments (see figure 4). In the polished and micro-blasted (P/mb) substrate treatment case, the coated inserts with nano-interlayer

thickness of 200 nm exhibit the best performance. In the ground and micro-blasted substrates (G/mb), the tool life was increased, as the nano-interlayer thickness grows. The afore described differences are caused by the coatings' adhesion changes exhibited before.

2.2 Multilayer nano-structured PVD coatings for restricting film brittleness

The deposition of multilayer nano-structured PVD coatings on cemented carbide tools contributes to a significant improvement of the coated tool life due to their capability to prevent the crack propagation [7]. Characteristic SEM photos demonstrating cross sections of nano-layered HPPMS PVD TiAlN coatings with film thickness of approximately 2 μm and 8 μm are shown in figure 5. The coating structure consists of successive TiAlN and TiN layers. The thicknesses of the individual TiAlN and TiN layers amounted to roughly 24 nm and 3 nm correspondingly. In this way, the resulting structure of a coating with thickness approximately equal to 2 μm, 4 μm and 8 μm is the sum of around seventy-five, or one hundred fifty, or three hundred TiAlN layers alternately with an equal number of TiN ones respectively. Furthermore, in figure 5, the roughness characteristics of the used coated inserts are illustrated. The roughness data are similar in all investigated coating thickness cases.
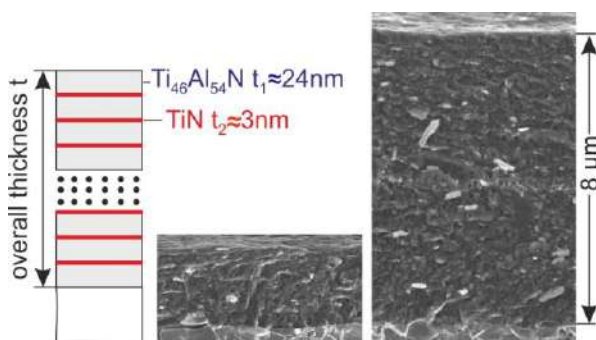
thickness	2	4	8
Rt [μm]	≈ 1.1	1.3	1
Ra [μm]	≈ 0.11	0.14	0.13

SPGN 120308, Ti$_{46}$Al$_{54}$N/TiN coating, substrate: HW-K05/K20, Deposition temp.=550°C, 3-fold substrate rotation

Figure 5. The employed nano-layered coatings with various thicknesses and their roughness characteristics

The strength properties gradations versus the film thickness for the investigated nano-layered coatings are presented in figure 6. For estimating the graded strength properties of the used HPPMS PVD coatings, it was assumed that the structures of the 8 μm, 4 μm and 1 μm thick coatings are described by four, two or one individual layers (Analytical Description's Layers (ADLs)) respectively, each one possessing a thickness of 2 μm and own uniform properties. Every layer after its deposition at the HPPMS process temperature is exposed to an annealing affecting its strength data. The annealing duration of each layer is associated with the rest time, up to the deposition of the overall coating thickness. Coated inserts with film thickness of 2 μm, 4 μm and 8 μm were annealed in vacuum at a temperature of 550 °C equal to the related one during the film deposition. The annealing duration was adequately varied. To estimate the strength properties of the ADLs of the manufactured PVD films, nanoindentations coupled with appropriate FEM simulations were carried out on annealed coated specimens [7].

HPPMS PVD (Ti$_{46}$Al$_{54}$)N/HW-K05/K20
Deposition/Annealing temperature=550°C
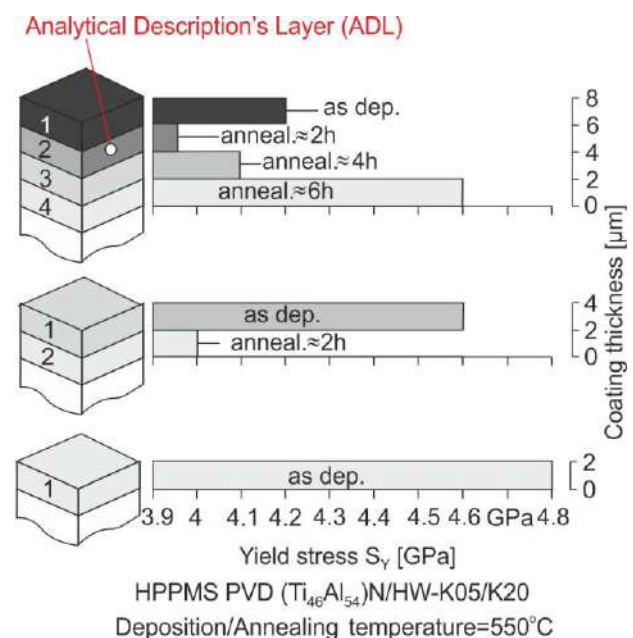
Figure 6. Prediction of the graded strength properties of 8 μm, 4 μm and 2 μm thick nano-layered coatings.

The R-rate is the ratio of the flank wear land width VB growth between two reference VB values divided by the overall removed chip length l$_c$ between these values. The latter parameter l$_c$ is

equal to the obtained number of cuts NC between the latter two VB values multiplied by the undeformed chip length l_{cu}. Figure 7 presents the R-ratio evolution versus the number of cuts NC and cutting time t_c in various film thickness cases.

v=200m/min, a_z=2mm, f_v=259mm/min, S=785rpm, D=81mm, α=11°, 42CrMo4 QT, down-milling, dry
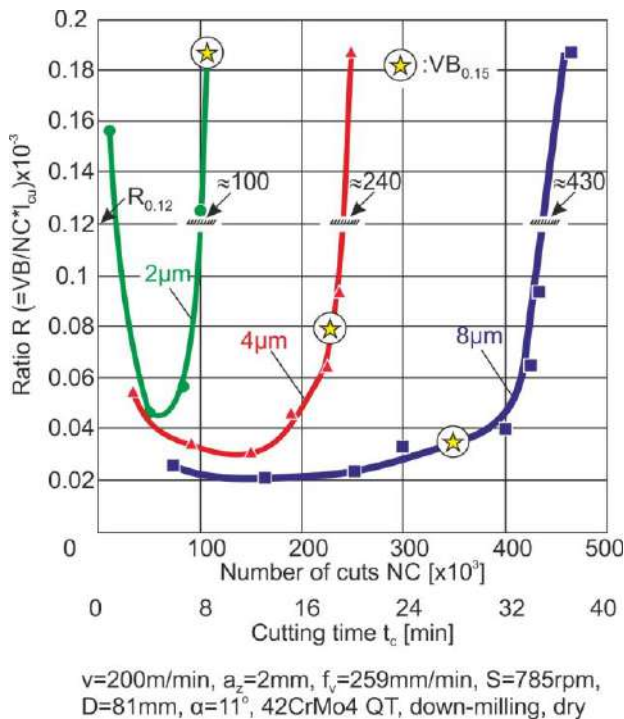
Figure 7. VB-evolution rate development versus the number of cuts of coated cemented carbides inserts with different film thicknesses

The R-rate was calculated at constant VB growth steps of 30 μm. The related number of cuts at the beginning and at the end of these steps were estimated by conducting milling experiments [7]. In the considered milling case, the undeformed chip length l_{cu} amounted to 16 mm. According to figure 7, the higher the coating thickness, the slower the R-rate evolution versus the number of cuts is. In the case of a 8 μm thick coating at a VB equal to about 150 μm, a low R-rate of roughly 0.04 × 10^{-3} [μm/mm] develops. On the contrary, in the case of a 2 μm thick coating, the R-rate at the same VB of 150 μm is roughly 4.5 times higher, equal to around 0.18 × 10^{-3} [μm/mm], thus rendering the tool change necessary. Hence, when using a 8 μm thick film instead of a 2 μm one, the obtained tool life was larger than 4 times at the same R-rate, as for instance at 0.12 × 10^{-3} ($R_{0.12}$ see figure 7). If the flank wear land width VB of 150 μm ($VB_{0.15}$) was used as criterion to compare the achieved tool lives when using a 2 μm and a 8 μm thick

coating, the previously mentioned tool life increase would be approximately only 3.5 times larger (see figure 7). In this way, it can be stated that the usage of multilayer nano-structured films facilitates the effective application of thicker coatings in milling processes due to their restricted brittleness.

3. DIAMOND COATINGS

3.1 Multi-layered diamond coating systems for restricting film brittleness

Diamond coatings on hardmetal tools are characterized by high residual stresses. The residual stresses in diamond films are associated with numerous reasons such as epitaxial crystal differences as well as the significantly smaller thermal expansion coefficient of the diamond coating compared to its cemented carbide substrate [9,10]. The employed deposition parameters affect significantly the level of residual stress in diamond film structure.

For investigating the described dependencies, three groups of coated inserts were produced by varying the deposition parameters. The cooling time was held constant and equal to 9 h. Applying a deposition time of 10 h, the NCD insert group was manufactured. At this deposition duration, the structural residual stresses were negligible and mainly thermal ones were developed in the nano-composite film structure. Moreover, two further groups were created possessing nano-composite (NCD/hsrs), or multi-layer film structure (MLD) with overall ten successive and alternate nano- and micro-structured layers. These nano- and micro-structured layers had approximately 0.34 and 0.66 μm thickness, respectively. In the latter two coating cases, the deposition time was intentionally shortened. As a consequence, structural compressive residual stresses developed in the diamond coating structure, which were overlaid with the also compressive thermal ones.

For determining the maximum residual stress in the investigated diamond coatings, the experimental-analytical procedure

described in [11,12] was employed. The experimental procedure comprises the conduct of inclined impact tests on the coated specimens. During this test, depending on the applied repetitive impact load, a fatigue failure in the NCD coating–substrate interface develops after a certain number of impacts causing the film detachment. After this damage, the highly compressive stresses in the NCD coating structure are released elevating the coating in the detached circular region up to a certain maximum height (bulge formation) [11]. Characteristic diamond film bulges developed at certain impact loads, after approximately the shown number of impacts are shown in figure 8. The bars at the right figure part demonstrate the determined thermal and structural equivalent stresses in the investigated coating cases. These stresses were determined by means of the mentioned analytical methods [11], taking into account the mechanical properties and the dimensions (diameter and height) of the formed bulges. In the case of NCD insert group, the structural residual stresses are negligible at ambient temperature compared to the thermal ones. On the contrary, the film residual stresses of NCD/hsrs and MLD coated inserts are attributed to both thermal and structural ones resulting during the CVD process and the subsequent cooling. The structural stresses in the MLD films are lower compared to the corresponding ones of the NCD/hsrs ones. Hereupon, it can be assumed that the micro-structured layers of the MLD coating absorb a part of the developed residual stresses, since they are more deformable compared to the nano-structured ones. The thermal residual stresses are reduced as the operational temperature grows, whereas the structural ones remain practically stable up to a temperature of roughly 400 $^{\circ}$C.

The cutting performance of the manufactured diamond coated tools was investigated in milling AA7075 T6. The experiment was performed without coolant or lubricant. For visualizing the coatings' wear evolution, the minimum coating thickness t_{rmin} in the tool wedge roundness, at diverse overall

chip lengths L_c, was determined with the aid of confocal microscopy measurements (see figure 9).
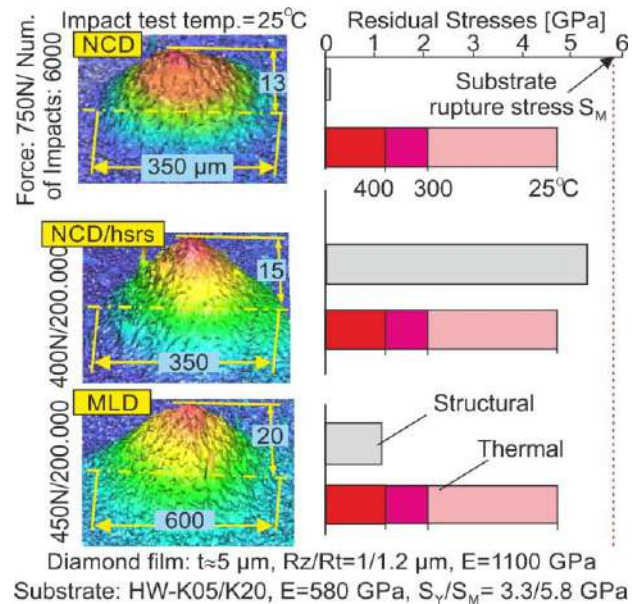
Figure 8. FEM-calculated thermal and structural stresses in the investigated coatings based on the dimensions of the developed bulges at various loads and number of impacts.
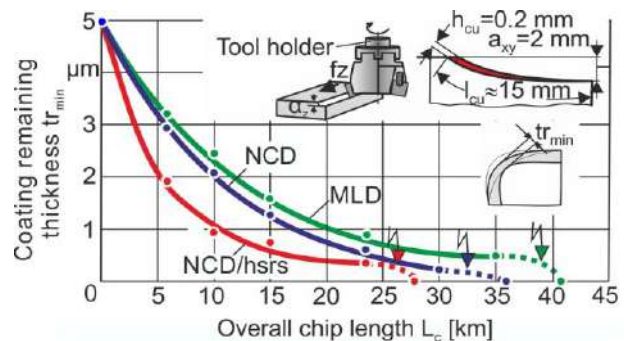
Figure 9. Coating remaining thicknesses t_{rmin} at various overall chip lengths L_c

The NCD/hsrs inserts demonstrated a worse cutting performance compared to the NCD and MLD ones. This can be attributed to the large compressive structural stresses in the NCD/hsrs films which may increase their brittleness and deteriorate the cutting performance. MLD coatings exhibited the best cutting performance reaching an overall chip length L_c of almost 40 km up to a substrate revelation at the cutting edge roundness region. Hereupon, the MLD coating withstands more effectively the repetitive impacts during milling, since the layer's interfaces obstruct the crack propagation and contributes to a tool life augmentation. Conversely, in the case

of NCD films, the cracks usually propagate straight down to the substrate, worsening their wear behavior in cutting.

3.2 Increased interfacial fatigue strength by controlling the developed residual stresses in the film structure

The cutting performance of diamond coated cemented carbide inserts is significantly affected by the film adhesion. Residual stresses in diamond films usually enhance the coating adhesion since they contribute to roughness locking in the coating–substrate interface. However, they may overstress the substrate material in its interface region, thus deteriorating the coating adhesion.

For determining the interfacial fatigue strength of the investigated coatings shown in figure 8, inclined impact tests were conducted. The experimentally detected maximum forces for avoiding the fatigue failure of the diamond coating–substrate interface after 10^6 impacts at diverse temperatures are illustrated in figure 10a. These critical impact forces and the temperature-dependent film residual stresses shown in figure 8 were the input data for calculating the shear failure stress (SFLS) according to the mentioned method described in [12]. The displayed SFLSs in Figure 10b represent temperature-dependent thresholds triggering an interfacial coating–substrate adhesive failure in every coating case after 10^6 repetitive impacts. The higher the operational temperature, the lower the maximum applied force and the SFLS are for avoiding an adhesive film fatigue failure.

At temperatures, less than approximately 200 °C, the lowest critical impact forces and SFLSs possess the NCD/hsrs coatings compared to the NCD and MLD ones. In this case, on the one hand, the sum of the structural and thermal residual stresses in the region of the film interface at temperatures less than approximately 400 °C is larger than the substrate rupture stress SM (Figure 8). Here, the temperature reduction to an ambient one leads to the formation of micro-cracks in the substrate interface region.
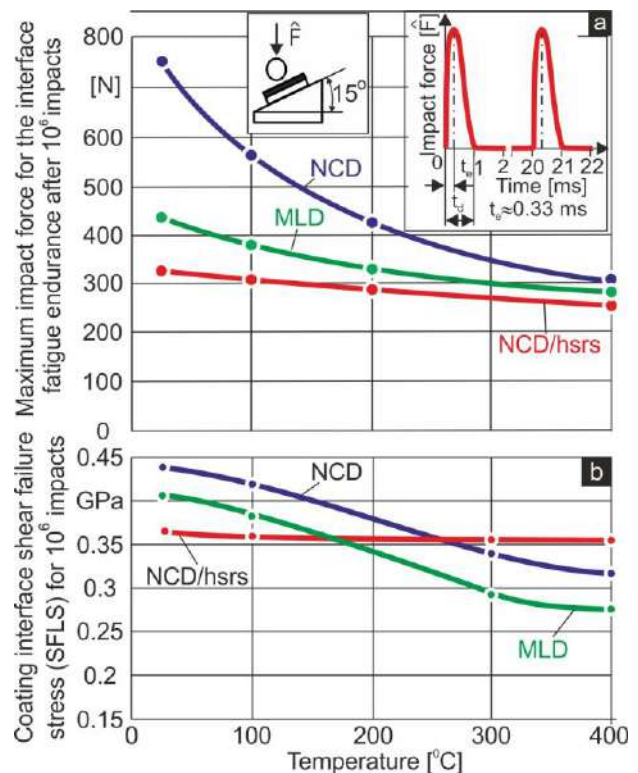
Figure 10. (a) Interface fatigue endurance impact force. (b) FEM-calculated SFLSs associated with the interface fatigue endurance at various temperatures.

In this way, the SFLS of NCD/hsrs films is lower compared to MLD and NCD coatings at temperatures less than about 100 °C. On the other hand, when the temperature grows, roughnesses between film and substrate in the interface region remain locked in the case of the NCD/hsrs films since the structural stresses are practically not affected. Hence, the related SFLS remains almost stable and over about 150 to 300 °C it is greater compared to the related ones of the MLD and NCD films, respectively. In the latter two cases, the temperature increase causes an unlocking of interface roughnesses, thus deteriorating the film adhesion.

4. CONCLUSION

In this paper, characteristic measures for an effective application of nano-structured PVD and diamond coatings on cemented carbide tools in milling were introduced. The goals of these measures are to achieve a sufficient film adhesion to the substrate and to avoid a rapid crack propagation due to a potential coating

brittleness increase. More specifically, in the case of HPPMS PVD coatings, the deposition of adhesive interlayers and application of multilayer nano-structured films for improving the film adhesion and brittleness respectively, are recommended. Moreover, multi-layered diamond coating systems prevent the steep crack propagation in cutting processes. In the case of diamond coatings, special care has to be given to the residual stresses of the film structure. The latter affect significantly the film adhesion.

REFERENCES

[1] K.-D. Bouzakis, N. Michailidis, G. Skordaris, E. Bouzakis, D. Biermann, R. M'Saoubi, Cutting with coated tools: Coating technologies, characterization methods and performance optimization, CIRP Annals - Manufacturing Technology, Vol. 61, No. 2 , pp. 703-723, 2012.

[2] K. Bobzin, High-performance coatings for cutting tools, CIRP Journal of Manufacturing Science and Technology, http://dx.doi.org/10.1016/j.cirpj.2016.11.004.

[3] K.-D. Bouzakis, S. Makrimallakis, G. Katirtzoglou, G. Skordaris, S. Gerardis, E. Bouzakis, T., Leyendecker, S. Bolz, W. Koelker, Adaption of graded Cr/CrN-interlayer thickness to cemented carbide substrates' roughness for improving the adhesion of HPPMS PVD films and the cutting performance, Surface and Coatings Technology, Vol. 205, No. 5, pp. 1564-1570, 2010.

[4] K.-D. Bouzakis, G. Skordaris, S. Gerardis, G. Katirtzoglou, S. Makrimallakis, M. Pappa, S. Bolz, W. Koelker, The effect of substrate pretreatments and HPPMS-deposited adhesive interlayers' materials on the cutting performance of coated cemented carbide inserts, CIRP Annals - Manufacturing Technology, Vol. 59, No.1, pp. 73-76, 2010.

[5] P. Eh. Hovsepian, A.P. Ehiasarian, R. Braun, J. Walker, H. Du, Novel CrAlYN/CrN nanoscale multilayer PVD coatings produced by the combined High Power Impulse Magnetron Sputtering / Unbalanced magnetron Sputtering technique for environmental protection of γ- TiAl alloys, Surface and Coating Technology, Vol. 204, pp. 2702-2708, 2010.

[6] K. Bobzin, T. Brögelmann, N.C. Kruppe, M. Engels, Influence of dcMS and HPPMS in a dcMS/HPPMS hybrid process on plasma and coating properties, Thin Solid Films, Vol. 620, pp. 188-196, 2016.

[7] G. Skordaris, K.-D Bouzakis., T. Kotsanis, P. Charalampous, O. Lemmer, S. Bolz, Film thickness effect on mechanical properties and milling performance of nano-structured multilayer PVD coated tools, Vol. 307, pp. 452-460, 2016.

[8] Aharon Inspektor, Paul A. Salvador, Architecture of PVD coatings for metalcutting applications: A review, Surface and Coating Technology, Vol. 257, pp. 138-153, 2014.

[9] Glen A. Slack, S. F. Bartram, Thermal Expansion of Some Diamond-like Crystals. Journal of Applied Physics, Vol. 46, pp. 89–98, 1975.

[10] N. Woehrl, T. Hirte, O. Posth, V. Buck, Investigation of the Coefficient of Thermal Expansion in Nanocrystalline Diamond Films. Diamond and Related Materials, Vol. 18, pp. 224–228, 2009.

[11] G. Skordaris, K.-D. Bouzakis, P. Charalampous, T. Kotsanis, E. Bouzakis , O. Lemmer, Effect of structure and residual stresses of diamond coated cemented carbide tools on the film adhesion and developed wear mechanisms in milling, CIRP Annals - Manufacturing Technology, Vol. 65, pp. 101–104, 2016.

[12] G. Skordaris, Effect of the temperature dependent residual stresses of diamond coated tools with different adhesion qualitis on their interfacial fatigue strength, Journal of the Balkan Tribological Association, Vol. 22, No 2A-I, pp. 1776–1786, 2016.

PERFORMANCE DEGRADATION BASED ON MIXED WEAR THEORY OF AVIATION HYDRAULIC PISTON PUMP

Shaoping WANG[1*], Mileta TOMOVIC[2], Lei HAN[3]

[1]School of Automation Science and Electrical Engineering, Beihang University, China
[2]Department of Engineering Technology, Old Dominion University, USA
[3]School of Automation, Beijing University of Poste and Telecommunications, China

Abstract: This paper focuses on the mathematical modeling of axial piston pump through dividing the failure development of friction pair into lubrication, mixed lubrication and abrasion. Directing to the wedge-shaped oil film between cylinder block and valve plate, the support force distribution under the temperature variance was obtained. Considering the rough peak of valve plate, the contact load model is modeled under plastic deformation and elastic deformation and the corresponding wear volume is calculated. Computing the wear and tear along the counter-clockwise, the total amount of friction and wear can be calculated. Simulation and preliminary wear particle monitoring test indicates that proposed modeling and analysis can reflect the real abrasion process of hydraulic piston pump.

Keywords: Axial piston pump, mixed wear, performance degradation, cylinder block, valve plate

1. INTRODUCTION

Aviation axial piston pump provides pressurized fluid to drive aircraft systems such as surface control system, landing gear system and nose wheel steering system. With the high efficiency and high power to weight ratio, axial piston pump is widely used in aircraft while its complicated structure makes it easy to fail due to the wear and tear of friction pairs. Based on the statistics, more than 70% failures of axial piston pump is the leakage due to the wear and tear of main friction pairs [1]. So many researches carried out the research on the failure mechanism under dynamic lubrication and abrasive wear.

The main friction pairs of axial piston pump consist of cylinder block/valve plate, piston/plunger chamber and piston shoes/swash plate. In normal condition, the main friction pairs operate in good lubrication condition. However, the complicated operational principle makes it easy enter boundary lubrication even abrasion, so the wear and tear plays major role in failures of axial piston pump. The failure analysis of axial piston pump divides into two types: one focuses on the lubrication and another emphasizes on the wear and tear. In 1986, Yagaguchi studied the lubrication between the valve plate and cylinder block, and gives the mathematical model of fluid oil [2]. Based on above model, he established the dynamic model of cylinder block, calculated its force and torque, and provided the stable condition of constant oil film between the valve plate and the cylinder barrel [3]. Through fixing up the displacement sensors along the valve plate, he got the oil film thickness between the valve plate and the cylinder block [3]. In order to get

the variation of oil film, Maring measured the oil film pressure between piston shoes and swash plate through experiment [4]. At the same time, Ivantysynova established the oil film model of cylinder block and valve plate considering the elastic deformation of the contact surface under high pressure [5]. She also analyzed the temperature influence between this friction pair considering the effects of viscosity and pressure change [6][7]. With the continuous operation of the axial piston pump, Greenwood and Williamson discovered the local contact when the oil film thickness is less than the roughness of the two surfaces, and built the Greenwood-Williamson model based on the elastic contact of rough surfaces [8]. In order to connect the bridge between the lubrication and abrasion of friction pairs, Patir and Cheng proposed a kind of Reynolds equation to solve the lubrication problem under local contact condition for the axial piston pump [9][10]. Yamaguchi analyzed the mixed lubrication based on Greenwood-Williamson model and Patir equation and built the test rig [11]. The corresponding experiment indicated that the proposed model can give the predict friction force and flow rate. Subsequently, many researches presented a series models to describe the multi scale characteristics of rough peak curvature in two surface contact [12][13]. Majumdar and Bhushan established the classification model of elastic plastic contact process on the rough peak, which means the plastic deformation connect each other and develop them to the elastic state [14]. Considering the rough peak deformation, Liou proposed a contact model based on height distribution of non Gauss distribution [15]. From the real micro profile monitoring, the wear and tear of friction pairs of axial piston pump depends on the pressure distribution, temperature distribution, oil film thickness variant and contact wear principle, so this paper establishes the mixed wear model considering the lubrication, boundary lubrication and abrasion, provides the performance degradation law and gives the estimation based on the on line wear debris monitoring.

The rest paper is organized as follows. Section 2 presents the mixed wear theory based on the lubrication, boundary lubrication and abrasion. Section 3 provides the performance degradation due to the wear and tear of the friction pairs. Section 4 shows the experimental results through on line contamination monitoring. Section 5 makes conclusions.

2. MIXED WEAR MODELING OF AXIAL PISTON PUMP

Fig.1 shows the structure of axial piston pump, in which the valve plate and swash plate are fixed, the shaft drives the cylinder block rotation and the pistons reciprocate in it when the axial piston pump operates. There are three friction pairs in axial piston pump, that is, cylinder block/ valve plate, slipper/swash plate and piston/ plunger cavity. The cylinder block-valve plate plays important role in axial piston pump because its failures predominate in maintenance.

Shaft   Swash plate   Cylinder block   Valve plate
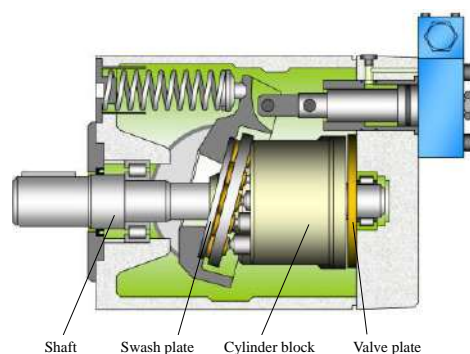
Fig. 1 The structure of axial piston pumpₚ

Through analyzing the surface morphology of the worn valve plate, its eccentric wear in high pressure area occupies the primary position. Since the axial piston pump is full of oil, its normal operation depends on the lubrication between friction pairs. Based on the tribology theory, most of the abrasive wear of the axial piston pump is caused by oil film damage between friction pair surfaces. In order to describe the failure development of abrasive wear, it is necessary to investigate the dynamic variation of the fluid film and abrasion rule between valve plate and cylinder block.

2.1 Dynamic lubrication model of cylinder block and valve plate

Since the imbalance pressure distribution between cylinder block and valve plate, the oil film between the friction pair is wedge-shaped shown in Fig. 2.
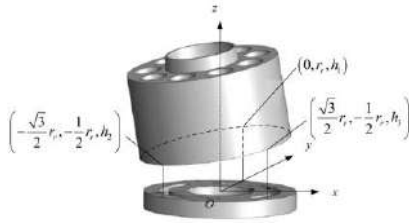
Fig.2 Wedge-shaped oil film between cylinder block and valve plate

For wedge-shaped oil film, the position of the whole cylinder block can be determined through measuring the height of 3 fixed points. Suppose three points in cylinder block are shown in Fig.4, the oil film thickness at arbitrary point can be determined as follows:

$$h(x,y) = \frac{h_3 - h_2}{\sqrt{3}r_r}x + \frac{2h_1 - h_2 - h_3}{3r_r}y + \frac{h_1 + h_2 + h_3}{3} \quad (1)$$

Where x, y is the coordinate at arbitrary point of valve plate, r_r is reference radius, h_1, h_2, h_3 are the height of oil film in distributed three points of valve plate. According to the Reynolds equation, the relation of support force and velocity can be described as:

$$\frac{\partial}{\partial x}(\frac{\rho h^3}{\mu}\frac{\partial p_l}{\partial x}) + \frac{\partial}{\partial y}(\frac{\rho h^3}{\mu}\frac{\partial p_l}{\partial y})$$
$$= 6[\frac{\partial}{\partial x}(v_x \rho h) + \frac{\partial}{\partial y}(v_y \rho h) + 2\rho\frac{\partial h}{\partial t}] \quad (2)$$

Where p_l is the support force of oil film, h is oil thickness, μ is dynamic viscosity which is related to the temperature and pressure.

2.2 Partial abrasion analysis of cylinder block and valve plate

Under ideal condition, there exists a layer of oil film between valve plate and cylinder block, which lubricate the operation of the friction pair shown in Fig. 3. Since the sealing strips separates the high pressure area of outlet and low pressure area of inlet, the periodic eccentric moment exists in valve plate

to cause out-of-balance between downward compressive stress F_B and upward support F_f. Then the cylinder block will contact the partial area of valve plate and cause the wear and tear.
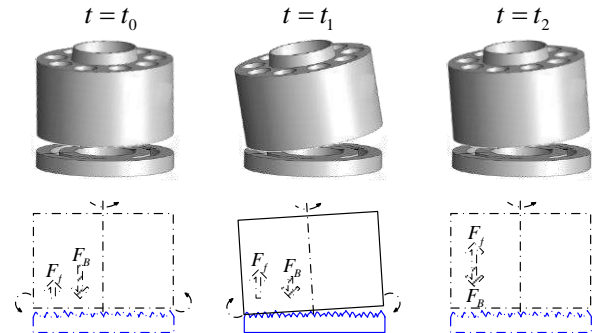
Fig.3 Friction pair of cylinder block and valve plate

In order to describe the contact of cylinder block and valve plate, Fig.4 enlarges the contact surface, in which $R(\alpha)$ indicates the radius of curvature of rough peak and $g(z)$ expresses the height distribution.
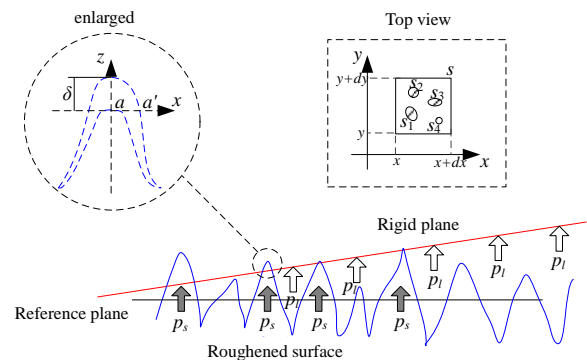
Fig.4 Mixed lubrication state

Suppose the contact surface between cylinder block and valve plate has the following characteristics:
1) The surface of cylinder block is ideal rigid smooth plane;
2) The surface of valve plate is non-rigid rough surface;
3) The top of the rough peak on a rough surface is nearly half spherical;
4) The curvature of rough peak R is related to the sectional area of rough peak α;
5) The upward support force of rough peak is p_s and oil film support force p_l.

According to the Hertz contact theory, the critical deformation area of rough peak can be described as

$$a_c = \pi \left(\frac{\pi H}{2E} \right)^2 R^2(a) \qquad (3)$$

Where H is material hardness, E is equivalent elastic modulus. When $a > a_c$, the contact asperity is elastic deformation. Otherwise, the contact asperity is plastic deformation.

In elastic deformation, the deflection can be described as

$$\delta_e = \frac{a}{\pi R(a)} \qquad (4)$$

Here $R(a)$ is complex curvature radius of rough peak.

Then the contact force of elastic deformation asperity is

$$f_e(a) = \frac{4}{3} E R^{1/2}(a) \delta^{3/2} = \frac{4E a^{3/2}}{3\pi^{3/2} R(a)} \qquad (5)$$

To the plastic deformation, the deflection can be obtained according to the volume conservation as

$$\delta_p = \frac{\delta_c(a)}{2} + \frac{a}{2\pi R(a)} \qquad (6)$$

The asperity contact area distribution of plastic deformation is shown as follows:

$$n_p(a) = \frac{A_a g(h)}{\pi a R(a)} \left| \frac{\pi \left(\frac{\pi H}{2E} \right)^2 R(a)}{2} \times \frac{dR(a)}{da} + \frac{1}{2} \left(1 - \frac{a}{R(a)} \times \frac{dR(a)}{da} \right) \right|$$

$$(7)$$

Where A_a is real contact area, $g(h)$ is the integrated surface height distribution of rough peak. The plastic deformation contact force is

$$f_p(a) = Ha \qquad (8)$$

Then the contact load can be expressed as [14]:

$$p_s(x,y) = \int_0^{a_c} f_p(a) n_p(a) \, da + \int_{a_c}^{a_L} f_e(a) n_e(a) \, da \qquad (9)$$

Where α_c is critical deformation area, α_L is maximum asperity contact area, n_p is asperity contact area probability density function of plastic deformation, n_e is asperity contact area probability density function of elastic deformation.

From Eq. (3) to Eq. (9), the pressure distribution of contact zone can be figured out.

2.3 Abrasive wear model of cylinder block and valve plate

If the eccentric wear between cylinder block and valve plate causes the particle and the particle size is larger than oil film, the abrasive wear will produce shown in Fig.5.
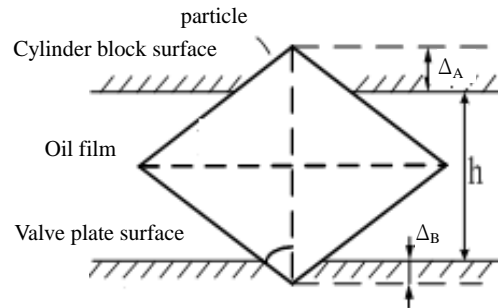
Fig. 5 Two-dimensional rhombic particle model

In Fig.5, D is the particle major axis, β is the angle to describe particle's shape, h is the separation of the surfaces, ΔA is the depth of the groove on the cylinder block and ΔB is the depth of the groove on the valve plate.

Assume that the particle hardness is much higher than hardness of sliding surfaces, the depth of a single abrasive particle embedded in the cylinder block and valve plate is

$$\begin{cases} \Delta_A(x,y,D) = \dfrac{H}{1+H} \left(\dfrac{D}{\tan \beta_d} - h(x,y) \right) \\ \Delta_B(x,y,D) = \dfrac{1}{1+H} \left(\dfrac{D}{\tan \beta_d} - h(x,y) \right) \end{cases} \qquad (10)$$

Where Δ_A is the depth of a abrasive particle embedded in the cylinder block, Δ_B is the depth of a abrasive particle embedded in the valve plate, H is the valve plate and cylinder block hardness ratio. Then we can get the wear volume of an abrasive particle in a certain time as

$$\begin{cases} \Delta V_A(x,y,D) = f \Delta_A^2(x,y,D) \tan \beta_d \, \omega r(x,y) \\ \Delta V_B(x,y,D) = f \Delta_B^2(x,y,D) \tan \beta_d \, \omega r(x,y) \end{cases} \qquad (11)$$

Where f is coefficient of wear, ω is velocity of pump, r is the radius at point (x,y).
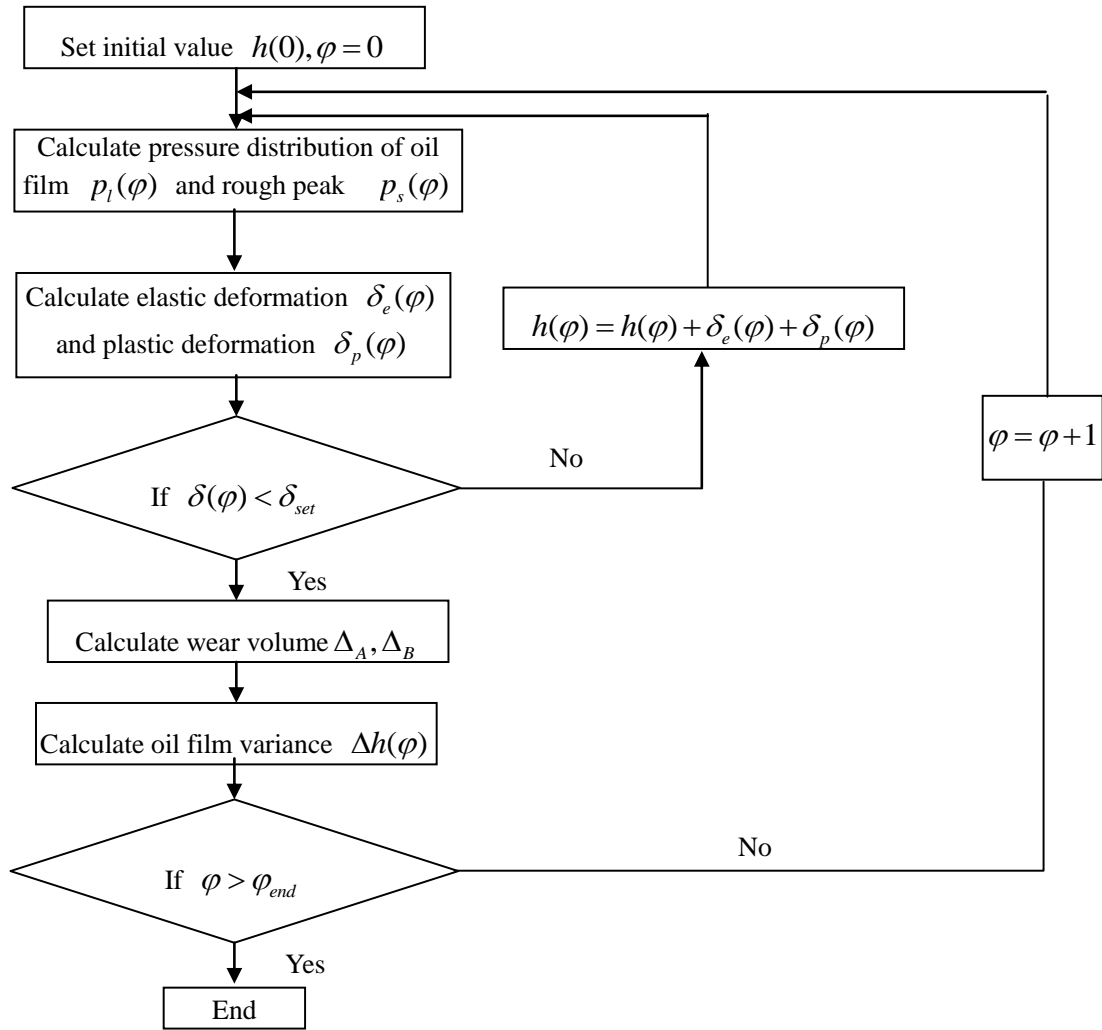
Fig. 6 Wear calculation under mixed lubrication condition

The total wear volume of friction pair within a certain period of time can be described as

$$v = \iint_{(x,y)\in\Omega} \lfloor V_A(x,y) + V_B(x,y) \rfloor \qquad (12)$$

Where Ω is the abrasive wear region.

In order to calculate the wear and tear along the circle of valve plate, the start angle $\varphi = 0$ and the positive direction is counter-clockwise. Then we get the flow chat to calculate the oil film and wear volume shown in Fig.6.

3. SIMULATION AND VALIDATION

The rated velocity of pump is 4000rpm, so we increase the angle from zero to 4000rpm and computer the oil film thickness distribution along the valve plate shown in Figure7.
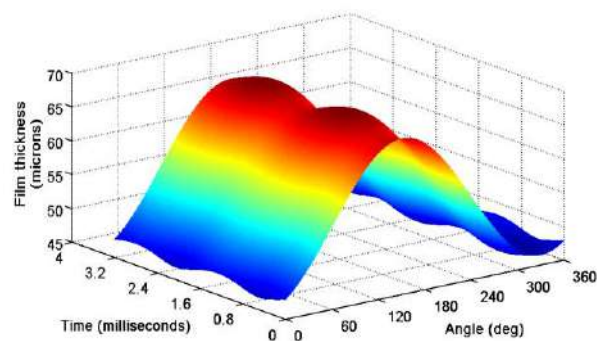
a) Outer sealing strip
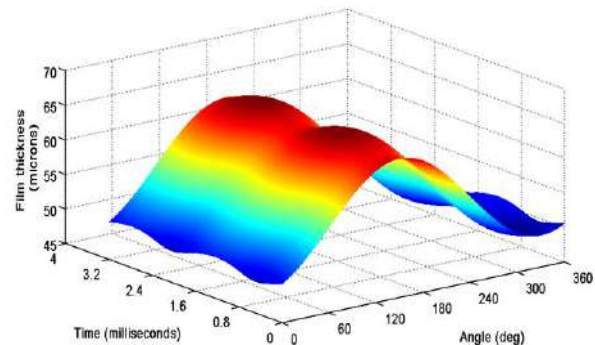
b) Inner sealing strip
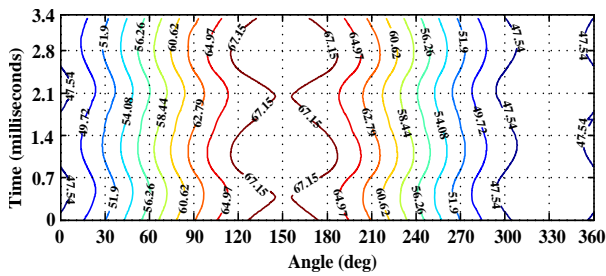
c) Oil film thickness distribution of outer sealing strip
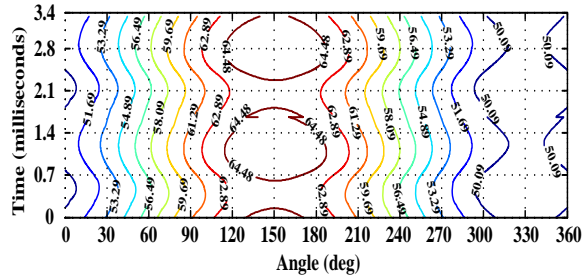
d) Oil film thickness distribution of inner sealing strip
Fig. 7 Dynamic oil film thickness of valve plate
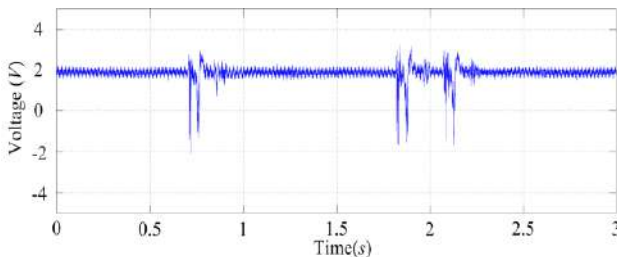
Fig. 8 The abrasive particle measured by inductive debris sensor
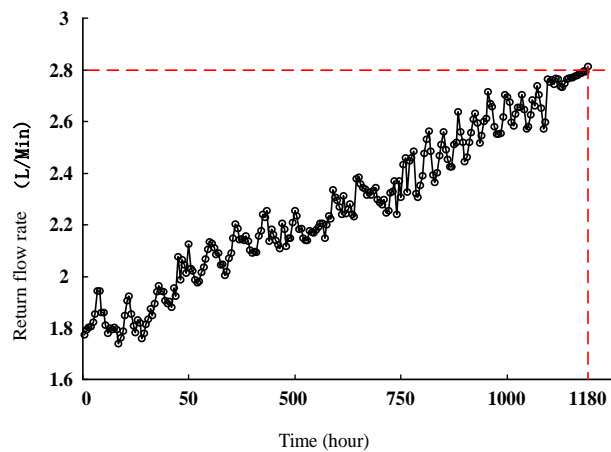
Fig. 9 Return flow rate of axial piston pump

Fig. 7 shows that the oil film thickness is time dependent and angle position dependent. The oil film thickness decreases from discharge port (150°) to inlet port (330°). The average film thickness of inner sealing strip is smaller than that of outer sealing strip in the angular range of 60° to 240°. The simulation results demonstrate good agreement with reference [16].

With the inductive debris sensor designed by our lab [17], we can detect the abrasive particle shown in Fig. 8.

The pulses in Fig.8 shows that the wear particles are produced due the wear and tear between cylinder block and valve plate. As the time goes on, the wear particles accumulate and will lead to the leakage shown in Fig. 9.

It is obvious that the return flow rate increases with the time, which means the wear and tear increases and causes more leakage.

4. CONCLUSIONS

This paper studies the performance degradation based on the complicated failure process including lubrication, mixed lubrication and abrasion. Based on Reynolds equation and Hertz abrasion theory, this paper establishes the dynamic abrasive wear model of cylinder block and valve plate from normal lubrication, partial abrasion to wear and tear. Simulation and validation indicate that the proposed mathematical model can reflect the integrated failure development process of axial piston pump, so its performance degradation is more consistent with the actual application.

REFERENCES

[1] Shaoping Wang, Mileta Tomovic, Hong Liu: *Commercial aircraft hydraulic systems*, Academic Press of Elsevier, 2016.

[2] Yamaguchi A: Formation of a fluid film between a valve plate and a cylinder block of piston pumps and motors: 1st Report, A Valve Plate with Hydrodynamic Pads, Bulletin of JSME, Vol.29, No.251, pp.1494-1498, 1986.

[3] Yamaguchi A: Formation of a fluid film between a valve plate and a cylinder block of

piston pumps and motors.(2nd report A valve plate with hydrostatic pads, JSME international journal, Vol.30, No.259, pp. 87-92, 1987.

[4] Manring N D.: Friction forces within the cylinder bores of swash-plate type axial-piston pumps and motors, Journal of dynamic systems, measurement, and control, Vol. 212, No.3, pp.531-537, 1999.

[5] Ivantysynova M, Lasaar R.: An investigation into micro-and macrogeometric design of piston/cylinder assembly of swash plate machines, International Journal of Fluid Power, Vol.5, No.1, pp.23-36, 2004.

[6] Huang C, Ivantysynova M.: A new approach to predict the load carrying ability of the gap between valve plate and cylinder block, Bath Workshop on Power Transmission and Motion Control, pp.225-240, 2003.

[7] Jouini N, Ivantysynova M.: Valve plate surface temperature prediction in axial piston machines, in: *Proceedings of the 5th FPNI PhD symposium*, Cracow, Poland, pp. 95-110, 2008.

[8] Greenwood J, Williamson J.: Developments in the theory of surface roughness, in : *Proc. 4th Leeds–Lyon Symp. on Tribology*, D. Dowson et al.[Eds.], Mechanical Engineering Publications, London, pp.167-177, 1977.

[9] Patir N, Cheng H S.: An Average flow model for determining effects of three-dimensional roughness on partial hydrodynamic lubrication, Journal of Lubrication Technology, Vol.100, No.1, pp. 12-17, 1978.

[10] Patir N, Cheng H.: Application of average flow model to lubrication between rough sliding surfaces, Journal of Lubrication Technology, Vol.101, No.2, pp.220-229, 1979.

[11] Yamaguchi A, Matsuoka H.: A mixed lubrication model applicable to bearing/seal parts of hydraulic equipment, Journal of tribology, Vol.114, No.1, pp.116-121, 1992.

[12] Kazama T, Yamaguchi A.: Application of a mixed lubrication model for hydrostatic thrust bearings of hydraulic equipment, Journal of tribology, Vol.115, No.4, pp. 686-691, 1993.

[13] Kazama T, Yamaguchi A.: Experiment on mixed lubrication of hydrostatic thrust bearings for hydraulic equipment, Journal of tribology, Vol. 117, No.3, pp. 399-402, 1995.

[14] Majumdar A, Bhushan B.: Role of fractal geometry in roughness characterization and contact mechanics of surfaces, ASME J. Tribol, Vol. 112, No.2, pp.205-216, 1990.

[15] Liou J L, Tsai C M, Lin J-F. : A micro contact model developed for sphere-and cylinder-based fractal bodies in contact with a rigid flat surface, Wear, Vol.268, No.3, pp. 431-442, 2010.

[16] J.M. Bergada, D.L. Davies, S. Kumar, J. Watton: The effect of oil pressure and temperature on barrel film thickness and barrel dynamics of an axial piston pump, Meccanica, No.47, pp. 639-654, 2012.

[17] Wei Hong, Shaoping Wang, Mileta Tomovic: A hybrid method based on band pass filter and cooreation algorithm to improve debris sensor capacity, Mechanical Systems and Signal Processing, No.82, pp.1-12, 2017.

COMPLEXITY OF CONTACT SYSTEMS: SELF-ORGANIZATION AND SYNERGETIC APPROACH IN TRIBOLOGY

Emilia ASSENOVA

The Society of Bulgarian Tribologists, Sofia, Bulgaria
E-mail: emiass@abv.bg

Abstract: *In front of sciences stay nowadays the topics of complexity and interdependence*. *Contact systems are adaptive complex entities whose specific structure* and behavior are *connected to the synergy effect* resulting *from the interaction of their* component*s*, and from *the interaction of the systems with the environment. Regarding tribological processes in contact systems, self-organization is observed as spontaneous creation of higher ordered patterns (secondary structures)* during the contact interaction. *Different approaches are found to* treat *self-organization* related to *compatibility of the tribosystems, structural adaptation in the formation of the secondary surface structures and of frictional or tribo-films, using of synergistic alloying of selfadaptive wearresistant coatings, particularity of the selective material transfer during friction, etc. The review is based on the concepts of tribology as interdisciplinary science, regarding contact interaction as the most general transfer process, and the adaptation to the dynamic conditions of* contact *existence by self-organization and synergy mechanisms* in *the selective material transfer resulting in high reduction of friction and wear.*

Keywords: complexity, synergy, self-organization, tribosystems

1. INTRODUCTION

One of the most highly developed skills in contemporary civilization is dissection: the split up of problems into their smallest possible components. We are good at it. So, that we often forget to put the pieces back together again. Our thinking and sciences appear to be the notions of fraction: partition, division, fragmentation, parceling, segmentation, splitting, etc. Every situation has limits, contours, borders, or margins. Limits together with the conviction of the lack of uncertainty for the classical science reflect the remoteness between science and the world we live in. However, in the last decades, science becomes much broader than to reflect and explain an artificially fractioned and definite world. And closer examination reveals that reality lies in the unity and wholeness of things. If we quote the Buddhist sage Nagardjuna many hundreds years ago, existence and essence of things are rooted in their mutual relationship and are nothing if taken alone.

Systems in real life are complex. [1,2] They consist of high number interacting components and subsystems. System properties are annihilated when a system is physically or theoretically decomposed into components. *Complexity* is generally used to characterize something with many parts interacting with each other in multiple ways, culminating in a higher order of emergence greater than the sum of its parts. *Complex* systems are

highly composite ones, built up from very large numbers of mutually interacting subunits whose repeated interactions result in rich, collective behavior that feeds back into the behavior of the individual parts.

Complex adaptive systems are complex systems with memory they can be influenced by, or can adapt themselves to, its environment and are very sensitive to the initial conditions. In complex adaptive systems perfect understanding of the individual parts does not automatically convey a perfect understanding of the whole system's behavior. In the sense of Murray Gel-Mann [2], they gather information about their surroundings and about themselves, at a certain level of coarse graining (coarse-grained materials or systems have fewer, larger discrete components). We shall consider contact systems as complex adaptive systems.

2. CONTACT INTERACTION AND SYNERGY

Overall said, systems can be regarded as contact systems in tribology. Two kinds of contacts can be considered for system's arrangement: the contact between system and environment – external contact and the contact between system components – internal contact.

Contact between system and environment – external contact: systems are immersed into their environment. They exchange energy-, mass- and information-flows with their surroundings. So, system and environment form an entity. The exchange of flows influences the interaction between system's components and their mutual contacts.

Contact between system components – internal contact: Contact systems are entities, the specificity of which (structure, properties, and behavior) is derivative from the communication and the mutual dependence of their components/subsystems. A process of transaction of energy, mass and information is disclosed. This is a simultaneous and interdependent interaction of their multiple components building the system's wholeness. When a system is decomposed into components, it is no more the same system; its properties are destroyed. The system is a wholeness of components. All listed above factors are connected to the **synergy** (συνεργία or cooperative work) effect between system's components and, on the other side, between system and surroundings.

The synergism of the interaction of elements brings that the elements, when combined and in co-operative coherent behavior, produce a total effect greater than the sum of the individual elements contributions. Synergy considers multi-component systems with the aim to reveal how the interaction of the components (e. g. on microscale) brings the emergence of secondary spatial, temporal or spatial-temporal structures in macroscale. Such behavior leads to increase of the order in the system, highly ordered structures emerge in the system of lower degree of order (chaotic) system: an order out of chaos system. **Synergetics** is the empirical study of systems in transformation, with an emphasis on total system behavior unpredicted by the behavior of any isolated components. [3-5] The focus is especially to the circumstances when the secondary structures emerge (it is a spontaneous act), as result of **self-organization**. A purpose is to disclose certain general principles leading the self-organization irrespective the nature of the subsystems. Since systems are identifiable at every scale from the quantum level to the cosmic, synergetics is a very broad discipline, and embraces a wide range of scientific and philosophical studies. It is an interdisciplinary area about the spontaneous, i. e. the self-organized morphology of the emerged secondary structures in far from equilibrium physical or non-physical systems. This branch of synergetics refers to the self-organizing structures of open systems explored by Hermann Haken [3].

3. TRIBOLOGY, SYNERGETICS, SELF-ORGANIZATION

Immanuel Kant used the term "self-organizing" in Critique of Judgement, 1790. At a later time the term was introduced to contemporary science in 1947 by W. Ross Ashby in the Principles of the Self-Organizing Dynamic System and by N.Wiener in cybernetics. After Ilya Prigogine's 1977 Nobel Prize, the thermodynamic concept of self-organization received attention of the public and scientific researchers [4,6]. There is not an agreeing hypothesis for self-organization definition and criteria.

The concept of self-organizing systems was applied further for contact and tribological

systems by V. Ebeling, G. Polzer, A.A.Polyakov, D.N. Garkunov, etc.[5, 7 -11]

The last decades showed the relatively fast development of tribology as science, research and interdisciplinary approach in the point-of-view of contact problems.[9, 11-13] The term has diffused into the international engineering field. Tribological studies involve the efforts of mechanical engineers, material scientists, chemists and physicists – tribology is a pointedly interdisciplinary science. New areas of tribological studies have been developed that are at the interface of various scientific disciplines: nanotribology, biotribology, the tribology of magnetic storage devices and microelectro-mechanical systems, green tribology (ecotribology), etc.

One of the new approaches of tribo-system research is based on synergetics and self-organization during friction searching the advent of new technologies and new techniques for surface and interface characterization, treatment and application, especially in the search of low friction and wear.

Regarding tribological processes, self-organization is observed as spontaneous creation of higher ordered patterns (spatial and temporal secondary structures) out of the local contact interactions. Hence, self-organization is difficult to be guided as it is a transition into a more organized form resulting in a spontaneous emergence of new structures in the *absence* of centralized control. Different approaches are found to resolving this contradiction: compatibility *of* the tribosystems, structural adaptation in the formation of the secondary surface structures and of frictional or tribo-films, the using of synergistic alloying of selfadaptive wear-resistant coatings, the particularity of the selective material transfer during friction, etc.

Theoretical treatment of the self-organizing processes in surfaces and interfaces is also focused. The principles of the thermodynamics of irreversible processes and of the nonlinear theory of dynamical systems are used to investigate the formation of spatial and temporal structures during friction. The transition to the self-organized state with low friction and wear occurs through destabilization of steady-state sliding. The destabilization is studied in different cases of formation of a protective film, micro-topography evolution and slip waves. The pattern formation may involve self-organized criticality and reaction–diffusion systems. A special self-healing mechanism may be embedded into the material by coupling the corresponding required forces. The analysis provides the structure–property relationship, which can be applied for the design optimization of composite self-lubricating and self-healing materials for various ecologically friendly applications and green tribology [5, 7,9,10,14,15].

Adaptation to the variable and complicated conditions in tribo-couples is realized by self-organization and synergy mechanisms. Synergy is regarded as two or more agents (contact body components) working together to produce a result not obtainable by any of the agents independently; the tribosystem being a complex adaptive system constituting of a set of coarse grained interrelated components working together with a common objective: fulfilling a designated need [2,5,7,9,16,17]. Tribosystems are considered as open systems exchanging material, energy and information with the milieu. The ability of a system "to forget" the external perturbations is related to system's self-organization. Due to the flow of mass, energy and information towards and from the system and far from equilibrium, new structures arise (new patterns like clusters, micro- and nano-clusters). Their formation is characterized by spontaneity. Furthermore, it is intentional, not fully arbitrary. The aim of the system is to survive in spite of the external perturbation. The latest only stimulates (unlocks) internal mechanisms in the system, as a result of which the new structures are formed.

In tribology are known many effects connected to self-organization: the effect of extremely low friction after irradiation of the surfaces with alpha-particles or ultrasound; the effect of selective transfer of material

between the contacting surfaces; the effect of surface-active additives in lubricants which cause decrease of surface strength; the effect of autovibrations, etc. In all cases formation of new structures is observed – these are secondary protective surface structures. The study of the secondary protective surface structures is a central question in the study of self-organization. Problems of optimizing the tribosystem are related to the possibility of optimizing the conditions, under which the system being introduced in operating regime, forms secondary protective structures. Generally, the affect is on the working surface (material, preliminary structure) and on the conditions of the process, in such way that the internal for the system factors of its self-organization could be switched on.

Interesting and non-trivial is the phenomenon of self-organization during **selective transfer of materials** in the contact of friction surfaces and the tribological processes that take place during friction under conditions of selective transfer. In 1966 D.N. Garkunov and I.V.Kragelskii registered as a scientific discovery the selective transfer of material from one contacting specimen to the other under special conditions. In investigation and application, D.N. Garkunov and G. Polzer are of the first researchers of the selective transfer of material during friction of Cu-containing contact surfaces with special surface-active substances, the corresponding formation of the "servovite layer" (notion adopted as per analogy with the contact in animal articulation), and the resultant high reduction in friction and wear [5,7,9,12,14,16-18]. Many studies on selective transfer [29, 40, 42-45,49] were also conducted with the transfer of layers different of copper. The surface passivation in selective transfer is accompanied by formation of a plastic film of secondary structures on the frictional surfaces.

Characteristic for the selective transfer in tribology applications is the fact that an inoxidable layer with low shift resistance is formed in the contact. This protective layer cannot accumulate dislocations and is highly antifrictional. The self-organization

phenomena depend also on the interface energy and the material exchange with the environment. Generation of that layer requires special combination of materials of the contact surfaces, as well as special lubricant between them. Conditions for the continuous reproducibility of the layer are also needed because of its not so long life in the contact body in some cases. Thus, synergy effect in the forming of new structures in the contact between surface materials and lubricant appears to be desirable as optimization of contact couple. A special role in the formation of the tribo-film during the selective transfer plays the presence of certain additives in the lubricating layer between the friction surfaces. The results have shown that the values of the tribological characteristics moment of friction, coefficient of friction and wear are for each load lower for oil and grease that contain the oil-soluble metal-plating composite additive VALENA additive [18,19].

4. CONCLUSION

The review aims to emphasize the possibility to optimize tribological contact systems through the investigation of the processes related to synergy, self-organization and selective transfer between the contacting surfaces. Important item is the focusing on the synergetic approach. It combines the effects of non-linearity and dissipation, randomness and coherence in open systems. The emergence of synergetics incited different sciences to match and to develop approaches related to self-organization process. The approach is regarded in connection with the development of tribology.

In tribology the contacts are under dynamic, variable, often very heavy conditions. So, the contact is in crisis. The system wants to protect itself and to survive in these conditions, i.e. to keep its integrity. We help the contact through tribology either by finding out the optimal material – that third body, which to be put in the contact, or by predicting the succession of events and phenomena by means of which the contact shall form its own

protective layer. The second case is related the opportunity to use self-organization processes in the contact body. They are connected to the adaptation of the tribosystem to the variable conditions and are realized by self-organization and synergy mechanisms. The *synergy* corresponds to the mutual work of two or more agents working together to produce a result not obtainable by any of the agents independently. At the s*elf-organization*, due to the flow of mass, energy and information towards and from the system, arise with **spontaneity** new structures – secondary protective surface structures. The aim of the system is to persist and keep on functioning in spite of the external perturbation. The later only stimulates (unlocks) internal mechanisms for the formation of the new structures.

The investigations of self-organization in the mode of selective transfer of materials have lead to the development of new lubricants, self-lubricating, wear-resistant and self-healing materials used in friction joints in heavy operating conditions, as in aircraft, mining industry, space research, etc.

Many of the problems are left inconclusive hinting or presenting just the opportunities and new tasks in tribology unwrapped by the concepts of synergetics and self-organization in non-living matter.

ACKNOWLEDGEMENT

REFERENCES

[1] G. Nicolis, Prigogine I., *Exploring complexity: An introduction*. W.H. Freeman and Company/New York, 1989.

[2] Murray Gell-Mann, *The Quark and the Jaguar: Adventures in the Simple and the Complex*. Henry Holt & Co., LLC, 1994.

[3] H. Haken, *Synergetics, an Introduction: Nonequilibrium Phase Transitions and Self-Organization in Physics, Chemistry, and Biology*, 3rd rev. enl. ed. New York: Springer-Verlag, 1983.

[4] M. Bushev. *Synergetics. Chaos, Order, Self-organization*. Sofia, 1992 (in Bulgarian).

[5] G. Polzer, W. Ebeling. Äussere Reibung fester Korper, dissipative Strukturen and Selbstorganisation, "Schmierungstechnik", Berlin, 17, 1986.

[6] G. Nicolis, Prigogine, I. *Self-organization in nonequilibrium systems: From dissipative structures to order through fluctuations*. Wiley, New York, 1977.

[7] D. N. Garkunov, *Scientific Discoveries in Tribotechnologies. No-wear effect under friction: Hydrogen wear of metals*. MAA Publishing House, Moscow, 2007.

[8] N. Manolov, Assenova, E., Danev, K., Über die Modellierung von selbstorganisierenden Tribo-systemen. Forschungswerke des Seminars "Neue Prinzipien und Prüfmethoden in der Tribotechnik", Zwickau, 1989.

[9] M. Nosonovsky, Entropy in Tribology: in the Search for Applications, Entropy, 12, p.p.1345-1390, 2010.

[10] E. Assenova, Kandeva, M., Self-organization in tribology: the role of synergism and selective transfer, 7th International Conference on Tribology Balkantrib, p.p.305-310, Thessaloniki, 2011.

[11] M. Kandeva, D. Karastoyanov, B. Ivanova, E. Assenova, *Tribological Interactions of Spheroidal Graphite Cast Iron Microalloyed by Tin*, Prof. Marin Drinov Publishing House of Bulgarian Academy of Sciences, Sofia, 2016.

[12] M. Kandeva, Vencl A., Karastoyanov D*., Advanced Tribological Coatings for Heavy-Duty Applications: Case Studies*, Prof. Marin Drinov Publishing House of Bulgarian Academy of Sciences, Sofia, 2016.

[13] E. Assenova, Majstorovic, V., Vencl, A., Kandeva, M., Green tribology and Quality of Life, International Convention on Quality 2012, Belgrade (Serbia), 05-07.06.2012, Proceedings, p.p. 32-38, Published in: Advanced Quality, 40, 2, p.p.26-32, 2012.

[14] G. Polzer, Tserma, Assenova E., Frictional coatings under conditions of selective

transfer. Proc. Int. Conf. BULTRIB'12, Sofia, 2012.

[15] W. Ebeling, *Strukturbildung bei irreversiblen Prozessen: e. Einf. in d. Theorie dissipativer Strukturen*, BSB Teubner Verlag, Stuttgart, 1976.

[16] E. Assenova, Green tribology, self-organization and quality. Tribological Journal BULTRIB, vol. 6, 2016, pp.53-58.

[17] E. Assenova, Gottlieb Polzer, Dr. Tsermaa, Mara Kandeva, Smart Coatings and Green Tribology. ID 885, World TribologyCongress, Torino, 2013.

[18] M. Kandeva, B. Ivanova, D. Karastoyanov, A. Vencl, E. Assenova, Influence of the metal-plating additive "Valena" on the wear of spheroidal graphite cast iron microalloyed by Sn, 14th International Conference on Tribology – SERBIATRIB'15, Belgrade (Serbia), 13-15.05.2015, Proceedings, pp.236-242.

[19] M. Kandeva, A, Vencl, E. Assenova. Influence of "Valena" metal-plating additive on the friction properties in ball bearings. Tribological Journal BULTRIB, vol. 4, 2013, pp.18-24.

ADDING ARAMID FIBRES TO IMPROVE TRIBOLOGICAL CHARACTERISTICS OF TWO POLYMERS

Mihail BOTAN[1], Andreea Elena MUSTEATA[2], Traian Florian IONESCU[2], Constantin GEORGESCU[2], Lorena DELEANU[2,*]

[1]INCAS - National Institute for Aerospace Research "Elie Carafoli", Bucharest, Romania
[2]"Dunarea de Jos" University of Galati, Galati, Romania
*Corresponding author: lorena.deleanu@ugal.ro

Abstract: *This paper presents the influence of the matrix on tribological properties of composites having 10% aramid fibres. Polyamide (Relamid) and PBT (Crastin) were used as matrix. The short aramid fibers (Teijin), were approximately 200...250 μm in length and 10 μm in diameter, with expended extremities due to manufacturing process. Tests were done on block-on-ring tribotester on a BRUKER-CETR®.UTM 2 system. The test parameters were: sliding speed (0.25, 0.50 and 0.75 m/s), the load (5, 10, 15 and 30 N) and the sliding distance of 5,000 m. There were analyzed the dependence of friction coefficient, temperature on the contact edge and wear of the polymeric materials. SEM images help identify wear mechanisms and pointed out the different behavior of the two matrixes. Adding aramid fibers into a matrix of either PA or PBT makes the resulting blends have better tribological characteristics: the wear is much lower, the friction coefficient slightly increases, but remaining in an acceptable range for actual applications as compared with the neat polymers. PBT + 10% wt aramid fibres had the lowest wear versus a slightly higher coefficient of friction as compared to that of PBT, for the tested regimes.*

Keywords: *dry sliding, aramid fibres, PBT, PA, wear*

1. INTRODUCTION

Global energy and resources crisis has been made plastics find their field of application in virtually all industries, from the food, automotive, aviation, medicine and hi-tech technologies, where the polymeric materials become non-replaceable.

Researchers have been focused on tribology of polymer composites and blends because friction couples with at least one element made of polymeric materials could have better behavior as compared to "classical" pair of materials, here including metal-metal contacts [1, 2, 3]. Tribological characteristics of polymers are improved by adding reinforcements (short fibres, nano and micro particles, made of metallic or ceramic materials) [4], solid lubricants, flame retardants etc. The most used fibres in polymeric matrixes are: glass fibres, carbon fibres, and recently introduced, aramid fibres. Companies [2, 5] offer on the market many composites with short fibres (carbon, glass, aramid) as reinforcement, giving mechanical characteristics of materials, but tribological characteristics are still reported by research institutes and academic stuff. For PBT, the mechanical characteristics are higher (Young modulus, tensile limit) adding 10% short fibres

carbon than other fibres (aramid, glass) [2, 6] but comparison of tribological features are still rare. Reports on polymeric blends with aramid fibers of various length were done: 6 mm [7, 8], 3 mm [9], 0.25 mm [10], 0.15...0.2 mm [11].

The aim of this study is to offer a comparison between two composites with the same quantity of short aramid fibres, PA6 and PBT, as concerning the tribological behavior.

2. TEST METHODOLOGY

The materials involved in this research study were produced at the Reseach Institute for Synthetic Fibres Savinesti, Romania, using a molding equipment type MI TP 100/50.

Polyamide grade Relamid and PBT grade Crastin were used as matrix (Tables 1 and 2). The short aramid fibers, as supplied by Teijin, were approximately 200...250 μm in length and 10 μm in diameter, with expended extremities due to the manufacturing process (Fig. 1) [12].
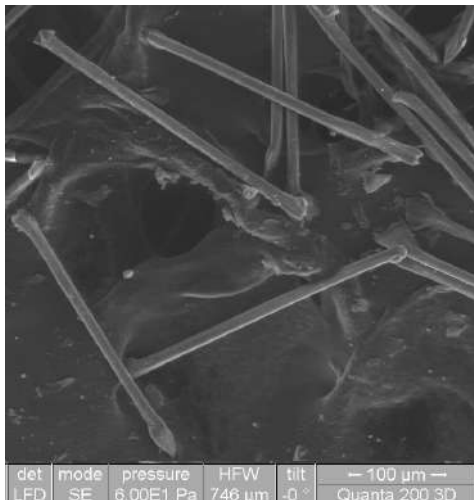
Figure 1. Shot aramid fibers, as supplied by Teijin

Table 1. Properties of PBT - CRASTIN 6130 NC010® [13, 14]

Caracteristic	Value
Maximum working temperature, [°C]	110...180
Tensile limit, [MPa]	65
Thermal conductivity, [W/m·K]	0.25
Thermal expansion coefficient, [K^{-1}]	90·10^{-5}
Young modulus, [MPa]	3300
Strain at yield, [%]	23
Melting temperature, [°C]	235.6

The composites with either PA6 or PBT matrix and addition of aramid fibers and black carbon (Table 4) were produced on a micropilot plant, by die molding, with a single-screw extruder (length to diameter L/D = 25, D = 60 mm, Table 3), the cooling bath for the blank polymer, a granulator, a rotary dryer and rotary drum granules for mixing the constituent.

Table 2. Properties of polyamide Relamid® [15]

Caracteristic	Value
Maximum working temperature, [°C]	90-110
Tensile limit, [MPa]	42
Thermal conductivity at melt, [W/m·K]	0.22
Thermal expansion coefficient, [K^{-1}]	200
Young modulus, [MPa]	922
Strain at break, [%]	109
Melting temperature, [°C]	232

Table 3. Caracteristics of the molding machine

Characteristic	Value
Worm diameter	33 mm
Number of heating zones	3+1 (nozzle)
Nominal power for pump	11 kW
Maximum molding volume	96 cm^3
Productivity	40 kg/h
Maximum molding pressure	114 MPa
Worm speed (under continously controlled load)	20-250 rpm
Maximum stroke of the nozzle	150 mm
Maximum force on the nozzle	35 kN
Temperature range for material heating	20-400 °C
Maximum pressure of hydraulic oil	14 MPa

Table 4. Tested materials

Symbol	Composition (%wt)
PA	100% PA
PAX	PA6 + 10% aramid fibers + 0.5% black carbon
PBT	100% PBT
PBX	PBT + 10% aramid fibers + 1% PA6 + 1% black carbon

The recommended parameters for polymer injection are [16]: temperature in feed zone - 220...240°C, temperature of matrix - 70...90°C, temperature in compression zone - 230...250°C, injection pressure - 80...120 MPa, temperature

in mixing zone - 240...270°C, the nozzle temperature - 250...260°C.

Tests were done on block-on-ring tribotester (Fig. 2), included in a system BRUKER-CETR®.UTM 2 [17, 18] with the parameters: sliding speed (0.25, 0.50 and 0.75 m/s), load (5, 10, 15 and 30 N) and the sliding distance of 5,000 m [15, 19, 20]. The speed of 0.5 m/s is the most used by producers of polymeric materials, for evaluating tribological properties [3].

There were analyzed the dependence of friction coefficient, temperature on the contact edge with the help of a thermo-camera PI160 and dedicated soft PI Conect and wear (as mass loss of the block) on the material.
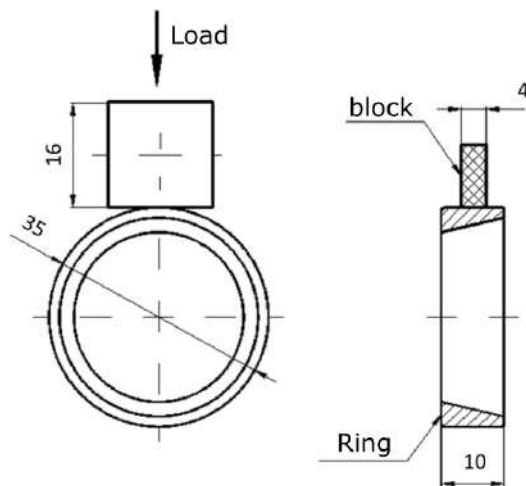
Figure 2. Tribotester block-on-ring

As one may notice from literature [19, 21, 22], the parameters for block-on-ring tests are in a wide range, especially for block dimensions, speed, load and sliding distance. After consulting many reports on this test, the authors considered that a sliding distance of 5000 m is satisfactory for making the friction coefficient and wear stable.

3. RESULTS

3.1 Friction coefficient

The average value of the friction coefficient (COF) was calculated for the running time of each test and in Figures 3 and 4, the minimum and maximum values of this parameter are also given.
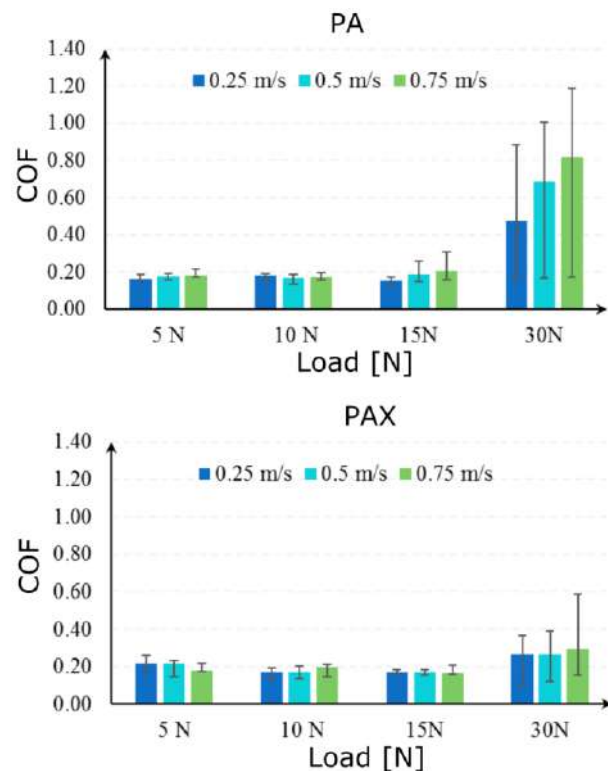
Figure 3. Average and spread range for friction coefficient characterising the couple PA-steel and PAX-steel.

Comparing the average values for the neat polymer and the blend PA + 10%wt aramid fibres, it is obvious that load has a high influence after 15 N, the friction coefficient at 30 N being about three times greater for PA as compared to the blend.

For materials based on PBT, the differences in the average values of the friction coefficient are in a narrow range, thus, this tribological parameter is not relevant in selecting one of these two materials and other tribological ones have to be compared (wear, running temperature, surface quality [19, 20] and even price.

In Figures 3 and 4, the smallest average values of COF (around 0.2) were obtained for the test parameters v = 0.25 m/s, F = 10 N. The lower value of the spread range was obtained for v = 0.25 m/s and F = 15 N. In some systems, where smooth operation is required, it is good to know this range.

The following discussion is based Czicosh's discussion on the friction coefficient [23] and Myshkin's studies [24].

PBT

PBX
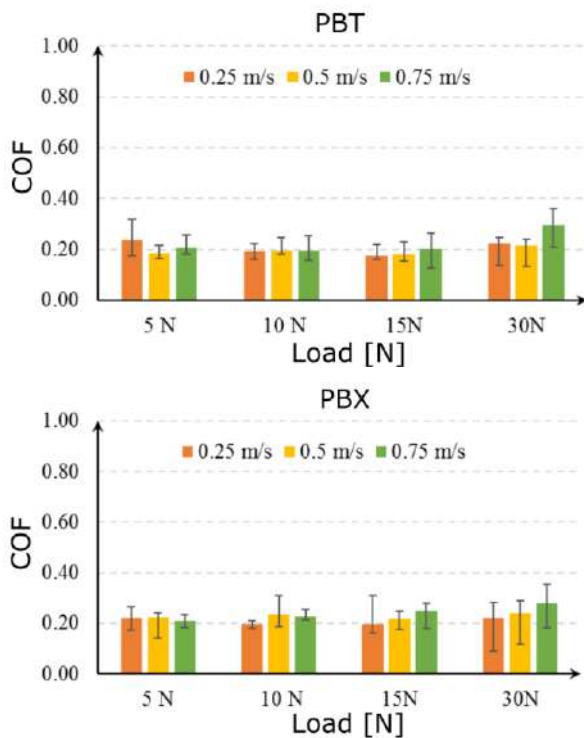
Figure 4. Average and spread range for friction coefficient characterising the couple PBT-steel and PBX-steel.

PA v=0.75 m/s

PAX v=0.75 m/s
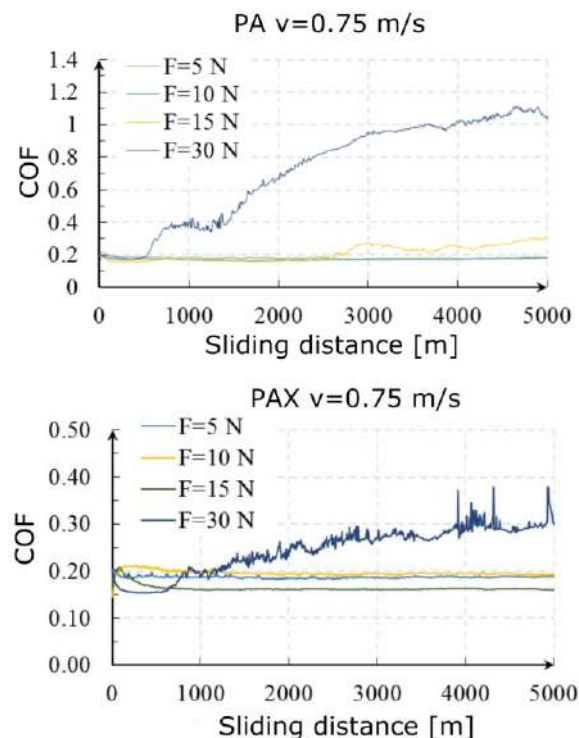
Figure 5. Examples of COF evolution in time for PA and PAX

For PA, one or two of these stages are missing and the friction coefficient evoluates smoothly for low loads, but for higher loads (15 N and 30 N), this parameter beggins to increase after 2500...3000 m for F = 15 N and

after a shorter sliding distance (L = 600...1000 m) for F = 30 N. This could be explained by the increasing temperature in contact (see Figs. 7-10) that favours the appearance of a soften/molten tribolayer that resist sliding more than the solid polymer. Adding 10% aramid fibres makes the friction coefficient becoming more stable for F = 5...15 N, but for F = 30 N, it increases and oscillates, not so severely as for the neat polymer.

For PBX, there could be indentified several stages, but some are overlapping or they are missing, L being the sliding distance:

- phase I (L = 0-200 m...500 m) of addapting surfaces and an increasing friction coefficient, a step of adjusting the surface to increase the coefficient of friction, less pronounced at higher forces;

PBT v=0.75 m/s

PBX v=0.75 m/s
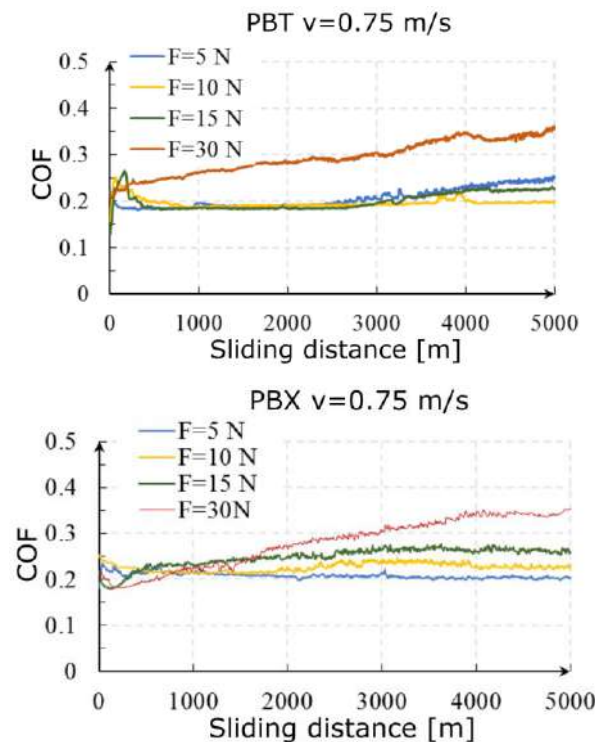
Figure 6. Examples of COF evolution in time for PA and PAX

- phase II (L = 200 m...500-1000 m) a step in which the friction coefficient decreases because of the surface smoothing;

- phase III (L = 1000 m...2500 m) the friction coefficient is maintained at low values, possibly with a slight tendency to increase, more pronounced in composites;

- phase IV (L = 2500 m...3000-5000 m) The development trend of the friction coefficient

depending on the combination (load, speed, materials in contact).

3.2 Wear and temperature on contact edge

In this work, the authors defined wear mass as the mass loss of the block, the difference between the initial mass and the final element.

Wear maps have become o good tool for pointing out the influence of different parameters on wear [25]. Maps were plotted using a cubic interpolation in MATLAB R2009b and surfaces are "obliged" to include the experimental data. A point on a map represents a test for the same set of parameters (F [N], v [m/s], L [m]), where F is the normal load, v is the sliding speed and L (5000 m) is the sliding distance. The values in temperature maps represent the temperature at contact edge, measured with a thermo-camera, just before the end of the test.

The following figures (Fig. 7 to Fig. 10) correlates the mass wear and the maximum temperature recorded on the edge of the contact. Looking at Figure 7, for F = 30 N, materials based on PA6 have a sharp increase in the wear mass, very strong for v = 0.75 m/s. For example, at v = 0.25 m/s and F = 30 N, the wear of the PA block is 4.25 times higher than for a halved force (F = 15 N) and for v = 0.5 m/s, wear of PA block is 12 higher than the wear at F = 15 N. The highest value was obtained at F = 30 N and v = 0.75 m/s. Based on these results, the authors recommend PA only in the field of F = 5...15 N and v = 0.25... 0.75 m/s.

PAX had better results, but its wear for F = 30 N was noticeably higher (see Fig. 8) for v = 0.50 m/s and v = 0.75 m/s, but having similar values, which means a reduced susceptibility to wear speed variation. From F = 15 N to F = 30 N, PAX wear was increased by 1.5 times, at v = 0.25 m/s, increased 2.25 times for v = 0.5 m/s and wear was 10 times higher for v = 0.75 m/s.

PBX wear is greater than that of the PBT for F = 5 N (for all tested speeds) (Fig. 11) it follows that the addition is not justified for small loads. Starting from F = 10 N, the wear

behavior of the two materials to a metal surface changes. Low values are obtained for the PBX. For F = 30 N, PBT wear is 2 times higher than that of the PBX, at v = 0.25 m/s and v = 0.50 m/s and 1.75 times for v = 0.75 m/s.

When comparing the values in Figs. 7 and 8, for the PA and PAX, to those in Figs. 9 and 10 for PBT and PBX, the following conclusions may be formulated.

For F = 5 N, PAX and PBX have higher mass wear, especially for low speeds as compared to the polymer PA and PBT, respectively. From F = 10 N to F = 30 N, additivated materials behaved better to wear, they have lost less material as compared to polymers without fibres.

Comparing wear values between PA and PBT, respectively PAX and PBX, favorable values (lower wear) are for PBT and PBX.

PBT and PBX are less sensitive to changes in speed, regardless of load, in other words, the authors recommend materials PBT and PBX, for processes where sliding speed changes substantially (in the range v = 0.25...0.75 m/s).

The maximum temperature recorded at the contact edge (Fig. 7 to and Fig. 10) ranks the tribological behavior more clearly for the tested materials. A designer will be interested in a material which is not easily heated and the load and speed variations of load will induce or increase the temperature as low as possible.

PA had the largest increase in temperature in the same zone of test parameters (F, v), where the coefficient of friction and wear were maximum. PAX and PBT have similar peaks in the same zone, but minimum values of temperature are lower for PBT.

PAX has the minimum temperature in the range of v = 0.25 ... 0.50 m/s and F = 10 ... 20 N, while PBT has a larger area of the combinations (F v), for a temperature increase only a few degrees above the ambient temperature. PBX does not exceed 60°C for any of the arrangements of test parameters.
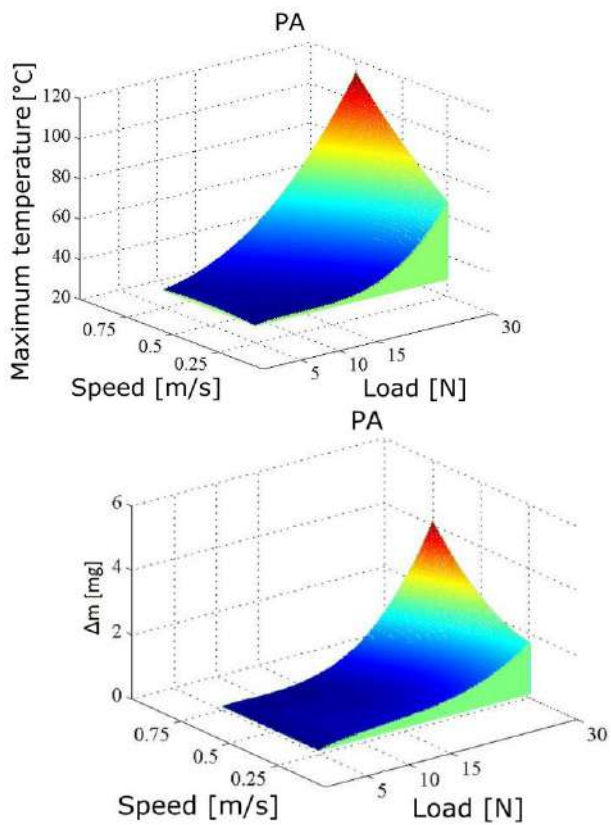
Figure 7. Maximum temperature at contact edge and mass wear for PA

Figure 8. Maximum temperature at contact edge and mass wear for PAX

Figure 9. Maximum temperature at contact edge and mass wear for PBT
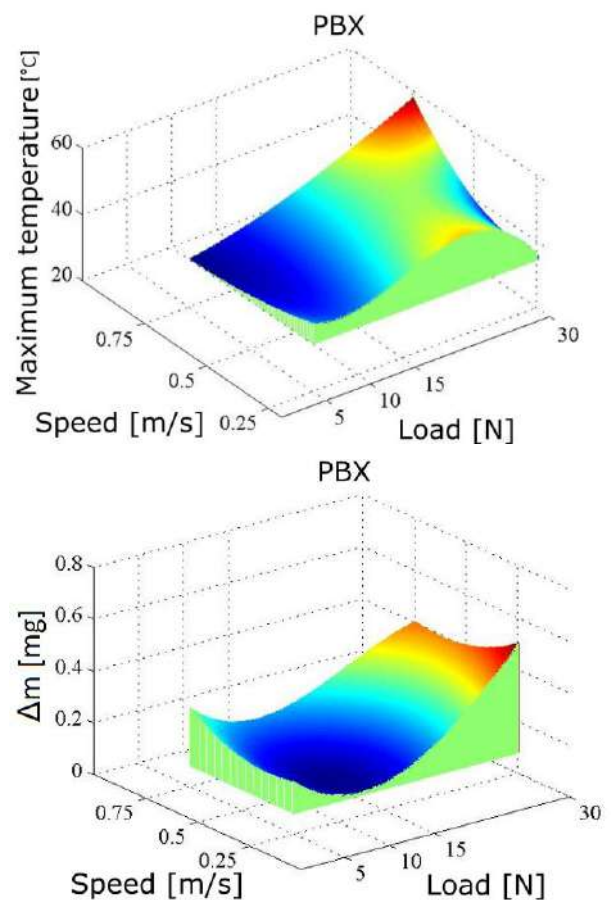
Figure 10. Maximum temperature at contact edge and mass wear for PBX

3.3 Wear mechanisms

Friction couples involving at least one element made of polymeric materials initiate and develop particular wear mechanisms: transfer, particle agglomerations and compacting zones, abrasion (Fig. 11), all these influencing the tribological behavior.
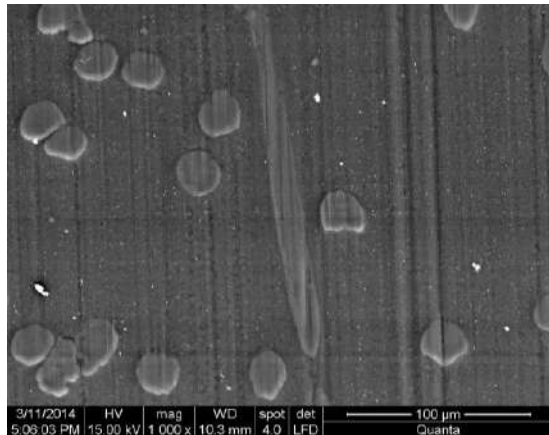
a) PAX, v = 0.25 m/s, F = 30 N
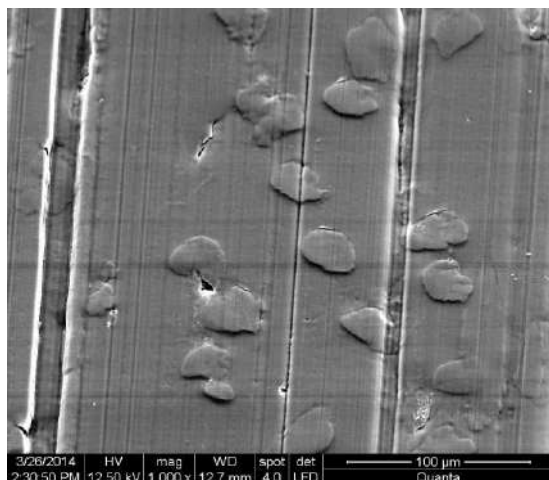
c) v=0.25 m/s, F=15 N, PBX
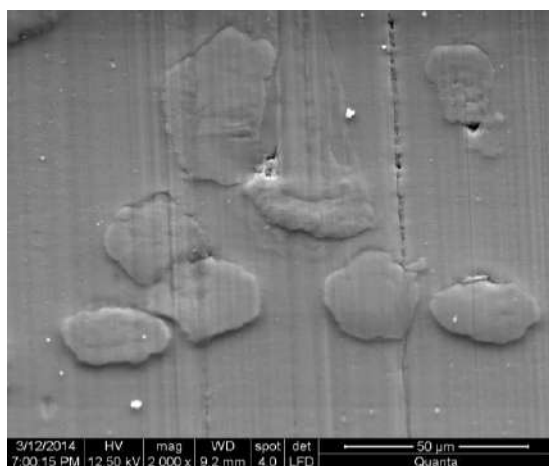
c) v=0.75 m/s, F=30 N, PBX

Figure 11. Abrasion process on the polymeric block

SEM images help identify wear mechanisms and pointed out the different behavior of the two matrixes.

Figures 12 and 13 shows a good bonding of the matrix around the fibres. Fibres are elastic and bend a little in the sliding direction, „opening" a small cavity between matrix and fibre, in front of the contact, as also described by Stachowiack [25].
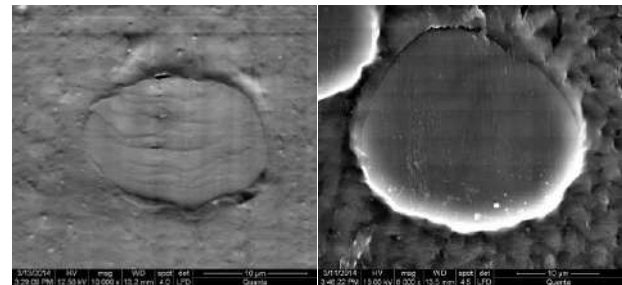
a) v = 0.25 m/s   b) v = 0.75 m/s

Figure 12. PAX, F = 30 N (sliding direction up-down)
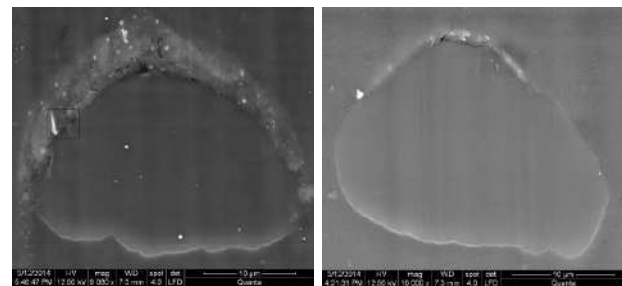
a) v = 0.5 m/s   b) v = 0.75 m/s

Figure 13. PBX, F = 30 N (sliding direction up-down)

Abrasion has ploughing as dominant process (Fig. 11.a and b). This process is less intense for higher speed due to the softening of the tribolayer and the recovery of the polymeric matrix. There is a debonding process between fibres and matrix, but the elasticity of aramid fibres diminish the process intensity and the cavity so formed is easily fill with the smallest wear debris (Fig. 13). It seems that fibres are not broken when they are still embedded in the matrix, but after a running time, the polymer matrix is more prone to be detached and lets the fibres to be tear off, especially when they are approximately positioned parallel to the sliding direction (Fig. 11.a and Fig. 14).
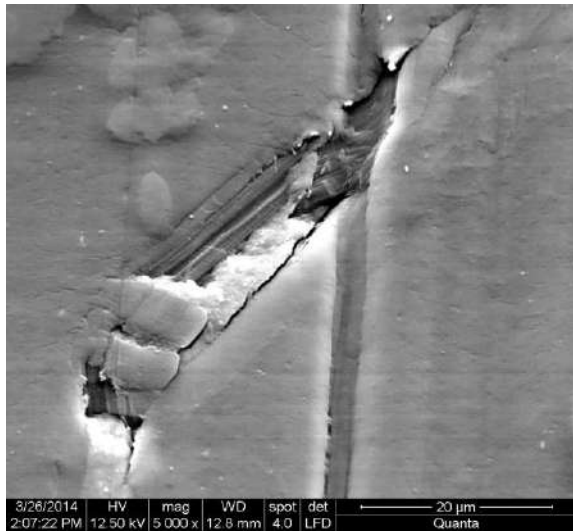
Figure 14. Damage of the superficial layer of a block made of PBX, F = 15 N, v = 0.75 m/s
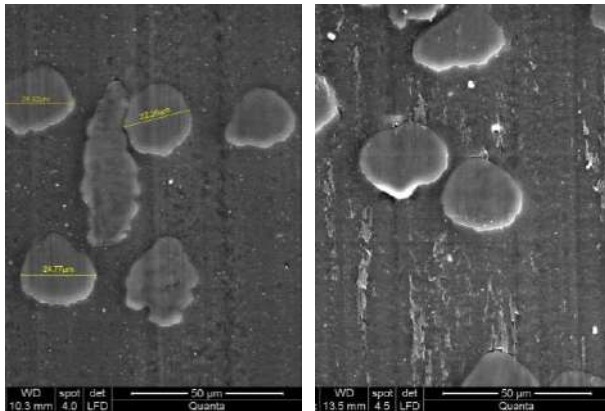
a) v = 0.5 m/s,   b) v = 0.75 m/s

Figure 15. Worn surface of a block made of PAX, F = 30 N

Figure 15 shows that at v = 0.75 m/s, for the block made of PAX, the running regime makes a very thin layer of polyamide to be soften and molt. At v = 0.5 m/s this thin layer is not noticeble (Fig. 15.a). Figure 16 presents a fibre detached from PAX, dragged and rolled in the contact (a), till break (b).
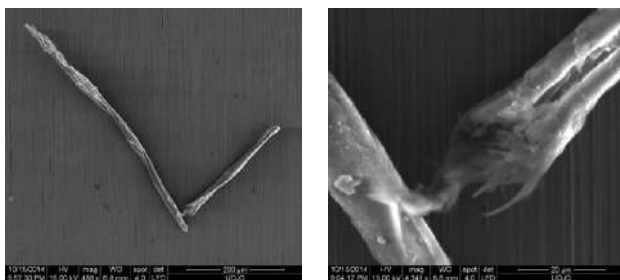
a) Detached fibre   b) Detail

Figure 16. Detached fibre, find on steel surface, PAX, F = 15 N, v = 0.25 m/s

Relatively low melt temperature combined with the low thermal conductivity of polymers ensures that frictional heat generated in contact can easily reach the melting point of the polymer and cause its surface to melt, at least to soften.

When the polymer melts, its friction and wear parameter are markedly altered. The melt process is taking place in a very thin layer but now, it could be easier detached or spread on the surface. When this mechanism is prevailing, the type of material loss is named 'melting wear' [3]. Also, the transfer of polymer could be intensified.
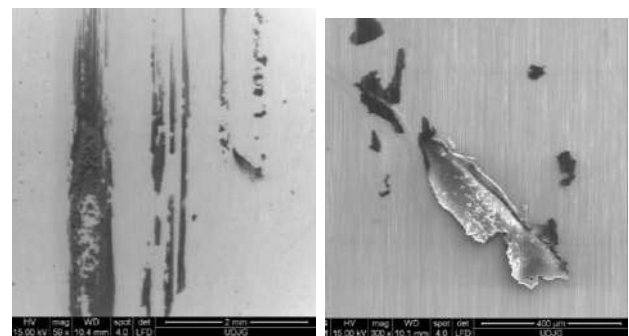
a) Lump transfer   b) Detail

Figure 17. Steel ring surface after running against PBX (F = 15 N, v = 0,75 m/s)
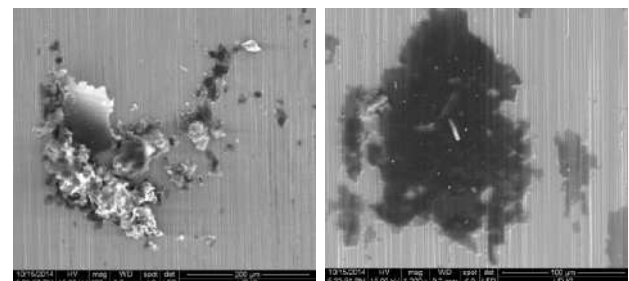
a) Adhesion and wear debris agglomeration   b) Lump transfer and trapped fragments of aramid fibres

Figure 18. Steel ring surface after running against PAX, F = 15 N, v = 0.25 m/s

Figures 17 and 18 present details of polymeric transfer on the steel surface of the ring and how the fibres are fragmented.

The separated fibres from the matrix do not break easily, but, in time, they are fragmented in small parts of several microns, as see in Fig. 19.b and Fig. 20.

a) Lump transfer   b) Detail
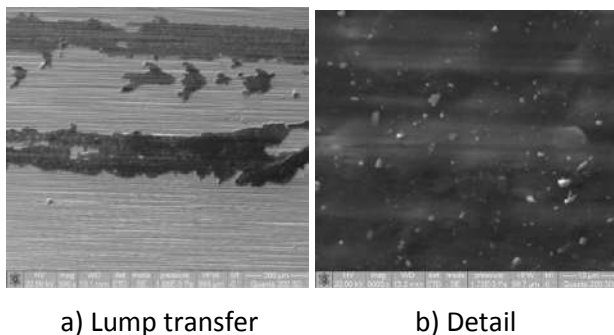
Figure 19. PBX transfer PBX on steel ring (F = 10 N, v = 0.25 m/s)

a) Fragment of aramid fiber ambedded in an island transferred film   b) Fragment of aramid fiber, trapped in the steel surface asperities
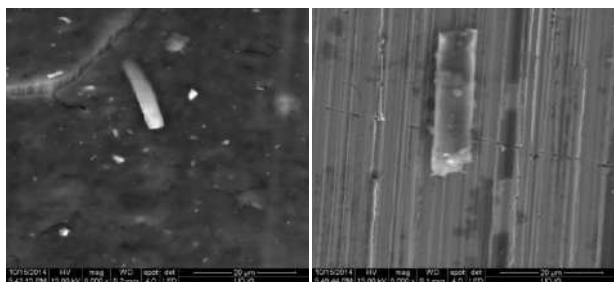
Figure 20. Fragments of aramid fibres on the metallic surface , block made of PAX, F = 15 N, v = 0.25 m/s

4. CONCLUSIONS

From this tribological study, it results that adding 10% wt aramid fibres in PA and PBT decreases wear and the temperature in contact. The friction coefficient slightly increases for the materials containing aramid fibres, but remaining in an acceptable range for actual applications.

The wear map of PA points out a zone with low wear for F = 5 ... 20 N (1.25 N/mm ... 5 N/mm) and v = 0.25 ... 0.75 m/s. For F = 20 ... 30 N (5 N/mm ... 7.50 N/mm) and v = 0.50 ... 0.75 m/s, the wear has a large gradient, indicating that the material should not be recommended for this regime.

Maps of wear recommend certain areas for load and speed in actual applications. Thus, it appears that PA and PAX wear is large for combination (high speed - high load), the polymer having a maximum of 4 times greater wear than PAX. PBT has an area of high wear for (high force - low speed) and the PBX had

the lowest wear values, with a weak dependence on the sliding speed, especially for high load (F = 30 N).

The addition of 10% aramid fibres in PA leads to flattening of the surface of wear map. The maximum value recorded for PAX is obtained for small forces and low speeds. So, this material has a much better wear behavior.

PAX performs better at high speeds and for F = 30 N, curve shape of wear departs only slightly from a straight line.

For PBT, the resulting map shows a better behavior between 12 ... 24 N and velocity v = 0.25 m/s ... 0.6 m/s. The greatest wear was obtained for the combination (the lowest force - the highest speed).

It has been found that PBT without reinforcement has a very good tribological behavior, the average coefficient of friction being low and also a relatively low wear, but the addition of 10% wt aramid fibres, causes a substantial improvement in the wear behavior. PBT + 10% wt aramid fibres had the lowest wear versus a slightly higher coefficient of friction as compared to that of PBT, for the tested regimes.

REFERENCES

[1] K. Friedrich, Z. Zhang, A.K. Schlarb: Effects of various fillers on the sliding wear of polymer composites, Composites Science and Technology, Vol. 65, No. 15-16, pp. 2329–2343, 2005.

[2] Wear Resistant & Low Friction Thermoplastic Compounds, available at: https://www.rtpcompany.com/products/wear-resistant/, accessed: 22.04.2017.

[3] B.J. Briscoe, S.K. Sinha: Tribology of polymeric solids and their composites, in: G.W. Stachowiack (Ed.): *Wear – Materials, Mechanisms and Practice*, Wiley, New York, pp. 223–267, 2005.

[4] S.K. Sinha, B.J. Briscoe: *Polymer tribology*, Imperial College Press, London, 2009.

[5] Low-Friction Mechanical Plastics, available at: http://www.dupont.com/products-and-services/plastics-polymers-resins/articles/mechanical-plastic-low-friction.html, accessed: 14.04.2017.

[6] M. Botan, C. Georgescu, C. Pirvu, L. Deleanu: Influence of aramid fibers on mechanical properties of two polymeric blends, in: *Proceedings of the 22nd International conference on materials and technology*, 20–22.10.2014, Portoroz, Slovenia, pp. 53.

[7] M. Arroyo, R. Zitzumbo, F. Avalos: Composites based on PP/EPDM blends and aramid short fibres. Morphology/behaviour relationship, Polymer, Vol. 41, No. 16, pp. 6351–6359, 2000.

[8] M.A. López-Manchado, J. Biagiotti, J.M. Kenny: Comparative study of the effects of different fibers on the processing and properties of polypropylene matrix composites, Journal of Thermoplastic Composite Materials, Vol. 15, No. 4, pp. 337-353, 2002.

[9] M. Shirazi, J.W. Noordermeer: Factors influencing reinforcement of NR and EPDM rubbers with short aramid fibers, Rubber Chemistry and Technology, Vol. 84, No. 2, pp. 187–199, 2011.

[10] G. Tang, W. Huang, D. Chang, W. Nie, W. Mi, W. Yan: The Friction and Wear of Aramid Fiber-Reinforced Polyamide 6 Composites Filled with Nano-MoS2, Polymer - Plastics Technology and Engineering, Vol. 50, No. 15, pp. 1537–1540, 2011.

[11] M. Sanchez-Soto, A. Gordillo, M.L.L. Maspoch, J.I. Velasco, O.O. Santana, A.B. Martinez: Glass bead filled polystyrene composites: morphology and fracture, Polymer bulletin, Vol. 47, No. 6, pp. 587–594, 2002.

[12] Teijin Aramid Properties of Twaron, available at: http://www.teijinaramid.com/aramids/twaron/, accessed: 10.04.2017.

[13] DuPont Engineering Polymers. Blow Moulding Processing Manual, available at: http://www2.dupont.com/Plastics/en_US/assets/downloads/processing/BM_PM_e.pdf, accessed: 10.04.2017.

[14] DuPont. Crastin® PBT. Thermoplastic polyester resin Crastin® 6130 NC010, available at: http://plastics.dupont.com/plastics/dsheets/crastin/CRASTIN6130NC010.pdf, accessed: 10.04.2017.

[15] M. Botan: *Caracterizarea mecanică şi tribologică a unei clase de compozite polimerice*, PhD thesis, „Dunarea de Jos" University, Galati, 2014.

[16] Crastin PBT. Molding Guide, available at: http://www2.dupont.com/Plastics/en_US/assets/downloads/processing/cramge.pdf, accessed: 14.04.2017.

[17] CETR UMT Multi-Specimen Test System, Software Operating Manual, Version 1.116, Build 222, 2007.

[18] CETR UMT Multi-Specimen Test System, Hardware Manual, 2007.

[19] C. Georgescu: *Studii şi cercetări privind evoluţia parametrilor stratului superficial în procesele de frecare şi uzură ale unor materiale compozite cu matrice de polibutilentereftalat*, PhD thesis, „Dunarea de Jos" University, Galati, 2012.

[20] L. Maftei: *Contribuţii la studiul comportării tribologice a compozitelor cu poliamidă şi microsfere de sticlă*, PhD thesis, „Dunarea de Jos" University, Galati, 2010.

[21] Z. Rasheva, G. Zhang, T.A. Burkhart: Correlation between the tribological and mechanical properties of short carbon fibers reinforced PEEK materials with different fiber orientations, Tribology International, Vol. 43, No. 8, pp. 1430–1437, 2010.

[22] G. Zhang, Z. Rasheva, A.K. Schlarb: Friction and wear variations of short carbon fiber (SCF)/PTFE/graphite (10vol.%) filled PEEK: Effects of fiber orientation and nominal contact pressure, Wear, Vol. 268, No. 7, pp. 893–899, 2010.

[23] H. Czichos: *Tribology: a systems approach to the science and technology of friction, lubrication, and wear*, Elsevier, Amsterdam, 1978.

[24] N.K. Myshkin, M.I. Petrokovets, A.V. Kovalev: Tribology of polymers: adhesion, friction, wear, and mass-transfer, Tribology International, Vol. 38, No. 11, pp. 910–921, 2006.

[25] S.M. Hsu, M.C. Shen: Wear Mapping of Materials, in G.W. Stachowiak (Ed.): *Wear – Materials, Mechanisms and Practice*, Wiley, New York, pp. 369-424, 2005.

Tribological Properties of Solid Materials

15th International Conference on Tribology – SERBIATRIB '17

17 – 19 May 2017, Kragujevac, Serbia

SERBIATRIB '17

15th International Conference on Tribology

Serbian Tribology Society

Faculty of Engineering University of Kragujevac

Kragujevac, Serbia, 17 – 19 May 2017

FRICTION COEFFICIENT OF MODIFIED EPIPHEN RESIN

Vasile BRIA[1], Iulia GRAUR[1,2*], Cristian ENI[1],Cristian MUNTENIŢĂ[1], Adrian CÎRCIUMARU[1,2]
[1]"Dunărea de Jos" University of Galati, Research and Development Centre for Thermoset Matrix Composites, Galaţi, Romania
[2]Diagnose and Measurement Group, Galaţi, Romania
*Corresponding author: iulia.graur@ugal.ro

Abstract: One commercial thermoset epoxy resin was used in this study namely Epiphen RE4020-DE 4020 (Bostik). In general, epoxy is not an ideal material used in tribological applications due to its three-dimensional network structure. This is why in this paper we made a study regarding friction coefficient of modified Epiphen epoxy resin. The tribological behaviour of Epiphen epoxy resin can be significantly improved by addition of suitable modifying agents. As modifying agents we used three concentrations of three organic solvents. Friction tests of formed composite materials were carried out on a pin-on-disc geometry. In this paper it is shown how load, sliding velocity, and distance affect friction coefficient of modified Epiphen epoxy resin.

Keywords: epoxy resin, Epiphen, friction coefficient.

1. INTRODUCTION

The name epoxy resins has over the years become synonymous with performance [1]. Epoxy resins constitute a major class of thermosetting resins and are extensively used as coatings, electronic materials, adhesives [2]. Some of their most interesting applications are found in the aerospace and recreational industries [3]. Many polymers and polymer based composites are widely used for sliding couples against metals, polymers and other materials [4].

The most common resin is based on bisphenol A and is referred to as the "diglycycidyl ether of bisphenol A" or DGEBA. The formation of the three-dimensional network can take place at room temperature or elevated temperatures depending upon the nature of the amine or anhydride [1,5]. Studies over the past two decades have shown the potential improvement in properties and performance of epoxy systems in which organic solvents are introduced [6]. The use of organic solvents to place modifying agents inside the polymer matrix had attracted increasing interest owing to their unique properties and numerous potential applications [7]. There are some well-known solvents as 1,4-Dioxane (1,4-D), 1-Methyl-2-Pyrrolidinone (NMP) and N,Ndimethylform-amide (DMF) that can be used [8, 9, 10]. It is desirable to conduct tribological tests to understand how organic solvents affect the friction coefficient of modified epoxy resin [11]. There have been numerous investigations exploring the influence of test conditions, contact geometry and environment on the friction behaviour of polymers [12, 13].

2. EXPERIMENTAL SECTION

The experiments were carried out with Epiphen RE 4020 - DE 4020 (Bostik) epoxy system. Friction coefficient studies of epoxy systems against steel disc are usually carried out at different load, sliding velocity, and distance conditions [14]. 1,4-D with a stated purity of 99.5% was purchased from Sigma Aldrich. NMP and DMF were also from Sigma Aldrich (with more than 99% and 99.8% purities, respectively). First of all, the chemical compatibilies of components (Epiphen epoxy resin and solvents) were made. The used amount of organic solvent are: 2.5%, 5% and 10%. The resin and the code designation for the test materials made from it are as follows: **E0**- epoxy resin; **E1.4D2.5%** - diluted epoxy resin with 2.5% 1,4-Dioxane; **E1.4D5%** - diluted epoxy resin with 5% 1,4-Dioxane; **E1.4D10%** - diluted epoxy resin with 10% 1,4-Dioxane; **EDMF2.5%** - diluted epoxy resin with 2.5% N,Ndimethylformamide; **EDMF5%** - diluted epoxy resin with 5% N,Ndimethylformamide; **EDMF10%** - diluted epoxy resin with 10% N,Ndimethylformamide; **ENMP2.5%** - diluted epoxy resin with 2.5% 1-Methyl-2-Pyrrolidinone; **ENMP5%** - diluted epoxy resin with 5% 1-Methyl-2-Pyrrolidinone; **ENMP10%** - diluted epoxy resin with 10% 1-Methyl-2-Pyrrolidinone.

R1, R2 and R3 represents the friction coeficient regimes used for composite materials tests.

The friction behaviour of epoxy resin and organic solvents diluted epoxy resin were investigated using a TRM 1000 tribometer from Wazau on pin-on-disk geometry, with the pin made of analyzed material and steel disk.
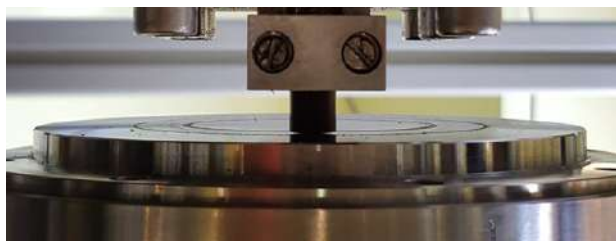
Figure 1. Tribometer TRM 1000 from Wazau

Tribological tests were done 23°C for 1000 m distance. The tests were performed at three different regimes with three loads and three sliding speeds in order to respect the same product load-speed (30N and 2m/s = **R1**; 40N and 1.5m/s = **R2**; 50N and 1.2 m/s = **R3**). The wear values of materials were also investigated. For each material three tests were run for each regime and the presented results are average values of the three tests.

During tribological tests, temperature values at the beginning and at the end of the test were measured with IP 160 Optris® imager.

3. RESULTS AND DISCUSSION

Figures 2, 3 and 4 shows the friction coefficient evolution of 1,4-D organic solvent materials for all three regimes. The results indicate that E1.4D2.5% and E1.4D5% materials shows a constant behavior close to that of the unmodified resin for all three regimes. In the case of E1.4D2.5% material, the friction coefficient values shows higher values than unmodified resin, while E1.4D5% material shows lower values than unmodified resin. In the case of E1.4D10% material, its behavior is approximately constant with the mention that the friction coefficient values for all three regimens are increasing, except within the three regime, where the values do not reach the friction coefficient of the modified resin, despite that the loss of material during the test it was a very small one, even lower than the unmodified resin (Table 1).
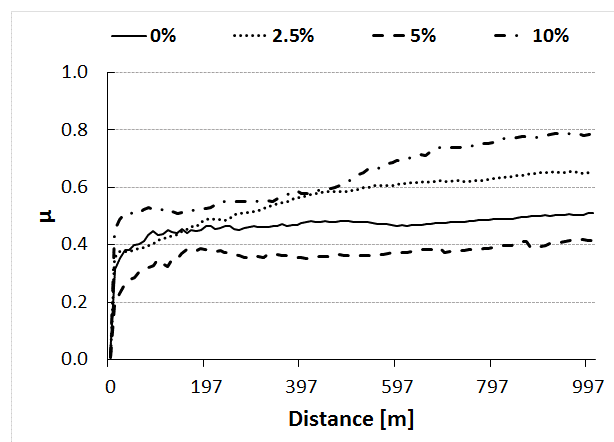
Figure 2. Friction coefficient of 1,4-D diluted Epiphen against steel (R1)
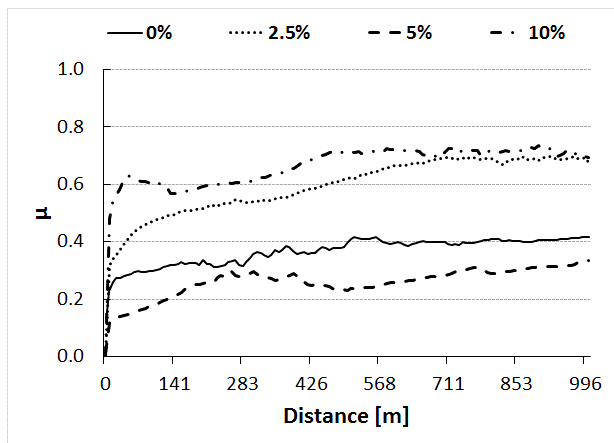
Figure 3. Friction coefficient of 1,4-D diluted Epiphen against steel (R2)
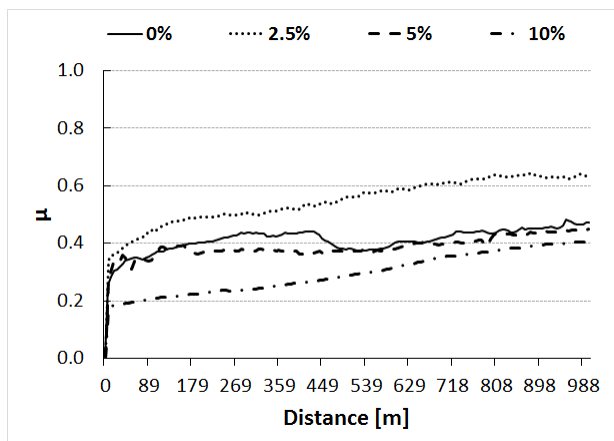
Figure 4. Friction coefficient of 1,4-D diluted Epiphen against steel (R3)

Table 1. Wear values of 1,4-D diluted Epiphen against steel

Wear rate x 10^{-5} [g/N*m]				
Regime	Values			
	0%	2.5%	5%	10%
R1	1.66	1.33	3.53	1.06
R2	2.5	5.25	1	7.5
R3	3	7.2	8	1.2

Although in case of the R3 regime, the friction coefficient values and the curve are very similar to that of the unmodified resin, the material loss of E1.4D5% material is two times higher, which leads to the idea that the phenomenon of abrasion in the case of this material it is a severe one.

Regarding the R3 regime, the E1.4D10% material showed the lowest mass loss, which makes this material to provide excellent tribological properties.
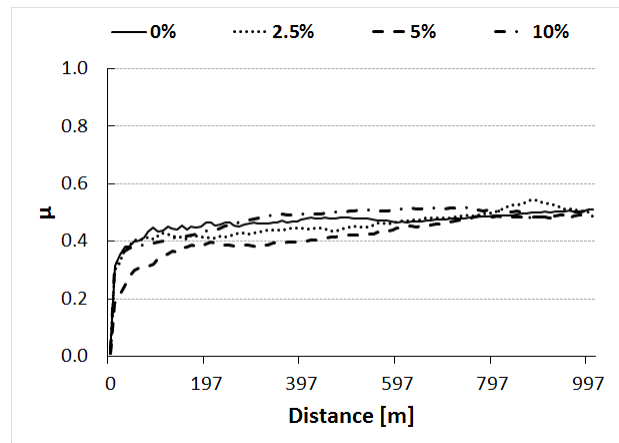
Figure 5. Friction coefficient of DMF diluted Epiphen against steel (R1)
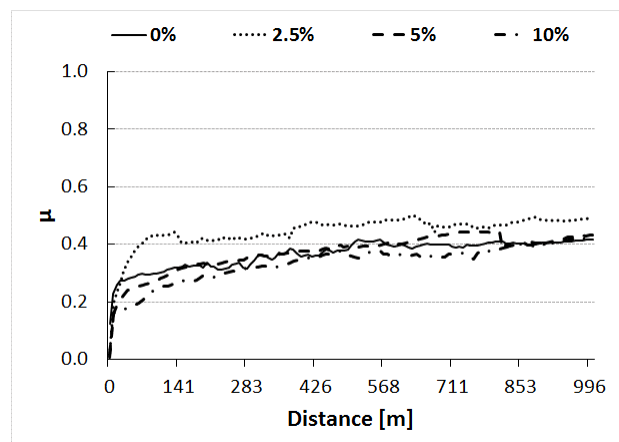
Figure 6. Friction coefficient of DMF diluted Epiphen against steel (R2)
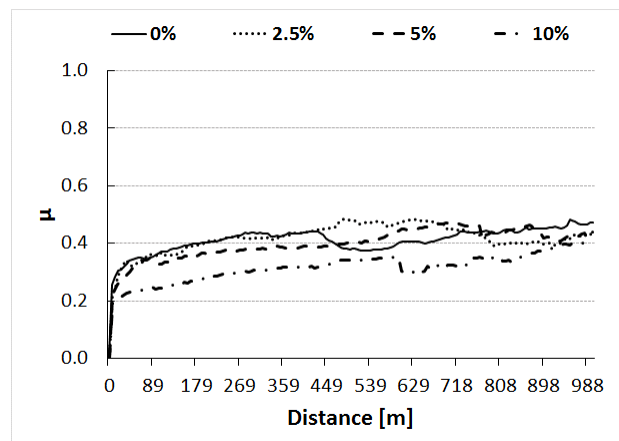
Figure 7. Friction coefficient of DMF diluted Epiphen against steel (R3)

Table 2. Wear values of DMF diluted Epiphen against steel

Wear rate x 10^{-5} [g/N*m]				
Regime	Values			
	0%	2.5%	5%	10%
R1	1.66	10	2.66	4.33
R2	2.5	6.75	5	8.75
R3	3	5	5.6	5.6

Figures 5, 6 and 7 shows the friction coefficient evolution of DMF organic solvent materials for all three regimes. The friction coefficient values for every material in this category, are close to those of unmodified resin, exhibit no significant variation leading to the idea that the percentage of DMF organic solvent can improve or worsen the the properties of those materials. From Table 2 it is clear that the materials with DMF organic solvent, regardless of the used amount, the mass loss were higher compared to the unmodified resin.
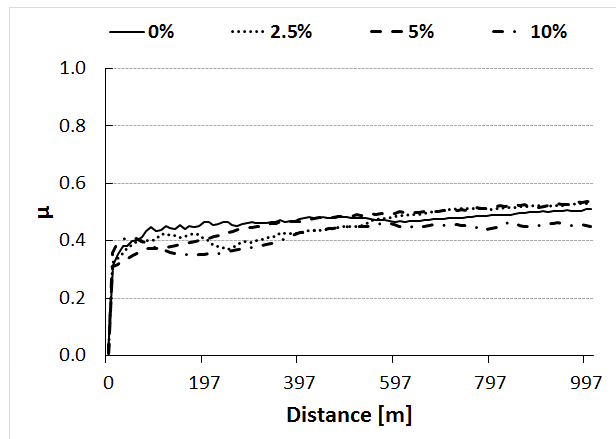
Figure 8. Friction coefficient of NMP diluted Epiphen against steel (R1)
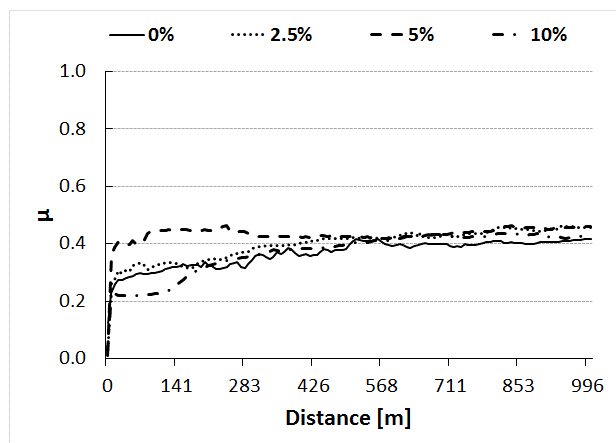
Figure 9. Friction coefficient of NMP diluted Epiphen against steel (R2)

Figures 8, 9 and 10 shows the friction coefficient evolution of NMP organic solvent materials for all three regimes. The largest weight loss during test was recorded for ENMP5% for R1 and R2 regimes (Table 3). Regarding the friction coefficient values we can say that, for all operating modes (R1, R2 and R3) the stabilization was recorded after about 400 m from the test was started. This

instability can be related to the compatibility between the contact surface of the material and the disc (pin-on-disc). If we refer to the mass loss, it is inversely proportional with raising force and directly influenced by the speed of the test. Thus, for this type of material R3 regime is optimal.
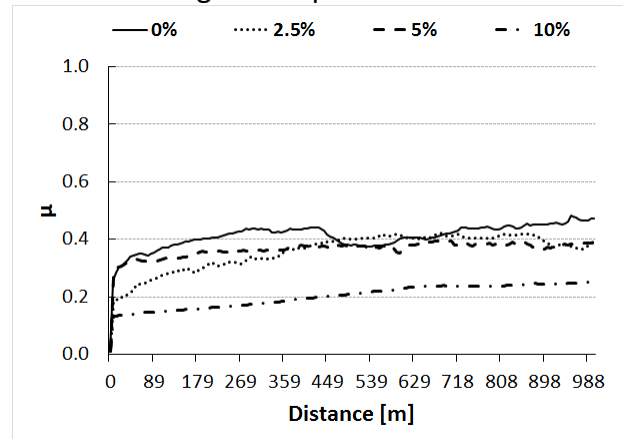
Figure 10. Friction coefficient of NMP diluted Epiphen against steel (R3)

Table 3. Wear values of NMP diluted Epiphen against steel

Wear rate x 10^{-5} [g/N*m]				
Regime	Values			
	0%	2.5%	5%	10%
R1	1.66	6.7	10	8.75
R2	2.5	6	7.5	3.4
R3	3	2.5	2.5	2.04

Tables 1-3 shows the degree of wear values calculated for each component. These values were determined using the following formula:

$$W_s = \frac{\Delta m}{F \cdot L}$$

Where Δm weight loss; F applied force; L sliding distance of 1000 m.

Analysis of the thermal field of the tribological system to the above listed materials leads to the conclusion that materials, due to friction, increase the temperature by approximate 19°C degrees for R1, 28°C for R2 and by 38°C for R3, for all organic solvents used (Fig.11).

This leads to the idea that the used organic solvent does not influence the temperature of materials during the tribological tests. The temperature increases with increasing test loads.
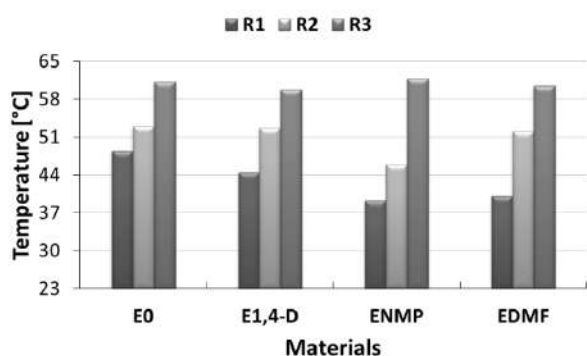
Figure 11. Thermal field of composite materials

4. CONCLUSIONS

Friction coefficient and wear tests of modified Epiphen resin containing different amounts of organic solvents were carried out using a pin-on-disc friction and wear machine.

The best behaviour of friction coefficient values is for DMF and NMP materials for all used concentrations.

Unstable behavior of friction coefficient values has been observed for all regimes for 1,4-D materials. They show some oscillations during tribological test. The oscillations are more pronounced in the case ofR2 regime, for an intermediate force of 40N. Can be noticed that 1,4-D materials does not comply the typical behavior of increasing friction coefficient values followed by its stabilization toward the end of the test.

The used organic solvent does not influence the temperature of materials during the tribological tests.

ACKNOWLEDGEMENT

REFERENCES

[1] C. Craver, C. Carraher, *Applied Polymer Science: 21st Century*, Elsevier, 2000.

[2] CA. May*, Epoxy resins-chemistry and technology,* Marcel Dekker, New York, 1988.

[3] J.P. Pascault, R.J.J. Williams*, Epoxy Polymers New Materials and Inovation,* Wiley, Germany, 2010.

[4] I. Hutchings, *Tribology friction and wear of engineering materials*, Edward Arnold, London, 1992.

[5] E.C. Dodds, W. Lawson*, Synthetic strogenic agents without the phenanthrene nucleus,* Nature, 1936.

[6] G. Mihu, I.Mihalache, M. Bodor, O. Mircea, I. Graur, Tribological Characterization of Modified Epoxy Systems, Materiale Plastice, Vol. 53, No.2, pp. 298-303, 2016.

[7] J. I. Paredes, S. Villar-Rodil, A. Martinez-Alonso, A., J. M. D. Tascon, Graphene Oxide Dispersions in Organic Solvents, Langmuir, Vol. 24, pp. 10560 -10564, 2008.

[8] J. Nakanishi, R. Makino, H. Kawasaki, M. Kishimoto, M. Gamou, *1,4-Dioxane*, Maruzen Press, 2004.

[9] A. Masahiro, K. Naoyuki, S. Hitoshi, O. Yoshirou, Degradation of 1,4-Dioxane Using Ozone Oxidation with UV Irradiation (Ozone/UV) Treatment, Journal of Environmental Science and Engineering A 1, pp. 371-379, 2012.

[10] G. John, V. S. Nandhibatla, Densities, Viscosities, Speeds of Sound, and Relative Permittivities for Water Cyclic Amides (2-Pyrrolidinone, 1-Methyl-2-pyrrolidinone, and 1-Vinyl-2-pyrrolidinone) at Different Temperatures, J. Chem. Eng. Data, Vol.49, pp. 235 -242, 2004.

[11] W. Brostow, V. Kovacevic, D. Vrsaliko, J. Whitworth, Tribology of polymers and polymer-based composites, Journal of Materials Education, Vol. 32, pp**.**273–290, 2010.

[12] C.J. Hooke, S.N. Kukureka, P. Liao, M. Rao, YK. Chen, The friction and wear of polymers in non-conformal contacts, Wear, Vol. 200, pp. 83 –94, 1996.

[13] KC. Ludema , D. Tabor, The friction and visco-elastic properties of polymeric solids, Wear, Vol. 9, pp. 329 –348, 1996.

[14] G. Mihu, I. Mihalache, I. Graur, C. Ungureanu, V. Bria: Comparative study regarding friction coefficient for three epoxy resins in *The 13th International Conference on Tribology ROTRIB'16* , September 22-24, Galați, RO, paper 77, 2016.

SERBIATRIB '17

15th International Conference on
Tribology

Serbian Tribology
Society

Faculty of Engineering
University of Kragujevac

Kragujevac, Serbia, 17 – 19 May 2017

FRICTION FACTOR OF THE FLUID FLOW THROUGH POROUS MEDIA

Nikola PALIC[1], Varun SHARMA[1], Nenad GRUJOVIC[1], Slobodan MITROVIC[1], Fatima ZIVIC[1,*]
University of Kragujevac, Faculty of Engineering, Serbia
*Corresponding author: zivic@kg.ac.rs

Abstract: *This paper deals with the theoretical foundations aimed for modeling and simulation of fluid flow through porous structures and related friction. Different approaches to determination of the analytical solution of the friction factor are presented, as well as formulas that are used in specific flow regimes. Review of fluid types from aspect of viscosity are shown, namely Newtonian and non-Newtonian fluids and related aspects of the fluid behaviour. Review of the established dependencies of the friction factor on the influential factors is presented, such as on Reynolds number, pore geometry, permeability and inertia coefficients. Differences between smooth and rough surfaces in contact with the fluid are observed, from aspects of friction. Geometry of the porous structure essentially influences the flow and governs the friction, as well as the surface roughness. The pressure drop within a porous structure is directly influenced by the permeability and drags force coefficients and can well characterise cellular materials. Wall roughness typically enhances the turbulence and transition from laminar to turbulent flows appears earlier for rough than for smooth surfaces. One short example of CFD modeling of the fluid flow through porous media is shown, as well as generation of the Voronoi based open cell pattern.*

Keywords: *friction factor, fluid flow, CFD, porous structure, Voronoi meshing.*

1. INTRODUCTION

Porous materials have gained much attention for numerous industrial applications, whereas the main property enabled is related to the lighter materials in otherwise robust elements. Porous material is a material containing voids in certain percentage. The solid portion of the material is often called the "matrix" or "frame". The voids or pores can be empty (e.g. in the case of shock absorbers) or filled with a fluid (e.g. in the case of filtration systems). Porosity is eminent property, but other features are also important, such as permeability, tensile strength, electrical conductivity or any other related to the end application. However, porosity is not a simple

term, because it is directly describing the material only in case of poroelastic medium. Porosity can be interconnected, thus making continuous network of solid matrix and open pores. In other case, porous material can have closed voids resulting in rather different methods of characterisation and design, from several aspects (fabrication, mechanical behaviour, etc.). For materials with open porosity, effective porosity (pore space accessible to flow) is also introduced as the process parameter.

Most of the natural materials exhibit some degree of porosity (rocks, soil, wood, biological tissues – bones), as well as many artificial ones (cement, concrete, ceramics) and numerous applications use its concept (e.g. filtration

systems that directly use porosity in its function). Fluid flow through open channels (e.g. river basin or pipes) is rather different than the flow through porous medium, whereas some part of the fluid is retained within pores constantly during the flow. The basic law related to the fluid flow through porous medium is Darcy's law, as given in equation (1), established by, Henry Darcy in 1856. It is based on his experiments with water passing through sand. It is a simple direct relationship between the discharge rate through a porous medium, pressure drop over certain distance and fluid viscosity.

$$Q = \frac{CA\Delta(P - \rho g z)}{L} \qquad (1)$$

where: Q is volumetric flow rate [m³/s]; P is pressure [Pa]; ρ is density [kg/m³]; g is gravitational acceleration [m/s²]; z is vertical coordinate (measured downwards) [m]; L is length of sample [m]; C is constant of proportionality [m²/Pa s]; A is cross-sectional area of sample [m²].

Darcy's law is valid in the case of macroscopic flow, that is, when flow regions are much larger than the pore sizes. However, when micro and nano voids are observed, different set of parameters must be taken into account. There are several influential parameters describing fluid flow through porous materials introducing complexity in calculations and theory. Observation of nano/micro scales only increase these complexities, and many issues are under investigation in scope of these new applications. For example, permeability is not a property related to the pore size. It is related to certain region that contains some number of pores and representative elementary volume (or length scale) needs to be defined. Dynamic behaviour of the fluid, especially in case of porous medium, often introduce Darcy friction factor, which is essentially different that friction coefficient in case of solid contacts. It describes the friction losses during the flow in pipes and open channels, and it is studied also for porous nano/micro structures.

Table 1. Historical approximations to the Colebrook–White relation: friction factor, f

Equation	Author	Year	Range	Ref.
$f = 0.0055(1 + (2 * 10^4 * \frac{\varepsilon}{D} + \frac{10^6}{Re})^{\frac{1}{3}})$	Moody	1947	$Re = 4000 - 5.10^8$ $\frac{\varepsilon}{D} = 0 - 0.01$	[1]
$\frac{1}{\sqrt{f}} = -2\log(\frac{\frac{\varepsilon}{D}}{3.71} + (\frac{7}{Re})^{0.9})$	Churchill	1973	Not specified	[2]
$f = 8\left[(\frac{8}{Re})^{12} + \frac{1}{(\Theta_1 + \Theta_2)^{1.5}}\right]^{\frac{1}{12}}$ where $\Theta_1 = \left[-2.457\ln((\frac{7}{Re})^{0.9} + 0.27\frac{\varepsilon}{D})\right]^{16}$ $\Theta_2 = (\frac{37530}{Re})^{16}$	Churchill	1977	Not specified	[2]
$A = 0.11(\frac{68}{Re} + \varepsilon)^{0.25}$ if $A \geq 0.018$ than $f = A$ and if $A < 0.018$ than $f = 0.0028 + 0.85A$	Tsal	1989	Not specified	[3]
$f = \left[-21\log(\frac{2.18\beta}{Re} + \frac{\varepsilon}{3.71})\right]^{-2}$ $\beta = \ln\frac{Re}{1.816\ln(\frac{1.1Re}{\ln(1 + 1.1Re)})}$	Brkić	2011	Not specified	[4]

Table 2. Examples of different fluids from aspect of viscosity

Viscoelastic	Amorphous polymers, semicrystalline polymers, biopolymers, blood clots, metals at very high temperatures, toothpaste, gelatine	combination of elastic and viscous effects under deformation
Time-dependent viscosity	Synovial fluid, printer ink, gypsum paste	viscosity increases with duration of stress
	Yogurt, aqueous iron oxide gels, gelatin gels, pectin gels, some clays, many paints, many colloidal suspensions	viscosity decreases with duration of stress
Non Newtonian Viscosity	Silica nano-particles are dispersed in a solution of polyethylene glycol; quicksand; corn starch in water	Shear thickening
	Blood, some silicone coatings, some silicone oils, sand in water, ice	Shear thinning (pseudoplastic)
	Water, Blood plasma	Generalized Newtonian fluids. Idealized fluid where viscosity is constant.

There is a number of existing phenomenological equations that enable calculation of Darcy friction factor, depending on the flow regime (laminar, transitional, turbulent in smooth or rough conditions, free surface), as well as many approximations, as given in Table 1. Friction factor has been studied by many research groups, but mainly for the pipe flow. The simplest formula is for the laminar flow in the pipe, for Reynolds number less than 2320, as given in equation (2).

$$f = \frac{64}{Re} \qquad (2)$$

Beside the Reynolds number, roughness ε is introduced and pipe diameter D. Development of the friction factor equations through years is given in Table 1. It only reflects complexity of the exact determination of the friction factor and additional issue of porous materials represents state-of-the-art subject of research nowadays. There are different parameters that can be observed as influential and a good review is given in [14, 19].

2. FRICTION FACTOR IN NON-NEWTONIAN FLUIDS IN POROUS MEDIA

Unlike the water, synovial fluids and blood belong to a group of non-Newtonian fluids. These fluids do not follow the Newton's Law of viscosity and exhibit viscosity that is dependent on the shear rate. Comparison of non-Newtonian, Newtonian, and viscoelastic properties and examples of fluids are given in Table 2 [6].

Flow of non-Newtonian fluids through porous materials is important for many applications, such as oil recovery, liquid polymer molding, blood flow through bone scaffolds, etc.

In general, non-Newtonian fluids can be classified as:
- Time-independent or generalized Newtonian fluids
- Time-dependent fluids
- Viscoelastic fluids

Friction coefficient can be calculated by using several equations, as previously mentioned, but in the case of porous structures it is still under development and is applied with more or less accuracy in modeling. Good reviews of possible approaches in modeling of flow through the porous structures are given in [18, 19, 20].

For single void, normalized friction coefficient calculated as the function of Reynolds number is shown in Fig. 1, whereas comparison of different pore sizes, flow lengths and empirical coefficients reflecting flow regimes are shown. The difference from idealized Newtonian fluid can be clearly seen. Another important parameter is the roughness of the surface over which the fluid is flowing, which essentially influence the friction in

boundary layers. Flow behaviour over smooth (Fig. 2a) and rough surfaces (Fig. 2b) usually relates to a different regimes and friction factor dependence on Reynolds number is shown in Fig. 2 [7] with obvious differences. The transition between laminar and weak turbulent flow can be clearly seen. Navier–Stokes equations are applied at the microscopic level, whereas these are reduced to Stokes equations when non-linear part is neglected. If only one width of the pore is presented for both cases of rough and smooth surfaces, very obvious difference in values of the friction factor can be seen in Fig. 3 [7]. It can also be seen that friction factor decreases with increase of Reynolds number, what can be typically expected. However, Figs. 2 and 3 shows that some opposite behaviour can be expected in certain ranges of Reynolds number. This can be especially well observed in Fig. 3, for both smooth and rough surfaces, but more pronounced in case of smooth surface. Wall roughness typically enhances the turbulence and transition from laminar to turbulent flows appears earlier for rough than for smooth surfaces (denoted by the sudden fluctuation of values in the presented curves). Tzelepis et al. [7] suggested the certain threshold on the factor dependence on the fracture width (or pore size if porous structure is considered) and roughness, meaning that after some value of Re, no dependence can be observed, but this needs further investigations.

However, there is a limited literature on fully porous structures related to the friction factor and all analytical solutions are mainly related to some approximations of those for pipe or open channel flows with introduction of wall roughness. Geometry of porous structure essentially influences the flow and some recent papers have started to deal with this topic, such as very good article on this subject is written by Kumar and Topin [8].
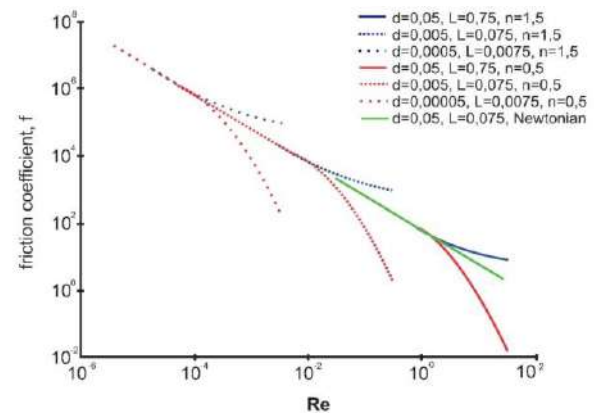
Figure 1. Friction coefficient dependence on Reynolds number for non-Newtonian fluids in comparison to Newtonian fluids [6]
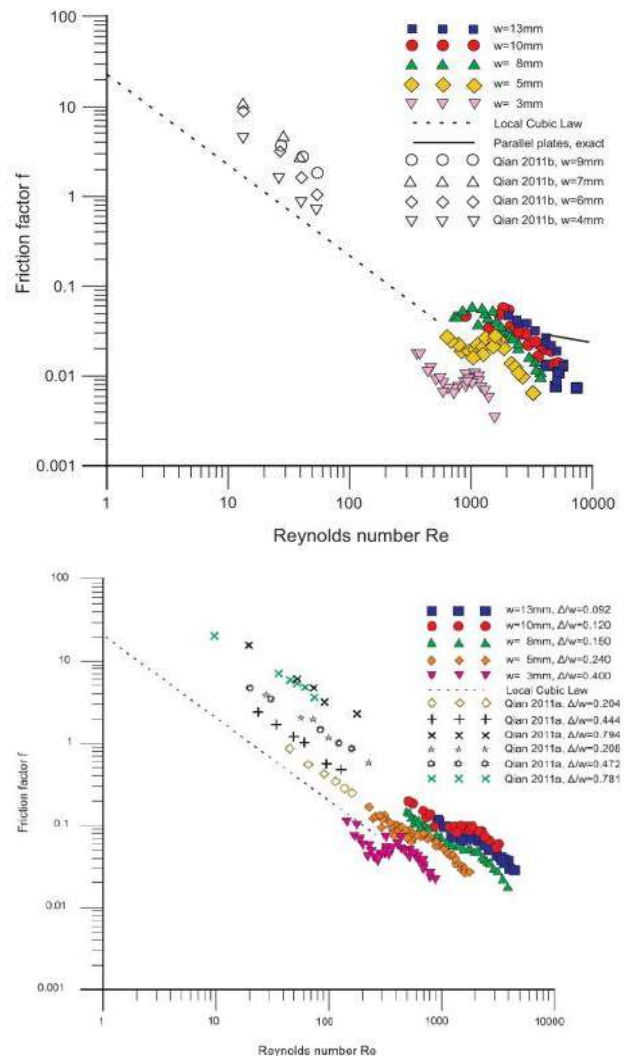
Figure 2. Constructed Moody diagram for all widths for a) smooth fractures and b) rough fractures [7]
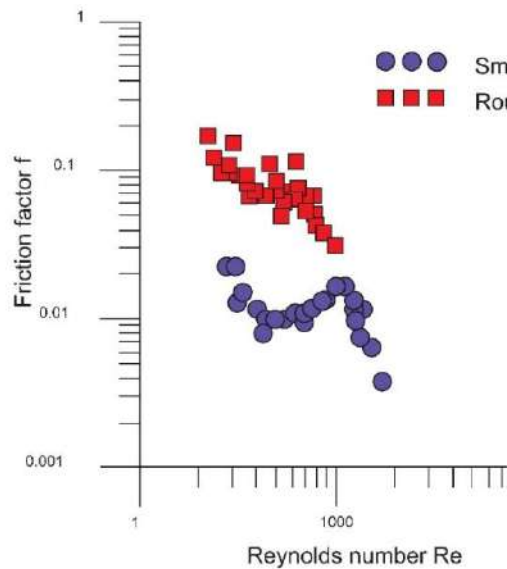
Figure 3. Constructed Moody diagram for 3 mm width – comparison of smooth fractures and rough fractures [7]

They enlisted several approaches in definition of properties of flow through open cell foams and analysed dependence of the particle diameter D_p on Reynolds number, used for pressure drop and friction factor calculations. This approximation considers the porous structure as the collection of grains closely packed, with the same specific surface area as the porous structure thus formed, what in reality can display rather large difference as can be seen in Fig. 4.
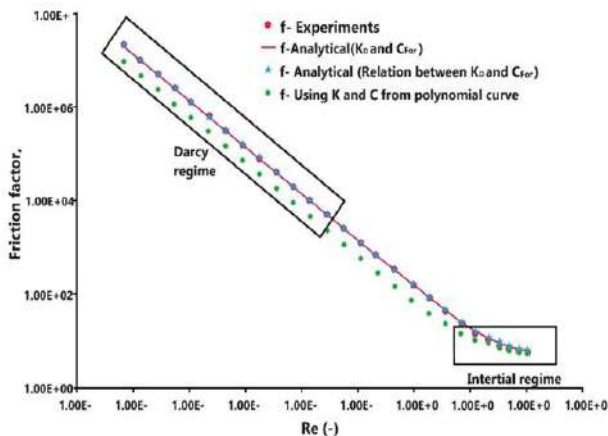
Figure 4. Comparison of analytical and experimental solutions for friction factor dependences on Reynolds number with influence of K and C coefficients [8]

Geometry of pores within the porous structure can be easily exactly determined, experimentally by using micro CT device [9]. Different formulas are used in different

regimes and several parameters are important, whereas flow characteristics, K – permeability and C – inertia coefficients, are commonly obtained by experiment and used for fitting of analytical curves.

Kumar and Topin [8] suggested analytical solution for friction factor by using pressure drop within a porous structure as given in equation (3) and proven by good fitting with experimental data as shown in Fig. 5. The pressure drop within a porous structure is directly influenced by the permeability and drag force coefficients and can well characterise cellular materials [8, 9].

$$f = \nabla\langle P\rangle . \frac{d_h}{\rho V^2} \qquad (3)$$
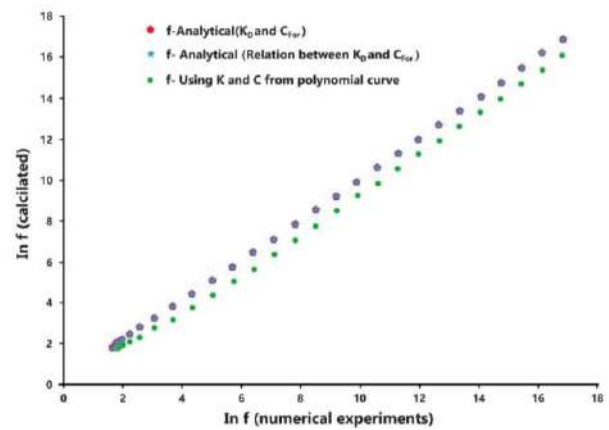
Figure 5. Comparison of analytical and experimental solutions for friction factor [8]
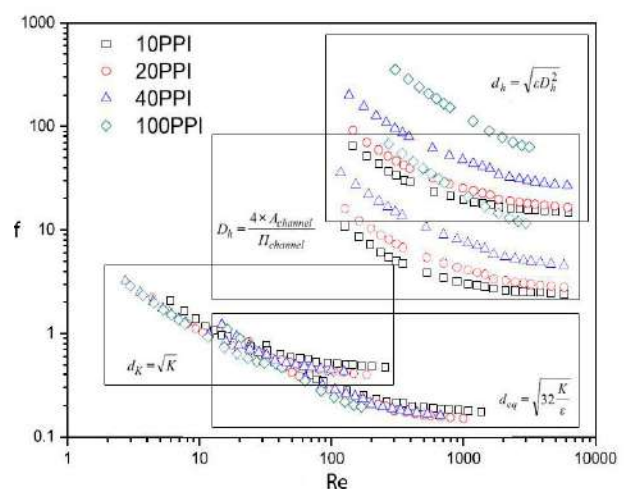
Figure 6. Friction factor dependence on: 1) the cross section area (D_h – central diagram); 2) equivalent diameter (d_{eq} – lower right diagram); 3) square root of permeability (d_k – lower left diagram) and 4) porosity (d_h – upper right diagram) [10]

Kim et al. [10] classified the relations between friction factor and Reynolds number for metal foams in several regimes: Re < 20, Re > 2000 and suggested that the dependence for foams is similar to classical Moody chart, as given in Fig. 6 [10].

The largest discrepancies with linear fit are exhibited for higher friction factors and inverse Reynolds number (1/Re), as well as for lower pore sizes and smaller cross section areas. Another correlation of the friction factor with Re for foams and different regimes is given in [16]. Approximations by using woven metal mesh screens have also been studied [17].

Besides the fundamental understanding of the friction within a fluid flow through the porous media and governmental basic parameters of the system, additional influences need to be considered as well, such as the temperature or magnetic field, especially in nano and micro domains and some recent research have been dealing with this. For example, magnetohydrodynamic nanofluids flow and transfer of heat are quite interesting for some new applications in micro systems [11, 12]. Those results indicated that volume fraction of nanoparticles can be related to some coefficients important for fluid dynamics, such as Nusselt number, but the type of the nanoparticle still remains the most important governing factor. However, magnetic field influence still needs clarifications.

Important areas of application are medical implants and human tissue represents the typical non-uniform porous structures [13]. The blood is known to be the non-Newtonian fluid, thus making modeling and simulation of the flow dynamics very complex and still under investigation from many aspects. In that sense, poroelasticity becomes important, as the property indicating interactions between the fluid flow and deformation of solids, during the flow through the porous structure [13].

3. Modeling of the fluid flow through porous media

Modeling of the fluid flow has been developed in the last decades in order to describe the system behaviour and predict its performance, as well as to determine the zones where the strengthening is needed. Determination of distributions of stress and strain within a porous structure is cutting edge research that will enable better material design. There are several approaches to the modeling of porous structures, but the majority still encounter principles used for solid structures and presence of voids still need to be comprehensively studied. One of the techniques used for modeling of the fluid flow through porous structure is by using Voronoi tessellation 3D effects. In the next example, dynamic behavior of pores under fluid effects is observed, by application of the simple steady sate viscous model based on commercial pre and post processing FEMAP TMG FLOW (CFD) software. A constant volumetric flow of water, Q = 2 l/s is applied and the structure is shown in Fig. 7. Mesh generation is schematically shown in Fig. 8 and Fig 9.
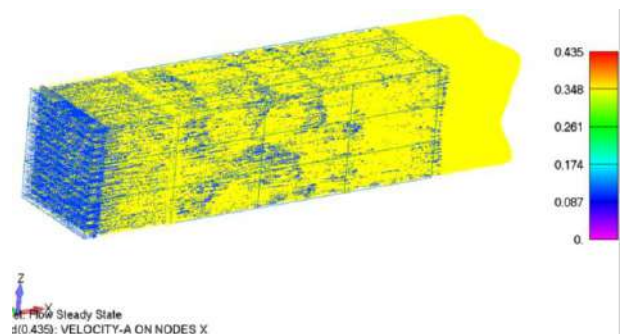
Figure 7. CFD modeling of the water flow through the porous structure

Initial conditions based on Navier–Stokes equations consider ambient temperature; mixing length laminar/turbulent flow model; and average Reynolds number of 14460. Distributions of the pressure and velocity are shown in Figs. 10 and 11, for the flow through the empty space represented by the given 3D structures in these images.
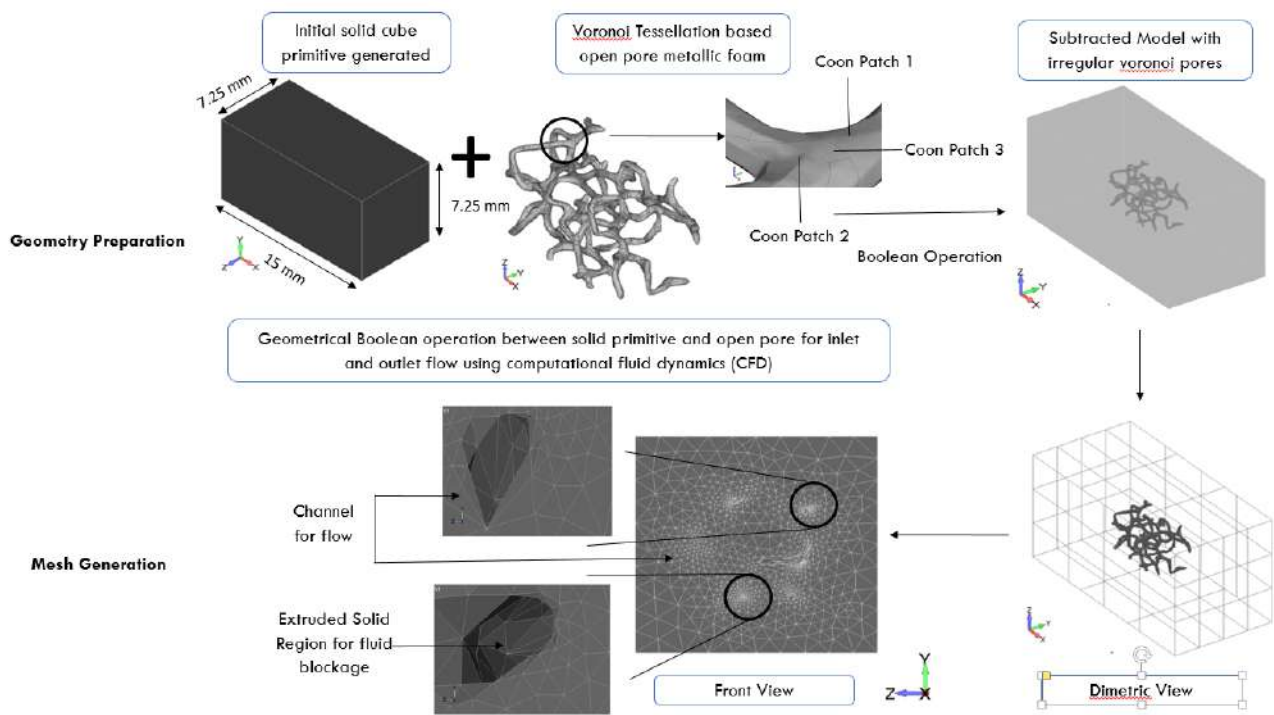
Figure 8. Design schematic and mesh generation procedure for the Voronoi based open pores pattern
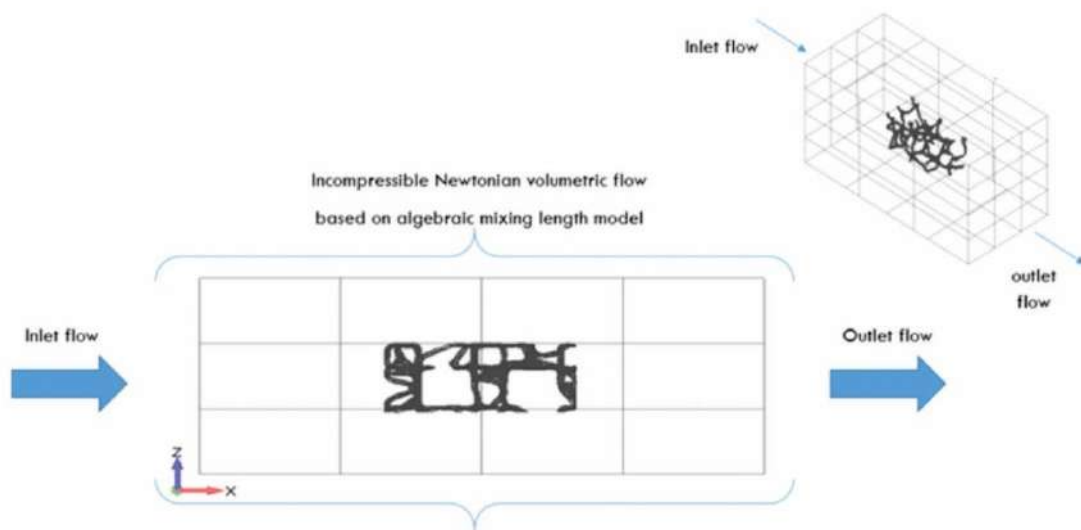
Figure 9. Computational domain definition for the incompressible Newtonian volumetric flow model based on algebraic mixing length model
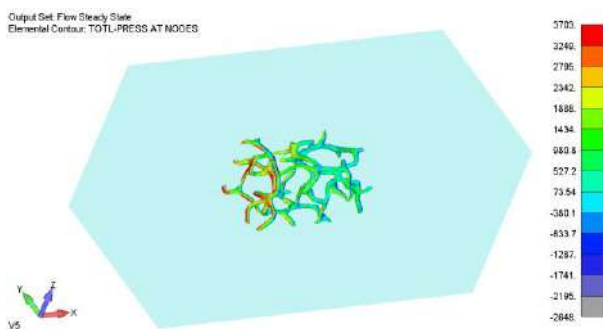
Figure 10. Pressure distribution at the boundary layers, in the x-direction
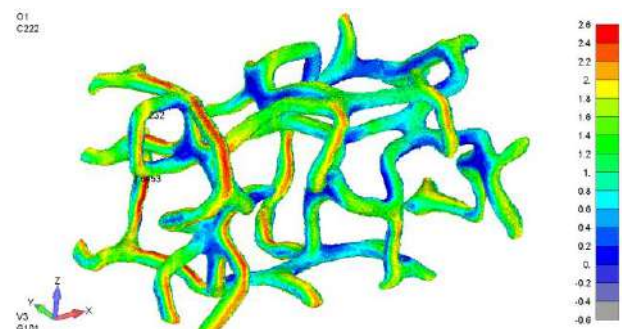
Figure 11. Velocity distribution at the boundary layers, in the x-direction

Skin friction drag pertains to the friction between the fluid and thin boundary layer on the surface of the object over which the fluid flows, usually consisting of the air. It is directly in connection with the properties of the material surface. The force that is exerted for dragging the layer of air attached to the surface of the object (e.g. inner pipe surface, or struts in porous structure) is called skin friction drag. Skin friction is due to the viscous drag within the boundary layer attached to the object surface, usually very thin, but it can become thicker within the rear zones, especially in the case of porous structures. Usually this zone exhibit laminar flow and transits to the turbulent in the rear zones. Shape of the surface greatly affects the zones with laminar and turbulent flow, and especially influences the transition point between the two of them. Good article on trasnsitional conditions is given in [15].

Various design methods are studied to provide laminar flow when it is possible. As in the previous case of the friction factor, skin friction coefficient can be calculated by using several equations, depending on the flow regime, and the basic one is given in equation (4).

$$C_f = \tau_w / q \qquad (4)$$

where τ_w is the local wall shear stress; q is the free-stream dynamic pressure. And for the turbulent flow, empirical formula is similar to the equation (2), as shown in the equation (4).

$$C_f = 0.074 / Re^{0.2} \qquad (5)$$

where Re is the Reynolds number.

The majority of theoretical equations are established for aerodynamic coefficients (e.g. for rockets) [5] and very limited literature exists related to the porous structures that represents the cutting edge current research related to several final applications, such as tissue scaffolds and associated processes.

CONCLUSIONS

Porous materials have gained much attention in the recent time due to many benefits that they can offer in both traditional applications as the substitution for heavy bulk materials, while retaining the strength and mechanical properties, and new applications, such as medical implants of new generations. However, the comprehensive properties of the porous structures are still under development, especially in the case of fluid flow through its voids. Dynamic fluid behaviour and its effects on mechanical integrity of the porous material elements (thin struts and matrix in general) is of the utmost importance for many new applications, including filtration systems, biomedical scaffolds and tissue engineering, or oil refining. Modeling and simulations represent valuable tool for determination of the weak points and further improvements, but also for prediction of its functional behaviour over time. Theoretical foundation for analytical solutions that are necessary for modeling is under development and many unanswered questions still exists. However, even with the existing ambiguities related to the transition between laminar and turbulent flow within the porous structure, distributions of pressures and velocities in boundary layers, and pressure drop over lengths, as well as the issue of all necessary influential factors, some new approaches have been studied and enabled rather well fitted analytical solutions related to the friction factor. Also, efficient new technologies, such as micro CT enabled exact determination of the real porous structure and opened up new avenues in this research topic.

ACKNOWLEDGEMENT

REFERENCE

[1] L.F. Moody: An approximate formula for pipe friction factors, Transactions of the ASME, Vol. 69, pp. 1005-1006, 1947.
[2] S.W. Churchill: Empirical expressions for the shear stress in turbulent flow in commercial

pipe, AIChE Journal, Vol. 19, No. 2, pp. 375-376, 1973. pp. 1005-1006, 1947.

[3] R.J. Tsal: Altshul-Tsal friction factor equation, Heating, Piping and Air Conditioning, No. 8, pp. 30-45, 1989.

[4] D. Brkić: Review of explicit approximations to the Colebrook relation for flow friction, Journal of Petroleum Science and Engineering, Vol. 77, No. 1, pp. 34-48, 2011.

[5] S. Box, C.M. Bishop, H. Hunt: Estimating the dynamic and aerodynamic paramters of passively controlled high power rockets for flight simulaton, February, 2009.

[6] H.E. Fayed: On Laminar Flow of Non-Newtonian Fluids in Porous Media, Springer Science+Business Media Dordrecht, Transport in Porous Media, Vol. 111, pp. 253–264, 2016.

[7] V. Tzelepis, K.N. Moutsopoulos, J.N.E. Papaspyro, V.A. Tsihrintzis: Experimental investigation of flow behavior in smooth and rough artificial fractures, Journal of Hydrology Vol. 521, pp. 108–118, 2015.

[8] P. Kumar, F. Topin: Investigation of fluid flow properties in open cell foams: Darcy and weak inertia regimes, Chemical Engineering Science Vol. 116, pp. 793-805, 2014.

[9] X.O.X. Zhan, T. Lowe, R. Blan, M.N. Ra, Y. Wang, N. Batai, C. Phamd, N. Shokri, A. Garforth, P. Withers, X. Fan: X-ray micro computed tomography characterization of cellular SiC foams for their applications in chemical engineering, Materials Characterization, Vol. 123, pp. 20–28, 2017.

[10] T.H. Kim, W. Lee, J.H. Jeong: Thermo-fluidic characteristics of open cell metal foam as an anodes for DCFC, part I: Head loss coefficient of metal foam, international journal of hydrogen energy, pp. 1-8, 2014.

[11] M. Sheikholeslami, M. Hatami, D.D. Ganji: Nanofluid flow and heat transfer in a rotating system in the presence of a magnetic field, Journal of Molecular Liquids, Vol. 190, pp. 112–120, 2014.

[12] M. M. Rashidi, S. Abelman, N. F. Mehr: Entropy generation in steady MHD flow due to a rotating porous disk in a nanofluid, International Journal of Heat and Mass Transfer Vol. 62, pp. 515–525, 2013.

[13] J.P. Gleghorn, A.R.C. Jones, C.R. Flannery, L.J. Bonassar: Boundary Mode Lubrication of Articular Cartilage by Recombinant Human Lubricin, December 2008.

[14] D. Edouard, M. Lacroix, C.P. Huu, F. Luck: Pressure drop modeling on SOLID foam: State-of-the art correlation, Chemical Engineering Journal, Vol. 144, pp.299–311, 2008.

[15] P. Venkataraman, P.R.M. Rao: Darcian, transitional, and turbulent flow through porous media, Journal of Hydraulic engineering, Vol. 124, No. 8, 1998.

[16] J.F. Liu, W.T. Wu, W.C. Chiu, W.H. Hsieh: Measurement and correlation of friction characteristic of flow through foam matrixes, Experimental Thermal and Fluid Science, Vol. 30, pp. 329–336, 2006.

[17] W. Bussière, D. Rochette, S. Clain, P. Andréa, J.B. Renard: Pressure drop measurements for woven metal mesh screens used in electrical safety switchgears, International Journal of Heat and Fluid Flow, Vol. 65, pp. 60–72, 2017.

[18] F. Macdonald, M. S. El-Sayed, K. Mow, F. A. L. Dullien: Flow through Porous Media-the Ergun Equation Revisited, Industrial & Engineering Chemistry Fundamentals, Vol. 18, No. 3, pp. 199-208, 1979.

[19] Genic et al: A Review of Explicit Approximations of Colebrook's Equation, FME Transactions, Vol. 39, pp. 67-71, 2011.

[20] V.B. Gawande, A.S. Dhoble, D.B. Zodpe, S. Chamoli: A review of CFD methodology used in literature for predicting thermo-hydraulic performance of a roughened solar air heater, Renewable and Sustainable Energy Reviews, Vol. 54, pp. 550–605, 2016.

TRIBOLOGICAL STUDIES ON COPPER-BASED FRICTION LININGS

Mara KANDEVA[1,*], Dimitar KARASTOYANOV[2], Galya NIKOLCHEVA[3], Blaža STOJANOVIĆ[4], Petr SVOBODA[5], Aleksandar VENCL[6]

[1]Tribology Center, Technical University of Sofia, Sofia, Bulgaria

[2]Institute for Information and Communication Technologies, Bulgarian Academy of Sciences, Sofia, Bulgaria

[3]Faculty of Industrial Technology, Technical University of Sofia, Sofia, Bulgaria

[4]University of Kragujevac, Faculty of Engineering, Kragujevac, Serbia

[5]Faculty of Mechanical Engineering, Brno University of Technology, Brno, Czech Republic

[6]University of Belgrade, Faculty of Mechanical Engineering, Belgrade, Serbia

*Corresponding author: kandevam@gmail.com

Abstract: The objects of this work were nine different copper-based friction linings produced from powder by pressing and sintering. Six copper-based friction linings contained 3 wt. % zinc (Zn) and variable content of tin (Sn), i.e. 1, 2, 4, 6, 8 and 10 wt. %. Three copper-based friction linings were with fixed contents of Zn (3 wt. %) and Sn (10 wt. %), and with different amount of SiC particles, i.e. 2, 4 and 6 wt. %. Tribological studies on these friction linings included determination of the static and kinetic coefficient of friction under different normal loads and unlubricated sliding conditions, as well as, determination of the abrasive wear resistance under different normal loads and unlubricated sliding/rolling conditions. The analysed results present the influence of Sn content and addition of SiC particles to the copper-based friction lining on its friction and wear properties.

Keywords: friction couplings, copper, tin, silicon carbide, friction, abrasive wear.

1. INTRODUCTION

Multiple-disc clutches (Fig. 1) are type of friction couplings which transmit motion and torque over the multiple friction plates (discs). They are used primarily in machine tools gearboxes, but also in the textile, construction and other machinery [1]. They also can be used as brakes. A multiple-disc clutch or brake is composed of friction lining discs and steel discs, which are internally or externally toothed and which upon activation are pressed against one another and transmit frictional torque [2]. By using multiple discs, a very large contact surface is obtained and more friction is achieved. Contact between the discs may be without or with lubrication, i.e. dry and wet clutches.
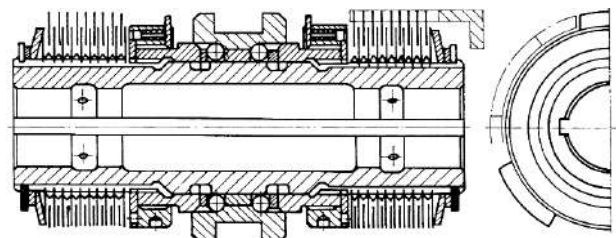
Figure 1. Schematic diagram of multiple-disc clutch

The friction materials (friction linings) must poses a complex of diverse and in many cases mutually exclusive properties. They should have high coefficient of friction, high wear

resistance and resistance to seizure, high thermal conductivity, high strength, good processing and machinability, high corrosion resistance, etc. Depending on the application and requirements, very different friction linings are used, i.e. organic friction linings (paper-based linings), metal friction linings (sintered bronze, iron and brass), carbon and carbon-containing friction linings, and ceramic and ceramic-containing friction linings [2,3].

The powder metal friction linings (sintered bronze, iron and brass) are based on a sintered metal matrix, into which mineral, metallic, non-metallic or ceramic agents, as well as abrasives and solid lubricants can be embedded. The production of powder metal friction linings includes compaction (densification) of powder and sintering. During sintering processes powder mixtures are heated to temperatures below the melting point, under pressure and controlled protective atmosphere. Thereby annealing, diffusion and recrystallization processes occur. These friction linings can be considered as mechanical coatings (solid state surfacing) [4], since the lining (coating) are bonded during sintering to the steel disc (substrate). Copper and iron are the most frequently used as the main metals forming the matrix of sintered materials for friction purposes [5]. Iron-based friction material has high temperature strength, hardness and thermal stability, while copper-based friction material has smaller but more stable coefficient of friction [6]. There is also a rapid increase in interest in composites as a promising class of friction materials [7].

The aim of this paper was to investigate the possibilities to increase the service life and coefficient of friction of multiple-disc clutches with copper-based friction linings. Relative to this, the influence of Sn content and addition of SiC particles to the copper-based friction lining on its friction and wear properties were investigated. All together nine different copper-based friction lining materials were tested, i.e. their static and kinetic coefficient of

friction and abrasive wear resistance in unlubricated conditions were analysed.

2. EXPERIMENTAL DETAILS

2.1 Materials

The substrate material for all copper-based friction linings was a high-carbon steel, in form of circular discs, with chemical composition shown in Table 1. Outer diameter of all circular discs was 89 mm, inner diameter was 60 mm, and thickness was 1.5 mm. Nine different copper-based powder mixtures were compacted and sintered on steel disc substrates. Their chemical composition is shown in Table 2. The powder mixtures were prepared by ball milling at 200 rpm for 90 minutes. After ball milling, the average particle size was 25 μm. All copper-based friction linings were compacted at a pressure of 320 MPa, and sintered at a temperature of 700 °C for 3 hours. Designation and hardness of the friction lining samples is shown in Table 2.

Table 2. Designation, chemical composition (wt. %) and hardness of tested friction lining samples

Sample designation	Powder chemical composition [wt. %]				Hardness HB
	Zn	Sn	SiC	Cu	
Cu-1Sn	3	1	–	Balance	75.5
Cu-2Sn		2			76.2
Cu-4Sn		4			81.5
Cu-6Sn		6			84.4
Cu-8Sn		8			89.2
Cu-10Sn		10			94.0
Cu-10Sn-2SiC		10	2		125
Cu-10Sn-4SiC			4		138
Cu-10Sn-6SiC			6		144

The thickness of friction linings was measure in 10 points by Pocket-LEPTOSKOP 2021 Fe, and the calculated average thickness of 150 μm was the same for all samples.

Table 1. Chemical composition (wt. %) of steel disc substrate

Element	C	Si	Mn	Ni	P	S	Cr	Fe
Percentage	0.7	0.28	1.1	0.18	0.03	0.02	0.25	Balance

2.2 Coefficients of friction testing

The coefficient of friction testing was performed on the test rig presented in Figure 2. Test sample (1) is mounted and fixed in the sample holder (3), which is connected through the non-elastic string with the dynamometer (6). Tangential force (T) is loaded to the sample through the very slow rotation of the micrometric screw (5) and displayed on the dynamometer (6). The counter-body (2) is stationary and in contact with the test sample (1). The normal force (F_n) is set by means of the weights (4). The test rig shown in Figure 2 enables determination of the two values, i.e. static and kinetic coefficient of friction. Both values are read from the same dynamometer (position 6 in Fig. 2).
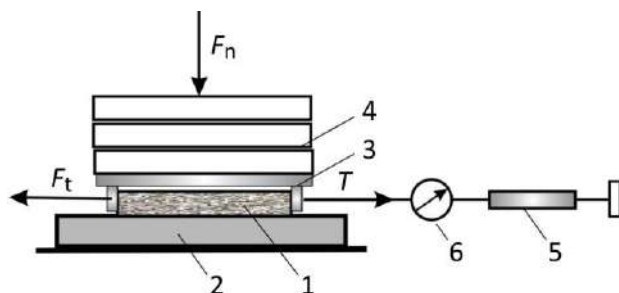
Figure 2. Schematic diagram of the coefficients of friction testing

Test parameters were as follows: four different normal loads, i.e. 40, 80, 120 and 160 N; dry contact condition, in ambient air at room temperature ($\approx 25\,°C$) and relative humidity of $40 - 45\,\%$. Test sample and counter-body were in the shape of circular disc with outer/inner diameter of 89/60 mm (Fig. 3). This gives the initial geometrical contact area of approximately 3394 mm². Taking into account this contact area, the specific loads were approximately 12, 24, 35 and 47 kPa. The resting time (time for the possible stress relaxation at the junctions) was 30 s for each contact pair.

2.3 Abrasive wear testing

Abrasive wear testing was carried out on Taber Abraser with a modified standard test conditions, i.e. only one abrasive roller was used (Fig. 4). A circular disc (1), having outer/inner diameter of 89/60 mm, with friction lining sample (2) is fixed on the horizontal turntable platform, driven with constant rotational speed (n) of 60 rpm by the electric motor (3). Abrasive roller (4), a Taber abrading wheel Calibrase® CS-10, is mounted on horizontal axis (5) and provides through weights (6) the necessary normal load (F_n). Abrasive wear of friction lining samples is calculated as their mass loss, i.e. as a difference between the initial mass of the sample and its mass after given number of abrasion cycles (N), counted by the counter (pos. 7 in Fig. 4). Mass of the samples is measured by the electronic balance with accuracy of 0.1 mg.
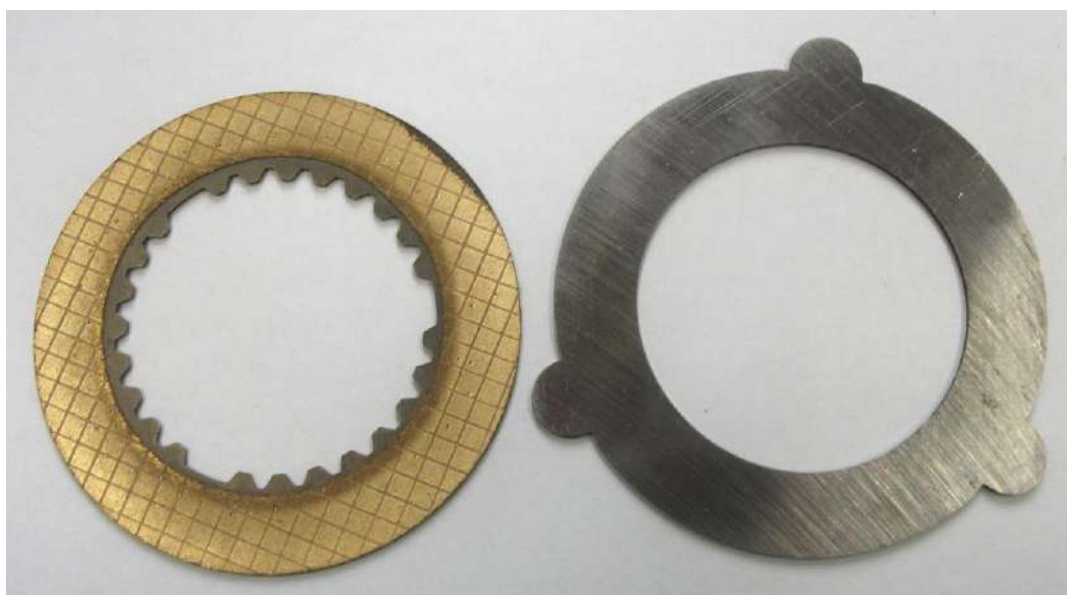
Figure 3. Appearance of the copper-based friction lining test sample (left) and the steel counter-body (right)
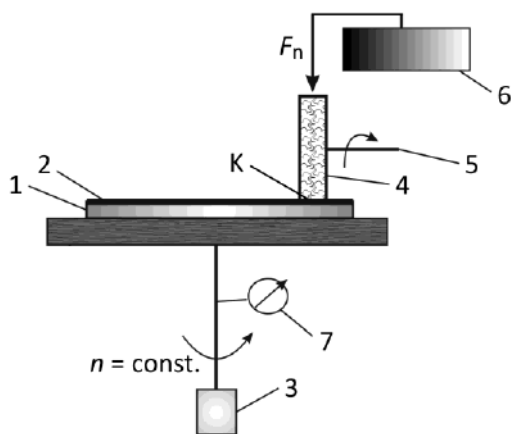
Figure 4. Schematic diagram of the abrasive wear testing

Abrasive roller (wheel) is driven by the rotating test sample. The wheels produce abrasion marks that form a pattern of crossed arcs over a circular ring. The width of the worn area (circular ring) is 12.7 mm, with the inner radius of 31.75 mm and outer radius of 44.45 mm (Fig. 5). Therefore, the distance between the rotational axis of circular disc sample (1) and mass centre of the contact area (K) is 38.1 mm, and the worn area is approximately 30 cm^2 [8]. The sliding action between the friction lining sample and abrasive roller is due to the relative motion between them which is characterised by the roller slip. This occurs because the axe of the roller is shifted from the centre of rotation of circular disc sample with the drifting angle of around 30° [9].

Figure 5. Wear track (lighter circular ring) on sample Cu-4Sn after 300 abrasion cycles (approx. 71.8 m)

Test parameters were as follows: normal load of 1 kg (9.8 N); average tangential velocity of friction lining sample of 0.239 m/s; sliding distance of N = 400 abrasion cycles (approx. 95.8 m); dry contact condition, in ambient air at room temperature (≈ 25 °C) and relative humidity of 40 – 45 %.

3. RESULTS AND DISCUSSION

3.1 Static and kinetic coefficient of friction

The obtained values of the coefficients of friction are presented in Figure 6. Values were in the range 0.22 – 0.34 for static coefficient of friction, and 0.15 – 0.32 for kinetic coefficient of friction. These values more or less correspond to the values for sintered friction clutch materials under dry sliding conditions, which are 0.36 (static coefficient of friction) and 0.30 (kinetic coefficient of friction) [10]. The average coefficient of friction of modern friction materials is between 0.3 and 0.5 [11]. In our case, contact pressure was very small (from 12 to 47 kPa) and that could be the reason for smaller values of the coefficients of friction.

It is well known that the friction depends on the size of actual (real) contact area. The number and size of the contact point will increase with the increasing pressure. If the contact between asperities is elastic, the coefficient of friction will decrease with the increasing pressure. On the other hand, if the contact between asperities is plastic, the coefficient of friction will increase with the increasing pressure. In general case the coefficient of friction dependence on load possesses the minimum that is connected directly with transition from elastic to plastic contact (when load is increasing) and associated variation in the relative contribution of the friction components [12]. In fact, something similar can be noticed on Figure 6, which shows the influence of normal load on both, static and kinematic coefficient of friction. Both coefficients of friction, for all materials, mainly decrease as the normal load increase up to 80 N, and after that load starts mainly to increase.
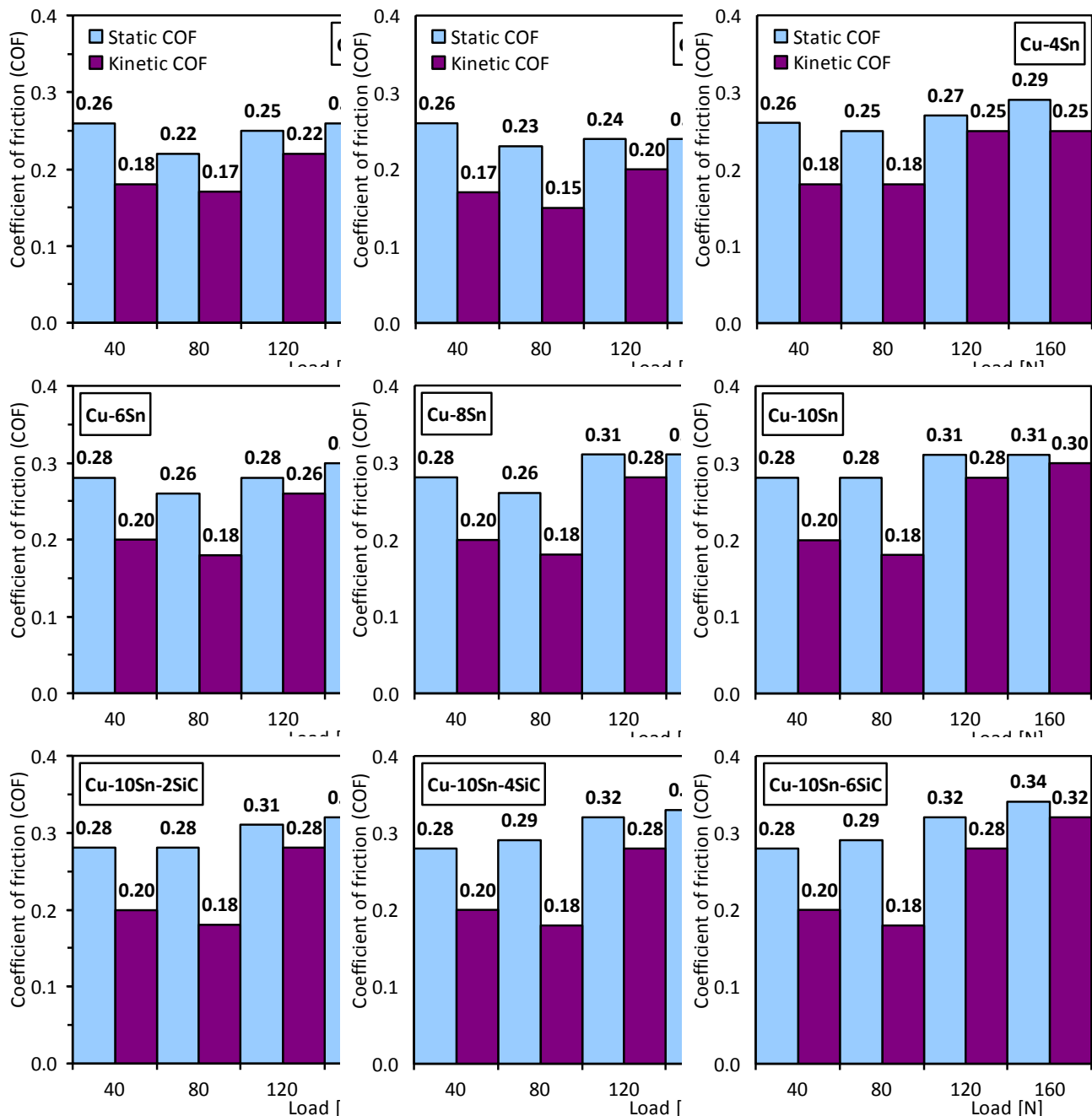
Figure 6. Static and kinetic coefficient of friction of tested materials (contact pairs) for different loads: Influence of load on coefficients of friction values

Differences between static and kinetic coefficient of friction did not differ too much between the samples. On the other hand, this difference changes with applied normal load. The average decrease of kinetic comparing to static coefficient of friction was 0.08 (31.2 %) for loads of 40 and 80 N, while for 100 and 120 N loads this average decrease was 0.03 (9.7 %). Static coefficient of friction is usually greater than kinetic coefficient of friction of about 20 to 30 % [13]. When the static coefficient of friction is noticeably greater than the kinematic one, the phenomenon of stick-slip

may occur, which is not desirable in terms of continuous torque transmission in friction couplings. This is due to the fact that before the onset of motion, a large stress relaxation at the junctions may occur, which causes an increase in the real area of contact and allows the adhesive forces to fully develop. This is particularly important in the contact that are mostly plastic and when the sliding surfaces are without contaminants [13].

Influences of tin (Sn) content and silicon carbide (SiC) particles content on the static and kinetic coefficients of friction are analysed
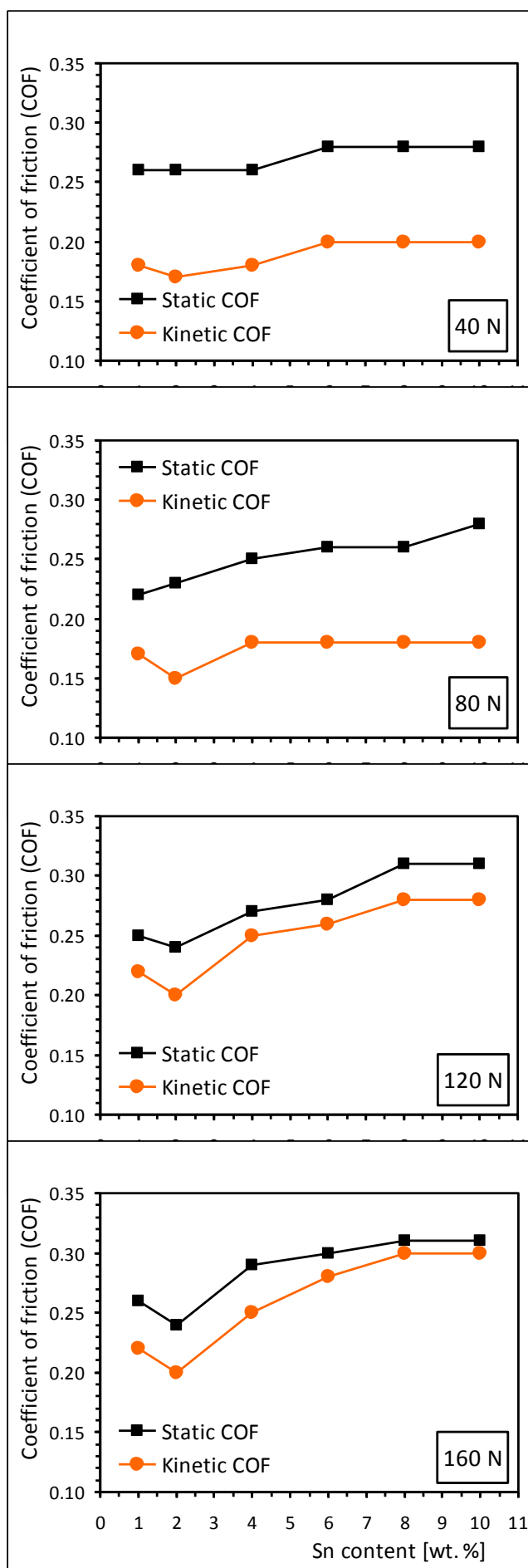
Figure 7. Dependence of static and kinetic coefficient of friction on Sn content, for different normal loads
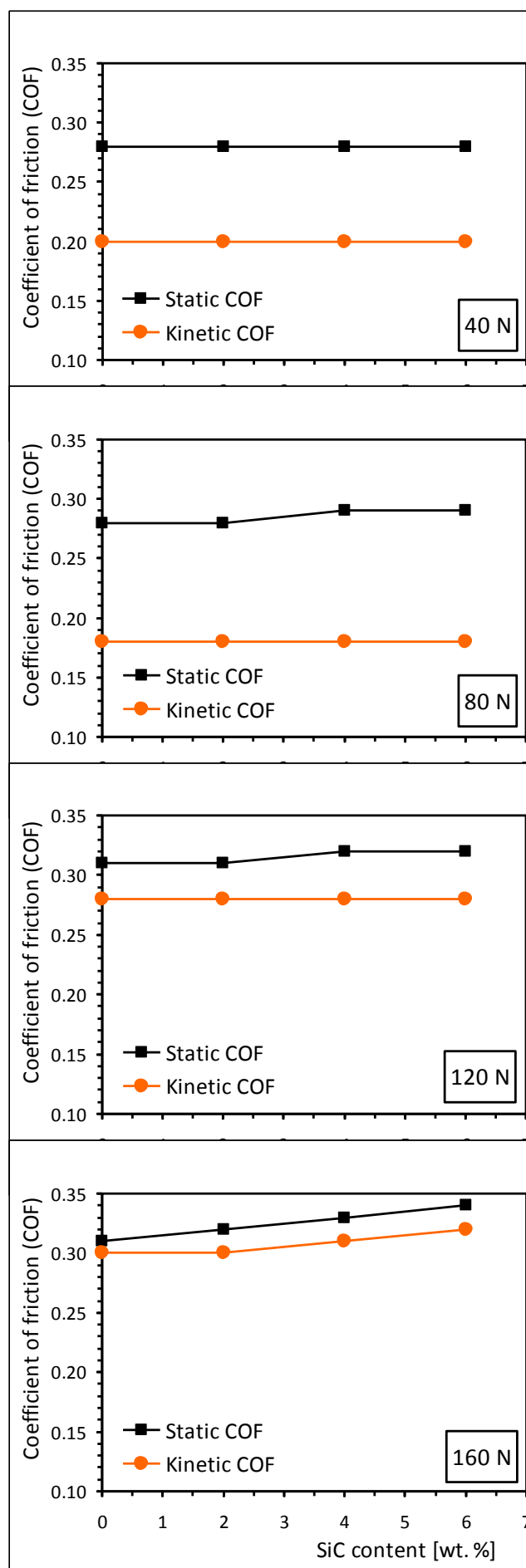
Figure 8. Dependence of static and kinetic coefficients of friction on SiC particles content, for different normal loads

separately. Based on the results given in Figure 6, appropriate diagrams are drawn for the dependences of coefficients of friction on Sn content (Fig. 7), and on SiC particles content (Fig. 8), for different loads. Once again, different behaviour is noticed for lower loads and for higher loads. Generally, both static and kinetic coefficient of friction are higher when the amount of Sn in copper-based friction lining is higher, but this influence is very small or do not exist at all for lower normal loads (Fig. 7). For higher loads this influence can not be neglected. As example, friction linings with 8 and 10 wt. % Sn, at highest applied load of 160 N, show the highest values. Their static coefficient of friction is higher by 0.07 (29.2 %) and kinetic coefficient of friction is higher by 0.10 (50.0 %), comparing to the friction lining with 2 wt. % Sn at the same load.

Similarly, addition of SiC particles to copper-based friction linings did not influence in significant meaner the values of the coefficients of friction at lower loads (Fig. 8). The more significant increase of coefficients of friction is noted only at the highest load of 160 N. At this load the highest values of coefficients of friction were for the friction lining containing the biggest amount of SiC particles (Cu-10Sn-6SiC). Static coefficient of friction of this friction linings at load of 160 N is higher by 0.03 (9.7 %) and its kinetic coefficient of friction is higher by 0.02 (6.7 %), comparing to the friction lining without SiC particles at the same load. Based on the percentage increase at 160 N load, it can be concluded that the addition of Sn has bigger influence on coefficients of frictions values than the addition of SiC particles.

If we analyse the mutual effect of Sn and SiC particles addition, the increase of the coefficients of friction is even higher. This is obtained by comparing friction lining which showed the highest values of coefficients of friction (Cu-10Sn-6SiC) with the friction lining which showed the lowest values of coefficients of friction (Cu-2Sn). In this case, at load of 160 N, the increase of static coefficient of friction of 0.10 (41.7 %), and kinetic coefficient of friction of 0.12 (60.0 %) is obtained.

3.2 Abrasive wear resistance

Abrasive wear of the friction linings was determined at various number of cycles, i.e. at N = 100, 200, 300 and 400, which corresponds to the following sliding distances: 23.9, 47.9, 71.8 and 95.8 m. Obtained mass losses for each number of cycle/sliding distance are presented in Table 3.

Table 3. Abrasive wear of tested friction linings

Sample designation	Number of cycles (N)			
	100	200	300	400
	Sliding distance [m]			
	23.9	47.9	71.8	95.8
	Mass loss [mg]			
Cu-1Sn	15.8	25.4	44.1	53.8
Cu-2Sn	14.8	16.6	33.2	36.2
Cu-4Sn	11.6	16.0	19.4	31.1
Cu-6Sn	12.8	14.7	27.7	29.2
Cu-8Sn	12.9	21.9	27.8	28.6
Cu-10Sn	12.0	23.8	24.5	25.0
Cu-10Sn-2SiC	10.0	14.6	18.5	20.1
Cu-10Sn-4SiC	8.0	12.2	16.8	18.1
Cu-10Sn-6SiC	5.0	10.2	14.8	16.1

Using the results from Table 3, mass losses are shown as a function of sliding distance, in the form of comparative wear curves (Fig. 9). The appearance of the constructed wear curves is similar for all tested friction linings, i.e. more or less linear dependence of wear on sliding distance is noticed. This suggests that the steady-state wear occurs from the beginning of the tests, which is common thing for the abrasive wear.

In order of easier comparison of different friction linings and influences of Sn and SiC particles content, values of total wear rates are calculated and presented in Figures 10 and 11. Total wear rates were calculated by using the highest mass losses and sliding distances, assuming that the steady-state wear occurred from the beginning of the tests. In addition to the wear data, the hardness of each of tested friction linings was determined (Table 2), as an ancillary mechanical property, to make appropriate correlations (Figs. 10 and 11).
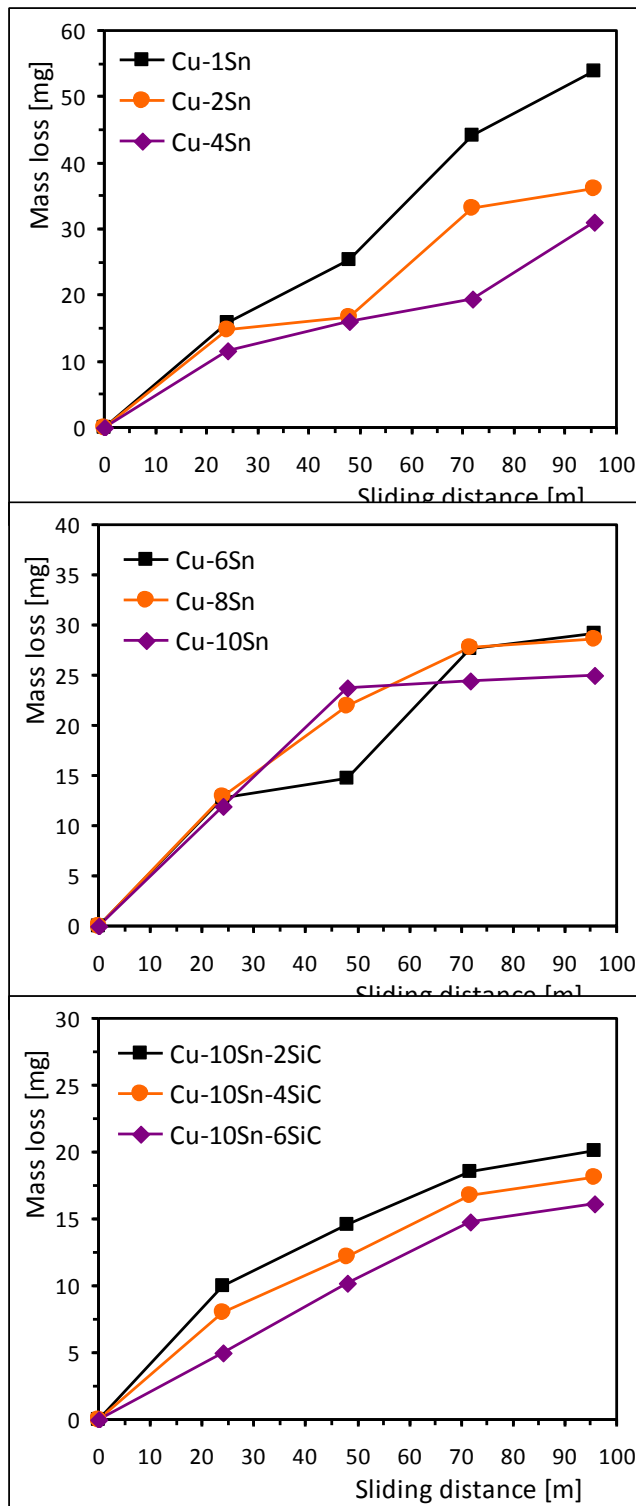
Figure 9. Mass loss vs. sliding distance (wear curves) for tested friction linings

The analysis of the results show that the presence of higher amount of tin (Sn) decreases the abrasive wear of tested friction linings (Fig. 10). The lowest wear rate of 2.61×10^{-1} mg/m shows sample Cu-10Sn, i.e. friction lining with the highest amount of Sn (10 wt. %). The increase of wear resistance for this friction lining is approximately 2.2 times in comparison to friction lining Cu-1Sn (sample with the lowest

amount of Sn of 1 wt. %) which shows the highest wear rate of 5.62×10^{-1} mg/m.

Presence of silicon carbide (SiC) particles also decreases the abrasive wear of tested friction linings, and this decrease is higher as the amount of SiC particles increases (Fig. 11). The lowest wear rate of 1.68×10^{-1} mg/m shows sample Cu-10Sn-6SiC, i.e. friction lining with the highest amount of Sn (10 wt. %) and highest amount of SiC particles (6 wt. %). The increase of wear resistance for this friction lining is approximately 1.6 times in comparison to friction lining Cu-10Sn (sample with the same amount of Sn and without SiC particles) which shows the wear rate of 2.61×10^{-1} mg/m.

If we analyse the mutual effect of Sn and SiC particles addition, the increase of the wear resistance is even higher. This is obtained by comparing friction lining which had the lowest wear rate (Cu-10Sn-6SiC) with the friction lining which had the highest wear rate (Cu-1Sn). In this case, increase of wear resistance of approximately 3.3 times is obtained.

The noticed decrease of wear rate with the increase of Sn and SiC particles content is connected with hardness of the tested samples. The wear rate decreases as hardness increase, as it could be expected. The relationships between obtained abrasive wear values and hardness (Table 2) of tested friction linings are shown in Figures 10 and 11. The obtained correlations between wear rate and hardness of tested samples are almost linear, with the exception of sample Cu-1Sn. Indeed, the other friction linings showed good correlation, since the R-squared (R^2) value are relatively high (R^2 = 0.93 for samples without SiC particles and R^2 = 0.99 for samples with SiC particles).

4. CONCLUSION

In this study, the friction and wear behaviour of nine different copper-based friction linings, produced from powder by pressing and sintering, were investigated. Different samples were obtained by varying the amount of Sn (1, 2, 4, 6, 8 and 10 wt. %) and SiC particles (0, 2, 4 and 6 wt. %) in friction linings.
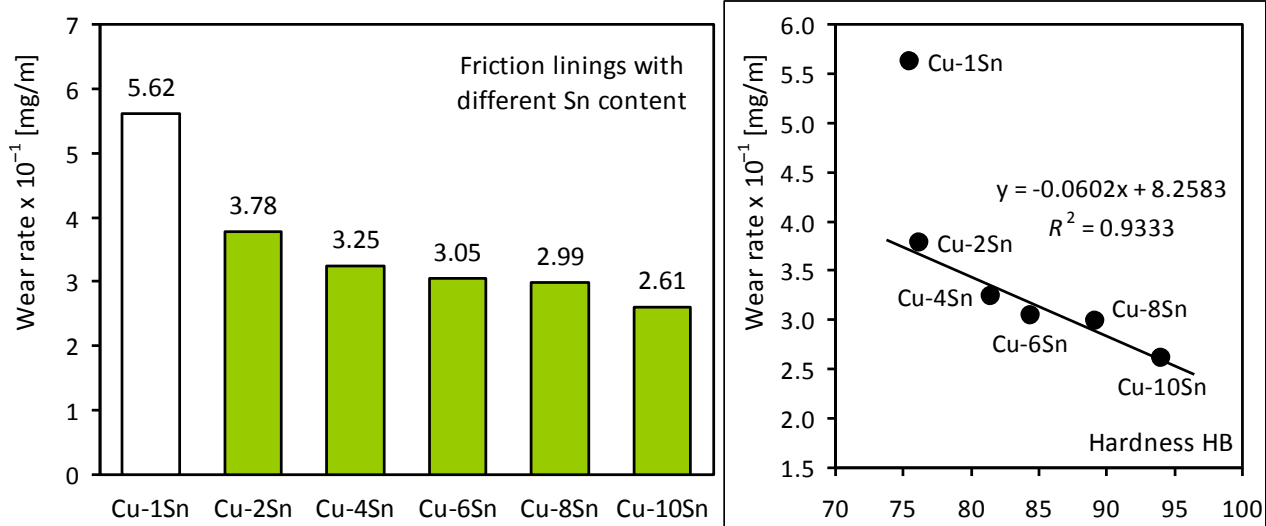
Figure 10. Friction linings with different content of Sn: total wear rates (left) and dependence of abrasive wear rate on hardness (right)
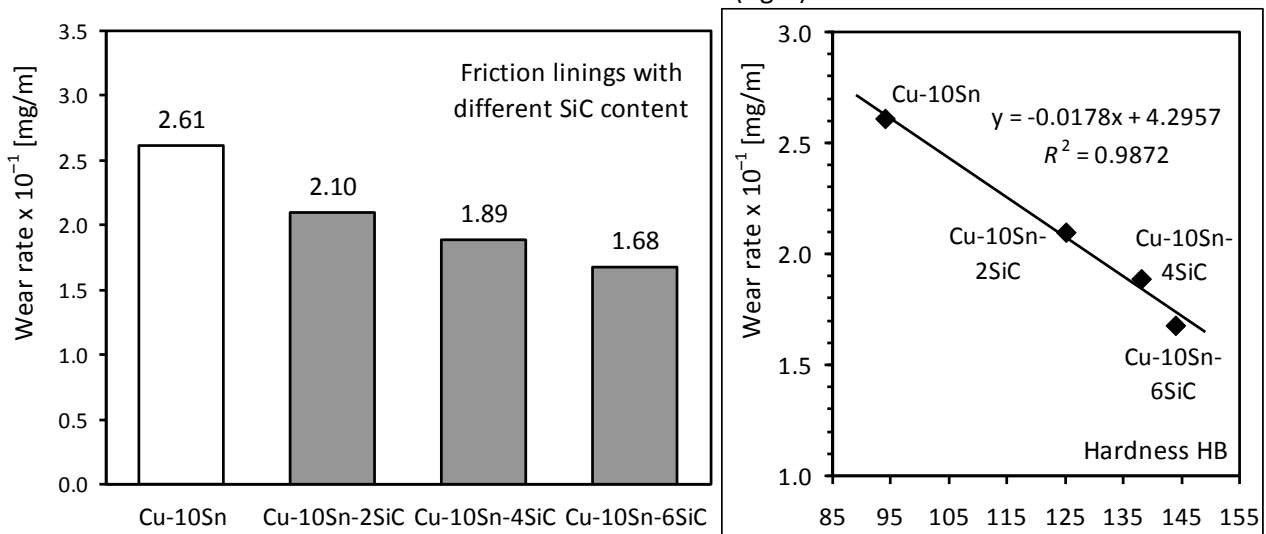
Figure 11. Friction linings with different content of SiC particles: total wear rates (left) and dependence of abrasive wear rate on hardness (right)

Generally, both static and kinetic coefficients of friction are higher when the amount of Sn in copper-based friction lining is higher, but this influence is very small or do not exist at all for lower normal loads. For higher loads this influence can not be neglected. Similarly, addition of SiC particles to copper-based friction linings did not influence in significant meaner the values of the coefficients of friction at lower loads, but only at the highest applied load. The analysis of the wear results show that the presence of higher amount of Sn decreases the abrasive wear of tested friction linings. Presence of SiC particles also decrease the abrasive wear of tested friction linings, and this decrease is higher as the amount of SiC particles increases.

The highest values of static and kinetic coefficient of friction and the lowest wear rate showed friction linings with the highest amount of Sn (10 wt. %) and SiC particles (6 wt. %). It was shown that with mutual effect of Sn and SiC particles addition, tribological characteristic can be increased up to 1.6 times (kinetic coefficient of friction) and up to 3.3 times (wear resistance).

ACKNOWLEDGEMENTS

REFERENCES

[1] M. Puljizević, Spojnice, u: Z. Savić (ur.): *Inženjersko mašinski priručnik, knjiga II*, Zavod za udžbenike i nastavna sredstva, Beograd, pp. 343-377, 1987, in Serbian.

[2] D. Frey: Wet multi disk clutches and brakes, in: T. Mang (Ed.): *Encyclopedia of Lubricants and Lubrication*, Springer, Berlin, pp. 2347-2362, 2014.

[3] J.Y. Jang, M.M. Khonsari: Wet clutch friction material: The surfaced groove effect, in: Q.J. Wang, Y.-W. Chung (Eds.): *Encyclopedia of Tribology, Springer*, New York, pp. 4102-4108, 2013.

[4] M. Kandeva-Ivanova, A. Vencl, D. Karastoyanov: *Advanced Tribological Coatings for Heavy-Duty Applications: Case Studies*, Prof. Marin Drinov Publishing House of Bulgarian Academy of Sciences, Sofia, 2016.

[5] V.M. Kryachek: Friction composites: Traditions and new solutions (review). I. Powder materials, Powder Metallurgy and Metal Ceramics, Vol. 43, No. 11, pp. 581-592, 2004.

[6] X. Xiao, Y. Yin, J. Bao, L. Lu, X. Feng: Review on the friction and wear of brake materials, Advances in Mechanical Engineering, Vol. 8, No. 5, pp. 1-10, 2016.

[7] V.M. Kryachek: Friction composites: Traditions and new solutions (review). II. Composite materials, Powder Metallurgy and Metal Ceramics, Vol. 44, No. 1, pp. 5-16, 2005.

[8] Taber Abraser (abrader), available at: http://www.taberindustries.com/taber-rotary-abraser, accessed: 10.04.2017.

[9] E. Csanády, E. Magoss, L. Tolvaj: *Quality of Machined Wood Surfaces*, Springer International, Cham, 2015.

[10] T.P. Newcomb, R.T. Spurr, H.C. Town: Friction clutches, in: M.J. Neale (Ed.): *The Tribology Handbook*, Butterworth-Heinemann, Oxford, pp. B7.1-B7.9, 1995.

[11] H. Heisler: Brake system, in: H. Heisler: *Advanced Vehicle Technology*, Butterworth-Heinemann, Oxford, pp. 450-509, 2002.

[12] Н.К. Мышкин, М.И. Петроковец: *Трение, смазка, износ*, Физматлит, Москва, 2007, in Russian.

[13] G. Straffelini: *Friction and Wear: Methodologies for Design and Control*, Springer, Cham, 2015.

THE TRIBOLOGICAL BEHAVIOR OF REINFORCED POLYTETRAFLUOROETHYLENE (PTFE) AGAINST GRAY CAST IRON IN LUBRICATED CONDITIONS

İsmail KAYA[1,*], Zeynep PARLAR[1], Vedat TEMİZ[1], Vildan GİRİŞTA KAYA[1]
[1]İstanbul Technical University, İstanbul, Turkey
*Corresponding author: kayaism@itu.edu.tr

Abstract: *In this study, tribological behavior of reinforced polytetrafluoroethylene (PTFE) against gray cast iron counter face is studied experimentally. In these experimentations pin on ring method is applied in order to obtain friction characteristics in lubricated conditions. In the tests, gray cast iron is used as ring (counter face) and PTFE materials having several reinforcing material ratios is used as pin element.*

Keywords: *PTFE, cast iron, lubrication, friction, wear, pin on ring, compressor, crankshaft.*

1. INTRODUCTION

Refrigerator is the only household appliance that does not have a switch on/off button, which means once it is plugged in, it works non-stop. Therefore, the increase of efficiency of a refrigerator may result in great amounts of energy savings. In order to increase efficiency, energy losses must be minimized as much as possible. Energy losses due to friction, which can be named as friction losses, mostly occur with the contact of relatively moving components.

In order to reduce friction losses, the material pair having the lowest possible coefficient of friction should be investigated.

Gray cast iron is commonly used as crankshaft material because of its low cost and ease of machinability. Polytetrafluoroethylene (PTFE) is a remarkable material known for its tribological behavior, and low weight. In order to improve wear resistance and frictional behavior PTFE is reinforced with some

additives [1,2] i.e. bronze, carbon, carbon fiber, glass-fiber, alumina [3,4,5].

2. EXPERIMENTAL STUDY

In this study, pin on ring method is used; friction coefficients and wear losses of various reinforced PTFE sliding against gray cast iron are investigated experimentally under lubricated friction conditions at different loads and speeds.

2.1 Test setup and materials

In pin on ring system, gray cast iron is employed as ring material and PTFE material having 3 different reinforcing material ratios are employed as pin component. Moreover, a commercially available refrigeration oil named as Suniso 1GS, is used to lubricate the contact surface of the ring and pin components. Schematic view of the pin on ring system and lubrication tank is shown is shown in Figure 1.
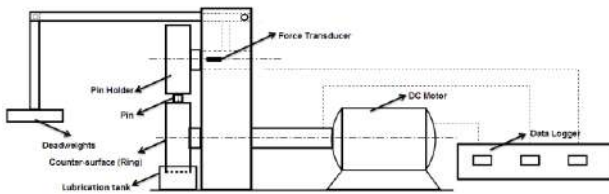
Figure 1. Schematic view of the test system

In order to determine friction and wear characteristics of the test samples, a pin on ring apparatus was employed. In this apparatus, pin stays stationary and in contact to the outer surface of the rotating ring. Because of this rotating motion, a friction force takes place between contact surface of pin and ring. The friction force is measured by a force transducer which is located on the fixed end of the pin holder. The force transducer has a range of ±200 N with a sensitivity of ±0,1 N. The ring is driven by a DC motor with rotational speed range of 30-900 rpm. The wear rate of the test specimens were computed based on the loss of mass and the mass was measured by using a scale which has 0,0001g accuracy. In addition, a three point infra-red thermometer, which has a range of -20 ℃ to 900 ℃ with a sensitivity of ±2 ℃, was used to measure the temperature of the contact surface.

In experiments, the rotating ring was made of GGG40 gray cast iron. The ring has as 59 mm in diameter and 15 mm in thickness. Pins are made of PTFE materials having 3 different reinforcement ratios, which have 10 mm diameter and 12 mm length, for the ease of assembly to the system. In experiments, wt. 25% glass fiber, wt. 60% bronze and wt. 35% carbon filled PTFE materials were used. In Figure 2, gray cast iron and reinforced PTFE samples are shown.

Figure 2. The ring and pin components

Furthermore, the above mentioned refrigeration oil which has approximately 11,5-14,5 cSt kinematic viscosity at 25 ℃ - 38 ℃ (according to ASTM D2161/D445) [6] and has specific gravity of 0,887-0,904 at 15,6 ℃.

2.2 Test procedure

At the beginning of experiments, counter face (ring) is attached to the DC motor shaft and pin is placed to the pin holder. After that, deadweights are placed to the lever arm of the system. In addition lubrication tank is filled with refrigeration oil and located underneath of the ring as it can be seen in Figure 3.

Figure 3. Assembly of the system.

In order to obtain proper surface contact between material pair, a pre-running operation was executed. Thus, undesired partial contact between pin and ring was prevented. Besides pin and ring surfaces were cleaned with carbon tetrachloride to make sure the absence of any contaminant.

In experiments 2 different normal loads were applied; 50 N and 100N at the linear velocity of 1 m/s. During the experiments friction force and temperature values were recorded. Also the mass of the pins were measured before and after tests. The wear rate is calculated according to the formula given below

$$K_s = \frac{\Delta m}{F \cdot L} \tag{1}$$

where, Δm is the loss of mass [g], F is the normal load [N], and L is the sliding distance [m]. Sliding distance was set to 2000 m for both friction and wear tests.
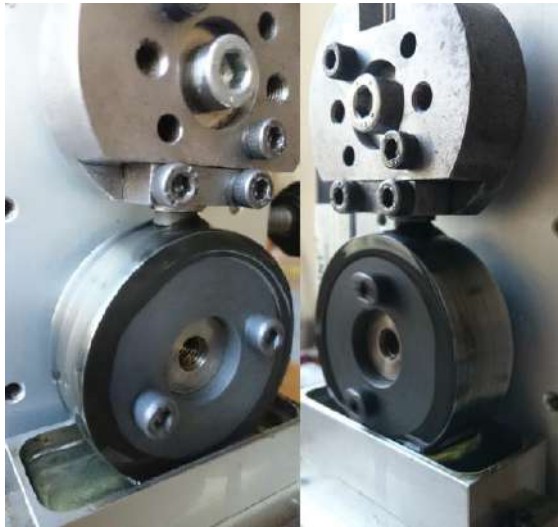
Figure 4. Pin holder and ring surface during the tests for lubricated conditions.

In figure 4, it can be seen that, oil bath lubrication was applied in the tests. Lubricant cap is filled with Suniso 1GS and placed under the ring. When ring rotates, proper amount of oil transfers to the ring surface and reaches to the contact surface. Thus mixed-film lubrication mechanism is ensured.

3. RESULTS AND DISCUSSIONS

In this study, tribological characteristics of various reinforced PTFE sliding against cast iron were investigated experimentally.
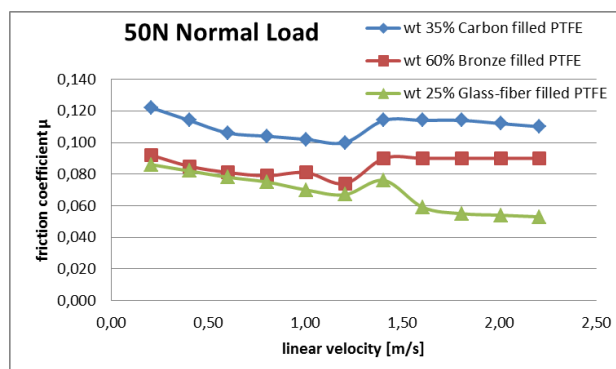
Figure 5. Variation of friction coefficient with sliding speed under 50 N load for lubricated conditions.

At the beginning, the effect of sliding speed on friction coefficient was investigated. Under

50 N load and lubricated conditions, the sliding speed of 2,5 m/s is reached with 0,2 m/s steps. Figure 5 shows these friction coefficient results of reinforced PTFE materials sliding against gray cast iron surface.

It can be said that all three filled PTFE has similar friction coefficient variations with sliding speed.
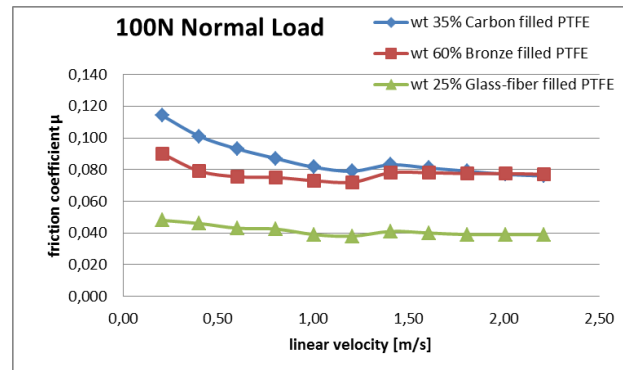
Figure 6. Variation of friction coefficient with sliding speed under 100 N load for lubricated conditions.

The same test was repeated under 100 N load and results are shown in Figure 6. Both friction coefficient curves and sequence of pin materials remained similar comparing to Figure 5.

After these results, linear velocity of 1 m/s was chosen as a constant parameter and the friction and wear test were performed until 2000 m sliding distance was reached.
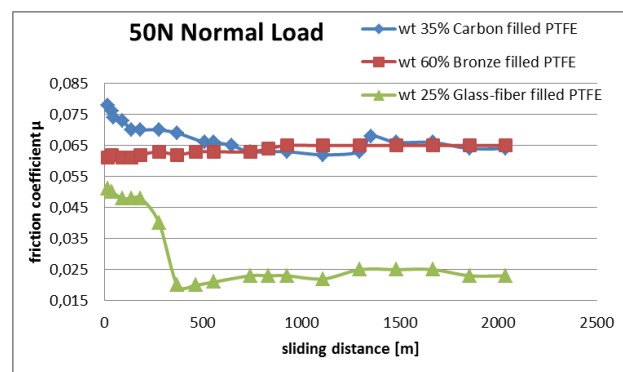
Figure 7. Variation of friction coefficient with sliding distance under 50 N load for lubricated conditions.

In the tests under 50 N normal load wt. 25% glass-fiber filled PTFE showed remarkably lower friction coefficients than other materials in Figure 7.

However, as the normal load increases the minimum friction coefficient values was

obtained for wt. 35% Carbon reinforced PTFE as seen in Figure 8.
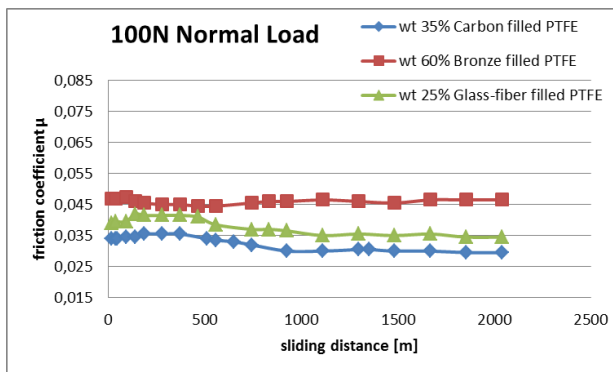
Figure 8. Variation of friction coefficient with sliding distance under 100 N load for lubricated conditions.

During tests, temperature of a portion of the ring which is very close to the contact surfaces was measured by using infra-red thermometer. Recorded data are given in Figure 9. As it can be seen from the Figure 9, good lubrication practice prevented the surfaces to reach high temperatures and slope of the curve decreased with sliding distance.
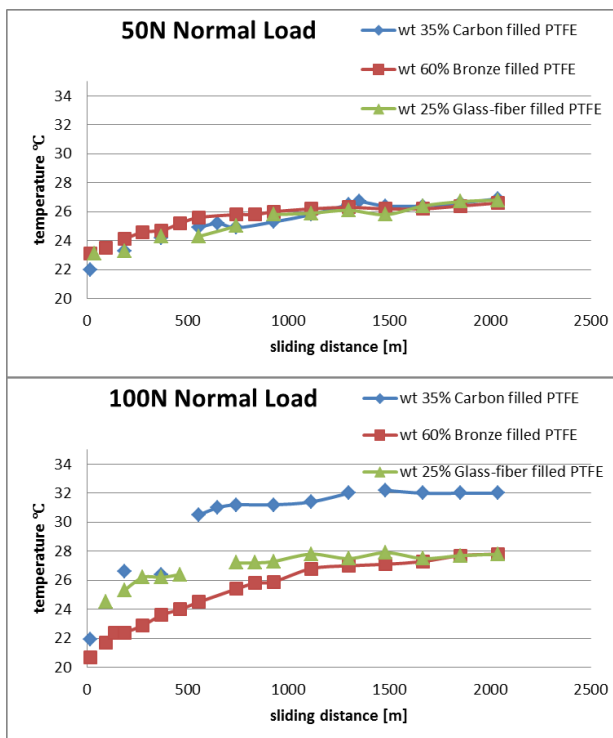
Figure 9. Temperature vs Sliding distance graph under 50 and 100 N loads and lubricated conditions.

The mass of the pin was measured before and after each experiment, and the loss of mass was recorded. Regarding the loss of mass,

applied loads and sliding distances, wear rates of each material were computed. The wear characteristics results can be seen in Table 1. After these systematical experiments, the sliding surface of the pins was examined under the optical microscope. Considering sliding direction, all specimens were placed in the same direction. Optical micrographs of these specimens were taken by a digital camera attached to optical microscope.

Table 1. Loss of pin materials per load and distance

	Under 50N load	Under 100N load
	10^{-9} [g/(N.m)]	10^{-9} [g/(N.m)]
wt. 35% Carbon	11	3
wt. 60% Bronze	26	44
wt. 25% Glass-fiber	19	4
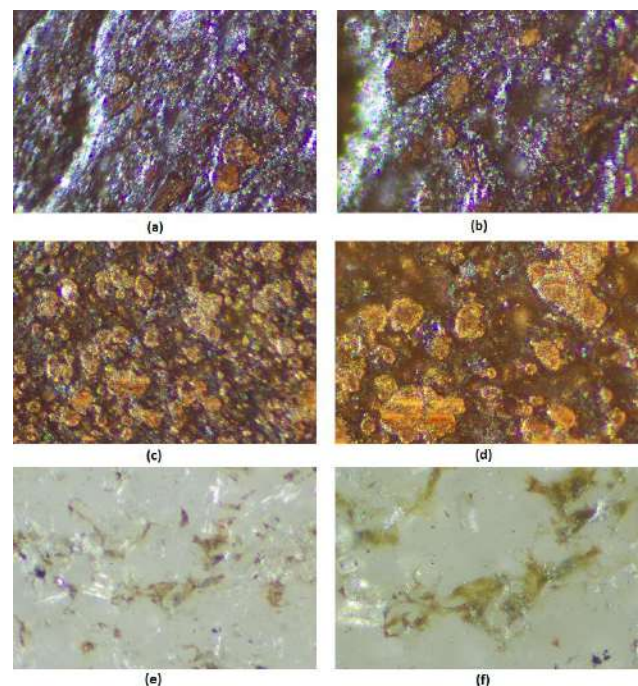
Figure 10. Micrographs of specimens after lubricated friction tests, from top to bottom, wt. 35% Carbon filled PTFE, wt. 60% Bronze filled PTFE, wt. 25% Glass-fiber filled PTFE; from left to right 100 times and 200 times growth, respectively.

In Figure 10, the optical micrographs of the pin surfaces are given for 100 and 200 magnification ratios respectively. In Figure 10, (a) shows wt. 35% Carbon filled PTFE with magnification ratio of 100; (b) shows wt. 35% Carbon filled PTFE with magnification ratio of

200; (c) shows wt. 60% Bronze filled PTFE with magnification ratio of 100; (d) shows wt. 60% Bronze filled PTFE with magnification ratio of 200; (e) shows wt. 25% Glass-fiber filled PTFE with magnification ratio of 100; (f) shows wt. 25% Glass-fiber filled PTFE with magnification ratio of 200.

4. CONCLUSION

Regarding the above discussions, the following results can be reached from this study.

✓ In the presence of lubricant, 25% glass-fiber filled PTFE gives the lowest friction coefficient values for all cases.

✓ For all materials, coefficient of friction decreases with increasing speed. This is caused by transfer of more oil in contact region reducing the dry contact points.

✓ The variation of coefficient of friction with sliding distance shows different pattern for lower and higher loads. In lower normal loads wt. 25% glass-fiber filled PTFE gives lower friction coefficient values through the 2000 m distance. As the normal load increases, wt. 35% carbon filled PTFE gives lower friction coefficient values. This caused by the lubricating effect of carbon taking effect after relatively higher surface pressures.

✓ In Figure 7, it can be seen that under 50 N normal load, friction coefficient of wt. 25% glass-fiber filled PTFE dramatically decreased around 500 m sliding distance and remained around same friction coefficient values.

✓ The increase of load resulted in decrease of both friction coefficient and wear rate. This finding can be explained by the ease of transfer film formation at higher surface pressure.

✓ The good thermal properties of bronze shows its effect at the surface temperatures (Fig.9).

✓ The wear rate of wt. 60% Bronze filled PTFE is remarkably higher than the other specimens (approximately 10 times disregarding specific weight). This is caused by the weak bonding between PTFE and bronze material. The increase in the wear rate of this material with increasing load supports this conclusion.

REFERENCES

[1] Y. Şahin, H. Mirzayev: Wear Characteristics of Polymer-Based Composites, Mechanics of Composite Materials, Vol. 51, No. 5, pp. 543-554, 2015.

[2] Z. Parlar, S. Samankan, V. Temiz: The Effect of Counter-face Roughness on the Tribological Behavior of Filled and Unfilled PTFE, Journal of Mechanics Engineering and Automation, Vol. 5, No. 11, pp. 609-615, 2015.

[3] W. G. Sawyer, K. D. Freudenberg, P. Bhimaraj, L. S. Schadler: A Study on the Friction and Wear Behavior of PTFE Filled with Alumina Nanoparticles, Wear, Vol. 254, No. 3-4, 254, pp. 573-580, 2003.

[4] R. K. Goyal, M. Yadav: The Wear and Friction Behavior of Novel Polytetrafluoroethylene / Expanded Graphite Nanocomposites for Tribology Application, Journal of Tribology, Vol: 136, 021601-1-5, 2014.

[5] İ. Kaya, V. G. Kaya, Z. Parlar, V. Temiz: The Investigation of Friction Coefficient and Wear Characteristic of Gray Cast Iron Against Reinforced Polytetrafluoroethylene (PTFE) in Refrigerator Compressors Crankshaft and Bearings, in : Tribological Journal Bultrib, 27-29.10.2016, Sofia, Bulgaria

[6] ASTM D2161-10 Standard Practice for Conversion of Kinematic Viscosity to Saybolt Universal Viscosity or to Saybolt Furol Viscosity, 2016.

THE ACCELERATED AGING EFFECT OF SALT WATER ON LIGNOCELLULOSIC FIBRE REINFORCED COMPOSITES

Cristiano FRAGASSA[1], Ana PAVLOVIC[1],*, Irena ZiIVKOVIC[2]

[1] Department of Industrial Engineering, University of Bologna, Viale Risorgimento 2, 40136, Bologna, Italy
[2] Faculty of Applied Arts, University of Arts, Belgrade, Kralja Petra 4, 11000 Belgrade, Serbia
* Corresponding author: ana.pavlovic@unibo.it

Abstract: In recent years natural fibre reinforced composite materials have received an increasing attention in consideration of their biodegradability and admirable mechanical properties. The present paper reveals the experimental observations and results of accelerated aging in the cases of ecological composite materials made by lignocellulosic fibres and an eco-friendly resin, when exposed to salt water and temperature. In particular, this research aims at verifying the potential of flax, as a natural fibre reinforcement, coupled with a vinylester with low content of styrene as matrix. Two types of specimens, dried and conditioned, were tested and results compared in terms of flexural strength. Fluid absorption was also monitored. In addition, surface characterization by 3D digital microscope was implemented. Results show an effectiveness of flax as reinforcement, but also a significant drop in flexural properties due to the water absorption which induced the degradation of the fibre/matrix interface.

Keywords: green composites, flax, vinylester, accelerated aging, salt water flexural strength, microstructures

1. INTRODUCTION

Nowadays, glass fibres surely represent the most preferred reinforcement for composites in the largest gamma applications, as of marine, thanks to a favourable combination of low-cost draft materials, efficient productive technologies [1-3] and high resistance to the effects of degradation. Whenever better properties in materials are necessary and extra costs can be accepted, then, carbon fibres are used to replace glass ones and autoclaves appear in processes [4]. But, unfortunately, neither glass, nor carbon fibres offer the ecosustainable option that meets the modern customers' expectations and desires.

Meanwhile, the use of lignocellulosic fibres (such as wood, flax, hemp, etc.) probably represents the most prominent eco-strategy for reinforcing composite materials by natural fibres [5-6]. In particular, in several investigations (as [7, 8]), it is highlighted that, although the mechanical properties of these eco-composites are usually lower than fibreglass [9] and material costs are often higher, they can even be appreciated in practical applications [10]. In the marine sector, this is the case, e.g., of applications for non-structural parts (such as coverings, panels, parts of deck, hatches [12]), where a slight loss in strength and higher costs can be offset by

the advantages of an environmental awareness.

Nevertheless, the hydrophilic character of the lignocellulosic fibres, together with a consequent reduction in mechanical properties [13-15], can represent a relevant obstacle for the application of natural reinforcements in marine industry or other outdoor constructions. Many researches tried to investigate and solve this criticality [16-19], without providing a definite response.

This research aims at enlarging the current knowledge on eco-composites focusing the attention on flax as natural reinforcement and on a specific vinylester with low content and emission of styrene, as eco-matrix.

Referring to the selection of reinforcement, in comparison with other lignocellulosic fibres, flax fibres present significantly better mechanical properties [20-21], but several precautions have to be taken in account, both in terms of production and use. For instance, previous researches [24] demonstrated that flax fibres start to slowly degrade between 200°C and 220°C. Above this temperature, the degradation of fibres is irreversible which sets a limit excluding the possibility of using thermoplastic polymers with a melting point higher than this value [23].

Referring to the selection of matrix, among all resins respecting this thermal limit, vinylester represents a very popular choice in marine industry [25, 26]. Anyway, considering the use of a reinforcement fibre (flax) quite uncommon for marine applications, a special attention has to be reserved during the experiment in investigating the correct interaction between matrix and fibres.

This aspect could be particularly critical in marine application considering the prolonged contact between composites and salt water. In fact, moisture absorption strongly influences interface adhesion between lignocellulosic fibre and polymer matrix, creating in turn poor stress transfer efficiency while causing a decline in the mechanical properties. In polymer matrix composites, diffusion of moisture occurs through three different mechanisms: diffusion between polymer chains; capillary transport into the flaws at the interface between reinforcement and matrix; and moisture transport into the fibres causing swelling of lignocellulosic composition [27, 28].

In comparison with other resins, vinylester shows low moisture absorption and a good resistance to ultraviolet rays whose nature plays a significant role in the aging behaviour of composites for marine purposes [29]. In particular, according to [30] eco-composites with vinylester matrix seem to show a limited surface damage even with long-term influence of moisture, but this damage can decrease flexural strength and impact resistance [31] of composites structures, as demonstrated for other fibres.

2. MATERIALS AND METHODS

This study aims at investigating the potential influence of a marine environment on the flexural properties of flax fibre reinforced vinylester ecomatrix composites. An accelerated aging was realized by submerging specimens in hot and salt water for a long period. Liquid absorption was monitored by measures of weight. Surface effects and other material damages were observed by 3D digital microscopy, comparing dry and conditioned specimens.

In particular, a commercial flax reinforcement (LINEO® FLAXPLY BL), consisting of 70% cellulose and characterized by 300 gr/m2 (flax weight per square meter), balanced fabrics (0°/90°) was used [32]. This bio-based eco-friendly reinforcement can be used with all conventional processes (RTM, infusion, hand lay-up…), In addition, it offers acceptable mechanical properties that, coupled with low density, enables a general weight reduction.

Referring to the matrix, a commercial vinylester (DISTITRON ® VEef 220 STZ), characterized by Low Styrene Emission (LSE) properties was used [33]. It is a thixotropic preaccelerated vinylester resin with interesting mechanical and thermal characteristics providing both excellent chemical resistance to prevent blistering

formation and low shrinkage to guarantee a good finishing. In order to comply with environmental requirements for VOC, the resin contains less than 35% of styrene, without including any other monomer in its formulation, to minimize emissions during application and a LSE system to block the during curing.

Properties of fibres and vinylester matrix declared by material manufacturers and vendors are shown, respectively, in Table 1 and Table 2. In the case of resin (Table 2), the values of strength, elongation and modulus represent the properties a cured (24h at 23°C + 3h at 100°C) unreinforced condition.

Table 1. Main properties of flax fibres [30]

Property	Unit	Value
Density	g/cm^3	1.40
Tensile strength	MPa	1034
Tensile modulus	GPa	51.0
Elongation at break	%	1.5

Table 2. Main properties of vinylester matrix [31]

Property	Unit	Value
Density at 25°C	g/cm^3	1.03 – 1.16
Viscosity at 25°C	mPa.s	1900 – 2550
Volatile content	%	<35
Gel time	Min	36 – 49
Curing time	Min	39 – 70
Glass transition T.	°C	115
Tensile strength	MPa	65
Tensile modulus	MPa	3500
Elongation at break	%	2.0
Flexural strength	MPa	105
Flexural modulus	MPa	3600

3. SPECIMENS PREPARATION

Laminates manufacturing was conducted by a wet lay-up hand laminating process overlapping 8 layers of flax balanced fabric and vinylester matrix, with a 24h long cure at room temperature followed by a 3h long post-cure at 100°C. After curing, composites were characterized by a total ratio of lignocellulosic reinforcement of 57.3% (in weight). After post-curing and cooling, the specimens were extracted out from the original laminate by diamond saw and tool machining. Half of the samples (dry) were prepared for flexural testing in dry conditions and the other half (conditioned) was subjected to the accelerated aging immerging them for 1000h in 35 ppt salt water at 80 °C. This solution, prepared with 35% g/L of NaCl, intends to represent the overall proportion of inorganic salts representative of ocean water (in accordance with ASTM D1141 [34]), but, for the sake of simplicity, without introducing each salt (as MgCl2, Na2SO4, …).

Immersed specimens in their bath are shown in Figure 1. The presence of plastic spacers and a frequent manipulation of specimens (for their reallocation) were used to guarantee a homogenous condition of immersion, even in the case of a little container, in accordance with the appropriate dimensions for the T-controlled oven at disposal.

Figure 1. Specimens in immersion in salt water

4. ABSORBTION MONITORING

In order to determine the stability of the composites, gravimetric water absorption analysis was done. The specimens were dried for 24h at 60C and cooled to room temperature in a desiccator and the initial weight (w0) was taken to the nearest 0.001g. The specimens were then immersed in the solution and weekly extracted for weight recording. In these monitoring events, the water on the surface was wiped away and the weight of each specimen was taken again (w). All specimens were analysed and the average

weight was taken. The percentage of water absorption (WA in %) was calculated using the Equation (1):

$$WA = \left(\frac{w\text{-}w_0}{w_0}\right) \times 100 \qquad (1)$$

where, wo represents the initial weight after drying and w the weight after water immersion.

In Table 3, the change in weight of specimens is reported along with a absorption rate estimative.

Table 3. Measure of weight and absorption estimation

Specimen	Weight [10^{-3} kg]		Absorption
	dry	aged	[%]
LVFC1	13.354	14.308	7.14
LVFC2	13.766	14.631	6.28
LVFC3	14.400	15.362	6.68
LVFC4	14.764	15.709	6.40
LVFC5	14.763	15.622	5.82
Mean	*14.209*	*15.126*	*6.46*
St. Dev..	*0.62*	*0.62*	*0.48*

Furthermore, with the aim at providing useful references for a better comprehension of the absorption phenomena in composites, laminates from other materials were also manufactured and their samples conditioned at the same environmental conditions (salt water at 15%, 80 °C, 1000hr). Specific resins and fibres were selected with the scope to be highly representative in respect to the main material under investigation (low-styrene vinylester, reinforced by flax). In particular, the same "green" vinylester was used as matrix, but reinforced by basalt or by a mix of basalt and flax fibres (as also reported in [35, 36]). In this way, the specific effect of flax on water absorption rate could be easily analysed thanks to the constancy of matrix. In addition, as inevitable reference, a fibreglass laminate was also realized, but selecting a standard vinylester.

A comparison among the different absorption tendencies is available in Table 4. Values are reported in terms of weight improvement (in %) in respect to the dry materials. 7 specimens for each materials were used. Weight was initially evaluated in wet conditions, after 6 hours from the first immersion, and, then, weekly till the end of the aging period (1000hrs).

Table 4. Weight improvement (regarding dry specimens) for different fibres and vinylesters

Matrix	Fibres	Wet	Aged
Vinylester^{stand}	Glass	0.40%	0.67%
Vinylester^{eco}	Basalt	0.31%	0.67%
Vinylester^{eco}	Basalt & Flax	2.01%	5.01%
Vinylester^{eco}	Flax	2.81%	6.18%

Table 4 shows that:
- vinylesters are not particularly sensitive to the aging effect of salt water, neither standard nor "green", confirming a behaviour quite different from Fick's theory of diffusion and a gain in weight much lower than other common commercial resins [37].
- fiberglass is extremely stable and inert confirming its properness for marine applications;
- basalt, an emerging and sustainable material, especially interesting for its extreme mechanical properties, offer a similar stability when compared with carbon [9, 35];
- flax seems to significantly accelerate the water absorption.

As a probable consequence of this last feature, it is expected that several material properties of flax fibre reinforced composites change in consideration of immersion in water.

5. EXPERIMENTAL TEST

The flexural strength in the case of dry and conditioned composites (before and after water immersion) was determined by an Instron 8033 servo-hydraulic testing machine, using a three-point bending test method. Tests were performed according to ASTM D7264 [38], an experimental standard for flexural properties determination of polymer matrix composite materials. Specimens were placed over two supports. Loads were applied midway by a bar with rectangular cross section and a crosshead speed of 2mm/min. A span of 80 mm was used in a 25 kN load cell. Test stages are shown in Figure 2. Photographs of

dry and conditioned specimens after flexural testing are shown on the Figure 3.

Figure 2. Sequential images from the flexural test
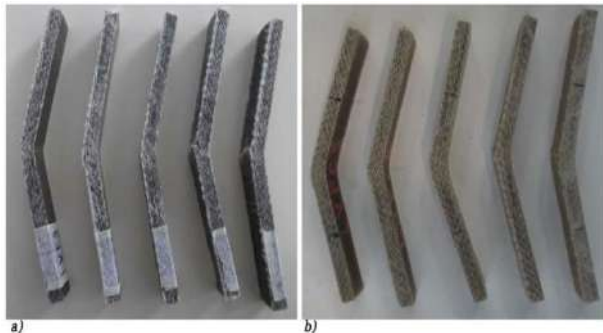
Figure 3. Specimens after three-point flexural testing: a) dry and b) conditioned

6. RESULTS AND DISCUSSION

Experimental results obtained during flexural testing are summarized in Table 5 while stress-strain diagrams are shown in Figures 4 and 5 for, respectively, dry and conditioned specimens

Table 5. Flexural strength and strain at break for dry and conditioned specimens

	Dry		Conditioned	
	Strength MPa	Strain %	Strength MPa	Strain %
	140.9	5.77	74.8	6.51
	122.9	5.25	76.3	6.48
	130.9	6.28	77.2	6.48
	120.6	5.23	79.8	7.14
	131.7	5.34	72.9	6.25
Mean	129.4	5.57	76.2	6.57
Dev.St.	8.1	0.45	2.6	0.33

Improvements in the flexural strength offered by the flax reinforcement can be immediately noticed. Comparing the values of flexural strength of cured, but unreinforced resin, as declared by vendor and reported in Table 2, with the experimental data, it is possible to estimate, on average, an increasing

of 22.8% (from 105 MPa to 129±8 MPa) in this property and a peak of 33% in the case of the specimen that, with 140 MPa, showed the best performance during tests.
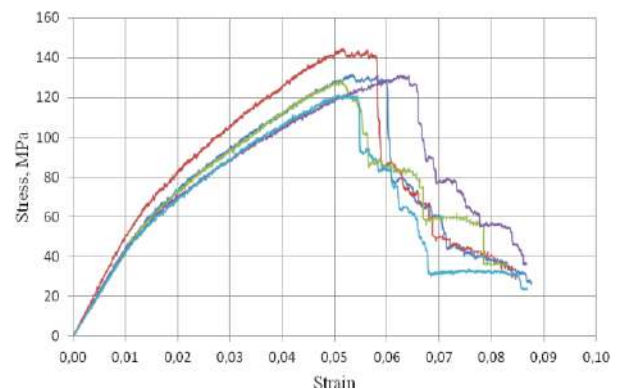
Figure 4. Flexural stress-strain diagrams for dry flax/vinylester composites
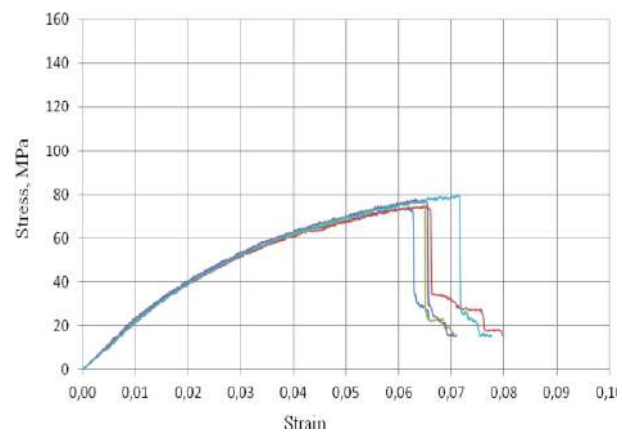
Figure 5. Flexural stress-strain diagrams for conditioned flax/vinylester composites

These results are in line with similar researches, as reported in [39], where the influence of direction of fibres on the flexural properties in a flax fibre-reinforced composite (with acrylated epoxidized soybean matrix) was analysed. In particular, it is demonstrated that significantly better improvements could be obtained when a unidirectional fabric is preferred to the balanced one. Material technical datasheet for this specific reinforcement highlights, for instance, an ultimate stress strength in flexion up to 300 MPa in the case of 12 layers of unidirectional fabrics [30]. But, with only 180 gr of flax/m² (instead of 300 gr) and 4 additional layers, this solution appeared less interesting in terms of productivity, costs and ecosustainability.

Meanwhile, a decrease in mechanical resistance of the conditioned specimens

compared to the dry specimens can be also immediately noticed. In particular, referring to the mean values, the flexural strength fall from 129.4 MPa to 76.2 MPa, losing more than 40%. On the contrary, the strain at break highlights a light increase, about +14%, from 5.57% to 6.57%. In other terms, accelerated aging by salt water and temperature improves the material ductility and reduces its mechanical resistance.

This phenomenon of brittle rupture is also suggested by the stress-strain diagram where the effect of first break, in the case of conditioned specimens, consists of a sudden and steeper fall.

Another noteworthy aspect, emerged from experiments, less evident at first sight, is related to the change in variability of the experimental values and its physical sense. In particular, Figures 4 shows a larger variability in the elastoplastic behaviour in the case of dry composites. Even if the strain at break is almost the same for all samples (6.57±0.33%) while the maximum stress shows relatively slight variances (129±8 MPa), their stress-strain diagrams look quite different between specimens. In contrast, the stress-strain diagrams for conditioned composites are identical to the ultimate stress, as shown in Figures 5. In other terms, water absorption and accelerated aging tend to level the difference in material structures and, as a consequence, in their mechanical properties.
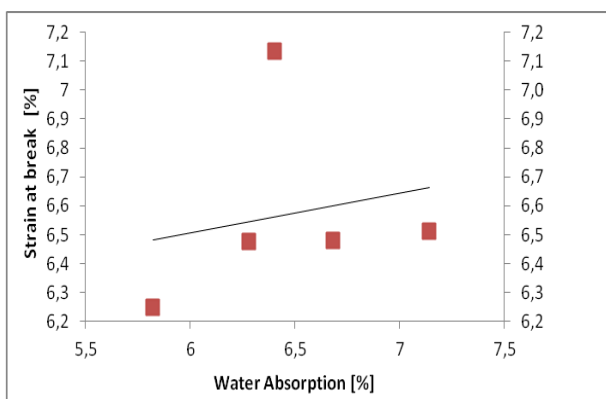
Figure 6. Relation between strain at break and water absorption

This supposition was also investigated trying to directly relate the flexural behaviour to the moisture absorption. In Figure 6, the strain at break is plotted versus the water absorption (expressed in %). Even if the reduced number of specimens and the variability of the phenomena do not permit a definite response, a slight incremental correlation can be initially observed. Further tests are necessary before any confirmation.

7. FURTHER CONSIDERATIONS

The degradation of mechanical properties can be related to the formation of hydrogen bonding between the water molecules and lignocellulosic fibres. Hydrophilic nature of lignocellulosic fibres with a large number of hydroxyl groups in the fibre structure enables formation of a large number of hydrogen bonds between the macromolecules of the cellulose and polymer matrix. This process is described in [38] and demonstrates that natural lignocellulosic fibres, such as flax, due to the intense presence of –OH groups, exhibit a very low resistance in the aquatic environment. In addition, the reduction in the interfacial adhesion between fibre and matrix causes dimensional variation and leads to decrease the mechanical properties these materials (as reported in [28, 41]).

The drop in strength seems too intense to be explained only by formation of a large number of hydrogen bonds between the macromolecules of the cellulosic reinforcement and polymer matrix: also polymer matrix degradation has to be present [42].

The hydrophilic flax fibre, attacked by the salt water, starts swelling, causing micro cracking of the brittle polymer matrix. At the same time, flax fibres, due to their high cellulose content, attract the water molecules which penetrate into the interface through these micro cracks activating capillarity transport of water to the interface region of composite material. Thus, the process of water diffusion through the matrix takes place, causing delamination and seriously damage of composite material (as detailed in [43]).

A validation of this hypothesis was investigated at the microscopic scale. Images obtained by HIROX multifocal 3D digital microscope are shown in Figure 7 and Figure 8.

These micrographs confirm that the vinylester embrittles with aging, but also highlight the presence of structural defects in materials as delamination and micro cracking.

The limit introduced by the hydrophilic nature of lignocellulosic fibres could be practically solved in applications with the addition a skin coat on the composite's surfaces. The skin coat can be composite laminate with water resistant reinforcement as basalt fibre, which can also improve mechanical properties of composite structure [27, 28].

Figure 7. Micrographs of composite surfaces, before (a) and after (b) the aging, showing the effect of embrittlement

☐ **Delamination**   ⬭ **Micro-cracking**

Figure 8. Micrograph of a specimen after aging, showing structural defects

8. CONCLUSIONS

The effect of the salt water on the mechanical properties of flax fiber reinforced vinylester matrix composites was investigated by accelerated aging, flexural tests and micrographs. Experimental results confirm that natural flax reinforcements really improve the properties of composites and that, in general, vinylester represents a valid solution as matrix in marine applications because of the good mechanical properties and low absorption rate it presents. Contemporaneously, the same results demonstrate that, in the case of vinylester reinforced by flax, a significant drop in flexural properties is due to the substantial water absorption that induces several phenomena, including the degradation of the fibre/matrix interface. Under the influence of moisture the hydrophilic flax fibre swells and micro cracking of the brittle polymer matrix occurs. Than the molecules of water penetrate into the interface and the process of water diffusion through the matrix causes delamination and seriously damage of the composite material. Microscopic analysis proves micro cracking and delamination damage mechanisms into the accelerated aged composite materials during flexural testing. It should be noted that vinylester resin continues to cure during accelerated aging which makes it more brittle than in dry condition. To overcome the problem of water absorption sensitivity authors recommended the usage of basalt fibre based skin coat on both sides of the lignocellulosic fibre reinforced composite material.

REFERENCES

[1] P. Compston, P-YB Jar, and P. Davies: Matrix effect on the static and dynamic interlaminar fracture toughness of glass-fibre marine composites, Composites Part B: Engineering, Vol. 29, No. 4, pp. 505-516, 1998.

[2] A. P. Mouritz, A. Kootsookos, and G. Mathys: Stability of polyester-and vinyl ester-based composites in seawater, Journal of materials science, Vol. 39, No. 19, pp. 6073-6077, 2004.

[3] F. Vannucchi de Camargo, C.E.M. Guilherme, C. Fragassa and A. Pavlovic,: Cyclic Stress Analysis of Polyester, Aramid, Polyethylene and Liquid Crystal Polymer Yarns, Acta Polytechnica, Vol. 56, No. 5, pp. 402-408, 2016.

[4] M. N. Alias and R. Brown: Corrosion behavior of carbon fiber composites in the marine environment, Corrosion science, Vol. 35, No. 1, pp. 395-402, 1993.

[5] O. Faruk, A.K. Bledzki, H.P. Fink and M. Sain: Biocomposites reinforced with natural fibers: 2000–2010, Progress in polymer science, Vol. 37, No. 11, pp. 1552-1596, 2012.

[6] S. De Paola, C. Fragassa, G. Minak and A. Pavlovic: Green composites: A review of state of art, in: 30th Danubia-Adria Symposium on Advances in Experimental Mechanics, DAS 2013 - Proceedings, 77-78, 2013.

[7] S. Kalia, A. Dufresne, B. M. Cherian, B. S. Kaith, L. Avérous, J. Njuguna, and E. Nassiopoulos: Cellulose-based bio-and nanocomposites: a review, International Journal of Polymer Science, Vol. 2011, Article ID 837875, pp. 1-35 , 2011, doi: 10.1155/2011/837875

[8] O. Adekomaya, T. Jamiru, R. Sadiku, Z. Huan: A review on the sustainability of natural fiber in matrix reinforcement–A practical perspective, Journal of Reinforced Plastics and Composites, Vol. 35, No. 1, pp. 3-7, 2016.

[9] A. Hyseni, S. De Paola, G. Minak and C. Fragassa: echanical characterization of ecocomposites, in: 30th Danubia-Adria Symposium on Advances in Experimental Mechanics, DAS 2013 - Proceedings, 175-176

[10] S. Pilla, Handbook of bioplastics and biocomposites engineering applications, John Wiley and Sons, 2011.

[11] J. B. Cleveland, The potential application of Natural Fiber Reinforced Bio-polymer (NFRbP) Composites in Architecture, ProQuest, 2008.

[12] C. Fragassa: Marine Applications of Natural Fibre-Reinforced Composites: A Manufacturing Case Study, In: Advances in Application of Industrial Biomaterials, Springer, 2017.

[13] K. G. Satyanarayana, G. G. C. Arizaga and F. Wypych: Biodegradable composites based on lignocellulosic fibers - An overview, Progress in polymer science, Vol. 34, No. 9, pp. 982-1021, 2009.

[14] A. K. Bledzki and J. Gassan: Composites reinforced with cellulose based fibres, Progress in polymer science, Vol. 24, No. 2, pp. 221-274, 1999.

[15] H. M. Akil, C. Santulli, F. Sarasini, J. Tirillò and T. Valente: Environmental effects on the mechanical behaviour of pultruded jute/glass fibre-reinforced polyester hybrid composites, Composites Science and Technology, Vol. 94, pp. 62-70, 2014.

[16] I. Zivkovic, A. Pavlovic and C. Fragassa: Improvements in wood thermoplastic matrix composite materials properties by physical and chemical treatments, International Journal of Quality Research, Vol. 10 , No. 1, pp. 205-2018, 2016.

[17] M.D.H. Beg and K. L. Pickering: Reprocessing of wood fibre reinforced polypropylene composites. Part I: Effects on physical and mechanical properties, Composites Part A: Applied Science and Manufacturing, Vol. 39, No. 7, pp. 1091-1100, 2008.

[18] M. Bengtsson and K. Oksman: The use of silane technology in crosslinking polyethylene/wood flour composites, Composites Part A: applied science and manufacturing, Vol. 37, No. 5, pp. 752-765, 2006.

[19] A. K. Bledzki, O. Faruk and M. Huque: Physico-mechanical studies of wood fiber reinforced composites, Polymer-Plastics Technology and Engineering, Vol. 41, No. 3, pp. 435-451, 2002.

[20] G. Romhány, J. Karger Kocsis, and T. Czigány: Tensile Fracture and Failure Behavior of Thermoplastic Starch with Unidirectional and Cross Ply Flax Fiber Reinforcements, Macromolecular Materials and Engineering, Vol. 288, No. 9, pp. 699-707, 2003.

[21] P. Wambua, J. Ivens, and I. Verpoest: Natural fibres: can they replace glass in fibre reinforced plastics?, Composites science and technology, Vol. 63, No. 9, pp. 1259-1264, 2003.

[22] J. Meredith, S. R. Coles, R. Powe, E. Collings, S. Cozien-Cazuc, B. Weager and K. Kirwan: On the static and dynamic properties of flax and Cordenka epoxy composites, Composites Science and Technology, Vol. 80, pp. 31-38, 2013.

[23] S. Alimuzzaman, R. H. Gong and M. Akonda: Nonwoven polylactic acid and flax

biocomposites, Polymer Composites, Vol. 34, No.10, pp. 1611-1619, 2013.

[24] B. Wielage, T. Lampke, G. Marx, K. Nestler and D. Starke: Thermogravimetric and differential scanning calorimetric analysis of natural fibres and polypropylene, Thermochimica Acta, Vol. 337, No. 1, pp. 169-177, 1999.

[25] A. M. Figliolini, and L. A. Carlsson: Seawater Aging of Vinylester and Carbon Reinforced Vinylester, Durability of Composites in a Marine Environment, Vol. 208, pp. 143-153, 2014.

[26] F. A. Almansour, H. N. Dhakal, Z. Y. Zhang and H. Ghasemnejad: Effect of hybridization on the mode II fracture toughness properties of flax/vinyl ester composites. Polymer Composites, 2015, doi:10.1002/pc.23743

[27] A. Espert, F. Vilaplana and S. Karlsson: Comparison of water absorption in natural cellulosic fibres from wood and one-year crops in polypropylene composites and its influence on their mechanical properties, Composites Part A: Applied Science and Manufacturing, Vol. 35, No. 11, pp.1267-1276, 2004.

[28] H. N. Dhakal, Z. Y. Zhang and M. O. W. Richardson: Effect of water absorption on the mechanical properties of hemp fibre reinforced unsaturated polyester composites, Composites science and technology, Vol. 67, No. 7, pp. 1674-1683, 2007.

[29] K. Shivakumar, G. Swaminathan and M. Sharpe: Carbon/Vinyl Ester Composites for Enhanced Performance in Marine Applications, Reinforced Plastics and Composites, Vol. 25, No. 10, pp. 1101-1116, 2006.

[30] A. Afshar, M. Alkhader, C. S. Korach and F. P. Chiang: Effect of long-term exposure to marine environments on the flexural properties of carbon fiber vinylester composites, Composite Structures, Vol. 126, pp. 72-77, 2015.

[31] I. Živković, C. Fragassa, A. Pavlovic, and T.M. Brugo: Influence of moisture absorption on the impact properties of flax, basalt and hybrid flax/basalt fiber reinforced green composites, Composites Part B: Engineering, Vol. 111, pp. 148-164, 2017.

[32] Lineo, Flaxply Technical Data Sheet, 2013.

[33] Polynt, DISTITRON ® VEef 220 STZ Technical Data Sheet, 2013.

[34] ASTM D 1141. An American National Standard Practice for the Preparation of Substitute Ocean Water, 2003.

[35] C. Fragassa: Effect of natural fibers and bio-resins on mechanical properties in hybrid and non-hybrid composites, in: AIP Conference Proceedings, Vol. 20118, No. 1736, 2016.

[36] S. Boria, A. Pavlovic, C. Fragassa and C. Santulli: Modeling of Falling Weight Impact Behavior of Hybrid Basalt/Flax Vinylester Composites, Procedia Engineering, Vol. 167, pp. 223-230, 2016.

[37] C. Baley, Y. Perrot, F. Busnel, H. Guezenoc and P. Davies: Transverse tensile behaviour of unidirectional plies reinforced with flax fibres, Materials Letters, Vol. 60, No. 24, pp. 2984-2987, 2006.

[38] ASTM D7264/D7264M, Standard Test Method for Flexural Properties of Polymer Matrix Composite Materials, 2015

[39] K. Adekunle, S. W. Cho, C. Patzelt, T. Blomfeldt and M. Skrifvars: Impact and flexural properties of flax fabrics and Lyocell fiber-reinforced bio-based thermoset, Journal of Reinforced Plastics and Composites, 2011, doi: 0731684411405874.

[40] N. Sombatsompop and K. Chaochanchaikul: Effect of moisture content on mechanical properties, thermal and structural stability and extrudate texture of poly (vinyl chloride)/wood sawdust composites, Polymer International, Vol. 53, No. 9, pp. 1210-1218, 2004.

[41] Y. Diamant, G. Marom and L. J. Broutman: The effect of network structure on moisture absorption of epoxy resins, Journal of Applied Polymer Science, Vol. 26, No. 9, pp. 3015-3025, 1981.

[42] Y. Perrot, C. Baley, Y. Grohens and P. Davies: Damage resistance of composites based on glass fibre reinforced low styrene emission resins for marine applications, Applied Composite Materials, Vol. 14, No. 1, pp. 67-87, 2007.

[43] A. Bismarck, I. Aranberri Askargorta et al.: Surface characterization of flax, hemp and cellulose fibers; surface properties and the water uptake behavior, Polymer Composites, Vol. 23, No. 5, pp. 872-894, 2002.

MICRO SCRATCH TEST CHARACTERISATION OF ZA-27/SiC NANOCOMPOSITES

Dragan DžUNIĆ[1], Miroslav BABIĆ[1], Slobodan MITROVIĆ[1], Marko PANTIĆ[1]*, Ilija BOBIĆ[2]
[1]University of Kragujevac, Faculty of engineering, Kragujevac, Serbia
[2]University of Belgrade, Institute for nuclear sciences, Vinča, Belgrade, Serbia
*Corresponding author: pantic@kg.ac.rs

Abstract: *In this study tribological properties of obtained nanocomposites were investigated using micro scratch tester. Tested nanocomposites were developed on well-known tribological ZA-27 alloy using compocasting technique. SiC nanoparticles (average size 50nm) in different volume fraction were used as reinforcement. Main scratch test results were coefficient of friction, penetration and residual depth. Obtained results for nanocomposites were compared to the obtained results for base ZA-27 alloy. Scratch test results and SEM revealed existence of structural irregularities such as porosity (trapped gas bubbles in material structure) and agglomerated nanoparticles. Existence of structural irregularities mainly diminishes positive effects that are expected from addition of hard nanoparticles.*

Keywords: *ZA-27, Nanocomposite, Scratch test, Wear, Friction, Penetration depth, Residual depth.*

1. INTRODUCTION

Engineers and researchers from all over the make an effort to obtain the material that is perfect in tribological manner, that has low coefficient of friction and therefore energy efficient and also it is necessary to have a great wear resistant or to be unswerving for a long time. Zink aluminium alloys are well known tribological material and they are widely used in various industrial applications. Zinc and aluminium are the main alloy constituents with low content of copper and magnesium. Content of aluminium can vary and regarding that exists several alloys with different content of aluminium 8% (ZA-8), 12% (ZA-12) and 27% (ZA-27). Casted zinc-aluminium alloys possess a great combination of strength, toughness and rigidity. Due to low copper content these alloys are very economical and energetically efficient replacement for numerous alloys based on non-ferrous metals. Regarding that they possess a good bearing capability, but from the other side they are characterised by lower casting temperature and cost effectiveness [1-4].

ZA alloys are widely used for plain bearings that work under conditions of low sliding speeds and high normal loads [5, 6].It should be mentioned that one of the main disadvantages of these alloys is their inferiority on higher temperatures [3, 7].

Further improvement of mechanical and tribological properties of ZA-27 alloys lead through development of their composites. Addition of hard ceramic particles improves wear resistance in comparison to the wear resistance of the base alloy [8-14], while addition of graphite particles improves

frictional properties [15-21]. Addition of graphite can also improve wear properties through generation of specific tribo-layer on both contact surfaces [6]. In order to improve wear and friction properties hard particles were simultaneously with graphite particles that acts like a solid lubricants [16, 18, 21, 22]. Recently researchers make great efforts to improve base alloys properties with addition natural biomaterials such as cassava leaves [23], coconut [24], palm kernel [25] and egg shell [26].

Beside all these scientific and research effort, influence of nanoparticles on the properties of base metals and their alloys is not fully understood and properly defined. Also numerous problems regarding dispersion, reactivity, and wettability are still present in order to obtain optimal distribution of nanoparticles in base material. Due to that the aim of this study is to investigate tribological properties of ZA-27 nanocomposites reinforced with different volume fraction of SiC nanoparticles obtained by compocasting technique.

2. MATERIAL

As is it previously mentioned ZA-27 alloy is reinforced with SiC nanoparticles, with average size around 50nm. Volume fraction of SiC nanoparticles was 1, 3 and 5%. Chemical composition of base ZA-27 alloy is presented in table 1.

Table 1. Chemical composition of the ZA-27 base alloy

Label	Chemical composition (wt. %)			
	Al	Cu	Mg	Zn
ZA27	25-27	2-2,5	0,015-0,02	Balance

Nanocomposites were obtained by the compocating procedure which comprise adding of nanoparticles in molten alloy under intensive mixing in order to achieve uniform distribution of nanoparticles and to avoid formation of agglomerates. Mixing time depends on volume fraction of nanoparticles. After casting obtained nanocomposites were hot pressed with 250 MPa pressure.

Tribological samples were prepared by milling, grinding and polishing, but making sure that the temperature does not exceed 100°C, which would result in degradation of mechanical properties [3, 7].

3. EXPERIMENTAL DETAILS

Tribological properties of obtained nanocomposites were investigated using CSM micro scratch tester (Figure 1). Micro scratch tests were performed using progressive normal load from 0 to 10 N, with loading rate 10 N/min, while sliding distance was 3 mm. Indenter was diamond Rockwell cone with a 100 μm radius on top. Results of these tests were presented through coefficient of friction, penetration and residual depth plots. Experiments on each sample were performed 15 times. Obtained results for nanocomposites were averaged compared to the base ZA-27 alloy.
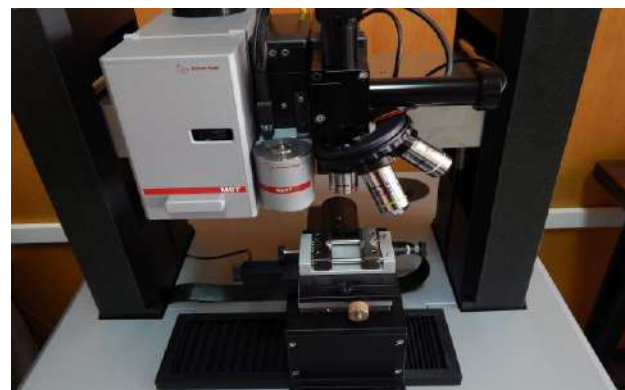
Figure 1. Micro scratch tester

4. RESULTS AND DISCUSSION

Scratch test was repeated on each investigated material 15 times while the distance between tracks were 0.5 mm, and this type of experiment organisation was in order to get a clearer picture of material distribution in surface layer of investigated materials. On figures 2, 3, 4 and 5 presents plots of coefficient of friction, penetration and residual depth for base ZA-27 alloy and for nanocomposites reinforced with 1, 3 and 5 vol. % of SiC nanoparticles. Presented plots are results obtain after one test while averaged values of all 15 tests is presented on figure 6.
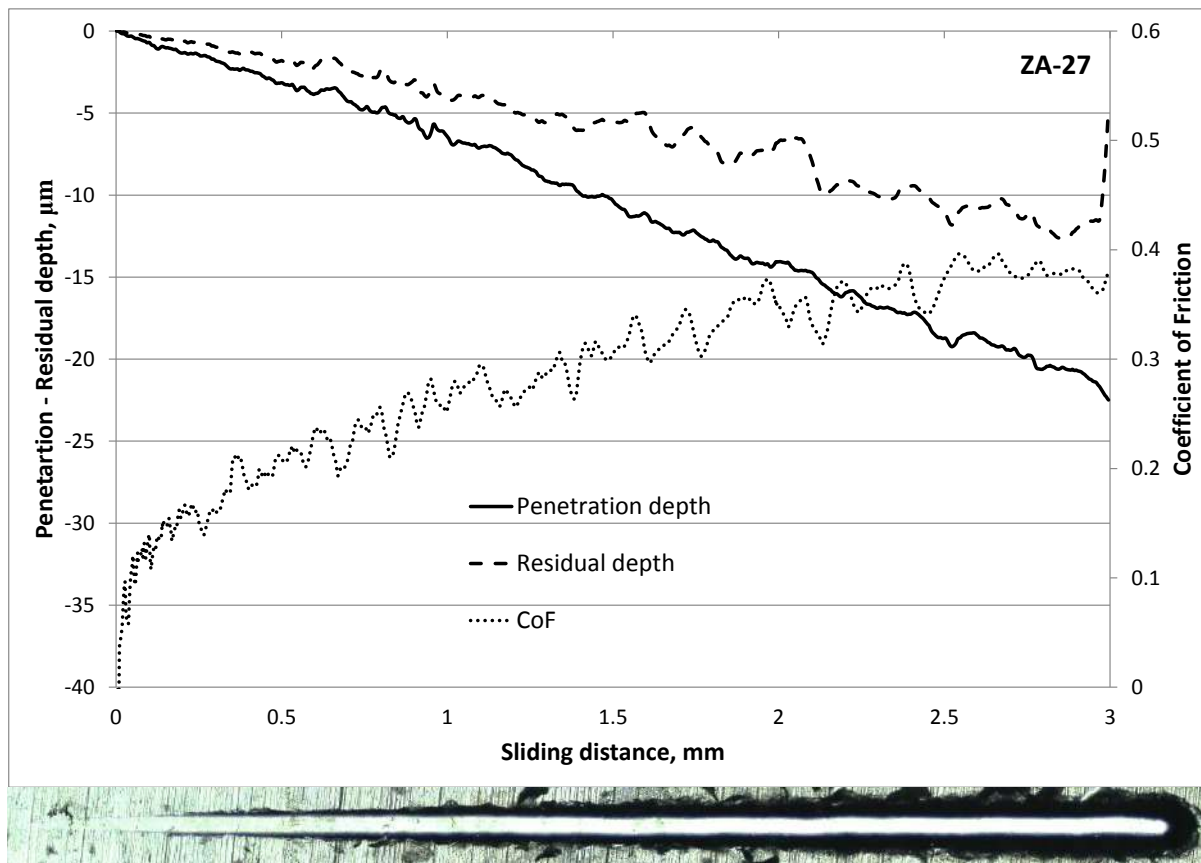
Figure 2. Penetration and residual depth, coeficient of friction and corresponding wear track (below) for ZA-27.
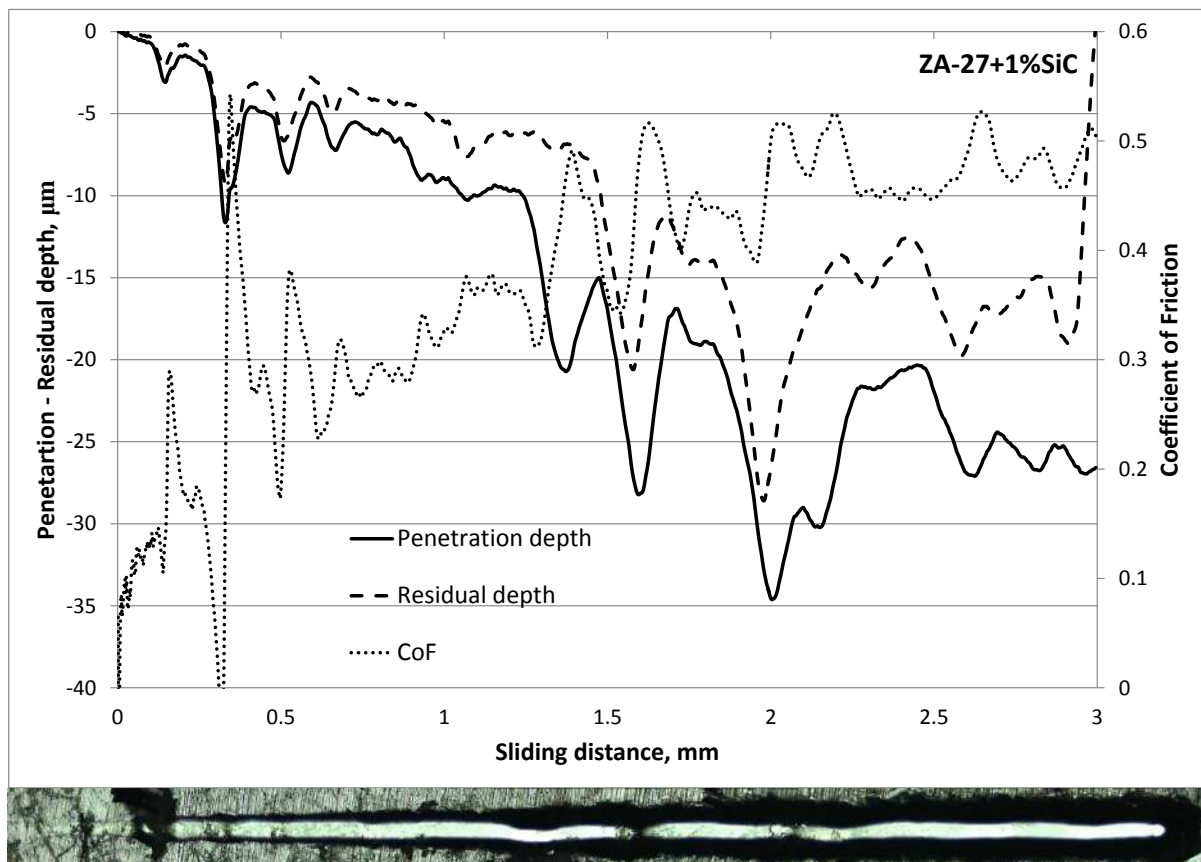
Figure 3. Penetration and residual depth, coeficient of friction and corresponding wear track (below) for ZA-27+1%SiC
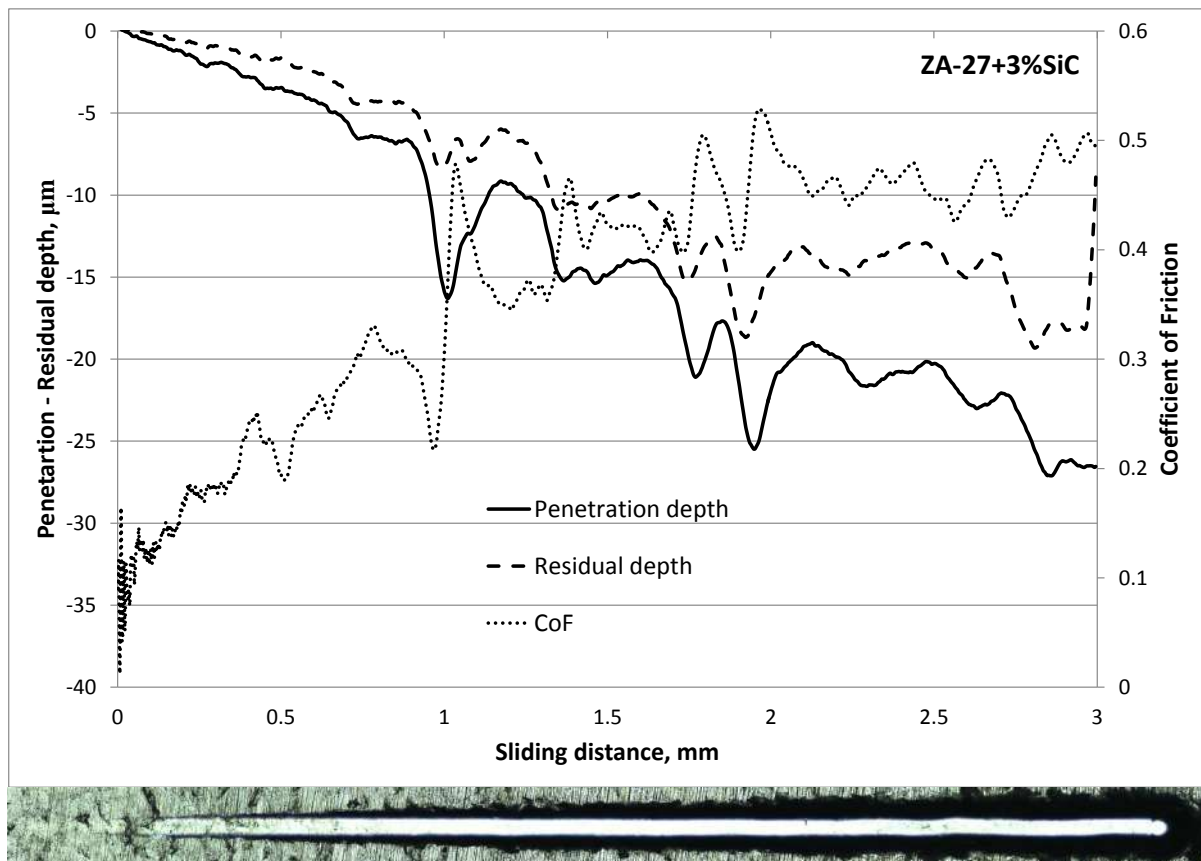
Figure 4. Penetration and residual depth, coeficient of friction and corresponding wear track (below) for ZA-27+3%SiC
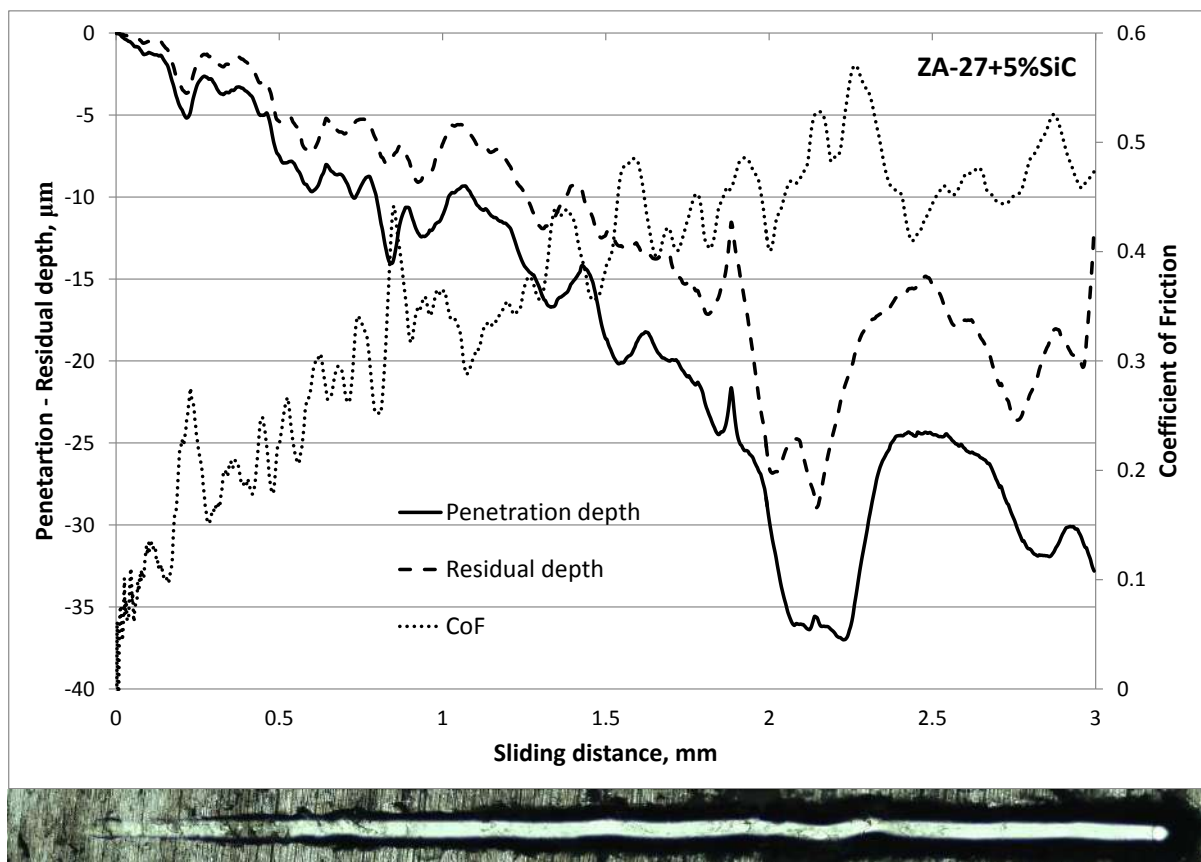
Figure 5. Penetration and residual depth, coeficient of friction and corresponding wear track (below) for ZA-27+5%SiC

Scratch tests results performed on obtained nanocomposites indicated existence of structural irregularities such as air bubbles and agglomerates while it was not the case with scratch test results obtained on base ZA-27 alloy. This conclusion is based on penetration depth curves analysis for nanocomposites where drastic changes are noticeable which refer to decline of indenter during sliding. Increase of penetration depth indicates on surface and subsurface defects. Numerous researchers noticed existence of structural irregularities generated with addition of hard nanoparticles and increase of their content in base material [27-31]. Due to nanoparticles nature gas bubbles generates around them (case when porosity is influenced by individual nanoparticles) or they are generated around agglomerated nanoparticles as a result of aggravated movement of molten metal during casting (case when porosity is influenced by agglomerated nanoparticles) [28]. Gas bubbles could occur due to low wettability between nanoparticles and base material, while generation of agglomerates is a result of increased friction between nanoparticles due to increased surface to volume ratio in comparison to the micro particles [32]. According to the appearance of presented plots for penetration depth of tested nanocomposite it could be concluded that number and size of structure irregularities along scratch track is different and unpredictable.

Change of penetration depth value causes changes of coefficient of friction value and results in higher average value of coefficient of friction in comparison to the coefficient of friction value of ZA-27 base alloy. From these plots it could be concluded that the degree of elastic relaxation is almost equal and constant for all examined materials, which means that is constant despite change of volume fraction of nanoparticles.

Averaged plots of coefficient of friction based on all 15 scratch tests are presented on figure 6. Analysing presented, it is obvious that ZA-27 exhibits lowest value of coefficient of friction during the scratch test sliding.

Coefficient of friction as it is previously mentioned highly depend on penetration depth of indenter and regarding that the coefficient of friction of nanocomposites is higher in comparison to the base ZA-27 alloy.
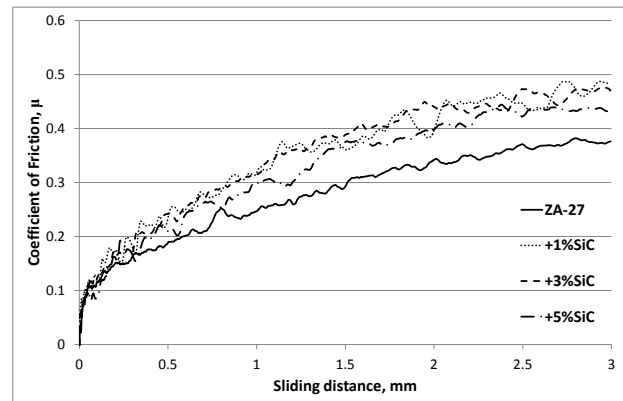
Figure 6. Averaged plots of coefficient of friction for tested materials

Figure 7 present comparative averaged plots of penetration depth for base alloy and obtained nanocomposites. Analysing presented plots it can be concluded that despite existence of trapped gas bubbles in material structure (figure 4) obtained nanocomposite reinforced with 3 vol.% of SiC nanoparticles has the lowest average value of penetration depth. In this case presence of nanoparticles of reinforcement managed to prevent movement of dislocations and on that to improve wear resistance and bearing capability [**Error! Reference source not found.**, **Error! Reference source not found.**]. Also it is noticeable that values of penetration depth for all tested materials are just slightly different in comparison to each other, but the higher differences could be noticed for higher value of normal load.
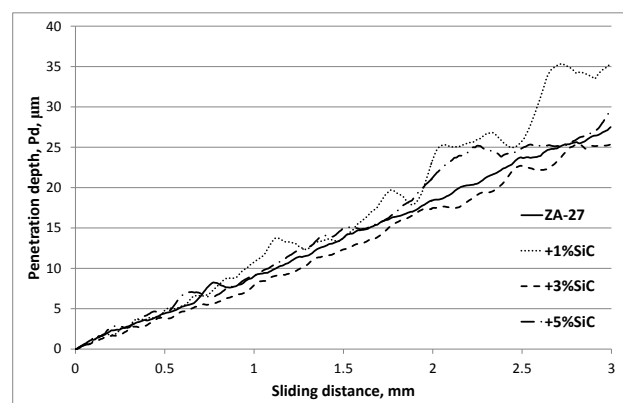
Figure 7. Averaged plots of penetration depth for tested materials.

The lowest average value of residual depth after scratch test exhibits base ZA-27 alloy than nanocomposite reinforced with 3 vol. % of SiC nanoparticles (Figure 8). This phenomenon could be explained by that the existence of trapped gas bubbles and agglomerates of nanoparticles cannot contribute to elastic relaxation of the nanocomposites. Scratch tests on base ZA-27 alloy revealed several smaller structural irregularities in comparison to the obtained nanocomposites.
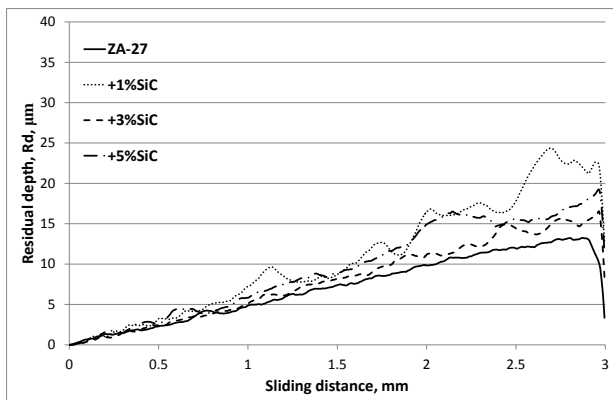
Figure 8. Averaged plots of residual depth for tested materials.

Obtained wear tracks were analysed using optical and scanning electron microscopy (SEM). Micro scratch tester is equipped with optical microscope which allows generating panoramic view of obtained wear track and matching with the corresponding results (coefficient of friction, penetration and residual depth plots). Generated panoramic view of obtained wear allows graphic presentation of noticed changes on plots. SEM equipped with topographic mode was used to analyse plastic deformation generated on the wear track sides (Figure 9).

SEM analysis of wear track shows that inside the wear track large number of small cavities is noticeable. Also analysing surrounding surface shows previously mentioned structural irregularities (Figure 9b and 9c). Pile up material on the sides of the wear track is apparently compact, especially at the end of the track where the material pile up is much bigger in comparison to the pile up on the side.
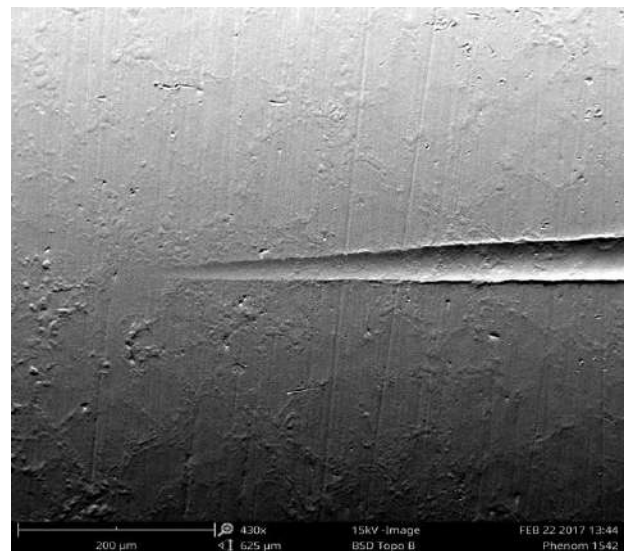
a)
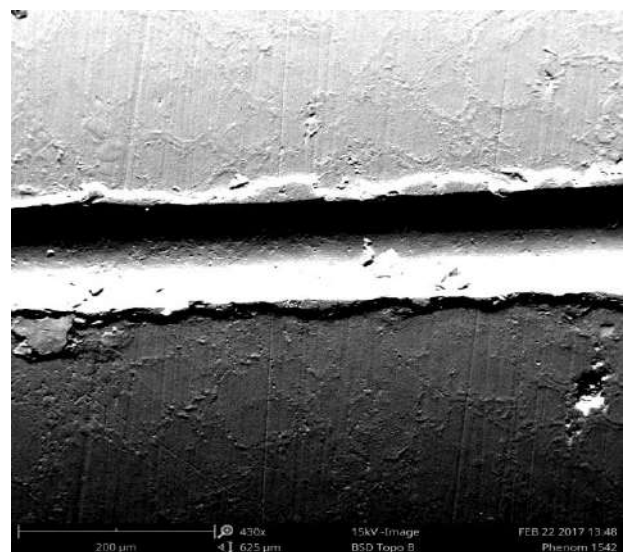
b)
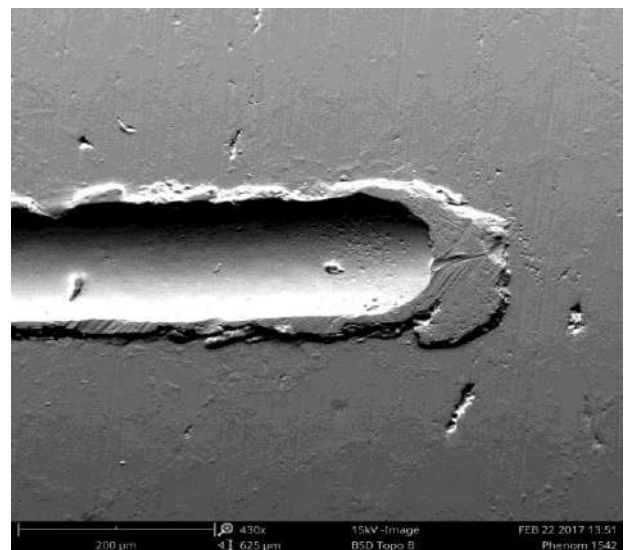
c)

Figure 9. Scanning electron microscopy of obtained wear track on nanocomposite reinforced with 1 vol. % of SiC: a) at the beginning, b) in the middle and c) at the end.

Regarding that it could be concluded that generated wear debris during the scratch is push in front of indenter, than deformed, compacted and pushed out due to conical geometry of indenter.

5. CONCLUSION

Micro scratch test was used to properly evaluate tribological properties of ZA-27 based nanocomposites reinforced with 1, 3 and 5 vol. % of SiC nanoparticles.

Micro scratch test revealed existence of structural irregularities of obtained nanocomposites. Structure irregularities such as gas bubbles and agglomerates of nanoparticles has a great influence on the penetration depth value.

The lowest averaged value of penetration depth during the scratch test exhibits nanocomposite reinforced with 3 vol. % of SiC nanoparticles.

Base ZA-27 alloy exhibits the lowest value of coefficient of friction during the scratch tests.

The lowest averaged value of residual depth exhibits base ZA-27 alloy.

SEM analysis of generated wear track showed plastic deformation and pile of material along the sides and at the end of the wear track.

ACKNOWLEDGEMENT

REFERENCES

References are to be listed in the order of their appearance in the text and numbered. Citation is by the number only which is to be put in square brackets, i.e. [1,2], [3], … etc. Please note that all references listed here must be directly cited in the body of the text.

In the reference list (Calibri 11 pt, Justify, Hanging 0.75 cm), journal papers [1], books [2], multi-author books [3], theses [4], conference Proceedings [5], standards [6,7] and websites [8] should be cited as in the following examples:

[1] M. Babić, R. Ninković: Tribological potential of ZnAl alloys, Faculty of mechanical engineering, Kragujevac, Serbia, 2007.

[2] M. Babić, S. Mitrović: Tribological properties of ZA-27 based composites, Faculty of mechanical engineering, Kragujevac, Serbia, 2007.

[3] S. Tjong, F. Chen: Wear behavior of As-cast ZnAl27/SiC particulate metal-matrix composites under lubricated sliding condition, Metall and Mat Trans A, vol. 28, no. 9, pp. 1951-1955, 1997.

[4] A. Rac, A. Vencl: Metallic materials for plane bearings: Physical, mechanical and tribological properties, Faculty of mechanical engineering, Belgrade, Serbia, 2004.

[5] T. Savaşkan, G. Pürçek, S. Murphy: Sliding wear of cast zinc-based alloy bearings under static and dynamic loading conditions, Wear, vol. 252, no. 9-10, pp. 693-703, 2002.

[6] M. Babic, M. Slobodan, D. Džunic, B. Jeremic, I. Bobic: Tribological Behavior of Composites Based on ZA-27 Alloy Reinforced with Graphite Particles, Tribol Lett, vol. 37, no. 2, pp. 401-410, 2010.

[7] T. Chen, C. Yuan, M. Fu, Y. Ma, Y. Li, Y. Hao: In situ silicon particle reinforced ZA-27 composites: Part 1 – Microstructures and tensile properties, Materials Science and Technology, vol. 24, no. 11, pp. 1321-1332, 2008.

[8] A. Vencl, I. Bobic, S. Arostegui, B. Bobic, A. Marinković, M. Babić: Structural, mechanical and tribological properties of A356 aluminium alloy reinforced with Al2O3, SiC and SiC+graphite particles, Journal of Alloys and Compounds, vol. 506, no. 2, pp. 631-639, 2010.

[9] A. Vencl, I. Bobić, M.T. Jovanović, M. Babić, S. Mitrović: Microstructural and tribological properties of A356 Al-Si alloy reinforced with Al2O3 particles, Tribology Letters, vol. 32, no. 3, pp. 159-170, 2008.

[10] S. Mitrović, M. Babić, I. Bobić, 'ZA-27 Alloy Composites Reinforced with Al2O3 Particles', Tribology in industry, Vol. 29, No. 3&4, pp. 35-41, 2007.

[11] S. Mitrović, M. Babić, F. Živić, I. Bobić, D. Džunić: Nanotribology Investigations of

Composites Based on Za-27 Alloy Reinforced by Al2O3 Particles, Tribology in industry, Vol. 30, No. 1&2, pp. 30-39, 2008.

[12] L. Davis, C. Andres, J. Allison: Microstructure and strengthening of metal matrix composites, Materials Science and Engineering: A, vol. 249, no. 1-2, pp. 40-45, 1998.

[13] M. Kok: Production and mechanical properties of Al2O3 particle-reinforced 2024 aluminium alloy composites, Journal of Materials Processing Technology, vol. 161, no. 3, pp. 381-387, 2005.

[14] T. Miyajima, Y. Iwai: Effects of reinforcements on sliding wear behavior of aluminum matrix composites, Wear, vol. 255, no. 1-6, pp. 606-616, 2003.

[15] S. Suresha, B. Sridhara: Effect of addition of graphite particulates on the wear behaviour in aluminium–silicon carbide–graphite composites, Materials & Design, vol. 31, no. 4, pp. 1804-1812, 2010.

[16] N. Miloradovic, B. Stojanovic: Tribological behaviour of ZA-27/10SiC/1gr hybrid composite, Journal of the Balkan Tribological Association, vol. 19, no. 1, pp. 97-105, 2013.

[17] F. Akhlaghi and A. Zare-Bidaki: Influence of graphite content on the dry sliding and oil impregnated sliding wear behavior of Al 2024–graphite composites produced by in situ powder metallurgy method, Wear, vol. 266, no. 1-2, pp. 37-45, 2009.

[18] B. Stojanovic, M. Babic, S. Mitrovic, A. Vencl, N. Miloradovic, M. Pantic: Tribological characteristics of aluminium hybrid composites reinforced with silicon carbide and graphite - a review, Journal of the Balkan Tribological Association, vol. 19, no. 1, pp. 83-96, 2013.

[19] P. Ravindran, K. Manisekar, P. Narayanasamy, N. Selvakumar, R. Narayanasamy: Application of factorial techniques to study the wear of Al hybrid composites with graphite addition, Materials & Design, vol. 39, pp. 42-54, 2012.

[20] P. Ravindran, K. Manisekar, R. Narayanasamy, P. Narayanasamy: Tribological behaviour of powder metallurgy-processed aluminium hybrid composites with the addition of graphite solid lubricant, Ceramics International, vol. 39, no. 2, pp. 1169-1182, 2013.

[21] I. Bobić, J. Ružić, B. Bobić, M. Babić, A. Vencl, S. Mitrović: Microstructural characterization and artificial aging of compo-casted hybrid A356/SiCp/Grp composites with graphite macroparticles, Materials Science and Engineering: A, vol. 612, pp. 7-15, 2014.

[22] M. Łągiewka, Z. Konopka: The Influence of Graphite Addition on the Abrasive Wear of AlMg10 Alloy Matrix Composites Reinforced with SiC Particles, Archives of Foundry Engineering, vol. 14, no. 3, 2014.

[23] F.O. Kolawole, S.K. Kolawole, J.O. Agunsoye, S.A. Bello, J.A. Adebisi, O.C. Okoye, S.B. Hassan: Cassava Leaf Nanoparticles (CLNPs) as a Potential Additive to Anti-Corrosion Coatings for Oil and Gas Pipeline, Tribology in Industry, Vol. 39, No. 1, pp. 63-72, 2017.

[24] J.O. Agunsoye, S.I. Talabi, S.A. Bello, I.O. Awe: The Effects of Cocos Nucifera (Coconut Shell) on the Mechanical and Tribological Properties of Recycled Waste Aluminium Can Composites, Tribology in Industry, Vol. 36, No. 2, pp. 155-162, 2014.

[25] I.A. Samotu, M. Dauda, F.O. Anafi, D.O. Obada: Suitability of Recycled Polyethylene/Palm Kernel Shell-Iron Filings Composite for Automobile Application, Tribology in Industry, Vol. 37, No. 2, pp. 142-153, 2015.

[26] S.B. Hassan, V.S. Aigbodion, S.N. Patrick: Development of Polyester/Eggshell Particulate Composites', Tribology in Industry, Vol. 34, No. 4, pp. 217-225, 2012.

[27] M. Karbalaei Akbari, H. Baharvandi, O. Mirzaee: Nano-sized aluminum oxide reinforced commercial casting A356 alloy matrix: Evaluation of hardness, wear resistance and compressive strength focusing on particle distribution in aluminum matrix, Composites Part B: Engineering, vol. 52, pp. 262-268, 2013.

[28] A. Mazahery, H. Abdizadeh, H. Baharvandi: Development of high-performance A356/nano-Al2O3 composites, Materials Science and Engineering: A, vol. 518, no. 1-2, pp. 61-64, 2009.

[29] H. Ezatpour, S. Sajjadi, M. Sabzevar, Y. Huang: Investigation of microstructure and mechanical properties of Al6061-nanocomposite fabricated by stir casting, Materials & Design, vol. 55, pp. 921-928, 2014.

[30] N. Nemati, R. Khosroshahi, M. Emamy, A. Zolriasatein: Investigation of microstructure, hardness and wear properties of Al–4.5wt.% Cu–TiC nanocomposites produced by mechanical milling, Materials & Design, vol. 32, no. 7, pp. 3718-3729, 2011.

[31] N. Hosseini, F. Karimzadeh, M. H. Abbasi, M. H. Enayati: A comparative study on the wear

properties of coarse-grained Al6061 alloy and nanostructured Al6061–Al2O3 composites, Tribology International, vol. 54, pp. 58–67, 2012.

[32] A. Yar, M. Montazerian, H. Abdizadeh and H. Baharvandi: Microstructure and mechanical properties of aluminum alloy matrix composite reinforced with nano-particle MgO, Journal of Alloys and Compounds, vol. 484, no. 1-2, pp. 400-404, 2009.

[33] M. Akbarpour, E. Salahi, F. Alikhani Hesari, H. Kim, A. Simchi: Effect of nanoparticle content on the microstructural and mechanical properties of nano-SiC dispersed bulk ultrafine-grained Cu matrix composites, Materials & Design, vol. 52, pp. 881-887, 2013.

[34] A. Fathy, F. Shehata, M. Abdelhameed, M. Elmahdy: Compressive and wear resistance of nanometric alumina reinforced copper matrix composites, Materials & Design, vol. 36, pp. 100-107, 2012.

STUDY OF ABRASIVE WEAR OF A THERMAL ALLOY OF Al-Mg-Nb

M. CASTILLO[*], M. J. VELÁZQUEZ, M. VITE
Instituto Politécnico Nacional, ESIMEZ, Cd de México, México
*Corresponding author: avinfer@hotmail.com

Abstract: *The aim of this work the aim of this work was to manufactured an alloy of aluminum - magnesium and niobium, The raw materials used for the manufacture of Al - 0.03 wt% Mg - Nb alloy specimens were electrolytic aluminum and magnesium with a purity of 99.3% and Al - Mg - Nb alloy. With a particle size of 100 µm. The aluminum, magnesium and niobium particles were placed in a graphite crucible and then melted in an induction furnace. The raw materials used for the manufacture of Al - 0.03 wt% Mg - Nb alloy specimens were electrolytic aluminum and magnesium with a purity of 99.3% and a particle size of 100µm. The aluminum, magnesium and niobium material was placed in a graphite crucible and then melted in an induction furnace. The ingots subsequently obtained were subjected to homogenization heat treatment for 14 hours at a temperature of 450 ° C, were preheated in a box oven for 30 minutes at 100 ° C and subsequently laminated to a final thickness of 13mm. After rolling the specimens were annealed for 45 minutes at a temperature of 350 ° C, 3 alloys were obtained, with a Brinell hardness of 250, 285 and 315 HB respectively. The micrographic analysis shows a fine dendritic structure. 3 specimens of each alloy were used for the respective dry abrasion tests according to ASTM G-65, entitled "Standard Test Method for Measuring Abrasion Using the Dry Sand / Rubber Wheel Apparatus". Where AFS 50/70 silica sand, whose size is approximately 250 µm, was used as the abrasive material. The load applied was 10N and a sand flow of 0.4 kg / min. It was observed that the niobium causes a grain refinement in the microstructure of the Al - Mg alloys, and increases the surface hardness, the increase of the Nb content in the Al - Mg alloys satisfactorily improves the abrasion resistance and one of The obtained alloys shows a lower hardness due to the absence of niobium and does not allow adequate thermal stability. For this reason, its resistance to abrasion proves to be less compared to the other two alloys manufactured.*

Keywords: *Aluminium alloy, magnesium, niobium, induction furnace, heat treatment, micrographic analysis, dry abrasion test.*

1. INTRODUCTION

The search for aluminum alloys that perform well in many applications has led to the search for new options such as lithium aluminum alloys, beryllium aluminum, aluminum matrix metal compounds developed through the process of powder metallurgy. The family of aluminum alloys lithium, are characterized mainly by their low weight in structures for the aeronautical industry, due to a significant reduction in density. A substitute in these lithium alloys is magnesium, which is an element that increases mechanical strength through the solid solution. However, aluminum magnesium alloys have not been competitive because reducing density is a significant challenge. Its application in the construction industry represents the largest market in the aluminum industry, thousands

of homes use aluminum for doors, windows screens, locks, nozzles and water pipes. Transportation is the second major market, many military and commercial aircraft are constructed entirely of aluminum [1, 2].

In previous decades aluminum magnesium alloys were developed with small additions of transition metals, such as scandium, which produces important improvements in the properties of these alloys, such as high mechanical strength, corrosion and abrasion. Due to the high mechanical strength and low weight, these alloys are used extensively in the automotive industry as well as in space and marine applications. The manufacturing industry is also very interested in these alloys.

However, scandium is a very rare and very expensive element for industrial applications [3]. Niobium is an abundant element, in alloys it is used as a grain refiner; it increases hardness, wear resistance and hot corrosion. Due to these properties, it is possible to use niobium in aluminum magnesium alloys [4, 5].

In addition, the first studies of importance and interest in the phenomenon of abrasion, using dry sand and a metallic disc with rubber as tribotester, were carried out by Haworth in the decade of 1940 [5]. Misra subsequently reviewed the abrasive wear of metals [6]. The tribological abrasion machine used for the experimental development of the present work was designed and manufactured by the team of Tribology researchers from SEPI-ESIME-IPN [7], in accordance with the international standard ASTM G-65 [8].

2. EXPERIMENTAL DEVELOPMENT

2.1 Materials

The raw materials used for the manufacture of Al - 0.03 wt. % Mg - Nb alloy specimens were electrolytic aluminum and magnesium with a purity of 99.3% and a particle size of 100μm. The aluminum, magnesium and niobium particles were placed in a graphite crucible and then melted in an induction furnace. The furnace was purged under a vacuum pressure of 10^{-2} Torr, using an argon

atmosphere to prevent oxidation of the elements. The melting point was about 750°C, within a copper matrix, cooled by circulating water. The ingots were obtained with a cross section of 50 x 50 x 300 mm, of three different aluminum alloys Al - 0.03 wt% Mg - 0.0003 wt% Nb (**I**), Al - 0.03 wt% Mg - 0.0006 wt% Nb (**II**) And Al - 0.03 wt% Mg (**III**), respectively. All ingots were manufactured under the same conditions. The chemical analysis of the three alloys obtained is shown in Table 1.

Table 1. Chemical analysis of aluminum alloys obtained

Element	Alloy		
	I	II	III
Si	0.000677	0.000622	0.001084
Fe	0.001573	0.001461	0.003664
Cu	0.000010	0.000010	0.000046
Mn	0.000080	0.000079	0.003459
Mg	0.03174	0.03216	0.03349
Zn	0.000050	0.000050	0.000050
Ni	0.000032	0.000030	0.000012
Cr	0.000010	0.000010	0.000018
Pb	0.000020	0.000020	0.000020
Ti	0.000028	0.000027	0.000064
V	0.000097	0.000097	0.000079
Co	0.000020	0.000020	0.000020
Sr	0.000001	0.000001	0.000001
Al	0.966	0.965	0.948

The specimens of the aluminum alloys obtained were subsequently subjected to a homogenization heat treatment for 14 hours at a temperature of 450°C within a box furnace in an argon gas atmosphere in order to avoid oxidation.

2.2 Heat Treatment and rolling

The specimens of the aluminum alloys obtained were preheated in a box oven for 30 minutes at 100 ° C and subsequently rolling to a final thickness of 13mm. After rolling, the specimens were annealed for 45 minutes at a temperature of 350°C using an argon atmosphere with a gas flow of 7.87 x 10^{-5} m^3 sec^{-1}.

2.3 Abrasive wear

Three specimens of each alloy were used for the respective dry abrasion tests according to ASTM G-65, "Standard Test Method for Measuring Abrasion Using the Dry Sand / Rubber Wheel Apparatus" [8]. Where AFS 50/70 silica sand, whose size is approximately 250 µm, was used as the abrasive material. The load applied was 10N and a sand flow of 0.4 kg / min., during all tests performed. While the mass loss of the aluminum alloy specimens was performed on an analytical balance with a sensitivity of 0.0001g. The development of abrasive wear tests is presented in figure 1.
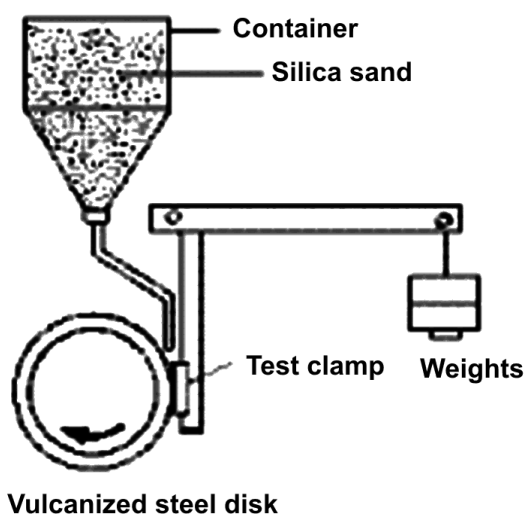
Figure 1. Schematic diagram of wear test

3. EXPERIMENTAL RESULTS

3.1 Determination of hardness

The hardness of the specimens of each alloy was obtained using a Brinell hardness tester. The load applied was 250 kg and with a sphere diameter in the indenter of 2.5 mm. The results obtained are shown in Table 2.

Table 2. Hardness of aluminum alloys

Alloy	I	II	III
Brinell hardness, **HB**	230	285	315

3.2 Abrasive wear

The abrasion resistance of the corresponding alloys was evaluated during 5

successive stages of wear tests, achieving a total trajectory of approximately 3590,835 m of sliding distance. The results are shown in Figure 2.
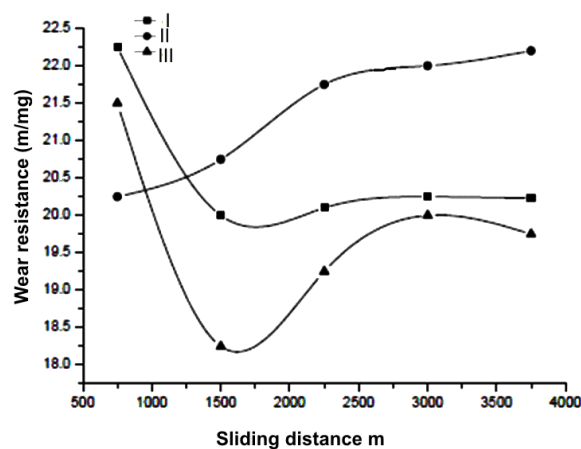
Figure 2. Wear behavior of the corresponding alloys

4. DISCUSSION OF RESULTS

4.1 Metallography

Aluminum alloys generally have a dendritic structure such as the Al-Mg alloy. Although the alloys including niobium are distinguished because they preferably have a fine dendritic structure as seen in Figure 3, obtained with the optical microscope.

It is assumed that at room temperature the solubility of the impurities is close to zero, and do not mix in the aluminum.

However, the second phases, shown in Figure 4, are only distinguishable using a high magnification in the scanning electron microscope.
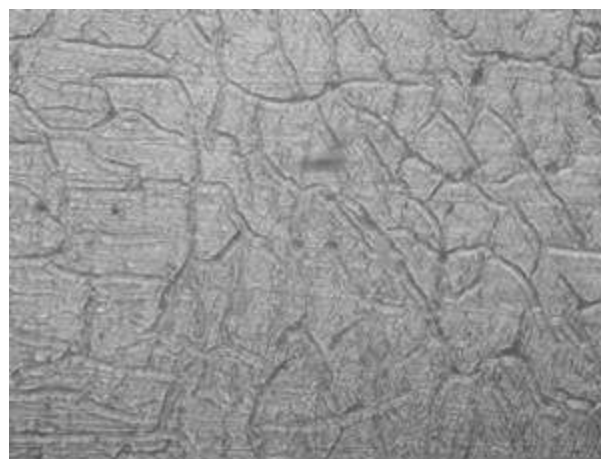
a) alloy **I**

b) alloy **II**
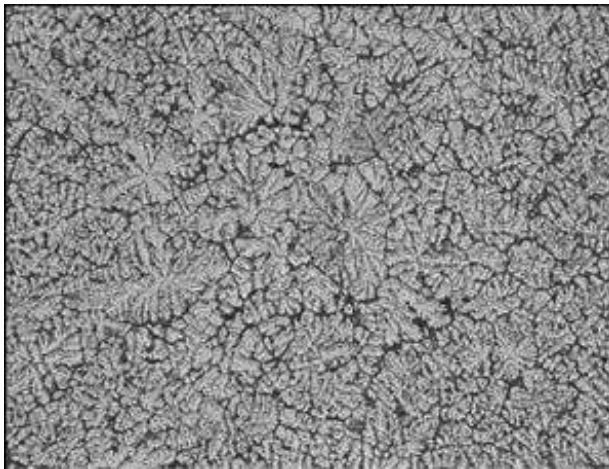
c) alloy **III**

Figure 3. Dendritic structure. 500X.
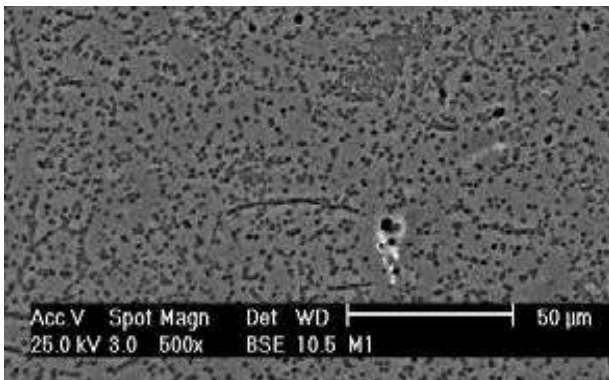
a) Alloy **I**
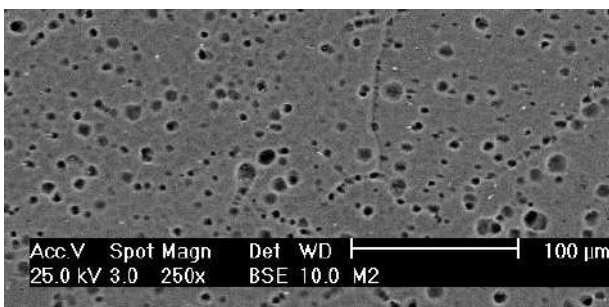
b) Alloy **II**
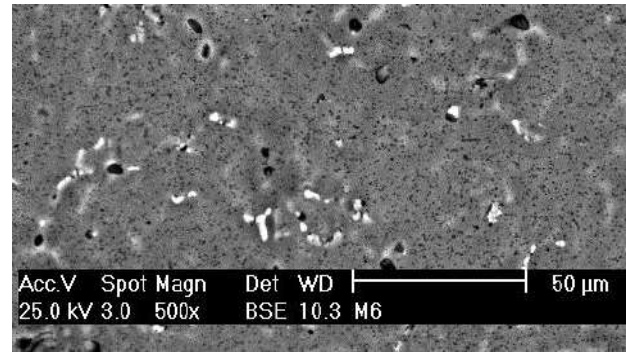
c) Alloy **III**

Figure 4. Second phases with SEM microscope.

Table 3 shows the percentage by weight of the second phases.

Table 3. Chemical Composition of the Second Phases of Aluminum Alloys

Element	Alloy		
	I	**II**	**III**
Al	0.966	0.965	0.958
Mg	0.03174	0.03216	0.03349
Si	0.000377	0.000622	0.001084
Fe	0.001573	0.001461	0.003664
Mn	0.000080	0.000079	0.003459
Nb	0.0003	0.0006	0.0000
other elements	0.000267	0.000265	0.000309

5. CONCLUSION

Niobium causes a grain refinement in the microstructure of Al-Mg alloys, and increases surface hardness.

Increasing the Nb content in Al-Mg alloys satisfactorily improves abrasion resistance.

The Al-0.03 wt. % Mg alloy shows the lowest hardness, due to the absence of niobium, and does not allow adequate thermal stability. For this reason, its resistance to abrasion is less compared to the other two alloys analyzed.

ACKNOWLEDGEMENT

REFERENCES

[1] Davis, R. Joseph (Ed.): *Aluminum and Aluminum Alloys,* ASM International, 1996.

[2] Dietrich, G. Altenpohl, *Aluminum: Technology, Applications and Enviroment*, 1998.

[3] Zaki Ahmad: *The Properties and Application of Scandium – Reinforced Aluminum*, Journal of Metals, February 2003.

[4]Rodriguez X, Dominguez D. *Tesis de Licenciatura UAM U. Azcapotzalco,* México. 2007.

[5] Haworth D, *The Abrasion Resistance of Metals.* Trans. Am. Soc. Met. Vol 41 (1949) pp. 819 – 869.

[6] A. Misra, I. Finnie: *A Review of the Abrasive Wear of Metals,* J. Eng. Mater. Technol, Trans. ASME 104 (1982) pp. 94 – 101.

[7] López E.: *Estudio Experimental del Desgaste Abrasivo en Aceros AISI 8620, D-2 Y H-13 con y sin Tratamiento Superficial, in:* Tesis de Maestría, SEPI ESIME IPN, México 2004.

[8] ASTM Standard G 65 – 94, *Standard Test Method for Measuring Abrasion Using the Dry Sand / Rubber Wheel Apparatus*.

MICROSTRUCTURE AND TRIBOLOGICAL PROPERTIES OF AUSTEMPERED DUCTILE IRONS WITH AND WITHOUT NANOADDITIVES

Julieta KALEICHEVA [1*], Valentin MISHEV[2], Zdravka KARAGUIOZOVA[3], Galina NIKOLCHEVA[2], Adelina MITEVA[5]

[1,2,4]Technical University of Sofia, Sofia, Bulgaria
[3,5]Bulgarian Academy of Sciences-SRTI, Sofia, Bulgaria
*Corresponding author: karazuzi@yahoo.com

Abstract: *The microstructure and tribological properties of austempered ductile irons (ADI) with structure of lower bainite and upper bainite with nanoadditives of titanium carbonitride and titanium nitride TiCN+TiN are investigated. For improvement of the particles wetting and distribution into the melt volume the electorless method for plating of the additives is applied using EFTTOM-NICKEL method.*

The microstructure of the patterns is observed by optical and quantitative metallography, X-Ray analysis, SEM and EDX analysis. Tests for hardness, wear resistance and intensity of wear are carried out.

The influence of the nanosized particles on the graphite phase modification is proved. Abrasion wear resistance increase of 23% (for structure of upper bainite) and of 73% (for structure of lower bainite) for austempered ductile irons with nanoadditives in comparison with irons without additives is determined.

Keywords: *detonation nanodiamond, electroless nickel coating, wear resistance, microhardness, and microstructure*

1. INTRODUCTION

The austempering of iron – carbon alloys in the bainitic area forms a structure with improved physical and mechanical properties. Austempering is a reason of formation of upper or lower bainitic structure characterized with a high strength and increased toughness. Austempering has a wide practical application in processing of the structural steel and spheroidal graphite cast irons [1,2]. Austempered ductile irons (ADI) are characterized with a high strength, toughness and wear resistance.

Graphite in the iron ensures resistance to a mechanical wear and improves its processing. Alloying or by heat treatment or using both of

this processes the graphite morphology and substrate structure could be changed with an aim to obtain irons with optimal properties. The investigation of new composition irons in cast condition or after heat treatment is an opportunity to extent the application area of this materials. Perspective to achieve this aim is the use of nanosized additives.

The role of added nanoparticles in the melt is in the changing of the graphite morphology for lamellar to vermicularis one [3], in the quantity graphite increase [4] and in the changing the substrate structure, which reflect in the increase irons' wear resistance [3-7].

The aim of the present work is to investigate the microstructure and tribological properties of austempered ductile irons (ADI)

with nanosized additives of titanium carbonitride and titanium nitride TiCN+TiN.

2. MATERIALS AND INVESTIGATION METHODS

The composition of the spheroidal graphite cast iron samples is: Fe-3,55C-2,67Si-0,31Mn-0,009S-0,027P-0,04Cu-0,025Cr-0,08Ni-0,06Mg wt%. The samples with and without nano-additves of titanium carbonitride and titanium nitride *TiCN+TiN* (Table 1) are studied. The *TiCN* and *TiN* nanosized particles are coated by electroless nickel coating EFTTOM-NICKEL [8] prior to the edition to the melt. The nickel coating improves the particles wetting into the melt and their uniformity distribution into the casting volume.

The microstructure of the cast iron samples before austempering is tested by quantity metallography, scanning electron microscopy (SEM) and energy-dispersive X-ray spectroscopy (EDX). Scanning microscopy EVO® MA10 „Carl Zeiss" Energy Dispersive X-ray Microanalyser - "Bruker" is used. The quantity metallographic analysis is performed by „Olympus MicroImage" Software and the data for an average diameter Dmid of the graphite grains, their roundness as well the volume parts of graphite, pearlite and ferrite are received.

The spheroidal graphite cast iron samples are undergone an austempering, including heating at $900^{\circ}C$ for an hour, after that isothermal retention at $280^{\circ}C$, 2h and at $380^{\circ}C$, 2h. The austempered ductile iron samples' microstructure is observed by means of an optical metallographic microscope GX41 OLIMPUS. The samples surface is treated with 2 vol. % nital solution. The austempered ductile iron samples are tested by X-Ray diffraction analysis the retained austenite quantity in the structure to be defined. The retained austenite quantity is determined before and after abrasion wear. For a phase identification X-ray powder diffraction patterns are recorded in the angle interval $20 \div 103^{\circ}(2\theta)$, on a Philips PW 1050 diffracto-meter, equipped with Cu Kα tube and

scintillation detector. The data for cell refinements and quantitative analysis are collected in θ-2θ, step-scan mode in the angle interval from 20 to 103° (2θ), at steps of 0.03° (2θ) and counting time of 3 s/step. A quantitative analysis is carried out by BRASS - Bremen Rietveld Analysis and Structure Suite [9].

The hardness test is carried out by Brinell method (for cast samples) and by Vickers method (for austempered samples).

The experimental study of the wear is carried out using method and device for accelerated testing in kinematic scheme "thumb-disc" under friction over a fixed abrasive [4,6]. The impregnated material *Smirdex 330 Duraflex P80 117SV* is used for the spheroidal graphite cast iron samples. The test data are: nominal contact pressure $P_a=0,21.10^6$[Pa]; average sliding speed, V=26,38[cm/s]; nominal contact surface, $A_a=50,24$[mm^2]; density, $\rho=7,80.10^3$[kg/m^3] [9]. The impregnated material Corundum 220 is used for the austempered ductile iron samples. The test data are: nominal contact pressure, $P_a=0,4.10^6$[Pa]; average sliding speed, V=24,5[cm/s]; nominal contact surface, $A_a=50,24$[mm2];density,$\rho=7,80.103$[kg/m^3][6].

3. RESULTS AND ANALYSIS

The tested spheroidal graphite cast iron substrate consists of ferrite and pearlite [4]. The quantity metallographic analysis is performed the influence of the nanosized additives on the graphite quantity, size and morphology as well as on the quantity ratio between ferrite and pearlite to be determined (Table 1). The analyses are carried out on three randomly chosen field of the ground joint and the average data are presented. Nanosized additives of TiCN+TiN in the spheroidal graphite cast irons don't change the graphite shape, but they decrease the average diameter of the graphite spheres Dmid from 11,00 to 10,50 µm (Figure 1a).

Nanosized additives increase the graphite phase quantity to 94% compared to this one of the irons without nanoparticles (Figure 1b).

Table 1. Nanoadditives, graphite characteristics, graphite, pearlite and ferrite quantity, hardness and tribological properties of spheroidal graphite cast irons.

№ of sampl	Nanosized additive	D_{mid} μm	Round-ness	Volume part of: [%]			Hardness HB	Intensity of wear i	Wear resistance I
				Graphite	Pearlite	Ferrite			
1	-	11,0	1,59	8,44	32,12	59,44	185	$0,124.10^{-6}$	$8,06.10^{6}$
2	*TiCN+TiN*	10,5	1,28	16,36	25,36	58,28	180	$0,08.10^{-6}$	$12,5.10^{6}$
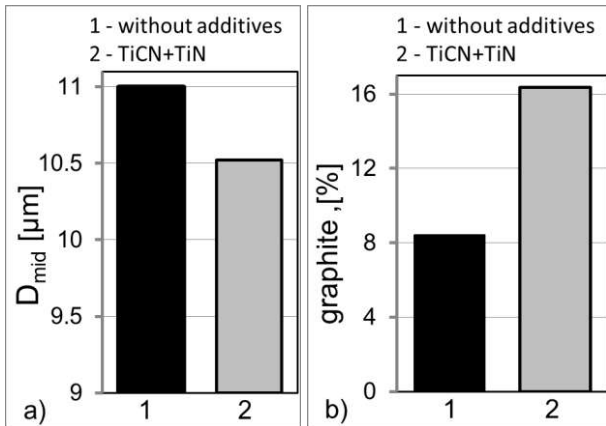
Figure 1. Average diameter of the graphite spheres Dmid (a) and graphite quantity (b) in spheroidal graphite cast irons: samples number – 1 and 2.

They change the quantity of the pearlite and ferrite in the structure of the cast iron samples (Table 1). The hardness of the tested irons is 185 HB for the sample 1 and 180 HB for the sample 2 (Table 1).

SEM analysis of the fracture of the impact destructed spheroidal graphite cast iron sample with TiCN+TiN nanoparticles additives (Figure 2) and EDX analysis of the graphite phase (Figure 3) are performed and the nanoparticles presence in the graphite is observed. These results and that achieved from the quantity metallographic analysis prove the modifying influence of the nanoparticles on the size and shape of the graphite phase in the iron samples.

In assessing the wear resistance of the iron base structure is necessary to take into account its ability to be changed as a result of a complex set of processes in operation. In the materials with a stable structure obtained after casting, improvement or normalization changes in the microgeometry, appearance of a sizable retained tension and strengthening of the surface layers by a formation of strips of sliding is observed.

Graphite in the gray cast iron structure has an essential role in their behavior in wear. In the dry friction in individual sections of the contact surface is not observed practically wear caused by adhesion. This is related to the presence of graphite in the structure, which has a lubricating ability and acts as a lubricant material.
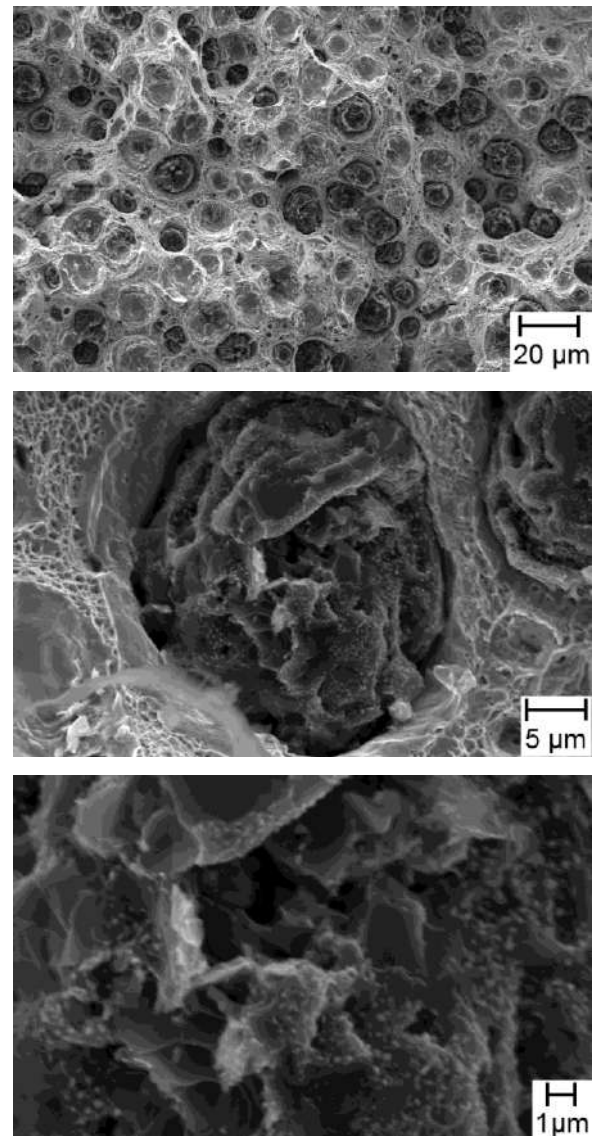
Figure 2. SEM analysis of the fracture of the impact destructive sample from spheroidal graphite cast irons with nanoadditives of TiCN+TiN (sample 2).

The wear resistance of the cast irons with a pearlite base at specified conditions of wear (contact pressure and sliding speed) is inversely proportional to the average distance between the graphite grains. By reducing the distance between the graphite grains the protective properties of the surface carbon layer improve and the wear resistance of the cast iron increases.
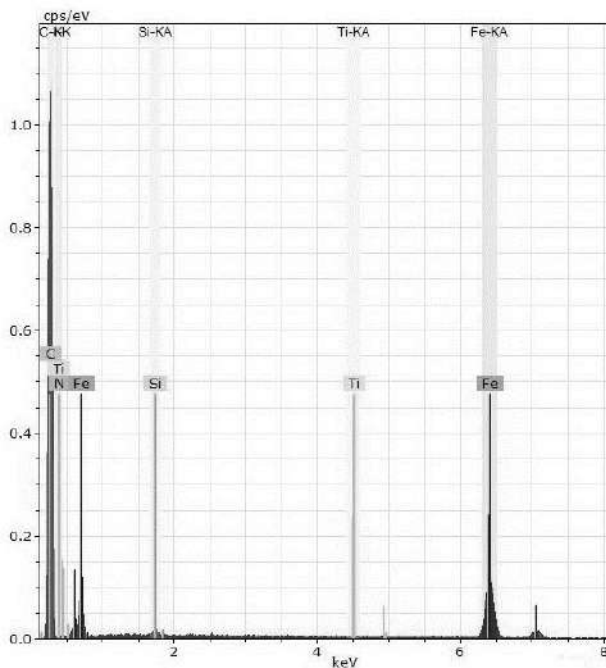
Figure 3. EDX analysis of the graphite phase in spheroidal graphite cast irons with nanoadditives of TiCN+TiN (sample 2).

The studied spheroidal graphite cast irons with or without nanosized particles have an equilibrium ferrite-pearlite structure of the substrate and inclusions of graphite spheres. The results of the quantitative metallographic analysis, SEM and EDX analysis show that the nano-sized additives possess modifying influence on the graphite and without changing its shape, increase its quantity leading to a reduction of the average distance between the graphite grains. The intensity of wear of the cast iron with nanoadditives of TiCN+TiN decreases and the wear resistance increases by 55 % compared to this one of the cast iron without nanoparticles (Table 1, Figure 4).

The wear resistance increase observed in the tested samples probably is connected not only with the defined changes in the quantity

and size of the graphite phase, but also with the nanoadditives influence on the surface strengthening in friction.
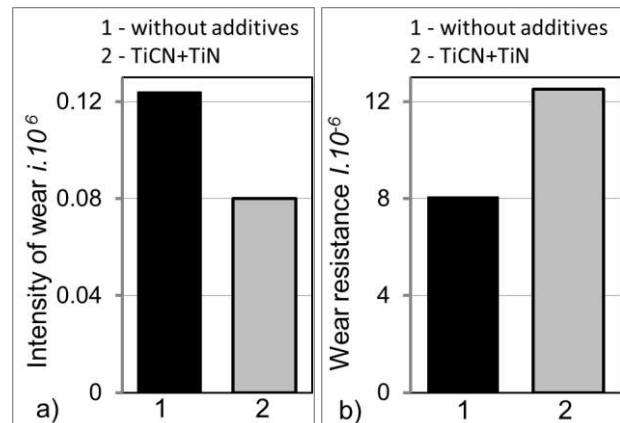
Figure 4. Intensity of wear i (a) and wear resistance I (b) of spheroidal graphite cast irons: samples number – 1 and 2.

The ductile cast irons are undergone to austempering in the bainitic area. The austempering mode includes austenitization at 900°C, 1 h followed by isothermal retention at 280 ^{o}C, 2 h with formation of a lower bainic structure (Figure 5) and isothermal retention at 380°C, 2 h with formation of a upper bainitic structure (Figure 6).
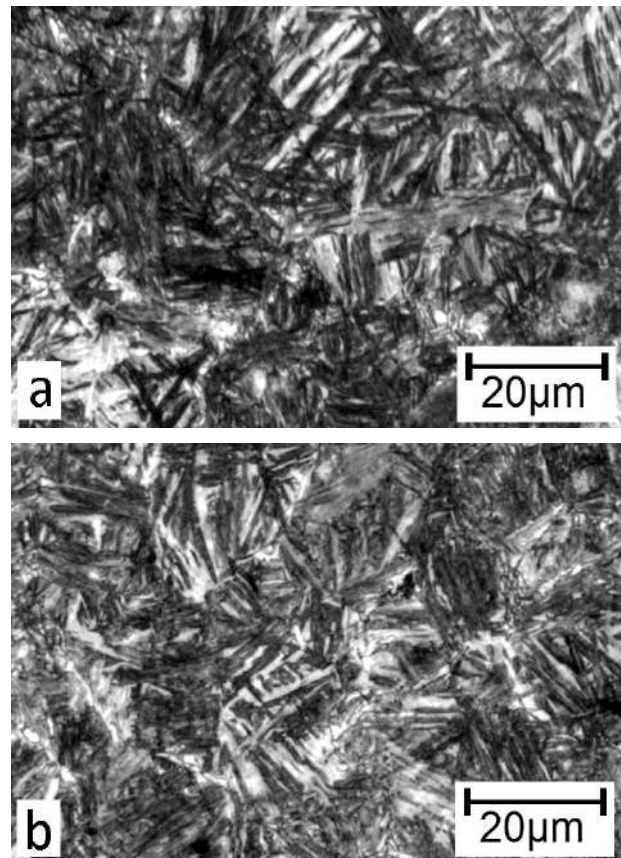
Figure 5. Lower bainite in uastempered ductile irons: a-sample 3; b-sample
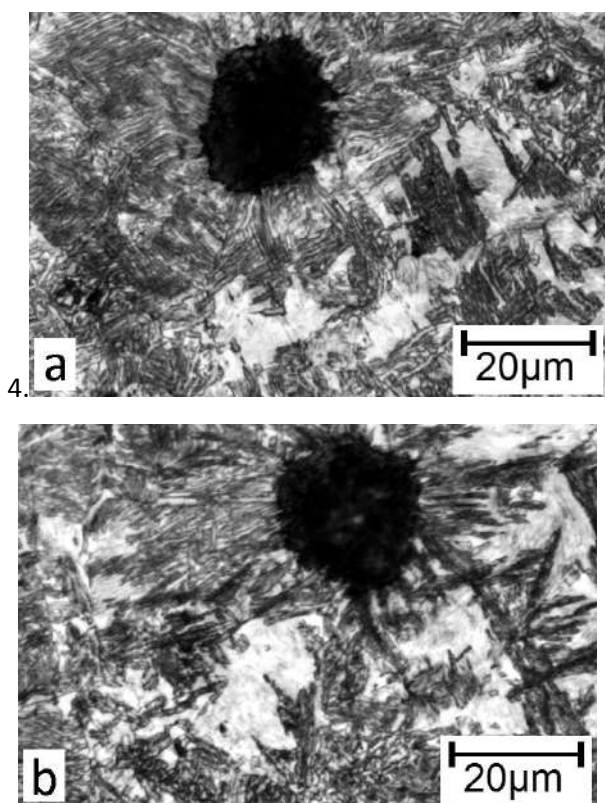
Figure 6. Upper bainite in austempered ductile irons: a-sample 5; b-sample 6.

Bainite is an oriented structure consisting of needles α - phase (bainitic ferrite), carbides and unconverted austenite. α-phase is formed by martensitic mechanism in austenitic areas with low carbon content [1,2,6]. Upon cooling on the temperature of isotherm to ambient temperature, the part of the unconverted austenite undergoes martensitic transformation, and another part thereof remains in the structure as a retained austenite A.

The austenite bainitic transformation begins with the formation of individual needles α-phase (bainitic ferrite) and is developed with the formation of new oriented needles located close to each other and forming a package of alternating plates α-phase and the unconverted austenite enriched with carbon A (c). Optical metallographic analysis shows this package as an individual needle in the low bainitic struiucture. Carbide phase is formed as a result of self-tempering of the α-phase or directly from A(c).

The microstructure and crystallographic characteristics of the lower and upper bainite are similar. The main difference is that the bainitic ferrite (α phase) in a lower bainite is supersaturated with a larger amount of carbon compared to this one of the upper bainite.

This means that the carbide particles in the lower bainite are separated mainly in the inner part of the ferrite plates, as in the upper bainite the carbide phase mainly is separated directly from the enriched with carbon austenite A (c).

Silicon in the spheroidal graphite cast irons (2-3%) hinders process of the carbide formation. A transformation to a bainitic ferrite and enriched with carbon unconverted austenite A(c) structure with high mechanical characteristics is realized at austempering for 2-4 hours. An austempering mode over 6 hours could lead to a decomposition of the enriched with carbon austenite to a composite of ferrite and carbide (α +carbide), which decreases the iron mechanical properties and practically not carried out [1,2].

The hardness HV10 of the tested austempered samples with a lower bainitic structure is in the range of 388 HV10 (sample 3) and 422 HV10 (sample 4), whereas this one of the upper bainitic structure is – 314 HV10 (sample 5) and 319 HV10 (sample 6) (Table2, Figure 7). The higher lower bainitic hardness is correlated to the higher carbon saturation of the α–phase and to the higher degree of the austenite transformation in the lower temperature range of the bainitic area.

The quantity of the retained austenite in the samples with upper bainitic structure is higher than this one in the samples with the lower bainitic structure after 2 hours austempering at 380 and 280°C (табл.2). This correlates with the characteristics of the bainitic transformation mechanism in the upper and lower temperature range of the bainitic area [1,2]. Nanosized additives of *TiCN+TiN* in the austempered ductile irons change the bainitic transformation kinetics and accelerate the austenite transformation to bainite. The retained austenite quantity decreases from 30,6% for the samples without nanoadditives to 24,9% for the samples with nanoadditives after 2 hours austempering at 280°C. For 2 hours austempering at 380°C the retained austenite quantity decreases

from 40,4 % to 27,1% for the samples with the same composition (Table 2).

Table 2. Tribological properties, hardness and retained austenite quantity of austempered ductile irons

№ of sample	Structure after austempering	Nanosized additive	Hardness HV10	Intensity of wear i	Wear resistance I	Retained austenite A, %	
						before wear test	after wear test
3	lower bainite	-	388	$0,14.10^{-6}$	$7,13.10^6$	30,6	25,0
4		TiCN+TiN	413	$0,08.10^{-6}$	$12,3.10^6$	24,9	12,2
5	upper bainite	-	314	$0,13.10^{-6}$	$7,67.10^6$	40,4	31,3
6		TiCN+TiN	319	$0,10.10^{-6}$	$9,42.10^6$	27,1	11,6
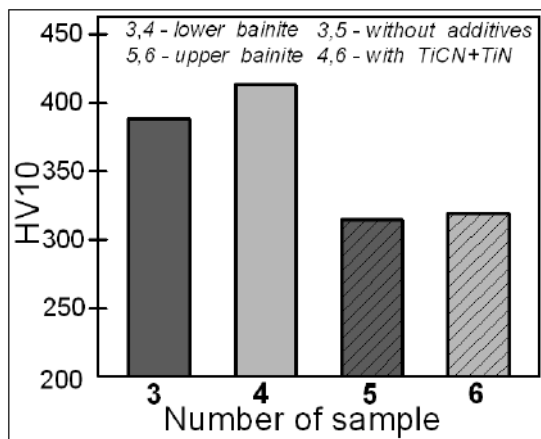
Figure 7. Hardness HV10 of austempered ductile irons with a lower bainitic structure (samples 3 and 4) and upper bainitic structure (samples 5 and 6).
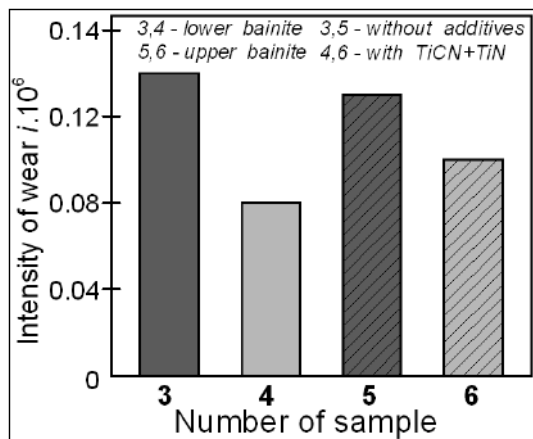
Figure 8. Intensity of wear i of austempered ductile irons with a lower bainitic structure (samples 3 and 4) and upper bainitic structure (samples 5 and 6).

The results achieved for the intensity of the wear i and for the wear resistance I of the tested samples of austempered ductile iron are shown in the Table 2 and Figure 8 and 9. The 4 and 6 samples with nanoadditives of *TiCN+TiN* possess higher wear resistance of 73% (for a lower bainitic structure) and of 23%

(for a upper bainitic structure) compared to the wear resistance of the samples 3 and 5 without nanoadditives.
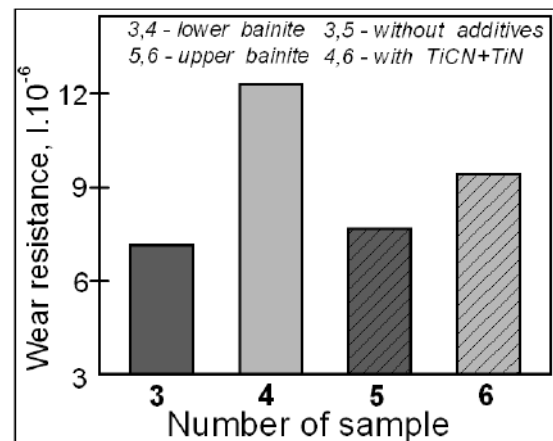
Figure 9. Wear resistance I of austempered ductile irons with a lower bainitic structure (samples 3 and 4) and upper bainitic structure (samples 5 and 6).

The tribological properties of the metal materials depend in a great extent on the structural condition, formed on the contact surface in friction. In the conditions of intensive plastic deformation of the metal in the area of the friction contact in the metastable structures (retained austenite, martensite, bainite) occur structural transformations that have a strong influence on the effective strength of the surface and, accordingly, on the tribological properties of the materials.

To the structural transformations of the α-martensite, initiated by plastic deformation, strain dynamic ageing or "strain tempering" of the martensite is connected. The processes of a strain dynamic ageing are characterized with a formation of segregates (atmospheres) of

carbon atoms on the emerging in friction dislocations. The strong fixing of the dislocations with dopands determines intensive strain strengthening of high carbon martensite in friction as well an increase in its resistance to various types of wear.

To the metastale structures refers also retained austenite, which undergoes strain induced γ→α martensite transformation in friction. In friction the retained austenite partially transforms to a strain induced martensite with the same quantity carbon as well a high carbon austenite and It appears untempered martensite with high hardness and capacity for intensive strengthening in a wear processing [6, 10].

X-Ray analysis is carried out for defining the possibility of martensite formation as a result of a strain induced γ→α martensite transformation in the area of the friction contact in the wear test. The quantity of the retained austenite is determined in the tested samples before and after the tribological testing (Table 2). It is found that the quantity of the retained austenite decreases in the all of the tested samples (Figure 10).
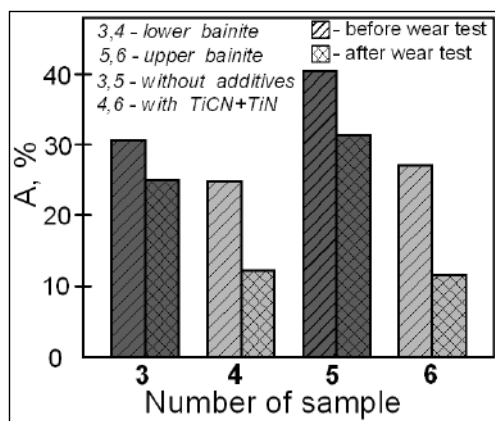
Figure 10. Quantity of the retained austenite A of austempered ductile irons with a lower bainitic structure (samples 3 and 4) and upper bainitic structure (samples 5 and 6) before and after tribological testing.

For the samples without nanoadditives (sample 3) the decrease is from 30,6% to 25,0% and from 40,4% to 31,3% (sample 5) and for the samples with nanoadditives of *TiCN + TiN* - from 24,9 % to 12,2 % (sample 4) and from 27,1 % to 11,6 % (sample 6) (Table2; Figure11; Figure12).
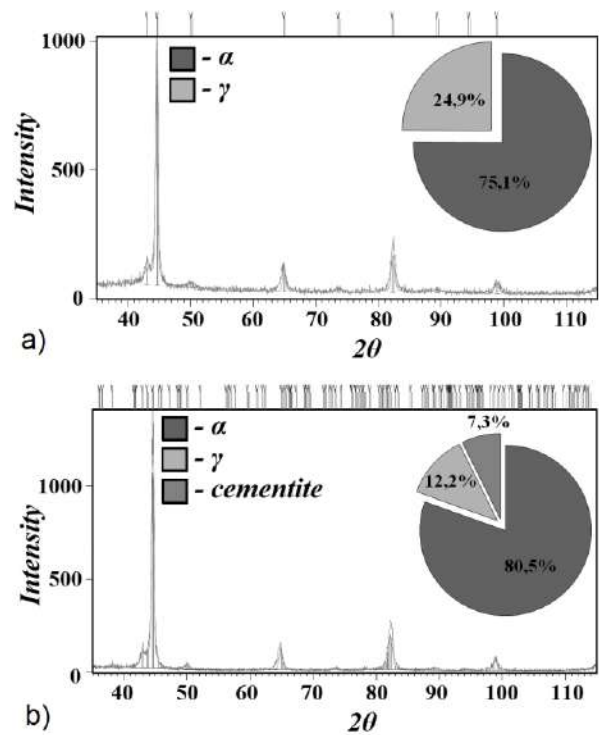
Figure 11. X– ray diffraction pattern of austempered ductile iron sample 4 before (a) and after (b) wear test
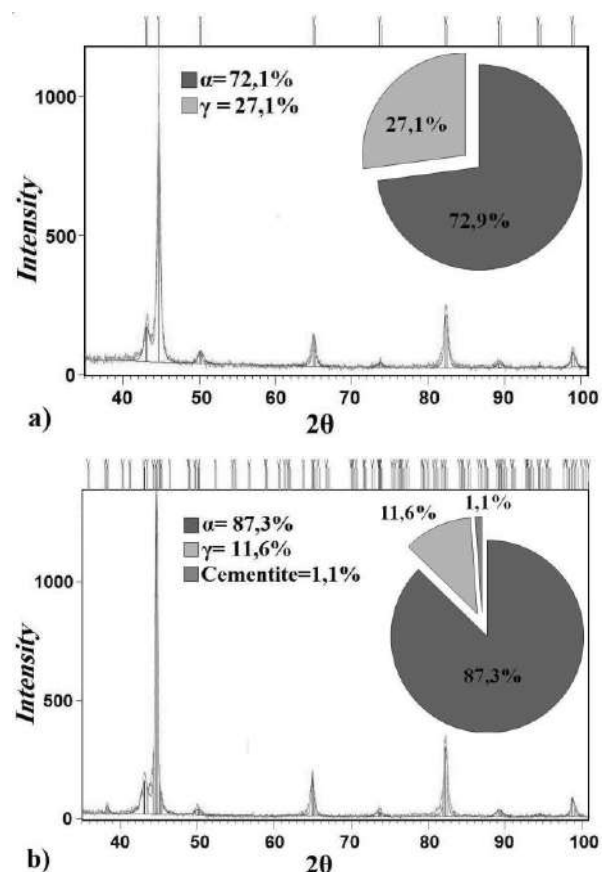
Figure 12. X– ray diffraction pattern of austempered ductile iron sample 6 before (a) and after (b) wear test.

In the area of the friction contact from the metastable retained austenite the strain

induced martensite is formed, which probably additionally increases the wear resistance of the austempered ductile irons. The tests performed show that in the irons with nanoadditives of *TiCN + TiN* the transformation of the retained austenite to strain induced martensite takes place in a greater extent in the wear and they have higher wear resistance compared to the irons without nanosized additives.

The observed effect of the nanoadditives on the graphite phase characteristics and on the extent of the transformation of the austenite to bainite, also the greater extent of the metastable retained austenite transformation to a strain induced martensite in the area of the friction contact in friction explain higher abrasion wear resistance of the tested austempered ductile irons with nanoadditives compared to the same without nanoadditives.

3. CONCLUSION

Nanosized additives of *TiCN + TiN* in the spheroidal graphite cast irons have a modifying effect on the graphite phase. Without changing the graphite shape, they decrease the graphite spheres size and increase the graphite quantity in the irons' structure. The spheroidal graphite cast irons with nanosized particles have a higher abrasion wear resistance compered to this one of the irons without nanoparticles.

It is specified that retained austenite in the structure of austempered ductile irons is partially transformed to a strain induced martensite in the wear testing as in a greatest extent, this conversion takes place in the cast irons with nano-sized additives of *TiCN + TiN.* These irons possess higher abrasion wear resistance compered to this one of the irons without nanoadditives. The increase of the wear resistance of the irons with nanoadditives is a result of the complex influence of the nanosized particles on the graphite phase chracteristics, on the kinetics

of the bainitic transformation under austempering and on the range of the metastable retained austenite conversion to a strain induced martensite in an wear testing.

REFERENCES

[1] E. Dorasil: *High-strenght Bainitic Nodular Cast Iron,* Academia, Prague, 1985.

[2] H.K.D.H. Bhadeshia: *Bainite in steels*, 2nd edit.London,Instution of Materials, Cambridge, 2001.

[3] Y. Wang, Z. Pan, Z. Wang, X. Sun, L. Wang: Sliding wear behavior of Cr–Mo–Cu alloy cast irons with and without nanoadditives, Wear Vol. 271, No. 11-12, pp. 2953– 2962, 2011.

[4] J. Kaleicheva, M. Kandeva, V. Mishev, Z. Karaguiozova: Wear Behavior of Ductile Cast Irons with Nanoparticle Additives, J. Chem. Chem. Eng., Vol.7, No 11, pp. 1044–1049, 2013.

[5] J. Li, M. Chen, H. Gao, Y. Zhao: Structures and Properties of Cast Irons Reinforced by Trace Addition of Modified SiC Nanopowders, Chinese Journal of Chemical Physics, Vol.20, No 6, pp. 625-631, 2007.

[6] J. Kaleicheva, V. Mishev, G. Avdeev, Z. Karaguiozova, B. Dineva: Influence of Nanoadditives on the Structure and Properties of Austempered Ductile Irons, in: *Proceedings of the European Conference on Heat Treatment and 21st IFHTSE Congress,* 12-15.05.2014, Munich, Germany, pp. 537-543.

[7] J. Kaleicheva: Wear Behavior of Austempered Ductile Iron with Nanosized Additives, Tribology in Industry, Vol. 36, No 1, pp. 74-78, 2014.

[8] G. Gavrilov: *Chemical (electroless) nickel-plating*, Portcullis Press, 1979.

[9] J. Birkenstock, R. X. Fischher, T. Messner,: *BRASS 2003: The Bremen Rietveld Analysis and Structure Suite,* Ber. DMG, Beih. z. Eur. J. Mineral. Vol. 15, No.1, 2003.

[10] A. Макаrov: *Wear resistance increase of iron alloys at the expense of metastable and nanocrystal structure formatio* , PhD thesis, Ural Department of the Mechanical Engineering Institute of the Russian Academy of Sciences, Chelyabinsk , 2009.

EFFECT OF GRAPHENE NANOPLATELETS (GNPs) ON TRIBOLOGICAL AND MECHANICAL BEHAVIORS OF POLYAMIDE 6 (PA6)

Ferda MINDIVAN[1,a,*]

[1]Department of Technical Programs, Bozuyuk Vocational College, Bilecik Seyh Edebali University, Bilecik, Turkey
[a]Biotechnology Application and Research Center, Bilecik Seyh Edebali University, Bilecik, Turkey
*Corresponding author: ferda.mindivan@bilecik.edu.tr

Abstract: *The effects of Graphene Nanoplatelet (GNP) on mechanical and tribological properties of Polyamide 6 (PA6) were studied. The composites were blended using twin-screw extruder and subsequently injection molded for test samples. Mechanical properties were investigated in terms of microhardness, scratch hardness and Young's modulus measurements and tensile test. The tribological behavior of composites was studied by using ball-on-disc reciprocating tribometer. Recent studies showed that the addition of GNP in PA6 matrix resulted in enhancement of mechanical and tribological properties.*

Keywords: *Graphene, composite, polyamide 6, scratch hardness, tribology.*

1. INTRODUCTION

Strong composite materials based on polymeric matrices are increasingly used in wide range of engineering applications, due to their higher stiffness-to-weight ratio in comparison with metallic materials as well as their enhanced corrosion-resistance. In order to improve their poor surface characteristics, various particles such as carbon nanotubes and boron carbide have been used especially in the recent decade [1, 2]. Due to its extraordinary mechanical properties with a reported Young's modulus of 1 TPa and a tensile strength of 130 GPa [3, 4], graphene nanoplatelets (GNPs) are an ideal reinforcement for strengthening polymer matrices. In order to improve the properties of GNP-polymer composite, the surface of GNPs is modified either physically or chemically [5]. It is generally considered that the surface

modification of GNPs is beneficial to improve the dispersal property of GNPs in polymer matrix. However, the modifying process is usually complicated and damages the structure of the GNPs and thereby greatly reduces their mechanical properties [6]. Thus, the enhancement effect of the GNPs will be weakened.

The objective of this paper is to fabricate PA6/GNP composites and investigate the effects of GNP loading content on the mechanical and tribological properties of the PA6/GNP composites without using any surface modification process.

2. EXPERIMENTAL METHODS

GNPs in this study were GRAFEN-IGP2 nanoplatelets (Grafen Chemical Industries, Turkey). These nanoparticles consist of short stacks of graphene layers having a lateral

dimension of ~5 nm and a thickness of ~5–8 nm. SEM observation (Fig. 1) of GNPs shows that the GNPs superimpose together and look like wrinkled or crumpled thin paper. Melt blending of PA6 and GNP was carried out in a co-rotating twin screw extruder (Thermoprism TSE 16 TC, L/D 24) at a screw speed of 100 rpm and barrel temperature profile of 230-230-230-230-230 °C, followed by granulation (3 – 5 mm long and 3 mm in diameter) in a pelletiser and drying. Prior to extrusion, the PA6 polymer and GNP were dehumidified in a vacuum oven at 90 °C for a period of 24 h. The GNP content in the PA6/GNP composites was varied from 1 – 4 wt. % (Table 1). The composite mixture was molded using a laboratory scale plunger type injection-molding machine (Micro injector, Daca Instruments) at a barrel temperature of 200 °C and mold temperature of 30 °C, for preparation of microhardness, scratch hardness, Young's modulus, tensile and tribological test samples.
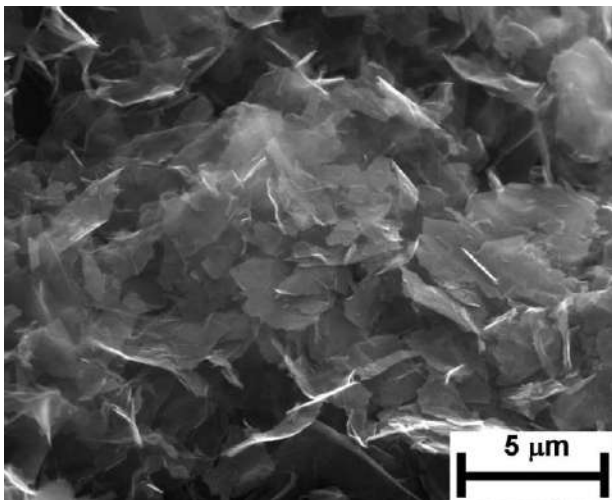
Figure 1. The SEM image of GNPs.

Table 1. Ratios and codes of GNP in the composites.

Samples	GN Content (in weight %)
PA6/GNP-1	1
PA6/GNP-2	2
PA6/GNP-4	4

Room temperature mechanical properties of the unfilled PA6 and PA6/GNP composites were determined according to microhardness and Young's modulus measurements, scrathch

hardness and tensile tests. Microhardness measurement was carried out on metallographic samples under the load of 50 g with a Vickers indenter. At least ten successive measurements were performed for each condition. The Impulse Excitation Technique (IET) was used to measure the Young's modulus of the sample series in accordance with the ASTM E 1876 standard [7]. Briefly, IET utilises the phenomenon of free mechanical resonance of flexural vibrations when these vibrations are excited by tapping the test sample. Analysis of the fundamental frequency of a specific vibration mode, which depends on sample mass, stiffness, and geometry, allows determining the Young's modulus by measuring the resonance frequency. The tensile test samples with a gage length of 80 mm were also tested according to the ASTM D 3822 standard [8] on Lloyd LR 5K tensile testing machine with a load cell of 10 N and the deformation rate was 20 mm/min. All the results represented an average value of five tests with standard deviations. The scratch tester, designed and built in our laboratory, was used to carry out scratch tests equipped with a Rockwell C-type conical indenter under laboratory environment condition (the temperature was 25 °C and the humidity was ~30-35 % RH). The tests were conducted at four different loads (5, 10, 15 and 20 N) with a constant tip velocity of 0,007 m/s. The length of the scratch was kept constant as 10 mm. In order to assess tribological properties of the unfilled PA6 and PA6/GNP composites, the friction and wear tests were conducted on a reciprocating wear tester under dry sliding conditions. The ambient temperature was approximately 25 °C and the relative humidity was nearly 40 ± 5 %. The wear tests on all samples were performed under a constant load of 10 N using a 10 mm diameter 304 steel ball at a sliding velocity of 1.7 cm s^{-1}. In all tests, the total sliding distance was kept constant at 50 m. The wear was calculated by analysing width and depth of wear scars developing on sample surfaces with the help of a contact stylus profilometer (SJ400). Following the wear tests, the steel counterface

surfaces were examined under an Optical Microscope (OM) in order to investigate the wear mechanisms. Then, scratch and wear scars on the surfaces of the unfilled PP and PA6/GNP composites were examined using a Scanning Electron Microscope (SEM- Carl Zeiss AG - SUPRA 40).

3. RESULTS AND DISCUSSION

Figure 2 showed XRD patterns of the unfilled PA6 and PA6/GNP composites. PA6 exhibited polymorphic structures containing two types of crystal form: monoclinic (α) and pseudo-hexagonal (γ).
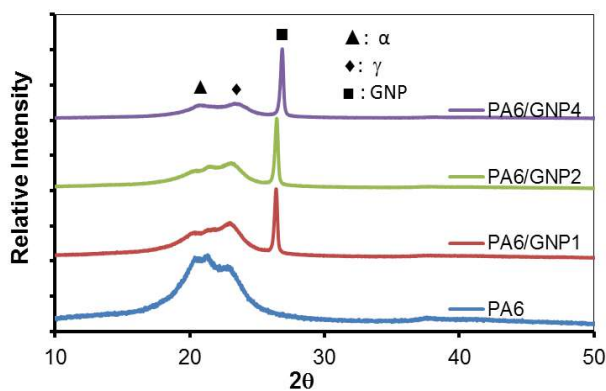
Figure 2. XRD patterns of unfilled PA6 and PA6/GNP composites.

The representative diffraction peaks observed at 2θ=20.4° and 21.8° corresponded to α and γ crystalline phases of the unfilled PA6 [9, 10], respectively. As shown in Fig.2, α phase was the dominant crystalline phase for the unfilled PA6. Also, all composites showed two peaks at 2θ=20.1° and 22.1°, corresponding to α and γ crystalline phases. When compared to the unfilled PA6, the diffraction peak corresponding to α-form crystal phase was observed only as a less pronounced shoulder at all GNP contents. However, the peak of γ form crystal phase in the PA6/GNP composites grew more obvious. However, referring to Fig. 2, in addition to the two reflections as seen in the PA6/GNP composites a other reflection was also detected at 2θ=26° which was related to the GNP [11]. According to these results, GNPs changed crystal structure of all composites. Gong et al. [12] reported that the diffraction

peaks of α-form crystals of modified graphene based PA6 composites become weaker with an increase of GNP loading content. Oneill et al. [3] showed that functionalized graphene oxide (GO) and functionalized reduced graphene oxide (rGO) could promote the formation of γ phase crystals in the PA6 matrix.

The mechanical properties of PA6/GNP composites are characterized by their tensile strength, Young's modulus, elongation at break and microhardness. The effects of GNP loading content on tensile strength and Young's modulus of the composites are displayed in Fig. 3. As shown in Fig. 3, the PA6/GNP composites show similar tensile strength compared to that of unfilled PA6. In addition, the Young's modulus of PA6/GNP composites increases with an increase in GNP contents (Fig. 3). The Young's modulus of the composite with 4 wt. % loading content of GNPs increased by 50 %, compared with that of unfilled PA6. The influences of GNP loading content on elongation at break and microhardness of the composites are presented in Fig. 4.
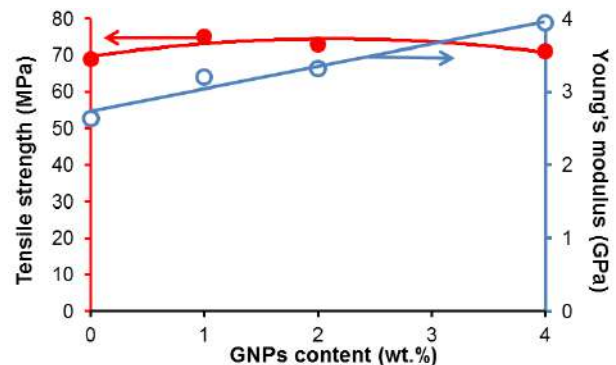
Figure 3. Tensile strength and Young's modulus of PA6 filled with various contents of GNPs
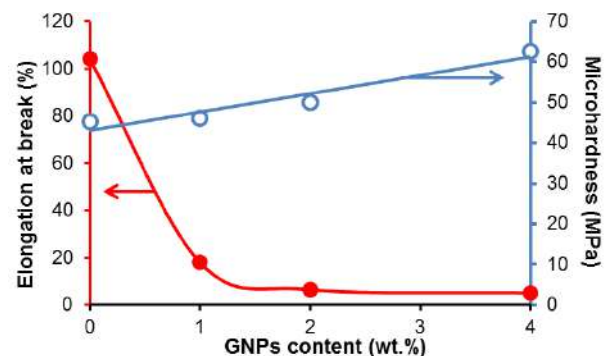
Figure 4. Elongation at break and microhardness of PA6 filled with various contents of GNPs

As seen from Fig. 4, the elongation at break of the composite decreases with an increase of GNP loading content and when the loading content is 4 wt.%, the value decreases by 95 % in comparison with that of unfilled PA6. However, the microhardness of composite increases with an increase of GNP loading content and when the loading content is 4 wt.%, the value increases by 38 % in contrast to that of unfilled PA6. The results of mechanical properties revealed that the incorporation of GNPs could improve the strength, but increase brittleness in the PA6/GNP composites due to alteration of the crystal structure of the PA6 matrix by the GNP (Fig. 2). Chatterjee et al. [6] reported that nanofillers could affect the mechanical properties of PA matrix by changing the crystallinity, which seems to be in compatible with my results.

In Fig. 5, by increasing the GNP content, scratch hardness showed a rising trend because of the existence of GNPs in the direction of the scratch test (Fig. 6) and decreased with increasing applied load. The rise of scratch hardness at a load of 20 N was sharper than the rise of the scratch hardness at lower loads (5, 10 and 15 N) because the role of the GNPs was diminished at smaller scratch depths.
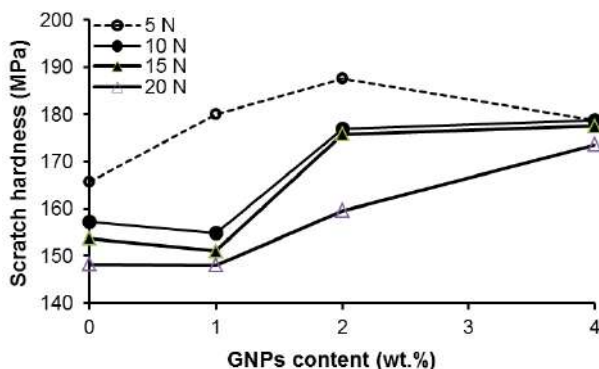
Figure 5. Scratch hardness of PA6 filled with various contents of GNPs

The effect of GNP addition on the tribological behavior of PA6 was investigated. It is shown that at small amounts of GNP, wear was reduced (Fig. 7) with a slight decrease in the average friction coefficient (from ~0.83 in the unfilled PA6 to 0.74 in the composite with 4 wt.% of GNP-4). Moreover, a larger number

of graphene sheets were obtained by adding more GNP into the PA6 matrix as illustrated in Fig. 8. A small increase in the basal spacing (the peak was shifted to the right) was also noted for the composites containing more GNP. These differences probably affected the tribological behavior.

(a)

(b)

(c)
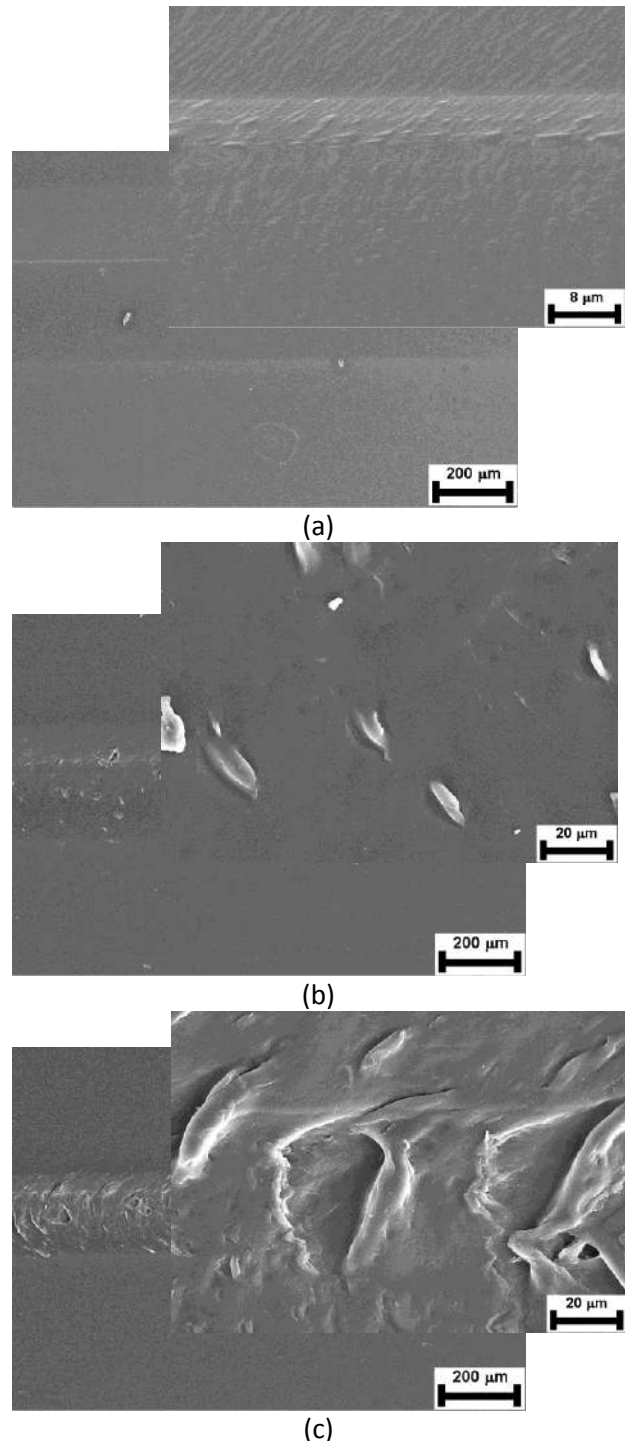
Figure 6. Low and high magnification SEM micrographs of scratch scars generated on the (a) unfilled PA6, (b) 2 wt.% PA6/GNP-2 composite and (c) 4 wt.% PA6/GNP-4 composite at a load of 20 N

It should be noted that the van der Waals forces in the composite with 4 wt.% of GNP-4 would have been lower than in the other composites, which could lead to a much easier way for the GNP layers to slide over each other.
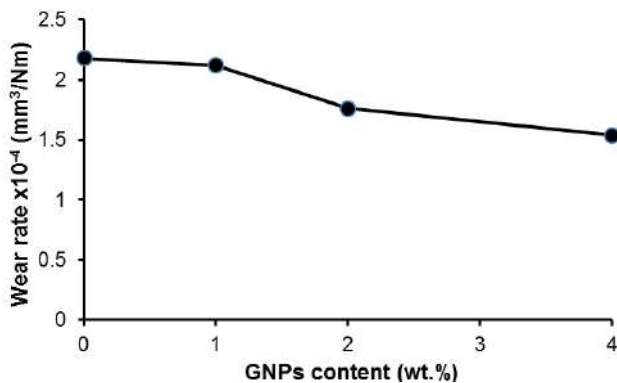
(a)
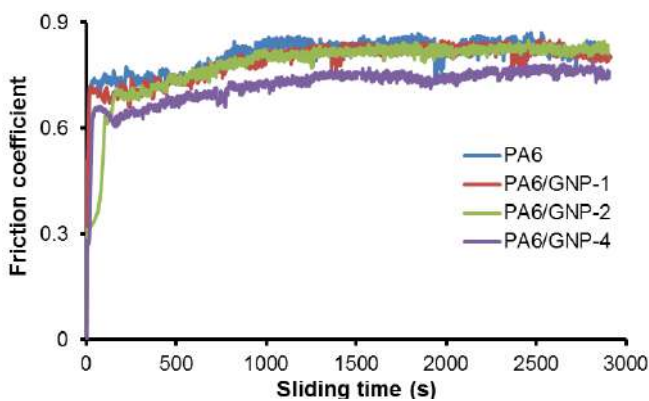
(b)

Figure 7. (a) Wear rate and (b) friction coefficient of PA6 filled with various contents of GNPs
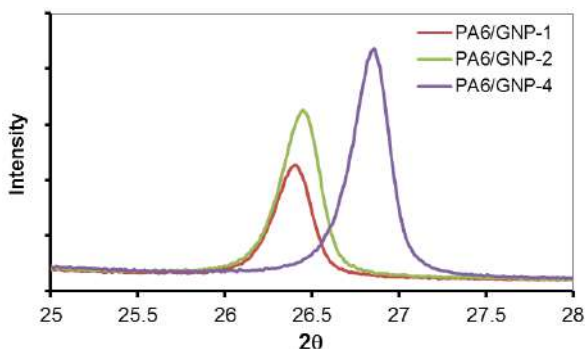
Figure 8. Comparison of GNPs' XRD Bragg peak at $2\theta \sim 26.5$ deg, confirming morphological differences of the composites containing 1, 2 and 4 wt. % of GNP

The SEM images of wear tracks for the unfilled PA6 and the composite with 4 wt.% of GNP-4 shown in Fig. 9 (all at the same magnification) are in accordance with the above analysis. For the unfilled PA6, the worn surface is rough and exhibits some scratch

grooves parallel to the sliding direction in the worn surface when sliding against the steel counterface. From the image of the composite with 4 wt. of GNP-4, it can be seen that nonuniform thin sheets are generated in the whole area investigated and thereby a rippled structure is formed, which is perpendicular to the sliding direction.
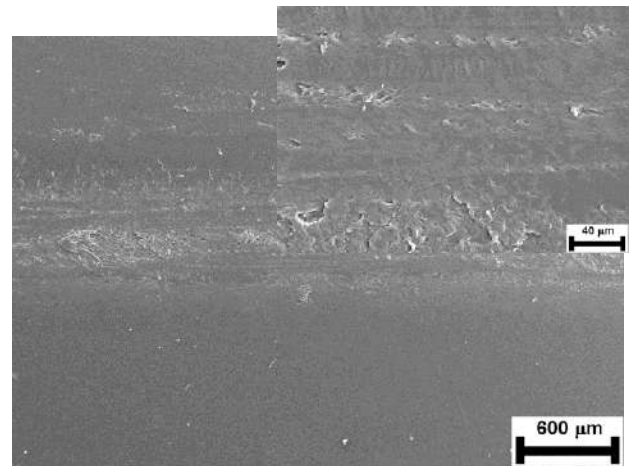
(a)
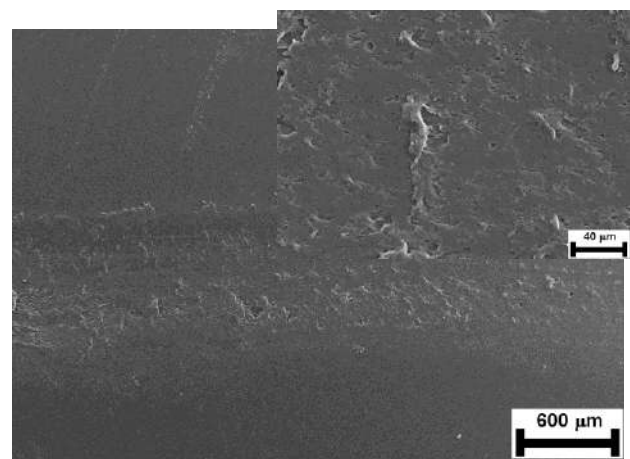
(b)

Figure 9. Low and high magnification SEM micrographs of wear tracks generated on the (a) unfilled PA6, and (b) 4 wt.% PA6/GNP-4 composite

Figure 10 shows OM images of the steel counter balls sliding against the unfilled PA6 and the composite with 4 wt. % of GNP after a sliding distance of 50 m. The rod like wear particles from the PA6 to the counter surface are white and adhere to the counter steel surface due to serious oxidization (Fig 10 a). It is evident that the temperature at the sliding interface has reached its melting point of PA6 during sliding, resulting in a poor wear property. On the other hand, some GNP particles reducing the friction by providing

interfacial sliding between the surface and steel counter ball were observed on steel ball surface sliding against the composite with 4 wt. % of GNP (Fig. 10 b). Dike et al. [1] have reported similar observations with CNTs in a polypropylene (PP) matrix and proposed that these fillers diminish the adhesion between the matrix and the counter surface; the digging phenomenon is thus reduced, and this results in a relatively higher wear resistance.
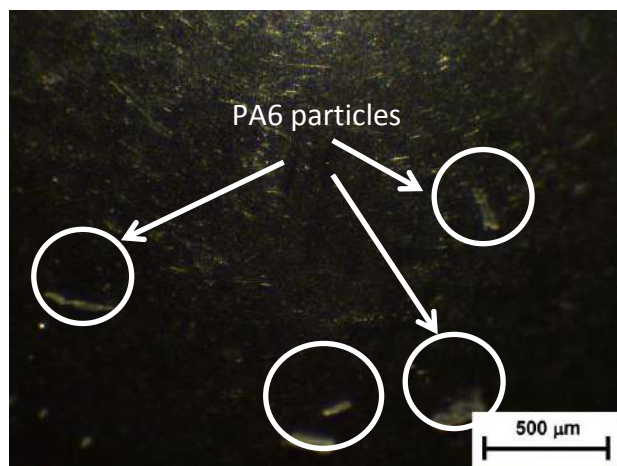
(a)
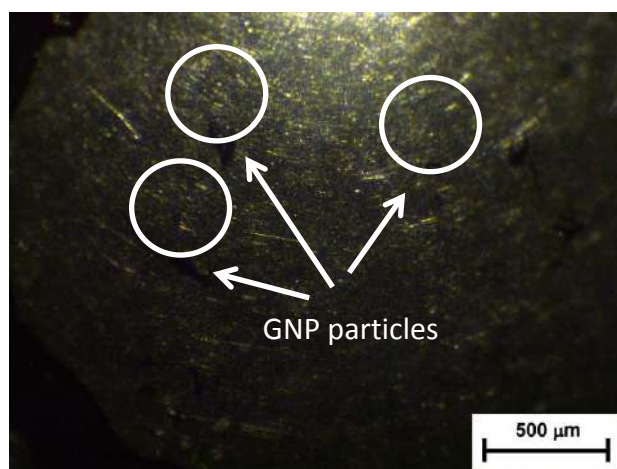
(b)

Figure 10. OM images of the steel balls sliding against the (a) unfilled PA and (b) composite with 4 wt.% of GNP

4. CONCLUSIONS

The addition of GNP has been proven an effective way to improve the Young's modulus, microhardness, scratch hardness and tribological performance of PA6-based polymer matrix without necessarily compromising tensile strength.

REFERENCES

[1] A.S. Dike, F. Mindivan, H. Mindivan: Mechanical and tribological performances of polypropylene composites containing multi-walled carbon nanotubes, International Journal of Surface Science and Engineering, Vol. 8, No. 4, pp. 292-301, 2014.

[2] A.S. Dike, F. Mindivan, H. Mindivan: Effect of B_4C content on the mechanical and tribological performances of polypropylene, Acta Physica Polonica A, Vol. 125, pp. 396-398, 2014.

[3] A. O'Neill, D. Bakirtzis, D. Dixon: Polyamide 6/Graphene composites: The effect of in situ polymerisation on the structure and properties of grapheme oxide and reduced graphene oxide, European Polymer Journal, Vol. 59, pp. 353–362, 2014.

[4] J.A. Puértolas, S.M. Kurtz: Evaluation of carbon nanotubes and graphene as reinforcements for UHMWPE-based composites in arthroplastic applications: A review, Journal of the Mechanical Behavior of Biomedical Materials, Vol.39, pp. 129–145, 2014.

[5] Y. Song, J.Yu, L. Yu, F.E. Alam, W. Dai, C. Li, N. Jiang: Enhancing the thermal, electrical, and mechanical properties of silicone rubber by addition of graphene nanoplatelets, Materials and Design, Vol. 88, pp. 950–957, 2015.

[6] S. Chatterjee, F.A. Nüesch, B.T.T. Chu: Crystalline and tensile properties of carbon nanotube and graphene reinforced polyamide 12 fibers, Chemical Physics Letters, Vol. 557, pp. 92–96, 2013.

[7] ASTM E 1876, *Standard test method for dynamic young's modulus, shear modulus, and poisson's ratio by impulse excitation of vibration*, American Society for Testing and Materials, 2001.

[8] ASTM D 3822, *Standard test method for tensile properties of single textile fibers*, American Society for Testing and Materials, 1997.

[9] T. Kashiwagi, R.H. Harris Jr, X. Zhang, R.M. Briber, B.H. Cipriano, S.R. Raghavan, W.H. Awad, J.R. Shields: Flame retardant mechanism of polyamide 6–clay

nanocomposites, Polymer, Vol. 45, pp. 881–891, 2004.

[10] P. Ding, S. Su, N. Song, S. Tang, Y. Liu, L. Shi: Highly thermal conductive composites with polyamide-6 covalently-grafted graphene by an in situ polymerization and thermal reduction process, Carbon, Vol. 66, pp. 576-584, 2014.

[11] J. Ma, Q. Meng, I. Zaman, S. Zhu, A. Michelmore, N. Kawashima, C. H. Wang, H.-C. Kuan: Development of polymer composites using modified, high-structural integrity graphene platelets, Composites Science and Technology, Vol. 91, pp. 82–90, 2014.

[12] L. Gong, B. Yin, L.-P. Li, M.-B. Yang: Nylon-6/Graphene composites modified through polymeric modification of graphene, Composites: Part B, Vol. 73, pp. 49–56, 2015.

OPTIMIZATION OF TRIBOLOGICAL PROPERTIES IN A356/10SiC/5Gr HYBRID COMPOSITE USING TAGUCHI METHOD

Blaža STOJANOVIĆ[1],*, Sandra VELIČKOVIĆ[1], Miroslav BABIĆ[1], Ilija BOBIĆ[2]

[1]Faculty of Engineering University of Kragujevac, Kragujevac, Serbia
[2]Department of Materials Science, Institute of Nuclear Sciences "Vinca",
University of Belgrade, Serbia
* Corresponding author: Blaža Stojanović: blaza@kg.ac.rs

Abstract: *In present study, the tribological behavior of hybrid composites with A356 aluminum alloy matrix reinforced with 10 wt.% of SiC and 5 wt.% of graphite was investigated using the Taguchi method. The composites were produced by the compocasting procedure. The tribological properties were studied using block-on-disk tribometer under lubricated sliding conditions at different normal loads (40N, 80N and 120N), sliding speeds (0.25 m/s, 0.5 m/s and 1 m/s) and sliding distances (150 m, 300 m and 1200 m). Analysis of the wear rate results was performed using the ANOVA technique. The lowest level of wear rate corresponded to the contact conditions with normal load of 40N, sliding speed of 1.0 m/s and sliding distance of 1200 m.*

Keywords: *Aluminum hybrid composites, optimization, SiC, Graphite, wear, Taguchi method*

1. INTRODUCTION

Composites with metal matrix (MMCS) are materials which possess excellent possibilities for development and contemporary material sciences. Lately, especially particle reinforced aluminum matrix composites, attract considerable amount of attention because they have the potentials of satisfying the recent demands of advanced engineering applications, such as for example demands of automobile and aerospace industries [1, 2].

Hybrid composites can have engineering combination of two or more forms of reinforcement like fibers, short fibers, particulates and whiskers. It can have different materials as reinforcement like silicon carbide - graphite (SiC - Gr), silicon carbide - alumina

(SiC - Al_2O_3), boron carbide - graphite (B_4C - Gr), graphite - alumina (Gr - Al_2O_3), and organic reinforcements are also used like fly ash etc [3, 4].

Just by choosing the right combination of particles for material reinforcement, their performance depends on it because some of the parameters for processing are directly connected with reinforcement particles. However, the final properties of the hybrid reinforcement depend on individual properties of the selected reinforcement and the matrix alloy. A few of such parameters are reinforcement type, size, shape, modulus of elasticity, hardness, distribution in the matrix among others [1-4].

The fabrication cost of aluminum metal matrix composites is low so it is manufactured

on a large scale and is one of the most extensively used product worldwide. Aluminum metal matrix composites (AMMCs) have many advantages, including higher strength, abrasion and impact resistant, higher wear resistance, higher thermal conductivity and lower coefficient of friction and exactly for already mentioned advantages they became the substitute for conventional materials. The application area of AMMCs is very wide and it is usually used for production of engine pistons, cylinders barrel, connection rods, elements of vehicles braking systems, cardan shafts, gears, valves, turbines, belt pulleys, turbo-compressors housings of pumps and supporting parts and so on [5-8].

Numerous scientists and researchers have done extensive research on mechanical and tribological behaviours of composite materials for their characteristics. Researches of these behaviours are still in the process because of the increased use in aerospace, automotive, marine, electronic and manufacturing industries.

Shubhranshu Bansal and J. S. Saini have conducted a research on mechanical and wear properties of composite materials. As matrix material they used Al359 reinforced by silicon-carbide particles and silicon carbide/graphite manufactured in stir casting process. They concluded that the hardness of Al359-silicon carbide composite is better than that of Al359-silicon carbide graphite composite. And in tribological testing they showed that the wear resistance of Al359 alloy is increased by reinforcement of material silicon-carbide/graphite in high load conditions, sliding speed and sliding distance [9].

B. Pavithranetet al. have completed the studies of mechanical and tribological properties of hybrid composites with Al6061 matrix. Experiments of wear were conducted on disc dry sliding test rig with sliding velocity of 2 m/s and 4m/s under load of 30N and 50N. Varying the reinforcement percentage of SiC (0% and 8%) and Gr (0%, 2% and 4%) they noticed that by increasing reinforcement percentage, wear rate decreases. They also concluded that by increasing sliding velocity, wear rate also increases, whereas the influence of load is minimal on the applied load range on wear rate [10].

Gajendra Dixit and Mohammad Mohsin Khan investigated the impact of the change graphite particle dimensions in partial lubricated sliding wear behavior of 10 wt.% SiC reinforced aluminum composites with the help of a pin on disc wear testing machine. Composited were prepared in liquid metallurgy route method whereas the tests on wear were done on pin-on-disc machine. They noticed that wear rate increased with load and speed. They concluded that samples' testing in oil plus graphite lubricated conditions led to less wear rate than that in oil alone. Then, that by adding 5 wt.% graphite (7-10 μm) to the oil lubricant led to minimum wear rate, and composites reached the lowest wear rate value whereas matrix alloy reached the highest. In the work they showed that wear rate coefficient decreases especially on samples at low loads, and additionally it reduces wit addition of graphite to the lubricating oil [11].

T. Pratheep Reddy and N. Amara Nageswara Rao using Taguchi's technique studied the effect of applied load, speed and track diameter on wear rate intensity. They studied the properties of wear and friction of hybrid metal matrix composite with Al6061 alloy as base material and reinforcements of SiC and Gr. Using Taguchi's technique they concluded that considered factors have an impact on wear rate intensity and friction coefficient and they calculated the optimal variant for reaching minimal wear intensity: load 50N, speed 1000 rpm and track diameter 110 mm. Also, they concluded that composite wear resistance increases by addition of SiC and Gr particles and that the wear intensity is relatively lower for composites in relation to pure material matrix [12].

Taguchi optimization was used by many researchers in order to optimize tribological properties in aluminum hybrid composite. Design of experiments Taguchi method has in

recent years become popular tool for engineering optimization due to its simplicity and robustness.

The aim of this work is to study tribological behavior of hybrid composites with A356 matrix reinforced with 10 wt.% of silicon carbide and with 5 wt.% of graphite. The experiments were conducted in lubricated conditions so as to find out new information and to carry out optimization of hybrid composites. The analysis of impact of load, sliding speed and sliding distance was performed using the Taguchi method.

2. EXPERIMENT

2.1 Materials and method of fabrication

In the present study, aluminum alloy A356 used as matrix, 10 wt.% of silicon carbide SiC (39 μm) and 5 wt.% of graphite (35 μm) as reinforcement. The composites were prepared in the compocasting process. A356 is an aluminum alloy of the following chemical composition: Si (7.20 wt.%), Cu (0.02 wt.%), Mg (0.29 wt.%), Mn (0.01 wt.%), Fe (0,18 wt.%), Zn (0.01 wt.%), Ni (0.02 wt.%), Ti (0.11 wt.%) and the rest is Al [13].

2.2 Wear analysis

The tests were performed in lubricated sliding conditions on the samples hybrid composites. Tribological tests are done on advanced and computer supported tribometer with block on disc contact pair in accordance with ASTM G77 standard. Samples are of 15.75 mm x 10.16 mm x 6.35 mm in size, whereas the counter body discs of 35 mm in diameter were made of steel 90MnCrV8 with the hardness of 62-64 HRC [14, 15].

Examinations were conducted according to the designed experiment plan where the values of loads are 40 N, 80 N and 120 N, of sliding speed are 0.25 m/s, 0.5 m/s and 1 m/s, and of sliding distance are 150 m, 300m and 1200m. The objective of the study is to achieve the minimum wear rate.

3. DESIGN OF EXPERIMENTS

The Design of the experiment (DOE) is used in Taguchi method to achieve the most significant data while conducting minimal number of experiments. Taguchi optimization is an experimental optimization technique that uses the standard orthogonal arrays for forming the matrix of experiments, which enables not only conducting minimal number of experiments but also reaching better value level of each parameter. Signal-to-noise (S/N) ratios are used in data analysis in Taguchi method. There are three basic categories to seek the best results of experiments; these are the nominal-the-better, the larger-the-better, and the smaller-the-better. The optimal setting is the parameter combination with the highest S/N ratio [16, 17, 18].

The S/N ratio for wear rate using smaller-the-better characteristic given by Taguchi is as follows:

$$S/N = -10\log\frac{1}{n}\left(\sum_{i=1}^{n}y_i^2\right), \qquad (1)$$

where y_1, y_2.....y_n are the response of wear rate and n is the number of observations.

In this study, the experimental design was according to an L27 orthogonal array (OA) based on the Taguchi method, while using the Taguchi OA would significantly reduce the number of experiments. The control factors were load (L), sliding speed (S), and sliding distance (D) (table 1). For each process variable, three levels were considered.

Table 1. Control factors with their levels and SI units

Control factors	Units	Level		
		I	II	III
Load (L)	N	40	80	120
Sliding speed (S)	m/s	0.25	0.50	1.00
Sliding distance (D)	m	150	300	1200

Experimental wear rate results, together with their transformations into S/N ratio, are shown in table 2.

The signal to noise ratio for each parameter is presented in figure 1 (a). In figure 1 (b) is shows interaction plot for each factor for which parallel plot denotes no interaction while crossing indicates significant interaction.

Table 2. L27 orthogonal array for experimentation

	Load	Sliding Speed	Sliding distance	Wear rate $(mm^3 \times 10^{-3}/m)$	S/N ratio (db)
1	40	0.25	150	0.926	0.668
2	40	0.25	300	0.813	1.798
3	40	0.25	1200	0.273	11.277
4	40	0.50	150	0.680	3.350
5	40	0.50	300	0.713	2.938
6	40	0.50	1200	0.239	12.432
7	40	1.00	150	0.564	4.974
8	40	1.00	300	0.551	5.177
9	40	1.00	1200	0.202	13.893
10	80	0.25	150	1.879	-5.479
11	80	0.25	300	1.328	-2.464
12	80	0.25	1200	0.458	6.783
13	80	0.50	150	1.426	-3.082
14	80	0.50	300	1.033	-0.282
15	80	0.50	1200	0.372	8.589
16	80	1.00	150	1.093	-0.772
17	80	1.00	300	0.818	1.745
18	80	1.00	1200	0.299	10.487
19	120	0.25	150	3.158	-9.988
20	120	0.25	300	2.322	-7.317
21	120	0.25	1200	0.756	2.430
22	120	0.50	150	1.941	-5.761
23	120	0.50	300	1.588	-4.017
24	120	0.50	1200	0.561	5.021
25	120	1.00	150	1.207	-1.634
26	120	1.00	300	1.059	-0.498
27	120	1.00	1200	0.423	7.473
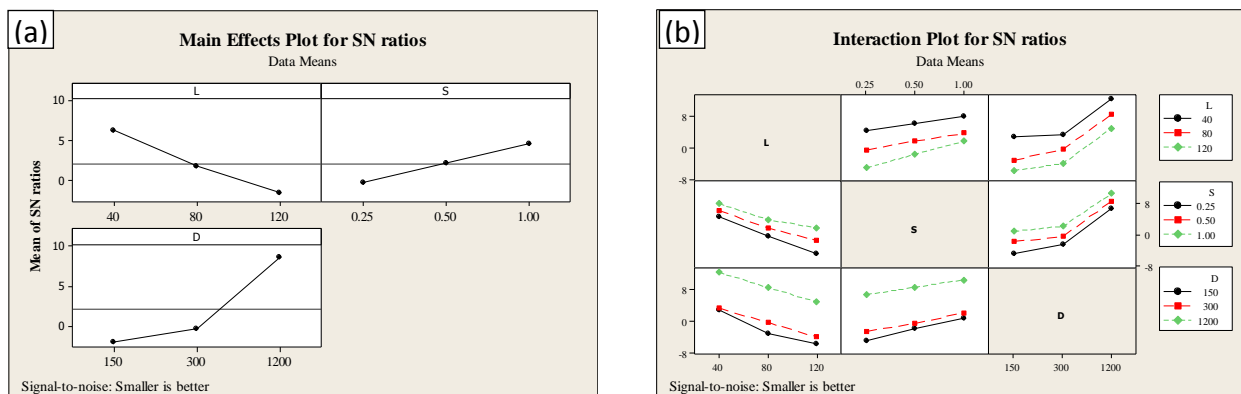
Figure 1. Graphical data of wear rate for smaller is better (a) main effects plot for S/N ratios (b) interaction plot for S/N ratios

According to signal to noise ratio for each parameter, factor levels can be determined for optimal wear rate base option. Factor optimal base option is L1S3G3, which means that the fist factor is on the first level, and the other two on the third.

4. RESULTS AND DISCUSSION

4.1 Wear analysis

Analysis of variance (ANOVA) is used for the analysis of experimental results and identification of factors which have significant impact on wear rate. The results of ANOVA analysis of considered factors and their interaction on wear rate ratio are given in table 3. The analysis was realized at 5 % significance level and a 95 % confidence level. The p values or probability values show the level of significance of each factor [19, 20]. In general the term having p-value less than 0.05 considered to have significant effect.

The percentage contribution by each of the process parameter in the total sum of the squared deviations was used to evaluate the importance of the process parameter change on the performance characteristic. From the sum of squares data contribution of each parameter was computed using equation (2).

$$\text{Contribution factor}(\%) = \frac{SS_f}{SS_T} \times 100 \qquad (2)$$

where SS_f is the sum of squares of factor and SS_T is the total sum of squares of all the parameters. This research was useful in achieving optimal value of considered factors so that the minimal wear rate value could also be achieved.

Analysis of Variance was carried out using Minitab 16. As it is given in table 3, the biggest impact on wear rate has the sliding distance with percentage contribution of 59.63%. Moreover, the impacts of the following factors can also be noticed: load (28.137%) and sliding speed (10.36%). To determine the model significance and individual parameter apart from probability (p-value), Fischer test (F-value) can also be applied. According to F-value the interaction between factors (load) x (sliding speed), (load) x (sliding distance) and (sliding speed) x (sliding distance) is also significant. The ranking of factors on the base of conducted analysis is given in table 4. The most influential factor is sliding distance, then follows load and finally sliding speed.

Table 4. Response table for signal to noise ratios

Level	L	S	D
1	6.279	-0.255	-1.969
2	1.725	2.132	-0.324
3	-1.588	4.538	8.709
Delta	7.867	4.793	10.679
Rank	2	3	1

According to conducted ANOVA analysis and results' analysis, the dependence among factors can be shown with respect to wear rate. Contour plots and 3-D surface plots were given so as to interpret results graphically.

Based on figures 2, 3, 4 (a) and (b) it is possible to calculate the parameter levels by which minimal wear rate values are achieved. More precisely, minimal wear rate value is achieved at lower load values and at higher sliding distance values. Wear rate depending on the sliding distance and sliding speed demonstrates that by increasing sliding speed wear rate decreases. The dependence between sliding speed and load clearly shows that at higher sliding speed values and at the lowest load value minimal wear rate value of hybrid composite is achieved.

Table 3. Analysis of Variance for S/N ratios

Source	DF	Seq SS	Adj SS	Adj MS	F	P	Pr
L	2	280.779	280.779	140.390	1170.56	0.000	28.137
S	2	103.381	103.381	51.691	430.99	0.000	10.36
D	2	595.043	595.043	297.521	2480.71	0.000	59.63
L*S	4	8.975	8.975	2.244	18.71	0.000	0.899
L*D	4	5.592	5.592	1.398	11.66	0.002	0.561
S*D	4	3.168	3.168	0.792	6.60	0.012	0.317
Residual Error	8	0.959	0.959	0.120			0.096
Total	26	997.897					100
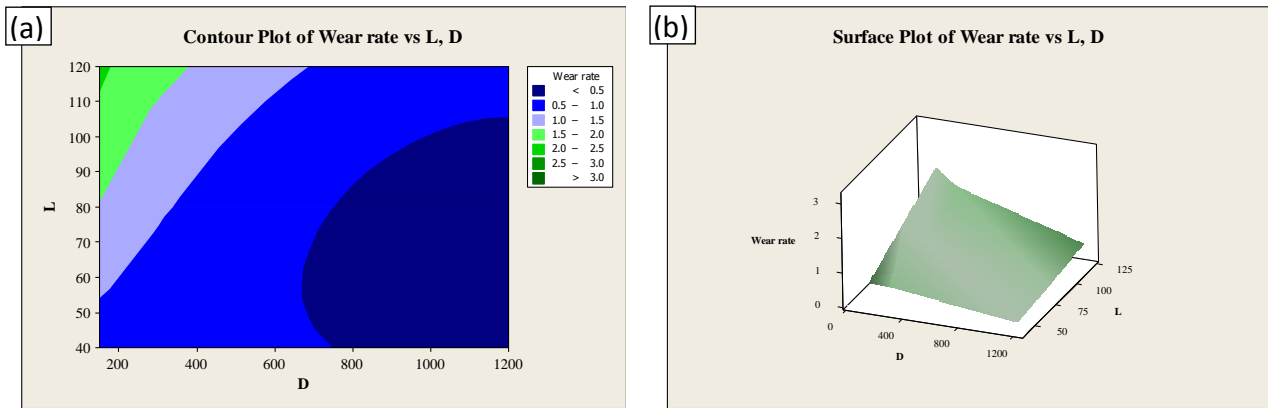
Figure 2. Dependence between wear rate of the load and sliding distance:
(a) contour plot, (b) surface plot.
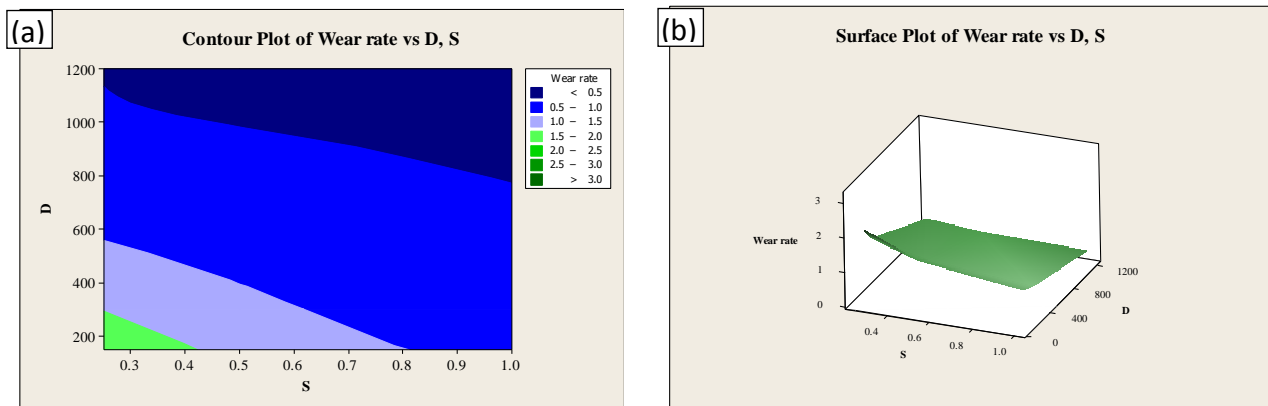
Figure 3. Dependence between wear rate of the sliding distance and sliding speed:
(a) contour plot, (b) surface plot.
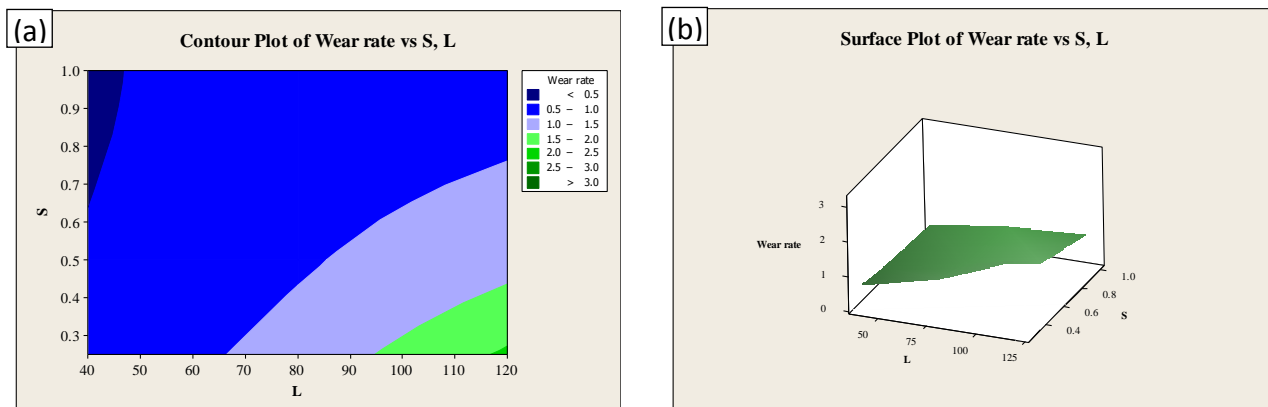
Figure 4. Dependence between wear rate of the sliding speed and load:
(a) contour plot, (b) surface plot.

4.2 Linear regression

The relationship between control factors and response for wear rate in term of S/N ratios was analyzed using Taguchi method. The 95% confidence level was achieved by accounting the complete experimental design data. The regression equation developed for the wear rate is as follows:

$$\mathrm{SNRA1} = 0.840 - 0.098L + 6.165S + 0.010D. \quad (3)$$

Equation (3) can be used for prediction of response wear rate at given levels of parameters. Table 5 demonstrates the estimation of linear model coefficients for S/N ratios in term of statistical parameters, standard error, T-test and probability value. Data given in this table clarify that the model was significant at the 95% confidence level since some p-values were less than 0.05.

Ratio with negative sign in equation is next to load factor, which means that wear rate decreases by increasing sliding distance. However, wear rate increases when load and sliding speed increase.

Table 5. The equation of regression coefficients

Term	Coef	SE Coef	T	P
Constant	0.840	0.688	1.222	0.234
L	-0.098	0.006	-16.110	0.000
S	6.165	0.639	9.643	0.000
D	0.010	0.000	23.548	0.000

By substituting the predicted optimum factor levels in the regression equation the estimated optimum Wear rate = 0.173356 mm^3 x 10^{-3}/m. Further validation experiments were conducted for the predicted optimum conditions and wear rate from the validation experiments was obtained as 0.202 mm^3 x 10^{-3}/m. The percentage error was also calculated and found to be 14.18% confirming the success of statistical analysis.

5 CONCLUSION

In this research work, the effect of various factors levels and factors (load, sliding speed and sliding distance) on wear rate hybrid composite was studied using Taguchi orthogonal array. Conclusions drawn from this experimental work are as follows:

• The hybrid composites have been successfully fabricated by compocasting process for the study of tribological properties.

• Taguchi's robust design method is suitable to analyse the wear rate as described in the present work.

• According to ANOVA analyses, the percent contributions of the L, S, and D factors on the wear rate were found to be 28.137%, 10.36% and 59.63%, respectively. Sliding distance (factor D) was found on the wear rate most effective parameter.

• It is concluded that combinations for minimum wear rate is L1S3D3 i.e. 40N load, 1 m/s sliding speed, and 1200 m sliding distance. Optimum wear rate is determined as 0.202 mm^3 x 10^{-3}/m.

REFERENCES

[1] M. O. Bodunrin, K. K. Alaneme, L. H. Chown: Aluminium matrix hybrid composites: a review of reinforcement philosophies; mechanical, corrosion and tribological characteristics, Journal of Materials Research and Technology, Vol. 4, No. 4, pp. 434-445, 2015.

[2] S. A. Mohan Krishna, T. N. Shridhar, L. Krishnamurthy: Research significance, applications and fabrication of hybrid metal matrix composites, International Journal of Innovative Science, Engineering & Technology, Vol. 2, No. 5, pp. 231-243, 2015.

[3] P. Sharma: Determination of Mechanical Properties of Aluminium Based Composites, International Journal on Emerging Technologies, Vol. 3, No. 1, pp. 157-159, 2012.

[4] D.S. Prasad, A. Rama Krishna: Tribological Properties of A356.2/RHA Composites, Journal of Materials Science and Technology, Vol. 28, No. 4, pp. 367-372, 2012.

[5] A. Vencl: Tribology of the Al-Si alloy based MMCS and their application in automotive industry, Engineered Metal Matrix Composites: Forming Methods, Material Properties and Industrial Applications, Magagnin, L. (Ed.), Vol. 28, No. 4, pp. 127–166, 2012.

[6] B. Stojanović, L. Ivanović: Application of aluminium hybrid composites in automotive industry, Technical Gazette, Vol. 1, No. 22, pp. 247-251, 2015.

[7] B. Stojanović, J. Glišović: *Automotive Engine Materials*, in: Saleem Hashmi (editor-in-chief) Reference Module in Materials Science and Materials Engineering, (Elsevier B.V., Amsterdam), 2016.

[8] A. Vencl, A. Rac, I. Bobić: Tribological behaviour of Al based MMCs and their application in automotive industry, Tribology in industry, Vol. 26, No. 3 and 4, pp. 31-38, 2004.

[9] S. Bansal, J. S. Saini: Mechanical and wear properties of SiC/Graphite reinforced Al359 alloy-based Metal Matrix Composite, Defence science journal, Vol. 65, No. 4, pp. 330-338, 2015.

[10] B. Pavithran, J. Swathanandan, N. Praveen, S. R. Prasanna Kumar, D. Senthil Kumaran: Study of mechanical and tribological properties of Al6061 reinforced with silicon carbide and graphite particles, International journal of technology enhancements and emerging engineering research, Vol. 3, No. 4, pp. 60-64, 2015.

[11] G. Dixit, K. Mohsin Mohammad: Sliding Wear response of an aluminium metal matrix composite: effect of solid lubricant particle size, Jordan Journal of Mechanical and Industrial Engineering, Vol. 8, No. 6, pp. 351-358, 2014.

[12] T. PratheepReddy, N. Amara Nageswara Rao: Wear optimization of Al/SiC/Gr hybrid MMC using Taguchi and ANOVA, International Journal of Innovative Research in Science, Engineering and Technology, Vol. 3, No. 11, pp. 17205-17210, 2014.

[13] B. Stojanović, M. Babić, N. Miloradović, S. Mitrović: Tribological behaviour of A356/10SiC/3Gr hybrid composite in dry-sliding conditions, Materials and technology, Vol. 49, No. 1, pp. 117-121, 2015.

[14] B. Stojanovic, M. Babic, S. Mitrovic, A. Vencl, N. Miloradovic, M. Pantic: Tribological characteristics of aluminium hybrid composites reinforced with silicon carbide and graphite. A review, Journal of the Balkan Tribological Association, Vol. 19, No. 1, pp. 83-96, 2013.

[15] M. Babić, B. Stojanović,S. Mitrović, I. Bobić, N. Miloradović, M. Pantić, D. Džunić: Wear properties of A356/10SiC/1Gr hybrid composites in lubricated sliding conditions, Tribology in Industry, Vol. 35, No. 2, pp. 148-154, 2013.

[16] V. Kumar, P. Kumar, S. Sharma: Wear characterization of Aluminium/SiC/Al_2O_3 hybrid metal matrix composite using Taguchi technique, International Journal of Innovative Research & Development, Vol. 3 , No. 1, pp. 34-40, 2014.

[17] B. Stojanović, M. Babić, S. Veličković, J. Blagojević: Tribological behavior of aluminum hybrid composites studied by application of factorial techniques, Tribology Transactions, Vol. 59, No. 3, pp. 522-529, 2015.

[18] S. Veličković, B. Stojanović, M. Babić, I. Bobić: Optimization of tribological properties of aluminum hybrid composites using Taguchi design, Journal of composite materials, Vol. 0, No. 0, pp. 1-11, ISSN 0021-9983, Doi 10.1177/0021998316672294, 2016.

[19] S. Miladinović, S. Veličković: Optimization and prediction of safety coefficient for surface durability of planetary gear box using Taguchi design and Artificial Neural Network, in: *3rd International scientific conference COMETa 2016*, 7-9.12.2016, Jahorina, B&H, RS, pp. 139-146.

[20] S. Miladinović, S. Veličković, M. Novaković: Application of Taguchi method for the selection of optimal parameters of planetary driving gear, Applied Engineering Letters, Vol. 1, No. 4, pp. 98-104, 2016.

ON THE EFFECT OF LATTICE DEFECT CONCENTRATION OF KAOLIN ON THE MECHANICAL STRENGTH OF FABRICATED POROUS CERAMICS

David O. OBADA[1]*, David DODOO-ARHIN[2,3], Muhammad DAUDA[1], Fatai O. ANAFI[1], Abdulkarim S. AHMED[4], Olusegun A. AJAYI[4] , Samaila UMARU

[1]Department of Mechanical Engineering, Ahmadu Bello University, Zaria, Nigeria
[2]Department of Materials Science and Engineering, University of Ghana, Legon, Ghana.
[3]Institute of Applied Science and Technology, University of Ghana, Legon, Ghana
[4]Department of Chemical Engineering, Ahmadu Bello University, Zaria, Nigeria.
*Corresponding author: obadavid4@gmail.com

Abstract: *Dehydroxylation of kaolinites during heating plays a key role in the structural integrity of kaolin based ceramics. The utilization of Kankara and Kibi kaolinite clay as raw materials in fabrication of porous ceramics has been tested by laboratory scale experiments and a correlation of its porosity and crushing strength drawn. This correlation has been buttressed by the metakaolinization effect during sintering. Porous ceramics with three different pore formers were fabricated by the sintering of kaolin clay and porogenic materials (sawdust, styrofoam and powdery high density polyethylene). The porosities of the ceramic bodies were experimentally determined, while the structure and chemistry of the materials were elucidated via ex-situ X-ray diffraction (XRD) and scanning electron microscopy (SEM). The respective compressive strength of the porous clay ceramics were found to exhibit a downward trend with increasing porosity. It was concluded that the elastic properties (mechanical strength) of the porous ceramic bodies reflect the changes in the structure of the body and the processes in it which are linked to escape of the physically bound water and dehydroxylation during firing and also the solidifying of the glassy phase during the cooling stage of firing.*

Keywords: Porosity, pore formers, kaolinite clay, mechanical property, dehydroxylation

1. INTRODUCTION

Recently, porous ceramics have recieved increasing attention for their successful industrial application as filters, catalyst supports, bioceramics, hot gas filters, desiccants, insulators, acoustic absorbers, sensors, and membrane reactors [1-5].Usually, these porous ceramics can be made by a conventional powder-processing route also referred to as solid state sintering with the incorporation of some pore-forming agents such as sawdust, starch, graphite, and organic particulates [6], or by injection molding [7], or

by gelcasting [8]. The pore-forming *in-situ* technique exploiting the decomposition of starting materials is known to be a good way to prepare porous ceramics with well-distributed pores and its eco-friendliness is an interesting attribute [4-5, 9]. Porous ceramics are fabricated by mixing clay with a combustible or pore forming material (usually sawdust, flour and rice husk) with a binder (water). The resulting homogenous mixture is then pressed using a mechanical device, or in some cases by manual molding using pottery wheel, or as the name implies by hand into the desired shape provided the mixture has some plasticity [10].

There are numerous kaolinite clay deposits in Nigeria and Ghana, and these deposits differ in a number of ways: *e.g.* the type and amount of impurities, colour, mineralogical content and nature, plasticity, and the characteristics of the fired product. As with clays of any origin, the above properties are expected to influence the ceramic and refractory properties of the clays. Kaolin deposits are wide spread throughout Nigeria. The three most extensively studied deposits are the Ozubulu deposits, Kankara deposits and Porter deposits in Plateau state [11]. The Kibi kaolin deposit in Ghana is also receiving attention [12].

Firing of silicate ceramics, which are made of clays with high contents of kaolinite, transforms a green body into a ceramic product [13, 14]. The green body showcases significant changes of its elastic properties resulting from dehydration at low temperatures, phase changes during dehydroxylation, high-temperature reactions and densification during sintering [15, 16]. All these changes significantly have an influence on the mechanical properties of the fired body as well as its other physical properties. Therefore, to save some ample time and energy, it is desirable to conduct the firing in the shortest time possible without necessarily damaging the fired ceramic body.

The porous nature of kaolin based ceramics makes them susceptible to failure. This leads to breakage during processing, transportation and usage. There is, therefore, a need to relate the mechanical properties of the porous clay ceramics to their porosity. This is expected to give the correlation of these properties vis-à-vis the industrial applicability. Svinka et al. [17] studied the production of porous alumina ceramics by the slurry casting method and investigated pore formation by elimination of hydrogen as a result of a chemical reaction of aluminium powder with water. The purpose of their study was to determine various ways of producing high porosity alumina ceramics having high mechanical strength and other properties significant for refractory ceramics. Yakub et al [10] fabricated porous ceramics with three different porosities by the sintering

of redart clay and woodchips (sawdust) with a view to developing a ceramic based water filter. The measured mechanical and physical properties were then incorporated into finite element models for the computation of stress distributions due to hydrostatic pressures exerted on the porous clay ceramics by the water in filter with different geometries and supporting configurations. The implications of the results were discussed for potential scale-up and design of a mechanically robust porous ceramic for water filtration.

In this paper, clay ceramics with three different pore formers were produced by the sintering of clay/sawdust, styrofoam and high density polyethylene mixture with varying ratios by weight. The porosity and cold crushing strength were investigated using experiments with a view to correlating the synergistic effects of these properties on the final ceramic products. It is also noteworthy that the use of powdery high density polyethylene as a pore former to the best of our knowledge has not been explored as a porogenic material in castable ceramics.

2. EXPERIMENTAL

2.1. Materials and processing

The clay materials that were used in this study were obtained from Kankara and Kibi Kaolin deposits in Nigeria and Ghana respectively. The X-ray pattern of the two clays is given in Figure 2. The sawdust (woodchips) used was obtained from a local sawmill in Ghana. The styrofoam and powdery high density polyethylene powders were processed at the Materials Laboratory of the University of Ghana. Clay was mixed with the sawdust, styrofoam and powdery high density polyethylene in four different ratios (clay-to-pore formers) by weight (Table 1). Prior to mixing, the pore formers were reduced into sizes using an analytical mill. The clay was blended with the pore formers according to batch formulations as presented in Table 1, using water as the binding agent.

Table 1. Composition of test Samples by weight (Total weight = 100g)

Sample code	Kaolin (g)	Plasticizer (Kibi Kaolin) (g)	Saw dust (g)	Styrofoam (g)	High density polyethylene (HDPE) (g)
0% CS	80	20	-	-	-
5%SD	75	20	5	-	-
10%SD	70	20	10		
15%SD	65	20	15		
20%SD	60	20	20		
5%SYF	75	20	-	5	-
10%SYF	70	20	-	10	-
15%SYF	65	20	-	15	-
20%SYF	60	20	-	20	-
5%HDPE	75	20	-	-	5
10%HDPE	70	20	-	-	10
15%HDPE	65	20	-	-	15
20%HDPE	60	20	-	-	20

The resulting mixture (clay, pore formers and water) were formed by completely filling into a mold and pressed to the same level to ensure compactness and dimensional homogeneity. The as-prepared green body samples were removed from the mold and dried in laboratory air (temperature of 25 °C, humidity of 43%) for 3 days on boards after which they were further dried at 100 °C in an oven for one hour (to make the green body safer to handle) by removing moisture. After drying, the green bodies were subjected to thermal treatment by heating to the sintering temperature of 1150°C in the muffle furnace with holding time of 2 hours.

Figure 1. Green bodies during drying at ambient temperature.

The samples were heated at 5 °C/min till final sintering temperature. Figure 1 shows the green bodies during drying in laboratory air.

2.2 Materials characterization.

The porosities of the samples were calculated using Eq. (1) [18]:

$$\text{Apparent Porosity} = \left(\frac{W\text{-}D}{W\text{-}S} \right) \times 100 \qquad (1)$$

Where: D = Weight of fired specimen, S = Weight of fired specimen suspended in water, and W = Weight of soaked specimen suspended in air

X-ray diffraction (XRD) was performed on powders of kaolin clay and porous clay ceramics to determine their phase compositions. This was done on an empyrean diffractometer (Bruker AXS,D8 Advance) with theta/theta geometry, operating a Cu Kα radiation tube (λ = 1.5418 Å) at 40 kV and 30 mA. The XRD patterns of all the randomly oriented powder specimens were recorded in the 10.0°- 90° 2θ range with a step size of 0.017° and a counting time of 14 s per step. The surface morphology of the porous ceramics was carried out using an ultra-high vacuum and high resolution FEI, Xl-30 scanning electron microscope. Samples were metalized with gold/platinum coating prior to the analysis. Images were acquired at

magnifications of 2000X.The thermal stability of the various phases in the samples was studied by DTA/TG under air flow of 50mL/min. The samples were thermally analysed by placing ≈25mg of the specimens in an alumina (Al_2O_3) crucible (100mg capacity), subjected to a linear heating ramp between 100°C and 700°C at a rate of 20°C/min in NETZSCH, STA 449C Jupiter TG/DTA instrument. The test measurements were made for the mass change (loss) of the sample as a function of the temperature and the phase changes by the adsorption or the emission of energy.

2.3. Strength measurements

Mechanical property tested for was cold compression strength. This was used to determine the compression strength at failure for each sample, an indication of its probable performance under load. The compressive strength testing was carried out on an hydraulic testing machine (Carver Press, USA) The strengths of the porous clay ceramics were obtained by compressive loading of samples prepared according to ASTM C133-97 (ASTM C133-97, 2003). In total, five specimens were used for the CS measurement and plots were made based on the average values of the results. Cold crushing strength of control and porous samples were calculated from the equation:

$$CS = P/BW \quad (2)$$

Where P =load at failure and B and W are the respective width and breadth of the specimens.

3. RESULTS AND DISCUSSION

3.1 Materials characterization

The X-ray diffraction analyses of the kaolin clays and porous ceramics are presented in Figs. 2 and 3. Figure 2 shows the XRD pattern of the Kankara kaolin and Kibi Kaolin. It could be observed from the XRD patterns that the peaks at Bragg's angles of 12.35, 19.89, 20.38,

24.88, 34.94, 35.95, 36.06, 38.35, 45.24, 54.88 and 62.37° responsible for the kaolinite mineral are prominent [19]. The main characteristic peaks of kaolinite (12.35 and 24.88°) for the two patterns are intense.
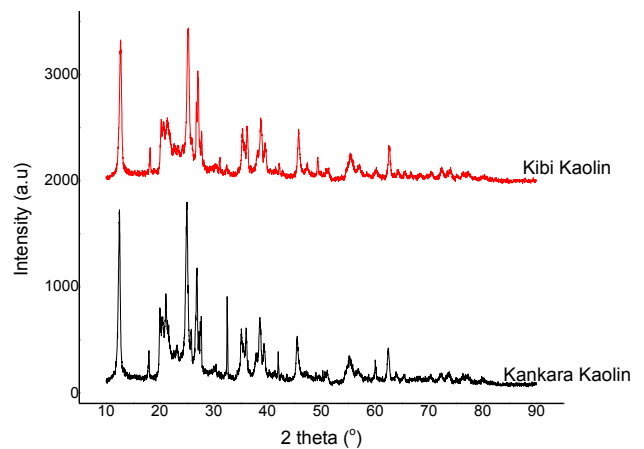
Figure 2: XRD pattern of Kankara and Kibi Kaolin
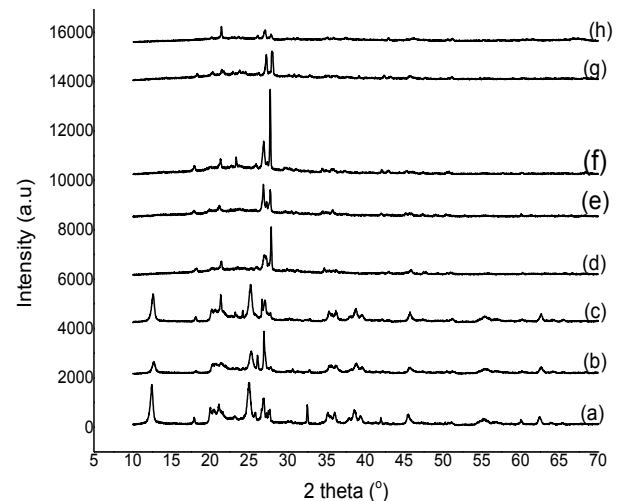
Figure 3: XRD pattern of Kibi kaolinite heated from 30–900 C (**a**: 30°C; **b**: 300°C; **c**: 400°C; **d**: 500°C **e**; 600°C; **f**: 700°C; **g**: 800°C; **h**: 900°C
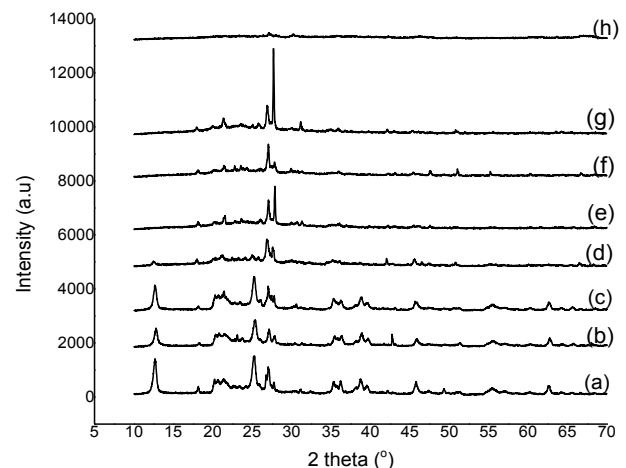
Figure 4: XRD pattern of Kibi kaolinite heated from 30–900 C (**a**: 30°C; **b**: 300°C; **c**: 400°C; **d**: 500°C **e**; 600°C; **f**: 700°C; **g**: 800°C; **h**: 900°C

Kaolinite ($Al_2O_3.2SiO_2.2H_2O$), the essential component of kaolin, loses the OH units in its crystal structure at approximately 450° C, forming an almost amorphous material known as metakaolinite ($Al_2O_3.2SiO_2$). Metakaolinite structure is quite unstable, and at about 1000° C its phase is transformed to γ-alumina, cristoballite (SiO_2) and primary mullite crystals [22-23]. Figures 3-4 shows the calcination of Kankara and Kibi kaolin at different temperatures. This is to further buttress the effect of thermal treatment on the transformation of kaolinites. It can be noticed that at 500^oC (d), the peaks responsible for the kaolinite mineral have deteriorated. This result suggests that some very weakly bound hydroxyl groups of the amorphous phase, as detected by XRD, are realeased within this temperature range. This finding is in agreement with other results presented elsewhere [24]. At 900^0C (h), it is noticed that the low intensity peaks observed for Kankara clay are all of residual quartz remaining in the clays [25].
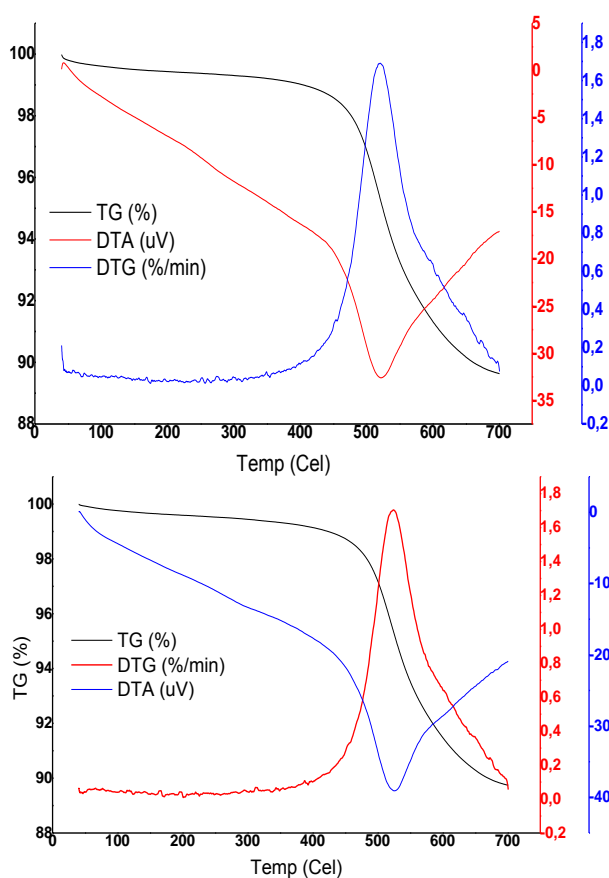
Figure 5: Thermal analyses (TG,DTG and DTA) of kaolin (Kankara (top) and Kibi (bottom)

The TG curves (Fig 5) show the weight loss associated with thermal treatment of Kankara and Kibi kaolin up to 700°C. It can be observed that the remarkable loss occurred between 450°C and 600°C and stabilized at about 700°C for both kaolinite clays. The endotherm as shown in Figure 5 which corresponds to the dehydroxylation temperature range may be attributed to loss of the hydroxyl units (removal of the chemically bound water) and complete removal of the structure water of the kaolinite structure forming an almost amorphous material which is identified as metakaolin[22,26,29-30]. This results corroborates findings from the XRD data in this study. The dehydroxylation temperature of the Kankara and Kibi Kaolin are 526.2^o C and 521.3^o C at enthalpies of -39.07uV and -32.60uV respectively.

The X-ray diffraction analyses of the porous ceramics are presented in Fig 6. The results show that the porous ceramics exhibit similar diffraction patterns. This is expected because the pore formers had decomposed during heat treatment and therefore plays no role in the pattern orientation as presented. The kaolin clay which is the base material for ceramic fabrication consists predominantly of illite and kaolinite mineral. Approximately above 500 ^0C, the kaolinite mineral undergoes an endothermic dehydroxylation process. This transforms it into a disordered alumino-silicate, metakaolinite [20,21]. The kaolin clay, which was originally crystalline, is now transformed into metakaolin which is amorphous. The phases of the porous ceramic samples after combined mechanical (force exerted by hydraulic press) and thermal treatments shows the transformation phase to mullite which should occur at relatively lower temperature as used in this study (1150^oC) than for the original kaolinites. Equations 3, 4 and 5 explain this trend:

$$Al_2O_3.2SiO_2.2H_2O \xrightarrow{\approx 400-500^\circ C} \underset{Metakaolinite}{(Al_2O_3.2SiO_2)} + H_2O$$

(3)

$$2\left(Al_2O_3.2SiO_2\right) \xrightarrow{\approx 950°C} Si_3Al_4O_{12}+SiO_2$$
<div style="text-align:center">metakaolinite (amorphous)   (Al-Si Spinel)</div>

<div style="text-align:right">(4)</div>

$$3Si_3Al_4O_{12} \xrightarrow{>1050°C} 2\left(3Al_2O_3.2SiO_2\right)+5SiO_2$$
<div style="text-align:center">(Al-Si Spinel)   Mullite</div>

<div style="text-align:right">(5)</div>
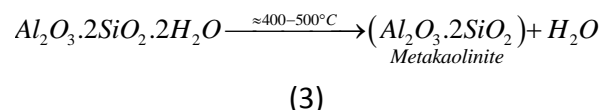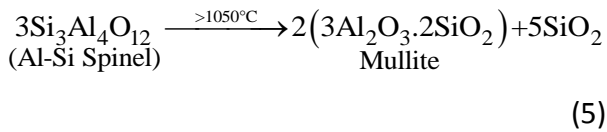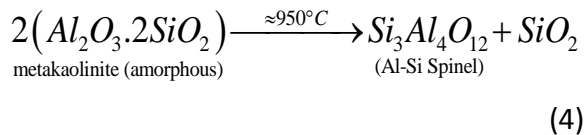
As the temperature increases, the kaolinite undergoes dehydroxylation and recrystallization. Recrystallization of the resulting metakaolinite to cristoballite (SiO_2) and γ-Al2O$_3$ or mullite results in an exothermic reaction between 950 and 1050°C [22].
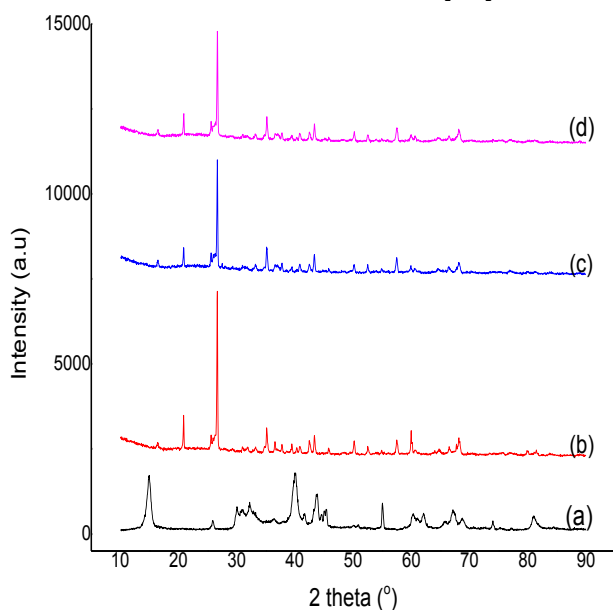
Figure 6: XRD pattern of Kankara clay (a) and porous ceramics with different pore formers (b;styrofoam; c: HDPE; d: sawdust).

Figure 7 shows the sintered ceramics with the different pore formers. The control sample (d) is without any pore forming agent hence the structure noticed.

<div style="text-align:center">(a)   (b)</div>

<div style="text-align:center">(c)   (d)</div>
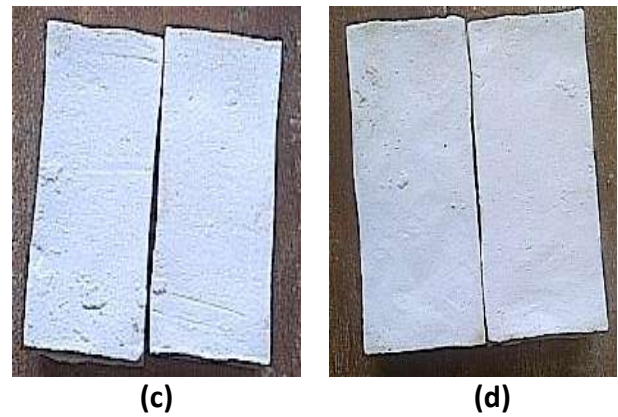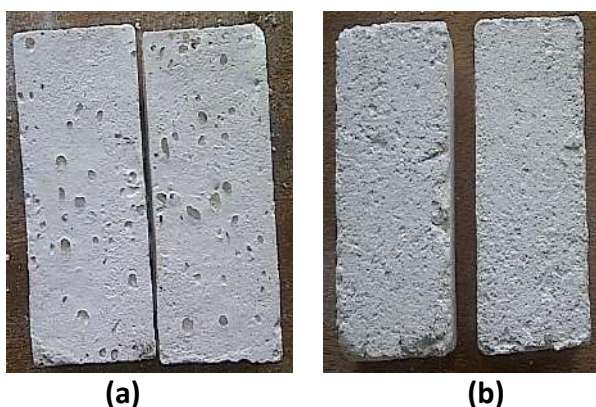
Figure 7: Sintered bodies a) Sample with styrofoam b) Sample with PHDPE c) Sample with sawdust d) Sample without pore formers.

Observing the other sintered bodies, open pores and closed pores are inherent. Figure 8 shows the scanned images of the porous ceramics and the control sample used in this study. Micrographs of the surface of the three porous clay ceramic with highest pore former content (20%) are presented in Fig.8(a)–(c), while the micrograph of the control sample is given in Fig 8(d). One hypothesis is that the ceramic body with a higher pore former content burns off faster than a ceramic body with a lower pore former content. This is by virtue of larger pathways and available channels for removal of the combustion products (mainly carbon dioxide). As a result, the ceramic body with the higher pore former content has more time to sinter which may be due to the relatively early expulsion of the pore formers.
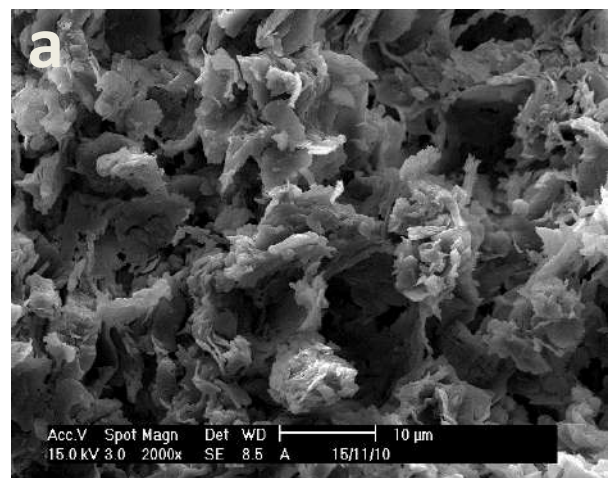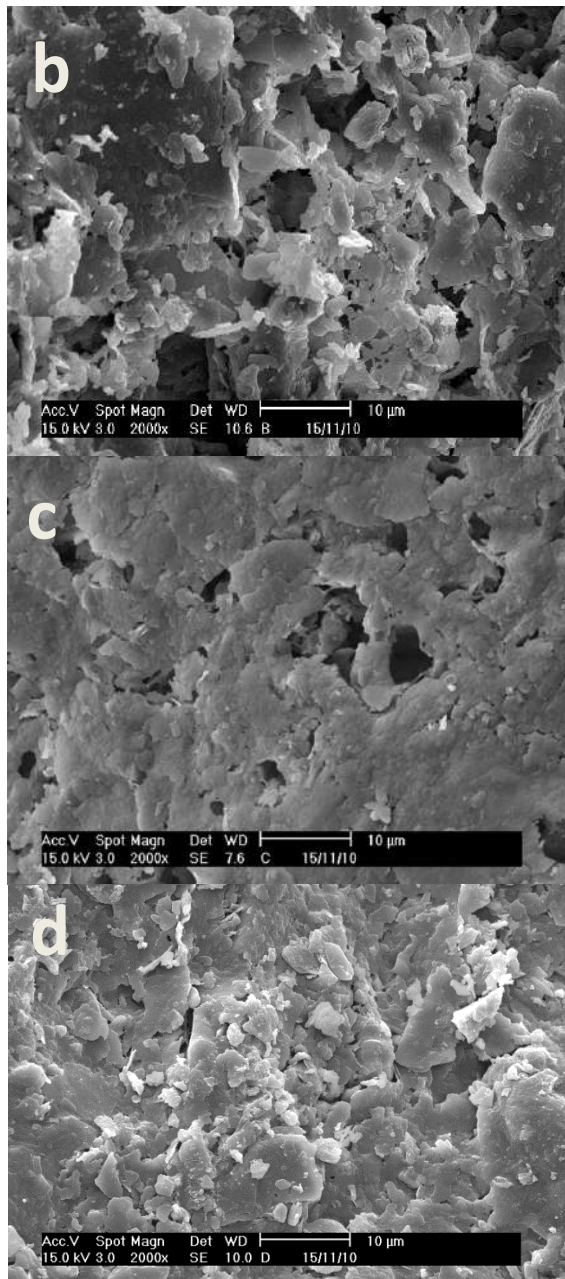
Figure 8: Scanning electron microscopy micrographs of (a) 80:20 sawdust as pore former (b) 80:20 styrofoam as pore former, (c) 80:20 powdery high density polyethylene as pore former (d) 100% kaolin.

3.2 Correlation of porosity and mechanical strength of samples.

The porosities and compressive strengths of the porous samples were evaluated by the expressions described earlier (Equations 1&2). Five sets of samples were used for each batch formulation and the average porosities and compressive strengths recorded. Figures 9 and 10 reveal the variation of percentage inclusion of pore formers to compressive strength and

also a composite plot of the variation of compressive strength with porosity. It was important to establish this relationship so as to obtain a realistic correlation for the fabricated bodies based on apparent porosity and cold crushing strength properties, as these could be said to have a significant effect on the industrial applicability of porous ceramics. The plots show that the strength decreases linearly as apparent porosity increases. The compressive strengths decreased linearly with increasing porosity (Fig. 10). The ceramic samples with HDPE as pore former by reason of its very high porosity have the least strength. This corroborates the linear correlation obtained. A better fit can be obtained considering a wider range of porosities, similar trends have been observed by other researchers [10, 31-33]. The implications of this study are noteworthy. First, the result shows that the mechanical properties of porous ceramics are not a simple function of its density, shrinkage, water absorption among other properties, but depends largely on porosity. Other possible factors that could affect the mechanical strength of porous ceramics include: surface and internal defects (such as cracks) during processing and transportation (mechanical vibration). One way of eliminating this hurdle is to fabricate porous ceramics from homogeneous mixtures of clay and pore formers.
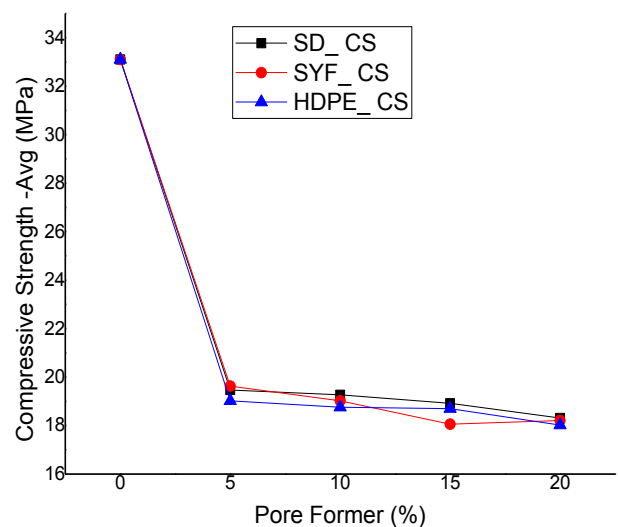
Figure 9: Variation of percentage pore formers against compressive strength
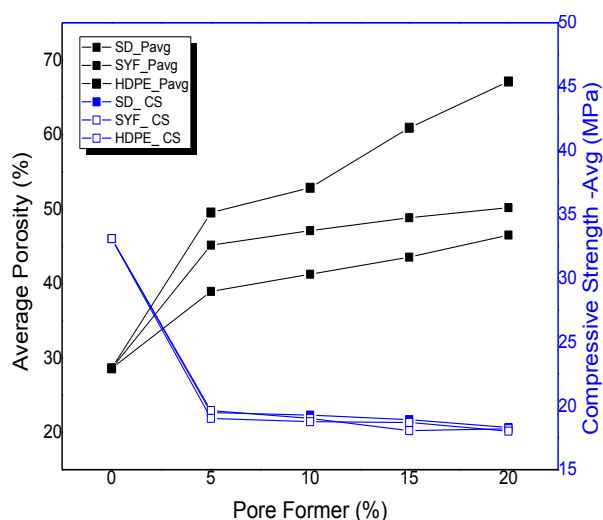
Figure 10: A composite plot of the variation of percentage pore former against average values of porosity and compressive strength.

The samples after firing exhibited some thermal stability and compactness without indications of severe surface cracks or distortions. This is attributed to the lower melting temperatures of the pore formers. It is commonly believed that the relatively large volume change which accompanies the $\beta \rightarrow \alpha$ transformation of the unsolved quartz grains ($\Delta V/V = -0.68$ % for free quartz grain) is the basic source of micro-cracking. After removing the weakly bound physically absorbed water, the sample loses the rest of this water and a small amount of the volatile material. The values of the thermal expansion increase up to $\sim$500 °C when dehydroxylation occurs, which leads to a contraction of the sample and dropping of its mass. Following the realease of the physically bound water, there is no further change in the structural configuration and composition. The temperature interval of dehydroxylation can be considered a critical stage of the firing process. It is known that an inadequate high rate of heating or cooling leads to cracking of the ceramic body. This was only observed on samples with HDPE as pore former which can also be attributed to the high porosity of the samples. It is noted that the new pore former used in this study produced ceramic bodies with porosity as high as 67%. Figure 11 shows the micro cracks observed on the sample which could be as a result of large volume change accompanying

phase transformations and sensitivity to the dehydroxylation phase.

Figure 11: Porous Ceramic with HDPE as pore former showing micro cracks.

Mechanical properties like the compressive strength is much more sensitive to defects created by dehydroxylation. Its values run through a clear minimum at $\sim$450 °C as shown in Figures 3 and 4. Very similar results were published in [34]. An increase of compressive strength during the continuing dehydroxylation (above 450 °C) is a complex phenomenon hence may not be easy to explain. It is known that other constituents (quartz and feldspar) hardly lose their mechanical properties, and metakaolinite, by virtue of its high concentration of crystal defects, must be considered a mechanically weak material [35]. The structure of metakaolinite does not change until $\sim$950 °C, so the effect of the compressive strength increase should be attributed to improving the interface synergy between metakaolinite crystals. Solid phase sintering which has been employed in this study could be a possible relevant mechanism. The cooling stage of the sintered bodies may also be of significance as have been reported elsewhere [36]. The cooling interval can be divided in two parts viz: Above 570 °C, the volume of the quartz grain remains approximately constant, and the glassy cladding tends to contract its volume. The grain is now under the compressive stress and no circumferential cracks can arise. But in the streamlined temperature interval around the $\beta \rightarrow \alpha$ transition of quartz, the quartz grain volume quickly contracts and the circumferential microcracks can then appear

around the grains. The microcracks are the outcome of the release of the mechanical stress caused by the difference in the thermal expansion between the quartz grains and the glass matrix [36-39]. All of these could influence the mechanical properties of porous ceramics.

4. CONCLUSIONS

The porosity of clay ceramics increases with increasing volume fraction of pore formers. The compressive strength decreases with increasing porosity. The mechanical strength of the sintered ceramic body reflects the changes in the structure of the body and the processes therein. They are linked to: escape of the physically bound water, dehydroxylation, the $\alpha \rightarrow \beta$ quartz phase transition, high-temperature reactions and solid-phase sintering during the heating stage of firing.

The main conclusions drawn from this study can be summarized as follows:

1. The X-ray diffraction patterns of the kaolin-based porous samples sintered at 1150°C indicated that they composed of transformed mullite phase which indicates some recrystallization effects. Other minor phases which are present in small quantities could not be detected by XRD analyses.

2. The SEM micrographs show that the open pores were distributed on the surface because of larger pathways and available channels of eviction of the pore formers.

3. The differential thermal analyses (DTA) and thermogravimetric (TGA) measurements of the kaolin used in this study showed broad endotherms at the dehydroxylation temperature of 526.2^{o} C and 521.3^{o} C at enthalpies of -39.07uV and -32.60uV respectively.

4. Compressive strength decreases linearly as apparent porosity signifying its correlation. It has also been shown that metakaolinization plays a huge role as to the structural integrity of porous ceramics.

5. It is noted that the new pore former used in this study produced ceramic bodies with porosity as high as 67% and hence the least compressive strength.

REFERENCES

[1] A.R. Studart, U.T. Gonzenbach, E. Tervoort: Processing routes to macroporous ceramics: A review, *J. Am. Ceram.Soc.*, 89, No.6, p.1771, 2006.

[2] R. Barea, M.I. Osendi, P. Miranzo: Fabrication of highly porous mullite materials, *J. Am. Ceram. Soc.*, 88, No.3, p.777, 2005.

[3] T. Tomita, S. Kawasaki, and K. Okada: A novel preparation method for foamed silica ceramics by sol-gel reaction and mechanical foaming, *J. Porous Mater.*, 11, No.2, p.107, 2004

[4] W. Yan, N. Li, and B.Q. Han: High-strength lightweight spinel refractories, *Am. Ceram. Soc. Bull.*, 84, No.4, p.9201, 2005.

[5] W. Yan and N. Li: Pore-size distribution and strength of porous mullite ceramics, *Am. Ceram. Soc. Bull.*, 85, No.12, p.9401, 2006.

[6] J.H. She and T. Ohji: Fabrication and characterization of highly porous mullite ceramics, *Mater. Chem. Phys.*,80, No.3, p.610, 2003.

[7] Z. Xie, J. Yang, Y. Huang, *et al.*, Study on binder removal process of ceramics injection molding, *Bull. Chin. Ceram.Soc.*, 2, No.2, p.18, 1998.

[8] Y.F. Liu, X.Q. Liu, H. Wei: Porous mullite ceramics from national clay produced by gelcasting, *Ceram. Int.*,27, No.1, p.1, 2001.

[9] Z.Y. Deng, T. Fukasawa, M. Ando: Microstructure and mechanical properties of porous alumina ceramics fabricated by the decomposition of aluminum hydroxide, *J. Am. Ceram. Soc.*, 84, No.11, p.2638, 2001

[10] I. Yakub, J. Du, and W.O. Soboyejo :Mechanical properties, modeling and design of porous clay ceramicsMaterials Science & Engineering A 558 ,21–29, 2012.

[11] B. S. Badmus and O. B. Olatinsu: International Journal of Physical Sciences Vol. 4 (10) pp. 592-606, October, 2009

[12] J. K. Efavi, A. Yaya, S. Adeborna, J. Fobil,: Development and Comparative Analysis of Aluminosilicate Based Ceramic Filters for Ground Water Defluoridation, Advanced

Materials Research, Vol. 936, pp. 822-828,2014.

[13] Z. Pospíšil, Z. and A Koller.: Fine Ceramics, Basics of Technology. SNTL/ALFA, Praha (inCzech), 1981.

[14] Pytlík, P. – Sokolář, R: Building ceramics – technology, properties, applications. Akad. nakladatelství CERM, Brno (in Czech), 2002

[15] F.H Norton: Fine ceramics – Technology and Application. McGraw-Hill Book Co., New York 1970.

[16] V Hanykýř, and J. Kutzendorfer : Technology of Ceramics. Silis Praha a Vega Hradec králové,Praha (in Czech) 2000.

[17] R. Svinka, V. Svinka, I Zake., and A Butlers: Influence of Some Additives on the Properties of Porous Alumina Ceramics,". ISSN 1392-1231, 2009.

[18] A.R Chesti: Refractories: manufacture, properties, and applications, Delhi, Prentice Hall of India Private Limited, 1986.

[19] N. Salahudeen: Development of Zeolite Y and ZSM-5 composite catalyst from Kankara Kaolin. A Ph.D thesis submitted to the Department of Chemical Engineering, Faculty of Engineering, Ahmadu Bello University, Zaria, Nigeria, 2015.

[20] W.D. Kingery, H.K. Bowen, D.R. Uhlmann: Introduction to Ceramics, 2nd ed.,Wiley, New York, 1976.

[21] M. Bellotto, A. Gualtieri, G. Artioli, S.M. Clark: Kinetic study of the kaolinite-mullite reaction sequence. Part I: kaolinite dehydroxylation." *Physics and chemistry of minerals* 22.4: 207-217, 1995.

[22] I. Štubňa, G. Varga and A. Trník: *Investigation of kaolinite dehydroxylations is still interesting",* Építôanyag ,58, évf. 1, szám, 2006.

[23] S. Agathopoulos, H. Fernandes, D. Tulyaganov, and J.Ferreira: *Preparation of mullite whiskers from kaolinite using $CuSO_4$ as fluxing agent",* Mater. Scie. Forum, 455-456, 818-821,2004.

[24] F. Gonza´lez Garcı´a, M. T. Ruiz Abrio, and M. Gonza´lez Rodrı´guez: Effects of Dry Grinding on Two Kaolins of Different Degrees of Crystallinity, *Clay Miner.,* **26** [4] 549–65 1991.

[25] A.S Kovo, O. Hernandez, and S. M. Holmes: Synthesis and characterization of zeolite Y and ZSM-5 from Nigerian Ahoko Kaolin using a novel, lower temperature, metakaolinization technique. *Journal of Materials Chemistry* 19.34: 6207-6212, 2009.

[26] S. Sayin: Origin of kaolin deposits: Evidence from the Hisarcik (Emet-Kutahya) deposits, Western Turkey", Turkish J. Earth Sci., 16, 77-96, 2007.

[27] V. Dodson: A study of the reaction between oxygen and mixtures of kaolinite and certain metal chlorides at elevated temperatures", The Ohio J. of Scie., 57(1), 1957.

[28] I. Štubňa and A. Trnik: Young's modulus of porcelain mixture after firing in the dehydroxylation region", Ceramics – Silikáty, 51 (2), 102-105, 2007.

[29] B. Sonuparlak, M. Sarikaya and I. Aksay, "Spinel Phase Formation during the 980ºC Exothermic Reaction in the Kaolinite-to-Mullite Reaction Series", J. Am. Ceram. Soc., 70 (11), 837-42, 1987.

[30] C. Ward and D. French: *Analysis and Significance of Mineral Matter in Coal*, 21st Annual Meeting of The Society for Organic Petrology, at The University of New South Wales, Sydney, New South Wales, Australia, 2004.

[31] F.P Knudsen: Dependence of mechanical strength of brittle polycrystalline specimens on porosity and grain size. *Journal of the American Ceramic Society* 42.8 1959: 376-387.

[32] A.S. Wagh, R.B. Poeppel, J.P. Singh: Open pore description of mechanical properties of ceramics. *Journal of materials science* 26.14: 3862-3868, 1991.

[33] D.M. Liu. Influence of porosity and pore size on the compressive strength of porous hydroxyapatite ceramic. *Ceramics International* 23.2 : 135-139, 1997.

[34] T Kozík, and I Štubňa,: Mechanical strength of ceramic material in dehydroxylation region. Silikáty, 25, 237-241 (in Slovakian), 1981.

[35] F Freund: Kaolinite-metakaolinite, a model of a solid with extremely high lattice defect concentration. Ber. Deutsche Keram. Ges., 44, 5-13, 1967.

[36] J Liebermann, Avoiding quartz in alumina porcelain for high-voltage insulators. Keramische Zeitschrift, 53, 683-686, 2001.

[37] F. Porte, R. Brydson, B. Rand, and F.L Riley: Creep viscosity of vitreous china. J. Amer.Ceram. Soc., 87, 923-928, 2004.

[38] W.M Carty, and B.M Pinto: Effect of filler size on the strength of porcelain bodies. Ceram.Engineering and Science Proceedings, 23, 95-105, 2002.

[39] S.R Braganca, and C.P Bergman: Porcelain microstructure and technical properties. Cerãmica, 50, 291-299, 2004.

INFLUENCE OF FRETTING MECHANISM ON FATIGUE STRENGTH AND LIFE OF Al 6061-T6 CONSIDERING ROTATING BENDING PHENOMENA

M.A. KOWSER, M.A. CHOWDHURY*, Q.M.Z. SHAH, M.M. SHAHIN, M.S. RANA
Dhaka University of Engineering and Technology, Gazipur, Bangladesh
* Corresponding author: asadzmn2014@yahoo.com

Abstract: *Being a prime constituent in various sophisticated applications like aerospace design, Aluminum alloys has ranked the apex point of interest for researchers in the field of fatigue. Since wear and other surface decaying process can risk the lifespan of valuable properties, surface modification and other fatigue reducing works are being adopted for Aluminum alloys. In this research work, fretting fatigue effect on heat treated Al-Mg-Si alloy (Al 6061-T6) has been studied. Experimental observation has been authenticated by developing a FEM model using simulation software ANSYS 14.5. It has been observed that fretting reduces the lifetime of Aluminum abruptly than normal fatigue.*

Keywords: *Fretting fatigue, FEM analysis, Fatigue life, ANSYS, S-N curve.*

1. INTRODUCTION

Fretting, which is gradual wear of something by rubbing or gnawing, is a wear process that occurs at the contact area between two materials under load and subject to minute relative motion by vibration or some other forces (Hattori et al., 1988). Although several articles on fretting fatigue are available in the literature, research on bending fretting fatigue is limited. Fretting fatigue occurs when one body in contact with another tries to slide or roll over that body. Hattori et al. (1988) and King and Lindley (1980) proved that fatigue strength during fretting decreases to less than one-third of that without fretting. Bending fretting fatigue occurs when the relative movement is influenced by cyclic bending load. Common examples are found in contact pairs, bolts, railway axles, turbine dove-tail-like blades, nuclear reactors, pressure vessels, and overhead electrical

conductors (Ebara and Fujimura, 2006; Hills and Nowell, 1994; Hoeppner et al., 2000; Mayama et al., 2008; Nowell et al., 2006). The initiation and propagation of fatigue cracks are severely characterized by the microstructure of materials. The dislocation seriously affects the plastic deformation, and the relationship between dislocated structures and plastic deformation is a fundamental subject of concern (Yaguchi et al., 2001). A small number of studies (Kubota et al., 2011; Yaguchi et al., 2001) have demonstrated the relationship between plain fatigue and dislocated structure of materials. The study in Peng et al. (2011) focused on the role of ecological hydrogen on the fretting fatigue quality of austenitic stainless steel. The relationships between the reaching surfaces and little cracks within the materials have been investigated, including the role of hydrogen gas. A 316L austenitic stainless steel was taken as the specimen because it possesses the crystal structure of

face centered cubic (FCC) lattice, and its dislocation configurations are easy to locate (Zalnezhad et al., 2013; Zhu et al., 2016). An experimental evaluation was conducted to investigate the fretting fatigue life of multilayer Cr–CrN-covered AL7075-T6 alloy specimens with high adhesion strength of the substrate. In fact, the bond quality of coating stands out among the most basic issues in magnetron sputtering system (Luo, 2013; Peng et al., 2013). Previous research (Peng et al., 2014) investigated the bending fretting fatigue of 7075 aluminum alloy. The work focused on behaviors of bending fretting fatigue, which are affected by the applied bending stress and the number of cycles on the same ratio. The objective was to identify the life reduction caused by the fretting induced by the pure bending load, and to determine the relationship between the bending fretting fatigue behavior and dislocation structures of microstructures. The behavior of soft bending fretting fatigue of medium carbon steel (LZ50 steel), aluminum alloy (7075) (Peng et al., 2014), and stainless steel (316L steel) (Zalnezhad et al., 2013) have been investigated (Majzoobi and Minaii, 2013). Recently, 30CrNiMo8 and 17CrNiMo6 alloy steels were investigated under the same conditions. The impact of deep rolling on the bending fretting fatigue resistance of Al7075 is studied using the rotating bending fretting fatigue tests conducted on a Moore rotary bending mechanical assembly (Zalnezhad et al., 2014). A test assessment by a rotating bending mechanical assembly (Song et al., 2014) was conducted to investigate the fretting fatigue life of multilayer Cr–CrNcovered AL7075-T6 composite specimens with higher adhesion quality to substrate, given that the covering grip quality is vital among the most basic issues in magnetron sputtering system (Peng et al., 2014). Fretting damage failure of a Chinese carbon railroad axle RD2 was investigated by using a small-scale axle-test apparatus and recreating tests at different rotator rates of 1800 and 2100 r/min (Gutkin and Alfredsson, 2008). Rotating bending was studied for crack growth in a press-fitted test rig (Savaria et al., 2016; Yang et al., 2014; Yuan et al., 2014). In recent years, a number of studies on bending fatigue (Dao and Vu, 2016;Haidyrah et al., 2016; Hwang et al., 2016; Kamaya, 2016; Li et al., 2016; Ma et al., 2015) and fretting fatigue have been reported (Foletti et al., 2016; Huang et al., 2016a, 2016b; Shi et al., 2016; Winkler et al., 2015), whereas comparatively less studies were performed on bending fretting fatigue (Ding et al., 2014; Johnson, 1995; Liu et al., 2013). It was found that the stress concentration for two close pitting holes is an exponential function of the separation between the two holes, under uniaxial loading (Jesús VILLALON LOPEZ, 2010). In order to investigate the fatigue limit micro-mechanism of a precipitation-hardened Al–Mg–Si alloy (6061-T6) (Hiroshi Noguchi, 2014), the alloy was subjected to very-high-cycle fatigue (VHCF) of over 109 cycles by an ultrasonic fatigue method. In this report, tensile properties of AA 6061 are determined as basic information for conducting fatigue test (*R.C. Prasad ,* 2 0 0 8).In this present work, effect of fretting fatigue is observed by applying fretting bolts using ring type fretting arrangement.

2. METHODOLOGY

2.1 Chemical and mechanical properties

Table 1 and Table 2 present the Chemical and mechanical properties of the AL 6061-T6.

Table 1: Chemical properties of Al 6061-T6

Mg	Al	Si	Cr		Mn	Fe
1.75	94.42	0.79	0.20		0.32	0.47

Table 2: Mechanical properties of Al 6061-T6

Density	UTS	YTS	Young's Modulus	Poison's ratio	Elastic limit
2.7 g/cc	310 MPa	276 MPa	68.9 MPa	0.33	96.5 MPa

There are some dimensions of the specimen is shown in Figure 1.

a

b
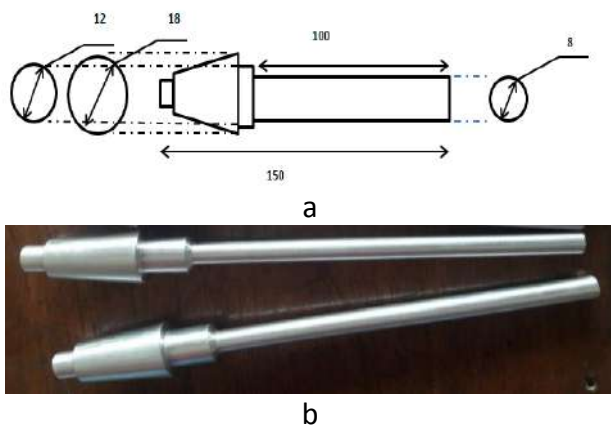
Figure 1. Designed specimen (dimensions are in mm) (a), prepared Specimens (b)

Experimental setup

General rotating bending machine with jockey load is used here. Friction fatigue is applied with the use of screwed friction points that is perpendicularly movable only to the specimen as shown in Figure 1 while fretting fatigue is applied with the help of screwed ring that is capable of rotating with specimen.

In Figure 2, power (on/off) is controlled by switch (1) which starts the motor (3) by supplying current to its coil. From rotation per minute of motor shaft, running cycles can be recorded which is shown in (2). Two bearing supports (4) are mounted to smoothen the rotation without tilting. Chuck and screw system (5) is used to grab the fixed portion of specimen. Friction arrangement (6) is provided with both side screwed bolt support which is allowed to move only to each other. Jockey load can be applied with the rotation of wheel (7). An automatic power cut-off switch is provided just below the jockey to discontinue power at fracture which is not shown in the Figure 2.

Figure 2. Experimental setup for fatigue test

When experimental setup with friction/fretting mechanism is ready (as shown in Figure 3.a) then, specimen tail is inserted into the setting hole attached with jockey load and head is inserted through chuck into hollow shaft attached with main motor. Wrench/spanner set is used to tighten the fixed portion. Cut-off switch sensor is held upward outside the tail setting set. Screwed wheel is rotated in jockey load to ensure the desired load applicable to the specimen. Frequency and rpm is set up with the help of inverter/VFD (here, constant frequency is 50 Hz, rpm 2800). Switch is turned on to start the motor, at the same time, stopwatch is used to measure the total time. When the specimen fractures as shown in Figure 3.b), motor is automatically off with the help of cut-off sensor. Just that time of stoppage, stop watch is also stopped. Cycles can be counted by following formulas:

N (cycle) = Time (minute) x RPM (2800).

Stress, S = Force/Area.

Obtained Stress and Cycles are plotted in S-N curve. Similar procedure is repeated for specimen with fretting load.

a

b

Figure 3. Fretting arrangement (a) and fractured specimens in this experiment (b)

2.3 Numerical Simulation

For FEM analysis, ANSYS 14.5 was used here. CONTA 174 and TARGE170 has been used as contact and target element. Refinement for meshing has been adopted for result convergence. Co-efficient of 0.2 has been taken between contacts. Fretting force of 1000 N has been taken as constant loading on pads. Figure 4 shows the FEM analysis for life under applied loading.
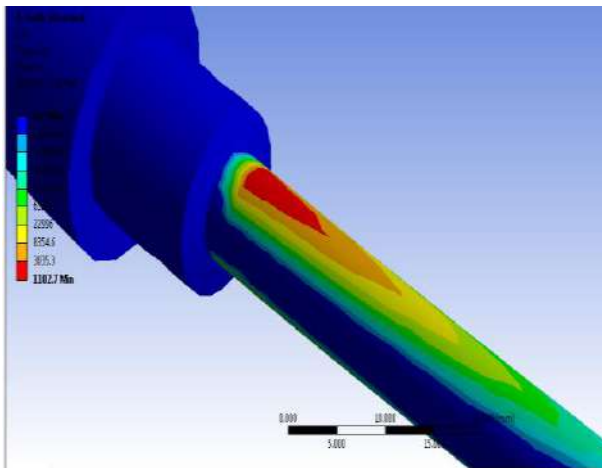
Figure 4. FEM analysis for life under applied loading

3. RESULTS AND DISCUSSIONS

Figure 5 and Figure 6 shown FEM result with respect to S-N curve of Al 6061-T6. From S-N diagrams, it is obvious that, fretting reduces fatigue life considerably. For higher order loading it coincides with general fatigue life but as load level decreases for 1000 N fretting load life cycles decreases abruptly. In other words, it can be said that effect of notch and edge corner has much more impact on specimen than fretting load of even 1000 N at high bending loading. Fretting effect becomes obvious for low order loadings.

Solving the above equation by taking log both sides yields the values of A and B from which we can get the value of endurance limit. We find from figure 6 that fatigue limit as well as endurance limit is 94 MPa at 10^7 cycles for normal fretting whereas for fretting fatigue, it becomes 77 MPa at 10^7 cycles.
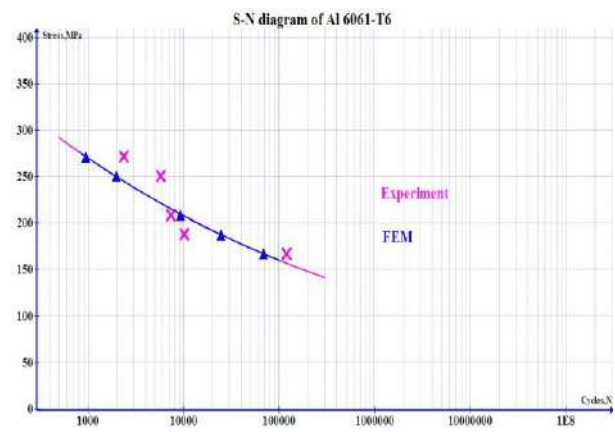
Figure 5. S-N curve obtained from experiment and FEM analysis
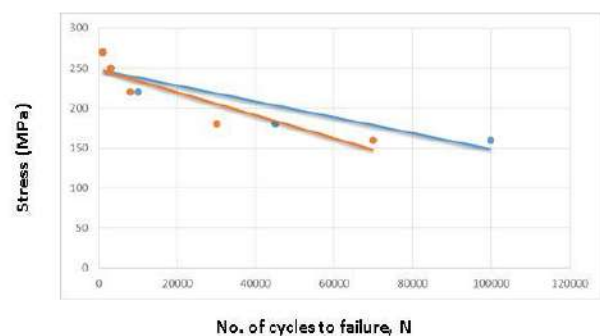
Figure 6. S-N curve obtained from normal and fretting fatigue.

From basquin equation, we know that

$$S= AN^B \qquad (1)$$

Endurance limit has been reduced of about 22% due to fretting of 1000 N while fatigue life time reduces 30-33% for low order loading.

4. CONCLUSION

On the basis of above discussed results, it can be said that fatigue associated with fretting affects the lifetime of Al 6061-T6 badly than the normal one. However, at the peak value bending loading with greater stress it is difficult to differentiate individual effect of sharp corner and fretting effect, respectively. Here, preference of fillet edged corner over sharp edged object subjected to cyclic loading comes afore. Fretting effect is pre dominant for lower valued bending stresses by reducing the fatigue limit. So, concentration should be equally paid to the cases of both fretting and edged corners of valuable structures.

REFERENCES

[1] Bethune B and Waterhouse R Adhesion of metal surfaces under fretting conditions I. Like metals in contact, Wear, Vol. 12, No. 4, pp. 289–296, 1968.

[2] Chen L and Wei Y (2014) Overall mechanical behavior of nanocrystalline materials accompanied by damage evolution on grain boundaries, International Journal of Damage Mechanics, Vol. 23, No. 1, pp. 25–42.

[3] Chuanfu YWZWD and Zenye Z, Study on spectrum load fatigue behaviors, fracture mechanism and fractography of two ultra-high strengh steels, Journal of Materials Engineering, Vol. 0, No. 2, pp. 10-14, 1992.

[4] Cortese L, et al., Prediction of ductile failure in materials for onshore and offshore pipeline applications, International Journal of Damage Mechanics, Vol. 23, No. 1, pp. 104–123, (2014)

[5] Dao NH and Vu MN, Load sequence effects on the fatigue crack growth in a cylinder subjected to combined rotary bending moment and axial force loads, Theoretical and Applied Fracture Mechanics, Vol. 82, pp. 117–124, 2016.

[6] Das RR and Pradhan B, Delamination damage analysis of laminated bonded tubular single lap joint made of fiber-reinforced polymer composite, International Journal of Damage Mechanics, Vol. 23, No. 6, pp. 772–790, 2014

[7] Ding J, et al., Finite element analysis on bending fretting fatigue of 316L stainless steel considering ratchetting and cyclic hardening, International Journal of Mechanical Sciences, Vol. 86, pp. 26–33, 2014.

[8] Ebara R and Fujimura M, Fretting fatigue behaviour of Ti–6Al–4V alloy under plane bending stress and contact stress, Tribology International, Vol. 39, No. 10, pp. 1181–1186, 2006.

[9] Foletti S, Beretta S and Gurer G, Defect acceptability under full-scale fretting fatigue tests for railway axles, International Journal of Fatigue, Vol. 86, pp. 34–43, 2016.

[10] Genet M, Marcin L and Ladeveze P, On structural computations until fracture based on an anisotropic and unilateral damage theory, International Journal of Damage Mechanics, Vol. 23, No. 4, pp. 483–506, 2014.

[11] Gutkin R and Alfredsson B, Growth of fretting fatigue cracks in a shrink-fitted joint subjected to rotating bending, Engineering Failure Analysis, Vol. 15, No. 5, pp. 582–596, 2008.

[12] Haidyrah AS, Newkirk JW and Castan~o CH, Weibull statistical analysis of Krouse type bending fatigue of nuclear materials, Journal of Nuclear Materials, Vol. 470, pp. 244–250, 2016.

[13] Hattori T, et al., Fretting fatigue analysis using fracture mechanics, JSME International Journal, Ser. 1, Solid Mechanics, Strength of Materials Vol. 31, pp. 100–107, 1988.

[14] Hills D and Nowell D, *Mechanics of Fretting Fatigue,* Kluwer Academic Publishers, 1994.

[15] Huang L, et al., Fatigue and fretting of mixed metal self-piercing riveted joint, International Journal of Fatigue, Vol. 83, pp. 230–239, 2016a.

[16] Huang Y, Wang Z and Zhou Q, Numerical studies on the surface effects caused by inhomogeneities on torsional fretting. Tribology International, Vol. 96, pp. 202–216, 2016b.

[17] Hwang B, Kim T and Han SM, Compression and tension bending fatigue behavior of Ag nanowire network, Extreme Mechanics Letters, 2016.

[18] Iwabuchi A, Kayaba T and Kato K, Effect of atmospheric pressure on friction and wear of 0.45% C steel in fretting, Wear, Vol. 91, No. 3, pp. 289–305, 1983.

[19] Johnson K, Contact mechanics and the wear of metals. Wear, Vol. 190, No. 2, pp. 162–170, 1995.

[20] Johnson K and Greenwood J, An adhesion map for the contact of elastic spheres, Journal of Colloid and Interface Science, Vol. 192, No. 2, pp. 326–333, 1997.

[21] Kamaya M (2016) Development of disc bending fatigue test technique for equi-biaxial loading. International Journal of Fatigue 82: 561–571.

[22] King RN and Lindley TC, Fretting fatigue in a 3/2 Ni–Cr–Mo–V rotor steel, In: Francosis D (ed.) In: Proceedings of ICF5. Oxford: Pergamon Press, pp. 631, 1981.

[23] Kubota M, et al., Mechanism of reduction of fretting fatigue limit caused by hydrogen gas in SUS304 austenitic stainless steel, Tribology International, Vol. 44, No. 11, pp. 1495–1502, 2011.

[24] Lee H and Mall S, Investigation into effects and interaction of various fretting fatigue variables under slip-controlled mode, Tribology International, Vol. 39, No. 10, pp. 1213–1219, 2006.

[25] Gonzalo M. DOMINGUEZ ALMARAZ1, Victor H. MERCADO LEMUS1, J. Jesús VILLALON LOPEZ, Rotating bending fatigue tests for aluminum alloy 6061-T6, close to elastic limit and with artificial pitting holes 1, Procedia Engineering, Vol. 2, No. 1, pp. 805–813, 2010.

[26] Yoshimasa Takahashi, Hiroaki Yoshitake, Ryota Nakamichi, Takuya Wada, Masanori Takuma, Takahiro Shikama, Hiroshi Noguchi, Fatigue limit investigation of 6061-T6 aluminum alloy in giga-cycle regime, Materials Science & Engineering, Vol. 614, pp. 243–249, 2014.

[27] B.F. Jogi , P.K. Brahmankar , V.S. Nanda, R.C. Prasad , (2 0 0 8) Some studies on fatigue crack growth rate of aluminum alloy 6061, Journal of materials processing technology, Vol. 201, No. 1-3, pp. 380–384.

HIGH FRICTION COEFFICIENT MATERIALS

Katarina LEKOVIC, Varun SHARMA, Nenad GRUJOVIC, Dragan ADAMOVIC, Slobodan MITROVIC, Fatima ZIVIC*

Faculty of Engineering, University of Kragujevac, Serbia

zivic@kg.ac.rs

Abstract: *This paper presents some insights into the materials characterised by the high friction coefficient. Friction coefficient is one of the essential parameters for evaluation of the contact development, but it still needs further investigations, especially from nano and micro aspects. There are several approaches to the determination and quantification of the static and dynamic coefficients, whereas methodology involving energy dissipation has gained attention for the nano and micro contacts. High friction is applied in systems where good adhesion is needed, such as breaks or in the case of dry adhesives – fitting of the elements together. Material combinations are reviewed, that exhibit high friction coefficients during contact. Two types of materials are presented from friction aspects: Ti-based alloys for medical implants where high friction is a negative property and Al-based alloys for which this feature has been used in various friction welding applications. In the case of Ti-based alloys, many approaches have been tried to overcome high friction and associated high detrimental wear, but it is still the evident problem. For aluminium alloys, it is used for joining two parts in different systems, such as car body, ship elements, or various rail wagon related elements.*

Keywords: *friction coefficient, adhesion, Ti alloys, Al alloys, contact.*

1. INTRODUCTION

Friction coefficient was introduced a very long time ago, by Leonardo Da Vinci, who defined it as the ratio of frictional force and normal component [1]. Friction coefficient is very commonly taken as the parameter which is either a known value for the system under observation from the tables in the literature (as in the case of many modeling methods), or it is experimentally determined in scope of tribological testing [2-7]. However, fundamental understanding of the governing influences on the value variations is still rather ambiguous, what is even more odd, considering the fact that friction coefficient is one the essential parameters in numerous calculations and system definitions. On the other hand, if the two relative surfaces in contact are observed, it is quite obvious that many influential factors determine the contact behaviour and from this point of view, friction coefficient is no more a simple parameter because it reflects all of these influences. In most of the engineering cases, only macro behaviour of the contact zone is satisfying enough for the system description and maintenance. However, if the scale is lowered down to micro and especially to nano levels, many factors become interlinked and under

debate, thus making a question of friction coefficient very complex one.

In general, friction coefficient depends on the materials in contact, their geometry, surface roughness, environment and temperature. Static or dynamic friction coefficient can be studied as: static to reflect the start of the motion, and dynamic or kinetic one, related to the maintenance of the motion. Difference between static and dynamic friction coefficient was noticed by ancient Greeks. They recognized that it is easier for the object to continue its movement than to start it from the inaction. The classical law of friction was first defined by Leonardo Da Vinci, who is sometimes considered to be the pioneer of tribology, whose work was documented in notes but not published at that time (year of 1493). These principals were discovered and first time published by Amontons in 1699 who defined friction force and dependence on applied load and independence of the contact area. In general, 1st and 2nd Amontons' laws of friction are still valid in cases of dry friction. In 1750, Belidor and Euler introduced the difference between static and dynamic friction. The first comprehensive study of the friction was realised by Coulomb in 1785 who studied the various influences originating from the materials in contact, contact geometry, external loading, velocities, time in contact, temperature, humidity. Coulomb stated that kinetic friction is independent of the sliding velocity. It was not until 1950 that surface roughness was essentially recognised as the highly influential factor, when Bowden and Tabor showed that contact surfaces on micro level are very small and introduced the term 'real contact surface', whereas the real contact surface is significantly smaller than previously considered the macro contacts.

For a very long time, common understanding has been that the friction coefficient can only have a value between 0 and 1 and also that static coefficient is higher than its dynamic value. Frictional energy, created during the motion of the two surfaces in relative contact, is partially transformed into heat, deformation and wear of the surfaces. At micro and nano scale, thermodynamics, as well as several other influences (chemistry, micro/nano roughness, etc.) start to govern the process. Work created due to friction can be transformed into deformations and heat can affect surface properties which can be used in polishing process. Work induced with friction can be used in material mixing and merging in frictional welding [11].

Definition of the factors that influence friction on micro and nano scale still represents a complex issue and several approaches has been proposed. There are many proposed friction models in the literature, that consider geometry (roughness), mechanical properties (stress, strain), fluid dynamics, electrostatic forces between surface atoms, chemical compatibility, shear strength of the adhesive junctions and other. Methodologies considering energy dissipation modes are considered to be the promising ones to provide general friction theory at micro/nano scale [8-10]. In different tribosystems, energy due to the work of friction is distributed in different ways, from the heat that simply increase internal energy of the materials in contact, or forming of new surfaces and wear debris by forming and breaking the micro-welded zones, and deformation of the contact films. The relationship between friction and wear is evident and yet there is no direct general theory to quantify it, except experimental dependences within separate tribo testing.

Energy transformed as friction effect can be stored inside the tribosystem or distributed in several ways, as per eq. 1.

$$E_f = E_{out} + E_{st} \qquad (1)$$

where: E_f - total energy resulting from friction; E_{out} – energy that left the system; E_{st} – energy stored within the system.

For example, energy created by mechanical sliding can be transformed into heat, vibrational energy (sound), material deformation, or wear. Therefore, energy can be stored within a material, in a form of microstructural defects. Accordingly, two materials with the same value of the friction

coefficient can experience different levels of wear because of different energy distribution between and inside materials. Relationship between friction and wear can change over time within one system and usually is changing, thus additionally introducing complexity in investigation of friction and wear.

Recent investigations, both theoretical and experimental, indicate that from simple energy approach, friction is related to 1) adhesion of the micro-contacts leading to material damage after breaking of those bonds and 2) plastic deformation of surface asperities [10]. However, energy dissipation in atomic-scale friction is much more complex than this approach [8, 9].

Frictional energy dissipates during microscopic deformations of surface asperities and converts into heat. Down to micro and nano scale, frictional force depends of interactive physical and chemical properties, loads, relative velocity, and temperature within small contact zones of surface asperities. As the direct consequence, generated heat is not equally distributed between the two surfaces in contact. Heat distribution level depends of heat conductivity, heat capacity, relative velocity, interspace and many other factors. Localized plastic deformation can significantly change heat distribution, because part of the energy is retained within a material microstructures (e.g. uniaxial strain test always store some energy in the microstructure in a form of residual stresses) and it can be as much as 80 - 100% of the total energy input.

Perceived knowledge on the friction coefficient has changed during last decades and values of the coefficient higher than 1 are proven from many experimental results. Consequently, materials that can exhibit these high friction coefficients has been studied and several practical applications have been recognised.

2. REVIEW OF THE MATERIALS WITH HIGH FRICTION COEFFICIENT

Static coefficient of friction is related to the initiation of motion, whereas dynamic friction coefficient pertains to the maintaining of the motion. Two opposite areas can be observed related to the friction coefficient exhibited in the process: low and high friction coefficient levels. Low friction coefficient is desired property in the cases when smooth rolling or sliding is requested during the contact between two different elements. Opposite to this approach, very high friction coefficients are studied for development of specific applications such as brake systems, or locking the elements together during assembly of some systems (zero slip), or cold welding, and others. High friction materials were mainly focused on brake materials earlier and did not have that much attention until last decades, and especially with advent of nanotechnologies they became interesting subject of research. Well known gecko feet effect [12] provoked very interesting investigations to mimic such materials and surface structures to enable high friction and low adhesion for many new nano/micro-related applications. The extraordinary natural surface design of the gecko feet lies within the set of arrays with hundreds of flexible fibers thus providing very high adhesion and friction on the opposite surface, for all surfaces, from rough to smooth or hydrophobic and hydrophilic surfaces, by using only weak van der Waals forces. This principle has been studied for application in dry adhesives.

It is usually considered that static coefficient of friction is always higher than the dynamic values. It is most often so, but there are numerous cases when dynamic values can be dramatically higher than static ones (even 40-50% higher), because it strongly depends on the materials in contact, as well as the contact conditions (surface roughness, load or pressure, velocity, environment and especially the temperature).

Table 1 presents several common combinations of materials in contact that result in high friction coefficients, with average values under ambient temperature. Comparison of changes in material combinations related to the friction coefficients is given in Table 2. It is obvious

that materials in contact have major influence on the frictional values, but also the environment can result in significant changes. For example, car tires are significantly easier to start moving on the asphalt than on the grass (or in the case of the rubber - wet asphalt/concrete/road vs. rubber - dry asphalt/concrete/road), which is commonly known fact in life, really nicely represented by the frictional values in Table 2. It can also be seen that even changes within the material compositions or structures, can decrease by half the frictional values (e.g. copper – cast iron vs copper – mild steel). Also, environment can have major influence, like in the case of graphite –graphite contact (in vacuum 0.5-0.8 down to 0.1 without the vacuum).

Table 1. Material combinations that result in high friction coefficient [13]

Material combinations		Static coefficient of friction		Dynamic coefficient of friction	
		Dry contact, Clean surfaces	Lubricated	Dry contact, Clean surfaces	Dry contact, Clean surfaces
Aluminum	**Aluminum**	**1.05 - 1.35**	**0.3**		
Aluminum	Mild Steel	0.61			
Cast Iron	**Cast Iron**	**1.1**		**0.15**	**0.07**
Car tire	Asphalt	0.72			
Copper	Copper	1	0.08		
Copper	Cast Iron	1.05		0.29	
Glass	Glass	0.9 - 1.0	0.1 - 0.6	0.4	0.09 - 0.12
Glass	Nickel	0.78	0.56		
Graphite	Graphite (in vacuum)	0.5 - 0.8			
Ice	Steel	0.03			
Iron	Iron	1.0	0.15 - 0.20		
Nickel	Nickel	0.7 - 1.1	0.28	0.53	0.12
Nickel	Mild Steel			0.64	0.178
Platinum	**Platinum**	**1.2**	**0.25**		
Rubber	**Rubber**	**1.16**			
Rubber	Dry Asphalt	0.9		0.5 - 0.8	
Rubber	Dry Concrete			0.6 - 0.85	
Silver	**Silver**	**1.4**	**0.55**		
Skin	Metals	0.8 - 1.0			
Steel	Steel	0.5 - 0.8	0.16		
Tungsten Carbide	Iron	0.8			
Tire, dry	Road, dry	1			
Zinc	Cast Iron	0.85		0.21	
Zinc	Zinc	0.6	0.04		

Table 2. Comparison of changes in material combinations that result in significant changes in friction coefficient values

Material combinations		Static coefficient of friction		Dynamic coefficient of friction	
		Dry contact, Clean surfaces	Lubricated	Dry contact, Clean surfaces	Dry contact, Clean surfaces
Car tire	**Asphalt**	**0.72**			
Car tire	Grass	0.35			
Copper	**Cast Iron**	**1.05**		0.29	
Copper	Mild Steel	0.53		0.36	0.18
Graphite	**Graphite (in vacuum)**	**0.5 - 0.8**			

Graphite	Graphite	0.1	0.1		
Rubber	**Dry Asphalt**	**0.9**		**0.5 - 0.8**	
Rubber	Wet Asphalt			0.25 - 0.75	
Rubber	**Dry Concrete**			**0.6 - 0.85**	
Rubber	Wet Concrete			0.45 - 0.75	
Tire, dry	**Road, dry**	**1**			
Tire, wet	Road, wet	0.2			
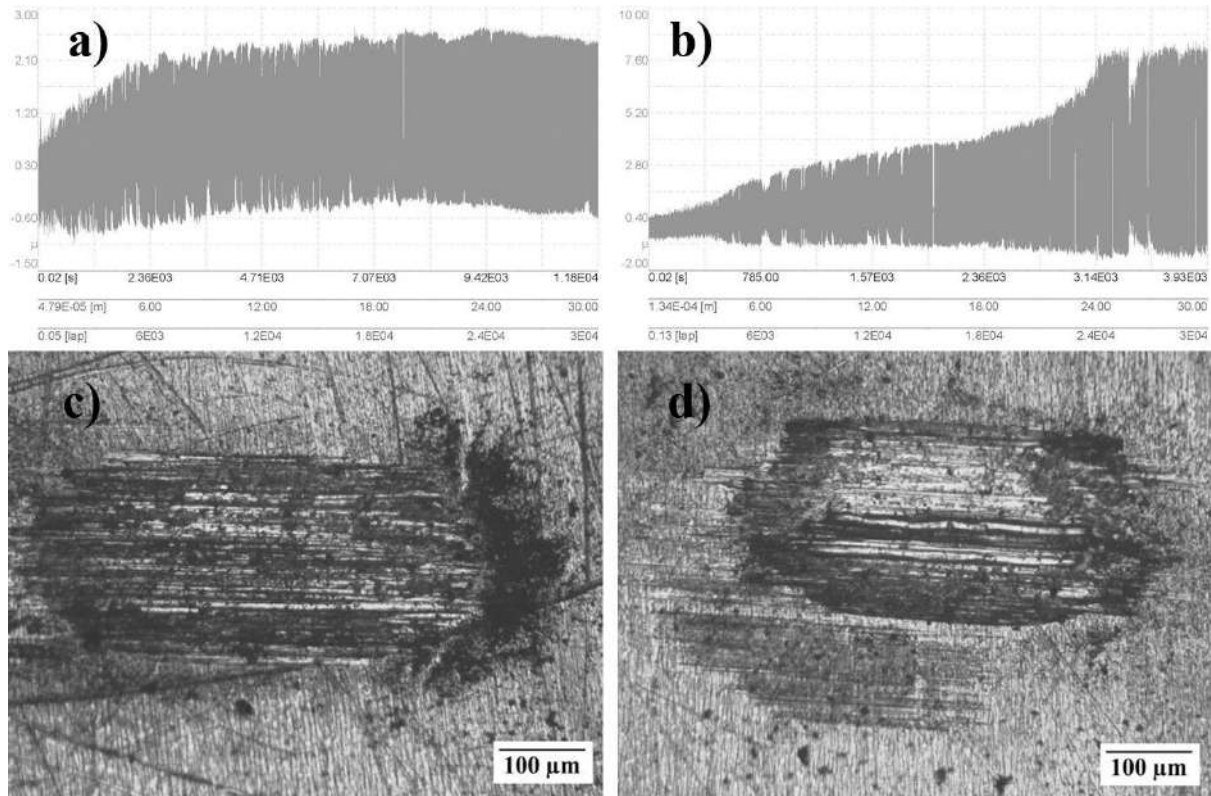
Figure 1. Sample 2: Diagrams of friction coefficient and optical micrograph showing wear track on Ti6Al4V sample: a), c) Ringer, v=4 mm/s; FN=100mN; b), d) Ringer, v=12 mm/s; b FN=100mN

The influence of the temperature is also very significant. Moving surfaces in relative contact to each other always results in frictional heating, thus the contact zone temperature is always higher than ambient temperature, even in the cases when contact is maintained without externally elevated temperatures. On the other hand, the increase of the temperature within the contact zone is strongly influenced by the material types in contact, velocities and loading, as well as the environment. So called flash temperatures and especially at micro/nano scale represents complex problem, still with many debates related to its origin and its influence on the development of motion.

Some materials are especially prone to detrimental effects of the frictional heating,

inducing such high frictional coefficients thus resulting in micro galling and micro-welding. For example, some α-β microstructures of medical grade Ti alloys (e.g. Ti6Al4V) can exhibit dynamic friction coefficients significantly higher than 1, as given in Fig. 1, sample 2 selected from 4 types of Ti6Al4V in contact with alumina ball (ball-on-flat).

This particular contact resulted in detrimental abrasive and adhesive wear with very high flash temperatures that can be concluded even without measuring the temperatures, due to the black burnt wear debris widely spread all around the contact zone (Fig. 1 c, d). This is commonly recognised problem with these Ti alloys and many new approaches have been studied to overcome it in order to use these alloys in medical implants.

Table 3. Chemical Composition of Al based element widely employed in friction stir welding process

(wt. %) of 5083 – O Thin Plate [13]									
Si	Fe	Cu	Mn	Mg	Cr	Zn	Ti	V	Al
0.35	0.29	0.08	0.67	4.32	0.12	0.18	0.07	-	Bal.

(wt %) of aluminum alloy 2024 – T4 (wt %) [14]								
Si	Fe	Cu	Mn	Mg	Zn	Ti	Others	Al
0.5	0.5	3.8 – 4.9	0.3 – 0.9	1.2 – 1.8	0.3	0.15	Ni: 0.1, Fe + Ni:0.5	Bal.

(wt %) of AA1050 [15]								
Si	Fe	Cu	Mn	Mg	Zn	Ti	Cr	Al
0.08	0.27	0.02	0.01	0.01	0.02	0.02	-	Bal.

(wt %) of AA 5754 [15]								
Si	Fe	Cu	Mn	Mg	Zn	Ti	Cr	Al
0.4	0.4	0.1	0.5	2.6 -3.2	0.2	0.15	0.3	Bal.

(wt %) of 7075 – T6 [16,28]								
Si	Fe	Cu	Mn	Mg	Zn	Ti	Cr	Al
0.58	0.35	1.2	0.12	2.1	5.1	-	-	Bal.

(wt %) of AA6061 - T6 [17,29]								
Si	Fe	Cu	Mn	Mg	Zn	Ti	Cr	Al
0.4 - 0.8	0.7 (max)	0.15 – 0.4	0.15 (max)	0.8 – 1.2	0.25 (max)	0.15 (max)	0.04 – 0.35	95.85 – 98.56
Others (0.05 each – max) – total 0.15								

(wt %) of AA 7020 [18]									
Si	Fe	Cu	Mn	Mg	Cr	Zn	Ti	Others	Al
-	0.35	0.10	0.24	1.30	0.14	4.70	0.08	7.65	85.44

(wt %) of A 6082 [19]									
Si	Fe	Cu	Mn	Mg	Cr	Zn	Ti	Others	Al
1.0	0.15	0.02	0.7	1.15	0.15	0.02	0.1	-	Bal.

(wt %) of 6061 Al [20]									
Si	Fe	Cu	Mn	Mg	Cr	Zn	Ti	Others	Al
0.6	0.7	0.2	0.15	0.9	0.1	0.25	-	-	Bal.

(wt %) of AA 2024 – T351 [21]									
Si	Fe	Cu	Mn	Mg	Cr	Zn	Ti	Others	Al
0.06	0.15	1.3	0.02	2.4	0.19	5.8	0.07	-	Bal.

(wt %) of AA 5052 – [22]									
Si	Fe	Cu	Mn	Mg	Cr	Zn	Ti	Others	Al
0.25	0.4	0.1	0.15-0.35	2.2 – 2.8	0.1	-	-	-	Bal.

(wt %) of 2A70 [23]									
Si	Fe	Cu	Mn	Mg	Cr	Zn	Ti	Ni	Al
0.35	1.1	2.01	0.20	1.57	-	0.30	0.03	0.95	85.44

(wt %) of 2219 T87 [24]									
Si	Fe	Cu	Mn	Mg	Zr	Zn	Ti	Ni	Al
0.08	0.18	6.38	0.32	-	0.18	-	0.06	0.03	Bal.

(wt %) of AA5010 [25]									
Si	Fe	Cu	Mn	Mg	Zr	Zn	Ti	Ni	Al
0.62	0.33	0.28	0.06	0.9	-	0.02	0.02	-	Bal.

(wt %) of AA 2219 [26]									
Si	Fe	Cu	Mn	Mg	Zr	Zn	Ti	V	Al
0.49	0.23	6.48	0.32	-	0.2	0.04	0.06	0.08	92.1

(wt %) of A6111 [27]									
Si	Fe	Cu	Mn	Mg	Zr	Zn	Ti	V	Al
1.041	0.036	0.803	0.066	0.592	-	-	-	-	Bal.

(wt %) of A5023 [27]									
Si	Fe	Cu	Mn	Mg	Zr	Zn	Ti	V	Al
0.110	0.090	0.200	0.005	5.680	-	-	0.090	-	Bal.

Accordingly, Ti alloys are avoided to use in implant elements where there is any type of motion.

One of the materials that exhibit very high friction coefficients when mated to itself is aluminium (Al), hence very suitable for frictional welding applications. It is commonly used for frictional welding in different combinations of devices, technologies and working regimes [11, 13-27]. Chemical compositions of Al-based alloys used for frictional welding are given in Table 3.

General application is in sheet metal industry and light weight engineering applications, and especially in transportation industry (shipbuilding industry, rail and automotive industry). However, these technologies, as well as material properties are further studied for improvements, most often by using simulation and modeling approaches, such as stress – strain localization models, thermo-mechanical finite element (FE) modeling and analysis. Usual demands upon joints formed in such way are certain level of loading (including shear stress), usually also with reversals during the lifetime, during which it must not exhibit wear, creep or micro cracking and other forms of failure.

3. CONCLUSION

The role of the friction used in some practical applications where high friction coefficients of the materials are used, can be observed in several ways: to lock elements together during the assembly procedure; to provide very strong joining (solid state welding); or to provide better adhesion of elements also under conditions of dry contact. Several existing material combinations presented in this paper are those already commonly used but many more are yet to appear, especially if joining of two different materials are further considered.

ACKNOWLEDGEMENT

REFERENCES

[1] I.M. Hutchings: Leonardo da Vinci's studies of friction, Wear, Vol 360–361, pp 51–66, 2016.

[2] P.J. Blau: The significance and use of the friction coefficient, Tribology International, Vol. 34, No. 9, pp. 585-591, 2001.

[3] H. Czichos, T. Saito, L. Smith (Eds.): Springer Handbook of Materials Measurement Methods, Berlin 2006.

[4] P.J. Blau: Introduction to the Special Issue on Friction Test Methods for Research and Applications, Tribology International, Vol. 34, No. 9, pp. 581-583, 2001.

[5] N.K. Myshkin, A.Y. Grigoriev, S.A. Chizhik, K.Y. Choi, M.I. Petrokovets: Surface roughness and texture analysis in microscale, Wear Vol. 254, pp. 1001–1009, 2003.

[6] E. Gnecco, E. Meyer: Elements of Friction Theory and Nanotribology, Cambridge University Press, 2015.

[7] G. Straffelini: Friction and Wear, Methodologies for Design and Control, Springer Tracts in Mechanical Engineering, Springer International Publishing Switzerland 2015.

[8] Y-Z. Hu, T-B. Ma, H. Wang: Energy dissipation in atomic-scale friction, Friction, Vol. 1, No. 1, pp. 24–40, 2013.

[9] Z. Xu, P. Huang: Application Of Energy Principle To Dry Sliding Friction, Proceedings of WTC2005, World Tribology Congress III, September 12-16, Washington, D.C., USA, WTC2005-63931, 2005.

[10] D. Maharaj, B. Bhushan: Friction, wear and mechanical behavior of nano-objects on the nanoscale, Materials Science and Engineering, Vol. 95, pp. 1–43, 2015.

[11] R.S. Mishra, P. Sarathi, N. Kumar: Fundamentals of the Friction Stir Process, Springer International Publishing Switzerland 2014.

[12] Y. Tian, N. Pesika, H. Zeng, K. Rosenberg, B. Zhao, P. McGuiggan, K. Autumn, J. Israelachvili: Adhesion and friction in gecko toe attachment and detachment, Proceedings of the National Academy of Sciences of the United States of America, Vol. 103, No. 51, pp. 19320–19325, 2006.

[13] Material Properties, Engineering toolbox, *www.engineeringtoolbox.com*.

[14] Y-G. Kim, I-J. Kim, Y-P. Kim, S-M. Joo: A Feasibility Study on the Three-Dimensional Friction Stir Welding of Aluminum 5083-O Thin Plate, Materials Transactions, Vol. 57, No. 6, pp. 988 – 994, 2016.

[15] J-G. Ren, L. Wang, D-K. Xu, L-Y. Xie, Z-C. Zhang: Analysis and Modeling of Friction Stir Processing-Based Crack Repairing in 2024 Aluminum Alloy, Acta Metall Sin (Engl. Lett.), Vol. 30, pp. 228–237, 2017.

[16] A. Ramadan S. Essa, M. Mohamed, Z. Ahmed, A-K. Yousif, A. Mohamed, A.E. El-Nikhai: An analytical model of heat generation for eccentric cylindrical pin in friction stir welding, The Journal of Materials Research and Technology, Vol. 5, pp 234-240, 2016.

[17] E Maleki: Artificial neural networks application for modeling of friction stir welding effects on mechanical properties of 7075-T6 aluminum alloy, IOP Conf. Ser.: Mater. Sci. Eng. Vol. 103, No. 012034., 2015.

[18] P. Singh, P. Biswas, S.D. Kore: A three-dimensional fully coupled thermo-mechanical model for Self-reacting Friction Stir Welding of Aluminium AA6061 sheets, J. Phys.: Conf. Ser. 759 012047, 2016.

[19] B. Panda, A. Garg, Z. Jian, A. Heidarzadeh, L. Gao: Characterization of the tensile properties of friction stir welded aluminum alloy joints based on axial force, traverse speed, and rotational speed, Front. Mech. Eng., Vol. 11, pp. 289–298, 2016.

[20] J-H Cho, S.H. Han, C.G. Lee: Cooling effect on microstructure and mechanical properties during friction stir welding of Al-Mg-Si aluminum alloys, Materials Letters, Vol. 180, pp. 157–161, 2016.

[21] W. Zhang, Y. Shen, Y. Yan, R. Guo: Dissimilar friction stir welding of 6061 Al to T2 pure Cu adopting tooth-MARK shaped joint configuration: Microstructure and mechanical properties, Materials Science & Engineering A, Vol. 690, pp. 355–364, 2017.

[22] M.M. Hasan, M. Ishak, M.R.M. Rejab: Effect of backing material and clamping system on the tensile strength of dissimilar AA7075-AA2024 friction stir welds, The International Journal of Advanced Manufacturing Technology, In Press, pp. 1-17, DOI: 10.1007/s00170-017-0033-7, 2017.

[23] S. Aliasghari, M. Ghorbani, H. Karami, M. Movahedi: Effect of plasma electrolytic oxidation on joining of AA 5052 aluminium alloy to polypropylene using friction stir spot welding, Surface & Coatings Technology, Vol. 313, pp. 274–281, 2017.

[24] Q. Zheng, X. Feng, Y. Shen, G. Huang, P. Zhao: Effect of plunge depth on microstructure and mechanical properties of FSW lap joint between aluminum alloy and nickel-base alloy, Journal of Alloys and Compounds, Vol. 695, pp. 952-961, 2017.

[25] S. Zhao, Q. Bi, Y. Wang, J. Shi: Empirical modeling for the effects of welding factors on tensile properties of bobbin tool friction stir-welded 2219-T87 aluminum alloy, The International Journal of Advanced Manufacturing Technology, Vol. 90, pp. 1105-1118, 2017.

[26] M. Ahmadnia, S. Shahraki, M.A. Kamarposhti: Experimental studies on optimized mechanical properties while dissimilar joining AA6061 and AA5010 in a friction stir welding process, The International Journal of Advanced Manufacturing Technology, Vol. 87, pp. 2337–2352, 2016.

[27] G. Sun, Y. Chen, S. Chen, D. Shang: Fatigue modeling and life prediction for friction stir welded joint based on microstructure and mechanical characterization", International Journal of Fatigue, Vol. 98, pp. 131–141, 2017.

[28] T-J. Yoon, J-G. Yun, C-Y. Kang: Formation mechanism of typical onion ring structures and void defects in friction stir lap welded dissimilar aluminum alloys, Materials and Design, Vol. 90, pp. 568–578, 2016.

[29] S. Rajakumar, C. Muralidharan, V. Balasubramanian: Influence of friction stir welding process and tool parameters on strength properties of AA7075-T6 aluminum alloy joints, Materials & Design, Vol. 32, pp. 535-549, 2011.

[30] ASM Material Data Sheet Al6061-T6, material property.

EXPERIMENTAL EVALUATION OF PROPERTIES OF 500W AND 400D GRADE TMT HIGH STRENGTH STEEL BAR

Mohammad Asaduzzaman CHOWDHURY[1,*], MD. Arefin KOWSER[2], Mohammad Abdul HYE[3]
[1]*Dhaka University of Engineering & Technology,DUET,Gazipur-1700,Dhaka,Bangladesh*
Corresponding author: asadzmn2014@yahoo.com

Abstract: In this paper, high strength TMT steel re-bars (500W and 400D) of various diameter have been investigate at different water pressure. Mechanical properties (ultimate strength, yield strength, % of elongation, hardness) of both graded re-bars with rib and without rib are also investigated experimentally. Microstructure of different re-bars at different water pressure also observed to compare and identify the best one.The singnificant outcomes of the results indicate that increase in water pressure its consequently improved the mechanical properties of TMT steel re-bars both graded (500W and 400D) TMT bar with rib are better than without rib TMT bar.However the chemical composition and surface roughing are also showns some significant role to improveing the mechanical and tribological properties in industry.

Keywords: Thermo mechanical treatment, low alloy steel, 400D TMT re-bars, steel structure, 500W TMT re-bars.

1. INTRODUCTION

Quenching of the TMT re-bars is main process in TMT manufacturing process. In this process the hot bar enters the quenching box from one end. In the box the bar is quenched into the water to make outer surface hard. The inner surface remains soft.The experiments were conducted and experimental data was recorded and analyzed by excel statistical method. The graph of main effect plot of factors was drawn, which was used to find the main effect on response. The parameters were controlled properly to minimize variation in yield strength and obtained the desired quality of bar. Here it is found that water pressure had the largest effect on the yield strength with ultimate strength, ratio (T/Y), % elongation. The water pressure was controlled at different re-

bars diameter such as 8 mm and 16 mm level for many experiments and yield strength for each experiment was noted. The mechanical properties experimental data analyses were done by various polt grap with copmary to re-bars with rib and without rib. We found the optimum level of parameters setting of water pressure contorl to get optimum level of Yield strength, For this action plan was designed to control water pressure to a specific level as per the conclusion of this experimentation. Then the action plan had been implemented. The re-bars were produced and checked for its quality; we found satisfactory quality re-bars diameter 8 mm, having optimum Yield strengt, ultimate strength, ratio (T/Y), % elongation. The conclusion has been found that the cooling rate affects on yield strength, but cooling rate is controlled by water pressure which is operated

using control valve. Hence water pressure has been controlled in quenching process to get the desired quality with minimum variation from standard value. The re-bars of 8 mm and 16 mm was produced by controlled rolling and quenching process. Speed of rolling was kept constant and PLC control water pressure valve was used instead of manual control valve for controlling the water pressure.

2. INTRODUCTION
2.1 Chemical composition

The chemical compositions of the TMT high strength steel re- bars diameter are presented in Table 1.

From this table, it is clear that the chemical compositions of the steel re-bars are slightly differed from each other. In order to know the combined effect of the alloying elements of the steel bars, their carbon equivalent (CE) values were also calculated using a widely used Eq. 1 in line with other investigators [29,30]. The CE values thus obtained are also presented in Table 1.

$$CE = \%C + \left(\frac{\%Mn + \%Si}{6}\right) + \left(\frac{\%Cr + \%Mo + \%V}{5}\right) + \left(\frac{\%Cu + \%Ni}{15}\right) \quad (1)$$

From Table 1, it is revealed that the percentage of Carbon (C) and Manganese (Mn) for TMT re-bars of 500W grade (Table 1). With the increase of C and Mn contents strength increases in steels [12]. But, for TMT high strength steel, strength is increased through work hardening and heat treatment techniques rather than increase of C. Here, C

content is remained low to increase steel's weldablity. The phosphorus (P) and sulphur (S) contents are lower for all steels has higher copper (Cu) content than others which play role in increasing corrosion resistance [12, 13].

From Table 1, for 500W TMT re-bars the carbon contents of re-bars diameter 8 mm and 16 mm and the carbon equivalents (CE) of the re-bars are 0.39% and 0.36% in order of re-bars given in Table 1.

From Table 2, it is revealed that the percentage of Carbon (C) and Manganese (Mn) for TMT re-bars of 400D grade (Table 2). With the increase of C and Mn contents strength increases in steels [12]. But, for TMT high strength steel, strength is increased through work hardening and heat treatment techniques rather than increase of C. Here, C content is remained low to increase steel's weldablity. The phosphorus (P) and sulphur (S) contents are lower for all steels has higher copper (Cu) content than others which play role in increasing corrosion resistance [12, 13]. From Table 2, for 400D TMT re-bars the carbon contents of re-bars diameter 8 mm and 16 mm the carbon equivalents (CE) of the re-bars are 0.42% and 0.45% in order of re-bars given in Table 2.

2.2 Tensile properties

Tensile strength of samples has been performed in the Universal Testing Machine. For each size of re-bars three specimens have been tested. Re-bars 12 inch in length was used as tensile test sample.

Table 1. Chemical Compositions of 500W TMT Re-Bar

Grade (TMT)	Dia. (mm)	C (%)	Si (%)	Mn (%)	P (%)	S (%)	Cr (%)	Mo (%)	Ni (%)	Cu (%)	V (%)	CE
500W	8	0.22	0.38	0.71	0.040	0.036	0.180	0.018	0.050	0.180	0.003	0.3939
500W	16	0.22	0.25	0.70	0.018	0.012	0.100	0.009	0.040	0.050	0.007	0.3659

Table 2 Chemical Compositions of 400D TMT Re-Bar

Grade (TMT)	Dia. (mm)	C (%)	Si (%)	Mn (%)	P (%)	S (%)	Cr (%)	Mo (%)	Ni (%)	Cu (%)	V (%)	CE
400D	8	0.25	0.28	0.78	0.034	0.024	0.110	0.016	0.050	0.140	0.008	0.4200
400D	16	0.27	0.30	0.81	0.040	0.030	0.130	0.019	0.060	0.180	0.005	0.4500

The gauge length was taken 200 mm. The data produced by the machine is presented in tables below.

Two kinds of surface condition for the tensile test of the re-bars diameter 8 mm and 16 mm have been experimented. Firstly, the as-received re-bars with ribs on surface are directly tested, the test result has been shown in the Table 3

From the Table 3, it can be seen that the maximum strength has been achieved from the re-bars diameter 16 mm with the lowest percentage of elongation is 16%. Re-bars diameter 8 mm and 16 mm these re-bars are to have 500 Mpa yield strength from the company. But, experimentally, showed yield stress above 500 MPa. Re-bars diameter 16 mm showed higher ductility than re-bars diameter 8 mm respectively. Although, re-bars diameter has higher ductility, it shows in table 3. It is possible setting actual water pressure control also define diameter wise water pressure.

Two kinds of surface condition for the tensile test of the re-bars diameter 8 mm and 16 mm have been experimented. Firstly, the as-received re-bars with ribs on surface are directly tested. The test result has been shown in the Table 4.

The ribs of some specimens of steel bars have been peeled off from the surface by machining keeping the case. Though, some portions of the case of the samples have been removed as a result of machining. The machined samples are re-bars diameter 8 mm and 16mm and 12 inch long. These samples were tested in UTM again. The gauge length was taken 200 mm of the length. The tensile test result of steel re-bars without ribs has been shown in Table 5.

Table 5 states that, the maximum ultimate strength has been achieved from the re-bars diameter 16 mm with the lower percentage of elongation which is 17%. Although, re-bars diameter 16 mm has higher ductility, it shows in Table 5. It is possible setting actual water pressure control also define diameter wise water pressure.

Table 3. Tensile Properties of 500W TMT Re-Bar with Rib

Grade (TMT)	Nominal Dia. (mm)	Yield Strength (Mpa)	Ultimate Strength (Mpa)	Ratio (T/Y)	Elongation (%)	Water Pressure (kg/cm^2)
500W	8	527	626	1.19	17.5	3.8
500W	16	540	643	1.19	16	6

Table 4. Tensile Properties of 400D TMT Re-Bars with Rib

Grade (TMT)	Nominal Dia. (mm)	Yield Strength (Mpa)	Ultimate Strength (Mpa)	Ratio (T/Y)	Elongation (%)	Water Pressure (kg/cm^2)
400D	8	450	562	1.25	17	2.25
400D	16	447	567	1.27	17	3.5

Table 5. Tensile Properties of 500W TMT Re-Bars without Rib

Grade (TMT)	Nominal Dia. (mm)	Yield Strength (Mpa)	Ultimate Strength (Mpa)	Ratio (T/Y)	Elongation (%)	Water Pressure (kg/cm^2)
500W	8	510	600	1.18	18	3.8
500W	16	520	625	1.20	17	6

Table 6. Tensile Properties of 400D TMT Re-Bars without Rib

Grade (TMT)	Nominal Dia. (mm)	Yield Strength (Mpa)	Ultimate Strength (Mpa)	Ratio (T/Y)	Elongation (%)	Water Pressure (kg/cm^2)
400D	8	435	555	1.28	17	2.25
400D	16	435	550	1.26	18	3.5

Table 7. Rockwell hardness of case and core with carbon equivalent and case depth of 500W TMT re-bars various diameters.

Sl. No.	Re-bar Diameter (mm)	Case Depth (mm)	Case Hardness, HRC	Core Hardness, HRB	CE (%)
1	8	1.8	30	90	0.394
2	16	1.9	32	90.8	0.366

Table 8. Rockwell hardness of case and core with carbon equivalent and case depth of 400D TMT re-bars various diameters**.**

Sl. No.	Re-bar Diameter (mm)	Case Depth(mm)	Case Hardness, HRC	Core Hardness, HRB	CE (%)
1	8	1.8	29	88	0.42
2	16	1.9	29.5	88.5	0.45

The ribs of some specimens of steel bars have been peeled off from the surface by machining keeping the case and core intact. Though, some portions of the case of the samples have been removed as a result of machining. The machined samples are re-bars diameter 8 mm and 16 mm and 12 inch long. These samples were tested in UTM again. The gauge length was taken 200 mm of the length. The tensile test result of steel re-bars without ribs has been shown in Table 6.

Table 6 states that, the maximum ultimate strength has been achieved from the re-bars diameter 8 mm with the lower percentage of elongation which is 17%. It shows in Table 6. It is possible setting actual water pressure control valve also define diameter wise water pressure.

Rockwell hardness Test is performed for various diameter of TMT 500W & 400D re-bars. The Rockwell hardness test for hardened zone and softer zone has been performed separately. For hard Case Rockwell C scale is used and for soft core Rockwell B scale is used to measure hardness.

Table 8 shows the average Rockwell hardness values for both hardened (Case) and softer zones (Core) with the depth of the hardened zone and Carbon Equivalent (CE).
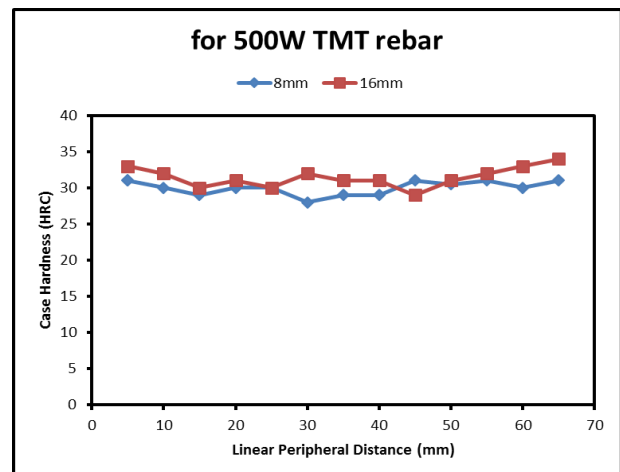
Figure 1. Rockwell hardness (HRC) of case along the periphery of 500W TMT steel re-bars.
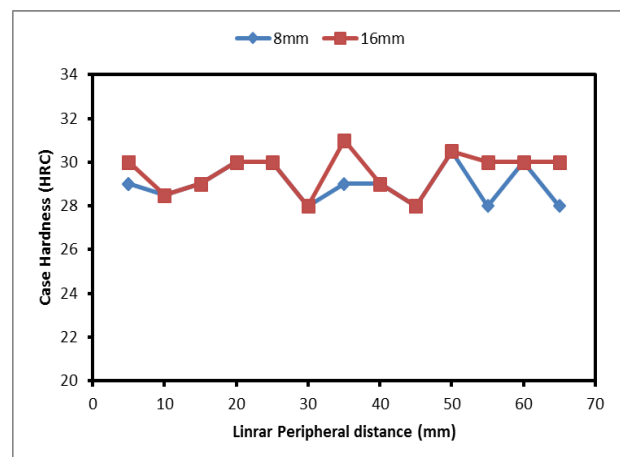
Figure 2. Rockwell hardness (HRC) of case along the periphery of 400D TMT steel re-bars

From the table 2.7 and figure 1, it is said that, higher carbon equivalent gives higher hardness for the 500W TMT 16 mm diameter re-bars has the highest carbon equivalent having higher case hardness of 32 HRC and core hardness of 90.8 HRB. From the table 2.8 and figure 2, it is said that, higher carbon equivalent gives higher hardness for the 400D TMT 16 mm diameter re-bars has the highest carbon equivalent having higher case hardness of 29.5 HRC and core hardness of 88.5 HRB.

3. CONCLUSION

The mechanical properties of 500W TMT and 400D TMT re-bars are varied differently. The yield strength and ultimate strength of 500W and 400D TMT re-bars with rib are slightly higher than that of without rebar. The case and core hardness 500W TMT is more as compared to 400D TMT. The properties of 500W TMT is more preferable in comparison of 400D TMT re-bar. The change of chemical composition, thin film coating process and nano-particles reinforcement can be suggested to enrich the properties of both of the steel re-bars. The improvement of the mechanical and shock absorbing properties can be considered for crtical construction system in relation to sustainability.

REFERENCES

[1] D.L. Doushanov: Control of Pollution in the Iron and Steel Industry, in: Encyclopedia of Life Support Systems (EOLSS), Vol. 8, pp.1-5.

[2] Report on *Available and Emerging Technologies for Reducing Greenhouse Gas Emissions from the Iron and Steel Industry*. by Office of Air and Radiation, United States Environmental Agency, September 2012.

[3] C. Kopczynski: High Strength Rebar Expanding Options in Concrete Towers, Structure Magazine, Vol.31, pp.1-2, 2008.

[4] G. Jha, A.K. Singh, N. Bandyopadhyay,O.N. Mohanty, Seismic Resistant Reinforcing Bars, Journal of Practical Failure Analysis, ASM International, Vol.5, pp.53-56, 2001.

[5] S. Fazal, J. Kwok, O. Salah: *Application of High-Strength and Corrosion-Resistant ASTM A1035 Steel Reinforcing Bar in Concrete of High-Rise Construction*, The Council on Tall Buildings & Urban Habitat's, 8th World Congress, Dubai, pp.1-6, 2008.

[6] M.S. Bari: *Use of 500 Grade Steel in the Design of Reinforced Concrete Slab*, BSRM Seminar, pp.1-19, 2008.

[7] M. Takashi, O. Kawano, T. Hayashida, R. Okamoto, H. Taniguchi: *High Strength Hotrolled Steel Sheet for Automobiles*, Nippon Steel Technical Report No. 88, pp.1-12 2003.

[8] D. Beynon, T.B. Jones, G. Fourlaris: Effect of High Strain Rate Deformation on Microstructure of Trip Steels Tested under Dynamic Tensile Conditions, Materials Science and Technology, Vol. 21, No.1, pp.103-112, 2005.

[9] Y. Tomota, H. Tokuda, Y. Adachi, M. Wakita, N. Minakawa, A. Moriai, Y. Morii: Tensile Behavior of TRIP-aided Multiphase Steel Studied by In-situ Neutron Diffraction, Acta Materialia, Vol. 52, No. 20, pp. 5737-5745, 2004.

[10] K. Hulka: The Role of Niobium in Cold Rolled TRIP steel, Materials Science Forum, Vol. 473-474, pp. 91-102, 2005.

[11] M.A. Islam: Thermomechanically Treated Advanced Steels for Structural Applications". *Proceedings of MARTEC 2010, the International Conference on Marine Technology*, 11-12 December, 2010.

[12] B.K. Panigrahi, S. Srikanth, G. Sahoo: Effect of Alloying Elements on Tensile Properties, Microstructure and Corrosion Resistance of Reinforcing Bar Steel, Journal of Materials Engineering and Performance, ASM International, Vol. 18, pp. 1102-1108, 2009.

[13] Manoharan, R., Jayabalan, P. and Palanisamy, K., "Experimental Study on Corrosion Resistance of TMT Bar in Concrete". ICCBT, pp.239-25, 2008.

[14] Prabir C. Basu, P. Shylamoni, A.D. Roshan: Characterisation of Steel Reinforcement for RC Structures: An Overview and Related Issues, The Indian Concrete Journal, pp.19-30, 2004.

[15] Technology, http://abulkhairsteel.com/technology.php; accessed on 2 June 2014.

[16] A. Golodnikov, Y. Macheret, A.A. Trindade, S. Uryasev, G. Zrazhevsky: Statistical Modelling of Composition and Processing Parameters for Alloy Development, Journal of Materials Science and Engineering, Vol.13, pp .633-644, 2005.

[17] M. Gaško, G. Rosenberg: Correlation between Hardness and Tensile Properties in Ultra-high Strength Dual phase Steels, Journal of Materials Engineering, Vol.18, pp. 155-159, 2011.

[18] E. George, J.R. Dieter: *Mechanical Metallurgy*, International student edition, McGraw-Hill, New York, pp. 282, 1961.

[19] *Metals handbook*, 8th ed., Vol. 11, Nondestructive inspection and quality control', Materials Park, OH, and American Society for Metals, pp. 425, 1976.

[20] M. Umemoto, Z.G. Liu, K. Tsuchiya, S. Sugimoto, M.M.A. Bepari: Relationship between hardness and tensile properties in various single structured steels, Journal of Material Science and Technology, Vol. 17, pp. 505-511, April 2001.

[21] S. Chenna Krishna, N.K. Gangwar, A.K. Jha, B. Pant: On the Prediction of Strength from Hardness for Copper Alloys, Journal of Materials, Vol. 2013, pp. 1-6, 2013.

[22] O. Takakuwa, Y. Kawaragi, H. Soyama: Estimation of the Yield Stress of Stainless Steel from the Vickers Hardness Taking Account of the Residual Stress, Journal of Surface Engineered Materials and Advanced Technology, Vol. 3, pp. 262-268, 2013.

[23] J. Moteff, R.K. Bhargava, W.L. McCullough: Correlation of the Hot- Hardness with the Tensile Strength of 304 Stainless Steel to Temperatures of 1200 C" Metallurgical and Materials Transaction A, Vol. 6A, pp. 1101–1104, 1975.

[24] M.O. Lai, K.B. Lim, On the prediction of tensile properties from hardness tests, Journal of Materials Science, Vol. 26, No. 8, pp. 2031–2036, 1991.

[25] M.A. Noor, A.U. Ahmed: Study on Grade 75 and 60 Reinforcement in RC Design, BSRM Seminar, pp.1-12, 2008.

[26] Workshop "Structural Steels for Civil Engineering Applications", held at Bangladesh university of Engineering and Technology, Dhaka, Bangladesh, 21 June, 2013.

[27] I.R. Kabir, M.A. Islam: Hardened Case Properties and Tensile Behaviours of TMT Steel Bars, American Journal of Mechanical Engineering, Vol. 2, No. 1, pp. 8-14, 2014.

[28] E.P. Degarmo, J.T. Black, R.A. Kohser: *Materials and Processes in Manufacturing*, 9th ed., Wiley, pp. 388, 2003.

[29] M. Mukherjee, C. Datta, A. Halder: Prediction of Hardness of the Tempered Martensite Rim of TMT Rebars, Journal of Materials Science and Engineering: A, Vol.543, pp.36-43, 2012.

[30] R. Datta, R. Veeraraghavan, K.L. Rohira: Weldability Characteristics of Torr and Corrosion-Resistant TMT Bars Using SMAW Process, Journal of Materials Engineering and Performance, ASM International, vol.11, pp.369-375, 2002.

PREDICTION OF TRIBOLOGICAL BEHAVIOR OF ALUMINIUM MATRIX HYBRID COMPOSITES USING ARTIFICIAL NEURAL NETWORKS

Slavica MILADINOVIĆ[1,*], Vesna RANKOVIĆ[1], Miroslav BABIĆ[1], Blaža STOJANOVIĆ[1], Sandra VELIČKOVIĆ [1]

[1]University of Kragujevac, Faculty of Engineering, Kragujevac, Serbia
*Corresponding author: slavicam@kg.ac.rs

Abstract: *Prediction of tribological characteristics of hybrid composites with A356 matrix using artificial neural networks (ANN) was performed in this paper. During experiment next parameters were varied: sliding speed, load, sliding distance and wt.% of reinforcement. The obtained experimental results were used to form the artificial neural network in which were varied number of neurons in the hidden layer, number of layers, the activation function and the function of training. Training of the neural network was performed for the wear rate, and optimal regression coefficient was equal to 0.994, for the network 4-15-10-1. Using neural networks to predict the wear rate greatly reduces the time and cost of experiment.*

Keywords: *prediction, wear rate, artificial neural network, coefficient of friction.*

1. INTRODUCTION

The increasing demands of today's industry that seeks to reduce the price and weight of the construction, as well as, to increase their working life, have contributed to the development of new materials. Under the concept of new materials, in this case, it refers to the composite materials obtained by combining two or more materials. One constituent of the composite represents its basis, while other constituent or more of them make reinforcements. The application of composite materials has increased in relation to the materials that constitute its basis for the purpose of improved characteristics [1-4].

In the engineering industry, the most attention is given to composites with a metal base. Aluminium, magnesium, iron, cobalt and others are mainly used as the basis for these composites, while the ceramics are most commonly used as the reinforcements, such as, for example, silicon carbide.

Many researchers have studied the production of the composites in terms of variations in parameters during the process of obtaining and the combination of contents, types and size of the reinforcing particles. For the processing of the experimental data often are used Taguchi method, factor design, Taguchi Grey relation analysis, and in recent years the use of artificial neural networks is increased [5-10].

The artificial neural network is a non-linear statistical technique that is used for data processing when it is very difficult or impossible to apply a statistical method [11-16].

Babić and Mitrović studied the effect of adding the reinforcement Al_2O_3 in the base alloy ZA-27. The tests were performed on the

tribometer with block on disc contact geometry in conditions without lubrication. The study plan was implemented with the variation of the wt.% of reinforcement, as follows: 3%, 5% and 10%; normal load of 10 mN, 50 mN, 100 mN and 120 mN; and the sliding speed: 10 mm/s, 20 mm/s and 30 mm/s. They concluded that that the composites with the addition of Al_2O_3 have a much lower coefficient of friction than the base alloy ZA-27 in all test conditions. The composite with the highest wt.% of Al_2O_3 particles (10%) has the best friction characteristics [17].

Basavarajappa et al. studied the tribological wear behaviour of Al2219/SiCp-Gr composites in conditions without lubrication. The tests were performed on the tribometer with pin on disc contact geometry, for sliding speeds up to 6 m/s and for the normal forces up to 60 N. According to the obtained results, it was concluded that the wear resistance of composites was increased with addition Gr and SiCp [18].

Stojanović performed the investigation of wear of the composite with A356 base and silicon carbide and graphite reinforcements, sliding speed, sliding distance, normal load and the percentage of reinforcement's content varied during the testing. The tested materials were: A356 base material, as well as composite materials with 10 wt.% SiC and 1, 3 and 5 wt.% Gr. The composite material with 10 wt.% SiC, and 1 wt.% Gr had the lowest wear rate at all test conditions [2].

Saravanan et al. performed the prediction of the wear rate and the friction coefficient of composites with aluminium base and Rice Husk Ash (RHA) reinforcement by applying artificial neural network [19]. To form the network, they used the following parameters: the normal load, sliding speed, particle size of RHA reinforcement and the wt.% of RHA reinforcement. After training, they obtained the value of the regression coefficient of 0.99. Based on the conducted analysis, they concluded that the trained neural network can be used for predicting the wear rate and the friction coefficient with up to 95% accuracy [19].

Rashed et al. used a neural network to predict the of wear rate of A356/SiC composites. They used normal load, test temperature, SiC particle size and their wt.% in the composite as the input. The neural network has proven to be a very effective tool for predicting the tribological behaviour of composites [20].

Maheswaran et al. studied the wear of hybrid composite Al6061-Al_2O_3-Gr, where the sliding speed, sliding distance, normal load and the percentage of the reinforcement varied. By comparing the experimental results and the one obtained by training the neural network, they showed that the neural network was a useful tool for predicting the wear of a hybrid composite in comparison to other experimental research [21]. Likewise, Varol et al. concluded that the neural network was a very powerful tool for predicting the physical and mechanical properties of composites based on the comparison of experimental results and the results obtained by training the neural network. They studied the characteristics of the composite Al2024–B_4C, for different size and wt.% of the reinforcement which formed the input of the neural networks, while density, hardness and tensile strength were used as the output. After training the network, the regression coefficient was 0.99 [22].

Altinkok et al. predicted the mechanical characteristics of Al_2O_3/SiC composites by using artificial network. They used the neural network with back propagation for predicting density and tensile strength, and the results of the regression coefficient had a satisfactory accuracy [23]. Hayajneh et al. studied the addition of copper as an alloying element and as the reinforcement on tribological behaviour of Al–4Mg composite with the help of neural networks [24]. Different alloys Al-Cu were subjected to examination in the temperature conditions without lubrication for the normal load of 40 N. They came to the conclusion that the addition of SiC has a good effect on increase of the wear resistance of composites. The neural network was formed with the help of obtained results, and its total error value was 2.40 %, which was satisfactory and this

neural network can be effectively used to predict tribological behaviour of the composite Al-4Mg [24].

Durmus et al. used a neural network to predict the wear loss and surface roughness with the aluminium alloy AA 6351. They compared the results obtained by experimental tests with the results obtained by using neural networks, and they noticed there was a coincidence to a large extent [25]. Vettivel et al. concluded that, for prediction of the tribological behaviour of sintered Cu-W composites, the neural network was better for prediction than polynomial regression based on the percentage error [26]. As the parameters of the neural network, they used wt.% of tungsten, sintering temperature, load and sliding distance in order to predict the characteristics such as the hardness, specific wear rate and coefficient of friction. They obtained very good coincidence of the experimental results and the results obtained with the help of neural networks [26].

Based on the paper overviews, it can be concluded that the artificial neural network is used to predict the behaviour of tribological, frictional and mechanical characteristics of composites. In this paper, there is the prediction of the tribological characteristics of hybrid composites by using the artificial neural network based on the obtained experimental results.

2. EXPERIMENTAL TESTING

The material obtained from compo-casting method was tested in this paper. This procedure has often been used in obtaining composites and hybrid composites with aluminium base [2, 3, 27].

Tribological characteristics of hybrid composites with aluminium base in conditions without lubrication were performed in the Tribology Center of the Faculty of Engineering in Kragujevac. The test was performed on the computer supported tribometer TR-95 with a block-on-disc contact geometry for the following parameter values: a normal load of 10 N, 20 N and 30 N; sliding speed of 0.25 m/s, 0.5 m/s and 1 m/s; and sliding distance of

30 m, 60 m, 90 m, 150 m, 300 m, 600 m and 900 m.

2.1 Test results

Tribological behaviour of hybrid composite with A356 matrix was followed through several phases. The tests were performed in conditions without lubrication on samples with the best structural, mechanical and anti-corrosion characteristics. The wear rate was measured during the testing.

The wear rate, as one of the major parameters for wear monitoring, was obtained based on the volume of the worn material, and as a function of sliding distance. Values of wear rate depending on the sliding speed, normal load and sliding distance for tested materials are given in Table 1. Due to the extensiveness of the obtained results, a partial number of experimental values of wear rate is shown in the Table 1.

First, the testing of base material - aluminium alloy A356, was performed, and then 10 wt.% SiC was added in the base. The wear rate decreased by adding silicon carbide to the base material of the composite. A graphite was added to the previous composite in order to obtain a hybrid composite. The wear rate of the composite significantly reduced by adding only 1 wt.% Gr. With the increase of graphite to 3 wt.%, the wear rate increased in certain intervals, while in others it decreased. When the percentage of graphite increased to 5 wt.%, the wear rate increased.

2.2 Artificial neural networks

A neural network is a form of implementation of artificial intelligence system, which represents a system consisting of a number of interconnected nodes, which are called artificial neurons. The body of neurons is called node or unit, and each neuron has a local memory which memorizes the information that are processed. The data that are exchanged in this way are usually numerical [28].

Table 1. Experimental results of wear rate

Material	Sliding speed, m/s	Normal load, N	Sliding distance, m	Wear rate, $mm^3 x10^3/m$
A356	0.25	10	30	0.389
			60	0.358
			90	0.324
			150	0.306
			300	0.361
			600	0.577
			900	0.901
A356/10SiC	0.25	10	30	0.037
			60	0.095
			90	0.13
			150	0.115
			300	0.12
			600	0.367
			900	0.776
. . .	. . .	. . .	. . .	. . .
A356/10SiC/1Gr	0.5	20	30	1.243
			60	1.434
			90	1.422
			150	1.307
			300	1.07
			600	0.909
			900	1.509
. . .	. . .	. . .	. . .	. . .
A356/10SiC/3Gr	1	30	30	3.735
			60	4.447
			90	4.274
			150	3.662
			300	2.96
			600	2.952
			900	3.477
A356/10SiC/5Gr	1	30	30	4.622
			60	5.134
			90	4.757
			150	4.299
			300	3.702
			600	3.57
			900	3.877

Artificial neural networks are simplified mathematical models of human brain function and they represent a new generation of information processing systems [29]. These mathematical models simulate some of the properties of biological nervous systems in order to solve different problems, where classical methods do not give satisfactory results. In biological systems, the learning is done through regulation of synaptic connections that connect the axons and dendrites of neurons. The learning of typical

events through examples is achieved through training or discoveries to the accurate sets of data inputs - outputs which train the algorithm by repeating and adjusting the weight coefficients of connections (synapses) [25]. It is necessary to collect as many data as possible for network to behave precisely in later use.

Neural networks are not programmed, they are trained, which means that it takes a long time for their training before they start to be used. The training of neural networks is done in a way that the weight coefficients are updated in order to get the output closer to the given value next time. During the training, the user assign the input and desired output values, and the programme attempts to obtain the corresponding output value [11, 28].

Matlab software [30] (Matlab R2016) was used for the neural network prediction of wear rate of tested materials.

The parameters of tribological tests are used as the input data: material, sliding speed, load and sliding distance (Table 1), while the obtained wear rate is used as the output. When training the network, there was a variation of the following: number of neurons in the hidden layer (for two hidden layers 15-10, 10-15, 8-10, 7-8, and for one hidden layer 20, 15, 10, 8, 6, 5, 4) and the activation function (log sigmoid transfer function - LOGSIG, hyperbolic tangent sigmoid transfer function - TANSIG). The output network function is linear transfer function (PURELIN), while the training function is Levenberg-Marquardt (TRAINLM). Table 2 presents the total regression coefficients (ALL) for different numbers of neurons and activation function.

It is necessary for the total regression coefficient to be greater than or equal to 0.95 in order for neural network to be acceptable. All obtained regression coefficient are acceptable, except for the coefficient obtained for LOGSIG activation function and 4 neurons in the hidden layer. The neural network with two hidden layers, 15 and 10 neurons in the hidden layers and the LOGSIG activation function has proven to be the best for predicting the wear rate.

Table 2. Variated network parameters

No. of hidden layers	No. of neurons in hidden layers	Wear rate for activation fuction:	
		LOGSIG	TANSIG
1	4	0.93647	0.9795
1	6	0.98282	0.98514
1	8	0.98236	0.98334
1	10	0.98552	0.98533
1	15	0.98959	0.99376
1	20	0.99283	0.99312
2	7-8	0.99185	0.99381
2	8-10	0.99389	0.98917
2	10-15	0.99114	0.99004
2	15-10	0.99401	0.98794

The regression coefficient obtained by training this network is shown in Figure 1.
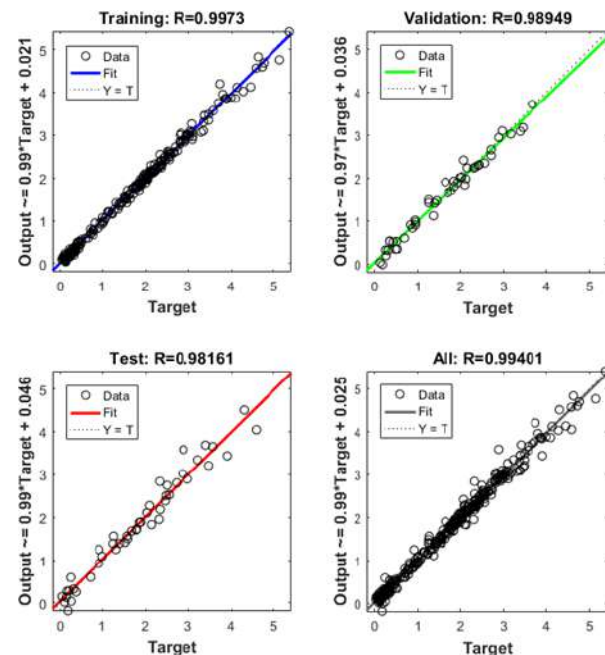
Figure 1. Regression coefficient for predicting wear rate

By training the artificial neural network, the obtained regression coefficient is 0.994, which indicates a very good coincidence with the experimental results.

In addition to the regression coefficient, a diagram of validation performance is obtained, which is shown in Figure 2.
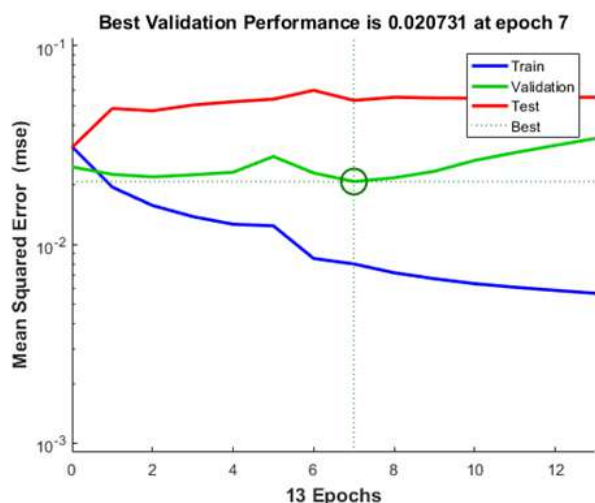
Figure 2. Validation performance

Figure 2 shows that the best validation performance is for iteration 7 and it is 0.020731; the training continued for 6 more iterations before the training stopped.

The errors representing the difference between targets and outputs are obtained after training the neural network, and they are given in Figure 3.
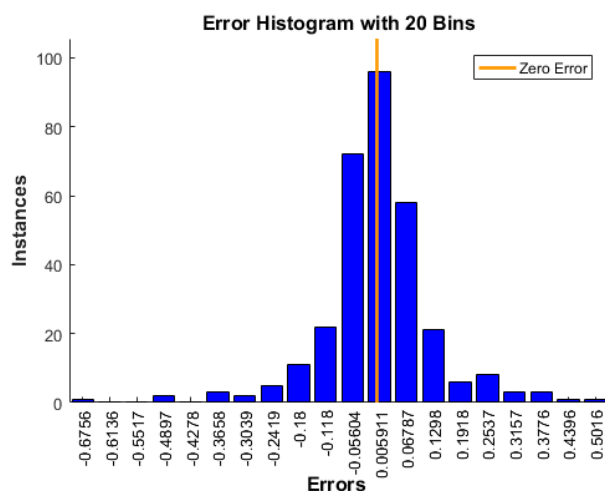
Figure 3. Error histogram

Figure 3 shows that there is a slightest deviation between the predicted and experimental values and it is 0.006911.

3. CONCLUSION

Based on the performed experimental tribological tests, it can be concluded that the wear rate decreases by adding reinforcement such as silicon-carbide to the aluminium alloy. However, poor mechanical properties can cause excessive content of SiC in the aluminium alloy. In order to improve these characteristics, the graphite, which considerably affects the decrease of wear rate, is added to a previous composite.

Based on the performed tribological tests, it can be concluded that a hybrid composite material with 10 wt.% SiC and 1 wt.% of graphite, i.e. A356/10SiC/1Gr, has the best tribological characteristics, or the least wear rate, in all test conditions compared to other tested composites.

An artificial neural network was used in order to reduce the number of experiments, and the predictions of the tribological behaviour of hybrid composites. The neural network was modelled in the Matlab software in the paper.

According to the obtained results for the regression coefficient, the neural network with two hidden layers, TRAINLM training function and LOGSIG activation function was adopted. The regression coefficient for this network was 0.994.

Satisfactory values of wear rate were obtained in comparison to the experimentally obtained values. The regression coefficient obtained by training the neural network is quite high, so therefore the neural network can be used for predicting tribological parameters of hybrid composites.

The obtained regression coefficient for predicting the tribological characteristics is similar to those that can be found in the available literature [17-24].

The results obtained by training the neural network for the wear rate show good coincidence with experimental results.

ACKNOWLEDGEMENT

REFERENCES

[1] F. L. Xavier, P. Suresh: Studies on dry sliding wear behaviour of aluminium metal matrix composite prepared from discarded waste particles, International Journal of Advanced Engineering Technology, Vol. 7, No. 1, pp. 539-543, 2016.

[2] B. Stojanović: *Tribological behaviour of hybrid composites with A356 matrix*, PhD thesis, Faculty of Engineering, University of Kragujevac, Kragujevac, 2013.

[3] N. Miloradović: *Tribological characterization of hybrid composites based on ZA27 alloy*, PhD thesis, Faculty of Engineering, University of Kragujevac, Kragujevac, 2013.

[4] P. Sharma, D. Khanduja, S. Sharma: Dry sliding wear investigation of Al6082/Gr metal matrix composites by response surface methodology, Journal of Materials Research and Technology, Vol. 5, No. 1, pp. 29-36, 2016.

[5] S. Veličković, B. Stojanović, M. Babić, I. Bobić: Optimization of tribological properties of aluminum hybrid composites using Taguchi design, Journal of Composite Materials, DOI: 10.1177/0021998316672294, 2016.

[6] B. Stojanovic, M. Babic, S. Veličković, J. Blagojević: Tribological behavior of aluminum hybrid composites studied by application of factorial techniques, Tribology Transactions, Vol. 59, No. 3, pp. 522-529, 2016.

[7] S. Dharmalingam, R. Subramanian, K. Somasundara Vinoth, B. Anandavel: Optimization of tribological properties in aluminum hybrid metal matrix composites using Gray-Taguchi method, Journal of Materials Engineering and Performance, Vol. 20, No. 8, pp. 1457–1466, 2011.

[8] A. K. Rout, A. Satapathy: Study on mechanical and tribo-performance of rice-husk filled glass–epoxy hybrid composites, Materials & Design, Vol. 41, pp. 131-141, 2012.

[9] S. Miladinović, S. Veličković, M. Novaković: Application of Taguchi method for the selection of optimal parameters of planetary driving gear, Applied Engineering Letters, Vol. 1, No. 4, pp. 98-104, 2016.

[10] S. Miladinović, S. Veličković: Optimization an prediction of safety coefficient for surface durability of planetary gearbox Taguhci design and artificial neural network, *Proceedings of the Conference on Mechanical Engineering Technologies and Application,* 07-09.12.2016., Jahorina, Republika Srpska, BiH, pp. 139-146.

[11] V. Ranković: *Intelligent control*, Faculty of Mechanical Engineering, Kragujevac, ISBN 978-86-86663

[12] M. Vincek: *Model Reference Adaptive Control Based on Neural Networks,* Thesis No. 1533, Faculty of Electrical Engineering and Computing, University of Zagreb, Zagreb, 2006.

[13] D. Milčić, B. Anđelković, M. Mijailović: *Decisions making in design process–examples of artificial intelligence application*, Machine Design-Monograph, University of Novi Sad, Faculty of Technical Sciences, ADEKO–Association For Design, Elements And Constructions, pp. 13-20, 2007.

[14] O. Stojanović: Electroencephalography: method and instrumentation, Thesis, Faculty of Sciences- Department of physics, University of Novi Sad, Novi Sad, 2013.

[15] M. Petrović, Basis of ANN and the importance of their application, *Journal of Faculty of Civil Engineering, Subotica*, No. 20, pp. 47-55. 2011.

[16] V. Ilić: Neuronske mreže, available at:, http://solair.eunet.rs/~ilicv/neuro.html - accessed: 17.06.2016.

[17] M.Babić, S.Mitrović: Tribological characteristics of composites based on ZA alloy, Monograph, Faculty of Mechanical Engineering, University of Kragujevac, Kragujevac, 2007.

[18] S. Basavarajappa, G. Chandramohan, K. Mukund, M. Ashwin, M. Prabu: Dry Sliding Wear Behavior of Al 2219/SiCp-Gr Hybrid Metal Matrix Composites, Journal of Materials Engineering and Performance, Vol. 15, No. 6, pp. 668-674, 2006.

[19] S. D. Saravanan, M. Senthilkumar: Prediction of Tribological Behaviour of Rice Husk Ash Reinforced Aluminum Alloy Matrix Composites Using Artificial Neural Network, Russian Journal of Non Ferrous Metals, 2015, Vol. 56, No. 1, pp. 97–106, 2015.

[20] F.S.Rasheda, T.S.Mahmoud: Prediction of wear behaviour of A356/SiCp MMCs using neural networks, Tribology International, Vol. 42, No. 5, pp. 642–648, 2009

[21] P. Maheswaran, C.J.Thomas Renald: Investigation on Wear Behaviour of Al6061-Al2o3-Graphite Hybrid Metal Matrix Composites using Artificial Neural Network, International Journal of Current Engineering and Technology, Special issue 2, pp. 363-367, 2014.

[22] T. Varol, A. Canakci, S. Ozsahin: Artificial neural network modeling to effect of reinforcement properties on the physical and mechanical properties of Al2024–B4C composites produced by powder metallurgy, Composites: Part B engineering, Vol. 54 pp. 224–233, 2013.

[23] N. Altinkok, R. Koker: Modelling of the prediction of tensile and density properties in particle reinforced metal matrix composites by using neural networks, Materials & design, Vol. 27, No. 8, 625-631, 2006.

[24] M. Hayajneh, A. M. Hassan, A. Alrashdan, A. T. Mayyas: Prediction of tribological behavior of aluminum–copper based composite using artificial neural network, Journal of Alloys and Compounds, Vol. 470, No. 1, pp. 584-588, 2009.

[25] H.K. Durmus, E. Ozkaya, C. Meric: The use of neural networks for the prediction of wear loss and surface roughness of AA6351 aluminium alloy, Materials and Design, Vol. 27, No. 2, pp. 156–159, 2006.

[26] S.C. Vettivel, N. Selvakumar, N. Leema: Experimental and prediction of sintered Cu–W composite by using artificial neural networks, Materials and Design, Vol. 45, pp. 323–335, 2013.

[27] D. Džunić: *Friction and wear analisys o metal matrix nanocomposites,* PhD thesis, Faculty of Engineering, University of Kragujevac, Kragujevac, 2015.

[28] Obučavanje veštačih neuronskih mreža u C# programskom jeziku, available at: https://www.automatika.rs/projekti/svi-projekti/obucavanje-vestackih-neuronskih-mreza-u-c-programskom-jeziku.html, accessed: 21.06.2016.

[29] I. Živković, Neuronske mreže: http://docslide.us/documents/neuronske-mre-ze-neural-networks.html accessed: 06.03.2017.

[30] MATLAB® 7: Getting Started Guide, The MathWorks, Inc, 2008.

A STUDY ON EROSIVE WEAR BEHAVIOR OF E-GLASS FIBER REINFORCED PLASTIC

U.K. DEBNATH, M.A. CHOWDHURY, M.A. KOWSER, M.M. SHAHIN
DhakaUniversity of Engineering and Technology, Gazipur-1700, Bangladesh
*Corresponding author: asadzmn2003@yahoo.com

Abstract: *The present paper presented the solid particle erosion nature of E-glass fiber reinforced plastic. The solid particle erosion rates of E-glass fiber reinforced plastic have been experimentally appraised at different experimental operating condition. The E-glass fiber reinforced plastic showed semi-ductile erosion behavior. Taguchi's orthogonal arrays are applied to design of experiments and test the specimens on compressed air jet type erosion test arrangement. The experimental results of erosion rate are in significant agreement with the values from the theoretical model develop to determine the erosion rate. An optimal parameter combination is also determined, which leads to the minimization of erosion rate. An analysis of variance (ANOVA) is used in present experiment and to find out the measured data and S/N (signal to noise) ratios at different operating conditions. A scientific connection, steady with the trial perceptions is proposed as a predictive equation for estimation of erosion rate for E-glass fiber reinforced plastic.*

Keywords: Erosion, E-glass fiber, Taguchi design, ANOVA.

1. INTRODUCTION

Solid particle erosion is a dynamic process which is the dynamic loss of unique material from a solid surface due to mechanical interaction between that surface and solid particles. E-glass fiber reinforced polymer composites used worldwide. It has are extensively used in engineering applications because to their excellent mechanical and physical specific property. Composites are now used in helicopters, space air craft, satellites, ships, submarines, automobiles industry, sporting goods, civil construction, and high speed vehicles and aircraft operating in desert environments[1, 2]. Composites have risen as

imperative materials due to their light weight, high strength and stiffness, good fatigue resistance and remarkable erosion resistance contrasted with most basic metallic alloys, for example, steel and aluminum.

It has been accounted for in the literature that polymers and their related composites material are widely utilized as a part of erosive wear situations[3]. Numerous analysts have explored the solid particle erosion conduct of its composites. Polymers that have been contemplated incorporate polystyrene[4], polypropylene [5, 6], and polymeric composites [7-9]. Nonetheless, various analysts Barkoula and Karger-Kocsis [10], Tewari et al. [11]have assessed the resistance of different sorts of

polymers and their composites to solid particle erosion. It is broadly perceived that polymer and their composites have poor erosion resistance. Their erosion rates (Er) are extensively higher than metals. Likewise, it is notable that the erosion rate of polymer composites is much higher than that of slick polymers as detailed by Häger et al [11]. The solid particle erosion conduct of polymer composites as a component of fiber substance has been examined to a restricted degree by specialists like Miyazaki and Takeda [7]. Tilly and Sage [12] have explored the impact angle, impingement angle, erodent size and weight of affected abrasives on different composite and plastic.

In this manner, the goal of the present research work is to deliberately explore the erosive wear execution of E-glass fiber reinforced plastic with extraordinary reference to examine the ideal level of control components utilizing Taguchi plan. A hypothetical model for estimation of erosion wear rate under numerous effect conditions and connection of erosion rate with U. NO is produced.

2. EXPERIMENTAL DETAILS

2.1 Materials Properties and Preparation and Test rig

The deliberate mechanical properties of tested E-glass fiber reinforced plastic are recorded in Table 1. Rectangle sort examples with a size of 50mm-30 mm and 5 mm thickness in measurements were cut utilizing a precious stone cutter from infusion formed plaques. Before the erosive wear tests all examples were cleaned with acetone. Extraordinary care was given to guarantee clean surface previously, then after the fact wear tests. Sand and tidy particles were cleaned after erosion test with air blasting and after that balanced carefully.

Present study sand blast erosion test rig has been deplored. One mechanism is utilized of keeping up the separation between nozzle and target material and other system is utilized for fluctuating the angle of the test samples.

Table 1. Mechanical properties of E-glass fiber reinforced plastic.

Material	Physical and mechanical properties	
E-glass fiber reinforced plastic	Density (kg/m^3)	2500
	Tensile strength (MPa)	2000
	Tensile Modulus (GPa)	72.45
	Hardness (Hv)	32

The utilized technique for measuring impact velocity of the erodent particles is the double disc method

2.2 Signal-to noise (S/N) ratio

Design of experiment is an important powerful analysis tool for examining and deciphering controlled tests to assess the ideal variables. The most essential stage in the outline of test lies in the choice of the control elements (variable) and settled parameters. The Control variables are impact velocity (A), angle of impingement (B), erodent size (C) and standoff separation (D). Other hand settled parameters are Nozzle breadth 5mm, Erodent encourage rate 4.56 gm/sec, particle micro-hardness42-44Hv and erodent is dry silica sand and Irregular shape, Test temperature is surrounding temperature, Therefore, a large number of factors are included so that non-significant variables can be identified at earliest opportunity. In-depth literature survey on erosion behavior of E-glass fiber reinforced plastic material reveals that parameters viz., impact velocity, angle of impingement, erodent size and stand- off distance etc. The influences of four such parameters at four levels are contemplated utilizing L27 (4^3) orthogonal array plan.

The exploratory perceptions are changed into a signal-to noise (S/N) ratio. There are a few S/N proportions accessible relying upon the kind of qualities. The S/N proportion for least erosion rate going under littler is better characteristic. This can be figured as

logarithmic change of the misfortune work as demonstrated as follows.

Smaller is the better characteristic:

$$\frac{S}{N} = -\log \frac{1}{n}\left(\sum y^2\right) \qquad (1)$$

where 'n', the number of observations, and y, the observed data. "Lower is better" characteristic, with the above S/N ratio change, is appropriate for minimizations of erosion rate.

3. RESULTS AND DISCUSSION

3.1 Influence of impact velocity

The steady-state erosion rate (E) can be communicated as a simple power function of particle impact velocity (v), it can be expressed as follows:

$$E = kv^n \qquad (2)$$

where n the velocity exponent, the constant of proportionality (k),incorporates the effects of all of the various factors. The influence of impact velocity on erosion rate of polymer composites has been researched to a constrained degree. The velocity exponent (n) is typically range between 2 and 3 for polymeric materials behaving in ductile nature and between 3 and 5 for polymer composites behaving in brittle nature[13]. Fig. 1shows the steady-state erosion rate dependence of E-glass fiber reinforced plastic for different impact velocities at an impingement angle of 90˚. The least-squares fit to the data points have been obtained by using the power law.

Using the tested data, the determine velocity exponents are taken in the range of 4.19–4.3 for E-glass fiber reinforced plastic at 50 m/sec impingement velocity. This implies that the finding of velocity exponents are nearer to the exponents range mentioned by the distinctive scientists for similarity of ductile nature of E-glass fiber reinforced plastic. E-glass fiber reinforced show semi-ductile nature and the velocity exponents are in congruity with Pool et al. [13].
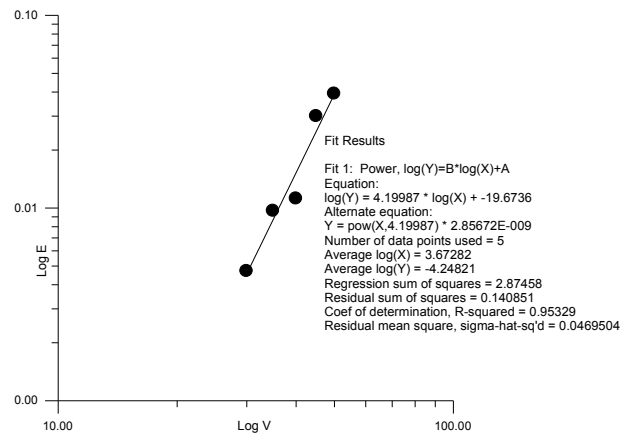
Figure 1. Curve fitting using Power law Equation for Experimental Data between Erosion rate and Impact Velocity [Test sample: E-Glass Fiber Reinforced Plastic, Impact angle 60 Degree]

3.2 Dimensional Analysis

Let:

$$E_R = F(V, f, P, D) \qquad (3)$$

Where, E_R-Erosion rate= MT^{-1}, V-Impact velocity= LT^{-1}, f- Sand flow rate= MT^{-1}, P-Particle size=L, D-Distance between nozzle and target material=L

$$E_R = kf[D/P]^d$$
$$\text{or, } E_R = K[D/P]^d \qquad (4)$$

Where, "d" and "K" are arbitrary constants. The dimensional deposition parameter D/P is hereby called "Uttam Number" and abbreviated as U. No.

Figure 16, shows the plot of erosion rate (E_R) versus U. No. for glass fiber reinforced plastic under impact velocity 50 m/sec and impact angle 30^0.The curves of the figures show that erosion rate decreases linearly with the increase of U. No. and is represented by the following equations:

E_R= 0.050-[0.48 (U. No.)] For E-glass fiber reinforced plastic

In Fig. 2square scatter points show the experimental results of erosion rate with U. No. Using these experimental values, linear regression and correlation are found using ORIGIN Software. Continuous lines showed in the figure indicate the regression lines. The

coefficient of correlation (r) is calculated to obtain -0.89743 for E-glass fiber reinforced plastic. As a subjective measure of relationship between experimental data with trend line, the mentioned coefficient of correlation signifies that there are strong negative relationships between erosion rate and UttamNumber. Therefore, it may be concluded that the experimental results are in good agreement with the theoretical calculations.

3.3 Steady state erosion E-glass fiber reinforced plastic

The overall mean for the S/N proportion of the erosion rate is determined to be – 67.1161 dB. Fig. 3 indicates graphically the impact of the four controls considers on erosion rate. The investigation is made utilizing the famous software particularly utilized for design of experiment applications known as MINITAB 15. Prior to any endeavor is made to use this simple model as a predictor for the measures of performance, the conceivable collaborations between the control factors must be considered.

Along this factorial design incorporates a simple means of testing for the presence of the interaction effects. Examination of the outcome leads to the conclusion that factor combination of A1, B3, C1 and D3 gives minimum erosion rate. The interaction diagrams are appeared in Fig. 4 (a-c). With respect to as minimization of erosion rate is concerned, factors A, B, C and D have huge significant effect. It is seen from Fig. 4 (b) that the interaction between A✕C shows most noticeable effect on erosion rate all tested conditions. But the factors A and B individually have greater dominating factor on output performance, and their combination of interaction with factor A and B is appeared in Fig. 4 (a) have less effect on erosion rate and the factors B and C individually have greater contribution on output performance, and their combination of interaction with factor B and C is shown in Fig. 4(c) have less effect on erosion rate and then can be neglected for further

study. Figure 4(d) shows the interaction plot between impingement angle and Impact velocity. The increase in impact velocity from 30 to 50 m/s, the erosion rate increased from 30 degree to 60 degree with maximum value between 60 degrees then started decreasing from 60 degree to 90 deg. From Fig. 4(e) it can be reasoned that with the increase in erodent size to the erosion rate increased from 30 degree to 60 degree with maximum value between 45 degree and 60 degree impingement angles. Figs. 4(d-f) demonstrate the counter plot of erosion rate with various combinations of experimental conditions. These counter plots approve the patterns of the experimental results.
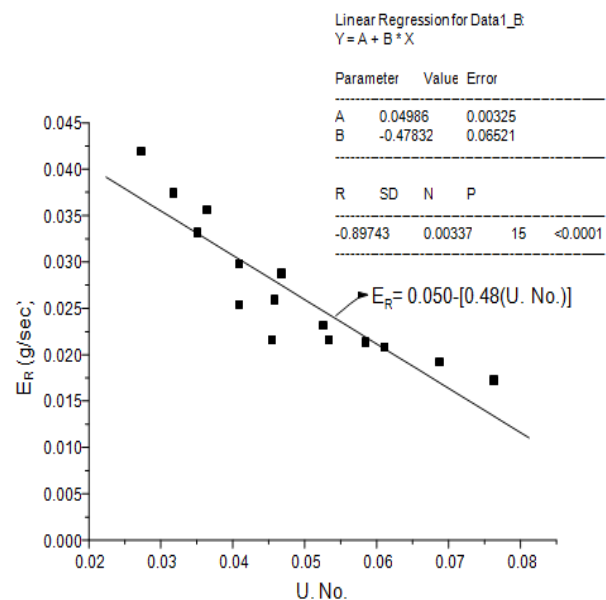
Figure 2. Erosion rate as function of U.No. for E-glass fiber reinforced plastic.
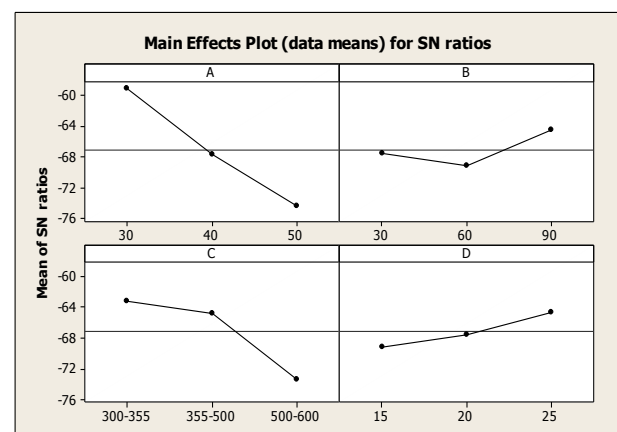
Figure 3. Effect of control factors on erosion rate of E-glass fiber reinforced plastic
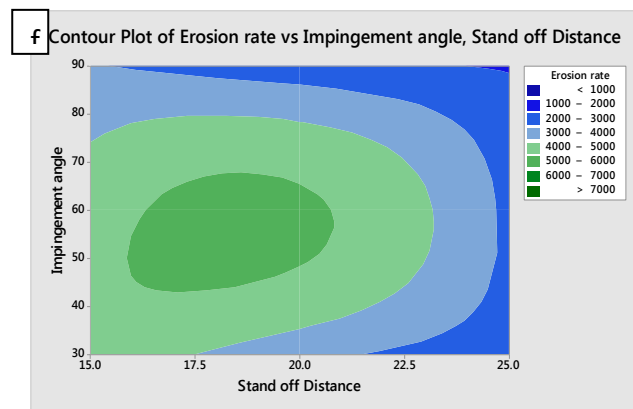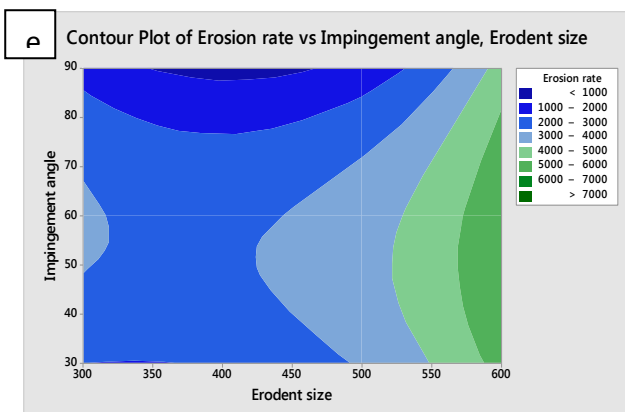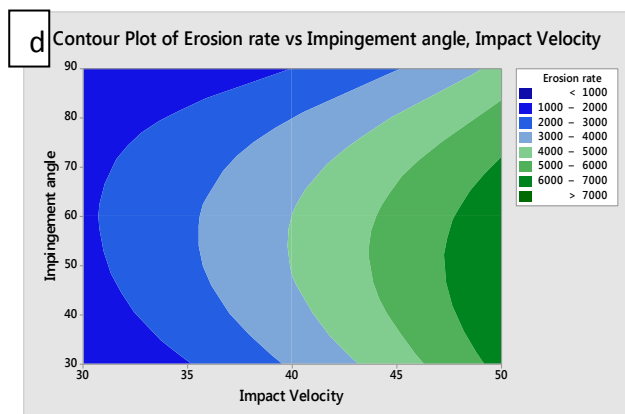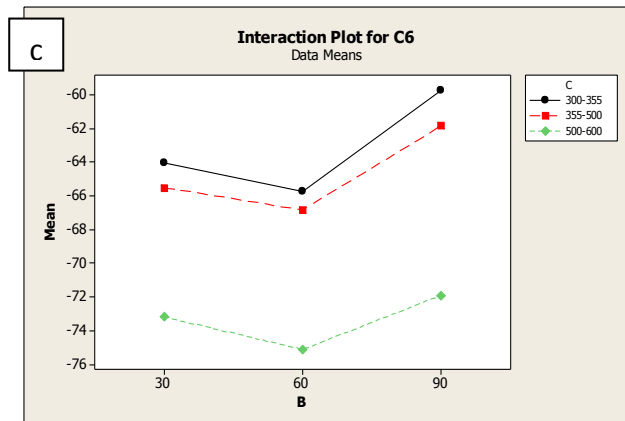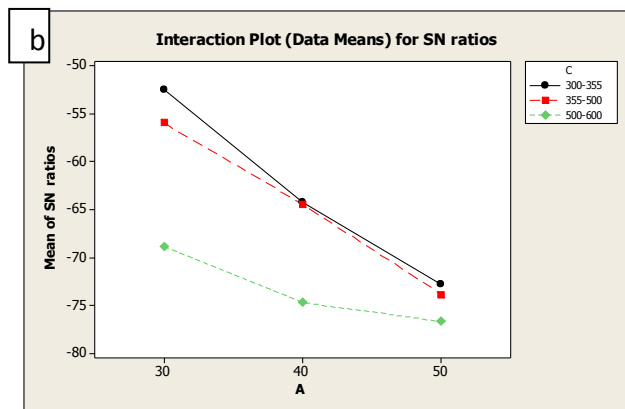
Figure 4. Interaction graph between(a) A✕ B, (b)A ✕ C, (c) B ✕ C, for erosion rate of of E-glass fiber reinforced plastic and contour plot for(e) steady-state erosion rate vs impact velocity,(d) Impingement angle and(f) Stand -off distance

3.4 ANOVA and the effects of E-glass fiber reinforced plastic

With a specific end goal to understand a concrete visualization of impact of different factors, it is attractive to create investigation of variance (ANOVA) table to discover out the order of significant factors. Table 2demonstrates the results of the ANOVA with the erosion rate. This investigation was attempted for a level of confidence of noteworthiness of 5 %. The last column of the table indicates that the main effects are exceptionally noteworthy (all have very little p-values). From Table 2, we can watch that the velocity of impact (p = 0.000), angle of impingement (p = 0.004), erodent size (p = 0.000) and, stand-off distance (p = 0.005) have extraordinary impact on erosion rate. The interaction between velocity of impact ✳ erodent size (p = 0.007) show significance of contribution on the erosion rate and the factor velocity of impact ✳ angle of impingement (p = 0.760), angle of impingement ✳ erodent size(P = 0.628) present less significance of contribution on erosion rate.

Table 2. ANOVA table for erosion rate of E-glass fiber reinforced plastic.

Source	DF	Seq SS	Adj SS	Adj MS	F	P	%
A	2	1064.420	1064.420	532.210	160.59	0.000	53.58
B	2	103.611	103.611	51.806	15.63	0.004	5.23
C	2	546.631	546.631	273.316	82.47	0.000	27.52
D	2	98.950	98.950	49.475	14.93	0.005	4.98
A*B	4	6.127	6.127	1.543	0.47	0.760	0.30
A*C	4	137.876	137.876	34.469	10.40	0.007	6.94
B*C	4	9.070	9.070	2.268	0.68	0.628	0.46
Error	6	19.884	19.884	3.314			1.00
Total	26	1986.615					100

3.5 Confirmation experiment of E-glass fiber reinforced plastic

The last stride of the Taguchi method is the affirmation tests conducted for examining the quality attributes. The affirmation test is performed is performed by taking a discretionary arrangement of factor level combination and compare with experimental results. The assessed S/N ratio for erosion rates can be ascertained with the help of following predictive equations:

$$\overline{\eta}_1 = \overline{T} + (\overline{A}_2 - \overline{T}) + (\overline{B}_2 - \overline{T}) + (\overline{C}_1 - \overline{T}) + (\overline{D}_2 - \overline{T}) + [(\overline{A}_2 \overline{C}_1 - \overline{T}) - (\overline{A}_2 - \overline{T}) - (\overline{C}_1 - \overline{T})] \quad \dots(5)$$ (5)

Where $\overline{\eta}_1$ is the predicted average; $\overline{T}$ is overall experimental average; $\overline{A}_2$, $\overline{B}_2$, $\overline{C}_1$ and $\overline{D}_2$ is the mean response for factors at designated levels.

By combining like-terms, the equation reduces to

$$\overline{\eta}_1 = \overline{A}_2 \overline{C}_1 + \overline{B}_2 + \overline{D}_2 - 2\overline{T}$$ (6)

A new combination of factor levels A2, B2, C1 and D2 is utilized to predict deposition rate through prediction equation and it is found to be. $\overline{\eta}_1$ = - 66.860 For every performance measure, an experiment was conducted for a different factors combination and the outcome with the result obtained from the predictive equation as shown in Table 3

Table 3. Results of the confirmation experiments for erosion rate

Optimal control parameters	Prediction	Experimental
Level	A2, B2, C1. D2	A2, B2, C1. D2
S/N ratio for erosion rate (dB)	-66.860	-66.332

The subsequent model is by all accounts equipped of predicting erosion rate to a sensible precision. An error of 0.789 % for the S/N ratio of erosion rate is watched. Nonetheless, the error can be further reduced if the number of measurements is increased. This approves the advancement of the scientific model for anticipating the measures of execution in light of information of the info parameters.

4. CONCLUSIONS

The solid particle erosion studies of E-glass fiber reinforced plastic, following conclusions are drawn:
1. The E-glass fiber reinforced plastic demonstrated maximum erosion at 60° impingement angle indicating semi-ductile nature.
2. In E-glass fiber reinforced plastic the steady-state erosion rate (E) is related to impact velocity (v) as $E = kv^n$. The exponent 'n' is closer to the standard rage for ductile materials.

3. Solid particle erosion characteristics of the E-glass fiber reinforced plastic can be effectively analyzed utilizing Taguchi experimental design scheme. Taguchi method provides a simple, systematic and efficient methodology for the optimization of the control variables.

4. The outcomes show that erodent size, impingement angle and impact velocity are the significant factors in a declining sequence affecting the erosion rate.

REFERENCES

[1] Hager, A. and M. Davies, Short-fibre reinforced, high temperature resistant polymers for a wide field of tribological applications, Advances in composite tribology, Vol 8, pp. 107-157, 1993.

[2] Bijwe, J. and M. Fahim, Tribology of high performance polymers-state of art, Handbook of Advanced Functional Molecules and Polymers, pp. 265-321, 2001.

[3] Barkoula, N.-M. and J. Karger-Kocsis, Review processes and influencing parameters of the solid particle erosion of polymers and their composites, Journal of materials science, Vol. 37, No. 18, pp. 3807-3820, 2002.

[4] Thai, C., K. Tsuda, and H. Hojo, Erosion behavior of polystyrene, Journal of Testing and Evaluation, Vol 9, No. 6, pp. 359-365, 1981.

[5] Walley, S., J. Field, and P. Yennadhiou, Single solid particle impact erosion damage on polypropylene, Wear, Vol. 100, No. 1-3, pp. 263-280, 1984.

[6] Friedrich, K., Erosive wear of polymer surfaces by steel ball blasting, Journal of materials science, Vol. 21, No. 9, pp. 3317-3332, 1986.

[7] Miyazaki, N. and N. Takeda, Solid particle erosion of fiber reinforced plastics, Journal of Composite Materials, Vol, 27, No. 1, pp. 21-31, 1993.

[8] Miyazaki, N. and T. Hamao, Solid particle erosion of thermoplastic resins reinforced by short fibers, Journal of Composite Materials, Vol. 28, No. 9, pp. 871-883, 1994.

[9] Harsha, A., U. Tewari, and B. Venkatraman, Solid particle erosion behaviour of various polyaryletherketone composites, Wear, Vol. 254, No. 7, pp. 693-712, 2003.

[10] Barkoula, N.-M. and J. Karger-Kocsis, Effects of fibre content and relative fibre-orientation on the solid particle erosion of GF/PP composites, Wear, Vol. 252, No. 1, pp. 80-87, 2002.

[11] Tewari, U., et al., Solid particle erosion of unidirectional carbon fibre reinforced polyetheretherketone composites, Wear, Vol. 252, No. 11, pp. 992-1000, 2002.

[12] Tilly, G. and W. Sage, The interaction of particle and material behaviour in erosion processes, Wear, Vol. 16, No. 6, pp. 447-465, 1970.

[13] Pool, K., C. Dharan, and I. Finnie, Erosive wear of composite materials, Wear, Vol. 107, No. 1, pp. 1-12, 1986.

SERBIATRIB '17

15th International Conference on Tribology

Serbian Tribology Society

Faculty of Engineering
University of Kragujevac

Kragujevac, Serbia, 17 – 19 May 2017

FRICTION COEFFICIENT OF REINFORCED EPOXY LAMINATES

Iulia GRAUR[1,2]*, Mara DIMOFTE[3], Cristian MUNTENIŢĂ[1], Radu BOSOANCĂ[1,2], Vasile BRIA[1], Marina BUNEA[1]

[1]"Dunărea de Jos" University of Galati, Research and Development Centre for Thermoset Matrix Composites, Galaţi, Romania
[2] Diagnose and Measurement Group, Galaţi, Romania
[3]International Computer High School of Bucharest, Romania
*Corresponding author: iulia.graur@ugal.ro

Abstract: *A very attractive direction of composite studies is the one of fabric reinforced composites with thermoset matrix. In other studies we observed that it is possible to control the elastic parameters of epoxy resins by modifying them with some organic solvents. The studied materials are formed with a graduated matrix and reinforced with different types of fabrics. In this paper we are presenting a tribological analysis of such type of materials to point out an eventual change in the friction coefficient of materials. The friction tests for all types of composite were carried out using pin-on-disc tribometer TRM 1000 (Wazau®, Germany) in the Polymer Composites Laboratory of Dunărea de Jos University of Galați.*

Keywords: *Friction coefficient, epoxy laminates, composite materials.*

1. INTRODUCTION

The composite materials are used in all domains, especially the fiber or fabric reinforced composites with polymeric matrices, due to their good mechanical properties, lightweight and low cost. Recent are studied the fabric reinforced thermoset matrix materials, which exhibit multifunctional properties in dependence of fiber, fabric, thermoset matrix properties and fiber-matrix interface quality. Beside of mechanical, electrical and thermal properties of fabric reinforced thermoset material, the tribological properties of those materials are very important. The properties of reinforced polymeric composites can be maneuvered by using of fillers or solvents in matrix structure. More researches showed that the modified

epoxy matrices with fillers exhibited better wear resistance, in dependence of particle dimensions, as it was found that the smaller size of particle improve the tribological properties [1, 2].

The tribological performance of fabric reinforced thermoset materials depends on fiber length, fiber volume fraction, fiber orientation [3], fiber type (carbon, glass, aramid,), fabric weave type (plain, twill, satin, unidirectional, etc.), fabric specific density, properties of used fillers or solvents and their volume fractions in matrix componence and thermoset matrix (epoxy, polyester, vinyl ester, polyimide, etc.) properties. Regarding the type of thermoset matrix, for example, the glass fiber epoxy materials showed a higher wear resistance than glass fiber polyester materials [4]. Many researchers study the tribological

behavior of fiber reinforced polymeric composites, in whose structure they are using like reinforcements the waste and natural fibers due to their bio degradability, low density, high specific strength, low cost [5-8]. But most often the tribo-materials are reinforced with carbon, graphite, glass and aramid fibers (shorts, longs, woven) [9]. The carbon fiber reinforcement reduces the friction coefficient, the wear volume lost, the wear track damage and the debris formation of the thermoset epoxy materials [10]. In ref. [11] was determined that the wear debris of carbon nanofibers had a lubricating effect and reduced significantly the wear rate of PEEK-CNF material.

The soft epoxy matrix reinforced with high strength carbon fibers offers a low wear resistance, which can be improved by using of hard coating [12]. Also, the tribological behavior of composites can be improved by surface treatment of carbon fibers, which makes stronger the interactions between fiber and matrix [13]. The wear rate varies in dependence of fiber orientation, so as in case of polymeric materials reinforced with 60 % carbon fibers the wear rate increases in order N (Normal) → AP (Antiparallel) → P (Parallel) indifferent of the normal load variation and sliding speed [14]. The fiber orientation at various angles influences insignificantly the tribological performance of GFRP [15], but the unidirectional glass fiber reinforced epoxy composites exhibit lower wear resistance than bi-directional reinforced composites [16]. Therefore, often, the fabric reinforcement is used, because it improves the abrasion resistance of polymers [17]. For improving the tribological properties of fabric reinforced epoxy composites, these composites can be made of multiple layers of different fabric types. So, it will be formed the hybrid materials which will combine the properties of all used fabrics like reinforcement, considering that wear resistance of carbon, glass and aramid fibers increases in order carbon → glass → aramid. In ref. [18], it was determined that the carbon/aramid mixed fabric reinforced epoxy composite showed a reduced

friction coefficient by 35 % in comparison with glass fabric reinforced epoxy composite.

For this research were studied the friction coefficient and wear values of hybrid reinforced composites with aramid, carbon/aramid and different carbon fabrics and modified epoxy matrix with 1-methil-2-pyrrolidone organic solvent.

2. MATERIALS

For study the tribological performance of thermosetting composites, it was formed four hybrid fabric reinforced epoxy laminates by wet lay-up method. These composites are similar regarding the reinforcement configuration, but the difference between them being the epoxy matrix types. So, as matrix were chosen four epoxy systems: EPIPHEN RE4020-DE4020, L-CL, HT2 and C. The laminates were reinforced with 15 layers of different types of simple plain fabrics, as it can be seen in table 1. The used plain fabrics were carbon fabrics with 160 g/m^2 specific density denoted C 160, carbon fabric 240 g/m^2 specific density denoted C 240, aramid fabric with 61 g/m^2 specific density denoted A 61, mixed carbon/aramid fabric with 68 g/m^2 specific density denoted C/A 68 and carbon TEXtreme with 60 g/m^2 specific density and 20 mm tape width denoted CT 60. The hybrid epoxy laminates had been denoted C, E, H and L. For improving the tribological properties of composites, the epoxy matrix was modified with 1-methil-2-pyrrolidone organic solvent, whose weight ratios had been increased with 5 % at each three layers.

Tribological characterization was performed using TRM 1000 tribometer (Wazau®, Germany) on tribological test module dedicated to pin-on-disc tests that allows setting and viewing of control and measured parameters: test rotational speed, loading force and friction coefficients. The pin is made of the composite material to be analyzed and is secured in the support of the machine, positioned perpendicularly and parallel to the disc.

The length was set at 1000 meters and speed test between 0.6 [m/s] and 1 [m/s]. Testing regimes have been established as follows:

R1: speed testing of 0.6 [m / s], load of 15N, distance 1000 meters.

R2: speed testing of 0.75 [m / s], load of 20N, distance of 1000 meters.

R3: speed testing of 0.6 [m / s], load of 25N, distance of 1000 meters.

Table 1. Structure of materials

Layers	Layers orientation	Fabric types	Weight ratios of solvent
01-03	0°	C 240	0 %
04-06	45°	C/A 68	5 %
07-09	0°	C 160	10 %
10-12	45°	A 61	15 %
13-15	0°	CT 60	20 %

So as, the epoxy matrix of composites exhibits various properties from bottom external layers modified with 0 % weight ratio of solvent till upper external layers modified with 20 % weight ratio of solvent, for each three layers.

According technical specifications of epoxy systems, the laminates were thermally cured after formation. Then were extracted the samples according to standard for determination of tribological properties by cutting on water jet machine.

3. RESULTS AND DISCUSSION

The friction coefficient was investigated by parallel and perpendicular modes, which are defined by the position of reinforcement layer relative to sliding speed. The perpendicular modes were performed on rigid surfaces and on elastic surfaces.

How it can be seen in figs. 1-3, the friction coefficient of investigated composites with H epoxy matrix by parallel mode and perpendicular mode on rigid surface exhibited higher values compared with other materials. While by perpendicular mode on elastic surface the composites with L epoxy matrix

exhibited the highest values of friction coefficient. This variation of friction coefficient values it is due to matrix and matrix-fiber interface properties.
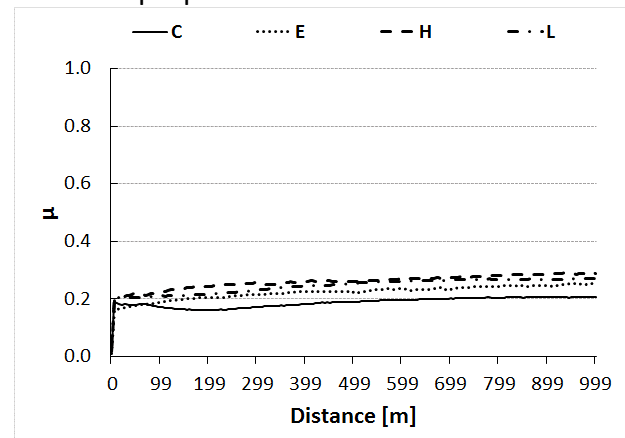
Figure 1. Friction coefficients of hybrid composites investigated by parallel mode and R1 testing regime

Figure 2. Friction coefficients of hybrid composites investigated by perpendicular mode on elastic surface and R1 testing regime

Figure 3. Friction coefficients of hybrid composites investigated by perpendicular mode on rigid surface and R1 testing regime

Table 2. Wear rate of hybrid composites investigated by parallel mode

Wear rate x 10^{-5} [g/N*m]			
Regime	Values		
	C	E	H	L
R1	1.26	1	0.66	0.66
R2	0.85	1.6	1.5	0.5
R3	1.08	0.8	1.2	0.4

Analyzing the wear rate of hybrid composites showed in table 2, it can be noticed that the composite with L epoxy matrix type exhibited the lowest values.

For R2 regime, where the force is intermediate, the values of friction coefficient it was not exhibited the significant variations, the behavior of materials being almost linear during the tests. The same behavior of hybrid materials it can be observed and for R3 regime for perpendicular modes.

Figure 4. Friction coefficients of hybrid composites investigated by parallel mode and R2 testing regime

Figure 5. Friction coefficients of hybrid composites investigated by perpendicular mode on elastic surface and R2 testing regime
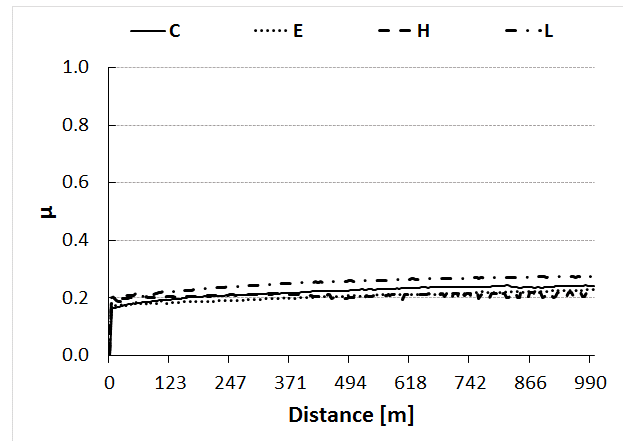
Figure 6. Friction coefficients of hybrid composites investigated by perpendicular mode on rigid surface and R2 testing regime

The increasing of friction coefficients it can be remarked by parallel mode for hybrid composite with L epoxy matrix.

Regarding the wear rate, the behavior of composites it is unstable. According to the values of wear rate of composites from tables 3 and 4, the perpendicular modes on rigid or elastic surfaces, it does not lead to significant variations of wear rates.

Table 3. Wear rate of hybrid composites investigated by perpendicular mode on elastic surface

| Wear rate x 10^{-5} [g/N*m]			
Regime	Values		
	C	E	H	L
R1	1.67	2	1.32	2.3
R2	1.5	1.65	1.75	1.37
R3	0.8	1.2	1.6	1.75
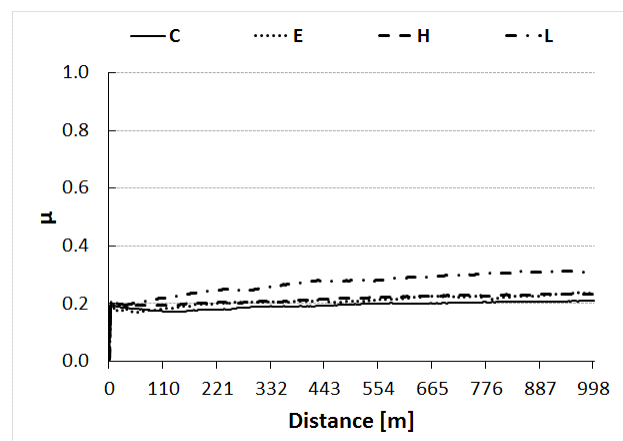
Figure 7. Friction coefficients of hybrid composites investigated by parallel mode and R3 testing regime
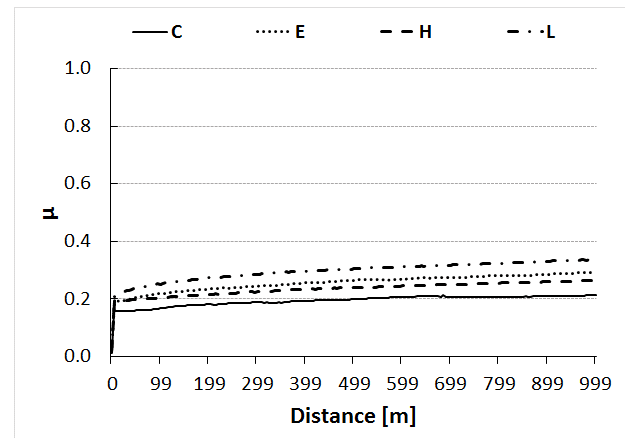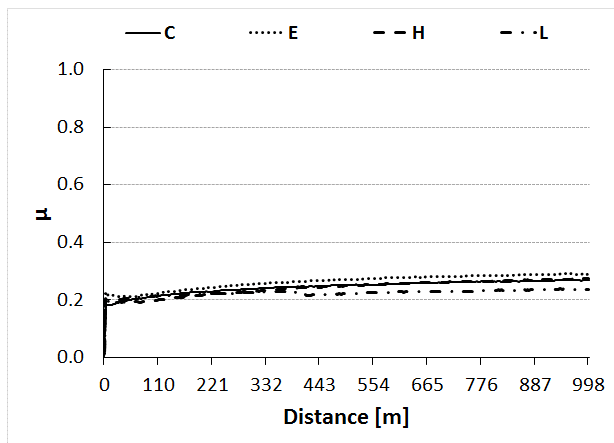
Figure 8. Friction coefficients of hybrid composites investigated by perpendicular mode on elastic surface and R3 testing regime
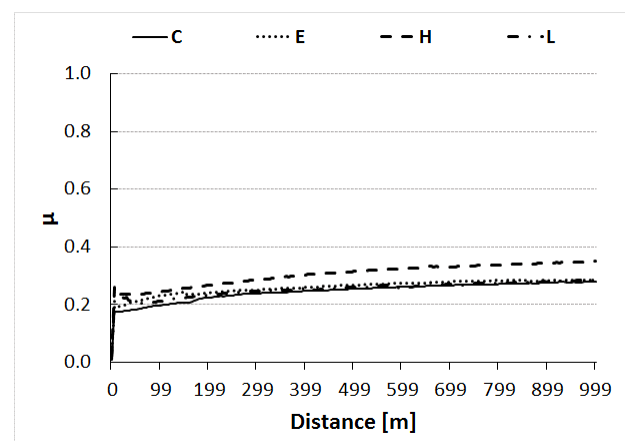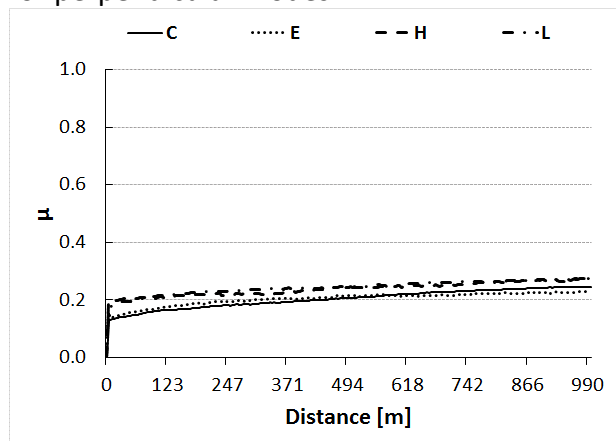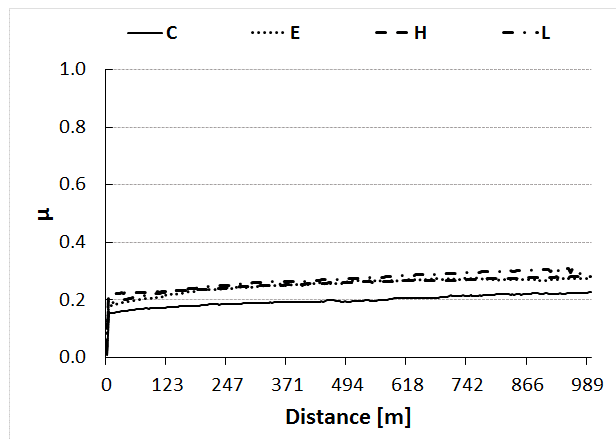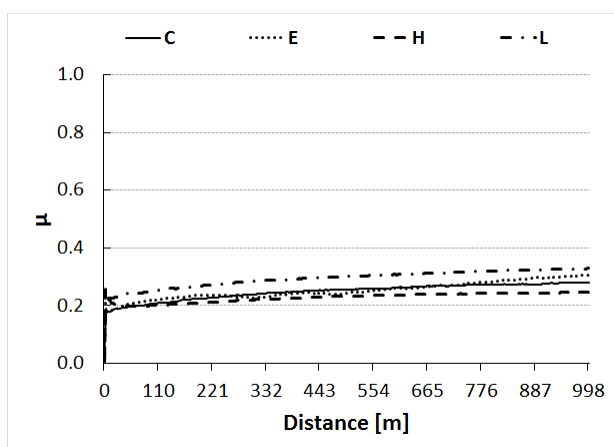

Figure 9. Friction coefficients of hybrid composites investigated by perpendicular mode on rigid surface and R3 testing regime

Table 4. Wear rate of hybrid composites investigated by perpendicular mode on rigid surface

Wear rate x 10^{-5} [g/N*m]			
Regime	Values		
	C	E	H	L
R1	1.74	2	1.27	2.33
R2	1.25	1.16	2.16	1.04
R3	1.06	1.33	1.67	1.2

4. CONCLUSION

Based on obtained tribological results, it can be formulated the following conclusions:

• The friction coefficient of investigated composite materials with L and H epoxy matrix types showed the highest values for both modes and all regimes of tribological experiments, excepting the friction coefficients of hybrid composites investigated

by perpendicular mode on elastic surface and R3 regime, where the composite with C epoxy matrix type exhibited the highest value.

• The wear rate of composite materials it is not very significant.

ACKNOWLEDGEMENT

REFERENCES

[1] B. Aldousiri, A. Shalwan, C. W. Chin: A Review on Tribological Behaviour of Polymeric Composites and Future Reinforcement, Advance in Materials Science and Engineering, Vol. 2013, pp. 1-9, 2013.

[2] Th. Ø. Larsen: *Tribological Studies of Polymer-matrix-composites*, Frydenberg a/s, Copenhagen, Denmark, 2007.

[3] H. Parikh, P. P. Gohil: Tribology of fiber reinforced polymer matrix composites – A review, Journal of Reinforced Plastics & Composites, Vol. 34, No. 16, pp. 1340-1346, 2015.

[4] H. Pihtili: An experimental investigation of wear of glass fibre-epoxy resin and glass fibre-polyester resin composite materials, European Polymer Journal, Vol. 45, No 1, pp. 149-154, 2009.

[5] H. Aireddy, S.C. Mishra: Tribological behavior and mechanical properties of Bio-waste reinforced polymer matrix composites, Journal of Metallurgy and Material Science, Vol. 53, No. 2, pp. 139-152, 2011.

[6] L. Mohammed, M. N. M. Ansari, G. Pua, M. Jawaid, M. S. Islam: A Review on Natural Fibers Reinforced Polymer Composite and Its Applications, International Journal of Polymer Science, Vol. 2015, 2015.

[7] K. Subramanian, R. Nagarajan, J. Sukumaran, W. Thangiah, P. De Baets: Dry sliding wear properties of Jute/polymer composites in high loading applications, Mechanical Engineering Letters, Vol. 12, pp. 7-18, 2015.

[8] M. P. M. Prasad, B. Vinod., Dr. L.J. Sudev: Effect of Fiber Orientations on Tribological Behaviour of PALF Reinforced Bisphenol-A Composite, International Journal of Engineering Research and General Science, Vol. 2, No. 4, pp. 809-814, 2014.

[9] J. Bijwe, M. Sharma: Nano and Micro PTFE for Surface Lubrification of Carbon Fabric Reinforced Polyethersulphone Composites, Tribology of Nanocomposites, Materials Forming, Machining and Tribology, pp. 19-39, 2013.

[10] H. Dhieb, J.G. Buijnsters, J.P. Celis: Degradation of Carbon Fiber Reinforced Epoxy Composites under Sliding in Ambient Air, Sustainable Construction and Design, Vol. 2, No 1, pp. 53-58, 2011.

[11] V. Altstaedt, P. Werner, J. Sandler: Rheological, Mechanical and Tribological Properties of Carbon-nanofibre Reinforced Poly (ether ether ketone) Composites, Polimeros: Ciencia e Tecnologia, Vol. 3, No. 4, pp. 218-222, 2003.

[12] J.M. Lackner, B. Major, W. Waldhauser, A. Mzyk, L. Major, M. Kot, Roughness Influence on Macro- and Micro-tribology of Multi-layered Hard Coatings on Carbon Fibre Polymer Composite, Archives of Metallurgy and Materials, Vol. 60, No. 3, pp. 2145-2151, 2015.

[13] X. R. Zhang, P. Zhao, X. Q. Pei1, Q. H. Wang, Q. Jia: Flexural strength and tribological properties of rare earth treated short carbon fiber/polyimide composites, eXPRESS Polymer Letters, Vol.1, No.10, pp. 667–672, 2007.

[14] R. Caliman: Friction Behaviour of Polymeric Composite Materials Mixed of Carbon Fibers Having Different Orientation Layout, IOP Conference Series: Materials Science and Engineering, Vol. 133, pp. 1-8, 2016.

[15] M.T. Mathew, Naveen V. Padaki, L.A. Rocha, J.R. Gomesa, R. Alagirusamy, B.L. Deopura, R. Fangueiro: Tribological properties of the directionally oriented warp knit GFRP composites, Wear, Vol. 263, No. 7-12, pp. 930-938, 2007.

[16] T. Madhusudhan, M. Senthilkumar, D. Athith: Mechanical Characteristics and Tribological Behaviour Study on Natural - Glass Fiber Reinforced Polymer Hybrid Composites: A Review, International Research Journal of Engineering and Technology (IRJET), Vol. 03, No. 04, pp. 2243-2246, 2016.

[17] B. R. Raju, B. Suresha, R. Parameshwarappa Swamy, B. Swamy Gowda Kanthraju: Investigations on Mechanical and Tribological Behaviour of Particulate Filled Glass Fabric Reinforced Epoxy Composites, Journal of Minerals and Materials Characterization and Engineering, Vol. 1, No. 4, pp. 160-167, 2013.

[18] T.Ø. Larsen, T. L. Andersen, B. Thorning, A. Horsewell, M. E. Vigild: Comparison of friction and wear for an epoxy resin reinforced by a glass or a carbon/aramid hybrid weave, Wear, Vol. 262, No. 7-8, pp. 1013-1020, 2007.

STUDY OF HIGH TEMPERATURE TRIBOLOGICAL PROPERTIES OF HYBRID ALUMINIUM BORON CARBIDE FLY ASH COMPOSITES

Canute XAVIER[1*], Manik Chandra MAJUMDER[1]
[1]National Institute of Technology,Durgapur,India
*Corresponding author: xcanute@gmail.com

Abstract: *The use of fly ash as the reinforcement in the production of metal matrix composites is increasing throughout the world. The main objective of the current investigation is to manufacture aluminum-boron carbide-fly ash composites with improved tribological and mechanical properties and to study the effect of load, sliding velocity,temperature on friction coefficient.The high temperature wear test was performed by the pin heating method. Analysis of variance technique was used to explore the effect of wear parameters on the friction coefficient. The results of the investigation reveal that the load had the highest significance, followed by temperature and sliding velocity. The coefficient of friction increased with an increase in input parameters. The pin surface was studied with a high-resolution scanning electron microscope.The developed composites can be used in the production of automobile and aircraft parts requiring high wear, friction and thermal resistance.*

Keywords: *Stir Casting,Hybrid MMC,Wear,Friction,Delamination*

1. INTRODUCTION

The main responses of tribology are friction and wear. The tribological characterstics of a material depend on surface roughness, material properties, tribochemical changes and material transfer mechanisms [1].

Lightweight materials which are suitable for nuclear,automotive and aerospace applications. The phenomenon of wear plays a vital role in the various mechanical parts such as gears, brakes and clutches. The important applications of aluminium cast metal matrix composites are engine blocks, brake rotors and connecting rods [2].

Boron Carbide is a potential reinforcement material compared to silicon carbide and Aluminium oxide because of its low density, high hardness and good thermal stability [3].

Aluminium boron carbide composites have good wear resistance and high strength. Aluminum boron carbide composites were used in the production of neutron absorber and armor plate materials.These composites have good fatigue strength and wear resistance [4]. The addition of boron carbide in Al/B_4C composites increases the wear resistance [5].

The important applications of aluminium flyash composites are brake rotors and pistons. ALFA composites with low fly ash percentage are used in the various automotive parts like manifolds, brackets and housings,household extruded parts and yard tool covers [6]. The addition of fly ash as reinforcement material increases yield strength, compression strength and hardness [7].

The tribological properties of hybrid composites are less when compared with

aluminium cast alloys. The addition of fly ash particles increases the wear resistance and frictional resistance, which is due to the presence of alumina silicate [8].The wear of resistance of aluminium flyash particles with course grain size was superior when compared with fine grain size [9]. AMMC's with higher reinforcement particle has greater wear resistance [10]. The addition of strontium to aluminium boron carbide composites, wear resistance was considerably increased [11].

The specific wear rate is expressed as volume loss per sliding distance and load. The friction is caused by contact between sliding surfaces of the material involved and heat is generated [12].

The coefficient of friction defined the ratio of frictional forces between sliding pairs and the force pressing them together. The effect of applied load has a significant effect on the wear rate of the composites[13]. Yalcin and Akbulut [14] found that friction coefficient value reduced with an increase in reinforcement content and applied load. Rodríguez et al [15] conducted the study with aluminium lithium alloy reinforced with silicon carbide and found that the coefficient of friction of Al/SiC composites were higher than the cast aluminium alloy.The sliding pairs and process parameters has considerable effect on friction coefficient. The friction coefficient and wear rate depend on the surface roughness,relative motion,stick slip,lubrication and vibration.The coefficient of friction decrease with the increase of sliding speed and load [16].The wear rate increases with an increase in sliding speed and load. Lower friction values were observed with higher sliding speeds [17]. The main objective of current research is to develop a composite with increased specific strength, yield strength, wear resistance, fatigue strength and thermal shock resistance suitable for high temperature resistant parts to be used to be used in automobile and aircraft industries.

2. MATERIAL AND METHODS

Aluminium A356 alloy is mixed with boron carbide powder (4%) by the stir casting method. Boron carbide powder (63 microns) was as reinforcement material. Fixed weight percentage (4%) of fly ash particles (10-100 microns) was used as the secondory reinforcement material Magnesium powder was added to increase strength and reduce casting fluidity and surface tension in aluminum. Strontium based master alloy (Al10Sr) was added to enhance mechanical properties and grain refinement.

2.1 Stir Casting

The reinforcement particles is heated to 750° C for three hours and added in the melt. Aluminium cast metal was charged into the stir-casting furnace and the temperature was augmented to 850°C. The temperature decreased progressively until it reaches to semisolid state.Hexachloroethane tablets were added to melt to eliminate the trapped air and porosity. Potassium flurotitatnate powder, aluminium-strontium master alloy and magnesium were added in required proportions. The melt was agitated uninterruptedly for 15 minutes. The pouring temperature was maintained at 720°C.

2.2 Wear Test

Wear tests of Al-B$_4$C composites were performed by pin-on-disc equipment. Schematic diagram is shown in Figure 1.The pin is inserted in the collet which is surrounded by heater coil. The pin is held pressed against EN 32 steel disc. The wear tests were conducted at different loads (10N, 20N and 30N),sliding velocity(1, 2 and 3 m/s) and temperatures 60°, 120° and 180°). Track diameter of disc of 110 mm was used for the entire test.
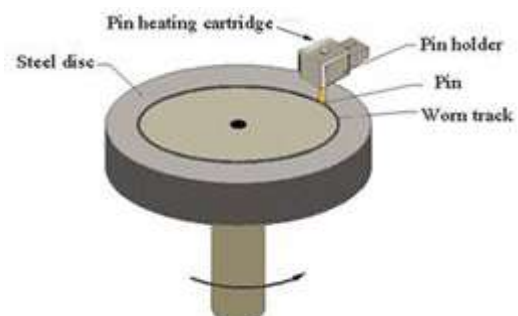
Figure 1. Schematic diagram of POD setup

3. PLAN OF EXPERIMENTS

The plan of experiments was designed considering taguchi principles and DOE. The parameters considered were load(L), sliding velocity (V) and temperature (T).The experimental conditions levels and parameters are publicised in Table 1.

Table 1. Levels and Parameters

Level	L	V	T
1	10	1	60
2	20	2	120
3	30	3	180

The orthogonal array used for the study is L9. The data analysis was carried through MINITAB 16 software. The experimental data were converted to signal to noise ratio.

4. RESULTS AND DISCUSSION

The details of the results of the various tribological and metallurgical examinations are described in this section. The readings of the wear test were recorded and results of wear analysis calculation are tabulated (Table 2). The effect of the load, speed and temperature on the frictional coefficient was analyzed by MINITAB 16 software.

Table 2. Experimental results

Level	L	V	T	COF	SN ratio
1	10	1	60	0.302	10.3999
2	10	2	120	0.250	12.0412
3	10	3	180	0.414	7.6600
4	20	1	120	0.370	8.6360
5	20	2	180	0.394	8.0901
6	20	3	60	0.362	8.8258
7	30	1	180	0.445	7.0328
8	30	2	60	0.395	8.0681
9	30	3	120	0.410	7.7443

The parameter with the highest S/N ratio gives minimum friction coefficient. The optimal friction coefficient was observed at 10N load with sliding velocity, 2 m/s temperature, 120°C.Load and sliding velocity

are more significant when compared to temperature. From the main effects plot for means, wear rate increases with load. When sliding velocity is increased the contact between the disc and the pin decreases. Hence the friction coefficient is decreased. Response table for Signal to Noise ratio is shown in Table 3 and means is shown in Table 4. The main effects plot for S/N ratio is shown in Figure .2. The main effect of plots for means is shown in Figure.3.

Table 2. Response table for S/N ratio

Level	L	V	T
1	10.034	8.690	9.098
2	8.517	9.400	9.474
3	7.615	8.077	7.594
Delta	2.419	1.323	1.880
Rank	1	3	2

Table 3.Response table for means

Level	L	V	T
1	0.3220	0.3723	0.3530
2	0.3753	0.3463	0.3433
3	0.4167	0.3953	0.4177
Delta	0.0947	0.0490	0.0743
Rank	1	3	2

From the response table for S/N ratios it is inferred that the load has the significant effect, followed by temperature and sliding velocity. The S/N ratio analysis predicts the optimal value of friction coefficient occurs when the load is at level 1(10N), sliding velocity at level 2 (2 m/s) and temperature at level 2 (120°C). Wear rate advances with applied load. Wear rate increase with the rise in temperature due to softening of the material [18]. Abrasive wear increases with an increase in temperature. Hardness, flow stress and yield strength decrease when temperature increases [19].

ANOVA analysis was performed with a 95 % confidence level and 5% significance level.
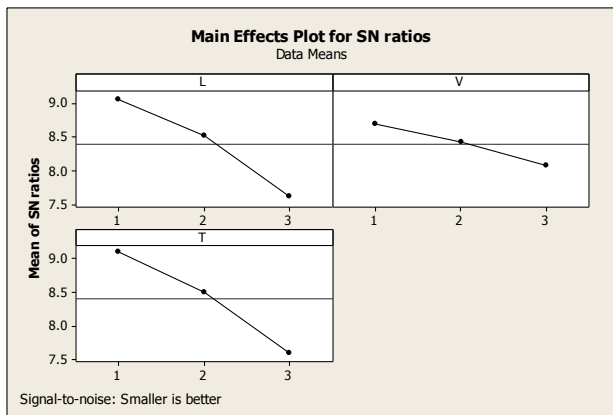
Figure 2. Main effects plot for S/N ratio

Figure 3. Main effect of plots for means

The applied load has the greater statistical influence (45.91%) and followed by temperature (33.29%) and sliding velocity (12.25%). The values of regression coefficient (R^2) for friction coefficient is 91.46%.

A regression equation was generated by the correlation of process parameters like load, sliding velocity and temperature Regression equation establishes the equation between the parameters like load, sliding velocity and temperature.

$$COF = 0.189 + 0.0473333 \times L + 0.0115 \times V + 0.0323333 \times T \qquad (1)$$

From the above relation, it was observed that the coefficient associated with load, sliding velocity and temperature was positive. This clearly reveals that as load, sliding velocity and temperature increases, the friction coefficient the hybrid composite also increases. The friction coefficient decreases with the increase in the content of the boron carbide particles. The boron carbide particles

form a protective layer between the surface of pin and counterface material [20]. The wear rate and friction coefficient rate are higher for aluminium alloy at all levels of temperature.

The wear rate of aluminium composites is less compared with base alloy. The wear rate and friction coefficient increases with an increase in the temperature. The contact area between pin and steel increases with the increase in temperature [20].

SEM investigation of the worn pin surface for load, 10N, sliding velocity, 2m/s and temperature, 120°C is shown by Figure.4. Fine and shallow grooves formed at low applied load and speed due to abrasive wear. The particles of the steel disc penetrate into the pin and hence wear on the pin is accelerated. Hard reinforcement particles remove material from the wear surface when the load increases, which is attributed by delamination.

Delamination wear is more at higher temperature. The phenomenon of adhesive wear is predominant at maximum load, 30 N. Wear tracks tend to disappear at this juncture. boron carbide particles tend to gather at the boundaries of α-aluminium dendrites in the casting [21].

SEM image of the worn out pin surface at L=20N, S=3 m/s, T=60°C is shown in Figure.7. The grooves widen with increased load. The mechanism of wear rate is greatly affected by the two sliding surface interaction. The frictional heat between the sliding pairs is increased by the load and duration of the test [22].
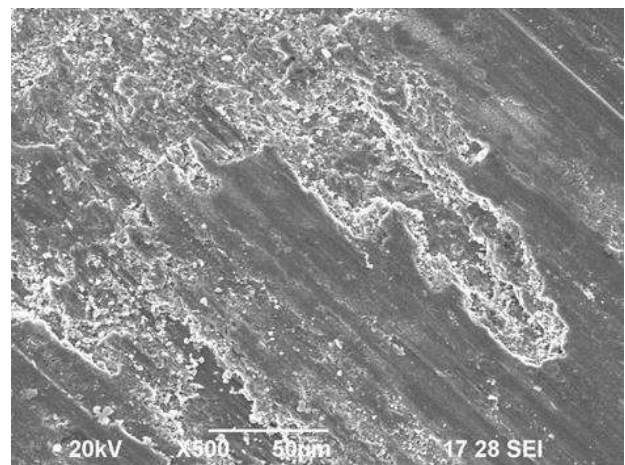
Figure 4. SEM image (10N,2 m/s,120°C)

Wear behavior of the composites is increased linearly with increasing the operating temperature at high load. This effect is due to the formation of the oxide film and glazing layer on sliding components.
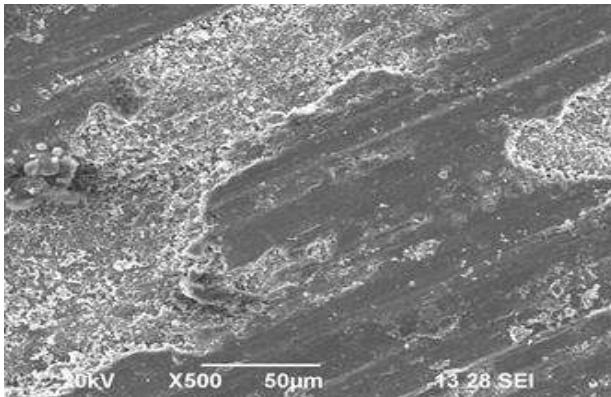
Figure 5. SEM image (20N.2m/s,180°C).

These layers prevent the direct metal-to-metal contact of sliding surfaces during sliding motion.
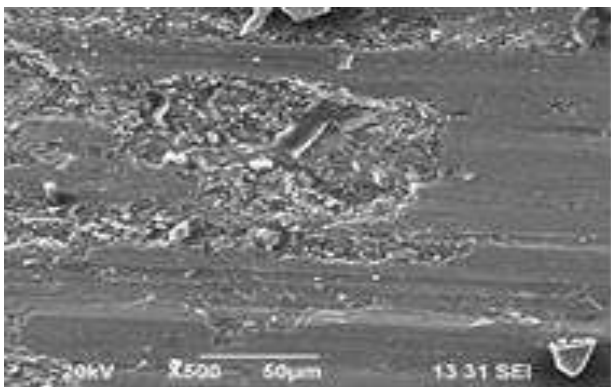
Figure 6. SEM iamge (30N,2m/s,60°C).
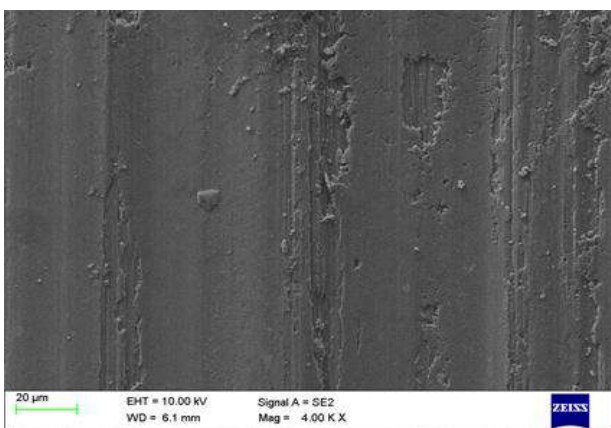
Figure 7. SEM image (L=20N S=3 m/s T=60° C).

Table 7. Confirmation tests

Parameter	Optimal	Pred.	Expt.	Error
Coeffficient of friction	10N,2 m/s,120°C	0.368	0.386	4.66%

The confirmation tests (Table.7) were conducted with optimum parameters arrived by taguchi analysis [24]. The error found to be less than 5%.

5. CONCLUSION

The optimal conditions for minimum COF is dermined by signal to noise analysis. It is inferred that the optimal conditions for minimum friction coeffient is given L=10N,V=2m/s and T=120°C).

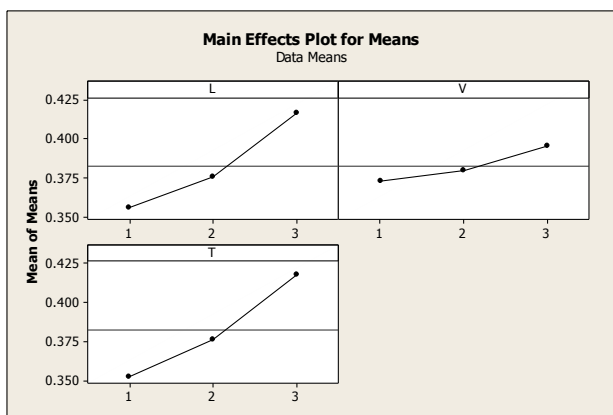From the ANOVA analysis,the applied load has the greater statistical influence (45.91%) and followed by temperature (33.29%) and sliding velocity (12.25%). The values of regression coefficient (R^2) for friction coefficient is 91.46%.

The friction coefficient increases with an increase in applied load, sliding velocity and temperature. Delamination wear is more at higher temperature. The phenomenon of adhesive wear is predominant at maximum load,30 N. Wear rate increases with load and temperature.

Regression analysis shows an extensive association between load,sliding velocity, temperature and friction coefficient.The confirmation experiment revealed that the error between the experimental values and optimal predicted values were less than 5% and hence the experimental results are validated.

The developed composites can be used in the fabrication of automobile and aircraft parts requiring high temperature and wear resistance. The tribological properties of Aluminium boron carbide flyash composites an be enhanced by selecting course grain fly ash particle with the addition of intermetallic alloys and titanium based master alloys.Graphite and Molybdenum disulphide can added toreduce the friction coefficient.

REFERENCES

[1] K. Kato: Wear in relation to friction-a review, Wear, Vol. 241, pp. 151–157,2000.
[2] S. Prasad, R. Asthana: Aluminum Metal-Matrix Composites for Automotive Applications:

Tribological Considerations, Tribology Letters Vol. 17, No.3, pp. 445–453,2004.

[3] J.Jung, S. Kang: Advances in manufacturing boron carbide-aluminium composites, Journal of American Ceramic Soceity, Vol.87, No.1, pp.47-54, 2004.

[4] K. U. Kainer :*Metal Matrix Composites. Custom-made materials for Automotive and Aerospace Engineering*, Wiley-Vch, EY-VCH Verlag GmbH & Co. KGaA, Weinheim, 2006.

[5] N. Radhika, T. Balaji: Studies on mechanical properties and tribological behavior of LM25/SiC/Al$_2$O$_3$, Journal of Engineering Science and Technology, Vol. 10, No. 2, pp. 134-144, 2015.

[6] T.P.D. Rajan, R.M. Pillai, B.C. Pai, K.G. Satyanarayana, P.K. Rohatgi: Fabrication and characterization of Al-7Si-0.35Mg/fly ash metal matrix composites processed by different stir casting routes, Composites Science and Technology, Vol.67, pp. 3369-3377, 2007.

[7] H.C. Anilkumar, H.S. Hebbar, K.S. Ravishankar: Mechanical Properties of flyash reinforced aluminium alloy (Al6061) composites, Journal of Mechanical and Materials Engineering (IJMME), Vol.6, No.1, pp.41-45, 2011.

[8] M.K.Sudarshan, Surappa: Synthesis of flyash particle reinforced A356 Al Composites and their characterization, Material Science and Engineering: A, Vol.480, No. 1-2, pp. 117-124, 2008.

[9] K. Ravikumar,K.M. Mohanasundaram, G. Aramaikkannu, R. Subramanian: Effect of particle size on mechanical properties and tribological behavior of aluminium/flyash composites, Science and Engineering Composite Materials, Vol.19, pp.247-253, 2012.

[10] P. Joshua, D. Ashkenazi, M. Ganor: The influence of a third element on the interface reactions in metal–matrix composites (MMC) Al–graphite system, Materials Science and Engineering A, Vol. 281, No.1-2, pp. 239-247, 2000.

[11] D.G. Mallapur, K.Rajendra Udupa, A. Kori: Influence of Ti,B and Sr on the microstructure and mechanical properties of A356 alloy, *IJMET*, Vol.1, No.1, pp.49-59, 2010.

[12] S.C. Lim, Ashby: Wear mechanism maps, Acta Metallurgica, Vol.35, No.1, pp. 1-24, 1987.

[13] D.P.Mondal, S.Das: High stress abrasive wear behavior of aluminum hard particle composites:effect of experimental parameters, particle size and volume fraction, Tribology International, Vol.39, pp.470–478, 2006.

[14] Y.Yalcin,H.Akbulut: Dry wear properties of A356-SiC particle reinforced MMCs produced by two melting routes, Materials and Design, Vol. 27, No. 10, pp. 872–881, 2006.

[15] J. Rodríguez, P. Poza, M.A. Garrido, A. Rico: Dry sliding wear behaviour of aluminium-lithium alloys reinforced with SiC particles, *Wear,* Vol. 262, No. 3-4, pp. 292–300, 2007.

[16] D. Kakas, B. Skoric, S. Mitrovic, M. Babic,P. Terek, A. Miletic, M. Vilotic: Influence of Load and Sliding Speed on Friction Coefficient of IBAD Deposited TiN, Tribology in industry, Vol. 31, No. 3&4, pp. 3-10, 2009.

[17] M. Uthayakumar, S. Thirumalai Kumaran, S.Aravindan: Dry sliding friction and wear studies of flyash reinforced AA-6351 metal matrix composites, Advances in Tribology, Vol.6, pp. 1-6, 2013.

[18] N. Radhika, A. Vaishnavi, G.K. Chandran: Optimisation of Dry sliding wear process parameters for Aluminium Hybrid Matrix composites, Tribology in Industry, Vol.36, No.2, pp. 188-194, 2014.

[19] M. Lindroos, M. Apostol, V. Heino, K. Valtonen, A. Laukkanen, K. Holmberg, V.T. Kuokkala: The deformation, strain hardening and wear behavior of chromium-alloyed hadfield steel in abrasive and impact conditions, Tribology Letters, Vol.57, No.3, pp. 1-17, 2015.

[20] N. Selvakumar, T. Ramkumar: Effects of High Temperature Wear Behaviour of Sintered Ti–6Al–4V Reinforced with Nano B$_4$C Particle, Transactions of the Indian Institute of Metals, Vol. 69, No. 6, pp.223-231, 2016.

[21] P.K. Rohatgi, R.Q. Guo: Low Cost Cast Aluminium – Fly Ash Composites for Ultralight Automotive Application, *TMS Annual Meeting, Automotive Alloys*, pp. 157-168, 1997.

[22] G. Dixit, M.M. Khan: Sliding Wear Response of an Aluminium Metal Matrix Composite: Effect of Solid Lubricant Particle Size, Jordan Journal of Mechanical and Industrial Engineering, Vol. 8, No.6, pp. 351 – 358, 2014.

A REVIEW ON TRIBOLOGICAL PROPERTIES OF MICROCOMPOSITES WITH ZA-27 ALLOY MATRIX

Filip VUČETIĆ[1],*, Sandra VELIČKOVIĆ[2], Aleksandar MILIVOJEVIĆ[3], Aleksandar VENCL[3]

[1]University of Belgrade, Innovation Center of the Faculty of Mechanical Engineering in Belgrade, Belgrade, Serbia
[2]University of Kragujevac, Faculty of Engineering, Kragujevac, Serbia
[3]University of Belgrade, Faculty of Mechanical Engineering, Belgrade, Serbia
*Corresponding author: fvucetic@mas.bg.ac.rs

Abstract: Manufacturing and testing of novel composite materials are one of the topics that had caught attention of many researchers. There are a vast number of possibilities for improving many characteristics of the base (matrix) material significantly with addition of relatively small amounts of different material to the matrix. This paper should give an overview on tribological properties of microcomposites with ZA-27 alloy as a matrix material. Following characteristics were taken into consideration in the process of making this overview: type, amount and size of reinforcement; manufacturing process; apparatus used for testing; and test parameters and conditions.

Keywords: ZA-27, microcomposites, manufacturing process, friction, wear.

1. INTRODUCTION

Zinc-aluminium (ZA) alloys are materials well known for their good physical and mechanical properties, high corrosion resistance in atmospheric conditions, excellent casting properties, easy machining, and good tribological properties [1-7]. They have become a good, cost effective substitute for conventional materials such as bronzes, aluminium alloys and cast irons [1,5-11].

One of the most frequently used member of ZA alloy family is ZA-27 casting alloy with 25 – 28 wt. % Al, 2 – 2.5 wt. % Cu, and 0.01 – 0.02 wt. % Mg. It has been often used in applications intended for high load and low to moderate speed applications, especially for sliding bearings [4-8,10,11]. Due to its overall good properties, ZA-27 alloy has been

interesting in past decades by many researchers. In order to obtain better mechanical and tribological properties, ZA-27 alloy was used for development of metal matrix composites (MMC). Improvement of these properties of ZA-27 composites was made by adding suitable amounts of improvers and reinforcements. In the case when two or more reinforcements are added to the matrix material a hybrid composite is produced.

This paper gives the overview of tribological properties of ZA-27 microcomposites with respect to the equipment used for testing, amount, type and size of reinforcements, manufacturing process, and test parameters (load, sliding speed and sliding distance) and conditions (dry or lubricated). Erosion test investigations, in situ manufactured ZA-27

microcomposites, and high temperature tribological investigations were not taken in consideration in this overview.

2. MANUFACTURING PROCESS

Production of metal matrix composites with casting techniques presents quite a challenge from the aspect of reinforcement material distribution in the matrix and thus obtaining desired properties. Difficulties emerge from the fact that reinforcement distribution in the melt is hard to control due to many factors, such as: properties of the reinforcement, viscosity of the slurry, wettability, effectiveness of agglomerates breaking with mixing, entrapped gas, etc. [12].

Most common production processes of ZA-27 microcomposites can be broadly divided in two groups:
- liquid state processes, which include different casting processes such as stir casting, centrifugal casting and ultrasound enhanced casting;
- semisolid process, i.e. compocasting.

Within these two groups, stir casting and compocasting processes are the most often used, i.e. in approximately 90 % of the reviewed papers [13-31]. Stir casting represents a process very similar to the conventional casting. The difference is that the stirring of the melt is introduced in order to obtain better distribution of the reinforcement in the matrix. Reinforcement in this process is infiltrated into the overheated melt of the matrix. Compocasting method is similar to the stir casting and the main difference is that the matrix is not in liquid state, but in semisolid [32].

On the other hand, there are much less publications for other mentioned processes. Centrifugal casting [21] was done on the machine consisting of a rotation system and a mould fixed on the centrifugal casting equipment; unidirectional solidification is enforced by the unidirectional heat transfer through the mould. Exposing melt to the ultrasound [24], and the cavitation effect that it induces is used to refine the grain size of the matrix during solidification. High intensity of

ultrasound also introduces agitation of the melt which can, in combination with cavitation effect, give a better distribution of reinforcement.

Reinforcements in the form of particles have been used in almost all the cases with ZA-27 microcomposites. This can be explained by cost effectiveness of particles when compared to other types of reinforcements. The most frequently used reinforcements were hard particles, such as Al_2O_3, SiC and minerals, followed by graphite (Gr), fly ash, etc. There are also cases when two reinforcements were used to obtain hybrid microcomposites; besides SiC and Gr, there are also hybrid microcomposites with various of different weight percents combinations of Al_2O_3 and fly ash on one side and Al_2O_3 and Gr on the other.

Amount of reinforcement varied and it was usually up to 10 wt. %. Differences in particle sizes are also significant. Minimum and maximum particle size along with minimum and maximum weight percent of each reinforcement is given in Table 1.

Table 1. Reinforcement amount and size ranges in ZA-27 microcomposites

Reinforcement	Amount [wt. %], min – max	Size [μm], min – max
SiC	1 – 15	5 – 80
Al_2O_3	3 – 25	10 – 250
Graphite	1 – 5	25 – 150
Other	1 – 20	4 – 70

3. TRIBOLOGICAL PROPERTIES OF ZA-27 MICROCOMPOSITES

Great number of factors influencing the tribological properties of microcomposites makes the comparison between different studies and examinations difficult, and in some cases even impossible. Only the studies with ZA-27 alloy matrix are reviewed and presented in Table 2, through the influencing factors such as: manufacturing processes, type, amount and size of reinforcement, test apparatus (type of contact) and testing parameters (load, sliding speed and sliding distance), and test conditions (unlubricated or lubricated).

Table 2. Tribological properties of ZA-27 microcomposites with influencing factors

Manufacturing processes	Compocasting			
Reference	Ranganath et al. [15]	Babic et al. [16]	Babic et al. [18]	Sharma et al. [19]
Apparatus	Pin-on-disc	Block-on-disc	Block-on-disc	Pin-on-disc
Reinforcement	Garnet	Al_2O_3	Graphite (Gr)	Zircon ($ZrSiO_4$)
Amount of reinforcement	2, 4 and 6 wt. %	3, 5 and 10 wt. %	2 wt. %	1, 3 and 5 wt. %
Size of reinforcement	30 – 50 μm	220 μm	30 μm	30 – 50 μm
Counter-body material	Steel EN24	Steel 30CrNiMo8 (55 HRC)	Steel 30CrNiMo8 (55 HRC)	Steel EN24 (57 HRC)
Sliding speed	7.35 – 31.5 m/s	0.26, 0.5 and 1 m/s	0.26, 0.5 and 1 m/s	1.86 m/s
Load	20, 30, 40 and 50 N	20, 50 and 80 N	10 – 50 N (dry); 20 – 80 N (lubricated)	20, 40, 60, 80, 100 and 120 N
Sliding distance	2 km	1 km	0.5 km (dry); 1 km (lubricated)	0.5 – 2.5 km
Test conditions	Dry sliding	Lubricated sliding (ISO VG 46)	Dry and lubricated sliding (ISO VG 46)	Dry sliding
Coefficient of friction	/	0.04 – 0.13	0.2 – 0.48 (dry); 0.018 – 0.05 (lubricated)	/
Wear	$1 - 47 \times 10^{-3}$ mm^3/m	$0.01 - 0.74 \times 10^{-3}$ mm^3/m	$0.2 - 6.8 \times 10^{-3}$ mm^3/m (dry); $0.2 - 11 \times 10^{-5}$ mm^3/m (lubricated)	$1.8 - 16.2 \times 10^{-3}$ mm^3/m

Manufacturing processes	Compocasting			
Reference	Almomani et al. [20]	Mitrović et al. [25]	Sharma et al. [26]	Mitrović et al. [29]
Apparatus	Pin-on-disc	Block-on-disc	Pin-on-disc	Ball-on-block
Reinforcement	Fly ash; Al_2O_3; fly ash + Al_2O_3	SiC + graphite (Gr)	Short glass fibres	Al_2O_3
Amount of reinforcement	2, 4 and 6 wt. %; 2, 4 and 6 wt. %; every combination of previous wt. %	5 wt. % SiC + 1 wt. % Gr	1, 3 and 5 wt. %	3, 5 and 10 wt. %
Size of reinforcement	44 μm (fly ash); 10 μm (Al_2O_3)	/	$4 - 6 \times 400 - 600$ μm	250 μm
Counter-body material	Stainless steel (644 HV)	Steel 90MnV8 (62 HRC)	Steel EN24 (57 HRC)	Steel ball
Sliding speed	0.314 m/s	0.25, 0.5 and 1 m/s	1.86 m/s	10, 20 and 30 mm/s
Load	70 N	10, 20 and 30 N	20, 40, 60, 80, 100, 120 and 140 N	10, 50 and 100 mN
Sliding distance	95 – 565 m	30, 60, 90, 150 and 300 m	0.5, 1, 1.5, 2 and 2.5 km	Reciprocating motion
Test conditions	Dry sliding	Dry sliding	Dry sliding	Dry sliding
Coefficient of friction	/	/	/	0.075 – 0.48
Wear	$0.2 - 6.8 \times 10^{-3}$ mm^3/m	$0.59 - 4.34 \times 10^{-3}$ mm^3/m	$1.6 - 15.6 \times 10^{-3}$ mm^3/m	/

Table 2. *Continued*

Manufacturing processes	Compocasting		Ultrasound enhanced casting	Centrifugal casting
Reference	Mitrović et al. [30]	Mitrović et al. [31]	Tjong and Chen [21]	Jyothi et al. [24]
Apparatus	Block-on-disc	Pin-on-disc	Block-on-disc	Pin-on-disc
Reinforcement	Al_2O_3	Fly ash	SiC	Al_2O_3
Amount of reinforcement	3.5 and 10 wt. %	1, 2 and 3 wt. %	5, 10 and 15 wt. %	5, 10, 15, 20 and 25 wt. %
Size of reinforcement	12 and 250 μm	3 – 5 μm	5, 20 and 80 μm	20, 40, 60, 80 and 100 μm
Counter-body material	Steel 30CrNiMo8 (55 HRC)	Steel	Steel GR15 (60 HRC)	Steel
Sliding speed	0.26, 0.5 and 1 m/s	1.56 m/s	0.47 m/s	100 – 500 rpm
Load	20, 50 and 80 N	20, 40, 60, 80, 100 and 120 N	294, 588 and 882 N	10, 20, 30, 40 and 50 N
Sliding distance	156, 300 and 600 m (dry); 936, 1800 and 3600 m (lubricated)	0.5, 1, 1.5, 2 and 2.5 km	846 m	1 km
Test conditions	Dry and lubricated sliding	Dry sliding	Lubricated sliding (SAE 20)	Dry sliding
Coefficient of friction	/	/	0.05 – 0.085	/
Wear	0.36 – 3.62 mm (wear scar width)	$3 – 18 \times 10^{-3}$ mm^3/m	1.18 – 56.7 mm^3/m	$0.23 – 0.57 \times 10^{-3}$ mm^3/m

Manufacturing processes	Stir casting			
Reference	Auras and Schvezov [23]	Joshi et al. [13]	Prasanna Kumar et al. [14]	Sharma et al. [17]
Apparatus	Pin-on-disc	Pin-on-disc	Pin-on-disc	Real bearings
Reinforcement	SiC	Al_2O_3 + graphite (Gr)	Garnet	Graphite (Gr)
Amount of reinforcement	8 and 16 wt. %	3, 6 and 9 wt. % Al_2O_3 each with 3 wt. % Gr	5, 10, 15 and 20 wt. %	1, 3 and 5 wt. %
Size of reinforcement	4.2 – 6.3 μm	/	50 – 70 μm	80 – 120 μm
Counter-body material	Steel (27 HRC)	Steel	Steel EN24 (57 HRC)	Steel EN24 (58 – 60 HRC)
Sliding speed	2 m/s	1, 2, 3, 4 and 5 m/s	1.25 – 3.65 m/s	0.019 m/s
Load	30, 50 and 80 N	10, 20, 30, 40 and 50 N	50, 100, 150 and 200 N	98, 196, 294, 392 and 490 N
Sliding distance	7.2 km	200, 400, 800 and 1000 m	1.19 – 2.8 km	7.2 km
Test conditions	Dry and lubricated sliding	Dry sliding	Dry sliding	Dry, semidry and lubricated sliding (SAE 10)
Coefficient of friction	/	/	0.25 – 0.7	0.13 – 0.45 (dry); 0.035 – 0.175 (semidry); 0.022 – 0.085 (lubrica.)
Wear	$2 – 82 \times 10^{-3}$ mm^3/m (dry); $0.15 – 3.6 \times 10^{-5}$ mm^3/m (lubricated)	10 – 340 mg	0.3 – 26 mg	/

Pin-on-disc tribometer was used more than all other testing apparatus, so the type of contact in most of the studies was conformal (surface) contact, which indicates the possible applications of these microcomposites (Fig. 1). It is followed by block-on-disc with non-conformal (line) contact. Since the contact area in line contact is much smaller than in the case of pin-on-disc, there is always a potential danger of conducting tests on a region without reinforcement (depending on the distribution of reinforcement on the surface).
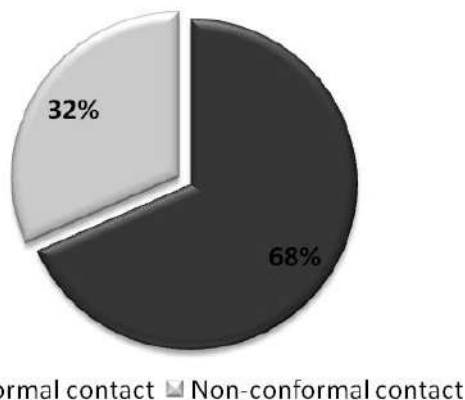

■ Conformal contact ▨ Non-conformal contact

Figure 1. Share of contact types in tribological tests of ZA-27 microcomposites

As for test conditions, unlubricated (dry) sliding conditions are present in 70 % of the studies; the rest was in lubricated sliding conditions. Some of the authors conducted tests in both dry and lubricated conditions in order to obtain better insight in tribological behaviour of their microcomposites. Since the environment (temperature, humidity, surrounding medium) was usually not stated, it is taken under the assumption that tests were conducted at room temperature in air, with standard humidity.

3.1 Coefficient of friction

The coefficient of friction was not studied in all of the reviewed papers. There are only several papers with investigations of coefficient of friction, which is insufficient to understand the tribological behaviour of ZA-27 microcomposites properly. Nevertheless, some regularities could be observed.

Results of dry sliding friction were easier to compare since the influence of normal load

and sliding speed is less pronounced. Coefficient of friction varies from 0.13 to 0.7, with an exception of 0.075 which was the lowest coefficient of friction value recorded in the paper of Mitrović et al. [29] on nanotribometer. With the increase of normal load the coefficient of friction increased in all cases [14,17,18,29]. Influence of sliding speed on coefficient of friction can be seen only in one paper [18], where the increase of speed lowered the coefficient of friction. Generally, lower friction was observed in microcomposites when compared to the coefficient of friction of the matrix itself, which indicates the positive effect of reinforcement addition on friction in dry sliding conditions. In case when the graphite was added to the microcomposites [17,18], it smeared on the surface and enabled the decreased probability of direct metal-to-metal contact and thus reducing the coefficient of friction. Effect of coefficient of friction decrease with addition of hard particles such as garnet [14] and alumina [29] was not elaborated by the authors.

There are also several results of friction investigations in lubricated sliding condition. Variation of coefficient of friction values is between 0.018 and 0.13. Here, the normal load and siding speed variations have significant influence on the coefficient of friction value. The increase of normal load also increases the coefficient of friction [16-18]. Tjong and Chen [21] had varied three different loads but only presented the results of coefficient of friction under the highest load. Higher speeds gave lower friction in all cases. Reinforcement addition had favourable effect on friction [17,18], as well as the adverse effect [16]. This can be explained with difference in reinforcement type, i.e. graphite particles provided solid lubrication by forming the graphite-rich film on the surface [17,18] which lowered the coefficient of friction. Increased level of coefficient of friction of microcomposites over that of the matrix alloy in study conducted by Babic et al. [16] was attributed to two-body and three-body abrasive action caused by Al_2O_3 particles of reinforcement.

3.2 Wear

Different authors have led investigations under different test parameters which makes comparison of their results very difficult. In addition, wear values were not always presented in the same way. Increase of load raised the wear value in almost all of the analyzed studies (in dry and lubricated sliding conditions) [13-16,18,19,21,22,25-28,30,31], with exception in the work of Auras et al. [23], who reported ambivalent behaviour of microcomposites with increasing of the load under lubricated sliding condition. There was no clear rule for the influence of the sliding speed on wear of microcomposites. Higher sliding speed in dry sliding conditions in some cases raised wear [14,15,18,25,28,30,31], but also in some other cases lowered it [22,27]. As for lubricated sliding, higher sliding speed sometimes increases wear [16], but also sometimes decreases it [18,30].

Increase of the reinforcement amount was beneficial to wear resistance of the ZA-27 microcomposites in all studies [13-16,18-28,30]. Table 3 shows the increase of wear resistance for each study and type of reinforcement. Highest amount of reinforcement in each investigation was the one with the best contribution to wear resistance of the matrix, so the wear resistance increase values in Table 3 were calculated for maximum amount of reinforcement with consideration of variations of test parameters in each investigation (that is if variations exist). For instance, if the investigation was done under two different sliding speeds and two different loads, maximum and minimum increase of wear resistance was picked out of four that were calculated for maximum amount of reinforcement under:
- lowest sliding speed with minimum and maximum load (two percentages); and
- highest sliding speed with minimum and maximum load (two percentages).

Addition of hard particles such as oxides, carbides and minerals improve wear resistance significantly. Hard phases provide protection of the ZA-27 alloy matrix of direct contact which leads to less wear in composite as compared to the matrix alloy, but can cause higher wear of counterpart [16]. Graphite reinforcement, as a solid lubricant, can get smeared onto the sliding surfaces in both dry and lubricated conditions, thereby preventing a metal-to-metal contact and decreasing the wear [22].

Table 3. Influence of reinforcement type and amount on wear resistance

Reinfor-cement	Ref.	Maximum reinforcement amount [wt. %]	Increase of wear resistance [times], min / max
Al_2O_3	[16]	10	3 / 16
	[20]	6	4.6
	[30]	10	1.12 / 2.54 (dry); 1.6 / 2.6 (lubricated)
SiC	[21]	15	8 / 24
	[23]	16	1.76 / 3 (dry); * (lubricated)
	[27]	5	1.24 / 1.36
Gr	[22]	5	1.38 / 1.56
	[18]	2	1.26 / 3 (dry); 1.14 / 5 (lubricated)
SiC + Gr	[28]	9 SiC + 3 Gr	2.18 / 2.78
	[25]	5 SiC + 1 Gr	1.17 / 1.33
Al_2O_3 + Gr	[13]	9 Al_2O_3 + 3 Gr	3.0 / 16.5
Fly ash + Al_2O_3	[20]	6 fly ash + 6 Al_2O_3	11.5
Garnet	[14]	20	2.00 / 2.33
	[15]	6	1.78 / 7.67
Zircon	[19]	5	1.67 / 5.37
Short GF	[26]	5	1.70 / 6.28
Fly ash	[20]	6	2.3
	[31]	3	1.75 / 5.70

*up to no wear; Gr – graphite; GF – glass fibre

4. CONCLUSIONS

Through the comparison of tribological properties of ZA-27 microcomposites, obtained in different investigations and manufacturing and testing conditions, some conclusions can be made, such as:
- Stir casting and compocasting are the most popular processes for production of these microcomposites.

- Ceramic particles such as Al_2O_3 and SiC are the most frequently used reinforcements, followed by graphite and other reinforcements like garnet, zircon, fly ash and short glass fibres. Reinforcement amount was usually up to 10 wt. %.
- Coefficient of friction values are in the range of $0.018 - 0.13$ for lubricated conditions, and $0.13 - 0.7$ in case of unlubricated (dry) sliding conditions. Increase of sliding speed and normal load increases the coefficient of friction in both dry and lubricated conditions.
- Microcomposites exhibited lower wear than ZA-27 alloy and with increase of reinforcement amount wear value decreases in all cases. Increase of load raised the wear value in almost all analyzed studies (in dry and lubricated sliding conditions), while there was no general rule for the influence of sliding speed on wear value.
- Intended application for ZA-27 microcomposites is mainly for tribological pairs with conformal contact, since most of the studies simulated this type of contact.

ACKNOWLEDGEMENT

REFERENCES

[1] B.K. Prasad: Effect of microstructure on the sliding wear performance of a Zn-Al-Ni alloy, Wear, Vol. 240, No. 1-2, pp. 100-112, 2000.

[2] R. Lyon: High strength zinc alloys for engineering applications in motor cars, Metals and Materials, No. 1, pp. 55-57, 1985.

[3] E. Gervais, R.J. Barnhurst, C.A. Loong: An analysis of selected properties of ZA alloys, Journal of Metals (JOM), Vol. 37, No. 11, pp. 43-47, 1985.

[4] E.J. Kubel Jr.: Expanding horizons for ZA alloys, Advanced Materials & Processes, Vol. 132, No. 1, pp. 51-57, 1987.

[5] R. Ninković, M. Babić, A. Rac: Yugoslav Zn-Al alloys as bearings material, Tribology in Industry, Vol. 22, No. 1-2, pp. 14-18, 2000.

[6] M. Babić, R. Ninković: Zn-Al alloys as tribomaterials, Tribology in Industry, Vol. 26, No. 1-2, pp. 3-7, 2004.

[7] R.J. Barnhurst: *Zinc Aluminium Alloy Design Manual for Continuous Rotation Bearings*, Noranda Research Centre, 1988.

[8] M. Babić, S. Mitrović, R. Ninković: Tribological potencial of zinc-aluminium alloys improvement, Tribology in Industry, Vol. 31, No. 1-2, pp. 15-28, 2009.

[9] P.P. Lee, T. Savaskan, E. Laufer: Wear resistance and microstructure of Zn-Al-Si and Zn-Al-Cu Alloys, Wear, Vol. 117, No. 1, pp. 79-89, 1987.

[10] B.K. Prasad, A.H. Yegneswaran, A.K. Patwardhan: Characterization of the wear response of a modified zinc-based alloy vis-à-vis a conventional zinc-based alloy and a bearing bronze at a high sliding speed, Metallurgical and Materials Transactions A, Vol. 27, No. 11, pp. 3513-3523, 1996.

[11] T. Savaşkan, G. Pürçek, S. Murphy: Sliding wear of cast zinc-based alloy bearings under static and dynamic loading conditions, Wear, Vol. 252, No. 9-10, pp. 693-703, 2002.

[12] J. Hashim, L. Looney, M.S.J. Hashmi: Particle distribution in cast metal matrix composites – Part I, Journal of Materials Processing Technology, Vol. 123, No. 2, pp. 251-257, 2002.

[13] A.G. Joshi, R.S. Desai, M.V. Prashanth, S. Sandeep: Study on tribological behavior of ZA-27/Al_2O_3/Gr MMC, International Journal on Emerging Technologies, Vol. 7, No. 2, pp. 117-122, 2016.

[14] M. Prasanna Kumar, K. Sadashivappa, G.P. Prabhukumar, S. Basavarajappa: Dry sliding wear behaviour of garnet particles reinforced zinc-aluminium alloy metal matrix composites, Materials Science (Medžiagotyra), Vol. 12, No. 3, pp. 209-213, 2006.

[15] G. Ranganath, S.C. Sharma, M. Krishna: Dry sliding wear of garnet reinforced zinc/aluminium metal matrix composites, Wear, Vol. 251, No. 1-12, pp. 1408-1413, 2001.

[16] M. Babic, S. Mitrović, F. Zivic, Effects of Al_2O_3 particle reinforcement on the lubricated sliding wear behavior of ZA-27 alloy

composites, Journal of Materials Science, Vol. 46, No. 21, pp. 6964-6974, 2011.

[17] S.C. Sharma, B.M. Girish, R. Kamath, B.M. Satish: Graphite particles reinforced ZA-27 alloy composite materials for journal bearing applications, Wear, Vol. 219, No. 2, pp. 162-168, 1998.

[18] M. Babic, S. Mitrović, D. Džunic, B. Jeremic, I. Bobić: Tribological behavior of composites based on ZA-27 alloy reinforced with graphite particles, Tribology Letters, Vol. 37, No. 2, pp. 401-410, 2010.

[19] S.C. Sharma, B.M. Girish, D.R. Somashekar, B.M. Satish, R. Kamath: Sliding wear behaviour of zircon particles reinforced ZA-27 alloy composite materials, Wear, Vol. 224, No. 1, pp. 89-94, 1999.

[20] M. Almomani, M.T. Hayajneh, M. Draidi: Tribological investigation of Zamak alloys reinforced with alumina (Al_2O_3) and fly ash, Particulate Science and Technology, Vol. 34, No. 3, pp. 317-323, 2016.

[21] S.C. Tjong, F. Chen: Wear behavior of as-cast ZnAl27/SiC particulate metal-matrix composites under lubricated sliding condition, Metallurgical and Materials Transactions A, Vol. 28, No. 9, pp. 1951-1955, 1997.

[22] K.H.W. Seah, S.C. Sharma, B.M. Girish, S.C. Lim: Wear characteristics of as-cast ZA-27/graphite particulate composites, Materials & Design, Vol. 17, No. 2, pp. 63-67, 1996.

[23] R. Auras, C. Schvezov: Wear behavior, microstructure, and dimensional stability of as-cast zinc-aluminum/SIC (metal matrix composites) alloys, Metallurgical and Materials Transactions A, Vol. 35, No. 5, pp. 1579-1590, 2004.

[24] P.N. Jyothi, M.C. Jagath, K. Channakeshavalu: Wear characteristics of ZA-27/Al_2O_3 composites processed by centrifugal casting, International Journal of Materials Science and Engineering, Vol. 3, No. 4, pp. 310-318, 2015.

[25] S. Mitrović, N. Miloradović, M. Babić, I. Bobić, B. Stojanović, D. Džunić: Wear behaviour of hybrid ZA27/SiC/graphite composites under dry sliding conditions, Tribological Journal BULTRIB, Vol. 3, pp. 142-147, 2013.

[26] S.C. Sharma, B.M. Satish, B.M. Girish, R. Kamath, H. Asanuma: Dry sliding wear of short glass fibre reinforced zinc-aluminium composites, Tribology International, Vol. 31, No. 4, pp. 183-188, 1998.

[27] S.C. Sharma, B.M. Girish, R. Kamath, B.M. Satish: Effect of SiC particle reinforcement on the unlubricated sliding wear behaviour of ZA-27 alloy composites, Wear, Vol. 213, No. 1-2, pp. 33-40, 1997.

[28] T.S. Kiran, M. Prasanna Kumar, S. Basavarajappa, B.M. Viswanatha: Dry sliding wear behavior of heat treated hybrid metal matrix composite using Taguchi techniques, Materials & Design, Vol. 63, pp. 294-304, 2014.

[29] S. Mitrović, M. Babić, F. Živić, I. Bobić, D. Džunić: Nanotribology investigations of composites based on ZA-27 alloy reinforced by Al_2O_3 particles, Tribology in Industry, Vol. 30, No. 1-2, pp. 33-39, 2008.

[30] S. Mitrović, M. Babić, I. Bobić: ZA-27 alloy composites reinforced with Al_2O_3 particles, Tribology in Industry, Vol. 29, No. 3-4, pp. 35-41, 2007.

[31] S.C. Sharma, M. Krishna, D. Bhattacharyya: Dry sliding wear behaviour of flyash reinforced ZA-27 alloy based metal matrix composites, International Journal of Modern Physics B, Vol. 20, No. 25-27, pp. 4703-4708, 2006.

[32] A. Vencl: Tribology of the Al-Si alloy based MMCs and their application in automotive industry, in: L. Magagnin (Ed.): *Engineered Metal Matrix Composites: Forming Methods, Material Properties and Industrial Applications*, Nova Science Publishers, New York, pp. 127-166, 2012.

Surface Engineering and Coating Tribology

15th International Conference on Tribology – SERBIATRIB '17

17 – 19 May 2017, Kragujevac, Serbia

THE ANTIFRICTIONAL COATINGS ON THE MOLYBDENUM BASE.

A. SAGALOVYCH[*], V. SAGALOVYCH, V. POPOV, A. KONONYHIN, V. BOGOSLAVZEV
Scientific technological Corporation "FED", Kharkov, 61023, Ukraine
*Corresponding author: iht@kharkov.ua

Abstract: *Friction and wear of the antifrictional complex coatings on the molybdenum base were under investigation. Coatings were obtained using complex vacuum-plasma technologies under reactive coatings deposition utilizing vacuum arc deposition of Mo-N coating and RF-magnetron deposition of MoS_2. Total coating thickness is 10 mkm.*

It was shown by means wear track profilography and acoustic emission investigation that such coatings are very effective working in pairs with hard coatings Ti-Al-N. During run-in period of exploitation such coatings shows low friction coefficient close to MoS_2, but they have much more resistance to wear in many times greater than MoS_2, and significantly more stable friction coefficients.

Keywords: *vacuum-plasma technologies, tribology, reactive coatings deposition*

1. INTRODUCTION.

Scientific technological Corporation "FED" conduct extensive work in the area of development and practical utilization of novel nanomaterials and technologies of obtaining such materials (multicomponent, mono and multilayer, nanostructured, gradient) of different functional application (antifrictional, hardening and others) for improvement performance of materials, units and samples of aircraft aggregates, as well as in the field of development of technological processes for the application of such coatings and equipment for their implementation.

The basis of technology is the processes of atomic-ion surface modification and the formation of nanolayer coatings from various elements and chemical compounds under the influence of a nonequilibrium low-temperature plasma.

The peculiarity of the developed coating processes lies in their complexity: different coating methods (plasma CVD, vacuum-plasma PVD (vacuum arc, magnetron), ion saturation and ion surface treatment) are combined in a single technological cycle.

For the application of functional multilayer composite coatings, experimental and technological equipment was developed and developed - the automated system Avinit [1], which allows the implementation of complex coating methods.

Avinit coatings are deposited on high-grade precision surfaces roughness (up to V = 11-12) without reducing the surface cleanliness class. Precipitation is carried out at low temperatures that do not exceed the tempering temperatures of the base material, which ensures the preservation of mechanical characteristics and the absence of warpage of the articles to be coated.

Correct choice of individual layers materials, deposition methods and optimization of technological parameters create prerequisites for the synthesis of materials with a complex of unique properties, including with exceptionally high hardness, strength, chemical stability, low coefficient of friction and increased wear resistance.

When developing new design solutions, the development of advanced technologies and materials with enhanced technical characteristics are of primary importance. One of the important areas of work in this regard is to increase the reliability and service life of friction units.

In connection with the sharp difference in the requirements for the properties of friction components in the volume and in the thin near-surface layer that determines the parameters of friction and wear, it is increasingly important to use new technologies for the application of protective, wear-resistant, antifriction and run-in coatings that enhance the possibilities of forming working layers.

MoS_2 (molybdenum disulphide) is the most widely used solid lubricant. Molybdenum disulphide has an extremely low coefficient of friction, lower than that of Teflon and graphite. The achievable friction coefficient is less than 0.05, varying depending on humidity and friction conditions.

Various low-temperature processes of deposition of MoS_2 coatings by magnetron sputtering are worked out.

The thickness of the coatings can vary, usually ranging from 1 to 10 microns. Coatings can be extremely thin and ultra-thin (0.1 micron or less), which is extremely important when coating the precision components.

The most significant drawback of such coatings is their very low wear resistance.

To increase their practical use, it is highly desirable that coatings, while maintaining a low friction coefficient at the level of pure molybdenum disulphide, have a significantly higher wear resistance.

It was shown in [2-4] that tribosystems based on superhard coatings (based on MoN

TiAlN) have low friction coefficients at a level of less than 0.07-0.09. After testing such friction pairs for wear no signs of increased wear, the working planes of samples covered with ▼ 10 *Avinit* C320 (310) and ▼ 10 *Avinit* C220 were not detected.

Such tribosystems have already found practical applications [5, 6].

Further improvements are associated with the creation of tribocouple designs with even lower coefficients of friction and increased wear resistance.

The technological capabilities of the *Avinit* installation allow us to proceed with the development of antifriction coatings based on the strengthened molybdenum disulphide of the following type:

- strengthened nanostructured coatings;
- strengthened nanolayer coatings;
- strengthened composite coatings (based on molybdenum disulphide == molybdenum nitride on surfaces with low roughness followed by mechanical run-in during operation).

In this paper, the results of studies of reinforced composite coatings of *Avinit* on the basis of molybdenum and a study of their tribological characteristics are presented.

2. RESEARCH METODOLOGY.

For the coatings deposition, the *Avinit M* and *Avinit C* units of the *Avinit* installation were used. The coatings were applied on the samples used in the tests on the friction machine, according to a specified program, in which the time, sequence and operating conditions of the evaporators, the reaction gas supply system were set.

Metallographic studies of samples with coatings (microsections, hardness of coating, determination of surface geometry after coating) were carried out using metallographic, chemical, X-ray and micro-X-ray spectroscopy, microhardness and roughness measurements of friction surfaces. The surface roughness of the samples before

and after the coating was measured on a profilometer - profilograph.

Metallophysical studies of the obtained coatings were performed with a scanning electron microscope JSM T-300.

Tribological studies on friction and wear were carried out using an improved serial friction machine 2070 SMT-1 in the "ring-ring" scheme.

Before the tests, the samples were washed with gasoline, dried at a temperature of 70°C. Before and after the tests, the samples were weighed on analytical scales VLR-200 with an accuracy of 10^{-5} g to assess the wear resistance of coatings.

Friction mode - boundary lubrication conditions (working fluid consumption - 2 liters / hour).

Working fluid - aircraft fuel TS-1 with a class of purity 6 ... 8.

Friction conditions:

- speed of rotation of a driving shaft 500 min^{-1};

- a stepwise increase in the load until the scoring is formed or to the maximum possible value;

- dwell time at each load stage 15 ... 20 min.

Working fluid for lubrication was supplied through the internal openings of the samples.

In the course of experiments, we recorded:

- the friction moment (recalculated in the coefficient of friction), the magnitude of which was judged on the mechanical losses in tribosystems;

- The temperature of the elements was continuously recorded in real-time tests in close proximity (1 mm) from the friction zone, using a sliding thermocouple.

To determine the scuffing of the surface layers of materials of friction pairs, the load was carried from P_{min} to the critical value P_{cr} at which the scuffing takes place.

In addition, we measured the rate of wear by the acoustic emission method. The wear rate was recorded for a time of 20 msec in relative wear units.

To reproduce the test results for wear, the surface of the end surfaces was controlled by

the contact area: not less than 90% of the working surface of each sample.

3. EXPERIMENTAL PART.

3.1. The essence of the design.

The tribocouple (the main sample A and the counterpart sample B) is similar to that tested in [2-5] - a sample A with a coating of ▼10 *Avinit* C320 (310) (based on TiAlN) 1.5-2 µm thick and sample B with a coating ▼10 *Avinit* C220 (based on MoN) with a thickness of 1.5-2 µm.

However, the counter sample B has a working surface grindedwith a roughness class ▼ 7 … 8, on which is deposited an unseparated MoN coating with a thickness of ≈ 10 µm with a roughness class of ▼ 7 … 8. Then MoN coating is applied to the MoS_2 coating with a thickness of ≈ 5 … 10 µm RF magnetron sputtering. Finally, the working surface has a roughness across the topography: - Ra 1.9 (▼ 6b). It is assumed that the MoS_2 coating fills the submicroscopic irregularities of the MoN rough microrelief. During operation, as the MoS_2 coating wears out on the working surface, an dispersed structure is formed on the basis of MoN- MoS_2 remaining in the unevenness of the microrelief, providing higher antifriction values in the operating loading range

1. Preparation of samples A (steel 30X3VA, 30 … 35 HRC) under Ti-Al-N deposition.

The working surface is machined to: - non-flatness ≤ 0.002 mm, roughness -Ra 0.104 (▼ 10). Samples A are nitrided *Avinit N* [7] h = 0.2 … 0.3 mm, H> 700 HV. After nitriding, the working surface has a roughness: - Ra 0,397 (▼ 8). To reduce roughness, the working surface of samples A is lapped manually on a cast iron plate without the use of abrasive. Lapping time - 2 … 3 min. Before obtaining on the entire working surface a new lapping relief with a roughness: Ra 0.020 (▼ 12). The surface of samples A is coated with Ti-Al-N (Avinit C310). Finally, the working surface has a roughness: - Ra 0.060 (▼ 10в … 11б).

2. Preparation of samples B (30X3VA, 28 … 33 HRC) under (MoN + MoS$_2$)

The working surface of the samples is grinded with a cleanliness class of ▼ 7 … 8. On the working surface, an unseparated MoN coating with a thickness of ≈ 10 μm is deposited. MoN coating is coated with MoS$_2$ coating with a thickness of ≈ 5 … 10 μm RF magnetron sputtering. Finally, the working surface has a roughness across the topography: - Ra 1.9 (▼ 6b).

Stage 1. Conducting tests to determine the coefficient of friction and wear resistance of the tribosystems Avinit C310 (TiAlN) - MoN = 10 μm + MoS$_2$ = 5 … 10 μm (operating time 0 … 8 hours).

Tribopair No. 1 for testing in phase 1
- Sample A - Avinit C310 coating (TiAlN);
- sample B - coating MoN = 10 μm + MoS2 = 5 … 10 μm

Changes in the friction coefficient and temperature in the contact zone along the test time are shown in Fig. 1.
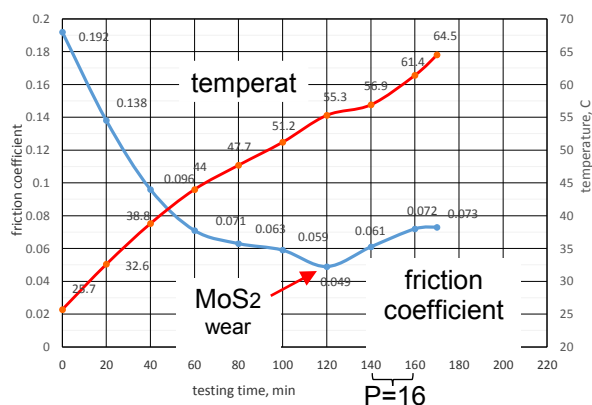

Fig. 1.

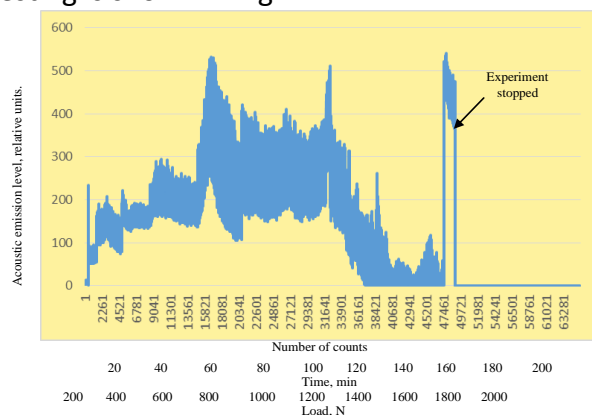The level of acoustic emission by time of testing is shown in Fig.2

Fig. 2.

The best level of antifriction the tribosystem shows in the load range from 1000 to 1200 N, which is apparently explained by the operation of the MoS$_2$ coating, which fills submicroscopic irregularities in the microrelief providing high antifriction rates in the operating loading range. Tribosystem has a high level of bullying (more than 2000 N).

The change in the level of acoustic emission (based on the results of three experiments) indicates an almost complete run-in of the tribosystem in the range of loads 1200 … 1600 N.

Above the loads of 1000 - 1200 N, the level of tribotechnical characteristics and acoustic emission is unsatisfactory. The level of the acoustic emission signal increased sharply and persisted for 5 minutes. At a load of more than 1000 N there is a transition from normal wear to microcutting.

At the end of the tests for bullying, on the working surface of sample A local crescent wear of the Ti-Al-N coating was revealed up to the main material, adjacent to the inner cylinder of the sample. Scraps of coating on the boundaries of the worn zone are not available. The weight wear of sample A was 1 mg, the weight wear of sample B was 0.0000 mg.

The working surface of sample B is in a satisfactory state

This behavior of the tribosystem is not typical for fatigue wear (by the nature of acoustic emission and the change in the friction moment). A possible cause is the presence of "grinding" of the surface of sample A by the surface of sample B.

At the same time, the profilogram of the sample surface shows that during the test, some running-in of the sharp cutting edges of the MoN coating occurred.

Since the working surface of sample A was worn out and the surface of specimen B was in satisfactory condition with improved profilographic characteristics and allowed to be used for subsequent tribological tests, it was decided in the second stage to test the tribocouple with a new sample A and sample B tested in the first stage.

Stage 2. Conducting tests to determine the coefficient of friction and wear resistance of the tribosystems Avinit C310 (TiAlN) - MoN = 10 μm + MoS2 = 5 ... 10 μm (operating time 8 ... 16 hours).

Tribopair No. 2 for testing in phase 2

- Sample A - Avinit C310 (TiAlN) coating, manufactured for both Stage 1;
- Sample B - Sample B after the first stage.

The coefficient of friction and temperature in the contact zone in time for wear resistance tests are shown in Fig. 3.
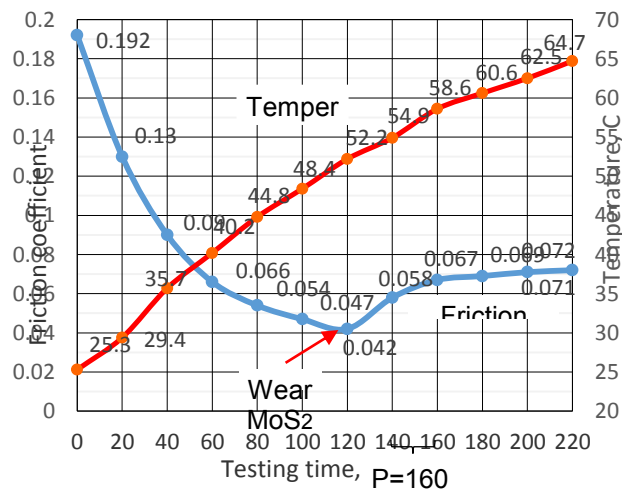

Fig. 3.

The level of acoustic emission by the time of the test is shown in Fig. 4.

The change in acoustic emission signals is not typical for fatigue wear (continuous emission), and the level of acoustic emissions signals practically does not change during the test, being approximately 10 rel. Units. It can be assumed that there is a mutual process of "grinding" of the working surfaces of samples A and B during the testing.
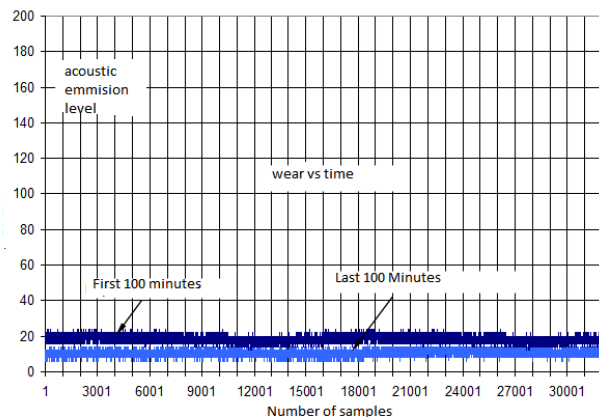

Fig. 4.

The analysis of the profilograms shows that the surface roughness of sample A remains practically unchanged (the surface roughness of sample A after the tests is Ra 0.046); the surface roughness of specimen B is substantially improved (the surface roughness of sample B after the tests is Ra 0.705).

At the same time, the wear rate is significantly lower than that of pair No. 1, both in terms of acoustic emission indexes and in terms of weight wear. The weight wear of sample A is 0.0001 g; Sample B 0.0002 gr.

According to the level of tribotechnical characteristics and acoustic emission, Tribopar No. 2 has fairly good indicators.

Taking into account the good condition of the tribo-pair No. 2 after the tests, which allows its use for subsequent tribological tests, it was decided to continue the trial of tribo-pair No. 2 at the third stage.

Stage 3. Conducting tests to determine the coefficient of friction and wear resistance of the tribosystems Avinit C310 (TiAlN) - MoN = 10 μm + MoS2 = 5 ... 10 μm (operating time 16 ... 24 hours).

Tribopair No. 3 for testing in Phase 3

- continuation of tribopair test No. 2.

The initial state of the working surface profile of sample A coating of Avinit C310 (TiAlN) is shown in Fig. 5 (roughness Ra 0.04)
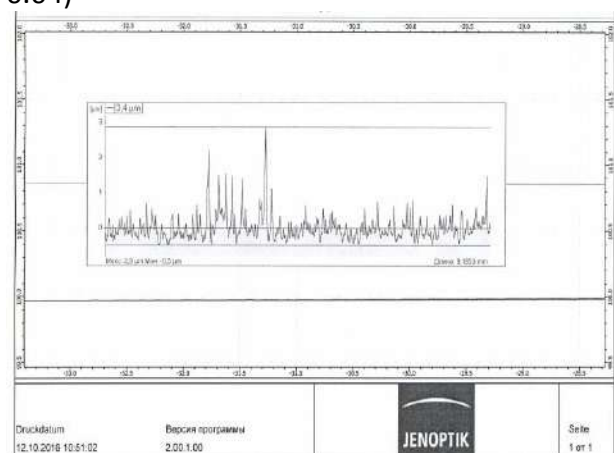

Fig. 5

The initial state of the working surface profile of sample B is MoN = 10 μm + MoS2 = 5 ... 10 μm (operating time 8 ... 16 hours) is shown in Fig. 6.
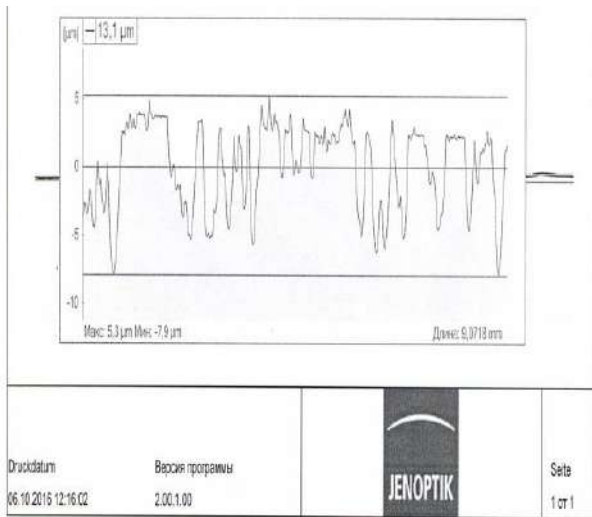
Fig. 6.

The coefficient of friction and temperature in the contact zone in time are shown in Fig. 7.
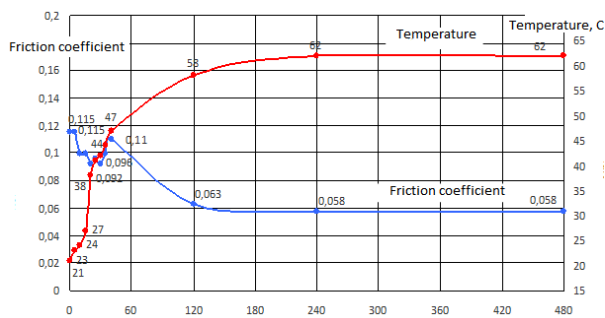
Fig. 7.

The level of acoustic emission by the time of the test is shown in Fig. 8/
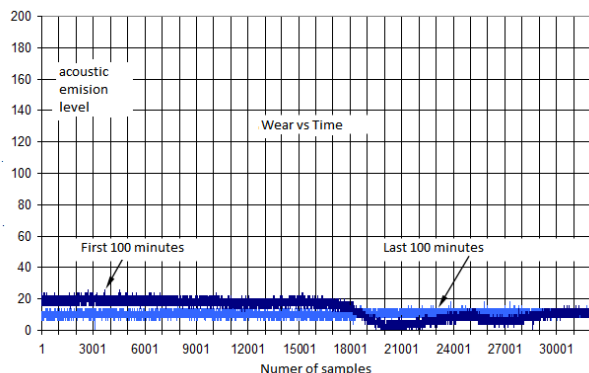
Fig. 8.

It is noted that the area of the working surface of sample B, which has a sheen (run-in visually), increased in comparison with the state after the first 16 hours of wear testing. The surface roughness of sample A after the tests R a 0.025. The roughness of the surface of sample B after the wear tests is Ra 0.108. Weight wear of sample A - 0.0001 gr, sample B - 0.0001 gr.

The tribosystem has an abnormally low rate of wear rate.

On the level of tribotechnical characteristics and AE, tribopar No. 3 has high indexes, better than pairs No. 1 and No. 2.

The condition of the profile of the working surface of sample A is the coating of Avinit C310 (TiAlN) shown in Fig. 9 (roughness Ra 0.02).
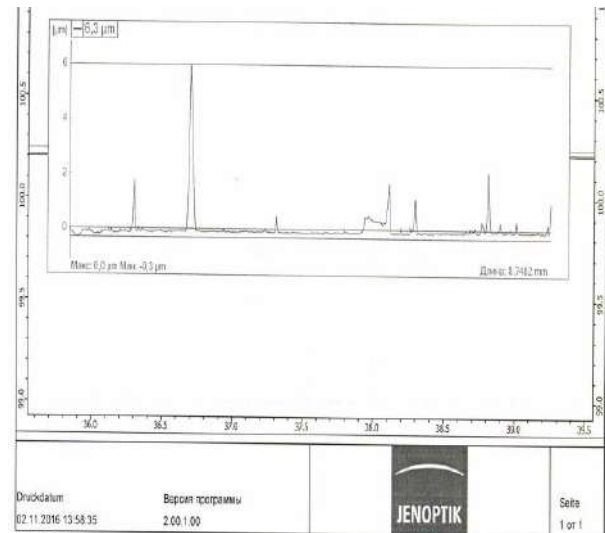
Fig. 9.
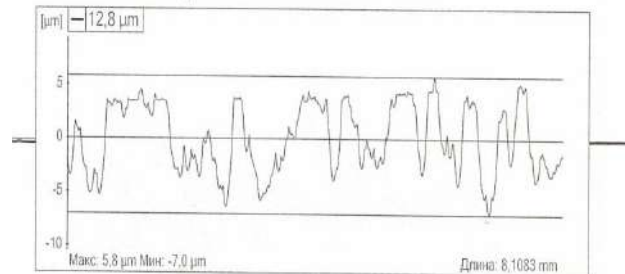
Fig. 10.

The state of the profile of the working surface of the sample is shown in Fig.10. The coating MoN = 10 μm + MoS2 = 5 ... 10 μm (operating time 16 ... 24 hours).

4. CONCLUSIONS

Tribological tests using the method of acoustic emission and profilographic measurements have shown that the improved antifriction hardened composite coatings of **Avinit** MoN-MoS$_2$ have high tribological characteristics when operating in pairs with superhard coatings based on Ti-Al-N. During the run-in during operation, keeping low

values of friction coefficients close to MoS_2, they have a much higher resistance to wear, many times higher than the resistance of MoS_2, and much more stable friction coefficients, which is explained by the MoS_2 coating that fills submicroscopic irregularities of the microrelief providing High rates of antifriction in the operating load range.

5. REFERENCES.

[1] O. Sagalovych, V. Popov, O. Kononikhin, V. Sagalovych, Avinit device for coating multilayer functional coatings, Physical engineering of a surface, Vol. 8, pp. 336-347, 2010.

[2] O. Sagalovych, V. Sagalovych, V. Popov ea., Coating Avinit Experimental stydiing – Aviacionnajo-kosmicheskaja tehnika I technologija, Technologia proizvodstva letatelnih apparatov, pp. 5-15, 2011.

[3] O. Sagalovych, V. Popov ea.,The Tribological Investigation of Multicomponent Multilayered Ion-plasma Coatings Avinit, Proc. 12th Intern. Conf. on Tribology SERBIATRIB '11, Kragujevac, Serbia.

[4] O. Sagalovych, V. Popov ea. The Tribological Investigation of Multicomponent Multilayered Ion-plasma Coatings *Avinit*. Tribology in industry, Vol. 33, No. 1, pp. 79-86, 2011.

[5] O. Sagalovych, V. Sagalovych ea. Pat. UA № 108279, 10.04.15.

[6] O. Sagalovych, V. Sagalovych ea. Pat. UA № 109053, 10.07.15.

[7] O. Sagalovych, V. Sagalovych ea. Pat. UA № 107408, 25.12.14.

TRIBOLOGICAL PROPERTIES OF WC-Co/NiCrBSi AND Mo/NiCrBSi PLASMA SPRAY COATINGS UNDER BOUNDARY LUBRICATION CONDITIONS

Aleksandar VENCL[1],*, Mihailo MRDAK[2], Pavol HVIZDOS[3]
[1]University of Belgrade, Faculty of Mechanical Engineering, Belgrade, Serbia
[2]Research and Development Centre, IMTEL Communications a.d., Belgrade, Serbia
[3]Institute of Materials Research, Slovak Academy of Sciences, Košice, Slovakia
*Corresponding author: avencl@mas.bg.ac.rs

Abstract: *The tungsten carbide based WC-Co/NiCrBSi (50/50) and molybdenum based Mo/NiCrBSi (75/25) coatings were investigated under boundary lubricated sliding conditions, and their tribological properties were analysed and compared. These two coatings are in service for a long time, but there are very few papers dealing with their tribological properties, especially in lubricated sliding conditions. The NiCrBSi self-fluxing alloy is one of the popularly used materials for thermal sprayed coating, with relatively high hardness, reasonable wear resistance and high temperature corrosion. Tungsten carbide (WC) is one of the most widely used commercial hard coating materials, and is added to the NiCrBSi coating to improve its hardness and wear resistance. Molybdenum (Mo) is added to the NiCrBSi coating to reduce its coefficient of friction, i.e. to improve its dry sliding wear resistance. The results showed that WC-Co/NiCrBSi coating was more wear resistant, but caused higher wear of the counter-body material. Coefficients of friction were similar for both coatings.*

Keywords: *coatings, tungsten carbide, molybdenum, atmospheric plasma spraying, boundary lubrication, friction, wear.*

1. INTRODUCTION

Thermal spraying is widely used coating deposition method because it presents process flexibility and coating quality in combination. It represents a group of techniques for the coating deposition in which both, thermal and mechanical energy is applied for deposition of the material. There are several different processes for thermal spray coating deposition, and the main classification, into two categories, can be performed according to the thermal energy source used for melting of the feedstock material: flame (combustion) and electrical (electrical discharge) energy. The most widely used processes for thermal spray coating deposition are: flame spraying, electric arc wire spraying, atmospheric plasma spraying and high velocity oxygen fuel spraying [1].

One of the popularly used materials for hard thermal sprayed coating is a NiCrBSi self-fluxing alloy. This coating have several interesting properties, e.g. relatively high hardness, reasonable wear resistance and high temperature corrosion [2]. However, numerous

studies have been undertaken with the aim of improving the wear resistance of this coating, and these studies have pointed in the direction of adding ''hard'' particles like (WC, NbC, Cr_3C_2, TiC, SiC, VC, WC-Ni) to the base formed by the secondary material [3]. Among commercial hard coating materials, tungsten carbide (WC) is the most widely used for wear resistance coating for its high hardness. Cobalt (Co) binder prealloyed tungsten carbide powder was generally used to complementing its limited toughness [4], so the WC-Co powder particle consists of the hard tungsten carbide grain imbedded in tough cobalt matrix. The NiCrBSi self-fluxing coating performs well as a wear resistant coating under low stress. However, at higher stress in unlubricated sliding condition it begins to deform, which may cause seizure as the stress increases. Molybdenum (Mo) is added to the coating to reduce the coefficient of friction, thus, improving its dry sliding wear resistance [5]. In addition, Mo can form metallurgical bonding with many metals and decrease cracking sensitivity of coating in thermal spray processes [6].

The first powder used in this research (WC-Co/NiCrBSi) was a blend of powders composed of 50 wt. % hard phase constituent WC-Co and 50 wt. % self-fluxing alloy NiCrBSi. According to the powder manufacturer, deposited coating has high erosive and abrasive wear resistance. The WC-Co/NiCrBSi coatings are very dense, hard and smooth, with good adherence between coating and substrate. The second powder used in this research (Mo/NiCrBSi) was a blend of powders composed of 75 wt. % Mo and 25 wt. % self-fluxing alloy NiCrBSi. According to the powder manufacturer, deposited coating has high wear resistance, low coefficient of friction and good scuffing resistance. It is compatible with the most of the materials, especially with iron base alloys. The Mo/NiCrBSi coatings are homogenous with

less than 3 % of porosity and with good adherence between coating and substrate. Both coating can be used unfused, resulting in no metallurgical bond to the substrate.

These two coatings are in service for a long time, but there are very few papers dealing with WC-Co/NiCrBSi [4,7-9] and Mo/NiCrBSi [5,6,10-13] tribological properties, especially in lubricated sliding conditions [14]. The aim of this paper is to investigate and compare the tribological properties of these two coatings under lubricated sliding conditions.

2. EXPERIMENTAL DETAILS

2.1 Materials

Two spray powders were used in the experiment, i.e. tungsten carbide based powder (Metco 34F) and molybdenum based powder (Metco 505). The chemical compositions of the powders are shown in Table 1.

The Metco 34F powder is composed of a fine tungsten carbide-cobalt powder blended with a fine nickel-chrome self-fluxing alloy powder. It contains 50 wt. % of tungsten carbide-cobalt and 50 wt. % of nickel-chrome self-fluxing alloy. Particle granulation of this spray powder blend was −53/+15 μm. The Metco 505 powder is a blend of molybdenum and nickel-chrome self-fluxing alloy. The share of the individual powder in the blend was 75 wt. % of molybdenum and 25 wt. % of nickel-chrome self-fluxing alloy. This spray powder blend shows spherical morphology with particle granulation −90/+15 μm. The substrate material was a stainless steel (EN X15Cr13). This substrate material was used without any heat treatment. For the convenience, coatings attained using Metco 34F and Metco 505 powders are hereafter referred to as 34F and 505, respectively.

Table 1. Chemical composition (wt. %) of used powders

Powder*	WC12Co	Mo	Ni	Cr	B	Si	Fe	C
Metco 34F	50	–	33	9	2.0	2.0	3.5	0.5
Metco 505	–	75	17.75	4.25	0.8	1.0	1.0	0.2

*Commercial brand names of Metco Inc.

Atmospheric plasma spraying (APS), with Plasmadyne SG-100 plasma spray gun, was utilized in the experiment, for both coatings deposition. In both cases specimen holder was rotated at constant speed of 500 mm/s, while the traverse speed of a spraying gun was maintained constant at 4 mm/s. Fusing of both coatings after the deposition was not performed, i.e. coatings were tested in unfused conditions. Before the spraying process, the surface of the substrates was activated and preheated. Activation (roughening) was done with white fused alumina (Al_2O_3) using particle sizes of 700 – 1500 μm. Before the deposition, the substrates were preheated to 200 °C. The coating thickness for all specimens (after deposition and machining) was approximately 300 μm. The detailed spray parameters are summarised in Table 2 [15].

Table 2. APS spray parameters values used for coating deposition

Spray parameter	Coating	
	34F	505
Primary plasma gas (Ar), l/min	47	47
Secondary plasma gas (H_2), l/min	12	10
Electric current, A	500	500
Electric potential difference, V	64	64
Powder carrier gas (Ar), l/min	4	5
Powder feed rate, kg/h	1.8	2.4
Spray distance, mm	125	130

2.2 Microstructure analysis and hardness testing

The microstructure of the coatings was analyzed with scanning electron microscope (SEM), equipped with energy dispersive spectrometer (EDS), where the coatings were sectioned perpendicular to the coated surface. Metallographic samples were prepared in a standard way, applying grinding and polishing, with no etching.

Measurements of the surface microhardness (HV 0.3 and HV 1) were performed on surface of the samples (not on cross-section) using Vickers microhardness tester under the loads of 300 g and 1 kg, and dwell time of 5 s. Microhardness HV 0.3 is the standard parameter for thermal sprayed coatings, while the microhardness HV 1 is measured to diminish the influence of different hardness of coatings phases/layers (WC-Co and NiCrBSi, i.e. Mo and NiCrBSi). At least five measurements were made for each sample in order to eliminate possible segregation effects and to obtain a representative value of the coating microhardness.

2.3 Tribological testing

Tribological testing were carried out on block-on-disc tribometer, under lubricated sliding conditions, in ambient air, at room temperature (about 25 °C), in accordance with ASTM G 77 standard [16]. A schematic diagram of the tribometer is presented in Figure 1. Rectangular blocks (6 × 16 × 12 mm) of the tested coatings were used as wear test specimens. The disc of 45 mm diameter and 10 mm thickness was made of steel C60E (428.6 HV 1). The length of the line contact between the block and the disc was 6 mm. Lubrication was provided by the rotation of the disc which was sunk into the oil container (Fig. 1). The lubricant was mineral engine oil (SAE 15W-40, ACEA E3). Surface roughness of blocks and discs was approximately *Ra* = 0.3 and 0.5 μm, respectively.
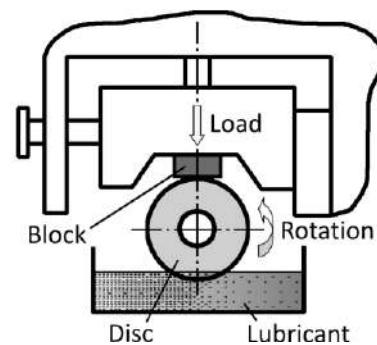
Figure 1. Schematic diagram of block-on-disk testing

Before and after testing, blocks and discs were degreased and cleaned with benzene. Wear scars on blocks were measured according to [16] with accuracy of 0.05 mm, after each test, to calculate the volume loss. Discs were weighed with accuracy of 0.1 mg, before and after each test, to calculate the mass loss. Mass loss is then converted to volume loss using the known value of disc density (7.85 g/cm^3).

Values of the oil temperature, coefficient of friction, normal and friction force were continuously monitored during testing and through data acquisition system stored in the PC. After testing, worn surfaces of blocks were examined using the SEM/EDS analysis.

The tests were carried out under the following conditions: sliding speed of 0.5 m/s, sliding distance of 3000 m and normal load of 400 N. In order to achieve a higher confidence level in evaluating test results, at least three replicate tests were conducted for each coating.

3. RESULTS AND DISCUSSION

3.1 Microstructure and microhardness

The microstructures of the investigated coatings (Fig. 2) were typical for thermal spray coatings and consist of elongated splats of molten powder, which form a curved lamellar structure, and oxide layers and inclusions in between [1]. Microstructure of the coating 34F (Fig. 2a) consists of WC-Co and NiCrBSi layers, which is confirmed with the EDS analysis (Figs. 3a and 3b). Presence of micropores was also noticed (denoted with arrows in Fig. 2a). In the microstructure of coating 505 (Fig. 2b), two distinct layers could be also clearly noticed. There are the Mo layers which form a base of the coating, and the NiCrBSi layers which are evenly distributed between the Mo layers. This is also confirmed with the EDS analysis (Fig. 3c

and 3d). Micropores, as well as, interlamellar pores were noticed in coating 505 (denoted with arrows in Fig. 2b). Detail microstructural analysis of the obtained coatings is presented elsewhere [15,17,18].

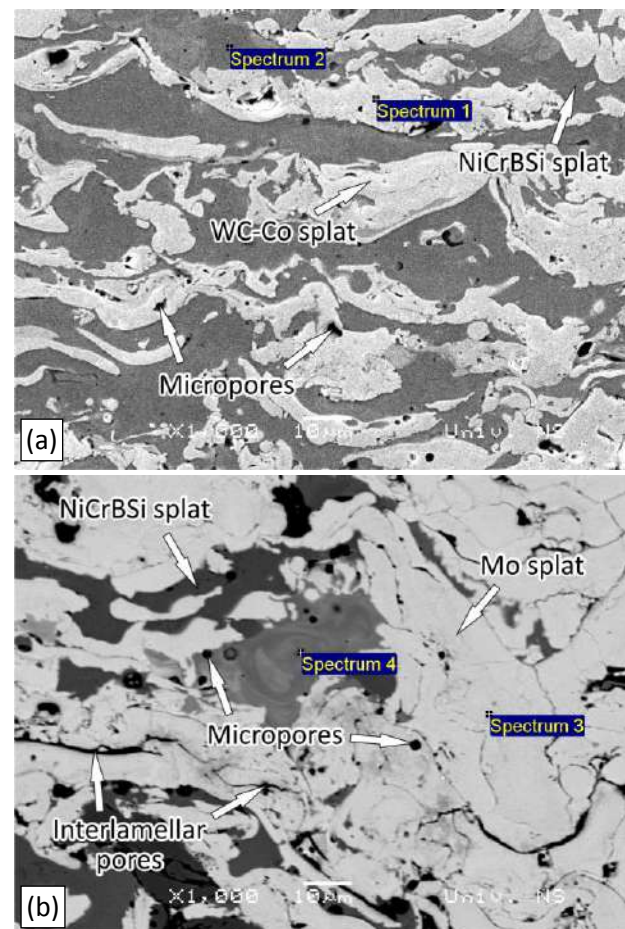**Figure 2.** Microstructures (SEM) of the obtained coatings, no etching: (a) coating 34F and (b) coating 505
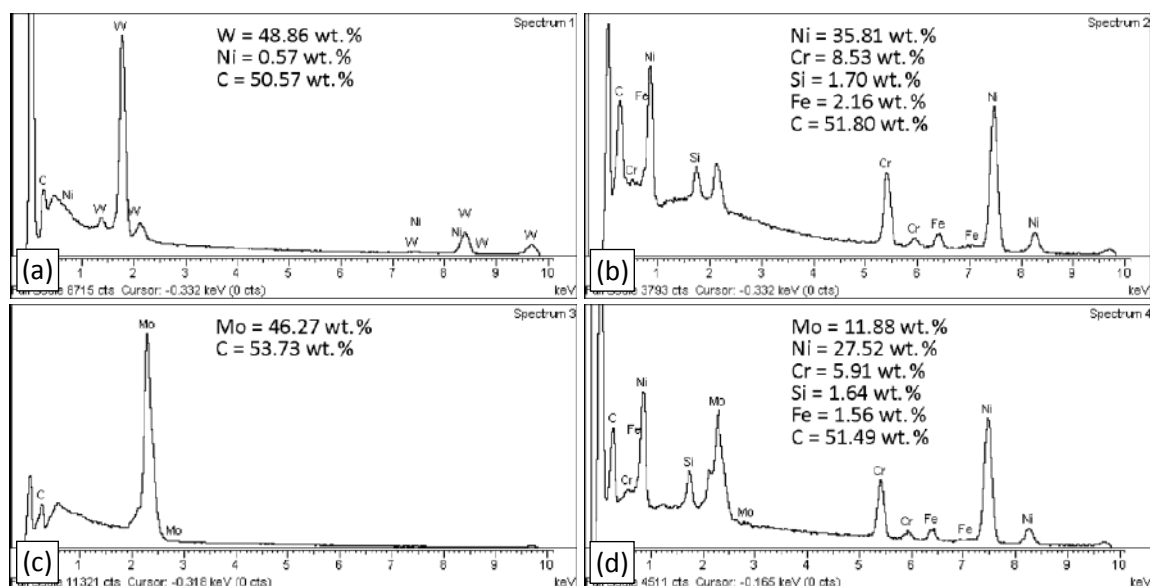

Figure 3. Results of EDS analysis of: (a) and (b) coating 34F (WC-Co/NiCrBSi) and (c) and (d) coating 505 (Mo/NiCrBSi), see Figure 2

The results of hardness measurements are shown in Figure 4. As expected, hardness values measured with higher load (HV 1) were slightly lower. The variation in hardness for both coatings was satisfactory (about 5 %). Microhardness values of coating 34F (WC-Co/NiCrBSi) was higher than values of coating 505 (Mo/NiCrBSi) due to the presence of hard WC phase. Obtained values are in correlation with cross-section values of the microhardness, taking into account that the hardness of NiCrBSi layers is significantly lower than the hardness of WC-Co layers [17], i.e. significantly higher than the hardness of Mo layers [18]. No matter what, hardness of discs (428.6 HV 1) was lower than both coatings and than all coatings layers.
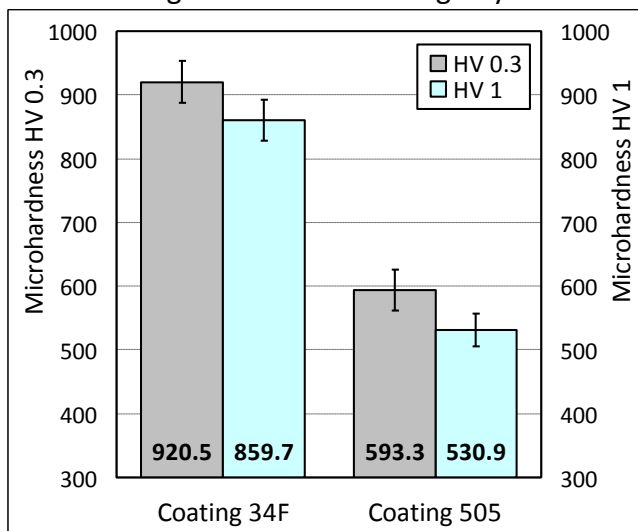

Figure 4. Microhardness of tested coatings

3.2 Tribological properties

Obtained average steady-state values of the coefficient of friction are presented in Figure 5. The results indicate good repeatability of the test, i.e. standard deviations were less than 8 %. The lubricant temperature was also continuously monitored during the tests. Since it was not controlled, it was rising during the tests and reaches the near steady-state values at the end of the tests. These near steady-state values are used to calculate the temperature rise during each test, having in mind that the lubricant temperature at the beginning of the tests was close to room temperature (about 25 °C). The average values of these temperature rises are also presented in Figure 5.
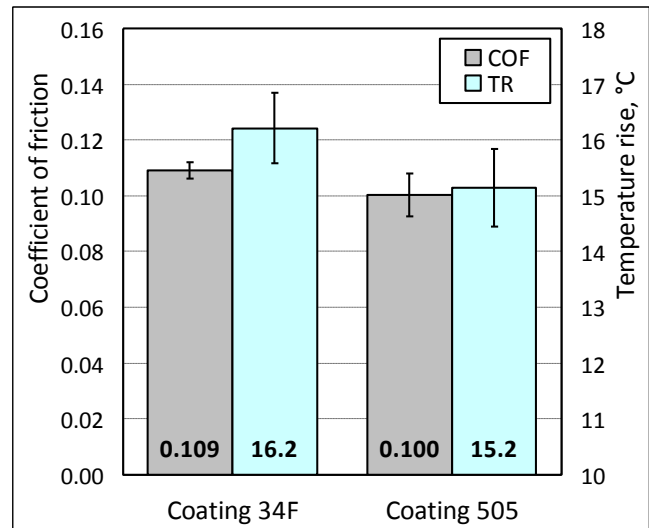

Figure 5. Steady-state values of the coefficient of friction and lubricant temperature rise during testing

Values of both coefficients of friction correspond to the approximate experimental values for contact pairs under boundary lubrication conditions, which are from 0.05 to 0.15 [19,20]. According to the elastho-hydrodinamic theory for line contact, calculated lubricant minimal film thickness were very low (approximately 0.3 µm) for both contact pairs. This also suggest that the sliding was performed in the boundary lubrication regime, since the approximate values of the surface roughness of blocks and discs was approximately Ra = 0.3 and 0.5 µm, respectively. Since most of the energy lost due to the friction is released as heat, higher coefficient of friction will induce higher temperature. This explains the correlation between these two values obtained in this study for different contact pairs (Fig. 5).

Coefficient of friction and oil temperature change during the test were similar in all tests and for both contact pairs. Between two contact pairs, coating 505 (Mo/NiCrBSi) gives slightly lower coefficient of friction. It is, most probably, due to the presence of Mo in this coating, which should decrease the dry sliding friction [5]. Relatively high value of the coefficient of friction that gives coating 34F (WC-Co/NiCrBSi) could be due to the presence of protruded hard WC phase and unfavourable proportion of the components in powder blend. Kekes et al. [9] investigated, under dry sliding conditions, WC-Co-Cr/NiCrBSi coatings with different fractions (from 0 to 100 wt. %) of WC-

Co component, and showed that 50 wt. % of WC-Co-Cr give the highest coefficient of friction.

Values of the wear rate of both of contact pair elements (block and disc) are presented in Figure 6. The wear rate of counter-body (disc) is very meaningful when the total clearance between tribological elements is of importance, and that is why it was also calculated. Taking into account significant differences in structure homogeneity of the coatings (Fig. 2), the repeatability of the wear rates of blocks, in terms of standard deviations, is satisfactory (within 10 %). Since the wear values were not measured continuously, i.e. during the test, the results in Figure 6 show total wear rates, which are usually higher than steady-state values.
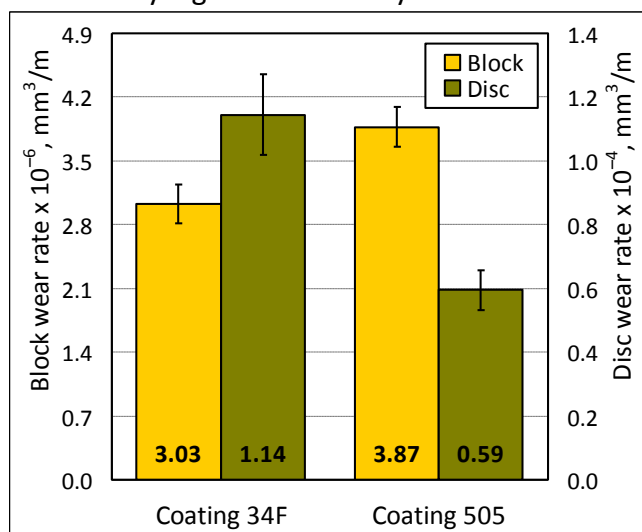

Figure 6. Total wear rates of tested contact pairs, i.e. blocks (coatings) and discs

Taking into account normal load of 400 N, wear factor values could be calculated [21] as: 7.6×10^{-9} mm^3/Nm (coating 34F), 9.7×10^{-9} mm^3/Nm (coating 505), 2.9×10^{-7} mm^3/Nm (disc in contact with coating 34F) and 1.5×10^{-7} mm^3/Nm (disc in contact with coating 505). These wear factor values (both for coatings, as well as, for steel discs) correspond to the literature data for metallic materials in sliding contact, under boundary lubricated condition, which are from 10^{-9} to 10^{-6} mm^3/Nm) [22]. It is interesting to notice that coating 34F wear less, but caused higher wear of the counter-body (disc) material.

Obtained wear values of investigated coatings (Fig. 6) are in correlation with their hardness values (Fig. 4), i.e. coating 34F (WC-

Co/NiCrBSi) was harder and showed higher wear resistance, and vice versa. In the case of coating 34F, hard WC particles protruded from the matrix protected the matrix from wear. Something similar was observed, although in slurry erosive wear testing, by Lu et al. [8]. The protruded WC particles also caused higher wear of steel disc when it was in contact with coating 34F (Fig. 6). On the other hand, coating 505 (Mo/NiCrBSi) showed higher wear value due to the fact that this blend mixture of Mo and NiCrBSi powders do not show the best wear resistance under dry sliding conditions. Niranatlumpong and Koiprasert [5] investigated, under dry sliding conditions, Mo/NiCrBSi coatings with different fractions (from 0 to 100 wt. %) of Mo powder in the blend, and showed that 75 wt. % of Mo had the highest wear.

Disc wear rates were much higher than blocks wear rates in both cases (more than 37 and more than 15 times, for contact with coating 34F and with coating 505, respectively). This is partially due to the lower hardness of the discs and partially due to the high initial roughness of the discs. Taking into account the diameter of the discs (45 mm) and length of the line contact between the block and the disc (6 mm), wear rate of 1×10^{-4} mm^3/m corresponds to the volume of the hollow cylinder of approximate thickness of 0.4 μm. This thickness corresponds very well to the initial roughness of the discs (Ra = 0.5 μm).

Wear mechanism analysis showed that the dominant wear mechanism was light two-body abrasion (Fig. 7). There is no evidence of the adhesive wear or plastic flow of the coatings material on the surface. Only shallow abrasive scratches can be noted in the sliding directions (denoted with black arrows in Fig. 7). Discs roughness was relatively high, but the hardness was much lower, so the main wear of the coatings was in the running-in period. Diagonal abrasive traces are consequences of machining (initial coating roughness). These machining traces are still visible on both coatings worn surfaces, suggesting low intensity of wear. Nevertheless, machining traces on coating 34F worn surfaces are more visible, confirming the lower wear of this coating.
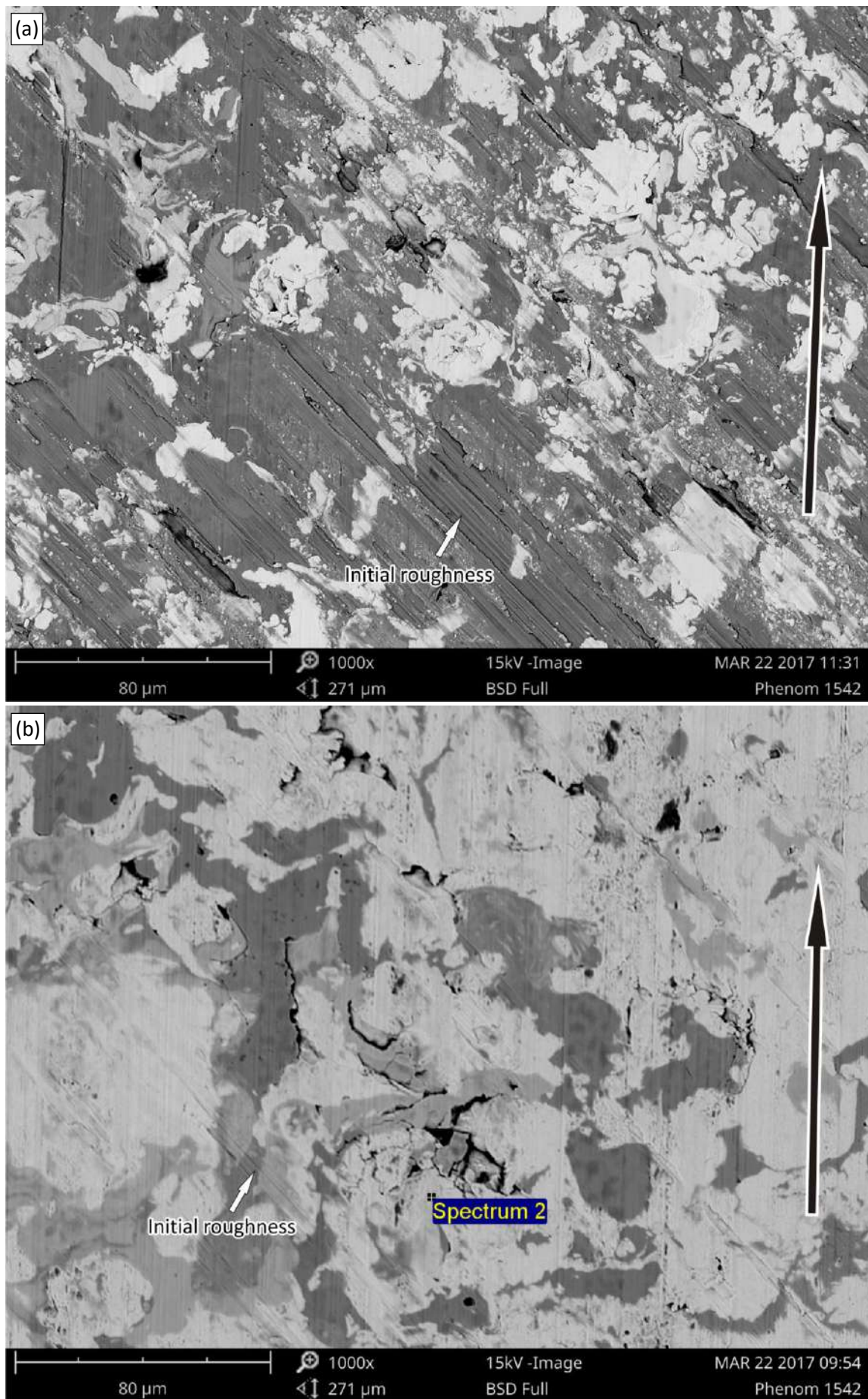
Figure 7. Worn surfaces (SEM): (a) coating 34F and (b) coating 505; counter-body sliding directions are denoted with black arrows

Worn surface of coating 34F was covered with small white particles (Figs. 7a and 8a). These particles are the result of larger WC particles fragmentation, which is confirmed with the EDS analysis (Spectrum 1 on Fig. 8a). The results of EDS analysis are shown in Table 3. These small and hard WC particles probably contributed, through the tree-body abrasion, to the higher wear of steel disc, when it was in contact with coating 34F (Fig. 6). Direction of WC fragmentation is the same as the direction of machining, so it is reasonable to conclude that the fragmentation mainly occurred before wear testing, i.e. during machining. These small WC particles were impressed into the softer NiCrBSi layers, which can be seen on SEM surface topography image (Fig. 8b). Presence of protruded larger WC particles, which protected the matrix, could be noticed on the same image.

Figure 8. Worn surface (SEM) of coating 34F: (a) backscatter electron detector image and (b) surface topography image

Figure 9. Worn surface (SEM) of coating 505: (a) backscatter electron detector image and (b) surface topography image

Table 3. Results of EDS analysis on the worn surfaces of coatings (chemical composition are in wt. %)

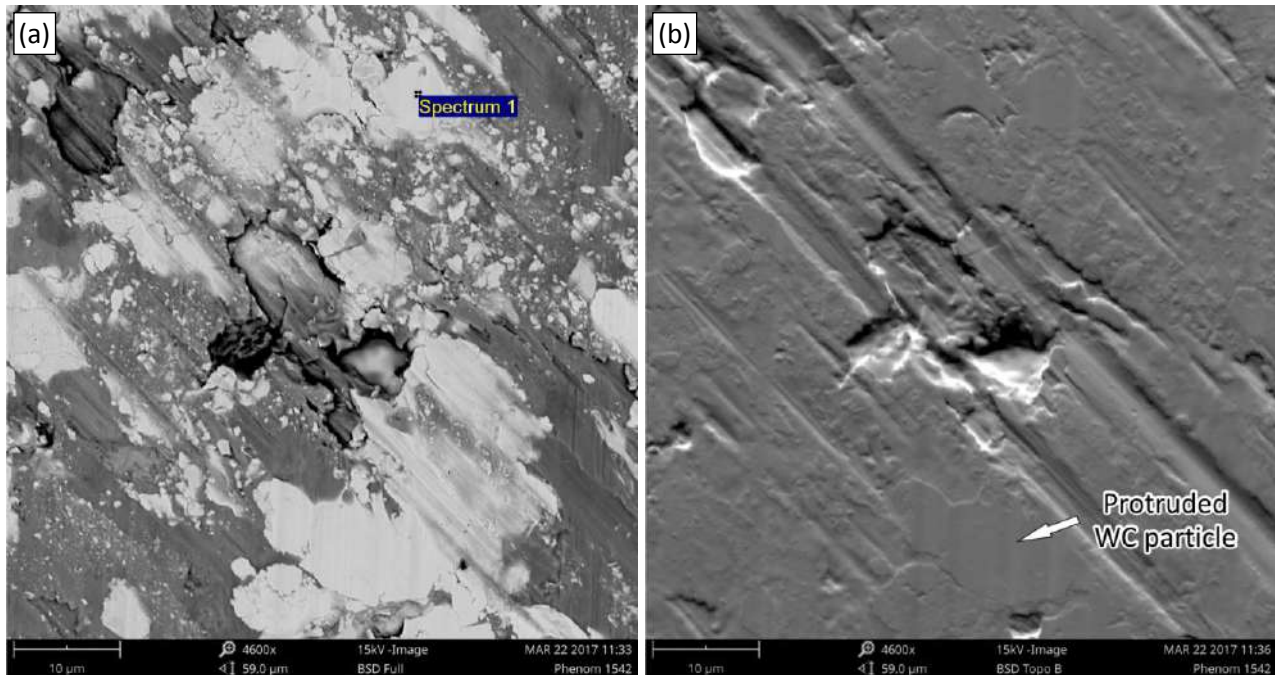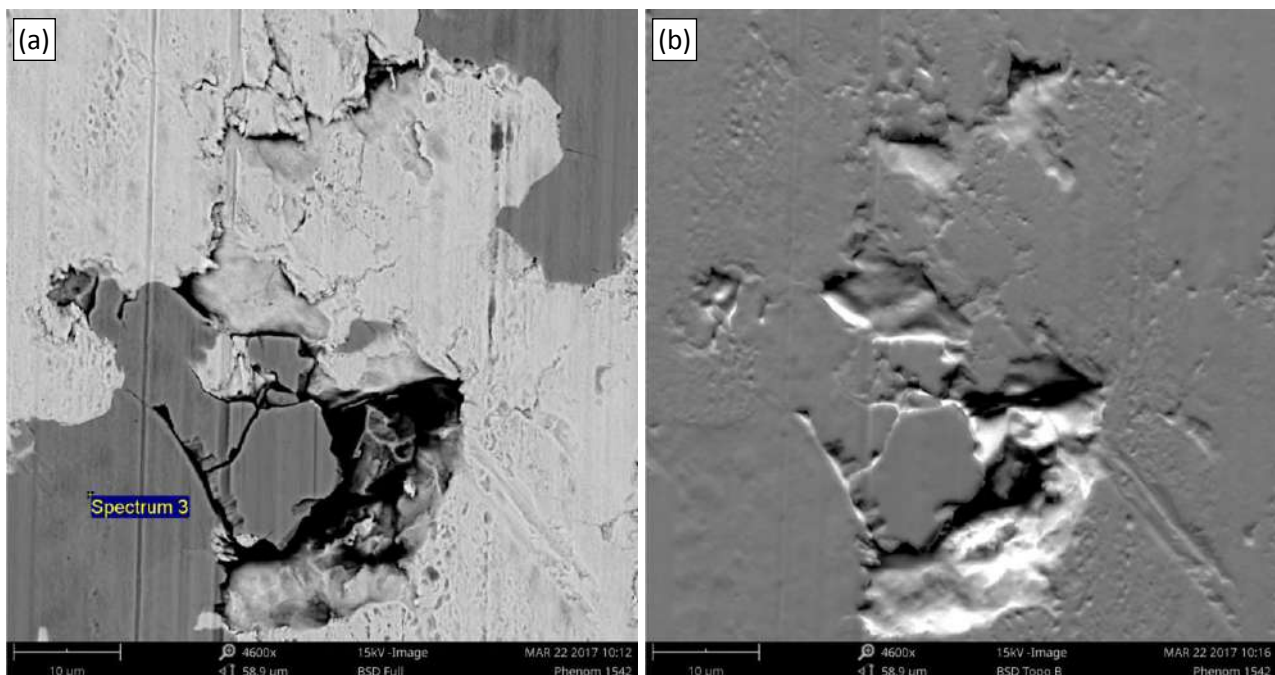| Spectrum	W	Co	Mo	Ni	Cr	B	Si	Fe	C
Spectrum 1	78.8	1.7	–	–	–	–	–	–	19.5
Spectrum 2	–	–	68.8	–	–	–	–	–	31.2
Spectrum 3	–	–	5.2	53.8	12.3	–	3.4	2.3	23.0

Analysis of the coating 505 worn surface showed presence of interlamellar pores and cracks (Fig. 7b). The cracks occurred mainly in the Mo-rich areas (Spectrum 2 on Fig. 7b), but also in harder Ni-rich areas (Spectrum 3 on Fig. 9a). In the case of coating 505, worn surface topography did not show any protruded particles (Fig. 9b). This means that the whole surface was in contact, having as a consequence higher wear of this coating.

4. CONCLUSIONS

In this study, the tribological properties of WC-Co/NiCrBSi and Mo/NiCrBSi plasma spray coatings under sliding lubrication conditions were investigated and compared. Both coatings showed microstructures typical for thermal spray coatings, which consist of elongated splats of molten powder, which form a curved lamellar structure, and oxide layers and inclusions in between.

Coefficient of friction values suggest that the sliding was performed in the boundary lubrication regime. Between two contact pairs, Mo/NiCrBSi coating gives slightly lower coefficient of friction, most probably due to the presence of Mo in this coating, and consequently slightly lower rise of lubricant temperature during testing.

The wear values showed that WC-Co/NiCrBSi coating was more wear resistant than Mo/NiCrBSi coating, but caused higher wear of the counter-body material. Higher wear resistance of WC-Co/NiCrBSi is due to the higher hardness of this coating, as well as due to the presence of protruded hard WC particles, which protected the softer matrix. The dominant wear mechanism for both coatings was light two-body abrasion.

REFERENCES

[1] M. Kandeva-Ivanova, A. Vencl, D. Karastoyanov: *Advanced Tribological Coatings for Heavy-Duty Applications: Case Studies*, Prof. Marin Drinov Publishing House of Bulgarian Academy of Sciences, Sofia, 2016.

[2] Y.-H. Shieh, J.-T. Wang: Alloying and post-heat-treatment of thermal-sprayed coatings of self-fluxing alloys, Surface and Coatings Technology, Vol. 58, No. 1, 1993, pp. 73-77.

[3] A. García, M.R. Fernández, J.M. Cuetos, R. González, A. Ortiz, M. Cadenas: Study of the sliding wear and friction behavior of WC + NiCrBSi laser cladding coatings as a function of actual concentration of WC reinforcement particles in ball-on-disk test, Tribology Letters, Vol. 63, No. 3, 2016, Paper 41.

[4] H.S. Ahn, C.H. Lee: A study on the wear characteristics of plasma sprayed NiCrSiB/WC-12Co mixed coating, in: *Proceedings of the 15th International Thermal Spray Conference*, 25-29.05.1998, Nice, France, 175-180.

[5] P. Niranatlumpong, H. Koiprasert: The effect of Mo content in plasma-sprayed Mo-NiCrBSi coating on the tribological behavior, Surface and Coatings Technology, Vol. 205, No. 2, 2010, pp. 483-489.

[6] X.-C. Yang, G.-L. Li, H.-D. Wang, T.-S. Dong, J.-J. Kang: Effect of flame remelting on microstructure and wear behaviour of plasma

sprayed NiCrBSi-30%Mo coating, Surface Engineering, DOI: 10.1080/02670844.2016.1226053.

[7] S. Lu, Y. Guo, L. Chen: Microstructure and properties of WC-Co/NiCrBSi brazing coating, Journal of Materials Science & Technology, Vol. 15, No. 3, 1999, pp. 283-285.

[8] S.-P. Lu, O.-Y. Kwon, Y. Guo: Wear behavior of brazed WC/NiCrBSi(Co) composite coatings, Wear, Vol. 254, No. 5-6, 2003, pp. 421-428.

[9] D. Kekes, P. Psyllaki, M. Vardavoulias: Wear micro-mechanisms of composite WC-Co/Cr-NiCrFeBSiC coatings. Part I: Dry sliding, Tribology in Industry, Vol. 36, No. 4, 2014, pp. 361-374.

[10] V. Fervel, B. Normand, C. Coddet, M. Delaet: Tribological properties of Mo/NiCrBSi thermal spray deposits, in: *Proceedings of the 15th International Thermal Spray Conference*, 25-29.05.1998, Nice, France, 237-241.

[11] S. Usmani, S. Sampath, D.L. Houck: Effect of microstructure and alloy additions on the sliding friction and wear of plasma sprayed molybdenum alloy coatings, in: *Proceedings of the 15th International Thermal Spray Conference*, 25-29.05.1998, Nice, France, 127-131.

[12] T. Valente: Air plasma sprayed metallic coatings for sour environments, British Corrosion Journal, Vol. 35, No. 3, 2000, 189-194.

[13] S.C. Modi, E. Calla: A study of high-velocity combustion wire molybdenum coatings, Journal of Thermal Spray Technology, Vol. 10, No. 3, 2001, pp. 480-486.

[14] B. Denkena, J. Kästner, T. Göttsching: Tribological mechanisms of microstructures, in: B. Denkena, A. Rienäcker, G. Knoll, F.-W. Bach, H.J. Maier, E. Reithmeier, F. Dinkelacker (Eds.), *Microstructuring of Thermo-Mechanically Highly Stressed Surfaces*, Springer, Cham, 2015, pp. 119-145.

[15] A. Vencl, S. Arostegui, G. Favaro, F. Zivic, M. Mrdak, S. Mitrović, V. Popovic: Evaluation of adhesion/cohesion bond strength of the thick plasma spray coatings by scratch testing on coatings cross-sections, Tribology International, Vol. 44, No. 11, 2011, pp. 1281-1288.

[16] ASTM G 77 *Standard Test Method for Ranking Resistance of Materials to Sliding Wear Using Block-On-Ring Wear Test*.

[17] M.R. Mrdak: Karakterizacija WCCo/NiCrBSi prevlake otporne na habanje, Vojnotehnički glasnik, Vol. 58, No. 2, 2010, pp. 43-52, in Serbian.

[18] M. Mrdak, A. Vencl, M. Ćosić: Microstructure and mechanical properties of the Mo-NiCrBSi coating deposited by atmospheric plasma spraying, FME Transactions, Vol. 37, No. 1, 2009, pp. 27-32.

[19] A. Rac: *Osnovi tribologije*, Mašinski fakultet Univerziteta u Beogradu, Beograd, 1991, in Serbian.

[20] B.J. Hamrock, S.R. Schmid, B.O. Jacobson: *Fundamental of Fluid Film Lubrication*, Marcel Dekker, New York, 2004, Ch. 1.

[21] A. Vencl: Tribological behavior of ferrous-based APS coatings under dry sliding conditions, Journal of Thermal Spray Technology, Vol. 24, No. 4, 2015, pp. 671-682.

[22] K. Kato, K. Adachi: Wear mechanisms, in: B. Bhushan (Ed.), *Modern Tribology Handbook*, CRCPress, Boca Raton, 2001, Ch. 7.

ENHANCEMENT OF THE WEAR RESISTANCE OF ZIRCONIUM MODIFIED TiO2 NANOSIZED SPRAYED COATINGS

Irina STAMBOLOVA[1]*, Vladimir BLASKOV[1], Mara KANDEVA[2], Silviya SIMEONOVA[3], Konatantin BALASHEV[3], Sasho VASSILEV[4], Alexander ELIYAS[5], Maria SHIPOCHKA[1], Nina G. KOSTOVA[5]

[1]Institute of General and Inorganic Chemistry, BAS, Sofia, Bulgaria
[2]Technical University-Sofia, Faculty of Industrial Engineering, Tribology Center, Sofia, Bulgaria
[3]Sofia University, Faculty of Chemistry and Pharmacy, Sofia, Bulgaria
[4]Institute of Electrochemistry and Energy Systems, BAS, Sofia, Bulgaria,
[5]Institute of Catalysis, BAS, Sofia, Bulgaria
*Corresponding author: e-mail: stambolova@yahoo.com

Abstract: Non-modified and Zr modified titania sprayed coatings have been deposited on aluminium substrate. The coatings were characterized by AFM, XRD and XPS analyses. The tribological properties of the coatings were studied. All the films possess nanosized anatase crystallographic phase. The non-modifed TiO2 film has average crystallites size 43 nm, while the modifed films have crystallite size in the range 22-24 nm. The XPS analysis proved the presence of Ti^{4+}, Zr^{4+} and O^{2-} ions. The zirconium additive greatly decreases the surface roughness and inhibits the grain growth. The Zr modification of TiO2 coatings (up to 10 %) increases significantly the wear resistance due to the smaller crystallites size and smooth surface. It has been shown using AFM analyses that after wear tests the coatings preserve their adhesion to the substrate.

Keywords: wear resistance, spray pyrolysis, tribology, thin films,surface topography

1. INTRODUCTION

Titanium dioxide is a multifunctional material with promising sensor, catalytic, photocatalytic, biomedical etc. properties. An increasing interest in TiO2 coatings due to their good wear and corrosion resistance, low friction, biocompatibility etc. is observed during the last years [1]. Some titania coatings with significant wear resistance were prepared by physical methods [2]. These methods require expensive and complicated apparatus and technique or applying high temperatures, which could destroy the original nanostructure [3]. The chemical techniques are preferable and cheap alternative for deposition of titania

coatings. Nevertheless the studies on the tribological properties of chemically deposited TiO2 coatings are very scarce [1, 4]. To the best of our knowledge there are only few studies on the tribological properties of TiO2 coatings deposited by conventional spray method [5]. Recently the interest is growing up with a view to control the physical and chemical properties of TiO2 by doping with metals. The choice of the dopant could play a crucial role in the crystalline structure and phase transformation temperature of TiO2.

According to some authors [6] the presence of some dopants could improve also the mechanical stability of thin films. Some studies revealed the influence of Ag, Au and Si as

dopants on the wear resistance of TiO_2 films [7-9]. Interest in Zr doped TiO_2 arises from the fact that Zr has the same valence structure and state as that of Ti [10]. Zr atoms occupy sub-stitutional sites in the TiO_2 lattice with an increase in the bond length to form $Ti1-xZrxO_2$ solid solutions, stabilize the anatase phase and inhibit the growth of the crystallites [10,11]. The molecular mixing of these components is vital in regard to transforming the properties of the mixed oxides.

Piwonski et al. [12] have proved enhanced wear stability of titania sol-gel coating with embedded zirconia nanoparticles in comparison to pure titania coatings.

To the best of our knowledge the effect of Zr dopant on the surface roughness, crystallites size and wear resistance of TiO_2 sprayed films has not been studied yet. The aim of this work was to investigate the effect of dopant type and concentration on the phase composition, surface morphology and wear resistance of TiO_2 sprayed films.

2. EXPERIMENTAL

Titanium chloride, dissolved in isopropanol, was used as titanium precursor solution. For the preparation of Zr modified TiO_2 coatings, $ZrOCl_2.8H_2O$ was dissolved in isopropanol and it was mixed with the corresponding quantity of titanium chloride solution. The concentrations of additive in the so obtained mixed solutions were varied within in the range between 0 and 30 at % with respect to the Ti content. The so obtained precursor solutions was sprayed onto aluminium foil sheets substrate, heated at 280-300°C. The deposits were finally treated at 400°C for 1 hour. The samples were labeled as TZ followed by number, which denotes the concentration of Zr in atomic percents.

The phase composition of the samples was studied by X-ray diffraction (XRD) with CuKα-radiation (Philips PW 1050). The crystallite size was estimated based on XRD patterns. The film compositions and electronic structure were investigated by X-ray photoelectron spectroscopy (XPS). The measurements were

carried out on AXIS Supra electron-spectrometer (Kratos Analytical Ltd.) using monochromatic AlKα radiation with a photon energy of 1486.6 eV and charge neutralization system. The binding energies (BE) were determined with an accuracy of ±0.1 eV. The chemical composition in the depth of the films were determined monitoring the areas and binding energies of C1s, O1s, Ti2p and Zr3d photoelectron peaks. Using the commercially provided data-processing software of Kratos Analytical Ltd. the concentrations of the different chemical elements (in atomic %) were calculated by normalizing the areas of the photoelectron peaks to their relative sensitivity factors. The surface topography was studied by means of Atomic Force microscope (AFM) (NanoScopeV system, Bruker Inc.) operating in tapping mode in air at room temperature. The silicon cantilevers (Tap 300 Al-G, Budget Sensors, Innovative solutions Ltd, Bulgaria) were used with 30 nm thick aluminium reflex coating. The cantilever spring constant, reported by the producer, was within the range of 1.5–15 N/m, the resonance frequency was 150 ± 75 kHz and the tip radius was less than 10 nm. The scan rate was set at 1 Hz and the images were captured in the height mode with 512 512 pixels in a JPEG format. Subsequently, all the images were flattened by means of the Nanoscope software.

The obtained samples were subjected to wear resistance tests. The experimental runs of abrasive wearing resistance of the coatings were realized by means of the test rig TABER ABRASER according to the kinematical scheme „disk-on-disk" [13]. The device used for this test is shown in Figure 1. Specimen (1) is mounted on a horizontal bearing plate (2), which is driven by an electric motor at a constant angular velocity (5) of 60 [rpm]. Abrasive roller (antibody) made of plastic abrasive material CS 10, is mounted on a horizontal axis in the device. The procedure of the experimental study on abrasive wearing off is realized in the following sequence of operational steps:
- Cleaning of lubricants and drying of the identical specimens. The specimens represent

disks of diameter 100 mm having 3 mm thickness of the deposited coatings;

- Measuring of roughness of the contact surfaces of the specimens before and after the wear test

- Measuring of specimens mass m_o before and its mass m_i after a given friction path L by electronic balance WPS 180/C/2 of accuracy 0.1 mg. Before every measurement the specimens are cleaned with appropriate solution against static electricity;

- The specimen 1 is fixed on the carrying horizontal disk 3; then the normal load P is set. The friction path length L is determined by the number of cycles counted by revolution counter 8.

Abrasive wearing off for all coatings is obtained under fixed identical operating conditions – nominal contact pressure given with the normal load P, average sliding speed V and parameters of the abrasive surface. The following parameters of mass wearing off are studied:

- Absolute mass m worn off;

- Average rate of mass dm/dt, [mg/min] wearing off;

- Absolute intensity of mass wearing off $i, [mg/m]$:

$$i = m/S \qquad (1)$$

- The friction distance S is calculated using the corresponding number of cycles N and the distance R between the axis of rotation and the mass center of the nominal contact site by the formulae:

$$S = 2\pi R N \qquad (2)$$

- Absolute wear resistance by mass I, $[m/mg]$:

$$I = 1/i = S/m \qquad (3)$$

3. RESULTS AND DISCUSSION

The X-ray diffraction analyses of all the samples revealed pure anatase crystallographic phase, presented by (101) peak with nanosized crystallites in all samples (Figure 1). The degree of crystallization of anatase phase decreases with the increasing of concentration of the ZrO_2.
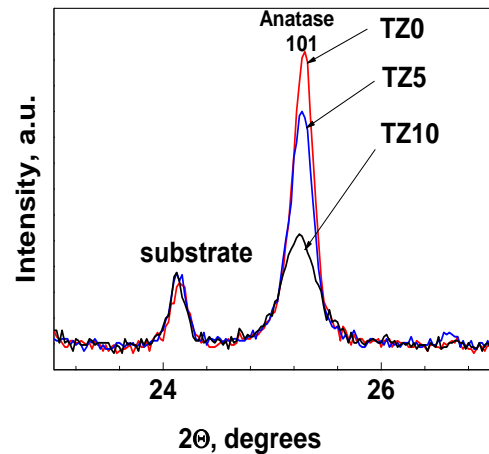
Figure 1. XRD patterns of non modified TiO_2 film and Zr modified TiO_2 film

The modifying of TiO_2 by ZrO_2 also leads to a decrease in the size of the crystallites in the nanometer range. The non-modifed TiO_2 film has average crystallites size 43 nm, while the modifed films have crystallite size within the range 22-24 nm. Similar inhibition of grain growth was obtained with Zr^{4+} doped TiO_2 nanoparticles by Wang et al [10]. It has to be noted that the anatase phase and the size of the crystallites were preserved after 400 cycles of friction.

The surface composition and chemical state of the TiO_2 layers were investigated by XPS. The TiO_2 layers doped with different quantity of zirconia show similar features. The $Ti2p_{3/2}$ peaks have a maximum at 458.6 eV, typical for the Ti^{4+} oxidation state (Fig.2).

Figure 2. Ti2p and Zr3d core level spectra of Zr modified TiO_2 films

The content of titanium dioxide on the surface is 25 at. %. The O1s spectra are wide and asymmetric. The mean peak at 529.8 eV is assigned to lattice oxygen in TiO_2 and a shoulder at ~531.8 eV is attributed to adsorbed hydroxyl species. On the surface zirconia with binding energy of $Zr3d_{5/2}$ peak at 182 eV is observed.
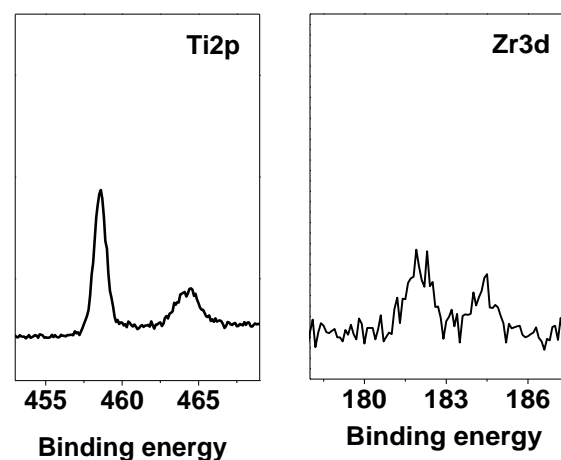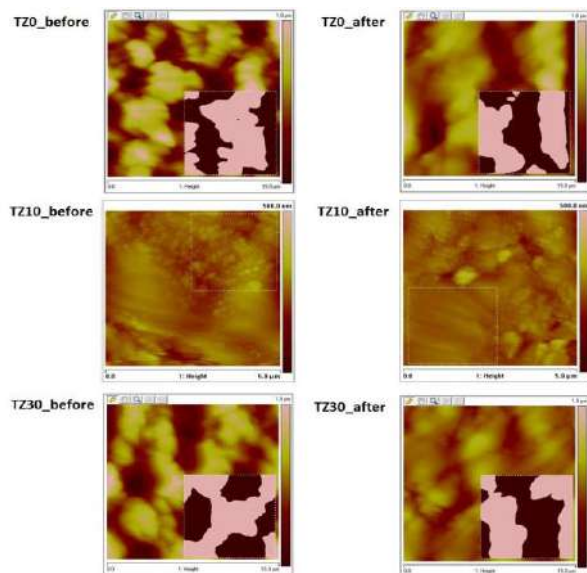

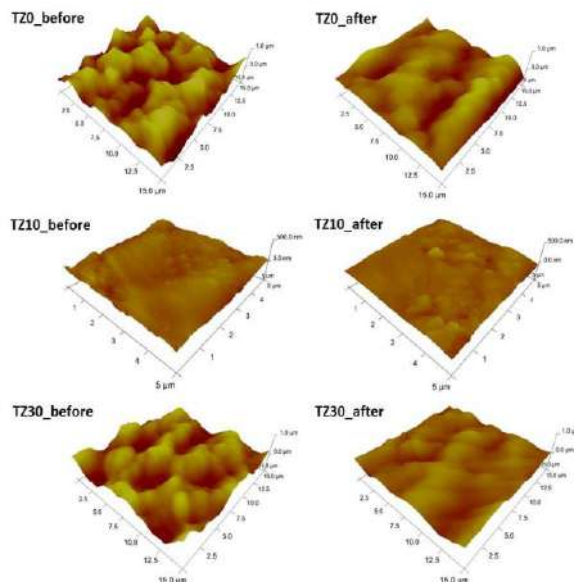**Figure 3.** AFM images of Zr modified TiO_2 coatings in 2D format

Figure 4. AFM images of Zr modified TiO_2 coatings in 3D format

Typical topographical images of the surface of non-modified TiO_2 coatings before and after 400 abrasive cycles in 2D and 3D format are shown in Figures 3 and 4, respectively. The performed analysis of the degree of roughness shows a profound difference in the surface structure of the non-modified and modified with 10% Zr samples. Pure TiO_2 films exhibit rough surface with many aggregates. The titania coating, modified with 10% Zr possesses very fine grained smoother surface. The mean roughness Ra of TZ0 coatings is about 187 nm, while that for TZ10 has value of 25 nm (Table 1).

Table 1. Roughness Ra of the titania coatings in nm before and after tribological test

Code	Image before	section before	Image after	section after
TZ0	187	179	132	113
TZ10	25	25	18	9
TZ30	165	167	75	75

The films roughness increases significantly with the increasing of ZrO_2 in TiO_2 above 10%. The comparison of the AFM images of non-modified and modified TiO_2 coatings clearly demonstrates that after 400 abrasive cycles the films surface becomes smoother and the corresponding values of the surface roughness become lower.

All the Zr modified TiO_2 coatings exhibit higher wear resistance of the aluminium substrate compared with those of coated with non-modified titania film.
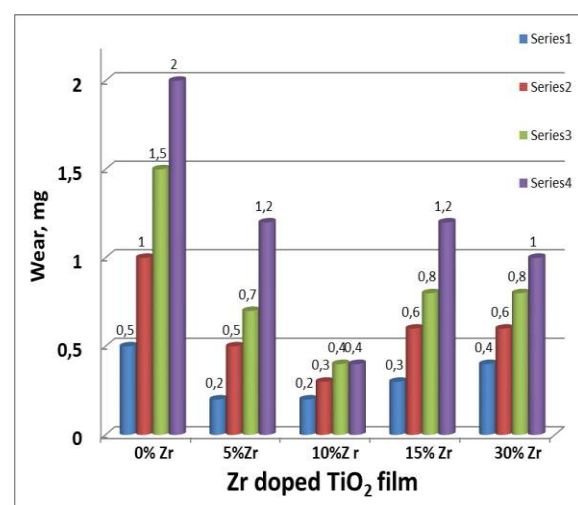

Figure 5. Wear of Zr modified TiO_2 films after 100 (series 1), 200(series 2), 300 (series 3) and 400 (series 4) abrasive cycles

As the zircoium content increases the wearing velocity and wear degree decrease (Figure 5 and 6), while the wear resistance increases (Figure 7).
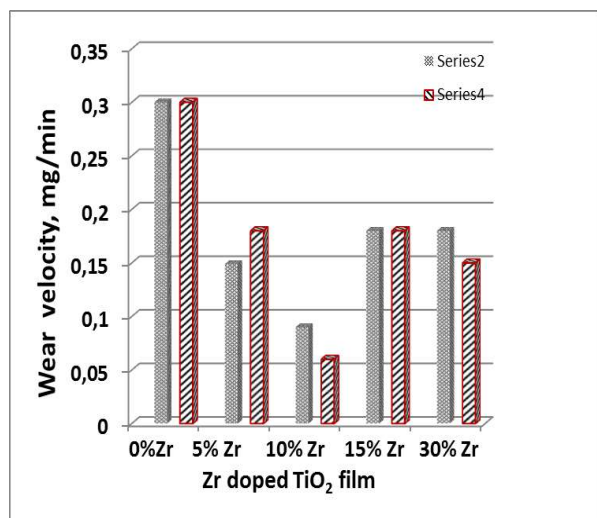

Figure 6. Wearing velocity of Zr modified TiO_2 films after 200 (series 2), and 400 (series 4) abrasive cycles

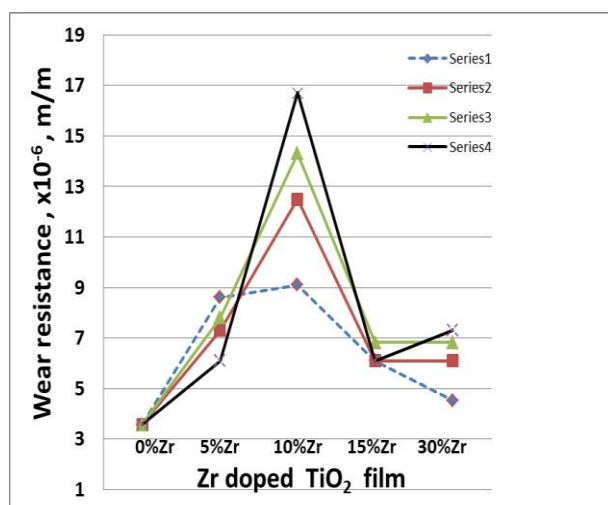The films obtained from solution with 10% Zr manifest the highest wear resistance.

Figure 7. Wear resistance of Zr modified TiO_2 films after 100 (series 1), 200(series 2), 300 (series 3) and 400 (series 4) abrasive cycles

All the doped samples have smaller crystallites size /about 20-25 nm/ than that of the non-modified film. This is in accordance with the results, obtained for TiO_2 sol gel coatings [9]. The authors stated that the finer grain size would greatly improve resistance of films to micro-fracturing. Another reason for the higher wear resistance of modified films is probably the smoother and compact surface than that of the non-modifed. Ji et al. [13] have proved that the wear resistance of ceria doped TiO_2 films is greatly improved with the decreasing of the films roughness. Nickel doped titania films possess higher wear resistance due to their smoother surface and smaller grains size [14]. The combination of suitable surface topography and size of the crystallites probably determines the wear protection properties of the Zr modified TiO_2 coatings.

4. CONCLUSIONS

Non-modified and Zr modified titania sprayed coatings have been deposited on aluminium substrate. The XRD study revealed nanosized anatase crystallographic phase, which shows tendency of decrease in the degree of crystallinity and grains growth of titania with the increasing of the zirconium content. The modification of TiO_2 coatings with ZrO_2 (up to 10 %) increases significantly the wear resistance in comparison with the reference sample. The best protection is manifested by TiO_2 samples, modified with 10% ZrO_2 due to the smaller crystallites size and smoother surface. It was shown using AFM analyses that after wear tests the particles of modified coatings preserve their adhesion to the substrate.

ACKNOWLEDGEMENT

REFERENCES

[1] G.X. Shen, .C. Chen, C.J. Lin: Corrosion protection of 316L stainless steel of TiO_2 nanoparticle coating prepared by sol gel method, Thin Solid Coatings, Vol.489, pp. 130-134, 1996.

[2] H.-F. Wang, W. Tang, H.-Y. Li: Microstructure and wear resistance of N-doped TiO_2 coatings grown on stainless steel by plasma surface

alloying technology, J. Iron Steel Res. Int. Vol. 18, No 7, pp. 73-78, 2011.

[3] A. Rico, P. Poza, J. Rodríguez: High temperature tribological behavior of nanostructured and conventional plasma sprayed alumina-titania coatings, Vacuum, Vol. 88, No 2, pp. 149-154, 2013.

[4] W. Zhang, W. Liu, C. Wang: Tribological behaviour of sol-gel TiO_2 coatings on glass, Wear, Vol. 253,No 3-4, pp. 377-384, 2002.

[5] M. Kandeva, V. Blaskov, I. Stambolova, N. Kostova, A. Eliyas, S. Vassilev: Study of wear resistance of TiO_2 sprayed coatings. Correlation between deposition parameters and wear properties, in: *Proceedings of 11th International conference "THE A Coatings"*, 1-3. 10. 2014, Thessaloniki, Greece, pp. 203-210,

[6] D. S. Ren, X. L. Liu, Q Zhang: Characteristics of SiO_2-TiO_2 Complex Thin Films Prepared by Sol Method, Acta Physicochim. Sinica, Vol. 19, No 9, pp. 829-833, 2003.

[7] R C. Adochite, D. Munteanu, M. Torrell, L.Cunha, E. Alves, N. P. Barredas, A. Cavaleiro: The influence of annealing treatments on the properties of Ag:TiO_2 nanocomposite films prepared by magnetron sputtering, Appl. Surf Sci., Vol. 258, No. 8, pp. 4028-4034, 2012.

[8] W. M. Lu, Y. X. Chen, G. T. Rou, T. Xu, D. C. Sun: Characterization and mechanical/tribological properties of nano Au–TiO_2 composite thin films prepared by a sol–gel process, Wear, Vol. 254, No10, 994-1000, 2003.

[9] Q. Jia, Y. Zhang, Zh. Wu, P. Zhang: Tribological properties of anatase TiO_2 sol-gel films controlled by mutually soluble dopants, Tribology Letters, Vol. 26, No.1, pp. 19-24, 2007.

[10] J. Wang, Y. Yu, S. Li, L. Guo, E. Wang, Y. Cao: Doping behavior of Zr^{4+} ions in Zr^{4+}-doped TiO_2 nanoparticles, J. Phys. Chem. C, Vol.117, No. 51, pp. 27120–27126, 2013.

[11] P.E. Lippens, A.V. Chadwick, A. Weibel, R. Bouchet, P. Knauth: Structure and chemical bonding in Zr-doped anatase TiO_2 nanocrystals, J. Phys. Chem. C, Vol. 112, No. 1, pp. 43–47, 2008.

[12] I. Piwonski, K. Soliwoda, A. Kisielewska, R. Stanecka-Badura, K. Kadziola: The effect of the surface nanostructure and composition on the antiwear properties of zirconia–titania coatings, Ceram. Int., Vol. 39, No. 2, pp.1111–1123, 2013.

[13] M. Kandeva, D. Karastoyanov, A. Andonova: Wear and tribothermal effects of nanostructured nickel chemical coatings, Appl. Mechan. Mater., Vol. 157-158, pp. 960-963, 2012

[14] G. Ji, Z. Shi, W. Zhang, Ge Zhao: Tribological properties of titania nanofilms coated on glass surface by the sol-gel method, Ceram. Int., Vol..40, No 3, pp. 4655-4662, 2014.

[15] Y. Wang, Zh. Xu, W. Chao, J. Zhang: Sol-gel derived nickel-doped TiO_2 films as wear protection coatings, J. Exp. Nanosci., Vol 8, No 5, pp. 618-623, 2013.

THERMAL OXIDATION OF COLD SPRAYED Ti-Cu-Fe₃O₄ COATING

Ahmet Hilmi PAKSOY[1], Onur TAZEGUL[1], Dogukan CETINER[1], Murat BAYDOGAN[1], Erdem ATAR[2], Hasan GÜLERYÜZ[3], Huseyin CIMENOGLU[1]

[1]Department of Metallurgical and Materials Engineering, Istanbul Technical University, Istanbul, Turkey
[2]Department of Materials Science Engineering, Gebze Technical University, Gebze, Kocaeli
[3]Department of Metallurgical and Materials Engineering, Sinop University, Sinop, Turkey
*Corresponding author: baydogan@itu.edu.tr

Abstract: Cr-Co-Mo alloys are widely used in biomedical applications due to good combination of their high strength, wear and corrosion resistance in human body. However, short service life, relatively low bioactivity, infection and inflammation risks are some of the major problems for these alloys. In that respect, the study aims to investigate the microstructural and mechanical properties of the multilayered coating on Co-Cr-Mo alloy with well-known bio-active TiO2 at the outermost surface. Additionally, iron oxide and copper are added to the deposited powder mixture to utilize the bio-active property of iron oxide and antimicrobial effect of copper.

In the present study, coatings were deposited via cold spray (CS) method with the feedstock containing titanium, copper and iron oxide (magnetite form) powders. After that, coated samples were thermally oxidized at 600oC for 60 h in order to obtain wear resistant, bioactive and anti-bacterial oxide layer on the outermost surface. Microstructural characterization of the coating are conducted by X-ray diffraction method (XRD) and microscopic examinations. Additionally, mechanical properties include tribological performance and hardness measurements investigated in comparison with Co-Cr-Mo alloy. Experimental results show that, CS'ed coatings were successfully deposited without any discontinuity at substrate/coating interface with well distribution of copper. Furthermore, after thermal oxidation sustainable oxide layer was formed on surface. Moreover, wear tests indicate that, multilayer coating have better wear resistance in dry, serum and simulated body fluid media with the higher hardness at the surface compared to the Cr-Co-Mo alloy.

Keywords: Cold spray, thermal oxidation, titanium, bio-material, wear

1. INTRODUCTION

Co-Cr alloys are one of the most frequently used metallic material in biomedical implants owing to high strength and good tribological performance [1-4]. However, limited service life is the main problem for this alloy group due to localized corrosion and dissolution of their surfaces. Furthermore, when the biological properties are of concern, Co-Cr alloys are bio inert materials and have very low osteointegration ability. For these reasons, formation of stable and bioactive ceramic coatings on Co-Cr alloys by utilizing different surface modification techniques is one of the current topics [5-8].In this study, titanium based powder mixture was deposited onto the Co-Cr alloy by cold spraying (CS) process and then thermal oxidation process was applied to form homogenous oxide layer on the

outermost surface in the form of titanium dioxide which is known as highly bio-active material [9-11]. Additionally, copper and iron oxide (in magnetite form) used as an additive in titanium matrix to gain the anti-bacterial property and bio-activity, respectively. Copper and its' ionic compounds are well known with the antibacterial property with superior biological activity [12,13]. Otherwise, iron oxide which has high stability in human body and frequently used in bio medical applications including, targeted drug delivery, magnetic separation of biological materials, contrast agent in magnetic resonance imaging (MRI) and molecular/cellular tracking [14,16]. Fabricated titanium based multi-layered coating on Co-Cr alloy characterized with X-Ray diffraction analyses, microstructural examinations from the cross section and surface. In addition, mechanical properties of coating including hardness measurements and tribological test compared with Co-Cr substrate.

2. EXPERIMENTAL

In the present study, feedstock containing 5 wt.% copper (Alfa-Aesar, spherical, <475 mesh, purity of %99), 3 wt.% iron oxide in magnetite form and 92 wt.% Titanium powder (Alfa-Aesar, spherical, <325 mesh, purity of %99) were prepared and deposited on F75 grade Co-Cr-Mo alloy by CS process. For the production of the coatings, RUSONIC Model K-201 CS equipment was utilized. 6 bar (600 kPa) inlet pressure of air was used as a process gas and traverse speed was fixed at 5 mm/s for all the cases. Stand–off distance, beam distance and powder feeding rate were set as 10mm, 2mm and 2 (equipment setting scale of 8), respectively. After the deposition, surface of the coatings was ground, polished and exposed to thermal oxidation during 60 hours at a temperature of 600ºC under air condition. Oxidation process were performed in muffle furnace (Nabertherm) and heating rate of 5 ºC/min. and cooling rate of 1 ºC/min. were adjusted.

Microstructural characterization of the coatings was executed by X-Ray diffraction (XRD) analyses and microscopic examinations. XRD analyses were performed with Cu Kα radiation between the angles of 10°-90° on GBC MMA XRD equipment to identify the different phases in the coatings. Microscopic characteristics were determined by scanning electron microscope (SEM, Hitachi TM-1000) and image analyser (Clemex Vision PE 6.0.027) was utilized to measure the thickness coating and oxide layer. Additionally, elemental distribution of the different phases, shown in the SEM images of the coatings, was analysed by the EDS attachment of the SEM.

Hardness of the coating from the polished cross-sections and hardness of the oxide layer from the surface determined by Wilson microhardness tester with a Vickers indenter under a load of 25 g. Tribological performance of the coating and substrate were specified in dry, serum (0.9 wt.% NaCl, solution and simulated body fluid (SBF) media under 1 N for all cases by using of Tribotech^{TM} reciprocating wear tester. For the dry and Serum environments temperature fixed at room temperature. In contrary, testing in SBF environment temperature fixed at 36.5 ^{o}C to simulate human body conditions. During wear test, Al_2O_3 ball with a diameter of 6 mm was used as a counter body. Moreover, sliding velocity, sliding stroke and total sliding length were fixed as 10mm/s, 5mm and 25m, respectively. Coefficient of frictions were recorded by wear tester throughout the testing period. 2-D profiles of the wear tracks were obtained by Veeco Dektak 6M surface profilometer. Additionally, wear scars of coating and substrate were investigated by SEM.

3. RESULTS and DISCUSSION

XRD patterns of the coatings before and after thermal oxidation were given in Figure 1. Before thermal oxidation only α-titanium and copper peaks were detected while no presence of iron oxide peaks due to deposited amount less than 3 wt.%. This result directly match with contains of the feedstock and showed that, during cold spraying process no chemical reaction have taken place between

deposited materials. Otherwise after thermal oxidation, only peaks of titanium and titanium dioxide in the form of rutile was appeared in the XRD patterns. Additionally, it is clearly seen that, α-titanium preserved the existence in the oxidised coatings' spectrum due the penetration of X-rays beneath the oxide layer during analyses. Moreover, shifting of α-titanium peaks to the left around 0.7^0 after oxidation was detected and this condition showed that titanium phase beneath the oxide layer is in the form of solid solution due to the oxygen penetration and diffusion of copper.
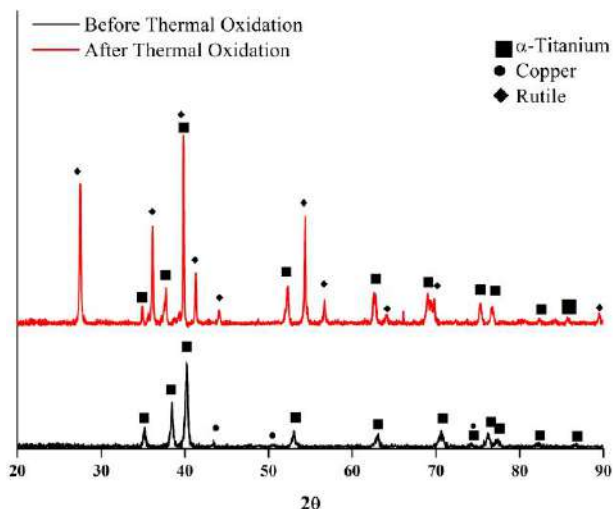

Figure-1. XRD patterns of the coating before and after thermal oxidation

Microstructure of cold sprayed and thermally oxidized coatings' was determined from the cross-sectional investigations and spliced SEM images at same magnification were given in Figure 2a. After thermal oxidation, coating has multi-layered structure which consist of homogenous oxide layer at the outermost surface with a thickness of approximately 3μm and intermediate region respectively. When interfaces between coating and substrate examined, no discontinuity could be detected. Also different phases in the coating structure can be easily distinguished with the differences in colours from the SEM images. In that respect; dark regions refer iron oxide, light grey regions refer titanium, whitish regions refer copper and relatively dark grey regions around copper and titanium particles refer solid solution compounds. Additionally, increment in porosity concentration of the coating from 5.7 ± 0.6 vol.% to 35±4.2 vol.% is

another result which could see from the SEM examinations and measurements conducted by the image analyses software. This phenomenon could be explained with the Kirkendall effect of diffusion mechanism which is thought between titanium, copper and oxygen.
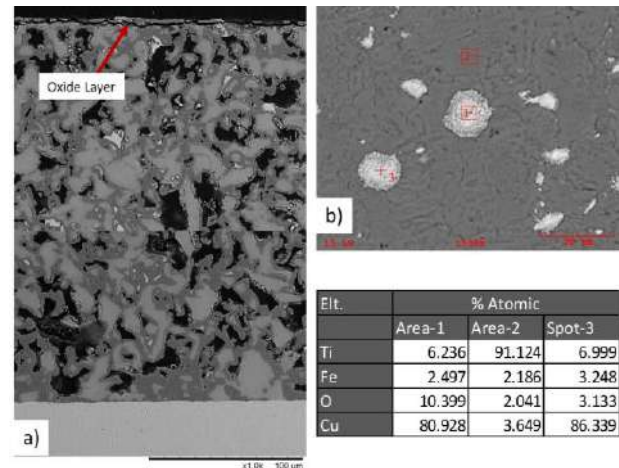

Elt.	% Atomic		
	Area-1	Area-2	Spot-3
Ti	6.236	91.124	6.999
Fe	2.497	2.186	3.248
O	10.399	2.041	3.133
Cu	80.928	3.649	86.339

Figure-2. SEM images of coating from crossection (a) and EDX analysis conducted on surface (b)

Moreover, EDX analysis conducted from the surface of thermally oxidized coating to determine elemental distribution on surface of oxide layer. Depicted results in Figure 2b shows that, copper and iron oxide additives have homogenous distribution also on the surface of coating.

Hardness of the coating was determined before and after thermal oxidation from the crossection and found as 48±14 and 326±74 $HV_{0.025}$ respectively. This dramatic increment in hardness while increasing of porosity can be mainly related with the diffusion of the oxygen and copper into the titanium and formed the solute solution in the coating according to phase diagram of titanium-oxygen and titanium-copper[17-18]. Besides the hardness measurement from the crossection, hardness of the oxide surface were determined under same testing load and measured as 525 ± 20 $HV_{0.025}$. This relatively low distrubition on the hardness of coatings' surface also supports the SEM examinations and showed homogenus formation of the oxide layer on outermost surface.

Tribological performance of Co-Cr susbtrate and oxidized coating determined in dry, serum and SBF environment respectively. Friction coefficient values obtained during the wear

testing were given in Figure 3 for Co-Cr substrate and coating. For all the cases, friction coefficient increases up to the specific level and become stable running in period. Furthermore, while in any environment Co-Cr substrate shows the similar chracteristics, in dry testing condition, friction coefficient of coating is lower than that of Co-Cr substrate in contrast to the serum and SBF conditions. This result could be explained from the SEM investigations of worn surfaces in dry condition. Whereas none effect of wear test could be detected from the worn surface of coating, clear wear grooves obtained from the surface of the Co-Cr alloy in contrary (Figure 4). In our best knowladge, during dry sliding wear testing of coating, between the counter body material (Al$_2$O$_3$ ball) and the oxide layer on the outermost surface lubricant effect was observed because of ceramic-ceramic interaction. Otherwise, tribological performance of thermally oxidized coating is of concern in Serum and SBF environment relatively higher friction coefficient and more apparent impressions on worn surface were spotted in Figure 3 and 4, respectively.

Figure 4. SEM images of the worn surfaces of Co-Cr substrate and coating.
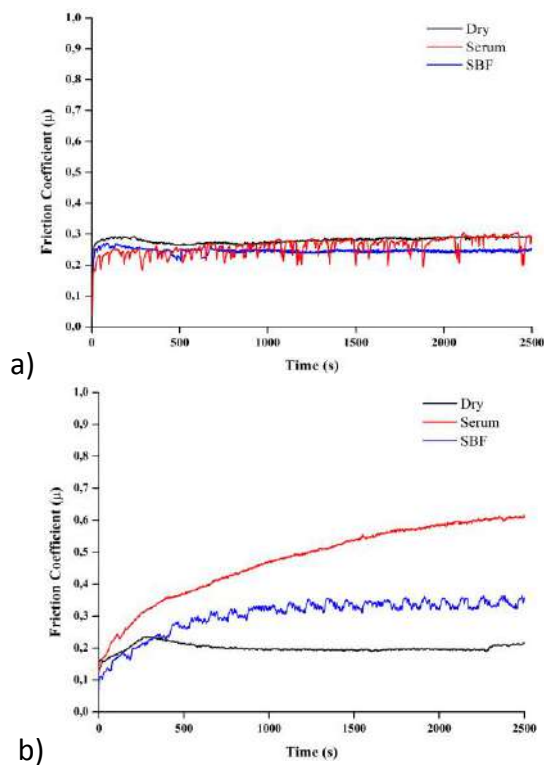

a)

b)

Figure-3. Friction coefficients curves of (a) Co-Cr substrate and (b) coating in different environments.
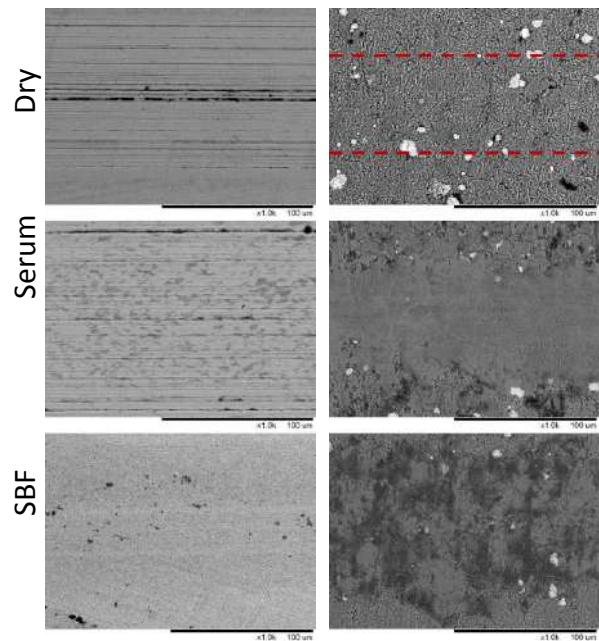
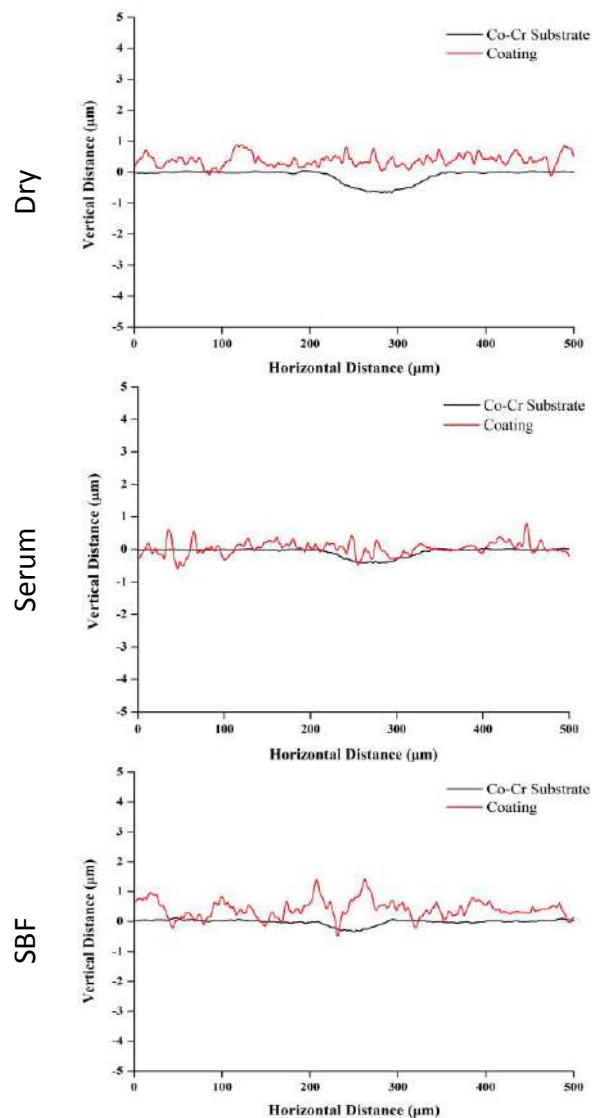Co-Cr Substrate   Coating

Figure 5. 2-D profiles of wear tracks in different environment

Serum and SBF are corrosive isotonic salt solutions because of the corrosive ions eg. Cl⁻ and $H_2PO_4^-$ etc. In addition, these ions react with titanium oxide and formed the lubricant passive film on the surface [19-20]. However, under the wear testing load of 1N which creates 840 MPa Hertzian contact pressure on the contact surface of the coating and this extreme contact pressure destroyed passive lubricant film during the wear test, then caused an increment on the friction coefficients.

2-D surface profiles of Co-Cr substrate and the coatings in Figure 5 show that apparent wear could not be formed on the coating in any environment media where as, clear wear scar profile obtained from the surface of the Co-Cr alloy.

4. CONCLUSION

Titanium based powder mixture (composition of 89 wt.%Ti + 8 wt.%Cu + 3 wt.%Fe₃O₄) were successfully deposited onto the surface of CoCr alloy by cold spray process. Thermal oxidation carried out at 600°C for 60 hours in air produced multi-layered coating comprising an inner titanium (titanium matrix composite) layer and an outer oxide layer (mainly rutile) on the surface of Co-Cr substrate. Titanium based multi layered coating represent superior performance with respect to the Co-Cr substrate in dry, serum and SBF wear testing environment. All of the examinations indicate that this method can be a solution to remove the drawbacks exist for the Co-Cr alloys without adverse effect to the mechanical properties. Effect of copper and iron oxide reinforcements on biological properties of coating going to be investigated in future studies of the project.

ACKNOWLEDGEMENT

REFERENCES

[1] S. Spriano, E. Vernè, M.G. Faga, S. Bugliosi, G. Maina: Surface treatment on an implant cobalt alloy for high biocompatibility and wear resistance, Wear, Vol. 259, No. 7-12, pp. 919–925, 2005.

[2] G. Mani, C.E. Macias, M.D. Feldman, D. Marton, S. Oh, C. Mauli Agrawal : Delivery of paclitaxel from cobalt-chromium alloy surfaces without polymeric carriers. Biomaterials, Vol. 31, No. 20, pp. 5372–5384, 2010.

[3] A. Marti: Cobalt-base alloys used in bone surgery Injury, Vol. 31, No. 4, pp. 18–21 2000.

[4] G.S. Matharu, H.G. Pandit: The cobalt to chromium ratio "may be" a key marker for adverse local tissue reactions in metal-on-metal hips. *J Arthroplasty*, Vol. 31, No.6, pp. 1374–1375, 2016.

[5] R. Martínez, J.C. Escobedo, D.A. Cortés, G.G. Alves, A.B.R. Linhares, J.M. Granjeiro, M. Pradoe, J.C. Ortiz, J.M. Almanza, E.M. Múzquiz-Ramos: In vitro bioactivity and biocompatibility of a Co-Cr-Mo alloy after heat treatment in contact with different bioactive Systems, *Ceramics International* Vol. 39, No. 2, pp. 2003-2011, 2013.

[6] M. Bahrami, M. Fathi, M. Ahmadian :The effect of nanobioceramic reinforcement on mechanical and biological properties of Co-base alloy/hydroxyapatite nanocomposite, Mater Sci Eng C, Vol. 48, pp. 572–578, 2015.

[7] M.İ. Coşkun, İ.H. Karahan, T.D. Golden: Computer assisted corrosion analysis of hydroxyapatite coated CoCrMo biomedical alloys. Surf Coat Technol, Vol. 275 pp. 1–9 2015.

[8] M Plecko, C Sievert, D Andermatt, R Frigg, P Kronen, K Klein, S Stübinger, K Nuss, A Bürki, S Ferguson, U. Stoeckle, B. Rechenberg: Osseointegration and biocompatibility of different metal implants - a comparative experimental investigation in sheep, BMC Musculoskeletal Disorders, pp. 13-32, 2012.

[9] H. Çimenoglu, M. Gunyuz, G.T. Kose, M. Baydogan, F. Ugurlu, C. Sener: Micro-arc oxidation of Ti6Al4V and Ti6Al7Nb alloys for biomedical applications, Materials Characterization, Vol. 62, No. 3, pp. 304-311, 2011.

[10] Z Lin, L Wang , X Xue, W Lu, J Qin, D Zhang: Microstructure evolution and mechanical properties of a Ti–35Nb–3Zr–2Ta biomedical alloy processed by equal channel angular

pressing (ECAP). Materials Science and Engineering C, Vol. 33, No. 8, pp. 4551–4561, 2013.

[11] A Arifin, Abu B Sulong , N Muhamad, J Syarif, M I Ramli: Material processing of hydroxyapatite and titanium alloy (HA/Ti) composite as implant materials using powder metallurgy: A review. Materials and Design Vol. 55, pp. 165–175 , 2014.

[12] H.W. Chai, L. Guo, X.T.Wang, Y.P. Fu, J.L. Guan, L.L. Tan, L. Ren, K. Yang: Antibacterial effect of 317L stainless steel contained copper in prevention of implant-related infection in vitro and in vivo, J. Mater. Sci. Mater. Med. Vol. 22, No. 11, pp. 2525–2535, 2011.

[13] J Ye, J He, C Wang K Yao, Z Gou: Copper-containing mesoporous bioactive glass coatings on orbital implants for improving drug delivery capacity and antibacterial activity. Biotechnol Lett, Vol. 36, No. 5, pp. 961–968 2014.

[14] O. Ziv-Polat, M. Topaz, T. Brosh, S. Margel : Enhancement of incisional wound healing by thrombin conjugated iron oxide nanoparticles. Biomaterials, Vol. 31, No. 4, pp. 741–747, 2010.

[15] J.K. Vasir, V. Labhasetwar: Targeted drug delivery in cancer therapy. Technol. Cancer Res. Treat, Vol. 5, pp. 363–374, 2005.

[16] S. Sharifi, H. Seyednejad, S. Laurent, F. Atyabi, A. A. Saei, M. Mahmoudi: Superparamagnetic iron oxide nanoparticles for in vivo molecular and cellular imaging. Contrast Media Mol. Imaging Vol. 10, No. 5, pp. 329–355, 2015.

[17] J. L. Murray : *Binary Alloy Phase Diagrams, 2ndEdition*, ASM International, OH, 1990.

[18] U. Diebold: The surface science of titanium dioxide, Surf. Sci. Rep. Vol. 48, No. 5-8, pp. 53-229, 2003.

[19] V.A. Alves, R.Q. Reis, I.C.B. Santos, D.G. Souza, T. de F. Gonçalves, M.A. Pereira-da-Silva, A. Rossi, L.A. da Silva: In situ impedance spectroscopy study of the electrochemical corrosion of Ti and Ti–6Al–4V in simulated body fluid at 25 °C and 37 °C, Corrosion Sciense, Vol. 51, No. 10, pp. 2473–2482, 2009.

[20] Z Wang,W Huang, Y Ma: Micro-scale abrasive wear behavior of medical implant material Ti–25Nb–3Mo–3Zr–2Sn alloy on various friction pairs, Materials Science and Engineering C, Vol. 42, pp. 211–218, 2014.

SERBIATRIB '17

15th International Conference on Tribology

Serbian Tribology Society

Faculty of Engineering University of Kragujevac

Kragujevac, Serbia, 17 – 19 May 2017

IMPROVEMENT OF THE SURFACE PROPERTIES OF ELECTROLESS NICKEL-NANODIAMOND COATINGS PLATED ON IRON ALLOYS

Zdravka KARAGUIOZOVA[1*], Julieta KALEICHEVA[2], Valentin MISHEV[2], Galina NIKOLCHEVA[2]
[1]Bulgarian Academy of Sciences-SRTI, Sofia, Bulgaria
[2]Technical University of Sofia, Sofia, Bulgaria
*Corresponding author: karazuzi@yahoo.com

Abstract: An advanced technology for production of novel Nickel-phosphorus-nanodiamond (Ni-P-ND) nanocomposite coatings on iron alloys is developed. The technology is based on the combination of sol-gel and electroless deposition technique. The ND sol is added directly to the electroless Ni-P solution. Electroless plating is performed by utilization of an EFFTTOM –NICKEL Method. A suitable surfactant is added to achieve well-dispersed ND particles in the electroless solution to facilitate their embodiment and equal distribution in the coating. Substrates of steel 17CrNiMo6 and spheroidal graphite cast irons are used for the manufacture of the iron alloys specimens.

The surface morphology and microstructure observation performed by scanning electron microscopy (SEM) and optical metallography confirms the influence of the ND particles on the coating structure. The structural phase investigation by X Ray analysis indicates that by heat treating, the amorphous phase changed to crystalline phases such as Ni, Ni3P. The microhardness by Knoop Method and wear resistance of Ni-P and Ni-P-ND composite coatings are evaluated and compared with each other. The hardness and wear resistance of Ni-P composite coatings increased in the presence of ND particles, whereas the increase of the microhardness to 1,6 – 3 times and to 33-37% of the wear resistance are achieved in heat treated coatings at 290 °C for 6 h.

Keywords: detonation nanodiamond, electroless nickel coating, wear resistance, microhardness, microstructure

1. INTRODUCTION

The co-deposition of metals with strengthening particles by chemical and electrochemical mechanism is a wide used method to obtain materials with superior properties, suitable for use in a broad range of industrial applications. There are many studies proving the materials properties improvement in the presence of additives as hard micro and nanosized particles. Electroless method for nickel based composite coating deposition is especially important seeing the expectation to replace the toxic Cr-containing coatings [1].

Additionally, it has been demonstrated the benefits of the electroless nickel plating over the electrolytic processes. One of the most important is that the obtained matrix by electroless method is nickel alloy, while the pure nickel is produced by electrolytic process [2]. The as plated nickel alloy matrix is harder than the pure nickel (HK 0, 02 ≈ 450-550), and yields to hardness increase (HK 0,02 ≈ 950-1450) after low temperature treatment

(~290°C,6h). The chemical process mechanism ensures uniform, density coatings with fine crystalline or X-Ray amorphous structure, which is the answer for high corrosion resistance, increased wear resistance and good adhesion to the coated surface [3, 4].

The authors in [5] analyze the influence of two kinds of particles, SiC and Si3N4 on the codeposition process and on the electroless Ni-P composite coatings properties. The result shows there is no influence of the particles type on the incorporation mechanism for the micron sized particles, while the type of particles is very important for nanosized condition. Moreover, the nanoparticles modify the metallic matrix growth mechanism much more than the micron-sized ones.

The discovery of ultra-dispersed diamonds (nanodiamonds) in the 1960s opened new prospects for unique materials exploration in this area. Many authors prove the improved coatings properties in the presence of nanodiamond in the bath solution [6-10]. But the opinions about the action mechanism of nanoparticles are controversial. Some of the researches believe the properties improvement is due to the nanodiamond incorporation into the Ni-P matrix, while others attribute this improvement to the change of the reaction conditions, which results in the coatings morphology [11]. These authors prove the Ni-B coatings' mechanical properties improvement because of residual pores filling. The nanodiamond particles addition to the solution for Ni-B plating bath leads to a dendrite structure refinement which is supposed to be the reason of hardness increase and tribological properties improvement. It is ascertained that the coatings' thermal processing affects only the hardness of the diamond-less sample, increasing it. There is no influence on the coating hardness, produced from diamond containing plating bath. It is assumed the nanodiamond additives facilitate amorphous structure formation due to the inhibition of the grain formation.

Deposition of nickel–phosphorus alloy and composite nickel coatings on low alloy cast iron surfaces using electroless deposition method improves its surface characteristics [12]. The evaluation and comparison of the wear properties of composite nickel coatings (Ni+SiC) with those of cast iron, nickel coatings (Ni), phosphate coating, and chromium plating indicate that not only the hardness of the Ni–P/SiC composite coating is high, but its wear resistance is better than that of the Ni–P coating, chromium plating, cast iron substrate, and the phosphatising coating. Under the given experimental conditions, the wear volume of the Ni–P/SiC composite coating is the lowest. Authors [13] prove that the graphite presence in the samples is of great importance for the electroless nickel plating strength on cast iron. Evaluating the strength of the plating film by bending tests it is found that the film cracks on cast iron are initiated by the graphite existing at the interface between the plating film and the substrate and it depends on the amount increase of graphite than on the graphite shape.

The aim of the present work is to investigate the microstructure and physical and mechanical properties of electroless nickel coatings with strengthening particles of detonation nanosized diamond ND, plated on the 17CrNiMo6 steel samples and spheroidal graphite cast iron. It is supposed the ND shape and particles size (4÷6 nm), as their specific nature and high surface activity ensure higher density and others functional qualities.

2. MATERIALS AND INVESTIGATION METHODS

On the 17CrNiMo6 steel samples and spheroidal graphite iron samples monolayer of nickel coatings are plated as double layer, consists of first nickel layer Ni and second layer of nickel with integrated particles of detonation nanosized diamond ND (Ni/Ni+ND). The EFTTOM-NICKEL technology for elctroless nickel plating developed in TU-Sofia is applied [14]. Detonation nanosized diamond with particles'' size of 4÷6 nm is used as a strengthening material. Nanosized diamond is produced by explosive method, developed in

Table 1. Properties of Ni and Ni-ND coatings on 17CrNiMo6 steel samples

Number of the sample	Sample material	Heat treatment	Coating		Microhardness HK0,02	Thickness δ, μm	Wear, g
			Composition	Heat treatment			
1	steel 17CrNiMo6	Normaliza-tion	Ni	-	494	8,7	7,5
2			Ni	290 °C, 6 h	1452	8,7	5,8
3			Ni /Ni + ND	-	712	9,3	8,0
4			Ni /Ni + ND	290 °C, 6 h	1112	7,3	4,8

Table 2. Properties of Ni and Ni-ND coatings on ductile cast iron and ADI samples

Number of the sample	Sample material	Coating				Wear resistance l
		Composition	Heat treatment	Microhardness HK0,02	Thickness δ, μm	
1	ductile cast iron	Ni	-	430	10	$0,27 \cdot 10^7$
2		Ni	290 °C, 6 h	878	9	$0,31 \cdot 10^7$
3		Ni /Ni + ND	-	466	8	$0,30 \cdot 10^7$
4		Ni /Ni + ND	290 °C, 6 h	950	8	$0,47 \cdot 10^7$
5	ADI	Ni	-	538	9	$0,37 \cdot 10^7$
6		Ni	290 °C, 6 h	850	8	$0,31 \cdot 10^7$
7		Ni /Ni + ND	-	588	8	$0,44 \cdot 10^7$
8		Ni /Ni + ND	290 °C, 6 h	1112	7	$0,49 \cdot 10^7$

SRTI-BAS [15]. The coating composition is shown in Table 1 and Table 2.

Prior to plating process the samples are undergone trough normalization (Table 1). The iron spheroidal graphite samples are copper alloyed composition: Fe-3,63C-2,59Si-0,30Mn-0,010S-0,034P-0,53Cu wt%. The spheroidal graphite cast irons and austempered iron samples ADI are used (Table 2). Austempering is performed under a regime: heating at 900°C 1 h and austempering at 290°C, 2 h in salt bath.

Two kinds of coatings are produced: electroless nickel coating (Ni) and composite nickel - nanodiamond coating (Ni/Ni+ND).

The process of electroless nickel plating is held on one stage for the electroless nickel coating (Ni) and in two stages for the composite nickel - nanodiamond coating Ni/Ni+ND using developed "EFTTOM-NICKEL" Method:
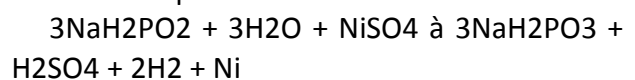
- Electroless Nickel layer formation process is performed at the following working conditions:
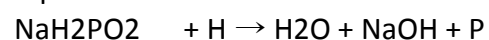   - pH = 4.6 ÷ 4.7
   - T = (92 ÷ 95) °C

- Coating time = 15 min (in one stage process; 10 min (in a two stage process).

- Optimal uses of the solution 7 ÷ 8 times per hour.

Chemical process of nickelization is:

$3NaH_2PO_2 + 3H_2O + NiSO_4$ à $3NaH_2PO_3 + H_2SO_4 + 2H_2 + Ni$

Part of the sodium hypophosphite is undergone to reduction process with phosphorous formation:

$NaH_2PO_2 + H \rightarrow H_2O + NaOH + P$

Hereby the coating obtained is amorphous alloy consists of nickel and phosphorous.

This layer works as a snubber in a two stage process, enhancing the coating ability to take a contact load and improves the adhesion between the sample base and coating.

- Composite nanostructured Ni layer is formed by nickelization in an electroless nickel solution with addition of super hard particles. The work is carried out under the conditions, performed in the first stage of the plating process with particles concentration of: 2 ÷ 5 g/l, determined in [16].

The comparative experimental study of the coatings' wear is carried out. The wear resistance tests of the coatings plated on spheroidal graphite cast iron and austempered ductile cast iron substrates are performed in fixed grinder conditions on TABER – ABRASER test machine by developed by authors method [17]. While the wear of the coatings plated on the samples of 17CrNiMo6 steel are tested by friction wear tests performed under 50MPa loading conditions – in accordance with the Polish Standard PN-83/H-04302.

The samples surface microstructure before and after tribological test is investigated by scanning electron microscope РЭММА 101-A at magnification x1000.

3. RESULTS AND ANALYSIS

3.1. Electroless composite nickel coatings on 17CrNiMo6 steel samples

Figure 1 represent the coating view and the microstructure of the steel base (17CrNiMo6 steel), obtained in an as-plated condition (Figure 1 a, b) and after thermal processing at 290°C, 6h (Figure 1 c, d). The coating appears as a white strip, following the surface topography and filling defects as micro pores and micro cracks. The samples are put to normalization before plating. The base material microstructure consists of ferrite and granular, sorbite shaped pearlite (Figure 1 a-d).

The coatings thickness δ is 8, 7 µm for Ni-coating and in the range of 7,3 – 9,3 µm for Ni/Ni + ND coating.

Figure 2 and 3 show the X-ray diffraction (XRD) patterns of the tested samples. As Ni - coating and Ni/Ni+ND coating (samples 1 and 3) show amorphous structure in an as-plated condition (Figure 2). The peaks of the diffraction patterns angles at $44,6^o$ (2θ) and $64,8^o$ (2θ) are due to the iron (Fe), containing in the substrate (steel 17CrNiMo 6). The coatings' structure (as Ni and Ni/Ni+ND) becomes crystalline after thermal processing at 290^oC, 6h (Figure 3). The diffraction patterns of the samples 2 and 4 prove the presence of Ni3P and Ni phases in the coatings' structure.
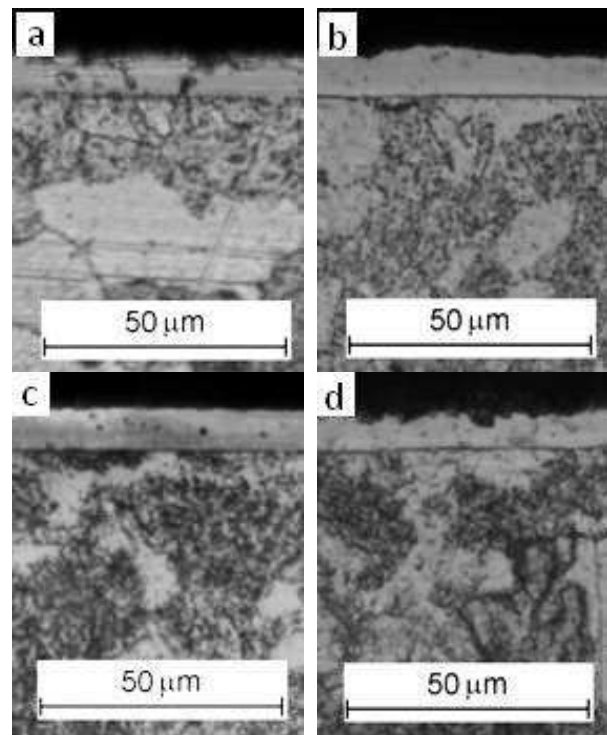

Figure 1. Microstructure of Ni (a, c) and Ni/Ni+ND (b, d) coatings on 17CrNiMo6 steel samples; a, b – coatings in as-plated condition;   c, d –thermal treated coatings at 290°C,6h
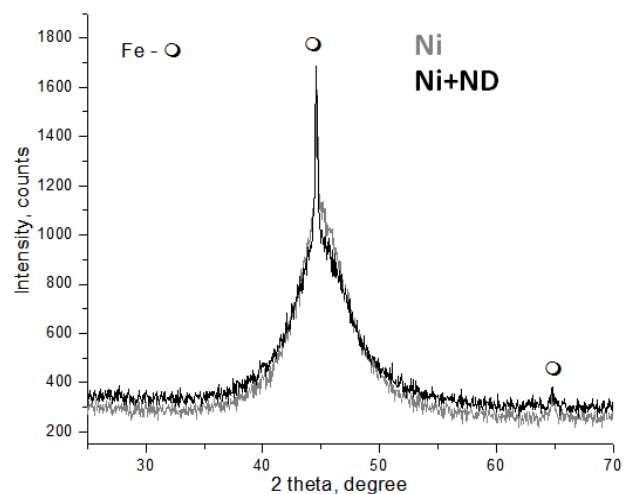

Figure 2. X– ray diffraction pattern of samples 1 (Ni coating) and 3 (Ni/Ni+ ND coating) in an as-plated condition

The coatings microhardness in an as-plated condition and after thermal processing is shown in Table 1 and Figure 4 a. The thermal processing of the coatings at 290^oC, 6h results in about threefold microhardness increase (from 494 HK0,02 to 1452 HK0,02) for Ni coating and about one and a half increase (from 712 HK0,02 to 1112 HK0,02) for Ni/Ni + ND coating.
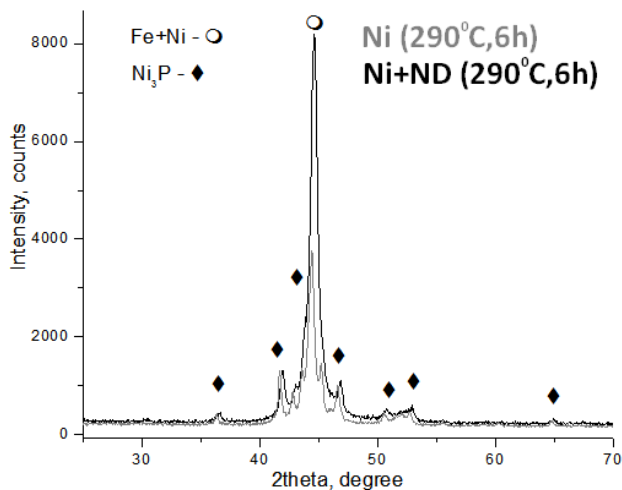
Figure 3. X– ray diffraction pattern of samples 2 (Ni coating) and 4 (Ni/Ni + ND coating) after thermal processing at 290°C, 6h.
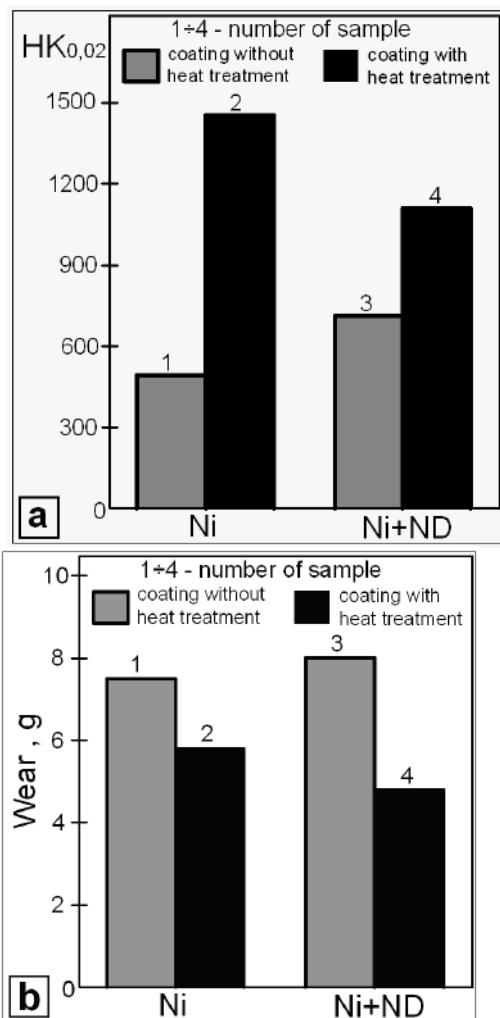

Figure 4. Microhardness HK 0,02 (a) and wear (b) of Ni and Ni/Ni+ND coatings plated on steel 17CrNiMo6 samples (Table 1)

Coating microhardness increase after annealing at 290°C, 6h is related to dispersion strengthening by a reason of dispersive crystal phase formation of Ni3P. The higher microhardness of the 2 and 4 samples after heat treatment at 290°C, 6h explains their higher wear resistance (Figure 4b).

3.2. Electroless composite nickel coatings on spheroidal graphite cast iron samples

The results for microshardness $HK_{0,02}$ testing of different coatings are presented in Table 2 and Figure 5. Thermal treating after plating – hardening at 290°C for 6 hours increases the microhardness about 2 times. Highest microhardness is achieved in the coatings with nanosized diamond, deposited on cast iron (950 HK $_{0,02}$) and austempered cast iron ADI (1112 $HK_{0,02}$) after thermal processing at 290°C for 6 hours.
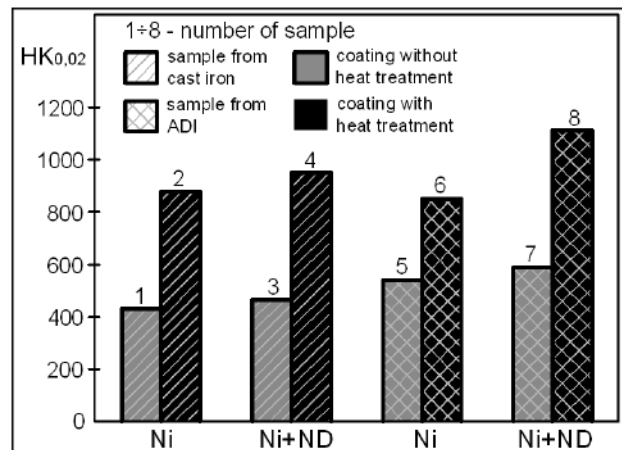

Figure 5. Microhardness HK 0,02 of Ni, Ni/Ni + ND coatings , deposited on ductile cast iron (samples № 1-4) and austempered cast iron ADI (samples № 5-8) (Table 2)

The microstructures of the padding and coatings are presented in Figure 6 and 7. The cast iron structure consists of ferrite, pearlite and graphite after casting (Figure 6a), while after austempering at 290°C, 2 h – of lower bainite and graphite (Figure 7a). The coatings appear as a white strip, following the sample surface relief (Figure 6 b; Figure 7 b). The coating thickness is in the range 7-10 μm (Table 2).

The following could be concluded analyzing the received results of the wear testing (Table 2 and Figure 8). The composite nickel coatings with nanosized diamond Ni/Ni+ND show higher wear resistance compared to this one of the samples coated with nickel. The

measured higher microhardness (Figure 5) of the thermal processed coatings (samples № 2,4,6,8 in Table 2) compared to this one of the coatings without thermal processing (samples № 1,3,5,7 in Table 2) corresponds to higher wear resistance (Figure 8).The lack of a correlation between the coatings microhardness and wear resistance of the sample 6, probably due to the low adhesion of the coating to the iron for the graphite presence in the iron structure. Maximum wear resistance ($I = 0,49 .10^7$) possesses sample № 8 with coating Ni/Ni+ND after thermal processing at 290°C, 6 hours, which correlates with the maximum coating microhardness 1112 HK0,02.
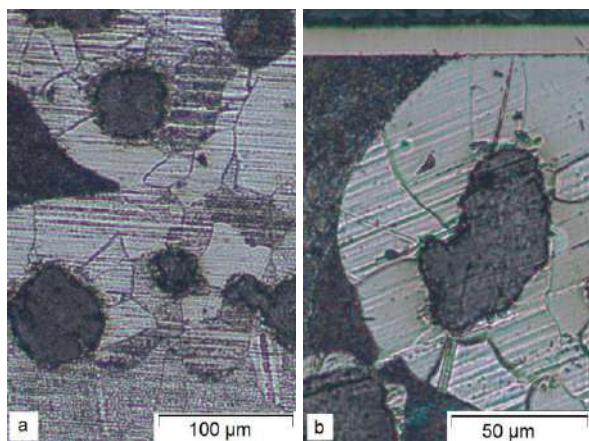

Figure 6. Microstructure of ductile cast iron samples without coating (a) and with Ni (b) coating with thermal processing at 290°C, 6 h.
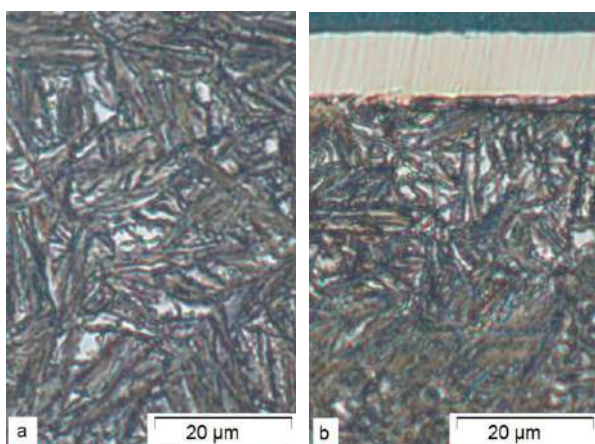

Figure 7. Microstructure of austempered cast iron samples ADI without coating (a) and with Ni/Ni+ND (b) coatings with thermal processing at 290°C, 6 h.

Electron microscopic analysis of the samples surface before and after tribological testing (Figure 9) shows the following:

In the initial state it is observed elements of a relief due to mechanical treatment of the samples (Figure 9 a, c). The coatings copy this sample's relief.
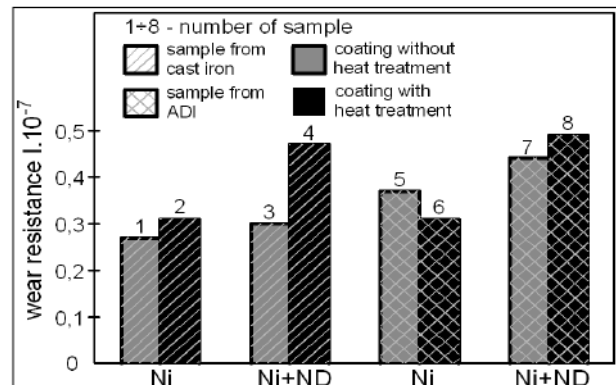
Figure 8. Wear resistance of cast iron samples (№ 1-4) and austempered cast iron samples ADI (№ 5-8) with Ni, Ni/Ni+ND coatings (Table 2)
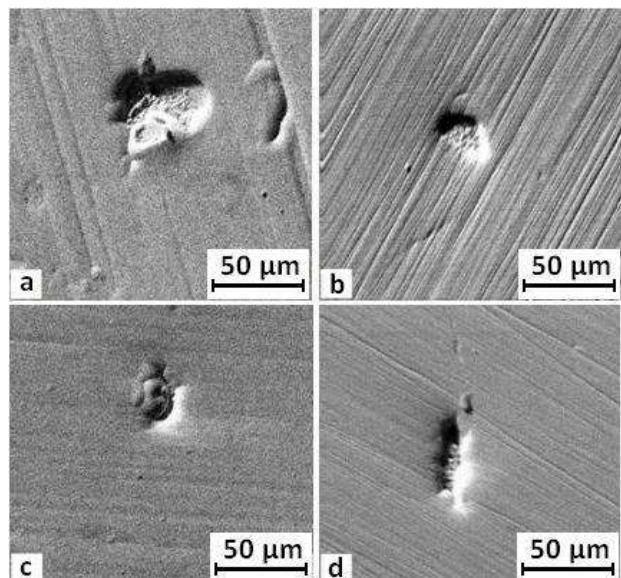
Figure 9. SEM images of surface structures: coated sample surface without heat treatment before (a) and after (b) wear test; coated sample surface with heat treatment (290°C, 6 h) before (c) and after (d) wear test.

The sample's surface is changed after wear test. It is observed developed relief with furrows due to surface wear of the sample with coating without thermal processing (b) and single furrows due to surface wear of the coated sample with thermal processing at 290°C, 6 h (d).

The surface morphology peculiarities of the samples after tribological testing (Fig.9) correspond with the received results of their wear resistance (Figure 8).

3. CONCLUSION

The following data are received for the coatings plated on the 17CrNiMo6 steel samples:

- 1.6 to 3 times increase in the microhardness after thermal processing at 290°C, 6 h. The higher hardness heat treated samples correlates with the higher wear resistance;

- amorphous structure of the coatings in as-plated condition;

- crystal formation of Ni_3P and Ni phases in the coatings' structure after heat treatment at 290°C, 6 h.

For the coatings plated on spheroidal graphite cast irons and austempered ductile iron (ADI) it is found:

- Two times increase in the microhardness HK0,02 after thermal processing at 290°C, 6 h;

- 52% (for ductile cast iron) and 58% (for ADI) higher wear resistance for nickel coatings with nanosized diamond Ni/Ni+ND compared to this one of the coatings without ND after heat treatment at 290°C, 6 h.

REFERENCES

[1] M. Feldstein: The Environmental Benefits of Composite Electroless Nickel Coatings, in Product Finishing, Cinncinati, Vol. 66, No. 11, pp. 52-56, 2002.

[2] Electroless Nickel Plating, available at: http://erieplating.com/electroless-nickel, accessed: 29.08.2015.

[3] Z. Karaguiozova, J. Kaleicheva, V. Mishev, G. Avdeev, S. Stavrev: Microstructure and Properties of Electroless Composite Nickel Coatings with Nanodiamond, Nanoscience & Nanotechnology: Nanostructured materials applications and innovation transfer, Vol. 13, pp. 74-77, 2012.

[4] Z. Karaguiozova, S. Stavrev, T. Babul, Al. Ciski: Influence of cubic nanostructure additions on the properties of electroless coatings, IJNM, Vol.5, No 1-2, pp. 129-138, 2010.

[5] M. Sarret, C. Müller, A. Amell: Electroless NiP micro- and nano-composite coatings, Surface and Coatings Technology, Vol. 201, No. 1-2, pp. 389-395, 2006.

[6] H. Xu, Z. Yang, M.K. Li, Y.L. Shi, Y. Huang, H.L. Li: Synthesis and properties of. electroless Ni–P–nanometer diamond composite coatings, Surface and Coatings Technology, Vol. 191, No. 2-3, pp.161-165, 2005.

[7] H. Matsubara, M. Kobayashi, H. Nishiyama, N. Saito, Y.Inoue, M. Mayuzumi: Co-deposition Characteristics of Nanodiamond Particles in Electrolessly Plated Nickel Films, Electrochemistry , Vol. 72, pp. 446-448, 2004.

[8] H. Matsubara, Y. Abe, Y. Chiba, H. Nishiyama, N. Saito, K. Hodouchi, Y. Inoue: Co-deposition mechanism of nanodiamond with electrolessly plated nickel films, Electrochimica Acta Vol. 52, No. 9, pp. 3047–3052, 2007.

[9] A. Miteva: Functionally graded materials in tribology, Trib. Journal Bultrib Vol. 3, No. 3, pp. 371-375, 2013.

[10] A. Miteva: On the Microstructure and Mechanical Properties of Nanocomposites, in: *Proceedings of the eighth scientific conference with International Participation S E S 2012,* 26.11.2012, Sofia, Bulgaria, pp. 220-225.

[11] A. Gurga, V. Mochalin, D. Pepe, C. Picardi, Y. Gogotsi: Nanoindentation Study of the Effect of Nanodiamond Additives on Electroless Deposition Nickel-Boride Coating, Advances in Technology of Materials and Materials Processing Journal, Vol. 10, No. 1, pp. 47-52, 2008.

[12] Y.C. Wu, G.H. Li, L. Zhang: Wear resistance of electroless deposited Ni–P and Ni–P/SiC composite coatings on low alloy cast iron, Surface Engineering, Vol. 16 No. 6, pp. 506-510, 2000.

[13] T. Yamada, A. Yamamoto, M. Fujiwara, Y. Kunugi: Strength evaluation and effect of graphite on strength of electroless nickel plating on cast iron, Journal of Materials Science, Vol. 28, No. 13, pp.3513-3518, 1993.

[14] G. Gavrilov, C. Nicolov: *Electroless Nickel and Composite Coatings*, Tehnika, Sofia, 1985.

[15] S. Stavrev, S. Lazarov, K. Stoev, L. Markov, V. Ivanov: Method for production of ultradispersed diamond, US Patent No. 5353708, 1994.

[16] Plating of composite coatings with nanodiamond powder by EFTTOM-NICKEL Method, Project BAS-SRTI 1460-5/1991.

[17] J. Kaleicheva, M. Kandeva, Z. Karaguiozova, V. Mishev, P. Shumnaliev: Investigation on wear resistance of ductile cast iron covered with nanostructured composite nickel coatings, in: *Proceedings of the 9th Int. Conf. The "A" Coatings in Manufacturing engineering,* 3. 10. – 5.10.2011, Thessaloniki, Greece, 2011, pp. 405-414.

TRIBOLOGICAL PROPERTIES OF NANOCOMPOSITE TiSiN AND MONOLAYER TiAlN COATING

Aleksandar MILETIĆ[1],*, Peter PANJAN[2], Pal TEREK[1], Lazar KOVAČEVIĆ[1], Dragan KUKURUZOVIĆ[1], Branko ŠKORIĆ[1]

[1]University of Novi Sad, Faculty of Technical Sciences, Novi Sad, Serbia
[2]Jožef Stefan Institute, Ljubljana, Slovenia
*Corresponding author: miletic@uns.ac.rs

Abstract: *In this paper, mechanical and tribological properties of coatings intended for application in lubricant free high speed machining of hard materials such as hardened steel, are presented. Materials used for such an application should be resistant to abrasive wear, resistant to oxidation and thermally stable up to very high temperatures ($\approx$800 °C). These requirements can be achieved by applying advanced nitride coatings on machining tools. In this study, nanocomposite TiSiN coating was deposited and characterized. Its properties were compared to TiAlN coating which has been mostly used coating for high speed machining in the last few decades. Both coatings were prepared in an industrial magnetron sputtering unit. Nanoindentation technique was used to measure mechanical properties. Tribological properties were evaluated by conducting ball-on-plate (alumina ball) tests in air. Stylus profilometry, scanning electron microscopy, and energy dispersive X-ray spectroscopy were applied to study generated tribo-tracks.*

We found that nanocomposite coating has considerably higher resistance to abrasive wear than monolayered TiAlN coating. Wear rate of TiAlN coating of ~14 x 10^{-6} $mm^3N^{-1}m^{-1}$ was twice as high as wear rate of nanocomposite coating (7 x 10^{-6} $mm^3N^{-1}m^{-1}$). On the other hand, almost no differences in friction coefficient were found. A value of around 0.75 was measured for both coatings. Higher wear resistance of nanocomposite coating is attributed to its higher hardness (H_{TiSiN} = 46 GPa, H_{TiAlN} = 24 GPa), higher cracking resistance (H^3/E^{*2}_{TiSiN} = 0.88, H^3/E^{*2}_{TiSiN} = 0.1), and lower surface roughness (Sa_{TiSiN} = 44 nm, Sa_{TiAlN} = 66 nm).

Keywords: *Nanocomposite coating, TiSiN, TiAlN, wear, friction, H^3/E^{*2} ratio*

1. INTRODUCTION

Increasing productivity, while decreasing production costs, along with meeting the harsh ecology standards is very demanding when it comes to tool materials. For high speed machining of hard materials, with low or without lubrication materials, materials of high hardness, high oxidation resistance, and high temperature stability are required. Even cutting-edge high-speed steels do not meet these requirements. Application of hard ceramic coatings on machining tools have proved as the best solution.

Hard nitride coatings have been widely used for increasing the efficiency and lifetime of tools for several decades. Among them, TiAlN and CrAlN have been the most usually applied on cutting tools. Both coatings are characterized by high hardness ($\approx$ 32 GPa), high oxidation resistance ($\approx$ 800 °C), and high temperature stability ($\approx$ 900 °C) [1–6].

Nowadays, great attention is given to special nanocomposite coatings. Great attention is devoted to TiSiN coating which consists of TiN nanocrystals surrounded with a thin amorphous Si_3N_4 matrix. TiSiN coatings exhibit high hardness (> 40 GPa), high oxidation resistance ($\approx$ 850 °C) and high thermal stability (up to 1100 °C) [7]. For increased oxidation stability Al can be added to TiSiN to form TiAlSiN nanocomposite coating [8].

In this study, conventional TiAlN and nanocomposite TiSiN coatings were deposited and characterized. Their mechanical and tribological properties are presented.

2. EXPERIMENTAL DETAILS

An industrial magnetron sputtering unit (CC 800/9) was used for coating deposition. The unit is equipped with four DC powered magnetron sources. During deposition of both coatings only two sources were active. Nanocomposite TiSiN coating was deposited from TiSi targets, while TiAlN coating was deposited from TiAl targets. Thickness of both coatings was around 3.5 µm. Polished cold work tool steel EN X160CrMoV121 was used as a substrate material. More details about coating preparation are given in the reference [9].

Mechanical properties were determined by instrumented nanoindentation technique. For this purpose, Fischerscope H100C equipped with Vickers indenter was used. The maximum penetration depth was less the 10% of coating thickness. Oliver-Pharr method [10] was used to calculate hardness (H) and modulus of elasticity (E). Besides these two properties, H^3/E^{*2} ratio was calculated and load at which coatings starts to crack was determined (F_{crack}).

Ball-on-plate test was used for evaluation of tribological properties. Test were conducted in atmospheric air which was at room temperature. As a counter-body an alumina ball with a diameter of 6 mm was used. All tests were conducted with the following parameters: linear speed of 5 cm/s, normal load of 5 N, stroke length of 5 mm, number of cycles from 1000 to 3000.

Taylor-Hobson Form Talysurf Series 2 was engaged for 2D measurements of wear tracks. Same device was used for 3D imaging of surface topography prior to wear tests. Morphology of wear tracks was studied by scanning electron and atomic force microscopy. Energy dispersive X-ray spectroscopy was used for elemental analysis of wear tracks.

3. RESULTS AND DISCUSSION

Mechanical properties are presented in Table 1. Nanocomposite TiSiN coating is characterized by significantly higher hardness, lower modulus of elasticity, and markedly higher H^3/E^{*2} ratio and cracking load.

Table 1. Mechanical properties

	TiAlN	TiSiN
H [GPa]	23.9 ±2.6	45.8 ±2
E [GPa]	345 ±18	310.5 ±6
H^3/E^{*2} [GPa]	0.1	0.88
F_{crack} [mN]	75	200

Large differences in mechanical properties can be attributed to large differences in design and microstructure of two coatings. TiAlN coating is of a single layer design, and as such grows in columnar fashion which is typical for magnetron sputtered coatings [9]. Relatively higher degree of porosity in columnar microstructure of this coating, and unhindered motion of dislocations inside crystalline grains are main mechanisms leading to lower hardness. On the other hand, TiSiN coating consists of tightly packed nanocrystals which size is around 5 nm. Absence of porosity between nanocrystals and of dislocation activity inside them are main factors leading to superhardness of TiSiN coating [9]. Due to different microstructure, these coatings also crack differently. TiAlN coating cracks preferentially by sliding of columnar grains [11]. On the other hand, inside TiSiN coating cracks form and propagate between nanocrystals with high amount of branching [12]. Thereby, higher load is required for crack initiation and propagation inside

nanocomposite coating than for sliding of columnar grains. Indeed, considerably lower load was needed to initiate cracks inside TiAlN coating than inside TiSiN coating (Table 1). Lately H^3/E^{*2} ratio is used as an indicator of cracking resistance. In this study, H^3/E^{*2} ratio correlates with the cracking load fully.

Figure 1 reveals that growing defects, which are typical for PVD coatings [13], dominate when it comes to surface morphology of both coatings. However, wider and higher defects grow inside TiAlN coating. Accordingly, lower average surface roughness was measured on nanocomposite coating (Sa_{TiSiN} = 44 nm, Sa_{TiAlN} = 66 nm).
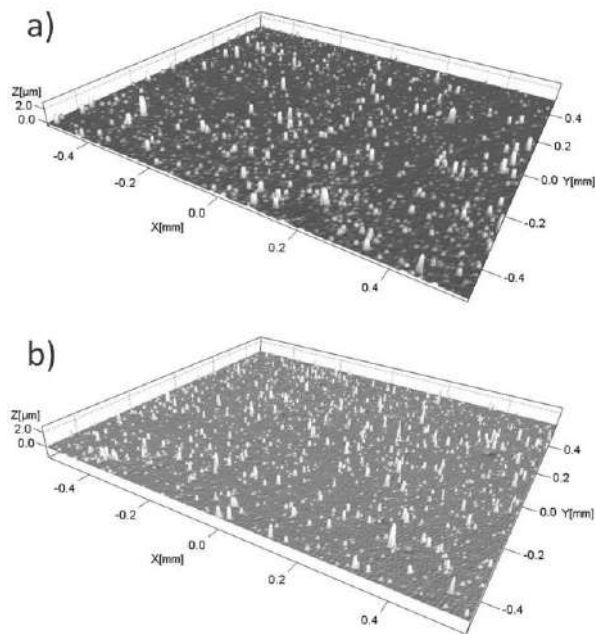

Figure 1. Surface topography of: a) TiAlN, b) TiSiN coating.

Curves representing change of friction with the number of cycles are presented in Figure 2. Friction curve of TiAlN coating exhibits three stages, running-in, transitional, and steady-state stage. On the other side, for TiSiN coating steady state was not reached even after 3000 cycles. During running-in stage friction coefficient increases rapidly and reaches value of around 0.5 for both coatings. Transitional stage begins after approximately 50 cycles with the decrease in friction coefficient. After short period friction coefficient continues to grow relatively steeply and without large sudden variations. For TiAlN coating steady value of 0.8 was reached after

around 2100 cycles. Approximately same friction coefficient was recorded for TiSiN coating at the end of the test.
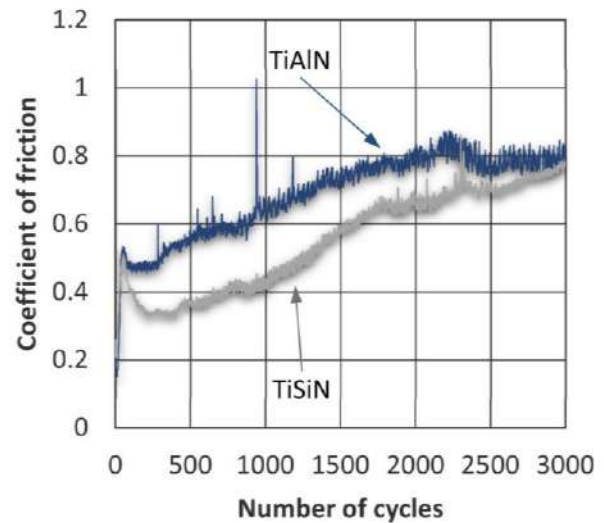
Figure 2. Evolution of friction coefficient.

Figure 3 shows that size of wear tracks progressively increases with the increase in cycle number which indicates that tribo test have good repeatability. Much deeper and wider wear tracks were produced in TiAlN coating. However, neither coating was completely worn-off after 3000 cycles.

Figure 3. Wear track profiles of: a) TiAlN, b) TiSiN.

2D profiles were used to calculate wear loss. For each coating, and each tribo test a number

of profiles was made in order to obtain realistic wear rate values. Calculated wear rates, along with friction coefficient, are presented in Figure 4. The presented va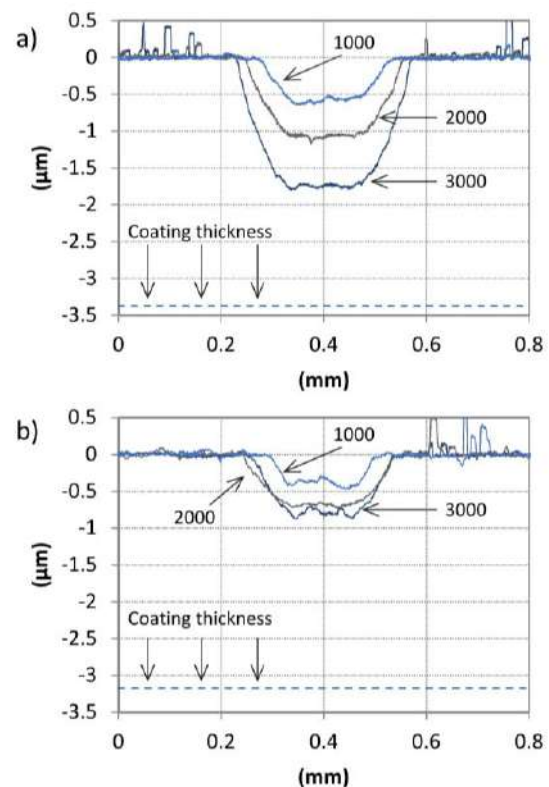lues are average values of tests conducted with different number of cycles. On one side, both coatings are characterized by similar and relatively high friction coefficient of around 0.75, which is typical for TiAlN and TiSiN coating in contact with an alumina ball [14,15]. On the other side, wear rate of TiAlN coating was twice as high as wear rate of TiSiN coating.
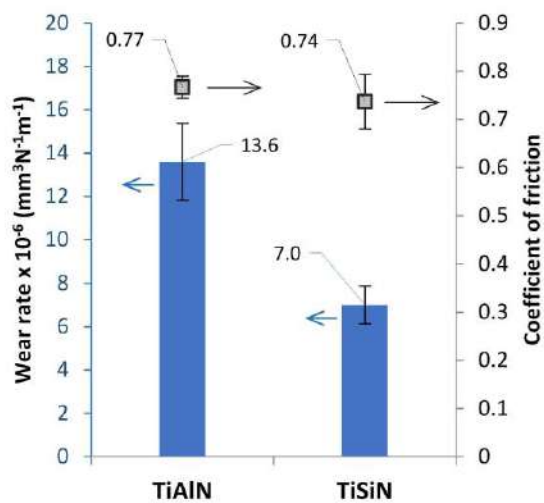

Figure 4. Wear rate and friction coefficient.

In order to better understand the tribological behavior of investigated coatings, tribo tracks were analyzed by scanning electron microscopy, energy dispersive spectroscopy, and atomic force microscopy. SEM images and results of EDS analysis of the tribo tracks produced after 2000 cycles are presented in Figure 5. Both tribo tracks are relatively smooth and clean. Wear debris are mostly agglomerated at the end of tribo tracks, and some smaller amount can be found at the edges of wear tracks. EDS analysis showed that main component of wear debris is oxygen. On the other hand, no oxygen was found inside the wear tracks, or around them.

Considering that SEM is somehow limited when it comes to 3D representation, tribo tracks were further analyzed by atomic force microscopy. AFM images of the edges of the wear tracks produced after 2000 cycles are presented in Figure 6. These images confirm that wear tracks of both coatings are relatively

smooth and without wear debris. However, wear track of TiSiN coating is considerably smoother, apart from several scars, the rest of wear track looks like it was polished.

Point	Atomic percent (at.%)				
	O	N	Al	Ti	Fe
1	51.66	19.31	17.13	11.9	
2		51.93	26.27	21.29	0.5
3		51.05	26.33	22.62	

Point	Atomic percent (at.%)					
	O	N	Al	Si	Ti	Fe
1	73.03		1.38	4.3	21.29	
2		54.81		7.29	37.3	0.6
3		52.99		7.63	39.38	
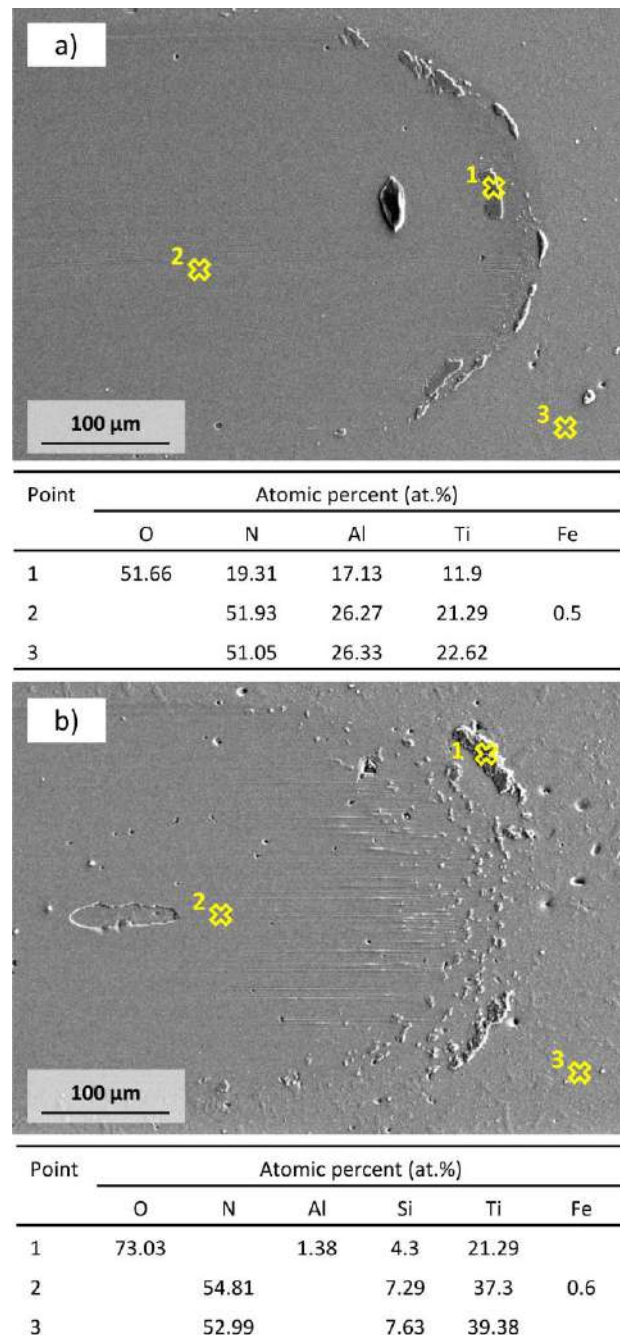
Figure 5. SEM images of wear tracks and results of EDS analysis: a) TiAlN, b) TiSiN. Points at which EDS analysis was made are marked with crosses.

According to the EDS analysis, ratio of oxygen and aluminum inside wear debris does not correspond to the typical Al_2O_3. It may be presumed that a part of wear debris are oxides generated during wear test. Oxides regularly appear during wear test due to heating induced by friction [16,17]. Based on coating

composition, and on results of the EDS analysis, formation of TiO_2 [18], Al_2O_3 [19], and smaller amount of SiO_2 [20] might be expected. Presence of hard Al_2O_3 and TiO_2 oxides in tribo contact, along with high hardness, i.e. high shear strength of TiAlN and TiSiN coatings, are key factors which lead to high values of friction coefficient of these coatings in contact with alumina ball.
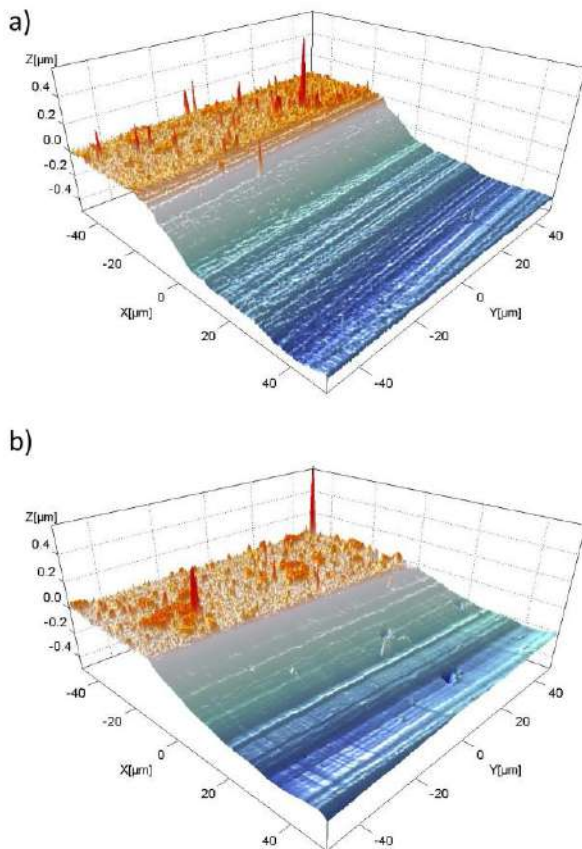

Figure 6. AFM images of wear tracks: a) TiAlN, b) TiSiN.

SEM and AFM images, together with results of the EDS analysis suggest that main wear mechanisms of boat coatings were mild abrasion and tribochemical wear. However, abrasion marks are more pronounced for TiAlN coating, which has remarkably lower wear resistance when compared to nanocomposite TiSiN coating. Lower hardness, lower cracking resistance, and higher surface roughness are main factors leading to lower wear resistance of TiAlN coating. Due to lower hardness and porous microstructure this coating cracks much easier than nanocomposite coating. During cracking, hard,

relatively large debris form, which in tribo contact intensify wear. On the other hand, cracks are not easily generated in nanocrystalline TiSiN coating. As a consequence, fine particles form and act as a polishing substance leaving smooth wear track (Figure 6b).

4. CONCLUSION

In this paper, study of mechanical and tribological properties of nanocomposite TiSiN and monolayer TiAlN coatings is presented. Owing to its nanocomposite structure, TiSiN coating is considerably harder, more resistant to cracking, and of lower roughness. Consequently, TiSiN coating expressed twice greater resistance to wear than monolayer TiAlN coating. Main wear mechanisms of both coatings were mild abrasion and tribochemical wear. High friction coefficient of around 0.75 was recorder for both coatings. High shear strength and formation of hard oxides in tribo contact were main factors leading to such high values of friction coefficient. Based on the results of the presented study, it may be concluded that TiSiN coating have high potential to replace TiAlN coatings in high speed machining of hard materials.

ACKNOWLEDGEMENT

REFERENCES

[1] A. Vennemann, H.R. Stock, J. Kohlscheen, S. Rambadt, G. Erkens: Oxidation resistance of titanium-aluminium-silicon nitride coatings, Surface and Coatings Technology, Vol. 174–175, pp. 408–415, 2003.

[2] A. Horling, L. Hultman, M. Oden, J. Sjolen, L. Karlsson: Mechanical properties and machining performance of TiAlN-coated cutting tools, Surface and Coatings Technology, Vol. 191, pp. 384–392, 2005.

[3] L. Chen, J. Paulitsch, Y. Du, P.H. Mayrhofer: Thermal stability and oxidation resistance of Ti-Al-N coatings, Surface and Coatings Technology, Vol. 206, pp. 2954–2960, 2012.

[4] J. Lin, B. Mishra, J.J. Moore, W.D. Sproul: Microstructure, mechanical and tribological properties of Cr1–xAlxN films deposited by pulsed-closed field unbalanced magnetron sputtering (P-CFUBMS), Surface and Coatings Technology, Vol. 201, pp. 4329–4334, 2006.

[5] H.C. Barshilia, N. Selvakumar, B. Deepthi, K.S. Rajam: A comparative study of reactive direct current magnetron sputtered CrAlN and CrN coatings, Surface and Coatings Technology, Vol. 201, pp. 2193–2201, 2006.

[6] J. Lin, B. Mishra, J.J. Moore, W.D. Sproul: A study of the oxidation behavior of CrN and CrAlN thin films in air using DSC and TGA analyses, Surface and Coatings Technology, Vol. 202, pp. 3272–3283, 2008.

[7] S. Veprek, M.G.J. Veprek-Heijman, P. Karvankova, J. Prochazka: Different approaches to superhard coatings and nanocomposites, Thin Solid Films, Vol. 476, pp. 1–29, 2005.

[8] L. Zhu, M. Hu, W. Ni, Y. Liu: High temperature oxidation behavior of Ti 0.5Al 0.5N coating and Ti 0.5Al 0.4Si 0.1N coating, Vacuum, Vol. 86, pp. 1795–1799, 2012.

[9] A. Miletić, P. Panjan, B. Škorić, M. Čekada, G. Dražič, J. Kovač: Microstructure and mechanical properties of nanostructured Ti–Al–Si–N coatings deposited by magnetron sputtering, Surface and Coatings Technology, Vol. 241, pp. 105–111, 2014.

[10] W.C. Oliver, G.M. Pharr: An improved technique for determining hardness and elastic modulus using load and displacement sensing indentation experiments, Journal of Materials Research, Vol. 7, pp. 1564–1583, 1992.

[11] S. Bhowmick, V. Jayaram, S.K. Biswas: Deconvolution of fracture properties of TiN films on steels from nanoindentation load - displacement curves, Acta Materialia, Vol. 53, pp. 2459–2467, 2005.

[12] J.M. Cairney, M.J. Hoffman, P.R. Munroe, P.J. Martin, A. Bendavid: Deformation and fracture of Ti–Si–N nanocomposite films, Thin Solid Films, Vol. 479, pp. 193–200, 2005.

[13] P. Panjan, P. Gselman, D. Kek-Merl, M. Čekada, M. Panjan, G. Dražič, et al.: Growth defect density in PVD hard coatings prepared by different deposition techniques, Surface and Coatings Technology, Vol. 237, pp. 349–356, 2013.

[14] Z.B. Qi, P. Sun, F.P. Zhu, Z.T. Wu, B. Liu, Z.C. Wang, et al.: Relationship between tribological properties and oxidation behavior of Ti0.34Al0.66N coatings at elevated temperature up to 900°C, Surface and Coatings Technology, Vol. 231, pp. 267–272, 2013.

[15] Y.H. Cheng, T. Browne, B. Heckerman, E.I. Meletis: Mechanical and tribological properties of nanocomposite TiSiN coatings, Surface and Coatings Technology, Vol. 204, pp. 2123–2129, 2010.

[16] T. Niebuhr, H. Bubert, H.-D. Steffens, D. Haumann, K. Kauder, U. Dämgen: Examination of wear mechanisms of hard coatings, Fresenius' Journal of Analytical Chemistry, Vol. 358, pp. 278–280, 1997.

[17] K. Holmberg, H. Ronkainen, A. Matthews: Tribology of thin coatings, Ceramics International, Vol. 26, pp. 787–795, 2000.

[18] N. Fateh, G. a. Fontalvo, G. Gassner, C. Mitterer: Influence of high-temperature oxide formation on the tribological behaviour of TiN and VN coatings, Wear, Vol. 262, pp. 1152–1158, 2007.

[19] G.S. Fox-Rabinovich, K. Yamomoto, S.C. Veldhuis, a. I. Kovalev, G.K. Dosbaeva: Tribological adaptability of TiAlCrN PVD coatings under high performance dry machining conditions, Surface and Coatings Technology, Vol. 200, pp. 1804–1813, 2005.

[20] I.W. Park, D.S. Kang, J.J. Moore, S.C. Kwon, J.J. Rha, K.H. Kim: Microstructures, mechanical properties, and tribological behaviors of Cr–Al–N, Cr–Si–N, and Cr–Al–Si–N coatings by a hybrid coating system, Surface and Coatings Technology, Vol. 201, pp. 5223–5227, 2007.

TRIBOLOGICAL PROPERTIES OF B_4C REINFORCED ALUMINIUM BASED COLD SPRAYED COATINGS

Osman KARAKUS[1], Onur TAZEGUL[1], Huseyin CIMENOGLU[1,*]

[1] Department of Metallurgical and Materials Engineering, Istanbul Technical University, 34469, Istanbul, Turkey

*Corresponding author: cimenogluh@itu.edu.tr

Abstract: *Aluminium and its alloys are widely used in the automotive and aerospace industries due to their high corrosion resistance, high specific strength (strength/weight) and thermal conductivity properties. Despite these advantages, its use is limited due to its low wear resistance. In industry, boric acid is used as a lubricant to reduce the wear rate of the metallic materials. In this study, aluminium and B_4C reinforced aluminium matrix coatings were deposited on Al 6061 substrate by cold spraying method to obtain sustainable lubricity by considering the reaction between B_4C and water. In that respect, microstructural characterization of the coatings was performed by X-ray diffraction analyses and microscopic examinations. Mechanical performances were executed with hardness measurements and wear tests in dry and water condition. Results of the experiments revealed that coatings were deposited without any discontinuities at the interface and any reaction between the constituents of the powder mixture. Furthermore, the hardness of the coatings increases with the addition of B_4C. Coatings exhibited better tribological performance in water than dry medium.*

Keywords: *Aluminium, B_4C, wear, water lubricity, Cold Spray*

1. INTRODUCTION

Due to its low weight and high specific strength, aluminium and its alloys have been widely used in the automotive and aviation industries in recent years. However, the low hardness and strength limit the use of these materials in tribological applications. Along with the developing technology, methods that increase the wear resistance of aluminium have been studied. One of the most prevalent methods today is ceramic particle reinforced aluminium based composite coatings [1,2]. Al_2O_3, SiC, and B_4C compounds come to the fore in metal matrix composite coatings made to improve the tribological properties of aluminium alloys. However, Al-B_4C composites are attractive material for applications with lower density, higher modulus of elasticity and higher specific stiffness, especially for abrasion and lightness, compared to Al-SiC and Al-Al_2O_3 composites [3].

One of the methods used to improve the wear behaviour of materials is to use lubricants. However, the fact that oil-based lubricants are harmful to nature has forced scientists to find harmless lubricants [4,5]. Studies have shown that pure water can be used as a lubricant for ceramics [6-8].

According to the above explanations, we focused on to improve wear resistance of aluminium by utilizing water lubricity properties of B_4C by depositing aluminium matrix B_4C reinforced composite coating. For

this purpose, pure aluminium and 60 vol.% B_4C + 40 vol.% Al powder mixtures were deposited by Cold Spraying method. Moreover, microstructural characterisations and reciprocating wear tests in dry and water conditions were performed to visualize the lubricity effect of water.

2. MATERIALS AND METHODS

In the present study, coatings were deposited on a 6061-grade aluminium alloy with a feedstock containing 60 vol.% B_4C powder (Alfa-Aesar, irregular, <325 mesh, purity of %99) + Al powder (Alfa-Aesar, irregular, <325 mesh, purity of %99) and 100 vol.% Al powder (Alfa-Aesar, irregular, <325 mesh, purity of %99). RUSONIC Model K-201 equipment was used for CS coating process. 1 mm/s traverse speed was set and 6 bar (600 kPa) inlet pressure of air was used for spraying. Beam distance, stand-off distance, and powder feeding rate were set as 2mm, 10 mm, and 3 (equipment setting scale of 8), respectively.

Phase analysis and microstructural examinations of the coatings were done by a X-Ray Diffractions equipment and an optical microscope, respectively. Phase analysis was made by GBC MMA XRD equipment using Cu $K\alpha$ radiation (λ = 0.154 nm) at 35 kV and 28.5 mA between angles of 20°-90° (0,020° step, 2°/min scanning speed). Leica DM750M optical microscope was used for optical analysis. The ratio of entrapped B_4C in coatings are determined by Clemex Vision PE image analyser from the optical microscope images.

Mechanical properties were investigated by hardness measurements and wear tests under dry and water conditions. The hardness of the coatings measured by Wilson micro Vickers Hardness tester under a load of 200 mN ($HV_{0,02}$). Hardness of the coatings were determined as an average of ten successful indentations.

Wear test were made by Tribotech reciprocating wear tester in dry and water conditions against Al_2O_3 ball which has a diameter of 6mm. Coefficients of friction (COF) were recorded during the test. 1N was used as test loads for all cases. Sliding velocity, total sliding length, and sliding stroke were set as 10 mm/s, 30 m, and 5 mm, respectively. Coating surfaces were ground with 1200 grit SiC emery paper before the wear test to obtain flat surface. Width and depth of the wear tracks were measured by Veeco Dektak 6M surface profilometer and worn volume was calculated.

3. RESULTS AND DISCUSSION

Cross-sectional optical microscopic images and XRD patterns of the coatings deposited by containing Al and Al+60 vol% B_4C are shown in Figure 1 and Figure 2, respectively. XRD patterns were shown that there is no other peak different from the feedstock (Figure 1). Only Al and B_4C peaks are observed in the pattern. Optical microscope images are shown that the B_4C particles were homogenously dispersed and porosities were barely detected in the structure (Figure 2). No discontinuity between the coating and the substrate was observed, which indicates a good bonding.
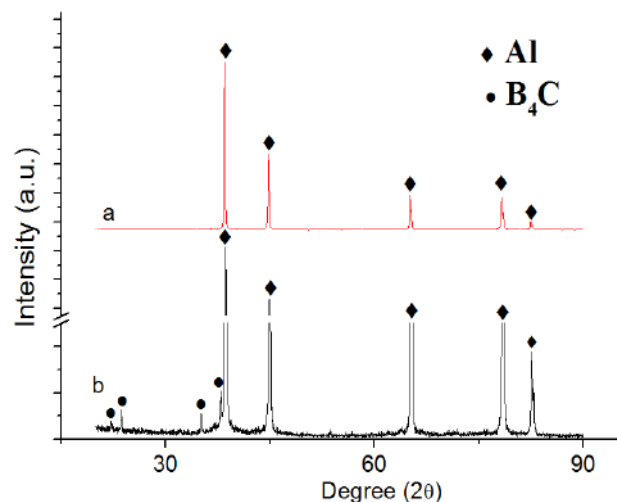

Figure 1. XRD patterns of coatings deposited by (a) B_4C Free and (b) 60 vol% B_4C feedstock

Table 1. The volume fraction of B_4C's entrapped in the coatings and surface hardness of coatings.

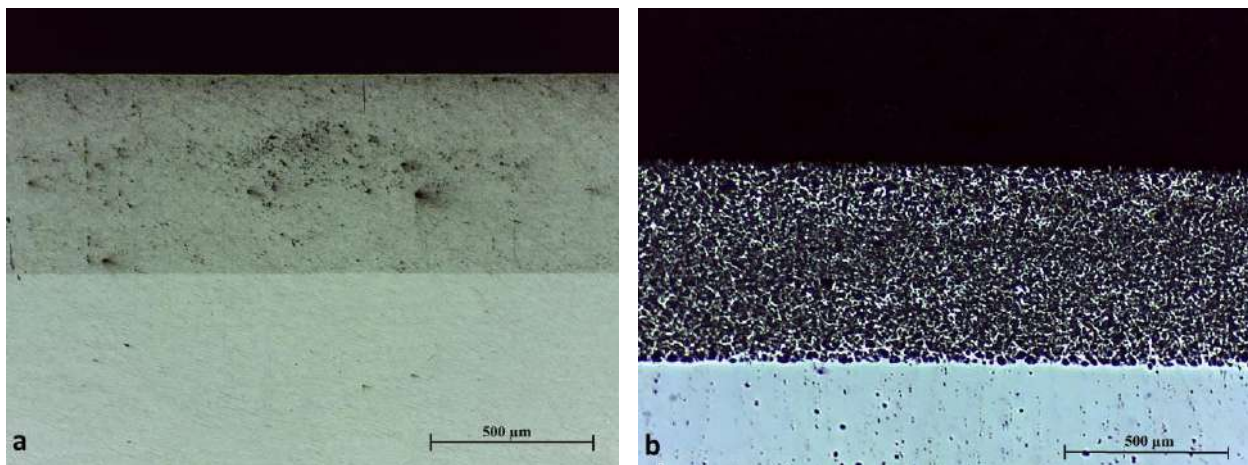| Feedstock	B_4C in the coating (vol%)	Hardness of the coating (HV_{200})
Al	-	67,4 ± 0,5
60 vol% B_4C	47,3 ± 0,4	82,7 ± 1

Figure 2. Optical microscope images of the coatings deposited by (a) B$_4$C Free and (b) 60 vol% B$_4$C feedstock.

Table 1 shows the volume fraction of B$_4$C's entrapped in the coating and the average values of the coatings. Given that the CS process is based on the principle of particles crashing rapidly to the surface, the hardness of the coatings is increased due to the excessive plastic deformation during coating [9,10]. Due to the low plastic deformation capability of the B$_4$C particles, the volume fraction of B$_4$C in the coating is lower than the feedstock. This case can be related to the B$_4$C particles bounce back during spraying [11,12].

Friction curves and 2-D wear track profiles of the coatings are presented in Figure 3 and Figure 4, respectively. In the case of wear in water condition, B$_4$C reinforced coating has a significantly lower average friction coefficient than the B$_4$C-free coating. The dry condition friction coefficient curve of the B$_4$C-free coating is not available because of its higher friction coefficient than the measurement limit of equipment. In addition, it has been observed that B$_4$C reinforced coating has a better average friction coefficient in water than dry condition.

It can be stated that when the friction curves are examined, B$_4$C reinforced coating showed a different friction characteristic than the B$_4$C-free coating. B$_4$C reinforced coating is given a fluctuating friction curve, while the B$_4$C-free coating is given a near-line friction curve.
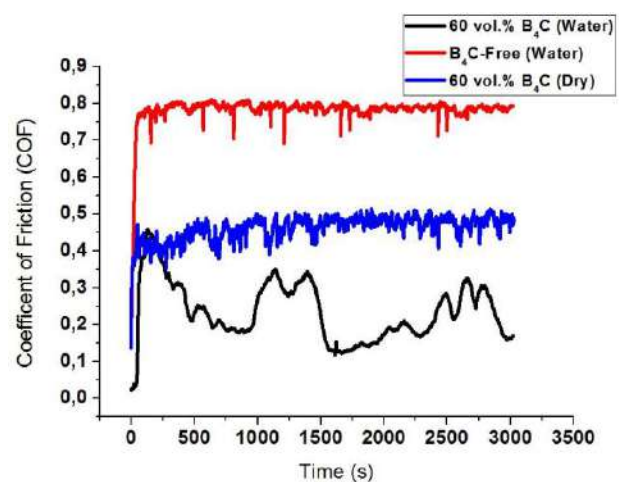

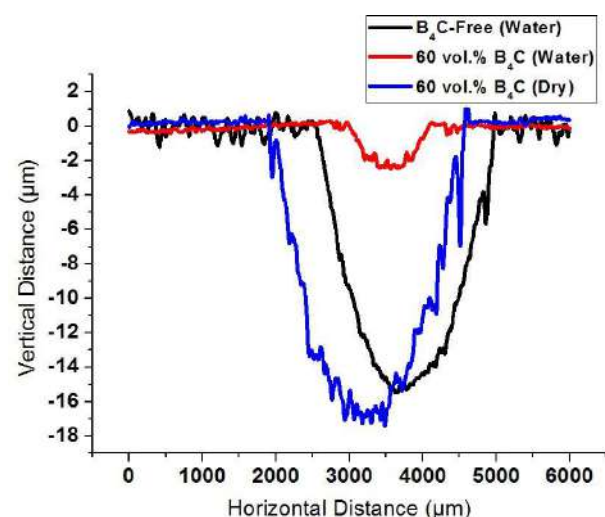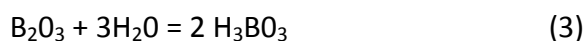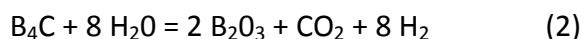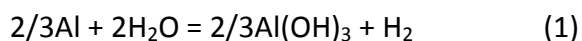**Figure 3**. Friction curves of the coatings under dry and water sliding conditions.

Figure 4. 2-D wear track profiles of the coatings under dry and water sliding conditions.

In addition, B$_4$C reinforced coating similarly has different friction characteristics in dry and water conditions. According to the literature, water triggers the following tribochemical reactions during sliding [13,14]:

$$2/3Al + 2H_2O = 2/3Al(OH)_3 + H_2 \qquad (1)$$

$$B_4C + 8 H_2O = 2 B_2O_3 + CO_2 + 8 H_2 \qquad (2)$$

$$B_2O_3 + 3H_2O = 2 H_3BO_3 \qquad (3)$$

It has been reported that boric acid (H_3BO_3) has a lubricating effect on aqueous wear conditions [15-17]. Boric acid which is the result of the tribochemical reactions forms a lubricating layer between the surfaces thanks to its lamellar structure [16]. The fluctuations in the friction curve of the B_4C reinforced coating in water condition indicate this formation. Boric acid layers which formed by local pressure and temperature increase during sliding are deteriorated due to load and pressure [14,16]. This case causes fluctuations in the friction curve.

Figure 4 presents the 2-D wear track profiles of the coatings. Wear in water is generated notably smaller wear tracks than the dry sliding condition. Contribution of B_4C also improves wear performance and allows for smaller wear track. Wear tracks of the B_4C reinforced coating is fluctuated due to detached B_4C particles during wear.
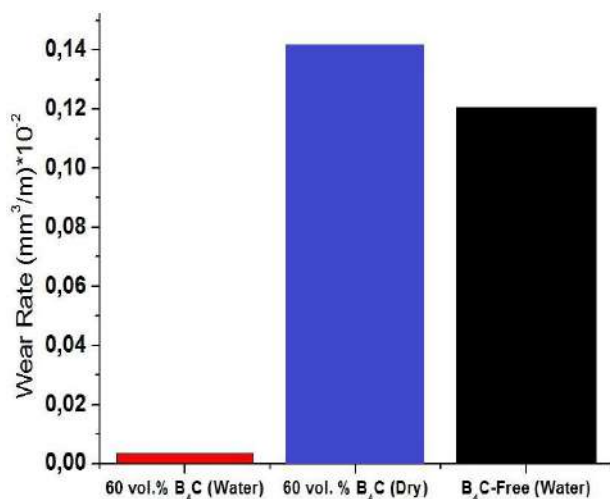

Figure 5. Wear rates of the examined coatings in dry and water condition.

Wear rates are calculated from the 2-D profiles of the wear tracks and presented in Figure 5. B_4C reinforced coating is exhibited 26 times better wear performance than B_4C-free coatings in water. In addition, B_4C reinforced coatings are exhibited 28 times better wear performance in water than dry condition.

4. CONCLUSION

Tribological performance of cold sprayed Al coatings improved by the addition of B_4C particles. B_4C contribution was more effective in water sliding conditions, due to the possible lubricating effect of the boric acid formed on the B_4C particles. Therefore, water may be used as a lubricant with B_4C that produce compounds with lubricant effect. Characterizations to prove the reactions occurring during friction and the resulting compounds are to be made in further studies.

ACKNOWLEDGEMENT

REFERENCES

[1] Surappa, M. K.: Aluminium matrix composites: Challenges and opportunities", Sadhana, vol.28(1-2), pp.319-334, 2003.

[2] Al-Haidary, J.T. ve Al-Kaaby, A.S.J.: Evaluation study of cast Al–SiCp composites, Materials Science-Poland, vol.25, pp.155-165, 2007.

[3] Hu, H.M., Lavernia, E.J., Harrigan, W.C., Kajuch, J. ve Nutt, S.R.: Microstructural investigation on B4C:Al-7093 composite, Materials Science and Engineering, pp.94–104, 2001

[4] I.M. Hutchings, Tribology: Friction and Wear of Engineering Materials, Edward Arnold, London, 1992.

[5] G.M. Stachowiak, A.W. Batchelor, Engineering Tribology, 4th ed. Butterworth-Heinemann, United States of America, 2001.

[6] J.F. Li, J.Q. Huang, S.H. Tan, Z.M. Cheng, C.X. Ding: Tribological properties of silicon carbide under water-lubricated sliding, Wear 218, pp.167–171, 1998.

[7] J. Xu, K. Kato: Formation of tribochemical layer of ceramics sliding in water and its role for low friction, Wear 245, pp.61–75, 2000.

[8] M. Chen, K. Kato, K. Adachi: Friction and wear of self-mated SiC and Si3N4, sliding in water, Wear 250, 2001.

[9] A.N. Papyrin, V.F. Kosarev, S.V. Klinkov, A.P. Alkhimov, V.M. Fomin: Cold Spray Technology, pp. 130-135, Elsevier, 2007

[10] Champagne V.K: The Cold Spray Materials Deposition Process Fundamentals and Applications, Woodhead Publishing Limited, England, 2007

[11] X. Luo, C.X. Li, F.L. Shang, G.J. Yang, Y.Y. Wang, C.J. Li: High velocity impact induced microstructure evolution during deposition of cold spray coatings, Surf Coat Technology 254, pp. 11–20, 2014

[12] Li, W.Y., Liao, H., Li, C.J, Coddet, G.L.C. ve Wang, X.: On High Velocity Impact of Micro-Sized Metallic Particles in Cold Spraying, Applied Surface Science 253, 2006

[13] U.S. Department of Energy. Reaction of Aluminum with Water to Produce Hydrogen, 2008.

[14] Dr. Yury G. Gogotsi, Professor Dr. Vladimir A. Lavrenko: Corrosion of High-Performance Ceramics, Springer Verlag Berlin, 1992

[15] Xiuqing Li, YiminGao, Qingxia Yang, Wu Pan, Yefei Li, Zhichao Zhong, Liancheng Song: Evaluation of tribological behavior of B4C–hBN ceramic composites under water-lubricated condition, Elsevier, 2015

[16] A.Erdemir, G.R.Fenske, R.A.Erck:A study of the formation and self-lubrication mechanisms of boric-acid films on boric oxide coatings, Surf. Coat. Technology, pp.588–596, 1990.

[17] C. Liu, J.Sun: Erosion behaviour of B4C-based ceramic composites, Ceramic International, pp.1297–1302, 2010.

THERMAL SPRAY COATINGS FOR WEAR CRC THE CHARACTERISTICS OF DIFFERENT SUBSTRATES

Yamg CHIALING[*], Tso Pei LUM

Department of Power Mechanical Engineering ,National Tsing Hua University, Hsinchu Taiwan

*Corresponding author: s9833815@m98.nthu.edu.tw

Abstract: *The most common thermal spray coating is CrC, commonly used arc spraying. Thermal spraying used in the automotive industry, aviation industry, power industry, textile industry, printing industry, medical industry, anti-corrosion industry. Different working conditions will affect the selection of paint and substrate selection, and one of the key parameters is the coating thickness (6 different thermal spray thickness). In this experiment, commercially available 316,2205 and C276 were selected as the thermal spraying substrate. Experiments with point - surface contact configuration, for measuring the influence of the microstructure and CrC coating thickness of the coating is abrasion wear behavior of unidirectional sliding conditions. The abrasion test is close to the actual working environment, with common working conditions: dry grinding, water, greases; 3 different loads. Spheres made of wear and 2.5 inch size tungsten carbide (WC). Due to the large number of experimental variables, all the variables will produce 162 test pieces, in order to simplify the number of test pieces, the application of Taguchi experimental method will be simplified to 6 test pieces. Preliminary observation CrC to wear behavior under different experimental variables, the experiment found that the greatest impact of the environment on the wear behavior. Experimental environment for maximum abrasion amount of water, and the specimen thickness and wear, and does not load the results of the experiment a significant impact.*

Keywords: Thermal spraying; microstructure; friction; wear; Taguchi experimental method

1. INTRODUCTION

Used in high-speed processing equipment components, the surface is often required to have high wear resistance, high corrosion resistance, the need for good friction and mechanical properties. Commercial coatings that conform to the foregoing properties are typically of a specific engineering application and are very thin in thickness and can not meet the wear of a high-speed machine under mutual operation. Thermal spray coating a few millimeters thickness; coating composition which is a mixture of various metal powders, metal powder melting at a high temperature, high pressure and then spraying it manner onto a substrate, so that the surface of the thermal spraying is generally very rough and mechanical properties will vary depending on the ratio of metal components subject to change. CrC is a common thermal spray coating, currently only know its performance for abrasive wear, erosion wear, sliding wear and heat wear and so on. Its mechanical properties and the applicable environment is not known, even MatWeb [1] material library

can provide the information is very few. And general thermal spray coating surface is very rough, can not be achieved using nano-indentation related mechanical properties of the coating, which limits the applied thermal spray product development time. CrC thermal spray wear related information is rare. The goal is to assess the impact CrC thermal spray coating microstructure and thickness of the friction properties.

2. EXPERIMENTAL PARAMETERS
2.1 Substrate and spray material

The basic principle of thermal spraying (Fig. 1) is to heat the material melting, in the gas belt to send high-speed impact attached to the substrate surface, accumulation, solidification to form a film thickness or coating, to anti-corrosion, rust, wear, adiabatic and other purposes. Selection of commercial 316,2205, C276 thermal spray base. The above three kinds of substrate made ⌀25 mm × 6 mm thick test piece, and then CrC powder to the arc thermal spraying method, spray to the test piece. While the thickness of the spray has 0.05, 0.10, 0.15, 0.20, 0.25 and 0.30 mm.
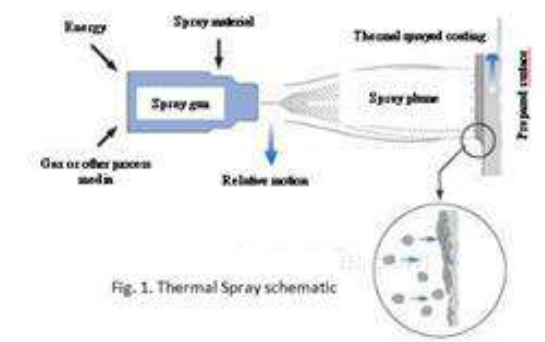

Figure 1. Thermal spray schematic

2.2 Experimental planning

The experiment is carried out in a one-way point -to-surface structure (Fig. 2). The ball is 1/2 inch tungsten steel ball. [2] [3] Side of the disc turning movement, the discharge test specimen, test temperature is room temperature。 See Table 1 for experimental variables. If the experiment in accordance with Table 1 variables, there will be 162 with a large number of test pieces, it is necessary to simplify the number of test pieces.
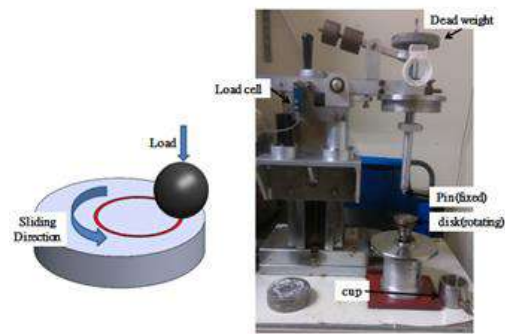

Figure 2. Ball on flat testing unidirectional testing

Experimental conditions for a minimum of three factors, so the selection of the Taguchi method to simplify the perpendicular. Choose the simplified software Minitab16, with the results shown in Table 2.

Table 2. Taguchi straightforward method

No.	Thickness (mm)	Substrate	environment	Load (g)
Y1	0.05	2205	Wet grinding	1000
Y2	0.10	2205	Oil grinding	1500
Y3	0.15	316	Dry grinding	1500
Y4	0.20	C276	Wet grinding	500
Y5	0.25	316	Oil grinding	500
Y6	0.30	C276	Dry grinding	1000

3. RESULTS AND DISCUSSION
3.1 Test piece and tungsten steel ball wear

In this study, there are three wear environment, dry mill, wet mill(water), oil mill (greases). Fig 3 is a wear test specimen after the total mass is determined by Y1 in FIG test strip to be worn most, Y4 abrasion test strip is least, the experimental environment, the two test pieces are in the water; Y1 test load of 1000g, Y4 load of 500g.
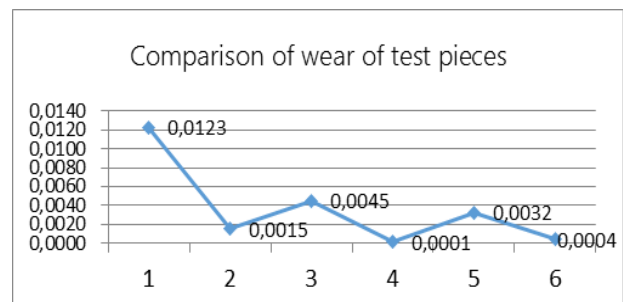

Figure 3. Comparison of wear of test pieces

Oil mill experimental test piece of Y2, Y5, respectively 1500g load test and 500g. Dry grinding experimental test piece of Y3, Y6, respectively, 1500g load test and 1000g. Y4 & Y6 wear amount is very small, its value can directly be omitted. Figure 3 observed Y1 & Y4, Y2 & Y5, Y3 & Y6 three groups of different environments wear test piece, found that the amount of wear and load is not directly related. The test can also be interpreted load given for thermal spray coating CrC too light, despite 4 thousand turn after wear, still can not CrC thermal spray coating do significant damage to wear.
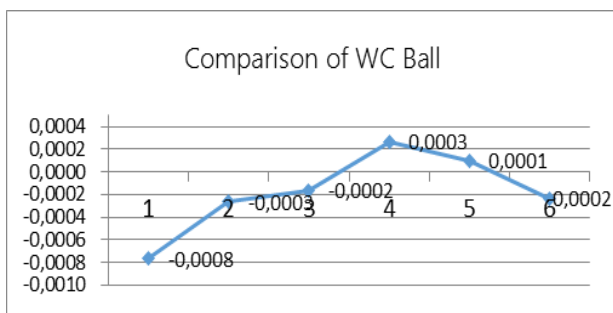

Figure 4. Comparison of WC Ball

The chosen hardness of tungsten ball RHA 92, is a conventional metal balls hardest material. Fig 4 is a mass after the ball test tungsten, Y1, Y2, Y3, Y6 in the value after abrasion is negative, showing a tungsten ball after the experiment, the weight of its mass than the mass before experiment. This phenomenon may be the test film in the wear process, the coating peeling off, the peeling off the debris happens to wear trajectory, so tungsten steel ball once again through the wear trajectory, the debris was adhered to the tungsten steel ball, quality after the experiment than before the experiment heavy. Y4, Y5 quality is positive, but its value is very small, may be due to the quality of the process before and after the test, the air dust or the measurement vehicle is not clean and clean dust adhesion to tungsten steel ball.

3.2 SEC Photo

Fig 5 is a photograph after the SEC experiment, the wear track was observed under different conditions, two kinds of photo capture SEC magnification, magnification X100, X500. The wear trajectory recognition is Y4>Y1>Y3>Y6>Y5>Y2, Y4 & Y1 is wet grinding; Y3 & Y6 is dry grinding; Y5 & Y2 is oil mill. The wear track, found in the state of the environment of water, the test strip is the most severe wear, and can also be found within a track has a coating flaking phenomenon. This phenomenon is possible, is a component of the CrC coating in the water to produce a chemical reaction, to promote the coating easy to wear. Fig 5 is a test piece Y1 & Y3 obvious track, or the coatings can be removed in the abrasion entire course of the experiment. SEC can only watch the faces of the specimen track, wear track can not get other features; It is then used to retrieve the function test strip EDS more specific location and obtain the analysis component, in order to facilitate understanding after the abrasion test, the change of the coating composition.

3.3 EDS

Fig 6 is a table showing experimental component coating material of the three substrates. Each test piece is extracted from 5 to 7 EDS photos, due to limited layout, this article each environment to take a test piece of EDS photos, to explore the wear test, the test piece changes.

Fig 7 shows the EDS of Y1. Fig 7-a is a result of composition analysis, and thermal spray coating the surface topography capture point. Fig 7-b shows the surface morphology of the wear trajectory and the results of the analysis of the capture points. The red box represents the components that are not shown in Fig 6-a & Fig 6-b.

Fig 8 shows the EDS of Y2. Fig. 8-a is a result of composition analysis, and thermal spray coating the surface topography capture point. Fig 8-b shows the surface morphology of the wear trajectory and the results of the analysis of the capture points. The red box represents the components that are not shown in Fig. 6-a & Fig. 6-b.
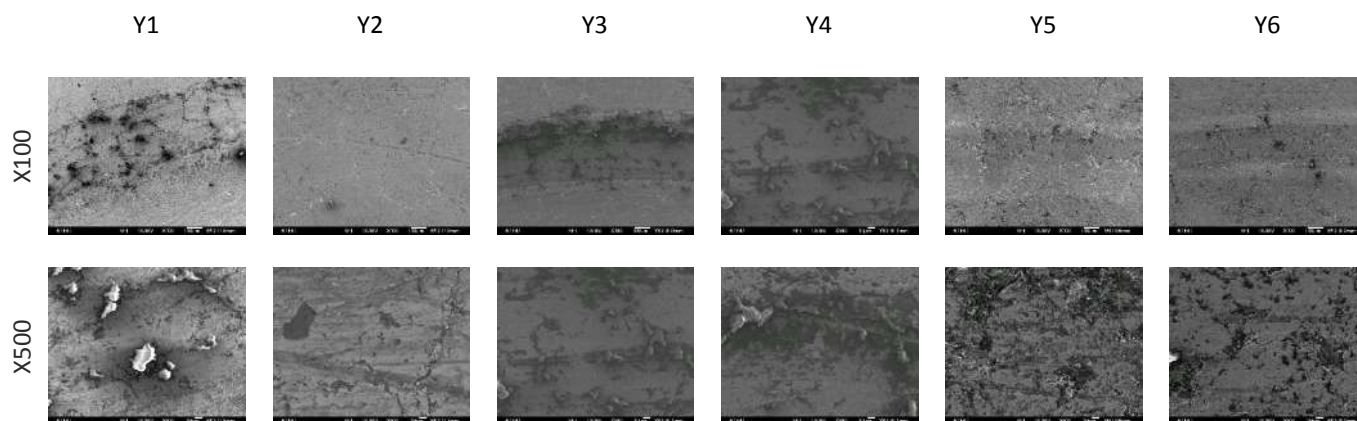
Y1 Y2 Y3 Y4 Y5 Y6

X100

X500

Figure 5. SEC photo based on design results in Table 2 (X100, X500)

Chemistry	
Carbon (total)	
Chromium	
Nickel	
Total All Other	

Component Elements Properties	Metric
Carbon, C	0.020 %
Chromium, Cr	22 %
Iron, Fe	68.71 %
Molybdenum, Mo	3.1 %
Nickel, Ni	6.0 %
Nitrogen, N	0.17 %

Component Elements Properties	Metric
Carbon, C	<= 0.080 %
Chromium, Cr	16 - 18 %
Iron, Fe	61.8 - 72 %
Manganese, Mn	<= 2.0 %
Molybdenum, Mo	2.0 - 3.0 %
Nickel, Ni	10 - 14 %
Phosphorous, P	<= 0.045 %
Silicon, Si	<= 1.0 %
Sulfur, S	<= 0.030 %

Component Elements Properties	Metric
Carbon, C	<= 0.010 %
Chromium, Cr	14.5 - 16.5 %
Cobalt, Co	<= 2.5 %
Iron, Fe	4.0 - 7.0 %
Manganese, Mn	<= 1.0 %
Molybdenum, Mo	15 - 17 %
Nickel, Ni	55 %
Phosphorous, P	<= 0.040 %
Silicon, Si	<= 0.080 %
Sulfur, S	<= 0.030 %
Tungsten, W	3.0 - 4.5 %
Vanadium, V	<= 0.35 %

a. Coating composition   b.2205   c.316   d.C276
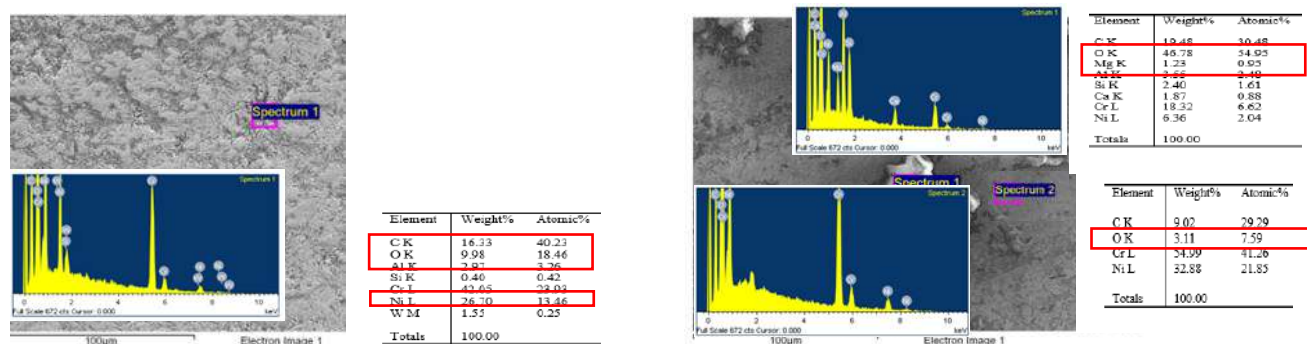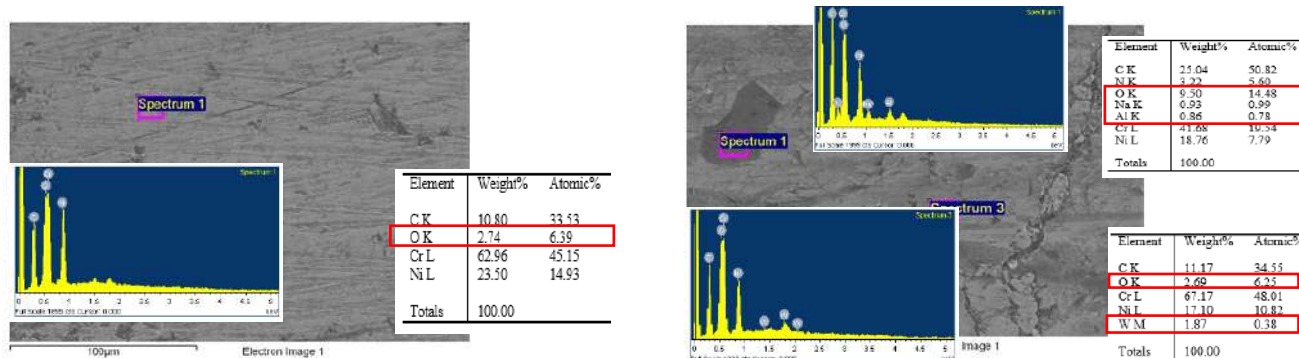
Figure 6. CrC thermal spray coating and substrate composition

a. Coating original morphology & Spectrum

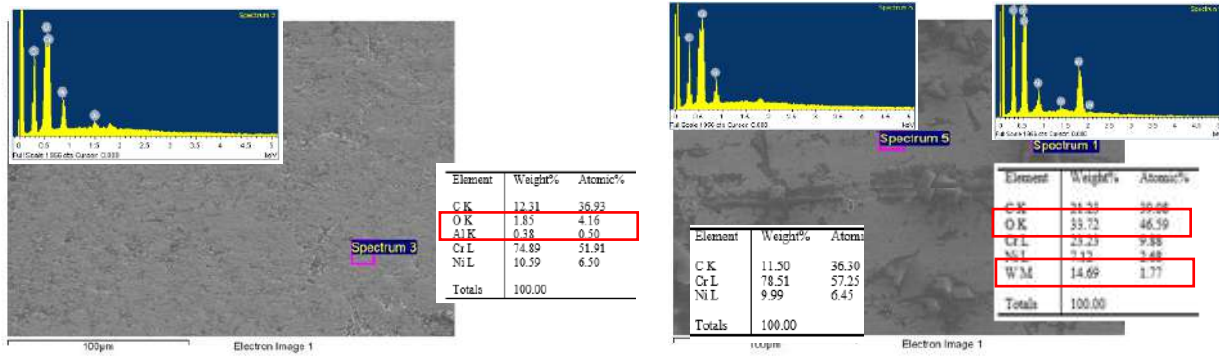b. Wear trajectory morphology & Spectrum

Figure 7. Y1 Original and Wear Traces within X500 EDS Photo

a. Coating original morphology & Spectrum

b. Wear trajectory morphology & Spectrum

Figure 8. Y2 Original and Wear Traces within X500 EDS Photo

a. Coating original morphology & Spectrum

b. Wear trajectory morphology & Spectrum

Figure 9. Y31 Original and Wear Traces within X500 EDS Photo

Fig. 9 shows the EDS of Y1. Fig 9-a is a result of composition analysis, and thermal spray coating the surface topography capture point. Fig 9-b shows the surface morphology of the wear trajectory and the results of the analysis of the capture points. The red box represents the components that are not shown in Fig 6-a and Fig 6-c.

From Fig. 7 - 9, the results of the spectrum can be found in the value of x is the largest and each analysis of the table are, this phenomenon may be after the experiment, with propanol cleaning test pieces and remain. The other elements of composition analysis arise, because the content ratio of less than 10%, it can be ignored explored.

4. CONCLUSION

Fig 3 observed Y1 & Y4, Y2 & Y5, Y3 & Y6 three groups of different environments wear test pieces, found that the amount of wear and load is not directly related.

Fig 5 shows that the coating thickness of this experiment is not absolutely related.

Fig 5 shows the wear trajectory, found in the state of environmental water, the test piece is the most serious wear, not generally recognized dry grinding. The reason may be composed of some of the ingredients within CrC, chemical reaction with water, and the coating which easily cause abrasion.

REFERENCES

[1] http://www.matweb.com/
    H. Czichos, D. Klaffke, E. Santner, M. Woydt: Advances in tribology: the materials point of view, Wear, Vol. 190, No. 2, pp. 155-161, 1995.

[2] C.L. Martin, O. Ajayi, A. Erdemir , G.R. Fenske, R. Wei: Effect of microstructure and thickness on the friction and wear behavior of CrN coatings, Wear, Vol. 302, No. 1-2, pp. 963–971, 2013.

[3] C.T. Wang , N. Gao , M.G. Gee, R. J.K. Wood, T.G. Langdon: Processing of an ultrafine-grained titanium by high-pressure torsion: An evaluation of the wear properties with and without a TiN coating, Journal of the mechanical behavior of biomedical materials, Vol. 17, 166–175, 2013.

CHARACTERISTICS OF THE MULTILAYER COATING FABRICATED ON AZ91 ALLOY BY MICRO ARC OXIDATION AFTER COLD SPRAYING OF Al-Cu POWDER MIXTURE

Faiz MUHAFFEL, Onur TAZEGUL, Huseyin CIMENOGLU*

Department of Metallurgical and Materials Engineering, Istanbul Technical University, Istanbul, Turkey

*Corresponding author: cimenogluh@itu.edu.tr

Abstract: *Magnesium alloys are attractive lightweight materials for the applications of aircraft-aerospace, chemistry, food, biomedical, automotive, electric-electronic, and communication industries. Besides magnesium and its alloys exhibit low density and high strength/weight ratio, their applications are broadly limited due to their low corrosion resistance and poor wear characteristics. To overcome these limitations, various surface modifications and coatings are applied on magnesium alloys, however many of the surface modification techniques have difficulties arising from low melting point of magnesium alloys, distortion and undesirable microstructure owing to excessive heat, environmental drawbacks or incapabilities to coat complex structures. Therefore, low temperature processes are gaining attention for protecting magnesium alloys from corrosion- and wear-related damages without altering the microstructure of the alloy.*

In the present study, cold gas dynamic spraying (CS) and micro arc oxidation (MAO) processes were applied subsequently on AZ91 magnesium alloy at low temperature conditions (<200 C). One group of samples was covered with monolithic aluminum and the other group was covered with a mixture of powder containing aluminum and copper. Later, the CS'ed layers were oxidized by MAO process in order to generate a protective alumina layer over AZ91 magnesium alloy. The effect of copper addition into the aluminum powder on the mechanical behaviour of the multi-layers were investigated in details.

Keywords: *AZ91 magnesium alloy, aluminium, cold gas dynamic spraying, micro arc oxidation, oxide coating.*

1. INTRODUCTION

Micro-arc oxidation (MAO) is a process that has used to form an oxide layer on the surface of the coating at low process temperature and in the environment friendly electrolytes [1]. It is possible to oxidise light metals such as aluminium, magnesium, titanium, etc. Corrosion and wear resistances of the metal substrate can be significantly improved by this method [2,3]. On the other hand, brittle and the porous nature of the oxide layer formed by the micro-arc oxidation process may reduce the fatigue resistance of the substrate in contrast to high surface hardness [4]. The effect of the process could be generated from easy propagation of the cracks because of the imperfect structure and brittle characteristics of the oxide layer.

In the scope of these explanation, we focus on the elimination of drawbacks about fatigue performance of the micro-arc oxidised samples by incorporated copper powders with different ratios which cannot be oxidised. In

this study, we characterised tribological performance of the oxide coatings with and without copper addition to determine the effect of copper to the oxide layer. In this sense, cold spray (CS) and MAO processes were sequentially applied to obtain multilayer coating on magnesium substrate containing oxide layer at the outermost surface and metallic layer beneath it. Moreover, X-Ray diffraction (XRD) and scanning electron microscopy (SEM) examinations were utilized for microstructural characterisation. Scratch and dry sliding wear tests were performed for tribological characterisation of the coatings.

2. MATERIALS AND METHOD

Cylindrical samples cut from AZ91 rod were used as the substrate. Prior to MAO process, monolithic aluminium and aluminium/copper mixtures were sprayed on the samples by CS process. The amount of copper added to aluminium powders were 30 and 60 wt.%. CS process was conducted by Rusonic Model K-201 equipment so that feeding powders were accelerated by air at inlet pressure of 6 bar. The CS layers were gently grinded and polished prior to MAO process. MAO was employed in sodium aluminum oxide (NaAlO2, Alfa Aesar), potassium hydroxide (KOH, Aldrich) containing electrolyte. The positive and negative voltages were selected as 400 and 80, respectively. During the MAO process the temperature of the electrolyte was kept at 20 ± 2 °C by the cooling system in order to regulate the chemical reaction rate on the surface of the samples. After the MAO process samples were cleaned ultrasonically in ethyl alcohol, distilled water and dried in air.

The surface morphology and cross-sectional microstructural analyses were conducted by a scanning electron microscope (SEM, Hitachi TM-1000). Phase composition of the coatings was examined between 20-80° 2θ degrees using X-ray diffractometer (XRD, GBC, MMA 027) with a Cu-Kα source. The accelerating voltage and applied current were 35 kV and 28.5 mA, respectively. The adhesion and scratching characteristics were examined by a

micro-scratch tester (CSM Instruments). The wear resistance of the samples in dry sliding conditions were evaluated by utilizing a computer controlled reciprocal wear tester (TriboTechnic Oscillating Tribometer). 6 mm silicon nitride ball was used as abrasive tool and sliding speed was 10 mm/s. The sliding distance, length of the wear track and load were 25 m, 5 mm, and 3 N, respectively. The wear area (μm^2) was calculated from the wear track cross-section by a profilometer (Dektak Veeco 6M). Relative wear resistance (RWR) of the samples was calculated as the ratio of the lowest wear area sample to the wear area of other samples.

3. RESULTS AND DISCUSSION

The XRD spectra belonging to the MAO-Cu-0, MAO-Cu-30 and MAO-Cu-60 samples are shown in Figure 1. On the XRD spectra, peaks of α-alumina, γ-alumina and aluminium were detected for all the samples. It should be mentioned that copper peaks have been detected and increased with the higher amount of copper in the mixture sprayed on the substrate. Peaks of aluminium appeared owing to the penetration of X-rays beyond the oxide layer. A small amount of copper oxide was observed in the spectrum of MAO-Cu-60 due to oxidation of copper during MAO process, however, the amount of copper oxide was relatively lower than alumina in the oxide layer.
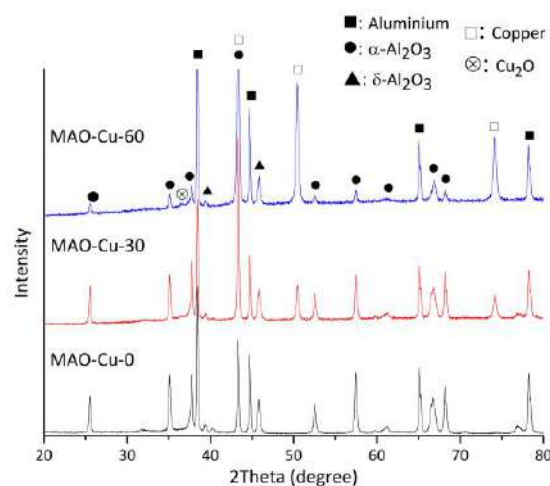

Figure 1. XRD spectra of samples after MAO process.

Surface SEM micrographs of the oxidized surfaces are presented in Figure 2. According to the SEM micrographs of the surfaces, the oxide layer on Cu-free MAO sample was covered with micro-pores with different sizes so that their characteristic porous nature was identified. The pores were homogenously distributed on the surface of the oxide layer. However, with the addition of copper into the CS'ed layer caused discontinuities on the surface as seen in Figure 2(b)-(c). The addition of 60 wt.% altered the coating surface morphology and created deep valleys and irregular pores.
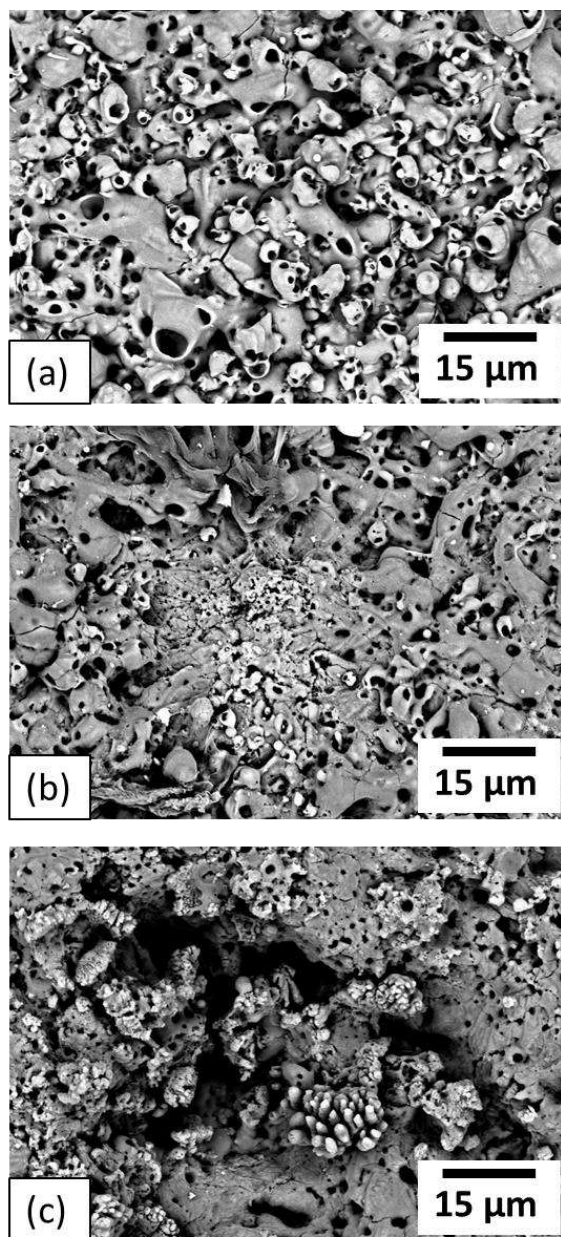

Figure 2. Surface SEM images of MAO'ed samples, (a) MAO-Cu-0, (b) MAO-Cu-30, (c) MAO-Cu-60.

Cross-sectional SEM micrographs of the oxidized samples are shown in Figure 3. Cross-section SEM examinations revealed that oxidized surfaces were covered with an oxide layer and the thickness of the samples are decreasing with increasing amount of the copper in the CS'ed layer (from about 20 μm to 10 μm). The copper particles were easily observed as the shiny particles embedded in the CS'ed layer as shown in Figure 3(b)-(c).
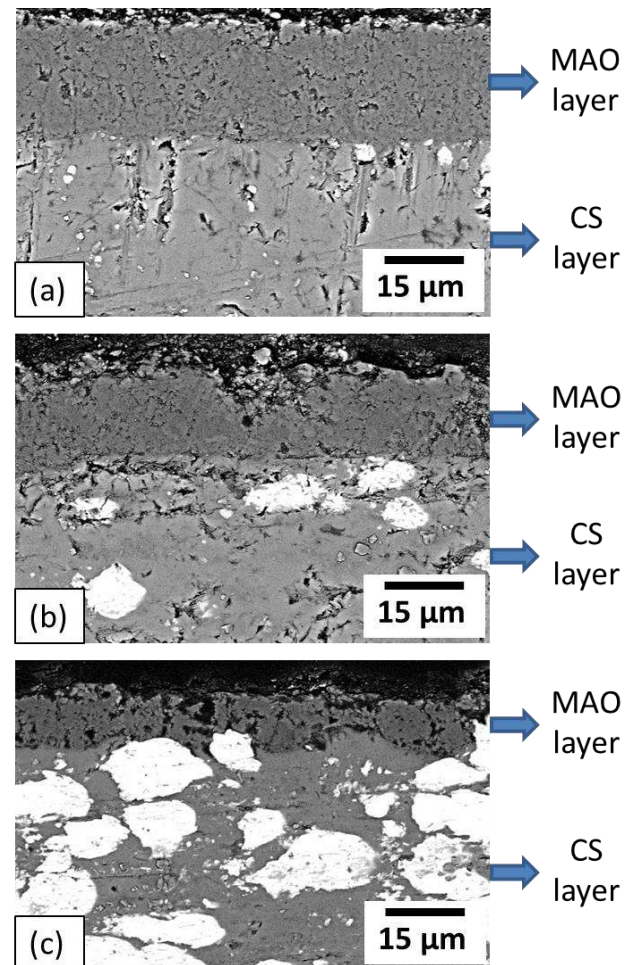
Figure 3. Cross-sectional SEM micrographs of MAO'ed samples, (a) MAO-Cu-0, (b) MAO-Cu-30, (c) MAO-Cu-60.

SEM micrographs of the scratch tracks for MAO'ed samples are shown in Figure 4. Due to high thickness and brittle microstructure of MAO-Cu-0 samples, cracks arising from the scratch track were easily observed on the surface. However, it is obviously seen that copper addition into the CS layer prevented the formation of cracks. This phenomenon can be explained by a beneficial composite

combination of alumina and copper containing aluminium layers generating a hard but also ductile multi-layer coating on AZ91 magnesium alloy.
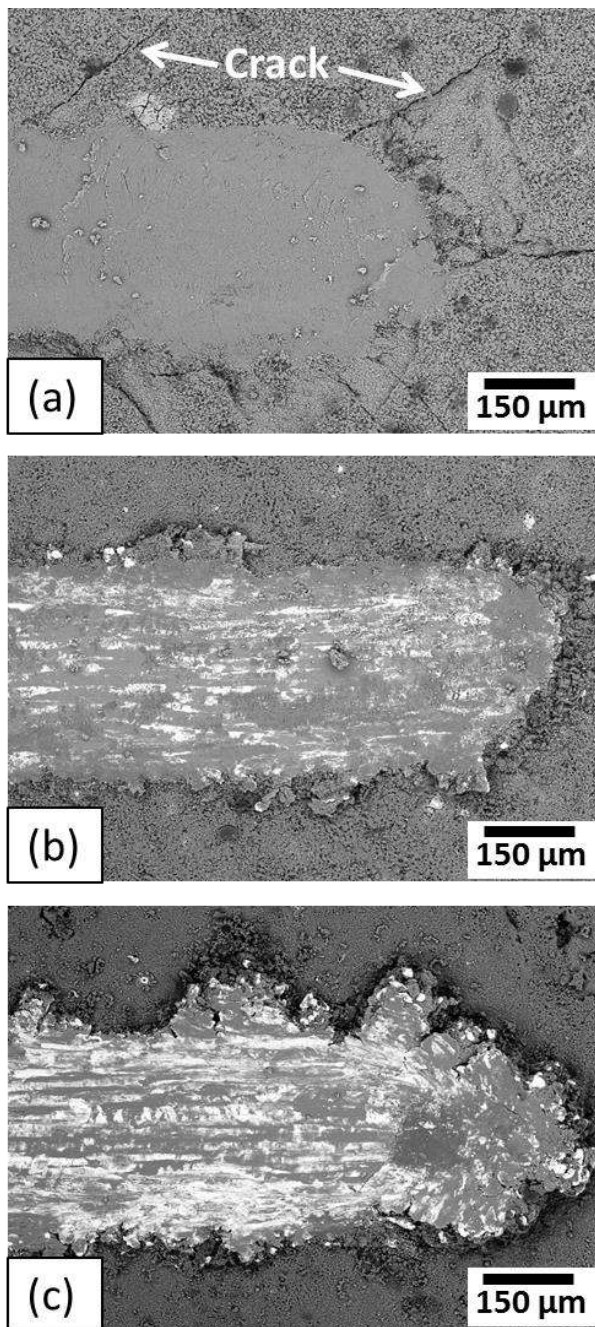

Figure 4. SEM micrographs of scratch tracks of MAO'ed samples, (a) MAO-Cu-0, (b) MAO-Cu-30, (c) MAO-Cu-60.

The friction coefficients of the wear tests at room temperature and under 3 N load under dry sliding conditions are shown in Figure 5. It can be seen that both samples containing copper in the CS layers showed relatively lower friction coefficient than MAO-Cu-0 sample during their startup periods. However, friction coefficient of MAO-Cu-

60 showed a rapid increase and reach to a value nearly similar to that of MAO-Cu-0 sample in the end of the wear test. Unlike the MAO-Cu-60 sample, MAO-Cu-30 sample exhibited a nearly stable friction coefficient curve until the end of the wear test.
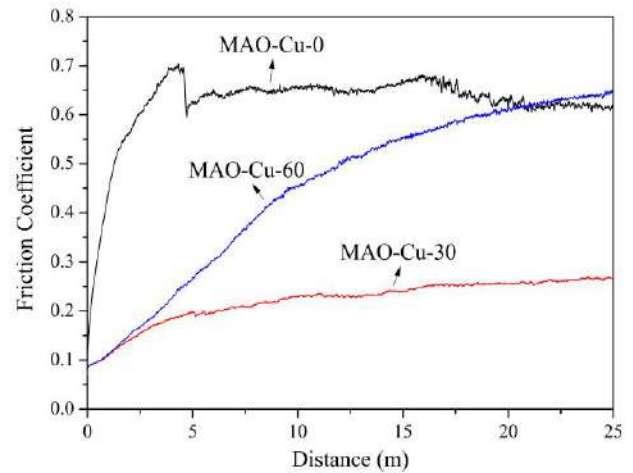

Figure 5. Friction coefficient curves recorded during wear tests for MAO'ed samples.

The RWR values calculated from the cross-section profiles are illustrated in Table 1. It is suggested that the MAO-Cu-30 sample exhibited higher RWR than MAO-Cu-0 and MAO-Cu-60 samples. While the friction coefficients of the MAO'ed samples were of concern, the high wear resistance of MAO-Cu-30 sample was consentient with these results. Reduced friction coefficient of MAO-Cu-30 sample may be explained by lubricating effect of copper oxide formed during sliding [5-7]. However, higher amount of copper reduced the wear resistance possibly due to the generation of inhomogeneous, thin and porous MAO layer.

Table 1. RWR values calculated from the wear tests.

Sample	MAO-Cu-0	MAO-Cu-30	MAO-Cu-60
RWR	1.5	2.1	1

4. CONCLUSION

The MAO coatings exhibited different structural and wear characteristics with respect to the copper content of the CS layers. While 30 wt.% copper addition into the CS layer improved the wear and scratch behaviours, 60 wt.% copper in the microstructure of CS layer altered both microstructural and tribological performances.

REFERENCES

[1] R. F. Zhang, S. F. Zhang, N. Yang, L. J. Yao, F. X. He, Y. P. Zhou, X. Xu, L. Chang, S. J. Bai: Effects of tannic acid on properties of anodic coatings obtained by micro arc oxidation on AZ91 magnesium alloy, Surface and Coatings Technology, Vol. 207, pp. 170-176, 2012.

[2] H. Solimana, A. S. Hamdy: Comparative study of micro-arc oxidation treatment for AM, AZ and MZ magnesium alloys, Protection of Metals and Physical Chemistry of Surfaces, Vol. 51, No. 4, pp. 620–629, 2015.

[3] Y. Eraslan: Wear performance of in-situ aluminum matrix composite after micro-arc oxidation, Transactions of Nonferrous Metals Society of China, Vol. 23, No. 2, pp. 347-352, 2013.

[4] A. L. Yerokhin, A. Shatrov, V. Samsonov, P. Shashkov, A. Leyland, A. Matthews: Fatigue properties of Keronite coatings on a magnesium alloy, Surface and Coatings Technology, Vol. 182, No. 1, pp. 78-84, 2004.

[5] A. Moghanian, F. Sharifianjazi, P. Abachi, E. Sadeghi, H. Jafarikhorami, A. Sedghi: Production and properties of Cu/TiO2 nano-composites, Journal of Alloys and Compound, Vol. 698, pp. 518-524, 2017.

[6] L. Yu, H. Zhao, H. Ju, J. Xu: Influence of Cu content on the structure, mechanical and tribological properties of W2N-Cu films, Thin Solid Films, Vol. 624, pp. 144-151, 2017.

[7] O. Tazegul, O. Meydanoglu, E. S. Kayali: Surface modification of electrical contacts by cold gas dynamic spraying process, Surface and Coatings Technology, Vol. 236, pp. 159-165.

Tribology of
Machine Elements

15th International Conference on Tribology – SERBIATRIB '17

17 – 19 May 2017, Kragujevac, Serbia

SERBIATRIB '17

Serbian Tribology
Society

**15th International Conference on
Tribology**

**Faculty of Engineering
University of Kragujevac**

Kragujevac, Serbia, 17 – 19 May 2017

INVESTIGATION OF TRIBOLOGICAL CHARACTERISTICS OF THE SAMPLES TAKEN FROM VALVE ON GAS PIPELINE SYSTEM J.P."SERBIAGAS"

Željko ALEKSIĆ[1], Pavel KOVAČ[2], Bogdan Nedić[3] , Dušan JEŠIĆ[4]

[1]J.P. "SRBIJAGAS", Srbija, aleksic@srbijagas.com
[2] Univerzitet u Novom Sadu, Fakultet Tehničkih Nauka, Srbija,
[3]Fakultet Inženjerskih nauka, Kragujevac, Srbija
[4] Međunarodna Tehnološko Menadžerska akademija,Srbija

*Corresponding author: aleksic@srbijagas.com

Abstract: The objective of this research based on samples taken from the real system of exploitation, comes to value of tribological parameters that are taking place in the boundary lubrication under high contact pressures and low sliding speeds. Various sliding speeds and pressure contact have been performed with materials taken from valves which have a constructive possibility of lubrication and are on the gas pipeline system J.P. "Serbiagas". The analysis of the obtained values shows that the coefficient of friction decreases with increasing the contact load.

Keywords: boundary lubrication, contact, grease, pressure, sliding

1. INTRODUCTION

Determining the hermetic, leakage of stopping organ wich play a critical role in the pipeline system is one of the very complex requirements uprising from the nature of stopping organs function – valves wich are at numerous of cases buried togather with the pipeline and the level of their hermetic level in that case is very hard to detremined. In the event of an accident or need for stopping of natural gas play a important role. Not a small number of times the requirements for valve leakage were disturbed and caused multiple additional operations on pipeline and increased costs. In responsible sections of the gas pipeline as well as distribution nods are in

use lubricating ball valves larger diameters (from DN 400 ÷ DN 1200, expressed in mm).

Contact compounds inside the valves which need to hermetic are under enormous forces with low speed sliding of materials in connection. They can be contact-type metal-metal and metal - PTFE (or the corresponding polymer). Almost every ball valve has the ability to be injected with grease of special formulation so that we have three body contact. Tribological system is defined by two contact element while the third element is a grease and all ball valve is under high pressure of 50 bar as well and more in natural gas environment.

2. OBJECT OF INVESTIGATION

The aim of this research is that on the basis of samples taken from the real system, valves, which were in service and parts that establish contact, along with the formulated grease FAM 2 through model testing occurs tribological values of parameters that have so far been unknown.

The area in which observed tribological process operates belongs to boundary lubrication and there is no possible access to "brightness" phenomenology than the experimental research, that was done in this case at the Faculty of Mechanical Engineering in Kragujevac on tribometer TPD-93 and belong to a group of model tests.
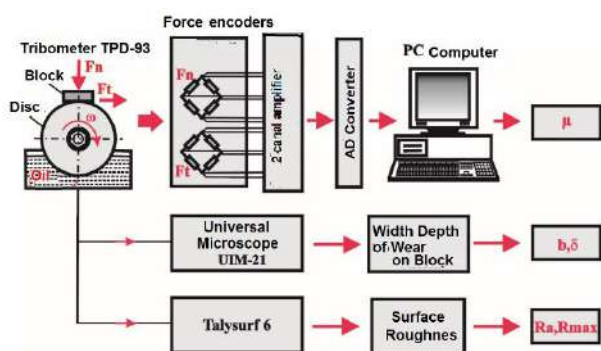

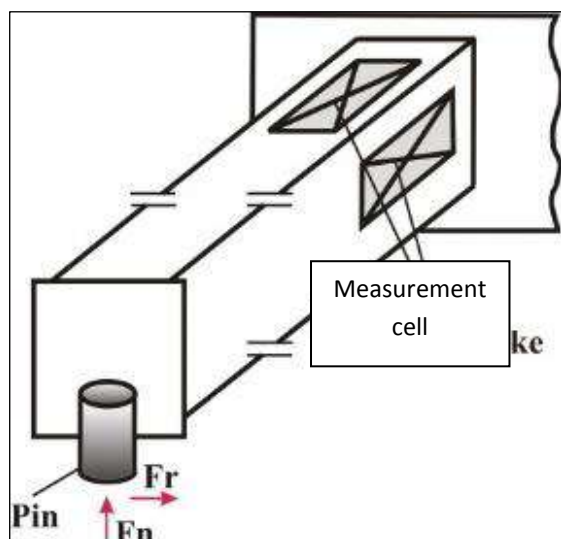**Figure 1.** Measuring equipment for tribological tests

Figure 2. Scheme of dynamometer

Material for making balls, in ball valves AISI 420 with the following characteristics chemical composition and mechanical properties, are shown in Table1.
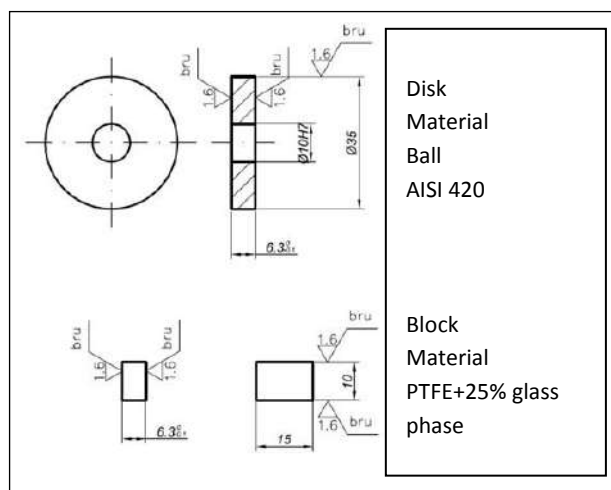
Figure 3. Geometry and drive of block

Table 1. Chemical composition and mechanical properties of AISI 420

C %	Si %	Mn %	Cr %	P %	S %	Tensile strength Rm	Yield strength Re
0,15	Max 1	Max 1	12-14	0.04max	0,03max	650-800 MPa	450 MPa

(Martensitic steel)[8].

Features thermoplastic material PTFE (polytetrafluoroethylene) with 25% glass phase for the blocks are given in Table 2.

Table 2. Physical, mechanical and thermal properties of PTFE with 25% glass phase [8]

Performance	Unit	PTFE +25% Glass phase
Density	g/cm^2	2,24
Breaking strength	N/mm^2	14
Elongation	%	250
Hardness indentation ball	N/mm^2	31
Thermal conductivity	W/mk	0,35
The thermal coefficient of linear expansion	K^{-1}	$1,0 \cdot 10^{-4}$
Temperature range of application	°C	-200÷+260

Figure 4. Enlarged part of the samples of metal balls. The body of valve and PTFE sealing ring (lost contact geometry due of exploitation process)

In Figure 4 are shown enlarged part of the samples of metal balls. On the body of valve and PTFE sealing ring are visible loss of contact geometry due of exploitation process. In Figure 5 is shown layout of blocks made of original sealing ring material for study. On the figure 6 is shown the process of making discs of selected material from the valve sphere in exploitation

Figure 5. Layout of blocks made of original sealing ring material

Figure 6. The process of making discs of selected material from the sphere in exploitation

3. EXPERIMENTAL TEST RESULTS

The study included the determination of the coefficient of friction tribological couple "block (PTFE) - disk (big ball AISI 420)" with the use of grease FAM 2. During the tests change were the sliding velocity and normal load. The obtained results are shown in Figure 7 - 10[th][7] The conditions during the experiment were:

Type of grease: grease FAM 2, from the manufacturer FAM Kruševac.
Block: Polytetrafluoroethylene -PTFE
Disk: Great ball-VK, material AISI 420
Normal load: Fn = 100 N, 200 N
Time test: t = 10 min
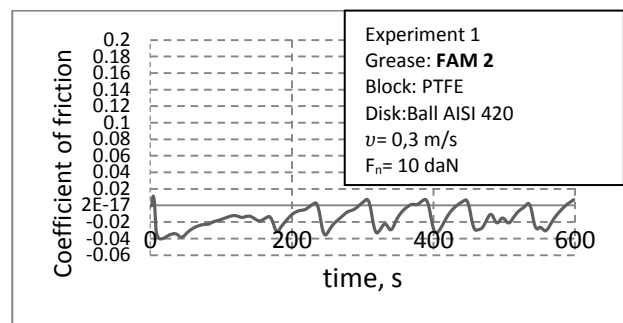The sliding speed of values were: v = 0.3 m/s, 0.5 m/s

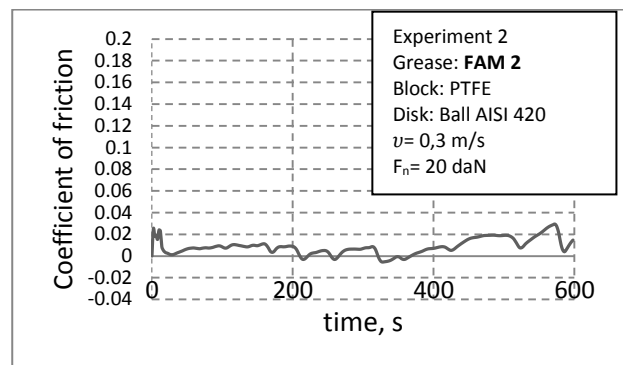**Figure 7.** Coefficient of friction versus time

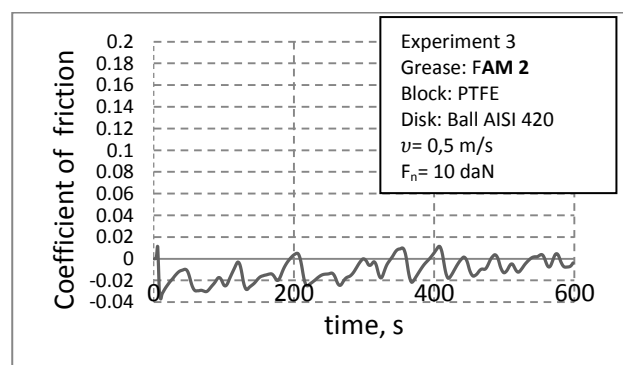**Figure 8.** Coefficient of friction versus time

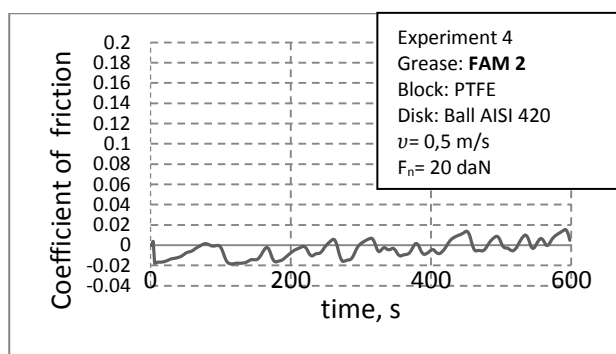**Figure 9.** Coefficient of friction versus time

Figure 10. Coefficient of friction versus time

Sliding speeds, normal load and average values - "calculated value" coefficient of friction during the test with a lubricant FAM 2 and tribo couple; block - PTFE and disc - Ball AISI 420, is shown in Table 3.

Table 3. The calculated values of the coefficient of friction for the investigated conditions [7]

Grease	FAM 2	FAM 2	FAM 2	FAM 2
Sliding velo	0.3 m/s	0.5 m/s	0.3 m/s	0.5 m/s
Normal load	10 daN	10 daN	20 daN	20 daN
Average values of friction coefficient	0.016	0.011	0.009	0.007

-Note about the way of calculating the coefficient of friction

Grease is due to the high density and high adhesion to a disc accumulate on the block directly to the contact, hardly passing through contact area and measurement console of dynamometer was moving backward – oppositely from the rotating disc direction.

For these reasons, the measuring device registered a "negative coefficient of friction."

In these diagrams, the friction coefficient must be replaced by another term - "calculated values" as the ratio between the measured forces which load the carrier block in the direction of sliding speed and normal load Fn.

Due to this phenomenon on measuring equipment, in order to determine mean values during this test was performed segmentation of the curve values that is in negative area. Its display is expressed as an absolute value of measured values to obtain a measure of the "friction coefficient", which, is seen from the physical aspect cannot be negative.

4. ANALYSIS OF RESULTS OF EXPERIMENTS

When lubricants FAM 2 (participation in the composition of MoS_2) revealed a large adhesive power of stickiness (capacity) retention on the surface. This caused the accumulation of grease in front of the disc and block. As a result, there was a moving of measuring console in the opposite direction, thus measuring device registered it as a "negative" coefficient of friction. In fact, this is expressed as a calculated value. The calculated value shows the characteristic traits that increase the load reduces the measured values, with 100 N to 200 N. Shown in Figure 11. [1,2,3,4]
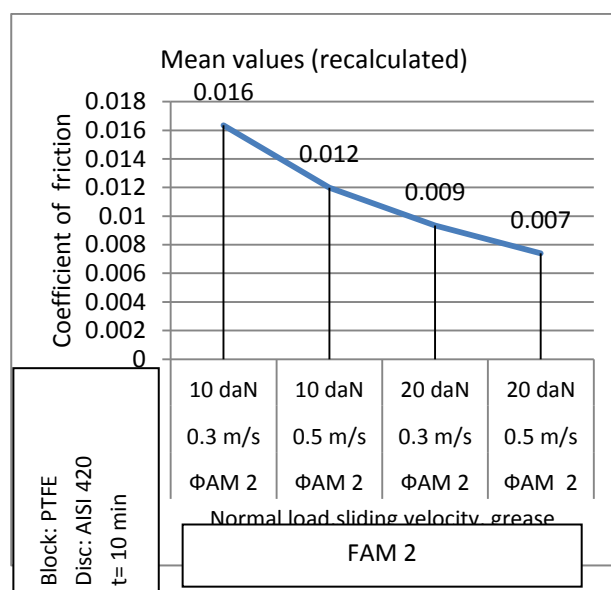
Figure 11. Mean values obtained by recalculating of the measured values [7]

Effect of MoS_2 composed specially formulated lubricants FAM2 and operation of PTFE with 25% glass phase in tribological test pair contributed to the synergistic effect that can be seen in Figure 11. The decline in the coefficient of friction.

The MoS_2 has excellent adhesion properties and high strength to cope with direct application to the surface (in this case the material AISI 420) while PTFE due fillers (filling)

in its matrix significantly raises the abrasive properties.

Improved anti-wear properties, with accessories can be the reason of forming a continuous and strong adhesive film that is transferred to the contact surface in contact with PTFE.

PTFE shows on the basis of experiments, decline of friction coefficient with increasing slip stress (load), which is illustrated and displayed in the results shown in Figure 11 and which are in accordance with the phenomenology [1,2,3,4].

In the Table 4 are shown characteristics of grease FAM 2 used in experiment.

Table 4. Characteristics of grease FAM 2

PRODUCT TYPE		FAM 2
Characteristics	Method	
Color	Visually	Black
Look at 20^0S	Visually	Homogenous
Unworking penetration,mm/10	ASTM D 217	175-205
NLGI	ASTM D 217	4
Dropping point,^0S	ASTM D 2265	>300
Oil separation,%	BS 2000 part.121	0
Slip tendency 4h/100^0C	GOST 19538-74	-
Resistance to water, degree	DIN 51 807/1	
15 min/90^0C		0
3 h/90^0C		1
Corrosion Cu,3h/100^0C	ASTM D 4048	1
Corrosion Cu,24h/100^0 C	ASTM D 4048	1

[FAM laboratory]

5. CONCLUSION

An experimental tribological research with samples taken from the real system (after several years of exploitation) in the field of boundary lubrication, gave a collective of experimental results so far, due to their nature were not so known.

Successful experimental research has shown that there is great potential for further research in this area and the impact on safety and reliability of operation of valves on the system of JP "Srbijagas".

ACKNOWLEDGMENT.

REFERENCES

[1] Briscoe, B.J: Material aspects of polymer wear, Scripta Met. Material, Vol. 24, pp 839-844, 1990.

[2] Jamison,W.E.: Plastic and plastic matrix composites, in CRC Handbook of Tribology and Lubrication, CRC Press, Boca Raton, Vol 3, pp. 121-147, 1994.

[3] Rabinowicz E.: Friction and wear of materials, 3rd edn. Wiley, New York, pp. 34, 1995.

[4] Gresham R.M. : Bonded solid lubricants, CRC Handbook of lubrication: Theory and practice of tribology, E.R. Booster (ed.), CRC press, Boca Raton, Vol. 3, pp. 167-181, 1997.

[5] Ivković B., Rac A., "Tribologija", Jugoslovensko društvo za tribologiju, Kragujevac, 1995.

[6] War office: USA, *Boudary lubrication, Scientific and technical applications forecast*, 1972.

[7] Aleksić Ž.:*The Application of tribological research on primary parts of valves in the gas systems, (In Serbian)*, PhD Thesis, Faculty of Technical Sciences, Novi Sad, 2016.

[8] www.api.org, American Petroleum Institute, "Represents America's Oil and Natural Gas Industry", 1996-2016.

DETERMINING THE RESISTANT FRICTION FORCES THAT OCCUR DURING SWITCHING PROCESS OF DIRECTIONAL CONTROL VALVES USED IN HYDROSTATIC DRIVES

Corneliu CRISTESCU[1]*, Catalin DUMITRESCU[1], Radu RADOI[1], Polifron CHIRITA[1]
[1]Hydraulics and Pneumatics Research Institute INOE 2000-IHP, Bucharest, Romania
*cristescu.ihp@fluidas.ro

Abstract: The article presents some research conducted in the Hydraulics and Pneumatics Research Institute INOE 2000-IHP, Romania, regarding the determination / evaluation of the total resistant frictional forces, that occur during the switching process of directional control valves used in hydrostatic drives. In the first part of the paper, there are presented some theoretical considerations on the possibility of quantifying / assessing / calculating the total frictional forces that needed to be known, to be overcome in switching process by the actuating mechanism, in order to change the direction of fluid flow. In the second part, the paper presents some experimental results obtained in the laboratory, which emphasize not only the value of these resistant forces, but also the dynamics of switching process of directional control valves, and, through the presented results, the article demonstrates its important practical value.

Keywords: Tribology, dynamic seals, frictional forces, viscous frictional forces, hydrostatic drive, testing bench, working fluid.

1. INTRODUCTION

It is known that in the structure of hydrostatic drive systems, in addition to the hydrostatic pumps and motors, an important role is played by elements directing the flow of pressurized fluid, currently known as the directional control valves.

In terms of construction hydraulic directional control valves are classified in: directional spool valves, directional ball valves, directional cam valves, directional poppet valves, seal closing valves, but the most used are directional spool valves.

For carrying out the process of directing fluid under pressure or to stop it, it is required a certain way to generate the switching force of the spool valve, force that can be generated: in a manual, hydraulic, pneumatic, electric etc. way.

The force required for switching / moving the spool of directional valve includes several types of forces and it depends on several factors, namely: working pressure, flow conveying through, speed of the fluid through the directional valve, fluid viscosity (viscous friction), dry friction (Coulomb) coefficient, etc. Generally, a directional valve, Figure 1, comprises the following major components: body of the directional valve (1), spool (2), compression springs (3), and depending on the drive various subparts are attached, for example two electromagnets (4) or a drive mechanism (5) [1].
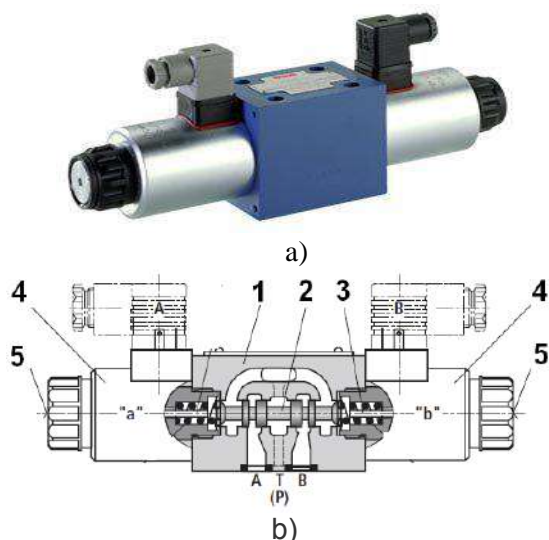
Figure 1. Spool hydraulic directional control valve [1]

The spool (or distributor) is the mobile element that connects the inlet port (P) to the outlet ports (A, B); the outlets, and in some versions also P, are also connected to the tank (outlet port T).

There are directional valves with 2, 3 or 4 ports or ways, and 2 or 3 working positions (E.g. 4/2, 4/3).
During the switching operation, which is performed by the movement of spool, the drive mechanism (actuating mechanism) must develop the force necessary to overcome the resistance forces.

That's why, it is very important to determine the resistance forces in both theoretical and the experimental way, especially when a drive electromagnet must be designed.

It is known that single stage directional valves are preferred because they are cheaper and most reliable, but increasing the rated size of coils / solenoids, electric actuators, they no longer cope, no longer develop the force required to switch spool, so for large sizes , i.e. high flow rates, there are preferred multistage directional valves [2].

The article presents theoretical considerations concerning the determination of resistance friction forces, and in the second part we present an experimental research that led to the determination of resistance forces when switching the directional control valve from a working position to another.

2. THEORETICAL CONSIDERATIONS ON QUANTIFYING TOTAL REZISTANT FORCES

Switching the hydraulic directional control valve from one position to another, for example, to achieve the flowing of the fluid Q under the pressure p transmitted by the pump through the port P to the hydraulic consumer connected to the port A of the directional valve where the flow rate Q_1 reaches, as a low flow rate q_a drains through metal-to-metal seal of spool, as shown in Figure 2, the actuator must develop an axial force F_{ax} at least equal to or greater than the sum of forces opposing the movement of spool [3].
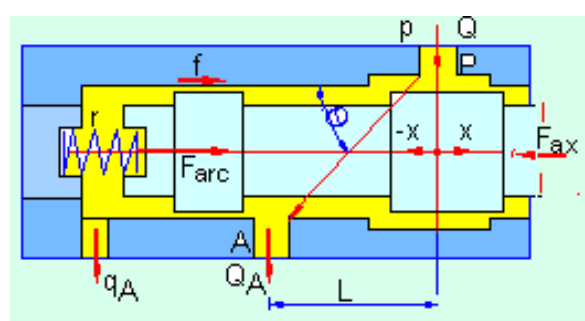

Figure 2. The fluid flow when switching spool

From Figure 2, it can be noted that, in addition to the dynamic forces related to the spool movement, of mass m, it entrains a quantity of fluid that is on the length L between the ports P and A, which varies over time, and a frictional viscous force which depends on the speed of movement v and the viscous friction coefficient f. In addition to these dynamic forces that vary over time, there also occur static forces represented by the force in the spring which varies with spool stroke x an spring constant r, and also the hydrodynamic force of the flow of fluid stream through the distributor, which is calculated on the basis of theorems of impulse and kinetic momentum, Euler's theorems, leading finally to the relation:

$$F = pvQ = \rho S \qquad (1)$$

where: ρ is the fluid density, v is the velocity of flow through the directional valve, S is the section through which flow rate Q of the fluid is flowing. As shown in Figure 2, the flow takes place at an angle θ of about 69°, so that the

projection of the axis of directional valve is given by the following equation:

$$F = pvQ \cdot \cos \theta \qquad (2)$$

Writing the balance equation through projection of the direction of travel, on the X axis, of all static and dynamic forces mentioned above, there is obtained the required axial force to be developed by the actuator of the directional valve (solenoid, etc.) according to the equation below:

$$F_{ax} = F_{din} + F_{st} =$$
$$= \left(m \frac{d^2x}{dt^2} + f \frac{dx}{dt} + \rho L \frac{dQ}{dt} \right) + \qquad (3)$$
$$+ (rx + \rho vQ \cos \theta)$$

In addition to the forces considered, in spool switching there also occur others; more significant is the bonding force, commonly called stick-slip, which is important to the long stay of the spool on a certain position.

Stick-slip is the spontaneous jerking motion that can occur while two objects are sliding over each other, with a corresponding change in the force of friction.

If the directional valve is left to stand under pressure for a few moments, in the next switching the stick-slip phenomenon occurs, which results in a higher than the normal operating resistance.

This additional resistive force disappears after several successive switching operations of the directional valve.
To reduce these forces, there is practiced execution of radial channels, called grooves, on the spool surface.

On the one hand, this force is added to the calculated value, and on the other hand it causes discontinuity of the spool movement, respectively of the supplied flow, and finally discontinuity of the hydraulically driven working machine.

But these bonding forces are difficult to assess, so it is necessary to experimentally determine total resistance forces that occur when switching the spool of hydraulic directional valve. Such an experimental determination is shown in the following.

3. PRESENTATION OF EXPERIMENTAL RESEARCH INFRASTRUCTURE

In order to determine the total resistance forces occurring during operation of directional valves, there has been designed and developed an experimental device, able to simulate, in the laboratory, the real operating conditions of a directional valve.

This device has been installed on a test bench arranged with help of some components existing in the laboratory, capable of generating the working fluid on the pressure and, also, a working device to assure the working load.

3.1. Constructive principle of the experimental device

The principle at the basis of developing the experimental device has consisted in using a manual directional control valve, being in the current manufacturing of company REXROTH BOSCH GROUP, from its market documents [4], shown in figure 3.

Figure 3. Manual directional control valves [4].

The basic idea used is that, in order to measure the resistant forces in switching of hydraulic directional valves, there should be used for switching the original actuating mechanism, and between the actuating mechanism and the directional valve spool there should be interposed a force transducer.

3.2. Presentation of the experimental device

For the physical development of the experimental device for measuring the forces

of total resistance, which occur in switching of hydraulic directional control valves there has been designed a constructive solution which was based on the use of a hydraulic directional control valve with manual control, of the size 10, existing in the Laboratory of Tribology of INOE 2000-IHP, shown in Figure 4. In order to achieve the device there has been detached body of the directional control valve (1a) from the mechanism for manual control (1b), for placing a force transducer FT on the axis of the directional valve spool, on the one hand, and, on the other hand, for performing actuation of directional control valve during tests precisely with the original control mechanism of the directional valve.
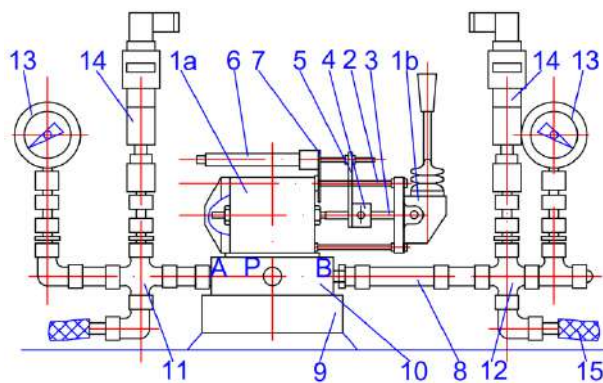

Figure 4. Layout of experimental device for measuring switching forces

For connecting / coupling the two parts of the main directional control valve, 1a and 1b, there were used four threaded rods (2) which replaced the original screws, thus achieving a space between the two parts of the main directional control valve. In this way, the possibility is created to insert, by means of threaded sleeves (3), a force transducer (4), between the control rods of the directional valve spool. To measure the stroke achieved by the spool, a rigid blade (5) is attached to the force transducer (4), which drives the rod of a potentiometric stroke transducer (6) which is fixed to the body of the directional valve by a supporting plate (7). The directional control valve is mounted by means of screws, on a compatible distribution plate (8) which is placed on another supporting plate (9). From the ports A and B of the distribution plate (8), pressurized fluid passes via two manifolds (11)

and (12), to the gauges (13) allowing direct reading of the pressure, and also to the pressure transducers (14), by which pressure variations are acquired by the computer system, and through the flexible hoses / piping (15), the fluid reaches the hydraulic motor actuated by the directional valve drive.

Physical development of the test device is shown in Figure 5, where one can see the actual technical solutions for developing it.
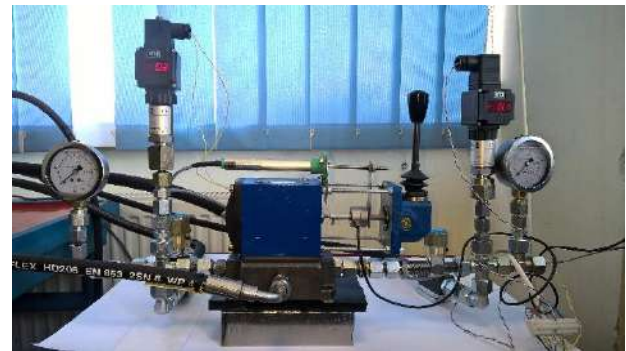
Figure 5. Physical development of the test device

3.3. Presentation of the experimental stand

To conduct the experimental research in order to determine the hydraulic resistance forces when switching directional valves, in the Laboratory of Tribology of INOE 2000-IHP there was arranged a test stand, in accordance with the diagram shown in Figure 6.

Figure 6. Concept daigram for arranging the experimental stand

Besides the experimental device ED which contains a force transducer FT, a stroke / displacement transducer ST, two pressure transducers PTA and PTB, and two manometers MA and MB, the stand also includes a hydraulic mini-station for generating pressurized fluid HG, a rotating mechanism RM driven by a rotating hydraulic

motor RHM and a system for data acquisition and processing ITS, consisting of a data acquisition board DAQ, National Ins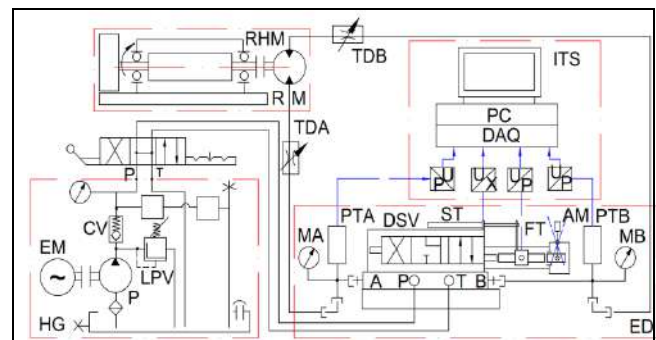truments type, and a PC type computer. The hydraulic generator GD is composed of a gear pump P driven by an electric motor EM, and assisted by a pressure limiting valve LPV, a check valve CV and a manual directional valve MDV through which pressurized fluid is sent to the ports A or B of the test device, and from here, through the throttles TDA and TDV, it reaches the rotating hydraulic motor RHM.

Figure 7 presents an overview of the experimental stand, and in Figure 8 one can see in detail the data acquisition and IT system.

Figure 7. Overview of the experimental stand

Figure 8. View of the IT system

By means of special electric cables all signals provided by transducers reach the acquisition board installed on the computer, and this one, based on specialized software, allows capturing, storage and processing of the measured data.

4. SOME EXPERIMENTAL RESULTS

In order to measure and record the variation of total resistance forces which occur on the spool of the directional spool valves, there has been conducted experimental research which led to obtaining a lot of graphical experimental results; some of them are presented bellow.

The object subjected to an experimental research was a hydraulic directional spool valve, directly operated, with manual actuation, size 10, manufactured by Rexroth Bosch Group, code 4 WMM 10 J 31/, which is a four-way distributor, with three operating positions, the central position providing communication of ports A and B to the tank T and the pump port P, closed, [5].

To this end, there has been necessary to set the parameters of interest and define a testing methodology.

Regarding the switching process in hydraulic directional spool valves, parameters of interest are:
- spool stroke x, measured by the stroke transducer ST in Figure 6, item 6 in Figure 4;
- resistive force Fax that opposes the spool movement, which is measured by the force transducer FT in Figure 6, item 4 in Figure 4;
- pressure at the port A, p_A, which occurs when opening the port A, measured by the pressure transducer PTA in Figure 6, item 14 in Figure 4;
 - pressure at the port B, p_B, which occurs when opening the port B, measured by the pressure transducer PTB in Figure 6, item 14 in Figure 4.

4.1 The test methodology

The test methodology consists of the following sequence:
- Start the PC computer systems and launch the data acquisition and processing software;
- Adjust, at the pressure limiting valve LPV in Figure 6, the desired pressure;
- Manually control the directional valve MDV in Figure 6, which opens the way for the pressurized fluid to the port P of the experimental device ED;
- Activate the data acquisition software;
- Manually control the tested directional valve DSV to open ways / ports, A and / or B for supplying the rotating hydraulic motor RHM, which begins to rotate the mechanism in one direction or the other. The command is for a

specified duration of tens of seconds, about a minute to a full cycle of control, which requires opening one at a time, both ports A and B;
- Stop data acquisition at the end of the control stroke of the directional control valve;
- Save the data acquired in the computer memory;
- Display and analyze the graphs of variation of parameters of interest;
- Repeat the sequences to get 2-3 records in the same case for a certain level of pressure;
- Repeat the sequences for other pressure levels;
- Stop PC computer system and end the testing session.

Following the developed experimental research, there have been obtained a lot of complete sets of experimental results, for 4 steps of pressure: 25 bar, 50 bar, 75 bar and 100 bar. For each pressure step, each measurement having 3 complete working cycles, for each half of cycle 3 determination, which means 6 determination and, also, for each quarter of cycle 3 determination, which means 12 determination. In total, there were 21 experimental determinations for each pressure step. For 4 pressure steps there were obtained 4x21 = 84 determinations.

One example of one complex graphic obtained is presented in Figure 9.

4.2 Analysis of the graphs obtained

After analyzing complex graphs obtained there were drawn some important conclusions, namely:
- graphs of variation of each parameter of interest have a logical progression, normal and repeatable;
- pressure values correspond to those directly read on the gauges MA and MB. They are slightly lower than the pressure values set at pressure limiting valve LPV because of pressure losses / drops along rotating hydraulic motor RHM circuits;
- the overall shape of the graph of spool stroke corresponds to a full work cycle in the drive / control mechanism with positive or negative values corresponding to the direction of movement of the control handle. Imperfections, small variations on the graph are due solely to the uneven manual drive by the human operator;
- the graph of resistance forces at spool is variable from one quarter of cycle of work to another, and also along individual quarter of cycle of work, but the differences between the maximum and minimum values are not very high, being in the range of (0-50) N, where it is admissible;

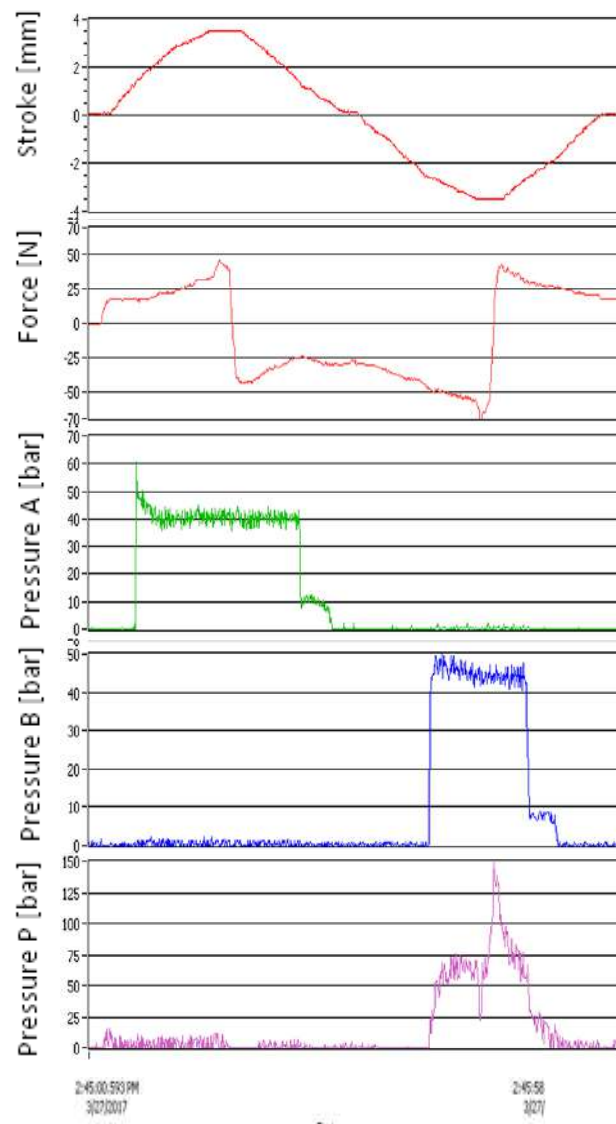**Figure 9**. Complex graphs for pressure step of 50 bar

- with the exception of the peaks, mean values of the resistance forces over a quarter of a stroke, are within the range (20 - 30) N [5], when extending the spool, and within the range (30 - 40) N, when compressing the spool, respectively the force transducer, which seems logical and corresponds to the recommendations in the literature [6];

- from a comparative analysis of graphs of variation of the resistant forces for the four pressure levels, no significant differences appear in proportion to the increase of pressure value. This may be due to internal balances based on special profiles of surfaces of elements in relative motion.

5. CONCLUSION

In the paper there are presented the research infrastructure and the results obtained following the development of an experimental research, on assessment of total resistance forces occurring in switching process of a directional spool valve.

Following the design and development of an experimental device and a testing stand, there have been obtained several complex numerical data and variation graphs for the parameters of interest, which enabled assessment of resistance forces, which occur during the switching process of the directional spool valves.

After analyzing numerical data and graphs obtained, it was concluded that the graphs of variation of parameters of interest, especially resistive force, have a normal form, and the mean values of them fall in a range of values close to the values mentioned in technical literature of reference [5].

Another important conclusion is that we cannot talk about a significant variation in the resisting forces with increasing working pressure, the pressure having a reduced influence on the switching force.

Through the numerical results and graphics, and especially through the conclusions reached following comparative analysis, this paper has special scientific and technical value and further research is required.

REFERENCES

[1] Rexroth Bosch Group. Spool hydraulic directional control valve direct-operated / 4/3-way WExx73xxA12, available at: http://www.directindustry.com/prod/bosch-rexroth-industrial-hydraulics/product-9143-1268489.html, accessed: 29.03.1017.

[2] Y, Qinghui, Y. Li. Perry: Using Steady Flow Force for Unstable Valve Design: Modelling and Experiments. In: Journal of Dynamic Systems, Measurement and Control, available at:http://dynamicsystems.asmedigitalcollection.asme.org/article.aspx?articleid=1410901, accessed: 27.march.2017.

[3] V. Marin, R. Moscovici and D. Teneslav: *Hydraulic Systems for Automatic Drive and Control* Technical Publishing House, Bucharest, Vol, pp 46-61, 1981.

[4] Rexroth Bosch Group. Directional spool valves, directly operated, with manual actuation, available at: https://www.boschrexroth.com/en/us/products/product-groups/goto-products/goto-hydraulics/directional-valves/4wmm-and-4wmr/index, accessed: 30.03.2017.

[5] Rexroth Bosch Group. Directional spool valves, directly operated, with manual and fluid logics actuation (size 6). available at: https://dcus.resource.bosch.com/media/us/products_13/product_groups_1/industrial_hydraulics 5/pdfs_4/re22280.pdf, accessed: 30.03.2017.

[6] Rexroth Bosch Group. Directional spool valves, directly operated, with manual and fluid logics actuation (size 10), available at: https://dc-us.resource.bosch.com/media/us/products_13/product_groups_1/industrial_hydraulics 5/ pdfs_4/ re22334.pdf, accessed: 30.03.2017

SERBIATRIB '17

15th International Conference on Tribology

TRIBOLOGICAL REINFORCEMENTS FOR CYLINDER LINER OF ALUMINUM - EXAMPLE COMPRESSORS FOR BRAKE SYSTEMS OF TRUCKS AND BUSES

Saša MILOJEVIĆ*, Dragan DžUNIĆ, Dragan TARANOVIĆ, Radivoje PEŠIĆ, Slobodan MITROVIĆ
University of Kragujevac, Faculty of Engineering, Kragujevac, Republic of Serbia
*Saša Milojević: sasa.milojevic@kg.ac.rs

Abstract: Aluminum gained in importance as a material for lightweight design of reciprocating engines and compressors. The application of aluminum alloys contributes to lower fuel consumption and exhaust emissions. The benefit of using aluminum is evident due to the reduced weight of the parts, but in parallel there is a problem due to the lower strength of this metal. Surface texturing and oils of low viscosity are used successfully to improve the tribological characteristics of sliding parts. For research purposes, the inner surface of cylinder which was produced of aluminum was reinforced by integrating tribological inserts. Their task is to reduce friction and wear between the piston and cylinder and to increase strength of the cylinder liner. Tribological optimization was made on the basis of the measurement results of the coefficient of friction. It is confirmed that the tribological properties of the cylinder with the tribological reinforcements are more optimal, compared to the case of aluminum construction (coating or honing of the cylinder liner). For this purpose is currently being brought into operation the test bench in the Laboratory for Engines as well as Tribology of the Faculty of Engineering University of Kragujevac.

Keywords: brake systems, tribology, cylinder liner, aluminum, optimization.

1. INTRODUCTION

Heavy-duty vehicles (HDVs), trucks and buses are responsible for about a quarter of carbon dioxide (CO_2) emissions from road transport in the EU and for some 6% of total EU emissions. Transport is the only major sector in the EU where greenhouse gas emissions are still rising. The European Commission has therefore set out a strategy to curb (CO_2) emissions from these (HDVs) over the coming years. Emissions from transport could be reduced to more than 60% below 1990 levels by 2050 [1].

In city buses and trucks a lot of fuel energy is engaging for power of auxiliary units. Specifically, the fuel energy is engaged for

drive of periphery units on engine, as example, for the air compressor, the alternator, the steering pump, the oil pump, the coolant pump, the fuel high pressure pump and the fuel delivery pump, as well as for air conditioning (A/C) compressor. The share of auxiliaries on the total power consumption is especially high for city buses due to (A/C) system and additional consumers of electricity and pressurized air, Figure 1 [1,2]. As a result, an increasing losses resulting in increase of fuel consumption, that is directly proportional to emission of (CO_2).

Reasons for this are the higher air demand of the wheel brakes, fewer headwinds for the engine cooling or more steering in curves i.e. the main influence factors on fuel

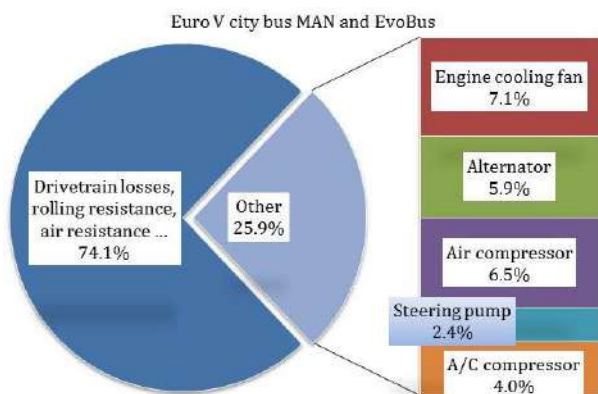consumption are the engine off heat or the wheel brakes air demand.

Figure 1. Percentage of driving resistances and auxiliary power demand on the fuel consumption of the city bus

Generally, city buses (classes with gross vehicle weight GVWR 18 t and length 12 m) are associated with 4.4% of total (CO_2) emissions [1]. City buses are frequently purchased by public institutions and thus they are in the public eye, yet may be the focus of cost-cutting measures [2-5].

Vehicles equipped with a conventional combustion engine can be still further improved by minimizing the internal friction of the mechanical parts in order to reduce (CO_2) emissions [6].

Potential actions to reduce friction in vehicles include the use of advanced coatings and surface texturing technology on engine and transmission components, new low-viscosity and low-shear lubricants and additives, and tire designs that reduce rolling friction [7-10].

In accordance with the above mentioned facts, we have realized the research in the field of optimal design of reciprocating aluminum engines and compressors. Consequently, we investigated new option for increasing strength and tribological characteristics of the tribo-system piston-cylinder liner [9-15].

The result of researches is patented prototype of aluminum piston and cylinder whose contact surfaces are coated or modified with reinforcements based on the tribo-materials [9].

2. PRODUCTION METHODS FOR ENGINE BLOCK AND CYLINDER SURFACES

If one compares the diverse options for realizing the engine block, Figure 2, and compares them with a view of today's requirements, on arrives at the conclusion that the profile is best met by an aluminum engine block [16]. The casting processes have become so advanced that the dynamic strengths demanded can be achieved by reducing casting faults, improving the microstructure and by targeted application of heat treatment.
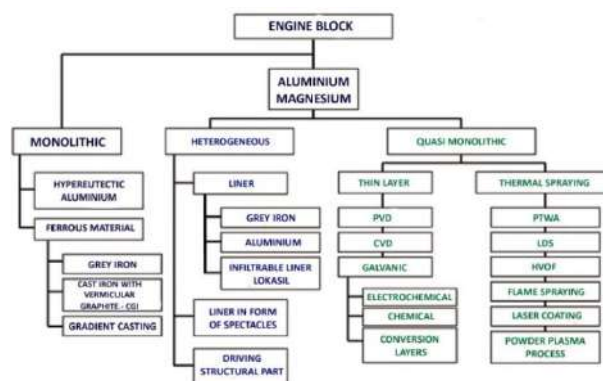
(PVD and CVD-physical and chemical vapor deposition; PTWA-plasma transferred wire arc; LDS-twin wire arc; HVOF-high velocity oxygen fuel)
Figure 2. Production method for engine block and cylinder surfaces

As the mechanical efficiency of the combustion engine i.e. reciprocating machines is strongly influenced by the tribological situation between piston, piston ring and cylinder surface, the properties of the cylinder surface become particular significant. Specifically, because the tribological properties of pure aluminum are poor compare with grey cast iron. Currently, one of solutions to resolve these problems is the use of cast iron liners. But, this is not the best solutions because of needed specific wall thickness, increasing dimensions and weight.

Another option is to provide protection of aluminum alloy, and chemical and thermal spray coatings are most predominant surface treatments. Today, any makers utilize thermal spraying to manufacture fully sprayed cylinder consisting of (Fe-Al) composite [10,11,13].

Looking from the second side, liquid-type lubricants have effectively served in reducing the friction and wear of various mechanical devices. However, in compressor components, the liquid-type lubricants have negative effects on their thermodynamic efficiencies, and also the state of lubrication in these components is usually not known and is considered to be in the boundary and mixed lubrication regimes. Recently, research interest and efforts are on oil-less compressor conditions to eliminate the adverse effects of liquid-type lubricants and to further improve the performance of compressors. Consequently, it becomes necessary to develop advanced coating materials that exhibit lower friction and higher wear resistant under compressor specific conditions [17].

2.1 New concept of aluminum cylinder with tribological reinforcements

Generally, according to real machining conditions, the full contact between piston rings and cylinder is not possible. This fact leads us to the idea that by casting tribological inserts in the cylinder, we can determine in forward, contact area between piston rings and cylinder liner.

With the aim to achieving strength as well as tribological characteristics similarly as in case of the application grey cast iron, we patented the cylinder of composite material for reciprocating air compressor with the reinforcements consisting of tribological materials, Figure 3 [9].

The internal surface of the aluminum cylinder as base material-matrix, (alloy EN AlSi10Mg), was modified by putting tribological inserts of cast iron that are arranged in the form of continuous pads, the plates or like discrete tribological plugs in the form of spheres (nodule), or particles spherical shape, as reinforcements, Figure 3 [9].

By transferring the contact between the piston rings and cylinder made of aluminum on the tribological inserts, we reduce the wear. This technology extends the service life of cylinder and piston rings.

Figure 3. Photography of patented aluminum cylinder with tribological reinforcements

This optimization can lead to reduce machine weight as well as reduced friction and wear. A reduction of friction between piston rings and the cylinder running surface is particularly effective, because the majority of frictional losses in the reciprocating machines are generated inside of this tribological system [14].

3. EXPERIMENTAL RESEARCHES

Wear is progressive loss of material caused by friction resistance between contact surfaces. The present work wants to investigate and evaluate the effect of tribological plugs as reinforcements on tribological behavior of patented aluminum cylinder.

Tribological tests were carried out on CSM nanotribometer with ball-on-plate contact pair for different normal loads, sliding speeds and distances without lubrications. Generally, tribological tests are based on variation of three different normal loads (0.3, 0.6 and 0.9) *N* and three different speeds (3, 9 and 15) $mm \cdot s^{-1}$. Duration of each test was 500 cycles (distance of 1 *m*), whereat one cycle is represented by full amplitude sliding distance (half amplitude is 0.5 *mm*).

The friction coefficient was automatically recorded during the testing, by using data acquisition software. Simultaneously, the friction coefficient curve was recorded and plotted during experiments.

4. RESULTS OF TRIBOLOGICAL TESTS AND DISCUSSION

4.1 Optical microscopy analysis

Experiments were carried out with the base material for cylinders (aluminum alloy) and with the material for reinforcements made of cast iron. Figure 4 presents optical microscopy of base aluminum alloy surface, where grey phases, which are noted on the surface presents eutectic silicon.
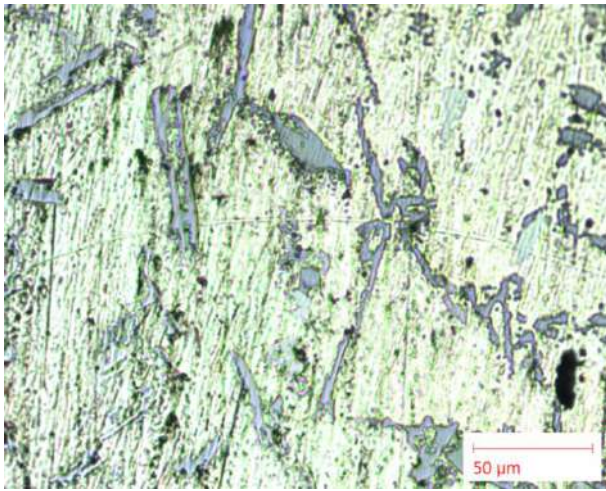

Figure 4. Optical microscopy of base aluminum alloy

Figure 5 presents surface of cast iron nodular discrete pads (reinforcements). Deeper analysis of the presented surface revealed that black lines across the surface are not micro cracks but graphite inclusions in the cast iron.
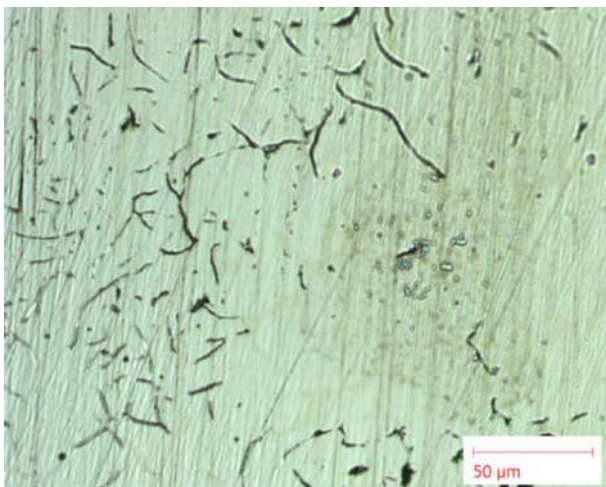

Figure 5. Optical microscopy of cast iron discrete nodular inserts

4.2 Coefficient of friction and penetration depth

Diagrams of friction coefficient (COF) and penetration depth during reciprocating sliding are shown in (Figure 6) for base material (aluminum) and in (Figure 7) for tribological inserts of cast iron.
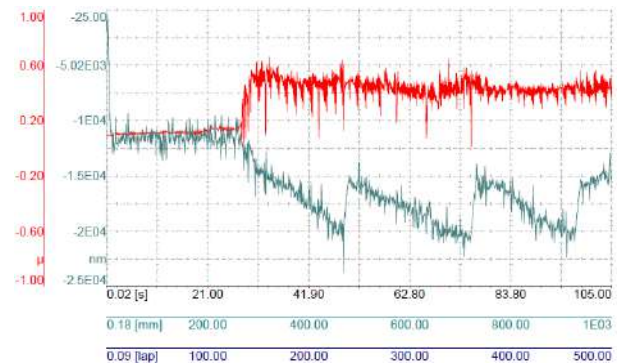
Figure 6. Coefficient of friction and penetration depth for base material $(F_N = 0.3\ N;\ V = 15\ mm \cdot s^{-1})$
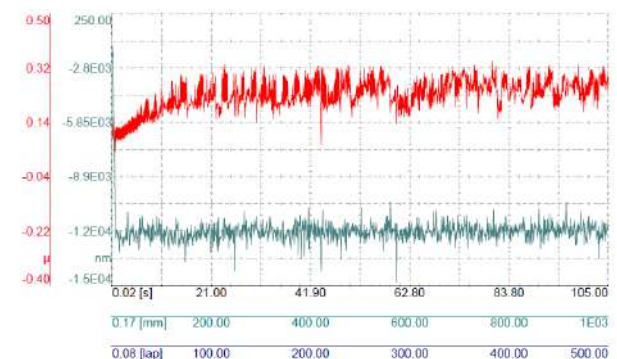
Figure 7. Coefficient of friction and penetration depth for tribological inserts (nodular discrete pads) under $(F_N = 0.3\ N;\ V = 15\ mm \cdot s^{-1})$

The values of the friction coefficient for tribological inserts were ranging from (0.041 up to 0.344), and these maximal values are lower to the results of base material (0.016 up to 0.662). This decrease was specifically lower for higher values of sliding speed and higher regimes of load. A steady-state value for the friction coefficient was reached shortly after the beginning of the test. Penetration depth of tribologically optimized material has relatively stable and constant values compared to base material.

On the Figure 6 it is noticeable that coefficient of friction sharply rises after a certain period of sliding as result of material transfer on counter body steel ball. After the material was transferred on the steel ball contact between transferred aluminum and aluminum as a base material was achieved. The latter results at that moment penetration depth also register a change in comparison to the previous period of contact. A cyclic change of penetration depth indicates that transfer of material on the counter body is cyclic process that means transferred material accumulates on counter body surface and after certain period fall off and became wear debris. In addition to this conclusion Figure 8 presents the profile of the steel ball before and after sliding test. Figure 8.b clearly indicates accumulated transferred material on the counter body surface.

(COF) and penetration depth obtained for cast iron discrete nodular insert are presented on Figure 7. In the case of cast iron there is no drastic change in (COF) and penetration depth in steady state regime.

4.3 Wear analysis

Optical microscopy was also used to examine obtained wear tracks. Figure 9.a and 9.b present wear tracks obtained under the same sliding conditions, but on two different materials. Comparing obtained wear tracks it is noticeable that wear of aluminum is higher than cast iron sample due to transfer material and increase of coefficient of friction which occurs for aluminum. Based on that it is fully justified the presence of cast iron discrete nodular inserts in aluminum that is widely used for engine cylinders.

a)

b)

Figure 8. Optical microscopy of the counter body steel ball profile a) before and b) after sliding test
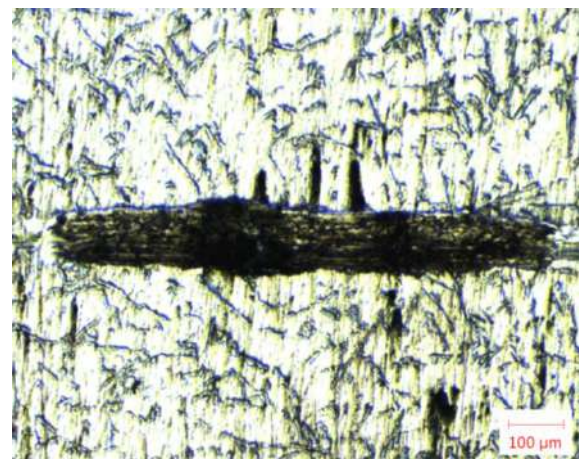
a)

b)

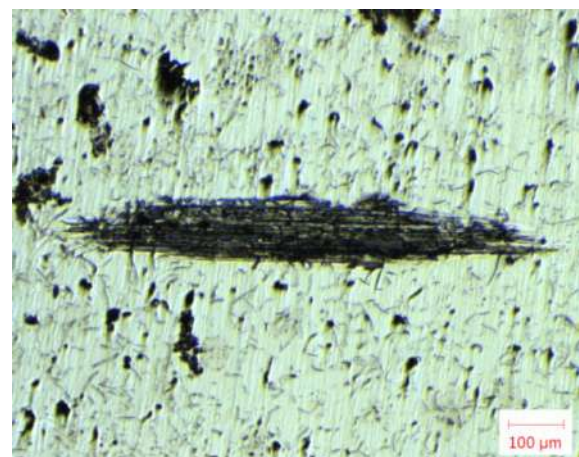**Figure 9.** Wear tracks of a) aluminum and b) cast iron under ($F_N = 0.3\ N$; $V = 15\ mm \cdot s^{-1}$).

Deep grooves in wear track of both tested material indicates that abrasive wear is the most dominant wear mechanism.

5. CONCLUSIONS

In trucks and city buses a lot of fuel energy is engaging for power of auxiliary units of engine, as it is air compressor inside braking system, reciprocating compressor for air conditioning system, pump of the steering system, alternator etc.

Aluminum continues to gain in importance as a material for lightweight machine design. One of the applications is replacing of material for engine blocks, which has been traditionally produced of gray cast iron. Application of aluminum contributes also to reducing fuel consumption that has a direct impact on reducing exhaust emissions.

Coatings of the tribo-materials on contact surfaces between the parts of system in sliding contact contribute to reducing friction while increasing resistance to abrasion.

Inside the paper are presented the realized researches in the field of optimal and tribological design of reciprocating aluminum compressors.

Presented results of the researches, obtained during tests of materials from which consisting cylinder, shows that by transferring the contact between the piston rings and cylinder made of aluminum on the reinforcements, it is possible to reduce the friction and wear. This technology extends the service life of cylinder and piston rings.

Penetration depth of tested material which is used for reinforcements has relatively stable and constant values compared to the base material, named as the matrix.

Comparing obtained wear tracks it is noticeable that wear of aluminum is higher than cast iron sample due to transfer material and increase of coefficient of friction which occurs for aluminum.

The values of the friction coefficient for reinforcements were ranging from (0.041 up to 0.344), and these maximal values are lower to the results of base material-matrix (0.016 up to 0.662).

ACKNOWLEDGEMENT

REFERENCES

[1] Road transport: *Reducing (CO₂) emissions from vehicles*, available at: http://ec.europa.eu/clima/policies/transport/vehicles/index_en.htm, accessed: 03.02.2017.

[2] S. Milojević, R. Pešić: *CNG buses for clean and economical city transport*, Int. J. Mobility and Vehicle Mechanics, Vol.37, No.4, pp. 57-71, 2011.

[3] S. Milojević: *Reconstruction of existing city buses on diesel fuel for drive on Hydrogen,* Int. J. Applied Engineering Letters, Vol.1, No.1, pp. 16-23, 2016.

[4] S. Milojević, D. Gročić, D. Dragojlović: *CNG propulsion system for reducing noise of existing city buses*, Journal of Applied Engineering Science, Vol.14, No.3, pp. 377-382, 2016.

[5] S. Milojević: *Sustainable application of natural gas as engine fuel in city buses – Benefit and restrictions*, Journal of Applied Engineering Science, Vol.15, No.1, pp. 81-88, 2017.

[6] M. Kennedy, S. Hoppe, J. Esser: *Piston ring coating reduces gasoline engine friction*, MTZ Motortechnische Zeitschrift , Vol.73, No.5, pp. 40-43, 2012.

[7] S. Mitrović, M. Babić, B. Stojanović, N. Miloradović, M. Pantić, D. Džunić: *Tribological Potential of Hybrid Composites Based on Zinc and Aluminium Alloys Reinforced with SiC and Graphite Particles,* Int. J. Tribology in Industry, Vol.34, No.4, pp. 177-185, 2012.

[8] B. Stojanovic, J. Glisovic: *Automotive Engine Materials*, in: Saleem Hashmi (Ed), Reference Module in Materials Science and Materials Engineering, Oxford: Elsevier, 2016, pp. 1-9.

[9] R. Pešić: *ASMATA–Automobile Steel Material Parts Substitution with Aluminum*, Int. J. Vehicle Mech., Engines and Transportation Syst., Faculty of Mechanical Engineering, University of Kragujevac, 2004.

[10] A. Vencl: *Optimization of the Deposition Parameters of Thick Atmospheric Plasma Spray Coatings*, Int. J. Balkan Tribological Association, Vol.18, No.3, pp. 405-414, 2012.

[11] A. Vencl, A. Rac, I. Bobic*: Tribological behaviour of Al-based MMCs and their application in automotive industry,* Int. J. Tribology in Industry, Vol.26, No.3-4, pp. 31-38, 2005.

[12] A. Vencl, A. Rac: *New wear resistant Al based materials and their application in automotive industry*, Int. J. Vehicle Mech., Engines and Transportation Syst., 30(2004): 115-139, Special edition.

[13] R. Pesic, S. Milojevic: *Efficiency and Ecological Characteristics of a VCR Diesel Engine*, Int. J. Automotive Technology, Vol.14, No.5, pp. 675-681, doi 10.1007/s12239–013–0073–4, 2013.

[14] S. Milojević, R. Pešić, D. Taranović: *Tribological Principles of Constructing the Reciprocating Machines*, Int. J. Tribology in Industry, Vol.37, No.1, pp. 13-19, 2015.

[15] S. Milojevic, R. Pesic, D. Taranovic: *Tribological optimization of reciprocating machines according to improving performance,* Int. J. Balkan Tribological Association, Vol.21, No.3, pp. 690-699, 2015.

[16] B. Gand: *Coating for cylinder surfaces in aluminium engine blocks,* MTZ Motortechnische Zeitschrift , Vol.72, No.1, pp. 34-39, 2011.

[17] T. A. Solzak, A. A. Polycarpou: *Tribology of Protective Hard Coatings for use in Oil-Less Piston-Type Compressors,* available at: http://docs.lib.purdue.edu/icec/1790, accessed: 03.02.2017.

TRIBOLOGICAL BEHAVIOR OF RADIAL PLAIN BEARING MADE OF TiN-BASED WHITE METAL ALLOY -TEGOTENAX V840

Amir ALSAMMARRAIE [1], Dragan MILČIĆ[2], Milan BANIĆ[3], Miodrag MILČIĆ[4]

[1] Univercity of Tikrit, Iraq, amircraft.2011@yahoo.com
[2] Faculty of Mechanical Engineering in Nis, Serbia, milcic@masfak.ni.ac.rs
[3] Faculty of Mechanical Engineering in Nis, Serbia, banicmilan@hotmail.com
[4] Faculty of Mechanical Engineering in Nis, Serbia, milcic.miodrag@gmail.com

Abstract: The present paper investigates experimentally the effect of sliding distance, rotation speed of shaft and normal load on friction, surface roughness special position on bearing inner surface and wear property of radial plain bearing made of tin-based white metal alloy -TEGOTENAX v840 under lubricated contact sliding against stainless steel shaft, to do that, a test rig apparatus was designed and fabricated. Experiments were carried out under normal load 1000,1500 and 2000 N and speed 750,1000, 1500 rpm. Results show that the wear rates increase with the increase of sliding speed and normal load. It is also found that friction coefficient increases with the increase of sliding speed and decreases with increase normal load. It is also found that the roughness change with sliding distance in special position bearing inner surface.

Keywords: radial load, roughness, distance sliding, coefficient friction, wear.

1. INTRODUCTION

Under conditions of full-film lubrication, the thickness of the lubricant film is supposed to be large enough to separate the roughness peaks on the surfaces of journal and bushing completely. If full-film lubrication of a bearing cannot be guaranteed during its entire lifetime, the wear rate (defined as the gradual loss of material of the bearing bush, caused by mechanical contact with the journal, i.e. the journal is assumed not to suffer from wear, and erosion and surface fatigue do not occur) of the bearing material is an important quality criterion that should be taken into account by designers and users. This is particularly true if the bearing is designed to function dry, in

which case a polymer based bearing material will often be used [1]. It is known that loaded contacts in relative movement give rise to wear phenomenon, which depends on several parameters such as roughness of rubbing surfaces, nature and microstructure of materials [2]. However, wear results at a micro geometrical scale by weight loss and sublayers deformation that lead to the formation of a third body called debris. The later plays a significant role in the wear process [3]. Tribological and mechanical properties of journal bearings manufactured from copper-based CuSn10 bronze and CuZn30 brass were investigated. Moreover, the effect of alloy elements of Cu, Sn and Zn on tribological and

mechanical properties of journal bearings was evaluated [4].

Savaskan [5] tested the friction and wear alloy AL-25Zn-3Cu-3 Si on tribometer by change pressure and sliding speed. He is found that the coefficient of friction of the alloy increases with sliding speed, but decreases with increasing pressure up to 1.5 MPa, above which the direction is reversed. However, the temperature and the extent of wear alloys are constantly increasing with increasing pressure and sliding speed. Ozsarac's [6] bearing wear tests were carried out using the new machines. On the machine were tested three types of behavior samples. These were based on tin bronze and lead RB-1, RB-7 RB-4 designs. Wear tests were carried out under a load of 10, 20 and 40 N and a sliding speed of 0.5 m / s using a sample in the form of a ring. Upon completion of the tests were measured, the weight of samples, calculate the value of the coefficient of friction, conducted the optical and SEM tests and eventually wear characterized with conventional alloys to be used for sleeve bearings. Guida [6] investigated the parameters of dry friction on the control system of the cart-pendulum. was used a geometric approach to analyze the influence of friction on the bearing. Conclusion is that the relationships that make it possible to assess how the parameters of friction bearings affect performance of the control system of the cart-pendulum.

Javorova *et all* [7] studied the performance of a finite length journal bearing, taking into account effects of non-Newtonian Rabinowitsch flow rheology and elastic deformations of the bearing liner. According to the Rabinowitsch fluid model, the cubic-stress constitutive equation is used to account for the non-Newtonian effects of pseudo plastic and dilatant lubricants. Sonam's [8] research work is directed on the development of new materials for industrial applications. From review of literature, it was found that the conventional bearing material (Babbitt and bronze) leads to high rates of wear, as well as a high coefficient of friction. Friction loss has been typically determined based on measurements of torque or heat flow caused by the friction. Andersson and Lintula [9] and Andersson *et al.* [10] determined the coefficient of friction of water-lubricated journal bearings by using a force transducer to measure friction torque reaction force in a lever arm.

The aim of the present work is to address lack of experimental data in order to ensure a better understanding of the influence of supply conditions on bearing made of tin-based white metal alloy -TEGOTENAX v840 under lubricant condision.

2. THEORETICAL FOUNDATION OF THE WEAR AND FRICTIONAL HYDRODYNAMICALLY

Wear can be defined as the removal of material from solid surfaces by mechanical action. Wear can appear in many ways, depending on the material of the interacting contact surfaces, the operating environment, and the running conditions. The most common wear model is named Archard's Wear Law [11], although Holm [12] formulated the same model much earlier than Archard:

$$V = K \frac{F_N}{H} s ,$$ (1)

where V is the wear volume, K is the dimensionless wear coefficient, F_N is the normal load, H is the hardness of the softer contact surface and s is the sliding distance. However, studies have found that wear coefficient is more suitable. The reason being that it takes the wear rate, the applied load, and the hardness of the wear material into account. Therefore, the wear coefficient K in the abrasive model is defined as:

$$K = \frac{H \cdot V}{F_N \cdot s},$$ (2)

as V can be evaluated from weight loss W and the density ρ, the wear coefficient can also be expressed as:

$$K = \frac{H \cdot W}{F_N \cdot s \cdot \rho}.$$ (1)

As shown in Fig. 1 the coefficient of friction generated between journal bearing and lubricant can be determined by following equation:

$$\mu = 2 \cdot \pi \cdot \frac{r^2 \cdot B}{c} \cdot \frac{\eta \cdot \omega}{F}, \qquad (4)$$

where μ is coefficient of friction [-], r is radius bearing[m], $h=c$ is thickness of clearance [μm], η is dynamic viscosity [Ns/m^2], ω is angular speed [1/sec], F is normal load [N] [13].
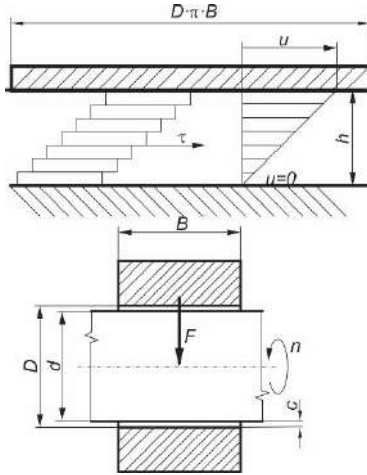

Fig. 1. Schematic friction model for journ

3. EXPERIMENTAL STUDIES

3.1. Preparation of experimental materials and conditions

In this study, radial plain bearing specimens made of tin-based white metal alloy - TEGOTENAX V840 were used as journal bearing and AISI 440C stainless steel was used as shaft. The chemical compositions of the journal and bearing materials used in the experiments were given in Table 1. The specimens were robbed by radial journal

bearing wear test rig under lubricated condition. The tribological parameter were measured under lubricated conditions of (1000, 1500 and 2000) N loads, (750, 1000, 1500) rpm equals to (1.75, 2.09, 3.14) m/s and every 1 h for change coefficient friction, 5 h for wear losses each specimen. The lubrication was achieved by using ISO VG32 oil.

Before and after testing, the specimens were cleaned by cleaner FLUXO S190 and dried using cotton and convection oven at 60 °C for a period of half an hour to remove humidity, as the weight of the samples was measured using a digital balance and recording the values before and after the test for each test. The surface profiles of the plain journal bearing were determined prior the tests by using the Perthometer SJ-301. The bearing was drilled with hole (dimension r =1.5 mm) in radial direction to ease lubrication oil flow into the contact zone. Circumferential groove was also made onto the outer surface of bush (width 2 mm, depth 0.5 mm) to include that lubrication oil arrives into the radial hole. as well, the spiral groove is made onto inner surface of sample (width 2 mm, average depth of 30 μm) to improve the lubrication process between the shaft and the bush. Each sample was marked with four perpendicular lines in order to investigate roughness changes of the bush surface, as shown in Fig. 2.

Table 1. Chemical composition of AISI440C wt- (%). and bearings materials wt- (%)

TEGOTENAX (V480) (big sticks), in TKL NOVA TVORNICA KLIZNIH LEZAJEVA (SLIDING BEARING MANUFACTURING), CROATIA											
WM	Sn	Sb	Cu	As	Bi	Ni	Pb	Cd	Fe	Al	Zn
Actual Value %	88.7	7.6	3.7	0.009	0.002	0.003	0.008	0.010	0.009	0.000	0.002
The alloy is free of lead and free of cadmium in compliance with RoHS Regulation (EU-Directive 2002/95/EC)											
AISI 440C	C	Si	Mn	Ni	Cr	Mo	P	S	-	-	-
	1.2	1	1	1	18	0.75	0.04	0.03	-	-	-
Mechanical Property Requirements For Material in the Annealed Condition to 1) AS2837 - 1986 440C and 2) ASTM A276-98b 440C											

Table 2. Material and physical proprieties of bearing

| White metal (WM) alloy TEGOTENAX				*440C stainless steels*	
Hardness	HB 10/250/180 (DIN ISO 4384 part 2)	20 [°C]	23	Tempering Temperature	260
		50 [°C]	17	Tensile Strength (MPa)	1960
		100 [°C]	10	Yield Strength 0.2% Proof (MPa)	1830
		150 [°C]	8	Elongation (% in 50mm)	4
Young´s modulus	E	56500 [N/mm²]		Hardness Rockwell (HRC)	57
Density	ρ	7,4 [kg/dm³]		Density (kg/m^3)	7650
Lower melting point	T_{lm}	233 [°C]		Elastic Modulus (GPa)	200
Upper melting point	T_{hm}	360 [°C]		Thermal Conductivity (W/m.K) at 100°C	24.2
Casting temperature	Tc	440 [°C]		-	-
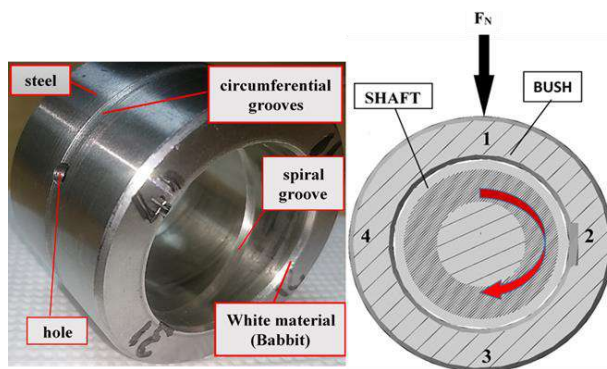
Fig.2 The modification to the samples (bush) design was conducted in the engineering workshops

3.2 Radial journal bearing wear test rig

Bearings materials in journal bearings are generally selected from materials, which have lower wear strength than the shaft material, that way dropping the wearing of the shaft safely. Therefore, journal bearing wear test apparatus are designed to examine the wearing of bearing materials. In Fig. 3a Shows the test rig which was modified specifically for this research to use in determining tribological properties of the bearings [14]. Therefore, it is possible to investigate different bearing and shaft materials and the effects of heat treatments on these materials. This test rig is divided into three main systems: Hydraulic Loading System, Rotation System, Lubrication system of the bush as shown in Fig. 3a. Hydraulic Loading System includes rotating electrical machines (REM) type CEM, IEC (0.75KW, 380V, 1420-1745 rpm, 50Hz), which is mounted on the hydraulic tank 20*l* and connected into high-pressure hydraulic flexible tubes which feed hydraulic into the hydraulic cylinder. The hydraulic cylinder is in contact with radial force sensor (U9c/10kN) which is located below it. The testing was done with the oil type ISO VG32. The Rotation System is consists of an asynchronous induction motor (AIM) (ABB, 400V, 3Ph, 50Hz, 3KW, 2860 rpm), which is attached by a flexible coupling to a shaft. The shaft is supported by two roller bearings and the test bearing is mounted between these two bearings as shown as Fig. 3a. Lubrication system of the bush contains electric lubrication pump (ELP) AMGP-03C, 05C Series (1450rpm, 500W, 220V, 50Hz) which was mounted on the hydraulic tank (10*l*). The lubricant is supplied by the ELP to the housing bearing through two flexible tubes which are threaded up the housing through an assembly steel tube. E540 - Wireless / Point laser was used for shaft alignment. The same type of oil, ISO VG32, was used in the testing.
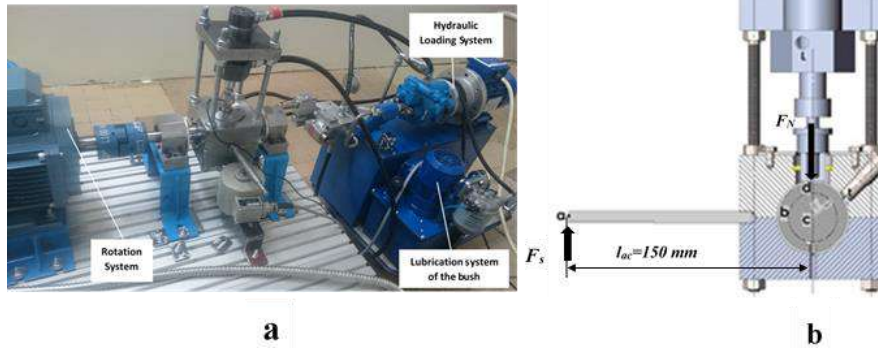
Fig. 3. View of hydrodynamic journal bearing test rig

3.3 Test specimen and procedure

Load and friction coefficient as a function of time in the touch of two real bodies is associated by Coulomb equations:

$$F_f(t) = \mu(t) \cdot F_N(t) . \qquad (5)$$

As a function of time the moment of friction was calculated as the result of the normal force of the sleeve (using reaction force transducer) and the distance on lever between the center of the bush and contact point of the force transducer:

$$M_f(t) = F_s(t) \cdot l_{ac} = F_f(t) \cdot r \qquad (2)$$

As shown in Fig. 3b. From (5) and (6):

$$\mu(t) = \frac{M_f(t)}{r \cdot F_N(t)} = \frac{F_s(t) \cdot l_{ac}}{r \cdot F_N(t)} \qquad (7)$$

Where M_f is Frictional moment [Nm], F_s is Reactional force sensor [N], l_{ab} leg distance of lever [m]. The temperature change and the values of the radial force on the bush were calculated by LabVIEW program which is installed into the computer. The data was transmitted to the recorder and this enabled monitoring and recording of the signals. The data about coefficient of friction, radial load and sensor force were applied for 1/20 s, temperature of lubricating oil and load for 5 s. The most common solution is to beging operate the bearing with no apparent pressure at the test rig's maximum speed as in [15]. This pattern of operation causes the shaft to converge as near to zero eccentricity as possible and ideally provides a measurement of the location at which the shaft and the bearing centers identify. Tests were performed for 5 hours' duration regarding wear test and one hour's duration as regard coefficient of friction test. Tin-based alloy was cleaned then starting an actual test of wear process and the hard substance cleaner FLUXO S190 with cotton and dry well was registered height and weight of samples accurately to provide a very precise and digital recording of all data using technics LabVIEW program.

4. RESULTS AND DISCUSSION

Values of surface roughness before and after wearing process were shown in Fig. 4 the profiles of plain journal bearing were investigated, it was found that total average roughness (Ra) of inner surface of four specimens tested 1, 2 and 3 are 0.4, 0.585 and 0.208 µm respectively and average roughness (Ra) of shaft is 0.23 µm, it means that even the presumably smooth plain journal bearing has some in dents and protrusions.

At all the positions marked 1, 2, 3 and 4 roughness surface journal bearing material decreases with increasing sliding time perhaps because of the roughness of surfaces are still in the process of stability, the roughened shaft may in turn cause change inner surface roughness of bearings, surface roughness has been stabilized and the bearing surface has conformed to the shaft surface after about 25 h for all positions as shown in Fig. 4. Biggest drop in the roughness occurred in positions 1 than 4, while the decrease in the positions 2, and 3 was a slight, may be due to that position 1 and 4 in the direction of radial loading, shaft rotating and continuous contact with the shaft rub.
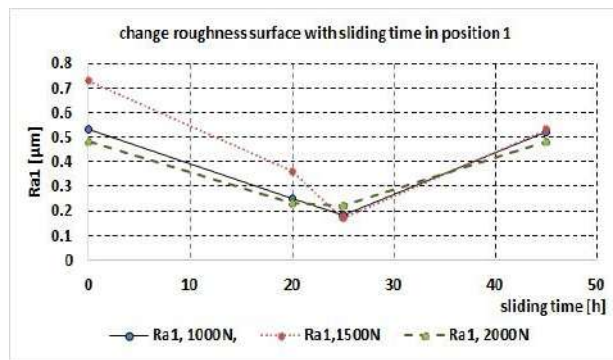
a
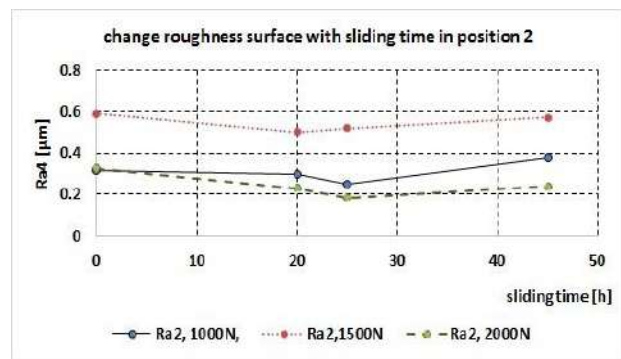
b
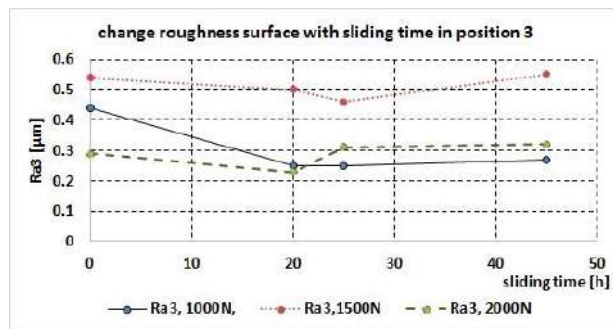
c

d

Fig. 4. Change Roughness surface with sliding time inner journal bearing surface depending on position. a), b), c) and d) are positions 1, 2, 3 and 4 respectively

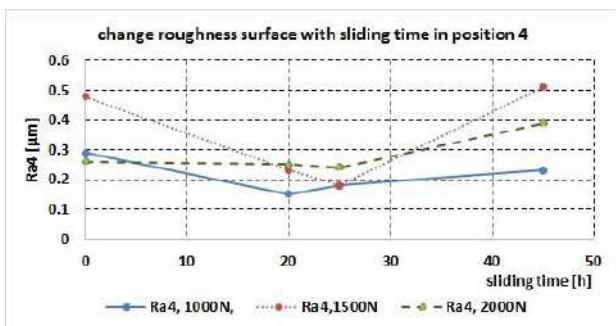The continuing slide was causing increasing roughness for all positions, a significant degradation of the surface in position 1 followed by position 4, while slightly increase in average roughness in position 2 and 3, which may be attributed to the direction of rotation speed of shaft and direction and region of impact of load, that drives debris toward the two positions.
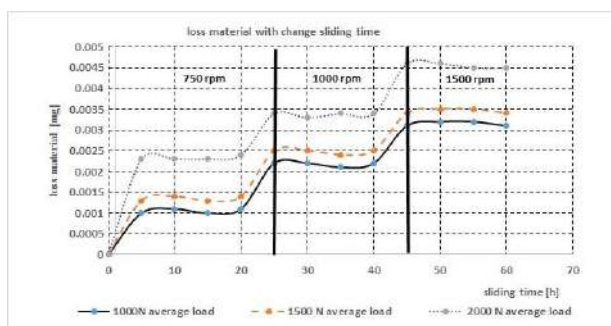

Fig. 5. Relationship between weight loss and sliding distance**.**

The wear of materials has been described by weight loss. In Fig. 5, were investigated of tin-based white metal alloy -tegotenax v840 bearing in lubricant sliding at different average

radial load 1000,1500 and 2000 N vs sliding time (0- 60) h, and variation rotation speed of shaft 750, 1000 and 1500 rpm.

In Fig. 5 shows three unsteady-state zones and three steady-state zones. First unsteady-state zone has Sharply wear increases vs sliding time for all average radial load 1000,1500 and 2000 N, value loss material about 0.001, 0.0013 and 0.0023 mg respectively. At the beginning of sliding process until access first steady-state wear process at 5 h sliding time. Time period of first steady-state zone is 15 h, i.e. change rotation speed. Average loss material in first steady-state wear process was 0.00105, 0.00135 and 0.0023 mg under 1000,1500 and 2000 N radial load respectively, and rotation speed 1000 rpm. The cause of rapid loss of material at the beginning of Operation i.e. first unsteady-state may be due to get to the case of compatibility between shaft and bush. At change rotation speed from 750 to 1000 rpm lead to a second unsteady-state zone wear process for 5 h sliding time, value loss material about 0.0022

0.0025 and 0.0034 mg under (1000-2000) N average radial load respectively, followed by second steady-state wear process zone, time period of second steady-state zone is 15 h an average loss material in second steady-state wear process 0.0022, 0.0025 and 0.0034mg under (1000-200) N average radial load respectively. Finally, third unsteady-state zone under which changes rotation speed of shaft from 1000 to 1500 rpm, Where the amount of loss material 0.0031, 0.0034, 0.0046 mg under (1000-2000) N average radial load respectively, time period unsteady-state zone 5h sliding time, followed by third steady-state wear process zone which time period 15 h, average loss material in third steady-state wear process 0.0031, 0.00345 and 0.0046 mg under (1000-2000) average radial load respectively as shown in Fig. 5. It is clear that lost material increases as increase radial forces and sliding speeds vs increase sliding time but effect sliding speed of shaft biggest than radial load. In fact, the effect of sliding speeds of shaft is implicit effect of sliding distance i.e. sliding time.
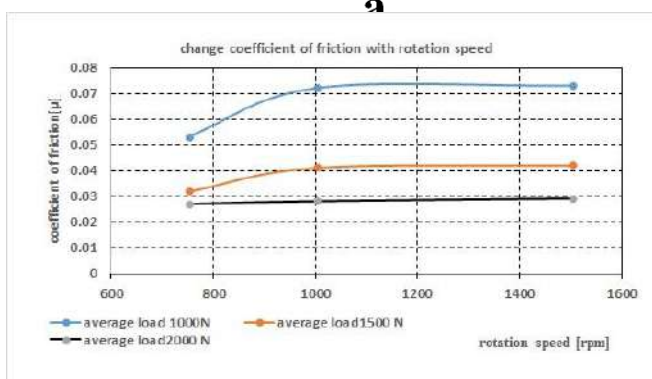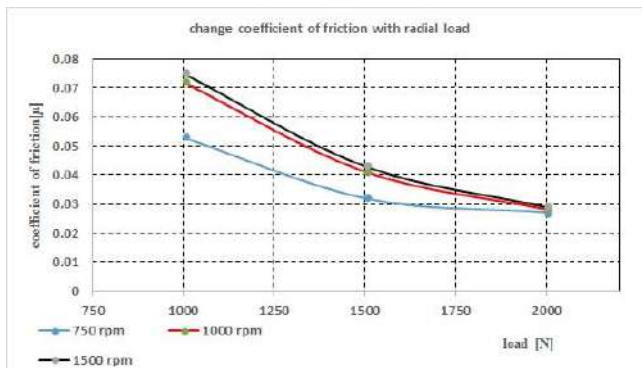

a

b

Fig. 6. Change coefficient of friction with, a) radial load, b) sliding speed

Typical curves of variations in friction coefficient with test duration (one hour) for different average normal loads 1000, 1500 and 2000 N and different sliding speeds 750, 1000 and 1500 rpm are shown in Fig. 6a and b. Friction coefficient was specific as a function of radial and friction force as in eq. (7). It has been observed that the coefficient of friction decreases extremely when increasing the radial load of journal bearing for all average impact radial load and each sliding speed, the highest friction coefficients 0.075 occurred in average radial load 1000 N and 1500 rpm sliding speed, whereas the lowest friction coefficients 0.027 occurred in highest average radial load i.e. 2000 N and rotate shaft speed 750 rpm. Change coefficient of friction values take the form of converging curves toward increasing the radial load at increasing rotate shaft speeds 750, 1000 and 1500 rpm as shown in Fig. 6a.

Fig. 6b illustrates the relationship between friction coefficient and rotation speeds of shaft, friction coefficient increases with the increase of rotating shaft speed 750 to 1000 rpm for average radial load 1000 and 1500 N, whereas remaining almost constant at radial load 2000 N. The friction between rotate shaft, bush and lubricant causes temperature growth of lubricant which results decrease in the shear stress of lubricant that lead to lowing viscosity of lubricant thus decrease coefficient of friction as shown in eq. 4.

Therefore, the coefficient of friction at highest load and lowest rotation speed of shaft have been lowest values, Vice versa as regards lowest radial load and highest sliding speed coefficient of friction have highest values. In Fig. 6b, it was noted increases slightly coefficient of friction with increasing sliding speed (1000-1500) rpm of shaft for all radial loads, which may be attributable to larger shear layers' lubricant thus increases friction drag i.e. coefficient of friction.

5. CONCLUSION

Tribological properties in conditions of sliding time contact can vary over many orders

of magnitude. In this study, the tribological behaviour of radial plain bearing made of tin-based white metal alloy -TEGOTENAX v840 under lubricant condision was evaluated and focusing on the effect of sliding time in change of roughness, loss material and coefficient of friction surface contact of. The following conclusions can be drawn:

a) Results tests is noted three unsteady-state zones and three steady-state zones, According to change in the speed of rotating shaft.

b) The highest wear loss 0.045 mg in steady-state zones occurred in load 2000 N and rotation speed 1500 rpm at sliding time 60 h, under similar tribological conditions, wear decreases as decrease radial load to lowest wear loss material 0.0031 mg happened in load 1000N, it is reduced by almost third. That mean wear loss tin-based bearing material directly proportional to increase the radial load.

c) The highest wear loss 0.0023 mg in unsteady-state zones occurred in load 2000 N and rotation speed 1500 rpm at sliding time 5h i.e. At the beginning of the test.

d) Change rotation speed, causing the wear loss of sliding surface bearing material to also be in an unsteady-state wear process, then constantly sliding surfaces go back to steady-state wear process.

e) Friction coefficient with respect to radial load is lowest in highest radial load for each shaft rotational speed, it decreases extremely when increasing the radial load of journal bearing.

f) Change coefficient of friction values take the form of converging curve toward increasing the radial load at increasing rotate shaft speeds.

g) Coefficient of friction increases slightly with an increase rotation speed of shaft for same average radial load.

h) The coefficient of friction at highest load and lowest rotation speed of shaft have been lowest values, Vice versa as regards lowest radial load and highest sliding speed coefficient of friction have highest values.

i) was found that surface roughness of bearings have Specific value before the test although presumably smooth plain journal bearing has some in dents and protrusions.

j) Roughness of surface bearing upon area contact effect of radial load more vulnerable to roughness change, in th us tests have been position 1 than 4.

REFERENCES

[1] D.J. Ligterink and A. W.J. de Gee, Measurement of Wear in Radial Journal Bearings, Tribology Section, Vol. 3, No. 1, p.p. 45-54, 1996.

[2] M.A. Chowdhury, D.M., Nuruzzaman, A.H. Mia, M.L. Rahaman: Friction coefficient of different material pairs under different normal loads and sliding velocities, Tribology in Industry, Vol. 34, No. 1, p.p. 18-23, 2012.

[3] O. Barrau, C. Boher, R. Gras, F. Rezai-Aria: Wear mecahnisms and wear rate in a high temperature dry friction of AISI H11 tool steel: Influence of debris circulation, Wear, Vol. 263, No. 1-6, p.p. 160-168, 2007.

[4] S. Bekir, Unlua, A. Enver: Evaluation of effect of alloy elements in copper based CuSn10 and CuZn30 bearings on tribological and mechanical properties, Journal of Alloys and Compounds, Vol.489, p.p. 262–268, 2010.

[5] Savaşkan, T., Bican, O.: Dry sliding friction and wear properties of Al–25Zn–3Cu–3Si alloy, Tribology International, Volume 43, Issue 8, p.p. 1346-1352, 2010.

[6] D. Guida, F. Nilvetti, C.M. Pappalardo: Dry friction of bearings on dynamics and control of an inverted pendulum. Journal of Achievements in Materials and Manufacturing Engineering, Volume 38 Issue 1, p.p. 80-94, 2010.

[7] Javorova, J., Mazdrakova, A., Andonov, I., Radulescu, A.: Analysis of HD journal bearings considering elastic deformation and non-Newtonian Rabinowitsch fluid model. Tribology in Industry, 38 (2), p.p. 186-196, 2016.

[8] Sonam M. Gujrathi, Prof. L.S. Dhamande and Prof. P.M. Patare,: Wear Studies on Polytetrafluroethylene (PTFE) Composites: Taguchi Approach. Bonfring International Journal of Industrial Engineering and Management Science, Vol. 3, No. 2, p.p. 47-51, 2013.

[9] Andersson, P., Juhanko, J. Nikkilä, A.-P., and Lintula, P.: Influence of topography on the running-in of water-lubricated silicon carbide journal bearings. Wear, Vol. 201, pp. 1-9, 1996.

[10] Andersson, P., and Lintula, P.: Load-carrying capability of water-lubricated ceramic journal bearings. Tribology International, Vol. 27, No. 5, pp. 315-321, 1994.

[11] Archard, J.F.: Wear theory and mechanisms. In: M.B. Peterson, W.O. Winer (eds.). Wear Control Handbook. ASME, 1980.

[12] Holm, R.: *Electric Contacts*. Almqvist & Wiksells Boktryckeri AB, Uppsala, 1946.

[13] Adatepe, H., Bıyıklıoglu, A., Sofuoglu, H.: An experimental investigation on frictional behavior of statically loaded micro-grooved journal bearing, Tribology International, Volume 44, Issue 12, Pages 1942–1948, 2011.

[14] Nada Bojic, Dragan Milcić, Milan Banic ,: Effect of coverage of graphite on self- lubricating plain bearings*, Serbiatrib '15*, May 13-15.5. 2015, Belgrade, p.p. 309-313.

[15] Antti Valkonen, *Oil film pressure in hydrodynamic journal bearings,* PhD thesis, Helsinki University of Technolog Faculty of Engineering and Architecture Department of Engineering Design and Producti, 2009.

COMPARISON OF THEORETICAL AND EXPERIMENTAL INVESTIGATIONS OF THE VIBRATION AMPLITUDE OF THE TURBOCHARGER ROTOR AND BEARING TEMPERATURES

Elena ZADOROZHNAYA[1,*], Sergey SIBIRYAKOV[2], Nikita LUKOVICH[1], Llad HUDYAKOV[1]

[1] South Ural State University, Chelyabinsk, Russia
[2] RPA "TURBOTEKHNIKA", Protvino, Moscow region, Russia
*Corresponding author: zadorozhnaiaea@susu.ru, elena-nea@rambler.ru

Abstract: One of the most urgent issues of the modern world and domestic automobile and tractor production is the problem of the production of efficient and reliable turbochargers. The rotor bearings largely determine the reliable operation of the turbocharger. By increasing the degree of the forcing of the engine the turbocharger rotor speed and the load increases significantly. Working conditions of bearings also complicated because of the temperature rise. In this case the bearing of the turbine and the compressor bearing works in different thermal conditions. The definition of the thermal state of the bearings can be performed experimentally. However, to perform these studies the sophisticated experimental equipment must be used. Researchers can't perform experiments for each type of turbocharger. Therefore, the applying of the theoretical approaches becomes more relevant. The peculiarity of the considered problem is the design of the bearings, which are made in the form of multilayer bearings with floating rings. Such designs increase the number of the parameters that affect the behaviour of the rotor. For the calculation of the multilayer bearings and turbocharger rotor dynamics a method and calculation algorithm was developed. A plan of the experiment based on the orthogonal central composite plan was drawn up. The regression equations for rotor amplitude and bearing temperature were obtained. As variable parameters the clearances (external and internal), rotor speed, pressure and lubricant temperature were used. The results of the calculation were compared with experimental results obtained at the plant. Non-Newtonian properties of the lubricants were taken into account in the calculations. Comparative results showed good agreement. In this way the resulting function can be applied to studies of the similarly multilayer bearings without complicated experimental studies.

Keywords: rotor of the turbocharger, multilayer bearings, thermal state, precession amplitude, calculation method.

1. INTRODUCTION

The currently, the boost is the main way to achieve the current requirements for power ratings, economic and environmental indicators of internal combustion engines [1]. Manufacturing of efficient and reliable turbochargers is one of the most pressing issues of the modern world and domestic automobile and tractor production. The rotor bearings largely determine the reliable operation of the turbocharger. By increasing the degree of forcing engine the turbocharger rotor speed and the load of the rotor is

significantly increased. Working conditions of bearings are also complicated because of the temperature rise [2-4].

Kucinschi B. and Fillon M. [5] presented a study, which shows the determination of the temperature distribution in the plain journal bearing, which is loaded with a constant force. The main focus was on hydrodynamic pressure, temperature distributions at the film/bush interface, oil flow rate, power losses and film thickness. The obtained results demonstrated that: for highly loaded bearings operating at low speed, critical parameters are film thickness and maximum pressure; for high speed operating bearings submitted to a light load, the shaft being almost centered, heating becomes very significant and maximum temperature becomes the critical parameter.

Pankaj Khatak and H. C. Garg [6] analyzed of the capillary compensated hybrid journal bearing by considering combined influence of thermal effects and a micropolar lubricant. The results obtained by numerically indicate that the bearing is significantly affected by increase in temperature. Hence, it is essential to consider the thermal effects for bearing operating with micropolar lubricant to produce realistic bearing characteristic data.

The shearing of lubricant at high loads and speed in journal bearings results in generation of large amounts of heat. The lubricant viscosity will decrease with increase in temperature. Many authors have studied the thermal effects of lubricant on the performance of hybrid journal bearings.

Moes H. et al. [7] presented a method of taking into account the thermal effects when simulating dynamically loaded, flexible, journal bearings. The method is an extension of Van der Tempel's model for a flexible, short journal bearing under severe dynamic duty, with partial circumferential supply grooves, cavitations and etc. It incorporates the heat generation due to the viscous dissipation and the cooling due to the axial and circumferential flow of lubricant. The results for the film thicknesses, the lubricant flow, the viscous dissipation and the temperature

distribution in two specific connecting-rod bearing configurations will be presented.

A theoretical model of slot entry hybrid bearing was developed by Sharma et al. [8], in which viscosity variation due to thermal effects was considered. It was reported that minimum fluid film thickness reduces for all the configurations of bearing due to thermal effects. They further reported that lubricant supply, stiffness, and damping coefficients change appreciably when thermal effects are considered.

Garg et al. [9] developed the slot entry hybrid bearing model to include the non-Newtonian and thermal effects of lubricant. It was observed that oil requirement in hybrid journal bearings was enhanced by increase in temperature and non-Newtonian effects in lubricant. These available studies indicate that performance characteristics of journal bearings are significantly affected by the temperature increase of the lubricant.

Thermal analysis of finite journal bearings with micropolar lubrication has been performed by few researchers [10, 11]. Khonsari and Brewe [10] compared the isothermal results of the micropolar lubricated finite journal bearing with thermohydrodynamic solutions. They showed the significant reduction in load-carrying capacity of the journal bearings when thermal effects are considered.

Edgar J. Gunter presented some results of the linear and nonlinear dynamics of the rotor, which rotates in the rotating floating ring bearings for the typical turbocharger [12]. He computed the linearized stability of the system for the various ratios of inner and outer clearances. He also represented the analysis of the critical speed and showed several fluctuation forms of the rotor.

A.Tartara [13] had conducted experiments and concluded, that remarkable effects of stabilizing system can be expected, when the bearings with floating rings are used. Namely, the ring starts rotating as soon as the whirl occurs, and the further stable operation is realized as the journal speed increases. The stabilizing effect of the floating-ring bearing is

conspicuous when the ratio between inner and outer clearances and the absolute clearances are large

Additionally, researchers should take into account the mutual influence of multi-layered bearings on each other. For example, in paper [14] authors presented an algorithm for solving the problem of rotor dynamics. The authors take into account the flexibility of the rotor. An algorithm for solving thermal problem for the plain bearing is represented in papers [15, 16].

However, experimental studies [17, 18] had shown that the bearings of the turbine and compressor operate in different thermal conditions. The temperature difference for the turbine and compressor bearings can be 30...50 °C.

Studies on thermal aspects of bearings considered with different bearing temperatures are very limited.

Consequently, the evaluation of the thermal state of each bearing and accounting them thermal state in the calculation of the rotor dynamics is an urgent task. At the same time the position of the rotor relative to the bearing must be determined at each time point. The flexibility of the rotor must be taken into account.

An attempt has been made in this paper to seek more realistic functions for the amplitude of the oscillations of the rotor and the temperature in each bearing.

2. METHOD OF THE THEORETICAL ANALYSIS

The problem of the hydrodynamic theory of friction units is characterized by a set of methods for solving several interrelated tasks: the determination the conditions of stability and parameters of the journal nonlinear oscillations on the lubricating film; the calculation of its trajectory; the calculation of the field of hydrodynamic pressure in the lubricating layer, which separates the friction surfaces of the journal and bearing, taking into account an arbitrary law of their relative motion; the calculation of the temperature of the lubricating film.

The methodology of the dynamics calculation of the flexible non-symmetric rotor on the multi-layer sliding bearings is based on methods of integrating the motion equations of movable elements of the bearings and rotor. The motion equations include forces that are associated with the presence in the system "rotor – bearings" the lubricating layers having substantially nonlinear characteristics. Bearing with rotating rings containing two lubricant layers and the direction of movement of lubrication is shown at figure 1.
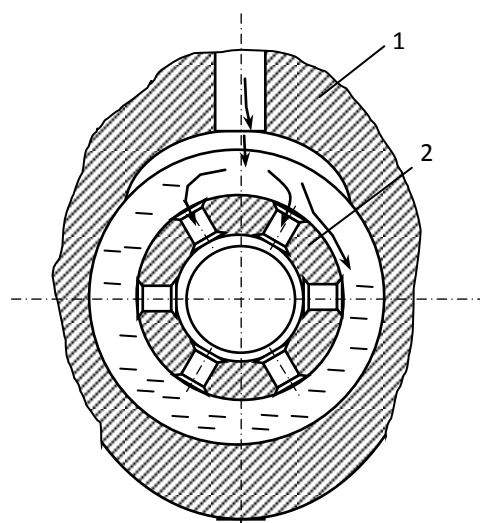

Figure 1. Bearing with rotating rings:
1 – turbocharger housing, 2 – rotating rings

The nonlinear reactions of the lubricating layer are determined by integrating the hydrodynamic pressures diagram. These diagrams are calculated at the each time step by numerical integration of the differential equation Reynolds.

The methodology for calculation the dynamics of the flexible non-symmetric rotor on the multi-layer sliding bearings is based on the methods of integration of the motion equations for movable elements of the bearings and rotor. The equations of motion include forces associated with the presence in the system "rotor–bearings" lubricating layers having substantially nonlinear characteristics. Among the factors considered in the modeling of the rotor vibration at the bearings with floating the rotating ring (contains two lubricating layers, fig.1) is included the gyroscopic and inertial forces, and the

kinematic excitation, resulting from the fluctuations of the foundation.

The nonlinear reaction of the lubricating layer is determined by integrating the diagram of the hydrodynamic pressures. Those diagrams are calculated at each time step by numerical integration of the differential Reynolds equation. The use of the multigrid method [19] for the numerical solution of the Reynolds equation allows one to take into account movable and immobile sources of lubrication in various forms, which are performed on the friction surfaces of the hull and bushings. These sources are taken into account by setting the boundary conditions for the pressures to the grid step.

The non-isothermicity of the lubricant flow is taken into account by the correction of its viscosity at each step of calculating the trajectory of the rotor and the floating bushings [14]. The heat balance equation is used to determine the temperatures of each lubricating layer. This equation takes into account the energy supply through the lubrication sources, the recirculation of the lubricant into the groove, the energy extraction through the journal and the bearing.

The degree of perfection of bearings with floating bushings is estimated by calculations of the stability characteristics of mobile elements and hydro-mechanical characteristics [20], which include friction losses, dissipation in lubrication, the thickness of the lubricating layer and temperature, the values of the hydrodynamic pressures. Those characteristics allow you to directly or indirectly estimate the heat release rate and the fatigue life of bearings, wear and tendency to galling of friction surfaces.

The system of equations of the motion for a flexible asymmetric rotor, which leans on multilayer bearings, is presented by V. Prokopiev et al [20], P. Taranenko et al. [14].

The lubricant is considered as a design element of any friction units. Non-Newtonian properties of the lubricant had been described by the function presented in [21]. Temperatures of lubricating layers were corrected by using the heat balance equation

at the each step of the calculation of the trajectory motion of the journal [15]. The system of equations of motion of the rotor elements are integrated by the Runge-Kutta method. Variable step integration over time is automatically selected by using Merson amendment. An algorithm for solving the task of rotor dynamics has been presented in the article [21].

3. EXPERIMENT

The experiment was carried out by employees of RPA "TURBOTEKHNIKA". To estimate the thermal state of the rotor elements and bearings the thermocouples were used. Measurement range is 0 ... 350°C. The installation scheme of thermocouples is shown in figure 2.
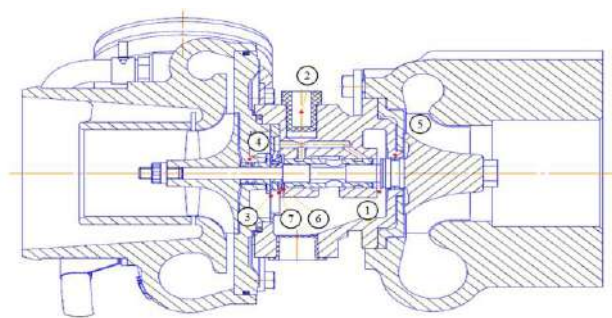

Figure 2. The scheme of installation of thermocouples

The figure shows: 1 is the draining the oil from the radial bearing from the turbine side; 2 is the oil supply to the bearing housing; 3 is the draining of oil from the thrust bearing from the compressor side; 4 is the seal on the compressor side; 5 is the seal on the side of the turbine; 6 is the draining of oil from the radial bearing from the compressor side; 7 is the draining the oil from the thrust bearing from the turbine side. Additional channels were made in the bearing housing to installation and attachment of thermocouples.

The measurements were carried out in 5 stages. The input parameters, varied during the tests, are given in table 1.

The airflow through the compressor was measured at 5...6 points on each branch of the compressor's characteristic from the surging boundary to the stop point.

Table 1. The input parameters

	Step number				
Parameter	1	2	3	4	5
Circumferential speed at the outer diameter of the compressor wheel, m / s	250 400 500 550	400 500	400 500	400 500	400 500
Oil temperature at the entrance to the bearing housing, ^{0}C	90	90	70	90	105
Input oil pressure, MPa	0,4	0,3	0,4	0,14	0,4

The parameters to be registered are:
- temperatures at the points of installation of thermocouples;
- the temperature at the oil drain from the turbocharger (bench thermocouple);
- degree of pressure increase in the compressor;
- the oil flow through the turbocharger;
- the air temperature at the compressor output;
- the gas temperature at the input to the turbine.

4. REZALTS OF EXPIRIMENT

The results of the first stage showed that at a peripheral speed of 250 m/s, there is a significant difference in the temperature of the oil from the compressor and turbine side. From the turbine side, the oil temperature on the drain from the radial bearing is 6 ... 7° higher. At circumferential speeds of 400 ... 550 m/s, there is no significant difference.

The maximum temperature of the oil was 122°C, that is, the gain relative to the inlet temperature is 30°. The maximum oil temperature in the thrust bearing was ~121°C, and it does not significantly differ from the temperature in the radial bearing.

The air temperatures at the output of the compressor and gas at the input to the turbine are shown in figure 3.
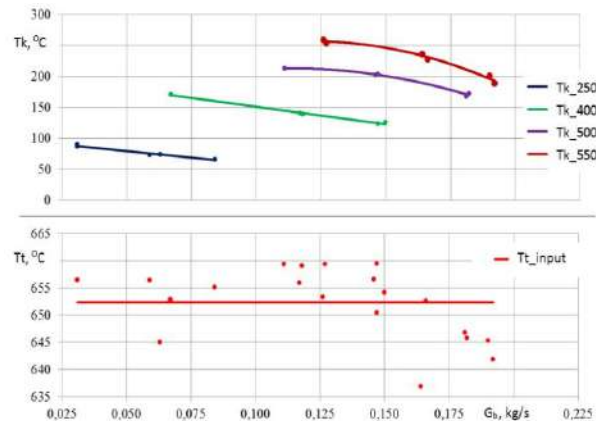

Figure 3. Air temperature at the output of the compressor (Tk) and gas at the input to the turbine (Tt) from the air flow through the compressor G_b.

At the second stage of the experiment, it was found that when the supply pressure of the lubricant increases, the temperature in the radial bearing increases to 5.5 °C.

The results of the measurements in the fourth stage when the oil supply pressure was reduced to 0.14 MPa showed that the increase the oil temperature on the drain from the radial bearing was 7...10°C from the compressor side and 10...15°C from the turbine side.

The results of measurements in the fifth stage showed that the temperature of the oil on the drain from the radial bearing increased by an average of 12.5°C. The dependence of the oil temperature at the radial bearing drain on the oil temperature at the input to the turbocharger is shown in figure 4.
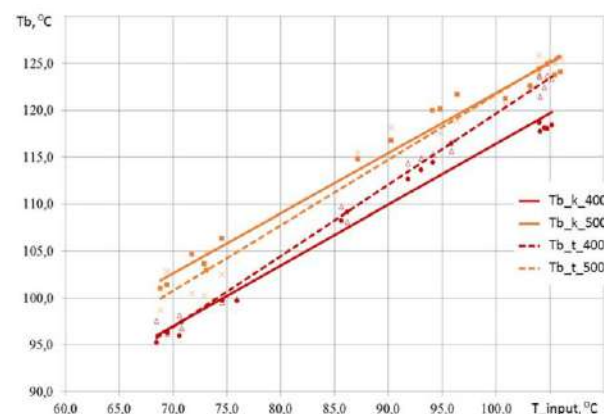

Figure 4. The oil temperature (Tb) in the radial bearing

5. RESULTS OF CALCULATION

A plan of the experiment based on the orthogonal central composite plan was drawn up. The regression equations for the function of the rotor amplitude and bearing temperature were obtained. As variable parameters the clearances (external and internal), rotor speed, pressure and lubricant temperature were used. The coefficients of the regression equation for the fluctuations amplitude of the journal and the bearing temperature are shown in Table 2.

Table 2. The coefficients of the regression equation

Coefficients	The fluctuations amplitude of the journal	The bearing temperature
b_0	-12,7034	88,54901
b_1	0,788164	-4,5208
b_2	-0,46852	7,919623
b_3	0,00019644	0,00285239
b_4	-12,4847	17,74234
b_5	0,174299	-0,12758
b_{12}	-0,03059	0,040477
b_{23}	$-7,9513 \cdot 10\text{-}6$	$-8,7008 \cdot 10\text{-}6$
b_{34}	0,000545	0,000367
b_{45}	0,083428	-0,02839
b_{11}	-0,00854	0,048233
b_{22}	0,088224	0,36404
b_{33}	$-7,7 \cdot 10\text{-}9$	$-7,3 \cdot 10\text{-}8$
b_{44}	-8,93225	-44,9515
b_{55}	-0,00109	0,005644

Figures 5 show the precession amplitude of the rotor and the bearing temperature by external and internal bearing clearances. In this case the oil pressure is 0,05 MPa, temperature is 95°C.

With increasing the rotor speed, the precession amplitude of the rotor decreases, the oil temperature increases. In the range of rotor speed from 14500 to 19100 c^{-1}, the changes of estimation parameters are slightly less than 0.5 microns for precession amplitude of the rotor and less than 10°C for the bearing temperature.

When the clearances were changing within tolerance the maximum amplitude of the rotor precession is about 7,5...11 mkm, the maximum bearing temperature is about 110...120°C.

Figure 5 shows the dependence of the precession amplitude of the rotor and oil temperature at the output of the bearing on the outer and inner clearances in the bearing at various rotational speeds of the rotor. The oil pressure is 0.05 MPa, the temperature is 95°C. At the figure 5 the internal clearance is assumed to be constant and equal to the maximum values.
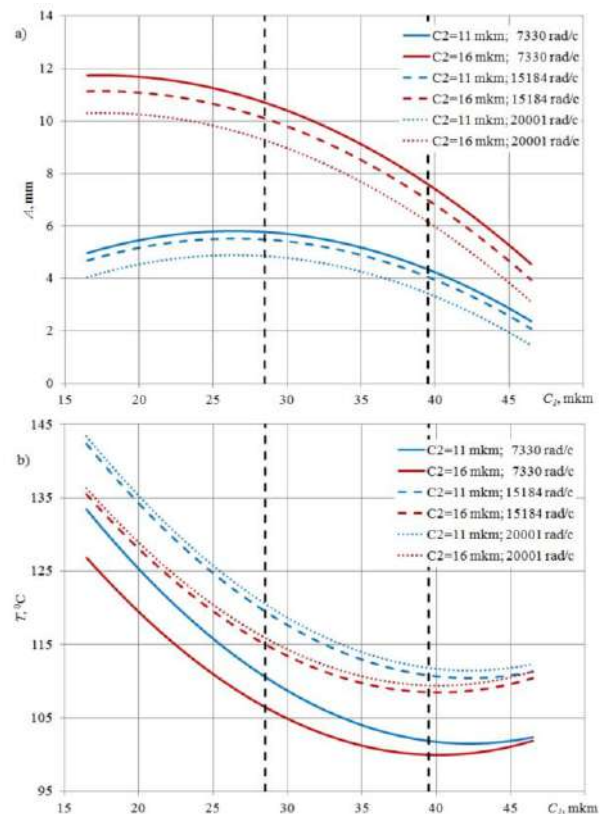

Figure 5. The precession amplitude of the rotor (a) and the bearing temperature (b) depending on the outside clearance at various rotor speeds

The results of the calculation showed that the amplitude of the precession of the rotor decreases with increasing the external clearance. The temperature at the exit from the bearing is minimal in the range of external clearances of 40...45 mkm and it grows when the clearance is changed.

With increasing the rotor speed, the precession amplitude decreases, the oil temperature at the output increases. If the clearances vary within the tolerance, the maximum amplitude of precession of the rotor is 7.5...11 mkm, the maximum temperature at the exit from the bearing is 110 ... 120°C.

Figure 6 shows the dependences of the estimated bearing parameters on the ratio of the outer clearance to the internal clearance (C1/C2).
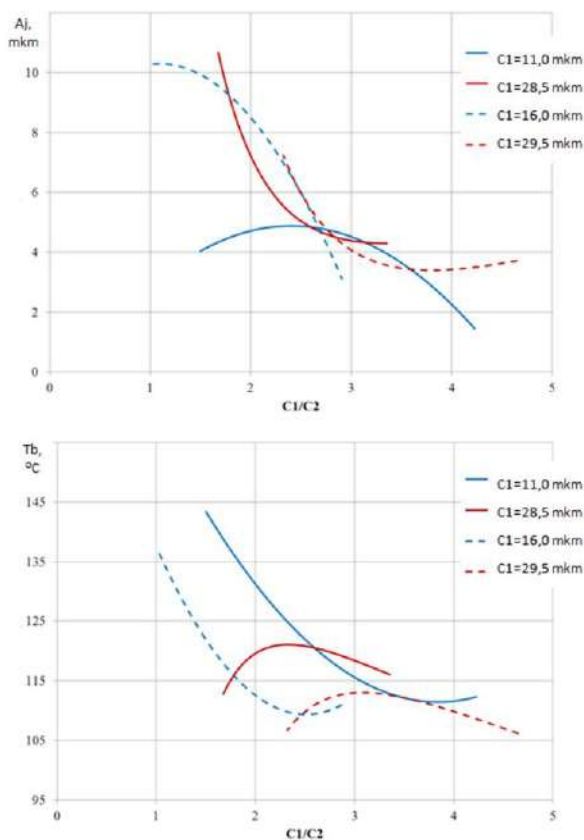

Figure 6. Dependence of the estimated bearing parameters on the clearance ratio

It can be seen from the graph that the optimal interval for the clearance is 2.5 … 3.

At the last stage, the results of the calculation of the bearing temperature were compared with the experimental results.

Figures 7 and 8 shows the results of comparing the calculated bearing temperature with the results of the experiment.
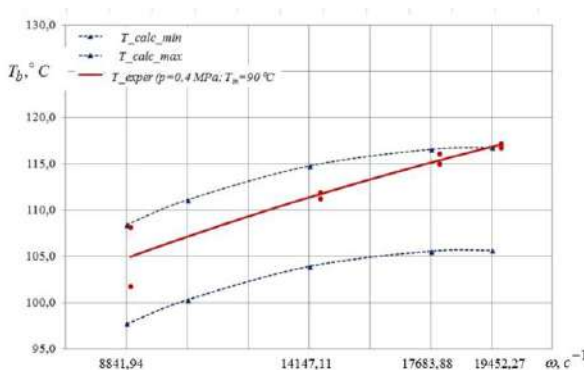

Figure 7. The dependence of the bearing temperature on the rotation speed of the rotor. p=0,4 MPa; Tin=90°C

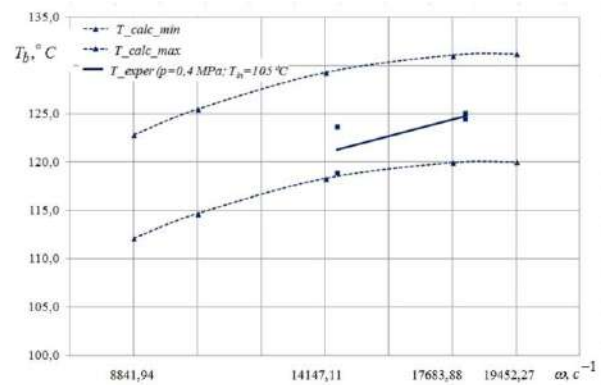**Figure 7.** The dependence of the bearing temperature on the rotation speed of the rotor. p=0,4 MPa; Tin=105°C

Comparative results showed good agreement.

6. CONCLUSION

The method of calculating the dynamics of the flexible asymmetric rotor on the radial plain bearing can be used for research of the turbocharger with other size. Regression equations were obtained for the rotor amplitude and bearing temperature, and were verified. Calculation results showed that the precession amplitude of the rotor at all modes is less than 11 microns. This indicates that the direct contact of the rotor and the radial bearing rings is absent. The increment of temperature in the bearing is 15 … 25°C and only slightly dependent on the lubricant supply conditions.

The regression function can be applied to studies of the similarly multilayer bearings without complicated experimental studies.

ACKNOWLEDGEMENT

REFERENCES

[1] V.V. Sinyavskij, I.E. Ivanov: *Forcing Engines. Systems and Units of Supercharging*, MADI, Moscow, 2016. (in Russ.).

[2] Yu.B. Morgulis et al.: Investigation of the thermal state of the turbocharger bearing unit, Tractors and agricultural machinery, No. 6, pp. 12–14, 1972 (in Russ.).

[3] R. Boncompian, M. Fillon, J. Frene: Analysis of thermal effects in hydrodinamic bearings; J. Tribol., Vol. 108, No. 2, pp. 219-224, 1986.

[4] H. McCallion, F. Yousif, T. Lloyd: The analysis of thermal effects in a full journal bearing, J. of Lubrication Tech, Vol. 92, No. 4, pp. 578-587, 1970.

[5] B. Kucinschi, M. Fillon: An Experimental study of transient thermal effects in a plain journal bearing, J. Tribol, Vol. 121, No. 2, pp. 327-332, 1999.

[6] P. Khatak, H.C. Garg: Performance analysis of capillary compensated hybrid journal bearing by considering combined influence of thermal effects and micropolar lubricant, J. Tribol, Vol. 139, No. 1, pp. 011707 (12 pages) , 2016.Paper No: TRIB-16-1044

[7] H.Moes, P.B.Y. Ten Hoeve; J. Van der Helm: Thermal effects in dynamically loaded flexible journal bearings, J. Tribol., Vol. 111, No. 1, pp. 49-55, 1989.

[8] S.C. Sharma, V. Kumar, S.C. Jain: Thermohydrostatic analysis of slot-entry hybrid journal bearing, Tribol. Int., Vol. 35, No. 9, pp. 561–577, 2002

[9] H.C. Garg, V. Kumar, H.B. Sharda: Performance of slot-entry hybrid journal bearings considering combined influences of thermal effects and non-Newtonian behavior of lubricant, Tribol. Int., vol. 43, No. 8, pp. 1518–1531, 2010.

[10] M.M. Khonsari, D.E. Brewe: Effect of viscous dissipation on the lubrication characteristics of micropolar fluids, Acta Mech., Vol. 105, No. 1, pp. 57–68, 1994.

[11] X.-L. Wang, K.-Q. Zhu: Numerical analysis of journal bearings lubricated with micropolar fluids including thermal and cavitating effects, Tribol. Int., vol. 39, No. 3, pp. 227–237, 2006.

[12] E.J. Gunter, W.J. Chen: *Dynamic analysis of a turbocharger in floating bushing bearings*, ISCORMA-3, Cleveland, Ohio, 2005.

[13] A. Tartara: An experimental study of the stabilizing effect of floating-bush journal bearings, Bull. JSME, Vol. 13 , No. 61, pp. 858-863, 1970.

[14] P. Taranenko, O. Sliva, E. Zadorozhnaya: Dynamics analysis of flexible rotor supported by floating ring bearings, Mechanisms and Machine Science, Vol. 21, pp. 1103-1113, 2015.

[15] E.A. Zadorozhnaya: Solving a thermohydrodynamic lubrication problem for complex-loaded sliding bearings with allowance for rheological behavior of lubricating fluid, Journal of Machinery Manufacture and Reliability, Vol. 44, No. 1, pp. 46-56, 2015.

[16] Y. Rozhdestvensky, E. Zadorozhnaya: A simulation of the thermal state of heavily loaded tribo-units and its evaluation, Bulletin of the South Ural State University, Series: Mathematical Modelling, Programming and Computer Software, Vol. 7, No. 4, pp. 51-64, 2014.

[17] V.N. Kaminskiy et al.: Experience in the development of supercharging systems for KAMAZ EURO-4 engines, "Zurnal AAI", Vol. 5, pp. 16, 2012, (in Russ.).

[18] V.N. Kaminskiy et al.: Development of test-benches for control and research tests of turbochargers, Scientific journal "Izvestiya MGTU MAMI", Vol. 1, No. 2(14), pp. 143-148, 2012, (in Russ.).

[19] V.N. Prokop'ev, A.K. Boyarshinova, E.A. Zadorozhnaya: Multinet integration algorithms of Reynolds equation in the dynamics problems of complex-loaded plain bearings, Problemy Mashinostraeniya i Nadezhnos'ti Mashin, No. 5, pp. 16-21, 2005.

[20] V.N. Prokop'ev, A.K. Boyarshinova, E.A. Zadorozhnaya, A.S. Fisher: Hydromechanical properties of bearings with a floating bushings stack, Problemy Mashinostraeniya i Nadezhnos'ti Mashin, No. 6, pp. 15-21, 2004.

[21] E.A. Zadorozhnaya, S.V. Cherneyko, M.I. Kurochkin, N.A. Lukovich: A study the axial and radial rotor stability of the turbo machinery with allowance the geometry of the surface and properties of the lubricating fluid, Tribology in Industry, Vol. 37, No. 4, pp. 445-463, 2015.

WEAR ANALYSIS OF PVD HARD COATINGS FOR HIGH PRESSURE DIE CASTING TOOLS

Lazar KOVAČEVIĆ[1],*, Pal TEREK[1], Aleksandar MILETIĆ[1], Dragan KUKURUZOVIĆ[1], Branko ŠKORIĆ[1], Peter PANJAN[1]

[1]University of Novi Sad, Faculty of Technical Sciences, Novi Sad, Serbia
[2]Jožef Stefan Institute, Ljubljana, Slovenia
*Corresponding author: lazarkov@uns.ac.rs

Abstract: High pressure die casting is a widely used process for mass production of complex near net shape aluminum alloy castings. During the mold filling stage of the process, metal reaches high velocities that cause substantial wear of the tool components. This wear is additionally augmented by the tendency of the molten aluminum to react with the tool steel. This process limits die lifetime, reduce product quality, and increases machine downtime due to regular removal of the soldered layer during production. In order to mitigate this problem, different surface treatments are sometimes employed for high production tools. Most common treatments are nitriding and PVD deposition of hard coatings. Numerous industrial and laboratory scale studies show a notable decrease in wear rate during casting production after employing these treatments on critical parts of the tool. However, results show different and often diverging trends between various treatments. This indicates an existence of uncontrolled influential parameters and, therefore, a necessity for analysis of worn surfaces during industrial trials. Within this study, two duplex hard coatings, CrN and TiAlN, were deposited on core pins by physical vapor deposition (PVD) process. Core pins were tested in four industrial production runs of an automotive component. In every run, the tool was mounted with one pin that was PVD coated, and one that was gas nitrided. Nitrided core pins were used as a base standard since they are most commonly used surface treatment. TiAlN coated pins were able to complete full production run of 22000 shots without significant damage. CrN coating showed somewhat higher soldering tendency and erosion rates. Considering that the untreated steel core pins were able to withstand only 5500 shots, it can be concluded that PVD coatings can significantly improve die lifetime. Additionally, results indicate that often disregarded variances in casting temperature or in cleanliness of ingots used in production can significantly change wear rates of HPDC tools.

Keywords: tool wear, die casting, PCD coatings, nitriding, aluminum alloy, core pins.

1. INTRODUCTION

High pressure die casting (HPDC) is a widely used process for mass production of complex near net shape light alloy castings [1]. This process involves injection of molten metal into a mold cavity under high pressure between 10 MPa and 65 MPa. During mold filling stage molten metal can reach velocities above 50 ms^{-1}. Metal impingement over large number of cycles can cause notable erosion of the exposed tool components. To mitigate this problem HPDC tools are made from steel hardened to withstand high temperatures and

extreme pressures. Therefore, HPDC tools are very expensive and induce high start-up production costs.

When casting aluminum alloy, tool wear is additionally augmented by the chemical reaction between the steel and molten aluminum. Although HPDC cycles incorporates spraying of die lubricants on top of the working surfaces, harsh process conditions cause significant damage on the tool surface [2]. Depending on the dominant operating mechanism, different failure modes are distinguished [3]: die soldering (corrosion and sticking), washout (erosion) and heat checking (thermal fatigue cracking).

In order to mitigate the problem of HPDC tool wear, numerous investigations were performed to develop adequate surface engineering technologies [4-8]. Nitriding and physical vapor deposition (PVD) emerged as the most appropriate technologies for this purpose [4]. Numerous industrial and laboratory scale studies show a notable decrease in wear rate during casting production after employing these treatments on critical parts of the tool [1,9]. However, results show different and often diverging trends between various treatments [3]. This indicates an existence of uncontrolled influential parameters and, therefore, a necessity for analysis of worn surfaces during industrial trials.

In this study, duplex hard coatings, TiAlN and CrN, were deposited on several core pins that were subsequently incorporated in HPDC tooling. Wear analysis of core pins after full scale industrial production is presented.

2. MATERIAL AND METHODS

Core pins used in this research were made of hot-working tool steel DIN 1.2344 (AISI H13). Samples were prepared using typical industrial production process for core pins. After CNC machining, samples were subjected to progressive grinding with 100 to 1,000 grit silicon carbide sandpaper. All samples were then subjected to gas nitriding. During the process the temperature was controlled in the range between 510 °C and 520 °C. Four samples received no further surface treatment and were used as a base standard for comparison.

Four additional core pins were subjected to PVD hard coating deposition. Two samples were coated with CrN coating, and two samples were coated with TiAlN coating. In order to remove compound layer, prior to deposition samples were subjected to progressive grinding with 400 to 1,000 grit silicon carbide sandpaper. Two different industrial deposition units were used for coatings preparation. CrN coating was deposited in a thermionic arc ion plating system BAI730 (Balzers) and TiAlN coating was produced in an unbalanced magnetron sputtering system CC800 (CemeCon).

Wear analysis of the core pin surfaces before and after casting was performed by light optical microscope SZH 10 (Olympus) and scanning electron microscope JSM-7600F (Jeol).

Core pins were tested using an in-plant die casting production. For normal operation, prior to every shot to prevent the aluminum from sticking to the die steel, the die was sprayed with a water-diluted lubricant with the dilution ratio of approximately 50 : 1. The aluminum alloy used in the trial was AlMg2Mn. Casting production was performed using the Buhler H400 SCD HPDC machine. Furnace temperature of the molten alloy was controlled in the range 720 - 740 °C. Melt speed at the entrance into the mold cavity was set to approximately 40 ms^{-1}.

Initial production runs of the same casting have shown that the core pins that received no surface treatment were able to withstand approximately 5,500 cycles. Therefore, investigation was conducted in four production runs. Two production runs (No. 1 and No. 2) were scheduled to stop at 5,000 cycles in order to investigate the wear of duplex PVD coated core pins, and compare them to the core pins that were subjected to only gas nitriding. Two more production runs (No. 3 and No. 4) were scheduled to run required maximum of 22,000 cycles. Since the

mold cavity was symmetric, during each run mold was equipped with one PVD coated core pin, and one gas nitrided core pin.

3. RESULTS AND DISCUSSION

Cross section optical micrographs of the core pins after 5,000 cycles are presented in Figure 1. Cross sections were made in a plane of maximum melt velocities, where the molten metal impinges the core surface. Core pins are grouped according to production runs. Top micrographs, Figures 1a and 1b, are from the first production run, and bottom micrographs, Figures 1c and 1d, are from the second production run. Locations where wear is the most pronounced are marked with arrows.
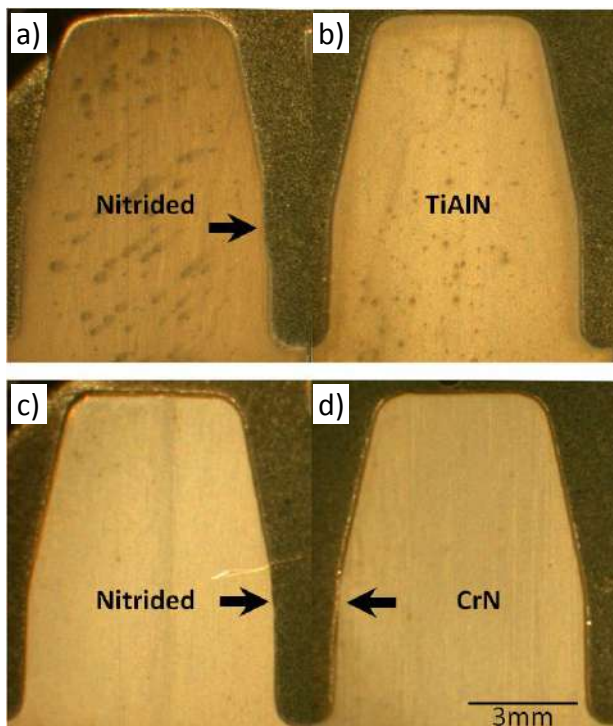

Figure 1. Cross sections of core pins after 5,000 cycles: a) nitrided pin from production run No. 1; b) TiAlN pin from production run No. 1; c) nitrided pin from production run No. 2; d) CrN pin from production run No. 2

Most pronounced wear marks can be found on nitrided core pins. Both core pins suffered severe wear. On the marked location nitrided layer is completely worn off. Core pins with deposited hard coatings have suffered lower wear. TiAlN core pin had markedly higher wear resistance, as optical micrographs do not reveal any notable wear marks.

Cross section optical micrographs of the core pins after maximum number of cycles are presented in Figure 2. Production run No. 3, with CrN core pin, had to be stopped after 14,000 cycles due to severe wear on nitrided core pin, Figure 2c, that caused unsatisfactory castings. However, even duplex hard coated CrN core pins have suffered notable wear that started to change geometry of the core, Figures 2d and 3.
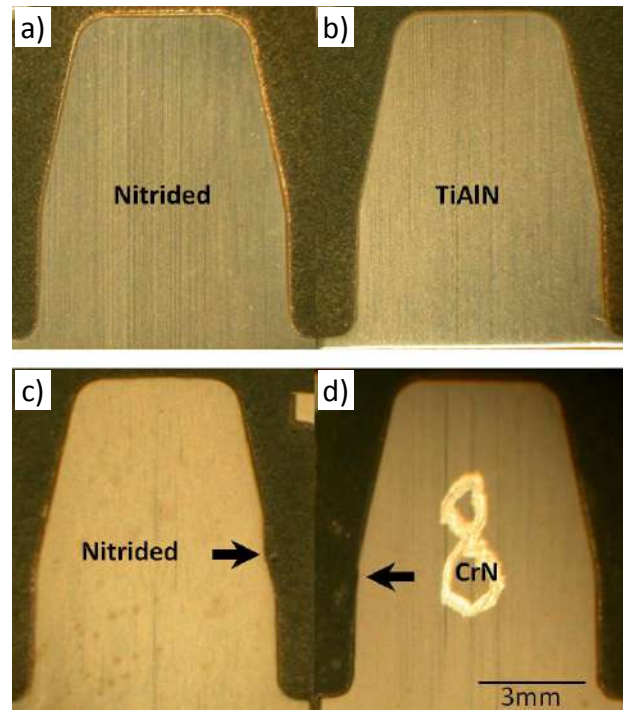

Figure 2. Cross sections of core pins after maximum number of cycles: a) nitrided pin from production run No. 4; b) TiAlN pin from production run No. 4; c) nitrided pin from production run No. 3; d) CrN pin from production run No. 3

Figure 3. CrN core pin after 14,000 cycles

Both core pins from production run No. 4 were able to withstand maximum number of

cycles, i.e. 22,000. Core pins retained geometry at the satisfactory level, and without forming notable undercuts. Pitting corrosion can be observed on all surfaces of the core pins, Figure 4a.
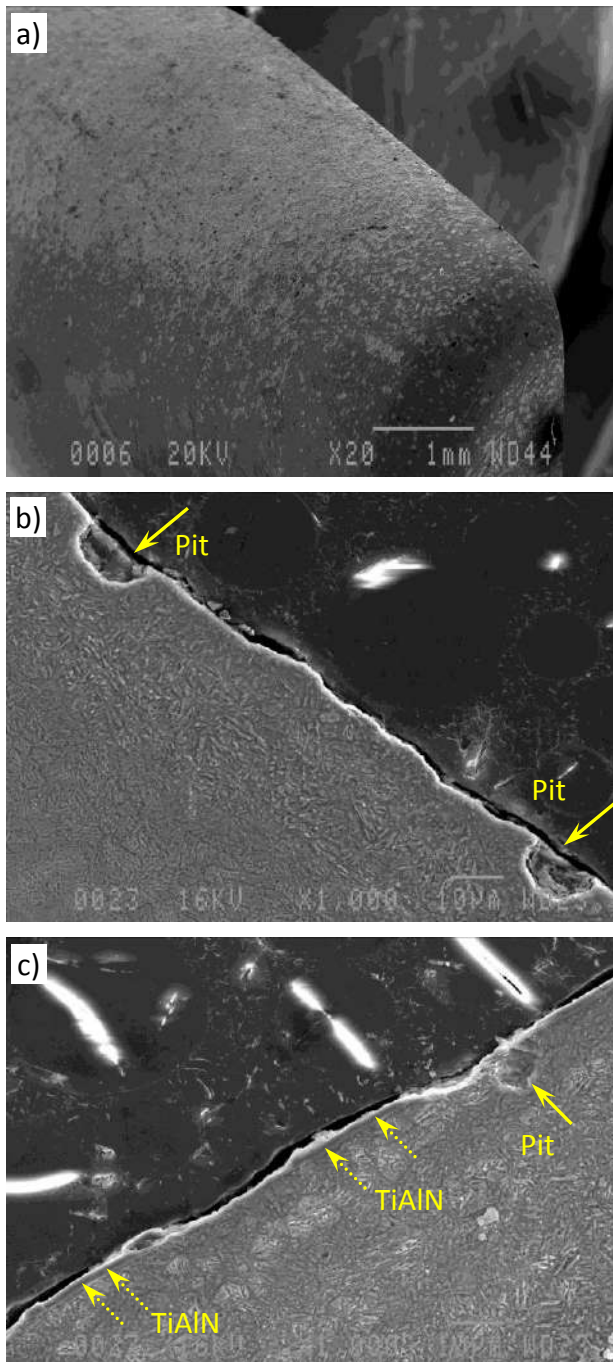

Figure 4. SEM images of the TiAlN core pin after 22,000 cycles: a) general appearance; b) cross section at the side directly under the impact of molten metal; c) cross section at the side opposite to the impact

Severity of the corrosion on two sides of the TiAlN core pin is notable. The coating was completely removed from the surface that was directly under the impact of molten metal,

Figure 4a. However, on the opposite side of the core pin, the coating was largely intact and is absent only on locations of corrosion pits, Figure 4b. Pits form at the location of the coating defects generated during deposition process [1,7]. Molten metal penetrates these defects and attacks underlying material. On the surfaces that are under the impact of the molten metal, coating can be delaminated and completely removed from the surface.

On all core pins that have observable wear marks, the most pronounced wear is located in the area where molten metal first reaches the pin and impinges its surface. This indicates that the dominant mechanism of wear is erosion.

During mold filling process, molten metal continuously loses its heat and for usual process parameters melt starts to solidify before the mold is completely filled. Since investigated core pins are located away from the ingates, it can be expected that the melt impinging the cores has some amount of solidified particles, i.e. primary dendrites. Additionally, excessive surface turbulence of HPDC process can induce formation of significant amount of aluminum oxide films. The repeated impact of high speed mixture of mixture of molten metal and solid particles can augment erosive wear and cause notable mass loss in the area of initial contact [2].

Wear marks on nitrided core pins used in first two production runs (5,000 cycles) were comparable. Therefore, it can be postulated that there were negligible differences in wear conditions of these two production runs. Since the CrN core pin from the first production run had significantly larger wear marks than TiAlN core pin from the second production run, it can be postulated that for tested conditions TiAlN duplex coatings exhibit higher wear resistance than CrN coatings. This is in agreement with previous results dealing with erosion behavior of hard coatings. Erosion performance is dependent on hardness (H), elastic modulus (E), and impingement angle [10,11]. For investigated experimental conditions, higher H/E ratio of the surface layer should give lower erosion rates of the

core pins. As previous results have shown, H/E ratio of duplex TiAlN surface layers is almost two times higher than that of the duplex CrN coating [3]. Therefore, TiAlN coating should have higher erosion resistance, as presented results have shown when comparing first and second production runs, as well as production runs No. 3 and No. 4.

It should be noted that the results of production run No. 4 show noticeable deviation from results of the first three production runs. During first three production runs, nitrided core pins have exhibited highest erosion rates and had largest wear marks that formed undercuts in core geometries. However, nitrided core pin from production run No. 4 had no noticeable erosion marks after 22,000 cycles, unlike nitrided pins that had been subjected to significantly lower number of cycles in previous runs, Figures 1 and 2. Since the core pins were from the same batch and had comparable properties, it can be postulated that wear conditions of production run No. 4 were somehow changed. The explanation could be found in small variances in the HPDC process. As previously stated, erosion behavior during HPDC can be significantly influenced by solid particles that are suspended in the molten metal. Cleanliness in the ingots used for initial preparation of the alloy can contain various amounts of oxide inclusions [12]. Additionally, small variations in the melt furnace temperature, metal dosage speed, tool temperature, and chemical composition of molten metal that minutely influences liquidus temperature, can change the fraction solid of the alloy at the time of impact. Hence, variance in the amount of solid particles impinging the core surface can be large even when the usually monitored parameters of the casting process are tightly controlled. Therefore, in order to adequately compare wear behavior of different surface treatments for HPDC tools, one must use only results obtained from the same production run, or implement known surface treatment in all production runs in order to confirm comparable wear conditions, as it was done in this study.

4. CONCLUSIONS

The dominant wear mechanism of core pins studied in this investigation was erosion.

Highest wear resistance was found for duplex TiAlN coatings, followed by duplex CrN coatings. Nitrided core pins exhibited lowest wear resistance during casting trials.

Significant scatter in results was present. Although TiAlN coated pins showed highest wear resistance, large variance in wear of nitrided core pins indicates that the production run when they were able to withstand maximum number of cycles had less severe erosion conditions.

Small and regularly disregarded variances in casting temperature or in cleanliness of ingots used in production can significantly change wear rates of HPDC tools. Therefore, when conducting industrial evaluations of surface treatments, one can only compare results obtained from the same production run.

REFERENCES

[1] A. Persson: *On Tool Failure in Die Casting*, PhD thesis, Uppsala University, 2003.

[2] R. Shivpuri, M. Yu, K. Venkatesan, Y.-L. Chu: A study of erosion in die casting dies by a multiple pin accelerated erosion test, Journal of Materials Engineering and Performance, Vol. 4, pp. 145–153, 1995.

[3] P. Terek: *Application of surface engineering technologies for improvement of diecasting tools quality*, PhD thesis, University of Novi Sad, Serbia, 2016.

[4] P. Terek, L. Kovačević, A. Miletić, P. Panjan, S. Baloš, B. Škorić, D. Kakaš: Effects of die core treatments and surface finishes on the sticking and galling tendency of Al–Si alloy casting during ejection, *Wear*, Vol. 356–357, pp. 122–134, 2016.

[5] A. Srivastava, V. Joshi, R. Shivpuri, R. Bhattacharya, S. Dixit: A multilayer coating architecture to reduce heat checking of die surfaces, Surface and Coatings Technology, Vol. 163–164, pp. 631–636, 2003.

[6] N. Dingremont, E. Bergmann, P. Collignon: Application of duplex coatings for metal injection moulding, Surface and Coatings Technology, Vol. 72, No. 3, pp. 157–162, 1995.

[7] C. Mitterer, F. Holler, F. Üstel, D. Heim: Application of hard coatings in aluminium die casting — soldering, erosion and thermal fatigue behaviour, Surface and Coatings Technology, Vol. 125, No. 1-3, pp. 233–239, 2000.

[8] J. Lin, S. Carrera, A.O. Kunrath, S. Myers, B. Mishra, P. Ried, J.J. Moore, D. Zhong: Design methodology for optimized die coatings: The case for aluminum pressure die-casting, Surface and Coatings Technology, Vol. 201, No. 6, pp. 2930–2941, 2006.

[9] C. Mitterer, F. Holler, D. Reitberger, E. Badisch, M. Stoiber, C. Lugmair, R. Nöbauerc, T. Müllerc, R. Kullmerc: Industrial applications of PACVD hard coatings, Surface and Coatings Technology, Vol. 163–164, pp. 716–722, 2003.

[10] F. Cai, X. Huang, Q. Yang: Mechanical properties, sliding wear and solid particle erosion behaviors of plasma enhanced magnetron sputtering CrSiCN coating systems, Wear, Vol. 324–325, pp. 27–35, 2015.

[11] A. Leyland, A. Matthews: On the significance of the H/E ratio in wear control: a nanocomposite coating approach to optimised tribological behaviour, Wear, Vol. 246, No. 1-2, pp. 1–11, 2000.

[12] N. V. Okladnikova, A.L. Uskova, T.N. Drozdova, T.A. Orelkina, M.M. Antonov: Studies of the Effect of Nonmetallic Inclusions and Refining of Melt on the Quality of Ingots and Shapes from Alloy AD31, Metal Science and Heat Treatment, Vol. 57, No. 1, pp. 69–73, 2015.

MECHANOCHEMICAL SYNTHESIS AND GAS PERMEATION PROPERTIES OF POROUS KAOLIN BASED MEMBRANES

David O. OBADA[1]*, David DODOO-ARHIN[2,3], Muhammad DAUDA[1], Fatai O. ANAFi[1], Abdulkarim S. AHMED[4], Olusegun A. AJAYI[4], Laminu S. KUBURI

[1]Department of Mechanical Engineering, Ahmadu Bello University, Zaria, Nigeria
[2]Department of Materials Science and Engineering, University of Ghana, Legon, Ghana.
[3]Institute of Applied Science and Technology, University of Ghana, Legon, Ghana
[4]Department of Chemical Engineering, Ahmadu Bello University, Zaria, Nigeria.
*Corresponding author: obadavid4@gmail.com

Abstract: *Porous kaolin based membranes using styrofoam (STY) and sawdust (SD) have been prepared by mechano-chemical synthesis method with porogen content wt% between (0 -20) % by die pressing. Pellets were fired at 1150°C and soaking time of 4 hrs. The raw materials were characterized using XRD and TGA/DTA.The membranes cast as circular disks were subjected to characterization studies using XRD and SEM and analyses were conducted to evaluate the effect of the sintering temperature and pore former content on porosity, density, water absorption and mechanical strength. Obtained membranes show good porosity with maximum at about 43 and 47% respectively for styrofoam and sawdust porogens but with a slightly low mechanical strength that does not exceed 19 MPa. These membranes can be considered as efficient regarding the results shown in the gas permeation tests at different sintering temperature. A STY and SD percentage of 20% was considered and a sintering temperature of 1,150°C was chosen as the optimum for gas permeation based on enlarged pore diameter of sintered membranes.*

Keywords: *Porosity, pore formers, kaolinite clay, Physico-mechanical properties, permeation*

1. INTRODUCTION

Ceramic membranes which can be utilized at relatively higher temperatures are finding increasing relevance, because it is more realistic to carry out many chemical reactions and separation at elevated temperatures [1-5]. Ceramic membranes have been widely investigated for energy and environmental applications due to its unique advantages such as high thermal stability, chemical and mechanical stability, environmentally friendliness, and low energy-consumption [6]. However, because ceramic membranes have higher cost than polymeric counterparts, their applications have been retarded in some

traditional industries such as food, beverage, and pharmaceutical. Also, limited types of membrane materials (such as Al_2O_3, ZrO_2, TiO_2, and their composite oxides) hinder their further applications [7-8]. Among the many technologies for gas separation, membranes are drawing interest because of their reduced energy consumption, steady or continuous operation, and huge potentials for pilot scale set-up which can be combined with other traditional separation technologies [9,10]. The most utilized membranes are categorized as polymeric, metallic and ceramic while their glassy counterparts are not quite important because of their low selectivity.

Ceramic membranes most times take the form of metal oxides and can be porous or highly dense [10]. The oxides mostly used are alumina (Al_2O_3), zirconia (ZrO_2), titania (TiO_2), and silica (SiO_2). The mixtures of these metal oxides are a very interesting option too. Their key advantages are good stability at high operating temperature and resistance to chemicals. In order to obtain a high permeability and the desired selectivity, usually the porous ceramic membranes are supported with a very open pore structure, and a thin top-layer with smaller pores. Sometimes the pores in the thin top layer are enlarged by embedding porogenic agents in the matrix. Due to their good chemical and thermal stability, these types of membranes are mainly used for applications in severe conditions of temperature (up to 600 °C) or in aggressive chemicals.

From an economic point of view, research is devoted to other raw materials that would be of low cost and suitable as a standard raw material replacement. Clays have been identified as best cost-effective raw materials for membrane applications [11-13].

In a recent study [14], the potentials of fabricating porous ceramics bodies from kaolinite clay using different pore formers was investigated. Therefore, the objective of this study is to fabricate ceramic membranes with clay/saw-dust and styrofoam mixture with varying ratios by weight to prepare macroporous membranes. The physical and mechanical properties of the kaolin based ceramic membranes and gas permeability test results are also presented.

2. MATERIALS AND METHODS
2.1. Materials and processing

The clay materials that were used in this study were obtained from Kankara and Kibi deposits in Nigeria and Ghana respectively. The powdery high density polyethylene powder was processed at the Materials Laboratory of the University of Ghana. Clay (Kankara and Kibi) was mixed with the powdery high density polyethylene in four different ratios (clay-to-pore formers) by weight (Table 1). The XRF and XRD of kaolinite used for membrane fabrication has been presented in our previous work [14]. It was observed that the composition of the clay was mainly alumina silicates while the spectrum suggested that the clay consists of mainly kaolin, illite, mica and montmorillonite.

2.2 Materials Characterization
2.2.1 Zeta potential

The zeta potential of dispersed kaolin was performed using a Horiba Scientific, SZ-100 nanoparticle analyser. After 15 min ultrasonication of the suspension, the zeta potential was measured as a function of pH by titration with HCL and NaOH

2.3 Membrane fabrication

The raw materials (see Table 1), were mixed in a ball mill at 50 rpm for 30 min. The resulting powdery mix was then compacted in a hydraulic pressing machine at a pressure of 3.5 MPa with the help of stainless steel die. The obtained circular shaped membranes were first dried at ambient temperature before further drying at 150˚C for 24 h in a hot air oven. This was to remove moisture and also reduce any thermal stresses which may hamper the successful fabrication of the ceramic membranes. Subsequently, the membranes were sintered at 1150˚C for 4 h in a muffle at 5°C/min.

Table 1. Composition of test Samples by weight

Sample code.	KnKaolin (g)	KiKaolin (g)	STY	SD
0% CS	80	20	-	-
5%STY	75	20	5	-
10%STY	70	20	10	-
15%STY	65	20	15	-
20%STY	60	20	20	-
5%SD	75	20		5
10%SD	70	20	-	10
15%SD	65	20	-	15
20%SD	60	20	-	20

Kn-Kankara (base kaolin); Ki-Kibi (Plasticizer); STY-styrofoam; SD-Sawdust; CS-Control sample

After sintering, the compact and porous ceramic membranes were polished on both sides using silicon carbide abrasive paper to obtain ceramic membranes with uniform surface. Then these membranes were washed with deionized water in an ultrasonic for 15min to remove the loose particles adhered on the surface of membranes.

2.3.1 Characterization of Ceramic Membranes

Apparent Porosity, Bulk Density and Water absorption

The apparent porosity (the amount of void or pores within a volume of porous solid) of the as-sintered membranes was calculated using equation 1:

$$\text{Apparent Porosity} = \left(\frac{W\text{-}D}{W\text{-}S} \right) \times 100 \qquad (1)$$

Their respective bulk density, apparent density and percentage water absorption were also calculated using the formulae as proposed [15]

$$\text{Bulk Density} = \frac{D}{(W\text{-}S)} \times 100 \left(g/cm^3 \right) \qquad (2)$$

$$\text{Water Absorption} = \frac{W}{(W\text{-}S)} \times 100 \qquad (3)$$

Where: D = Weight of fired specimen, S = Weight of fired specimen suspended in water, and W = Weight of soaked specimen suspended in air.

2.3.2 Mechanical Strength

Mechanical property tested for were cold compression strength and flexural strength. The compressive strength is an indication of the membranes' probable performance under load. The membrane samples were dried in an oven at a temperature of 110 ^{0}C and allowed to cool. The compressive strength testing was carried out on an hydraulic testing machine (Carver Press, USA) The compressive strengths of the porous clay ceramics were obtained by compressive loading of samples and cold crushing strength, of standard and conditioned samples were calculated from the equation:

$$CS = \frac{P}{BW} \qquad (4)$$

Where P =load at failure and B and W are the respective width and breadth of the specimens.

The flexural strength of the membranes was tested with a three-point bending with rectangular bars using Universal Testing Machine. The flexural strength was evaluated by the expression

$$\text{Flexural Strength} = \frac{3PL}{2bd^2} (MPa) \qquad (5)$$

Where, P = maximum load applied on test specimen (N)
L = support span/gauge length (mm)
b = width of specimen tested (mm)
d = thickness of specimen tested (mm)

2.3.3 Permeability Tests

The permeability of the porous samples obtained was tested using N_2 as permeate with a laboratory designed set up. For this experimentation, the membranes were sintered at 850, 1000 and 1150°C for 4h in a muffle at 5°C/min. This was to investigate the effects of sintering temperatures on gas permeability through the membranes. The gas cylinder was connected to a mass flow controller and the set point was such that 10 mL/min of gas was released at the out flow. This was measured by the use of a flow rate meter. The mass flow controller was then connected to the end of the quartz tube were the membrane was placed for the gas permeability tests. The gas flow rate was measured at the out flow of the tube connected to valves for the control of inlet and outlet. The pressure supplied was varied as the permeability of gas was measured at the gas exit using a flow meter.

3. RESULTS AND DISCUSSION

Figure 1 shows the zeta potential of kaolinite (Kankara and Kibi) used for membrane fabrication as a function of the pH of dispersant (H_2O). It is known that to obtain dense ceramic components, a number of stages, including mixing, incorporating

additives, shape forming, drying and sintering are required. Water (H_2O) has been used as a binder and dispersant hence a need to evaluate dispersion stability by the zeta potential measurements. Particles in aqueous solution becomes charged. The charge, measurable by the zeta potential, is an important parameter in determining the stability of dispersion. If the particles have a large zeta potential they will repel each other, and the dispersion is stable. If they have low zeta potential values, then there is no force to prevent the particles from coming together, meaning the dispersion is unstable and particles aggregate [16]. It is well known that kaolin has positively charged edge faces and negatively charged basal faces. With increasing pH the dissociation of the silanol groups present on the basal plane of kaolin particles increases and so they are effecitve in the aqueous dispersion. The curves (Figure 1) show mostly a negative zeta potential in the pH range from 2 to 10. The isoelectric point (the point where the value of the zeta potential is zero) is about pH 2 for the kaolinites. Dispersions with a pH near the isoelectric point are unstable. Thus in pH range of 2, particles are oppositely charged and dispersion flocculates. The interaction is very strong and in this range it is impossible to disperse mixture of kaolin powder and to obtain slurry of good quality without any additives.
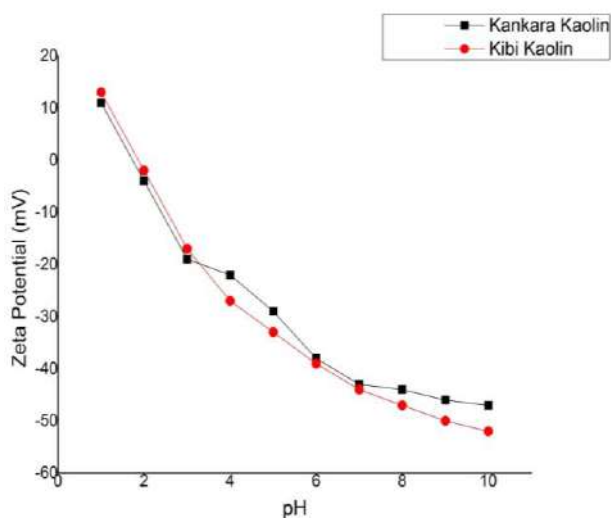

Figure 1. The zeta potential of kaolin in H_2O as a function of pH

The porosity (ε) of the membrane was determined by the achimedes principle. Figs. 2 - 6 summarizes the porosity, density, water absorption and compressive and flexural strengths and of the membranes varying with pore former addition.

Fig. 2 shows the variation of membrane porosity with varying pore former addition. The membrane porosity increases from 39.20% to 46.17% for sawdust addition whereas for styrofoam addition, porosity increases from 33.93% to 42.54% when pore former content varies from 5%-20%. This is due to the fact that with increase in pore former content, porosity of the structure increases due to decomposition of the pore formers during sintering.
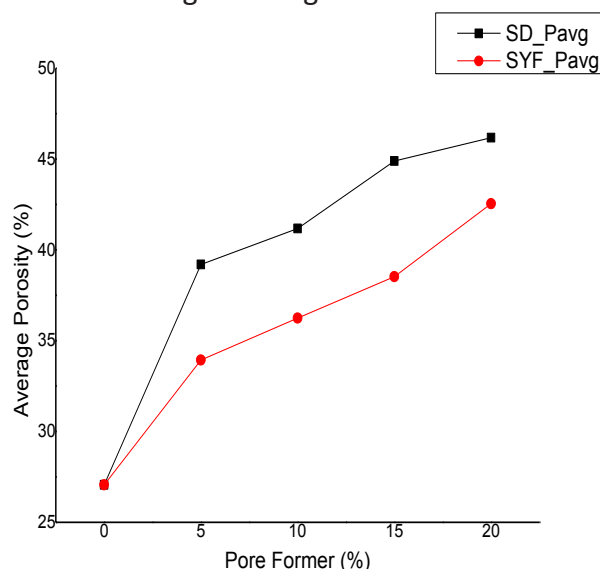

Figure 2. Porosity of membranes with varying weight of pore formers.

The water absorption rate, which is the weight of the moisture in the pores as a fraction of the weight of the sintered membranes, is an effective index of the quality of porous ceramic membranes. Fig. 3 shows the effect of increase in pore former content on the apparent porosity and water absorption of the sintered ceramic membranes. The plots show a similar trend, which is an increasing water absorption tendency with increasing pore former content.

The membranes apparent density as shown in Fig. 4 decreases from 2.05 g/cm^3 to 1.97g/cm^3 and 1.54 g/cm^3 to 1.48g/cm^3 when pore former content varies from 5%-20% for sawdust and styrofoam pore formers

respectively, thereby reducing the densification of the porous membrane structures.
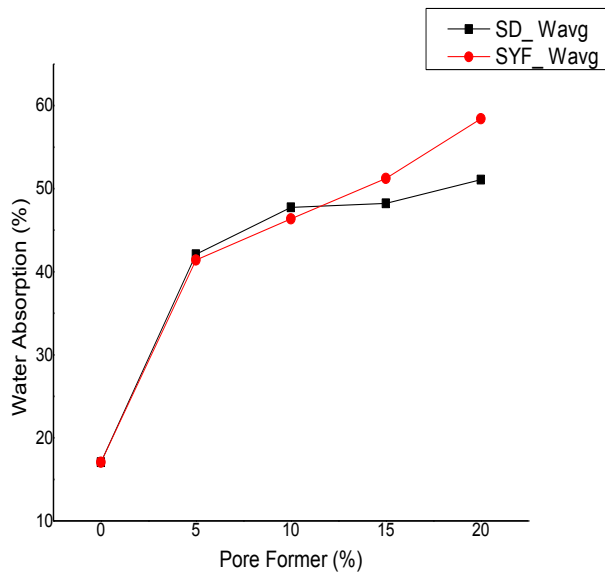

Figure 3. Water absorption of membranes with varying weight of pore formers
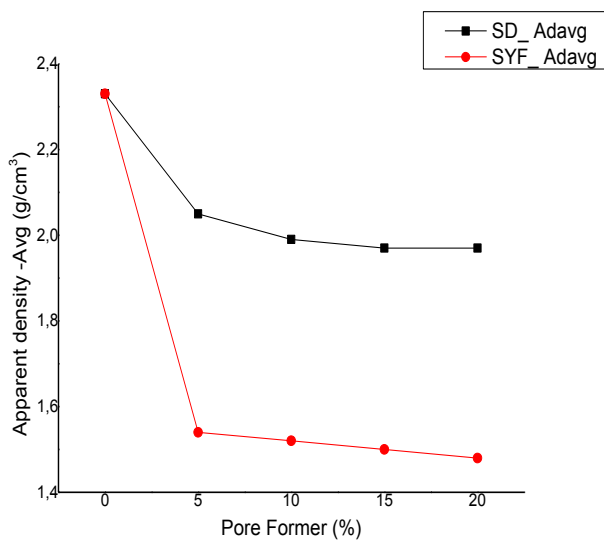

Figure 4. Apparent density of membranes with varying weight of pore formers

The flexural strength of the prepared membranes was performed using the three points bending strength method. The flexural strength of the membranes at different pore former content is presented in Figure 5. It can be seen that the flexural strength decreases (18.04 MPa at 5%) with increasing pore former content (10.14MPa at 20%) and (22.23 MPa at 5%) with increasing pore former content (11.27MPa at 20%) for sawdust and styrofoam as porogens respectively. The decrease in flexural strength is attributed to the reduced densification of the clay materials with increasing pore former content of the samples. This result is in good agreement with the trends found in literature [11,17].
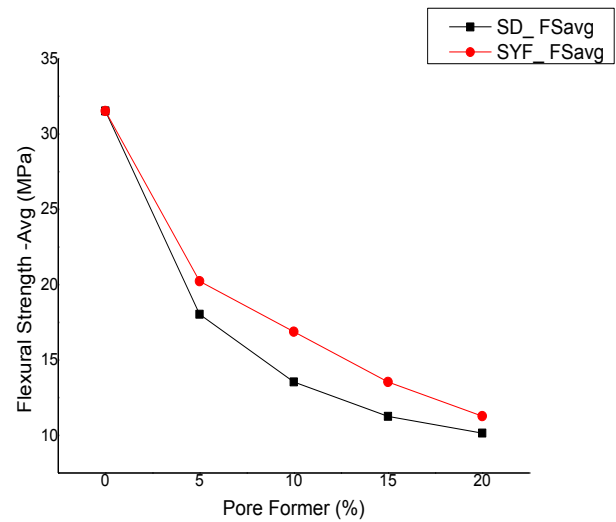

Figure 5. Flexural strength of membranes with varying weight of pore formers

Fig. 6 shows that the cold crushing strength is higher for the control sample (0% pore former content) in comparison to samples with pore formers due to higher porosity in the latter samples. Higher porosity implies fewer loads bearing capacity. Therefore, the strength decreases at higher pore former content. However the value of compressive strength, 18.31Mpa and 18.21Mpa obtained at maximum pore former content (20%) for sawdust and styrofoam as pore formers respectively at the sintering temperature used in this study (1150^0C) is considered to be within tolerable limits.
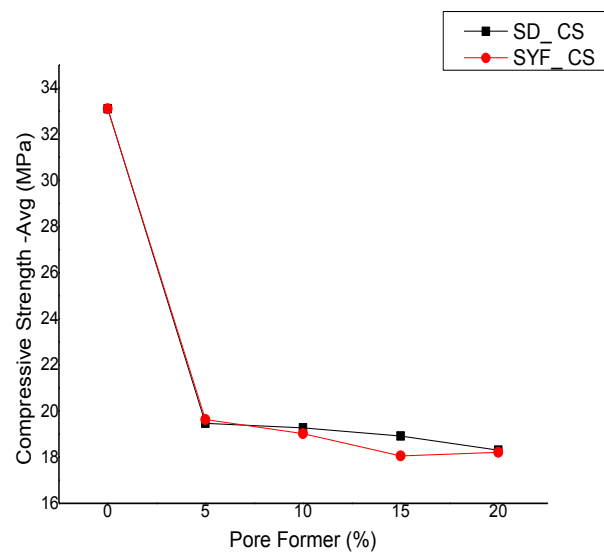

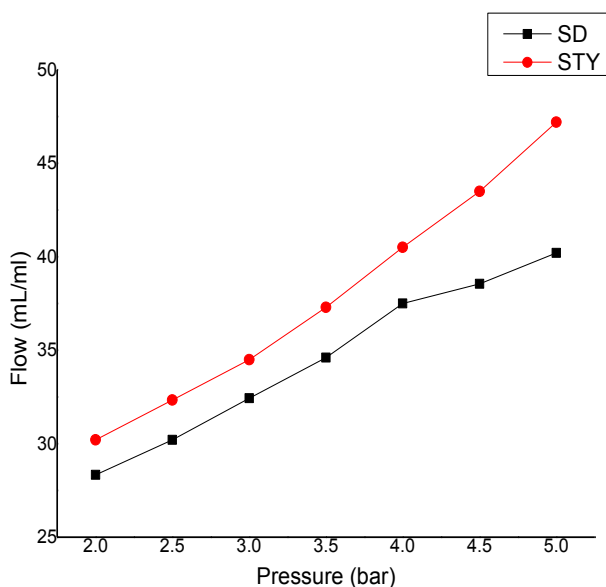**Figure 6.** Compressive strength of membranes with varying weight of pore formers

Figure 7. Flow evolution with pressure for membranes heated at 1,150°C

Fig. 10 shows the flow evolution with pressure for membranes heated at 1,150°C. A near linear evolution of the flow vs. pressure can be noted. At a maximum pressure of 5bar, the flow evolution is 40.20mL/min, 47.20mL/min at 1,150°C for sawdust and styrofoam porogens respectively. The outcome could be directly related to the bigger pore size generated by the high sintering temperature. It is known that pore nucleation or cavitation precedes pore growth in ceramics at high temperature. This result confirms that the pore size is more important for the permeability than the total pore volume. The increase of the heating temperature closes the porosity and also induces the pore coalescence which engages a bigger pore size. Usually, average pore diameter of the membrane increases with increasing sintering temperature due to which membrane permeability also increases. Similar trends are reported in literature [11,17] for the other type of clay based inorganic membrane fabrication.

4. CONCLUSION

This study indicates that ceramic membrane can be fabricated with higher contents of kaolin (80%) and pore formers. The membranes provided good mechanical strength and the obtained permeation values show an increase of permeability with the at a high sintering temperature in relation to increase of gas pressure. These results suggest that membranes could also be tested to evaluate their performance for liquid permeation. These results provide significant opportunities to develop ceramic micro-filtration membranes with flexible pore sizes for industrial applications.

REFERENCES

[1] Q. Xu, and M.A. Anderson: Sol-Gel Route to Synthesis of Micro- porous Ceramic Membranes: Thermal Stability of Ti0,-Zr02 Mixed Oxides, Journal of the American Ceramic Society, Vol. 76, 2093, 1993.

[2] Y. Li, X. Zhang, J. Wang: Preparation for ZSM-5 membranes by a two-stage varying-temperature synthesis, Separation and purification technology, Vol. 25, No. 1, pp. 459-466, 2001.

[3] J.S Church, N. W. Cant, D. L. Trimm: Surface Area Stability and Characterization of a Novel Sulfate-Based Alumina Modified by Rare Earth and Alkaline Earth Ions, Applied Catalysis A: General, Vol. 107, No. 2, pp. 267-276, 1994.

[4] F.K Mizukami, M. Maeda, K. Watanabe, T. Masuda, T. Sano, K. Kuno: Preparation of Thermostable High-Surface-Area Aluminas and Properties of the Alumina-Supported Pt Catalysts, Proceedings of the catalysis and Automotive Pollution Control II, 10-13.9.1991, Brussels, Belgium, p. 557.

[5] C.A LeDuc, J. M. Campell, J. A. Rossin: Effect of Lanthana as a Stabilizing Agent in Titanium Dioxide Support, Industrial & Engineering Chemestry Research, Vol. 35, No. 7, pp. 2473 – 2476, 1996.

[6] X. Dong, G. Zhang, Z. Liu, Z., Zhong, W., Jin, N. Xu: CO_2-tolerant mixed conducting oxide for catalytic membrane reactor, Journal of Membrane Science, Vol. 340, No. 1, pp. 141-147, 2009.

[7] J.Z Hamad, C. Ha, M.D Kennedy. G.L Amy: Application of ceramic membranes for seawater reverse osmosis (SWRO) pre-treatment, Desalination and Water Treatment, Vol. 51, No. 25-27, pp. 4881-4891, 2013.

[8] P. Pandey, R.S Chauhan: Membranes for gas separation, Progress in Polymer Science, Vol. 26, No. 6, pp. 853-893, 2001.

[9] M. Mulder: *Basic Principles of Membrane Technology*, 2nd edition, Kluwer Academic Publishers, Boston, Dordrecht, 2016.

[10] A.G. Dixon: Recent research in catalytic inorganic membrane reactors, International Journal of Chemical Reactor Engineering, Vol. 1, No. 1, pp. 1 - 35, 2003.

[11] N Saffaj, H Loukili, S.A Younssi, A. Albizane, M. Bouhria, M Persin, A. Larbot: Filtration of solution containing heavy metals and dyes by means of ultrafiltration membranes deposited on support made of Moroccan clay, Desalination, Vol. 168, pp. 301-306, 2004.

[12] S. Khemakhem, A. Larbot, R.B. Amar: Study of performances of ceramic microfiltration membrane from Tunisian clay applied to cuttlefish effluents treatment, Desalination, Vol. 200, No. 1, pp. 307-309, 2006.

[13] M.R Weir, E. Rutinduka, C. Detellier, C.Y Feng, Q. Wang, T. Matsuura, R. Le Van Mao: Fabrication, characterization and preliminary testing of all-inorganic ultrafiltration membranes composed entirely of a naturally occurring sepiolite clay mineral. *Journal of Membrane Science*, Vol. *182*, No.1, pp. 41-50, 2001.

[14] D.O Obada, D. Dodoo-Arhin, M. Dauda, F.O Anafi, A.S Ahmed, O.A Ajayi: Potentials of fabricating porous ceramic bodies from kaolin for catalytic substrate applications. Applied Clay Science, Vol. 132, pp. 194-204, 2016.

[15] A.R Chesti: *Refractories: manufacture, properties, and applications,* Delhi, Prentice-Hall of India Private Limited, 1986.

[16] Z. Dohnalová, L. Svoboda, P. Šulcová: Characterization of kaolin dispersion using acoustic and electroacoustic spectroscopy, *Journal of Mining and Metallurgy B: Metallurgy*, Vol. *44*, No. 1, pp. 63-72, 2008.

[17] F. Bouzerara, A. Harabi, S. Achour, A. Larbot: Porous ceramic supports for membranes prepared from kaolin and doloma mixtures, Journal of the European Ceramic Society, No. 26, pp. 1663–1671, 2006.

SERBIATRIB '17

15th International Conference on Tribology

Kragujevac, Serbia, 17 – 19 May 2017

SOLVING THE INTERCONNECTED PROBLEM OF DYNAMICS AND LUBRICATION FOR THE CRANKSHAFT BEARINGS SYSTEM OF IC ENGINES

Yury ROZHDESTVENSKY[1], Nadezhda KHOZENIUK[1,*], Sergey SUROVTSCEV[1]

[1] South Ural State University (National Research University), Chelyabinsk, Russia,
rozhdestvenskiiyv@susu.ru; khozeniukna@susu.ru; ssw-92@yandex.ru
*Corresponding author: khozeniukna@susu.ru

Abstract: The article presents the solution to the interconnected problem of main bearings dynamics for the forced internal combustion (IC) engine. For the crankshaft main bearings system of the (IC) engines it is necessary to consider the cross-coupling effect of the tribounits arising from elastic links of bearings and journals (by means of an engine crankcase and a crankshaft).

The results are received by the solution of four interrelated problems: 1) the dynamics of a journals on the lubricant layers under the influence of non-steady external forces and reactions of the lubricant layers; 2) the hydrodynamic theory of lubrication to determine the pressure distribution in the lubricant films for each bearings taking into account the design features of tribo-units and the rheological properties of the oil; 3) a determination of the thermal state of the bearings for the correction of the lubricant viscosity; 4) a definition of the loads operating on all bearings of a multisupporting elastic crank shaft as a redundant system. The technique is based on the iterative scheme of the solution of four tasks given above. It analyzes not only the influence of macrogeometry parameters of each main bearing and the influence of non-Newtonian properties of lubricant, but also elastic characteristics of a crankshaft and crankcase and supports displacements caused by the thermal deformation of an engine crankcase. The influence of technological coaxiality tolerance for bearings and necks of a crankshaft is also estimated. The modeling results of two types of engines are compared to various design of a crankcase. The research shows the necessity of applying the integrated approaches which allow to consider simultaneously both the features of autonomous bearings and many facts of their interaction.

Keywords: main bearing, lubricant, crankshaft, crankcase, elastic deformation, internal combustion engine.

1. INTRODUCTION

Performance assurance of the hydrodynamic tribosystem is one of the basic problems in the creation and operational development of internal combustion engines design. Mainly it is caused by complexity and interconnectivity of the processes and factors defining the reliability of the fluid friction units.

For the performance assurance of the hydrodynamic tribosystem it is necessary to take into account the following data: geometry of the tribounits, macro- and micro geometry of the friction surfaces, velocity and loading parameters, viscosity-temperature and rheological properties of the liquid lubricant dividing the complex loaded surfaces of the friction. Together with these parameters

considered in the autonomous tribounits simulation, for the system of crankshaft main bearings of the internal combustion engines it is necessary to consider the cross-coupling effect of the tribounits arising from elastic links of bearings and journals (by means of an engine crankcase and a crankshaft).

Moreover, the factors determining a relative position of its journals and bearings influence significantly the reliability of the main bearings system. Among these factors one should mention technology and thermal factors. The technology factors are correlated with coaxiality tolerance of the holes into the crankcases and a run-out tolerance of the crankshaft journals. Modeling the influence of thermal stress state of a crankcase on hydromechanical characteristics of main bearings of diesel engines requires a detailed description of thermal fields. This description requires modeling a heat emission in cylinders and liquid flows in the cooling system of the engine heads and crankcases.

The existing methods of modeling the interconnected processes of lubricant flow in thin liquid layers and nonlinear dynamics for a system of "a crankshaft - lubricating films - a crankcase" are reduced to the separate subtasks solution [1-3].

Such methods are mostly used for heavy-loaded autonomous (isolated) hydrodynamic bearings. However, they do not allow to estimate the influence of design and technological factors such as different values of elastic compliances of crankshaft supports, misalignments of journals and main bearings and so on.

The fullest model was suggested by S. M. Zakharov [4], D. Bonneau et al. [5-9]. The technique [4] considered the deviations of the necks of the crankshaft and the angular compliances of the crankshaft supports, but for obtaining the results the authors were compelled to apply an approximation method (Holland`s method). The complete models [9] simultaneously consider the bearings as a whole with their relative displacements under the deformation effect of the engine block and the crank shaft, but authors didn't analyze

influence of admissions on coaxiality of pins of a shaft, other technological and thermal factors on operability of main bearings system.

2. METHOD DESCRIPTION

The efficiency of hydrodynamic tribounits can be estimated by calculating the standard set of hydromechanical characteristics (HMC) in order to predict the fatigue durability and wear resistance of bearing antifriction layers, friction losses, thermal loading of tribosystems, and solve the problem of optimizing the design parameters [10, 11]. The most important HMC for main bearings are: instant values of the minimum film thickness $h_{\min}(t)$ and the maximum hydrodynamic pressure $p_{\max}(t)$ of a lubricant layer, and also their extremes $\inf h_{\min}$, $\sup p_{\max}$ and averages $h_{\min}^{*}$, $p_{\max}^{*}$ magnitudes per cycle of loading; effective temperature of a lubricating layer T^{*}, instant and average power losses to friction $N(t)$, N^{*} lubricant flow rates $Q(t)$, Q^{*}.

HMC determination of main bearings system for IC engine is based on the solution of four interrelated problems: 1) the dynamics of a journal on the lubricant layer under the influence of non-steady external forces and reactions of the lubricant layer; 2) the hydrodynamic theory of lubrication to determine the pressure distribution in the lubricant film taking into account the design features of tribounits and the rheological properties of the oil; 3) a determination of the thermal state of the bearing for the correction of the lubricant viscosity; 4) elastic model for determination the interrelation between elastic compliance of crankshaft and crankcase and bearing reactions.

2.1 Dynamic subtask

The position of each central of crankshaft necks $X^{j}(\tau), Y^{j}(\tau)$, $\alpha^{j}(\tau), \beta^{j}(\tau), j = 1, .., n+1$ (where n is number of cranked port of shaft) defined by the decision of the dynamic

equation system (the subscript j isn't specified):

$$m\ddot{\bar{U}} = \bar{F}(\bar{U}, \dot{\bar{U}}, \bar{\gamma}, \dot{\bar{\gamma}}, \tau) + \bar{R}(\bar{U}, \dot{\bar{U}}, \bar{\gamma}, \dot{\bar{\gamma}}, \tau)$$

$$J\ddot{\bar{\gamma}} = \bar{M}_F(\bar{U}, \dot{\bar{U}}, \bar{\gamma}, \dot{\bar{\gamma}}, \tau) + \qquad (1)$$

$$+ \bar{M}_R(\bar{U}, \dot{\bar{U}}, \bar{\gamma}, \dot{\bar{\gamma}}, \tau) + \bar{M}_G(\bar{U}, \dot{\bar{U}}, \bar{\gamma}, \dot{\bar{\gamma}}, \tau),$$

where
$\bar{U} = \{X, Y\}$, $\bar{\gamma} = \{\alpha, \beta\} = \{-\gamma \cdot \cos\varepsilon, \ \gamma \cdot \sin\varepsilon\}$,
$\dot{\bar{U}}, \dot{\bar{\gamma}}, \ddot{\bar{U}}, \ddot{\bar{\gamma}}$ are vectors of linear and angular coordinates, velocities and accelerations of the journals respectively; γ is the skewed angle between the neck and bearing axis; ε is the angle between the skewed and coordinated planes; m, J are the journal inertial characteristics; $\bar{F} = \{\tilde{F}_X, \tilde{F}_Y\}$, $\bar{M}_F = \{\tilde{M}_X, \tilde{M}_Y\}$ are forces and moments acting on the bearing (they are defined by solving the system (5); $\bar{R}, \bar{M}_R$ are the resultant vectors of forces and moments received by integration of the Reynolds equation for the lubricant pressure; $\bar{M}_G$ is the gyroscopic torque.

Unlike autonomous bearing, the vectors for non-autonomous bearings system depends on elastic characteristics of all supports and thus coordinates and accelerations of all crankshaft journals centers.

2.2 Hydrodynamics subtask

For the definition of a hydrodynamic reaction of each bearing lubricated by non-Newtonian liquid it is necessary to know a hydrodynamic pressure distribution in a thin lubricant layer $p(\varphi, z, \tau)$. This function is obtained by solving Reynolds' differential equation [2, 12, 13]

$$\frac{\partial}{\partial \varphi}\left[\bar{h}^{k+2}\left(\bar{\varphi}_2 - \frac{\bar{\varphi}_1^2}{\bar{\varphi}_0}\right)\bar{\rho}\frac{\partial \bar{p}}{\partial \varphi}\right] +$$

$$+ \frac{\partial}{\partial \bar{z}}\left[\bar{h}^{k+2}\left(\bar{\varphi}_2 - \frac{\bar{\varphi}_1^2}{\bar{\varphi}_0}\right)\bar{\rho}\frac{\partial \bar{p}}{\partial z}\right] = \qquad (2)$$

$$= \frac{\partial}{\partial \varphi}\left[\bar{\omega}\,\bar{\rho}\bar{h}\left(1 - \frac{\bar{\varphi}_1}{\bar{\varphi}_0}\right)\right] + \frac{\partial}{\partial \tau}(\bar{\rho}\bar{h}),$$

where $\bar{\rho}$ is lubricant density; $\bar{p} = (p - p_a)\psi^2 / \mu_0\omega_0$, $\bar{h}$ are a non-dimensional hydrodynamic pressure and film thickness respectively; p, p_a are a dimensional hydrodynamic pressure and the atmospheric pressure value; ψ, ω are relative values of a bearing clearance and angular velocity; $\bar{z}$ is a non-dimensional coordinate in the direction of a bearing width; φ is an angular bearing coordinate; k is an index characterizing the degree of non-newtonian behavior of a lubricant;

$$\bar{\varphi}_k = \int_{\bar{y}_1}^{\bar{y}_2} \bar{y}^k / \bar{\mu}^* \, d\bar{y}, \ k = 0, 1, 2,$$

$\bar{y}$ is a non-dimensional coordinate on the frictional surface normal; $\bar{\mu}^*$ is a non-dimensional value of viscosity which depends of viscosity versus shear rate, pressure and temperature

$$\bar{\mu}^* = (\bar{I}_2)^{(k-1)/2} \times C_1 \times e^{(C_2/(T_e + C_3)) + \beta(T_e)\cdot p}, \qquad (3)$$

where $\bar{I}_2 = (\partial \bar{V}_x / \partial \bar{y})^2 + (\partial \bar{V}_z / \partial \bar{y})^2$ is the second invariant of the shear rate; T_e is the temperature of the lubricant layer; C_1, C_2, C_3 are the constants, which are the empirical characteristics of the lubricant; $\beta(T_e)$ is a piezoelectric coefficient of viscosity which depends on the temperature and chemical composition of the lubricants. The empirical procedure for determining the characteristics of a lubricant is proved in [14].

The dimensional function of the film thickness taken into account the skewness of axes is:

$$h(\varphi, Z_1, \tau) = h^*(\varphi, Z_1) -$$

$$-e(\tau)\cos(\varphi - \delta(\tau)) + \qquad (4)$$

$$+ Z_1\frac{2S(\tau)}{B} \cdot \cos(\varphi - \varepsilon(\tau)) + L_p,$$

where $e(\tau)$ is the displacement of the journal mass centers relative to the bearing; $\delta(\tau)$ is the angle taking into account the skewness of axes of the bearing and the journal; $S(\tau)$ is the distance between the geometric centers of the

journal and the bearing at the ends of the tribounit; B is the bearing width, $Z_1 \in [-B/2; B/2]$; $h^*(\varphi, Z_1)$ is the bearing layer thickness with non-ideal geometry at the central journal position; L_p is elastic deformations of bearing.

At integration of the equation (2) the Stieber-Swift boundary conditions are used.

The lubricant thermal state (1-4) is based on the isothermal approach. It assumes that the calculated current temperature is the same at the all points of the lubricant film. This temperature is a highly inertial parameter and it is determined by solving the bearing heat balance equation for correcting of the lubricant viscosity. The calculating method for the autonomous bearing is in more detail presented in work [12, 15].

2.3 Elastic subtask

The mechanical model presented on Fig. 1 is a statically indeterminate 3D beam system on an elastic foundation. Forces and moments, acting to the j-th bearing $\tilde{F}_X^j(\tau), \tilde{F}_Y^j(\tau), \tilde{M}_X^j(\tau), \tilde{M}_Y^j(\tau)$ are defined by redundant problem solving. The solution of this problem is based on equation of five moments

$$[\delta] \times \{M\} = \{R\}, \qquad (5)$$

where $[\delta]$ is the band matrix of the influence coefficients $\delta_{ij} = \delta_{ij} \left(K_{s,x}^{\lambda, j=1,n}, K_{s,y}^{\lambda, j=1,n}, K_{L,x}^{\lambda, j=1,n}, K_{L,y}^{\varphi,j}, K_{s,x}^{\varphi,j}, K_{s,y}^{\varphi,j}, K_{L,x}^{\varphi,j}, K_{L,y}^{\varphi,j} \right)$; $\{M\}$ is the vector of unknown moments; $\{R\}$ is on the right part of Eq. (5), each vector entry is the deflection under external forces and moments $R_i = R_i (F_X^{j=1,n,(s)}, F_Y^{j=1,n,(s)}, K_{s,x}^{\lambda, j=1,n}, K_{s,y}^{\lambda, j=1,n}, K_{L,x}^{\lambda, j=1,n}, K_{L,y}^{\varphi,j}, \Delta_{case}, \Delta_{necks})$; Δ_{necks}, Δ_{case} are misalignments of necks and main bearings.

Usually these misalignments are correlated with technology and thermal factors. The technological misalignments are caused by a coaxiality tolerance of the holes into the crankcase and a run-out tolerance of the crankshaft journals. The technique of thermal state definition is presented in works [16, 17].

Identification procedure of the elastic properties of the shaft and linear $K_{s,x}^{\lambda,j}, K_{s,y}^{\lambda,j}$ and angular $K_{s,x}^{\varphi,j}, K_{s,y}^{\varphi,j}$ compliances is presented in work [18].
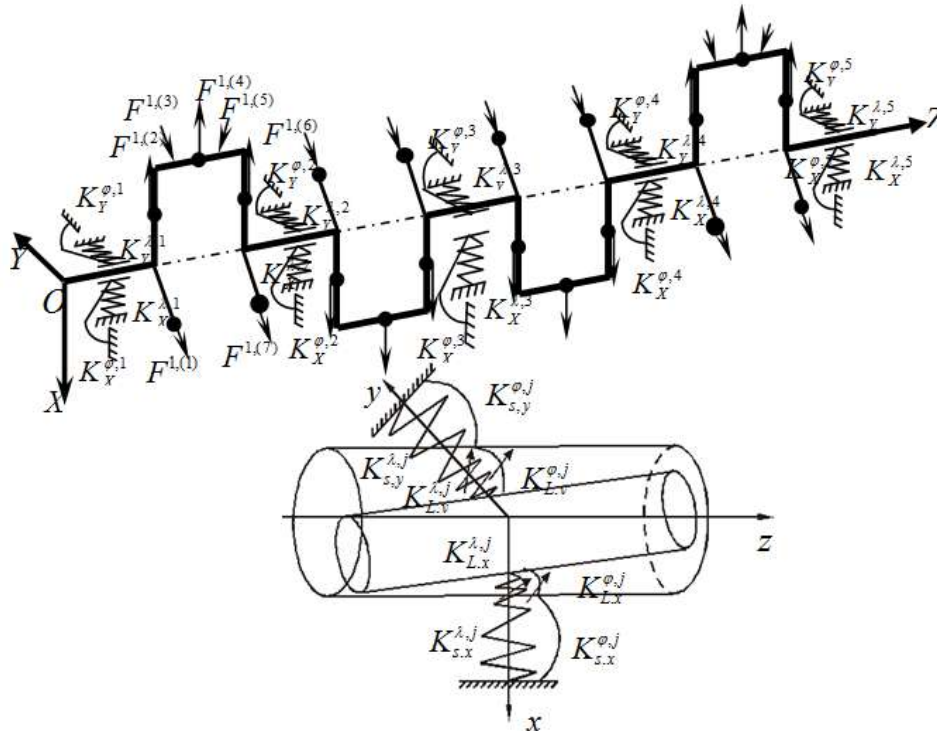

Figure 1. Dynamic model of the crankshaft (a) and bearing (b)

Influence of the lubricant layers dividing friction surfaces of the main bearing journals of a crankshaft and a crankcase of the IC engine is modeled by means of non-linear elastic elements with the compliances $K_{L,x}^{\lambda,j}(\tau), K_{L,y}^{\lambda,j}(\tau), K_{L,x}^{\varphi,j}(\tau), K_{L,y}^{\varphi,j}(\tau)$.

These compliances depend on the lubricant layers thickness which varies with time because the centers of the journals move on some trajectories under the loads $F^{i,(s)}$, where i is number of the cranked port of shaft, $s = 1,..,7$ is number of the external force (see Fig. 1).

Instant values of the compliances can be defined by the expressions

$$K_{L,x}^{\lambda,j}(\tau) = X^j(\tau)/\tilde{F}_X^j(\tau);$$
$$K_{L,y}^{\lambda,j}(\tau) = Y^j(\tau)/\tilde{F}_Y^j(\tau);$$
$$K_{L,x}^{\varphi,j}(\tau) = \alpha^j(\tau)/\tilde{M}_X^j(\tau); \qquad (6)$$
$$K_{L,y}^{\varphi,j}(\tau) = \beta^j(\tau)/\tilde{M}_Y^j(\tau),$$

where $\tilde{F}_X^j(\tau), \tilde{F}_Y^j(\tau), \tilde{M}_X^j(\tau), \tilde{M}_Y^j(\tau)$ are instant values of the forces and moments, acting to the j-th bearing; $X^j(\tau), Y^j(\tau), \alpha^j(\tau), \beta^j(\tau)$ are the position of the center of the jth main bearing journal of the crankshaft.

At the performance evaluation of non-autonomous main bearings (main bearings system), the determining methods of the autonomous bearings HMC are combined by an iterative process with the calculation of the loads. The iterative process is based on the continuous scheme of the multisupporting crankshaft on the elastic foundation. The elastic structural properties (a crankshaft and a crankcase), the misalignment of the journals and the main bearings, the nonlinear damping properties of the lubricant layers can be considered in the calculation of acting loads. For the solution to this problem it is offered to use the iterative algorithm which requires consistent calculation of loads, acting on bearings, and trajectories of movement of the centers of their journals into bearings. For calculating loads not only gas and inertial parts are considered, but also elastic properties of supports and a shaft. They are defined by

means of three-dimensional finite element models of the engine crankcase and crankshaft. The finite differences method by the multigrid technique for the Reynolds equation was applied for the definition of the main journals movement trajectories. The method allows to consider a dependence of viscosity on temperature, pressure and shear rate. In addition the scheme of oil supply in each bearing layer, macrogeometrical characteristics of friction surfaces and other parameters are taken into account.

3. RESULTS

The described method is applied to the calculations of the main bearings system of 4-cylinder in-line and 6-cylinder in-line engines (cylinder bore is 13 cm, stroke of piston is 15 cm). Input dates are given in Fig. 2 and in table 1. FEA models of the crankshaft and a crankcase for two engines (see Fig. 3-4) are used.

Table 1. Input dates

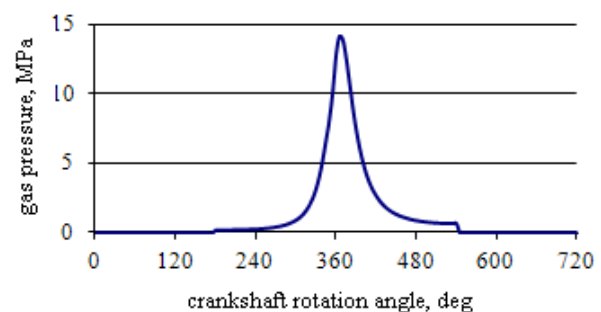| Parameter	Value
angular velocity of bearing, rad/sec	219,0
main bearing diameter, m	0,105
main bearing width, m	0,035
main bearing clearance, m	0,000103
oil feed hole diameter into the journal, m	0,007
oil feed hole angle, deg.	90, 270
groove start angle at the bearing surface, deg	100
groove finish angle at the bearing surface, deg	260

Figure 2. Gas pressure

3.1 Influence of elastic properties of supports

Calculations of the main bearing systems for the two types of a crankcase of 4-cylinder and 6-cylinder engines are made. The comparison of HMC is presented in Fig. 7 and in Table 2 (bearings and necks are coaxial).
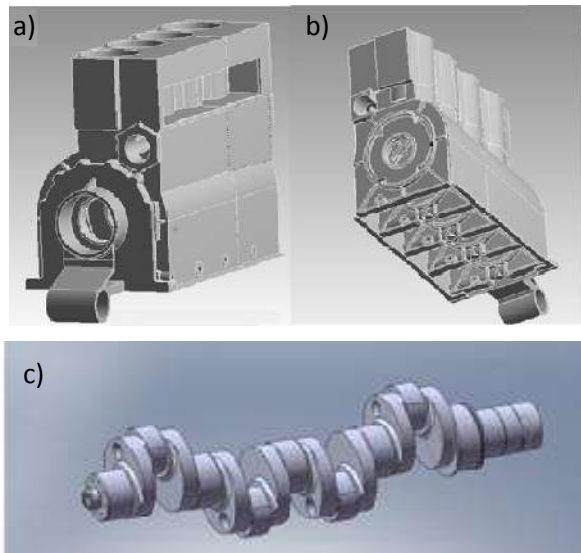

Figure 3. Models of the crankcase and crankshaft of 4-cylinder engine: model of the crankcase design No 2 (a), the crankcase design No 1 (b), the crankshaft model (c)
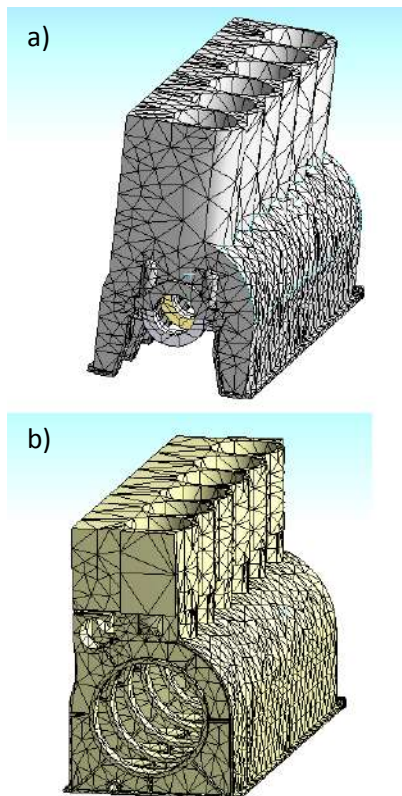

Figure 4. Model of the crankcase of the 6-cylinder engine of design No 2 (a) and design No 1 (b)
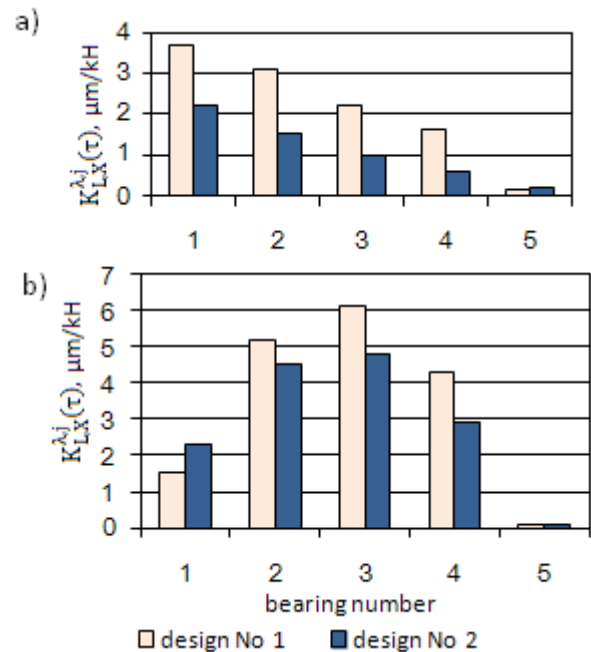
Figure 5. The elastic compliance coefficients (m/N) of the supports for the 4-cylinder engine for XOZ plane (a), YOZ plane (b)
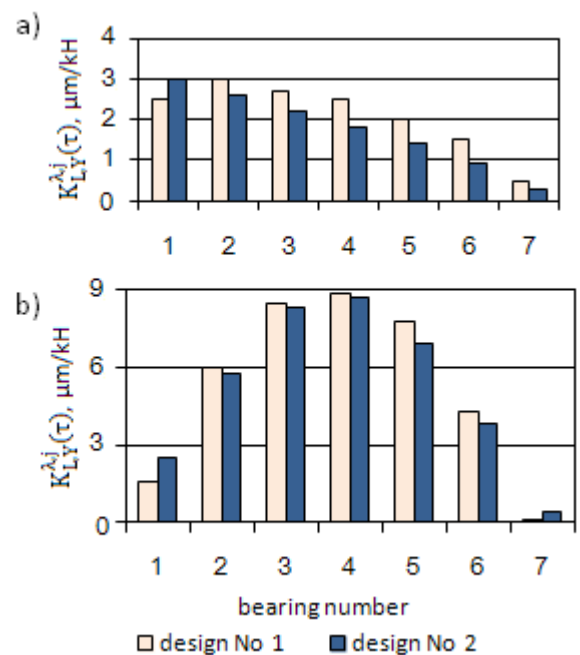
Figure 6. The elastic compliance coefficients (m/N) of the supports for the 6-cylinder engine for XOZ plane (a), YOZ plane (b)

If supports and necks are coaxial then the increase of elastic compliance coefficients of support most often positively influences the HMC of main bearings (see Fig. 7). Minimums of film thickness are 5 − 29% more (for a design No. 1) and 12 − 36% more (for a design No. 2) than for the case with absolutely rigid supports of a crankshaft.
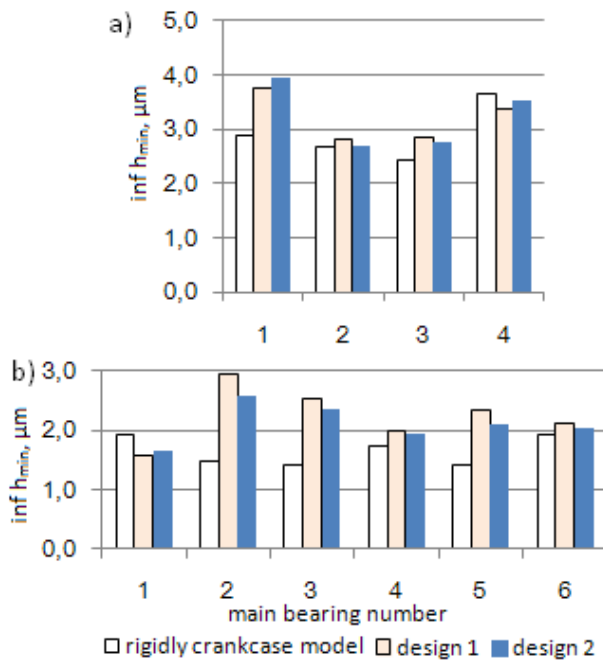
Figure 7. Comparison of HMC for 4-cylinder (a) and 6-cylinder (b) engines (bearings and necks are coaxial)

Table 2. Hydromechanical characteristics of main bearings for the 4-cylinder engine

Bearing number	$\inf h_{min}$, μm	$\alpha_{h_{min}}$, deg	h^*_{min}, μm	$\sup p_{max}$, MPa	p_{max}, MPa	N^*, W
1	2,89[1]	70	11,95	79	15	544,8
	3,74[2]	184	7,83	108	19	593,5
	3,93[3]	184	8,23	98	17	579,5
2	2,68	243	9,10	225	40	650,8
	2,81	15	11,53	156	25	584,1
	2,69	15	12,98	180	29	584,5
3	2,68	243	9,10	225	40	650,8
	2,81	15	11,53	156	25	584,1
	2,69	15	12,98	180	29	584,5
4	3,64	609	11,00	148	26	587,9
	3,37	15	12,99	130	26	559,0
	3,51	15	12,95	121	25	560,7

1) rigidly crankcase model; 2) crankcase of design No1; 3) crankcase of design No 2.

Comparison of the main bearings HMC for designs No. 1 and No. 2 of the engine crankcase between themselves shows that the twofold increase by elasticity does not lead to unambiguous change of values $\inf h_{min}$: the film thickness of the second and third bearings increase by 5–4,5%; however at the same time the film thickness of the first and fourth bearings decrease by 4–5%. Apparently, the change of structural elasticity of a crankcase leads to the redistribution of the loadings acting on main bearings and corresponding change of HMC.

3.2 Influence of displacement of crankshaft supports and necks

The distribution of possible displacements of the crankshaft supports and necks were set on the basis of coaxiality tolerance of the holes into the crankcases and a run-out tolerance of the crankshaft journals according to technical documentation of the engine. Possible versions of displacements for design No 2 are presented in Fig. 8. The most dangerous displacement distributions are chosen by calculations of main bearings HMC considering crankcase elasticity and different combinations of supports and necks relocation (see Fig. 8, highlighted in red).

Modeling results of the main bearings system for the most dangerous misalignment distribution are presented in Fig. 9-10. The accounting of misalignment of the crankshaft supports and necks leads to decrease $\inf h_{min}$ by 20–80% for both designs of the crankcase for a 4-cylinder engine. At the same time for more elastic crankcase of design No. 1 the minimum thickness of the first (third) bearing is 6% (28%) lower than rather similar value received for the crankcase of design No. 2. Values $\inf h_{min}$ are approximately at the same level for the second and fourth bearings. For the 6-cylinder engine the values $\inf h_{min}$ are reduced by 2.5 times.

It should be noted that the maximum difference of the supports displacement for design No. 1 is nearly 8 times higher than design No. 2. At the same time the change of the corresponding values $\inf h_{min}$ is insignificant. It demonstrates desensitization to misalignment of crankshaft supports and necks by increasing the crankcase elasticity.
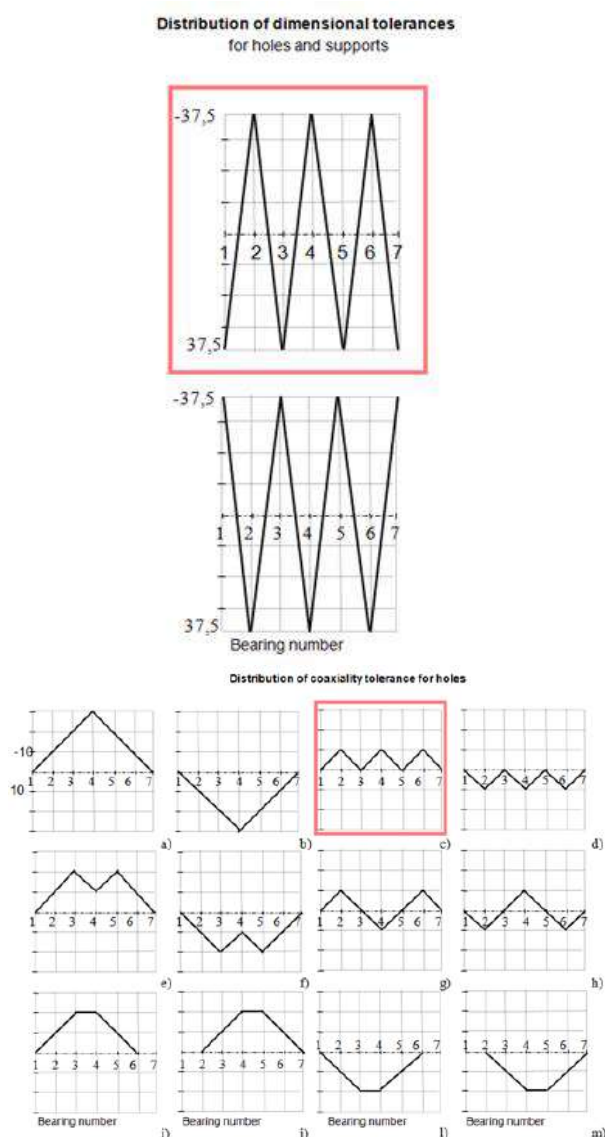
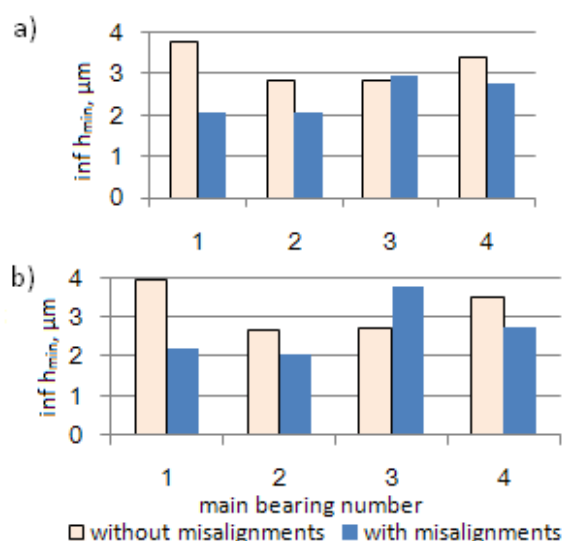**Figure 8.** Possible misalignment distribution for supports

Figure 9. Comparison of HMC for a 4-cylinder engine: (a) design No 1of crankcase, (b) design No 2 of crankcase
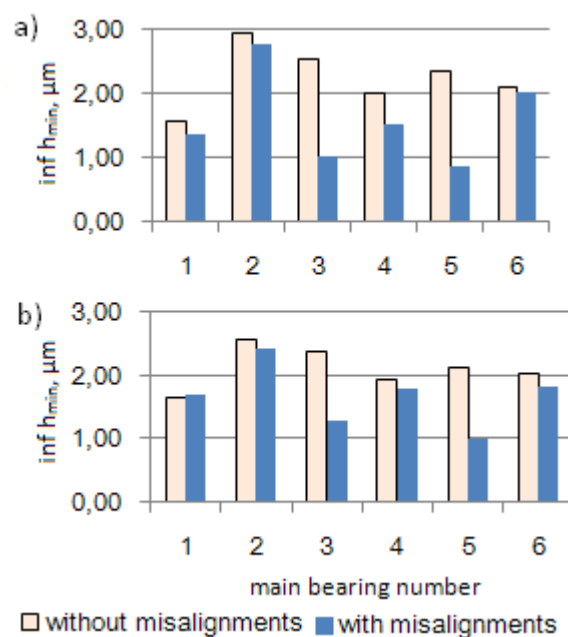

Figure 10. Comparison of HMC for the 6-cylinder engine: (a) design No 1of crankcase, (b) design No 2 of crankcase

3.3 Thermal effects

The thermal field leads to crankcase deflection from the axis OZ and arouses a misalignment of the hole for bearings installation. The technique of a thermal state definition of a crankcase and the respective field of deformations is in detail considered in work [16, 17]. The misalignments caused by various reasons are shown in table 3 and the modeling results are presented in Fig. 11 for the 4th cylinder engine (rigidly crankcase model), were type 1 is bearings misalignments caused by thermal deformation, μm; type 2 is technological misalignments for the bearings, μm; type 3 is technological misalignments for the journals of the crankshaft, μm.

Table 3. Comparison of values of the misalignments caused by various reasons

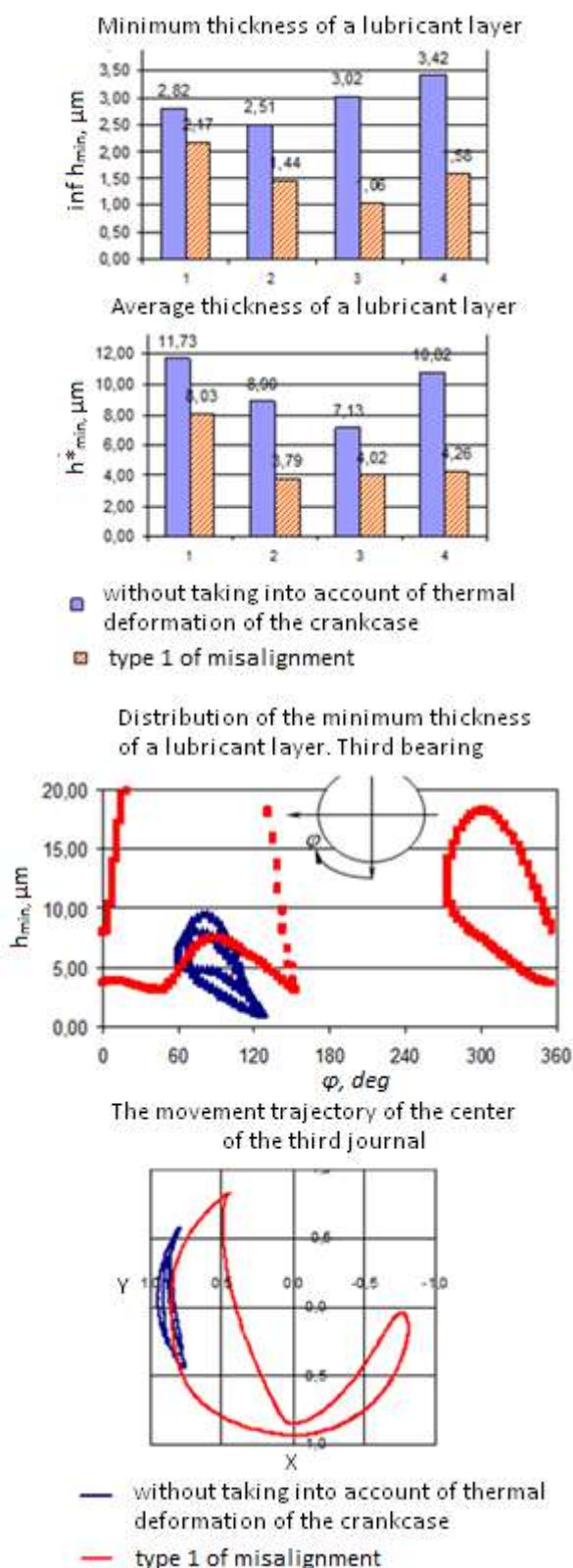| Types of misalignment	Number of the crankshaft support				
	1	2	3	4	5
Type 1	-65	67	127	69	-71
Type 2	0,0	10	0,0	10	0,0
Type 3	10	-20	30	-20	10

Figure 11. Influence of thermal deformation of a crankcase on a hydromechanical characteristics of the main bearings system

Distributions of the minimum film thickness on the bearing surface and also a journal trajectory for the 3rd main bearing are shown in Fig. 11. It is obvious that misalignments

from OZ rotation axis significantly influence the performance assurance of the main bearings system.

4. CONCLUSION

The research shows the necessity of applying the integrated approaches which allow to consider simultaneously both the features of autonomous bearings and many facts of their interaction.

ACKNOWLEDGEMENT

REFERENCES

[1] K.P. Oh, P.K. Goenka: The elastohydrodinamic solution of the journal bearing under dynamic loading , ASME Journal of Tribology, Vol. 107, pp. 389-395, 1985.

[2] R. Paranjpe, S. Tseregounis, M. Viola: Comparison between theoretical calculations and oil film thickness measurements using the total capacitance method for crankshaft bearings in a firing engine, Tribology Transaction, Vol. 43, pp. 345–356, 2000.

[3] C. H. Li, S. M. Rohde: On the steady state and dynamic performance characteristics of floating ring bearings, ASME Transactions Journal of Lubrication Technology, Vol. 103, No. 3, pp. 389–397, 1981.

[4] S.M. Zaharov, V.I. Sirotenko, I.A. Zharov: Work modeling of tribosystem "a crankshaft bearings - support of the block of cylinders" of internal combustion engines, Friction and Wear, Vol. 16, pp. 47–54, 1995.

[5] D. Bonneau, A.M. Chomat-Delalex, T. Garnier, et al.: Influence of the engine block/crankshaft design on the 3D EHD lubrication of a four cylinder inline automotive engine, in *Proceedings of the 10th World Congress on Theory of Machines and Mechanisms*, University of Oulu, 1999, Finland, pp. 2488–2495.

[6] D. Bonneau, A.M. Chomat-Delalex, T. Garnier, et al.: 3D EHD lubrication optimised design of a four cylinder in line automotive engine

crankshaft, *Proceedings of the 26th Leeds-Lyon Symposium., Thinning Films and Tribological Interfaces*, 2000, Elsevier (ed.), Amsterdam, pp. 391–398.

[7] A. Fatu, M. Hajjam, D. Bonneau: An EHD model to predict the interdependent behavior of two dynamically loaded hybrid journal bearings, Journal of Tribology, Vol. 127, pp. 416–424, 2005.

[8] T. Garnier, D. Bonneau, C. Grente, Three-dimensional EHD behavior of the engine block/crankshaft assembly for a four-cylinder inline automotive engine, Journal of Tribology, Vol. 121, pp. 721–730, 1999.

[9] D. Bonneau, A. Fatu, D. Souchet: *Internal combustion engine bearing lubrication in hydrodynamic bearing,* Wiley, 2014.

[10] V.N. Prokopiev, Yu.V. Rozhdestvensky, V.G. Karavaev, E.A. Zadorozhnaya, N.A. Khozeniuk: *Dynamics and Lubricant of Piston and Rotor Tribounits. Vol. 1*: SUSU publishing, Chelyabinsk, 2010.

[11] V.N. Prokopiev, Yu.V. Rozhdestvensky, V.G. Karavaev, E.A. Zadorozhnaya, N.A. Khozeniuk: *Dynamics and Lubricant of Piston and Rotor Tribounits. Vol. 2*: SUSU publishing, Chelyabinsk, 2011.

[12] V.N. Prokopiev, E. A. Zadorojznaya, V.G. Karavaev et al.: Improvement of a calculation method of heavy loaded bearings of the sliding greased by non-newtonian oils, Problems of mechanical engineering and reliability, No. 1, pp. 63–67, 2010.

[13] R. Zhang, H. Xueming, S. Yang et al.:, Perturbation solution of non-Newtonian

lubrication with the convected Maxwell model, Transaction of the ASME, Vol. 127, pp. 302–305, 2005.

[14] I.G. Levanov: Method of calculation of hydromechanical characteristics of heavy loaded bearings of sliding of the piston and rotor cars greased by non-Newtonian oils, Vestnik of SUSU, Series «Mashinostroenie», Vol. 18, pp. 34–44, 2011.

[15] V.N. Prokop'ev, A.K. Boyarshinova, E.A. Zadorozhnaya: Multigrid algorithm for integrating the Reynolds equations in dynamic problems concerning slip bearings under complex load, Journal of Machinery Manufacture and Reliability, Vol. 34, pp. 7, 2005.

[16] Y. Rozhdestvensky, N. Khozeniuk, A. Mylnikov,, I. Levanov, V. Romanov: Modeling of the main bearings of a multi-supporting crankshaft of the internal combustion engine, in: WTC2013 Proceedings,08.-13.09.2013, Torino, Italy, pp. 1825-1828.

[17] Y. Rozhdestvensky, N. Khozenjuk, A. Mylnikov et al.: Modeling of a multisupporting cranckshaft tribo-system of internal combustion engine, in: *Proceedings of the 15th Nordic Symposium on Tribology «NORDTRIB 2012»*, 2012, Trondheim, Norway, p. 163.

[18] A.A. Mylnikov: Experimental research of elastic characteristics of a crankshaft and block case of the four-cylinder in-line engine of ChN 13/15 type, Vestnik of SUSU, Series «Mashinostroenie», Vol. 271, No. 12, pp. 218–222, 2012.

STUDY VIBRATION CONDITION OF BALL BEARINGS UNDER DIFFERENT OPERATING CONDITIONS

Vyara POZHIDAEVA[1], Mara KANDEVA[2], Svetlozar TOKMAKCHIEV[1]
1University of Mining and Geology "St. Ivan Rilski"-Sofia,Bulgaria
[2]Tribology Center, Technical University – Sofia, Bulgaria
*Corresponding author: vpojidaeva@abv.bg

Abstract: This paper presents the results of experiments conducted using a specially designed laboratory bench for the studying the vibration of rolling bearings. The developed experimental arrangement allows examination of both different sizes and shell construction of the roller elements and modeling of different loads, damage and impact over them. The designed laboratory bench allows the application of different methods and approaches for vibration control depending on the equipment and software, which results in the opportunity to conduct research with a different focuses.

Keywords: rolling bearings, method vibration control

1. INTRODUCTION

The continuous process in the enterprises of the mining industry places high demands on security and reliability of mining mechanization. One of the priority areas to achieve flawless operation and improvement and modernization of the repair work in recent years is the introduction of diagnostic systems to control the technical condition. The mining technique has different constructions, but overall their technical condition is determined by the state of bearings and drive. There is a variety of different structure and dimensions of roller elements operating at different loads and frequencies. The application of methods for diagnosing technical condition based on vibration control required preliminary research.

2. EXPERIMENTAL STUDY

In connection with the objectives to study the vibrations arising in bearings of different size, built in various mining machines, a laboratory bench is designed for experiments and modeling of different loads, damages and influences. The principle scheme of the experimental set-up is shown in Figure 1. The experiments were conducted with double-row ball bearings type 2208, item 7 and item 15, in addition to the vibrations in them, their working temperature has also been controlled.

Vibrations in the bearings 7 and 15 are perceived by accelerometers 17 and 20 and the signal is fed into the apparatus Robotron M1302 for vibration measurement and analysis.
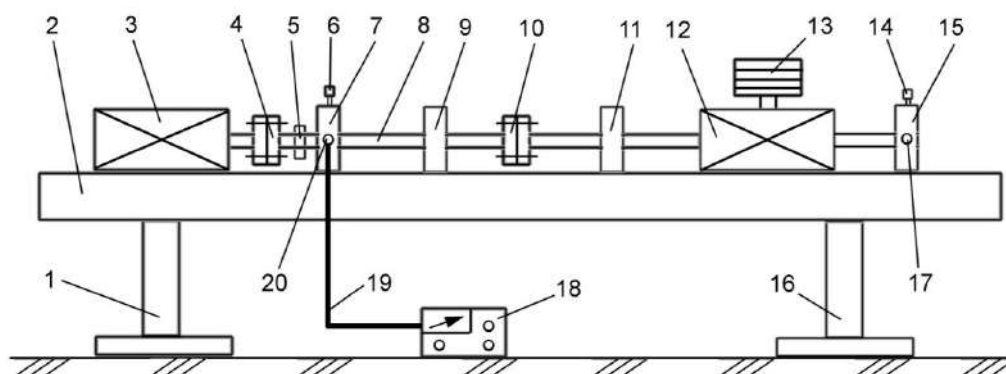
Figure 1. 1 - support; 2 - base; 3 - motor; 4 - connector; 5 - dynamic load; 6 - thermocouples; 7 - bearing; 8 - load cells shaft; 9 - bearing; 10 - connector; 11 - bearing; 12 - generator; 13 - static load; 14 - thermocouples; 15 - bearing; 16 - support; 17 - transducer; 18 - equipment for vibration measurement ; 19 - connecting cable; 20 - transducer

The apparatus Robotron M1302 provides an opportunity for measure vibration in different frequency bands and allows for direct calculation on a parameter which characterizes the friction in bearings by analogy with the Kurtozis method. The operating temperature in the bearings is controlled by a thermocouple type platinum-platinium-iridiy 6 and 14 and recorded by a specialized apparatus 18 of type 21N1. Dynamic load 5 caused by two types of centrifugal forces to the size of 850 N and 1700 N and static load 13 generated by the standard weight of about 450 N act upon the bearings. The studies were conducted in two stages: a new bearing type 2208 and the same type bearing, which has zones with visible wear on the inner ring.

3. RESULTS AND DISCUSSION

The experimental results are shown in the Table 1. Measurements were carried out in the individual frequency bands at a constant static load of 450 N and variable dynamic loads, the size respectively 850 N and 1700 N, in the radial and axial direction. Changes in vibro-velocity and temperature are illustrated in Fig. 2 and Fig. 3 forthecases of a new bearing and a bearing with zones of wear.

The results are a basis to evaluate the vibration behavior of the bearings, namely in the presence of wear and/or defects on the bearing surfaces, the vibration speed is almost doubled.
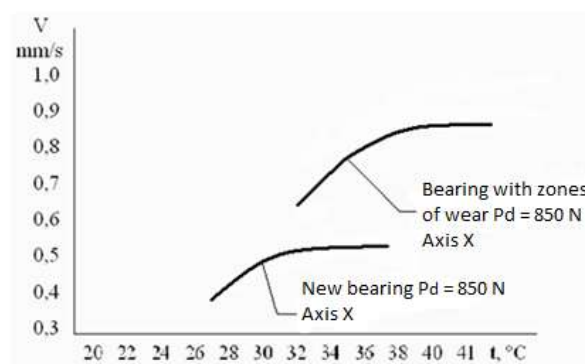

Figure 2. Changes in vibro-velocity and temperature for a new bearing and a bearing with zones of wear
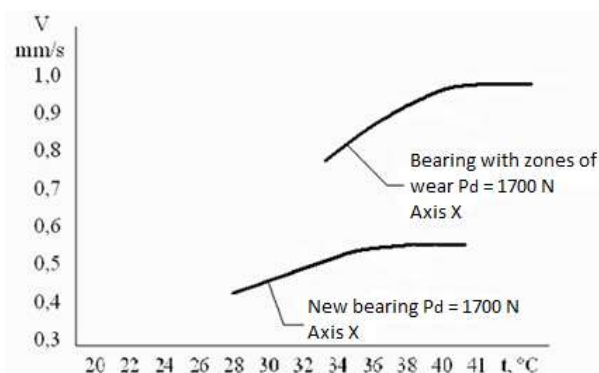

Figure 3. Changes in vibro-velocity and temperature for a bearing with zones of wear

This difference in readings is a reason to believe that the spectral analysis of vibration signals of individual damage will occur in the harmonic sequence in accordance with specified in formulas 1-3 frequencies, namely:

Table 1. Experimental results

Коорд, ос	Frequency Spectrum, Hz																								
	31,5			63			125			250			500			1000			2000			4000		
	U, mV	V, mm/s	t, °C	U, mV	V, mm/s	t, °C	U, mV	V, mm/s	t, °C	U, mV	V, mm/s	t, °C	U, mV	V, mm/s	t, °C	U, mV	V, mm/s	t, °C	U, mV	V, mm/s	t, °C	U, mV	V, mm/s	t, °C
New Bearing – P_d = 850 N, $P_{st.}$ = 450 N																								
x	3,25	0,32	28	3,25	0,33	29	3,5	0,35	29,5	3,5	0,35	30	3,5	0,35	29	3,5	0,35	30	3,5	0,35	31	3,2	0,32	32
y	3.2	0.20	28	3,25	0,33	29	3,25	0,32	29,5	3,2	0,32	30	3,2	0,32	29	3,2	0,32	30	3,5	0,35	31	3	0,30	32
z	3	0,30	28	3,35	0,33	29	3,25	0,32	29	3,1	0,31	30	3	0,3	29	3	0,3	30	3	0,30	31	2,9	0,29	32
New Bearing – P_d = 1700 N, $P_{st.}$ = 450 N																								
x	4.2	0,42	28	4,3	0,43	30	4,6	0,46	32	4,6	0,46	33	4,61	0,46	34	4,6	0,46	35	4,5	0,45	36	4,2	0,42	37
y	3,8	0,38	28	3,9	0,39	30	4,1	0,41	32	4,12	0,41	33	4,2	0,42	34	4,2	0,42	35	4,1	0,41	36	3,7	0,37	37
z	3,5	0,35	28	3,50	0,35	30	3,7	0,37	32	3,72	0,37	33	3,8	0,38	34	3,7	0,37	35	3,5	0,35	37	3,4	0,34	39
Bearing, which has zones with visible wear – P_d = 850 N, $P_{ст.}$ = 450 N																								
x	6,8	0,68	30	7,1	0,71	32	7,4	0,74	33	7,6	0,76	34	7,8	0,78	35	7,7	0,77	37	7,6	0,76	38	7,6	0,76	39
y	5,9	0,59	30	6,3	0,63	32	6,5	0,65	33	6,8	0,68	34	6,9	0,69	35	6,9	0,69	37	6,8	0,68	38	6,7	0,67	39
z	4,8	0,48	30	4,9	0,49	32	5,1	0,51	33	5,1	0,51	34	5,2	0,52	35	5,2	0,52	37	5,1	0,51	38	5,1	0,51	39
Bearing, which has zones with visible wear – P_d = 1700 N, $P_{ст.}$ = 450 N																								
x	7,8	0,78	33	7,9	0,79	34	8,2	0,82	36	8,4	0,84	38	8,6	0,86	39	8,5	0,85	40	8,4	0,84	41	8,1	0,81	40
y	6,7	0,67	33	6,8	0,68	34	7,1	0,71	36	7,3	0,73	38	7,7	0,77	39	7,4	0,74	40	7,3	0,73	41	6,9	0,69	40
z	5,4	0,54	33	5,5	0,55	34	5,8	0,58	36	6,1	0,61	38	6,3	0,63	39	6,1	0,61	40	6,0	0,6	41	5,7	0,57	40

- frequency of appearance of defects on the outer or inner ring:

$$f = \frac{n}{2} f_r \left(1 \mp \frac{BD}{PD} \cos \beta \right), \text{Hz} \qquad (1)$$

- frequency of appearance of defects on the rolling elements:

$$f_{er} = \frac{PD}{BD} f_r \left[1 - \left(\frac{BD}{PD} \cos \beta \right)^2 \right], \text{Hz} \qquad (2)$$

- frequency of appearance of defects in the separator:

$$f_C = \frac{1}{2} f_r \left(1 + \frac{BD}{PD} \cos \beta \right), \text{Hz} \qquad (3)$$

where:
- n - number of rolling elements;
- f_r - speed of rotation of the bearing, min^{-1};
- BD - diameter of the rolling rings, mm;
- PD - diameter of the stationary rings, mm;
- β - contact angle, rad.

An experiment for a total qualification of the bearings in the three-tier gradation "good condition - warning level - damage requiring replacement of the bearing" is performed by the apparatus Robotron M1302. For this purpose, as diagnostic's indicator K, is measured, which is similar to the Kurtozis-factor:

$$K = \int_{-x}^{+x} \frac{(x - \bar{x})}{\sigma^4} P(x) dx \qquad (4)$$

where:
- x - instantaneous amplitude of vibration, mm;
- $\bar{x}$ - average amplitude, mm;
- σ - standard deviation of vibrations, mm;
- $P(x)$ - the likelihood of defects.

Diagnostic parameter K is calculated by hardware after introducing values for respective primary vibro accelerations from according to the formula:

$$K = \frac{\bar{a}(0) \cdot \hat{a}(0)}{\bar{a}(t) \cdot \hat{a}(t)} = 1 \div 0,01 \qquad (5)$$

where:

$\bar{a}(0), \hat{a}(0)$ are respectively effective and peak vibration acceleration at the starting point of the operation of nodes (in this case data from the measurement of new bearing from the beginning of the experiment have been taken);

$\bar{a}(t), \hat{a}(t)$ are respectively effective and the peak value of vibration acceleration at a time of operation of the node (in this case data from the measurement of bearings with areas of wear at different times from the beginning to the end of experiment have been taken);

The measurement of the diagnostic parameter K is realized only at a load of 1700 N and the graph is constructed and shown in Fig. 4.
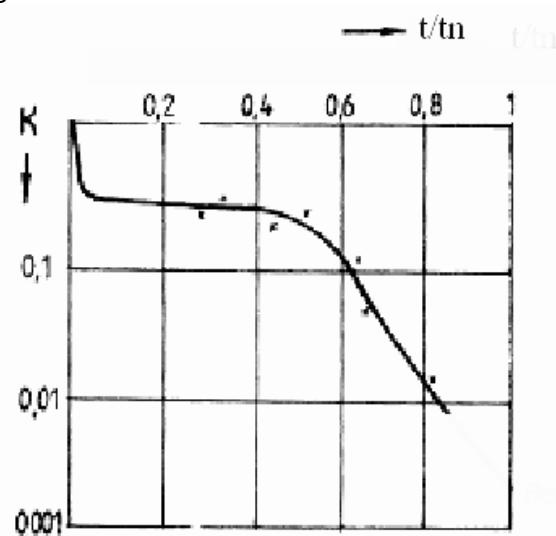

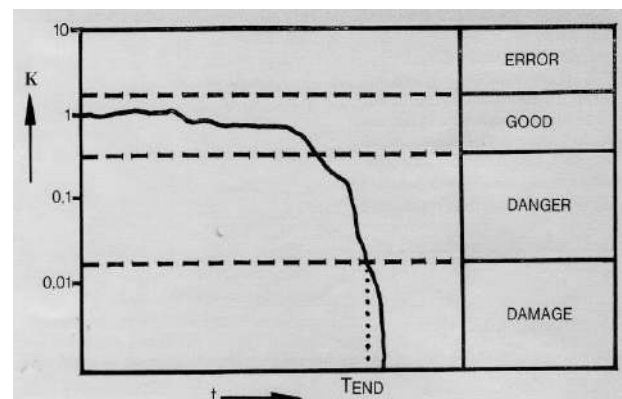**Figure 4.** Diagnostic parameter K, realized at a load of 1700 N

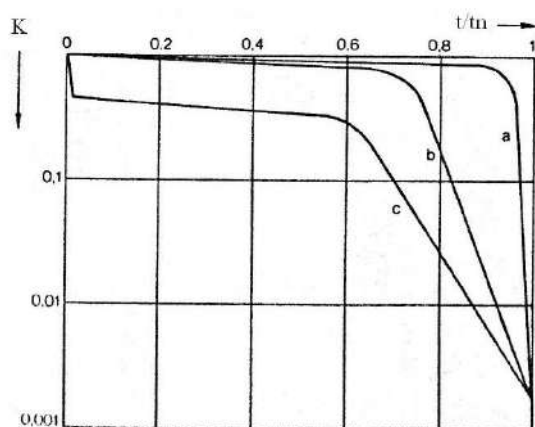**Figure 5.** Experimental curve of the variation of K

Figure 6. Theoretical curves of the variation of K

4. CONCLUSION

The research resulted in the following conclusions:

1. Develop laboratory bench provides opportunities for study of various sizes bearings and modeling of different loads, damage and affect them in satisfying the requirements of this study.
2. The research done clearly shows the sensitivity of vibration control approach to the technical condition of the researched object. Of the two control parameter in the range of the experiment - velocity and temperature, the vibration indicator is more dynamically changing.
3. The resulting initial results correlate well with the theoretical formulations and in the presence of an appropriate apparatus, research can be realized to a greater depth.

REFERENCES

[1] A. Mazioud, L. Ibos., A. Khlaifi, J.F. Durastanti, Detection of Rolling Bearing Degradation Using Infrared Thermography, *9*[th] *International Conference on Quantitative Infrared Thermography*, July 2-5 , 2008, Krakov, Poland.

[2] M. Barret, J.F. Durastanti, K. Madani, Diagnostic vibratoire base sur la transformee en ondelettes, Congres CNRIUT03, Mai 2003, Tarbes (France).

[3] R.F. Staidel, *An Introduction to Mechanical Vibration*, WILEY, New York, 1989.

[4] Tachnical instruction: *Vibrodiagnosis apparatus Robotron M 1302*, VEB ROBOTRON-MESSELEKTRONIK, OTTO SCHON, DRESDEN, 1980.

FRICTION INFLUENCE REDUCING BY USING LINER BEARINGS AND BALL SCREW SHAFTS IN MINI-PLATFORMS

Miloš MATEJIĆ[1,*]**, Nenad PETROVIĆ**[1]**, Nenad KOSTIĆ**[1]**, Mirko BLAGOJEVIĆ**[1]**, Nenad MARJANOVIĆ**[1]

[1]University of Kragujevac Faculty of Engineering, Kragujevac, Serbia
*Corresponding author: mmatejic@kg.ac.rs

Abstract: *With the constant progress of technology in mechanical engineering, a very rapid development of linear units and elements is present. Linear units and elements involves exercise and installations for rectilinear movement. This paper is an analysis of mini-platforms that uses plain bearings and power screw with trapezoidal thread. Friction resistance of platform movement is analyzed as well as its influence over the power of the machine drive. For the analysis of the friction resistance the known analytical models for plain and linear bearings and power screws are used. In terms of platform manufacturing, an analysis of the disadvantages of usage of these elements was also conducted. After the analysis with plain bearings and the power screw with trapezoidal thread, the change has been made to the replacement of these elements with linear bearings and ball screw shaft. After the change of mini-platform elements a comparative analysis related to the previous situation has been conducted. Through the paper the benefits of using these types of linear elements is highlighted. Paper concludes with given directions and possibilities for further investigation of this attractive research topic.*

Keywords: *platform, friction, linear bearing, ball screw shaft, plain bearing, power screw.*

1. INTRODUCTION

Modern tendencies in design consider a lower energy consumption, decreased cost of production and maintenance, increase of efficiency, etc. In order to meet these demands, it is necessary to implement adequate tribological design into the design process. Adequate tribological design includes decreasing operational friction resistance, thereby improving efficiency and decreasing energy use for machine operation. This aspect includes a decrease of friction resistance in the interaction of two or more machine elements. This is particularly the case with parts of machines where any kind of bearing, plain, joint, etc. is present. Tribological characteristics in this case are improved by using standard parts from the ranks of linear technics.

Linear technics include various types of guides, plains, threaded spindles, bearings, etc. which have the sliding friction resistance replaced with the rolling resistance using many small balls. Numerous researchers have worked on researching and testing aiming to improve these elements. A group of authors [1], researched how decreasing the ball size will influence ball screw shafts. Zhang et al. [2] examined how large momentary increases of speed influence ball screw shafts. A very important aspect of this research is dynamics

[3]. Using linear bearings, researchers tested small oscillations of balls in the bearing, [4]. These bearings are also examined for appearances linked to friction on a nano level, [5].

A small number of researchers have, however, worked on the connecting all these elements as a whole, and their influence on the decrease of friction resistance in machines as opposed to conventional solutions. This research tries to improve characteristics of a mini-platform by implementing observed elements. As the research was conducted in cooperation with a local company, and some parts are protected by a non-disclosure agreement, this paper will only give the key elements of the research. The paper concludes with notable indicators of improvement of the mini-platform construction.

2. PROBLEM FORMULATION

In the initial version the mini-platform used bronze sliding bearings. In this part the largest contact friction was apparent with the sliding of bronze on steel. The threaded spindle also had a bronze on steel contact. The initial mini-platform version is shown on figure 1.
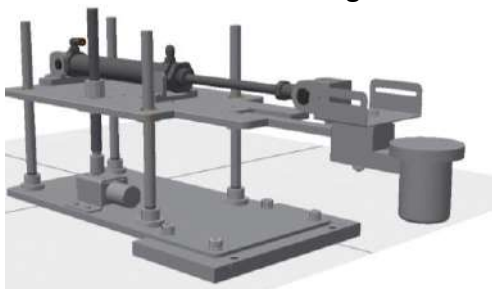
Figure 1. Initial version of mini-platform

Such a construction requires small tolerances and heat treatment of guides. This design also has a large energy use due to the stronger motor needed to overcome friction resistance.

2.1 Sliding friction resistance in plain bearings

In the initial platform design contact is achieved by sliding bronze bearing and heat treated steel guides. This type of sliding with friction resistance is shown in figure 2.
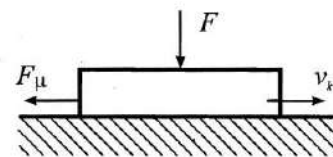
Figure 2. Plain bearing friction resistance

Figure 2 shows a segment of the plain bearing. The platform has sliding bearings and guides with a circular cross section. The relationship between force and friction is given in the expression (1).

$$F_\mu = F \cdot \mu. \tag{1}$$

Where:
F_μ – Friction, N;
F – Force acting on the bearing, and
μ – Friction coefficient between the guide and bearing.

In this case of contact the friction coefficient from equation (1) is $\mu=0,16$, [6].

2.2 Friction resistance in threaded spindles with trapezoidal thread

In the treaded spindles with trapezoidal thread there is a significant sliding friction resistance. Efficiency here is calculated using expression (2).

$$\eta = \frac{\tan\varphi}{\tan(\varphi+\rho_n)}. \tag{2), [7].}$$

Where:
η – Efficiency;
φ – thread taper angle, and
ρ_n – Friction angle.

From expression (7) in can be seen that the efficiency on the threaded spindle in this case is directly linked to the geometry of the connecting elements. According to the calculations the initial threaded spindle had an efficiency of $\eta=0.36$. This data later was shown as very precise.

3. MODIFICATION OF THE DESIGN USING LINEAR TECHNICS

In order have the mini platform improved (to decrease its friction resistance and with it

the needed power for operation), the following actions were taken:

- Sliding bearings were replaced with linear bearings, and
- The trapezoidal threaded spindle was replaced with a treaded spindle with balls.

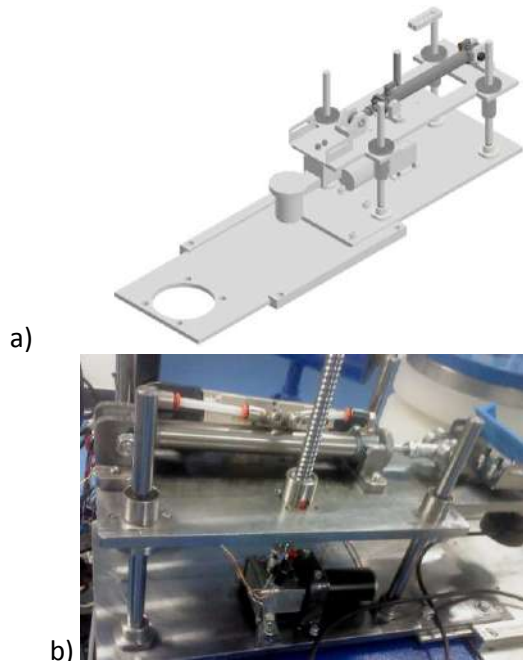After the implemented improvements, the mini-platform looked as shown in figure 3.

a)

b)

Figure 3. Mini-platform after improvements: a) 3D model; b) completed assembly

3.1 Replacing plain bearings with linear bearings

With a goal to increase efficiency and decrease friction resistance, the sliding bearings were replaced with linear bearings on the mini-platform. Linear bearings were selected from the LMFK series. The installed linear bearings are shown in figure 4.

Figure 4. Installed LMFK series linear bearing, [8]

The replacement of sliding linear bearings was done due to the nature of friction of these

two bearings. In plain bearings the mechanism of sliding friction is present, while linear bearinfs have rolling. Rolling friction is favorable for this type of mini-platform, making linear bearings more favorable.

3.2 Replacing conventional threaded spindle with ball screw

Conventional threaded spindles with an internal and external thread are replaced with threaded spindles with balls. The ball screw is shown in figure 5.

Figure 5. Installed ball screw, [9]

This type of threaded spindle has the mechanism of sliding friction replaced by rolling. Many researchers have explored the efficiency of ball screws, [10]. Figure 6 shows the diagram of efficiency of a ball screw.
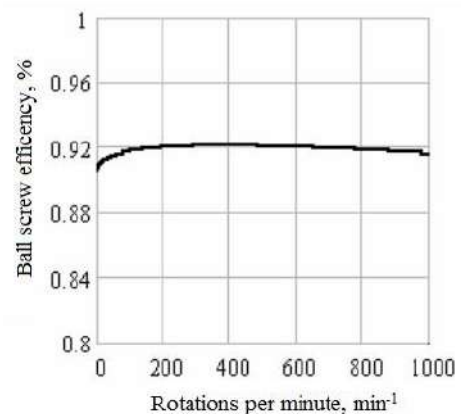

Figure 6. Efficiency of ball screw, [10]

From the diagram in figure 6 it can be seen that the efficiency of the ball screw is between 90 and 92%. At lower speeds the efficiency is lower, while the increase of speed leads to higher efficiency up to 800 min^{-1}, after which it declines. For this platform, a moto reducer with an output speed of 200 min^{-1}, which means the efficiency is around 91%. This data correlates with catalogue data.

4. CONCLUSION

Installing linear technics elements, linear bearings and ball screws achieved the following improvements:
- Friction decreased three times,
- Power needed to operate the platform decreased three times,
- Decrease of power decreases the moto reducer, thereby leaving more space for installing automated control platforms,
- Simplification of platform production,
- Specific elements can be created in wider tolerances.

All improvements were discovered by testing the initial and modified mini platforms.

There are some drawbacks as well:
- Decreased loading capacity of linear bearings from plain bearings,
- Decreased loading capacity of ball screw from threaded spindle,
- Increased difficulty of assembling due to possibility of balls falling out, from both the bearing and spindle.

Further research on this topic will be creating a mathematical model which would determine the energy savings and influence on improvement of efficiency of linear bearings compared to sliding bearings. This research will be conducted in general numbers due to non-disclosure agreements within the project.

ACKNOWLEDGEMENT

REFERENCES

[1] T. Miuraa, A. Matsubarab, D. Konob, K. Otakab and K. Hoshide: Design of high-precision ball screw based on small-ball concept, Precession Engineering, Vol. 47, pp. 452-458, 2017.

[2] J. Zhang, H. Zhang, C. Du, and W. Zhao: Research on the dynamics of ball screw feed system with high acceleration, International Journal of Machine Tools & Manufacture, Vol. 111, pp. 9-16, 2016.

[3] C. G. Zhou, H. T. Feng, Z. T. Chen and Y. Oua: Correlation between preload and no-load drag torque of ball screws, Machine Tools & Manufacture, Vol. 102, pp. 35-40, 2016.

[4] H. Syamsula, T. Oiwab, T. Tanakac and J. Asamaba: Positioning error improvement based on ultrasonic oscillation for alinear motion rolling bearing during sinusoidal motion, Precession Engineering, Vol. 38, pp. 517-527, 2014.

[5] X. Dong, D. Yoon and C. E. Okwudire: A novel approach for mitigating the effects of pre-rolling/pre-sliding friction on the settling time of rolling bearing nano-positioning stages using high frequency vibration, Precession Engineering, Vol. 47, pp. 375-378, 2017.

[6] http://www.engineershandbook.com/Tables/frictioncoefficients.htm, accessed in December 2016.

[7] V. Nikolić: *Machine elements*, in Serbian, Mechanical Engineering Faculty, University in Kragujevac, 2004.

[8] http://www.znzbearing.com/en/producttitle.asp?id=2118, online catalogue, accessed in February 2017.

[9] http://www.hiwin.com/ballscrews.html,online catalogue, accessed in February 2017.

[10] D. Olaru, G. C. Puiu, L. C. Balan and V. Puiu: *A New Model to Estimate Friction Torque in a Ball Screw System*, Product Engineering, Technical University "Gh. Asachi" of Iasi, Chapter, pp. 333-346, 2005.

SERBIATRIB '17

15th International Conference on Tribology

EXPERIMENTAL DETERMINATION OF THE WEAR FACTOR OF THE SLIDING BEARINGS MADE OF POLYMER BASED COMPOSITE

Miloš STANKOVIĆ[1]*, Aleksandar MARINKOVIĆ[2], Radivoje MITROVIĆ[2], Žarko MIŠKOVIĆ[2]
[1]Innovation Center of the Faculty of Mechanical Engineering, Serbia
[2]Faculty of Mechanical Engineering, University of Belgrade, Serbia
*Corresponding author: mstankovic@mas.bg.ac.rs

Abstract: Wear intensity is very important in terms of determining life cycle of machine elements. Experimental analysis of wear factor of certain material in contact with other specific materials are inevitable for this prediction. This paper provides two methods of determination of wear factor of polymer based sliding bearings – volume loss method and mass loss method. Volume loss method is based on capturing wall thickness before and after wearing process. The capturing was performed by means of 3D microscope. On the other hand, mass loss method is based on measuring mass of bearing sample before and after wearing. This measuring was performed by means of high accuracy balancing device. Afterwards, it was performed comparison of the results by connecting mass and volume through density. The tested specimen is sliding bearing of PTFE-Polyamide composite. The wearing was performed on the machine USL 5-30. Operational parameters are: velocity - 1m/s, pressure - 1MPa and sliding distance - 20000 m.

Keywords: wear factor, experimental wear determination, polymer based composites, sliding bearings

1. INTRODUCTION

Sliding bearings made of polymer based composites are widely applied, especially when it comes to the special requirements, such are self-maintaining, absence of lubrication or some dimensional constraints [1]. Only some examples of applications of these bearings are in food industry or in production of household appliances. Their application is economically justified due to quite low price if compared to metal, roller bearings. But their disadvantage is significantly lower load capacity.

Since these bearings operate in sliding contact, usually with sleeve made of steel, their tribological properties are essentially important for proper functionality. In this paper it was presented two methods to determine wear factor of these sliding bearings. The wear intensity was evaluated through mass loss, and volume loss determination.

2. EXPERIMENT DESCRIPTION

Experiment could be divided into 3 stages:
1. Pre-wear stage
2. Wear stage
3. Post-wear stage

In the first stage it was performed balancing of the samples, in order to determine mass of the unworn bearings. There were also taken the high magnification photographs of the bearing wall in the zone of expected wear

occurrence in order to determine wall thickness of the unworn bearing.

The second stage assumes the wearing process of specimens under predefined conditions. Those conditions are to follow:

- Radial load of 1 MPa applied onto the specimens outer cylindrical surface
- Sliding velocity of the sleeve in contact 1 m/s
- Sliding distance between specimen and sleeve during one experiment - 20 km.

Consequently, the duration of the wearing process was 20000 seconds. The experiments were conducted under the room temperature.

Before the second stage, the samples are initially lubricated with one single drop of lubricant. Besides the experiment runs in dry sliding conditions. During the experiments it was monitored the temperature in sleeve-bearing contact, by means of thermocouple fixed onto the outer surface of the bearing. It was also monitored the friction torque in this tribo pair in order to evaluate friction coefficient, by means of straingauges.

After the process of wearing, the samples are cleaned in ultrasonic cleaner. As the cleaning fluid it was used gasoline at the temperature of 50°C.

In the post-wear stage there were retaken the magnified photographs of the worn zone and the samples were rebalanced in order to calculate worn volume and worn mass.

2.1 Specimen description

PTFE Polyamide combines a thermoplastic as a base material, with PTFE additives and glass-fibre, which results in self-lubricating and low wear performance. They are designed for dry operation, but their performance could be improved by initial lubrication. With a supply of grease, oil, water or other liquid, the operating speed of these bushings can be increased. These bushings are resistant to most lubricating oils and greases. They offer many features and advantages such as:

- Maintenance-free operation
- Cost efficiency

- Excellent resistance to corrosive conditions
- Electrically insulating properties

Dimensions of examined bushings are Ø20x Ø23x20 mm. Additional properties of these bearings are given in Table 1.

Figure 1. PTFE polyamide bushing

Table 1. Characteristics of PTFE polyamide bushing

Permissible load, N/mm^2 (dynamic/static)	40/80
Permissible sliding velocity, m/s	1
Friction coefficient μ	0.06..0.15
Temperature range, °C	-30..+110
Density, kg/m^3	1380

2.2 Description of the equipment

For the first and third stage of the experiment (mass and volume measurements), there were used high precision balance with accuracy of 1×10^{-3} g (Figure 2) and 3D microscope (Figure 3).
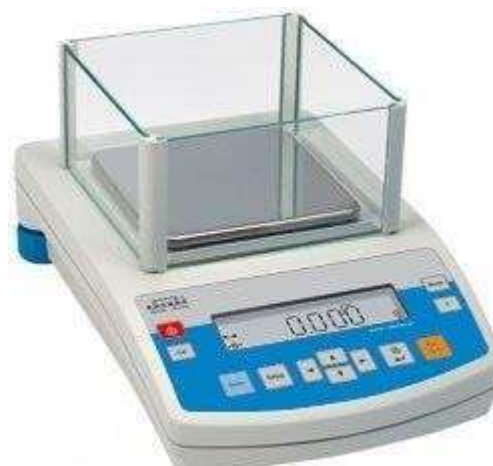

Figure 2: Balancing device "RADWAG" (accuracy 1×10^{-3} g)

Figure 3: HIROX KH-7700 3D Microscope

The second stage, i.e. tribological experiments on composite sliding bearings are conducted by means of custom made equipment USL 5-30. This equipment was described in more details in one of the previous papers [2]. The principle of its functioning could be seen at the Figure 4.
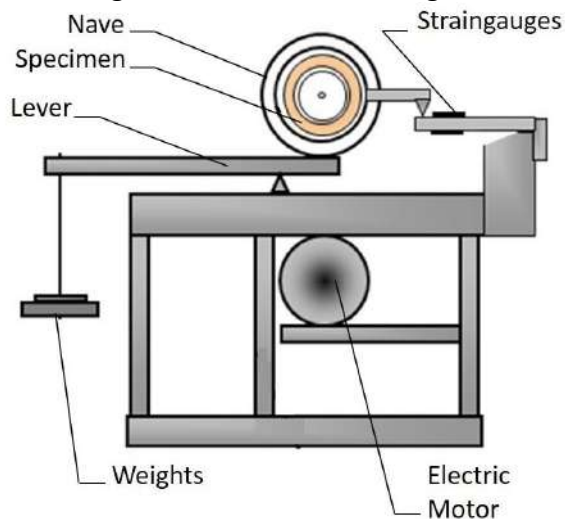

Figure 4: USL 5-30 test rig system

The shaft which is in contact with specimen is driven by means of electric motor and belt transmission. The radial load is applied through the lever. One end of the lever is in contact with nave in which the specimen is placed, while on the other end of the lever there are hanged the weights. The ratio of lever ends is 10:1. The radial load could be varied by applying different combination of weights, while the rotation speed of shaft could be also varied through the frequency inverter.

3. RESOULTS AND ANALYSIS

The masses of 3 bearing samples before and after process of wearing is presented in Table 2. There can be noticed excellent

repeatability of the results, but values of the worn mass are very low (7-8 mg). Since the polymers are usually well-known for high humidity absorption, these values should be carefully taken into account, since there is possibility of mass increase due to liquid absorption. In another words it is very likely that the worn mass of specimen is partially replaced by the amount of mass of the fluids (lubricant and gasoline) absorbed by specimen.

Table 2: Measured mass of specimens in different stages of the experiment

Specimen Number	Before wear [g]	After wear [g]	Decrease [g]
1	2.833	2.825	0.008
2	2.81	2.802	0.008
3	2.812	2.805	0.007

Analysing the other method of wear intensity evaluation, volume method, it could also be seen excellent repeatability for all of the samples. What was actually measured, it was a wall thickness of the sample before and after wearing (Figure 5), and through it was calculated inclination of the shaft into the specimen. Assuming that the profile of worn volume is uniform along the specimen, measuring inclination makes it possible to calculate the worn volume. The flow of this method was actually the assumption of the uniform wear distribution along specimen. At the moment, this assumption cannot be confirmed.
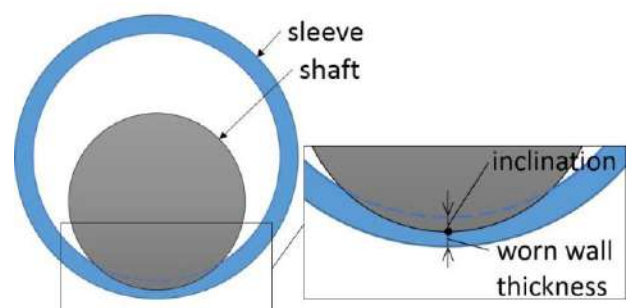

Figure 5 : Wall thickness after wearing process

Finally, these two methods are comparable by connecting appropriate values of mass and volume with already known density.

$$m = \delta \cdot v \qquad (1)$$

Taking into account values of volume from the Table 3 and the density of examined bearings $\rho=0.00138$ g/mm^3, it was calculated the masses of worn volume and compared to masses from Table 2. The compared results are presented in Table 4.

Table 3: Wall thickness before and after wearing process

Speci-men Number	Before wear [mm]	After wear [mm]	Inclina-tion [mm]	Volume [mm^3]
1	1.544	1.247	0.297	93.99
2	1.576	1.278	0.298	94.37
3	1.570	1.260	0.310	98.86

Table 4: Comparison of measured and calculated masses.

Specimen Number	Measured mass [g]	Calculated mass [g]	Ratio m_m/m_c [%]
1	0.008	0.130	6.1
2	0.008	0.130	6.1
3	0.007	0.136	5.1

Analysing the results from Table 4, it could be noticed huge deviation of masses obtained by two different methods. This is explained by previously mentioned flaws of each methods. Since the "mass method" is giving the lowest possible value of wear (probably additionally decreased for the value of absorbed liquids), and the "volume method" is giving the highest possible value of wear (the assumption of uniform wear distribution along the specimen gives the highest value of wear), this deviation is expected in a certain way. What we can claim for sure, is that the wear in above specified conditions is not less than the one determined by "mass method", and not greater than the one determined by "volume method".

4. CONCLUSION

In this paper it was presented determination of wear intensity of polymer based composite sliding bearings by two different methods:

"mass method" and "volume method". Although the repeatability of the results of wear determination by two methods is excellent, the comparison between them did not give good superposition. Anyway, having the frame in which the wear intensity is placed could be considered for a certain progress.

Further improvement in wear intensity determination is planned for the future investigation by means of high precision 3D scanner able to scan the worn surface in 3 dimensions. That will certainly improve the "volume mass" results obtained in this investigation.

REFERENCES

[1] A. Marinkovic, M. Stankovic: Advantages and Applications of Self-Lubricating Plastic Bearings, in: Proceedings of the 13th International Conference on Tribology – SERBIATRIB '13, 15-17.05.2013., Kragujevac, Serbia, pp. 247-250.

[2] M. Stankovic, A. Marinkovic: Tribological Properties of Selflubricating Sliding Bearings Made of PTFE and POM-Based Composite Materials, in: Proceedings of the 14th International Conference on Tribology – SERBIATRIB '15, 13-15.05.2015., Beograd, Serbia, pp.314-318.

[3] SKF bushings catalogue, Publication 4741 E

[4] B. Sadık Ünlü, E. Atik, S. Köksal: Tribological properties of polymer-based journal bearings, Materials and Design, Vol. 30, No. 7, pp. 2618–2622, 2009.

[5] M. T. Demirci, H. Düzcükoglu: Wear behaviors of Polytetrafluoroethylene and glass fiber reinforced Polyamide 66 journal bearings, Materials and Design, Vol. 57, pp. 560–567, 2014.

[6] V. Krsmanović, R. Mitrović: Klizni i kotrljajni ležaji, ISBN: 978-86-17-19284-4, 2015

[7] B. Sadık Ünlü, E. Atik, S. Köksal: Determination of Friction Coefficient in Journal Bearings, Materials and Design Vol. 28, No. 3, pp. 973–977, 2007.

THE INFLUENCE OF FRICTION CHARACTERISTICS IN SIMULATING THE IMPACT BULLET - STRATIFIED MATERIALS

Traian Florian IONESCU[1], Catalin PIRVU[2], Simona BADEA[3], Constantin GEORGESCU[1], Lorena DELEANU[1,*]

[1]"Dunarea de Jos" University of Galati, Galati, Romania
[2]INCAS - National Institute for Aerospace Research "Elie Carafoli", Bucharest, Romania
[3]Scientific Research Center for CBRN Defense and Ecology, Bucharest, Romania
*Corresponding author: lorena.deleanu@ugal.ro

Abstract: *This paper present a study on the influence of friction coefficient in simulating the impact between a bullet and a stratified material. There are compared results obtained for models with and without friction. The FEM model used Ansys 14.5. The layer material is introduces as an isotropical material, with maximum equivalent plastic strain of 0.06. All materials are considered to have bilinear isotropic hardening behavior. The model was designed as isothermal because thermal influence of the impact is considered low for run impact velocities (150...400 m/s). The simulation of the impact bullet - stratified panel, using different values for the friction coefficient between the layers, pointed out that the bullet top head velocity during the impact depends on this parameter, especially for the cases where the bullet make total or partial penetration of the panel. For cases where the bullet is rebound after impacting the panel, the friction has a low influence, when the bullet slides against the deformed first layer. For all run cases, the model without friction has produced the highest value of the top head bullet velocity after impact, for velocity range 250...400 m/s. These simulated cases suggest that friction increase V_{50}, with 10...30 m/s, at least for the studied ranges of the initial velocity of the bullet and the friction coefficient, also the bullet velocity after penetration is lowered.*

Keywords: *bullet impact simulation, friction coefficient, stratified panel, FEM.*

1. INTRODUCTION

Reports on ballistic impact simulation are published, from micro-scale [1, 2, 3] to macro one [4, 5, 6, 7], including mezo level as it is the models for woven fabrics [8, 9, 10], unidirectional ones [11, 12, 13], and laminated [14, 15]. Some models are based on simplifying hypotheses, as, for instance, considering a rigid projectile [16]. The influence of friction processes in impact and especially in projectile-target impacts was comming into research focus in the last decades of the XXth century and it has been continuing till now because of the interest in protecting army and law enforcement personel and civilians, also operators and equipment involved in industrial processes with higher risks of impacts [17, 18]. Complex friction processes with different friction couples are described and analysed [19, 20, 21]. Friction couples were systematized in

tribology taking into account the contact shape and the motion between rubbing surfaces. It is clear that the projectile could have a sliding and pivotating relative motion against the target. Analysing a projectile-target system, friction occurs between projectile and target, but also among their components. Thus, there is friction between the bullet jacket and its core. For target made of fabrics, friction appears between the fibers of the yarns and their coating (if it is added), the microlevel of such a system, between yarns - the mezo level, between layers, between the projectile and the stratified panel, the macro level.

Today, woven or multi-directional fabrics, made of fibers with high impact resistance [4, 22], are used for individual protection armors [23]. The models for impacting a panel with a projectile have become more and more complex and particularly elaborated to give answers to punctual questions (certain threats only, certain materials). Grujicic et al. [13, 24] modeled a stratified panel at mezo and macro level. Narayanamurthy run a simulation for a plate impacted by a round top projectile [25], but without friction. Velmurugan et al. [26] presented an analytical model for stratified systems, but they consider that energy lost in friction between projectile and composite is negligible as well as the heat generated during the projectile composite interaction.

Models for impacted stratified composites were proposed by da Silva [27], Soltani et al. [28], Tan et al. [29], Zhu al. et [30] (with spherical rigid penetrator), Kreculj [31], Gower [32], Sadighi [33], Scott [34]. Lopez-Puentes et al. [35] proposed even an analytical model of cylindrical projectiles impacting carbon/epoxy laminates.

The aim of this paper is to run a simplified simulation of the impact bullet - stratified pack for restraining one or more parameters involved in the pack testing.

2. THE MODEL

This model is considered isothermal for the simulation conditions (bullet velocity and mass), based on specialized literature [9, 10,

13, 26] and it has 6 solid bodies: 4 identical layers, considered a group of bodies (with the option *multiple materials)*, overlapped and rigidly fixed on their contour, and 2 bodies for the bullet (also *multiple materials)* with bonded connections (Table 1). The structura analysis was solved with Lagrangean method, in Explicit Dynamics, using AutoDyn [36, 37, 38]. The dimensions of one layer is are 6.10^{-2} m x 6.10^{-2} m x $0.6 \cdot 10^{-4}$ m, this thickness being similar to advanced fabrics. As the impact direction is the same to the symmetry axes of the model, the simulation is run for a quarter. The contact among bodies takes into account the friction. The friction coefficient between a layer and the bullet jacket is COF(b-l) = 0.3, except for the case without friction when both friction coefficients were zero. The friction coefficient between layers, COF(l-l), was varied in the range of 0.2...0.8, the lower values being characteristic for sliding polyethylene against itself and the higher for lightly bonded layers. But this case could have higher values, depending on the adhesive characteristics.

Table 1. Characteristics of the model

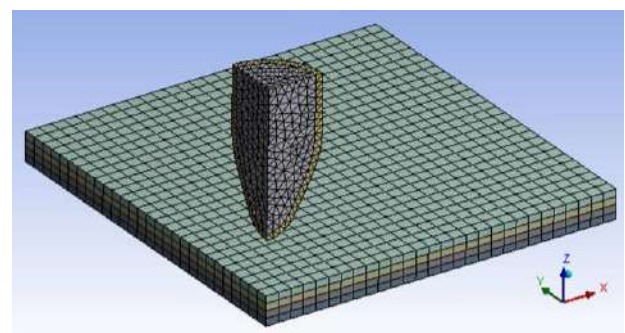| Body	Nodes	Elements
Layer	1250	576
Pack with 12 layers	18816	8748
Bullet (jacket + core)	1432	6289
Bullet jacket	739	2211
Bullet core	996	4078

Figure 1. Model meshing for a panel with 4 layers.

Figure 1 presents the mesh for the panel with 4 layers. The maximum side of an element is 5×10^{-4} m. Initial condition refers to the bullet velocity just before impact (here, cases with initial velocity between 150 m/s to 400 m/s were run). Many recent models accepted the rigid clamp on the contour [15],

even if, for body armor, the panel is simply supported on a visco-elastic material. The model was run for a maximum number of cycles is 10^7 and the maximum error for energy was 0.9. Materials are modeled as being hardening bilinear isotropic. This simplifying hypothesis could be justified for some fabrics by the arrangement of long aramid fibers, at four different angles (0, 90, 45, -45) [39] and for ceramics and metallic materials [40, 41]. After consulting the literature [7, 25, 31, 33], the failure criterion for layer material was the ultimate plastic strain, set for 0.06. The friction coefficient is considered as constant and it was set at 0.3 for the contact bullet jacket - layer. Thus, this study will point out the influence of friction between layers on the bullet velocity, stress and strain distribution.

Table 2. Material characteristics used for modeling the impact

Material Characteristic	Layer	Copper alloy	Lead
Young, Pa	7×10^{10}	1.1×10^{11}	1.6×10^{10}
Poisson ratio	0.35	0.34	0.30
Bulk modulus, Pa	7.77×10^{10}	1.14×10^{11}	4.44×10^{10}
Shear modulus, Pa	2.59×10^{10}	4.10×10^{10}	5.55×10^{9}
Yield limit, Pa	6.3×10^{8}	2.8×10^{8}	3×10^{7}
Tangent modulus	1.9×10^{10}	1.15×10^{9}	1.1×10^{8}

3. RESULTS AND DISCUSSION

The model was run for different values of COF(l-l), in the range 150...400 m/s. The selected values for COF(l-l) were 0.0, 0.2, 0.4 and 0.8. For COF(l-l) = 0.0, also COF(b-l) = 0.0, that being the case without friction for all bodies in contact. The following figures give the same moment for a certain velocity, but for different values of COF(l-l).

At v = 150 m/s, the influence of friction intensity is not obvious. Till t = 9×10^{-5} s the maximum stress is increasing than it decreases, the bullet begins to be rebound. At t = 1.3×10^{-4} s, the panel under the bullet is not significantly loaded (30...35 MPa), but high values of the stress (715...750 MPa) are still visible on the contact periphery. At 1.6×10^{-4} s, these values appear near the fixed edge of the panel.

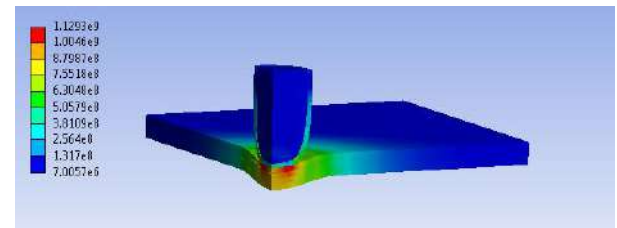a) COF(b-l) = 0.0, COF(l-l) = 0.0

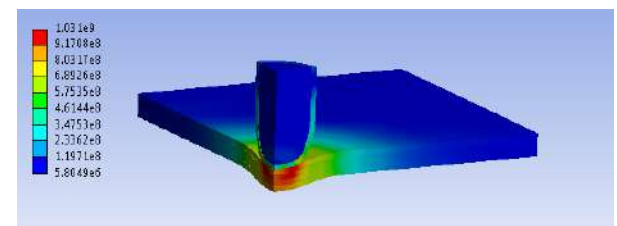b) COF(b-l) = 0.3, COF(l-l) = 0.2
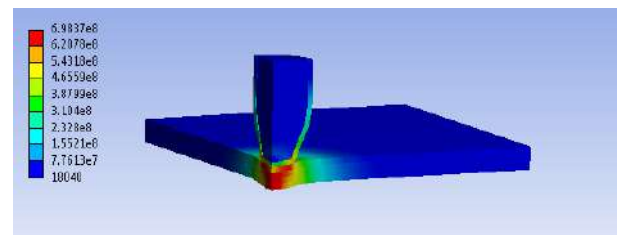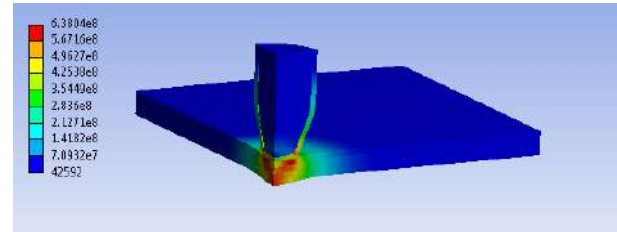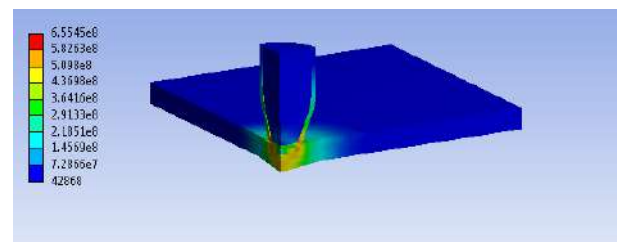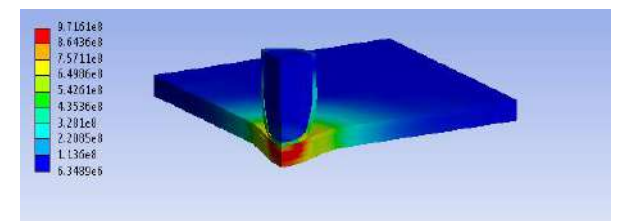

c) COF(b-l) = 0.3, COF(l-l) = 0.4

Figure 2. v = 150 m/s, 4 layers, t = 4×10^{-5} s (contact biggins at t = 2×10^{-5} s, von Mises stress distribution)

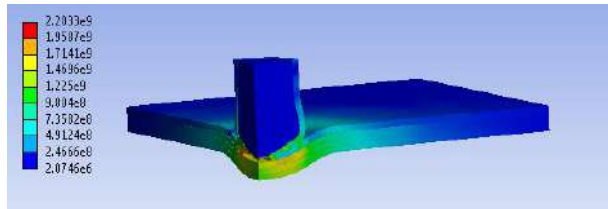
a) COF(b-l) = 0.0, COF(l-l) = 0.0
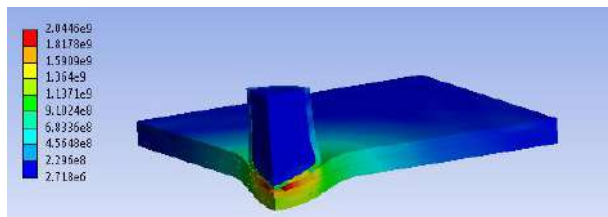

b) COF(b-l) = 0.3, COF(l-l) = 0.2

c) COF(b-l) = 0.3, COF(l-l) = 0.4

Figure 3. v = 150 m/s, 4 layers, t = 4×10^{-5} s (contact biggins at t = 5×10^{-5} s, von Mises stress distribution)
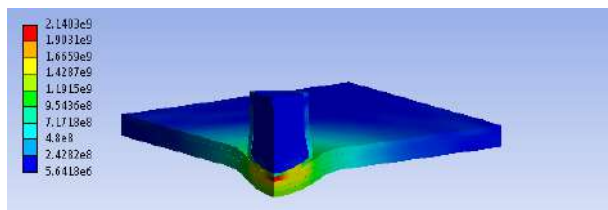
For the cases with friction, the stress concentration under the bullet seems to be a little delay (less than the time step selected for running, t = 10^{-5} s). Analysing Figure 12, the bullet rebounds more quickly when there is no friction, the rest of the plots v-t overlapping.
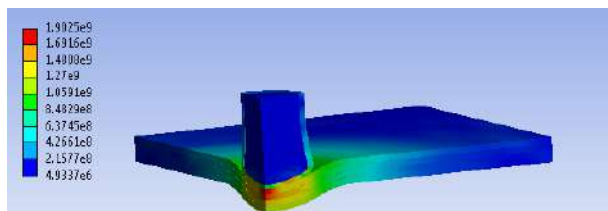

a) COF(b-l) = 0.0, COF(l-l) = 0.0

b) COF(b-l) = 0.3, COF(l-l) = 0.2
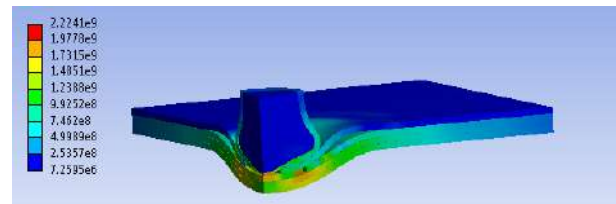

c) COF(b-l) = 0.3, COF(l-l) = 0.4

d) COF(b-l) = 0.3, COF(l-l) = 0.8

Figure 4. v = 330 m/s, 4 layers, t = $3x10^{-5}$ s (contact biggins at t = $1x10^{-5}$ s, von Mises stress distribution)

The ballistic limit, V_{50}, is the velocity at which the probability of penetration of an armor material is 50% [23]. To determine this characteristic, numerous ballistic tests are done, bullets are fired at higher and higher velocities until they start penetrating. Thus, V_{50} is a good measure of the upper limit of panel protection, or the "breaking point" for an armor. It is easier to approximate this limit by simulation and then restraining the tests that have to be done.

For the analysed model, the velocity V_{50} was determined as being more than 330 m/s and less than 335 m/s, for no-friction case, as for the first value the projectile does not break the last layer, but for v = 335 m/s, the fourth layers is broken (see Fig. 8). But for the cases with friction, V_{50} is higher than 335 m/s and lower than 350 m/s, depending on the value for friction coefficient.
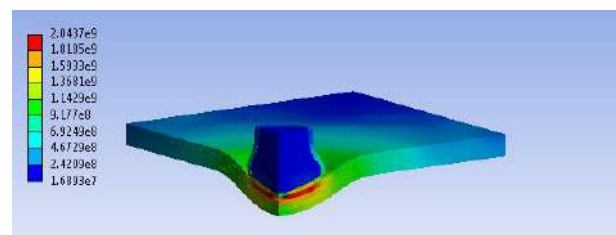
At 330 m/s, if the friction intensity increases, the layers, even broken, remain under the bullet, are compressed and the failure of the following layers are a little bit delayed (with a time interval of 1...$3x10^{-5}$ s). When COF is higher the bullet deforms more rapidly.
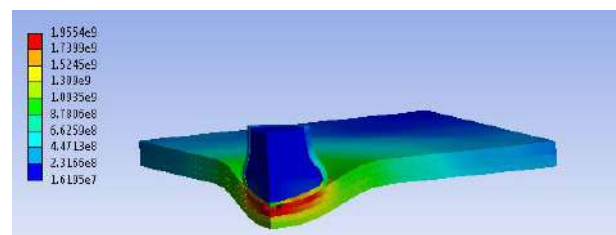

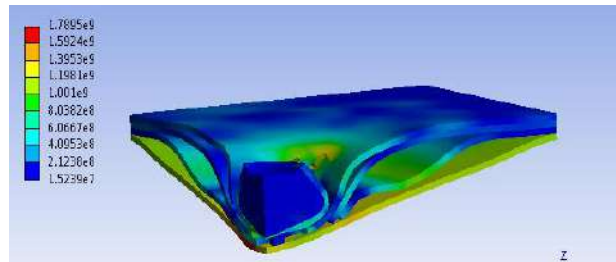a) COF(b-l) = 0.0, COF(l-l) = 0.0
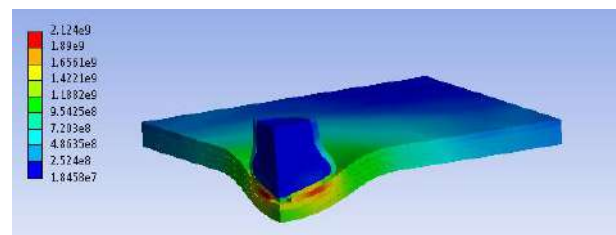
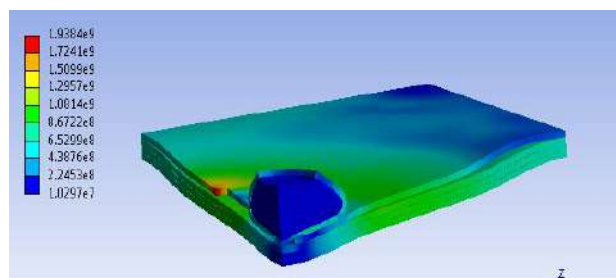b) COF(b-l) = 0.3, COF(l-l) = 0.2

c) COF(b-l) = 0.3, COF(l-l) = 0.4

d) COF(b-l) = 0.3, COF(l-l) = 0.8

Figure 5. v = 330 m/s, 4 layers, t = $4x10^{-5}$ s (contact biggins at t = $1x10^{-5}$ s, von Mises stress distribution)

The friction seems to have effect on the layers deformation in time. Without friction, layers are waving with higher amplitude. For instance, in Fig. 6a, after being broken, layers 2 and 3, are pushed away and they do not have the opportunity to remain under the bullet and to increase the resistance of the remaining layers, as it happens even when considering the COF(l-l) at the lowest analysed value (0.2). For higher values the layers remain in contact (Fig. 6c and d).
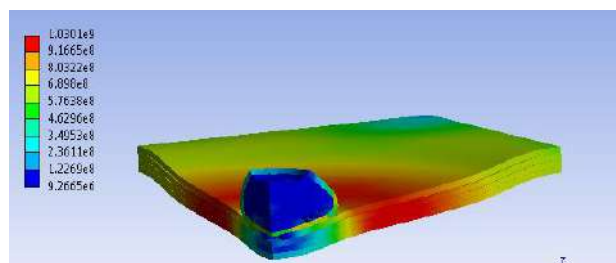

a) COF(b-l) = 0.0, COF(l-l) = 0.0
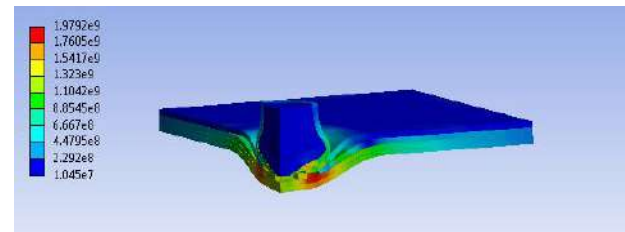

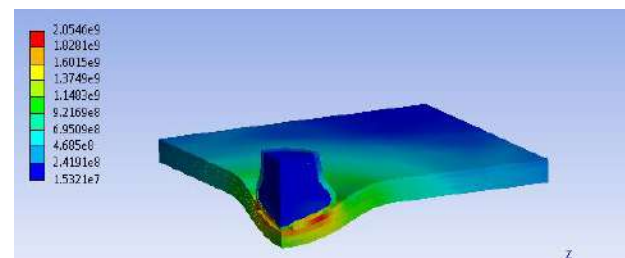b) COF(b-l) = 0.3, COF(l-l) = 0.2
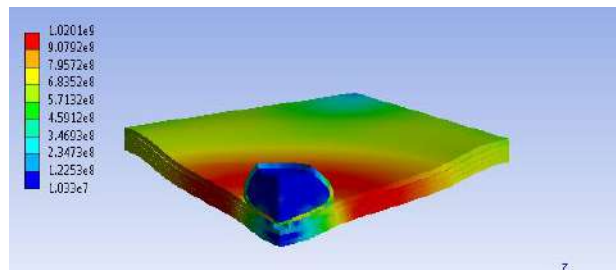
c) COF(b-l) = 0.3, COF(l-l) = 0.4

d) COF(b-l) = 0.3, COF(l-l) = 0.8

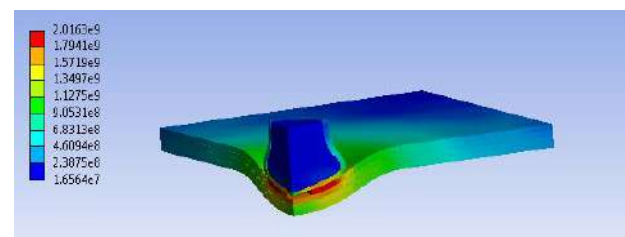**Figure 6.** v = 330 m/s, 4 layers, t = 9x10^{-5} s (contact biggins at t = 1x10^{-5} s, von Mises stress distribution)

At 335 m/s and moment t = 4x10^{-5} s (contact biggins at t = 2x10^{-5} s), for the case without friction, 3 layers are already broken, but for the cases with friction, only the first one is failed. At moment t = 7x10^{-5} s (contact biggins at t = 2x10^{-5} s), the running of the no-friction case reveals 3 broken layers and the high buckling of the first two layers (Fig. 7a).

a) COF(b-l) = 0.0, COF(l-l) = 0.0

b) COF(b-l) = 0.3, COF(l-l) = 0.2

c) COF(b-l) = 0.3, COF(l-l) = 0.4

d) COF(b-l) = 0.3, COF(l-l) = 0.8

Figure 7. v = 335 m/s, 4 layers, t = 4x10^{-5} s (contact biggins at t = 2x10^{-5} s, von Mises stress distribution)

The magnitude of the panel deformation in the velocity direction is much greater than that obtained for cases with friction (Fig. 8b-d). But, as the layers are trapped under the bullet, there are initiated high stress concentrator outside the contact bullet-first layer, as one may notice in Fig. 8b that will initiate the rupture of the layer.
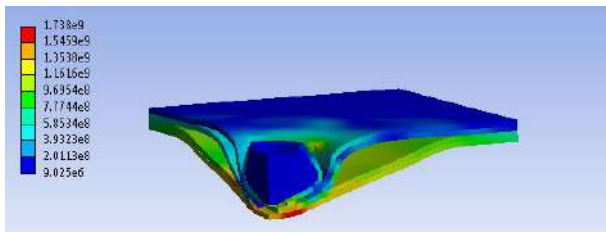
a) COF(b-l) = 0.0, COF(l-l) = 0.0
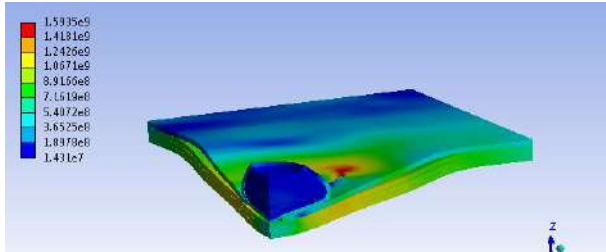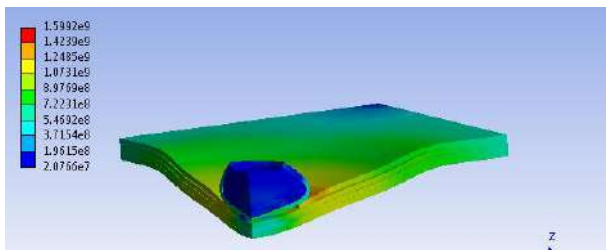
b) COF(b-l) = 0.3, COF(l-l) = 0.2
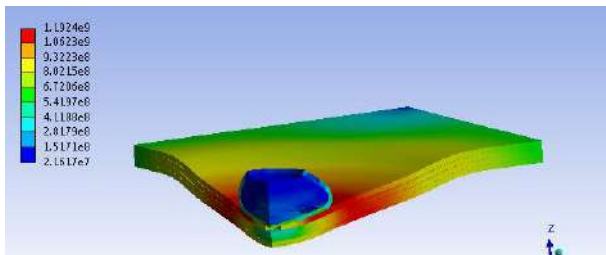
c) COF(b-l) = 0.3, COF(l-l) = 0.4

d) COF(b-l) = 0.3, COF(l-l) = 0.8

Figure 8. v = 335 m/s, 4 layers, t = 7x10⁻⁵ s (contact biggins at t = 2x10⁻⁵ s, von Mises stress distribution)
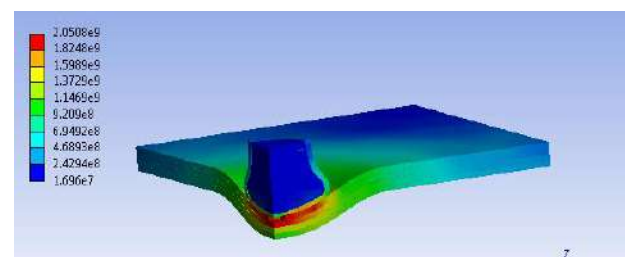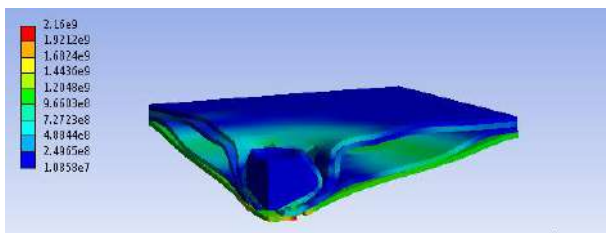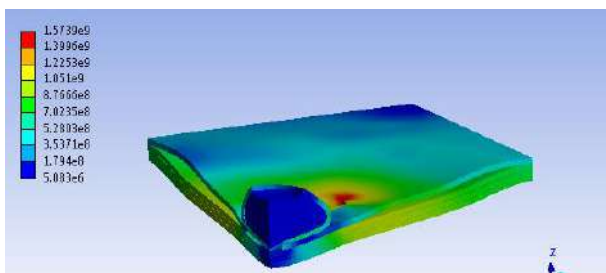

a) COF(b-l) = 0.0, COF(l-l) = 0.0
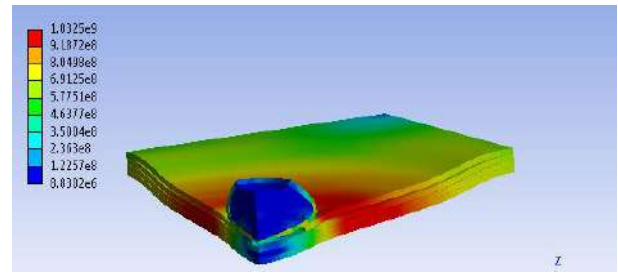
b) COF(b-l) = 0.3, COF(l-l) = 0.2
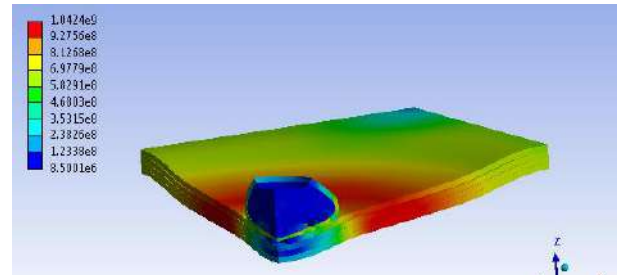
c) COF(b-l) = 0.3, COF(l-l) = 0.4

d) COF(b-l) = 0.3, COF(l-l) = 0.8

Figure 9. v = 335 m/s, 4 layers, t = 9x10⁻⁵ s (contact biggins at t = 2x10⁻⁵ s, von Mises stress distribution)
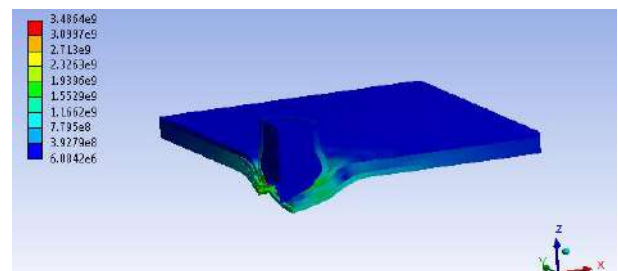
a) COF(b-l) = 0.0, COF(l-l) = 0.0
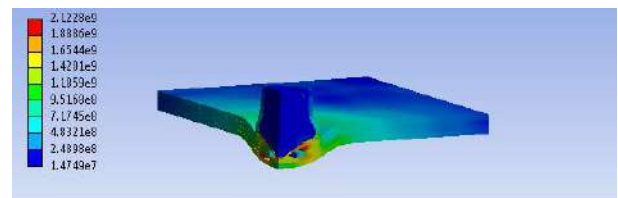
b) COF(b-l) = 0.3, COF(l-l) = 0.4
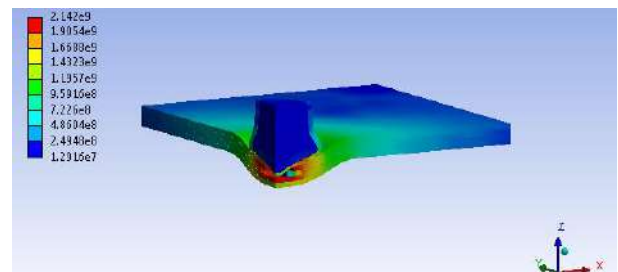
c) COF(b-l) = 0.3, COF(l-l) = 0.4

Figure 10. v = 400 m/s, 4 layers, t = 3x10⁻⁵ s (contact biggins at t = 1x10⁻⁵ s)

For v = 400 m/s, at moment t = 3x10-5 s (contact begins at t = 1x10-5 s), 3 layers are broken for the case without friction and with low COF(l-l) = 0.2.

For COF(l-l) = 0.4, only two layers are broken, but the third one is highly tensioned and it will probably break at future moments (Fig. 10). Figure 11 show that, at t = 5x10-5 s (contact begins at t = 1x10-5 s), all 4 layers are broken, but the deformation of the panel on impact diretion is lower when the friction coefficient COF(l-l) increases (from 0 to 0.4).

a) COF(b-l)=0.0, COF(l-l)=0

b) COF(b-l)=0.3, COF(l-l)=0.2

c) COF(b-l)=0.3, COF(l-l)=0.4
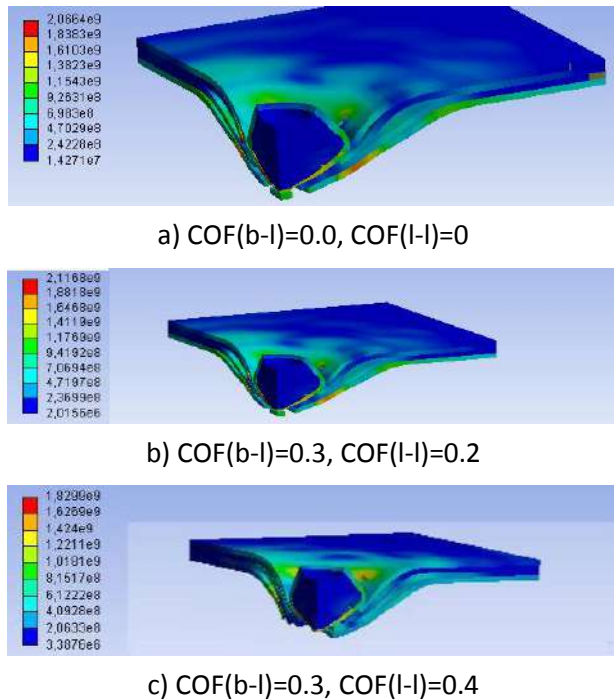
Figure 11. v = 400 m/s, t = 5x10^{-5} s (contact begins
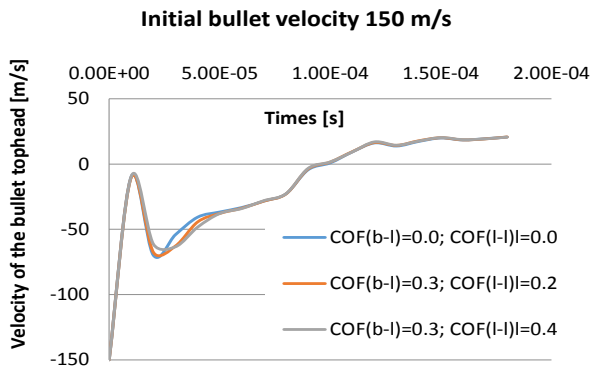
Figure 12. The velocity of the bullet top head for
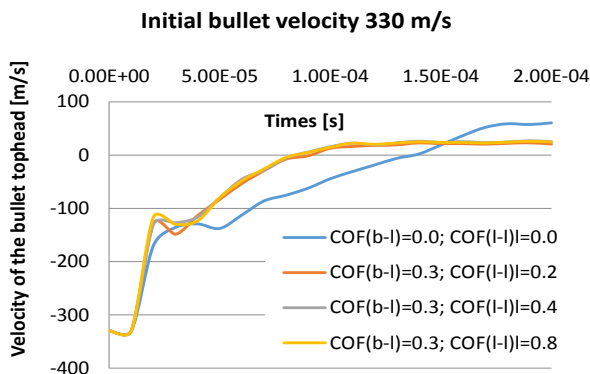
Figure 13. The velocity of the bullet top head for v = 330 m/s
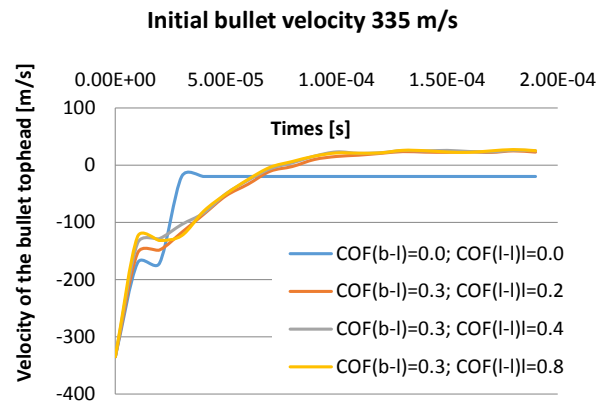
Figure 14. The velocity of the bullet top head for
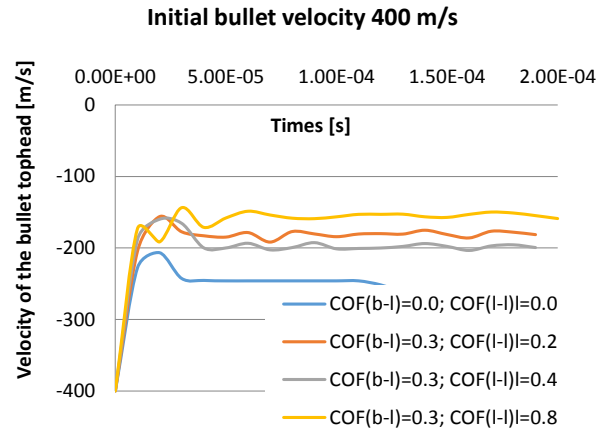
Figure 15. The velocity of the bullet top head for v = 400 m/s

4. CONCLUSION

The simulation of the impact between a bullet and a stratified panel, using different values for the friction coefficient between the layers of the panel, pointed out that the bullet top head velocity during the impact depends on this parameter, especially for the cases where the bullet make a total penetration of the panel. For cases where the bullet is rebound after impacting the panel, the friction has a low influence, when the bullet slides against the deformed first layer.

For all run cases, the model run without friction has produced the highest value of the top head bullet velocity for velocity range 250...400 m/s.

The friction becomes important in energy balance of the impact when the layers are broken. When the projectile velocity is not enough for destroying the layers (or at least one), and the projectile is rebound, the influence of friction is noticed on a reduced time interval, but the velocity plots are not

modified at the beginning and the end of the impact (Fig. 12).

These simulated cases suggest that friction increase V_{50}, with 10...40 m/s, at least for the studied range of the initial velocity of the bullet and also the bullet velocity after penetration is lowered (Figs. 14 and 15).

REFERENCES

[1] R. Barauskas, A. Abraitiene: Multi-resolution finite element models for simulation of the ballistic impact on non-crimped composite fabric packages, Composite Structures, Vol. 104, pp. 215-229, 2013.

[2] V.B.C. Tan, X.S. Zeng, V.P.W. Shim: Characterization and Constitutive Modeling of Aramid fibers at High Strain Rates, International Journal of Impact Engineering, Vol. 35, No. 511 pp. 1303-1313, 2008.

[3] L. Mishnaevsky Jr.: *Computational Mesomechanics of Composites. Numerical analysis of the effect of microstructures of composites on their strength and damage resistance*, John Wiley & Sons, New York, 2007.

[4] A. Bhatnagar: *Lightweight ballistic composites*, CRC Press, New York, 2006.

[5] M.V. Donadon, L. Iannucci, B.G. Falzon, J.M. Hodgkinson, S.F.M. de Almeida: A Progressive Failure Model for Composite Laminates Subjected to Low Velocity Impact Damage, Computers and Structures, Vol. 86, No. 11-12, pp. 1232-1252, 2008.

[6] B.K. Kumar, T.L. Kishore: Low Velocity Impact Analysis of Laminated FRP Composites, International Journal of Engineering Science and Technology, Vol. 4, No. 1, pp. 115-125, 2012.

[7] R.R. Kumar, K.S. Raghuram: Predictive Impact Analysis on Fiber Reinforced Laminates, Review of Research, Vol. 3, No.6, 2014.

[8] V. Ungureanu: *Contribuţii teoretice si experimentale la studiul proprietatilor mecanice ale unor compozite polimerice*, PhD thesis, "Dunarea de Jos" University, Galati, 2012.

[9] G. Nilakantan, M. Keefe, T.A. Bogetti, Jr.J.W. Gillespie: Multiscale modeling of the impact of textile fabrics based on hybrid element analysis, International Journal of Impact Engineering, Vol. 37, No. 10, pp. 1056-1071, 2010.

[10] G. Nilakantan, E.D. Wetzel, T.A. Bogetti, Jr.J.W. Gillespie: Finite element analysis of projectile size and shape effects on the probabilistic penetration response of high strength fabrics, Composite Structures, Vol. 94, No. 5, pp. 1846-1854, 2013.

[11] A. Tasdemirci, A. Kara, A.K. Turan, G. Tunusoglu, M. Guden, I.W. Hall: Experimental and Numerical Investigation of High Strain Rate Mechanical Behavior of a [0/45/90/- 45] Quadriaxial E-Glass/Polyester Composite, Procedia Engineering, Vol. 10, pp. 3068-3073, 2011.

[12] A. Tasdemirci, I.W. Hall: Development of Novel Multilayer Materials for Impact Applications: A Combined Numerical and Experimental Approach, Materials and Design, Vol. 30, No. 5, pp. 1533-1541, 2009.

[13] M. Grujicic, G. Arakere, T. He, W.C. Bell, B.A. Cheeseman, C.-F. Yen, B. Scott: A Ballistic Material Model for Cross-Plied Unidirectional Ultra-High Molecular-Weight Polyethylene Fiber-Reinforced Armor-Grade Composites, Materials Science and Engineering: A, Vol. 498, No. 1-2, pp. 231-241, 2008.

[14] R.J. Davies, S.J. Eichhorn, J.A. Bennett, C. Riekel, R.J. Young: Imaging Microstructure and Stress Fields within a Cross-ply Composite Laminate, Composite Science and Technology, Vol. 69, No. 5, pp. 567-574, 2009.

[15] V.P.W. Shim, Y.B. Guo, V.B.C. Tan: Response of woven and laminated high-strength fabric to oblique impact, International Journal of Impact Engineering, Vol. 48, pp. 87-97, 2012.

[16] B.P. Patel, S.K. Bhola, M. Ganapathi, D.P. Makhecha: Penetration of Projectiles in Composite Laminates, Defence Science Journal, Vol. 54, No. 2, pp. 151-159, 2004.

[17] B.S. Gupta: *Friction in Textile*, Woodhead Publishing House Ltd., Cambridge, 2008.

[18] A.R. Bunsell: *Handbook of tensile properties of textile and technical fibres*, Woodhead Publishing House Ltd., Oxford, 2009.

[19] G.W. Stachowiak: *Wear - materials, mechanisms and practice*, John Wiley and Sons Ltd, New York, 2005.

[20] T. Hasegawa: *Tribology research trends*, Nova Science Publishers Inc., New York, 2008.

[21] I. Crudu: *Tribosystem - tribomodel for studying the mechanical systems* (in Romanian), Galati University Press, Galati, 2008.

[22] P.M. Cunniff, M.A. Auerbach: High performance "M5" fiber for ballistics / structural composites, in: *Proceedings of the*

23th Army Science Conference, 02-05.12.2002, Orlando, SUA, pp. 1-8.

[23] ***: *Ballistic Resistance of Body Armor*, Nova Science Publishers, Inc., New York, 2009.

[24] M. Grujicic, J. Snipes, S. Ramaswami, V. Avuthu, C.-F. Yen, B. Cheeseman, Derivation of the material models for ultra-high molecular-weight polyethylene fiber-reinforced armor-grade composites with different architectures, Engineering Computations, Vol. 33, No. 3, pp. 926-956, 2016.

[25] V. Narayanamurthy, C.L. Rao, B.N. Rao: Numerical Simulation of Ballistic Impact on Armour Plate with a Simple Plasticity Model, Defence Science Journal, Vol. 64, No. 1, pp. 55-61, 2014.

[26] R. Velmurugan, R.S. Sikarwar, N.K. Gupta: Analytical Modeling for Ballistic Perforation of Angle-Ply and Hybrid Composite Laminates, in: *Proceedings of the IMPLAST 2010 Conference*, 12-14.10.2010, Providence, USA, 2010.

[27] M.A.G. da Silva, C.G. Chiorean, C. Cismasiu: Numerical simulation of ballistic impact on composite laminates, International Journal of Impact Engineering, Vol. 31, No. 3, pp. 289-306, 2005.

[28] P. Soltani, M. Keikhosravy, R.H. Oskouei, C. Soutis: Studying the Tensile Behaviour of GLARE Laminates: A Finite Element Modelling Approach, Applied Composite Materials, Vol. 18, No. 4, pp. 271-282, 2011.

[29] P. Tan: Numerical Simulation of the Ballistic Protection Performance of a Laminated Armor System with Pre-existing Debonding/ Delamination, Composites Part B: Engineering, Vol. 59, pp. 50-59, 2014.

[30] D. Zhu, A. Vaidya, B. Mobasher, S.D. Rajan: Finite element modeling of ballistic impact on multi-layer Kevlar 49 fabrics, Composites Part B: Engineering, Vol. 56, pp. 254-262, 2014.

[31] D. Kreculj, B. Rašuo: Review of Impact Damages Modelling in Laminated Composite Aircraft Structures, Tehnicki vjesnik, Vol. 20, No. 3, pp. 485-495, 2013.

[32] H.L. Gower, D.S. Cronin, A. Plumtree: Ballistic Impact Response of Laminated Composite Panels, International Journal of Impact Engineering, Vol. 35, No. 9, pp. 1000-1008, 2008.

[33] M. Sadighi, R.C. Alderliesten, R. Benedictus: Impact Resistance of Fiber-metal Laminates: A review, International Journal of Impact Engineering, Vol. 49, pp. 77-90, 2012.

[34] B. Scott: Unusual Transverse Compression Response of Non-Woven Ballistic Laminates, in: *Proceedings of the 26th International Symposium on Ballistics*, 12-16.09.2011, Miami, USA, pp. 1859-1871.

[35] J. López-Puente, D. Varas, J.A. Loya, R. Zaera: Analytical modelling of high velocity impacts of cylindrical projectiles on carbon/epoxy laminates, Composites Part A: Applied Science and Manufacturing, Vol. 40, No. 8, pp. 1223-1230, 2009.

[36] ***: *AutoDyne composite modeling*, ANSYS Inc., 2012.

[37] T. Delpero, G. Lepoittevin, A. Sanchez: *Finite Element Modeling with ANSYS*, Strukturlabor, 2010.

[38] V. Năstăsescu, A. Ştefan, C. Lupoiu: *Analiza neliniară prin metoda elementelor finite. Fundamente teoretice şi aplicaţii*, Military Technical Academy, Bucharest, 2001.

[39] Ballistics material handbook, available at: http://www.teijinaramid.com/wp-content/uploads/2016/05/Teijin-Aramid-Ballistics-Material-Handbook.pdf, accesed: 02.04.2017.

[40] C. Pirvu: *An Experimental and Numerical Study on the Ballistic Protection Packs Made of Aramid Fiber Fabrics* (in Romanian), PhD thesis, "Dunarea de Jos" University, Galati University Press, Galati, 2015.

[41] I. Safta: *Contribuţii la studiul teoretic şi experimental al mijloacelor individuale de protecţie balistică*, PhD thesis, Military Technical Academy, Bucharest, 2011.

INFLUENCE OF FRICTION ON INCREASE STIFFNESS OF MODULAR FIXTURE SYSTEMS

Marija MATEJIC[1], Milos MATEJIC[1], Bekir NOVKINIC[2], Milutin ZIVKOVIC[3], Branko TADIC[1]
[1]Faculty of Engineering, Kragujevac, Serbia
[2]Ministriy of Defense, Banja Luka, B&H
[3]Higher Technical School of Mechanical Engineering,Trstenik, Serbia
*Corresponding author: marija.jeremic@kg.ac.rs

Abstrakt: *The idea of development of modular fixture systems increased level of stiffness and flexibility based on modular fixture systems that are in the basic form of framed structures. It is assumed that the concept of forming assemblies of modular fixture systems provide greater rigidity and flexibility, greater reliability, which is especially important if you take into account the possible use of these accessories when processing on modern multi-axis numerical machines in which at once basing and tightening treatment performed with a number of different tools. The friction between structural elements of the modular fixture systems are analyzed.*

Keywords: *modular fixture systems, stiffnes, friction, structural elements.*

1. INTRODUCTION

The concept of modular fixture system composed of a number of interchangeable components originally developed in England at the beginning of World War II [1]. With the development of numerical machines (Numerical Control machine - NC) 1960 years, beginning more and more to develop and implement modular clamping accessories in the industry. Modular fixture systems play an important role in the modern manufacturing environment because they reduce the time and costs required for the design, and the time and costs during the changes fixture systems in a variety of manufacturing processes [2]. In addition, the modular fixture systems through the universal existence of exchangeable clamping elements allow for greater flexibility,

the quality and volume of production. The flexibility of modular fixture systems derives from a large number of clamping configuration, ie. different combinations of clamping elements which can be connected to this base plate. Modular fixture systems basically consist of a base plate on which is placed fixture elements standard type and are used for different shapes and sizes of workpieces. The elements of a modular fixture systems be in the form of vertical and horizontal elements for the positioning, both vertical and horizontal clamping elements with a role to base, positioned and clamped the workpiece in a given position. A method of designing a modular fixture systems may be divided into four phases [3]:
• preparation of input data,
• planning modular fixture systems,

- the design modular fixture systems,
- verification.

Generally speaking, the modular fixture systems can be divided into two groups according clamping surfaces [4]:

- the surface of the base the T - the grooves and,
- basing surfaces with holes and threaded bore.

Automated design of a modular fixture systems means the process in which, without human interaction projects a corresponding modular fixture systems for the workpiece. Considering that the in today's widespread use of 3D design software, as input to a system that is able to automatically design a modular fixture systems to use the 3D model of the workpiece, with the technological data such as tolerances, surface roughness and other [5]. Modular elements of the clamping would need to have some level of intelligence is required [6]. In previous research, a large number of systems for automated design of modular fixture systems, or complete automation of any system has not been developed. More or less essential human interaction in defining the input data into the system.

Previous studies in the field of application systems for automated design accessories CAFD, globally, can be divided into two prominent fields of research include: optimization of modular fixture systems and the development of modular fixture systems. Different techniques were used to optimize the modular fixture systems:

- the method of the finite element [7]–[9],
- genetic algorithms [10]–[13],
- a combination of genetic algorithms and neural networks [14], [15],
- the finite element method, and genetic algorithm [16],
- genetic algorithms and algorithms ant colony [17].

This type of research, more or less, is focused on defining the optimal number of necessary elements for positioning and clamping the workpiece in a modular fixture systems. When we talk about the

development of modular clamping kit, there are several systems that should be noted:

- a neural network [14], [15],
- case-based reasoning - CBR [18], [19],
- an expert system [20]–[23] and
- knowledge-based systems [24]–[26].

Analyzing literature which is directly related to this field of research has been observed that the systems of modular clamping of accessories based on the system console. A large number of studies designed to determine the performance of positioning, tolerance analysis, stability analysis, analysis of possible constraints, and optimize the clamping force. In addition, previous studies include: a method for determining automatic positioning and clamping the workpiece on the basis of mathematical models, algorithms to select the position for positioning and clamping, which provides maximum mechanical leverage, the kinetic analysis based on the planning of clamping tension arrangement and dependence shrinkage based on the analysis of the accessibility automatically select settings taking into account the tolerance factor, and the occurrence of possible failures of the clamping devices, as well as the geometrical analysis based n a 2D planning clamping accessories. Principles of clamping equipment and research based on the finite element method are also the subject of considerable research. The finite element method, it is in most cases used for analysis of the behavior of stress and strain of the system the workpiece / chucking device in relation to the applied force of processes of cutting and clamping process. It also carried out a large number of optimization and developed a large number of mathematical algorithms in order to minimize as much displacement and deflection.

The idea of development of modular fixture systems increased level of stiffness and flexibility based on modular fixture systems that are in the basic form of framed structures. It is assumed that the concept of forming assemblies of modular fixture systems provide greater rigidity and flexibility, greater reliability, which is especially important if you

take into account the possible use of these accessories when processing on modern multi-axis numerical machines in which at once basing and tightening treatment performed with a number of different tools.

2. BASIC SYSTEM CONFIGURATION OF MODULAR FIXTURE SYSTEMS

The basic configuration of a modular fixture systems of frame type is illustrated in Figure 1. The frame of the modular fixture systems is formed with the outer faces of the base plate which can be easily connected with other elements which are used for clamping work cartwheel within modular fixture systems. The above-described basic elements are mounted on a base plate which by means of screws fixed to the table working machines. The supporting structure of this type of modular fixture systems consists of a base plate, the pillar (guide rail) of the mounting plate and the carrier guide rail.
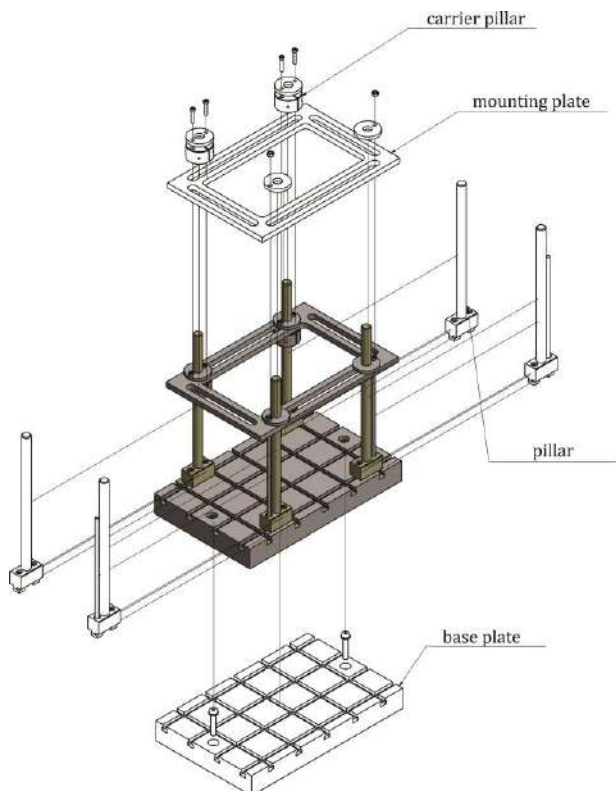
Figure 1. The basic configuration of the modular fixture systems

After defining the dimensions of the workpiece, with respect to the base plate, approach to the design of the modular fixture systems. Pillars can slide along the groove by the base plate and clamping elements can be fixed anywhere along the groove. Depending on your needs can be installed more poles. To increase the stiffness of the bearing structure of modular fixture systems, if necessary, the poles are placed stiffeners. After fixing pillars are mounting and fixing of the mounting plate by means of the carrier poles at a certain height.

3. THEORETICAL INVESTIGATIONS

Under the influence of the transverse external load bracket is bent, ie. comes to its bending axis. The focus of arbitrary cross section at a distance, z, from the left end moves perpendicular to the axis of the console size, u. This move is known as a deflection. The function u (z) is the equation of the elastic line bent axis bracket (Figure 5.4). In close the cross-section, at an infinitesimal distance dz, the deflection will be u + du, where du increment of deflection. Given that the distance is infinitely small, we can consider that the line CD is right, that is. that this line coincides with the tangent to the elastic line at point C. The angle φ which this tangent forms with the original axis of the bracket is known as a slope.

Theoretical consideration deflection and slope for a particular case console loaded by force F on the free end (Figure 2).
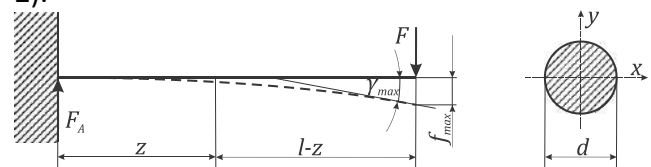
Figure 2. Elastic line console loaded at the free end

From the strength of materials known to the deflection console loaded by force F on the free end:

$$Bu = \frac{Fl^3}{6}\left[3\left(\frac{z}{l}\right)^2 - \left(\frac{z}{l}\right)^3\right]. \qquad (1)$$

respectively:

$$f_{max} = \frac{Fl^3}{3B}. \qquad (2)$$

At console with variable cross section shown in figure 2 at the calculation of the deflection are taken into account the moments of inertia of the increased moment of inertia of the work and the console of circular cross section. Calculation of deflection takes place over two fields (field AC and CB feld).
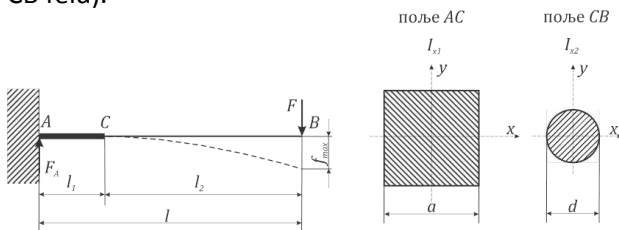
Figure 3. Deflection console with variable cross section

On the basis of the previously calculated deflection u_{AC}, u_C and u_{CB} the total deflection, or an elastic console line with variable cross section shown in Figure 2 would be:

$$u = \frac{Fl_1}{2B}(2l - l_1) + \sin\gamma_C \cdot \frac{180^o}{\pi} \cdot z_1 + \\ + \frac{Fl_2^3}{6B}\cdot\left[\left(\frac{z_1}{l_2}\right)^2 \cdot \left(3 - \frac{z_1}{l_2}\right)\right]. \qquad (3)$$

4. EXPERIMENTAL INVESTIGATIONS

The experimental investigations on the elements that make up the bearing structure of the modular frame of the fixture system are sufficient indicator of the impact of different sizes load at the behavior of the fixture system/ the workpiece.

During the presentation of experimental analyses it is used specially designed device that works on a mechanical principle, and to check the reading obtained independent parameters used coordinate measuring machine DEA Global Performance using measurement software PCDMIS.
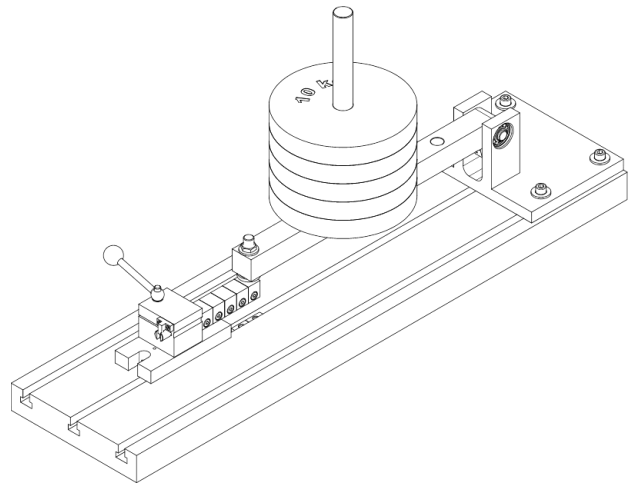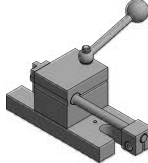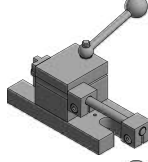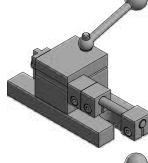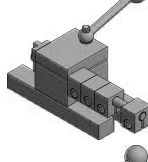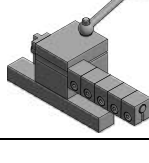
Figure 4. Mechanical measuring device

It was conducted five experimental tests. In conducting out of the experimental tests it was carried out by changing the cross section of the modular guide elements of the fixture system by the addition of stiffening. Each of the experimental tests is conducted and involved a load side guide to the values of normal load Fn, given in table 1.

Table 1. Experiment plan and program

Experiment no.	Stiffening elements	Fn, N
1.		44.99, 56.76, 68.54, 80.31, 92.08, 103.85
2.		44.99, 56.76, 68.54, 80.31, 92.08, 103.85
3.		44.99, 56.76, 68.54, 80.31, 92.08, 103.85
4.		44.99, 56.76, 68.54, 80.31, 92.08, 103.85
5.		44.99, 56.76, 68.54, 80.31, 92.08, 103.85

The result of experimental tests was to determine and compare the differences of elastic line guides with and without stiffening elements. Due to the volume of experimental data, the paper will be displayed only static processed results.

5. EXPERIMENTAL ANALYSES OF RESULTS

According to the experimental analyses described in chapter 7, and the results shown in Table 4, it was followed by analysis of the behavior of deflection under the action of the abovementioned loads. The obtained experimental results of the elastic line of the guide without the stiffening elements and the stiffening elements are shown as the diagram in Figure 5. The primary result of the experimental analyses is to show the real behavior of a structural element of the modular fixture systems to the effects of stress. It is believed that the experimental analyses conducted on a moving structural elements sufficient indicator of reliability and overall system rigidity modular fixture systems.

Analysis of the experimental results shown in Figure 5 a) can clearly see the reduction in the deflection f by the addition of stiffeners in relation to the guide without stiffeners. Reduction in the deflection f observed in the percentage of the measured end-point, in the guides with stiffening with respect to the guide without the stiffener is 37%. The deflection f, which is further observed reduction in, with two guides of the support in relation to the guide without the bracing of 36%. Deflection f, three guides with a stiffening element in relation to the guide of the support without it decreased by 54%, while the decrease of the deflection f, in the guides with a complete change of the cross-section, i.e. in the guides with four stiffening elements smaller in relation to the guide without stiffeners 57%. Based on the above, it can be concluded that the experimental research deflection f in the guides with a complete change of the cross section into a rectangular shape smaller by about 50% in relation to the guide of circular cross section.

a)

b)

c)
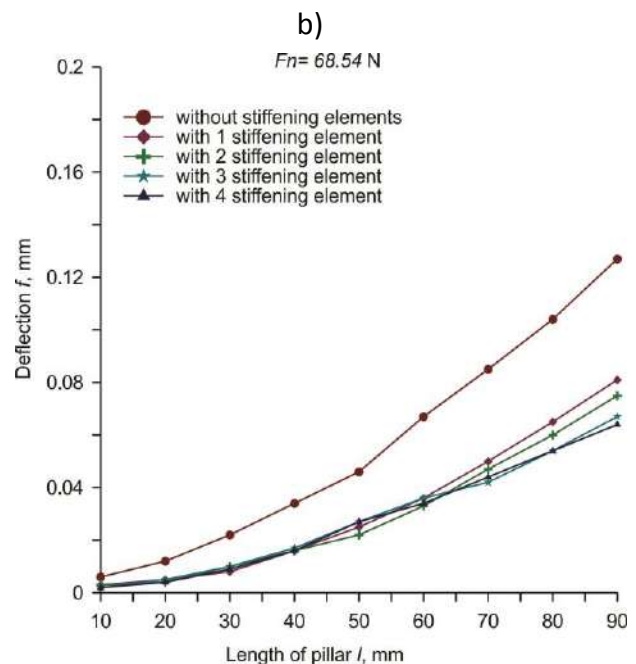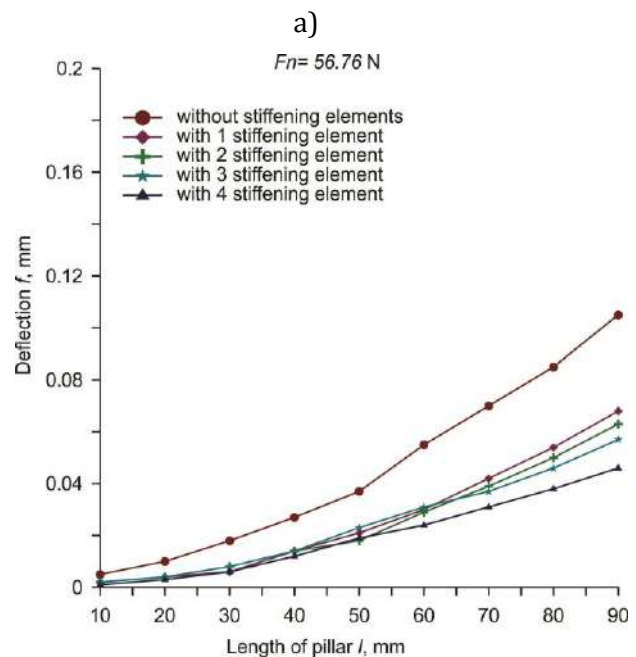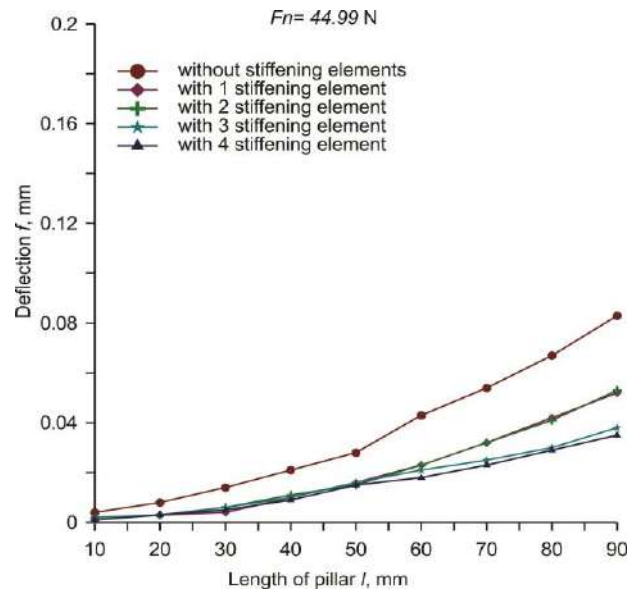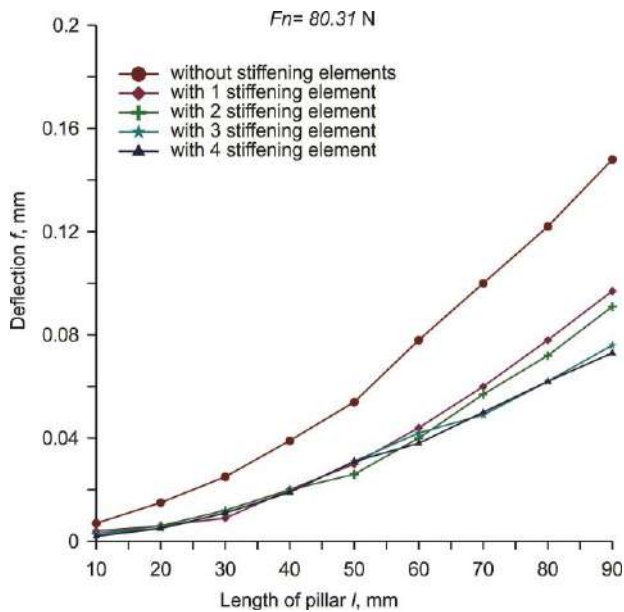
d)
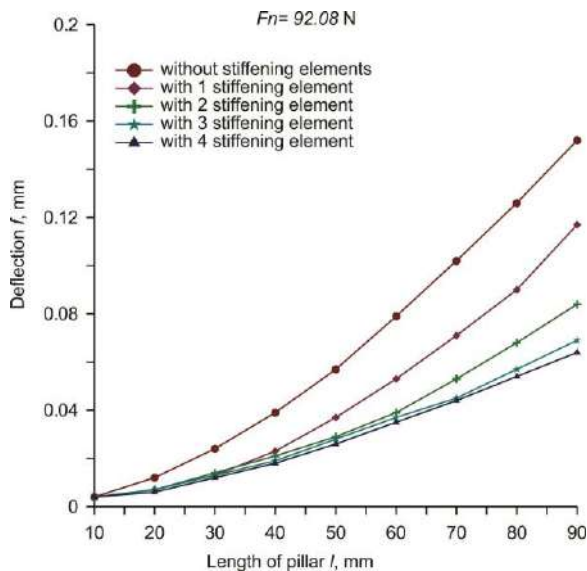
e)
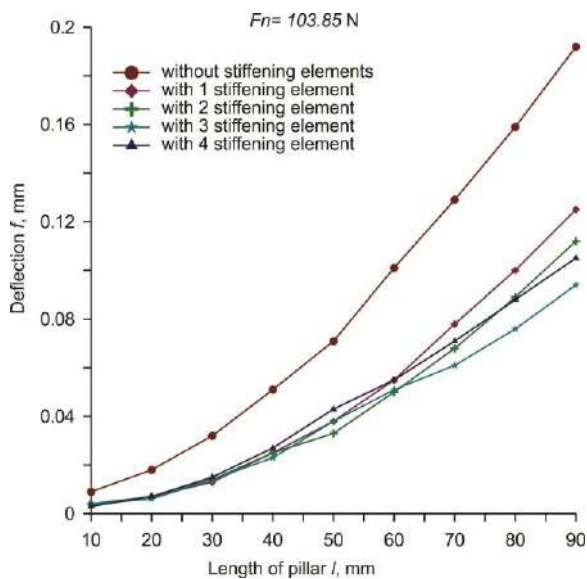
f)

Figure 5. Display the experimental results of the elastic line guides under load a) $F_n = 44.99\,N$, b) $F_n = 56.76\,N$, c) $F_n = 68.54\,N$, d) $F_n = 80.31\,N$, e) $F_n = 92.08\,N$ and f) $F_n = 103.85\,N$

Further examination of experimental research in fact load Fn is an increase deflection f. The increase of the deflection f, and increase of the load Fn, expressed as a percentage is 26%, 53%, 78%, 104% and 131%.

6. CONCLUSION

Significant improvements in the stiffness of frame type modular fixture systems can be achieved by choosing an appropriate cross-section of the structural elements. Theoretical considerations, as well as the results in conducted experiments confirmed the assumption that the stiffness of the guides rectangular cross-section greater by 35-40% as compared to the stiffness of the guides of circular cross section.

LITERATURE

[1] S. H. Bawa, *Manufacturing Processes - I*. Tata McGraw-Hill Education, 2004.

[2] Y. Kang, Y. Rong, and J. C. Yang: Computer-Aided Fixture Design Verification. Part 2. Tolerance Analysis, The International Journal of Advanced Manufacturing Technology, Vol. 21, No. 10, pp. 836–841, 2003.

[3] W. Neng, W. Zhan, R. Mo: An intelligent fixture design method based on smart modular fixture unit, The International Journal of Advanced Manufacturing Technology, Vol. 69, No. 9–12, pp. 2629–2649, 2013.

[4] Y. Rong, S. Huang, *Advanced computer-aided fixture design*, Academic Press Inc, Orlando, USA, 2005.

[5] A. Rétfalvi, M. Stampfer: The Key Steps toward Automation of the Fixture Planning and Design, Acta Polytehnica Hungarica, Vol. 10, No. 6, pp. 77–98, 2013.

[6] Z. M. Bi, W. J. Zhang: Flexible fixture design and automation: Review, issues and future directions, International Journal of Production

Research, Vol. 39, No. 13, pp. 2867–2894, 2001.

[7] N. Amaral, J. Rencis, Y. Rong: Development of a finite element analysis tool for fixture design integrity verification and optimisation, The International Journal of Advanced Manufacturing Technology, Vol. 25, No. 5, pp. 409–419, 2005.

[8] Y. Zheng, Z. Hou, Y. Rong: The study of fixture stiffness part I: a finite element analysis for stiffness of fixture units, The International Journal of Advanced Manufacturing Technology, Vol. 36, No. 9–10, pp. 865–876, 2008.

[9] R. Menassa, W. DeVries: Optimization methods applied to selecting support positions in fixture design, Journal of Engineering for Industry, Vol. 113, No. 4, pp. 412–418, 1991.

[10] S. Kamat, M. Srinivas, P. Rama Rao: Mixed mode I/III fracture toughness of Armco iron, Acta mater, Vol. 46, pp. 4985–4992, 1998.

[11] K. Krishnakumar, N. Melkote: Machining fixture layout optimization using the genetic algorithm, International Journal of Machine Tools and Manufacture, Vol. 40, pp. 579–598, 2000.

[12] K. Kulankara, S. Satyanarayana, N. Melkote: Interactive Fixture Layout and Clamping Force Optimization Using the Genetic Algorithm, Journal of Manufacturing Science and Engineering, Vol. 124, No. 1, pp. 119–125, 2002.

[13] S. Vallapuzha, E. C. De Meter, C. Shabbir, R. P. Khetan: An investigation of the effectiveness of fixture layout optimization methods, International Journal of Machine Tools and Manufacture, Vol. 42, No. 2, pp. 251–263, 2002.

[14] A. Kumar, V. Subramaniam, K. Seow: Conceptual design of fixtures using genetic algorithms, The International Journal of Advanced Manufacturing Technology, Vol. 15, pp. 79–84, 1999.

[15] A. Kumar, V. Subramaniam, T. Teck: Conceptual design of fixtures using machine learning techniques, The International Journal of Advanced Manufacturing Technology, Vol. 16, pp. 176–181, 2000.

[16] W. Chen, L. Ni, J. Xue: Deformation control through fixture layout design and clamping force optimization, The International Journal of Advanced Manufacturing Technology, Vol. 38, pp. 860–867, 2008.

[17] G. Prabhaharan, K. Padmanaban, and R. Krishnakumar: Machining fixture layout optimization using FEM and evolutionary techniques, The International Journal of Advanced Manufacturing Technology, Vol. 32, pp. 1090–1103, 2007.

[18] J.-S. Chou: Web-based CBR system applied to early cost budgeting for pavement maintenance project, Expert Systems with Applications, Vol. 36, pp. 2947–2960, 2009.

[19] G. Peng, G. Chen, C. Wu, H. Xin, Y. Jiang: Applying RBR and CBR to develop a VR based integrated system for machining fixture design, Expert Systems with Applications, Vol. 38, No. 1, pp. 26–38, 2011.

[20] O. Bartholomew, S. Alladin, P. Lyu: A framework for a rule-base expert fixturing system for face milling planer surfaces on a CAD system using flexible fixtures, Journal of Manufacturing Systems, Vol. 7, pp. 193–207, 1989.

[21] A. R. Darvishi, K. F. Gill: Knowledge representation database for the development of a fixture design expert system, Proceedings of the Institution of Mechanical Engineers, Part B: Journal of Engineering Manufacture, Vol. 202, No. 1, pp. 37–49, 1988.

[22] J. Fuh, C. Chang, M. Melkanoff: An integrated fixture planning and analysis system for machining processes, Robotics ad Computer – Integrated Manufacturing Journal, Vol. 10, pp. 339–353, 1993.

[23] B. O. Nnaji, P. Lyu: Rules for an expert fixturing system on a CAD screen using flexible fixture, Journal of Intelligent Manufacturing, Vol. 1, No. 1, pp. 31–48, 1990.

[24] A. Wallack, J. Canny, W. AS, J. Canny: Planning for modular and hybrid fixtures, Algorithmica, Vol. 19, No. 1, pp. 40–60, 1997.

[25] R. Brost, K. Goldberg, A complete algorithm for designing planar fixtures using modular components, IEEE Robotics & Automation Magazine, Vol. 12, pp. 31–46, 1996.

[26] A. Nee, A. Kumar, S. Prombanpong, K. Puah: A Feature-based classification scheme for fixtures, CIRP Annals – Manufacturing Technology, Vol. 41, pp. 189–192, 1992.

SERBIATRIB '17

15th International Conference on
Tribology

Serbian Tribology
Society

Faculty of Engineering
University of Kragujevac

Kragujevac, Serbia, 17 – 19 May 2017

TRIBOLOGICAL STUDY ON SPUR GEAR USING DIFFERENT GEAR OILS

M.M. SHAHIN*, M.A. CHOWDHURY, U.K. DEBNATH, Z. SHAH, M.A. KOWSER
Dhaka University of Engineering and Technology, Gazipur, Bangladesh
*Corresponding author: shahin.duet37@gmail.com

Abstract: *Power loss is the most dominating concern in mechanical power transmission system by any types of gear. Power loss is highly influenced by the friction force and friction loss between two gear contacts. Friction loss is affected by the energy consumption, gear operating temperatures, lower oil oxidation and speed. In the present study power losses minimization was obtained remarkebly by applying two main different approaches: using lower modulus of spur gears with significant positive profile shafts and using gear lubricant formulations with different types of base lubricants named as 5W30, 10W30, 10W-40 and 15W50 gear oil on the nylon gear and pinion. 15W30 gear oil indicated the lower power losses, friction coefficient and wear loss remarkebly due to higher viscosity effect and the selected geometries also minimized the power losses considerably approaching the thermal stabilization. An endurable thin Lubricant layer formulated to reduce coefficient of friction, wera rate and power loss as well signficantly that provide a positive approach in any gear mechanism.*

Keywords: Power loss, Sliding loss, Friction loss, Nylon Spur Gear, lubrication, Temperature.

1. INTRODUCTION

The purposes behind utilizing gear transmissions incorporate transferring secondary torques also evolving the crating different motion. The effectiveness of a gearbox will rely on upon high losses of the energy [1]. Gear lubricant is important substance to reduce friction force, temperature, corrosion and wear. Rubbing is decreased possibly by a dividing oil novel into a film alternately by additives transported of the rigging network by the ointment. That adequacy for cooling relies on the sum of ointment what's more entryway great it will be transported of the hot gear flanks. Energy losses could make divided under no load-dependent and load losses. Load-dependent losses would the individuals from gears what's

more bearings at torque is exchanged. No-load loss happen significantly without at whatever load continuously transmitted [2, 3]. They are because of the revolution of shafts, which reasons bearings and gears to be dragged in the lubricant. Energy losses when gears are dragged in the lubricant are called churning losses and are affected by the oil level, viscosity of the lubricant and rotational speed [4]. Gear churning losses can be a major contributor to the total energy losses in a gearbox. Running gearboxes with a lower oil level and lower viscosities can reduce these losses, but causes worse lubrication and thus higher temperatures. Hohn et al. [5] have studied possible gear failures due to increased temperature. The objective can be reached through different perspectives such as rise efficiency and cut down gear power loss,

minimize gear operating temperature, enhance reduce lubricant oil oxidation and rising lubricant life or accommodate the use of a less lubricant quantity, minimize friction force between gear teeth and pinion, progressing the resistance to micro pitting and scuffing and thus gear longevity, less the environmental impact of lubricants oil, using biodegrade-able, low toxicity gear lubricant oils [6, 7]. Load, geometry, friction coefficient would those determinant parameters that govern friction power loss and large number choices would accessible should control these variables. The dominating of the load stress and load can be effortless decreased adopt larger teeth or growing contact ratio. Friction coefficient perhaps limited by surface texture, lubrication regime or lubricant oil properties, and also by factors as sliding speed and the length of the contact path [6, 8].

In this study, an attempt is made to reduce the power loss, sliding loss, friction coefficient , wear rate etc and select the preferable operating conditions and gear oil as the lubricant. Moreover, this study can be used as a worthy source for the clarification of ongoing researches on gears for industrial applications. In this context, this study focused different gear oil (5W30, 10W30, 10W40 and 15W50) as lubricant which indicated different natures on the power loss, friction coefficient, wear rate and so on. Experimental results has been compared to the estimated results that provided alomost above 90% fitted in to each other. A significant lower friction coefficient, power loss and wear rate was attained using 15W50 gear oil producing stabilized lubricant layer in between gear meshing due to higher viscous effect rather than the other selected gear oils. A stabilized thermal nature in lubricant was observed indicating by gear oil temprature.

2. METHODOLOGY

2.1 Test equipment

Both running-in and proficiency tests were performed in a FZG back to back spur gear test

rig with a productivity test setup. In all tests, gears with the same geometry were utilized as a part of the test gearbox (1) and Digital Thermocouple (3). To stack the gear, deadweights were held tight the load clutch (2). The grease tank (4), Inverter (5) torque sensor (7), and motor (6) shown in the Figure.1 [9]. As new combines of apparatuses were utilized as a part of every test, the test rig must be dismantled and reassembled once more test. To change gears in the slave gearbox (1), the motor (5) and speed and torque sensor (7) were removed first. Both apparatus sets were then changed by removing the two front cover on the two gearboxes. The inverse system was taken after to reassemble the apparatus. The same get together methodology was utilized for all tests. The performance specifications of the torque transducers can be observed from the Table 1.

Table 1. Performance specifications of the torque transducers.

Transducer	Capacity (Nm)	Non-linearity (%)[a]	Hysteresis (%)[a]	Repeatability (%)[a]	Temperature range [b] (1C)
Input/ Output torque	5650/2250	±0.0026	±0.031	±0.05	+21 to+77

a is % of rated output and b is Compensated.
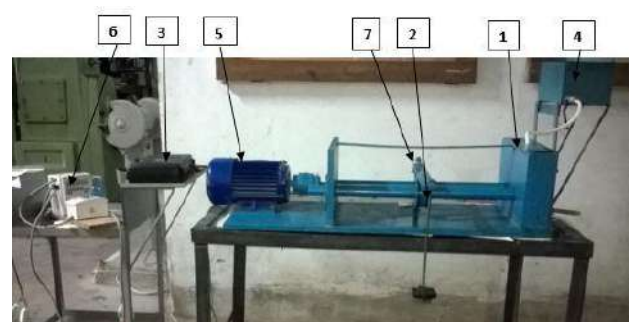
Figure 1. FZG gear test rig

2.2 Test gear box

Figure.2 demonstrates a schematic perspective of the test gearbox. This gearbox has two shafts where two pinions are

mounted. The both shafts are attached by ball bearing. The test gearbox permits the choice of two distinctive kinematic relations. Table 2 displayed the main geometric properties of the pinions used in the test gearbox.

Table 2. Geometrical parameters of the pinions in the test gearbox

Parameter	Units	Pinion number	
		1	2
Modulus (m)	mm	10	10
Number of teeth(z)		38	50
Addendum modificatio n(x)		0.415	0.3814
Face width(b)	mm	32	32
Pressure angle (α)		20	20

2.3 Lubricants

Four commercial gear oils were selected and characterized. The lubricants have been used as 5W-30, 10W-30, 10W-40, and 15W-50. The physical and chemical characterization of the lubricants is displayed in Table 3.

Table 3. Chemical and Physical Properties of the gear oil (synthetic, Mobil Co)

Parameter	Unit	5W-30	10W-30	10W40	15W-50
Viscosity @40°C	mm²/ sec (cSt)	61.7	78.1	95.9	114
Viscosity @100°C	mm²/ sec (cSt)	11.7	12	14.7	15
Pour Point	°C	-39	-37	-33	-30
Flash Point	°C	230	232	232	236
Density@1 5.6ºC	g/ml	0.856	0.86	0.860	0.876

2.4 Power loss analysis

O_1 and O_2 are two gears and pinion power has been transfered from gear O_1 to O_2 shown by the curve line in Figure 2. It was considered that both gear and pinion has been come to contact at point AB and all gear and pinion

rotation showing in this figure and transmitted force at gear point K. Gear and pinion rotated each other as result force shifted at point D and generated rolling friction.
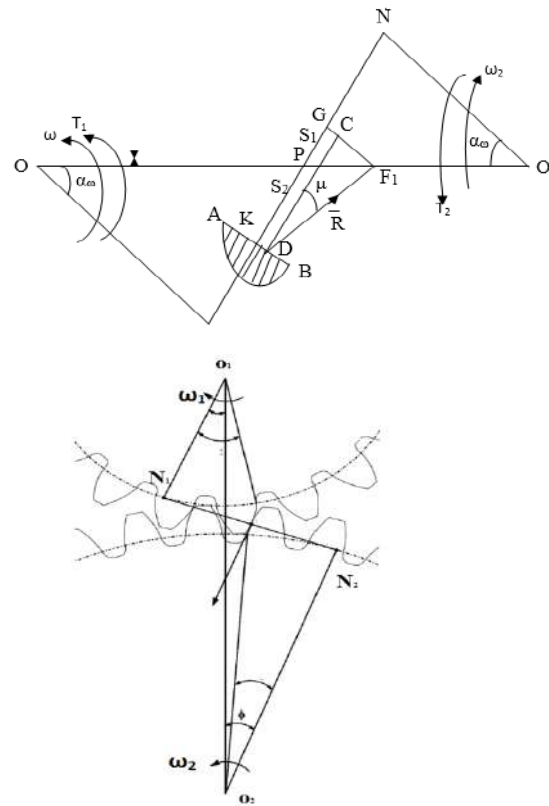
Figure 2. Schematic diagram of an external engagement of gear and pinion

The contact point does not coincide according to the kinematic pitch point at P, the gear has been generated at different speed and sliding friction therefore produced friction coefficient μ at triangle ΔCDF$_1$. Two types of friction has been occurred between gear and pinion teeth. The force R12 is shifted at point F_1 rotating way from at P in direction of the driven gear. The sliding loss has been calculated by using previous researcher at [10, 11]. The following equation was used:

$$\phi = \frac{H_1 - H_2}{H_1} \tag{1}$$

$$Power\ loss = H_1 - H_2 \tag{2}$$

$$H_1 = T_1 \cdot \omega \tag{3}$$

$$T_1 = \overline{R_{12}} \cdot O_1 \cdot F_1 \cdot \cos(\alpha_\omega + \mu) \tag{4}$$

Where H_1 is the power input at gear O_1 and H_2 is the power output at pinion O_2, ω is angular velocity of the gear O_1, T_1 is the torque of the gear O_1, $\bar{R}_{12}$ is the gear interaction force, α_ω is the pressure angle and μ is the friction angle.

$$\overline{H_2} = T_2 \cdot \omega \qquad (5)$$
$$T_1 = \overline{R_{12}} \cdot O_2 \cdot F_1 \cdot \cos(\alpha_\omega + \mu) \qquad (6)$$

Where ω is angular velocity of the pinion O_2, T_2 is the torque of the pinion O_2, $\overline{R_{12}}$ is the pinion interaction force, α_ω is the pressure angle and μ is the friction angle.

2.5 Friction coefficient analysis

Friction coefficient has been a valuable parameter to determine the power loss and sliding loss between power transmitted by the gear and pinion [12]. Friction coefficient is dominated by the different parameters such as surface roughness of the gear and pinion, viscosity of the gear oil, loading condition and sliding velocity. A large number of research recommended those experimental formulas for estimation of the friction coefficient [13-16]. In the present study misharin et al. [15] formula has been considered to determine the friction coefficient of the gear in power transmission system.

$$\mu = [0.325 \cdot V_s \cdot V_r \cdot \vartheta_k]^{-0.25} \qquad (7)$$

Where μ is the friction coefficient, V_s is the relative sliding velocity, V_r is the sum of the rolling velocity and v_k is the kinematic viscosity of the gear oil.

3. RESULTS AND DISCUSSIONS

3.1 Power loss and sliding loss

Just like oil stabilization temperature hierarchy, 5W-30 ranked slightly upper than other oils in case of power loss in watt for gradual increment of RPM [11, 17]. However, for sliding loss, 15W-50 remains lower significantly due to higher viscosity effect for all conditions with straight nature in lower torque (4 N-m), while 10W-30 shows inclined but straight line for highest (8 N-m) torque. For lower order torques, all types of oil tend to show affinity to become horizontal with increment of RPM. It also shows good agreement for lower RPM operation against variable torques. It means that power loss remains constantly minimum for low RPM torques and RPM. Experimental data as Figure 3 to Figure 7 and estimated results shown good agreement proving the authenticity of test rig

[9]. As the variation of torque lower power loss was observed while lower torque however, at 4 N-m the experimental results matched with estimated results as 100% using 15W50 gear oil shown in 6 (d).
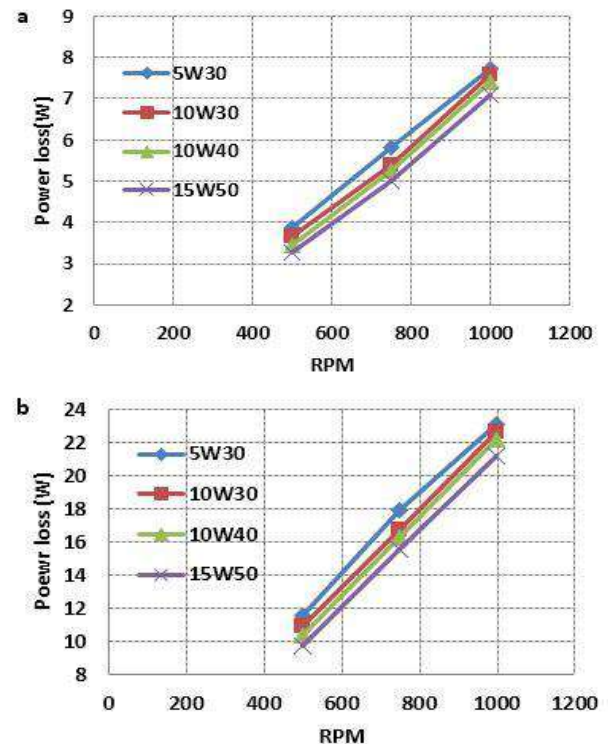
Figure 3. Power loss with RPM at different gear oil grade (a) 4 N-m and (b) 8N-m
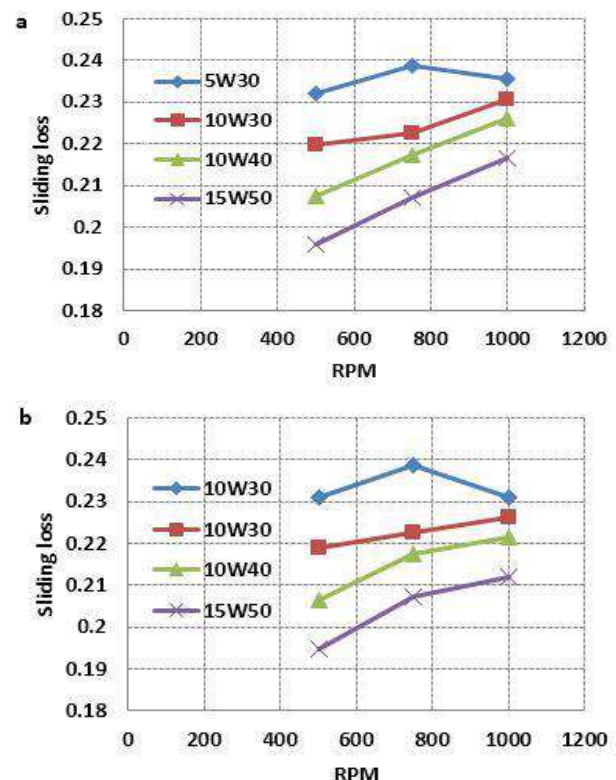
Figure 4. Sliding loss with RPM at different gear oil grade (a) 4 N-m and (b) 8N-m

Figure 6. Power loss with RPM at experiment and estimation result at 4 N-m torque (a) 5W30 (b) 10W30 (c) 10W40 and (d) 15W50

Figure 5. Power loss with RPM at different Torque (a) 5W30 (b) 10W30 (c) 10W40 and (d) 15W50
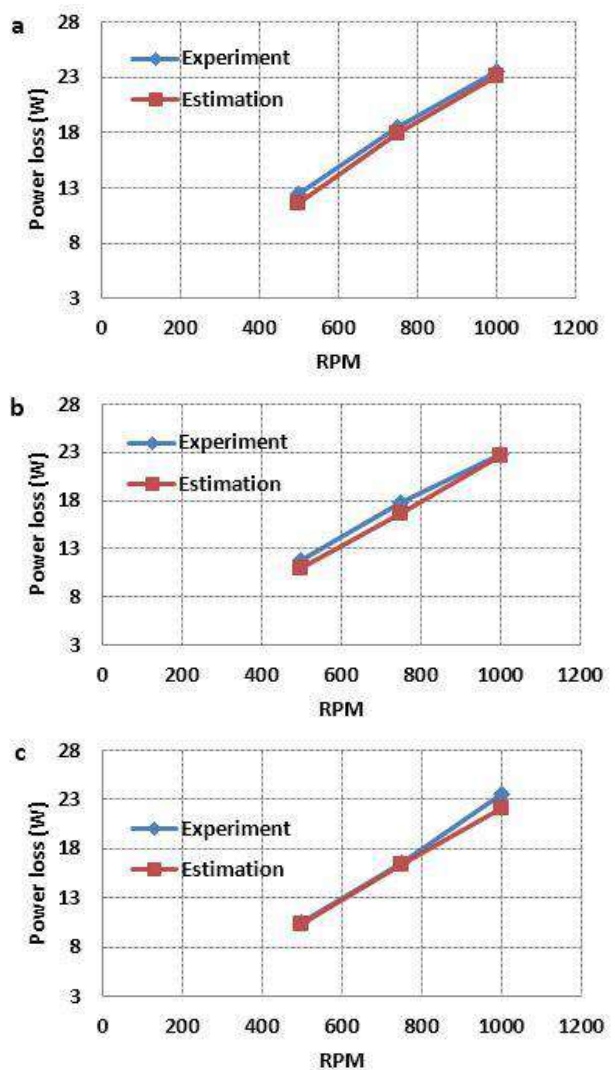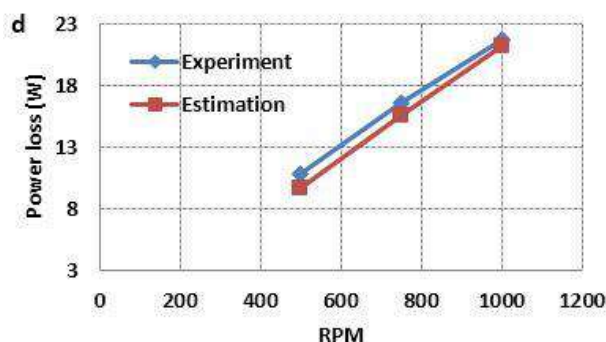
Figure 7. Power loss and RPM at experiment and estimation result at 6 N-m torque (a) 5W30, (b) 10W30 (c) 10W40 and (d) 15W50

3.2 Friction coefficient

Figure 8 demonstrated the relations among the friction coefficient, RPM and different gear oil. Effect of the speed on the coefficient of friction of the spur gear pair is studied at different operating conditions. In the Present study it has been observed that the tendency of the variation of the coefficient of friction as the speed increases opposite's case for all tested condition. As the rotational speed increases of the spur gear, the sliding velocity of the tooth interface increased, which enhanced the proper shear action of the film within the nominal contact zone that results decreasing coefficient of friction was obtained.
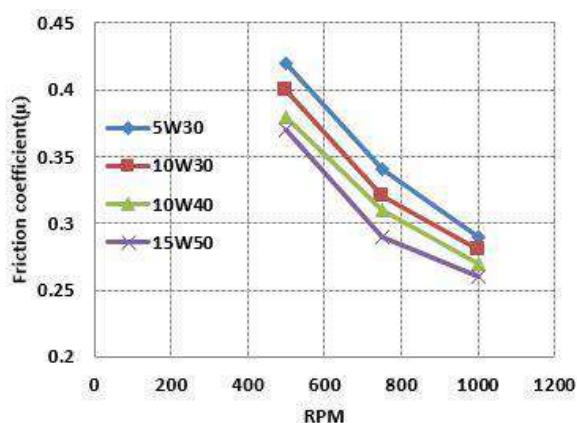
Figure 8. Friction coefficient with RPM using different types of gear oil

However, once the thermal effect is taken into account, as the speed increases, the temperature rise increases due to the higher sliding velocity, and this would lead to the decrease of the fluid viscosity, which further causes a increase of the coefficient of friction. A minimal friction coefficient is attained using

15W50 gear oil rather than the other gear oils. However, for all gear oil provided to lower coefficient of friction with the increase in rotaional speed (RPM) which are similar trend to previous study [12, 18, 19].

3.3 Wear rate of gear

From below mentioned Figures 9-11, it is obvious that at 500 RPM with variable torques, due to use of 5W30 grade lubrication wear amount (in mg) per hour rapidly increases than usual for terminal hour. However, for 500 and 1000 RPM, it did not show any regular characteristics. Meanwhile, other lubricants show little bit deviation for 750 RPM with high order torques.
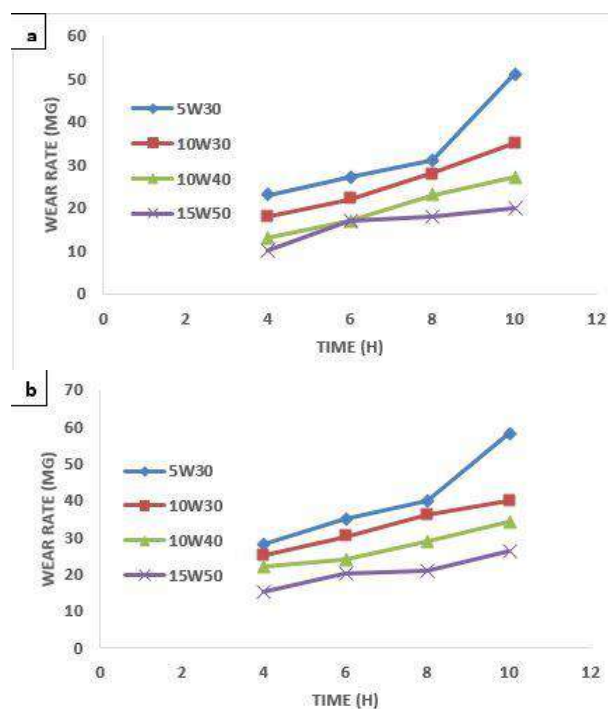
Figure 9. Wear rate with time duration using different gear oil at 500 RPM (a) 4 N-m torque (b) 6 N-m torque
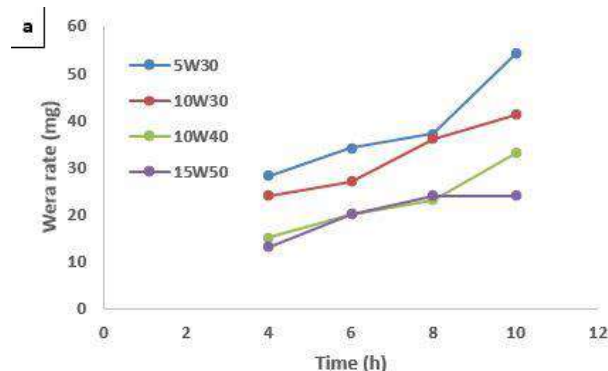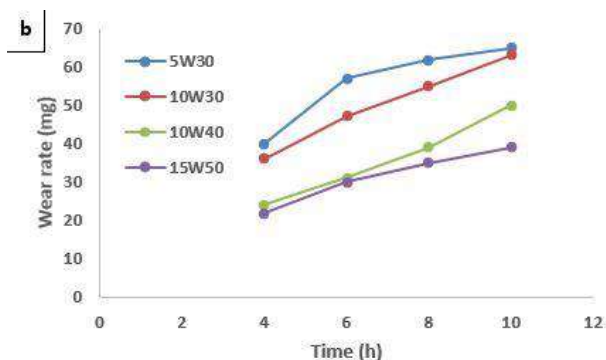
Figure 10. Wear rate with time duration using different gear oil at 750 RPM (a) 4 N-m torque (b) 6 N-m torque
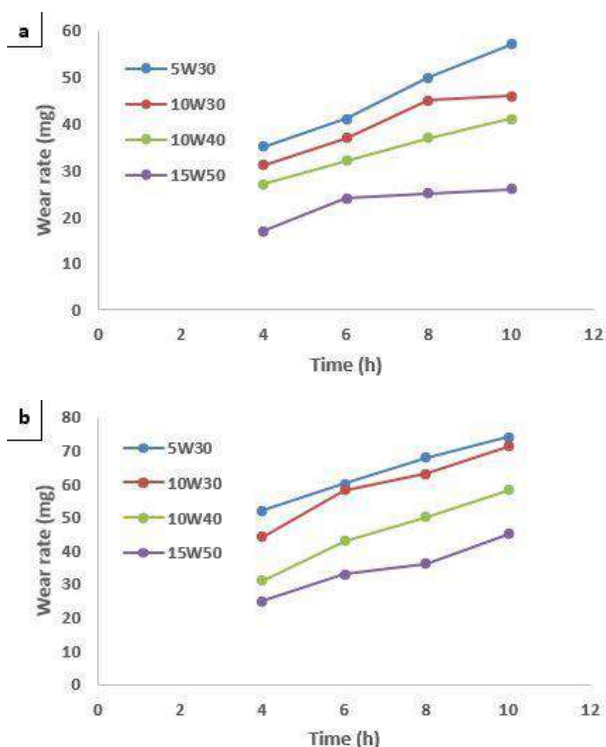
Figure 11. Wear rate with time duration using different gear oil at 750 RPM (a) 4 N-m torque (b) 6 N-m torque

Figure 10 shows that, wear rate takes a straight line shape showing regularity for 5W30 and 10W40 lubricants especially. High viscous effect [20] of 15W50 gaer oil indicated the lower wear in all conditions.

3.4 Thermal stabilization temperature effect

Thermal stabilization temperature and torque are noticeable parameter of the gear test [21]. The torque and stabilization temperatures were determined and recorded the testing time and the mean value of the last 60 minutes of the 10 hours test has been considered, Figure 12 show the oil sump stabilization temperatures ($\nabla T_{Wall} = T_{Oil} - T_{Room}$) from the analysis of Figure 12. It has been analyzed that there are highly variety of the all tested gear oil. 15W50 always promoted lower stabilization temperatures at any other of the selected gear oils, while 5W30 promoted the highest stabilization temperatures. Gear oil 10W30 and 10W40 also better then gear oil 15W50 for the all experimental conditions.

Figure 13 demonstrated the test results in a several way. On the abscissa the oil sump adjustment temperatures $\nabla T_{or} = T_{Oil} - T_{Room}$ are illustrated. On the ordinate the differences between the oil sump and outer gear box wall temperatures are determine by $\nabla T_{0w} = T_{Oil} - T_{wall}$. At the point when the warm adjust was achieved, the temperature in different points of the gearbox outer side was assessed utilizing a digital thermometer. This system was rehashed for various working conditions and it was checked that the temperature on the outside wall of the gearbox temperature was on steady condition. Regardless of the chose the gear oils uncovering altogether different oil sump thermal equilibrium temperatures, two roughly direct and oil independent curves can be distinguished in Figure 13. Since this connection is oil independent, it can be inferred that when the vigorous harmony is achieved the impact of the oil thermal properties on the plotted thermal balance temperatures is negligible, prompting a roughly uniform oil sump temperature. Because of the trial conditions the wind stream around the test gearbox for the most part relies on upon the air flow made by the turning shafts at low speeds. Several researchers have been study on the effect of thermal temperature of the gear oil and Hohn et al. [22] expressed that for low velocities around the test gearbox the oil thermal properties have little impact prompting a roughly uniform oil sump temperature.

All types of liquid dissemination brought about by the moving mechanical components in a

gearbox is firmly identified with the revolution of the pinions somewhat inundated in grease and the gearbox inside geometry. Gear oil course in a gearbox is created by the collaborations between the flow advanced by every one of the pinions and moving components inside the gearbox [20]. The heat that courses through the gearbox lodging is reliant on the way of the liquid flow close to the dividers which is pondered the temperatures.
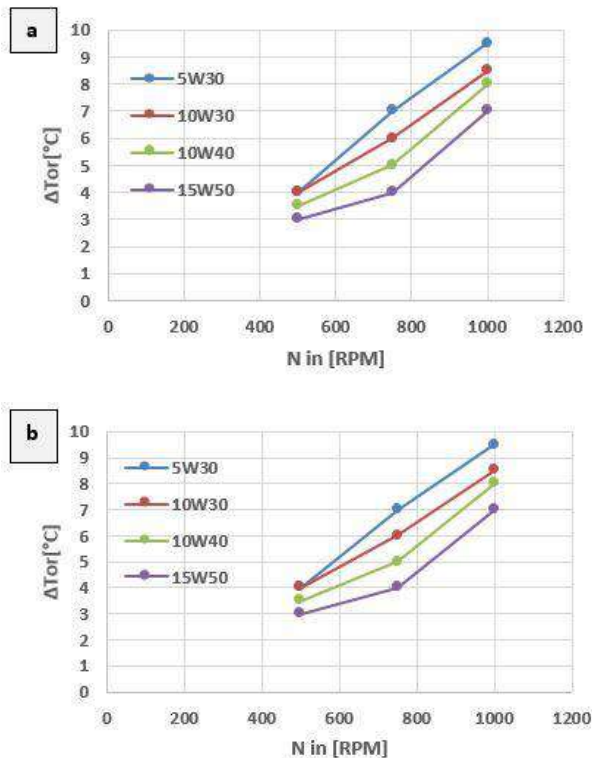
Figure 12. Oil sump stabilization temperature ($\nabla T_{or} = T_{Oil} - T_{Room}$) at (a) 2 N-m and (b) 3 N − m for nylon gear
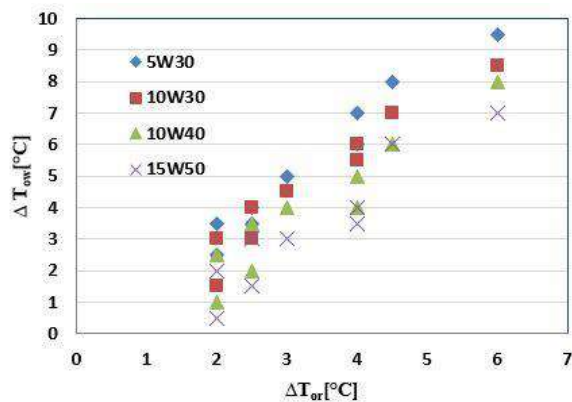
Figure 13. Difference between oil sump and external wall temperature of the housing $\nabla T_{0w} = T_{Oil} - T_{wall}$ of the test gearbox against the difference between oil sump and room temperatures $\nabla T_{or} = T_{Oil} - T_{Room}$
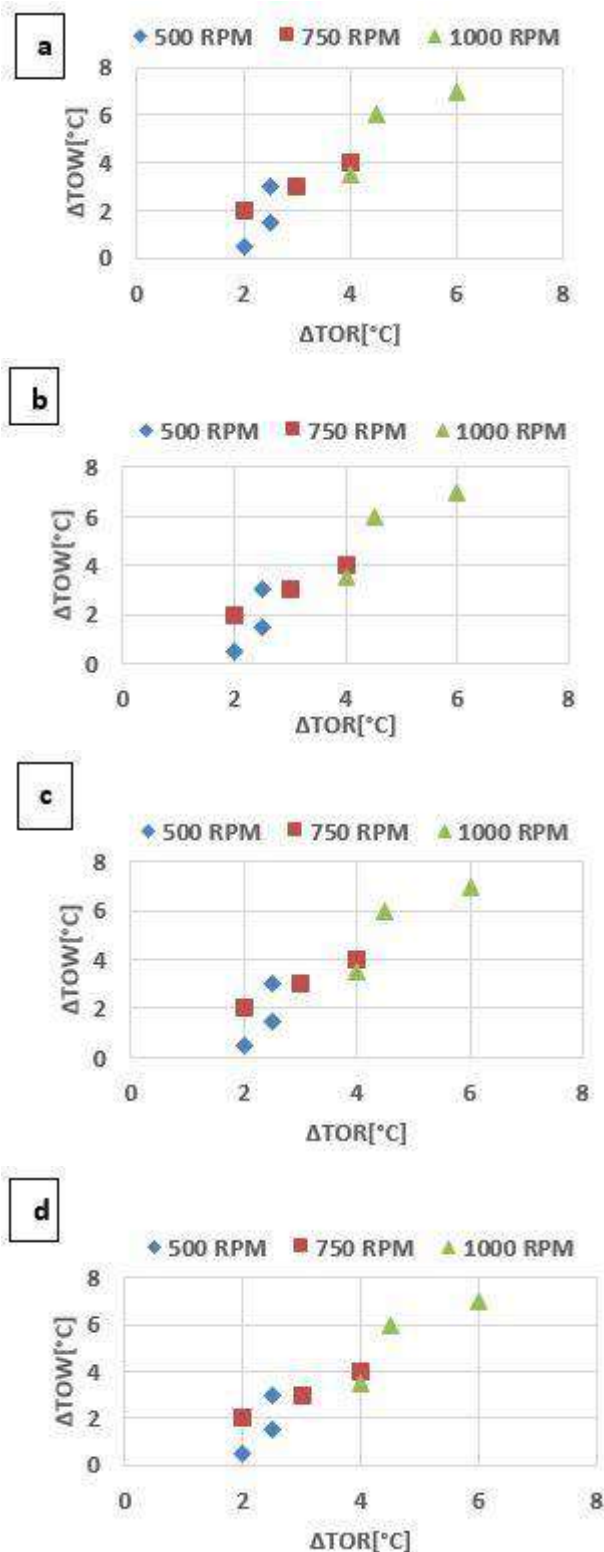
Figure 14. Difference between oil sump and external wall temperature of the housing of the test gearbox against the difference between oil sump and room temperatures (emphasizing the speed dependence) at (a) 5W30, (b) 10W30,(c)10W40 and (d)15W50

Higher heat exchange coefficients are related to turbulent flow, so a move from a laminar to a turbulent stream inside the test gearbox may

prompt the outcomes shown in Figure 13 and Figure 14. After these contemplations it was expected that the flow administration inside the gearbox coming about because of the turning gears halfway submerged in oil could be accessed through the investigation of the conduct of the thermal adjust temperatures.

4 CONCLUSION

As the lubricant, different types of gear oil was used in this work. Using 15W50 provided the lower power loss and sliding loss as well due to higher viscosity effect at increasing temperature rather than other gear oils.There is the approximately same trend of experimental value with estimated value regarding power loss analysis was found in this study. A significant lower trend of coefficient of friction and wear rate have been identified using 15W50 gear oil as compared to other tested gear oils. Stabilization temperature nature was found under 750RPM using the all tested gear oils. Estimated results fitted in to experimental results above 90% approximately regarding power loss, especially 100% at 4 N-m using 15W50 gear oil.

ACKNOWLEDGEMENT

REFERENCES

[1] Fernandes, C.M., et al., Influence of gear loss factor on the power loss prediction, in New Trends in *Mechanism and Machine Science*, Springer, pp. 799-806, 2015

[2] Seabra, J., et al., Influence factors on gearbox power loss. Industrial lubrication and tribology., Vol. 63, No. 1, pp. 46-55, 2011

[3] Fernandes, C.M., et al., Gearbox power loss. Part III: Application to a parallel axis and a planetary gearbox, Tribology International, Vol. 88, pp. 317-326, 2015.

[4] Höhn, B., K. Michaelis, and H. Otto, Flank load carrying capacity and power loss reduction by minimized lubrication, Gear Technology, pp. 53-62, 2011:

[5] Höhn, B.-R. and K. Michaelis, Influence of oil temperature on gear failures. Tribology International, Vol. 37, No. 2, pp. 103-109, 2004.

[6] Hohn, B., K. Michaelis, and A. Wimmer, Gearboxes with minimised power loss. VDI BERICHTE, Vol. 1904, No. 2, pp. 1451. 2005.

[7] Martins, R., N. Cardoso, and J. Seabra, Gear power loss performance of biodegradable low-toxicity ester-based oils. Proceedings of the Institution of Mechanical Engineers, Part J: Journal of Engineering Tribology, Vol. 222, No. 3, pp. 431-440, 2008.

[8] Höhn, B.-R., et al., *Thermal rating of gear drives: balance between power loss and heat dissipation,* American Gear Manufacturers Association, 1996.

[9] Fernandes, C.M., et al., Torque loss and wear of FZG gears lubricated with wind turbine gear oils using an ionic liquid as additive. Tribology International, Vol. 90, pp. 306-314, 2015.

[10] Ratanasumawong, C., et al., Estimation of sliding loss in a parallel-axis gear pair, Journal of Advanced Mechanical Design, Systems, and Manufacturing, Vol. 6, No 1, pp. 88-103, 2012.

[11] Brandão, J.A., et al., Calculation of gear tooth flank surface wear during an FZG micropitting test. Wear, Vol. 311, No 1, pp. 31-39, 2014.

[12] Martins, R., et al., Friction coefficient in FZG gears lubricated with industrial gear oils: biodegradable ester vs. mineral oil. Tribology international, Vol. 39, No 6,pp. 512-521, 2006.

[13] Benedict, G. and B. Kelley, Instantaneous coefficients of gear tooth friction. ASLE transactions, Vol. 4, No. 1, pp. 59-70, 1961.

[14] Drozdov, Y.N. and Y.A. Gavrikov, Friction and scoring under the conditions of simultaneous rolling and sliding of bodies. Wear, Vol, 11, No 4, pp. 291-302, 1968.

[15] Misharin, Y.A. Influence of the Friction Condition on the Magnitude of the Friction Coefficient in the Case of Rollers with Sliding, in Proceedings of International Conference on Gearing, Mechanical Engineering, London, 1958.

[16] O'donoghue, J. and A. Cameron, Friction and temperature in rolling sliding contacts, ASLE TRANSACTIONS, Vol. 9, No. 2, pp. 186-194, 1966.

[17] Fernandes, C., et al. FZG gearboxes lubricated with different formulations of polyalphaolefin wind turbine gear oils, *in International gear conference*, 2014.

[18] Castro, J. and J. Seabra, Coefficient of friction in mixed film lubrication: gears versus twin-discs, Proceedings of the Institution of Mechanical Engineers, Part J: Journal of Engineering Tribology, Vol 221, No. 3, pp. 399-411, 2007.

[19] Kleemola, J. and A. Lehtovaara, Experimental evaluation of friction between contacting discs for the simulation of gear contact, Lubrication Science, Vol. 13, No. 1, pp. 13-20, 2007.

[20] Brandão, J.A., et al., Measurement of mean wear coefficient during gear tests under various operating conditions. Tribology International, Vol. 102, pp. 61-69, 2016.

[21] Csobán, A., Tooth friction loss in simple planetary gears. Scientific Bulletin Series C: Fascicle Mechanics, Tribology, Machine Manufacturing Technology, Vol. 21, pp. 153, 2007.

[22] Höhn, B.-R., K. Michaelis, and T. Vollmer, Thermal rating of gear drives: balance between power loss and heat dissipation, American Gear Manufacturers Association, 1996.

A NUMERICAL ANALYSIS FOR PLUNGER PUMP IN ELASTOHYDRODYNAMIC LUBRICATION

Bora LEE[1],*, Yonghun YU[1], Yongjoo CHO[1]
[1] School of Mechanical Engineering, Pusan National University, Busan, South Korea
*Corresponding author: yjcho@pusan.ac.kr

Abstract: In this study, we evaluate the lubrication characteristics of the reciprocating plunger pump by hydrodynamic lubrication analysis considering elastic deformation of a barrel. The lateral motion of the plunger during plunger sliding barrel inside is called secondary dynamics.

This paper presents effects of elastic deformation of a barrel on the piston secondary motion in hydrodynamic lubrication. The rigid ringless piston and deformable cylinder-shaped barrel were considered. We use the two-dimensional Reynolds equation to evaluate lubrication characteristics with a variation clearance for an incompressible, unsteady state flow. Moreover, we use the equilibrium equation of moment and forces in the vertical and horizontal directions to determine the secondary motion of the plunger. Through numerical analysis, the orbit of plunger eccentricity and minimum film thickness are calculated for given conditions. We investigate the lubrication characteristics of the pump by comparing the minimum film thickness and surface roughness. After cyclic convergence, complete hydrodynamic lubrication conditions are achieved while plunger-barrel contact occurs for others. Through lubrication analysis, we found that there is optimum clearance between plunger and barrel, which depends on operation conditions. As barrel deforms as much as clearance scale, it is important to consider barrel deformation to figure out the secondary motion of plunger pump.

Keywords: plunger, barrel, lubrication, elastic deformation, clearance

1. INTRODUCTION

The fuel injection pump is one of the main components of the marine diesel engine. This pump is the device that pumps fuel into the cylinders of a diesel engine. High pressure and low viscosity of fuel cause scratches of the running surfaces and leads to accelerated wear or sticking in reciprocating fuel pumps. Thus, needs for understanding and design optimization are increasing to prevent wear and stick in the plunger pump, and that are compatible with the increased fuel pressure in modern medium-speed diesel engines.

The lateral motion of the piston during piston sliding cylinder inside is called secondary dynamics. This paper presents effects of elastic deformation of a barrel on the piston secondary motion in hydrodynamic lubrication. The rigid ringless piston and deformable cylinder-shaped barrel were considered. We use the two-dimensional Reynolds equation to evaluate lubrication characteristics with a variation of clearance for an incompressible, unsteady state flow. Moreover, we use the equilibrium equation of moment and forces in the vertical and horizontal directions to determine the

secondary motion of the plunger. Through numerical analysis, the orbit of plunger eccentricity of top and minimum film thickness are calculated for given conditions. After cyclic convergence, complete hydrodynamic lubrication conditions are achieved.

2. ANALYSIS MODEL

2.1 Geometry and Conditions

The numerical model of the fuel pump is simplified, as shown in Fig. 1. This system is consisted of plunger that has a reciprocal motion and deformable barrel. It is assumed that the center of moment in the plunger is placed on the bottom of it, and this point moves only on the center line of the barrel because the guide is installed the lower end of the plunger.

Plunger and barrel geometry parameters are shown in Table 1. The clearance between the plunger and barrel is 5 μm. The barrel pressure and plunger stroke is dependent on crank angle. Maximum value of plunger stroke and barrel pressure are 30 ㎜ and 800bar. 0.02Pa*sec oil is considered as lubricant.

Table 1. Geometry parameter

Parameter		Value	Unit
Plunger	length	150	mm
	radius	10	mm
Barrel	length	100	mm
	outer radius	20	mm
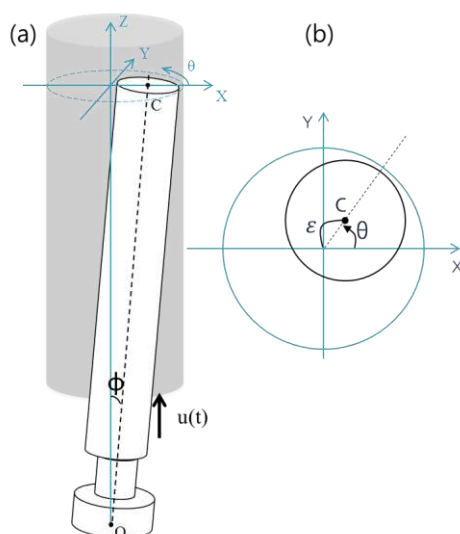
Figure 1. Geometry of pump

2.2 Numerical Methodology

The equations of motion in lateral direction are solved using the calculated oil film hydrodynamic pressure, hydro-frictional force, contact force, cylinder gas pressure and inertia. To calculate the hydrodynamic pressure acting on the piston, unsteady-state two-dimensional Reynolds equation is solved by finite difference method using a rigid piston-cylinder assumption as formula (1). Reynolds boundary conditions are used to consider cavitation boundary.

$$\frac{\partial}{\partial x}\left(\frac{\rho h^3}{12\eta}\frac{\partial p}{\partial x}\right)+\frac{\partial}{\partial y}\left(\frac{\rho h^3}{12\eta}\frac{\partial p}{\partial y}\right)=\frac{U}{2}\frac{\partial(\rho h)}{\partial x} \tag{1}$$

$$p = 0, \qquad \frac{\partial p}{\partial n}=0 \tag{2}$$

The cylindrical coordinates of center of the top plunger are shown in Figure 1.(b) The film thickness equation is expressed as formula (3).

$$h(y,\theta)=c-\varepsilon\cos\theta+h_d(y,\theta) \tag{3}$$

The equilibrium equation of moment at the O point in Figure 1. and the equilibrium of forces in the vertical and horizontal direction are used, as shown in formula (4) to determine the motion of the plunger. The moment at the O point is calculated with formula (5).
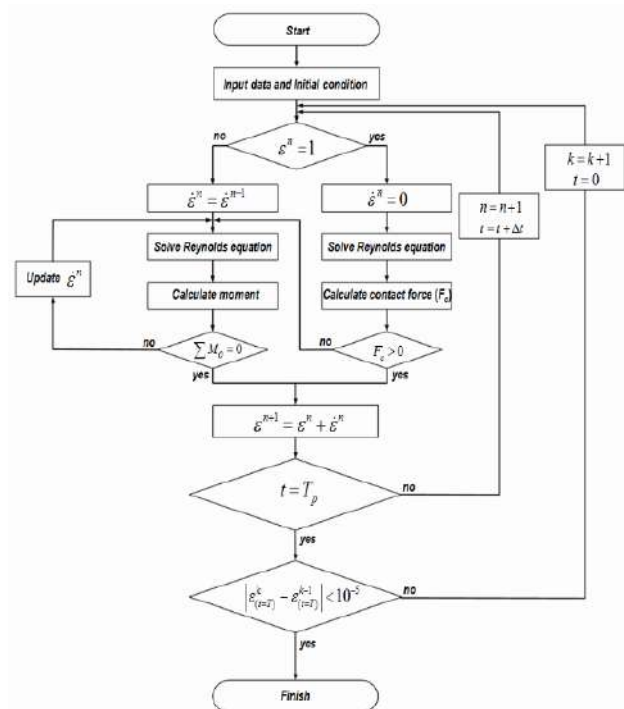
Figure 2. Analysis flow chart [2]

To satisfy the moment equilibrium at the bottom of the plunger, eccentricity of plunger is updated using the Newton Raphson method.

$$\sum F_X = \int_0^L \int_0^{2\pi} (p\cos\theta) rdzd\theta = 0$$

$$\sum F_Y = \int_0^L \int_0^{2\pi} (p\sin\theta) rdzd\theta = 0 \quad (4)$$

$$\sum M_X = \int_0^L \int_0^{2\pi} (pz\sin\theta) rdzd\theta = 0$$

$$\sum M_Y = \int_0^L \int_0^{2\pi} (pz\cos\theta) rdzd\theta = 0 \quad (5)$$

2.3 Barrel deformation

When plunger reciprocates, barrel go through elastic deformation and this displacement changes oil film thickness between plunger and barrel. We considered elastic deformation of barrel surface to examine the effect of elastic deformation on plunger secondary motion.

When radial point load is forced on specific spot A of barrel inner surface, the components of elastic displacement ux, uy at any point B on the barrel inner surface is dependent on the distance between A and B as shown in Figure 3.

We calculated elastic displacement ux, uy for all node using ANSYS APDL, which is used as influence function, $f(\xi,\psi)$. ξ and ψ are relative coordinate of forced spot from deformed point. Therefore, the radial displacement(u) of specific point on barrel is expressed as below.

$$u = \int_0^L \int_0^{2\pi} p \star f(\xi,\psi) rdzd\theta \quad (6)$$

We assumed that plunger is rigid and displacements of outer surface of barrel is constraints for all direction.
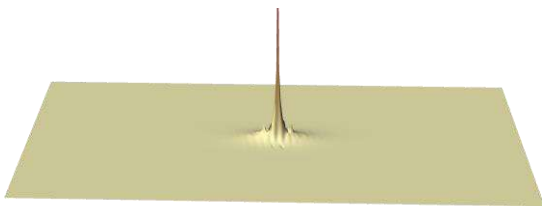
Figure 3. Distribution of dimensionless elastic deformation on surface for point load

3. RESULT

We compared minimum film thickness at the top of the plungers with different radial clearance after plunger motion stabilizing. The results are shown in Figure 4-5. Dimensionless time, T=0, 1 at BDC and T=0.2 at TDC.

Figure 4 presents (a) eccentricity ratio at the top of the plunger and (b) minimum film thickness during reciprocating motion. When radial clearance increases, plunger tilts more and maximum eccentricity ratio increases. However, minimum film thickness for plunger with 10um radial clearance was the smallest. Figure 5. demonstrate variation of minimum film thickness with dimensionless time for different radial clearance conditions. It can be shown that there is optimum clearance. The optimum clearance is about 5 μm at given conditon.
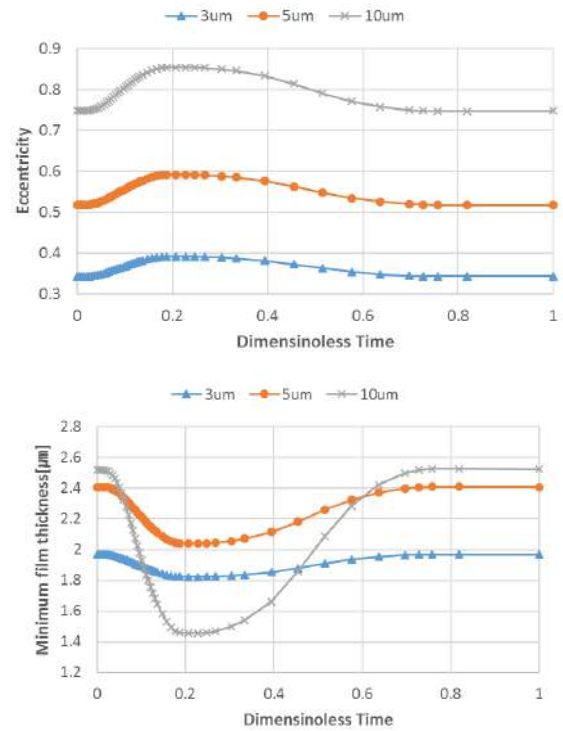
Figure 4. Plunger secondary motion for a cycle (a)eccentricity ratio (b)minimum film thickness

To evaluate the effect of barrel deformation on plunger lubrication properties, transition of eccentricity of plunger top and minimum film thickness in a cycle are presented on Figure 6-7. In both cases, plunger top is set in same position at BDC (T=0).
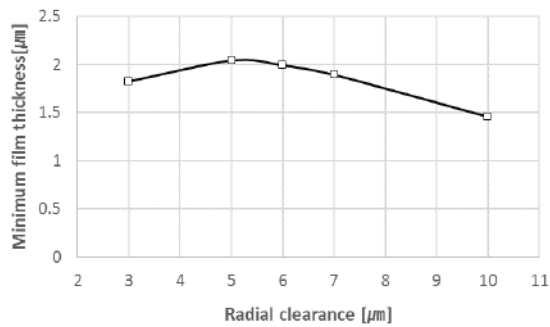
Figure 5. Minimum film thickness with clearance
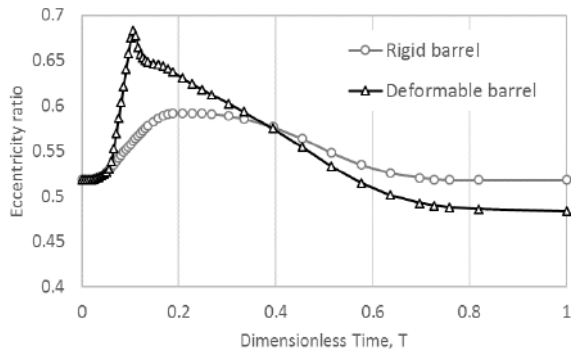
Figure 5. Effect of barrel elastic deformation on eccentricity ration of plunger top.

Figure 6. Effect of barrel elastic deformation on minimum film thickness

For rigid barrel condition, plunger approach to barrel wall during ascending stroke and film thickness become minimum at TDC(T=0.2). For the deformable barrel condition, however, plunger tilts more than rigid conditions and recovers oil film thickness before TDC. After 1 reciprocating motion, eccentricity ratio for elastic deformable barrel condition is larger. We can guess that after plunger motion stabilizing, plunger with deformable barrel condition would have less eccentricity ratio and larger film thickness.

4. CONCLUSION

In this study, the secondary motion of plunger pump is simulated and the lubrication characteristics of the plunger were investigated with various clearance. There is optimum radial clearance ratio, which was 5um for given conditions.

We considering barrel elastic deformation as well. For rigid plunger-deformable barrel condition, minimum film thickness increase and eccentricity ratio of plunger top is decrease compared with stabilized result of rigid barrel condition.

REFERENCES

[1] T. Prata: Dynamic Analysis of Piston Secondary Motion for Small Reciprocating Compressors, ASME J. Tribol., Vol.122, pp. 752-760, 2003.
[2] S. H. Hong, Lee, Y. J. Cho: Improvement of lubrication characteristics in the reciprocating fuel pump of marine diesel engines, Journal of Mechanical Science and Technology, Vol.30, No.11, pp.5225-5232, 2016.

Tribology of
Manufacturing Processes

15th International Conference on Tribology – SERBIATRIB '17

17 – 19 May 2017, Kragujevac, Serbia

CORRELATION OF SURFACE ROUGHNESS PARAMETERS WITH OPERATIONAL VARIABLES IN TURNING OF A NEW ALUMINUM MATRIX STEEL PARTICULATE COMPOSITE: A MULTI-PARAMETER ANALYSIS

Nikolaos M. VAXEVANIDIS[1]*, Athanasios G. MOURLAS[2], Nikolaos A. FOUNTAS[1], Georgios V. SERETIS[3], Christopher G. PROVATIDIS[3], Pandora P. PSYLLAKI[2], Dimitrios E. MANOLAKOS[3]

[1]Department of Mechanical Engineering, School of Pedagogical and Technological Education (ASPETE), Athens, Greece
[2]Piraeus University of Applied Sciences, Egaleo, Greece
[3]School of Mechanical Engineering, National Technical University of Athens, Greece
*Corresponding author: vaxev@aspete.gr

Abstract: *Present study concerns with a multi-parameter experimental and statistical analysis of surface texture in turning of stainless steel flakes reinforced cast aluminum matrix particulate composite (AMPC). Spindle speed, n (rpm) and feed rate, f (mm/rev) were assigned to an L_9 Taguchi orthogonal array as independent variables whilst depth of cut was kept constant. The response/output (performance characteristic) was an increased number of surface roughness parameters including amplitude, hybrid, statistical and fractal ones. The multi-parameter analysis of surface finish was selected since the evaluation of the roughness with one or two only parameter is ambiguous. The correlation of these parameters with the machining conditions was investigated. Then, statistical analysis and was applied to quantitatively allow exploration of the effect which each machining input yields on roughness outputs. Regression equations were constructed then, in order to develop prediction models with the possible lower estimation error.*

Keywords: *surface roughness, aluminum matrix particulate composite; stainless steel flakes; turning; multi-parameter analysis, regression equations.*

In Memoriam Prof. B. Ivković (1931-2016) and Prof. G.P. Petropoulos (1959-2010)

1. INTRODUCTION

Metal cutting operations are widespread in manufacturing industry and the prediction and/or the control of relevant machinability parameters always attracts interest. A basic machinability parameter is the surface texture, as it is closely associated with the quality, reliability and functional performance of

components [1, 2]. Turning is the primary operation in metalworking industry for producing axisymmetric components. These components, typically, possesses critical features that require specific surface finish and the best possible functional behaviour. Due to inadequate knowledge of the complexity of the process and factors affecting the surface integrity in turning operation [3], an improper

decision may cause high production costs and low machining quality. The proper selection of cutting tools and process parameters for achieving high cutting performance in a turning operation is a critical task [2-4].

The various manufacturing processes applied in industry produce the desired shapes of the components within prescribed dimensional tolerances and surface quality requirements. Therefore, any proposed description of a technological surface should take into account the features of the profile imparted by the machining process performed. This is a crucial point because the process can be controlled through surface texture recognition which also can be used to generate suitable profiles for tribological functioning [5].

In the common industrial practice surface roughness is evaluated by profile amplitude parameters such as R_a, R_t etc., which, however, do not provide information on the shape of the profile. Characteristics like inclination and curvature of the surface roughness asperities, "emptiness" or "fullness" of the profile, distribution of the profile material at various heights are included in the profile shape. The essential tribological aspects (e.g. friction, wear, conditions of lubrication) are highly dependent on profile shape [5, 6]. In this regard, the characterization of machined surface shapes is necessary; this can be achieved only, through multi- parameter statistical analysis [6-10].

The present study concerns with a multi-parameter experimental and statistical analysis of surface texture in turning of stainless steel flakes reinforced cast aluminum matrix particulate composite (AMPC). Spindle speed, n (rpm) and feed rate, f (mm/rev) were assigned to an L9 Taguchi orthogonal array as independent variables whilst depth of cut was kept constant. The response/output (performance characteristic) was an increased number of surface roughness parameters including amplitude, hybrid, statistical and fractal ones. The multi-parameter analysis of surface finish was selected since the evaluation of the roughness with one or two

only parameter is ambiguous. The correlation of these parameters with the machining conditions was investigated. Statistical analysis was applied to quantitatively allow exploration of the effect which each machining input yields on roughness outputs. Regression equations were constructed then, in order to identify prediction models with the possible lower estimation error.

It should be noted that for the study of the influence of operational parameters on machining performance during turning, besides statistical methods, soft computing techniques such as artificial neural networks and genetic algorithms can be applied see for example Refs [3, 11, 12] and [13] respectively.

2. SURFACE ROUGHNESS PARAMETERS

Surface roughness evaluation is very important for many fundamental problems such as friction, contact deformation, heat and electric current conduction, tightness of contact joints and positional accuracy. For this reason surface roughness has been the subject of experimental and theoretical investigations for many decades. The real surface geometry is so complicated that a finite number of parameters cannot provide a full description. If the number of parameters used is increased, a more accurate description can be obtained. This is the main reason for introducing new parameters for surface evaluation [5, 7, 10]. More than one hundred parameters have been proposed in the literature, owing to the fact that a real profile shape is usually very complicated, and the functional requirements for the components are very high in today's industry [5]. Since the estimation of the roughness performed with one parameter is ambiguous, the multi-parameter estimation of roughness is recommended [2, 5, 14]. Surface roughness parameters are normally categorized into three groups according to its functionality. These groups are defined as amplitude parameters, spacing parameters, and hybrid parameters [7]. The surface roughness parameters under study were:

- the arithmetic average, R_a;
- the maximum height of the profile; R_t or R_{max};
- the ten point height, R_z;
- the root mean square (RMS) roughness, R_q;
- the skewness of the amplitude distribution, R_{sk};
- the kurtosis of the amplitude distribution, R_{ku};
- the bearing or Abbott curve parameter at 1 μm under the highest peak, R_{tp};
- the fractal dimension, D.

3. EXPERIMENTAL

In this study for the fabrication of composite rod, an Al-Mn alloy containing Mg was used as matrix material. The purity of the matrix alloy was 96.6 %. Stainless steel 316L flakes (SSF) were used as reinforcing fillers. Al-Mn/SSF composite rods with SSF content equal to 0.25% wt were produced. The fabrication of the aluminum/stainless steel flakes composite by casting was reported in [15]; therefore it is not presented here, see also Ref. [16] for additional details on the fabrication technique.

Cutting experiments were performed on a Mondiale Gallic® 14 conventional lathe equipped with a NC positioning unit. The ISO 6 L1616 P20-grade brazed carbide cutting tool (PVD TiN coated) from Sandvic Coromant® with 0.8 mm tip radius for continuous turning was employed. Coolant was not used during the tests.

Spindle speed and feed rate were treated as the independent machining parameters whilst a number of roughness parameters (see section 2) were treated as the responses on an L_9 Taguchi orthogonal array design. The depth of cut was kept constant for all turning passes at a=1.0 mm.

The surface roughness analysis was performed using a Rank Taylor-Hobson® Surtronic 3 profilometer equipped with the Talyprof® software. The cut-off length was selected at 0.8 mm whilst three measurements were conducted on every pass at the longitudinal direction. Measured average values for all surface roughness parameters under study together with the corresponding cutting variables are tabulated in Table 1.

Table 1. Measured values for surface roughness parameters.

Exp.	n (rpm)	f (mm/rev)	R_a (μm)	R_t (μm)	R_z (μm)	R_q (μm)	R_{sk}	R_{ku}	R_{Tp} (%)	D
1	200	0.05	1.86	12.88	11.27	02.30	00.11	02.92	01.86	1.22
2	200	0.27	8.43	46.53	41.80	10.33	00.52	02.79	00.67	1.10
3	200	0.60	8.57	44.10	38.53	10.06	00.27	02.45	00.60	1.07
4	800	0.05	0.65	04.85	04.35	00.83	-00.21	03.10	07.71	1.36
5	800	0.27	8.20	45.67	41.03	10.05	00.04	02.48	00.63	1.07
6	800	0.60	7.77	47.00	39.80	09.65	00.54	03.67	00.63	1.01
7	1600	0.05	0.88	06.54	05.42	01.09	-00.19	02.84	03.80	1.37
8	1600	0.27	7.96	50.13	39.23	09.63	00.38	03.33	00.33	1.12
9	1600	0.60	8.49	51.50	43.30	10.51	00.44	03.33	00.56	1.10

4. RESULTS AND DISCUSSION

4.1. Experimental observations

The variation of R_a, R_t and R_z values with feed rate for all three spindle speeds applied is presented in Figures 1, 2 and 3 respectively. When turning under the lowest level for feed rate (i.e. f=0.05 mm/rev), R_a is kept low for all spindle speed levels, therefore it is deemed as the most influential parameter affecting R_a. Lowest value for R_a was obtained for spindle speed equal to 800 rpm with 0.05 mm/rev feed rate. For the same feed, R_a slightly increases when spindle reaches 1600 rpm. Experimental observations for R_t and R_z as well as for R_q are quite similar to those for R_a, as it is expected. Moreover, variation patterns

presented in Figures 1 and 2 are quite different from the ones observed in turning of pure Al-Mn alloy (matrix material) under the same experimental conditions; see Ref. [17].

Note, that arithmetic average roughness (R_a) is by far the most commonly used parameter in surface finish measurement and for general quality control. Despite its inherent limitations, it is easy to measure and offers a good overall description of the height characteristics of a surface profile. On the other hand, R_t is very sensitive to the high peaks or deep scratches. R_q (RMS) is more sensitive to peaks and valleys than R_a, but less robust whilst R_z is the most versatile process control parameter, very sensitive to process changes and relatively robust.
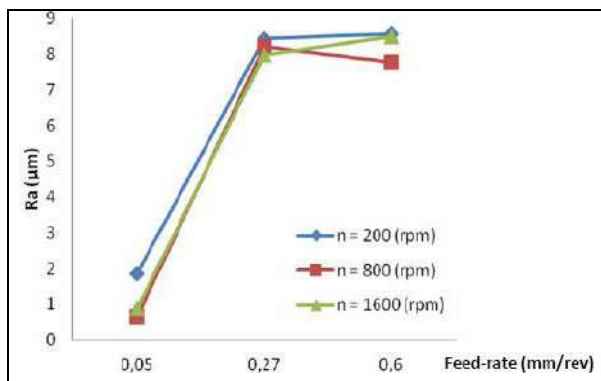
Figure 1. Variation of R_a in relation to operational parameters
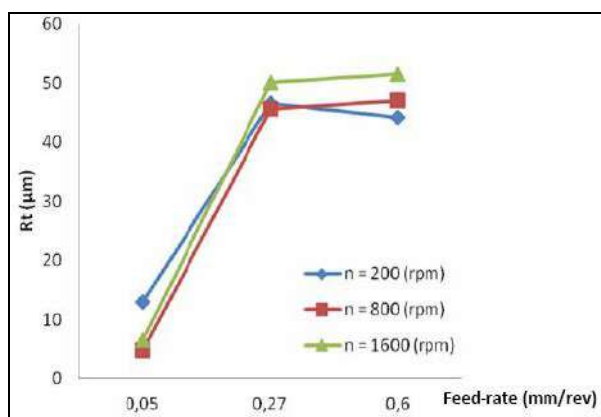
Figure 2. Variation of R_t in relation to operational parameters

Skewness parameter (R_{sk}) is typically used to measure the symmetry of the profile about the mean line and is sensitive to deep valleys or high peaks. A symmetrical height distribution, i.e. with as many peaks as valleys, has zero skewness. Profiles with peaks removed or deep scratches have negative

skewness. Profiles with valleys filled in or high peaks have positive skewness.
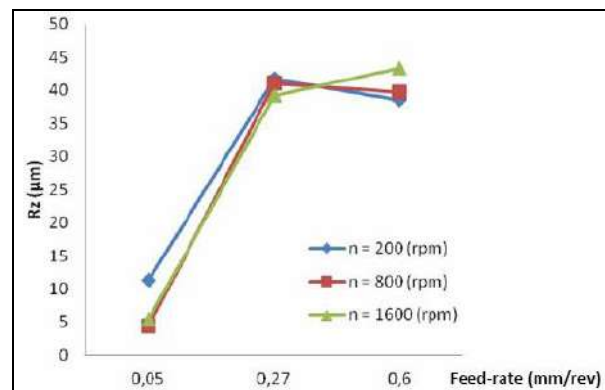
Figure 1. Variation of R_z in relation to operational parameters

The variation of R_{sk} with feed rate for all three spindle speeds applied is presented in Figure 4. R_{sk} reaches its highest value when turning the composite rod using a spindle speed equal to 800 rpm with a feed rate equal to 0.27 mm/rev.
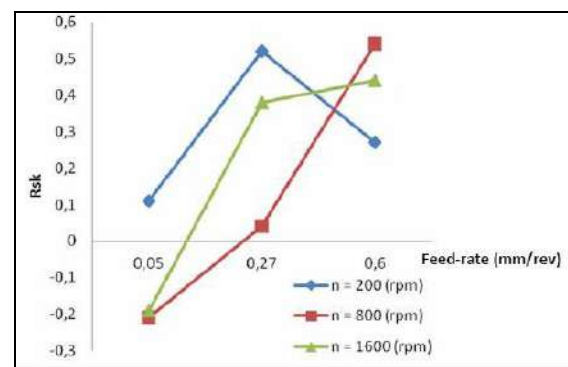
Figure 4. Variation of R_{sk} in relation to operational parameters

Kurtosis (R_{ku}) typically describes the sharpness of the probability density of the profile. When $R_{ku} < 3$ the distribution curve is said to be platykurtoic and has relatively few high peaks and low valleys. When $R_{ku} > 3$ the distribution curve is said to be leptokurtoic and has relatively many high peaks and low valleys. The variation of R_{ku} in relation to operational parameters is presented in Figure 5. Measured values of this parameter are in the range of around 3 indicating normally distributed high peaks and low valleys.

Bearing (Abbott) curves and bearing ratio parameters are useful tools for analyzing surface morphology in relation to tribological performance [18]. The R_{tp} (Abbot) parameter

representing the cross-section of surface material at 1 μm under the highest peak was determined for all conditions examined; see Figure 6. Note that R_{tp} is used primarily for the analysis of load carrying surfaces.
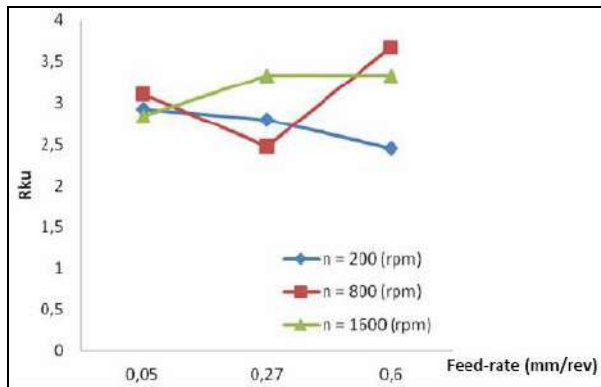
Figure 5. Variation of R_{ku} in relation to operational parameters
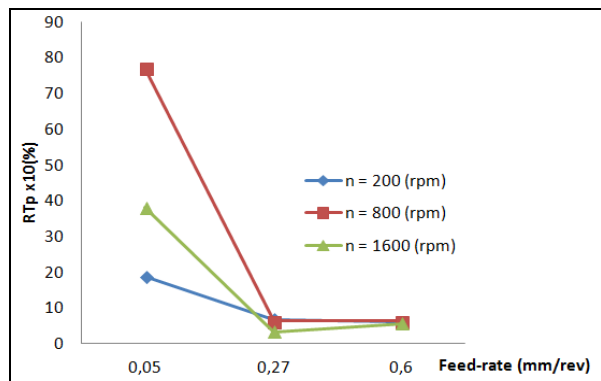
Figure 6. Variation of Abbott curve parameter R_{tp} vs. operational parameters
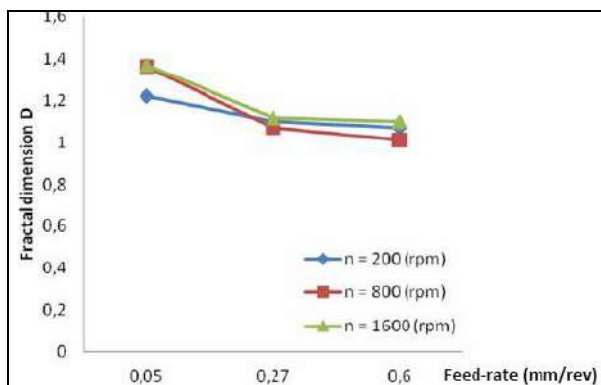
Figure 7. Variation of fractal dimension *D* with operational parameters

Fractal-based methods for describing surface texture have attracted great interest since they can provide information that conventional surface roughness parameters cannot [9]. The fractal dimension *D* was calculated via the power spectrum method and it appears rather insensitive to operational parameters; see Figure 7. Note that fractal analysis has not been introduced so far in ISO surface metrology standards; see for example ISO 4287: 1997, but it is used and calculated via in-house and commercial software [9]. Moreover, application of fractal analysis to machined surfaces obtained by tool of defined geometry, as in the case of turning, is still open to discussion.

4.2. Statistical analysis

Statistical analysis was performed in order to examine the effect of spindle speed and feed rate upon roughness parameters under examination. The statistical software MINITAB® 17 was used for conducting the corresponding analysis and to obtain the outputs for results interpretation. Main effects and interactions plots were generated to study the influence among parameters' levels and their combinations respectively, on R_a and R_t roughness parameters. Figure 8 shows that average roughness (R_a) is greatly affected by feed-rate, followed by spindle speed whilst significant interactions are noticed mainly between the second and the third level for spindle referring to the second level for feed-rate; see Figure 9.
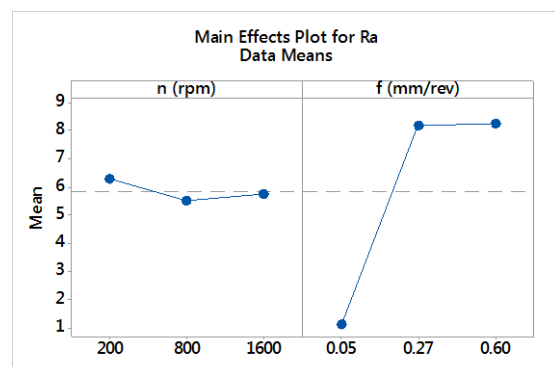
Figure 8. Main effects plot using the data means for R_a

Similar analysis was performed to interpret the effect of cutting conditions on maximum roughness (R_t). Figures 10 and 11 illustrate the main effects of independent variables and their interactions. According to these outputs, R_t is strongly affected by feed-rate which exert the largest influence against spindle speed considering the experiment's preset levels.
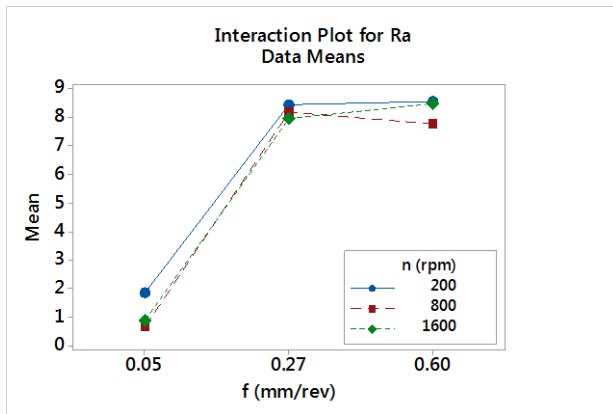
Figure 9. Interactions plot using the data means for R_a
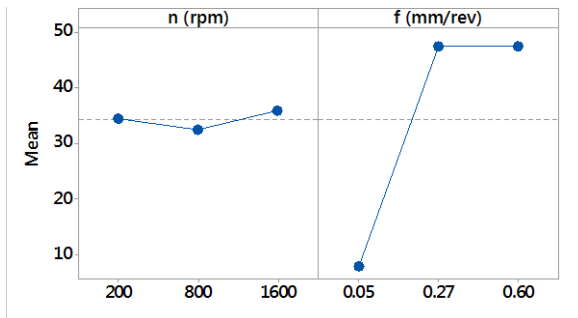
Figure 10. Main effects plot using the data means for R_t
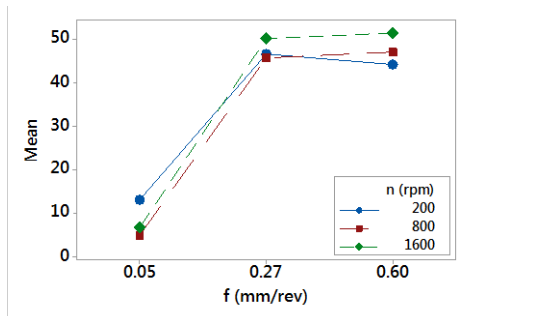
Figure 11. Interactions plot using the data means for R_t

More accurate results concerning the effects of machining parameters on the responses of R_a and R_t can be obtained by conducting ANOVA analysis; see for example Refs [12, 19].

4.3. Prediction models for roughness parameters

Based on the experimental results presented above; see also Table 1, several prediction models of different types can be formulated. These models typically include: a) the general linear model for first-order; b) the least squares approach – second order model and c) the exponential one [17].

During present investigation full quadratic models were developed for all roughness responses; see Table 2 whilst exponential models were implemented for R_a and R_t; see Table 3.

By examining coefficient of determination (R^2 values in Table2 it is evident that R_a, R_z, R_q, R_t and D parameters are highly correlated to their corresponding coefficients and independent parameter values; whilst the opposite is revealed for R_{sk} R_{ku} and R_{Tp}. These parameters remain uncorrelated and their models cannot be employed.

Exponential models; see Table 3, are characterized by lower coefficient of determination (R^2); therefore their use for prediction is not reccomended.

Table 2. Full quadratic regression equations for the prediction of roughness parameters.

Response	Regression model	R^2 (%)
R_a	= -0.107-0.0027×n+49.68×f+10^{-6}×n^2-57.97×f^2+10^{-2}×n×f	99.75
R_t	= 0.85-0.014×n+268.5×f+6×10^{-5}×n^2-324.7×f^2+0.016×n×f	99.54
R_z	= 1.57-0.011×n+230.6×f+3×10^{-5}×n^2-279.1×f^2+0.013×n×f	99.62
R_q	= -0.12-3×10^{-3}×n+59.8×f+10^{-5}×n^2-70.6×f^2+2×10^{-3}×n×f	99.78
R_{sk}	= 0.114-7×10^{-4}×n+2.3×f-2.8×f^2+6×10^{-3}×n×f	80.46
R_{ku}	= 2.8+6×10^{-4}×n-2.1×f+2.3×f^2+10^{-3}×n×f	49.32
R_{Tp}	= 32.7+0.074×n-267×f-4×10^{-4}×n^2+326×f^2-0.017×n×f	76.55
D	= 1.33+4×10^{-4}×n-1.41×f+0.01×n^2+1.62×f^2-12×10^{-3}×n×f	92.62

Table 3. Exponential equations for the prediction of R_a and R_t roughness parameters.

Response	Regression model	R^2 (%)
R_a	4.7×10^4×$n^{-18.17}$×$f^{15.82}$	75.00
R_t	1.12×10^4×$n^{-13.04}$×$f^{11.47}$	62.80

5. CONCLUSIONS

A multi-parameter experimental and statistical analysis of surface texture in turning of a new aluminum matrix steel particulate composite was presented. Spindle speed (n) and feed rate (f) were treated as the independent machining parameters whilst roughness parameters including R_a, R_t, R_z, R_q, R_{sk} R_{ku}, R_{Tp} and D were treated as the responses on an L9 Taguchi orthogonal array design.

Variation patterns of roughness parameters for the composite rod tested are in same cases different from the ones observed in turning of pure Al-Mn alloy (matrix material) under the same experimental conditions

The correlation of responses with cutting variables was successfully achieved for R_a, R_z, R_q, R_t and D parameters by using full quadratic regression equations. On the contrary, it was shown that R_{sk}, R_{ku} as well as R_{Tp} remain uncorrelated according to experimental results.

REFERENCES

[1] G.P. Petropoulos, N.M Vaxevanidis, C.N. Pandazaras, A.T. Antoniadis, Control of representative turned surface textures, Wear, Vol. 257, No. 12, pp. 1270-1274, 2004.

[2] G.P Petropoulos, C.N. Pandazaras, J.P. Davim, Surface Texture Characterization and Evaluation Related to Machining, in: J.P. Davim (Ed.): *Surface Integrity in Machining*, Springer, pp. 37-66, 2010.

[3] N.M. Vaxevanidis, J.D. Kechagias, N.A. Fountas, D.E. Manolakos, Evaluation of Machinability in Turning of Engineering Alloys by applying Artificial Neural Networks, Open Construction and Building Technology Journal, Vol. 8, pp. 389-399, 2014.

[4] N.M. Vaxevanidis, N. Galanis, G.P. Petropoulos, N. Karalis, P. Vasilakakos, J. Sideris, Surface Roughness Analysis in High Speed-Dry Turning of Tool Steel, in: *Proceedings ASME 2010 10th Biennial Conference on Engineering Systems Design and Analysis*, July 12-14, 2010, Istanbul, Turkey, paper ESDA 2010-24811.

[5] G.P. Petropoulos, C.N. Pandazaras, N.M. Vaxevanidis, A. Antoniadis, Multi-parameter identification and control of turned surface textures, International Journal of Advanced Manufacturing Technology, Vol. 29, No. 1-2, pp. 118-128, 2006.

[6] G. Petropoulos, N. Vaxevanidis, A. Iakovou, K. David, Multi-parameter modeling of surface texture in EDMachining using the design of experiments methodology, Materials Science Forum, Vol. 526, pp. 157-162, 2006.

[7] W. Grzesik, S. Brol, Hybrid approach to surface roughness evaluation in multistage machining processes, Journal of Material Processing Technology, Vol. 134, No. 2, pp. 265-272, 2003.

[8] G. Petropoulos, C. Pandazaras, N.M. Vaxeva-nidis, I. Ntziantzias, A. Korlos, Selecting subsets of mutually unrelated ISO 13565-2: 1997 surface roughness parameters in turning operations, International Journal of Compu-tational Materials Science and Surface Engineering, Vol. 1, No. 1, pp. 114-128, 2007.

[9] G. Petropoulos, N. Vaxevanidis, C. Pandazaras, A. Koutsomichalis, Postulated Models for the Fractal Dimension of Turned Metal Surfaces, Journal of the Balkan Tribological Association, Vol. 15, No. 1, pp. 1-9, 2009.

[10] N.M. Vaxevanidis, N.A. Fountas, I. Ntziantzias, A. Koutsomichalis, A. Vencl, Experimental investigation and statistical analysis of surface roughness parameters in milling of PA66-GF30 glass-fibre reinforced polyamide, in: *Proc. of the International Conference BULTRIB '16*, 27-29 October, 2016, Sofia, Bulgaria, Tribological J. BULTRIB, 6, pp. 304-314, 2016.

[11] T. Özel, Y. Karpat, Predictive modelling of surface roughness and tool wear in hard turning using regression and neural networks, International Journal of Machine Tools and Manufacture, Vol. 45, pp. 467-479, 2005.

[12] N.M. Vaxevanidis, N.A. Fountas, J. Kechagias, D.E. Manolakos, Estimation of main Cutting Force and Surface Roughness in turning of Ti-6Al-4V titanium alloy using Design of Experiments and Artificial Neural Networks, in: *Proceedings of the International Conference on Engineering and Applied Sciences Optimization (OPT-i)*, June 4-6, 2014, Kos, Greece, pp. 2889-2906, 2014.

[13] A.R. Yildiz, F. Ozturk, Hybrid enhanced genetic algorithm to select optimal machining

parameters in turning operation, Proceedings of the Institution of Mechanical Engineers, Part B: Journal of Engineering Manufacture, Vol. 220, No. 12, pp. 2041-2053, 2006.

[14] B. Nowicki, Multi parameter representation of surface roughness, Wear, Vol. 102, No. 3, pp. 161-176, 1985.

[15] G.V. Seretis, G. Kouzilos, A.K. Polyzou, D.E. Manolakos, C.G. Provatidis, Effect of stainless steel flakes content on mechanical properties and microstructure of cast aluminum matrix composites; submitted to International Journal of Metalcasting, 03-2017.

[16] G.V. Seretis, G. Kouzilos, A.K. Polyzou, D.E. Manolakos, C.G. Provatidis, Effect of Graphene Nanoplatelets Fillers on Mechanical Properties and Microstructure of Cast Aluminum Matrix Composites; Nano Hybrids and Composites, Vol. 15, pp. 26-35, 2017.

[17] N.M. Vaxevanidis, N.A. Fountas, G.V. Seretis, C.G. Provatidis, D.E. Manolakos, A multi-parameter experimental and statistical analysis of surface texture in turning of a new aluminum matrix steel particulate composite, in: *Proceedings of the 5th International Conference on Advanced Manufacturing Engineering and Technologies (NEWTECH 2017)*, 5-9 June 2017, Belgrade, Serbia, pp. 387-403, 2017.

[18] G.P. Petropoulos, A.A. Torrance, C.N. Pandazaras, Abbot curves characteristics of turned surfaces, International Journal of Machine Tools and Manufacture Vol. 43, pp. 237-243, 2003.

[19] B. Stojanović, M. Babić, L. Ivanović, Taguchi optimization of tribological properties of Al/SiC/Gr composite, Journal of the Balkan Tribological Association Vol. 22 No. 3, pp. 2200-2213, 2016.

SERBIATRIB '17

15th International Conference on Tribology

Serbian Tribology Society

Faculty of Engineering University of Kragujevac

Kragujevac, Serbia, 17 – 19 May 2017

INFLUENCE OF PROCESS PARAMETERS ON THE FRICTION COEFFICIENT IN AlMg3 ALLOY STRIP IRONING DRAWING TEST

Srbislav ALEKSANDROVIĆ [1]*, Slaviša ĐAČIĆ [2], Milan ĐORĐEVIĆ [3], Vukic LAZIĆ [1], Dusan ARSIĆ [1]

[1] Faculty of Engineering, University of Kragujevac, Kragujevac, Serbia
[2] Coal Mine, Pljevlja, Montenegro
[3] Faculty of Technical Sciences, University of Pristina, Kosovska Mitrovica, Serbia

Abstract: *Presented in this paper are the results of experimental investigations of influence on friction in the stripe ironing process with double thinning. Applied was modified mathematical model for evaluating influence of lateral force, contact pressure and average absolute roughness height on friction coefficient. Classical model in not suitable for small lateral and drawing forces, and give unreal negative friction coefficient values. Previously proposed and applied here, modified model is more appropriate. Calculated friction coefficient values in that model are more according to reality. 20 mm wide and 3.0 mm thick strips of AlMg3 alloy sheets were used in the single and three-phase process with a maximum thinning deformation of 27%. Appropriate lubricating grease was used in conditions of lower speed of 20 mm/min. Three phase process was realized with variable lateral force of 4, 8 and 12 kN. The applied experimental test procedure enables the precise quantification of lateral force, contact pressure and roughness influence on friction to be established. Test also enables evaluation of lubricants quality.*

Keywords: *modified stripe ironing test, Al alloy, friction coefficient.*

1. INTRODUCTION

Ironing is metal forming process which combine characteristics of sheet metal forming and massive (bulk) forming. Thinnig strain reach over 25%, and contact pressure over 1000 MPa [1]. It is well known application of the ironing process in manufacturing different kinds of thin walled cans. World annual production (especially for beverage cans) are more than billion pieces. In the tribologycal sense, ironing process is one of the most severe, owing to the high surface expansion, large plastic strains and high normal pressure at the tool-workpiece interface. Considering previous notice more researchers still interested in ironing. During

the last decade significant attention is paid on investigation of environmentally friendly lubricants application [1, 2, 3].

In order to quantify the performance of the individual lubricants, a different experimental test methods has been developed. Wide applying have double (or single) sided thinning stripe ironing test in different variations [4, 5, 6, 7, 8]. Following mathematical model is mainly so called Schlosser model [4]. Despite its evident deficiency or inaccuracy was indicated yet in article [5], and in [9] detailed motivated, however that model is applying even in recent extensive researches [8]. In authors investigations [9, 10, 11] proposed was different, or corrected mathematical model usable in all conditions with real results.

In this paper presented is another verification of above mentioned authors model. It is experimental investigation of process parameters (lateral force, nominal pressure, roughness) influence on friction coefficient in double sided ironing of AlMg3 alloy stripes.

2. EXPERIMENT

2.1 Device description, physical and mathematical model

The special device for physical modeling the symmetrical contact between the sheet strip and die was used for experimental investigation (Fig. 1 and Fig. 2). The sheet metal sample (strip 2) is placed in the jaws (1) vertically. In the initial phase the thinning makes such that the right-hand sliding tool element (6 right) acts upon the strip by lateral force F_D (Fig. 2). Due to the fixed left side tool element (6 left) and the action of right element, the even double sided ironing of the strip is realized.
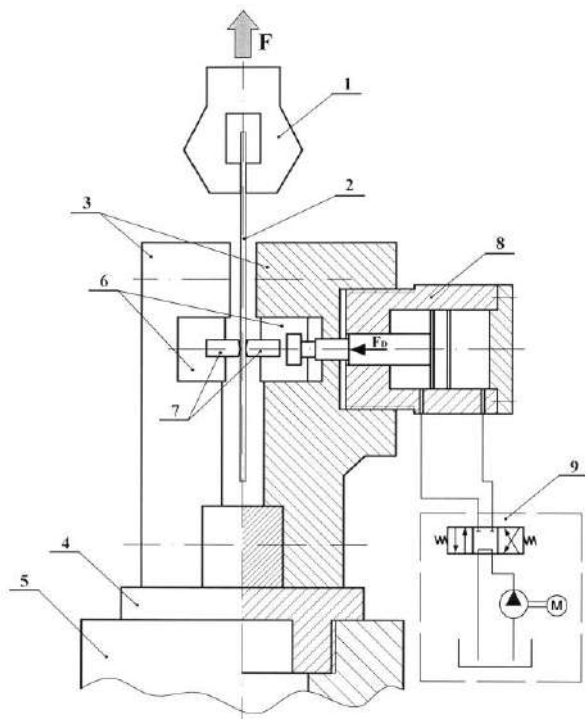
Figure 1. Experimental device scheme

After the initial thinning deformation was realized, the tensile force F (Fig. 2) begins to act, and the ironing process continues until the sample length is executed. The main action of

the ERICHSEN 142/12 laboratory hydraulic press is used as the tensile force across the range of 0-20 kN at speed of 20 mm/min. The lateral force is realized by the hydro-cylinder (8). The maximum range of the lateral force is 0-50 kN. The piston pushes right hand element (6) which is coupled to the sliding element (7). The hydro cylinder (8) is powered by the independent hydraulic aggregate (9), which contains the filter, electric motor, pump, two position directional control valve, adjustable control valve for lateral force and manometer. The data acquisition system measures drawing force dependence on the sliding length or time and the constant intensity of lateral force [10, 11, 12].
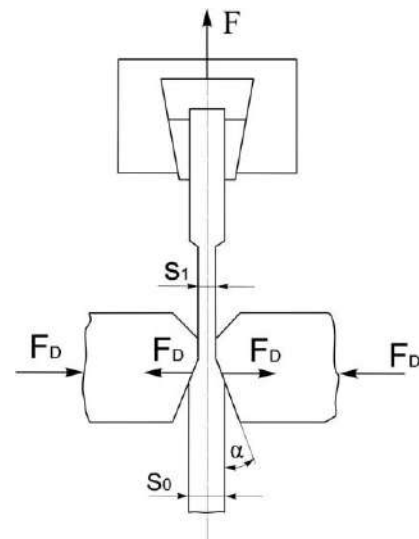
Figure 2. Forces acting scheme
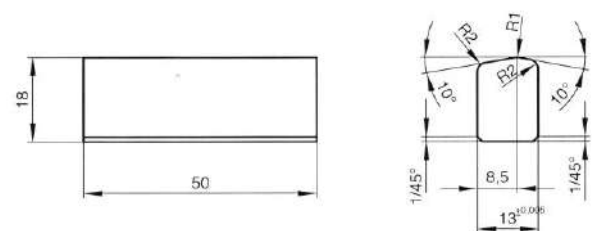
Figure 3. Tool elements geometry

Geometry of the tool elements are shown at Fig. 3. Physical appearance of elements and assembly can be seen at Fig. 4a and 4b.
For the contact elements material chosen was alloyed tool steel X160CrMoV12 with 62 HRC hardness after thermal treatment. Active surfaces are fine ground and polished with average absolute roughness height $R_a \approx 0,06$ μm.

Figure 4a. Tool elements physical appearance
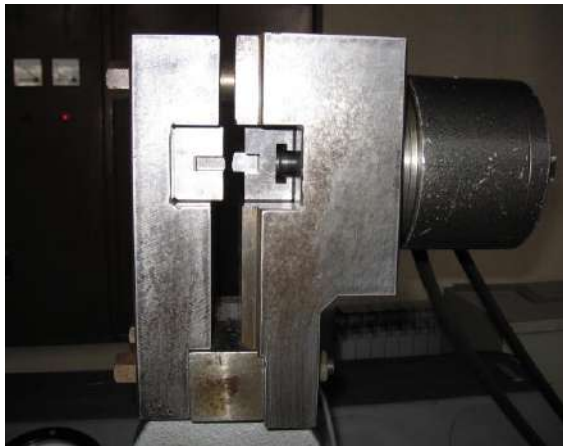
Figure 4b. View of tool assembly

According to established model [9] obtained are following formulas for friction coefficient and average calculated (nominal) pressure:

$$\mu = \frac{F}{2aF_D \cos^2\alpha + F\frac{\sin 2\alpha}{2} + 2(1-a)F_D} \quad (1)$$

$$\bar{p} = \frac{F\sin^2\alpha + aF_D \sin 2\alpha}{b(s_0 - s_1)} \quad (2)$$

Parameter "a" is determining distribution of side force F_D between inclined and small vertical contact surface and his value is in the range 0 to 1. It was adopted a=0.7 in this case. Change of parameter "a" is very small (about 1%). Inclination angle α is 10° as can be seen in Fig. 3.
Formulas (1) and (2) with current data for this experiment, are:

$$\mu = \frac{F}{0{,}171 \cdot F + 1{,}958 \cdot F_D} \quad (3)$$

$$\bar{p} = \frac{0{,}03015 \cdot F + 0{,}2394 \cdot F_D}{18{,}03(3{,}06 - s_1)} \quad (4)$$

2.2 Strip material properties

Geometry of the strip is shown in Fig. 5 and Tab. 1.
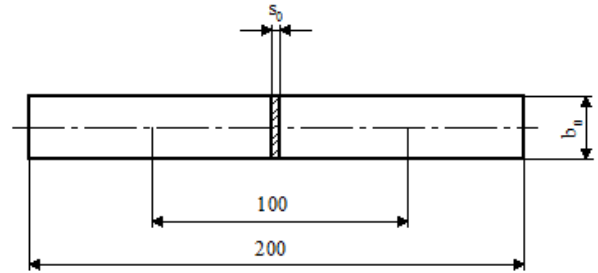
Figure 5. Strip geometry

Table 1. Strip dimensions

Material		l_0 [mm]	b_0 [mm]	s_0 [mm]
AlMg3	min	100	17,79	3,05
	average	100	18,03	3,06

For experimental investigations in this paper chosen was the aluminium alloy AlMg3. Specimens for mechanical properties were prepared accordin to standards SRPS EN ISO 6892 - 1.2012. Determined material characteristics are shown in Tab. 2.
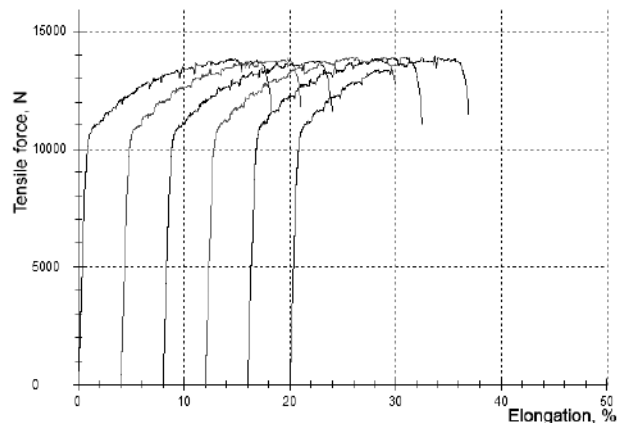
Figure 6. Tensile force - strain curves

Experimental tensile force - strain curves (Fig. 6) were obtained for six specimens with excellent repeatability. As can be seen, force

(or stress) curves have oscillatory dependence on strain which is common for Al alloys.

In Tab. 2 $R_{p0.2}$ is yield strength, R_M is tensile strength, A is percenage elongation et fracture and "n" is strain hardening exponent.

Table 2. Mechanical properties

Material		$R_{p0,2}$ [MPa]	R_m [MPa]	$R_{p0,2}/R_m$	A [%]	n
AlMg3	min	190,16	253,17	0,751	15,17	0,144
	aver.	191,31	253,56	0,754	16,29	0,150

3. RESULTS AND DISCUSSION

Within results of this experiment, diagrams of tensile forces are presented first (Fig.7, Fig.8, Fig.9). In the first case (Fig. 7) used are one phase process. Each stripe sliding process needs separate specimen with appropriate lateral force (F_D). Values are chosen according to empirical recommendation (4kN; 8 kN and 12 kN). Lateral force of 12 kN is above limiting and strip break occurs at sliding path of about 50 mm.
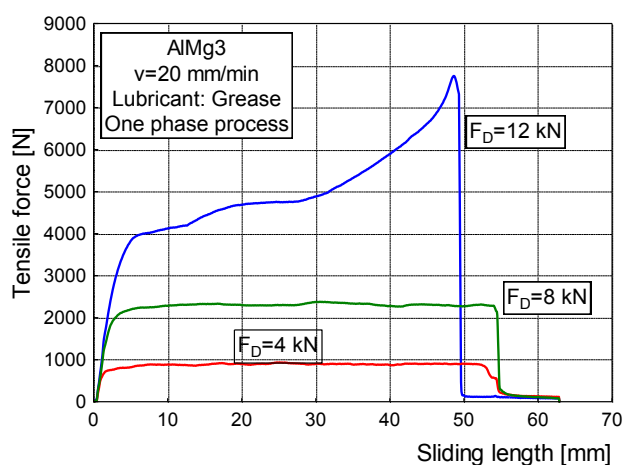
Figure 7. Tensile force vs sliding length curves

Fig. 8 represents more severe conditions. There is three phase process realized on the single specimen. First sliding is performed with lateral force of 4 kN at the path length of about 54 mm. Second phase is performed on the same specimen but ironing starts 20 mm after stripe path beginning. Lateral force was higher: 8 kN. Third sliding passage take place on the same strip also, after 40 mm path. Conditions was to severe and brake occur after about 18 mm sliding length.
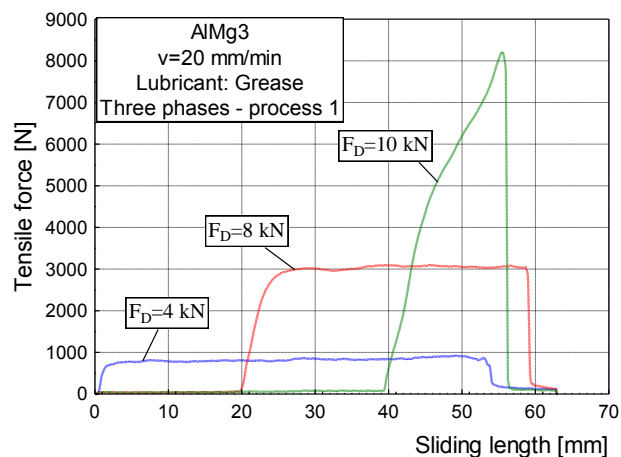
Figure 8. Tensile force vs sliding length curves

Lubricant in the process was grease (signed PRESS 626) of domestic producer, intended to drawing operations. Kinematic viscosity of that lubricant is 330 mm^2/s at 40° C.

Fig. 9 shows tensile force diagrams for three phase ironing process with constant lateral force of 8 kN in each phase. Second and third phase starts with 20 mm offset like in previous case. Sliding process is relatively smooth and no brake occurs.
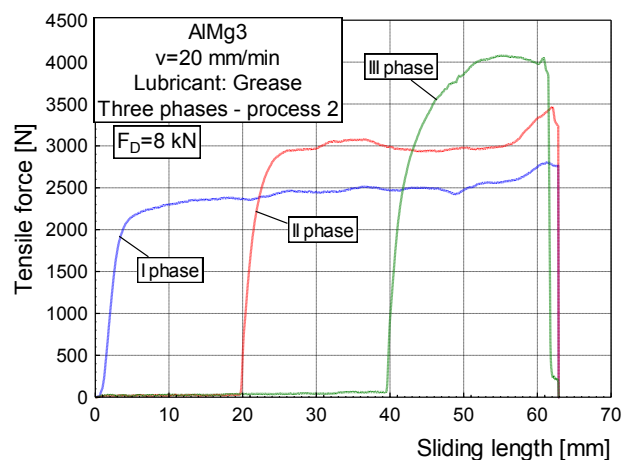
Figure 9. Tensile force vs sliding length curves

Figure 10. Strips after multi phase ironing

In Fig. 10 is the strips appearance after multi phase ironing.
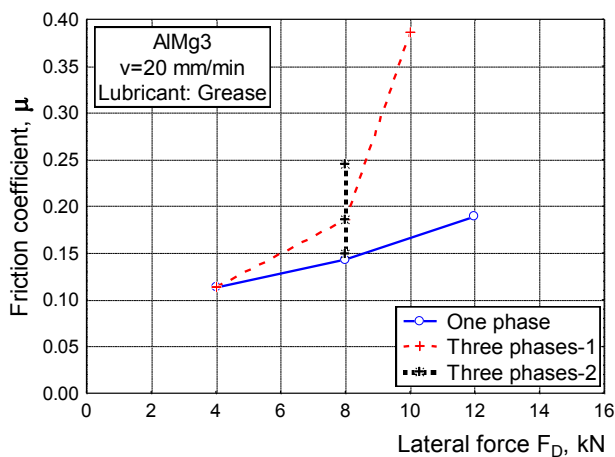
Figure 11. Friction coefficient dependence on lateral force

In this study investigated are the influences of lateral force, calculated (nominal) pressure and average roughness on the friction coefficient (Fig. 11, 12 and 13).

Dependences given at the. Fig. 11 determined are according to terms (1) and (3). For tensile force F intensities was adopted average values. For one phase process friction coefficient (μ) have relatively small values, even in case of 12 kN lateral force where break occurs.

Diagrams for three phase processes clearly shows that μ increase, and it is in accordance with heavier process conditions. Especially in the three phase process with lateral force increasing (proc. 1 in Fig. 11), μ reached maximum value.
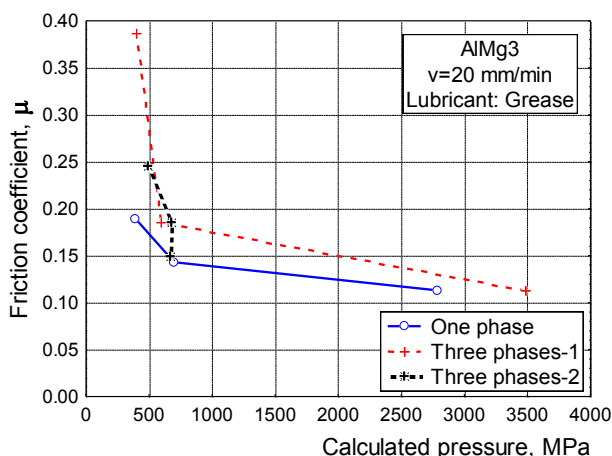
Figure 12. Friction coefficient dependence on calculated pressure

Fig. 12 shows friction coefficient dependence on calculated pressure according to terms (2) and (4). For that parameter must be noticed that it is only calculated or nominal parameter, which inversely depends on strip thinning strain. Because of that, pressure values are reached unreal intensities for very small thinning. So, calculated pressure need to be considered like parameter related to thinning strain, rather than real pressure.
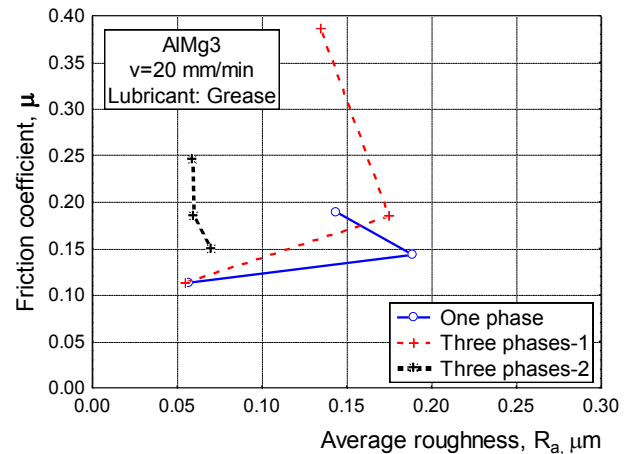
Figure 13. Friction coefficient dependence on average roughness

For diagrams at Fig. 12 need to be notice that the process starts at the high calculated pressure values and goes to lower values (from right to left side of diagram). As can be seen from Fig. 12 friction coefficient increasing with thinning strain increasing, or calculated pressure decreasing.

Relation between friction coefficient and average roughness R_a (Fig. 13) gives somewhat unexpected values in one phase and three phase (process 1) cases. In third stage μ increases while R_a decreases. Expectation is opposite. Possible explanation is in the way of μ calculation and R_a determination. μ is calculated according to formulas (2 and 4) and depends only of tensile force F and lateral force F_D . In other side R_a is determined experimentally, by measuring. Also, it is possible to occur polishing effect in the third stage and deceasing R_a and the calculated higher μ values at the same time.

4. CONCLUSIONS

Two types of analysis was accomplished in this study. First was application and testing of authors previously proposed formulas for coefficient of friction and calculated pressure

determination in strip ironing test. Results of this study, like in some other cases, confirms usableness of proposed formulas and model, in the lubricants evaluation par example. Proposed formulas have special significance in conditions of relatively small tensile and lateral forces intensities. That is the case in aluminium ironing process.

Second was particular experiment with intention to evaluate process parameters influence on the friction coefficient. Results shows the following annotations:

a) increasing of lateral and drawing forces both, influence on friction coefficient increasing (process type 1),

b) thinning strain increasing, i.e. calculated (nominal) pressure decreasing, caused friction coefficient increasing,

c) known influence of average roughness R_a is confirmed, but polishing effect occurred in the third stage of processes with high lateral force intensities.

For further evaluations of different influences on the Al alloys ironing process (especially multi phase) needs to continue extensive experiments in different conditions.

ACKNOWLEDGEMENT

REFERENCES

[1] N. Bay et al.: Environmentally benign tribo-systems for metal forming, CIRP Annals - Manufacturing Technology, Vol. 59, No. 2, pp. 760 – 780, 2010.

[2] Y. Sagisaka, I. Ishibashi, T. Nakamura, M. Sekizawa, Y. Sumioka, M. Kawano: Evaluation of Environmentally Friendly Lubricants for Cold Forging, Journal of Materials Processing Technology, Vol. 212, No. 9, pp. 1869–1874, 2012.

[3] M. Đorđević, D. Arsić, S. Aleksandrović, V. Lazić, D. Milosavljević, R. Nikolić: Comparative study of an environmentally friendly single-bath lubricant and conventional lubricants in a strip ironing test, Journal of Balkan Tribological Association, Vol. 22, No.1A-II, pp. 947-958, 2016.

[4] D. Schlosser: Beeinflussung der Reibung beim Streifenziehen von austenitischem Blech: verschiedene Schmierstoffe und Werkzeuge aus gesinterten Hartstoffen, Bander Bleche Rohre, No. 7-8, pp. 302-306, 1975.

[5] P. Deneuville, R. Lecot: The study of friction in ironing process by physical and numerical modelling, Journal of Materials Processing Technology, Vol. 45, No. 1-4, pp. 625–630, 1994.

[6] J.L. Andreasen, N. Bay, M. Andersen, E. Christensen, N. Bjerrum: Screening the performance of lubricants for the ironing of stainless steel with a strip reduction test, Wear, Vol. 207, No. 1-2, pp. 1-5, 1997.

[7] H.C.E. van der Aa, M.A.H. van der Aa, P.J.G. Schreurs, F.P.T. Baaijens a, W.J. van Veenen: An experimental and numerical study of the wall ironing process of polymer coated sheet metal, Mechanics of Materials, Vol. 32, No. 7, pp. 423-443, 2000.

[8] D. Adamovic, M. Stefanovic, V. Mandic: *Modelling of ironing process*, Faculty of Engineering, University of Kragujevac, Kragujevac, 2012. (In Serbian)

[9] S. Aleksandrovic, M. Stefanovic , V. Lazic, D. Adamovic, M. Djordjevic, D. Arsic: Different ways of friction coefficient determination in stripe ironing test, in: *Proceedings of the International conference on Tribology SERBIATRIB 2013*, 15–17. 05. 2013, Kragujevac, Serbia, pp. 359-363.

[10] S. Djacic: *Metal forming with double sided ironing*, Master thesis, Faculty of Engineering, University of Kragujevac, 2016. (In Serbian)

[11] M. Djordjević, S. Aleksandrović, V. Lazić, M. Stefanović, R. Nikolić, D. Arsić: Experimental analysis of influence of different lubricants types on the multi-phase ironing process, Materials Engineering - Materiálové inžinierstvo, Vol. 20, No. 3, pp. 147-152, 2013.

[12] M. Djordjević, S. Aleksandrović, D. Arsić, V. Lazic: Experimental-numerical analysis of contact conditions influence on the ironing strip drawing process, Industrial lubrication and tribology, the article DOI (10.1108/ILT-10-2015-0156), 2016.

EFFECT OF COATING THICKNESS ON DIE WEAR

Hülya ALKAN [1,*], Eyyup GERÇEKCİOĞLU[2]
[1]Boycelik Metal SAN.TİC.A.Ş, Kayseri, Turkey
[2]Erciyes University, Kayseri, Turkey
* Corresponding author: huyla.alkan@boycelik.com.tr

Abstract: *In wire drawing process, the high carbon including of 0.65 C% steel wire rods were coated with phosphate before drawing to make drawing process easy and gain corrosion resistance. Thickness of coating has many effects on drawing process. The most important effect of the coating thickness is about die wears. In this study, two different wire rods which have different coating thicknesses were investigated. Wire rods coated with phosphate by changing immersion time in phosphate bath so the thickness of coating was different. The coating thicknesses were measured by weigh difference method. The wire rods which were coated 5,28 g/ m^2 and 10,16 g/ m^2 have observed after cold drawn. The expansion of dies measure by digital micrometer. The first wire rod which was coated 5,28 g/ m^2 made the diameter of dies bigger average 18,1%. However the second wire rod which was coated 10,16 g/ m^2 made the diameter of dies bigger average 12,1%. This results Show us that the thickness of coating is so important in wire drawing process. The more thickness of coating means the more die life and less die wear per unit time.*

Keywords: *coating thickness, die wears, wire drawing, spring wire, phosphate coating*

1. INTRODUCTION

Wire drawing process is one of the most common process in metal working.Wire drawing process can be defined as thinning of thick-sectioned wire by going through the die [1].

Wire enters many dies which are placed consecutive to reach the final diameter. In wire drawing machine, the wire firstly goes into of the lubrication box and next it goes to the die box. After the die box wire is wrapped on the block. The blocks transfer the wire to another steps. In additon to this, the surface of blocks cool the wire. These steps are repeated for the number of blocks [2].

Figure 1. A section of wire drawing die

When two surfaces contact each other frictional force occur and this frictional force causes wearing on the surfaces [3]. It is impossible that you eliminate frictional force completely. However, it's not possible to

prevent wearing caused by friction for now the frictional force can be minimized by some methods. Thismeans that the reducing frictional force is to have more die life without wear on dies.
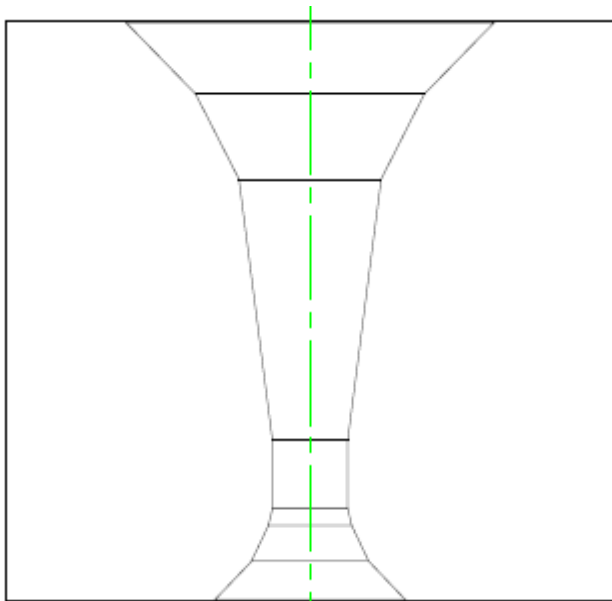
Figure 2. Technical drawing of die section
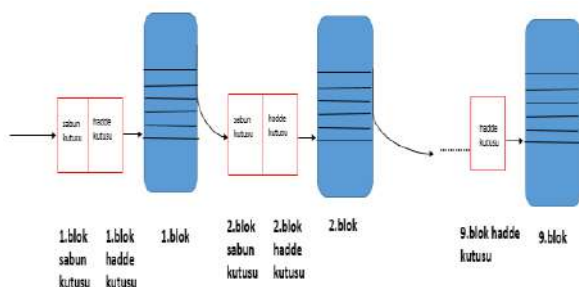
Figure 3. Wire drawing schematic representation

The wire drawing process is based on thinning wire through the die so there occur serious contact area between wire and die [4]. To reduce the friction because of contact,some additional things are used to reduce the frictional force caused by the contact. One of them is powder lubricants known as soap [5]. Another important method is to coat the surface of the wire rod with phosphate. Phosphate coating interacts with the soap and this ensures the wire more slipperness. However, the phosphate coating increases the corrosion resistance of the drawn wire.

With the development of technology high-speed wire drawing machines produce for more efficient production by increasing the production volume per unit time. However, it

is not enough to have only fast machines to achieve this. There will be many obstacles to overcome with high speed [6]. A faster process means more friction and more temperature formation. These parameters affect the wearing in a short time [7]. Therefore the most suitable equipment and technology should be provided for the working conditions and some improvement should be made.

The process of increasing the thickness of the phosphate coating on the surface of the wire rod is the first improvement on the coating side.In the wire drawing process, the coating thickness has certain limits determined by the plant's standard. It's expected that the wire which is coated according to the standart and under the limit of standard affect the wearing of die will be different. The wearing time rises with increasing coating thickness to a certain point. However, after a certain value, the curve of wear duration continues constantly.

2. COATING PROCESS

Before wire drawing, the wire rods go through a preliminary setup for he drawing process. This preliminary setup contains the cleaning of surface and coating. To get the good coating the first thing should be done is cleaning the surface of wire rod [8]. There are two different methods to clean the surface from the rust, scale etc. One of them is cleaning by mechanical desclaing and the other one is cleaning by chemicals[9]. It is generally use hydrocloric (HCl) acid and sulfuric acid (H_2SO_4). In this paper, the experiments made by using HCl. Hence wire rods immerse the HCl baths to clean the surface. After cleaning the surface, the wire rods go to the rinsing bath to get rid of the excess acid on surface. The wire rod which is cleaned by acid goes to the activation bath. Activation bath prepares the surface of wire rod to coating. Next step after activation, the bath is the most important one, phophate bath. The wire rod immerses the phosphate coating bath and stay here for a couple of minutes. The thickness of coating depends on

immersing time. The thickness of coating increases by immersing time in the bath but after a value it stays constant.If the rod stays overtime then the thickness of coating decrease because of the reverse reaction. The last step of this prosess is to immersing the rinsing and notralization bath. When these steps are completed the wire rod is ready to drawing.

Figure 4. Phosphate coating bath

Table 1. Ideal phpsphate bath parameters of a wire drawing plant

Total acidity point (a)	60
Phosohate point (b)	30
Stability of bath (a/b)	2
Temperature of bath	75 ^oC
Thickness of phosphate coating	8-12 g/m^2

3. EXPERIMENTAL TESTS

In this study, in order to obtain a coating thickness of 8-12 g/m², which is normally idealized in the operating conditions, two different wire rods observed which is stayed in the phosphate bath in 1 and 6 minutes. Because of the different immersing time these two wire rods have different phosphate coating thicknesses. While drawing these rods, some parameters measured to understand the effects of the coating thickness on the die wear. The coating thickness of wire rod which is stayed in the phosphate bath for 1 minute is measured as 5,28 g/m². On the other hand thickness of other wire rod which is stayed in the phosphate bath for six minutes is measured as 10,16 g/m².

Table 2. The measurement parameters ofphosphate coating

Rod Properties	sample	2.sample
Diameter (mm)	5,57	5,76
Length (mm)	1080	880
Initial weight (gr)	20,0177	16,8528
Final wieght (gr)	19,9985	16,8444
Immersing time (min.)	6	1
Coating thickness (g/m²)	10,16	5,28

In order to determine the relation of the coating thickness to the immersing time, the coating thickness was measured by immersing for 6 different periods in 6 different samples of phosphate coating bath. This experiment was repeated twice to ensure that the hypothesis was correct about the relations between immersing time and coating thickness and the results were recorded as shown in Fig.5.
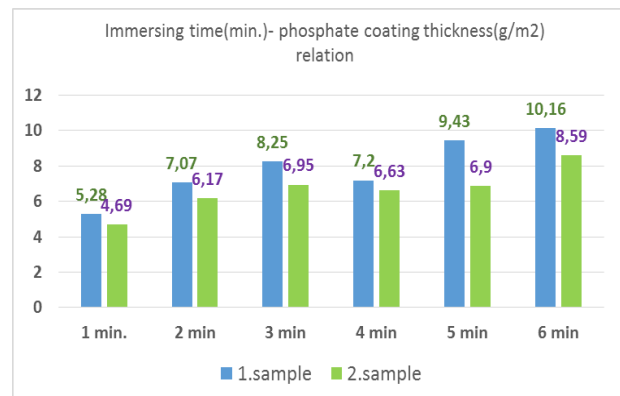
Figure 5. Relation between immersing time and phosphate coating thickness

The thickness of phosphate coating on wire rod was measured by the difference of weights [10].

3.1 Measurement method of phosphate coating thickness

First of all a special chemical soluion should be prepare. Thesolution is prepared by mixing the chemicals below.

1. 100 gr 0,1N NaOH
2. 90 gr EDTA
3. 4 gr TEA (treatonomil)
4. 1000 ml pure water

Next step is to put this solution in a beaker. After that some wire rod samples which is phosphate coated cut about 100 mm

length.The special solution which is prepared to measure the coating is heated to 75 ^{o}C.While the solution is heating, the weight of phosphate coated samples can weigh (initial weight) and record by using sensitive scale. Then the samples put the solution inside of the beaker and leave here for about five minutes. This solution helps to remove the coating on surface. After five minutes, the samples are taken out and rubbing the surface with a tissue to remove the coating on surface. Black colour is seen on the tissue after rubbing. The rubbing is continued until the black color is disappear. The coating is compeletely rinsed then the samples are washing with water and dried with air or some other tools to prevent any water on surface.As last step the samples are weigh again by using sensitive scale and record.

Figure 6. Wire rod samples after rubbing

By using the parameters recorded, the thickness of phosphate coating is calculated with the Equation (1).

$$mA = \frac{\Delta m}{A}\left(gr\!\!\left/m^2\right.\right)$$ (1)

Equation 1. The formulation of weight difference
Δm= Initial weight (gr)-Final weight (gr)
A=π.d.l
Π=3,14
d=diameter of wire rod sample (mm)
l= length of wire rod sample (mm)

The three wire rods which were left in the phosphate bath for one minuteused a wire drawing machine which has 9 blocks and drawn with 18 m/s from 5,50 mm to 2,38 mm. The phosphate coatings of these three rods are 5,28-5,93-7,05 gr/m^2,respectively. Before using these wire rods the diameter of wire

rods were measured and recorded. When these tree wire rods finish the diameter of dies measured and compared the initial measurement. The same process (same machine, same speed, same inlet and outlet diameter) repeated for other wire rods which were left in the phosphate coating bath for six minutes. The coating of this wire rods are 8,09-8,53-9,56 gr/m^2. The results shown at the Tables 3 and 4.

Table 3. The measurements of dies after using the wire rods which were left the phosphate bath for 1 minute.

Block number	Measurement-1 (before the trial)	Measurements of die's diameter (mm)			% die diameter growth (in the end of the
		Thickness of coating 5,28 gr/m2 Measurement-2 (After using 1.wire rod)	Thickness of coating 5,93 gr/m2 Measurement-3 (After using 2.wire rod)	Thickness of coating 7,05 gr/m2 Measurement-4 (After using 3.wire rod)	
1	4,880	4,888	4,891	4,891	22,5%
2	4,348	4,350	4,353	4,353	11,5%
3	3,900	3,900	3,902	3,902	5,1%
4	3,520	3,502	3,523	3,523	8,5%
5	3,200	3,201	3,204	3,203	9,4%
6	2,940	2,940	2,941	2,942	6,8%
7	2,704	2,706	2,707	2,723	70,3%
8	2,507	2,509	2,510	2,512	19,9%
9	2,372	2,368	2,372	2,374	8,4%

Table 4. The measurements of dies after using the wire rods which were left the phosphate bath for 6 minute.

Block number	Measurement-1 (before the trial)	Measurements of die's diameter (mm)			% die diameter growth (in the end of the
		Thickness of coating 8,09 gr/m2 Measurement-2 (After using 1.wire rod)	Thickness of coating 8,53 gr/m2 Measurement-3 (After using 2.wire rod)	Thickness of coating 9,56gr/m2 Measurement-4 (After using 3.wire rod)	
1	4,892	4,893	4,9	4,901	18,4%
2	4,363	4,365	4,366	4,367	9,2%
3	3,910	3,912	3,911	3,912	5,1%
4	3,534	3,533	3,535	3,536	5,7%
5	3,212	3,211	3,213	3,214	6,2%
6	2,954	2,953	2,955	2,955	3,4%
7	2,710	2,722	2,721	2,721	40,6%
8	2,525	2,525	2,527	2,528	11,9%
9	2,375	2,375	2,377	2,377	8,4%

4. CONCLUSION

The wire rods which are immersed in the phosphate coating bath for different times are coated with different thickness. One wire rod approximately 1500 kg. In this study,there are

two groups of wire rods. First group left the phosphate coating bath for one minutes and second group left the phosphate coating bath for six minutes. Each group has three wire rods and these wire rods were finished abut two hours in the wire drawing machine which worked 18 m/s.

For first group, the results shown that the diameter of dies grown up avarage %18,1 in two hours. Beside this for second group, the diameter of dies grown up avarage %12,1 in two hours.

It has been confirmed that the increase of coating thickness make the contact between die surface and wire rod by decrease the coefficient of friction while drawing. Because of this situation the wearing of die period extend. Thus the hypothesis was confirmed by experiments.

ACKNOWLEDGEMENTS

REFERENCES

[1] Ali Güzey, Demirsel tellerin üretim sürecinin incelenmesi, yük.Lis.Tezi, Trakya Üniv.Fen Bilm.Enst., 2009, Edirne.

[2] R.N. Wright: Wire Technology, Process Engineering and Metallurgy, pp. 286-287, 2011.

[3] W.T. Becker, R.J.Shipley: *Failure Analysis and Prevention*, ASM Handbook, ASM International, Vol.11, 2002.

[4] R.Chandramouli: Wire and Bar drawing-Basic concepts, Joint Initiative of IITs and IISc – Funded by MHRD pp. 1-8, Sastra University, Thanjavur- 613 401.

[5] V. Marrel, Wire Drawing Saop Lubrication: Principles and Factors Affecting Selection, September 2007.

[6] Z. Muskalski: Selected Problems From the High Carbon Steel Wire Drawing Theory and Technology, Vol. 59, pp. 532-533, 2014.

[7] P.A. Engel: *Impact Wear, Friction, Lubrication and Wear Technology*, ASM Handbook, ASM International, Vol.18, 1992.

[8] C. Zhang, Z Chu, F. Wei, W. Qin, Y. Yang, Y. Dong, D. Huang, L. Wang: Optimizing process and the properties of the sprayed Fe-based metallic glassy coating by plasma spraying, Surface and Coating, Vol. 319, pp. 1–5, 2017.

[9] P.Gillström, M. Jarl: Wear of die after drawing of pickled or reverse bent wire rod, Wear, Vol. 262, pp: 858–867, 2007.

[10] Weighing by Difference, available at: http://www.vanderbilt.edu/AnS/Chemistry/courses/chem104/experiment1/weighing/weighing_2.htm, accessed: 30.03.20

A RESEARCH OF CONTACT AND BENDING STIFFNESS ACCORDING TO SURFACE ROUGHNESS PARAMETERS AND APPLICATION FOR CURVIC MODEL

Yonghun YU[1], Bora LEE[1], Yongjoo CHO[1,*]

[1] School of Mechanical Engineering, Pusan National University, Busan, South Korea
*Corresponding author: yjcho@pusan.ac.kr

Abstract: This paper studied about the effect of contact stiffness in the coupling system by the surface roughness parameter. Coupling is connected elements between the axes. It is mainly used in motors, generators and decelerators, and so on. Coupling application can not only reduce the stiffness of the overall system, but it also changes dynamic behaviour. The roughness profile of the contact surface is the most important parameter to determine the contact stiffness. Many studies have been carried out from GW (Greenwood and Williamson) statistical model related to the contact behaviour. This study also had been applied to the contact and bending stiffness analysis by using the GW model and Hertz contact theory. The GW model assumed the contact of rough asperities to the contact of spheres which has the same radius. Based on the results of Nayak's random processor study, the contact stiffness is calculated by using three characteristics of rough surface: average radius of asperity, density of asperity and standards derivation of the asperity height distribution. We have investigated the changes in contact stiffness in the elastic and elastic-plastic regions according to the three surface parameters mentioned above. In addition, the GW model applied to RFR (Rod-Fastened Rotor) in this paper. In RFR, a Cuvic coupling is widely used in which the contact area is widened by machining gear teeth on the contact surface. Therefore, this research is to bring off the contact and bending stiffness analysis method of the Curvic coupling. For exact analysis, we calculated the tangential force on the contact surface due to the slope by dividing into two conditions: a slip, and no slip and considered exact orthogonal projection along with the geometric shape of the Curvic coupling. The result show that the Curvic coupling has bigger contact stiffness and lower bending stiffness than plane coupling.

Keywords: Contact stiffness, Bending stiffness, GW model, Curvic coupling model, RFR, roughness parameter

1. INTRODUCTION

Coupling is connected elements between the axes. It is mainly used in motors, generators and decelerators, and so on. Coupling application can not only reduce the stiffness of the overall system, but it also changes dynamic behaviour. The roughness profile of the contact surface is the most important parameter to determine the contact stiffness. The contact stiffness is calculated by using three characteristics of rough surface. We have investigated the changes in contact stiffness in the elastic and elastic-plastic regions per the three surface parameters. Also, Curvic model were compared to plain model

2. THEORY

This study had been applied to the contact stiffness analysis by using the GW model and Hertz contact theory. The GW model assumed the contact of rough asperities to the contact of spheres which has the same radius. Based on the results of *Nayak*'s random processor study, the contact stiffness is calculated by using the three characteristics of rough surface: average radius of asperity, density of asperity and the standards derivation of the asperity height distribution.

2.1 Standard deviation of summit height, σ_s

The distribution of surface height is assumed Gaussian distribution in GW model.

$$\phi(z) = \frac{1}{\sqrt{2\pi}\sigma} e^{-\frac{1}{2}\left(\frac{z}{\sigma}\right)^2} \tag{1}$$

The standard deviation of rough surface heights and summit height and the relation of the two parameters are Eq 2[7].

$$\sigma_s = \left(1 - \frac{0.8968}{\alpha}\right)m_0^{1/2} = \left(1 - \frac{0.8968}{\alpha}\right)\sigma$$

$$where, \ \alpha = \left(\frac{D_{extrema}}{D_{zero}}\right)^2 \tag{2}$$

The standard deviation of summit height is an important parameter to determine gap d between two surfaces.

2.2 Average summit radius, *R*

One of assume at GW model is that all summits have the same radius. Many summits have Average summit radius and the height is randomly distributed.

$$R = 1/\overline{\kappa_m}, \qquad where \ \ \overline{\kappa_m} = 8/3\sqrt{m_4/\pi} \tag{3}$$

2.3 Density of summit, η

The density of summit means the number of summits on unit area of contact surface. It is an important parameter to determine number of contact summits when two surfaces contact.

$$\eta = D_{sum} = \frac{1}{6\pi\sqrt{3}} \cdot \frac{m_4}{m_2} \approx 1.2 \ D_{peak}^2 \tag{4}$$

3. CURVIC MODEL

3.1 Projected area

The projected area of Curvic model represented in Fig. 1. It was considered shape and position of machining tool. We can calculate exactly contact and bending stiffness by calculating the exact projected area.

3.2 Contact stiffness

Curvic model has a contact angle so that it must be considered. Due to this contact angle the contact surface can easily slip. Therefore, tangential stress is calculated dividing into stick region and slip region. The contact angle and stresses were represented in Fig. 2. Contact stiffness can be calculated by Eq (5~6).

$$F = \sigma_z A_n = (\sigma_n \sin\alpha + \sigma_t \cos\alpha)A_n$$
$$= (k_n \delta_n \sin\alpha + \sigma_t \cos\alpha)A_n$$
$$where,$$
$$stick : \sigma_t = k_t \delta_t \qquad at \ \sigma_t \le \mu\sigma_n$$
$$slip : \ \sigma_t = \mu\sigma_n = \mu k_n \delta_n \ \ at \ \sigma_t > \mu\sigma \tag{5}$$

$$k_z = dF/d\delta \tag{6}$$

3.3 Bending stiffness

At very small area, very small load is same as Eq (7). Where A_P is projected area, A_n is contact real area, δ is displacement. Also, very small moment is same as Eq (8). For dividing into stick and slip region total moment and bending stiffness calculated by Eq (9~10).

$$dF_z = \sigma_z dA_n = (k_n \delta_n \sin\alpha + \sigma_t \cos\alpha)\frac{dA_p}{\sin\alpha}$$
$$= (k_n \delta \sin^2\alpha + \sigma_t \cos\alpha)\frac{dA_p}{\sin\alpha} = \left(k_n \delta \sin\alpha + \sigma_t \frac{\cos\alpha}{\sin\alpha}\right)dA_p \tag{7}$$

$$dM = ydF = y\left(k_n \delta \sin\alpha + \sigma_t \frac{\cos\alpha}{\sin\alpha}\right)dA_p$$

$$at \ no-slip \qquad\qquad at \ slip$$
$$= y\left(k_n \delta \sin\alpha + k_t \delta_t \frac{\cos\alpha}{\sin\alpha}\right)dA_p \quad = y\left(k_n \delta \sin\alpha + \mu k_n \delta_n \frac{\cos\alpha}{\sin\alpha}\right)dA_p$$
$$= y\delta\left(k_n \sin\alpha + k_t \frac{\cos^2\alpha}{\sin\alpha}\right)dA_p \quad\ = y\delta\left(k_n \sin\alpha + \mu k_n \sin\alpha\frac{\cos\alpha}{\sin\alpha}\right)dA_p \tag{8}$$
$$= y^2\theta\left(k_n \sin\alpha + k_t \frac{\cos^2\alpha}{\sin\alpha}\right)dA_p \quad = k_n y^2\theta(\sin\alpha + \mu\cos\alpha)dA_p$$

$$at \ no-slip \qquad\qquad\qquad at \ slip$$
$$M = \left(k_n \sin\alpha + \frac{k_t\cos^2\alpha}{\sin\alpha}\right)\int_A y^2 dA_p\theta \quad M = k_n(\sin\alpha + \mu\cos\alpha)\int_A y^2 dA_p\theta \tag{9}$$

$$at \ no-slip \qquad\qquad\qquad at \ slip$$
$$G_{eq} = \left(k_n \sin\alpha + \frac{k_t\cos^2\alpha}{\sin\alpha}\right)\int_A y^2 dA_p \quad G_{eq} = k_n(\sin\alpha + \mu\cos\alpha)\int_A y^2 dA_p \tag{10}$$

Figure 1. Contact angle, displacement and stresses of Curvic model
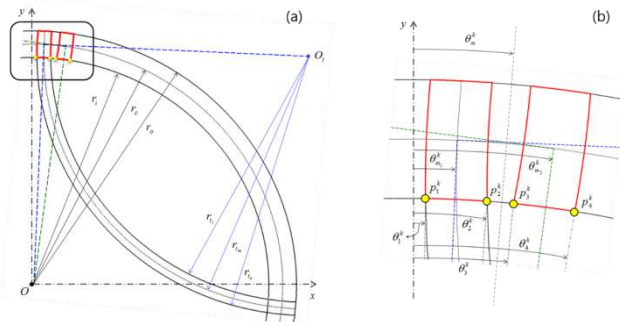
Figure 2. Projected area of Curvic model

4. MODEL
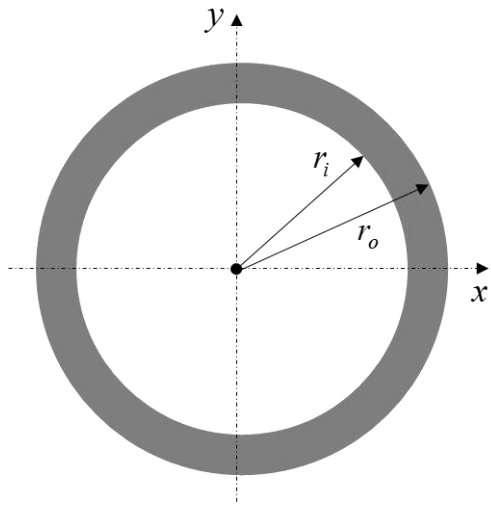
Figure 4. Projection area of contact surface

Table 1. Surface parameter

Element	R [μm]	η [1/m²]	σ_s [μm]
Value	11.59	1.525E10	0.761

Table 2. Shape and analysis condition

Element	r_i [mm]	r_o [mm]	r_{tm} [mm]	F_z [kgf]
Value	105	113.5	238.5	28,000

5. RESULT

5.1 Contact stiffness per surface parameter
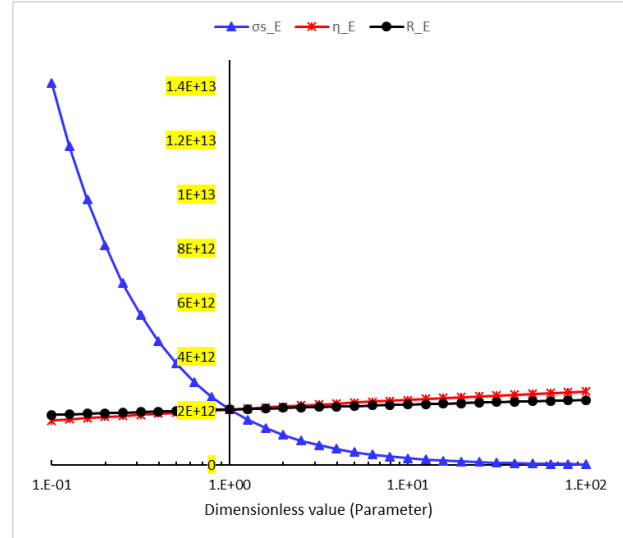
Figure 5. Contact stiffness per surface parameter
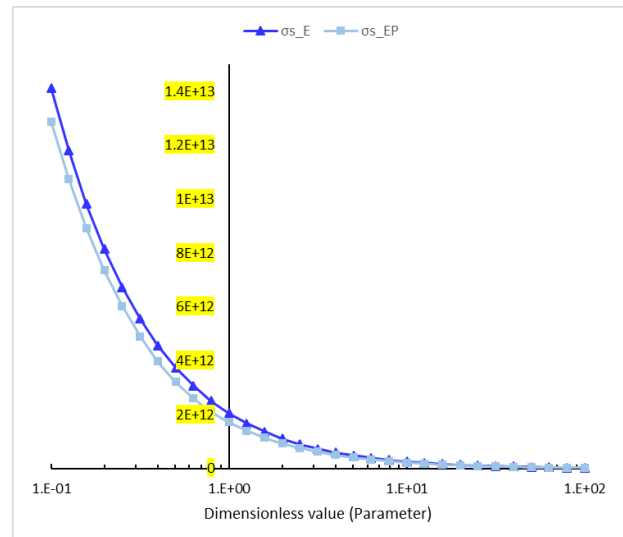
Figure 6. Elastic and Elastic-plastic contact stiffness per standard deviation of summit height
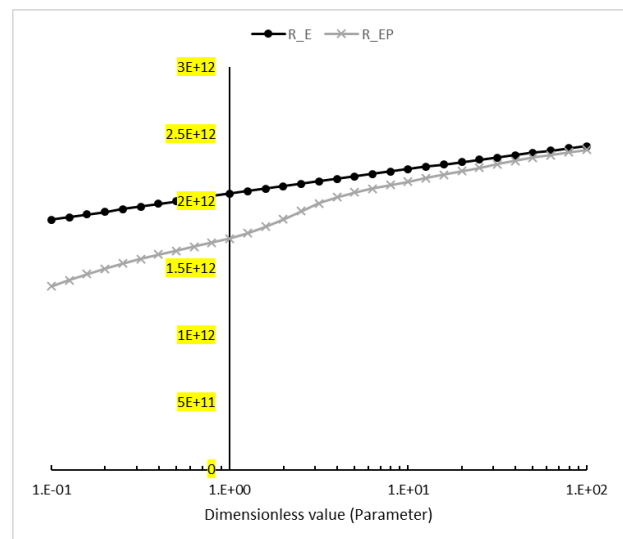
Figure 7. Elastic and Elastic-plastic contact stiffness per average summit radius
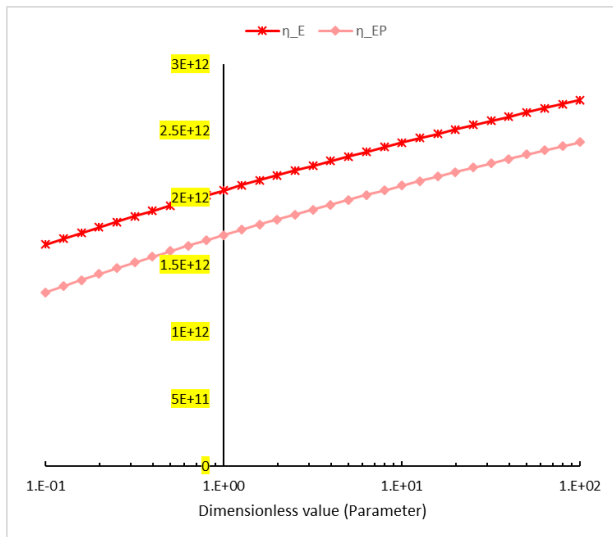
Figure 8. Elastic and Elastic-plastic contact stiffness per density of summit

5.2 Contact and bending stiffness (Curvic model)
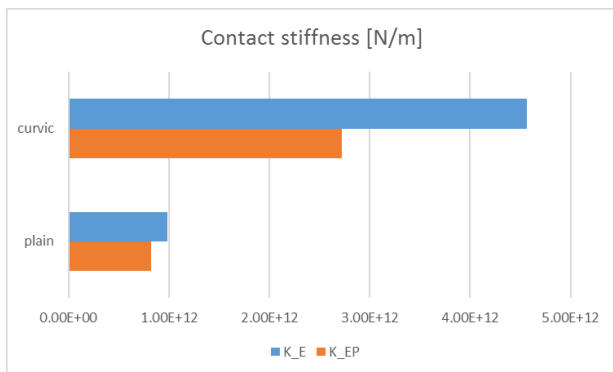
Figure 9. Contact stiffness plain and Curvic model (Elastic and Elastic-plastic region)
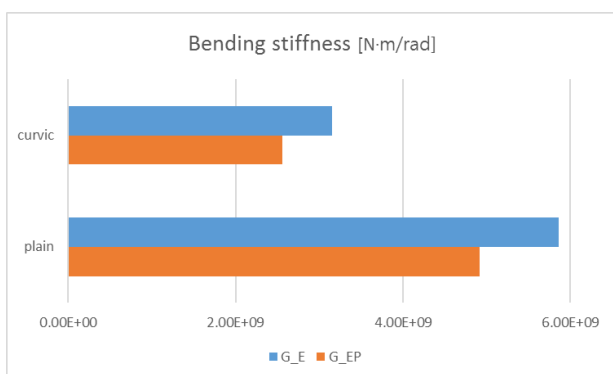
Figure 10. Bending stiffness plain and Curvic model (Elastic and Elastic-plastic region)

6. CONCLUSION

In this study, contact and bending stiffness per surface roughness parameters were calculated for elastic and elastic-plastic method. The results about two methods are same when the value is increasing for the standard deviation of summit height and average summit radius. The change of contact stiffness per standard deviation of summit height is high when the it has low value. Contact stiffness of Curvic model is higher about 3~4 times comparing with plain model and Bending stiffness is lower about 0.7 times.

REFERENCES

[1] NAYAK, P. Ranganath. Random process model of rough surfaces.
[2] YUAN, Qi, et al. Analysis of dynamic characteristics of gas turbine rotor considering contact effects and pre-tightening force. In: *ASME Turbo Expo 2008: Power for Land, Sea, and Air*. American Society of Mechanical Engineers, 2008. p. 983-988
[3] PENG, He, et al. Rotor dynamic analysis of tie-bolt fastened rotor based on elastic-plastic contact. In: *ASME 2011 Turbo Expo: Turbine Technical Conference and Exposition*. American Society of Mechanical Engineers, 2011. p. 365-373.
[4] YUAN, Shuxia, et al. Study on the Equivalent Stiffness of Heavy-Duty Gas Turbines Composite Rotor With Curvic Couplings and Spindle Tie-Bolts. In: *ASME 2011 Power Conference collocated with JSME ICOPE 2011*. American Society of Mechanical Engineers, 2011. p. 567-576.
[5] GAO, Jin, et al. Effects of bending moments and pretightening forces on the flexural stiffness of contact interfaces in rod-fastened rotors. *Journal of Engineering for Gas Turbines and Power*, 2012, 134.10: 102503.
[6] JOHNSON, Kenneth Langstreth; JOHNSON, Kenneth Langstreth. *Contact mechanics*. Cambridge university press, 1987.
[7] THOMAS, Tom R. *Rough surfaces*. World Scientific, 1998.

SURFACE ROUGHNESS ANALYSIS AT PLASMA CUTTING

Bogdan NEDIĆ[1,*], Marko JANKOVIĆ[2], Ivan PEKO[3]

[1]University of Kragujevac, Faculty of engineering, Kragujevac, Serbia
[2]Yugoimport SDPR, Belgrade, Serbia
[3] University of Split, Faculty of Electrical Engineering, Mechanical Engineering and Naval
Architecture, Split, Croatia
* Corresponding author: nedic@kg.ac.rs

Abstract: *This paper presents experimental results concerning the surface roughness variation at plasma cutting plate of structural steel St 52-3 N 4 mm thickness. For measuring roughness used Talysurf 6 device. The correlation between surface roughnes and the process input parameters is analyzed. The paper shows the effect of traverse rate, current intensity, gas pressure, and distance between the nozzle exit and the material on surfaces roughnes. Conclusions and theoretical considerations of other authors who investigated topography and quality of the surface after plasma cutting are presented.*

Keywords: Plasma arc cutting, experiment, quality of cut, process parameters, surface roughness.

1. INTRODUCTION

Plasma arc cutting is a non-conventional manufacturing process capable of processing a variety of electrically conducting materials. Stainless steel, manganese steel, titanium alloys, copper, magnesium, aluminums and its alloys and cast iron can be processed [1].

The interest in plasma arc cutting applications have increased due to the capability of this process to compete with laser cutting (higher quality but also more expensive) and oxygen-fuel cutting which is less expensive but lower cutting quality. Most of plasma arc cutting process was supported by the CNC attachment which benefits wide industries.

This method can be used with both economical and technical advantages, but this involves the development of full studies and amply theoretical and experimental

researches among all the technological system's links, in order to establish (chose) the optimal processing variant.

As in the case of other machining methods, at the plasma arc cutting, in order to obtain good results, [2] it is very important to well know the process, this meaning to exactly know what are the parameters involved in the process and their influences. Input parameters are those parameters that can be controlled, and their values are known and can be set by the operator. In this study our intention was to study the effects of plasma arc cutting parameters, such as traverse rate V mm/min, current intensity I A, gas pressure P Bar and distance between the nozzle exit and the material L mm, on surface roughness. Aim of the work was to find a better combination of these four parameters to achieve better surface roughness.

2. SOURFACE ROUGHNESS

Surface roughness is the measurement of the surface texture based on the vertical deviation of a real surface from its ideal form. The surface roughness test is conducted to determine the irregularities of the cutting surface, and gives information on whether the need for further processing.

Surface roughness is a function of material thickness defined [3] by ISO 9013, based on which can see that the thinner material have lower roughness. Surface finish by this standard is described as Rz5, the mean of 5 maximum peak-to-valley roughness depths in 5 successive sampling lengths. Unit is μm.
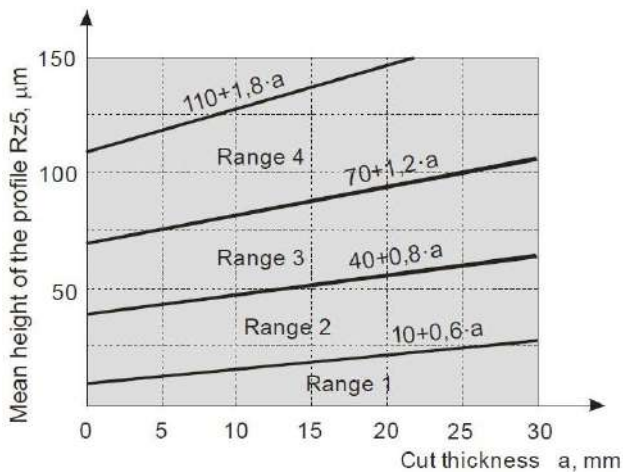
Figure 1. Influence of material thickness on Rz5 by standard "EN ISO 9013"

Researchers to analysed surface roughness mainly used Ra. Ra is the arithmetical mean of the sums of all profile values at evaluation length. Despite its inherent limitations, it is easy to measure and offers a good overall description of the height characteristics of a surface profile.

In experimental research [4] was developed mathematical model which also, shows that the thickness of the material has the greatest influence on surface roughness. This is logical because current and cutting speed is functions of material thickness.

Experimental research [5] showed that the surface roughness is inversely proportional MRR (material removal rate). Higher MRR will have lower surface roughness. This research also showed that dimensions of the dross

determine the quality of plasma arc cutting in terms of surface roughness. Small dimension of dross resulted better surface roughness.

Surface roughness is influenced by more input parameters, but the most influential are: traverse rate, current and material thickness.

In try to improve surface roughness by the concrete problems, thickness of the material can not be change, so the solution must be sought in other input parameters, therefore it is necessary to know the effect of these parameters on Ra.

Many experiments show that the most influential variable on Ra is traverse rate, but that does not mean that the optimal value of the surface roughness obtained only by changing speeds. The optimal value of Ra is generally receives with corresponding combination of traverse rate and current intensity, provided that less significant parameters are good (dimenzion of nozzles, gas pressure, nozzle distance from the work piece ..). Developed a lot of software and mathematical models which application may be input parameters that give optimum conditions for the corresponding Ra.

Experimental research [6] demonstrated that higher values of pressure gives lower values of Ra. The following factors such as traverse rate of plasma torch and plasma gas pressure have the most significant impact on the machined surface roughness. Other factors that are less important are diameter of the nozzle and the distance between the nozzle exit and the material. From the experimental results can be conclude that it is recommended to use higher pressures of plasma gas and appropriate traverse rate of plasma torch in order to reach higher quality of cut surface. It is known that surface roughness of the cut is not same by depth. This study showed that diameter nozzle has a larger effect on surface roughness on upper reaches of cutting (1 mm from the top edge) than in the lower zones (5 mm from the top edge).

Experimental research [7] shoved that surface roughness is different for the left and

right sides of the cut. Surface on the right are about 25% rougher than on the left side.

3. EXPERIMENTAL EXAMINATION AND DISCUSSION

In the experiment were done 26 samples of 80 mm length. Steel plate material St 52-3 N (Č0563) was 4 mm thick.

Cutting was performed at the Faculty of engineering in Kragujevac on FlameCut-2513 machine, manufacturers by Arpel. Width of the opening at the nozzle exit was 1.2 mm.

Figure 2. FlameCut-2513 plasma machine

In order to investigate the effect of each analysed input parameters, on surface roughness, an experiment was planned that when varying one input parameter, the three others will be constant.

Table 1. Used parameters and measured values

No. of Exp.	I, A	V , mm/ min	L, mm	P, Bar	Ra, μm	Rtm , μm
1	60	2000	1,5	6	2,24	12,9
2	60	2500	1,5	6	3	14
3	60	3000	1,5	6	3,5	15
4	60	3500	1,5	6	3,53	18,9
5	60	3800	1,5	6	3,8	19
6	80	2000	1,5	6	1,24	7,3
7	80	3000	1,5	5	2,09	13,1
8	80	3000	1,5	5,5	2,18	12,9
9	80	3000	1,5	6	2,3	12
10	80	3000	1,5	6,5	2	11
11	80	3000	1,5	7	2,3	12
12	80	3000	1	6	1,88	10,6
13	80	3000	2	6	2,465	13,2
14	80	3000	2,5	6	2,4	13
15	80	3500	1,5	6	2,6	13,4
16	80	4000	1,5	6	2,77	14,2
17	80	4500	1,5	6	2,73	14,9
18	100	2000	1,5	6	1,18	6,2
19	100	2500	1,5	6	1,21	5,9
20	100	3000	1,5	6	1,61	7,2
21	100	3500	1,5	6	1,43	8,2
22	100	3800	1,5	6	1,75	8,6
23	100	4000	1,5	6	1,64	8,6
24	100	4500	1,5	6	1,65	8,8
25	100	5000	1,5	6	1,74	10,1
26	100	5500	1,5	6	1,767	10,2

Surface roughness was analyzed by Ra and Rtm – medium value of maximum height profile of the reference length, the length of the evaluation. Roughness was measured on the Talysurf 6 device. Measurements were performed at the middle of cut cross section.

Figure 3. Talysurf 6 device

Figure 4 displayed analysis of the surface roughness when changes traverse rate at different current intensity. Pressure gas and distance between the nozzle exit and the material are constant.
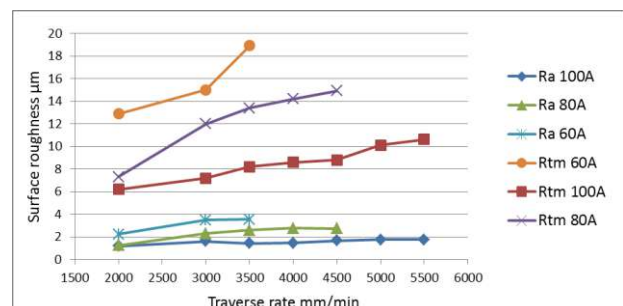
Figure 4. Surface roughness depending on changes traverse rate at different current intensity P=6bar, L=1,5 mm

Parameters Ra and Rtm have a bigger value by increase traverse rate. For better

understanding this effect, it's necessary to connected roughness of the cutting edge with stability of process.

When the traverse rate increases the torch moves fast and plasma arc loses stability with view to the cutting front. Therefore plasma arc can not remain perpendicular to front surface of the work piece, which is on surface cutting formed lynx. On the other side too low traverse rate lead to excessive melting in a work zone, resulting appearance of furrows.

Figure 4 also show that by increasing the current intensity surface roughness has a lower value. This result is logical because with increasing the current intensity, process becomes more stable. Thereby a larger quantity of heat, melted tips of micro irregularities and thereby obtain smaller values of Ra and Rtm.

So increase or decrease traverse rate and current intensity have different effects on surface roughness.
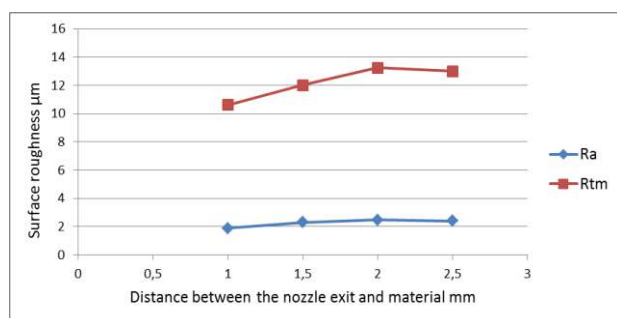
Figure 5. Surface roughness depending on changes distance between the nozzle exit and material I=80A, V=3000 mm/min, P=6 bar

When analysis experimental data at Figure 5 it has been found that by increase distance between the nozzle exit and the material gets worse Rtm parameters. The substance of the problem should be sought on connection between stability of process and this parameter. When the torch is too high positioning from work piece plasma arc is a long and curve. This phenomenon leads to the formation of surface waves, and lynx, and therefore to a higher Rtm. Changes in parameter Ra is very small, so it can say that input parameter distance between the nozzle exit and the material almost no influence on Ra.

Varying the pressure (Fig. 6), while the other input parameters are constant, almost do not have influence on Ra.

By increasing the pressure, the greater part of the melt products were blowing, which resulting in reduced Rtm.

Samples 18 have the lowest value of Ra, while the lowest value of Rtm has samples number 19. Which means that the best surface roughness achieved at maximum current intensity and of at two least traverse rate. This result is fully in accordance with theoretically consideration and earlier research.
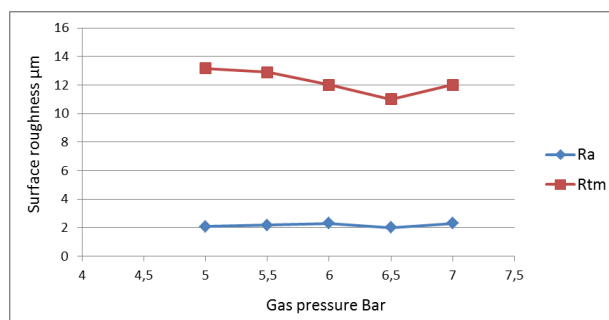
Figure 6. Surface roughness depending on gas presure I=80A, V=3000 mm/min, L=1,5 mm

4. CONCLUSION

Plasma cutting is technical system that represents the best relation between cost and quality value for most of the standard ports and small series production types. In addition, the processing speed is far greater than the technology of machining, and quality is comparable to the laser cutting technology.

The cut surface from the plasma arc process is normally rougher than that achieved by oxy-fuel cutting on carbon steels, and it is definitely rougher than most machining processes. In most metals, this roughness usually appears as a ripple along the cut surface. This is partly due to the output waveform of the dc power supply (the smoother the output, the smoother the cut), but it is also determined to an extent by the gases used and the torch design.

For a better analysis of the surface roughness is necessary to connect analysed parameters with the stability of process and with the input heat to the zone of the cut.

Based on the experimental results it can be concluded that traverse rate and current intensity have different effects on surface roughness.

Varying the pressure and distance between the nozzle exit and material, while the other input parameters are constant, almost do not have influence on Ra. On the other side, variation of these two parameters have opposite effect to Rtm.

ACKNOWLEDGEMENT

REFERENCES

[1] M.Radovanovic, M. Madic: *Modeling the plasma arc cutting process using ANN*, Nonconventional Technologies Review, Vol. 4, pp. 43-48, 2011.

[2] B.Nedic, M. Jankovic, M. Radovanovic, G. G. Lakic: *Quality of plasma cutting*, in: *13th International Conference on Tribology*, 15-17. 05. 2013. Kragujevac, Serbia, pp. 314-319.

[3] ISO 9013:2002, Thermal cutting - Classification of thermal cuts - Geometrical product specification and quality tolerances (E), 2002.

[4] I. Sanda-Maria, M. CoteaŃă, A. Munteanu: Experimental results concerning the variation of surface roughness parameter (Ra) at plasma arc cutting of a stainless steel workpiece, International Journal of Modern Manufacturing Technologies, Vol. 2, No. 1, pp. 31-36, 2010.

[5] R. Bhuvenesh, M.H. Norizaman, M.S. Abdul Manan: Surface roughness and mrr effect on manual plasma arc cutting machining, World academy of science, engineering and technology, Vol. 6, No. 2,pp. 459-462, 2012.

[6] M. Hatala, R. Čep, Z. Pandilov: Analysis of surface roughness and surface heat affected zone of steel EN S355J0 after plasma arc cutting, Mechanical Engineering Scientific Journal, Vol. 29, No. 1, pp. 1–6, 2010.

[7] A.P.Hoult, I.R. Pashby, K. Chan: Fine plasma cutting of advanced aerospace materials, Journal of Materials Processing Technology Vol. 48, No. 1-4, pp. 825-831, 1995.

INVESTIGATION OF FRICTION COEFFICIENT IN TRIBOPAIRS OF POLYMERS USED FOR RAPID PROTOTYPING DEPENDING ON SETTINGS OF 3D PRINTING

Svetlana PEREPELKINA[1],*, Pavel KOVALENKO[1], Roman PECHENKO[1], Karina MAKHMUDOVA[1]
[1]ITMO University, Saint Petersburg, Russian Federation
*Corresponding author: svetlana.yu.perepelkina@gmail.com

Abstract: This paper deals with the research of friction coefficient in tribopairs made of the polymers that are the most commonly used in rapid prototyping technologies. Parts manufactured with the use of a 3D printer with different settings of printing were chosen as samples for the experimental research. Friction coefficient and the temperature in the contact area during the runtime were measured using a universal friction machine MTU-1. The machine allows us to carry out tribological experiments using different contact schemes with or without lubricants. For this research, the scheme "plane to plane" was chosen. No lubricants were used. Wear of the samples was estimated after the experiments. Analysis of the experimental data has shown that changing of 3D printing settings has significant influence not only on the strength and stiffness of the parts, but also on the quality of the surface that affects the tribological properties of the tribopairs. The results of this research allow us to choose optimal settings for 3D printing depending on the required tribological properties of the parts, such as friction coefficient and wear.

Keywords: friction coefficient, tribological properties, wear, temperature in the contact area, rapid prototyping technologies, 3D printing settings, universal friction machine.

1. INTRODUCTION

Recently, rapid prototyping technologies, or 3D printing, also called additive manufacturing, have been widely used for design and manufacturing of various parts of systems and mechanisms [1]. These methods and technologies are used both in industry and academic institutions [2]. In medicine, additive manufacturing helps us design implants, individual prostheses, as well as the parts for various mechatronic systems for robotic rehabilitation, such as orthoses and exoskeletons [3].

A wide range of research has been carried out in the field of 3D printing in order to investigate mechanical properties of the parts manufactured with the use of such technologies. Strength, stiffness, weight and other properties of these parts depend on various conditions of 3D printing, such as layers' thickness and height, shell thickness, fill density, etc. Mechanical properties of 3D printed parts were investigated by Bellini et al. [4]. Song et al. paid attention to the measurements of the mechanical response of 3D printed parts made of PLA plastic [5]. Mechanical properties of coloured PLA plastics were described by Wittbrodt et al. [6]. Es-Said

et al. considered the influence of layer orientation on the mechanical properties, such as tensile strength, modulus of rupture, and impact resistance, for the parts made of ABS plastic [7]. Part orientation during 3D printing has its influence on the surface finish [1] and, therefore, it affects the tribological properties of the tribopairs. However, tribological properties of such parts have not been investigated well enough, which may lead to uncontrolled wear of tribopairs surfaces [8]. Dawoud et al. investigated the tribological properties, such as friction coefficient and wear, for the samples 3D printed with the use of ABS plastic.

In this paper, the tribological behaviour of the samples made of PLA plastic with the use of 3D printing with different settings is considered.

2. RAPID PROTOTYPING AND ADDITIVE MANUFACTURING TECHNOLOGIES

Most rapid prototyping technologies are based on the addition of material layer by layer according to the previously developed computer model. There are a lot of methods and technologies for additive manufacturing. Basic methods are: three dimensional printing (3DP), fused deposition modeling (FDM), stereolithography (SL), powder bed and inkjet 3D printing, selective laser sintering or melting (SLS or SLM), direct metal laser sintering (DMLS), laminated object manufacturing (LOM) and ultrasonic consolidation (UC) [9]. The most common methods for additive manufacturing and rapid prototyping are 3DP and FDM. These methods are based on the melting of the filaments that are usually made of thermoplastics. After being melted by the hot extruder, the material is deposited layer by layer through the nozzle that can move in vertical and horizontal directions. After extrusion from the nozzle the material hardens immediately due to the temperature change. The most commonly used materials for these methods are ABS (acrylonitrile butadiene styrene) and PLA (polylactic acid). No binders between layers are required.

Other additive manufacturing technologies, such as selective laser sintering, can use powders made of various materials, including plastics, metals or ceramic. In these methods, lasers are used to fuse the particles of the powder, therefore, binders are not used. The use of binders is required for other methods working with powders, such as powder bed and inkjet 3D printing [9].

Another rapid prototyping method is stereolithography. This technology is based on the use of liquid materials that are sensitive to the influence of light or ultraviolet. Layers harden being irradiated by the laser or ultraviolet due to the phenomena of photopolymerization.

All these methods allow us to produce parts with different inner structure and mechanical properties [10]. This diversity can be obtained by the use of different settings and various materials for additive manufacturing. Using 3D printing or fused deposition modeling it is possible to change some parameters, such as layers' thickness, fill density, porosity, layers' orientation, etc. These parameters affect the surface finish and, therefore, not only mechanical properties, but also tribological behaviour of the parts.

3. UNIVERSAL FRICTION MACHINE "MTU-1"

Recently, a wide range of measurement machines and methods have been developed for the estimation of tribological behaviour in various conditions [11]. 3D printing technology allows us to manufacture parts with varying accuracy [12] and degree of filling of the inner layers of the part. Deviations of the shape and roughness of the surface have significant influence on various properties of the part, including its reliability and wear [13].

Roughness of the surface layers, as a rule, does not depend on the filling factor. Therefore, it is of interest to investigate the tribological properties of tribopairs after abrasion of the surface layers. A universal friction machine MTU-1 was used for testing. (Fig. 1).
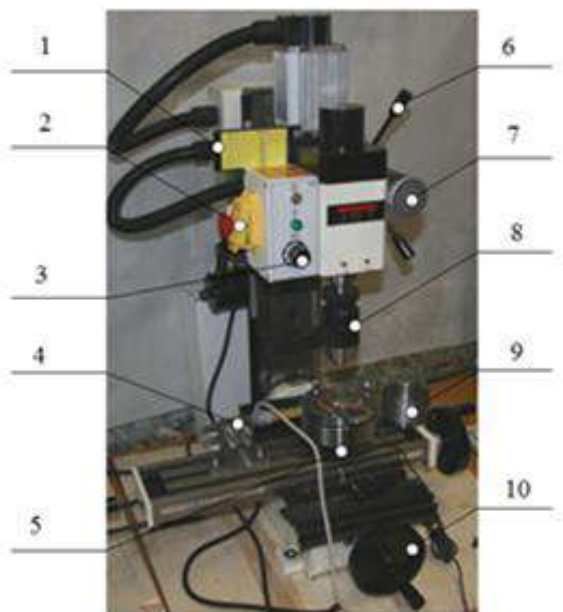
Figure 1. Universal friction machine "MTU-1"

In Figure 1, the following parts of the universal friction machine "MTU-1" are presented: 1 – the part used for the control of rotation speed; 2 – the power button; 3 – the speed control button; 4 – the friction torque measurement system with the elastic sensing element; 5 – the strain gauge for axial load measurement; 6 – the handle for fast loading; 7 – the handle for fine loading; 8 – the chuck for the upper sample; 9 – the lubricant reservoir; 10 – the handle for the displacement of coordinate table.

The structure of the universal friction machine "MTU-1" allows us to save the parallelism of the contacted surfaces, which increases the accuracy of measurements. The machine is resistant to the environmental influence, such as vibration, electromagnetic interference, dust, humidity and temperature fluctuations.

The testing method for "MTU-1" is based on a relative rotational movement of the upper sample to the lower stationary sample with or without lubricants using different test schemes, such as disc to disk, sphere to ring, pin to disk motion, etc.

The upper sample rotation speed without the load is adjustable up to 2500 rpm, the load on the samples can be varied from 50 to 1000 N [14].

4. EXPERIMENTAL RESULTS

Samples for the experimental research were made of various PLA plastics with different filling factor with the use of a 3D printer Picasso.

The samples for the first tribopair were made of plastic REC PLA with 100% filling. Experimental conditions: rotation speed is 300 rpm, starting load is 500 N.

In Fig. 2, the samples for the first tribopair before the experiment are shown.
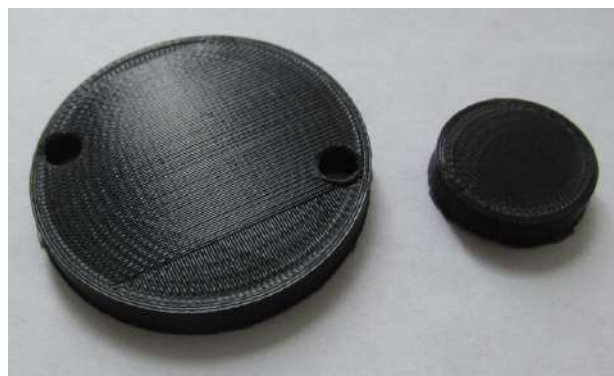
Figure 2. Samples of REC PLA with 100% filling

Figure 3 shows the graph of friction torque versus time for the samples made of REC PLA with 100% filling.
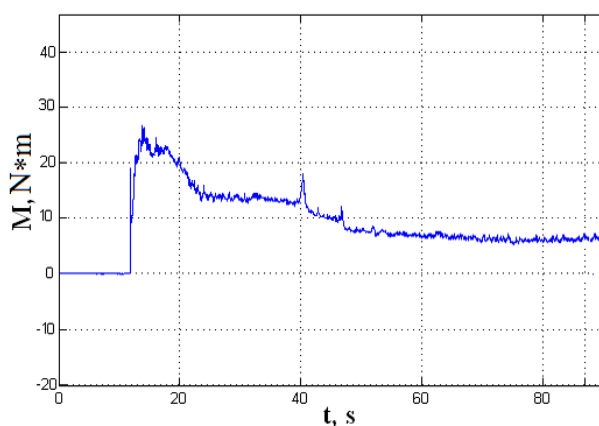
Figure 3. Graph of friction torque versus time for REC PLA with 100% filling

It can be observed from the graph in Fig. 3 that at the beginning of the experiment friction torque changed sharply, which is connected with the beginning of the process of running-in in the tribopair due to plastic flow of the samples.

In Fig. 4 and 5, respectively, the graphs of the temperature in the contact area and

friction coefficient versus time of the experiment are presented.
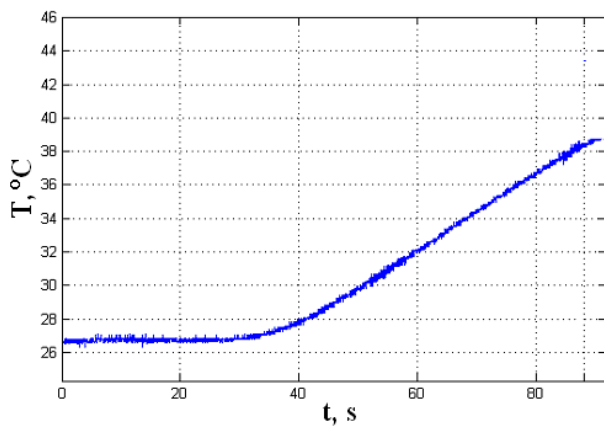
Figure 4. Graph of the temperature in the contact area versus time of the experiment

It can be seen from the graph in Fig. 4 that after approximately 40 seconds of the friction process the temperature in the contact area starts to rise. This is due to the jump of the friction torque, as well as the partial reflow of the material at the points of the real contact.
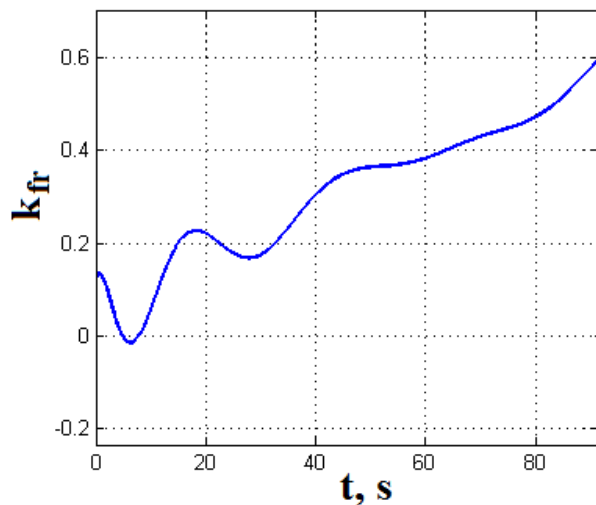
Figure 5. Graph of the friction coefficient versus time

It can be noticed from the graph in Fig. 5 that the maximum value of friction coefficient is 0.6. It is observed at the end of the experiment. The presence of extremum points on the graph is explained by the considerable plastic flow of the samples, as well as by the appearance and destruction of molecular cross-links between the samples.

Figure 6 shows the photographs of the surfaces of the samples before (Fig. 6, a) and after (Fig. 6, b) the experiment.
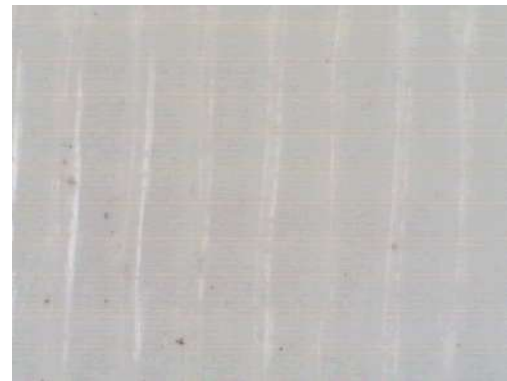
a)

b)

Figure 6. Photographs of the surface of the sample before (a) and after (b) the experiment (magnification is 88x)

In Fig. 6, b, the areas of scoring and fusion of the surface are clearly visible.

The second set of experiments was devoted to the research of the tribopairs made of REC PLA plastics with two different filling factors: 75% and 100%. The sample with 100% filling has different layers' orientation from the sample investigated in the first set of experiments. Experimental conditions are the following: rotation speed is 300 rpm, the starting load is 250 N.

In Fig. 7, the graphs of the friction torque versus time for two samples are shown.

a)

b)
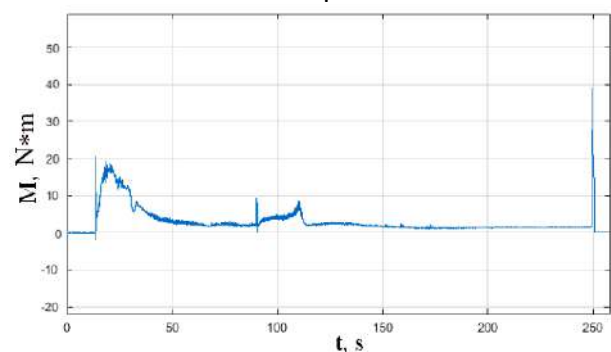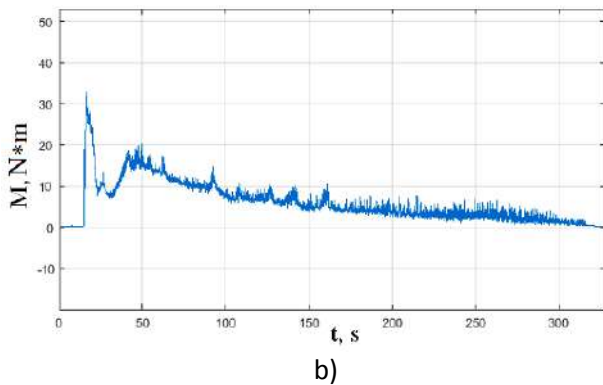
Figure 7. Graphs of the friction torque versus time: a) for the sample with 75% filling; b) for the sample with 100% filling

In Fig. 7 a, the results for the sample with 75% filling is presented. Fig. 7 b shows the results for the sample with 100% filling.

It can be seen in Fig. 7 that the friction torque for the samples with 100% filling after running-in changes smoothly, which is due to the more regular surface of the samples.

In Fig. 8, the graphs of the temperature in the contact area versus time for the samples made of REC PLA with 75% and 100% filling are shown.

a)

b)
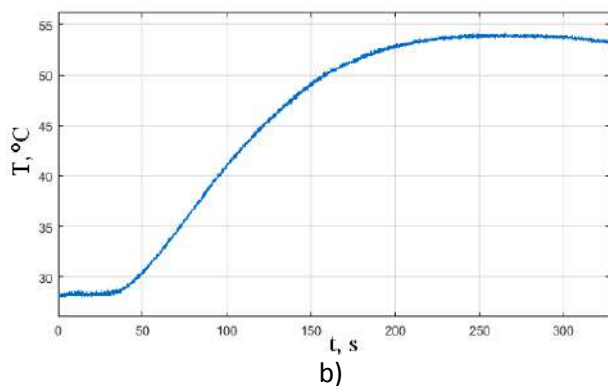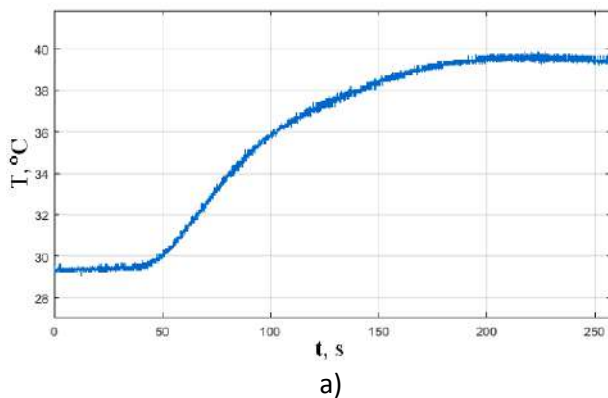
Figure 8. Graphs of the temperature in the contact area versus time: a) for the sample with 75% filling; b) for the sample with 100% filling

It can be seen from the graph in Fig. 8 that the temperature in the contact area is gradually increasing, which indicates the absence of scuffing in the tribopair. For the sample with 100% filling, the temperature in the contact area is higher, which is apparently due to a greater number of points of real contact in the tribopair.

In Fig. 9, the graphs of friction coefficient versus time for the samples with 75% (a) and 100% (b) filling are presented.

a)

b)
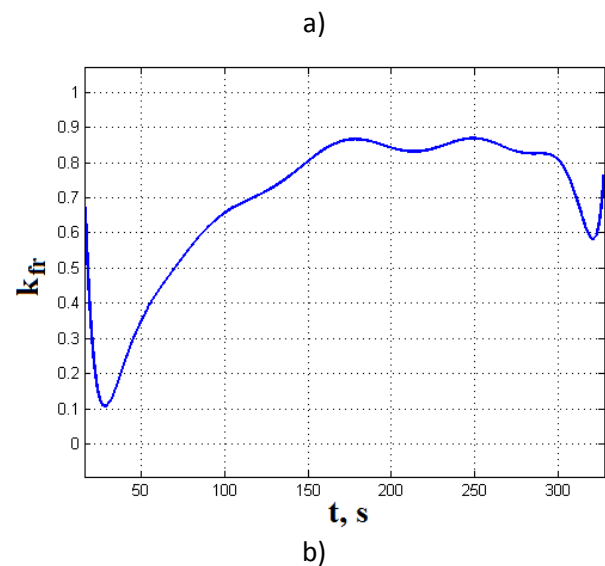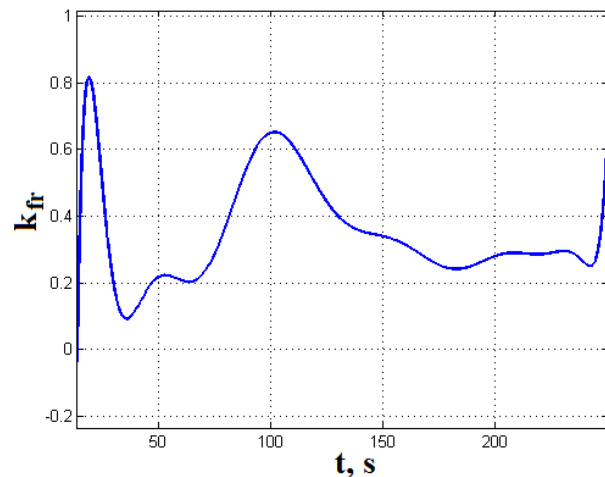
Figure 9. Graphs of friction coefficient versus time: a) for the sample with 75% filling; b) for the sample with 100% filling

It can be seen from the graph in Fig. 9 that friction coefficient for the sample with the filling factor 75% has extremum points, which, apparently, is due to the porosity of the material. When the surface layer is abraded, the contact is between inner layers of the material. These inner layers have the porosity

that is different from the porosity of the surface layer.

Friction coefficient for the sample with 100% filling changed more smoothly during the experiment. At the beginning of the experiment, friction coefficient decreased, which is due to the process of plastic flow in the tribopair. After that, friction coefficient increased, which is due to wear of the surface layers of the sample.

Figure 10 shows the photographs of the samples made of REC PLA with the filling factors 75% (Fig. 10 a) and 100% (Fig. 10 b) after the experiments.

a)

b)

Figure 10. Photographs of the samples made of REC PLA with 75% (a) and 100% (b) filling after the experiments

It can be observed from the figure 10 that a sample with 75% filling has more uneven wear than a sample with 100% filling. This is due to the greater porosity of the sample.

Figure 11 shows the photographs of the surface of the samples after the experiment.

a)

b)

Figure 11. Photographs of the surfaces of REC PLA samples with 75% (a) and 100% (b) filling after the experiments. Magnification is 88x.

In Fig. 11, the areas of plastic flow and reflow of the material surface in the contact area can be noticed.

5. CONCLUSION

Experiments have shown that the tribological properties in the tribopairs made of plastics for 3D printing depend on the filling factor. The presence of plastic flow in the contact area increases friction coefficient; and the temperature in the contact area exceeds the melting point of the material. Porosity of the material has a significant influence on the process of friction and wear of the samples.

Friction coefficient in the tribopair with 100% filling changes smoothly, which makes it possible to predict the behavior of the tribopair more accurately. The results of the research allow us to make a conclusion that it is preferable to use parts with 100% filling for design of tribopairs in mechanisms and systems.

In future work, it is of interest to investigate the influence of layers' orientation on the tribological properties of 3D printed parts made of PLA and ABS.

REFERENCES

[1] D.T. Pham, R.S. Gault: A comparison of rapid prototyping technologies, International Journal of Machine Tools and Manufacture, 38 (10-11), pp. 1257-1287, 1998.

[2] A.P. Nyaluke, D. An, H.R. Leep, H.R. Parasaei: Rapid prototyping in academic institutions and industry, Computer and Industrial Engineering, Vol. 29, pp. 345–349, 1995.

[3] K.F.Gretsch, H.D. Lather, K.V. Peddada, C.R.Deeken, L.B. Wall, C.A. Goldfarb: Development of novel 3D-printed robotic prosthetic for transradial amputees, Prosthetics and Orthotics International, Vol. 40, No.3, pp. 400-403, 2016.

[4] A. Bellini, S. Güçeri: Mechanical characterization of parts fabricated using fused deposition modeling, Rapid Prototyping Journal, Vol. 9, No. 4, pp. 252-264, 2003.

[5] Y. Song, Y. Li, W. Song, K. Yee, K.-Y. Lee, V.L. Tagarielli: Measurements of the mechanical response of unidirectional 3D-printed PLA, Materials and Design, Vol. 123, pp. 154-164, 2017.

[6] B. Wittbrodt, J. M. Pearce: The Effects of PLA Color on Material Properties of 3-D Printed Components, Additive Manufacturing, Vol. 8, pp. 110–116, 2015.

[7] O.S. Es-Said, J. Foyos, R. Noorani, M. Mendelson, R. Marloth, B.A. Pregger: Effect of layer orientation on mechanical properties of rapid prototyped samples, Materials and Manufacturing Processes, Vol. 15, No. 1, pp. 107-122, 2000.

[8] M. Dawoud, I. Taha, S.J. Ebeid: Effect of processing parameters and graphite content on the tribological behaviour of 3D printed acrylonitrile butadiene styrene, Materialwissenschaft und Werkstofftechnik, Vol. 46, No. 12, pp. 1185-1195, 2015.

[9] S. Kumar, J.-P. Kruth: Composites by rapid prototyping technology, Materials and Design, Vol. 31, pp. 850–856, 2010.

[10] I. Gajdoš, J. Slota: Influence of printing conditions on structure in FDM prototypes, Tehnicki Vjesnik, Vol. 20, No. 2, pp. 231-236, 2013.

[11] V.P. Sel'kin, S.V. Kopylov: Friction machine for testing materials under boundary lubrication, Journal of Friction and Wear, Vol. 37, No. 2, pp. 184-186, 2016.

[12] D. Dimitrov, W. Van Wijck, K. Schreve, N. De Beer: Investigating the achievable accuracy of three dimensional printing, Rapid Prototyping Journal, Vol. 12, No. 1, pp. 42-52, 2006.

[13] V.A. Pechenin, M.A.Bolotov, N.V. Ruzanov: Technique of decomposition of form deviation for freeform surfaces, Key Engineering Materials, Vol. 685, pp. 334-339, 2016.

[14] S. Perepelkina, P. Kovalenko, R. Pechenko: Investigation of Tribological Properties of Metallic Materials with the Use of the Universal Friction Machine "MTU-1", Procedia Engineering, Vol. 176, pp. 301-309, 2017.

ACTIVE TRIBOLOGY SYSTEMS

Velibor KARANOVIĆ[1,*], Mitar JOCANOVIĆ[1], Marko OROŠNJAK[1]
[1]University of Novi Sad, Faculty of Technical Sciences, Novi Sad, Serbia
*Corresponding author: velja_82@uns.ac.rs

Abstract: Recently, there was introduced a new tribology development direction, so called active tribology or tribotronics. Active tribology concept implies integration of tribology and electronics, which enables real-time control of machines and mechanisms based on energy losses, caused by friction and wear. Friction leads to energy loss and lower machine efficiency, while wear is responsible for shortened machine service life, machine failure and enormous losses due to degraded performances. Present tribological contacts are passive, which means that their components (such as geometry, material or lubricant characteristics) cannot adjust to the working conditions change. With possibility to adjust tribological system parameters in order to minimize losses due to friction and wear, we can significantly improve safety level, flexibility, working performances and reliability of tribological systems. Continuous tendency to make machines with high level of energy density, with high controllability, flexibility and presence of artificial intelligence, opening a high possibilities for smart tribological systems development and implementation. The concept of active tribology is presented and discussed in this paper. Also there are given some illustrative examples that show the feasibility of an active approach.

Keywords: active tribology, tribotronics, friction, wear, energy losses.

1. INTRODUCTION

Modern society have continuous demand for more reliable, safe and energy efficient machines. On the one hand we are obligated by laws and regulations, and on the other competition in the market. All machines (agricultural, industrial, transportational, for mining etc) that we use every day, involve numerous mechanical contacts between various surfaces. When surfaces are in motion relative to each other, these contacts will result in friction and wear. Friction leads to functional disturbances and energy loss that adversely affects machine efficiency and wear is responsible for failure and break down of machine assembly parts. To minimise this problems, different solutions are used, but the most common choice is lubrication.

Generally, with the application of the tribology principles, we achieve significant energy savings, a reduction in noise, vibration and the emission of harmful substances in the environment, and it extends the life of the machines. However, if one wants to provide an even greater contribution of the tribology, it is necessary to think about active systems that are capable of constant monitoring and adjustment according to the working conditions.

2. DEFINITION AND ELEMENTS OF AN ACTIVE TRIBOLOGY SYSTEM

Active tribological system, which is popularly called tribotronic system, is a system that integrates elements of tribological, electrical and IT systems [1]. While working it acts like a mechatronic system. Unlike mechatronic, tribotronical system is operated according to the parameters representing the losses, such as friction, temperature, vibration, fluid leakage, pressure drag, wear, and the like. Based on mentioned before, the purpose of tribotronic concept is to manage the system on the basis of operating parameters and loses in a way that will improve work performances, efficiency and reliability of tribological pairs and machines in general.

The design of such a system includes components such as sensors, actuators, control units and tribo-pairs (Figure 1). Based on the collected signals by sensors, the control unit, using tribological algorithms, determines what action should be taken, and the selected action is executed by triboactuator. After the measures taken, there is comparing of the parameters of the previous and the current situation, and accordingly new corrective action is taken. This allows "on-line" adjustment of the tribosystems, which is why these systems can be characterized as autonomous or self-aligning.
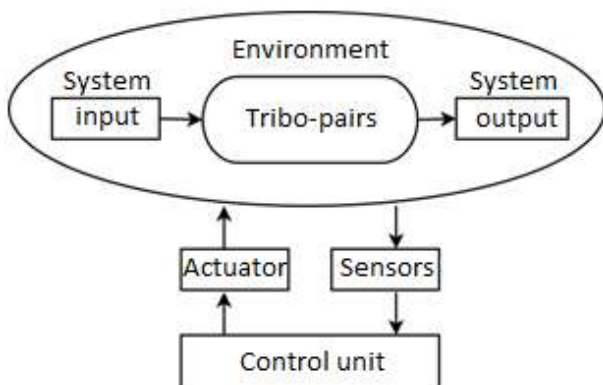
Figure 1. Tribotronic system configuration.

The correct choice of sensor is very important. The sensors used for equipment condition monitoring, if adequately adapted, could be used in tribotronic system. Their adaptation should provide more reliability and resistance to interference (noise) emitted by industrial equipment such as electro-magnetic field, vibrations, etc. Also, it is wise to think of sensors as modules which within themselves have the ability of measuring multiple parameters simultaneously, as well as the possibility of self-supply by converting mechanical energy into electricity [2,3].

Algorithms and computer units applied in tribotronical system should have a high degree of flexibility and quick response.

Selection of triboactuators represents the greatest challenge because there is no concept of their construction. Actuators for tribotronic application should be elements that have adequate size, strenght and especially adequate (fast) speed of reaction and accuracy.

3. EXAMPLES AND DISSCUSION

The usual method of friction and wear control is by elimination of direct contact between the surfaces of the tribo-elements with thin film lubrication. In this case, the wear of contact surfaces is minimized, while the friction is limited to the existence of viscous forces in the lubricant film. The problem that appears here is the problem of retaining lubricant in the contact zone which under the actionof load force is squeezed out. A classic example of this tribosystem is hydrostatic bearing (Figure 2).
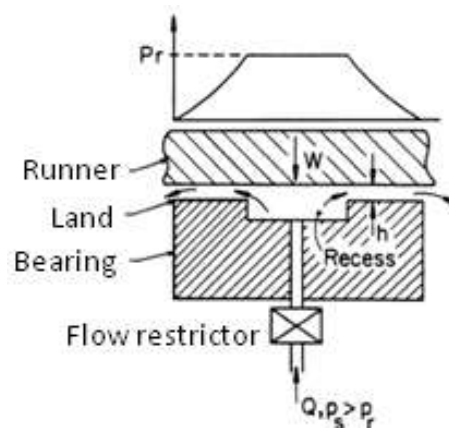
Figure 2. Hydrostatic bearing.

Parameters such as capacity and thickness of the lubricant film, can be managed by adjustment of pressure and lubricant flow into the hydrostatic bearing. In accordance with the possibility of online adjustment of flow and pressure, hydrostatic bearing may be considered as active tribological system.

Another significant problem with the systems, using lubricant as a means to reduce friction and wear, is the degradation of its properties during service. Lubricant condition has a very significant impact on performances, reliability and durability of elements of technical systems in which they are used. Therefore, it is quite clear that the implementation of the diagnostic system, for real-time monitoring and analysis of lubricants, is necessary if we want to increase the contribution tribosystems. In case of change of lubricant properties outside of the tolerated limits, corrective measures must be conducted. Those measures are realized with active conditioning systems, which include heaters, coolers, filter systems etc.

Another example of tribotronic system is a tilting-pad bearing (Figure 3). The tilting-pad journal bearing is a fluid-film bearing in which the shaft is supported by a number of stator pads. The pads independently tilt in response to the motion of the shaft. Additionally, the pivots supporting the pads may be adjustable in the radial direction thus changing oil film geometry. This method use change in oil film wedge at the inlet and outlet, to affect system performance. Another way to influence the work performance is the flow pattern control in the contact area. For this purpose can be used electro- and magneto-rheological fluids, which react to the formation and change of electric, or magnetic fields, with reverse possibility of changes in their rheological properties. In a strong field, the viscoelastic properties of the fluid are changing rapidly as the magnetic or electric field [4]. Such active control has the potential to compensate for a suddenly induced shaft imbalance or misalignment or a change in shaft speed and loading. It may further improve the stability and load capacity of the bearing system, reduce wear and power loss, and enable better tolerance of lubricant contamination and viscosity changes [5]. Active changes in the radial position of the bearing plate, are achieved with hydraulic cylinders or piezoelectric actuators customized for this application.
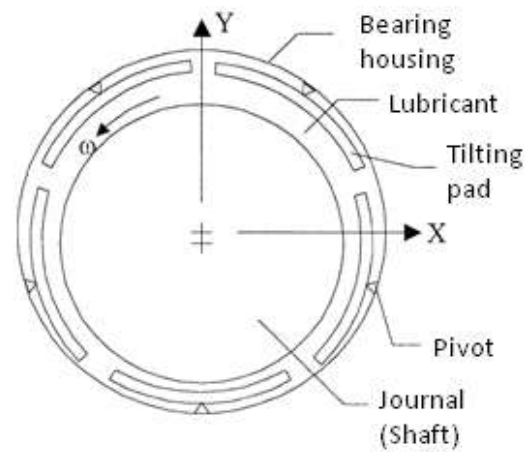
Figure 3. Tilting-pad journal bearing.

For its own needs, NASA developed solutions that provide the lubrication of bearings during the entire mission. Knowing that the losses of lubricant are related to its evaporation, degradation or leakage out of the contact zones, it was necessary to find a solution that will eliminate these problems. One of the solutions that can be said to fall within the scope of active system, are oil reservoirs in the form of cartridges that are made of porous material – Figure 4 [6]. In the pores of the reservoir is stored lubricating oil that is released by heating. Heating provides the heat produced due to increased friction, or by the micro-heater, which activates when the sensor detects an increase in the coefficient of friction. In this case, the role of the triboactuator has a micro-heater.
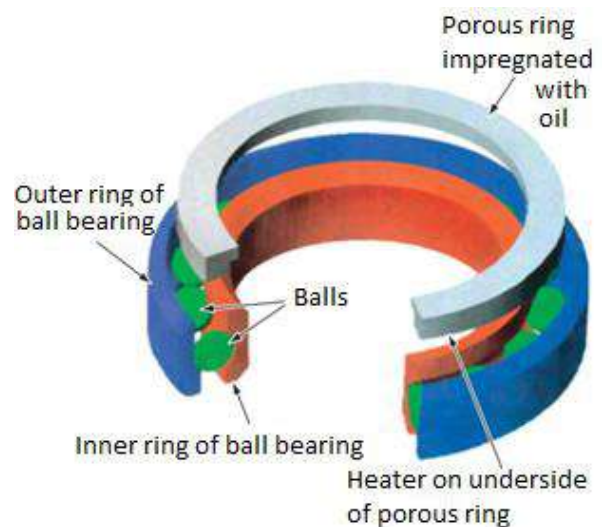
Figure 4. In situ, on demand oil lubricator for the ball-bearing rings.

Another approach is to provide bearing lubrication on demand with solid lubricants

such as indium, lead, silver, molybdenum disulphide. Micro-heater, as triboactuator, is activated depending on friction measured by the friction sensor. As a result of this action solid lubricant evaporates and lubricates the bearing thus lowering friction (Fig. 4).
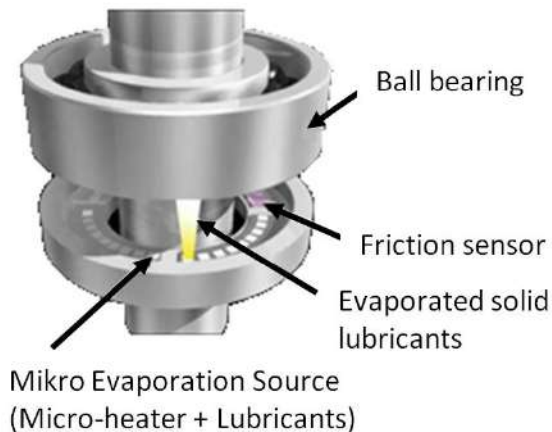
Figure 4. Conceptual image of a self-restored lubrication system for ball bearing with a micro evaporation source for tribo-coating [7].

Besides bearing applications, there are many other applications where it is possible to apply the active tribological concept, for example vibration control, friction control in transmission systems, tire pressure adjustment, etc. For example, mechanical vibrations are caused by mass imbalance and they are associated with fatigue, which can lead to a catastrophic failure. Therefore, vibrations must be attenuated. Active vibration control can be applied by introduce of a control force which is produced by magnetic bearings or piezoelectric stacks et cetera [8].

All these examples point to the fact that the implementation of tribotronic concept in future would be inevitable in order to achieve a higher level of self-sustainability of smart machines and next generation mechanisms.

4. CONCLUSION

Some examples of active tribology concept are presented in this paper. Environment, operational aspects so as reliability are three main reasons that motivate us to move away from the old technological solutions, to more efficient and modern alternatives. The purpose of introducing active tribology concept is to make technical systems more reliable, controlable, self sustainable and safer. Active tribology systems are complex but enables many improvements that extends life of the machines.

REFERENCES

[1] S. Glavatskih and E. Höglund: Tribotronics—Towards active tribology, *Tribology International*, vol. 41, no. 9-10, pp. 934-939, 2008.

[2] Z. Chi, Z.L. Wang: Tribotronics—A New Field By Coupling Triboelectricity And Semiconductor, *Nano Today*, vol. 11, no. 4, pp. 521-536, 2016.

[3] Z.L. Wang: Nanogenerators for Self-Powered Devices and Systems, Georgia Institute of Technology SMARTech digital repository, 2011.

[4] M.R. Jolly, J.W. Bender and J.D. Carlson: Properties and applications of commercial magnetorheological fluids, In *5th annual international symposium on smart structures and materials*, June 16th, International Society for Optics and Photonics, pp. 262-275, 1998.

[5] D.C. Deckler, R.J. Veillette, M.J. Braun and F.K. Choy: "Simulation And Control Of An Active Tilting-Pad Journal Bearing", *Tribology Transactions*, vol. 47, no. 3, pp. 440-458, 2014.

[6] M. Marchetti, W.R. Jones Jr, S.V. Pepper, M.J. Jansen, R.E. Predmore: In-situ, on-demand lubrication system for space mechanisms, *Tribology transactions*, vol. 46, no. 3, pp. 452-459, 2003.

[7] K. Adachi and K. Kato: In situ and on-demand lubrication by tribo-coating for space applications, *Proceedings of the Institution of Mechanical Engineers, Part J: Journal of Engineering Tribology*, vol. 222, pp. 1031-1039, 2008.

[8] R.C. Simoes, V. Steffen Jr, J. der Hagopian, J. Mahfoud: "Modal Active Vibration Control Of A Rotor Using Piezoelectric Stack Actuators". *Journal of Vibration and Control*, vol. 13, no. 1, pp. 45-64, 2007.

EJECTION PERFORMANCE OF COATED CORE PINS INTENDED FOR APPLICATION ON DIE CASTING TOOLS FOR ALUMINIUM ALLOYS PROCESING

Pal TEREK [1], [*], Lazar KOVAČEVIĆ [1], Aleksandar MILETIĆ [1], Dragan KUKURUZOVIĆ [1], Branko ŠKORIĆ [1], Aljaž DRNOVŠEK [2], Peter PANJAN [2]

[1] University of Novi Sad, Faculty of technical sciences, Novi Sad, Serbia
[2] Jožef Stefan Institute, Ljubljana, Slovenia
*Corresponding author: palterek@uns.ac.rs

Abstract: During high pressure die casting process of aluminium alloys molten metal severely damages the tool surfaces, hampers the casting ejection, reduces the casting quality and decreases the overall production efficiency. One of the wear mechanisms that induces such behaviour is cast alloy soldering which develops bonding between the cast alloy and tool material. Although a die lubricant is applied on tool surfaces it is removed by erosion effects of liquid metal and consequently the tool surfaces become exposed to cast alloy. In order to combat these issues thin ceramic PVD (physical vapour deposition) coatings are applied on tool surfaces. These hard coatings have high oxidation resistance and chemical inertness to liquid aluminium alloys. However, their performance greatly relies on surface topography which is usually overlooked. This investigation employed ejection test for the examination of soldering tendency of EN X27CRMOV51 steel, plasma nitrided EN X27CRMOV51 steel and CrN and TiAlN duplex PVD coatings, in contact with Al-Si-Cu alloy. Duplex PVD coatings were prepared to a range of surface roughness and morphologies. Ejection tests were performed by tensile testing machine and the sample surfaces were evaluated by profilometry, confocal optical microscopy and scanning electron microscopy. Contrary to the findings published so far, it was found that the ejection force is independent of the chemical composition of investigated materials. After the ejection, the cast alloy soldering layer was found on surfaces of all tested materials. This built-up layer formed by effects of mechanical soldering, without corrosion reactions. The coated samples displayed a pronounced dependence of ejection force on surface roughness and topography. By decreasing the roughness, the ejection force increased, which is a consequence of intensified adhesion effects. Presented findings are a novel information important for efficient application of PVD coatings in protection of high pressure die casting tools.

Keywords: Aluminium alloy casting, Die casting tool, Plasma nitriding, Duplex PVD coatings, Cast alloy soldering, Surface topography

1. INTRODUCTION

In production of aluminium alloy castings by high pressure die casting process the tool surfaces are exposed to severe environment which cause tool wear [1]. Due to wear, tool operation becomes difficult, production efficiency is reduced, castings lose tolerances and the quality of their surface finish is reduced [2]. By continuing the production with

worn tools both castings and tools integrities are endangered. Although a die lubricant is applied on tools surfaces, the tool wears by erosion, soldering and thermal fatigue which commonly occur simultaneously [1,3].

Nowadays the cast alloy soldering becomes a major concern in the industry [2]. Therefore, diffusion layers, thin ceramic coatings and their combinations are applied for increasing the wear resistance of high pressure die casting tools [1,3]. Coatings produced by physical vapor deposition (PVD) have a range of required mechanical properties and high chemical inertness in molten metals [1,3,4]. Ceramic coatings efficiently suppress different types of wear and especially the corrosion caused by molten aluminium [1,4]. However, PVD coatings are also prone to formation of cast alloy built-up layer (sticking) on their surfaces [2]. Such cast alloy built-up layer hampers the castings ejection and increase the tool maintenance. Therefore, it is essential to further investigate and develop PVD coatings tailored for application on high pressure die casting tools.

In this study ejection test is employed for the evaluation of soldering (sticking) tendency of Al-Si-Cu alloy toward EN X27CRMOV51 (AISI H11) steel, plasma nitrided EN X27CRMOV51 steel, CrN and TiAlN duplex PVD coatings. The effects of surface roughness on the performance of duplex coated samples are detailly evaluated.

2. EXPERIMENTAL

Investigation concerned quenched and tempered EN X27CRMOV51 hot-working tool steel, plasma nitrided EN X27CRMOV51 steel, CrN and TiAlN PVD coatings produced as duplex layers on plasma nitrided samples. Cylindrical pin-shaped samples ($\phi 15 \times 100$ mm) were produced by procedures regularly employed in production of high pressure die casting tool parts (Figure 1 a).

Plasma nitriding was performed using ION-25I (IonTech) unit, CrN coating was deposited by BAI730 (Balzers) unit and TiAlN coating by CC800/7 (CemeCon) unbalanced magnetron

sputtering system. In order to accurately compare the performance of different materials, samples were produced applying the same surface finishing treatments. However, the coated samples were prepared with two additional degrees of surface roughness. Samples used in this investigation are denoted as follows: EN X27CRMOV51 steel samples as H11, plasma nitrided samples as PN, PVD coated samples were denoted with their types as CrN and TiAlN. Additionally, suffixes are added after sample names to distinguish the samples with different surface roughness: rough-R; smooth-S; post deposition polished-PP.

Cast alloy soldering (sticking) tendency was practically evaluated by ejection test. In this test, pin sample is used as a core for production of simple casting with a hole (Figure 1 b, c). As a result of a casting process a pin-casting assembly is obtained (Figure 1 c). Using a tensile testing machine ZDM 5/91 (VEB) the pin sample is ejected from the casting and a force displacement curve is recorded (ejection curve). This test imitates the process of core removal from a casting produced by high pressure die casting technology. Therefore, the force recorded during the test carry information about the soldering tendency of cast alloy.
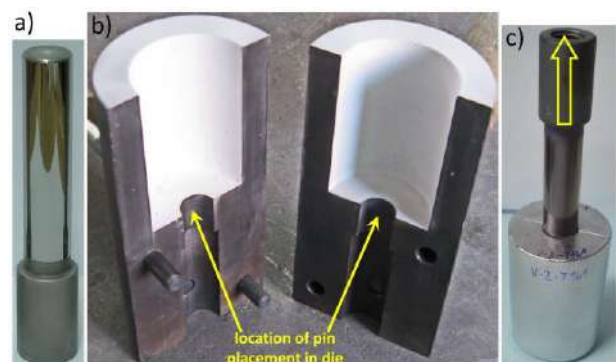
Figure 1. a) Pin sample, b) experimental casting die, c) pin-casting assembly

Casting process was performed by gravity melt pouring of EN AC-46200 alloy, at temperature of 730 °C, into a specially designed steel die, preheated to temperature of 320 °C. After each casting (solidification) cycle, the process is repeated for next sample.

Surface topography of samples was acquired by 3-D-profilometer (Taylor Hobson

Talysurf). Instrumented hardness tester H100C (Fischerscope) was employed for the evaluation of mechanical properties of layers and thin coatings, employing 100 mN indentation loads. After the ejection tests samples surfaces were evaluated by confocal optical microscope Axio CSM700 (Zeiss).

3. RESULTS AND DISCUSSIONS

All samples were produced of quenched and tempered EN X27CRMOV51 hot working tool steel with hardness of 455 HV_{30}. For plasma nitrided samples a maximal surface hardness of 1300 $HV_{0.01}$ was achieved, while the CrN and TiAlN coatings have 2575 $HV_{0.0025}$ and 3600 $HV_{0.0025}$ respectively. The hardness of investigated layers and coatings are appropriate for application on tools with increased wear resistance. Surface roughness parameters of all investigated samples are presented in Table 1. Roughness of all investigated samples belongs to the range of low surface roughness. In table 1 samples having nearly the same roughness are circled with dashed lines.

Table 1. Average values of surface roughness parameters of investigated samples

Sample group	R_a [µm]	R_{sk}	S_{dr} [%]
Rough samples (R)			
CrN-R	0.145	-0.179	0.055
TiAlN-R	0.153	0.990	0.157
Smooth samples (S)			
H11-S	0.198	-0.889	0.039
PN-S	0.183	-0.026	0.075
CrN-S	0.032	0.491	0.021
TiAlN-S	0.059	4.562	0.363
Post deposition polished samples (PP)			
CrN-PP	0.027	-1.162	0.020
TiAlN-PP	0.059	-0.947	0.016

Average values of maximal ejection force obtained for samples with comparable roughness are for different materials presented in Figure 2. Generally, values of measurement standard deviations (SD) are averagely less than 10 % of a measured value, which indicate a satisfactory experimental repeatability for this kind of examinations.

A small difference in ejection force, which is observed for investigated materials, falls in the range of test deviations. This means that investigated materials have nearly the same value of ejection force and the same soldering tendency. Therefore, the casting ejection performance from the die casting tool with a PVD coating would be the same as from the those made of X27CRMOV51 steel.
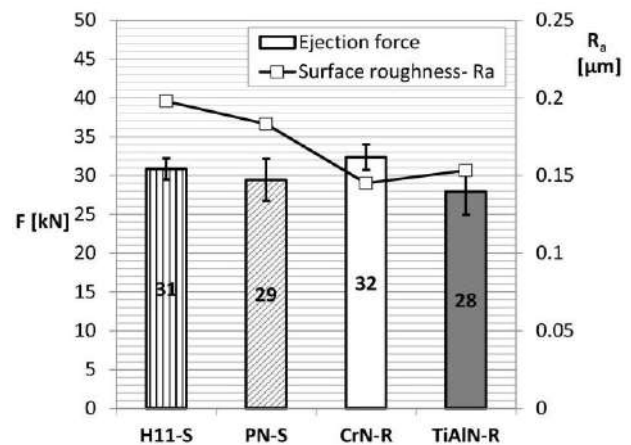
Figure 2. Average values of maximal ejection force recorded for different pin materials, error bars represent ±1 SD

Such finding is not in agreement with results published so far in literature, as in papers [1,3]. In their case, a considerably higher force was recorded for X27CRMOV51 steel and plasma nitrided X27CRMOV51 steel than for PVD coated samples. However, in these investigations the comparison between materials is not made on samples with the same roughness. Considering that surface topography affects the initial pin-casting interlocking conditions and the tribological performance during sliding [2], disregarding its influence could lead to inaccurate results interpretations. The effect of surface roughness on the ejection performance is in more detail elaborated by results obtained for coated samples with different roughness.

Surface morphology of pin samples after the ejection tests holds qualitative information about the soldering tendency of cast alloy toward pin material and galling processes that develop during the pin ejection. Macroscopic appearance of samples and confocal optical microscopy (CFM) images of surfaces with built-up layer are presented in Figure 3.

The cast alloy built-up layer is present on the surfaces of all investigated materials. It is distributed mostly inside the pronounced grinding marks, cavities, around asperities or coatings nodular defects (detail in Figure 3). For H11, CrN and TiAlN samples the built-up typically agglomerates inside grinding grooves. This is not typical for PN samples where the built-up distributes in form of lumps around asperities on the surface. For coated samples the built-up piles up around the nodular defects and on the sides of cavity defects. This suggests that both kind of coating defects (surface irregularities) have their own effect on distribution of cast alloy on pin surfaces. During ejection, nodular defects plough through the casting material and aggregate the cast alloy in front of them. On the other side, the cast alloy present in cavities, or in coating pinholes, is cut off the casting due to the shear stresses generated on pin-casting interface, during the ejection process. This means that both surface features also have their effect on the stress concentration during ejection and accordingly on the values of ejection force [2]. After examinations, the cast alloy was dissolved by NaOH solution and no remnants of built-up layer remained on the surfaces. This indicates that conditions in the employed test promotes only the effects of mechanical soldering (sticking).

Further, the investigation is directed toward performance evaluation of hard nitride coatings, as materials with highest corrosion resistance and great importance for practical application on die casting tools. A special attention is given to the influence of surface roughness on their ejection performance. The maximal ejection force measured for coated samples with different surface roughness are presented in Figure 4. It can be seen, that decrease in average surface roughness (R_a) induce a considerable increase of ejection force. The highest values of ejection force were recorded for post deposition polished samples of both kinds of coatings (CrN, TiAlN). However, a small difference in R_a parameter between the smooth (S) and the post polished (PP) samples resulted with a considerable difference in ejection force. This is a consequence of a large difference in surface morphology of these samples, which can be distinguished by other roughness parameters like skewness (R_{sk}) (Table 1, Figure 4).
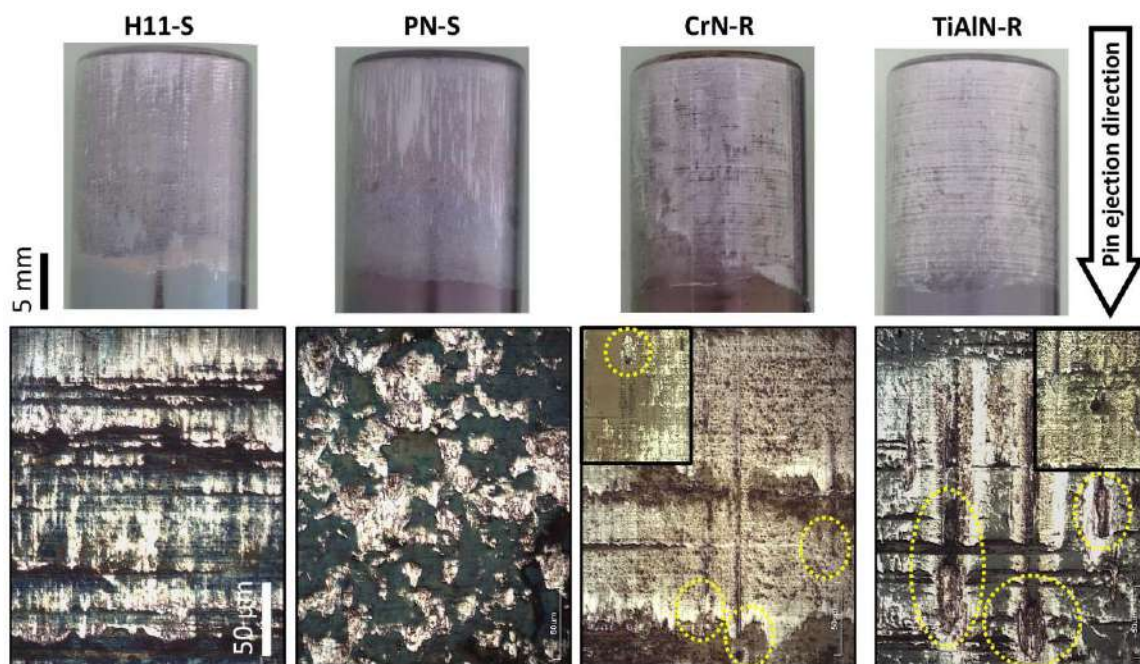
Figure 3. Appearance of the samples with built up layer, a) macroscopic images, b) confocal optical microscopy images of pin areas submerged 5 mm in the casting, image inserts with higher magnification; areas circled with dashed lines are typical locations around coating defects
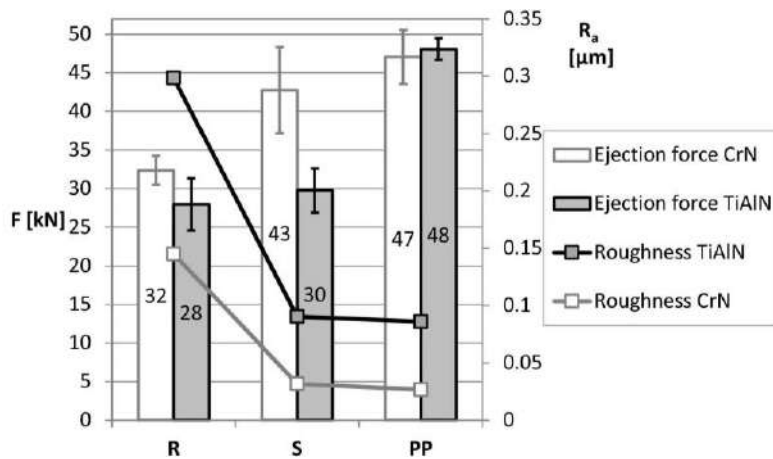
Figure 4. Average values of ejection force recorded for coated samples (CrN, TiAlN) prepared to a different degree of surface roughness, error bars represent ± 1 measurement standard deviations

By examining the representative topographies of coated samples, shown in Figure 5, it is clear that a great difference exists between the smooth and post polished samples. Surfaces of smooth coatings are characterized by a large quantity of peaks (nodular coating defects) and accordingly high values of R_{sk}, while the surfaces of post polished coatings are smooth, characterized by numerous cavities (wrenched defects) and accordingly negative values of R_{sk}. Surfaces of CrN coatings are generally smoother than of TiAlN coating. For CrN samples a decrease of roughness (R_a) is followed by almost gradual decrease of (R_{sk}) parameter and continuous increase of ejection force (Table 1, Figure 5). On the other side for TiAlN coatings a somewhat different behaviour is observed. The TiAlN-S samples have lower R_a parameter than TiAlN-R samples, but a considerably higher R_{sk} parameter. Accordingly, the values of ejection force for TiAlN-S are almost similar as for the TiAlN-R samples.

Explanation concerning the revealed behaviour could lie in the pin-casting interlocking conditions or in the nature of stress concentration that develops on the pin casting interface during ejection process. By cross sectional evaluations, not presented herein, it has been shown that casting exhibit a fully interlocked contact with CrN and TiAlN samples. Therefore, it is concluded that the ejection force required for pin release depends predominantly on the stress conditions in the pin-casting contact. During the ejection process, asperities of rough surfaces (CrN-R, TiAlN-R, TiAlN-S) induce shear stress concentrations on the pin-casting interface, which reduce the force required for the initial pin release. The morphology of built-up layer around surface features (marks, defects) undoubtedly support this theory (Figure 3). However, on very smooth surfaces (CrN-PP, TiAlN-PP), due to high tangential forces [5],
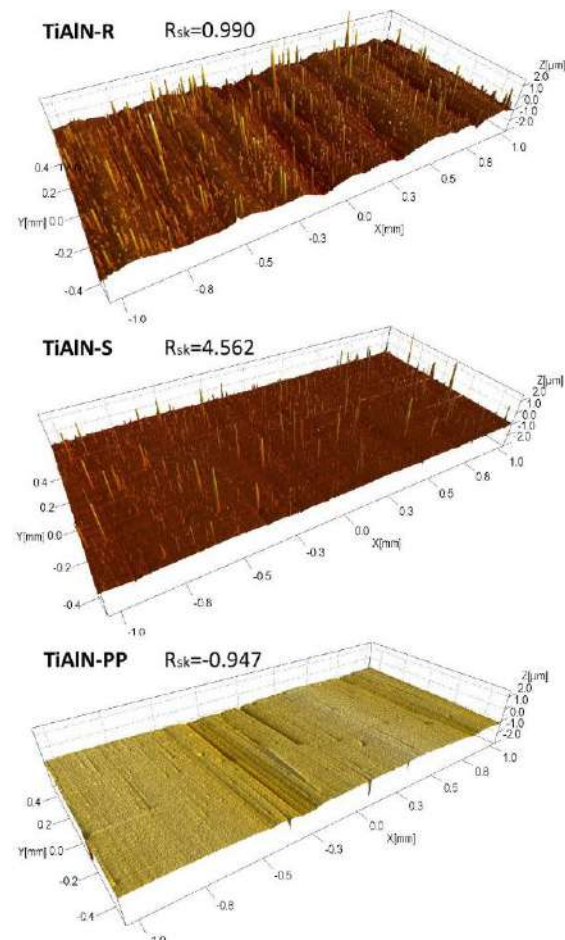
Figure 5. Surface topography images of TiAlN coated samples

adhesion is enhanced and consequently higher forces are needed for pin release.

Application of very smooth tool surfaces is beneficial for obtaining narrow casting tolerances and highest surface finishes. However, considering the results of presented investigation, together with the fact that coatings provide adequate protection against effects of cast alloy, coatings with post polished (very smooth) surfaces are not beneficial for efficient application on a high pressure die casting tool.

4. CONCLUSIONS

Presented investigation employed ejection test for the evaluation of Al-Si-Cu alloy soldering tendency toward different tool materials, layers and PVD coatings intended for application on high pressure die casting tools. The performance of PVD coating is evaluated on samples prepared to a range of surface roughness.

Mechanical characteristics of investigated plasma nitrided layer and duplex CrN and TiAlN coatings are adequate for the application of high performance high pressure die casting tools.

For investigated materials, prepared to the same degree of surface roughness it was found that the ejection force is independent of their surface chemical composition. This is a novel information revealed by considering the effect of surface roughness.

It was found that all investigated materials are prone to mechanical soldering by Al-Si-Cu alloy. The identified built-up layer of cast alloy formed by the effects of mechanical soldering.

The ejection performance of samples with CrN and TiAlN coating greatly depends on their surface roughness. The ejection force increase with decrease of their roughness. The highest values were recorded for post deposition polished surfaces for both kinds of coatings.

Performance of PVD coatings on high pressure die casting tools, beside surface chemistry greatly rely on surface roughness and surface morphology of tool parts.

ACKNOWLEDGEMENT

REFERENCES

[1] J. Lin, S. Carrera, A.O. Kunrath, D. Zhong, S. Myers, B. Mishra, P. Ried, J.J. Moore: Design methodology for optimized die coatings: The case for aluminum pressure die-casting, Surface and Coatings Technology, Vol. 201, No. 6, pp. 2930–2941, 2006.

[2] P. Terek, L. Kovačević, A. Miletić, P. Panjan, S. Baloš, B. Škorić, D. Kakaš: Effects of die core treatments and surface finishes on the sticking and galling tendency of Al–Si alloy casting during ejection, Wear, Vol. 356–357, pp. 122–134, 2016.

[3] V. Joshi, K. Kulkarni, R. Shivpuri, R.S. Bhattacharya, S.J. Dikshit, D. Bhat: Dissolution and soldering behavior of nitrided hot working steel with multilayer LAFAD PVD coatings, Surface and Coatings Technology, Vol. 146–147, pp. 338–343, 2001.

[4] K. Bobzin, T. Brögelmann, U. Hartmann, N.C. Kruppe: Analysis of CrN/AlN/Al2O3 and two industrially used coatings deposited on die casting cores after application in an aluminum die casting machine, Surface and Coatings Technology, Vol. 308, pp. 374–382., 2016.

[5] B. Bhushan: Adhesion and stiction: Mechanisms, measurement techniques, and methods for reduction, Journal of Vacuum Science & Technology B., Vol. 21, No. 6, pp. 2262-2296., 2003.

DAMAGE AND DESTRUCTION OF WORKPIECE AND TOOL SURFACES IN IRONING PROCESS

Dragan ADAMOVIC[1*], Miroslav ŽIVKOVIC[1], Tomislav VUJINOVIC[2], Slobodan MITROVIC[1], Jelena ŽIVKOVIC[1], Dragan DŽUNIC[1]

[1]Faculty of Engineering, University of Kragujevac, Kragujevac, Serbia, adam@kg.ac.rs, zile@kg.ac.rs, boban@kg.ac.rs, jelena.zivkovic@kg.ac.rs, dzuna@kg.ac.rs
[2] APEIRON University, Banja Luka, Bosnia and Herzegovina; tomo.vujinovic@yahoo.com
*Corresponding author: adam@kg.ac.rs

Abstract: *All metal forming processes have some common features (one of the contact pairs is significantly plastically deformed, tool is always in contact with new surfaces, etc.), but still, certain processes differ from one another, both in terms of the contact geometry and of the values of process parameters (speed range, specific pressures, operating temperatures, etc.). Change of friction parameters is reflected in different intensity of the tool wear and damage of the workpiece surface.*
Experimental studies presented in this paper were performed on the original tribo-model of ironing process and aimed to point out the changes that occur during the ironing process, as well as to consider the influence of certain factors (tool material, lubricant on die and punch) on the damage of sheet metal and tool surfaces.

Key words: ironing, galling, steel, aluminum, roughness, die, punch

1. INTRODUCTION

Basic factors that have influence on tribological phenomena in metal forming can be divided into five groups:
1. *Geometric factors* (macro- and micro-geometry of the contact, deformation of macro- and micro- zones of contact, surface of actual contact),
2. *Kinematic factors* (type and character of movement, speed, duration of contact),
3. *Dynamic factors* (distribution and value of normal pressures, character and change of the load),
4. *Physic-chemical factors* (type of contact pair material, chemical affinity of contact pair material, crystalline structure, type of oxide, type of lubrication) and

5. *Energy factors* (temperature of micro-zones of contact, energy balance in macro- and micro-zones of contact, results of the energy processes).

Factors 1 and 4 characterize the basic properties of contact pairs (internal factors), while others define the basic parameters of the friction process (input factors).

Assessment of the influence of various factors on the friction force value and the friction itself is required primarily for practical reasons. Depending on the change of friction characteristics the process characteristics are changing, and that is necessary to know for more accurate selection of equipment and technological process.

In practice, a number of factors simultaneously change, so despite the fact

that each of them has an influence on the process, it affects the change of some other factors' influence as well. For example, speed change affects the temperature change of contact pairs, change of specific pressure is closely related to the degree of deformation, and so on.

In other words, besides the individual influence of each factor there is also an interaction between some factors. Therefore, the value of friction coefficient is determined according to collective influence of all interconnected factors.

2. DAMAGE AND DESTRUCTION OF METAL SURFACE IN METAL FORMING

The question of optimal contact pairs according to their type of material was and still is the subject of many detailed tests, that have been carried out mostly on mechanical elements so far. The selection of optimal contact pairs also has the great influence in metal forming process. However, in the case of pairs of mechanisms contact elements can be chosen quite freely, while in the case of metal forming, the free choice is almost impossible since one of the contact pair materials, the one that is plastically deformed, has already been determined and represents an independent factor. Only material of the tool can be changed, and the choice of materials that could be used for creating the tool is quite limited (carbon or alloyed steel).

In the case of conventional plastic forming of steel the unfavorable contact pair is steel against steel, while in case of forming of non-ferrous metals, unfavorable contact pairs are: tool steel – nonferrous metal (for example Fe-Al, Fe-Zn, Fe-Cu, etc.). Intensive wear of the tool used for metal forming indicates that reduction of roughness and increase in tool hardness do not always give satisfactory results. In order to manage selection of contact materials and thus the process of tool wear one should know physical and chemical processes that occur in friction zones.

2.1 Micro-fractographic analysis of surface topography in the friction process

Specific (closed) system of the contact kinematic pair prevents direct observation of the contact zone and thus monitoring the phenomena that occurs there. Therefore, indirect tests of change of force or moments of friction are performed, and the effects of friction manifested as wear or damage of the contact surfaces are monitored. Based on the intensity and character of these changes, the type of friction is selected.

Analysis of the change of surface topography due to the effects of friction performed at the moment of big increase can provide a very detailed detection of phenomena that occur in the contact zone, as well as the evaluation of friction mechanism [1].

This analysis aims to show the mechanism of deformation in micro-zones of contact and transfer of material, as well as the way of its removal from the contact surfaces, i.e. introduction of the specific mechanisms of friction for higher values of pressure as well as developing a physical model of the friction process. Since the crystal structure is considered to be one of the main factors that affects the tribological properties of the metal and the friction mechanism, it is necessary to analyze the change of surface topography after friction in case of metals that are crystallized in various crystallographic systems.

2.2 Damage and destruction of metal surface in case of same material pairs

In order to examine the effect of the crystalline structure to the mechanism of metal transfer in micro-zones of contact and to present the friction mechanism between same metals it is interesting to consider a contact pair Fe-Fe.

Contact pair Fe-Fe. Examples of damage of mild steel specimens in friction process show visible plastically deformed adhesion compounds wherein the smaller elongation of micro-zone of the contact is observed

(compared to Al and Cu), indicating a greater reinforcement of the metal. This also leads to the notching (galling) and breaking the oxide. Micro cracks at the edges of the notches indicate the local metal reinforcement in the zones of contact with friction.

2.3 Damage and destruction of metal surface in case of different material pairs

Analysis of the change of surface topography in the friction process due to contact between two different metals is carried out considering the influence of the crystal structure and the chemical affinity of the micro kinematics of material transfer in the contact zone. Analyzed pairs are: Cu-Ni, metals that crystalize in the same crystallographic system (grid A_1[1]), then metals that crystallize in different crystallographic systems, for example Fe-Al, Fe-Cu (grid A_1-A_2) as well as the pairs where one of the metal has a hexagonal structure, for example Cu-Zn (grid A_2-A_3) and Fe-Zn (grid A_1-A_3).

Contact pair Fe-Al. In case of this contact pair the adhesion of aluminum on the steel surface can be observed. Adhesives of aluminum have the form of a very elongated strips, which indicates the great plasticity of the metal.

In case of these pairs destruction of adhesion compounds occurs in outer layer of aluminum, not on the initial contact surfaces. This shows that the resulting compound is characterized by higher strength regardless the low chemical affinity of these two metals. Mechanism of destruction of the adhesion compounds is analogous as in the case of regular metal grid A_1, A_2, which means that micro-zones of contact are strongly plastically deformed and then are separated without clearly visible slip planes. As a result of significant plastic deformation of adhesion compounds a relatively slight increase of the surface roughness occurs. Metals of this contact pair are significantly apart in the

periodic table, have different values of atomic radius and are not soluble in the solid state. These characteristics suggest that the intensity of formation of friction compounds is small. However, in the case of this contact pair extreme adhesion of aluminum on the steel workpiece surface is observed.

X-ray examinations [1] indicate that these are no fusion joints. Formation of no fusion compounds instead of diffusion ones is a result of a high tendency of aluminum to oxidation. The obtained aluminum oxides are very hard (approximately 1800 HV) and thus very brittle, so the destruction occurs even in the case of shear stress of 2MPa, which causes direct metal contact.

Contact pair Fe-Zn. Adhesives of the contact pair Fe-Zn have a layered character. Regardless of the relatively low chemical affinity of the metal of this contact pair, the destruction of adhesion compound does not take place on the surface of the initial contact, but in the outer layer of weaker Zn, where the layered character of the material transfer in micro-zones of contact is visible.

In the case of these metals, traces of pulling have not been observed but only the shear of adhesion compounds associated with a small strength to shear of Zn, which is a property of the metal with a hexagonal shape of crystal grid.

Given the small strength to shear of Zn, the frictional resistance is small, though transfer of the metal is significant, which cause a significant increase in surface roughness.

Summarizing the test results of contact pairs of the same and different metals it can be concluded that the crystal structure shows a substantial influence to frictional resistance and mechanism of deformation, as well as to destruction (shear) of adhesion compounds, mostly in the case of similar metals. In the case of a pair of dissimilar metals, the influence of the crystal structure and mutual chemical affinity of contact pair metals should be considered. The greater tendency to the formation of adhesion compounds occurs in the case of dissimilar metals. This is the result of a significant approaching of surfaces under

---

[1] In crystallography, A_1 denotes face-centered cubic grid, A_2 – body-centered cubic grid, A_3 compact hexagonal grid.

the influence of higher normal pressures and a significant increase in real contact zone. The result of such interaction is significant adhesion of one metal to another, whereby, as a rule, metal with lower melting point is pasted on the metal with higher melting point which can be explained by higher chemical activity of the first one.

Great adhesion leads to the fact that the resistance of adhesion compounds is higher than the resistance of at least one metal of contact pair regardless of the chemical affinity of these metals. Destruction of the compound occurs mainly in the outer layers of metal with lower strength and not on the initial contact surface. In contrast, the mechanism of micro deformation of adhesion compounds, and the way of their destruction (shear), are greatly dependent on the crystal structure, although there is some influence of the chemical affinity of contact pair metals.

In the case of metals with face or body centered grid (A_1 and A_2) which have a higher plasticity, the resulting adhesion compounds reach a significant plastic deformation during the friction as evidenced by the elongation of micro-zone of the contact. In contrast, quite different character of movement in micro zones of the contact occurs in the case when one of the metals of contact pair has a hexagonal grid. Then deforming of the metal in micro-zones of contact has a layered character. In the case of these contact pairs destruction of compounds is carried out always in the outer layers of the metal's hexagonal grid, regardless of the chemical affinity of metals of contact pair, which results from the low strength to shear of metal with A_3 grid, and great number of smooth zones is observed on a surface.

Effect of the chemical affinity to mechanism of surface damage can be observed in the case of contact of metals with cubic grid, body or face centered. If the metals of the contact pair have higher chemical affinity then the resistance of resulting compounds is greater than both of the metals of contact pair (those are always diffusion compounds), so in addition to plastic deformation, deep pulling

can be observed, followed by the increase of surface roughness. In the case of small chemical affinity of metals of contact pair classical deformation dominated in micro-zones of contact, and there is no pulling during the shear of adhesion compounds. The increase of surface roughness in that case is insignificant. [1].

From abovementioned considerations, it follows that, the crystal structure, as well as the chemical affinity of the contact pair metals belong to the factors that have a very large impact on:

- Friction resistance,
- Mechanism of destruction of adhesion compounds and consequently the way of moving the material,
- Type of damage of contact surfaces and in particular the increase of roughness,
- Intensity of wear.

3. EXPERIMENTAL RESEARCH

Experimental studies presented in this paper were performed on the original tribo-model of ironing process, which bilaterally symmetrically imitates the contact zone of die and punch. This model enables the realization of high contact pressures and respects the physical and geometrical conditions of the real process (material of die and punch, topography of contact surfaces, angle of die cone - α, etc.) [2].

The bent sheet metal band, U-shaped test piece, is assembled on the ''punch''. Holding force F_D acts on test piece by dies. Dies are assembled in supports, where the left support is motionless and the right support is movable together with the die. The test piece slides between the dies under the force that is applied at the punch head, whereby the thinning of the test piece wall thickness occurs. During ironing process, the outer surface of the test piece slides against die surface inclined by an angle α, and the inner surface of the test piece slides against plates attached to the punch body.

The device was realized with the compact construction of high rigidity, with the possibility

of easy changes of contact-pressing elements (die and plate), with simple cleaning of contact zones and suitable assembling of test pieces.

Plates and die can be made of various materials and with various roughnesses, and dies can also have a various inclination angle α.

For experimental tests in this paper material is selected from Al-alloys, in the form of sheet, mark AlMg3(.43)[2] (old mark: AlMg3-24; mark according to DIN: AlMg3 F24, mark according to EN AW-5754: AlMg3). This material is very important in modern industry. Mechanical properties of the tested material, determined for samples cut in the rolling direction of the sheet are: R_p=201.1 *MPa*, R_m=251 *MPa*, A=12 %, n=0.13545, r=0.40510, E=0,701×105 *MPa*.

Contact pairs ("die" and "punch") are made of alloy tool steel (TS) with high toughness and hardness, with mark Č4750 (DIN17006: X165CrMoV12). This steel is resistant to wear and is intended for operation in the cold conditions. Oil quenching and tempering is carried out before the mechanical treatment by grinding.

Hard coating of TiN is applied to one set of tools made from heat treated alloy steel Č4750.

4. RESULTS OF EXPERIMENTAL RESEARCHES

In case of deep drawing with thinning of the wall thickness, depending on the type of the contact pair (tool-die, the punch/sheet metals) and used lubricant, creating the adhesives on the tool can occur. Every adhesion on the tool deteriorates the surface quality (adhesion on punch, dies, etc. is reflected in the drawn parts) and is one of the main problems in technology of deep drawing with thinning of the wall thickness, both regarding the product quality as well as the wear of the tool. This phenomenon is often referred to as "*galling*" in literature and represents the subject of detailed study of many authors [3, 4, 5, 6].

Appearance of smooth and notched surfaces made by scratching due to aluminum adhesives is shown in Figure 1.

a)   b)
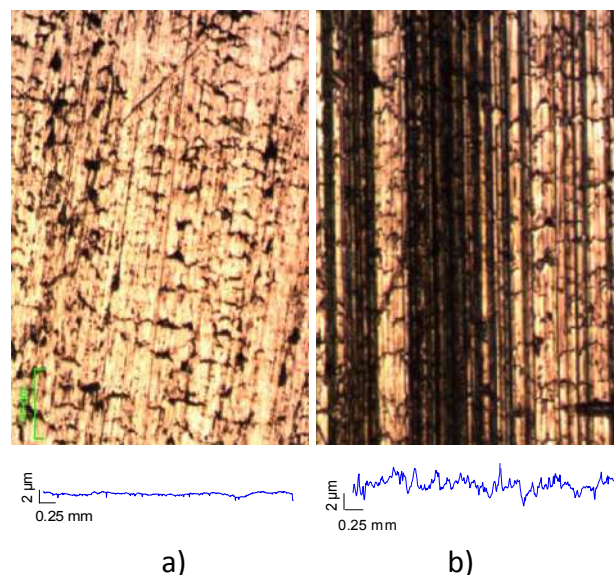
Figure 1. Smooth and notched surface Al samples and their roughness

As previously stated, adhesives especially occur in case of drawing of aluminum alloys, both on the punch and on the side of the die, Figure 2.
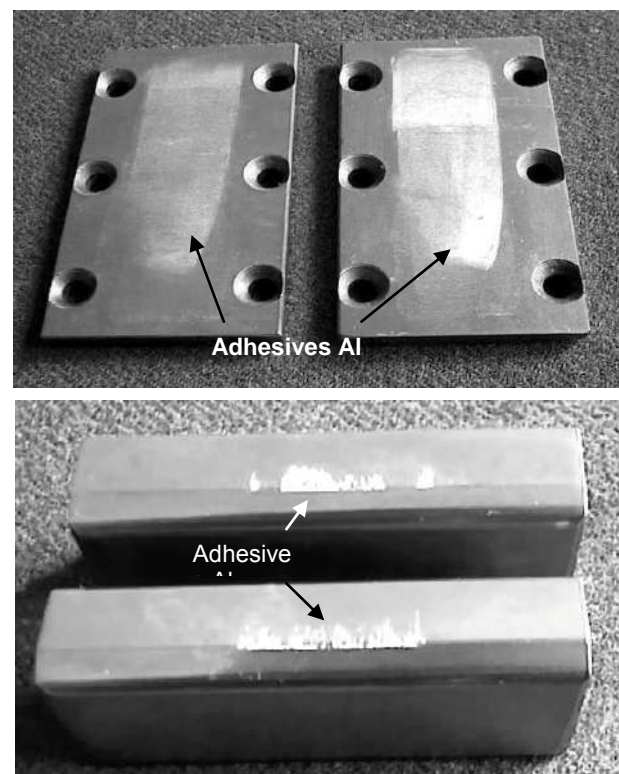
Figure 2. Aluminum adhesives on the punch and die surfaces

EDS analysis of the surface of the punch and the die with a TiN coating confirmed the presence of aluminum adhesives, Figure 3.

---

[2] - Mark AlMg3 will be used further in text
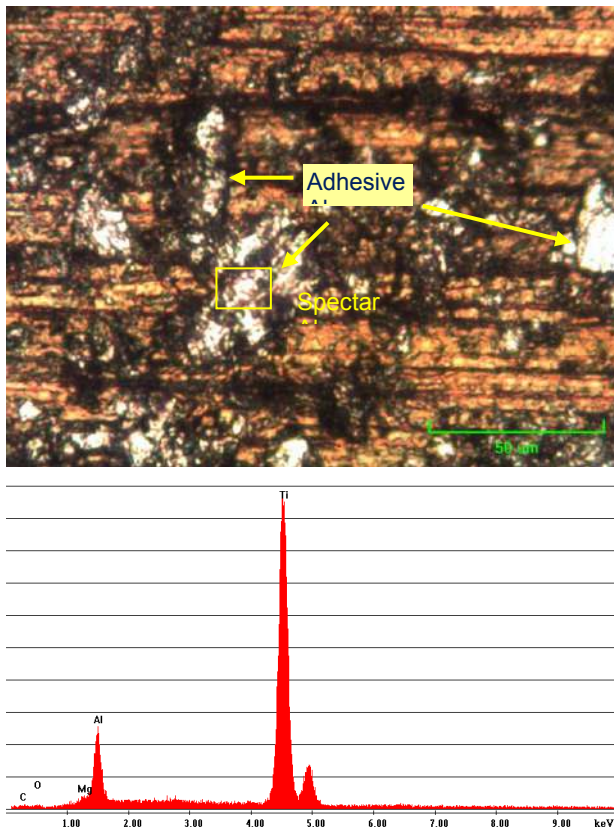
Figure 3. EDS analysis of aluminum adhesives on punch made from tool steel with TiN coating

Using inadequate lubricants, followed with the effect of greater holding force, in the process of deep drawing, regularly leads to the formation of adhesives and significant disruption of contact conditions, and therefore at each subsequent phase ironing force increases significantly (Figure 4).
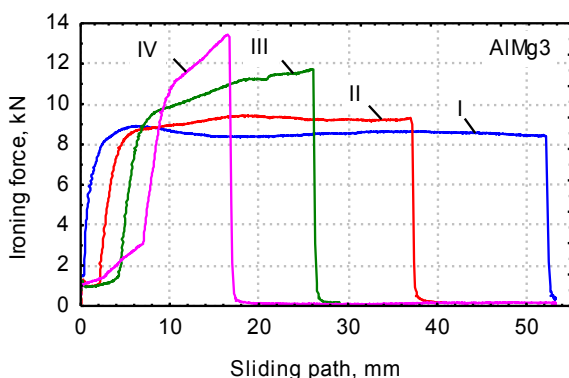
Figure 4. Change of ironing force at multiphase drawing of steel sheet metal and AlMg3 alloy samples

5. CONCLUSION

In the case of deep drawing process with thinning of wall thickness it is characteristic that if the coupled contact pair (tool-Fe, Ti/sheet metals-Al) is made from different metals (tool - Fe, Ti / sheet - Al), there is an intensive formation of aluminum adhesives on the surface of the tool.

As a result of preponderance of the adhesion forces to the resistance to plastic flow of adhesion layer, plastic deformation of formed adhesions occurs, i.e., their pulling and smudging. In the case of a sufficiently large thickness of adhesion layers, as a result of many times repeated process of their plastic deformation, the process of separating formed adhesives from the base metal (tool) begins, by means of flaking (shear) or pulling, whereby there is a considerable damage to the tool surface, and therefore an increase of the surface roughness of the workpiece. Such processes are especially typical in deep drawing with thinning of the wall thickness of sheets if adequate lubricant is not used.

ACKNOWLEDGMENT

REFERENCES

[1] Gierzynska M.: *Tarcie zużycie i smarowanie w obrobce plastycznej metali*, WNT, Warszawa, 1983

[2] Adamović D.: *The behavior of materials in contact during the cold plastic forming processes with high working pressures*, PhD Thesis, Faculty of Mechanical Engineering in Kragujevac, Kragujevac, 2002. (in Serbian)

[3] Schedin E., Lehtinen B.: Galling Mechanisms in Lubricated Systems: a Study of Sheet Metal forming, Wear, 170, 1993., 119-130

[4] Schedin E.: Galling Mechanisms in Sheet forming operations, Wear, 179, 1994., 123-128. (1978),

[5] Hirasaka M., Nishimura H.: Effects of the Surface Micro-geometry of Steel Sheets on Galling Behavior, Journal of Materials Processing Technology, 47, 1994., 153-166

[6] Ike H., Yoshida K.: Galling mechanism and requirements to lubricants, 3th Intern. Colloq., Esslingen, 1982., 18.1-18.19

IMPROVING THE TRIBOLOGICAL PROPERTIES OF CUTTING TOOLS BY CONTACTLESS ELECTRICAL SPARK DEPOSITION (LESD)

Todor PENYASHKI[1] Galina NICOLCHEVA[2,*], Georgi KOSTADINOV[3], Mara KANDEVA[4]

[1]Institute of Soil Sciences, Agrotechnologies and Plant Protection „N. Pushkarov" – Agricultural Academy –ISSAPP „N.-Pushkarov") Sofia, Bulgaria

[2]Technical University of Sofia (TU-Sofia) Sofia, Bulgaria

*Corresponding author e-mail: ginic@tu-sofia.bg

Abstract: *In this work contactless electrical spark deposition (LESD) with polycarbide composite electrodes based of WC and TiN is used to enhance the durability of turning tools from high speed steel. The complex influence of the electrical parameters of the deposition process, the electrode materials, (respectively the morphology and composition of the coatings) and of the cutting speed and feed onto the wear, the contact processes, the power and average temperature during cutting were investigated. From the results obtained it was found that the effect after the LESD varies far too widely. Depending on the used processes parameters, the wear of the layered tools is 1.3 to 2.4 times lower than that of the uncoated. Relatively constant effect after the LESD -1.8- 2 times lower wear is obtained in the speed range above the 30 m / min. However, for various cutting conditions optimum results are obtained at different values of the process parameters of LESD, i.e. it is not possible to determine a single material and regime, in which the wear of the layered instruments in all investigated cutting speeds and feeds to be minimized. It has been found the impact of different electrode materials on the quality characteristics of the resulting coatings and on the wear of layered tools. The wear analysis show that the LESD can successfully be used for increasing wear resistance of cutting tools, but in order to obtain maximum a durable and reliable tribological effectiveness is needed preliminary optimization parameters of the regime and materials for deposition according to the specific cutting conditions. The knowledge gained in this work can be used for obtaining advanced know-how for improvement of the wear resistance of cutting tools, for optimizing their qualities and prediction of their reliability and life.*

Keywords: *contactless electro-spark deposition, (W,Ti,Ta,Nb)C, friction, wear resistance, microstructure, microhardness, cutting tools, cutting speed.*

1. INTRODUCTION

Electrical spark deposition (ESD) is one of the progressive, dynamically developing branches of the metal science, which is distinguished by its low cost, simplicity, compactness and reliable equipment and allows being deposited locally coatings from any and onto all electrically conductive materials.

ESD is a simple, cheap and universal means of local deposition of single and multilayer coatings of any and on all kinds' conductive materials.

ESD coating has a high strength of adhesion to the substrate, the absence of heating and deformation of the material of layering device, simplicity and accessibility of the technology, simple, cheap and compact equipment, with low operation cost, low cost of materials and low energy consumption of the process. It process allows the deposition of coatings on strictly certain places without the need for means and measures to protect the rest of the surface overlay coating product. It is a promising high universal tribological resource for improving the wear resistance of any friction metal surfaces. Among its other applications, ESD creates prerequisites for deposition of wear resistant coatings that can potentially improve the efficiency of the cutting tools and the tool life.

Metal cutting is one of the most complicated tribological processes. It occurs at much higher pressures than in the most loaded friction parts / e. sliding bearings /. In the contact surfaces are realized normal stresses up to 1200 MPa and tangential stresses to 200-400 MPa, the temperature may reach up to $1000^{o}C$.

In these conditions occur intensive friction, adhesion and diffusion processes, sometimes chemically. Under these conditions it is not in force and the law of Amonton-Kulon for friction, the actual relationship between the friction force and pressure has exponential character, and the system of friction in cutting is thermodynamic unbalanced [1,2].

Currently, the process of shaping by cutting are specialized part of tribology. Tribology of metal cutting studyied the processes of interaction between the instrument and processed materials, the mechanism of wear, the influence of the physicochemical properties of the cultivated materials, geometric parameters of the tool, cutting conditions / kinematic scheme and parameters of the cutting / and the external environment on the wear and durability of tools, productivity processes.

Notwithstanding the advent of improved tool materials, HSS tools are the most common tool materials because of their low price and better strength characteristics. The main disadvantage of HSS is their lower hot hardness, which limits the use of HSS tools for high cutting speeds. For increasing tool life and allowable cutting speeds of HSS tools currently most commonly are used Surface engineering methods to deposit single and multilayer wear-resistant coatings.

The widespread and approved with its efficiency chemical vapor deposition (CVP) and physical vapor deposition (PVD) coatings from hard and superhard materials such as TiN, AlN, TiCN, CrN, TiAlN, TiS and others have a higher qualities than the electrical spark coatings. PVD and CVD the methods are expensive and require expensive equipment and high investments, until ESD unlike them, is cheap and accessible process and along with the many other applications he could also be used of strengthening of machine tools.

The experimental data in the literature and existing theoretical developments on the issue of ESD tools are in most cases defragged and have multidirectional and unsystematic character. The used in most studies presumptions of the influence the composition and structure of the resulting coatings on their properties do not reflect the actual dependencies as they does not consider the effects of multiple technological constituting factors and also the type of equipment for ESD.

Some authors reported absence of effect or minimal one, and others [3-6] for 50 - 400% increase in tool life. In [7] reported for five-times increase tool life of drill bits, and in [8] – for a 20-times increase in life of the layered tools.

Furthermore, some authors indicate that the durability of the instruments with tungsten carbide coatings [5-7] is higher than that of the ESD with other electrodes, and the others – [8,9,10] - that the tool life of coated with electrodes T15K6 and those based on TiN, TiCN, TiB_2 etc. is higher than that of the layered with tungsten carbide electrodes.

The reason for these differences is that these tests do not take into account the simultaneous impact of all factors influencing the process of wear - materials and conditions for electrical spark deposition, geometric

parameters of the cutting tool, the cutting conditions and properties of processed material defining the specificity of different contact processes and phenomena between the chip and the layered surface. This is mainly related to the lack of sufficient knowledge about the process of friction and wear mechanism of layered instruments.

In this regard, the objective of this work is to study the wear and to improve the surface properties and increase the working ability and tribo-efficiency of HSS tools by contactless electro-spark deposition with carbide materials based on WC, TiC and TiN and formation of wear-resistant surface structures.

2. METHODOLOGY

The effectiveness of LESD tools are essential many factors, the most important of which are the parameters of the regime and material for LESD and parameters of cutting modes. This study examine the complex influence of electrical parameters of the ESD process, the type of electrode material and the qualitative characteristics, composition, and structure of the resulting coatings on the wear properties of model cutting tools for turning at different speeds and feeds in order to achieve a hard, strong and endurance surface of tools.

For a comprehensive assessment of the qualities of the tools has been accepted their operational durability, whose main characteristics are wear and tool life, the force and temperature of cutting. Under tool life be understood the operating time until reaching the accepted criterion for wear.

2.1 Materials and Apparatus for ESD

Used in the vibration installations pulse energy to 5J [3,5-10] allows obtaining coatings with higher thickness, but with higher and in most cases unacceptable roughness and degree of unevenness. For obtaining uniform coatings with less roughness has been a necessary the use of mechanical equipment with low energy and duration of the pulses. These are machines for contactless ESD /LESD/

type "Elfa 541" Fig.1a [11,12]. The application of the coatings is carried out with a cylindrical rotating electrode – 1- Fig. 1b, with a diameter of 1÷1.5mm, trapped in the laminating head. Working pulses with energy $E=10^{-3}÷10^{-2}J$ and frequency up to 66 kHz are lodged by a pulse generator - 2 (Fig. 1b). Automatic regulator of inter-electrode distance - 3 maintain the necessary gap in which plasma spark discharges run and ensures high stability of the process. Mechanisms 4 provide moving of details with controlled speed along the X and Y axes during the drawing of the cover with the top surface of the laminating electrodes (Fig. 1b, c). It provides also automatic control over the inter-electrode distance at stratification with the lateral surface of the electrode– Fig. 1d.

The lamination product, fastened on the machine table is moved in the X and Y axes at controlled rates. The performance of the deposition is up to 0.5÷0.6 mm^2/s.

During the experiments the following primary adjustable parameters of the regime for LESD were used:
- Pulse current amplitude - I = 8-16A;
- System voltage /Circuit voltage/ - U = 90V;
- Pulse duration - Ti = 3, 5 8,12, 20; µs;
- Capacity – C = 0.2, 0.5, 0.7, 1 µF;
- Coefficient of filling of the pulses - τ = 0.1and 0.2 - τ = Ti/T, where T=Ti+Tp is the period of the pulse, and Tp- pause between the pulses; 1/T = f- frequency of the pulses;
- Speed of deposition /coverage rate/- V = 0.6 mm/s;
- Number of passages of the electrode - n = 2.
Apply coatings are single with two passes of hard facing electrode

2.2 Materials of electrodes

The next quick hard metal composite electrode materials with indications respectively P25 and TiN were selected and developed for wear-resistant coatings deposited on a steel substrate.
1. P25 -16%TiC+4.5 % (Ta, Nb) C+10.5%Co+WC. The presence of TiC, TaC and NbC suggests increasing resistance to wear and tear.
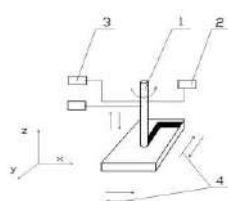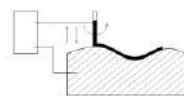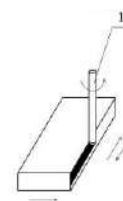
a) **b)** **c)** **d)**

Figure 1 Machine for contactless local electro-spark deposition type "ELFA -with semi-automatic control

Table 1. Parameters of coatings

№	Elect rode	I, A	C, μF	Ti, μs	τ -	Ra, μm	δ, μm	HV, x10³MPa
1	P25	14,4	1	12	0,1	1,38	6,8	15.7
2	P25	14,4	0,68	12	0,1	1,22	5.9	14.4
1	TH	14,4	1	12	0,1	1,15	5,7	12.7
2	TH	14,4	0,68	8	0,1	0.92	4.6	12.3

2. TiN - 80%TiN + Ni, Cr, Mo with micro additives of B, Al2O3 and Cu. TiN has a low coefficient of friction and high wear resistance. Moreover, it is chemically active, at least with respect to iron and may be an excellent barrier against the adhesion and diffusion wear.

2.3 Regimes for LESD

For the current research were selected two modes for LESD - medium and high for Machinery «Elfa» energy of a single pulse. LESD modes and values of roughness Ra, the thickness δ and HV hardness of the damage to the electrodes P25 and TiN coatings are given in Table.1

In LESD electrode P25 and TiN the main phases in the coating composition [4,13 to 15] are modified anode carbides of the type: Fe $(WMo)_4C$; Fe_3W_3C; W_2C, TiN_{1-x}; Ti $(CN)_{1-x}$; martensite (Fe-α) and modified austenite (Fe-γ).

The characteristic X-ray lines of austenite and martensite are broadened and shifted, which is indicative of the presence of solid solutions, crystal defects and internal stress.

By increasing the energy of the pulses (I, C, Ti) increases the amount of carbides, the amount of austenite and its degree of alloying. Grows and the degree of dispersibility of the coatings as at high energies (I≥14.4 A, C ≥1 μF and Ti≥ 12μs) at LESD with electrode P25 is observed austenitic, martensitic structure containing microcrystalline and amorphous metastable phases saturated with superdispersed carbides [13,14]. At LESD with electrode TN in the coatings are additionally observed in small quantities TiN, $TiCN_{1-x}$ and traces from Fe_2Ti, and Fe_2O_3, Fe_3O_4. The amount of the iron-tungsten carbide is less than those obtained with the electrode P25 coatings and is comparable to that of the substrate.

At the regime 1 in the coatings inflicted with electrode P25 in the white layer is obtained austenite-martensite structure of high heterogeneity saturated with super dispersed carbides up to amorphous state. Operational characteristics of pseudo amorphous coatings are not well studied and represent a significant interest due to they are included in these studies.

2.4 Scheme for deposition of coatings

The coating is deposit to the front surface of the major and minor cutting edges of the (inserts) plates in the form of line width 2.5-3 mm (see Fig.12) with two passes of hardfacing electrodes.

2.5 Machine tool

The experiments are carried out on a universal lathe trademark C10MB with stepless variation of speed.

2.6 Cutting tools

Used model cutting tools with square inserts type SPGN 120308 from high speed steel HS6-5-2 (1.3343) - / 6% W, 5% Mo, 4.2% Cr, 1.8% V, 0.9% C / with hardness of HRC 61-63. The inserts are polished to a roughness Ra = 0.63 μm. The radius at the tip of the cutting edges is 0.8 mm. The inserts are attached in toolholder with section 25x25mm and following geometrical parameters: front corner γ 5^0, rear angle α 6^0, chief Adjusting corner χr 75^0 auxiliary Adjusting angle 15^0.

2.7 Processed material

Processed material is from st.45 (0.45% C) with a hardness of 210-220 HB, an external diameter of 160mm and length of 500 mm. Used forced cooling with a 5% solution of boryol in water.

2.8 Methods of measurements

- ### *Tests of coatings*

The surface roughness Ra, μm and thickness δ, μm of the resulting coatings are measured by using profilometer -"Pertometer S5P"(Germany).

The microstructure and microhardness Hv of the coatings have been studied by optical microscopy on cross-sectional and micro-hardness tests under indentation load of 5 and 10 g by metallographic microscopes "Neofot 2" and "Metaval"(Germany). Microhardness of the layer, the sub-layer (in depth to the base) and the base itself has been measured.

Wear - the size of the craters are measured by instrumental microscope "BMI -1" or a place with Brinel pipe accuracy of reporting 0,01mm.

- ### *Tool-life test procedure*

For complex evaluation of the qualities of the tools has been accepted is tool wear and tool life. For the study of wear on cutting tools are carried out single-factor experiments. Explores is the effect of the cutting time factor t on the parameters of wear (hi). Controlled are the flank wear land width on the back surface - VB (the average width of the flank wear land) and depth of the crater on the front surface Kt (the depth of the crater given in μm). This indicator displays the most exact the role of the coating as a specific type a barrier for development of wear not only in front but on the back surface. The measurements are performed at regular intervals. Work up to the wear VB = 0.4 mm, but in some cases, this value may be smaller or larger.

The main cutting force Fz is measured by threecomponent electricinductive differential dynamometer, previously calibrated.

The temperature θ of the contact surfaces of cutting wedge tool is measured by natural thermocouple. For to be the results comparable, the strength and temperature of the cutting are measured simultaneously. The measurements are performed early in the first minute of the process immediately after stabilizing the testimony of instrumentation.

The levels of varying parameters of the cutting are:

Cutting speed V - 10 to 55 m/min, pass (feed) f - 0.11 - 0.37 mm/rpm. Because the cutting depth does not significantly affect on the wear, in all experiments it is assumed to be constant - 1 mm.

These types of conditions are seen as kinds of processing, characterized the contact of the cutting edge of the tool with the material being processed. Thus, the selected range of modes of cutting includes features and of other kinds of processing in which the shearing metal layer is a permanent and the cutting process is continuous. Is thus also the cutting modes are selected not as the typical for turning process, but as a real cutting data and of other kinds of

operations reporting the attainment of similar in types wear. The analysis of the possible combinations of speed and feed allows you to choose particular tools that given combination is appropriate and the resulting effect of LESD be valid for these instruments.

In the tests is study the influence of parameters of the regime for ESD and electrode material, i.e. the qualitative indicators, composition, structure and properties of coatings onto wear of tools.

The studies were conducted in three series of covered and standard (uncovered) instruments depending on the time of cutting.

At regular time intervals is measured wear of tools along the front and wear main surfaces - Kt and VB and built curves "Time-wear" - Kt, VB = f(t, V, f).

Under criteria of wear VB = 0.2 and 0.4 mm are reported relevant durability and are built speed – durability dependencies - T = f (V) for uncoated and layered with electrodes P25 and TiN tools.

3. RESULTS AND DISCUSSION

3.1. Coating characterization. Roughness Ra and thickness δ of coatings

The general appearance of the layered surface and the relief of coatings are shown in Fig. 2. Homogeneous, dense, smooth and adherent coating layers with good repeatability of the qualitative characteristics have been obtained during LESD experiments.

Figure 2. General View of coating from electrode P25 -I=14.4 A, Ti= 12μs C=1μF, τ = 0.1

The coating layers produced by the LESD with the two examined electrodes are illustrated in Fig. 3.

P25/HSS
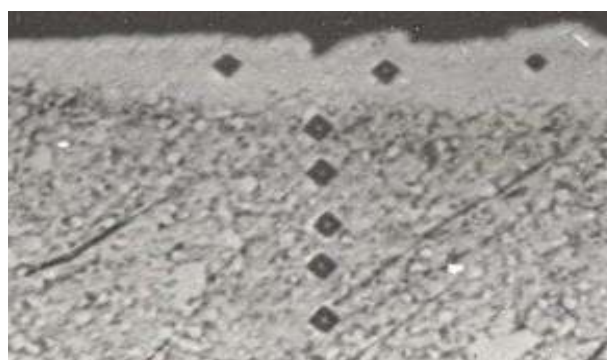
TiN/HSS

Figure 3. Cross-section photomicrograph of the coatings inflicted by LESD on HSS steel under a regime I = 14.4A, τ = 0.1, C=1, C=1μF, n =2 passes of electrode

Surface layers were clearly seen after the etching of the samples. The coatings have a compact and uniform microstructure- white layer with a low degree of porosity and does not mix with the substrate. Microscopic unevenness is observed on different locations on the surface of the coatings in the cross section. However, is seen uniform, equal, dense layers with about 6 μm thickness are seen, snugly connected with the substrate without visible microcracks and omissions. Could be seen, the prints from the measurement of the microhardness in a coating of TiN electrode are larger than those of the coating of electrode P25. Microhardness of the coatings is significantly improved compared with the substrate (Tabl.1).

Figure 4 shows the change of tool wear over time in cutting speed V = 30 m / min and feed f = 0.37 mm / rpm.
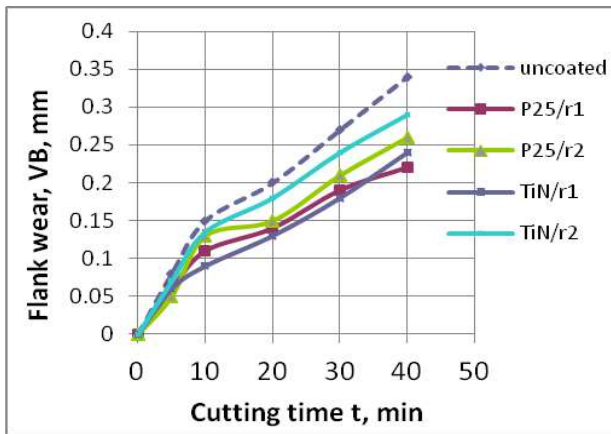
a) Development of flank wear VB in time
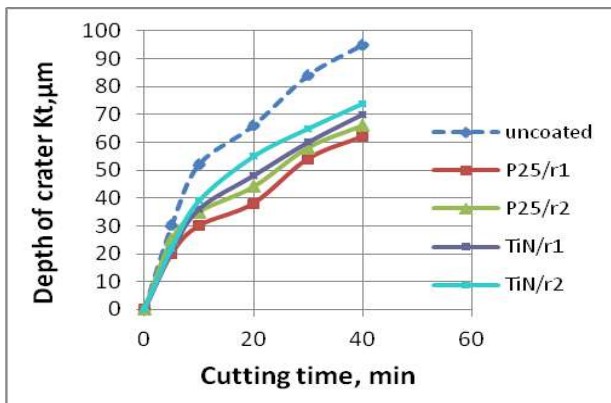
b) Development of Depth of crater Kt in time

Figure 4. Development of wear of uncoated and coated with P25 and TiN electrodes tools at regimes 1 and 2 in time= Cutting speed V=30 m/min, feed f=0.37 mm/rpm.

Fig. 5 shows an amendment of the tool wear in time at cutting speed of V = 40 m / min and feeding f = 0.37 mm / rpm.

Figure 6 shows the variation of wear of uncoated and layered with P25 electrode in modes 1 and 2 - Table 1 tools at different cutting speeds.
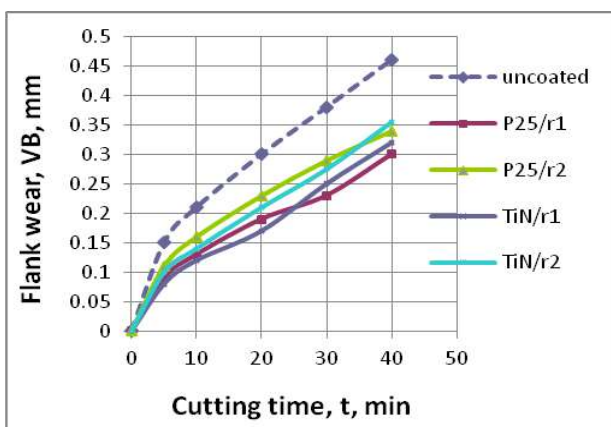
a) Development of flank wear VB in time
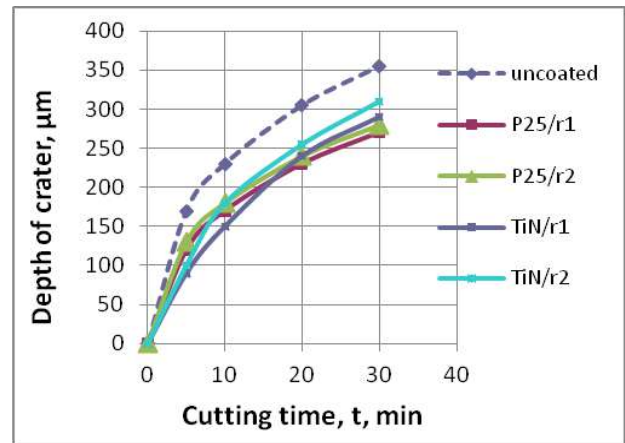
b) Development of Depth of crater Kt in time

Figure 5. Development of wear of uncoated and coated with P25 and TiN electrodes tools at regimes 1 and 2 in time. Cutting speed V=40 m/min, feed f=0.37 mm/rpm
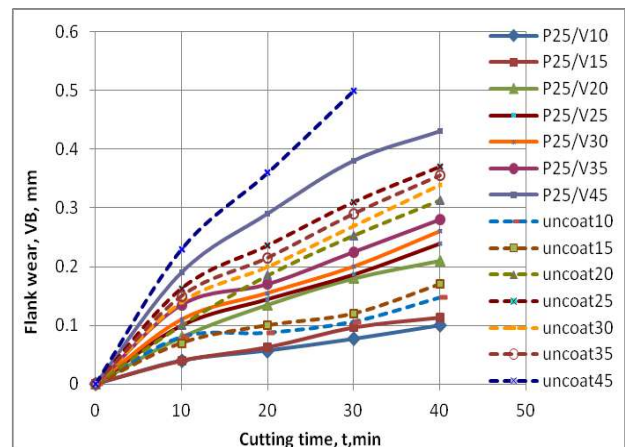
Figure 6. Development of wear of uncoated and coated with P25 electrode tools at regimes 1 and 2 at different cutting speeds V, feed f=0.37 mm/rpm

Figure 7 a, b, c, d shows the change of the wear of the tools in time at cutting speeds V = 30 and 35 m / min and feeding f = 0.21 mm / rpm.
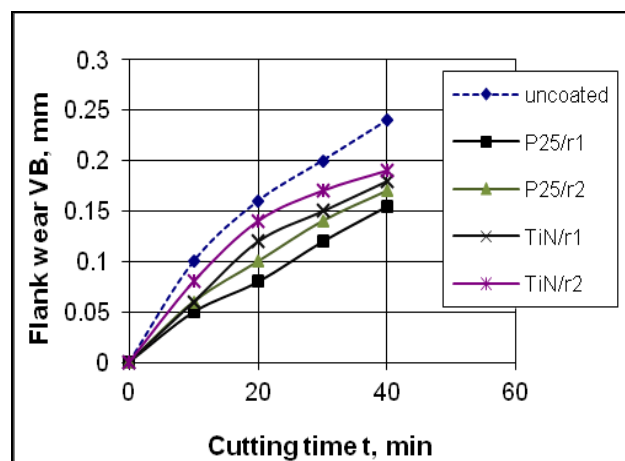
a) Development of flank wear V=30m/min
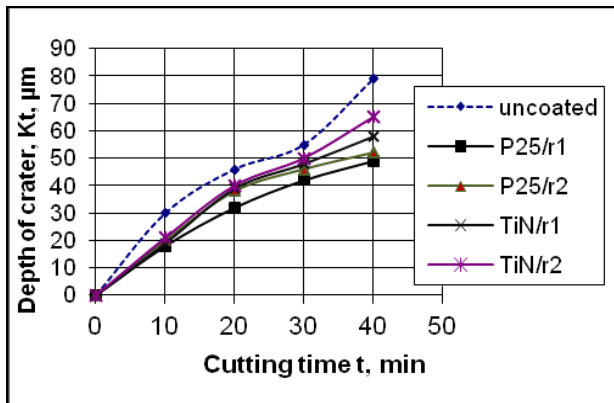
b) Development of Depth of crater V= 30m/min
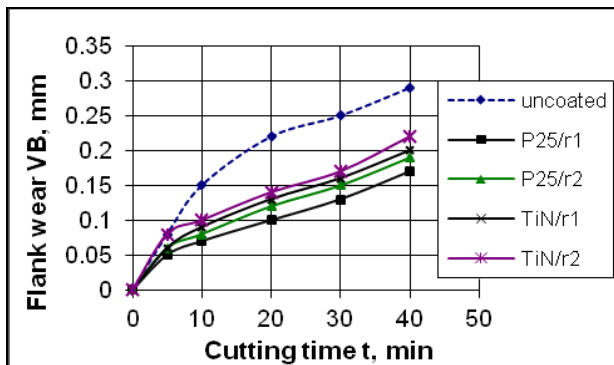
c) Development of flank wear V=35m/min
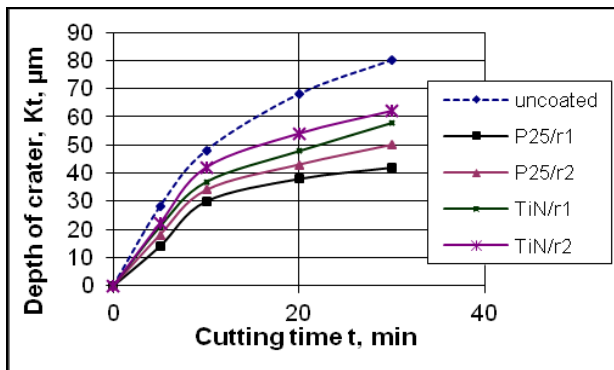
d) Development of Depth of crater V=35m/min

Figure 7. Development of wear of uncoated and coated with P25 and TiN electrodes tools at regimes 1 and 2 in time- Cutting speed V=30 and 35 m/min, feed f=0.21 mm/rpm

From Figure 4, 5, 6 and 7 it is seen that in all studied cutting data, the nature of wear of the LESD tools is like that of the uncoated. The differences are in the lower values of the parameters characterizing the wear. From the obtained curves it was found that the coating system reduces the wear of the tools both in the front and the back surfaces.

Wear of deposited tools under the front surface takes place in two stages. At the first coating is destroyed due to abrasion and delaminating from the substrate.

In the second phase wears out the rest out without of coverage substrate. The layer of basic material however remained stable and longer keeps their working capacity. The depth of the crater Kt is significantly less than that of uncoated tools. The values of Kt for LESD tools are always lower than those of uncoated - Fig.4b, 5b, 6b, 7b and d. The main reason for the reduced wear in this case is higher diffusion resistance, higher hardness and chemical resistance of the coating and of the sub coat layer of the tool steel.

The progressive increase in flank wear width VB with increasing of the cutting speed for feed 0.37mm/rpm is presented in Fig. 6. At all investigated cutting speeds (Figure 4, 5, 6, 7a and 7c), uncoated tools undergo flank wear with a higher rate compared with coated tools.

The differences appear at the beginning of the cutting process. With an increase in the time of cutting, these differences increase, reaching a maximum value within the range VB = 0.2-0.4mm - Fig. 4a, 5a, 6, and 7a and 7c, after which they remain rather constant.

A comparison of the influence of both experimented factors - processing energy and material of depositing electrode allows to establish that a stronger influence on the durability and the wear of the deposited tools provide processing energy.

In the mode with higher energy the wear of coated tools is lower. When comparing the influence of depositiong electrode is established that the differences in the wear of the tools deposited with two electrodes can reach to 20%.

The results obtained show that the influence of the electrode material is connected as with system of LESD, as well with the cutting speed and feed rate. At medium and low cutting speeds, lowest wear have deposited with an electrode P25 tools. At cutting speeds higher than 40m/min - Figure 6, the differences in the value of wear of the coated with the two electrodes tools are reduced and their wear is almost comparable,

but still the wear of the deposited tools with an electrode P25 remains lower.

Reduce the differences in the wear of the deposited and uncoated tools and effects of LESD in this range remain relatively constant - 70-100% lower wear than that of uncoated tools.

The highest differences in the wear of the LESD and uncoated tools - 150% less wear were obtained in the speed range V = 25-35 m/min. Figures 8 and 9 shows the variation of the main force and the average temperature of cutting at coated with electrodes P25 and TiN and uncoated tools. From Fig. 8 can be seen that the cutting force of layered tools is lower than that of uncoated throughout the speed range studied, but cutting force levels are comparable.
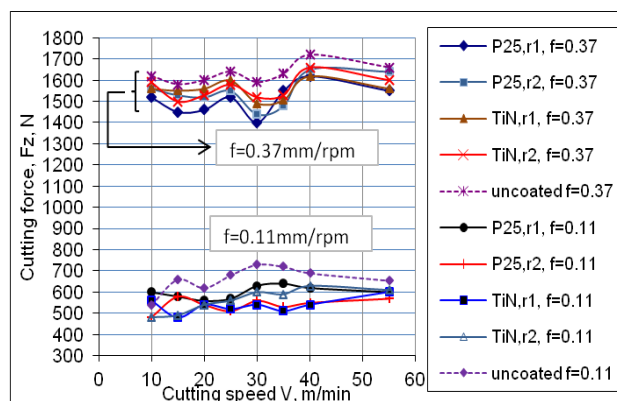
Figure 8. Development of cutting force of uncoated and coated with P25 and TiN electrodes tools at regimes r1 and r2 depending of cutting speed, feed f=0.11 and 0.37 mm/rpm
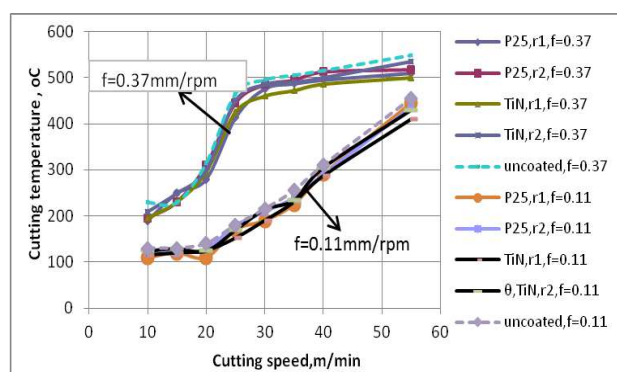
Figure 9. Development of temperature of uncoated and coated with P25 and TiN electrodes tools at regimes 1 (r1) and 2 (r2) depending of Cutting speed, feed f=0.11 and 0.37 mm/rpm.

Larger are the differences in the values of Fz when feed is f = 0.11 mm / rpm. They can reach to 20% in favor of deposited tools.

From the data it is seen that in the speed range V = 15-40 m / min the cutting force passes through the extremums, as at the feed f = 0.11mm / rpm, the maximums and minimums of the layered and uncoated tools are dephased as at speed, and also in values. At speeds over 40 m / min Fz gradually reduced. The probable reason for the presence of extreme values is complex influence of speed-temperature factor, the composition and structure of the surface layer on the contact process between the chip and the front surface of the tools. The cutting temperature is almost the same for deposited and uncoated tools - Fig.9.

It is evident from the data that, as soon as the tool comes in contact with the workpiece at the start of the cutting process, the values of temperature rise rapidly initially, at speeds V = 20 and 30 m / min and feeds respectively 0.11 and 0.37 mm/rpm increase calms down, and then increased progressively slower with increasing of cutting speed until it reaches the maximum value in the highest speeds.

The type of electrode material and the parameters of the mode of LESD slightly influence on on variation of Fz and θ - the lowest force and temperature of cutting are registered with the tools, LESD with TiN electrode in mode1, which can be explained by the higher content of TiN, which has a lower coefficient of friction in comparison to tungsten carbide. In regime 1 with higher energy extremum levels are more implicit than those of deposited with mode2 and of uncoated tools.

Figure 10 shows the speed-tool life relationships in logarithmic coordinates obtained with feed f=0.37 and 0.21mm/rpm at criterion of wear VB=0.2 mm. As can be seen, the life of the coated tools is higher than that of the uncoated tools at all spindle speeds. In analyzing the speed - tool life dependencies was found that in the speed range 20-35 m / min at uncoated and deposited in mode2 (lower energy) -Tabl.1 tools are obtained extreme values of tool life - minimums and maximums. Moreover, the maximum of the durability coincide at speed

with the minimum of the main cutting force Fz - Figure 8. At low cutting speeds wear is concentrated mainly on the back surface due to the unstable congestive underdeveloped area on front surface. At cutting speeds 20-35 m / min - Figc. 4,6 and 7 wear has adhesive and abrasive nature. Thanks of formed as a result of the coating stably developed congestive zone and resistant build -up edge (BUE), that defends the rear surface, the wear of the layered tools is lower, and their durability - higher - Fig.10a, wherein speed 25 and Fig.10 b - at a speed of 30 m / min.

a) f=0.37mm/rpm

b) f=0.21mm/rpm
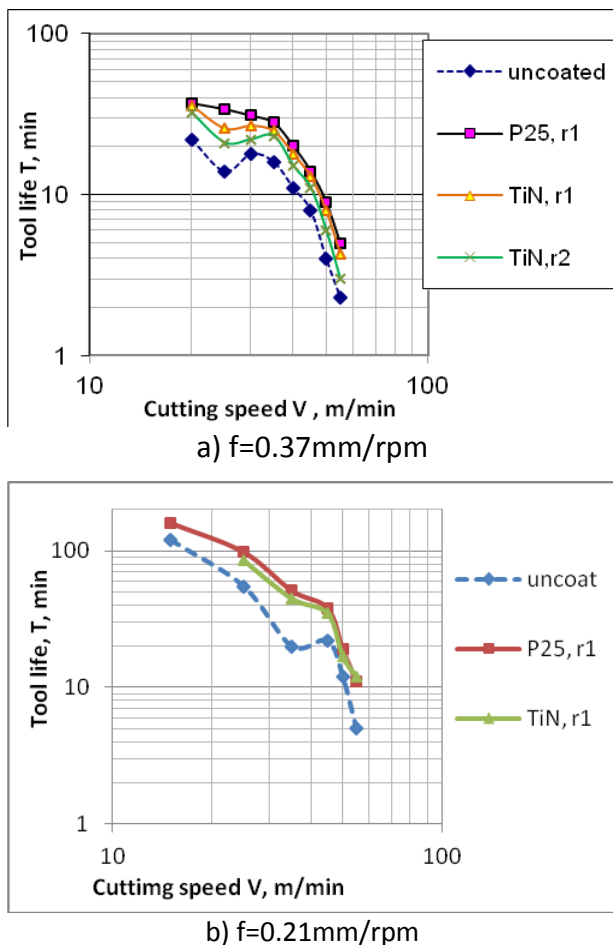
Figure 10. Tool life as a function of cutting speed in logarithmic scales at feed f=0.37 and 0.11 mm/rpm (At criterion of flank wear VB=0.2 mm)

It is noteworthy that the zone of maximum effect for tools coated with the test modes and electrodes for different values of the feed is displaced in the speed range 20-35 m/min. Moreover, in the area of the minima of the durability of the uncoated tools, the wear VB and Kt is maximal, but the wear of coated tools is with a reduced intensity (Fig.4-7)

compared with that of the uncoated tools. This fact allows making conclusion that extreme values of durability in speed- speed-tool life relationships are related with the specifics of friction and hence the impact of speed-temperature factor and **b**uild up edge (BUE). Minima of durability appear at the maximum height and angle of BUE. Therefore, the significant reduction of tool life in extreme speed range is caused by the instability of the process of forming BUE.

From studies of the contact zone, it was found that the coatings due to their little chemical affinity with processed material and the higher hardness and abrasion resistance change the nature of the contact processes between the front face and the chip as a result of a change in conditions of flow of the adhesive processes and the magnitude and influence of BUE on the wear are smaller.

By changing the thickness of the shear layer metal and the front corner γ of tools, the extremes of tool life vary both in speed and in absolute values - Figure 10a and 10b. The effect of LESD also varies depending on the degree of phasing speed of minimum and maximum of tool life.

The highest effect - 2.5 times increase in tool life is obtained by LESD whit electrode P25 at mode1 with the higher energy at cutting speed 25 m/min, corresponding to a minimum tool life of uncoated tools (Figure 10a). When layered by this mode tools minimums of the durability almost absent and this determines the highest effect. Under this mode, the coatings have a higher thickness, a greater quantity of carbides and ultradispersed structure containing micro crystalline and amorphous metastable phases [4,5,13,14,16]. This state is retained at the cutting temperature (300-500^{0}C- Fig.9) at this speed range [15], and directly influences on the adhesion processes between the front surface and the chip.

Formed in the process of LESD with an electrode P25 complex iron-tungsten carbides contribute to an increase the strength of the coatings and the bond strength with the substrate. The higher strength of these carbides than that of TiN and TiCN, and the small size of

the carbide grains reduces the possibility of adhesion wrenching. As a result, the adhesion is lower, Build -up size is less, the minima of tool life are not as clearly pronounced as in uncoated tools, the intensity of wear is lower. In the mode with lower energy the coatings are with more small thickness, a lower amount of carbides, with a lesser degree of dispersity and amorphous and carbide grains grows at lower temperatures [15]. As a result, the character of the speed-durability dependencies is as in uncoated tools - with extremums, and increase of tool life - lower than that of the layered with mode1 tools.

In uncoated tools the height of BUE is larger, and his exiting the outside of the cutting edge is greater (Fig.11). In its cyclical disruption part of the destroyed particles fall between the rear surface of the tool and the machined surface and act abrasive in contributing to the increased wear on the front and rear surfaces of the tool. Whit reduction of the plasticity of the processed material, the thickness of the cuttings layer and an increase in the front corner the parameters of built-up edge (BUE) will decrease. Extreme values of the durability will become more implicit, and the intensity of wear will also decrease. This is confirmed by comparison of the extreme values of durability T for feeding 0.21 and 0.37 mm/rpm- Fig.10 from where can finding that with the reduction of the feeding (respectively thickness of shear layer metal) the extreme values are more implicit, and the critical speed under that appear minima of tool life is moved towards speed of 30-35 m/min. At the same time the effect of LESD slightly decreases. In this speed range the effect of LESD is maximum, but could be and a minimal - where the extremes of the durability of the layered tools are dephased in speed i.e. when the maximum of the tool life of the uncoated tools coincides with minimum of tool life of the layered tools. For example, at speed of 30 and 35 m/min - Fig.10a, b, the comparison of the tool life of coated with TiN electrode and uncoated tools indicates that the effect from LESD is negligible - almost absent. Above

described mechanism is confirmed by photographs of the wear of the layered and uncoated tools worked at the extreme cutting speeds - Fig.11, 12.
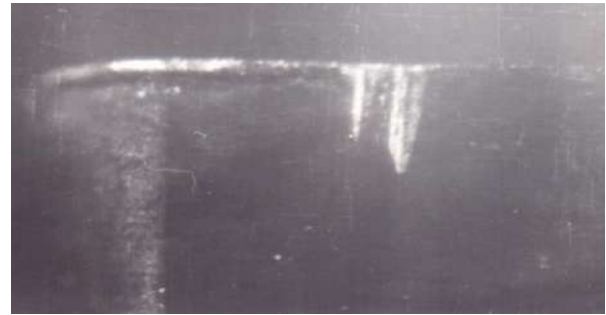
a) flank wear of LESD with electrode P25 at regime1-Tabl.1
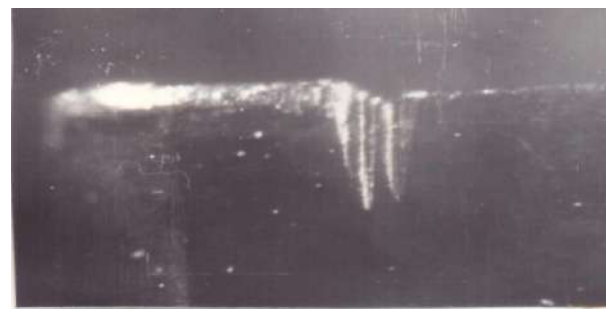
b) flank wear of uncoated tools

Cutting speed V 30m/minq f 0.21mm/rpm, cutting time 30 min
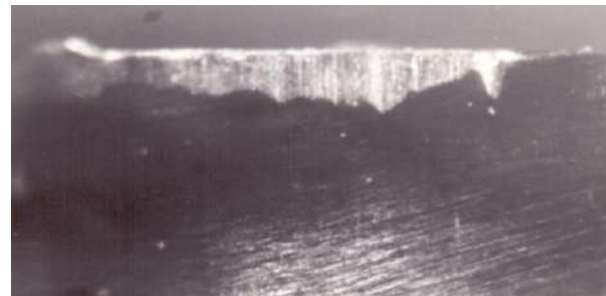
c) Flank wear of tools LESD with electrode P25 at regime 1-Tabl.1

d) Flank wear of uncoated tools

Cutting speed V 25m/min, f 0.37mm/rpm, cutting time 40 min

Figure 11. Width of flank wear of LESD and uncoated tools for different cutting speeds and feeds
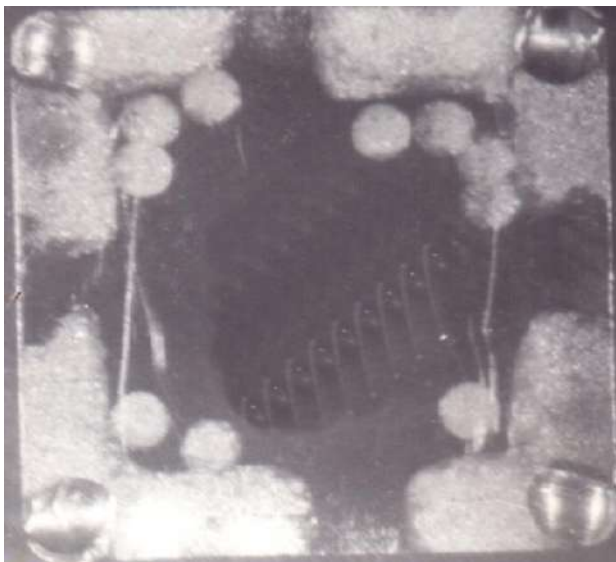
Figure 12. Wear of the face of LESD tools

From the pictures reveal that the traces of abrasion of uncoated tools (Fig 11) are obviously not caused by hard inclusions in the processed material, that they are with very small dimensions and cannot cause such large prints, but they are caused by particles from the ruined of BUE and of tools material.

This conclusion is consistent with the statements in [1,17] that at cutting speeds when there is no a plastic shearing or diffusion wear, there is a priority influence the separation of large fragments from tool steel by the action of the BUE.

With the further increase in speed over 35 m/min increases cutting temperature (Fig. 9), and the height and the front corner of the BUE decreases. Imbalances amorphous state of the coating gradually crystallizes and is passing to a more sustainable state. As a result of the increased thermal and mechanical load on the contact zone, the part of the adhesion wear reduces; take place the wear with diffusion-plastic nature and tool life are significantly reduced with increase of the speed.

Due to its high hardness, temperature stability and wear resistance the coating prevents diffusion between the tool and processed material and wear of coated tools is lower than that of uncoated.

As the impact of the part of adhesive wear decreases the effect from LESD also reduced to 1.7-2 times and remains relatively constant up to maximum surveyed speeds of 55 m/min. Since at these temperatures in the coatings

gradually begins increase the grain size, crystallization and increase the amount of austenite [14,15], the difference in the durability of the layered with the two electrodes and modes tools reduces too.

Under these conditions, wear of cutting proceeds simultaneously across the face and rear surfaces, but the accepted criterion of wear is reached sooner than the width of flank wear VB, therefore prevails is wear on the back surface VB.

The results obtained show that, depending on the cutting conditions, the nature and intensity of interaction between the tool and material being processed extrema of durability are moved to higher, or to lower cutting speeds and the absolute value of the durability are different.

In conclusion, it can be summarize that the life of LESD tools depends on simultaneous influence of qualitative characteristics, composition and structure of the coatings and cutting conditions, particularly speed-temperature factor and mechanism of formation of the BUE.

From the obtained results it can be concluded that LESD rather not a method to deposit wear resistant coatings like CVD and PVD methods where there is a sharp boundary between the properties of the coating and the substrate, this is a method for improving the surface properties of the tools material.

This study has demonstrated that it is possible to use the LESD process to improve the surface properties and the wear resistance of HSS tools as a result to increase the life of layered tools. It suggests that they may be efficiently used to strengthen rapidly wearing tools.

4. CONCLUSIONS

The LESD coatings enhance the life of the tools. Obtained extent of tool life enhancement is to 1.7- 2.5 times compared to the uncoated HSS tools, depending on the machining conditions employed for cutting.

Are examined the complex influence of the parameters of mode of cutting processes on a

contact, friction and wear mechanism of layered instruments.

The designating structural factors that provide increased wear resistance are the uniformity, the low roughness, the fine-grained structure and the high part of carbides and amorphous forming components of the coatings obtained by LESD, which change the nature of the contact and adhesion processes between the front surface of tool and the swarf.

It has been found that the minimums of the durability of the uncoated tools caused by the instability of the process of formation of the BUE can be prevented by LESD. When cutting in the area of critical speeds - where the BUE has a maximum size, the highest effect is obtained at LESD with electrode P25 in regimes with high energy pulse. At cutting speeds higher than the critical the effect of LESD with electrodes P25 and TiN is relatively constant and approximately equal.

From the obtained results it was found that among other applications LESD can be used to reduce wear and increase durability of cutting tools.

The resulting dependencies can be use for developing of promising energy- and resource-saving technologies by electrical spark coating for hardening of tools with different designation.

REFERENCES

[1] T. N. Loladze, *Prochnost' i iznosostoĭkost' rezhushtego instrumenta*, Moskva, Mashinostroenie, 1982.

[2] B.Eremich, M. Babich, S. Markovich, Tribologicheskie aspekty naneseniya pokrytii, Trenie i iznos, No. 1, 1990.

[3] A.E., itle vich, V.V. ikha lovand all., *Élektroiskrovoe legirovanie metallicheskikh po verkhnosteĭ*, Kishinev, Shtinitsa, 1985.

[4] G.A., Bovkun, Z.I.Vladkova, V. Molyar, T.Penyashki, Yu.G.Tkachenko, Research hardening of steels at a local electrospark deposition of metal carbides, Surface Engineering and Applied Electrochemistry, No. 1, pp. 10-12, 1988.

[5] V.N., Gadalov YU.V Boldyrev., p rochnenie rezhushtego instrumenta sposo om lokal'nogo l ektroiskrovogo naneseni a pokr ti , STIN, No. 9, pp. 18-20, 2006.

[6] V. N., Gadalov, R. E. Abashkin, Yu. V. Boldyrev, E. F. Balabaeva, A. I. Lytkin, *Cutting-tool wear and hardening of high-speed steel by local electrospark coating application*, Russian Engineering Research, Vol. 29, No. 4, pp. 419–422, 2009.

[7] K.R.C. Soma Raju , Nadimul Haque Faisal, D. Srinivasa Rao, S.V. Joshi, G. Sundararajan, Electro-spark coatings for enhanced performance of twist drills, Surface & Coatings Technology 202 pp. 1636–1644, 2008.

[8] E. Allen Brown, Gary L. Sheldon, Abdel E. Bayoumi, A parametric study of improving tool life by electrospark deposition,Wear, Vol. 138, No. 1–2, ,pp. 137-151, 1990.

[9] A.D.Verkhoturov, I. A. Podchernyaeva, L.F.Pryadko, F. F.Egorov, *Élektrodnye materialy dlya élektroiskrovogo legirovaniya*, M. Nauka, 1988.

[10] A.D.Verkhoturov, S.V.Nikolenko, Razrabotka i sozdanie élektrodnykh materialov dlya élektroiskrovogo legirovaniya, Uprochnyayushtie tekhnologii i pokrytiya, No. 2, 2010.

[11] B. Antonov, Device for local electric-spark layering of metals and alloys by means of rotating electrode, US Patent No. 3832514, 1974. - www.google.ch/patents/US3832514

[12] B. Antonov, St. Panayotov, O. Lyutakov, *Apparatus for the spark deposition of metals*, US Patent 4226697 Okt.1980. www.google.ch/patents/US4226697

[13] T.G.Penyashki and all: Izsledvane izmenenieto na fazoviya sŭstav i strukturata na povŭrkhnostniya slo v zavisimost ot energiyata za LEN", AMO, Vol. 89, pp.34, 1989.

[14] T.G. Penyashki, and others, Izsledvane na kachestvenite kharakteristiki na elektroiskrovo naplasteni pokritiya s amorfen stroezh, Tribological journal Bultrib (Bulgaria), pp. 130-140 ,2004.

[15] T.G. Penyashki: Study of the influence of the temperature on the structure of the deposited electrospark coatings, Tribological journal Bultrib (Bulgaria), No. 4, pp. 159-169, 2014.

[16] A. Lengerov, *Manufacturing Technologies, Plovdiv,* 2013.

[17] YU. G. Kabaldin, Issledovanie iznashivani a rezhushte chasti instrumenta iz strorezhushte stali. / . . a a ldin, N. E. Kozhevnikov // Trenie i iznos. t. 11, No. 1, pp. 130-135, 1990.

WEAR OF THE TOOLS FOR THE IRONING PROCESS AND METHODS FOR INCREASING THEIR LIFETIME

Dragan ADAMOVIC[1*], Miroslav ŽIVKOVIĆ[1], Tomislav VUJINOVIĆ[2], Fatima ŽIVIĆ[1], Marko TOPALOVIĆ[1], Marko PANTIĆ[1]

[1]Faculty of Engineering, University of Kragujevac,Kragujevac, Serbia, adam@kg.ac.rs, zile@kg.ac.rs, zivic@kg.ac.rs, topalovic@kg.ac.rs, pantic@kg.ac.rs
[2]University APEIRON, Banja Luka, Bosnia and Herzegovina; tomo.vujinovic@yahoo.com
*Corresponding author: adam@kg.ac.rs

Abstract: The influence of the tribological conditions in ironing has a significant influence, on the geometrical, kinematic and dynamic conditions which define conduction of the ironing process, as well as on the lifetime of used tools. In recent years a number of researchers studied this influence in both real processes and the tribo models. The process of tool wear, which is mainly reflected (in the case of abrasive wear) on the change in dimensions and shape, results in deterioration of the quality of the product. This deterioration leads to final products with greater dimensional deviation and a degraded quality of the surface.

Experimental research in the original tribo-model, implemented in this study was aimed to point out the changes occurring on the test samples of steel and aluminum alloys during the extraction, with a variety of materials of tools (tool steel, tungsten carbide) and a variety of surface states tool (Cr coating, TiN coating).

Keywords: ironing, galling, friction, wear, tool steel, hard metals, aluminum,

1. INTRODUCTION

Great intensity of wear in metal forming (MF) tools causes increased attention to be payed to the problem of determining tool lifetime. Previous studies have shown that friction has a significant impact on the geometric, kinematic and dynamic conditions of metal forming, and the tool lifetime, and thus affects the continuity of production. Wear progress (in the case of abrasive wear) is mainly reflected on the changes in tool size and shape, resulting in a gradual deterioration of the product quality. Tool wear causes greater dimensional tolerance of MF products, poor surface quality and even products with visible defects. These defects mostly occur in the form of notches and thickenings caused primarily by the formation of bulges on the tool. Tool lifetime also affects the reliable performance of the machine or machining systems. Frequent tool replacements lead to inevitable delays in machine operations, which affects efficiency, and therefore the cost of the production. The tool wear process is very complex, and the destruction of the tools can be caused by a number of related causes that act together. The process of tool wear is affected not only by the occurrence of the friction and respected abrasive wear, but also by other processes such as: fatigue (thermal and mechanical), corrosion and oxidation.

Therefore, the tool wear for MF is the result of the superposition of all the physical processes acting on the tool, and it will be more intense than wear caused by friction alone.

2. WEAR AND TEAR OF MF TOOLS

In order to effectively counter the destructive processes that limit the lifetime of MF tools it is necessary to know the mechanism and specificity of the basic processes of wear and tear. These processes vary for different tools.

Tools for cold MF are mainly subjected to mechanical loads and loads due to friction and wear. Characteristics of mechanical loads (static, dynamic) depends primarily on used machines. An important characteristic of mechanical loads is that they are mainly cyclical; so in the case of this group of tools we can speak of mechanical fatigue. However, as an essential process that determines the lifetime of MF tools, abrasive wear is taken. The increase in temperature of the outer layer of the tool is essentially insignificant and has no major impact on the change in mechanical properties of materials. Therefore, thermal fatigue processes can be ignored.

The most common cases of tool wear can be divided into the following groups:
- destruction of the die and punch
- abrasive wear and
- plastic deformation of certain zones in tool.

The destruction of the die and the punch is generally carried out by the entire cross-section, and the causes can be:
- incorrect heat treatment (too high residual thermal stresses)
- inadequate production of tools (stress concentrators)
- inappropriate use of tools, a particularly bad placing of tools on the body of machines, tools, etc. overload.

Tools designed for the cold MF are mostly demaged by the following types of wear:
- adhesive wear
- abrasive and
- fatigue (fragmentation).

Adhesive wear occurs mainly as a result of contact surfaces getting significantly closer, a considerable increase in surface area of real contact (final contact surface may be from 2 to 5 times larger than the initial surface) [1], as well as the introduction of new, not yet oxidized layers of material into contact with MF tools.

This causes a "cold welding" which leads to the appearance of deformed metal stickers on the tool. The number of these stickers keeps growing and their occurrances keep getting more frequent as the number of the process repetitions increases. Great adhesion strength of resulting connections, possibly diffuse in nature, affect the mechanism of their destruction. Traces of deep pulling, observed on the surface of the tool, testify that the destruction of the connection takes place in the upper tool, not on the original contact surface [1].

Destruction of contact connections results in a significant increase in roughness of the tool, which is transmitted in a negative way to the quality of the product surface, because the "bumps" which were created on the tool give rise to notching on the product.

Alongside adhesive wear, abrasive wear can also occur on the MF tools. It is caused by the effect of impurities on metal and partial fragmentation of "bumps". The intensity of abrasive wear in this case is not significant, and this process occurs only on certain part of the tools.

Interaction of micro fragmented parts with a working surface of tool leads to fatigue wear. Impulse characteristic of loads in micro contact zones, which is transferred to the outer layers of the tool, and the extrusion of the lubricant layer, leads to the occurrence of fatigue wear, which is characterized by fragmentation during the sliding friction.

Intense wear of the tool in the ironing process results from the fact that the entire working surface of the tool is in continuous contact with the work piece material. For this reason, the intensity of wear is greater in comparison with the other tools. Types of

wear that damage ironing tools can be divided into the following categories:

- adhesive wear that manifested by the appearance of the stickers ("bumps"),
- micro and macro cracks
- fragmentation and,
- the occurrence of loss of material in the shape of a ring which is the effect of abrasive wear.

The most influential types of wear for this type of tool is the appearance of so-called ring damage on work (conical) surface for compaction. This demage eliminates the necessary conditions for normal deformation of work piece and causes an additional friction with a significant increase punching force. The resulting damage can have a symmetrical or un unsymmetrical shape in nonaxial guidance of the workpiece or in case of excessively worn tool.

This mechanism of tool wear resulting from the kinetics of the material flow and pressure distribution in the cone of the punch. In the entrance area of the cone material which is being compressed suffers the largest deformations, therefore this is the area with the highest pressure per surface unit. Beside this, impurities, oxides, etc.. are retained on the working edges of the entrance to the conical part of the tool, so these impurities can act as abrasives which cause high intensity abrasive wear. Hence, in the central part of the cone a contact is formed between partially deformed workpiece material, released oxide and tool material. In regards to this, dominating process is adhesive wear.

In addition to adhesive wear, there is a frequent occurrence of damage in the form of cracks and fragmentation. This particularly applies to tools made of sintered carbides. This type of wear occurs mainly in the lower part of the tool, ie. outside of the calibration opening, especially if the tool has an inappropriate profile.

The technical condition of the tool, and especially the quality of its work surface have crucial impact on:

- surface quality and mechanical properties of the final product,

- productivity of processes and
- cost effectiveness of the production

3. METHODS FOR INCREASE OF THE LIFETIME AND RELIABILITY OF MF TOOLS

Durability MF tools depends on many factors that can generally be divided into three main groups:

- structural,
- production and
- exploitation.

Excluding structural and manufacturing defects, which are typically can be eliminated, increasing the lifetime of MF tools can be achieved:

- by replacing the currently used tool steel with materials with better resistance properties but also significantly more expensive,
- using the correct method for surface treatments which allow the achievement of the required properties of the surface layers, especially higher resistance to abrasion,
- using proper technological lubricant.

Deficiency of alloying elements, and their high price, make the high-alloyed steel tool used only in exceptional cases and for high stressed elements of the tool. Therefore, an effective and efficien increase of tool lifetime can be achieved by surface treatment. This solution for problem of low durability of productive tools makes processes of friction and wear, as well as fatigue, oxidation and corrosion mainly localized in the surface layers. Therefore, only surface layers are required to have greater resistance to wear, thermal fatigue, oxidation, corrosion, etc., without having to make the whole tool with these properties.

It should nevertheless take into consideration the fact that the surface layers of the tool, (created during the manufacturing process) are subjected to continuous changes during operation. These changes, may result from the cumulative wear process or originate from sudden individual changes (e.g., temperature changes, tool overload, etc.).

Therefore, when considering the role of surface layers and their impact on tool lifetime, one should bear in mind two aspects:

1. the initial state of the surface layers, obtained by the preferably selected processing method.
2. secondary changes that occur in the surface layers as a result of exploitation, causing a drop useful characteristics tools.

The final state of the tool, and in particular its features that are of interest to the user, as well as its durability and reliability, will be the result of a specific superposition of the original properties of the surface layers and the effects of wear (fatigue, corrosion, oxidation, etc.) which are inevitable during exploatation.

Therefore, in order to achieve the required tool lifetime, depending on the type of external loading that's being transferred (mechanical, thermal), as well as the operation environment influence (corrosion and oxidation processes), it is necessary to choose the optimum surface treatment.

MF tools are very often subjected to several types of loads together, which to a great extent limits choice of surface treatment. The processes of surface treatment which increase the wear resistance (e.g., hard coating obtained as a result of nitriding, plasma coating, etc.) have not proven effective in variable cyclical load cases. For this reason, the goal should be, in any case, to identify the main processes that determine the durability of the group of tools, and based on that knowledge, to select the appropriate surface treatment. In order to ease this selection, it is necessary to have knowledge of the outer layers after the surface treatment, and in particular: wear resistance (in a wide range of friction parameters), resistance to mechanical and thermal fatigue, tendency toward oxidation, corrosion and so on.

In search for the optimal properties of the surface layers, several treatment methods that enable achievement of the useful properties of the contact pairs are available. In addition to mechanical treatment, for which the correction of the tribological properties is achieved mainly as a result of an increase in the hardness of the outer layers (e.g., strengthening), in other cases, one of the essential objectives of surface treatment is to change the chemical composition (eg. by means of enrichment with compositions such as carbides of Cr , B carbides, nitrides of Al, Cr, Mo, V and so on.) which results in significantly increased resistance to abrasive wear. As a result of many studies, it has been found that the most resistant to abrasive wear are fine-dispersed hard phases (e.g., carbides, nitrides, etc.) [1].

Alloying elements in steel: V, W, Mo, Cr significantly increase resistance to abrasive wear of steel because they form stable carbides, if the steel has a sufficiently large C content, and if the parameters of heat treatment are properly selected. However, the main requirement to achieve good abrasive wear resistance is that the carbides are properly deployed in sufficiently resistant, and at the same time plastic basis.

One of the more preferred methods of surface treatments, which significantly increases the abrasion resistance, is a method of sulfatization (sulfo-nitriding, cyano-sulfation). In this case, good sliding properties can be achieved by enrichment of the outer layers with ingredients with the hexagonal lattice, which provide easy sliding over the baseline plains.

A specific group of modifications of the surface layer is a galvanic treatment, for example: hard chroming, phosphating etc.

The coating obtained by hard chroming is characterized by a relatively high hardness (1000-1200HV), as well as the typical network that represents the natural lubrication canals. As the result of this treatment of the surface layers, a significant increase of the abrasion resistance is achieved [2].

Phosphate coatings are crystalline coatings consisting of the phosphates of Zn, Mn or Fe, and they have somewhat different properties. The basic characteristics of phosphate coatings is their high porosity and good absorption of lubricants. Due to its porous structure, phosphate coatings have a very good ability to absorb grease, oil, soap, etc. which provides a good sliding properties [3].

In view of these properties, this method is used as a special lubricating coating of the MF process, whereby the phosphate layers are applied to a material that is plastically deformed.

With the aim of achieving good tribological properties, both at ambient and at elevated temperatures, plasma-coating technology has been developed. This technology utilizes the hardly soluble metals such as Cr, W, Co, Ti, or their compounds TiN, TiC and so on [4].

Also, in the group of surface treatment methods, which deserve attention, we must mention electro and chemical polishing. Defective layers which must be addressed originate from the pre-treatment (eg. cutting). As a result of the polishing defective layers are removed from the surface, and a new surface layer has significantly less surface roughness and lower, or very low levels of stresses. The surface layers obtained as a result of these processes are characterized by a significantly lower friction coefficient, higher resistance to abrasive wear as well as corrosion resistance.

4. EXPERIMENTAL RESEARCH

Experimental studies presented in this paper were performed on the original tribo-model of ironing process, which bilaterally symmetrically imitates the contact zone of die and punch. This model enables the realization of high contact pressures and respects the physical and geometrical conditions of the real process (material of die and punch, topography of contact surfaces, angle of die cone - α, etc.) [5].

The bent sheet metal band, U-shaped test piece, is assembled on the ''punch''. Holding force F_D acts on test piece by dies. Dies are assembled in supports, where the left support is motionless and the right support is movable together with the die. The test piece slides between the dies under the force that is applied at the punch head, whereby the thinning of the test piece wall thickness occurs. During ironing process, the outer surface of the test piece slides against die surface inclined by an angle α, and the inner surface of the test piece slides against plates attached to the punch body.

The device was realized with the compact construction of high rigidity, with the possibility of easy changes of contact-pressing elements (die and plate), with simple cleaning of contact zones and suitable assembling of test pieces.

Plates and die can be made of various materials and with various roughnesses, and dies can also have a various inclination angle α.

In this study, two materials were selected for experimental testing: steel, in the form of plate, designated as Č0148P3 (according to EN: DC04) and the aluminium alloy, also in the form of plate, designated as AlMg3(.43)[1] (old designation: AlMg3-24; designation according to DIN: AlMg3 F24, designation according to the EN AW-5754: AlMg3). Both materials are very common materials in modern industry. Mechanical characteristics of steel material determined for samples cut in the rolling direction of sheet are as follows: Rp = 186.2 MPa, Rm = 283.4 MPa, A = 37.3%, n = 0.2186, r = 1.31915, E = 1.957 x 105 Mpa. Mechanical characteristics of aluminium alloy, determined for samples cut in the rolling direction of sheet are as follows: Rp = 201.1 Mpa, Rm = 251 MPa, A = 12%, n = 0.13545, r = 0.40510, E = 0.701 x 105 MPa.

Contact pairs ("die" and "punch") are made of alloy tool steel (TS) with high toughness and hardness, with mark Č4750 (DIN17006: X165CrMoV12). This steel is resistant to wear and is intended for operation in the cold conditions. Oil quenching and tempering is carried out before the mechanical treatment by grinding.

In one set of tools, steel alloy Č4750 is heat treated, and on its surface, TiN hard coatings are deposited.

One set of tools is hard chrome plated (Cr) for the purpose of comparative testing. It should be noted that the tool base was made of heat-treated alloy tool steel Č4750.

One set of dies is made of hard metal (HM) marked with WG30 (DIN 4990: G30). Hard material (α-phase) is Tungsten carbide (WC), and bounding material is Cobalt (β-phase).

---

[1]- Here in after the acronym AlMg3 is used

The shape of "punch" and "die" is shown in Figures 1 and 2 respectively.
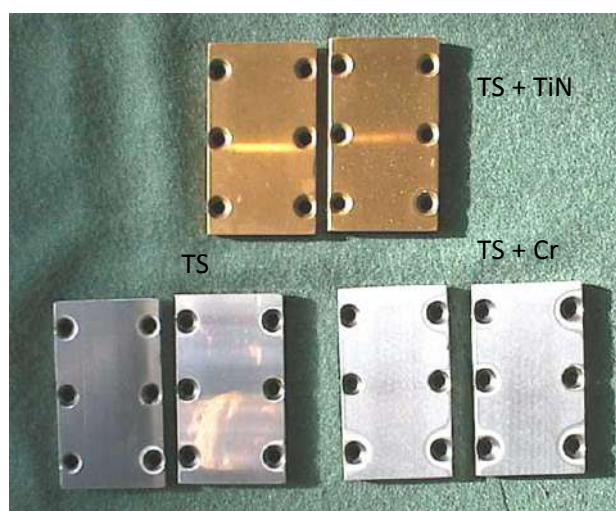
Figure 1. Images of the plates that simulate the surface of the „punch"
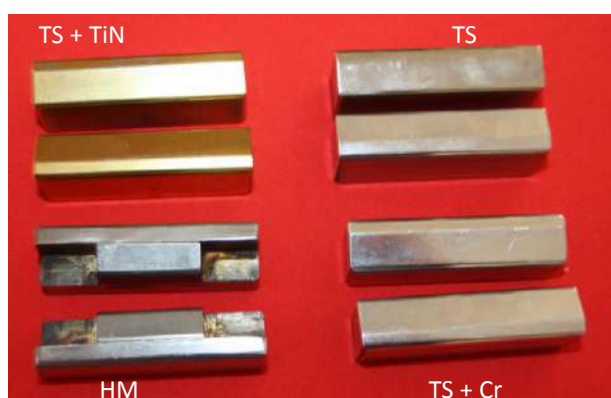
Figure 2. Images of „die"

5. RESULTS OF EXPERIMENTAL RESEARCHES

Under the influence of large normal pressures, surfaces are getting closer and adhesion compounds are formed, coupled with a substantial increase in the real contact area. The result of such interaction is the significant sticking of one metal, on the other, wherein as a rule, low-soluble metal is bonded to the surface of the metal with higher melting point.

As a rule, significant sticking results in the fact that the hardness of adhesion compounds, is higher than the hardness of at least one metal of the contact pair. Destruction of the compound occurs mainly in the outer layers of metal with low strength, and not on the original contact surface.

The surface of the die with stickers (TS + TiN), abrasions (TS TS + and Cr) and without damage (HM) is given in Figure 3.
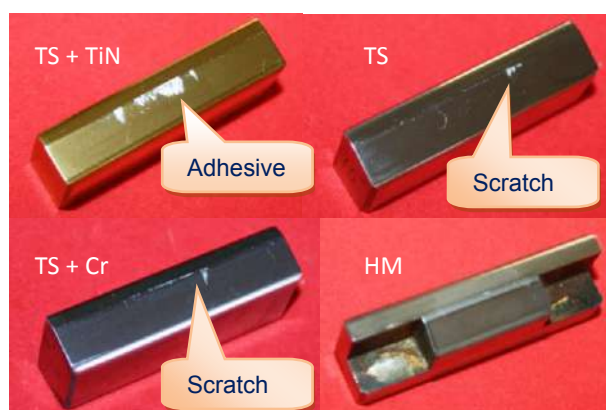
Figure 3. Surface of the die with stickers (TS + TiN), abrasions (TS and TS + Cr) and without damage (HM)

During ironing of Aluminium alloy sheets lubricant has a very important role; to separate surfaces of the test piece, and the surface of the tools. Lubricant also needs to prevent the creation of stickers on the tool surface, due to the great affinity of aluminum to sticking. If the proper lubricant is not used intensive aluminum sticking to the tool will occur. Stickers created on the die lead to rough damage on the sheet surface (galling).

EDS analysis of aluminium stickers formed on the die made of the tool steel coated with TiN is given in Figure 4.
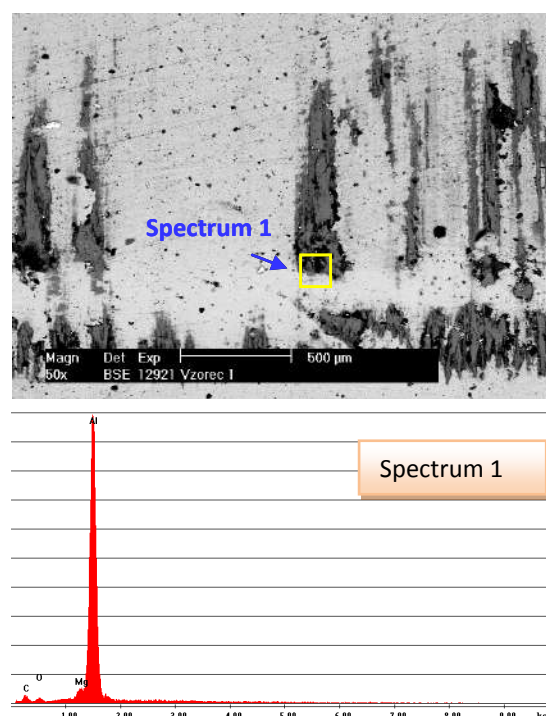
Figure 4. EDS analysis of aluminium stickers formed on the die made of the tool steel coated with TiN

While using punch with greater roughness and when the ironing is performed without lubrication of the punch, extensively sticking

aluminum on the surface of the punch was observed. When lubricants were used, stickers were significantly smaller, or not present. Formation of aluminum stickers on the punch (dark field) is shown in Figure 5. It should be noted that the resulting stickers formed on the punch are much easier to remove in comparison to those that have been created in the die.
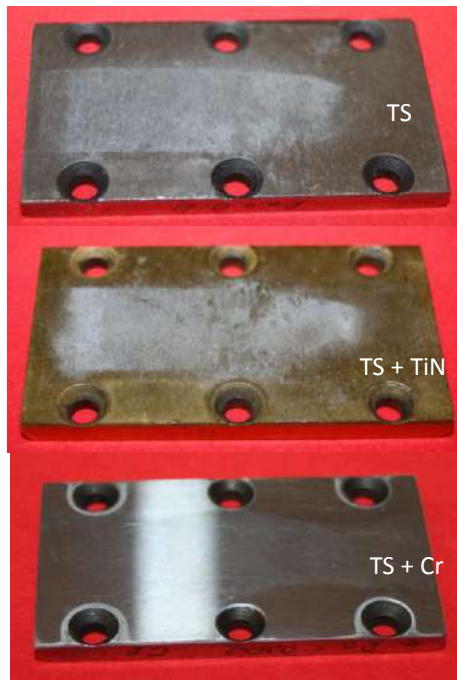
Figure 5. Punch with stickers
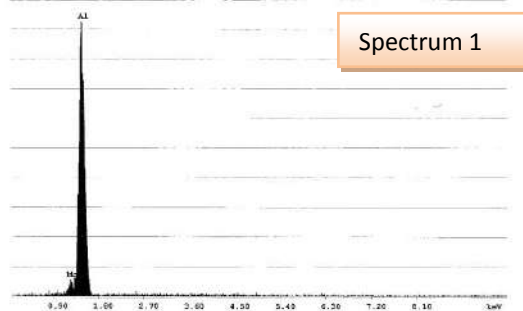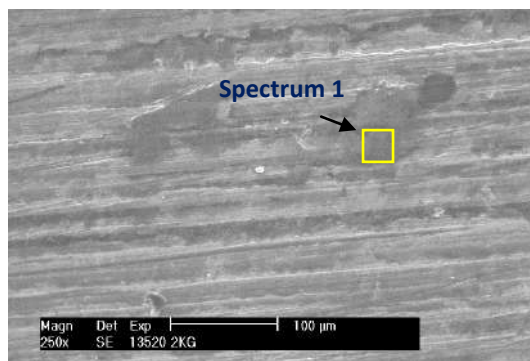
Figure 6. EDS analysis of aluminium stickers formed on the punch made of the tool steel

EDS analysis of aluminium stickers formed on the punch made of the tool steel is given in Figure 6.

Due to the high contact pressures and continuous formation and separation of stickers, damaging (scaling) of a TiN coating occurs. EDS analysis of the TiN coating damage on the die surface is given in Figure 7.
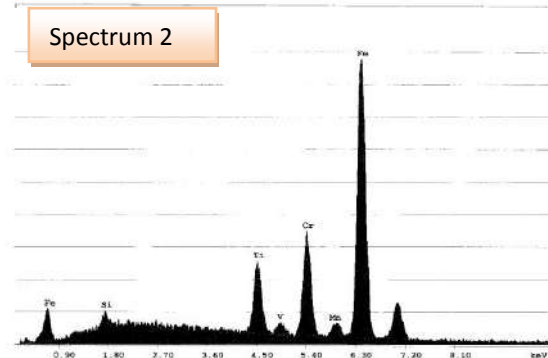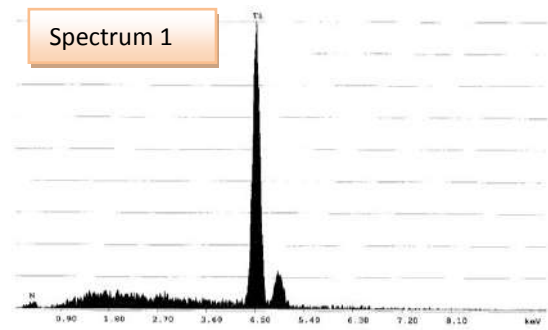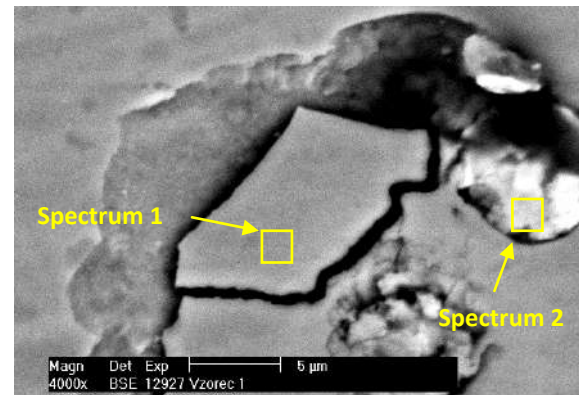
Figure 7. EDS analysis of the TiN coating damage on the die surface
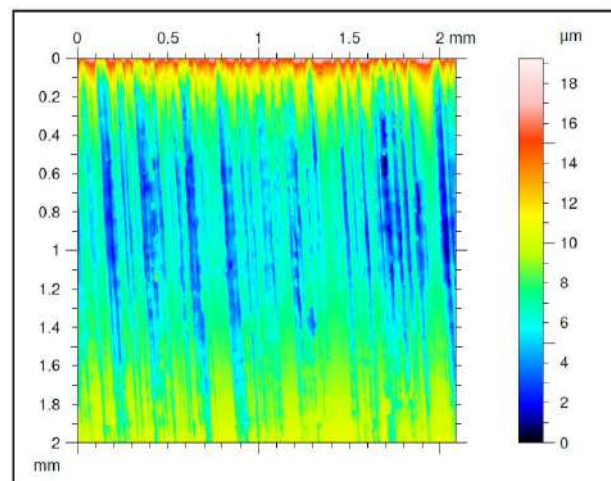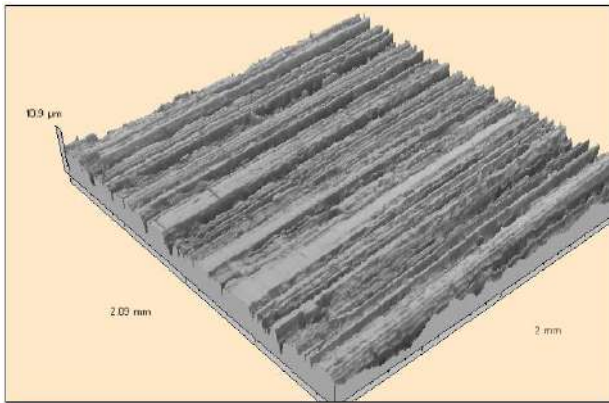
Figure 8. Topography and 3D rutted steel surface
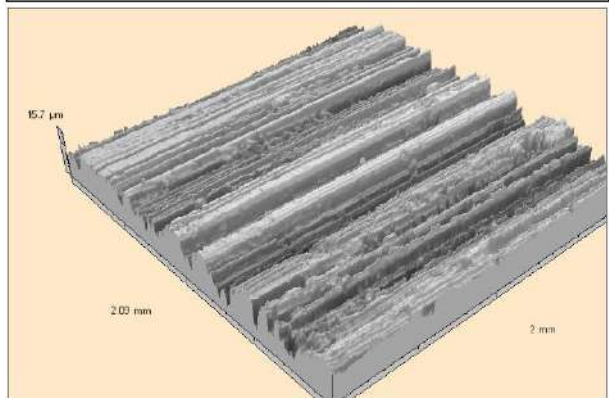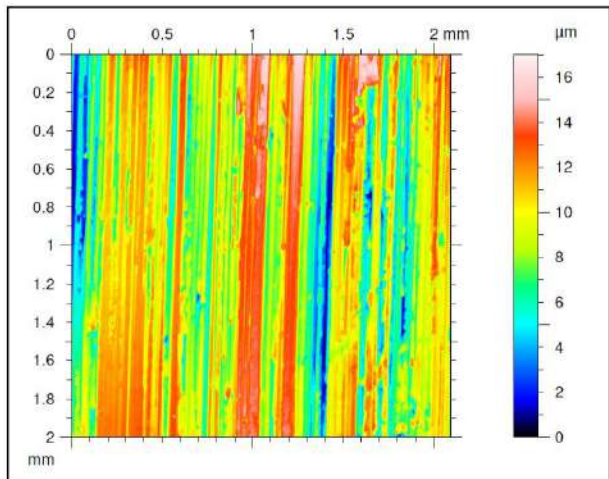
Figure 9. Topography and 3D rutted aluminium alloy surface

Analysis of the surface topography change due to the effects of friction was obtained at high magnification. This analysis can provide a very accurate detection of phenomenon that occur in the area of contact as well as evaluation of the friction mechanism.

The aim of this analysis to shed a light on the mechanism of deformation of the micro-zones of contact and transfer of materials. Method for removal of transferred material from the contact surfaces is also analyzed, so were specific mechanisms of friction for higher values of pressure.

Stickers on the tool surface deteriorate quality and are one of the main problems with the ironing technology, both with regards to product quality as well as with respect to tool wear. In literature, this phenomenon is known as "galling".

Grooved surface topography of the sheet, resulted from the stickers on the tool, is shown in Figures 8 and 9.
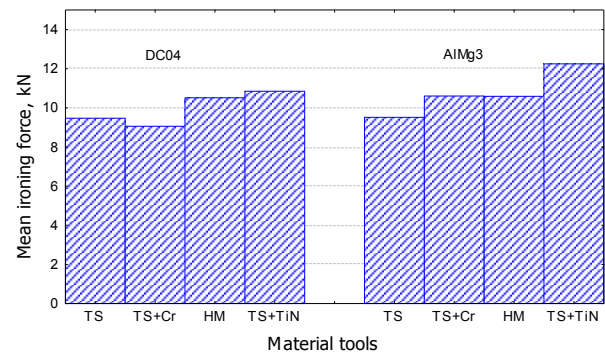
Figure 10. Mean value of the punch force for tools made of different materials

Changes in mean values of punching force for different tool materials are given in Figure 10, both for DC04 samples and for AlMg3 samples. It should be noted that the maximum value of mean punching force is obtained using the tool with the TiN coating. The reason for this is the most intense formation stickers on this kind of tools, as well as damages on coating that originated from the formation and fragmentation of stickers. Differences in the results obtained by testing steel and aluminum samples are a consequence of the nature of their interaction, and contact with the high contact pressures.

6. CONCLUSION

In order to achieve the goal of good tribological properties of tools for ironing process, treatment of contact surfaces is required. Contact surfaces of the tools (punch and die) can be treated with different methods:

- Applying a coating of hardly soluble metals such as Cr, W, Co, Ti, or their compounds TiN, TiC and so on.
- Mechanical hardening of the surface layers (for example flattening),

- Changing the chemical composition of the surface layers (eg. by means of enrichment with carbides of Cr and B, nitrides of Al, Cr, Mo, V, etc.).
- Making tools from high-alloy steel (V, W, Mo, Cr) which significantly increase the resistance of steel to wear,
- Methods of chemical-thermal treatment of surfaces (sulfo-nitriding, cyano sulfation);
- Modification of the surface layers using galvanic treatment (hard chromium plating of the tool surface, phosphating the surface of the workpiece, etc.),
- Surface treatment using polishing (electro and chemical polishing).

Which of the above mentioned methods or combination of methods will be used depends on the material to be treated. Also, it should be taken into account the stability of the surface layer and the possible process of sticking of the workpiece material to the surface of the tool (contact of dissimilar metals).

Stickers on the tool surface deteriorate quality and are one of the main problems with the ironing technology, both regarding product quality as well as in respect to tool wear.

During ironing process lubricant has a very important role. It is used to separate the metal surfaces of the tools and to prevent the creation of stickers on the tool surfaces.

ACKNOWLEDGMENT

REFERENCES

[1] Gierzynska M.: *Tarciezužycieismarowanie w obrobceplastycznejmetali*, WNT, Warszawa, 1983.
[2] METALS HANDBOOK – Heat Treating, Cleaning and Finishing, Vol.2, ASM, Metals Park, Ohio, 1964.
[3] Bay N.: The State of the Art in Cold Forging Lubrication, Journal of Materials Processing Technology, 46, 1994., 19-40.
[4] Dohda K.: *Tribological properties of thin hard coatings used in metal forming*, Proceedings of the Japan International Tribology Conference, Nagoya, 1990., 1973-1980.
[5] Adamović D.: *The behavior of materials in contact during the cold plastic forming processes with high working pressures*, PhD Thesis, Faculty of Mechanical Engineering in Kragujevac, Kragujevac, 2002. (in Serbian).

Lubricants and Lubrication

15th International Conference on Tribology – SERBIATRIB '17

17 – 19 May 2017, Kragujevac, Serbia

INFLUENCE OF COMPOSITION OF PLANT OILS ON THEIR TRIBOLOGICAL PROPERTIES

Nikolai K. MYSHKIN*, Andrei Ya. GRIGORIEV, Inna N. KAVALIOVA

Metal-Polymer Research Institute NASB, Gomel, Belarus
*Corresponding author: nkmyshkin@mail.ru

Abstract: *Sunflower, corn, rapeseed, olive, and linseed oils were used for investigation. Their fatty-acid compositions have been evaluated by gas chromatography. The tribological properties were determined on a four-ball machine. Flash and set points, static and dynamic viscosity of the oils were defined according corresponded standard methods. The results of tests on a four-ball machine show that refined plant oils possess better tribotechnical properties than a base mineral oil without additives. It was found that their antiwear and bearing resistance properties correlate with the structure of fatty acids molecules. It is demonstrated that the activation of unsaturated bonds as a result of the triglycerides oxidation has a positive influence on the friction interaction due to tribopolymerization and film formation on the wear surfaces.*

Keywords: *plant oils, lubricating ability, fatty-acid composition, length of alkyl radical, number of unsaturated bonds.*

1. INTRODUCTION

One of the goals of modern research in the area under consideration is the selection of base plant oils. However, unfortunately, there are the conflicting data in the published works in this area. Differences in tribological terms, such as wear, of similar oils reach 50% [1–3].

An analysis of the known data shows that the variability of the fatty acid composition of the oils can be the cause of the observed differences. Independent studies show that the triglyceride composition can vary by more than an order of magnitude, depending on the plant variety, agricultural methods, climatic and production factors [4, 5]. For example, the content of triglycerides of erucic acid in rapeseed oil varies from 1 to 60%. Furthermore, content of oleic acid in sunflower and corn oils can vary from 10 to 40%. It is obvious that mainly variability of the fatty acid composition is the main cause of the observed differences in the tribotechnical properties of oils. However, there is practically no study on analyzing this problem.

The purpose of this work is to investigate the influence of fatty acid content and structure of edible plant oil alkyls on their main tribotechnical properties.

2. MATERIALS AND METHODS OF RESEARCH

Edible grades of rapeseed, olive, corn and sunflower oils without additives are investigated. The choice of oil edible grade is determined by rigid sanitary and technical standards on their composition and impurity level.

Mineral oil without additives I-20 (GOST 20799-88), commonly used in low- and middle-loaded gears, ball bearings and slideway of machine tools and other mechanisms dispensed with specialized lubricants, is chosen for comparison.

The density of the lubricants is evaluated on Densito-30PX (Mettler, Spain). Oil flash-point temperature is determined in an open cup by the Vspyshka-A (Elektronpribor, Russia) in accordance with GOST 4333 (ISO 2592) and GOST 6356 (ISO 2719). Thermal characteristics (freezing point) are estimated with scan differential calorimeter Diamond DSC (PerkinElmer, USA) at the heating rate 8 °C/min. Kinematic viscosity is determined in accordance with GOST 33.

Composition of plant oil fatty acids is defined on the gas chromatograph Crystall-500 (Chromatec, Russia) in accordance with GOST 30418–96. The content of mono-, di- and triglycerides, as well as higher alcohols and free fatty acids, are evaluated by the method of ascending onedimensional paper chromatography in the hexane – diethyl ether – acetic acid system (18, 3 and 0.2 ml, respectively). The content of the main frictionally active elements is evaluated by means of X-Ray fluorescent spectrometer XEPOS (Spectro, FRG).

Load-carrying capacity, antiwear and antiwelding properties of oils are estimated on four-ball machine FBM-K1 (Ukraine), which has the test unit made as pyramid of four ball 12,7 mm in diameter down-dropped in a cup with lubricant. The balls are made of steel ShCh-15 (C – 1%, Cr – 1.5%; analog of USA 52100 steel USA). Three of them form the base of pyramid and rotate with cup about a top ball. Tests are carried out according GOST 9490-75 requirements. Friction surface morphology is studied on the scanning electron microscope Vega II-LSH (Tescan, Czech Republic).

3. RESULTS AND DISCUSSION

Data on basic physical, chemical mechanical and tribological properties of investigated lubricants are represented in Table 1.

Table 1. Functional properties of oils

Properties	I-20A	Sun-flower	Corn	Rape-seed	Olive	Linseed
Physical and mechanical properties						
Density, kg/m^3	885.2	919.7	917.7	918	910.3	930
Kinematic viscosity at 40°C, mm^2/s	33.1	33.8	35.6	34.3	41.7	15.22
Kinematic viscosity at 100°C, mm^2/s	5.3	8.1	8.5	8.6	8.8	6.33
Ignition Temperature, °C	222	245	232	280	316	>280
Solidification point, °C	-15	-17	-14	-10	+2	-21
Tribotechnical characteristics						
Parameter of wear (40 kg)	1.65	0.67	0.73	0.67	0.68	0.73
Critical load, kg	40	80	80	80	80	80
Welding load, kg	119	126	126	133	126	168
Load wear index	15	35	36	33	35	56

In common, the obtained data showed that basic properties of vegetable oil just as well or better than of standard mineral oil. For example, flash-point temperature of vegetable oils higher up by 30-50% than I-20 oil on the average. The freezing temperature of rape oil is close to minus 20°C, that lower than I-20 oil by 5%.

As can be seen, most of the mechanical properties of vegetable oils are fairly close in magnitude. The data of Table 2 show that the ratio of saturated and unsaturated fats for all oils is close to 1:8. The average lengths of the alkyl chains of these fatty acid groups are also similar. Differences in the content of potentially tribologically active substances are significant only for sulfur and phosphorus compounds. However, the concentration of these elements is too small to have a noticeable effect on frictional interaction processes.

Thus, the composition of the investigated oils, in terms of the ratio of the saturated and unsaturated acids content, their alkyl chain lengths and concentrations triboactive matters, looks alike.

Table 2. Composition of plant oils, wt %

Composition	Plant oil				
	sun-flower	corn	rape-seed	olive	linseed
Concentration of fatty acids, wt %					
C16:0. palmitic	7.6	12.3	6.1	11.2	5.6
C18:0, stearic	3.5	2.0	1.6	3.5	3.4
C18:1. oleic	24.8	29.0	54.6	77.3	15.3
C18:2. linoic	61.5	54.2	20.0	4.8	14.0
C18:3, linolenic	—	1.0	10.0	—	60.5
Average length of alkyl group	17.8	17.8	17.9	17.8	17.8
Average number of unsaturated bonds	1.51	1.43	1.35	0.9	2.5
FAs with the concentration of less than 1 %	2.6	1.7	7.7	3.2	1.2
Concentration of active elements. 10^{-4} wt %					
Phosphorus	4.1 ±0.4	—	—	—	27 ± 0.6
Sulfur	2.9 ±0.2	8.4 ± 0.3	3.20 ±0.2	1.9 ±0.2	44.2 ±0.5
Calcium	10.0 ±0.1	10.0 ±0.1	10.0 ±0.1	10.0 ±0.1	10.0 ±0.1
Zinc	0.3 ±0.1	0.4 ±0.1	<0.1	<0.2	0.3 ±0.1

Obviously, the proximity of the structural, physical and mechanical properties of plant oils is largely determined by the fact that with the exception of flaxseed oil, their tribological characteristics do not differ too. Thus, the results of testing the hypothesis of the equality of the average values of plant oil wear factors indicate that they are statistically insensitive with a significance level of 0.01. Consequently, the investigated oils from vegetable raw materials aren't different in wear indicators.

It is established in the work [6] that the wear of copper – steel pair is directly proportional to the length of alkyl radicals of cholesteric liquid crystals used as lubricants. We can assume that this is also true for the friction of samples in the media of plant oils. In this case, the constancy of the alkyl radical length of the triglycerides of the materials studied explains both their identical anti-wear properties and the range of action of the surfactants, estimated by the value of the critical load, which equals 80 kgf for all studied oils.

Analysis of oil antiwelding properties on the welding load and load wear index shows that linseed oil exceeds by these parameters the other materials by one or two stages of load according to GOST 9490–75. It is most likely that the observed advantage of flaxseed oil is associated with a high content of triglycerides of linolic acid, which is characterized by a relatively large number of unsaturated bonds (Fig. 1).
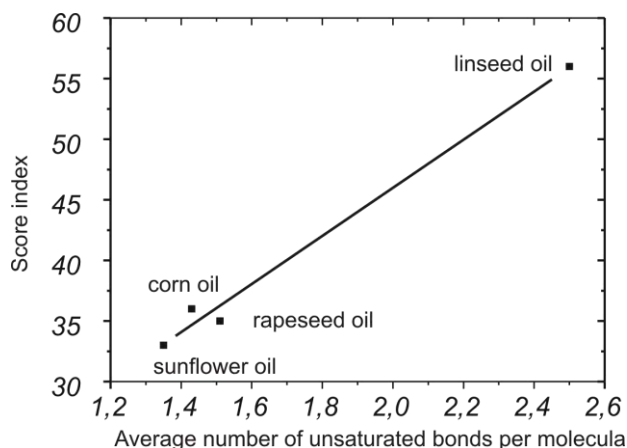
Figure 1 Correlation score index and relative number of their unsaturated bonds of plant oils

Under the influence of tribomechanical factors, unsaturated compounds are easily oxidized, initiating polymerization processes [7], contributing to increase in the bearing capacity of the oil.

The formation of high-molecular resinous substances is confirmed by the presence of the typical deposit in the friction zone, the area of which is the larger, the greater the average number of unsaturated bonds of triglycerides (Fig. 2).

a   b   c
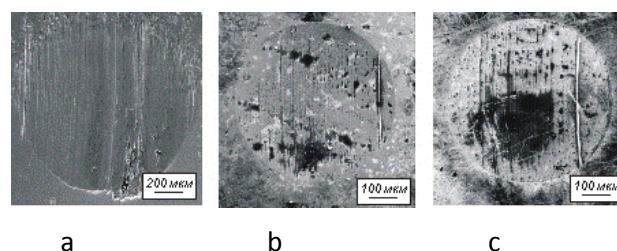
Figure 2 Contact area of samples after four-ball machine test in mineral (a), rapeseed (b) and linseed oil (b) correspondigly

The influence of high temperature and pressure promotes the process of hydrolysis and oxidation of fats. In the used oils should

The concentration of free fatty acids, mono- and diglycerides, mono- and oxy-acids must

increase, and, most significantly, the synthesis of polymeric compounds (tribopolymers) must be present in the waste oils. IR spectra of oils before and after tribotechnical tests are analyzed to assess the degree of chemical degradation of plant oils. The obtained data indicate their small differences (Fig. 3)
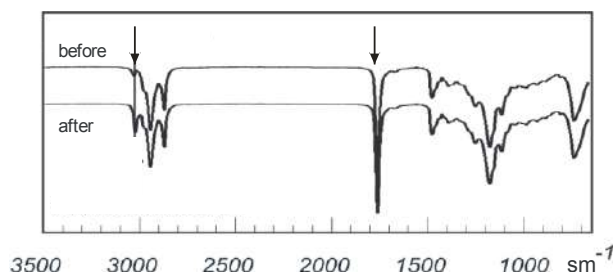
Figure 3. IR absorbtion spectre of linseed oil before and after test on the four-ball machine

Band intensity variation is observed at the frequency of 1746 cm^{-1}, typical of esters (C=O), and at the frequency of 3468 см$^{-1}$ specific to the functional group OH, and while analyzing oil associated with their hydrolysis and polymerization processes. Thus, according to the data obtained by gas chromatography, the fatty acid composition of the initial and used oils differs insignificantly. In general, the results of the analysis of IR spectra and gas chromatography indicate that there is no significant destruction of triglycerides after the tests. To clarify this information, the observations of oils using paper chromatography are carried out.
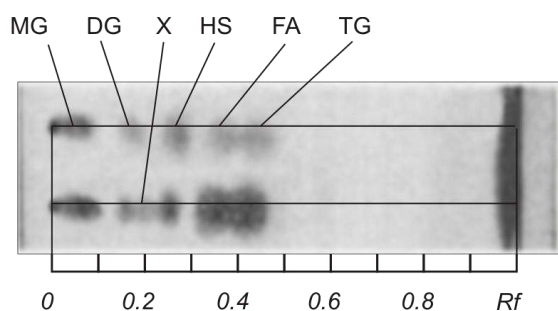
Fig 4. Chromatographic profile of linseed oil before (above) and after (below) test on the four-ball machine

The chromatographic profiles of the initial waste flax oil (the remaining oils have similar chromatograms) are shown in the Fig. 4. As can be seen, the relative spot intensities corresponding to mono- (MG) and

diacylglycerides (DG), fatty acids (FA), higher alcohols (HS), and triglycerides (TG) coincide rather well. The new X phase identified in the waste oil (Fig.4). Based on the position occupied on the chromatographic profile between diacylglycerol (DG) and higher alcohols (HS), it can not be attributed to high molecular weight products. It is most likely that this phase is glycerol, formed as a result of hydrolysis of oil lipids. The absence of areas that could be attributed to high-molecular products is likely due to their low concentration. This means that the processes of oxidation and tribopolymerization occur directly in the zone of frictional contact and do not enter significant amounts in the volume of the lubricant.

4. CONCLUSION

The results of tests on a four-ball machine show that refined plant oils have better complex of tribotechnical properties than the industrial base oil I20A. All investigated oils are characterized by the same anti-wear properties and surfactants effective range that is associated with equality of values of their alkyl radicals average lengths.

It is shown that activation of unsaturated bonds as a result of oxidation and thermomechanical effects during friction positively affects the processes of frictional interaction. It is established that the processes of tribopolymerization occur directly in the zone of frictional contact, and High-molecular products do not come in significant quantities in the amount of lubricant. A comparative analysis of the chemical composition of the oils before and after the tests on the four-ball machine does not reveal the products of destruction of triglycerides in significant amounts.

The obtained results suggest that decrease in the average length of alkyl radicals due to the introduction of lower unsaturated fatty acids into the triglyceride oils and the increase in the average number of unsaturated bonds by adding higher unsaturated fats can improve the tribotechnical characteristics of plant oils.

REFERENCES

[1] Bugaev, A.M., Influence of rapeseed oil on wear of the hydrosystem parts of agricultural machines, Mezhd. Nauch. Zh., 2008, no. 1, pp. 23–25.

[2] Krachun, A.T., Morar', V.U., and Krachun, S.V., Analysis of the lubricant composition of some vegetable oils, Trenie Iznos, 1991, vol. 11, no. 5, pp. 929–932.

[3] Evdokimov, A.Yu., Fuks, I.G., and Bagdosarov, L.N., Smazochnye materially na osnove rastitel'nykh i zhivotnykh zhirov (Lubricants from the Plant and Animal Fats), Moscow: Tsentr. Nauchno-Issled. Inst. Inf. Tekh.-Ekon. Issled. Mater.-Tekh. Snabzheniyu, 1992 (in Russian).

[4] Sakhno, L.A., Variability in the fatty acid composition of rapeseed oil: classical breeding and biotechnology, Cytol. Genet., 2010, vol. 44, no. 6, pp. 389–397.

[5] Khasanov, V.V., Ryzhova, G.L., Dychko, K.A., and Kuryaeva, T.T., Composition of fatty acids and steroids from the plant oils, Khim. Rastit. Syr'ya, 2006, no. 3, pp. 27–31.

[6] Ermakov, S.F., Shardin, V.A., and Shuldykov, R.A., Influence of length of the alkyl radical on lubricant and optical properties of cholesteric liquid crystals and their mixtures, Mater., Tekhnol., Instrum., 2007, vol. 12, no. 2, pp. 50–55.

[7] Voitov, V., Kravtsov, A., and Sysenko, I., Prospective use of the plant oils for production of lubricants, Motrol, 2013, vol. 15, no. 7, pp. 56–63.

THE INVESTIGATION OF THE BIODEGRADABLE UNIVERSAL TRACTOR OIL

Sreten PERIC[1*], Mile STOILKOVIC[2], Bogdan NEDIC[3], Mihael BUCKO[1]
[1]University of Defence in Belgrade, Military Academy, Belgrade, Serbia,
[2]NIS GAZPROMNEFT, Belgrade, Serbia
[3]University of Kragujevac, Faculty of Engineering, Kragujevac, Serbia,
Corresponding author: sretenperic@yahoo.com

Abstract: *Vegetable oils are potential substitutes for petroleum-based oils. Not only they are environmentally friendly, renewable and less toxic, but also they have excellent lubricating properties. Despite their safety, vegetable oils suffer from several drawbacks, for instance in terms of thermal and oxidative stability. The combination of additives in vegetable oils is the best option to overcome these problems. However, the additives are often combination of many substances which may be toxic.*
This paper presents the features of the oils based on rapeseed oil, sunflower, soya and mixture of rapes oil with mineral oil is, after corresponding testing, compared with the features of the commercially available mineral oil based UTTO.
According to the obtained results for physico-chemical properties of various oil samples, it may be concluded that almost all the investigated properties of biodegradable universal tractor oils, satisfy the John Deere and Massey Ferguson specifications, and some characteristics are even better when compared to the properties of universal mineral based oil. The exceptions are the oxidation stability and low temperature characteristics. The properties of vegetable oils were improved by the corresponding additives, specially designed for these oils.

Keywords: *biodegradable universal tractor oil, oil analysis, physical-chemical properties, tribological characteristics*

1. INTRODUCTION

By the end of the 19th century, only vegetable or animal oils and fats had been used as lubricants. The development of internal combustion engine stopped their application due to insufficient oxidation and thermal stability, as well as high prices in comparison with mineral lubricants. However, in the past ten years, the question of the application of mineral oils has risen due to environmental effects, and so lubricants derived from plant sources have been suggested as replacement [1].

Main advantages of vegetable oils over mineral oils is the fact that they are non-toxic, biodegradable, and made from renewable raw materials. The additional advantages are lower consumption due to lower evaporation loss, better lubricating properties, higher viscosity index, higher fire resistance due to higher ignition temperature, and better solubility of additives and oxidation products. Nevertheless, main disadvantages of vegetable oils would be lower oxidation stability, lower thermal stability, lower hydraulic stability, higher pour point and foam tendency, easier filter clogging, reactivity with seal elastomers and shorter storage life [2].

Vegetable oils as base oils for production of ecologically acceptable lubricants are triglycerides made up of complex mixtures of fatty acids having different chain lengths and number of double bonds. Triglycerides are very quickly biodegraded and have excellent lubricity properties.

Ecologically acceptable oils are the oils which in contact with the environment produce the minimum of harmful effects. The conditions for the ecological acceptance are biodegradability and no toxicity of lubricants. Besides, ecologically acceptable lubes are produced from the renewable sources (vegetable oil) thus reducing the dependence of mineral oils. The interest for the ecologically acceptable oils is growing every year especially in the field where the application of mineral oils can produce harm in the environment like the oil losses of motor saws, agricultural, forester and civil engineering machines, railroad and tramway crossings, outboard motors fit the motor boats, oils for mold release in civil engineering, steel ropes and chains and the other flow lubrications where the total quantity of lubricant remains in the environment. The lubricant producer's strategies are geared toward the production of ecologically acceptable lubricants. For many producers the market of the future is the market of biodegradable lubricants.

Agricultural machinery such as tractors, are ideal for use of biodegradable lubricants, because they operate in conditions where the lubricant can easily come in contact with soil, water and crops. The universal tractor transmission oil (UTTO) is used for lubrication of hydraulic and transmission systems as well as wet brakes in tractor [3,4].

2. PHYSICO-CHEMICAL PROPERTIES OF THE BIODEGRADABLE UNIVERSAL TRACTOR OIL

The features of oils based on rapeseed oil, sunflower oil, soybean oil and a mixture of rapeseed oil with mineral oil were, after the corresponding testing, compared with the features of the commercially available mineral-based universal tractor oil, UTTO (Table 1).

Table 1. Oil samples

Sample	Oil name	Oil code
1.	Rapeseed oil without additives	RE
2.	Soybean oil without additives	SO
3.	Sunflower oil without additives	SU
4.	Rapeseed oil with additives	REA
5.	Soybean oil with additives	SOA
6.	Sunflower oil with additives	SUA
7.	Rapeseed oil + additives + 10% SN150	REAM10
8.	Rapeseed oil + additives + 20% SN150	REAM20
9.	Mineral UTTO	MIN

The ASTM D 4951 and ASTM D 4927 AAS methods have been applied to obtain the elemental composition of the additives used in the test oils, as shown in Table 2 and Figure 1.

Table 2. The elemental composition of the additives used in the test oils

	P	Ca	Zn	S
	% m/m			
REA	0.07	0.08	0.13	0.19
SOA	0.06	0.07	0.14	0.19
SUA	0.06	0.07	0.14	0.19
REAM10	0.08	0.15	0.14	0.23
REAM20	0.09	0.18	0.15	0.28
MIN	0.11	0.34	0.15	0.54
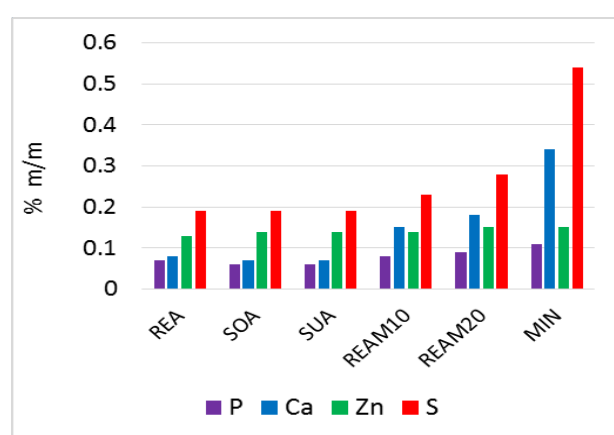
Figure 1. The elemental composition of the additives for the test oils

It can be seen from the Figure 1 that the elemental composition of additives is quite similar for all formulated vegetable based UTTO: REA, SOA and SUA. The reference mineral UTTO oil (MIN) contains a significantly

higher level of phosphorous, calcium and sulfur, than the ester-based oils. Zinc and phosphorous are parts of AW/EP additive package, while calcium is a typical element in a detergent additive. Samples REAM10 and REAM20 contain increased levels of phosphorus, sulfur and calcium, as they contain proportionally higher percentage of mineral oil.

Vegetable oils are generally less additivated than mineral oils, because they posses good lubricating properties due to their polar nature. This makes them good solvents for sludge and dirt, which would otherwise deposit on metal surfaces [5-8]. Because of these properties, it is possible to reduce the amount of friction modifiers, antiwear additive package, and dispersants, when formulating biodegradable universal tractor oils.

The physical and chemical properties of the vegetable oils were examined in accordance with standard methods (Table 3).

Table 3. Laboratory test methods

Method	Physical and chemical characteristics	Test method
1.	Pour point, °C	ASTM D 97 or ISO 3016
2.	Flash point, °C	ISO 2592, ASTM D 92
3.	Foaming, ml/ml 24 °C; 94 °C; 24 °C	ASTM D 892
4.	Deaeration, minutes	DIN 51381
5.	Oxidation stability, minutes	ASTM D 2272
6.	Corrosion on copper, 3 hours at 121 °C	ASTM D130
7.	P content, %	ASTM D 4927
8.	S content, %	ASTM D 2622
9.	Ca content, %	ASTM D 4628
10.	Zn content, %	ASTM D 4628
11.	Wear, (1h; 65 °C; 40 kg and 1500 rpm), mm	ASTM D 4172
12.	4-ball EP test - scuffing, kg	ASTM D 2783

The results of experimental testing of physico-chemical properties are presented in Table 4. Experimental work was carried out in accordance with the manufacturer specifications and proper standards, by using the necessary testing equipment.

Table 4. Physico-chemical characteristics of oils

Physico-chemical charact.	unit	RE	SO	SU	REA	SOA	SUA	REAM10	REAM20	MIN
Density at 15°C	kg/m³	916	918	920	918	921	922	912	907	877
Kinematic viscosity at 40°C	mm²/s	34.8	32.7	35.1	42.3	37.7	38.6	42.03	41.00	70.56
Kinematic viscosity at 100°C	mm²/s	7.9	7.82	7.93	9.49	9.17	9.27	9.23	9.18	10.05
Viscosity Index		210	224	209	218	227	226	211	201	126
Flash point	°C	322	326	328	254	260	250	248	246	234
Pour point	°C	-8	-13	-11	-23	-25	-24	-26	-27	-36
Oxidation stability, RBOT	minutes	13	8	10	109	60	70	120	149	214
Protection against corrosion, Test B		pass	pass	pass	pass	pass	pass	pass	pass	pass
Wear, (1h;75ºC;40kg and 1200 rpm)	mm	0.66	0.69	0.68	0.38	0.39	0.37	0.39	0.39	0.36
Corrosion on copper, 3 hours at 121 ° C	1A	1A	1A	1A	1A	1A	1A	1A	1A	1A

2.1 Oxidation stability

Most vegetable oils are triglycerides constituting a complex mixture of fatty acids with different chain length and instauration content [9-15]. The alcohol component (glycerin) is the same in all vegetable oils. The fatty acid components are plant-specific and therefore variable. The fatty acids differ in chain length and number of double bonds. From the fatty acid composition of the oils, it is observed that chain length C18 is dominating (Table 5). Main fatty acids with double bonds

are linolenic, linoleic and oleic. The oxygen absorption rate is 800:100:1 respectively, therefore less double bonds in a carbon chain result in better oxidation stability [16]. Generally the oxidation stability of vegetable based oils decreases with the increased level of instauration.

The content of polyunsaturated fatty acids (C18:2) is rather high for soybean (SO) and sunflower (SU) oil. Under thermal conditions, the double bonds in polyunsaturated fatty acids polymerize much faster than monounsaturated (C18:1 and C22:1) or saturated (C16:0 and C18:0) fatty acids. Unfortunately, the saturation of fatty acid degenerates the low temperature behavior or pour point of the oil.

Iodine value characterizes particular oil on the base of unsaturated fatty acids. Oils with high iodine values are more problematic for oxidation processes, however values fewer than 100 are not recommended since such oils are more problematic for changing the characteristics at lower temperatures.

Table 5. Fatty acid content and iodine value of vegetable base oil

Physicochemical characteristics	Rape seed oil	Soybean oil	Sunflower oil
Iodine value (gI$_2$/100g)	118.4	126.2	131.2
Fatty acid content	%		
C14:0 (Myristic acid)	0.06	0.05	0.04
C16:0 (Palmitic acid)	6.58	10.24	6.35
C16:1(Palmitoleic acid)	0.36	0.15	0.13
C18:0 (Stearic acid)	2.88	5.24	5.35
C18:1 (Oleic acid)	53.10	29.33	27.13
C18:2 (Linoleic acid)	28.72	47.95	58.53
C18:3 (Linolenic acid)	6.54	5.35	0.16
C20:0 (Arachidic acid)	0.41	0.52	0.41
C20:1 (Eicosenoic acid)	0.73	0.29	0.20
C22:0 (Behenic acid)	0.28	0.65	1.31
C22:1 (Erucic acid)	0.17		
C24:0 (Lignoceric acid)	0.10	0.20	0.35

The oxidation stability of oil samples was examined by the ASTM D2272 test (RBOT - Rotating Bomb Oxidation Test). As concerning the neat vegetable oils (without additives), rapeseed oil (RE) shows better oxidation stability as compared to the soybean (SO) and

sunflower (SU) oil. The reason is a high content of oleic acid and a low iodine value present in rapeseed oil. The oxidation stability of vegetable oils without additives is very low.

The improvement of the oxidation stability of vegetable oils was accomplished by adding the antioxidant additives and the mineral base oil. The concentration of the additives was the same for all vegetable oils. The oxidation stability values determined by RBOT method for neat vegetable oils, vegetable oils with additives and vegetable oils with mineral base oil, were compared with the values for commercial UTTO oil, as it is shown in Figure 5. The best oxidation stability shows sample REAM20 (149 minutes). The oxidation stability is improved by adding the antioxidant additive: for rapeseed oil, the improvement is more than eightfold. The stability is further increased by adding a mineral oil, but the biodegradability is reduced.

A low oxidation stability of newly formulated biodegradable oils limits their use for the production of motor oils and other oils that require high oxidation stability. Therefore, such oils may be used in the fields where the high oxidation stability is not required (flow lubricating oils, hydraulic oils, universal tractor oils), or in the agriculture and forestry, where a low toxicity and biodegradability of lubricants is mandatory [17-21].
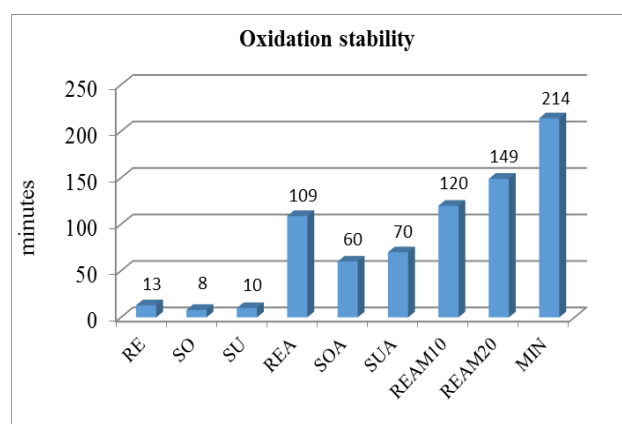
Figure 2. Oxidation stability, ASTM D2272 (RBOT)

2.2 Flash point

Flash point is important in transport and storage due to risk of fire. Vegetable oils have higher flash point values in comparison with mineral oils (Figure 3).
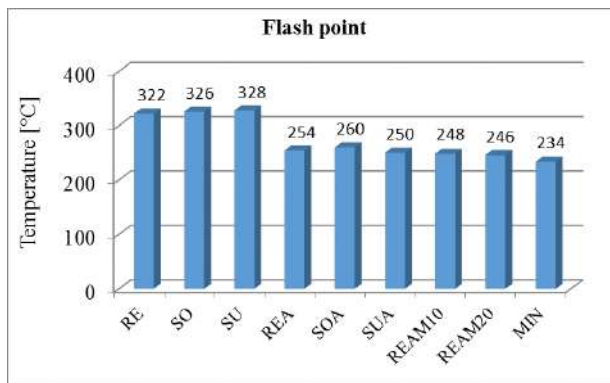
Figure 3. Flash point, ASTM D 92

Flash point for vegetable oils is higher than 300 °C. By adding a package of additives and mineral oil according to the formulation, the flash point is reduced, but it is far above the allowed values according to the specifications of tractor manufacturers (Massey Ferguson CMS M1141, Massey Ferguson_CMS M1143; John Deere J20C: Flash point ≥ 200 ^{0}C).

2.3 Pour point

The flowability of vegetable oils at low temperatures is extremely low, which limits their use at low operating temperatures (Figure 4). Vegetable oils form crystal structures at low temperatures, by agglomeration of triglycerides, wherein the oil flowability is reduced. In order to improve the low-temperature characteristics, vegetable oils are added additives labeled as pour point depressants (PPD). The function of these additives is to prevent the crystallization of the triglyceride molecules at low temperatures and their further grouping. The optimal concentration of additive PPD of 1% in the final formulation of vegetable oils, significantly improves their low temperature properties.
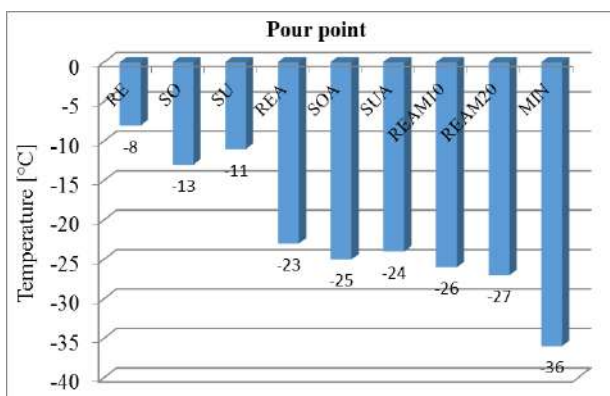
Figure 4. Pour point, ASTM D 97

2.4 Oil foaming

Foam affects the lubrication process very adversely, and also it accelerates the oil oxidation. Antifoaming additives have a role to prevent the occurrence of foam, by preventing the entry of air into the oil, which causes the foam. It is necessary to add this type of additives into the vegetable oils.

The tests of oil foaming have led to the interesting results. The neat vegetable oils free of additives have shown a good resistance to the appearance of foam (0/0; 0/0; 0/0) (Table 6). A mixture of vegetable and mineral oils gives also good results related to the appearance of foam, which means that the addition of mineral oil does not affect the foaming. However, after the addition of additives, there was an intense foaming (Table 6). Further laboratory analysis of oil with each individual additive, led to the conclusion that the foam occurrence is caused by additives named pour point depressants (PPD) and additives for protection against extreme pressures and shock loads (EP). On the contrary, the additives that protect against wear (AW) and oxidation (AO) did not initiate the appearance of foam.

Table 6. The laboratory analysis results of oil foaming, without antifoaming agents

Foaming	I seq., 24ºC	II seq., 94ºC	III seq., 24ºC
Unit	ml		
RE	0/0	0/0	0/0
SO	0/0	0/0	0/0
SU	0/0	0/0	0/0
REA	350/140	290/0	390/190
SOA	380/120	270/0	350/130
SUA	440/210	400/0	300/110
REAM10	500/280	680/0	180/60
REAM20	600/290	350/0	280/25

To solve the problem of vegetable oil foaming, the antifoaming agents were added. The application of conventional antifoaming additives did not give the required results. Better results were obtained with 30 ppm of the additive based on silicone (dimethylsiloxane), which improved the sequence II, or with the second additive (alkylmethacrylate) in an amount of 80 ppm,

which improved the sequences I and III. However, the results obtained (180/0; 50/0; 20/0) were not within the acceptable limits, according to the manufacturer's specifications. Only after the addition of 60 ppm of the substance based on silicone (dimethylsiloxane), and 160 ppm of alkylmethacrylate, the satisfying results were obtained. The oil foaming data are presented in Table 7.

Table 7. The laboratory analysis results of oil foaming, with antifoaming agents

Foaming	I seq., 24ºC	II seq., 94ºC	III seq., 24ºC
Unit	ml		
REA	25/0	20/0	20/0
SOA	15/0	20/0	20/0
SUA	30/0	20/0	10/0
REAM10	25/0	20/0	10/0
REAM20	20/0	20/0	10/0
MIN	5/0	20/0	5/0

2.5 Rust and corrosion

Rust is a product of reactions between a metal and corrosive environment. Corrosion is an electrochemical process, usually caused by the action of acidic chemical compounds on the metallic surface. Corrosion inhibitors (anti-corrosion additives) protect metal parts that are exposed to the rust and corrosion [22]. The basic mechanism of action of anti-corrosion additives is based on the formation of a protective layer on the metal surface, by physical and chemical adsorption [23]. Rust and corrosion inhibitors are commonly sulfonates, which are surface-active substances and provide good results in vegetable oils. Antioxidant additives are multifunctional and they can also protect metal against corrosion.

All of the oil samples showed good results in terms of protection against rust, according to the test B, ASTM D 665 method (the result was "passes") and corrosion according to the method ASTM D130 (the result was "1A"), as shown in Table 4.

2.6 Abrasion and high pressures resistance

Tests of the abrasion and high pressures resistance were carried out on the device with four balls ("four ball" test), and the results are shown in Table 8. The wear resistance testing was carried out according to the method ASTM D 4172.

The test conditions were as follows: the pressing force is 392 N, the top ball is rotated at 1200 rpm for 60 min., and the temperature of the test lubricant is regulated at 75°C. The limiting value of the scar diameter worn on the ball is maximum 0.4 mm for UTTO oil, according to the Massey Ferguson MF 1135 specification. The vegetable oil samples without additives (RE, SO, SU) did not pass the standard test, because the wear intensity was 70% higher than allowed. The wear parameters for other samples are presented in Figure 5, and it is seen that they are quite uniform, and within the allowed limits (< 40mm).

The measurement of extreme-pressure properties was performed according to the ASTM D 2783 (Four-ball method). The load is steadily increased until welding occurs, and the welding value of load is recorded as a maximum load which can be carried out by lubricant. The results in Table 8 indicate that vegetable based UTTO oils possess higher load values comparing to mineral oils, which means that they can better withstand extreme pressures and suddenly applied stress. The laboratory tests by using four-ball method have revealed that vegetable oils free of EP additives, possess even better results than mineral oils with the additives, as it is seen in Figure 6.

Table 8. The wear resistance test parameters and results

Characteristics	Wear	4-ball EP test
Unit	mm	kg
RE	0.66	140
SO	0.69	140
SU	0.68	140
REA	0.38	200
SOA	0.39	200
SUA	0.37	200
REAM10	0.39	200
REAM20	0.39	160
MIN	0.39	100
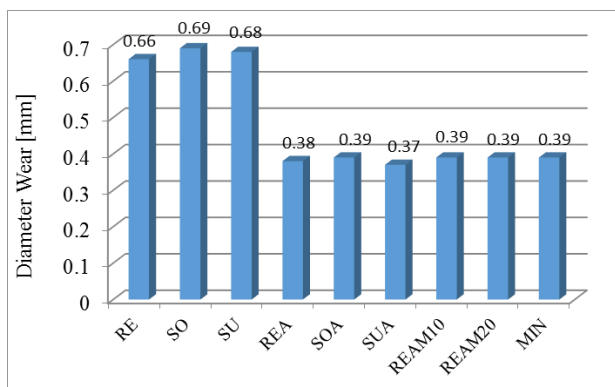
Figure 5. Wear resistance of vegetable oils and their mixtures
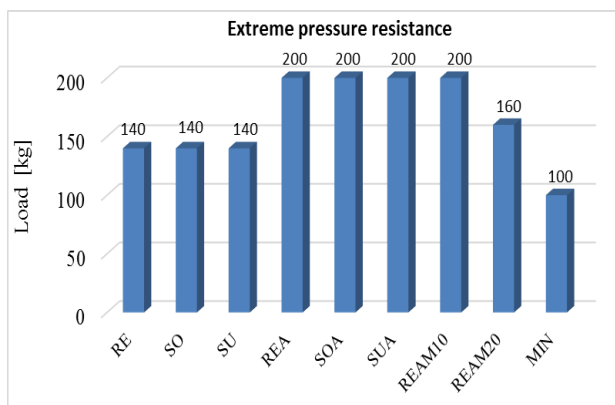
Figure 6. Extreme pressure resistance of vegetable oils and their mixtures

3. TRIBOLOGICAL PROPERTIES OF THE BIODEGRADABLE UNIVERSAL TRACTOR OIL

Most tribological properties are determined using defined standard tests, as shown in Table 9. For these purposes, some of the standard commercial tribometers such as Falex, Timken, Plint, Koehler, SRV, etc. can be used.

Table 9. Lubricant tribological characteristics tests

Standard	Contact geometry
Wear Preventive Characteristics	
ASTM D2670	Pin and Vee Block
ASTM D4172	Four-Ball
Extreme Pressure Properties	
ASTM D2782	Block on Ring
ASTM D2783	Four Balls
ASTM D3233	Pin and Vee Block
IP 240	Block on Ring
Friction characteristics	
ASTM D 5183	Four-Ball
Tribological behavior of lubricant in devices with real mechanical elements	
ASTM D5182	FZG – Gear Test Rig

The measuring system applied to determine tribological properties of the tribomechanical system elements is shown in Figure 7. It is composed of:

− a TPD-93 Tribometer for normal force, frictional force, and frictional coefficient measurements;
− thermopairs for temperature measurements of oil and elements in contact;
− a PQ-2000 particle quantifier;
− a microscope for wear parameter measurements (length, width, and depth of worn zone);
− Talysurf 6, a computerized measuring device for surface topography and wear parameter measurements.
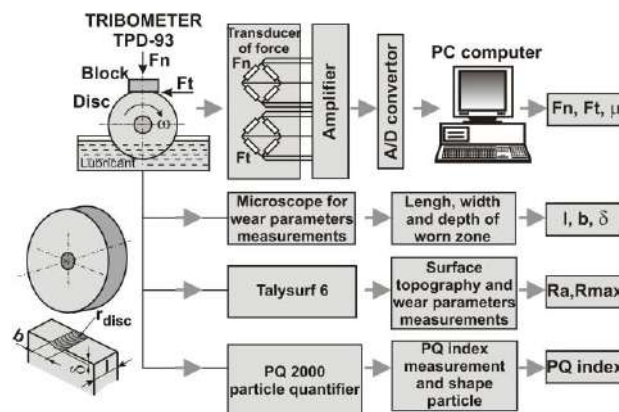
Figure 7. Measuring system applied for determination of tribological properties

The results obtained during the tests contain information about the friction coefficient, friction force, width and depth of the wear track, wear shape of the block's contact surface, change in the friction coefficient and temperature during the time of contact, block's and disc's surface topography parameters before and after the testing, etc. To investigate the dynamics of the contact process, the force and friction coefficient signals were recorded continuously for later processing.

The friction coefficients measured under various loads and in different periods are presented in Figure 8. In the first phase, the coefficient was measured under the force of 30N during 15 minutes, then the force increased to 100N for 15 minutes, and in the

final stage the force was 300N during 30 minutes.

Table 10. Tribological characteristics of oils

Oil	Friction coefficient μ			Boundary lubrication	
	Fn=30N t=15 min	Fn=100N t=15 min	Fn=300N t=30 min	Block's wear width (mm)	Block's wear depth (μm)
RE	0.058	0.065	0.062	1.117	8.9145
SO	0.092	0.095	0.098	1.278	11.670
SU	0.063	0.069	0.069	1.175	9.8645
REA	0.053	0.071	0.077	1.460	15.232
SOA	0.098	0.098	0.091	1.513	16.358
SUA	0.093	0.084	0.080	1.345	12.926
REA M 10	0.087	0.084	0.079	1.455	15.128
REA M 20	0.094	0.090	0.088	1.502	16.121
MIN	0.076	0.098	0.099	1.585	17.953
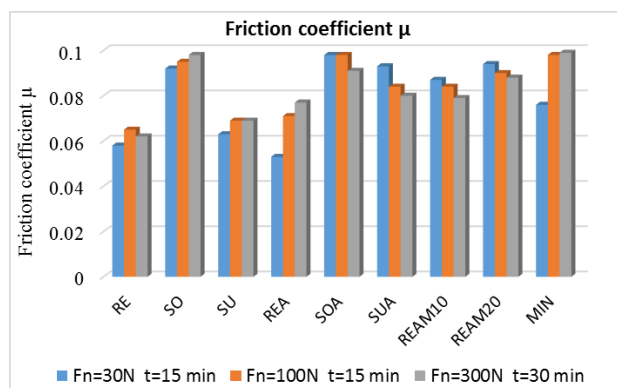
Figure 8. Friction coefficients measured under various loads and examination times

When low force is applied (30N), the lowest friction coefficient is recorded for rapeseed oil with additives (biodegradable UTTO oil based on rapeseed oil), while the highest coefficient is for the soybean oil with additives (biodegradable UTTO oil based on soybean oil). Under the middle load values (100N), the rapeseed oil without additives has the lowest coefficient, whereas the additive free soybean oil and mineral UTTO oil show the highest coefficient.

Finally, at the highest applied force (300N) during 30 minutes experiment, the additive free rapeseed oil again shows the lowest coefficient, and the highest value is again recorded for mineral UTTO oil.

It may be concluded from the diagram in Figure 8 that the friction coefficient significantly depends on the oil type, and that the rapeseed oil, which possesses the highest percent of monounsaturated fatty acids (oleic acid, C18:1) and the lowest iodine number (118.41 gI$_2$/100g), shows the lowest coefficient.

Figure 9. Block's wear width for different oil samples

Figure 9 illustrates the block's wear width measured after the examination of different oil samples. The highest width value was observed for the mineral UTTO oil sample (MIN UTTO, 1.585 mm), and the lowest for the rapeseed additive free oil sample (RE, 1.117 mm). The low block's wear width values for the RE, SO and SU samples indicate good lubrication properties of vegetable oils, i.e. they prove that the triglyceride structure of these oils is sufficiently effective against wear even at the highest pressures.

4. CONCLUSIONS

Flash point is higher for vegetable oils as compared to the mineral.
Low temperature fluidity of vegetable oils is far from satisfactory, thus limiting their use at low temperatures. However, PPD additive lowers pour point for these oils to -15 ^{0}C or even -23 ^{0}C, and these values satisfy most standards.
All vegetable oil samples show good protection against rust and corrosion.
Some of the additives used (PPD and EP) increase foaming above the allowed limits, but after the addition of antifoaming agent, good results are obtained.

Oxidation stability of vegetable oils without additives is very low. For instance, the result from RBOT test for additive free soybean oil is only 8 minutes. The improvement of this characteristic of vegetable oils has been accomplished by adding the antioxidant additive and mineral based oil. The mineral oil addition enhances the oxidation stability, but lowers the biodegradability of vegetable oils. The best oxidation stability was found for the rapeseed oil sample (REA=109 minutes), which was the expected result.

The wear resistance tests were performed on "four ball" device. The results from this examination were quite uniform for all samples and within the standard limits (< 40mm).

The extreme pressure (EP) resistance was tested by using "four ball" device. The vegetable UTTO oils show much higher ability to withstand extreme pressures as well as shock loads, in comparison to mineral oils. The laboratory tests give evidence that even vegetable oils without EP additives show better results than mineral oils with the additives.

The tribological testing consisted of measuring the change in the tribological properties of the elements which were in contact with the oil sample. The results obtained give information on the friction coefficient, friction force, width and depth of the wear track and wear shape of the block's contact surface, the change in the friction coefficient and temperature during the contact, block's and disc's surface topography parameters before and after the testing. The obtained results about the friction coefficient enabled identifying certain friction-connected tribological processes, while the data on block's wear width and depth enabled the explanation of the wear process.

The change in the friction coefficient for the rapeseed and sunflower oil samples is very similar, while soybean oil shows higher coefficient. Nevertheless, these three oils without additives possess lower friction coefficient than mineral based oil. It gives rise to the assumption that vegetable oils, due to

the triglyceride structure, possess excellent lubricating ability in all load phases. As a matter of fact, esters of naturally occurring fatty acids are even used as additives for the improvement of lubricating properties.

The friction coefficient of the vegetable oils with additives is higher when compared to these oils without additives, but it is still lower than the coefficient value for the reference mineral UTTO oil, particularly for high loads. The friction coefficient increases proportionally by adding the mineral oil, indicating that the lubricating property deteriorates.

The friction coefficient was measured under various loads and in different time periods. In the first phase, the coefficient was measured under the force of 30N during 15 minutes, then the force increased to 100N for 15 minutes, and in the final stage the force was 300N during 30 minutes. When low force is applied (30N), the lowest friction coefficient is recorded for rapeseed oil with additives (biodegradable UTTO oil based on rapeseed oil), while the highest coefficient is for the soybean oil with additives (biodegradable UTTO oil based on soybean oil). Under the middle load values (100N), the rapeseed oil without additives has the lowest coefficient, whereas the additive free soybean oil and mineral UTTO oil show the highest coefficient. Finally, at the highest applied force (300N) during 30 minutes experiment, the additive free rapeseed oil shows again the lowest coefficient, and the highest value is again recorded for mineral UTTO oil. The friction coefficient significantly depends on the oil type, so that the rapeseed oil, which possesses the highest percent of monounsaturated fatty acids (oleic acid, C18:1) and the lowest iodine number (118.41 gI_2/100g), shows the lowest coefficient.

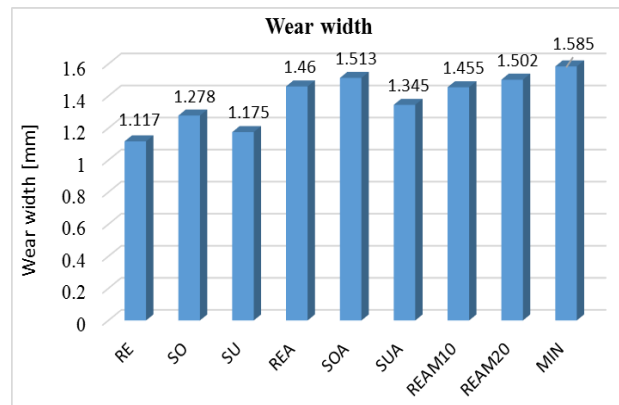After the examination of various oil samples, the block's wear width was measured. The highest width value was observed for the mineral UTTO oil sample, and the lowest for the rapeseed additive free oil sample. The low block's wear width values for the RE, SO and SU samples indicate good lubrication

properties of vegetable oils, i.e. they give evidence that the triglyceride structure of these oils is sufficiently effective against wear even at the highest pressures.

The block's and disk's surface roughness was measured by using Talysurf device. The surface peaks were clearly observed on the fresh block and disk surface. However, after the contact of coupled elements, where various oil samples were used as a tribological element, the peaks were deformed and torn. After the surface topography examination, it may be concluded that the smallest wear track was recorded for the additive-free rapeseed oil, while the widest track was observed when the mineral UTTO oil was used as a tribological element.

REFERENCES

[1] E. Beran: Experience with evaluating biodegradability of lubricating base oils. Tribol. Int., Vol. 41, No. 12, pp. 1212–1218, 2008.

[2] S. Erhan, B. Sharma, J. Perez: Oxidation and low temperature stability of vegetable oil-based lubricants. Ind. Crops Prod., Vol. 24, No. 3, pp. 292–299, 2006.

[3] C. Cecutti, D. Agius: Ecotoxicity and biodegradability in soil and aqueous media of lubricants used in forestry applications. Bioresour. Technol., Vol. 99, No 17, pp. 8492–8496, 2008.

[4] A. Adhvaryu, S.Z. Erhan, J.M. Perez: Tribological studies of thermally and chemically modified vegetable oils for use as environmentally friendly lubricants. Wear, Vol. 257, No. 3-4, pp. 359-367, 2004.

[5] N. Ravasio, F. Zaccheria, M. Gargano, S. Recchia, A. Fusi, N. Poli, R. Psaro: Environmental Friendly Lubricants Through Selective Hydrogenation of Rapeseed Oil over Supported Copper Catalysts. Applied Catalysis A: General, Vol. 233, pp. 1-6, 2001.

[6] A.J. Robertson, S.J. Randles: The use of laboratory techniques to simulate biodegradation of lubricants in the environment. JUGOMA Professional Publications, Vol. 205, 1990.

[7] B. Kržan, J. Vižintin: Use and Development of Biodegradable oils, in Tribology of Mechanical Systems, ASME Press, New York, 2004.

[8] B. Chen, N. Zhang, K. Liang, J. Fang: Enhanced Biodegradability, Lubricity and Corrosiveness of Lubricating Oil by Oleic Acid Diethanolamide Phosphate. Tribology in Industry, Vol. 34, No 3, pp. 152-157, 2012.

[9] D.R. Kodali: High performance ester lubricants from natural oils, Industrial Lubrication and Tribology, Vol. 54, No. 4, pp. 165-170, 2002.

[10] R.E. Gapinski, C.F. Kernizan, I.E. Joseph: Improved Gear Performance through New Tractor Hydraulic Fluid Technology, in Tribology 2000-Plus, 12th International Colloquium, 11-13.01. 2000, Gottingen, Germany, pp. 2269-2276.

[11] E. Kassfeldt, D. Goran: Environmentally adapted hydraulic oils. Wear, Vol. 207, pp. 41–45, 1997.

[12] L. Ulm, J. Vržina, V. Schiesl, M. Šateva: Biodegradability of water-resistant greases, in: International Conference on Tribology "Slotrib '98", 18-19.11.1998., Ljubljana, Slovenija, pp. 104-112.

[13] K. Lal, V. Carrick: Performance testing of lubricants based on high oleic vegetable oils. Journal of Synthetic Lubrication, Vol. 11, No. 3, pp. 189–206, 1994.

[14] Rhodes B.N., P. Mammel, P. Landis, F.L. Erikson: Water rejection of vegetable oil base stocks for tractor/hydraulic fluids. SAE Tech Paper, pp. 1–4, 1995.

[15] R. Sraj, J. Vizintin: Ecologically Acceptable Hydraulic Fluids Based on Rapeseed Oils. Proceedings of the International Conference on Tribology, 13-14.11.1996, Gozd Martuljek, Slovenia, pp 110-12.

[16] N. Ravasio, F. Zaccheria, M. Gargano, S. Recchia, A. Fusi, N. Poli, R. Psaro: Environmental Friendly Lubricants Through Selective Hydrogenation of Rapeseed Oil over Supported Copper Catalysts. Applied Catalysis A: General, Vol. 233, No. 1-2, pp. 1-6, 2001.

[17] G.W. Stachowiak, A.W. Batchelor: Engineering Tribology, Third edition, Elsevier, Amsterdam, 2005.

[18] E.M. Stempfel: Practical experience with highly biodegradable lubricants, especially hydraulic oils and lubricating greases. NLGI Spokesman, Vol 62, No. 1, pp. 8-23, 1998.

[19] N.S. Battersby: The biodegradability and microbial toxicity testing of lubricants + some recommendations, Shell Research and Technology Centre, Vol. 41, No. 7, pp. 1011-1027, 1999.

[20] A. Willing: Lubricants based on renewable resources - an environmentally compatible alternativeto mineral oil products, Chemosphere, Vol. 43, No. 1, pp. 89-98, 2000.

[21] B. Willson: Lubricants and Functional Fluids from Renewable Sources, Industrial Lubrication and Tribology, Vol. 50, No. 1, pp. 6-15, 1998.

[22] M. Bučko, J. Rogan, S.I. Stevanović, A. Perić-Grujić, J.B. Bajat: Initial corrosion protection of Zn–Mn alloys electrodeposited from alkaline solution, Corrosion Science, Vol. 53, No. 9, pp. 2861-2871, 2011.

[23] M. Bučko, U. Lačnjevac, J.B. Bajat: The influence of substituted aromatic aldehydes on Zn-Mn alloy electrodeposition, Journal of the Serbian Chemical Society, Vol. 78, No. 10, pp. 1-22, 2013.

THEORETICAL AND EXPERIMENTAL ANALYSIS OF LASER TEXTURED GREASE LUBRICATED BEARINGS

Victor Gabriel MARIAN[1,*], Adrian PREDESCU[1], Nicolae Alexandru STOICA[1], Ionuţ NICOLAE[2], Iuliana URZICĂ[2], Gheorghe CRISTIAN[3]

[1]University Politehnica of Bucharest, Bucharest, Romania
[2]National Institute for Laser, Plasma and Radiation Physics, Bucharest, Romania
[3]JNO Group, Romania
*Corresponding author: victormarian@omtr.pub.ro

Abstract: *The aim of this paper is to theoretically and experimentally analyze a laser textured grease lubricated bearing. The optimal textured surface area is determined using a contact model with the finite element method. The main parameters of the laser texturing process are presented. A UMT-Bruker test rig is used to determine the tribological parameters of the friction couple. It is shown that a slight improvement in the friction coefficient is observed for some values of contact pressure.*

Keywords: *laser texturing, mixed lubrication, finite element method, grease lubrication, tribology*

1. INTRODUCTION

It is well known that surface texturing of sliding bearings improves their performance by reducing friction, the microcavities being reservoirs of lubricant in case of boundary and mixed lubrication regime [1]-[9]. A reduction of consumed energy and an increase of life period of the friction couple is obtained. However the lubrication fluid was oil or water. Few studies were undertaken for bearings with Bingham fluids in hydrodynamic regime [10]. A review of recent developments on surface texturing is presented by Ibatan in [11]. In this paper it is outlined that the friction coefficient depends strongly on the textured surface area density and the geometry of the dimples. The effect of geometrical parameters of dimples under starved lubrication conditions on friction behaviour was studied

by Saedi [12] and Scaraggi [13]. Laurentis realizes in [14] an analysis on the influence of bearing grease on friction in rolling/sliding contacts. A similar analysis is made by Lugt in [15]. No studies in the case of mixed lubrication regime for textured surfaces using grease lubrication were found. The aim of this paper is to theoretically and experimentally analyze a laser textured grease lubricated bearing.

2. THEORETICAL MODELLING

In order to find the optimal textured area of the dimples, it is considered that after a worn height *dh*, the grease from the dimple reservoirs should be enough to completely fill the cavities of the rough surface. This condition translates into the following equation:

$$dh \cdot A_t \cdot \rho_t = dh \cdot (1 - \rho_t) \cdot A_t \cdot \rho_c \qquad (1)$$

where A_t is the total area of the textured surface, ρ_t is the area density of dimples (Area of dimples/A_t) and ρ_c is the fraction volume of the cavities of the rough surface (Figure 1).
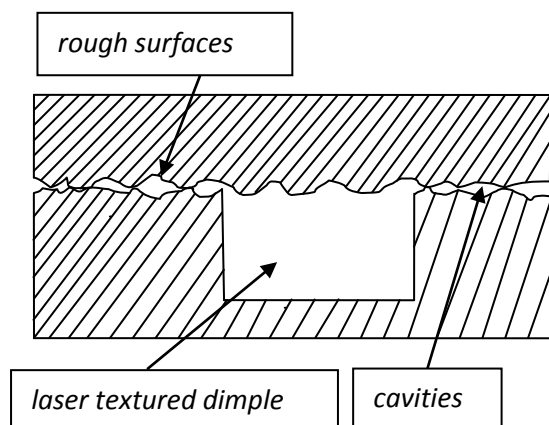
Figure 1. Schematic of a laser textured dimple

From equation (1) we obtain:

$$\rho_t = \frac{\rho_c}{1 + \rho_c} \qquad (2)$$

In order to determine the fraction volume of the cavities, a simulation using the nonlinear finite element program MARC was accomplished.

One of the bodies was considered plane rigid due to the fact that for the simulation we need less computational ressources. This hypothesis can also be sustained by the fact that one surface could be case hardened.

A schematic of the model is presented in Figure 2.
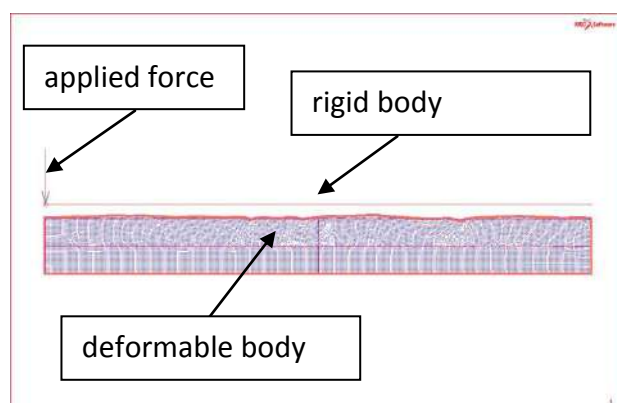
Figure 2. Schematic of the model

Due to computational ressources, plane strain conditions were assumed. The measured topography of the surface was imported in the finite element program by importing the coordinates of 500 points measured with a stylus surface profilometer. Then a cubic spline interpolation was used in order to obtain the top curve. QUAD elements with 8 nodes (parabolic shape function) were used for the deformable body mesh. Knowing the pressure on the bearing, the applied force on the rigid surface was computed. The material was considered to be elastic-perfectly plastic. A constant-time step with 50 steps was chosen for the stepping procedure of the contact simulation. In Figure 3 the equivalent plastic strain is presented.
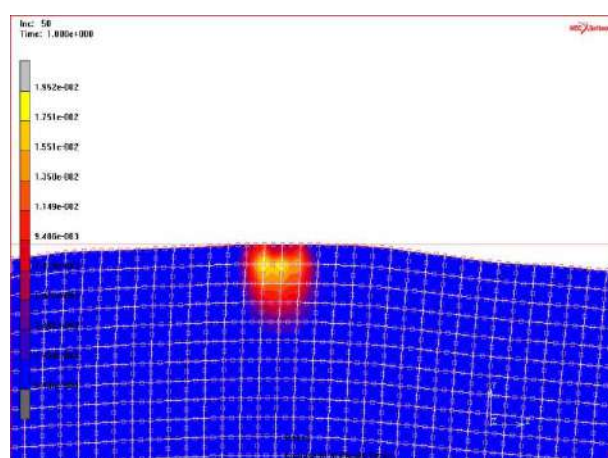
Figure 3. Plastic deformation of the material

After the contact simulation completed succesfully, a Python subroutine was created in order to compute de volume of the cavities and the volume fraction of the cavities. Due to the fact that the applied force depends on the textured area density ρ_t, the fixed point procedure was applied in order to determine ρ_t: an initial textured area density was considered, the force was computed, the volume fraction of the cavities was computed using the finite element software and the Python subroutine, the new textured area density was computed using formula (2) and so on until the textured area density converges.

The surface roughness changes in time, so if we introduce the measurea surface roughness before friction and we suppose that the asperities are becoming flattened, we ontain a maximal textured area density using this method.

3. EXPERIMENTAL SETUP

3.1 LASER TEXTURING PROCESS

The laser texturing setup consists of a Lumera Rapid 1064 nm laser radiation source with 8 ps pulse duration and a Nutfield XLR8 scanner with an f-theta objective and a 100 mm focal length. In order to drill the indentations, a spiral-shaped scanning trajectory with 0.005 mm rise was followed by the laser spot for each indentation. The process parameters are as follows: 1064 nm laser wavelength, 500 kHz laser pulse repetition rate, 2.4 Watt average laser power, 50 μm laser spot diameter, and 100 mm/s scanning speed. A textured circular bearing specimen is presented in **Figure 4**. The texturing process was applied to the bolt due to technological reasons.

Figure 4. Textured circular bearing sample

A plain bearing sample is presented in **Figure 5**. One half of the bearing is textured, the other is untextured.

Figure 5. Textured plain bearing sample

A closer look at the bearing surface is presented in **Figure 6**. The dimples have a diameter of 200μm and the textured surface area density is 10%.
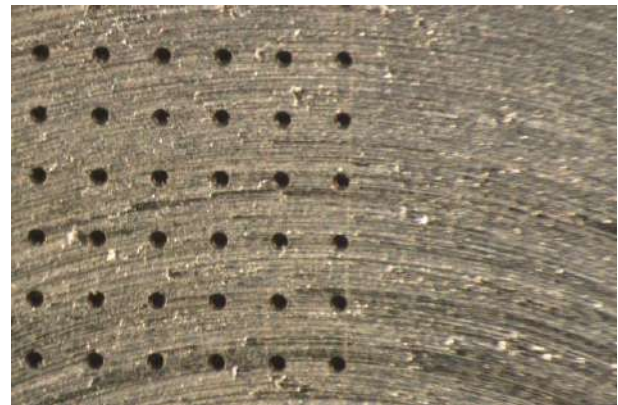
Figure 6. Microscope view of the textured plain bearing sample

A 3D measured profile is presented in **Figure 7** and **Figure 8**. The maximal value of the scale is 15μm and the minimal value is -55μm.
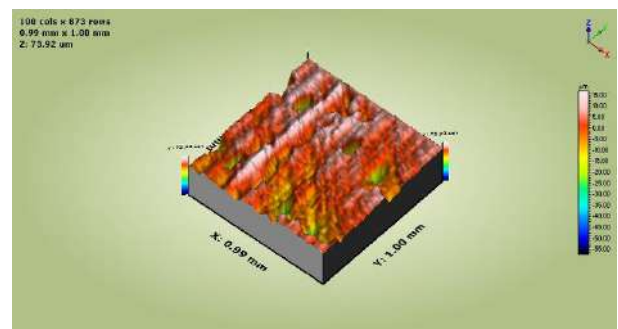
Figure 7. 3D measurement of the textured sample
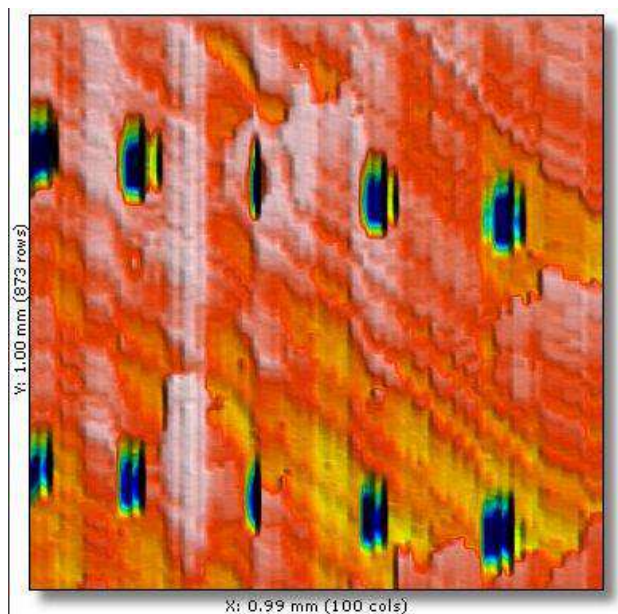
Figure 8. 3D measurement of the textured sample

3.2 Experimental testing

Reciprocating sliding tests were carried out in order to see if there is any improvement in the friction coefficient due to the laser surface texturing process.

The UMT-Bruker test rig is presented in Figure 9.

Figure 9. Reciprocating test rig

The grease used for testing is called Divinol Mehrzweckfett 2, produced by Zeller+Gmelin Gmbh & Co. KG. The grease was modeled using the Bingham rheological model. The rheological parameters were determined at 20°C using a Brookfield viscosimeter. Following values are obtained:

- Yield stress = 1573 Pa
- Dynamic viscosity = 1.2721 Pa·s.

4. RESULTS

For a measured roughness of the bearing surface and a yield stress of 1000Mpa of the material, the maximal textured area density obtained from the theoretical model is 25%. The plain bearing was produced with a textured area density of 10%.

The measured coefficient of friction for an oscilating motion having a total time of 1800s is presented in **Figure 10**. Only a fraction of the time is represented due to a more clear representation.

We obtain a mean value for the coefficient of friction of 0.1659 for the untextured sample and 0.1586 for the textured sample.
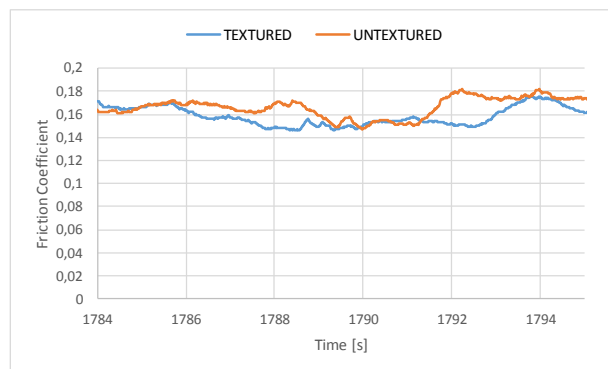
Figure 10. Friction coefficient (F=100N, v_{max}=2mm/s)
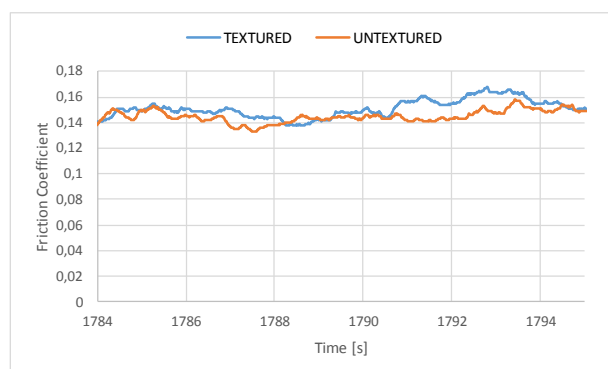
Figure 11. Friction coefficient (F=150N, v_{max}=2mm/s)

We obtain a mean value for the coefficient of friction of 0.150 for the untextured sample and 0.149 for the textured sample.

5. CONCLUSIONS

The theoretical model presented in the article can predict the maximal textured area fraction of the textured surface in order to have optimal lubrication.

Laser surface texturing proves to be a fast and reliable method to texture plain and cylindrical surfaces. The experimental tests showed that the friction coefficient is slightly lower in the case of textured surface for the applied pressure. Further tests are needed with an increased pressure and different materials in order to make a deeper investigation.

Development and Innovation Funding, project 29PTE/2016.

REFERENCES

[1] A. Ramesh, W. Akram, S.P. Mishra, A.H. Cannon, A.A. Polycarpou, W.P. King: Friction characteristics of microtextured surfaces under mixed and hydrodynamic lubrication, Tribology International, Vol.57, pp.170-176, 2013

[2] H. Zhang, M. Hua, G. Dong, D. Zhang, K-S Chin : A mixed lubrication model for studying tribological behaviors of surface texturing, Tribology International, Vol. 93, No.2 , pp.583-592, 2016

[3] P. Andersson, J. Hoskinnen, S. Varjus, Y. Cerbig, H. Haefke, S. Georgiou, B. Zhmud, W. Buss: Microlubrication effect by laser-textured steel surfaces, Wear, Vol. 262, pp. 369-379, 2007

[4] W. Koszela, P. Pawlus: The effect of oil pockets size and distribution on wear in lubricated sliding, Wear, Vol. 263, pp. 1585-1592, 2007

[5] U. Petterson, S. Jacobson: Influence of surface texture on boundary lubricated sliding contacts, Tribology International, Vol. 36, pp. 857-864, 2003

[6] A. Kovalcenko, O. Ajany, A. Erdemir, G. Fenske, I. Etsion: The effect of laser surface texturing on transitions in lubrication regimes during unidirectional sliding contact, Tribology International, Vol.38, pp.219-225, 2005

[7] X. Wang, K. Adachi, K. Otsuka, K. Kato: Optimization of the surface texture for silicon carbide sliding in water, Applied Surface Science, Vol.253, pp.1282-1286, 2006

[8] X. Wang, K. Kato, K. Adachi: Loads carrying capacity map for the surface texture design of SiC thrust bearing sliding in water, Tribology International, Vol.36, pp.189-197, 2003

[9] X. Wang, K. Kato, K. Adachi, K. Aizawa: The effect of laser texturing of SiC surface on the critical load for the transition of water lubrication mode from hydrodynamic to mixed, Tribology International, Vol. 34, pp.703-711, 2001

[10] K.P. Gertzos, P.G. Nikolakopoulos, C.A. Papadopoulos: CFD analysis of journal bearing hydrodynamic lubrication by Bingham lubricant, Tribology International, Vol. 41, pp. 1190-1204, 2008

[11] T. Ibatan, M.S. Uddin, M.A.K. Chowdhury: Recent development on surface texturing in enhancing tribological performance of bearing sliders, Surface&Coatings Technology, Vol. 272, pp.102-120, 2015

[12] F. Saeidi, B. Meylan, P. Hoffman, K. Wasmer: Effect of surface texturing on cast iron reciprocating against steel under starved lubricating conditions: A parametric study, Wear, Vol. 348-349, pp.17-26, 2016

[13] M. Scaraggi, F.P.Mezapesa, G. Carbone, A. Ancona, D. Sorgente, P.M. Lugara : Minimize friction of lubricated laser-microtextured-surfaces by tuning microholes depth, Tribology International, Vol. 75, pp.123-127, 2014

[14] N. De Laurentis, A. Kadiric, P. Lugt, P. Cann : The influence of bearing grease composition on friction in rolling/sliding concentrated contacts, Tribology International, Vol.94, pp.624-632, 2016

[15] P.M. Lugt: Modern advancements in lubricating grease technology, Tribology International, Vol.97, pp.467-477, 2016

EFFECTS OF CONTAMINATION OF SLIDEWAY OILS WITH WATER MISCIBLE METALWORKING FLUIDS

Marica DUGIĆ[1*], Branko DESPOTOVIĆ[2], Mirko Petković[3], Novak DAMJANOVIĆ[4], Pero DUGIĆ[5]

[1,2,3]Rafinerija ulja Modriča, BiH, majad@modicaoil.com; bane@modricaoil.com; pmirko@modicaoil.com
[4]"OPTIMA Grupa" d.o.o. Banja Luka, BiH, damjanovicn@optimagrupa.net
[5]Tehnološki fakultet Univerziteta u Banjaluci, BiH, pero.dugic@tf.unibl.org

Abstract: *Slideway oils have application in many industry branches, in all sliding parts, spindles for transferring work shift, moderately loaded worm gears, and all types of rails, linear and circular, and vertical and horizontal slideways. In machines that are used for metalworking, slideway oils come in contact with various metalworking fluids (MWF). Because of that, chemical compatibility of slideway oils and metalworking fluids is very important for effective functioning of machines with slideways and for lifetime expectancy of slideway oil itself, and also for metalworking fluid. Compatibility of these two lubricants is determined by demulsivity property that is the ability of separation of oil from MWF. During the metalworking process, even if the demulsivity characteristics are good, water and oil separation doesn't happen so fast, like in standing phase.*
Goal of this paper was to examine effects of different metalworking fluids formulations on antiwear characteristics of slideway oils. Most common viscosity grades of slideway oils are ISO VG 68 and ISO VG 220. Oils in these viscosity grades are treated with three types of emulsions of different chemical composition prepared in concentrations, that is normally used in production and that can satisfy several types of metalworking. Emulsions are added in different percentages, in order to evaluate its effect on lubricating properties of slideway oils, via applied wear tests.
This research shows which chemical type of metalworking fluid has unfavorable effect on antiwear properties of slideway oil and, at the same time, helps on choosing the type of lubricant.

Keywords: slideway oils, machine tool, metalworking fluids, emulsion, demulsivity, 4 ball wear

1. INTRODUCTION

Industry term „slideway"is associated with parts of metalworking machine that are called machine tools. Machine tools are made up of a number of elements, devices and mechanisms. Integral parts of machine tools are sliding surfaces, called slideways. During operation of the machine in production conditions, lead sliding surfaces where metalworking tool carrier is sliding, are intensely worn out. The intensity of wear of leading slideways may be affected by many factors. One can single out external effects that influences wear, and influence of composition and quality of materials they are made of. [1]

That's why a good choice of slideway lubricant is very important because it can affect productivity of machine tools that are used in various metalworking processes. Lubricating greases are used only in some places, while lubricating oils have wider

application. Slideway oil has great impact on production capability and precision of metalworking.

In machines that are used for metalworking, slideway oils come in contact with various metalworking fluids. Because of that, chemical compatibility of slideway oils and metalworking fluids is very important for effective functioning of machines with slideways and for lifetime expectancy of slideway oil itself, and also for metalworking fluid.

Quality of machined parts depends also on the movement of machine tool, respectively on the condition of slideway. If the friction is on minimized on the slideway, tool won't work correctly and the productivity will be decreased in the end, resulting in badly processed parts. Often mentioned stick-slip phenomenon on the slideway system can cause movements with twitching and stuck. [2]

Slideway oils have application in many industry branches. Large consumption is in the following branches of industry: automobile, food, beverage, packaging, and considerable amount are spent in small workshops. Market analyses showed that the most common viscosity grade is ISO VG-68, especially with numerous mobile and industrial applications, mostly with horizontal slideways. Then follows the ISO VS-220 gradation, that is used with heavily loaded horizontal and vertical slideways. [3]

On domestic and markets of wider region, also the most common gradations are VG-68 and VG-220.

Many researchers have tested the effect on quality and longevity of use of metalworking fluid itself, when there is contact with slideway oils. Some of them done research to what extend and at what characteristics affects coolant and lubricant in machining process, on lubricant itself and on slideway oil.

Researchers Mohan C., Gopalakrishna and authors, in paper „Coolant lubricity and coolant-lube compatibility with regard to slideway behavior", tested the effect of mixing these two lubricants, done demulgivity characteristics and the effect on tribological characteristics of slideway oil. [4]

2. EXPERIMENTAL WORK

Idea for this research came from need to get the information at which type of water miscible metalworking fluid has the greatest effect on degradation of slideway oils functional characteristics.

Lubricating oils for slideways that were used in this test fulfill these standards/specifications: ISO 6743/4 HG, CINCINNATI-MACHINE: P-47 (VG 68), P-50(VG 220), ISO 11158 HG (VG 68), ISO 6743/13 (VG 220) i ISO 19378 G-A (VG 220). [5]

Basic characteristics of slideway oil, whose values fulfill demands of afore mentioned specifications are:

- ensuring the continuity of the oil film and good adhesion to the sliding surface
- low static and dynamic friction coefficient, ensuring great antiwear protection, including work under extreme pressures
- avoiding stick-slip phenomenon
- excellent corrosion protection
- good compatibility with hydraulic oils and with all net cutting oils
- good chemical compatibility with all watersoluble metalworking fluids that are used as a coolant and lubricant during metalworking process
- good demulsivity characteristics with watermiscible metalworking fluids
- good compatibility with all machine tools, including materials they are build of and colors and [6]

Slideway oil samples of ISO VG-68 and ISO VG-220 viscosity grades are prepared according to formulations listed in table 1. One formulation that was in use at large number of consumers was chosen.

In both gradations the same additive package based on sulfur, phosphorus and nitrogen was used, which provides the completion of all the characteristics required by the aforementioned specifications. In order to ensure good adhesion of slideway oil to the

sliding surface, a specially designed polymer was added. By chemical composition it is polyisobutilen. It affects the improvement of adhesion and continuity of the lubricant film during the movement of the slideway. It also affects the demulsibility characteristics, is water-repellent or act by not allowing easy mixing with the water-soluble agents.

Table 1. Slideway oils formulations ISO VG-68 and ISO VG-220

	ISO VG 68, %	ISO VG 220, %
Base oil 1	35	40
Base oil 2	62,9	-
Base oil 3	-	57,9
Additive package	1,8	1,8
Tackiness additive	0,3	0,3

Table 2. Slideway oils characteristics ISO VG 68 i ISO VG 220

	ISO VG-68	ISO VG-220
Characteristics and testing method	Result	Result
Viscosity at 40 [^{O}C], mm^2/s, ASTM D 7042:2014	68,24	212,6
Viscosity at 100 [^{O}C], mm^2/s, ASTM D 7042:2014	8,11	18,4
Flash point, [^{O}C], ISO 2592:2002	246	282
Demulsivity at 54 [^{O}C] at 82 [^{O}C] (oil:water: emulsion), [mL], [minutes], ISO 6614:2000	40:40:0(0)	40:40:0(5)
Corrosion on Cu 3h/100, [^{O}C], stage, ASTM D 130:2004	1a	1b

Base oils that are in both formulations are combined from three oil gradations so desired viscosity is achieved. Base oils marked in Table 1., with 1 and 3 are manufactured by solvent neutral technology by renowned manufacturers, and base oil marked with 2, is manufactured by hydrockracking technology in domestic oil refinery.

Basic characteristics of slideway oils prepared for this research, ISO VG 68 and ISO VG 220 are shown in Table 2.

Classification of watermiscible metalworking fluids was done by ISO 6743/7 L-M, when mixed with water, they give:

- fully synthetic solutions, whose concentrates don't contain oil
- semi-synthetic solutions, whose concentrates contain 40-50% oil
- oil based emulsions, whose concentrates contain 60-85% of mineral oil

Every one of three types of MWF's is used in processing, so their water solutions come into contact with slideway oils.

For the purposes of the tests of each type of fluid are chosen formulations, which meet the following standards: ISO 6743/7: L-MAH, L-MAF and L-MAB. [7]

Fully synthetic fluid, type I, was formulated based on biodegradable alkanolamines, polyalkyl glycols, boric acid, biocides, antifoaming agent and water. Depending on the type of processing of steel and lightweight non-ferrous metal, the concentration of aqueous solutions is determined for drilling, grinding, turning, milling, threading. Particles sizes of transparent aqueous solution are 0,01-0,1 [µm].

Semi-synthetic type II MWF with water gives a semi-transparent micro-emulsion, with particle size 0,1-1 [µm], which are used for cooling and lubrication of tools for operations of drilling, turning, milling, and thread cutting. It contains emulsifiers, stabilizers, biocides, mineral oil, water and additives to improve lubricity.

Type III is the oil-based water soluble MWF, in an amount of about 70%, doesn't contain water, has added emulsifier, additives for improving the lubricity, inhibitors and biocides. With water it gives milky emulsions with particle size of 1-10 [µm], for a wide range of treatment at drilling operations and abrasion.

Of the concentrate of each type of MWF are blended with water in 5% concentrations, which are commonly used in a number of

different metal processing operations with users that use slideway oils produced according to the described formulations.

Testing the impact of MWF on slideway oils in this study was first conducted through demulsivity tests. Used test was developed by additives manufacturers in this area of lubricants in cooperation with tribology laboratory „SKC Gleitechnik" in Roedental, Germany.

This demulsivity test simulates situation where MWF comes in contact with slideway oil and in that way it contaminates it. Test is carried at room temperature. In a 10 mL graduated cylinder slideway oil and the aqueous solution of MWF is poured in a ratio of 80:20 (oil: aqueous solution of MWF), and 8 mL of slideway oil with 2 mL of an aqueous solution of MWF. After mixing for 30 seconds for ISO VG-68 and 60 seconds for ISO VG-220, separation is visually estimated. The first assessment is after 1 hour, the second after one day and the third after 7 days. [8]

If the test results of demulsibility after assessment after one hour are bad, it is assumed that this will have an impact on the anti-wear properties of the oil.

In the Figure 1. are shown mixtures (by modified method for demulsibility test „SKC Gleitechnik") after mixing of slideway oil ISO VG-68 with 5 % MWF: synthetic, semi-synthetic and oil emulsions.

In the Figure 2. are shown mixtures of ISO VG-220 with same emulsion types. The photographs were taken after 10 minutes of mixing of the two lubricants.

Figure 1. Photograph of mixture ISO VG-68 with 5 % synthetic, semi-synthetic and oil emulsion, after 10 minutes of standstill

In the photographs shown in Figures 1. and Figures 2. it is evident that after the standstill of the mixture for about ten minutes oil and

aqueous phases do not separate. Only after a rest time of an hour phase separation occurs, as shown in Figure 3. With mixture of both oil gradations with oil emulsion there is less separated water. This can be explained by a greater share of the emulsifier in the oil emulsion, which emulsifies water and oil phase during that time.

Semi-synthetic emulsion also contains an emulsifier and the content of separated water is noticeable in both gradations. In blends with synthetic emulsion content of the separated aqueous phase is greatest. It is favorable when operating processing machines that use synthetic emulsions that are mixed with slideway oils.

Figure 2. Photograph of mixture ISO VG-220 with 5 % synthetic, semi-synthetic and oil emulsion, after 10 minutes of standstill

Figure 3. Photograph of mixture ISO VG-68 (left) and VG-220 (right) with 5 % synthetic, semi-synthetic and oil emulsion, after one hour of standstill

Figure 4. shows the photographs of the condition of the same blend made after seven days. Only during the rest phase of the mixtures a better separation of the oil and aqueous phases will occur. In mixtures of gradation 68 with all three types of emulsions in standstill is separated more oil part than at VG-220, which is usual for lighter oil gradations. A mixture of VG-220 with oil emulsion has less separated water, which can

be interpreted as stronger influence of emulsifiers in heavier gradation.
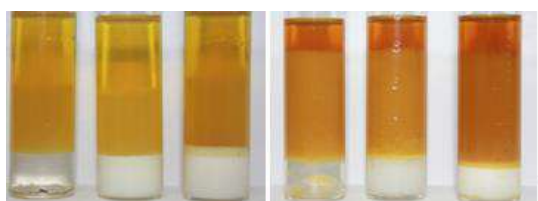
Figure 4. Photograph of mixture ISO VG-68 (left) and VG-220 (right) with 5 % synthetic, semi-synthetic and oil emulsion, after seven days of standstill

Since during the metal processing mixing of the lubricant happens continuously, in addition to good demulsibility characteristics of slideway oils, during operation may be difficult to separate the phases, which is illustrated in Figure 1.

To research the influence of mixing of those two lubricants on the antiwear properties, the series of tests was performed where in different percentages in slideway oil was added 5% emulsion of each type of MWF.

Wear tests were made using two apparatus, Reichert's balance and Four Ball Machine.

Reichert's balance is apparatus by which is determined how the lubricant layer tolerates specific pressure occurring between the contact surfaces of metals. The basic element of the test device consists of a roller and the ring. The roller is static, and the ring is dynamic element. Lubrication of tested elements is achieved in such way that the ring is partially submerged in the tested lubricant and during rotation it carries away part of lubricant. Testing is done up to 100 [m] of sliding path of a ring with constant strain on tested elements, 150 [N]. On the test roller remain traces of wear in the form of an ellipse. The size of the wear in [mm2] is recorded as test result on Reichert's balance. Calculation from surface wear gives specific ground pressure, in [N/mm^2]. [9]

The test result is better when the surface of wear is smaller, because it means that the specific surface pressure lubricant can endure is higher. [10]

The test conditions on Reichert's balance and characteristics of the apparatus at which

the samples are tested and the determination of the wear surfaces are:

- amounts of liquid and temperature: 75 [mL], room, about 21 [^{o}C]
- probes: ring and the roller
- material of the ring and roller: alloy steel (HRC 61-63)
- type of friction: sliding friction
- sliding speed: 1,70 [m/s], [900 ^{o}/minut]
- load: 150 [N]
- duration of the test: 100 [m] movement of the track, about 1 [minute]
- measured quantity: wear surface [mm^2]; uniform movement noise, [m]; specific ground pressure, [N/mm^2]; [11]

Wear test was done by method ASTM D 4172, Four Ball Method. Because of present water in samples, the testing was done at room temperature.

Testing conditions were as followed:
- Speed: 1200 ^{o}/min ± 60 ^{o}/min
- Duration of the test: 50 min ± 1 min
- Load: 400 N ± 20 N

Table 3. Tribological characteristics of mixures of ISO VG-68 with different percentage of synthetic emulsion

Characteristics	Ratio of 5 [%] synthetic emulsion in VG-68, [%]				
	0	20	30	50	100
Scar diameter [mm]	0,40	0,58	0,86	1,00	-
Scar area,[mm^2]	7,22	7,86	8,83	15,11	17,86
Specific surface pressure, [N/mm^2]	41,55	38,16	33,97	19,85	16,79

Results of tribological tests of mixtures of slideway oils VG-68 (Table 3.) and VG-220 (Table 4.) with synthetic emulsions are obtained by measuring the scar diameter wih Four Ball Method, and with wear test on Reichert's balance we measured the Scar area. Specific surface pressure values are obtained by calculations. In Tables 5. and 6. are shown test results of thonse tests for mixtures ISO VG-68 and ISO VG-220 with

semisynthetic emulsions, and in Tables 7. and 8. with oil emulsions.

Table 4. Tribological characteristics of mixures of ISO VG-220 with different percentage of synthetic emulsion

Characteristics	Ratio of 5 [%] synthetic emulsion in KS-220, [%]				
	0	20	30	50	100
Scar diameter [mm]	0,37	0,65	0,72	1,00	-
Scar area,[mm^2]	3,34	6,70	7,85	10,59	17,86
Specific surface pressure, [N/mm^2]	89,82	44,77	38,21	28,32	16,79

Table 5. Tribological characteristics of mixures of VG-68 with different percentage of semi-synthetic emulsion

Characteristics	Ratio of 5 [%]semi-synthetic emulsion in KS-68, [%]				
	0	20	30	50	100
Scar diameter [mm]	0,40	0,57	0,88	0,97	-
Scar area,[mm^2]	7,22	7,33	10,53	11,23	16,41
Specific surface pressure, [N/mm^2]	41,55	40,92	28,49	26,71	18,28

Table 6. Tribological characteristics of mixures of VG-220 with different percentage of semi-synthetic emulsion

Characteristics	Ratio of 5 [%]semi-synthetic emulsion in KS-220, [%]				
	0	20	30	50	100
Scar diameter [mm]	0,37	0,59	0,80	0,95	-
Scar area,[mm^2]	3,34	3,57	5,88	7,7	16,41
Specific surface pressure, [N/mm^2]	89,82	84,03	51,02	38,96	18,28

Table 7. Tribological characteristics of mixures of VG-68 with different percentage of oil based emulsion

Characteristics	Ratio of 5 [%] oil based emulsion in KS-68, [%]				
	0	10	30	50	100
Scar diameter [mm]	0,40	0,53	0,80	0,98	-
Scar area,[mm^2]	7,22	5,88	6,04	6,91	14,30
Specific surface pressure, [N/mm^2]	41,55	51,02	49,66	43,41	20,97

Table 8. Tribological characteristics of mixures of VG-220 with different percentage of oil based emulsion

Characteristics	Ratio of 5 [%] oil based emulsion in KS-220, [%]				
	0	10	30	50	100
Scar diameter [mm]	0,37	0,53	0,76	0,80	-
Scar area,[mm^2]	3,34	4,53	4,71	5,18	14,30
Specific surface pressure, [N/mm^2]	89,82	66,22	63,69	57,91	20,97
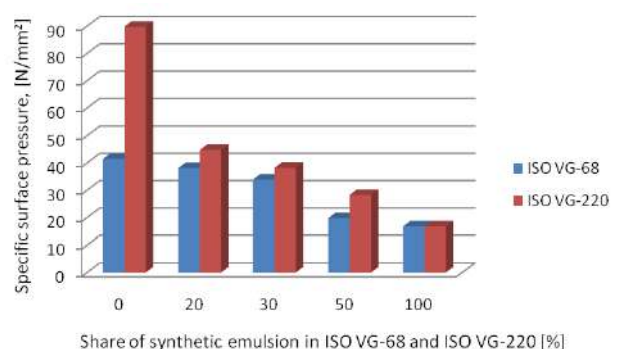
Figure 5. Specific surface pressure, comparison of mixture of slideway oil ISO VG-68 and ISO VG-220, with different percentage of synthetic emulsion

Figure 5. shows comparison of the value of the specific surface pressure of a mixture of two oil grades with different amount of synthetic emulsion.
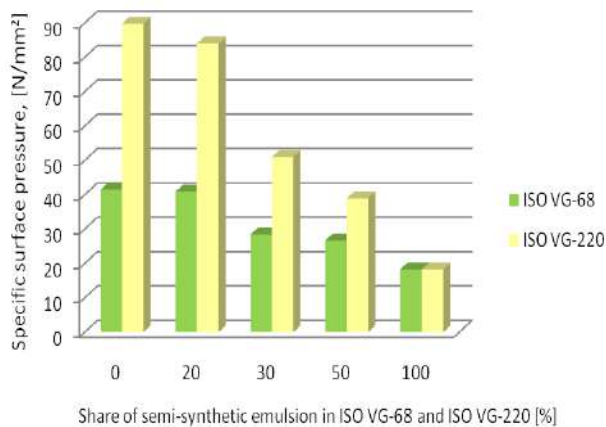
Figure 6. Specific surface pressure, comparison of mixture of slideway oil ISO VG-68 and ISO VG-220, with different percentage of semi-synthetic emulsion

Figure 6. presents a comparison of the value of the specific surface pressure of the mixture of two grades semi-synthetic emulsion, and in Figure 7., with a mixture of oil-based emulsion.
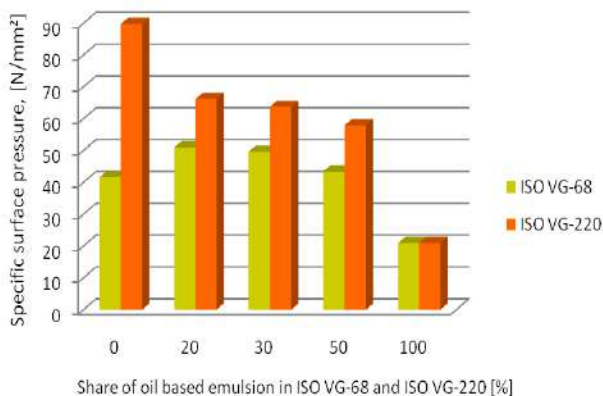
Figure 7. Specific surface pressure, comparison of mixture of slideway oil ISO VG-68 and ISO VG-220, with different percentage of oil based emulsions

Gradation ISO VG-220 compared to the VG-68 in all mixtures with all three types of emulsion can bear greater loads. Higher gradation oils have better adhesion and continuity of the lubricant film on the surface that is lubricated. This feature allows the submission of larger loads, even in situations where it is mixed with MWF.

Wear scar diameter value of mixture of slideway oil ISO VG-68 with a different amount of synthetic, semisynthetic and oil emulsions are shown in Figure 8., and Figure 9. in a mixture with the ISO VG-220.
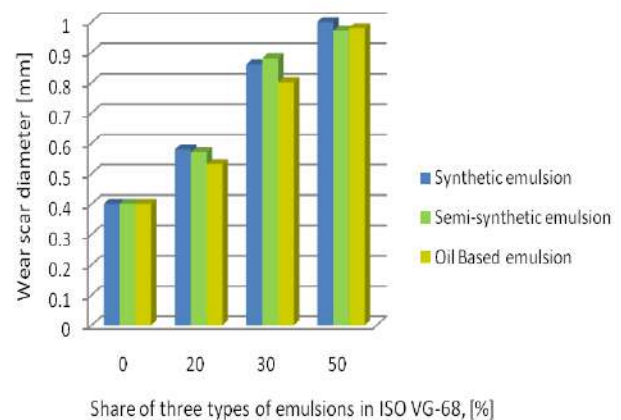
Figure 8. Wear scar diameter, comparison of mixture of slideway oil ISO VG-68 and ISO VG-220, with different percentage of semi-synthetic emulsion

It is evident that with the increase of MWF amount in slideway oil in both gradations there is an increase in wear. Participation of oil emulsions in VG-220 has the least effect on this characteristic.
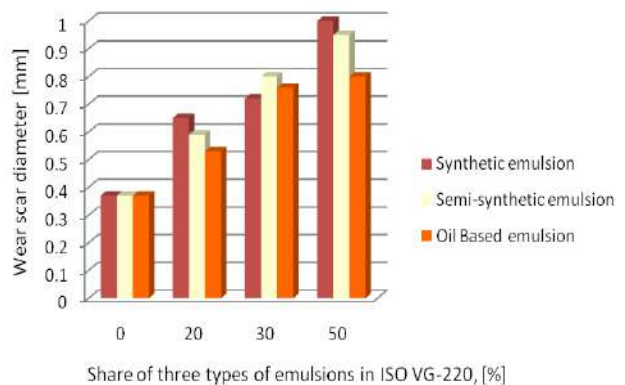
Figure 9. Wear scar diameter of mixture of slideway oil ISO VG-220 with different percentage of synthetic, semi-synthetic and oil based emulsions
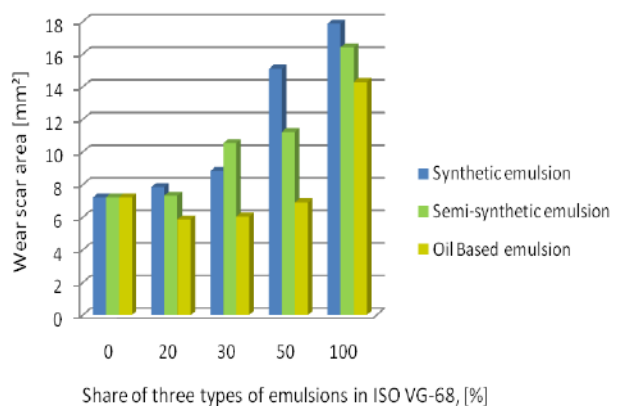
Figure 10. Wear scar area of mixture of slideway oil ISO VG-68 with different percentage of synthetic, semi-synthetic and oil based emulsions

Wear scar area characteristic with VG 68 (Figure 10.) and VG-220 (Figure 11.) is only slightly degraded in mixture with synthetic emulsion, especially with VG 68.
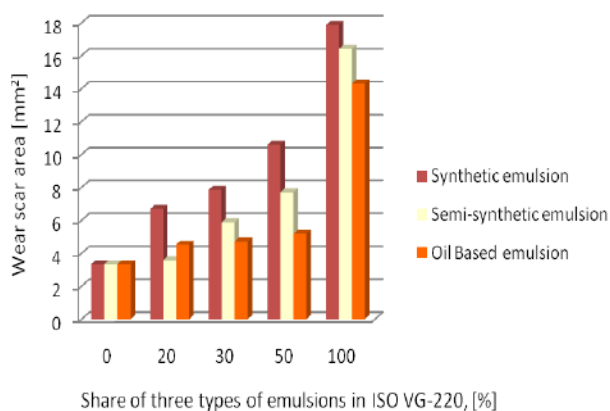
Figure 11. Wear scar area of mixture of slideway oil ISO VG-220 with different percentage of synthetic, semi-synthetic and oil based emulsions
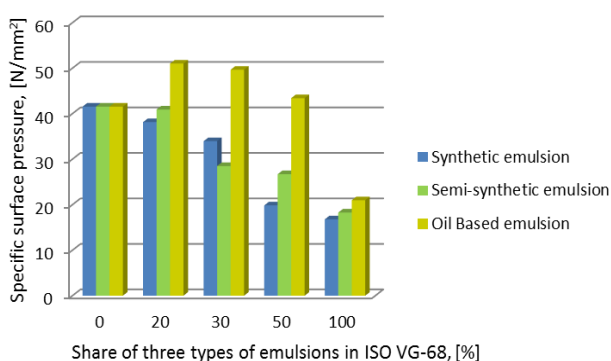
Figure 12. Specific surface pressure of mixture of slideway oil ISO VG-68 with different percentage of synthetic, semi-synthetic and oil based emulsions
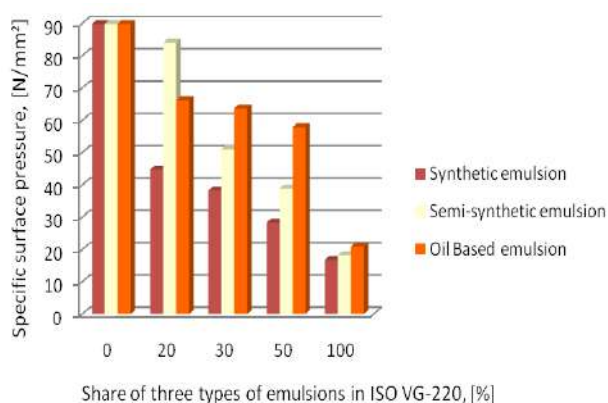
Figure 13. Specific surface pressure of mixture of slideway oil ISO VG-220 with different percentage of synthetic, semi-synthetic and oil based emulsions

Figure 12. shows comparison of specific surface pressure of slideway oil ISO VG-68 with a different amount of synthetic, semisynthetic and oil emulsions. Based on the results it can be seen that synthetic and semi-synthetic emulsion influence the reduction of specific surface pressure. The amount of oil emulsions in that gradation gave a bit higher values, which can be interpreted by the synergistic action of AW and EP additives in this type of MWF and better wetting of rollers during the test.

Figure 13. shows a comparison of specific surface pressure of mixture of slideway oil ISO VG-220 with a different amount of synthetic, semisynthetic and oil emulsions. Semisynthetic emulsions only in the case of participation of 20% has less affect on this characteristic. Oil emulsion added in different percentages in this oil grade has the least impact, while synthetic emulsion has the greatest impact on reducing the specific surface pressure.

3. CONCLUSION

This research showed that with demulsibility and wear tests by two methods, one can obtain results on which type of MWF due to mixing has greatest effect on functional characteristics of two most common gradations of slideway oils.

Demulsibility characteristics of the mixtures are worse in higher grades of slideway oils, but the effect on tribological characteristics is lower.

These data are significant in setting the demulsibility characteristics of slideway oils by adding a demulsifier.

Using the wear test results, we have learned that the greatest harmful affect on anti-wear properties have synthetic emulsions. They have better cooling and inhibition features, but have poorer lubricating function. Semisynthetic emulsions have a slightly lower effect on the anti-wear properties.

Oil emulsions are richer in their composition and have the least impact on the anti-wear properties.

The study of influence of three different types of emulsions on slideway oils yielded a series of results useful for manufacturers of both groups of lubricant, but also for consumers.

Lubricant formulations of samples selected for testing in this study are in use as a commercial product with many users. Their behavior was tested in exploitation conditions.

LITERATURE

[1] L. Yang, J.Wang, R.Wu, W.Wu: *Machine slideway wear to the precision of the whole machine impact*, Applied Mechanics and Materials, Trans Tech Publication, Switzerland, 229-231, 2012.

[2] Th. Mang, K. Bobzin, T. Bartels, Industrial Tribology, Wiley-VCH, Germany, 26-27, 2011.

[3] News from ReportBuyer, *Slideway Oil Market Analysis By Product,* London, July 13, 2016 /PRNewswire, **www.reportbuyer.com**

[4] Mohan. C. B., Gopalakrishna. K., Mahesh Lohith. K. S., Krishna Venkatesh, Divakar. C., Mithun. R. B., Naveen. T. N., *Coolant lubricity and coolant-lube compatibility with regard to slideway behavior,* J. Braz. Soc. Mech. Sci. & Eng. vol.30 no.4 Rio de Janeiro Oct./Dec. 2008

[5] Interni dokumenti Rafinerije ulja Modriča, Interni standard M.2.01.008

[6] Th. Mang, W. Dresel, Lubricant and Lubrication, Weinheim, 2007., 326

[7] Interni dokumenti Rafinerije ulja Modriča, Interni standard M.3.03.001

[8] SKC Coolant Separation Test, SKC Gleittechnik, Roedental, Njemačka

[9] Th. Mang, K. Bobzin, T. Bartels, Industrial Tribology, Wiley-VCH, Germany, 2011. , 26-27

[10] Th. Mang, W. Dresel, Lubricant and Lubrication, Weinheim, 2007., 740

[11] Reichert balance test

**Serbian Tribology
Society**

SERBIATRIB '17

**15ᵗʰ International Conference on
Tribology**

**Faculty of Engineering
University of Kragujevac**

Kragujevac, Serbia, 17 – 19 May 2017

ANTIWEAR PROPERTIES OF GREASES AND GEAR OILS WITH THE GEO-MODIFIERS OF FRICTION

Igor LEVANOV[1],*, Aleksey DOYKIN[1] , Elena ZADOROZHNAYA[1], Robert NOVIKOV[2]
[1]South Ural State University, Russia, kafat@susu.ac.ru
[2]Scientific and Engineering Center "RS LSM" UB RAS, Russia, sec@wekt.ru
*Corresponding author: levanovig@susu.ru

Abstract: *The article describes the influence of the geo-modifiers of friction on the antiwear properties of greases and gear oils. Geo-modifiers of friction are the fine powders of mineral materials. This work is directed on the investigation the influence of the geo-modifiers of friction in the form of the hard lubricant compositions, which based on a mineral serpentine, on the anti-wear properties of greases and gear oils. This composition is the fine powder serpentine with the addition of components such as chalk, borax, kaolin and talc. We compared the antiwear properties of the greases without geo-modifiers of friction and the antiwear properties of greases containing the geo-modifiers of friction from 0.5% to 3%. The Litol-24 and transmission oil TAD-17 was used for testihg. The four-ball machine of friction was used for tests accordance with GOST 9490-75. As geo-modifiers the serpentine was used, the fraction of which has a size from 0.87 microns to 2.2 microns. Such parameter as the wear scar diameter was used for evaluation of the antiwear properties of lubricants.*

As a result of tests it was established that the antiwear greases properties improved on 26-50% depending on the concentration of the geo-modifiers of friction based on the pure serpentine.

Keywords: *greases, gear oils, geo-modifiers of friction, antiwear properties.*

1. INTRODUCTION

Geo-modifiers of friction are natural minerals that are added to lubricants to improve their tribological properties, in particular anti-wear properties. In the early 90s of the last century it was established that the minerals of the serpentinite group possess the best tribological properties among a lot of rocks [1].

Many studies [2-8] indicated an increase of a wear resistance of friction units when the friction geo-modifiers type of serpentinite was added to the lubricant. However, the tribological properties of the lubricant composition depend on a chemical composition and a structure of serpentinite. Since serpentinite as the rock usually contains up to 45% -50% of serpentine, and the rest 7-8% of magnetite, up to 10% of aluminosilicates, titanium oxides, calcium (basalts) and silica. Many natural serpentinites are unsuitable for the production of additives to lubricants due to the increased content of abrasives such as SiO_2. The use the unknown composition of serpentinite can lead to a negative result [6].

Breki [2] investigated the effect of nanosized serpentinite on the tribological properties of aviation oil MS-20. He showed that nanosized serpentinite increases the

ultimate load capacity of the lubricating layer by 11-20%, reduces the wear spot by 15-33%, reduces the boundary friction by 26-41% relative to the MS-20 oil, which does not contain additives. The author also showed that a mass concentration of serpentinite 1-2% in the oil MS-20 provides the lowest values of the wear scar diameter. However, the work does not provide information about the composition of used serpentinite.

Nigmatullin et al. [3] investigated the effect of serpentine on the tribological properties of oxidized lubricants. Serpentine produced in the Republic of Bashkortostan was used. The authors concluded that a self-assembled protective metal-ceramic coating (film), which is characteristic of selective transfer (the effect of non-weariness), is formed on iron-containing friction surfaces when serpentine is added to an oxidized lubricant (industrial grade I-40 oil, compressor oil KS-19). Lubricating composition of oxidized oil KS-19 with the addition of serpentine (0.3%) and MnO_2 (0.05%) ensures the greatest efficiency of the friction units. The wear scar diameter is reduced by 40% when testing the lubricant composition on the four-ball friction machine. The authors also note an increase in the microhardness of the friction surface. Unfortunately, there is also no information about the structure of serpentine.

Medvedev et al. [4] investigated the effect of the particle size of serpentinite on the anti-wear properties of Litol-24 grease. The authors concluded that particle size of 1 μm does not have a positive influence on the antiwear properties of the lubricating composition. The anti-wear properties of the composition with particle serpentinite sizes 10 μm and 30 μm begin to appear at low concentrations. In [5], the authors studied the effect of a mixture of talc and serpentinite on the anti-wear properties of the grease plastic Litol-24. The particle serpentinite sizes were 10 μm, talc was 15 μm. The total mass concentration of the mixture was 10%. The authors showed that when the mixture of serpentinite and talc was added to the grease, the antiwear properties of the base lubricant are improved. In this case, the wear scar diameter depends

on the ratio of talc and serpentinite. The best results are achieved when the percentage of components in the mixture (talc relative to serpentinite) is 100% to 0%. Wear is slightly increased with the percentage of the mixture of talc-serpentinite 45/65%.

Duradji et al. [7] investigated the effect of the antifriction antiwear lubricant composition based on the natural mineral of the serpentinite group. The authors presented the phase composition of the antifriction anti-wear composition, in which 78-85% is serpentine $Mg_6[Si_4O_{10}](OH)_8$, the rest is additives and catalysts. The composition tested by the authors did not contain any abrasive particles, was chemically neutral, did not dissociate in oils, and did not change their viscosity. The authors investigated the tribological characteristics of the base plastic lubricants Litol-24, Solidol-G and others with the addition of the composition and showed that the friction coefficient is reduced in 1,5-2 times, wear is significantly reduced, abrasive wear is observed with the serpentine concentration of more than 30%. Serpentine in engine oil M-10DM significantly improves the running-in of the internal combustion engine and does not lead to a change in the microstructure and microhardness of the friction surfaces.

Skotnikova et al. [8] investigated the effect of minerals from the serpentinite group (antigorite, lizardite, chrysotile) on the antiwear properties of motor oils. The authors presented the dependences of the wear rate on the contact pressure and showed that the addition of the lizardite particles with sizes of 3-5 μm in mineral engine oil leads to improvements in their antiwear properties, but degrades anti-wear properties of synthetic oil with a balanced additive package. However, the contact pressure at which wear begins is higher for the modified synthetic oil.

This article presents the results of an experimental determination of the effect of friction on the basis of pure serpentine on the anti-wear properties of Litol-24 grease and TAD-17 gear oil.

2. GEO-MODIFIER OF FRICTION

The study used a solid-lubricating composition "Zvezda-5" based on pure serpentine, which is a further development of the friction geo-modifiers described in [9]. Figure 1 shows the size of pure serpentine, and Table 1 shows the chemical composition. The measurements were performed using the HORIBA Laser Scattering Particle Size Distribution Analyzer LA-950 spectrometer at the Institute of Solid State Chemistry, Ural Branch of the Russian Academy of Sciences.
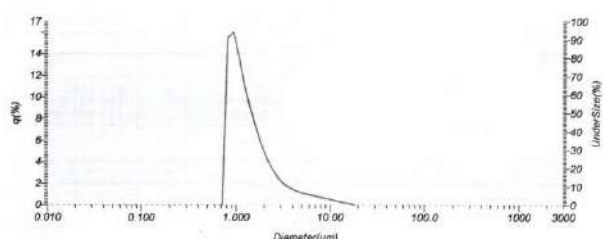
Figure 1. Serpentine size

Figure 1 shows that 90% of the particles have a diameter of 0.88 μm to 3.5 μm and 10% are particles with a diameter of 3.5 μm to 17.4 μm.

Table 1. Chemical composition of serpintine

	O	Mg	Si	Ca	Fe
Macca [%]	44.68	28.71	24.97	0.03	1.61
Atom [%]	57.09	24.14	18.17	0.02	0.59
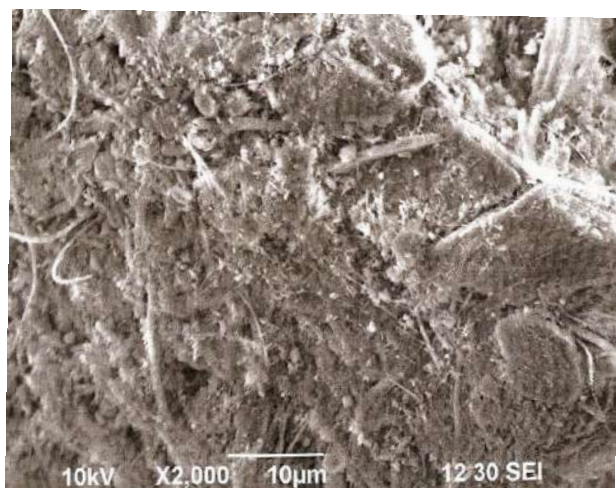
Figure 2. The image of serpentine under a microscope

The lubricating compositions were prepared for studies. One of them consisted of grease Litol-24 with the addition of geo-modifiers of friction from 0.5% to 3% by weight. Another composition consisted of transmission oil TAD-17 with the addition of geo-modifiers of friction from 1% to 3%. The choice of these lubricants is due to their wide application. Lithol-24 is antifriction multi-purpose waterproof grease. It is one of the most common in Russia. It is used for the main friction units of vehicles, industrial equipments, etc. TAD-17 is universal, mineral oil, which contains a multifunctional serophosphorus containing, depressant and antifoam additives. It is used to lubricate gears of cars, including conical and hypoid gears.

3. EXPERIMENT AND RESULTS

Antiwear properties of lubricants were evaluated on the four-ball friction machine (Fig.3) in accordance with GOST 9490-75. The principle of operation of four-ball friction machine is well described in the literature.

The anti-wear properties of the TAD-17 gear oil were additionally evaluated in accordance with the guidelines [10]. Dependence of the wear rate on the contact pressure for pure TAD-17 oil and for the lubricant composition TAD-17 with the addition of 3% the geo-modifiers of friction were constructed after the processing of the measurement results.

Figure 3. The Four ball tribometer

Litol-24 grease compositions were tested at a load of 196 N, but lubricants based on TAD-17 gear oil were tested at 392 N load. The test duration was a one hour, the test temperature was 20 ° C. After the end of the tests with the help of a microscope the value of the wear scar diameter of the lower balls was evaluated.

Figures 4, 5 show the measurement results of the mean wear scar diameter (MWSD). Figures 6, 7 show dependence of the wear rate on the contact pressure and on the time.

1 - TAD-17 oil; 2 - TAD-17 oil + 3% of the geo-modifiers of friction

Figure 7. Dependence of the wear rate on the time

4. CONCLUSION

The results of experimental studies allow us to draw the following conclusions:

1. The geo-modifiers of friction based on pure serpentine with the particle size of 0.88 μm to 3.5 μm significantly increases the antiwear properties of Lithol-24 grease. The wear scar diameter is reduced by 26-50%.

2. The geo-modifiers of friction (3% by weight) in the gear oil TAD-17 increases the wear scar diameter from 2.3% to 12.0%. However, the wear rate decreases more quickly. This fact indicates a decline in the running time of the friction unit.

Figure 4. Mean wear scar diameter at different concentrations of the geo-modifiers of friction (Litol-24 lubricant)
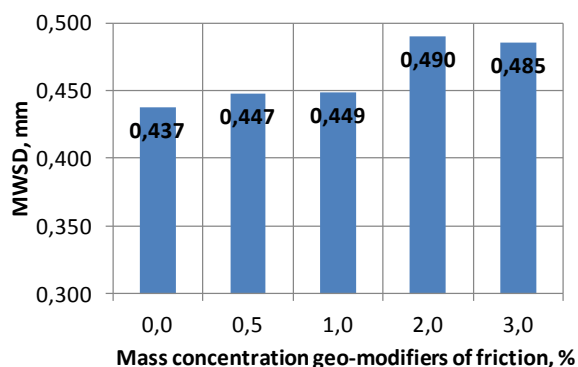
Figure 5. Mean wear scar diameter at different concentrations of the geo-modifiers of friction (TAD-17 gear oil)

1 - TAD-17 oil; 2 - TAD-17 oil + 3% of the geo-modifiers of friction

Figure 6. Dependence of the wear rate on the contact pressure

REFERENCES

[1] Usachev V.V., Pogodaev L.I., Teluh D.M., Kuzmin V.N. Introduction in a problem of use of natural layered geomodifiers in pairs of friction, Friction and lubrication in the machines and mechanisms, No. 1, pp. 36-42, 2010.

[2] Tribological properties of modified lubricating oils, available at: http://www.ipme.ru/ipme/edu/diss/albreki2011.pdf, accessed: 26.02.2017.

[3] R.G. Nigmatullin, B.Y. Sholom, L.S. Shuster and I.M. Nigmatullin: Improving the efficiency of lubricants with friction geomodificators, Bulletin USATU, Vol. 16, No. 1, pp. 51-56, 2012.

[4] Medvedeva V. V., Breki A. D., N. A. Krylov, M. A. Skotnikova and other: Investigation of Antiwear Properties of a Plastic Lubricating composite material containing dispersed particles of the Layered friction modifier, Proceedings of the SouthWest State University Technics and Technologies, No. 1 (64), pp. 75-82, 2016.

[5] Medvedeva V. V., Breki A. D., N. A. Krylov, S. E. Aleksandrov and other: Antiwear Properties of a Grease-Lubricating Composite Material Containing a Mixture of Hydrosilicates of Magnesium, Proceedings of the SouthWest State University Technics and Technologies, No. 2 (19), pp. 30-40, 2016.

[6] Nanotechnology antifriction powder composition (options), nanotechnology lubricating composition and method of lubrication nanotechnology, available at: http://www.freepatent.ru/patents/2415176, accessed: 26.02.2017.

[7] V.N. Duradji, D.E. Kaputkin, A. Duradji: Tribological Studies of Antiwear Antifriction Composition and its Application, Tribology in Industry, Vol. 38, No. 4, pp. 496-507, 2016.

[8] Medvedeva V. V., M. A. Skotnikova, Breki A. D. and other: Evaluation of the Influence of Particle Size and Concentration of Powereds of Rocks on the Antiwear Properties of Liquid Lubricant Compositions, News of Tula State University. Technical science, No. 11 (1), pp. 57-65, 2015.

[9] Solid lubricating composition, Patent of the Russian Federation. № 2553255, 2015. (on Russian).

[10] RD 50-531-85, *Providing wear resistance of products. The method of experimental evaluation of antiwear properties of lubricants in friction: methodical instructions*, 1986.

PERFORMANCE EVALUATION OF JATROPHA OIL AS A LUBRICANT IN TURNING OPERATION OF MILD STEEL

Samaila UMARU[1], David Olubiyi OBADA[1],*, Laminu Shettima KUBURI[1],
Muhammad Kaisan USMAN[1], Muyideen Bolarinwa BALOGUN[1]
[1]Department of Mechanical Engineering, Ahmadu Bello University, Zaria, Nigeria
*obadavid@gmail.com

Abstract: *Vegetable oil from non-edible materials is a promising alternative to fossils fuels in terms of environmental pollution and rapid depletion of world fossil fuel reserves. In this study, Jatropha Caurcas seed oil was produced using the Soxhlet apparatus and tests on the oil quality and suitability for turning operation of mild steel was carried out. Properties evaluated includes: absolute viscosity, kinematic viscosity, cloud point, density, flash point, pour point, iodine value, saponification value and free fatty acid value. A series of evaluations were also carried out to investigate chip thickness ratio, surface finish and temperature during the turning of mild steel. The free fatty acid value was obtained to be 8.742%. The experimental results obtained for the properties of the fluid in terms of oil quality and suitability during the turning operation showed that using Jatropha oil as a lubricant for machining operations for mild steel is a quite promising approach.*

Keywords: *Biolubricant, Jatropha oil, mild steel, turning operations, free fatty acid.*

1. INTRODUCTION

One of the most important aspects in metal cutting theory is turning operation as it leads to material removal using a single point tool from a work-piece to form a desired shape. Optimum selection of machining parameters and usage of cutting fluids significantly influence the tool life. It also leads to higher material removal and leading to surfaces with better finishing [1]. In addition to reducing or controlling friction, lubricants are usually expected to reduce wear and often to prevent overheating and corrosion.

Lubricants have been classified based on their sources into two major categories; the mineral oil lubricant and the biolubricant [2]. The mineral oil lubricants are obtained from crude oil sources and are harmful to the environment and human life. Biolubricants are environmentally friendly because they are sulphur free [3,4]. Steel and aluminium machining operations use lubricants that are designed to tolerate high temperature, withstand severe vibration and shock. Lubricants have been synthesized from plant oils and other environmentally friendly sources which are referred to as biolubricants and these are primarily triglyceride esters derived from animals and plants. There is an increasing demand for environmentally compatible lubricants, particularly in areas where they can come into contact with water, food or people [5].

Biolubricant possess lower volatility, higher flash/ fire points, less vapour emissions and oil

mist, and constant viscosity that makes them offer better safety. With regards to these, it is of great importance to search for non-edible seeds as bio-lubricants to reduce the cost of other available lubricants. When formulating the metal working oils, different compounds-additives are used in order to improve lubricant properties [6].

This work is aimed at evaluating the performance of Jatropha Oil as a lubricant in turning operation of mild steel. The influence of the oils on surface roughness, and temperature was conducted by varying machining parameters.

2. MATERIALS AND METHODS

Thermo-physico-chemical properties of the crude oil samples are determined to know whether the oil samples could be used as base oil for biolubricant production. These properties are: absolute viscosity, kinematic viscosity, cloud point, density, flash point, pour point, iodine value, saponification value and free fatty acid value.

2.1 Materials and Equipment

The materials and equipment used includes: mechanical grinder, viscometer, lathe machine, polish, Infra-red gun thermometer, beakers, electric oven, Jatropha seeds, mild steel work-pieces, micro meter screw gauge, hexane, and sodium hydroxide.

2.2 Biolubricant Synthesis

The Jatropha Curcas seeds were sourced from National Research Institute for Chemical Technology (NARICT) Zaria, Kaduna State Nigeria. The seed kernels were ground using a mechanical grinder and defatted in a soxhlet apparatus using hexane. The extracted seed oil was stored in a freezer at -2 °C for subsequent physico-chemical analysis.

Physico-chemical analysis of the Jatropha oil was carried using the ASTM standard in conformity with researches conducted by [2, 7]. The lubricant was synthesized by transesterification of the methyl ester with ethylene glycol in 50 ml batches using 0.5 M Sodium methoxide (prepared simply by dissolving sodium in 30% methanol) as catalyst. The weight ratio of oil-to-methanol used was 3.5:1, the amount of catalyst used was 0.8% w/w of the total reactants and the reaction was conducted at a temperature of 120°C for two hours thirty minutes (2hrs:30mins).

2.3 Machining of Mild Steel

The investigation of the performance of Jatropha oil was carried out using a turning operation was carried out using the centre lathe with speed range between 15 rpm and 1000 rpm. During the machining operation, one quantity (feed rate, depth of cut) was selected and varied while others were kept constant. The chips produced were measured using micro meter screw gauge and the corresponding thickness was calculated using the chip thickness ratio formula in equation 1:

$$Chip\ thickness\ ratio = \frac{depth\ of\ cut\ (d_c)}{chip\ thickness\ (t_c)} \quad (1)$$

During the operation, temperature was measured using infra-red gun thermometer while the surface roughness of the machined surfaces was determined using a surface comparison sample.

2.4 Test Procedure

Mild Steel was first machined using the biolubricant formed from Jatropha oil. Two different test procedures were carried out. In the first case, the speed is kept constant at 180 rpm and the depth of the cut at 2 mm while feed rate was varied between 0.35 mm/rev to 3.5 mm/rev in a five step sequence. During the process, lubricants were applied directly to the tool work piece interface using a plastic can while the temperature variations were measured using an Infra- red gun thermometer. In the second case, the speed and the feed rate were kept at 370 rpm and 0.5 mm/rev respectively and the depth of cut was varied between 0.5 mm and 2.5 mm in

steps of 0.50 mm. At the end of each of these processes, the chips formed as a result of machining were gathered and the thickness was evaluated using a micrometre screw gauge and surface generated on the work piece was evaluated for surface finishing in arithmetic mean (Ra) of roughness. The same procedure was carried out using soluble oil and readings recorded. The readings obtained from chip thickness was used to calculate the chip thickness ratio and recorded alongside the temperature and surface finish.

3. RESULTS AND DISCUSSIONS

In this section results observed were presented and discussed.

3.1 Physico-Chemical Properties of Jatropha Oil

Table 1 gives the properties of the Jatropha Curcas oil.

Table 1. Properties of the Jatropha Curcas oil

Properties	Value
Absolute viscosity 40°C	66.74 cst
Absolute viscosity 100°C	14.70 cst
Kinematic viscosity 40°C	71.72 cst/g/ml
Kinematic viscosity 100°C	16.475 cst/g/ml
Cloud point	-8 °C
Density 40°C	0.925 g/ml
Density 100°C	0.892 g/ml
Flash point	240 °C
Pour point	2 °C
Iodine Value	40.23 %
Saponification value	173.91 %
Free fatty acid value	8.742 %

From Table 1 it can be observed that the Jatropha oil can be used up to when a temperature of 240 °C is expected. This implies that the lubricant can be used for machining operations at low depth of cut.

3.2 Effect of Lubricant on the Temperature

Figure 1 and Figure 2 show the variation of temperature with the depth of cut and feed rate respectively.
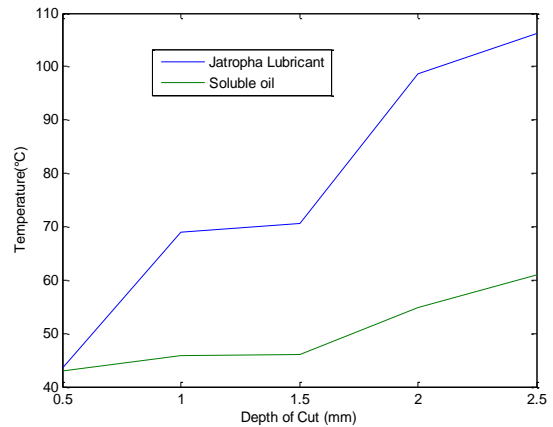
Figure 1: Variation of Temperature with Depth of Cut
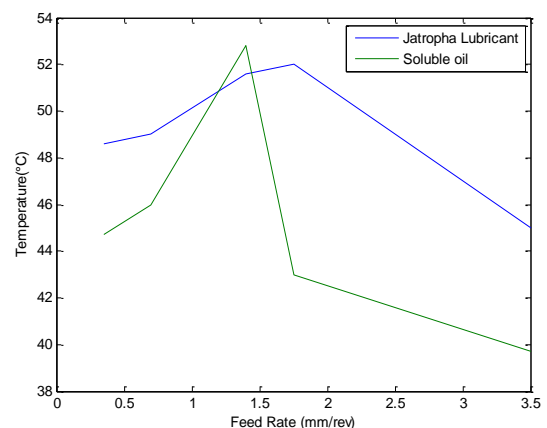
Figure 2. Variation of Temperature with Feed Rate

It shows that the temperature increase as the depth of cut increases in both lubricants but it is higher in the Jatropha lubricant than the soluble oil given the same depth of cut. Cutting force decreases with increase in speed and that since the quantity of heat generated is a product of force and velocity, more heat will be generated as speed increases. This shows that the Jatropha oil lubricant is not a good heat dissipater and this increase in temperature with increase in depth is due to the increase of cutting forces.

3.3 Effect of Lubricant on the Surface Roughness

Figure 3 and Figure 4 show the variation of surface roughness with the depth of cut and feed rate respectively.
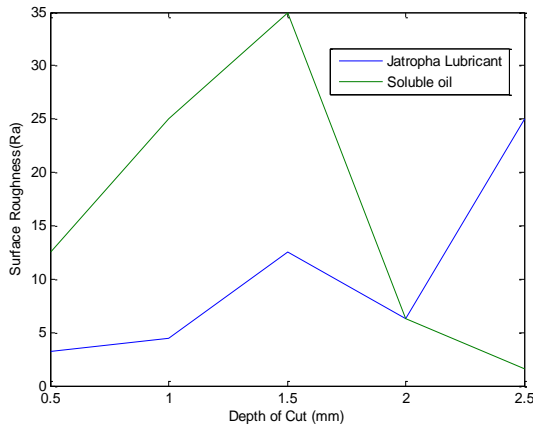
Figure 3. Variation of Surface Roughness with Depth of Cut
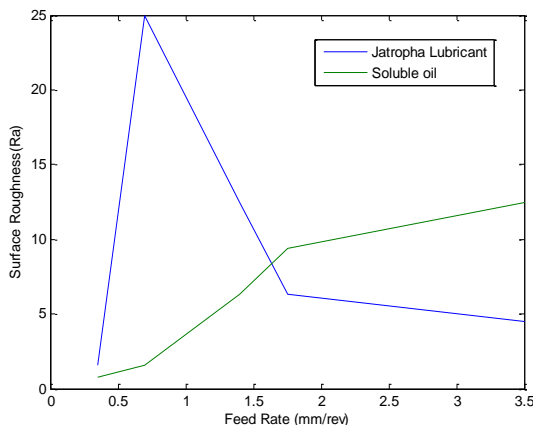
Figure 4. Variation of Surface Roughness with Feed Rate

As cutting fluids reduces adhesion of workpiece to cutting tool i.e. it reduces the formation of built up edge which however protects the tool surfaces, work piece and lowers the cutting force required on machine parts. Figure 3 and Figure 4 show that surface roughness increased with increase in depth of cut (Figure 3) and feed rate (Figure 4). This happens because higher feeds increase the cutting forces and temperature acting on the tool which in turn accelerates tool wear and hence affect the surface quality of the surface being machined.

3.4 Effect of Lubricant on the Chip Thickness Ratio

Figure 5 and Figure 6 show the variation of chip thickness ratio with the depth of cut and feed rate respectively.
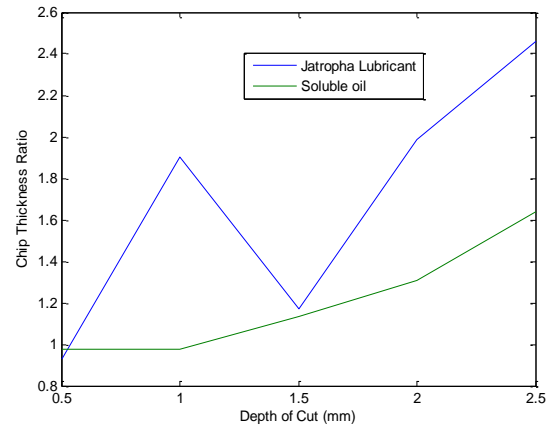
Figure 5. Variation of Chip Thickness Ratio with Depth of Cut
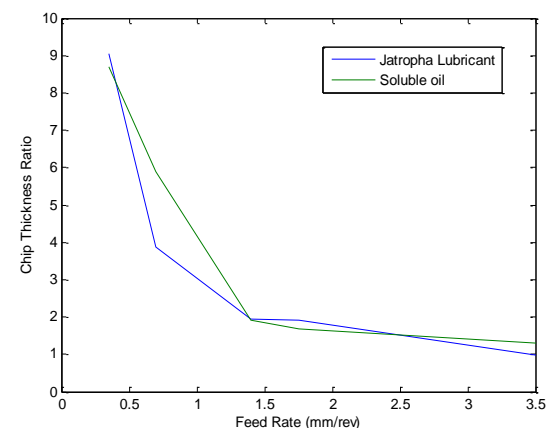
Figure 6. Variation of Chip Thickness Ratio with Feed Rate

Chip thickness ratio increased gradually with depth of cut for both oils at the initial stage and decreased for jatropha lubricant before increasing again (see Figure 5). While with feed rate the chip thickness ratio decreases with increase of feed rate. Showing that jatropha biolubricant has a lower chip thickness ratio when compared with soluble oil(see Figure 6). The quality of these surfaces is as a result of formation of chip continously with no built up edge as the feed rate and depth of cut increases.

4. CONCLUSION

Jatropha Curcas oil was extracted from the Jatropha seed using available equipment and procedures. The physical properties of the oil investigated found out to be: absolute viscosity at 100 °C (14.70 cst), kinematic viscosity at 100 °C (16.475 cst/g/ml), cloud point (-8 °C), density at 100 °C (0.893 g/ml), flash point (100 °C (14.70 cst), iodine value (40.23 %), saponification value (173.91 %) and free fatty acid value (8.74%). During the machining operation of mild steel under varying depth of cut and feed rate, the surface temperature, surface roughness and chip thickness ratio were investigated. It was observed that Jatropha lubricant gave a higher surface temperature but has a better surface finish than soluble oil. Therefore, when surface finish is of huge importance, Jatropha lubricant should be used instead of soluble oil.

REFERENCES

[1] S. A. Lawal, A. Choudhury, I. O. Sadiq and A. Oyewole: Vegetable-Oil Based Metalworking Fluids Research Developments for Machining Processes, Survey, Applications and Challenges, Manufacturing Rev. 1, P 22. 2014.

[2] S. Bilal, I. A. Mohammed-Dabo, M. Nuhu, S. A. Kasim, I. H. Almustapha and Y. A. Yamusa: Production of Biolubricant from Jatropha Curcas Seed Oil, Journal for Chemical Engineering and Material Science Vol 4(6), pp. 72-79, 2013.

[3] S. Supranto: Palm Oil Transesterification Processing to Biodiesel using a Combine of Ultrasonic and Chemical Catalyst, Pertanika J. Sci. & Technol. Vol 21 (2): 567-580. 2013.

[4] S. A. Lawal: A Review Of Application Of Vegetable Oil-Based Cutting Fluids In Machining Non-Ferrous Metals, Indian Journal Of Science And Technology, Vol: 6, Issue 1, 2013.

[5] M. F. Askew: *IENICA: Biolubricants Market Data Sheet. Central Science Laboratory, UK.* 2004.

[6] Bergstra: *Advanced Biolubricants and Re-refining. Biosynthetic.com– MTN Consulting Associates*, 2016.

[7] M. M. Aji, S. A. Kyari and G. Zoaka: Comparative Studies between bio lubricants from Jatropha oil, neem oil and mineral lubricant. (Engen super 20W/50), Applied Research Journal, Vol 1, Issue, 4, pp. 252-257, 2015.

EFFECT OF HOMOGENIZATION IN PRODUCTION PROCESS ON FUNCTIONAL CHARACTERISTICS OF LUBRICATING GREASES

Branka DUGIC KOJIC[1*], Pero DUGIC[2], Goran Dugic[3], Novak DAMJANOVIC[4], Mirko PETKOVIC[5]

[1,3,5] Oil Refinery Modrica, Republic of Srpska, branka@modricaoil.com; gdugic@modricaoil.com; pmirko@modricaoil.com
[2] Faculty of Technology, University of Banja Luka, Republic of Srpska, pero.dugic@tf.unibl.org
[4] ''Optima Group'' d.o.o. Banja Luka, Republic of Srpska, damjanovicn@optimagrupa.net

Apstrakt: *With the development of modern equipment that has improved performances, lubricating greases are set against increasingly strict requirements. The lubricating greases must meet technical and ecological requirements, but at the same time, they must be acceptable from an economical point of view.*

Regarding the composition, lubricating greases represents very complex group of lubricants, and are therefore very often subject of research by numerous reserchers and all of that is done for achieving better performances and application of new materials.

Homogenisation represents very important step in greases production process because homogenisation gives grease with stable colloidal structure. Depending on the type of colloid mill, or a homogenizer, the size of the opening through which the action of the high pressure pushes the grease, the values of pressure and temperature, it is possible to obtain the desired grease consistency and structure stability.

The goal of this paper is testing the effect of homogenization on rheological and other functional characteristic of greases. In this paper we used greases based on Li-soap, Al-complex greases, Li greases with solid additives and Li-greases for high temperature applicatios. For each type of grease are prescribed operating pressures at which process of homogenizaton is carried out. However, in case of changes in the composition of the raw materials it is necessary to investigate the influence of process variables on the quality of the product and to choose the optimal values.

The paper studies the influence of pressure in industrial homogenizer on the characteristic of product. For performance testing we used methods for determination the penetration of lubricating grease using cone ISO 2137, dropping point BAS ISO 2176:1995 (E), extraction of oil from lubricating greases under static conditions ASTM D 1742. The results shows that the homogenization mostly affects the penetration and colloidal stability which also represents the most important characteristic of lubricating greases.

Keywords: *lubricating greases, lubricating greases production, homogenization, rheological characteristics, testing methods, working pressure, penetration.*

1. INTRODUCTION

Lubricants market is experiencing constant changes. These changes, driven by the growing needs and expectations, put the lubricant manufacturers into increasingly greater challenges. They have to meet complex requirements and specifications that incorporate equipment manufacturers, at the same time adapting to the increasingly stricter global requirements. Industrial greases are one of the most important fluids extensively

used by the large variety of industrial branches. Their superior properties, durability, as well as availability are highly appreciated. Different types of greases are employed to protect equipment and machinery. Therefore, it is interesting to analyze the changes that occur, even during the manufacturing process, changing production parameters.

This paper studies the influence of homogenization on functional characteristics of lubricating greases. All samples which are analyzed were taken directly from the production process.

2. LUBRICATING GREASES

To definition which gives American Society for Testing Materials, lubricating greases represents solid or semifluid lubricants that are obtained by dispersing thickener in base oil, with the addition of additives for improvement of certain characteristics.

Lubricating grease contains:

base oil (mineral, sinthetic, vegetable); the proportion of base oil;75-95 %;

thickener (soap or no-soap); the proportion of thickener: 5-19 %;

additives (antioxidants, Aw and EP additives, additives for adhesion, corrosion inhibitors, friction modifier, and solid additive; the proportion of additives: 0-10 %.

The relatively small volume that additives occupy in grease is a reminder of the power of these compounds and complexes impart to a recipe for a lubricating grease.

Lubricating greases are used, when because of the construction solution liquid lubricant cannot be used, when constant presence of a lubricant on the lubrication place is required, because of high specific loads and lower speeds, and high temperatures.

A skillfully formulated grease can bring to the user a host of good things. These include consistency, oxidative and thermal stability, corrosion resistance, structural stability, load-carrying capability, low-temperature performance, high dropping point and elastomer compatibility.(14)

Total global prduction of lubricating greases in 2016 years was 1,1 milion tons, what makes only 3% of total world production of lubricants. Production of lubricating greases in Europe makes 17 % of total world production of lubricants [2].

2.1 Purpose and characteristics of lubricating greases

The main purpose of industrial greases is to minimize friction and wear between moving surfaces. A large number of greases currently available in the market are used in various element of rolling bearings. Lower quantities are used in plain bearings, gearboxes and on open gears. Normally, grease for a given industrial application is expected to provide adequate lubrication to reduce friction and to prevent harmful wear of bearing components. Simultaneosly, it protects surfaces in machinery against corrosion and acts as a seal that prevents access of dirt, moisture and water. Additionally, grease resists leakage, dripping or undesirable loss from the lubricated surfaces as well as intolerable change in structure or consistancy in the bearing especially during prolonged service. Nowdays, industrial grease have suitable physical characteristics adjusted to their application area. They are compatibile with seals and other types of construction materials in the lubricated portion of the mechanism to maximize the comfort of working and the overall performance. Advanced industrial grease tolerates even certain degree of contamination, for instance moisture, without loss of its characteristics.

High quality and innovative greases are significantly driving down maintenance costs and increasing the equipment life as well as the whole production plant productivity. There is a general trend toward continuously improving the quality and performance of industrial greases as end users are more demanding. Simultaneously, advanced grease protect the equpiment and machines better, enhance the reliability of working parts and improve the profitability. Therefore, major

trends and developments are related to the fact that often the choice and adaptation of greases for the right application can bring a huge challenge which needs to be addressed by manufaturers to meet the costumers needs [3].

2.2 Grease classification

Greases can be classified and referred to in many ways, but the main way is by consistency or stiffness as specified by National Lubricating Grease Institute (NLGI) grade. *NLGI grade* expresses a measure of the relative hardness of a grease used for lubrication.

NLGI's classification defines nine grades, each associated to a range of ASTM worked penetration values, measured using the test defined by standard ASTM D217 *"cone penetration of lubricating grease".*

The following table shows the NLGI classification and compares each grade with household products of similar consistency [4].

Table 1. Classification of lubricating greases by consistency

NLGI NUMBER	WORKED PENETRATION AT 25 $^{\circ}$C	APPEREANCE
000	445-475	FLUID
00	400-430	SEMI-FLUID
0	355-385	VERY SOFT
1	310-340	SOFT
2	265-295	NORMAL GREASE
3	220-250	FIRM
4	170-205	VERY FIRM
5	130-160	HARD
6	85-115	VERY HARD

Grease also can be referred to by thickener type such as lithium, aluminium or calcium grease (Figure 1) [5].

They can be classified by base oil types such as synthetic, mineral or biobased (Figure 2) [5].

Some classify grease by its ability to carry loads, whether it's an EP or non EP grease or by its application such as food grade, wheel bearing grease or steel mill grease.
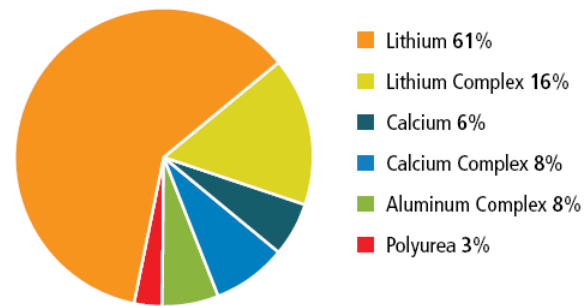
Figure 1. Grease classification according to thickener type
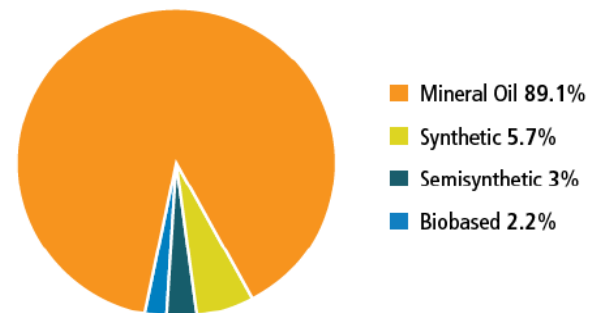
Figure 2. Grease classification according to base oil usage.

3. EXPERIMENTAL PART

The samples for the experimental part were taken directly from the production process, and the samples of lubricating grease are tested in the accredited laboratory in Oil refinery Modrica.

The production program includes grease based on Li soap, as they have multiple applications, greases based on Ca soap, Al complex greases and silica gel greases.

3.1 Lubricatin grease production process

In the domestic refinery we carried out batch production process of lubricating greases in 3 reactors with mixers.

The technological process was carried out in several phases.

<u>First phase-</u>base oil blending

Base oil blending, or the preparation of a base, was carried out in the way that each oil by the pump was transfered in the tank where the oil blending is done. When all oil is transfered, they are mixed with compressed air and recirculation.

<u>Second phase-</u>mixing and heating

Production process start with preparation for the heating system. After that, the base is dosing into the reactor. With the beginning of dosing mixing starts.

<u>Third phase-</u>component dosing

When the base oil has reached a certain temperature, the soap is added. The melt was further heated to a temperature of 110–120 °C. Then, the second part of base is added. By adding the base, temperature in reactor drops for a few degrees. The reactor then was sealed and heating continues to the temperature above 200 °C. After that, the furnace is turned off and the melt if stirred for 10 more minutes. Then, cooling is turned on and the last part of base is added. During the addition of a base, mixing takes place continuously. Grease is left to cool with stirring, then mixers are turned off and grease is left for crystalization.

<u>Fourth phase-</u>additive dosing

After phase of crystalization, it continues with mixing and cooling until certain temperature when additive is added, after which it is necessary to mix for 2-3h in the reactor.

<u>Fifth phase-</u>homogenization.

Homogenization starts by turning on the homogeniser and discharging the batch in the funnel. Lubricating grease passes through the filter to the discharge of the pump and come up with a homogeniser. Tightening the nozzle pressure homogenizer suppression of the homogenizer nozzles should reach a value of 100-300 bar, depending on the type of grease that is homogenized. Homogenized grease leads to funnel where in the circular flow venting of grease is done and over the two-way valve dosed in the packaging in which it is packed. [6]

3.2 Al complex grease production

Al complex grease production is carried out on a specific way, in two phase.

In the reactor, first is added dried base oil BU1, which is heated to a certain temperature. After reaching these conditions, heating is stopped and the soap is added, then it continues with mixing and further heating, then the acid is added and further continues with mixing.

The second phase involves blending base oil BU2 and Al tri isopropoxide. It is necessary to mix well and add to the reactor. After the addition, strengthen the mixing and continue with heating. Saponification reactions starts at temperature of about 100 °C and it ends at temperature of about 140 °C. After reaching this temperature, mixer is turned off, and the sample was taken for visual control to check whether there has been a sublimation acid. In this phase, the sample should be homogeneous, transparent and that there are no particles of acid and no specific odor.

After visual control of the sample, continue with heating and mixing until it reaches temperature below 200 °C. After reaching this temperature it is necessary to re-take a sample for a visual control. It should be homogenous and transparent.

The coling is turning on and the melt is cooled to a temperature below 100 °C, when additives are added, exept the solid additives. By addition of the additives, mixing continues for 1-1,5h, and in the same time the grease is cooling.

When the grease has additionaly cooled, solid additives are added, and the mixing continues for around 1h. Then, the grease is homogenized. [6]

3.3 The APV Manton-Gaulin Homogeniser

APV Manton-Gaulin Homogeniser is basically a high pressure pump with a special homogenising valve assembly fitted to the discharge side of the machine. The machine consists essentially of a floor-standing base assembly which accommodates electric motor,

drive shaft, eccentric shaft, pistons, cylinder block and homogenising valves.

An electric motor drives the triple-plunger pump through a multiple belt drive, the product is being drawn into the cylinder block from the supply line and then expelled at high pressure through the homogenising valves. Here the fluid is deflected by an impact ring at right angles to the flow and forced through a variable restriction which achieves the desired break-up of the fluid particles [7].

3.4 Methods for grease testing

Determination of oil separation from lubricating grease under static conditions DIN 51817:1998

Oil separation is the appearance of a liquid fraction from an otherwise homogeneous lubricating composition. It is the quantity of oil in the initaial sample mass that separates from the lubricating grease under the static conditions and that was accumulated in the oil collecting beaker at the end of the test.

A cylindrical test cell fitted with a conical wire mesh sieve is filled with the sample. After the surface of the sample is levelled off, a weight is placed on the sample. The pressure of the weight adds to the inherent pressure of the sample.

In the standard test, a temperature of 40 °C is maintained and the quantity of separated oil which has passed through the sieve is determined after a test period of 168 hours (7 days).

In the accelerated test, temperature of 40 °C is maintained and the quantity of separated oil which has passed through the sieve is determined after a test perion od 18 hours.

The oil separation is calculated as the ratio of the mass of oil separated from the initial sample mass. [8]

Determination of dropping point of lubricating grease ISO 2176:1995

Dropping point is an indicator of the heat resistance of grease. As grease temperature increases, penetration increases until the grease liquefies and the desired consistency is lost. The dropping point is the temperature at which a grease becomes fluid enough to drip. The dropping point indicates the upper temperature limit at which a grease retains its structure, not the maximum temperature at which a grease may be used.

Determination of dropping point is done by automatic device. The vessel is filled with sample and placed in a tray of cuvette. On the instrument you can set the parameters, the temperature to which it needs to be heated, and heating rate per minute. The sample in the cup is heated and the fall of the first drop on the sensor is read out as dropping point. After that, the device automatically starts with cooling and the result is dropping point. [9]

The cone penetration of lubricating grease is determined at 25°C by releasing the cone assembly from the penetrometer and allowing the cone to drop for 5s, and measuring the extent of the penetration.

Unworked penetrations are determined on test portions transferred with a minimum od disturbance to container suitable for test purposes.

Worked penetrations are determined immediately after working the test portion for 60 double strokes in a standard grease worker.

Prolonged worked penetrations are determined on test portions for more than 60 double strokes. [10]

4. RESULTS AND DISCUSION

Table 2 shows the composition of bases that were used in lubricant greases manufacturing process.

Table 2. Base composition

Component	B1	B2
Napht.	32%	30%
Paraf. (VG 460)	38%	50%
Paraf. (VG 100	30%	-
Hydrocracked	-	20%

Paraffin based base oils are manufactured by known manufacturers by solvent neutral technology and are different by viscosity and VGC.

Hydrocracked base oil is produced in domestic refinery. Napthenic base oil is produced by hydrotreating process in production plant in world renowned company. They differ from paraffinic and have higher VGC values, which in base fluids combinations gives better solubility and thickener dispersion in greases manufacturing [11].

In order to evaluate the base oil solubility abbility you can use different parameters. In order to gain the information on base oil solubility abbility, regarding the components that need to be dissolved in base oil, VGC is calculated (Viscosity-Gravity Constant). VGC is dimensionless constant that is based on mathematicaly calculated values by viscosity and density by method ASTM D 2501.

VGC constant shows the abbility of oil to dissolve other components, by evaluating the viscosity and chemical characteristics of oil, with reference to anilin point vaules and aromatic hydrocarbons content.[12].

Table 3. shows characteristic of base which are used for lubricating grease production.

Table 3. Characteristic of base for grease production

Characteristic	B1	B2
Viscosity at 40 °C, mm^2/s	143,88	148,06
Viscosity at 100 °C, mm^2/s	13,12	14,04
Viscosity index	81	90
Flash point, °C	253	270
Pour point, °C	-14	-13
Total acid number, mgKOH/g	0,006	0,014
Cu corrosion, 3h, 100° C	1a	1a
NOACK, volitality test, %	5,90	4,85
RBOT, Oxidation test, min	70	60
Aniline point	105	114
Refractive index	1,49384	1,49044
Specific gravity, kg/m^3	898,0	891,9
VGC(Viscosity-Gravity Constant)	0,828	0,817
C_A	7,00	5,79
C_P	45,65	45,64
C_N	47,35	48,57

Table 4 and 5 shows test result for Li grease which contains 9% of soap and it is prepared with B1.

Table 4. shows test results for grease at 50, 100 bar i 150 bar.

Table 4. Test results for grease at 50, 100 and 150 bar

CHARACTERISTIC	50 bar	100 bar	150 bar
Unworked penetration, mp, mm/10	291	278	257
Worked penetration, mpw$_{60}$, mm/10	278	260	250
Penetration mpw$_{10}$^{4}, mm/10	266	266	265
δw, %			
Dropping point °c	205	206	205
Oil separation in static conditions, 40°c, 7 dana; %	6,8	5,9	4,38
Oil separation in storage conditions, subjective evaluation, 4 months	-	A bit of separated oil	Higher gloss, possible separation

Table 5. shows test result of greases at pressures of 200 bar, 250 bar i 300 bar.

Table 5. Test result of greases at pressures of 200, 250 and 300 bar

	200 bar	250 bar	300 bar
Unworked penetration, mp, mm/10	257	278	257
Worked penetration, mpw$_{60}$, mm/10	259	260	250
Penetration mpw$_{10}$^{4}, mm/10	257	266	265
δw, %	-		
Dropping point °c	206	206	205
Oil separation in static conditions, 40°c, 7 dana; %	2,28	5,9	4,38
Oil separation in storage conditions, subjective evaluation, 4 months	No gloss	A bit of separated oil	Higher gloss, possible separation

VGC base 1 is higher and it has lower aniline point, which is advantageous for dissolution and dispersion of soap, process is carried out at lower temperature and for shorter time. This base give NLGI 2-3.

From the results showed at Table 4 and 5 can be seen that with increasing homogenization pressure, unworked as well as worked penetration are reduced, ie, harder greases are obtained. Big difference between unworked and worked penetration says that grease is not homogenized enough at 100 bar. It is enough to homogenize harder grease at pressure of 200 bar at our production conditions and with this type of soap.

Homogenization does not affect dropping point, but significantly affects on oil separation in static conditions.

Figure 3 graphically shows the results for unworked and worked penetration, and Figure 4 graphically shows the results for the percentage of oil separation.

Figure 3. Unworked/worked penetration according to pressure
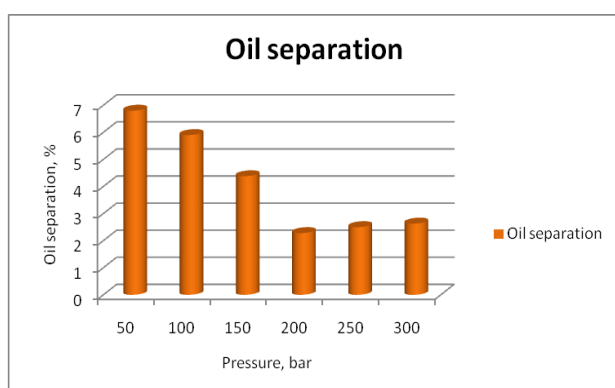
Figure 4. Oil separation according to pressure

Table 6 and 7 shows test result for Li greases prepared with 9 % of soap and with base B2. Table 6 lists the test result for grease at pressure of 50 bar, 100 bar and 150 bar, while Table 7 shows the test results for grease at pressure of 200 bar, 250 bar abd 300 bar.

Table 6. Test result for grease at 50, 100 and 150 bar

	50 bar	100 bar	150 bar
Unworked penetration, mp, mm/10	320	296	293
Worked penetration, mpw_{60}, mm/10	315	298	289
Penetration mpw_{10}^{4}, mm/10	300	307	303
δw, %	-	-	-
Dropping point ^{o}c	189	198	201
Oil separation in static conditions, 40°c, 7 dana; %	10,5	9,89	7.9
Oil separation in storage conditions, subjective evaluation, 4 mon	Oil at surface	A bit of separated oil	

Table 7. Test result for grease at 200, 250 and 300 bar

	200 bar	250 bar	300 bar
Unworked penetration, mp, mm/10	290	282	287
Worked penetration, mpw_{60}, mm/10	287	286	290
Penetration mpw_{10}^{4}, mm/10	305	296	303
δw, %	6,27	3,5	4,48
Dropping point ^{o}c	204	204	204
Oil separation in static conditions, 40°c, 7 dana; %	6,63	4,53	5,76
Oil separation in storage conditions, subjective evaluation, 3-4 months	Higher gloss	No	No

VGC of base is lower, has higher aniline point, which is worse for dissolving and dispersing the soap, so longer time and higher temperature are needed.

From the results showed at Table 6 and 7 can be noted that with increasing homogenization pressure, unworked as well as worked penetration are reduced, ie, harder greases are obtained. It is enough to

homogenize harder grease at pressure of 250 bar at our production conditions and with this type of soap. At pressure of 300 slight degradation of grease happens.

Homogenization does not affect dropping point, but significantly affects on oil separation in static conditions.

Figure 5 graphically shows the results for unworked and worked penetration, and Figure 6 graphically shows the results for the percentage of oil separation.

Figure 5. Unworked/worked penetration according to pressure
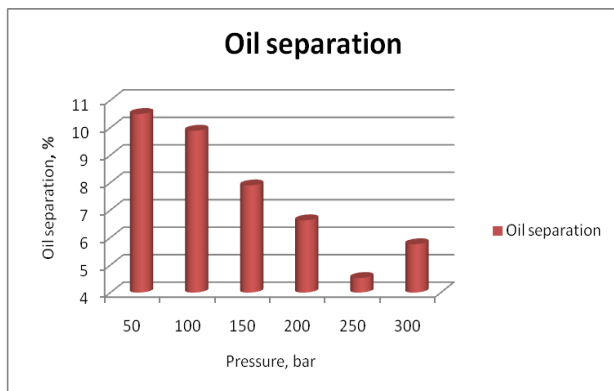
Figure 6. Oil sepation according to pressure

Table 8 and 9 shows the test results for Li grease which contains 8 % of soap and it is prepared with a base B1. Table 8 presents the test results for grease at pressure of 50 and 100 bar, while Table 9 gives the test results for grease at pressure of 200 and 300 bar.

VGC base 1 is higher and it has lower aniline point, which is advantageous for dissolution and dispersion of soap, process is carried out at lower temperature and for shorter time.

Table 8. Test results for grease at pressure of 50 and 100 bar

	50 bar	100 bar
Unworked penetration, mp, mm/10	308	299
Worked penetration, mpw_{60}, mm/10	305	295
Penetration mpw_{10}^{4}, mm/10	290	302
δw, %		
Dropping point ^{o}c	198	200
Oil separation in static conditions, 40°c, 7 dana; %	9,1	6,19
Oil separation in storage conditions, subjective evaluation, 3-4 months	Oil at surface	Higher gloss

Table 9. Test results for grease at pressure of 200 and 300 bar

	200 bar	300 bar
Unworked penetration, mp, mm/10	285	280
Worked penetration, mpw_{60}, mm/10	288	278
Penetration mpw_{10}^{4}, mm/10	292	290
δw, %	1,39	
Dropping point ^{o}c	203	204
Oil separation in static conditions, 40°c, 7 dana; %	4,93	3,57
Oil separation in storage conditions, subjective evaluation, 3-4 months	A bit of gloss	Excellent

In this case, soap from another batch was used. Every change in the formulation requires another production parameters, temperature, dissolution and dispergion speed and different homogenisation conditions. From the results showed at Table 8 and 9 can be seen that with increasing homogenization pressure unworked as well as worked penetration are reduced, ie, harder greases are obtained Homogenization does not affect dropping point, but significantly affects on oil separation in static conditions.

Figure 7 graphically shows the results for unworked and worked penetration, and Figure 8 graphically shows the results for the percentage of oil separation.
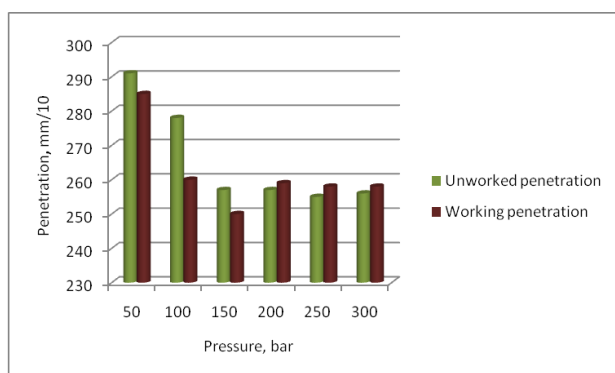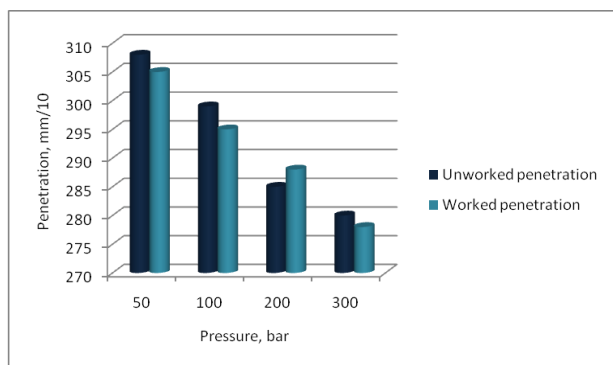
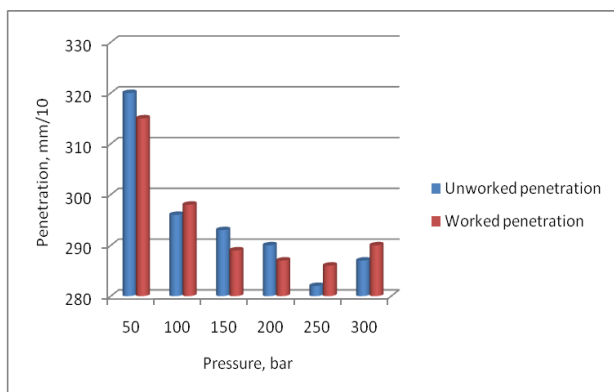**Figure 7.** Unworked/worked penetration according to pressure
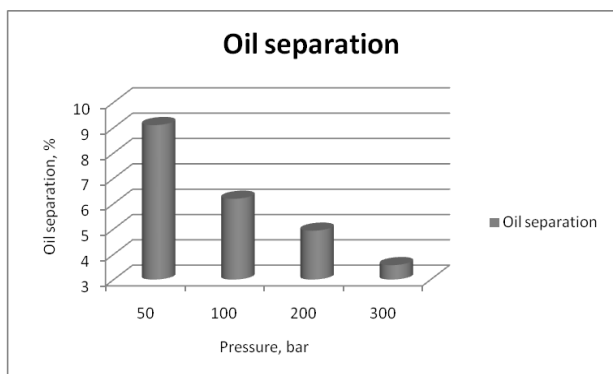
Figure 8. Oil separation according to pressure

Aluminium complex greases

Table 10 and 11 shows the test results for Al complex greases**.** Table 10 presents the test results for grease at pressure of 50 and 100 bar, while Table 11 gives the test results for grease at pressure of 150 and 200 bar.

Table 10. Test results for grease at pressure of 50 bar and 100 bar

	50 bar	100 bar
Unworked penetration, mp, mm/10	438	404
Worked penetration, mpw_{60}, mm/10	Liquid	385
Penetration mpw_{10}^4, mm/10	Not tested, too liquid	381
δw, %		-1,04
Dropping point ^{o}c	Liquid	
Oil separation in static conditions, 40°c, 7 dana; %	Not working	Not working
Oil separation in storage conditions, subjective evaluation, 3-4 months	A little bit	No

Table 11. Test results for grease at pressure of 150 bar and 200 bar

	15MPa (150 bar)	20MPa (200 bar)
Unworked penetration, mp, mm/10	398	382
Worked penetration, mpw_{60}, mm/10	**368**	377
Penetration mpw_{10}^4, mm/10	367	348
δw, %	-0,27	-7,69
Dropping point ^{o}c		
Oil separation in static conditions, 40°c, 7 dana; %		
Oil separation in storage conditions, subjective evaluation, 3-4 months	No	No

Based on results shown in tables 10 and 11, it can be concluded that with Al complex greases high pressures have negative effect. By applying high pressures the grease thickens, structural changes of grease occurs, polymer structure disturbes, chains are being broken, and stickiness decreases that this grease needs to provide. In this case, optimal pressure for homogenisation is 150 bar.

Figure 7. Unworked/worked penetration according to pressure

Figure 9 graphically shows the results for unworked and worked penetration, and Figure 8 graphically shows the results for δw

5. CONCLUSION

Based on the results that are displayed graphically and in tabular form, following conclusions may be adopted:

1. Lubricating greases represent very important group of lubricants that have wide application;
2. Lubricating greases manufacturing process is very complex and parameters need to be defined carefuly in order to get product with desired characteristics;
3. In this paper samples of Li lubricating greases and Al complex greases that were formulated with two different bases are analysed;
4. VGC is very important characteristic of base oil and its knowing can contribute to better selection of oil that is going to be used for lubricating grease manufacturing process;
5. Base oils that have higher VGC are better for lubricating grease manufacturing because better soap dissolution and dispersion conditions are achieved, and lower temperatures and shorter time is needed for process;
6. Base oils that have lower VGC are unfavorable for lubricating grease manufacturing because worse soap dissolution and dispersion conditions are achieved, and higher temperatures and longer time is needed for process;
7. Samples of lubricating greases are analysed at pressures of 50-300 bar;
8. Homogenisation has greatest effect on worked and unworked penetration of lubricating greases and also on percentage of separated oil in static conditions;
9. Lubricating greas that was formulated with B1 that has higher VGC, is enough to homogenise at pressure of 200 bar in order to get grease with satisfactory characteristics;
10. With homogenisation pressure rise the grease becomes harder;
11. With homogenisation pressure rise the percentage of separated oil is lowered;
12. Lubricating grease that was formulated with B2 that has lower VGC constant needed to be homogenised at higher pressures in order to obtain the grease with satisfactory characteristics. Optimal pressure in this case is 250 bar;
13. It is worth noting that every shipment of any feedstock can require another set of working parameters;
14. With Al complex greases lower pressures are needed because high pressure leads to grease destruction. Greases with worse characteristics are obtained and it cannot satisfy application demands;

REFERENCES

[1] G. Fish: Tribology, Lubrication and Technology: Additives for lubricating grease, Vol. 71, No 12, pp 18-19, 2015.
[2] Sustainability in the Grease Industry-Parameters Production Product, available at: www.fuchs.com, accessed:
[3] Emerging Trends in the Industrial Grease Market, available at: www.businesschemistry.org/article, accessed: October 2014
[4] National lubricating grease institute, available at: www.wikipedia.org/NLGI, accessed:
[5] B. Kamchev: Lubes and Greases EMEA: Grease Production Stays Flat, No 90, pp 10-15, 2016.
[6] Internal Documentation
[7] Internal Documentation of Equipment Manufacturer
[8] DIN 51817, *Determination of Oil Separation from lubricating grease under static conditions,* 1998
[9] ISO 2176, *Determination of dropping point of lubricating grease,* 1995.
[10] ISO 2137, *Determination of cone penetration of lubricating greases*, 2007.
[11] ASTM D 2501, *Standard test method for calculation of Viscosity-Gravity Constant (VGC) of Petroleum Oils.*
[12] H.Backstrom, Naphtenic Magazine Special issue on grease: Naphtenic Oils advanatgeous in grease making, 2006

MOLECULAR MECHANISMS IN BOUNDARY LUBRICATION

Jelena MANOJLOVIC[1]

1The Faculty of Mechanical Engineering, University of Niš, Niš, Srbija
*Corresponding author: jmanojlo@gmail.com

Abstract: *When the distance between surfaces is very small and lubrication is performed with a thin film of several to tens of nanometers in thickness, we usually talk about thin film lubrication (TFL), or extended boundary lubrication. In boundary lubrication molecules are absorbed on two solid surfaces, usually to avoid dry contact between them. Molecules form adsorbed layers on surfaces by various procedures. The adsorption of molecules from a surfactant solution on the solid surface is determined by electrostatic and hydrophobic interaction (physical adsorption). In some cases covalent or chemical bonds can be formed between surfactant molecules and the surface, which is usually called chemisorption. If the result of adsorption is a very well-ordered layer, the process of the surface self-assembly is defined. The kinetics of surfactants adsorption depends on many parameters such as the surfactant type, concentration, temperature of the solution and solvent. However, the results of the proces of self-assembly are influenced by the nature of a surface and its properties, such as surface charge and ion-exchange capacity. This paper deals with quaternary amonium surfactants and the procedure of their adsorption on muscovite mica.*

Keywords: boundary lubrication, chemisorption, self-assemble, ion-exchange

1. INTRODUCTION

Friction is an omnipresent byproduct of the shearing interface. When we measure friction we usually obtain a number, the coefficient of friction, described as the ratio of the friction force to the applied load. There are numerous surface parameters that affect friction [1]. This simple definition of friction neglects dynamic effects. In fact, friction is a non-equilibrium process and the coefficient of friction hence depends on dynamic parameters such as sliding velocity, temperature, load, molecular degrees of freedom and the architecture and orientation of surface molecules [2].

The basic principles of friction have been described very well in an empirical way, but the molecular mechanisms underlying friction are still not understood [3, 4, 5, 6]. Even when the atomic structure of the two surfaces is known, the details of friction energy dissipation cannot be predicted. Only in the last decades, after the development of new experimental probes [7], scientists have been able to study the origins of friction on the atomic scale. These studies are challenging, because the forces that must be measured at these dimensions are very small.

The atomic processes at the interface of two materials are very complex and thus it is important to better understand adhesion, friction, wear and lubrication [3, 5, 6] at the molecular level. Where the solid surfaces are very close together the contact between asperities on them is possible, and lubrication by a thin film liquid under such conditions is

usually very complex. The bulk properties of the liquid under this regime play little or no part in the friction and wear behavior [8]. Such a thin film of lubricant under confined conditions, between two solid surfaces at a very small distance, behaves much more differently than in the bulk state [9].

Researchers have tried to reduce friction in mechanical systems by improving the chemical composition of the lubricants between two moving parts. The forces between two surfaces with a liquid medium between them can be attractive, repulsive, or a complex function of the separation [1]. A number of investigations have shown that the force depends on the structure of the liquid molecules and the structure of the confining surfaces [1, 3, 5]. For example, the surfaces may induce solidification of the liquid if the thickness of the gap is only a few molecules in diameter.

Another possibility to protect surfaces and avoid dry contact between them is to coat surfaces by molecules with special properties. Boundary lubricants form an adsorbed molecular film on the surfaces and dry contact is excluded from boundary lubrication [11]. Most lubricants are oils. They are normally mixed with additives in order to modify the viscosity. There are different types of oil soluble boundary lubricant additives, however, oils are not desired here and the goal is to use a model system, self-assembled monolayers (SAMs) [12].

SAMs are a good model for boundary lubrication. They are molecular units that are spontaneously formed upon certain substrates (such as Au, mica) when immersed in an organic solvent. This way they change the properties of the surface. They have three parts: headgroup, chain and endgroup. The stability of the assembled system depends on van der Waals forces. SAMs can reduce friction and this has been proven in the literature [13]. Many self-assembled systems have been investigated, but probably the most studied are alkanthiolates on gold [14]. In particular, we are interested in monolayers and bilayers deposited onto mica. In these boundary layers,

the molecules have a defined orientation and are self-ordered into layers. The plan here was to evaluate quaternary ammonium surfactants, with the aim of producing well-characterized SAMs on mica.

2. EXPERIMENTAL PART

The experiments included making self-assembled monolayers of quaternary ammonium surfactants on mica. Single-tailed hexadecyltrimethylammonium bromide, CTAB, with the molecular structure $CH_3(CH_2)_{15}N^+(CH_3)_3Br^-$, was purchased from Fluka. As solvent, ultra pure water with the resistivity of $18.3M\Omega cm$ was prepared using a Barnstead EASYpure™ batch-fed water purification system. The same water quality was also applied for the sample rinsing, before drying with a clean nitrogen stream.

The bottles used in the experiments were cleaned by piranha solution and then rinsed with purified water to avoid any organic contamination. Piranha solution, a 7:3 mixture of sulfuric acid and 30% hydrogen peroxide, was used to remove the organic contamination. *Attention: piranha solution reacts violently with all organics and should be handled with care!* All the employed tools were previously cleaned in order to minimize the occurrence of molecular contamination, particularly on the high energy mica surface.

Muscovite mica purchased from Spruce Pine Mica Company Inc. (USA) was used for the adsorption experiments. Small mica samples of $1-1.5cm^2$ in size were cut by scissors. Then, they were freshly cleaved on both sides before immersion into the surfactant solution. The adsorption was performed from the surfactant solution in the volume of 20ml.

Every experiment consists of a few steps - adsorption, rinsing, drying and analysis (CA - contact angle measurements). In the experimental procedure it is possible to change many parameters, such as the surfactant solution concentration, adsorption time, rinsing time, experimental temperature, solution temperature and many others. All of

these possibilities will not be discussed here. The immersion and extraction of a mica sample into and out of the surfactant solution was defined as an adsorption protocol that was named "CTAB in/CTAB out", as shown in figure 1.
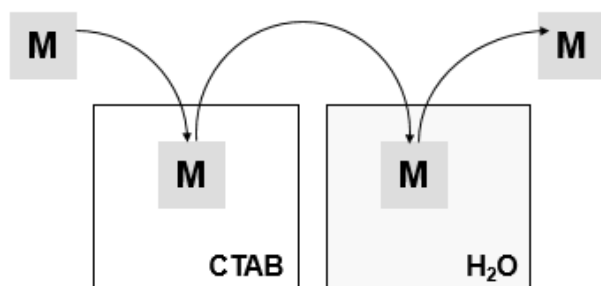
Figure 1. Adsorption protocol "CTAB in, CTAB out" experiment

This option involved the immersion (30sec) of the mica sample (M) and the extraction from the surfactant solution at the nominal concentration. In the rinsing step, the mica samples were dipped into 20ml of ultra pure water for 10sec to remove the excess solution and excess surfactant molecules.

In the series of adsorption experiments without temperature control, a 1000ml stock solution of 10^{-2}M (~10cmc) CTAB was prepared at room temperature. Since the solubility of CTAB in water was low at room temperature, the solution was heated to 30-35°C. By dilution of this solution, prepared by adding the appropriate volume of ultrapure water, we prepared surfactant solution concentrations ranging from 10^{-3}M (~cmc) to 10^{-6}M (~cmc/1000). The adsorption experiment shown in figure 1 was repeated at uncontrolled temperature and at controlled laboratory temperature, at 18°C and 30°C, at various concentrations.

3. RESULTS AND DISSCUSSION

Using the above preparation protocol, a significant number (several tens) of samples were prepared. Contact angle measurements were conducted on two representative samples obtained by the CTAB in/CTAB out protocol at a concentration below the cmc (10^{-4}M).

The contact angle (CA) is a quantitative measure of the thermodynamic surface energy balance between a solid, a liquid and a gas phase. Geometrically, CA is defined as the angle formed at the three-phase boundary, where the liquid, the gas and the solid meet.

The advancing and receding water contact angles measured under uncontrolled laboratory conditions (primarily temperature) were 85°/30° and 82°/22°, respectively. When the experimental temperature was controlled, the contact angle measurements detected on the samples were 85°/25° (at 18°C) and 85°/15° (at 30°C). Measurements were performed in several spots on the sample covered by the surfactant. The obtained results showed hydrophobic surface properties, but the AFM measurements [15] demonstrated very inhomogeneous surfactant layers.

The temperature dependence of the observed film morphology at 18°C and 30°C is summarized in the table below. Due to the variations determined in the different samples spots, both the results for water (advancing/receding) and hexadecane are given with errors.

Table 1. Contact angle results

	hexadecane	water
CTAB in/CTAB out(18°C)	27±2°	85°/35°
CTAB in/CTABout (30°C)	17±2°	85°/15°

Contact angle measurements indicate good wetting by very low (<30°) contact angles (e.g. water on hydrophilic surfaces), neutrality at a contact angle near 60°-90° and non-wetting is observed by a contact angle greater than 90° (determined on hydrophobic surfaces). For example, freshly cleaved mica has the contact angle of less than 10° and the contact angle on the SAM produced by CTAB adsorption on mica can be 140° [16]. The measurement of the dynamic contact angle gives not only practical information on wetting but also valid indications for chemical composition and stability of molecules at the surface.

In both groups of experiments, hydrophobic surfaces with advancing contact angles between 75° and 90° were obtained. The significant hysteresis suggests a chemical heterogeneity or roughness in the surfactant film [17]. Measurements of hexadecane contact angle represent one of the most sensitive tools to determine the conformational order of hydrocarbon thin films. High hexadecane contact angles are observed on hydrocarbon SAMs only when the monolayers are densely packed. Using hexadecane, we observed lower values than the expected 40° for ideally ordered films.

The aim was to produce homogeneous monolayers of surfactants on muscovite mica by the chosen quaternary ammonium surfactants. These substrates and surfactants are basically used to perform the SFA experiments (muscovite mica is an important part of this technique). Another reason to apply mica is to use the ion-exchange capabilities of the negatively charged mica substrate and positively charged head groups of the quaternary ammonium surfactants (primary cetyltrimethylammonium bromide-CTAB). The most favourable route to modify the mica surface is to exchange inorganic surface cations by organic ions, producing the hydrophobic monolayers of organic molecules ionically bound to the substrate (figure 2). Therefore, mica is of practical interest as an ion exchanger. The potassium ions K^+ on mica participate in this ion exchange [18,19].
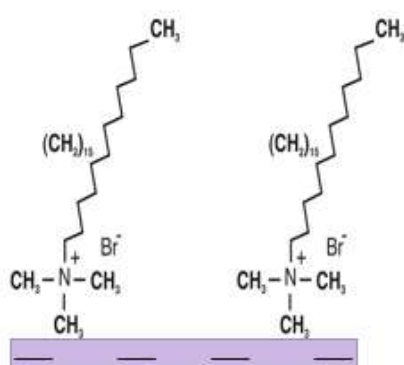
Figure 2. Surfactant CTAB adsorption on muscovite mica

According to some earlier studies described in the literature, one can produce well-ordered monolayers or bilayers on mica. However, numerous experiments that we have conducted [12], have pointed that it is difficult to create homogeneous hydrophobic monolayers on mica.

The adsorption mechanisms of the surfactant molecules at the solid-liquid interface play an important role in the preparation of CTAB films on mica substrates. Self-assembled monolayers (SAMs) can be prepared using different methods already proposed in the literature. Several new protocoles have been established and described [12,15].

When freshly cleaved mica is immersed into water, potassium ions will dissolve in water [20] being exchanged by hydrated protons [21]. In any aqueous surfactant solution the ion exchange on the mica surface will involve all species of solvated ions, including H_3O^+ ions, depending on pH. Hydronium ions will compete with any cationic surfactant to occupy the surface-charge sites.

The cation exchange capacity (CEC) is important in order to completely cover the mica surface by an organic monolayer. The CEC of mica is a measure for its negative charge and it is defined as the sum of all exchangeable cations at a certain pH value [22]. For an accurate determination of the exact amount of surfactant ions adsorbed onto the surface, it is essential to have a well-defined substrate surface. Mica surface is thus ideal for adsorption studies [12].

Another fundamental property of surfactant solutions with the influence on the solution structure and adsorption process is the capacity of surfactants to aggregate and form micelles. The aggregation process can be discussed in terms of the cmc and the aggregation number.

The critical micelle concentration (cmc) is defined as the surfactant concentration at which many measurable solution properties abruptly change, indicating monomer aggregation and micelle formation. Many solution properties, such as surface tension, conductivity, turbidity etc. markedly change at the cmc [12]. At low concentrations the

surfactant solution consists of dispersed monomers. When the cmc is reached, the surfactant molecules will start organizing into micelles. The shape of a micelle (figure 3) is the result of the subtle energy balance between the different terms originating in the amphiphilic nature of the surfactant.
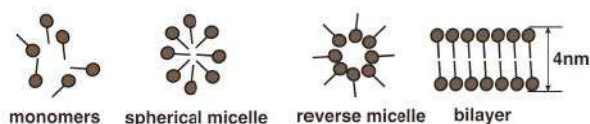

Figure 3. Monomers and different micelle shapes

The structure and the stability of the produced monolayer on mica can be verified by many techniques (reference), such as contact angle measurements in our experiments. We have found that temperature control can have a strong influence for CTAB solution properties below and above the critical micelle concentration (cmc) and in adsorption processes - to obtain reproducible films. In the process of solution heating and cooling, very much dependent on the Krafft temperature [24], significant changes in the surfactant solution structure can be detected. One can expect that these changes, as a function of the experimental conditions, have dramatically influenced the adsorption process. Therefore, the various SAM morphologies found in our adsorption experiments can be explained. It has been shown that the factors such as the temperature during solution preparation, frequently neglected, can have crucial influence on the surfactant solution struction and the adsorption mechanism on substrate. The variety of the CA results indicates very complex molecular mechanisms in the process of surfactant self-assembling and require the application of additional techniques in order to clarify the mechanisms that are happening on the nanoscale.

4. CONCLUSIONS

SAMs are good models for boundary lubricants because of their strong adhesion to the substrate and significant reduction of the friction between the two moving surfaces. Numerous surfactants can have configurations providing low-friction sliding under particular conditions, such as specific values of sliding velocity. Reduction of the friction force between hydrocarbon surfactants has been observed and detailed studies about these topics are included in the scientific research. The lubrication between two surfaces can be performed with very thin lubrication films, and it has been found that the static and dynamic properties of such films exhibit dramatic changes when the film thickness is of molecular dimensions. The experimental results in the investigation of SAMs on muscovite mica have shown a very complex behaviour, first of the surfactant solution and then of the molecular mechanisms of adsorption CTAB on mica, due to the fact that many experimental parameters are involved (temperature, solution pH, humidity, ion-exchange capacity of muscovite mica etc.).

REFERENCES

[1] M.M. Koura, M.A. Omar: The effect of surface parameters on friction, Wear, Vol.73, No. 2, pp. 235-246, 1981.

[2] M. Amiri, M.M. Khonsari: On the Thermodynamics of Friction and Wear-A Review, Entropy, Vol.12, pp. 1021-1049, 2010.

[3] B. Bhushan, J. Israelachvili, U. Landman: Nanotribology: friction, wear and lubrication at the atomic scale - Review article, Nature, Vol. 374, pp. 607-616, 1994.

[4] J.C.Fröberg, O.J. Rojas, P.M. Claesson: Surface forces and measuring techniques, International Journal of Mineral Processing, Vol. 56, pp. 1-30, 1999.

[5] E. Kumacheva: Interfacial friction measurement in surface force apparatus,

Review, Progress in Surface Science, Vol. 58, No. 2, pp. 75-120, 1998.

[6] N.J. Israelachvili: *Intermolecular and surface forces*, Academic press London, London, 1991.

[7] N. K. Myshkin: Devices for Tribotests at Micro/Nano Scale, Tribology in industry, Vol. 26, No. 3-4, pp. 15-20, 2004.

[8] W.E. Campbell: *Boundary Lubrication, an Appraisal of World Literature*, ASME, Houston, 1969.

[9] M. H. Müser: Lubricants under high local pressure: liquids act like solids, Mat.-wiss. u. Werkstofftech, Vol. 35, No. 10-11, pp. 603-609, 2004.

[10] B. Bhushan: *Modern tribology handbook*, films CRC Press , 2000.

[11] S.C. Bae, J.S. Wong, M. Kim, S. Jiang, L.Hong, S. Granick, S. Granick: Using light to study boundary lubrication: spectroscopic study of confined fluids, Phil. Trans. R. Soc. A, Vol. 366, No. 1869, pp. 1443–1454, 2008.

[12] J. Manojlovic: *Structure, Morphology and History Effects in Surfactant Self-assembly*, PhD. thesis, ETH Zurich, Switzerland, 2006.

[13] J. Manojlović: Dynamics of boundary lubrication, Tribology in Industry, Vol. 35, No. 3 pp. 200 207, 2013.

[14] A. Ulman: Formation and structure of self-assembled monolayers, Chem. Rev. Vol. 96, No. 4, pp. 1533-1554, 1996.

[15] J. Manojlovic: Preparation and characterization of quaternary ammonium surfactants in muscovite mica, in: *13th International Conference on Tribology–Serbiatrib'13*, 15-17.05.2013. Kragujevac, Serbia, pp. 177-183.

[16] B.G. Sharma, S. Basu, M.M. Sharma: Characterization of adsorbed ionic surfactants on a mica substrate, Langmuir, Vol. 12, No.26, pp. 6506-6512, 1996.

[17] Y.L. Chen, C.A. Helm, J.N. Israelachvili: Molecular Mechanisms Associated with Adhesion and Contact-Angle Hysteresis of Monolayer Surfaces, Journal of Physical Chemistry, Vol. 95, No. 26, pp. 10736-10747, 1991.

[18] J.F.Liu, W.A. Ducker: Surface-induced phase behavior of alkyltrimethylammonium bromide surfactants adsorbed to mica, silica, and graphite, Journal of Physical Chemistry B, Vol. 103, No. 40,pp. 8558-8567, 1999.

[19] S. Nishimura, et al.: Molecular-Scale Structure of the Cation Modified Muscovite Mica Basal-Plane, Langmuir, Vol. 10, No**.** 12, pp. 4554-4559, 1994.

[20] H. Terashima: A direct measurement of the ion-exchange capacity of muscovite mica using a Mettler ultramicrobalance, Journal of Colloid and Interface Science, Vol. 245, No. 1, pp. 81- 85, 2002.

[21] G.A. Carson, S. Granick: Self-Assembly of Octadecyltrichlorosilane Monolayers on Mica, Journal of Materials Research, Vol. 5, No. 8, pp. 1745-1751, 1990.

[22] M.A. Osman, U.W. Suter: Determination of the cation exchange capacity of muscovite mica, Journal of Colloid and Interface Science, Vol. 224, No. 1, pp. 112-115, 2000.

[23] Hiemenz, P.C., Rajagopalan R: *Principles of colloids and surface chemistry*, CRC Press, Dekker, 1997.

[24] J. Manojlovic: The Krafft Temperature of Surfactant Solutions, Thermal Science, Vol. 16, No. 2, pp. S631-S640, 2012.

EVALUATING LUBRICATION CAPABILITY OF SOYBEAN OIL WITH NANO CARBON ADDITIVE

George Catalin CRISTEA[1], Cosmin DIMA[1], Constantin GEORGESCU[1]
Dumitru DIMA[1], Liviu SOLEA[1], Lorena DELEANU[1,*]
[1]"Dunarea de Jos" University of Galati, Galati, Romania
*Corresponding author: lorena.deleanu@ugal.ro

Abstract: *This paper presents the influence of adding carbon black nanopowder (average size 13 nm, PlasmaChem) in soybean oil in different massic concentration (0.25%, 0.50% and 1%) on several tribological parameters: friction coefficient, wear scar diameter and wear rate. Tests are done on a four-ball machine. The test parameters were load: 100 N, 200 N and 300 N and the speed 1000 rpm, 1400 rpm, 1800 rpm.*
The test balls are lime polished, made of chrome alloyed steel, having 12.7±0.0005 mm in diameter, with 64-66 HRC hardness. The sample oil volume required for each test was 8 ml ±1 ml.
This type of anti-wear additive, because the particle distribution is not evenly in contact during the running and could not help improving the tribological behavior, as it does not reduced the friction coefficient and wear scar diameter as compared to the neat soybean oil. The authors think that the additive should be bonded (physically or chemically) for having better results.

Keywords: *soybean oil, four ball test, nano black carbon, wear scar diameter*

1. INTRODUCTION

Soybean oil could become a source for the base oil in fields of activities that require non-polluting processes and materials [1, 2, 3, 4]. As other vegetable oils, this one, too, has low viscosity [5] and research has been done for additivating this oil in order to increase its viscosity or/and to protect the rubbing surfaces by specialized additive (especially anti-wear and extreme pressure additives) [6]. But vegetable oil-based lubricants have several disadvantages as compared to mineral and synthetic ones, including low viscosity that not encourage the generation of a continuous film when the tribosystem runs, consequently, implying a mixt or boundary lubrication. This is why the additivation of such vegetable oils is

of great interests for researchers, producers and users [2].

Recent reviews of the mechanisms of friction reduction and anti-wear of nanoparticles in lubricants were published, pointing out lubrication mechanisms as rolling effect, protective film, mending effect and polishing effect [7, 8]. Shahnazar et al. [9] presented a classification of nano additives in lubricants. Those based on carbon were included in four main allotropic classes: zero-dimensional (fullerene), one-dimensional (nanotubes, nanowires, nanorodes), two-dimensional (graphene), three-dimensional (graphite, nano-sized diamonds)[10, 11].

Hwang [12] concluded that lubricants with nano additives improve the tribological behavior as compared to microaddition of the

same base oils. The nanoparticles play the role of nano ball bearings. He used several carbon-based additives tested on a disk-on-disk tribotester. For black carbon, the size was 54 nm.

Hu et al. [13] investigated the efficacy of the carbon black as an engine soot substitute and concluded that WSD increased with the content of black carbon in the range of 0...8% for a certain grade of engine oil, but for the other, the same parameter has lower values as those for the neat oil. Tested time was 0.5 h. Also, friction coefficient depends on the base oil and carbon concentration.

Many research reports used a pin-on-disk tribometer for evaluating the anti-wear additives [14], bur also, the four ball tribotester is favorable to compare experimental results [15].

This paper aims to report the influence of nano black carbon as additive in soybean oil on the tribological behavior of the formulated lubricants by the parameters friction coefficient and wear scar diameter.

2. TESTING METHODOLOGY AND MATERIALS

The lubricants formulated with soybean oil additivated and nano black carbon in different concentrations (0.25%wt, 0.50 %wt and 1% wt) were tested on a four ball machine. Table 1 presents the typical composition of this oil.

The nano black carbon was supplied by PlasmaChem and has the following characteristics [16]: average particle size: ~13 nm, specific surface: ~550 m²/g, ash content: < 0.02%, bulk density: ~120 g/L.

The degumming and refining process of soybean oil is done at Prutul SA Galati and prevents oil to form gum deposit and to ferment [17].

The test balls are lime polished, made of chrome alloyed steel (Table 2), having 12.7±0.0005 mm in diameter, with 64-66 HRC hardness. The sample oil volume for each test was 8 ml ±1 ml. The test method for investigating the lubricating capacity is given in [18].

Table 1. Typical fat acid composition for the tested soybean oil

Acid	Symbol	Concentration, %wt
Myristic acid	C14:0	0.11
Palmitic acid	C16:0	12.7
Palmitoleic acid	C16:1	0.13
Heptadecanoic acid	C17:0	0.05
Stearic acid	C18:0	5.40
Oleic acid	C18:1	21.60
Linoleic acid	C18:2	52.40
Linolenic acid	C18:3	5.70
Arachidic acid	C20:0	0.25
Gondoic acid	C20:1	0.20
Eicosadienoic acid	C20:2	0.50

Table 2. Chemical composition of the steel the balls are made of (wt%)

Element	C	Cr	Mn	Si	S	P
Steel grade EN31	1.0	1.3	0.5	0.35	0.05	0.05

The test parameters were: speed (1000 rpm, 1400 rpm and 1800 rpm corresponding to the following sliding speeds 0.383 m/s, 0.537 m/s and 0.691 m/s, respectively), normal force (100 N, 200 N and 300 N), testing time 1 hour.

The formulated lubricants were obtained in a small quantity of 200 ml each. The steps followed in this laboratory method were:

- weighting the additive and the dispersing agent with an accuracy of 0.1 mg,

- mechanical mixing of addtive and equal mass of guaiacol (supplied by Fluka Chemica), chemical formula being $C_6H_4(OH)OCH)_3$ (2-methoxyphenol), for 20 minutes; this dispersing agent is compatible with both additive and vegetable oils,

- adding gradually the soybean oil, measured for getting 200 g of lubricant with the desired concentrations of additive,

- stirring with a magnetic homogenizing device for 1 hour,

- sonication + cooling of 200 g lubricant for 5 minutes with the help of sonicator Bandelin HD 3200 (Electronic GmbH & KG Berlin); the lubricants is heating at approximately 70 °C; the cooling time was 1 hour; this step sonication + cooling is repeated 5 times for obtaining a total sonication time of 60

minutes. The parameters of sonicating regime are: power 100 W, frequency 20 kHz ±500 Hz, continuous regime.
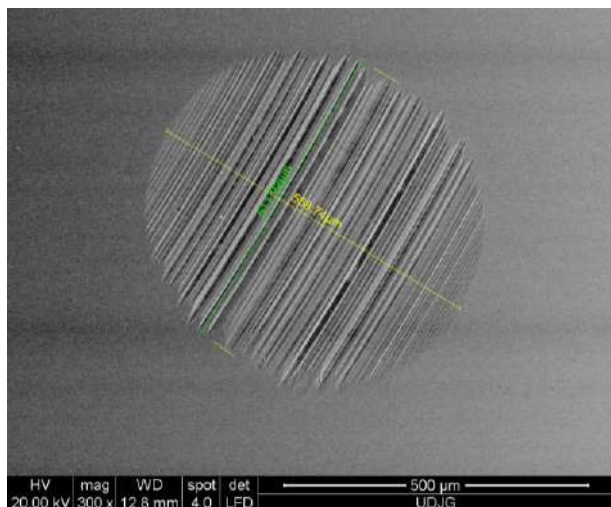
Figure 1. Exemple of WSD measurement. Test conditions: 1000 rpm, F=200 N, time 1 h, lubricant: soybean oil +1% nano black carbon, ball 1

3. RESULTS

SEM investigations reveal that the black carbon is on the rubbing surfaces as nano agglomerations, unevenly distributed on the surface texture.

The particles or their agglomerations seem to be rolled and it is very probable that they act like nano rolling elements, this explaining the low values of friction coefficient during the test (Fig. 1).

The problem is that, as one may notice, the particles are not evenly distributed on the contact surfaces, producing preferential wear on the zone without particles. As the particles migrate in running, these zones prone to direct contact are changing, this could be the explanation for the variation of the friction coefficient in time and with high amplitudes (Fig. 2).

The plots of the friction coefficient in Figures 3-5 is done using a moving average of 200 values, the record sample being 2 values per second.

The discussion upon the evolution of friction coefficient in time is based on comments done by Czikos [19].
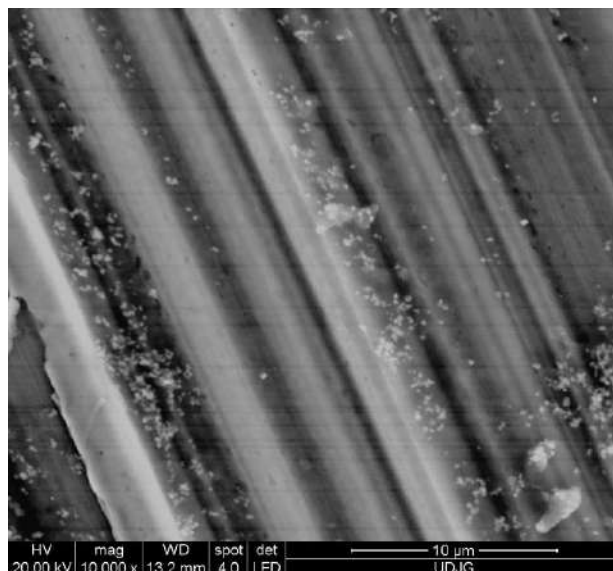
Figure 2. Particles of nano black carbon. Test conditions: 1000 rpm, F=200 N, time 1 h, lubricant: soybean oil +1% nano black carbon
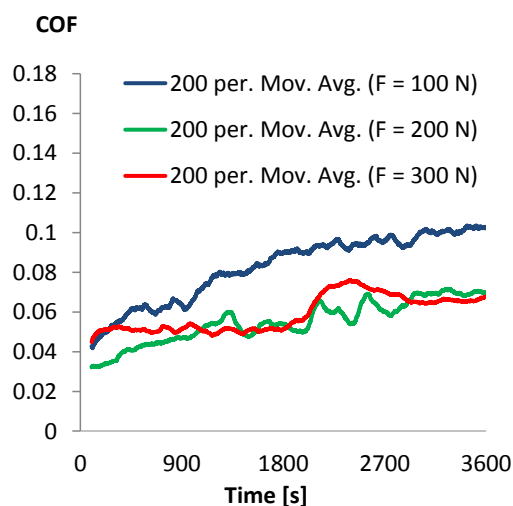
a) 1000 rpm
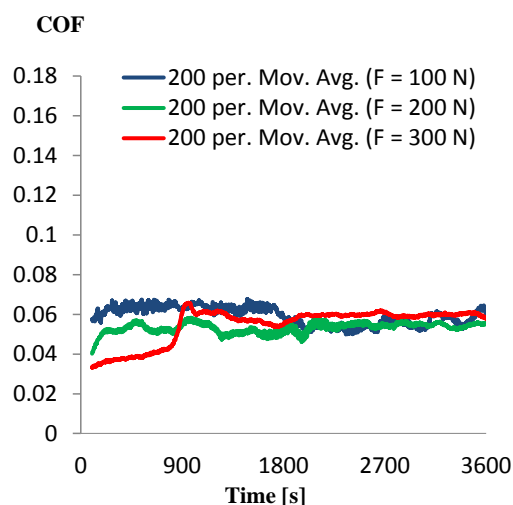
b) 1800 rpm

Figure 3. Evolution of friction coefficient in time for soybean oil (non-additivated)

Thus, the friction coefficient measured for soybean oil has a tendency to gradually increase in time for low speed and to remain in a narrow range, at almost the same value for the higher speed (Fig. 3). For the additivated lubricants, the tendency is to decrease the friction coefficient after a running period of 10...15 minutes.

Analysing Fig. 5, one may notice that, at a concentration of 1.0% of nano black carbon, the friction coefficient becomes lower for higher load (F=300 N) and high speed (v=1800 rpm). Also, this regime gives the less influence on the WSD (Fig. 6). Under the lowest tested load (F=100 N) the range of COF oscillations are the greatest.

a) 1000 rpm

c) 1800 rpm
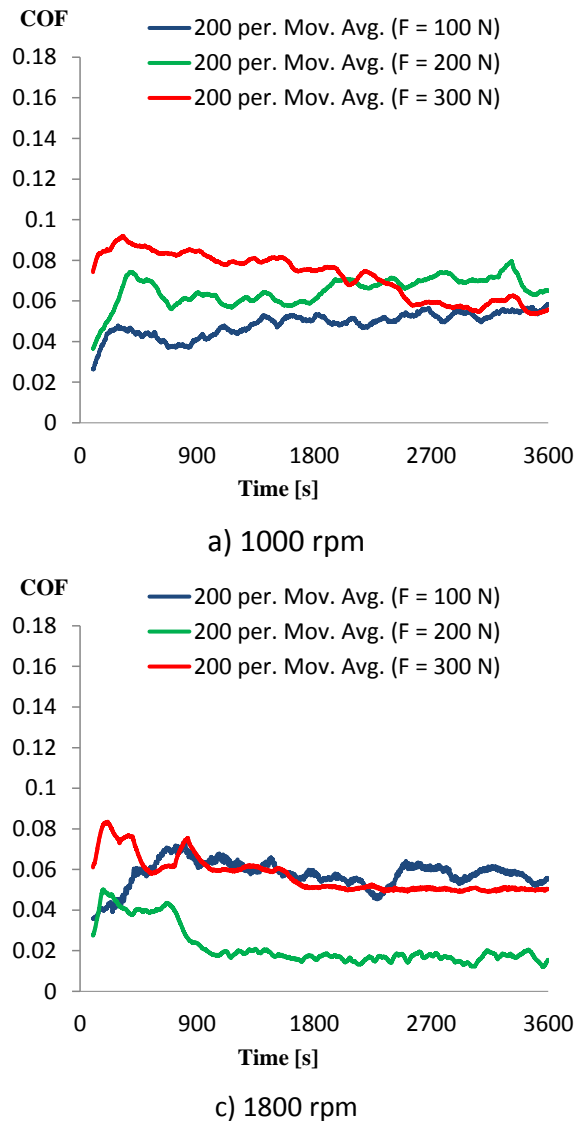
Figure 4. Evolution of friction coefficient in time for soybean oil +0.5% nano black carbon

All maps were plotted using a cubic interpolation and the surfaces are "obliged" to include the experimental data. A point on a wear map represents a test for the same set of parameters (F [N], v [rpm], C [%]), where F is the normal load on the four ball tester, v is the rotational speed (1000 rp,. 1400 rpm and 1800 rpm) and C is the massic concentration of the black carbon (0, 0.25%, 0.5%, 1.0%).

a) 1000 rpm

c) 1800 rpm
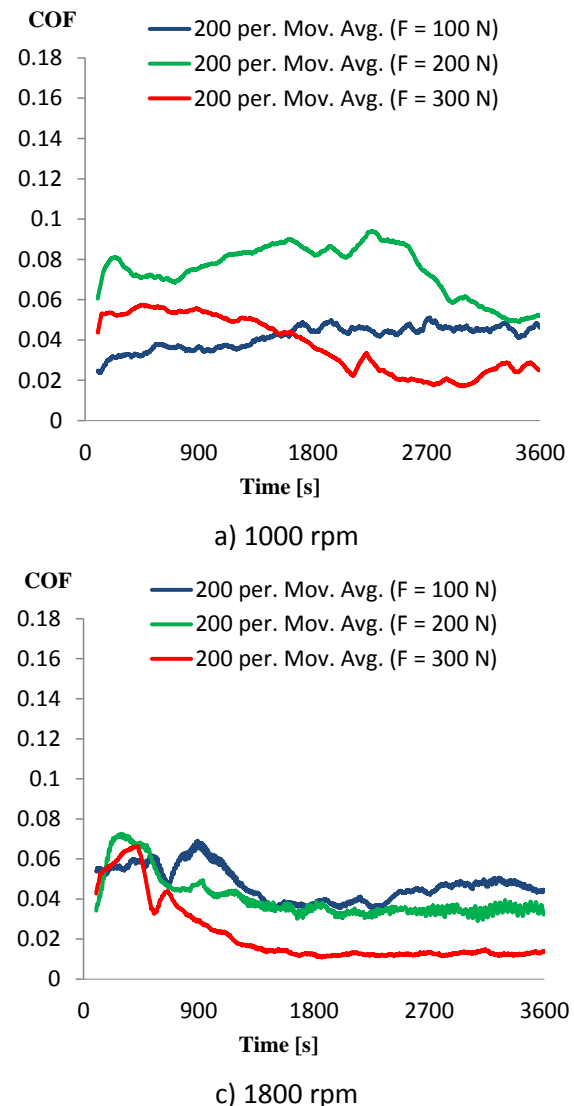
Figure 5. Evolution of friction coefficient in time for soybean oil +1% nano black carbon

In Fig. 6, the friction coefficient (COF) is the average value obtained during a test of one hour. COF is slightly reduced for the additivated lubricants and this tendency is more visible for the higher speed (1800 rpm).

Taking into account the map shape for 1400 rpm, it seems there are some changes in the regime, especially for the neat oil. The increase of load and speed makes the friction coefficient to increase for the soybean oil.

1000 rpm

1400 rpm

1800 rpm
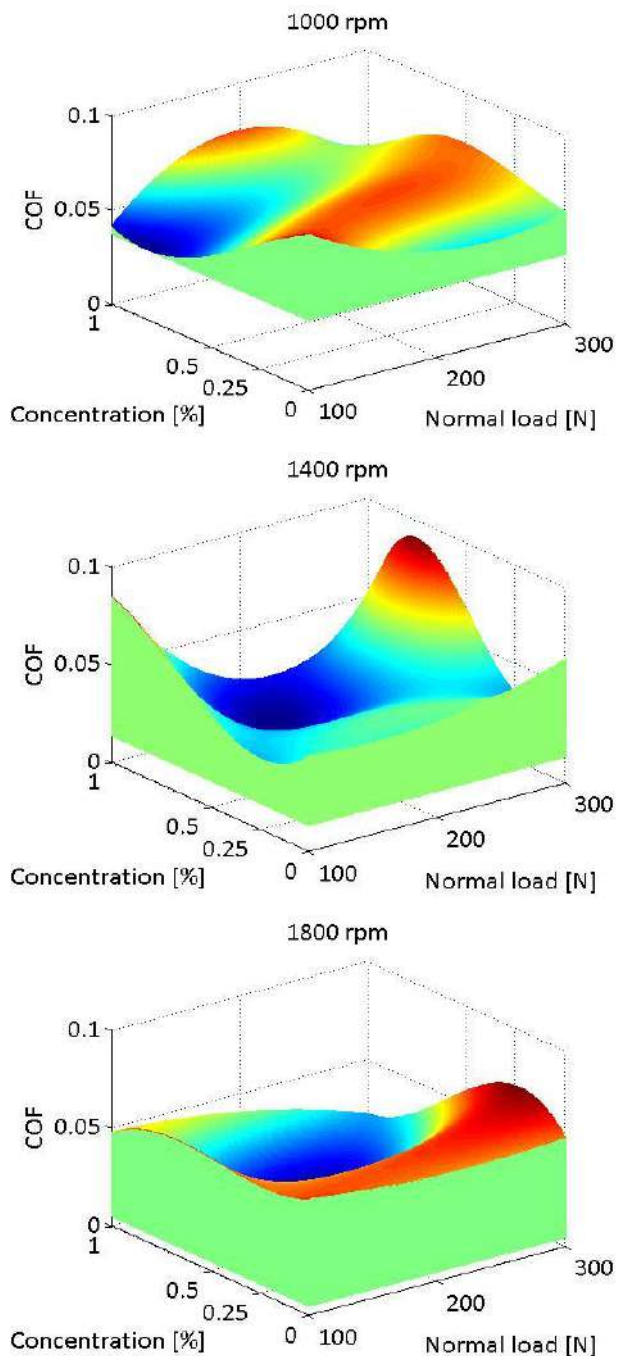
Figure 6. COF as a function of additive concentration and test conditions

1000 rpm

1400 rpm

1800 rpm
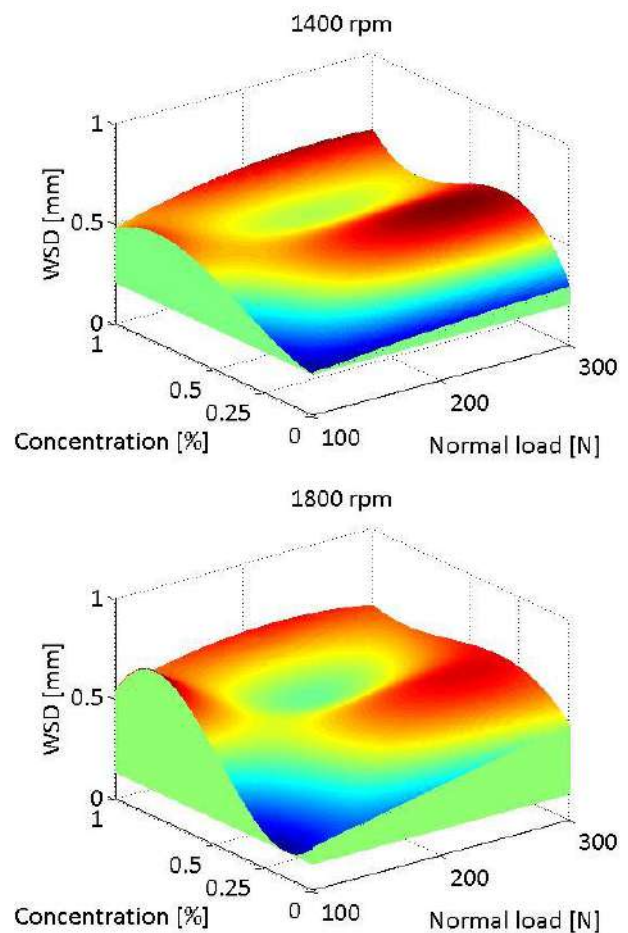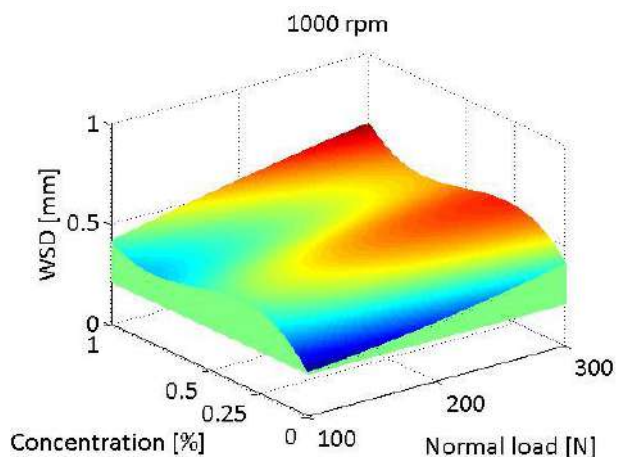
Figure 7. WSD as a function of additive concentration and test conditions

Wear scar diameter is the average values of six measurements, two of each fixed ball of a test. For each ball, there were measured the wear diameter in the sliding direction and perpendicular to it (Fig. 7).

For the additivated lubricants, WSD is less sensitive to concentration, especially for F=300 N. The non-additivated soybean oil could be recommended for mild regimes (equivalent to F=100...200N and speed v=1000...1800 rpm. The almost linear dependency of the WSD to load in each map in Fig. 7 suggests an abrasive wear due to a mixt regime.

4. CONCLUSIONS

For the tested regimes (F=100 N... 300 N and v= 1000...1800 rpm), the results are not in the favour of the additivated lubricant formulations.

The addition of nano black carbon increases the WSD. As comparing only the additivated oils, it seems that under low speed, when the load

increases the WSD increases, too. Under the loads of 200 N and 300 N WSD is less depending on speed and load for the concentrations of 0.5%wt and 1.0%wt black carbon.

It seems that this anti-wear additive - nano black carbon, does not a very clear influence on improving the tribological behavior of the soybean oil. Even if the mechanism of reducing friction exists in the presence of the additive, that is interposing nano particle of black carbon between the rubbing surfaces and having a third body friction, the migration of these particles (because they are not bonded to the surfaces) and the uneven distribution in contact make the tribosystem to behave more unstable than the neat soybean oil. In a statistical approach, at a moment there could enough particles in contact to reduce friction and wear but, during running, there could be moments when this number is low enough to have mixt regime and the oscillations between these two situations could explain the variations of the friction coefficient and the higher values for WSD.

This type of anti-wear additive, because the particle distribution is not even in contact during the running could not help improving the tribological behavior, as it does not reduced the friction coefficient and wear scar diameter as compared to the neat soybean oil. The authors think that the additive should be bonded (physically or chemically) for having better results.

REFERENCES

[1] L. R. Rudnick: *Natural oils as lubricants*, CRC/Taylor & Francis Group, 2006.

[2] J. C. J. Bart, E. Gucciardi, S. Cavallaro: *Biolubricants*, Woodhead Publishing Ltd, 2013.

[3] L. A. T. Honary, E. Richter: *Biobased lubricants and greases technology and products*, John Wiley & Sons, New York, 2011.

[4] P. Nagendramma, S. Kaul, Development of ecofriendly/biodegradable lubricants: An overview, Renewable and Sustainable Energy Reviews, Vol. **16**, No. 11, pp. 764-774, 2012.

[5] L. C. Solea: *Contribution on studying the rheological and tribological behavior of several biodegradable lubricants based on vegetable oils*, PhD thesis, "Dunarea de Jos" University, Galati, 2013.

[6] L. R. Rudnik: *Lubricant Additives. Chemistry and Applications*, Taylor&Francis, 2009.

[7] M. Gulzar, H. H. Masjuki, M. A. Kalam, M. Varman, N. W. M. Zulkifli, R. A. Mufti, R. Zahid: Tribological performance of nanoparticles as lubricating oil additives, J Nanopart Res, Vol. 18, 223, 2016.

[8] Z. Tang, S. Li: A review of recent developments of friction modifiers for liquid lubricants (2007–present), Current Opinion in Solid State and Materials Science, Vol. 18, pp. 119–139, 2014.

[9] S. Shahnazar, S. Bagheri, S. B. A. Hamid: Enhancing lubricant properties by nanoparticle additives, Intern. J. of Hydrogen Energy, Vol. 41, No. 17, 2016.

[10] Y. Gogotsi: *Carbon nanomaterials*, CRC Press Taylor & Francis Group, 2006.

[11] H. 0. Pierson: *Handbook of Carbon, Graphite, Diamond and Fullerenes. Properties, Processing and Applications*, Noyes Publications, New Jersey, 1994.

[12] Y. Hwang, C. Lee, Y. Choi, S. Cheong, D. Kim et al.: Effect of the size and morphology of particles dispersed in nanooil on friction performance between rotating discs, J Mech Sci Technol, Vol. 25, No. 11, pp. 2853-2857, 2011.

[13] E. Hu, X.Hu, T. Liu, L. Fang, K. D. Dearn, H. Xu: The role of soot particles in the tribological behavior of engine lubricating oils, Wear, Vol. 304, pp. 152-161, 2013.

[14] S. Bhaumik, S.D. Pathak, Effect of Nano and Micro Friction Modifier Based Lubricants on Wear Behavior between Steel-Steel Contacts, Tribology in Industry, Vol. 39, No. 1, 136-143, 2017.

[15] S. Baskar, G. Sriram, S. Arumugam, Experimental Analysis on Tribological Behavior of Nano Based Bio-Lubricants Using Four Ball Tribometer, Tribology in Industry, Vol. 37, No. 4, pp. 449-454, 2015.

[16] Nano materials and related product, 1st ed. Catalogue PlasmaChem, 2016.

[17] E. M. J. Deffense: *From organic chemistry to fat and oil chemistry*, Oléagineux Corps Gras Lipides/OCL, 2009.

[18] ISO SR EN ISO 20623 *Petroleum and related products. Determination of the extreme-pressure and anti-wear properties of fluids. Four ball method*, 2004.

[19] H. Czikos: *Tribology – A System Approach to the Science and Technology of Friction, Lubrication and Wear*, Elsevier, 1978.

RESEARCH OF TRIBOLOGICAL CHARACTERISTICS OF VARIOUS OIL APPLIED IN THE TRIBOLOGICAL SYSTEM

Pavel KOVAČ[1*], Dušan JEŠIĆ[2], Borislav SAVKOVIĆ[1], Marin GOSTIMIROVIĆ[1], Nikola GVOZDENOVIĆ[3]

[1]Univerzitet U Novom Sadu, Fakultet tehničkih nauka, Novi Sad, Srbija
[2]Tehnološko menadžerska Akademija, Novi Sad, Srbija
[3]Adeco, Srbija
*Corresponding author: pkovac@uns.ac.rs

Apstract: To test the tribological characteristics were selected two oils used in the process of synchronization gears. Tests were done on tribometer according to the method block on disc. The results show that the present system for testing tribological characteristics gives a very good and reliable results. The paper on the mentioned equipment specific coefficients of friction for the two types of oil during the test period, for different loads and different values obtained tear.

Keywords: motor oil, tribological properties, coefficients of friction

1. INTRODUCTION

The effect of lubricants on the development of tribological processes in mechanical systems and assemblies is very complex and still not fully understood. To enable the functionality, stability and reliability of the system in operation it is necessary to, on the basis of operating modes, choose the appropriate lubricant [1, 2].

Lubricant oil can be present as a mixture of base oil and additives. Although at first glance a simple definition, oil formulation is complex and requires extensive testing and continuous improvement.

Base oils are the basis for the production of all types and quality of lubricating oils. She determine the area of application, quality and price of lubricants, since some of the characteristics of lubricating oils are exclusively related to the quality of the used base oil and cannot be changed by adding additives.

The most important division is based on the origin, to: mineral and synthetic base oils.

Mineral base oils are derived from petroleum and are complex mixtures of various chemical structures of hydrocarbons and other organic compounds that contain sulfur, oxygen, nitrogen, and others. According to the group of hydrocarbons that dominate the base oil, there are: paraffinic, naphthenic and aromatic base oils.

Synthetic base oils are chemical compounds, which are obtained by chemical synthesis of different components of different technological processes. In this their properties "targeted" (expected and predictable), and the quality is repeatable. Good properties of these oils are low pour point, high viscosity index, low volatility, high oxidation stability and others. Lack of them is a

small compatibility with conventional additive packages and sealing materials, as well as the high cost [3, 4].

Because of determination of the characteristics of the lubricant conditions and work processes, for example: gears in automotive power train selected two engine oils of the same viscosity grades and formulated the same additive package. In the tests were used the oil for lubrication of all types of modern gasoline and diesel engines with and without catalytic converter, turbocharger of passenger cars and light trucks. Especially recommended for engines with multivalve divorce. In the paper conducted are the exploitation and tribological tests of two oils.

2. OBJECT OF INVESTIGATION

During the tests we used semi-synthetic motor oil of high quality. It is designed to lubricate highly loaded diesel engines of trucks, buses, construction and agricultural machines, with or without turbocharger. Manufactured to meet the requirements of the extended interval replacement motor oil the world's leading engine manufacturers, protecting and preserving the motor during the entire period of use. Meets the requirements of API CI-4 specification, which this oil makes it suitable for use in engines using EGR system for exhaust gas treatment, and ACEA E7 specification of engine oil indicates that it is suitable for use in Euro 1, 2, 3, 4 diesel engines , using the SCR system catalyst for reduction of nitrogen oxides (No_x) exhaust gases, and ACEA E7 specifications of the engine oil shows that is suitable for use in Euro 1, 2, 3, 4 diesel engines, which use v SCR system to reduce nitrogen oxides (NOx). It is not intended for use in engines loaded DPF system (particle filter). Ideal for mixed fleets, because it can be used in vans as well as in passenger cars with petrol and diesel engines. Another advantage of this oil are:

• Provides safe protection of the engine at high loads and temperatures,

• Reduced oil consumption and fuel,

• Extended oil change intervals (20,000 to 30,000 km depending on the engine manufacturer's recommendations) [5].

Physic-chemical properties of test oils are given in Table 1.

Semi-synthetic oil exploitation tests were carried out during the autumn (October-December month of 2014).

Table 2 shows the test engine oil between the two replacements in the engines installed in tractors.

From Table 2 it is clear that the loss of engine oil to the lower limit of normal loss, and can be performed following conclusion: The base engine oil is an ingredient of the engine oil is of high quality with high thermal stability.

Table 1. Characteristics of the universal semi-synthetic, multigrade engine oil SAE 10W-40

Characteristics, unit of measurement	The measured value	The method
Density at 15°C, g/cm^3	0.87	SRPS B.H8.015
Kinematic viscosity at 40°C, mm^2/s	93.5	SRPS ISO 3104
Kinematic viscosity at 100°C, mm^2/s	13.8	SRPS ISO 3104
Index viscosity	150	SRPS B.H8.024
Flash point, COC, °C	220	ISO 2592
Pour point, °C	-35	SRPS ISO 3016
TBN, mgKOH/g	7.5	SRPS ISO 3771
The foaming, ml/ml		SRPS ISO 6247
The sequence I	10/0	
The sequence II	50/0	
The sequence III	10/0	

Meets specifications:
API SL/CF, ACEA 2007, A3/B3/B4-04, Daimler V2007.1: MB 229.1, VW 501.01/505.00

Table 2. Consumption of oil between the two replacements

Name of machine	The amount of oil poured (l)				The amount of consumed fuel (l)	Consumption of motor oil %
	0 – 100 r/č	100 – 200 r/č	200 – 300 r/č	300 – 400 r/č		
Tractor Case 9220	2	0	2	1	6939	0,43
Tractor John Deere 8320	2	3			5273	0,57

3. TEST TRIBOLOGICAL CONDITIONS

3.1 Laboratory and measuring equipment

During the experiment, which included measuring the friction force, coefficient of friction and wear parameters were used following laboratory and measuring equipment:
- Tribometer TPD-93
- A / D converter,
- Booster - HBM, two-channel measuring bridge KWS273.A2,
- PC,
- A device for measuring roughness Talysurf (Taylor Hobson)
- The universal tool microscope UIM 21.

In Figure 1, the measuring system for tribological tests used in the realization of the experiment.

Talysurf 6 is computerized and measuring system for measuring and analyzing roughness, which provides the basic features entry contact surfaces. Identification of changes in the situation on the contact surfaces (the parameters of surface topography) was carried out by measuring surface roughness parameters, realized precisely on the device.

The universal microscope UIM-21, is used to measure the width of the trace of wear on the contact surface, as well as to analyze the results. When the measurement is carried out a comparison of the value change of the amount (depth) area which is the hub, with respect to an established reference point. The measure changes the height (depth) area which is the hub relative to the base represents the linear intensity of wear. For reference base used is part of the area that does not wear off, and is located right next to the battered surface.
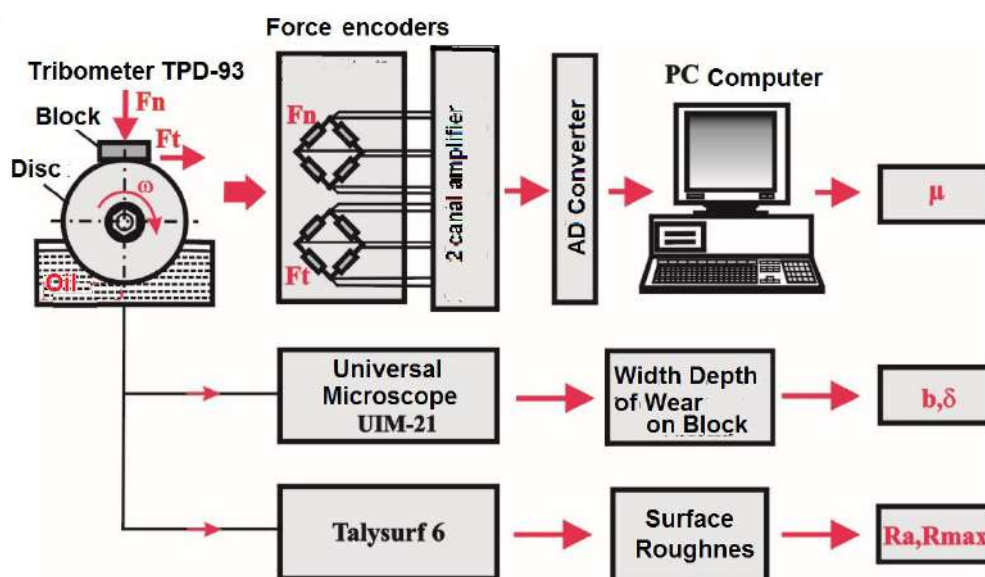
Figure 1. Measuring system for tribological tests used in the realization of the experiment

3.2 Terms of tribological tests

Tribological tests type "block on disk" was subjected to two samples of oil. Lubrication is carried out by passing through the lower part of the disk tank with lubricating oil, so that the disk encompassed a certain amount of oil, and do contact boundary lubrication. Between the surface of the block and the extensive surface of the disc is accomplished in-line contact. The special design provides a carrier block at all times fully fit the entire length of the contact block. The geometry of the drive and block tribological tests is shown in Figure 2. The material disk and block is soft annealed steel 16MnCr5 (Č4320) hardness of 35 HRC.

The total time duration of the test of each sample was t = 60 minutes. The value of speed skating in the contact zone is v = 0.8 m / s. The value of the normal external load (Fn) changes during the test:

Fn1 t1 = 30 N = 15 min
Fn2 = 100 N t2 = 15 min
FN3 t3 = 300 N = 30 min
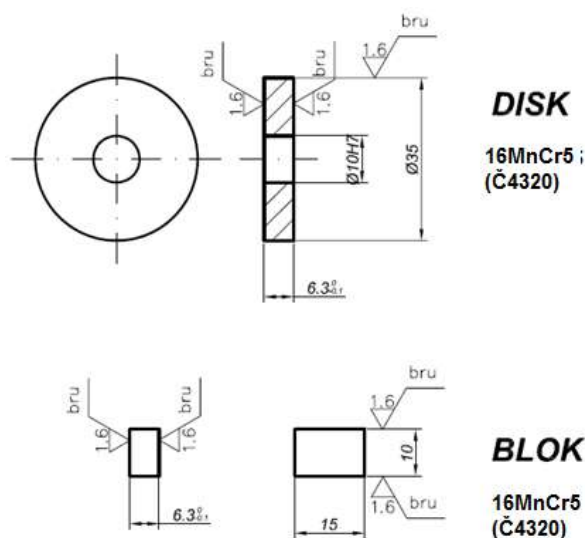
Figure 2. The geometry of the drive and block tribological tests

The main indicator of the tribological properties of the material change in the coefficient of friction over time. To obtain a clearer picture of what the character of the coefficient of friction in certain time intervals, the coefficient of friction values are recorded every 2 seconds. This gives the information

about the dynamics of the process that takes place on tribometer.

4. TEST RESULTS

In this part of the paper presents the results of tribological tests characteristic represented by a tribological system.

Figure 3 shows a trace of wear as a profile of unit 2 at the end of the test. In figure 4, 5 and 6 are shown the records of the friction coefficient as a function of time for different load tests for base oil SN 150. Figure 7 and 9 shows coefficients of friction as a function of time for different load tests for oil 10W40.
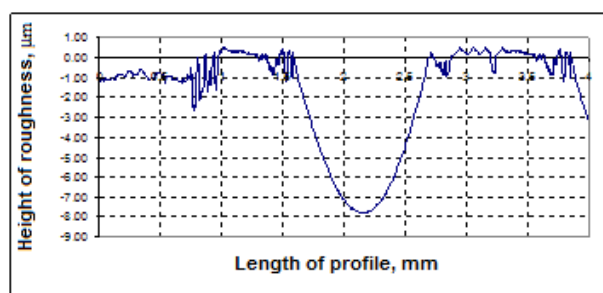
Figure 3. Profile of block 2 after the tests and experiments 2
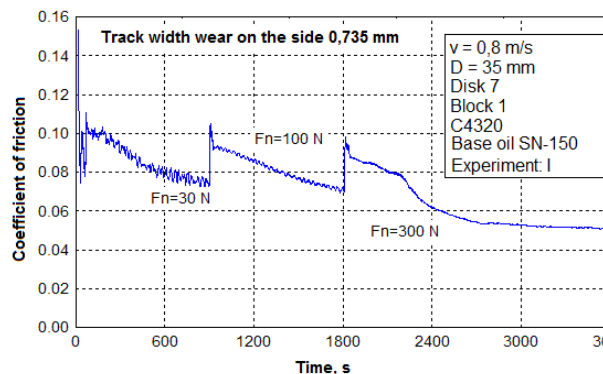
Figure 4. The friction coefficients of base oil
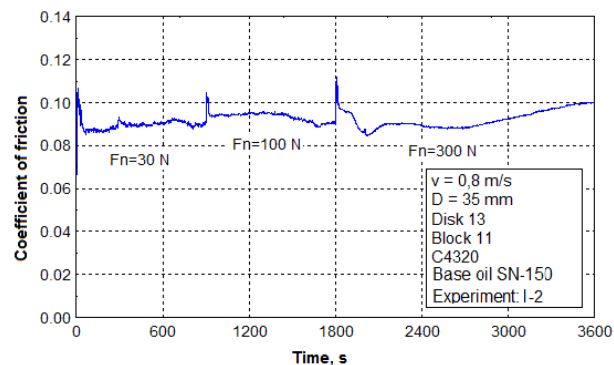
Figure 5. The friction coefficients of base oil

Slika 6. The friction coefficients of base oil

Figure 8. Coefficients of friction for oil 10W40

Table 3 presents the coefficients of friction for those tested oils for different intervals of tests as well as different levels of wear track width of the block.

Figure 9 shows a graphical presentation of changing the coefficients of friction at the time of testing for both sealing oil. In Figure 10 is a graph showing changes in track width of wear for all the tested oil.

Table 3 presents the coefficients of friction for those tested oils for different intervals of tests as well as different levels of wear track width of the block.

Figure 7. The coefficients of friction for oil 10W40

Table 3. The coefficients of friction and wear track width on the block tested oil

Experiment	Conditions	Coefficient of friction			Track wear on the block
		After 10-15 min	After 25-30 min	After 55-60 min	
1	Base oil SN-150 I	0.076	0.072	0.053	0.735
	II	0.090	0.091	0.10	0.665
	III	0.074	0.080	0.085	0.790
2	SHPD 10W40 I	0.057	0.082	0.098	0.840
	II	0.059	0.087	0.092	0.685
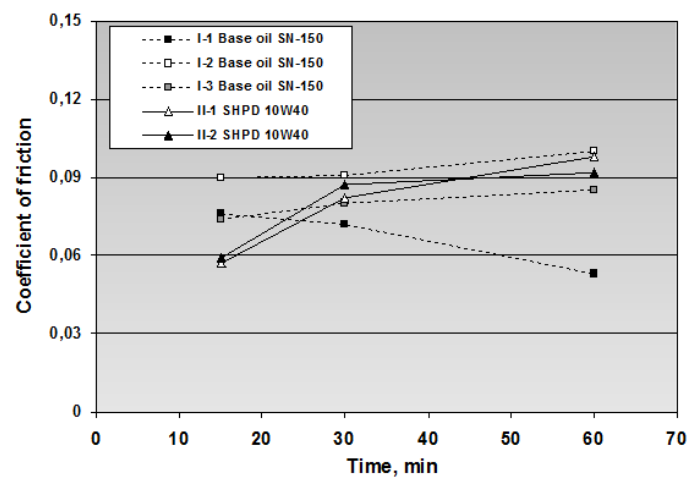
Figure 9. Comparative review of the coefficients of friction at the time of the contact zone
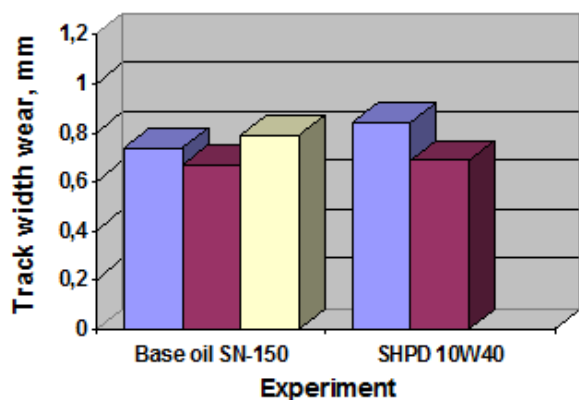
Figure 10. Track wear of tested oils

5. CONCLUSION

Test methodology developed with the use of the described equipment has been shown that in laboratory tests can be used to identify the characteristics and treibomechanical system. This approach to the study of tribological processes provides significant advantages compared to the test in real conditions, however, can be applied in circumstances where sampling does not disturb the functioning of the real system. In this case it is a sampling of lubricating oil. By use of the test method it was concluded that changes tribological characteristics of lubricating oil in the engine and transmission gear of the vehicle. These changes are directly depending on the condition of all elements tribomechanical system, and depending on their functional characteristics.

Figures 4 and 4 shows the dependence of friction coefficients depending on the duration of contact for track width of wear on the block.

Analysis of the results showed that it is supposed to do additional testing. For this is indicated in Figure 6 domiciles, especially oil 10W40. After repeated tests SHPD 10W40 oils are obtained and the expected satisfactory results.

The results for the base oil SN-150 are satisfactory especially if one takes into account the variability of the coefficient of friction lubrication when it comes to the process of running tribomechanical system.

REFERENCES

[1] D. Golubović, P. Kovač, D. Ješić, M. Gostimirović, V. Pucovski: Wear intensity of different heat treated nodular iron, Metalurgija, Vol. 51, No. 4, pp. 518-520, 2012.

[2] D. Golubovic, P. Kovač, D. Jesic, M. Gostimirović: Tribological properties of ADI material, Journal of the Balkan Tribological Association, Vol. 18, No. 2, pp. 165-173, 2012.

[3] D. Ješić, J. Pulić, P. Kovač, B. Savković, N. Kulundžić: Application of nodular castings in the modern industry of tribomechanical systems today and tomorrow, Journal of Production Engineering, Vol. 16, No. 1, pp. 55-58, 2013.

[4] D. Golubovic, P. Kovač, B. Savkovic, D. Jesić, M. Gostimirović: Testing the Tribological Characteristics of Nodular Iron Austempered by Conventional and an Isothermal Procedure, Materials and Technology, Vol. 48, No. 2, pp. 293-298, 2014.

[5] Katalog of firm ADECO, Temerinski put 109, Novi Sad, Srbija, 2015.

INFLUENCE OF COLLING AND LUBRICATION TECHNIQUE ON TOOL WEAR AND SURFACE ROUGHNESS IN HARD TURNING

Gordana GLOBOČKI LAKIĆ[1], Branislav SREDANOVIĆ[2], Davorin KRAMAR[3], Janez KOPAČ[4]

[1]University of Banjaluka, Faculty of Mechanical Engineering, Stepe Stepanovića 75, 78000 Banja Luka, Republic of Srpska, Bosnia and Herzegovina, e-mail: gordana.globocki@gmail.com,
[2]University of Banjaluka, Faculty of Mechanical Engineering, Stepe Stepanovića 75, 78000 Banja Luka, Republic of Srpska, Bosnia and Herzegovina, e-mail: sredanovic@gmail.com,
[3]University of Ljubljana, Faculty of Mechanical Engineering, Aškerčeva 6, 78000 Ljubljana, Slovenia, e-mail: davorin.kramar@fs.uni-lj.si,
[4]University of Ljubljana, Faculty of Mechanical Engineering, Aškerčeva 6, 78000 Ljubljana, Slovenia, e-mail: janez.kopac@fs.uni-lj.si
*Corresponding author: gordana.globocki@gmail.com

Abstract: *In this paper, experimental study on capabilities of two techniques of cooling and lubrication: conventional flooding and high pressure jet assisted machining in the turning was performed. Experimental research was conducted on hard-to-machine materials: hard-chromed and surface hardened steel Ck45 (58 HRc) and hardened bearing steel 100Cr6 (62 HRc). There were used coated carbide tools and highly cutting speed. The capability of cooling is characterized by tool wear and surface roughness parameters. Monitored parameters of tool wear are, as follows: flank tool wear (VB), the wear on minor flank face (VB') and crater wear. Tool life is evaluated for adopted value of criteria in depending on the machining time. During tool wear, surface roughness parameters, such as mean height of surfaces roughness (Ra) and maximum height of surfaces roughness (Ry), were evaluated. Connection between the tool wear and surface roughness is established. Results of experimental research show that the application of HPJAM offers many advantages such as: extended tool life, low intensity of tool wear, and surface roughness in acceptable limits.*

Keywords: *HPJAM, hard-to-machine materials, carbide tool, tool wear, surface roughness*

1. INTRODUCTION

In modern cutting processes, the general trend is dry machining. However, there are materials, which due to the high temperature that develops in the cutting zone, cannot be dry machined, even with the most modern tools with coatings. These are called hard - to - cut materials such as: austenitic stainless steels, high-temperature resistant nickel and cobalt alloys, titanium alloys, and hardened steels. Machining of these materials requires the use of a cooling and lubrication fluid (CLF). Machining process for workpiece materials that are hardened above 45 HRc and up to 65 HRc is a hard turning. In the manufacturing chain, the inductive hardening process is followed by finishing operation that generates the component's final geometry. Traditionally, the finishing operations are grinding processes,

but within the last years the performances of hard cutting operations have been drastically improved. The study of Klocke et al. (2005) has shown that hard cutting offer a higher flexibility, increased material removal rates, increased tool life, reduction of cutting temperature and tool wear, improvement of chip breakability, reduced power consumption and the possibility of machining with reduced coolant consumption [1].

In the literature, as well as in practices it can be traced to a variety of approach to the solution of this the problem and improve the machinability completely [2]. In order to increase productivity, quality of machining and machinability hard-to-cut materials, a variety of methods and techniques of cutting have been developed. One solution is a self-driven rotating turning tool. This mechanism bring some advantages such as significantly extended tool life, lower cutting temperatures, higher material removal rates, a very fine-treated surface, and very little change in the structure of the treated surface, in short, an improved machinability. Precision rotating tool shows some weakness in manipulating with them, especially with tools larger diameter, as well as that stepwise workpieces cannot be machined. In order to improve the machinability of complex materials many hybrid procedures with mechanical or thermal support for the cutting process, such as ultrasonic assisted turning, laser-assisted turning, and cryogenic cutting, are developed. Most implementations of hybrid technologies include turning, it is estimated that turning occupies 40% all treatments with the cutting, as well as its kinematics provides access support process. The previously described technology and required additional equipment, have an additional technical limitations and sometimes even higher processing costs. Development of materials (super alloy) for specific applications such as components for aircraft jet engines, gas turbines and biocompatible materials in medicine, require materials of high hardness, strength and toughness, resistance of corrosion and high temperature. In addition, the above-mentioned hybrid processes combinated with use of cutting with high pressure, the degree of material removal and machining productivity is significantly increased. The turning of the cooling and lubrication at high pressures is a very effective method that enables higher productivity, reduces temperature in the cutting zone and improved control chip formation, depending on the pressure and flow of CLF [3]. In addition, CLF have a direct impact on the environment and economy of production. By replacing the conventional type of cooling application with HP supply CLF significant reduce production costs related to the CLF is achieved [4, 5, 6].

Hard turning usually reqires high cutting speeds and advanced cutting tool materials such as CBN, PCD and ceramics. Hard cutting with coated carbide tools, low cutting speed and conventional cooling, usually results in significant problems concerning extremely long chips and severe adhesion wear mechanisms. By applying HPC at flow rate 1.4 l/min, the friction and the heat induced in the tool–chip interface can be reduced.

This paper presents the results of investigation of the author's team in area of hard turning [7, 8, 9, 10]. In this investigation the capabilities of conventional and HPC in hard turning on two hard-to-machine materials (hard-chromed and surface hardened steel Ck45 (58 HRc) and hardened bearing steel 100Cr6 (62 HRc)) are compared. All machining experiments are performed with coated carbide tools and cutting speeds up to 160 m/min (expect for steel Ck45 (58HRc) where the speed was up to 250 m/min. The performances of different cooling conditions are evaluated on the basis of tool wear, tool life, cooling efficiency and surface roughness.

2. EXPERIMENTAL DETAILS

The experimental investigation was performed on a conventional lathe (Figure 1). In the flooding technique, CLF was delivered at the top of the machining zone, from a distance of approximately 150 mm at 6 l/min. CLF was directed to the non-machined workpiece

surface and the rake surface of the cutting tool insert, Figure 2.
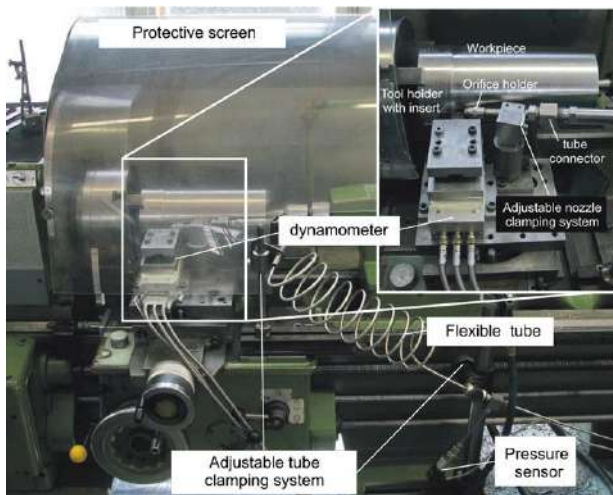
Figure 1. Machine in experimental work with HPJAM

Figure 2. Position of conventional flooding

In HPJAM, the jet was directed toward the cutting edge at a low angle directly between the rake face and the chip, Figure 3.
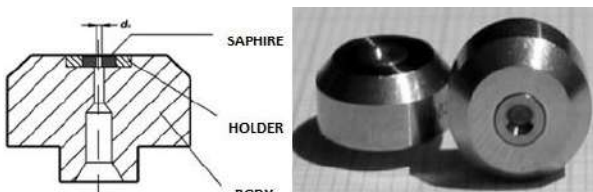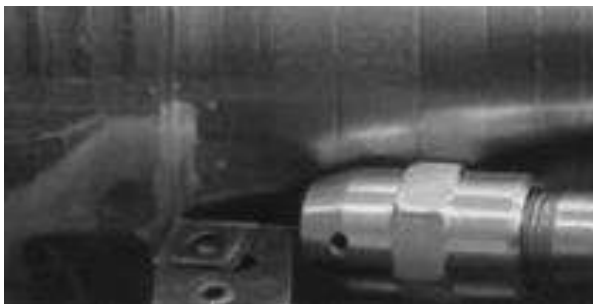
Figure 3. The jet injected directly between the rake face and the chip (above), sapphire nozzle (below)

For this application, a conventional universal lathe was fitted with a high pressure plunger pump with a flow rate capacity of 10 l/min and pressure of 150 MPa. The jet was directed normal to the cutting edge and under angle of 30° from clearance face at a low angle 5° with the tool rake face.

Monitoring and measurement of tool wear was performed using a tool microscope TM-MITOTOYO 510 equipped with high-resolution camera. Surface roughness was measured using a mobile measuring device MITOTOYO SURFTEST SJ-301, Figure 4.

Figure 4. Surftest SJ-301 and tool microscope

During the experimental investigation, following parameters were measured and analysed: flank tool wear (VB), wear on minor flank face (VB') and the size of the crater on the rake face (b_w). The measurement of the selected parameter of tool wear during cutting enables the creation of the experimental curves of wear [10]. By defining the wear resistance of tools for a given criterion VB_k, the tool life T can be determined. Due to wear of tools, values of surface roughness were measured, as follows: mean values of roughness (Ra) and maximum height of roughness (Ry).

2.1 Experimental work with Ck45 (58 HRc)

One of workpiece's materials used in the experimental investigation is construction steel used for highly loaded parts in mechanical engineering (untreated carbon steel Ck45 - surface induction hardened on 58 HRc). Experimental conditions are: tool - Al_2O_3 coated carbide cutting tools SNMA 120408 KR 432 without chip breaking geometry on the rake face (Figure 5), tool holder PSBNR 2020K 12 (producer Sandvik), CLF -5,5% emulsion of vegetable oil.

Figure 5. Coated carbide tool SNMA 120408 KR 432

For the analysis of the jet pressure influence on the cutting process, different CLF pressures were applied (10 - 200 MPa), while the cutting speed, v_c = 98.5 mm/min, feed rate, f = 0.25 mm/rev and depth of cut, a_p = 2 mm, were kept constant. Chip breakability is excellent in every case of HPJAM. During the experimental investigation, it was noticed that the pressure higher than 110 MPa is not achieved by further improving chip breaking, so that the test tool wear and surface roughness done in these conditions. Efficiency CLF techniques is analysed by means of tool wear and surface roughness in following conditions: cutting speed, v_c = 98.5 mm/min, feed rate f = 0.25 mm/rev and depth of cut, a_p = 2 mm, pressure 110 MPa, diameter nozzle 0,3 mm.

As a criterion of wear, the value VB_k = 0.1 mm was adopted, at which the tool life should be evaluated. Images in Table 1 and Table 2 show that wear on flank face is uniformly for both CLF techniques. It can be seen a small notch at the place where the cutting blade cuts workpiece surface. This is probably due to the hard surfaces of the workpiece coated with chromium and friction with chip sharp edges.

Table 1. Tool wear in conventional cooling in turning of Ck45 (58 HRc) [9]

Time T [min]	Wear on rake face	Wear on flank face
0,5		
1,20		
1,90		

Table 2. Tool wear in HPJAM of Ck45 (58 HRc) [9]

Time T [min]	Wear on rake face	Wear on flank face
1,4		
3,92		
9,98		
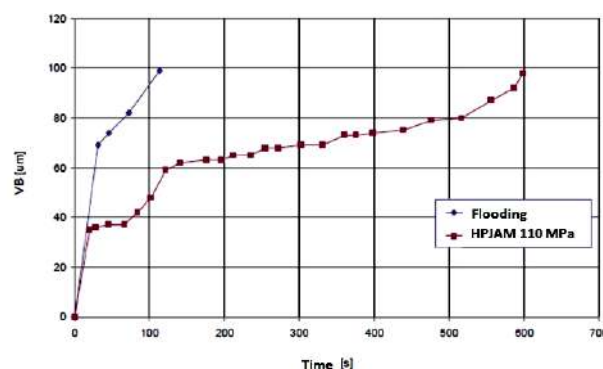
Figure 6. Wear of tool SNMA 1204 08 KR in turning Ck45 (58HRc), a_p=2mm, v_c=98,5m/min, f=0.25mm/rev [7]

Results on Figure 6 shows that tool is worn for less than 2 minutes using conventional

flooding for the selected criteria VB_k=0,1 mm, but for HPJAM tool is worn for about 10 minutes. The consumption of coolant in the case of HPC is more than four times lower than in the case of conventional cooling.
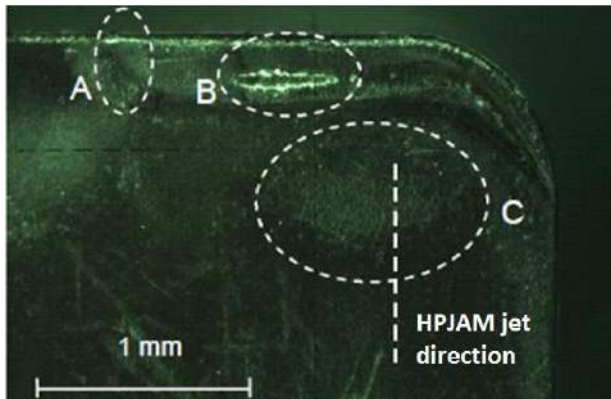
Figure 7. Types of tool wear in turning Ck45 (58HRc) with HPJAM, p = 110 MPa

The figure 7 shows types of tool wear SNMA 1204 08 KR in turning Ck45 (58HRc) using HPJAM: zone A – notch wear, zone B - crater wear on the rake face dimensions of about 0.45 x 0.08 mm, C - erosion wear in the area where the jet strikes the surface of the tool.
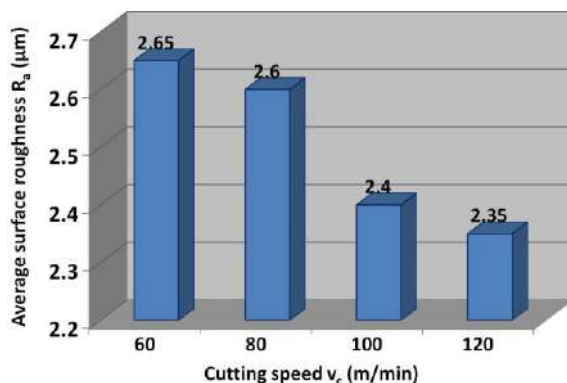
Figure 8. Surface roughness Ra in turning of Ck45 (58 HRc, SNMA 120408 KR 432, f = 0.25mm/rev, a_p = 2mm; flooding)
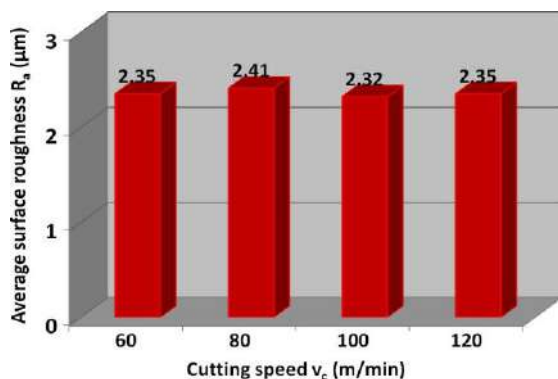
Figure 9. Surface roughness Ra in turning of Ck45 (58 HRc, SNMA 120408 KR 432, f = 0.25mm/rev, a_p = 2 mm; p = 110 MPa, D_n = 0.3 mm, HPJAM)

Figures 8 and 9 show the influence of the cutting speed and Figure 10 show influence of feed rate on surface roughness R_a.
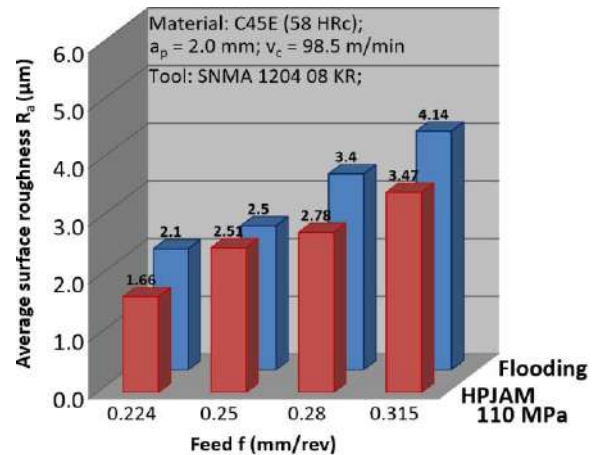
Figure 10. Surface roughness Ra in turning of Ck45 (58 HRc) for different CLF techniques

In Figure 10 it can be seen that the surface quality is slightly improved when HPJAM was used, compared to conventional flooding. Since the application of HPJAM was in the semi-finishing and roughing operations the effect is not so important. Influence of tool wear on surface roughness R_a in turning of Ck45 (58 HRc) are presented on Figure 11. With increase of tool wear, the surface roughness is increasing, as expected.
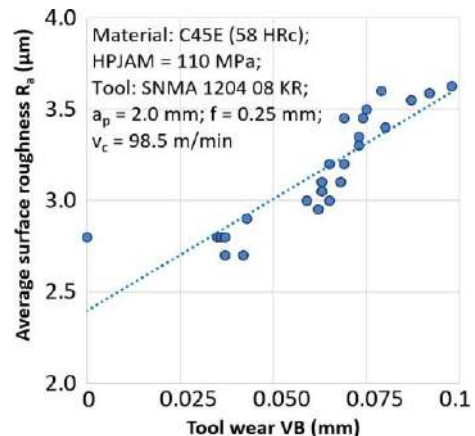
Figure 11. Influence of tool wear on surface roughness Ra in turning of Ck45 (58 HRc)

Basic conclusions in turning of steel Ck45 with hardness 58HRc regarding of tool life and surface roughness and the application of various CLF technique are as follows:

- the heat-treated steel can be adequately treated with the cutting insert, which is not suitable for this material (carbide tool without chip breaker),

- HPJAM is very important and allows the processing of hard materials without chip breaker,
- Excellent brittleness chips with HPJAM,
- using HPJAM can significantly increase the area of operability - technological window (for ~ 45% of the maximum cutting speed and ~ 25% of the maximum feed),
- For the selected criteria, in the case of HPJAM tool life was approximately five times longer than in the case of conventional cooling,
- The consumption of coolant in the case of HPC is more than four times lower than in the case of conventional cooling,
- For both CLF delivery techniques (conventional flooding and HPJAM) similar surface roughness was obtained.

## 2.2 Experimental work with 100Cr6 (62 HRc)

Second workpiece materials used in experimental investigation was alloy bearing steel 100Cr6, hardness of 62 HRC. This steel is very difficult to machined and dominantly is processed with CBN tool inserts. Main target was to investigate the capability of hardened steel processing using carbide tool insert and HPJAM, which is much cheaper than CBN tool insert.

Figure 12. Carbide insert CNMG 1204 08 MF5, internal designation TH1000 (SECO producer)

Cutting tool used in experiments was carbide insert with nano-coating CNMG 1204 08 MF5, SECO producer, tool holder: PCBNR 2525 M12 (Figure 12). Cutting fluid was 3% emulsion of vegetable oil. CLF technique was HPJAM, pressure was set to 50 MPa and flow rate to 2.0 l·min^{-1}, diameter of nozzle was 0,5 mm. Input parameter: cutting speed v_c (65, 85, 100, 120 m/min), feed f (0,08; 0,125; 0,16; 0,2 mm/rev) and constant cutting depth, a_p =0,5 mm.

Experimental testing of tool wear was conducted in specific cutting conditions: the flank wear reaches approximately 0.25 mm or an interval of time of cutting reaches value of 20 min (see Figure 13 and Table 3).
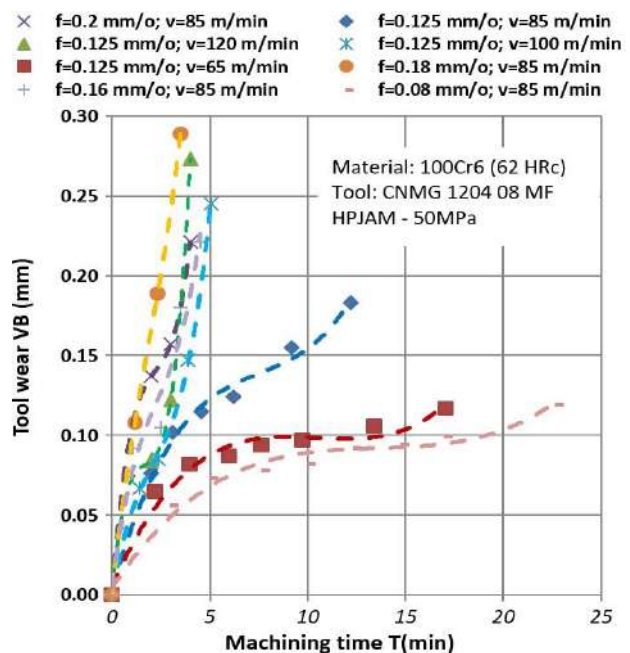
Figure 13. Tool wear in turning of steel 100Cr6 with HPJAM for different cutting conditions, a_p=0,5 mm

In Table 4, results of tool life and parameters surface roughness (R_a, R_y) for different cutting conditions are presented. Parameters Ra and Ry are presented for the first and last measured value of tool wear (at the moment immediately before the dismissal of tool). Analysis of results shows when feed and cutting speed increase, tool life decrease (see Table 3 and Table 4), but significantly increase productivity, i.e. material removal rates (MRR).

Table 3. Tool wear in turning steel 100Cr6 (HPJAM)

a_p =0,5mm f=0,125 mm/rev v_c=85 m/min	Time T [min]	2,6	13,2
	Wear on rake face		
	Wear on flank face		

Experimental studies have shown that, in terms of tool wear and productivity of processing, optimal results achieved with lower values of feed and cutting speed, i.e. cutting speed 85 m/min and feed 0.08 mm/rev (see Figure 13).

Table 4. Tool life and parameters Ra, Ry in turning steel 100Cr6 with HPJAM [11]

Dept of cut a_p [mm]	Feed f [mm/o]	Cutting seed v [m/min]	Tool life T [min]	R_a [μm]		R_y [μm]	
				Beginning	End	Beginning	End
0.5	0.200	85	4.0	0.91	0.96	3.98	4.51
0.5	0.125	85	13.2	0.48	0.50	2.51	2.88
0.5	0.125	120	4.0	0.52	0.57	2.61	2.93
0.5	0.125	100	5.1	0.53	0.58	2.86	3.62
0.5	0.125	65	17.1	0.58	0.63	3.18	3.28
0.5	0.180	85	3.5	0.86	0.99	3.93	4.67
0.5	0.160	85	4.5	0.85	0.97	3.90	4.22
0.5	0.080	85	22.7	0.36	0.62	2.12	3.35

Results in Table 4 show that the influence of cutting speed on tool wear is the higher, expressed in percentages, than feed. Intensive tool wear is a result of high contact pressure on the cutting tool edge and intense heat generation during machining of hard-to-machining steels such as 100Cr6.

In cutting conditions when feed increases, at the same values of cutting speed, the surface roughness significantly increases, but when the cutting speed increases, with the same values of feed, better quality of processing is achieved, see Figure 14.

Based on the presented results in processing hard-to-machine steel, it can be concluded that the processing of these materials can be achieved with carbide tools by applying HPJAM in conditions semi rough and rough machining.
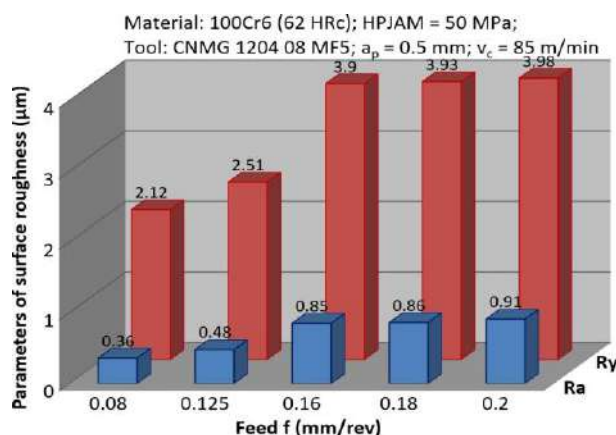
Figure 14. Surface roughness for different feed during machining of 100Cr6 [11]
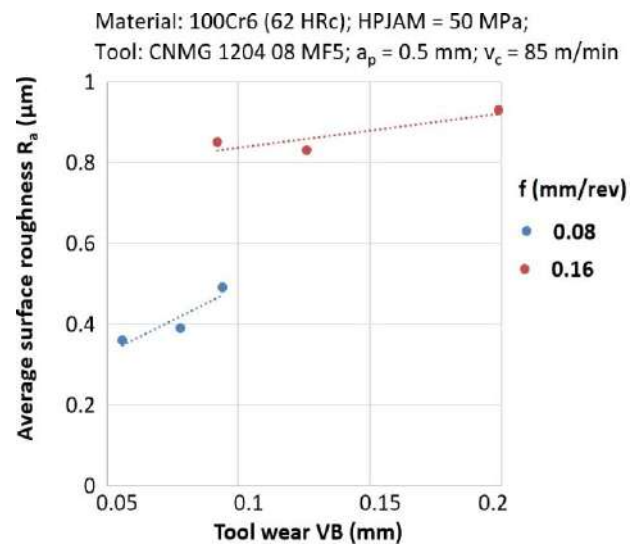
Figure 15. Dependence of surface roughness on tool wear during turning 100Cr6

The results in Figure 15 show that with increased tool wear, there is also an increase in the parameters of surface roughness, when applying HPJAM. The increase in parameters of surface roughness is more pronounced for higher values of feed.

3. CONCLUSION

Main target was to investigate the capability of hardened steel processing using carbide tool insert, because mentioned material are processed dominantly with CBN tool inserts, which are much more expensive than the carbide tool inserts. Experimental study on capabilities of two techniques of cooling and lubrication (conventional flooding and high pressure jet assisted machining in the turning) was evaluated in this paper.

Experimental research was conducted on two hard-to-machine materials: Ck45 (58 HRc), and 100Cr6 (62 HRc). There were used coated carbide tools and highly cutting speed (up to 160 m/min). The capability of cooling is characterized by tool wear and surface roughness parameters. During tool wear, surface roughness parameters (Ra and Ry), were evaluated, and relation between the tool wear and surface roughness is established.

Basic conclusions in turning of steel Ck45 (58HRc) regarding of tool life and surface roughness and the application of various CLF techniques are:

- for the selected criteria (VB = 0.1 mm), in the case of HPJAM tool life was approximately five times longer than in the case of conventional cooling.
- Tool wear in HPJAM is uniform and less notch wear is recognized compared to conventional CLF technique.
- The consumption of coolant in the case of HPC is more than four times lower than in the case of conventional cooling.
- The changes in roughness were noticed as a consequence of the increasing tool wear. Compared to conventional cooling can be noticed that the surface roughness the slightly higher in HPJA techniques due to action of high pressure jet to the surface.
- For both CLF delivery techniques (conventional flooding and HPJAM) similar surface roughness was obtained.

Results of experimental investigations indicate that HPJAM techniques can be successfully used for hard turning of steel 100Cr6 (62 HRc):

- The significant increase in chip breakability was achieved by use of HPJAM.
- Significantly reduction of the consumption of cutting fluid in comparison to conventional machining.
- The influence of cutting speed on tool wear is higher expressed in percentages than influence of feed. Intensive tool wear is a result of high contact pressure on the cutting tool edge and intense heat generation during machining.
- Experimental studies have shown that, in terms of tool wear and productivity of processing, optimal results were achieved with lower values of feed and cutting speed.

Results of presented experimental investigation show that the hard turning with carbide cutting tools and HP supply CLF provides numerous advantages from the techno-economic aspect: greater productivity, reduce of temperature in the cutting zone, improved control chip formation, longer tool life, significant reduce of production costs related to the CLF, similar surface roughness compared to conventional CLF technique.

REFERENCES

[1] F. Klocke, D.Lung, G. Eisenblätter, P. Müller-Hummel, H. Pröll, W. Rehbein: Mimimalmengenkühlschmierung - Systeme, Werkzeuge und Medien, Trockenbearbeitung prismatischer Teile, VDI-Berichte, Vol. 1375, pp. 197-210, 1998.

[2] M.C. Shaw: *Metal cutting principles*, Oxford series on advanced manufacturing 3, Oxford science publications, 1984

[3] E.O. Ezugwu: Key improvements in the machining of difficult-to-cut aerospace superalloys, International Journal of Machine Tools and Manufacture, Vol. 45, No. 12-13, pp. 1353-1367, 2005.

[4] P. Dahlman, M. Escursell: High-Pressure Jet-Assisted Cooling: A New Possibility for Near Net Shape Turning of Decarburized Steel, International Journal of Machine Tools & Manufacture, Vol. 44, No. 1, pp. 109-115, 2004.

[5] A. E. Diniz, R. Micaroni: Influence of the Direction and Flow Rate of the Cutting Fluid on Tool Life in Turning Process of AISI 1045 Steel, International Journal of Machine Tools & Manufacture, Vol. 47, No. 2, pp. 247-254, 2007.

[6] C. Courbon, D. Kramar, P. Krajnik, F. Pusavec, J. Rech, J. Kopac: Investigation of machining performance in high-pressure jet assisted turning of Inconel 718: an experimental study. International Journal of Machine Tools & Manufacture, Vol. 49, No. 14, p. 1114-1125, 2009.

[7] D. Kramar, P. Krajnik, J. Kopač: High pressure jet assisted turning of surface hardened piston rods, Int. J. Materials and Product Technology, Vol. 38, No. 4, pp.399-417, 2010.

[8] B. Sredanovic, G. Globočki-Lakić, Dj. Čiča, D. Kramar: Influence of Different Cooling and Lubrication Techniques on Material Machinability in Machining, Strojniški vestnik -

Journal of Mechanical Engineering, Vol. 59, No. 12, pp. 748-754, 2013.

[9] G. Globočki-Lakić, B. Sredanović, D. Kramar, J. Kopač, Machinability of C45E steel - Application of Minimum Quantity Lubrication and High Pressure Jet Assisted Machining Techniques, Transactions of Famena, Vol. 40, No. 2, pp. 45-58, 2016.

[10] G. Globočki-Lakić, D. Kramar, J. Kopač, *Metal cutting-theory and applications*, Faculty of Mechanical Engineering, Banja Luka and Ljubljana, 2014.

[11] B. Sredanovic: *Development of universal machinability model based on cutting process parameters*, MSc thesis (in Serbian), Faculty of Mechanical Engineering Banja Luka, University of Banjaluka, Banja Luka, 2012.

TRIBOLOGICAL PROPERTIES OF VEGETABLE AND MINERAL OILS

Mile STOJILKOVIĆ[1], Latinka DESPOTOVIĆ[1], Slavko BAČEVAC[1]

[1]NIS GAZPROMNEFT, Serbia, mile.stojilkovic@nis.eu, latinka.despotovic@nis.eu, slavko.bacevac@nis.eu

Abstract: *As a result of the increasing environmental pollution and reduction of crude oil reserves, has intensified the development of environmentally friendly lubricants. Environmentally friendly lubricants are rapidly biodegradable and non-toxic to living organisms. The most important raw materials for the formulation of environmentally friendly lubricants are vegetable oils.*

Vegetable oils are triglycerides that make up the complex mixture of fatty acids with different chain length and number of double bonds. Triglycerides are rapidly biodegradable and have excellent lubricity properties. Advantages of vegetable oils compared to mineral are reflected in the following characteristics: toxicity, rapid biodegradability, good lubricity, high flash point, high viscosity index and low volatility. Disadvantages of vegetable oils compared to mineral are: poor oxidative stability, poor flow ability at low temperatures and poor hydrolytic stability that limits their application.

The paper presents the tribological properties of vegetable oils, which was compared with the tribological properties of mineral oil.

Keywords: *environmentally friendly lubricants, vegetable oil, biodegradable oil, tribological characteristics, wear*

1. INTRODUCTION

The louder and more justified environmental requirements for the protection of the environment causes introduction of increasingly stringent requirements, rules and regulations. The two main aspects: saving and preservation of non-renewable resources and reduce the harmful effect of lubricants on the environment are core tasks. All these issues have increased public awareness and environmental conscience for the development of environmentally friendly lubricants. Terms of the environmental acceptability are biodegradability and non-toxicity lubricants. The most important raw materials for the formulation of environmentally friendly lubricants are vegetable oils, which, in addition to biodegradability and non-toxicity, is a renewable resource. Research suggests that vegetable oils have advantages and disadvantages in relation to the mineral.

Vegetable oils have a great advantage over mineral because they are non-toxic, biodegradable, less polluting, and they are particularly interesting because they are made from renewable raw materials. Besides that, they provide lower consumption due to the lower loss by evaporation, a better lubricating properties, higher viscosity index, higher resistance to fire because higher flash temperature, a higher solubility for additives and oxidation products.

The disadvantages of vegetable oils, comparing with a mineral are: they are less

thermally stable, in the presence of moisture are susceptible to hydrolysis forming corrosive acids, have a considerably higher pour point and a much greater tendency to foam, and have a shorter shelf-life and period of use.

With high probability it can be supposed that in the near future environmental requirements further increase and intensify. The direct and important role of tribology is the development of environmentally friendly lubricants. In this complex and long process tribology plays a very important role and can not be, as until now, considered a science or profession which deals with the reduction of friction and better lubrication.

2. EXPERIMENTS

2.1 Preparation of sample

Tests should show the difference that exists between the mineral and vegetable base oils in terms of their tribological properties, and their ability to additive. As a mineral oil was taken SN 150 base oil, which is used for the production of mineral lubricants. This mineral base oil will be in the following text labeled as MIN 30, and has a viscosity that is comparable to the viscosity grades of vegetable oil from the rapeseed which is labeled as REP 30. Physico-chemical characteristics of MIN 30, and the REP 30 are shown in Table 1, and physico-chemical characteristics of anti-wear additive in table 2, and the additive for extreme pressures in table 3. These additives are conventional and they use in the production of mineral lubricant.

Table 1. Physico-chemical properties of vegetable oils used in the experiment

Phisicalchemical characteristics	Unit	MIN 30	REP 30	Metods
Density at 20^{0}C	g/cm^3	0,89	0,92	ISO 3675
Kinematic viscosity, 40^{0}C	mm^2/s	29,15	34,07	ISO 3104
Kinematic viscosity, 100^{0}C	mm^2/s	5,3	7,84	ISO 3104
Index viscosity		98	213	ISO 2909
Flash point	^{0}C	207	322	ISO 2952
Pour point	^{0}C	- 15	-8	ISO 3016

Neutralisation number	mgKOH /g	0,007	0,3	ISO 6618

Table 2. Physicochemical properties of AW additives used in the experiment

Characteristics	Unit	AW additives	Metods
Density at 15^{0}C	g/cm^3	0,930	ISO 3675
Kinematic viscosity, 40^{0}C	mm^2/s	45,0	ISO 3104
Kinematic viscosity, 100^{0}C	mm^2/s	8,3	ISO 3104
Flash point	^{0}C	180	ISO 2952
Zink content	% w/w	4.5	ASTM D4628

Table 3. Physico-chemical properties of EP additives used in the experiment

Characteristics	Unit	EP additives	Metods
Density at 15^{0}C	g/cm^3	1,036	ISO 3675
Kinematic viscosity, 40^{0}C	mm^2/s	42,0	ISO 3104
Kinematic viscosity, 100^{0}C	mm^2/s	6,3	ISO 3104
Flash point	^{0}C	70	ISO 2952
Sulfur content	%w/w	30	ISO 8754
Phosphorus content	%w/w	0.5	ASTM D4628

Anti-wear (AW) additives

For protection metal surfaces, which are in contact, from wear occuring under conditions of moderate temperature and pressures standard anti-wear additives is used (Zinc alkyldithiophosphate). These are polar materials that form a film on the metal surface, wherein the polar ends directed at right angles to the metal surface, and which together make a more or less strong adhesive joint, Figure 1. The film formed between the metal surfaces reduces friction and provide metal to relatively easily slide one after the other. These

additives act only under mild conditions of loading and temperature conditions.

Due to the extreme pressures and shock loads in particular of gear transmissions, it happens the interrupt of oil layer. In that case, there is the danger that in touch points of gears happens destructive friction and wear and because of the high temperatures, which develops in the contact zone, welding metal surfaces is happening. In order to prevent that, an additive for improvement the capability to resistance the extreme pressures (Phosphoric acid esters / amine salt) is added.
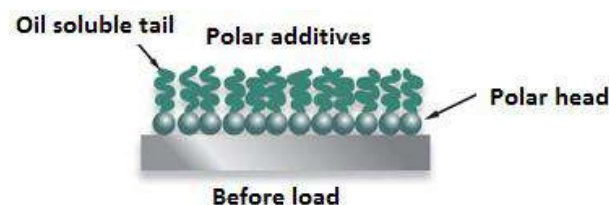
Figure 1. Polar additive

Additive for improving the capability of resistance to the extreme pressure (EP additives)

In condition of shock loads and extreme pressures this additive chemically reacts with the metal surface and builds a solid compound with high shear stability than of the metal, Figure 2.

This compound effectively performs the function of a solid lubricant and prevents the destructive friction and welding of contact surfaces of gear until new a layer of oil is form, that is a boundary lubrication.
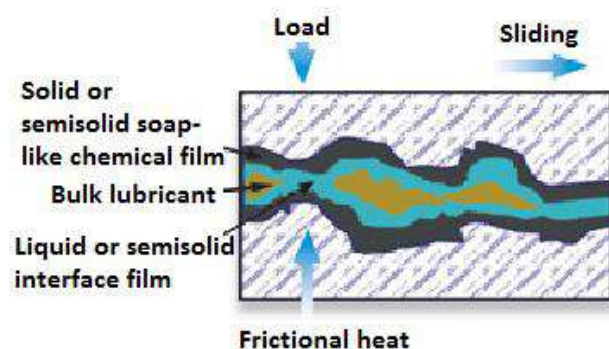
Figure 2. EP additive

2.2 Equipment and test methods

Antiwear properties (Four Ball Wear Test)

The test of wear resistance is done by the standard method ASTM D4172. This test show the efficiency of protection against wear, and it is used for determining the resistance to load of lubricating film in the mixed and mild boundary lubrication conditions. Basic test element consists of four balls that are in the form of a regular tetrahedron immersed in test oil. The three are beads in the carrier and fastened by a ring and immersed in oil. Fourth ball is attached with handle, which along with it, rotates around a vertical axis with 1,500 rpm, Figure 3. The load of 40 kg is transmitted through the upper rotating balls evenly on three immovable balls. Test duration was 60 minutes at a temperature of 65°C. At the end of test, diameter of worn surfaces (which is dome-shaped) of immovable three balls is measured, and the result is expressed as the average wear diameter in mm.

Wear of ball directly indicates the load resistance of the lubricating film. As the value of the mean diameter is smaller, resistance of the lubricating film is higher and inversely.

Figure 3. Four ball tests

Extreme pressures properties (Four Ball Extreme Pressure Test)

Testing the ability to resistance extreme pressures is done according to the standard method ASTM D 2783, a device with four balls. The difference from the previous wear test is that the load are gradually increased until scuffing or welding balls, Figure 4.

EP-device with four ball is used to determine the load that may be carrying by lubricants, or the strength of lubricants film in the boundary conditions of lubrication (EP properties). The basic test element consists of four balls that are in the form of a regular tetrahedron immersed in oil which is tested. Upper ball rotates at a constant speed around a vertical axis, touching the other three balls which are fastened to the base of the tetrahedron. With specific load of balls, the test takes 10 seconds. The load is increased until balls do weld. Load at which the ball is welded is expressed as the welding point and it is expressed in Newton (N). As the value of the point of welding is greater, greater is the strength of lubricating film.

Figure 4. Appearance of weld balls

2.3 Test results and explanations

Results of mesurements of testing samples

Measured values which were obtained in a device with four balls for rapeseed (REP 30) and mineral oil (MIN 30) are located in tables 4 and 5.

Table 4. Resistance to wear

Treat level of additives (%w/w)	REP 30 (mm)	MIN 30 (mm)
0,0	0,68	0,80
0,5	0,66	0,67
1,0	0,62	0,50
1,5	0,60	0,42
2,0	0,58	0,34
2,5	0,58	0,33
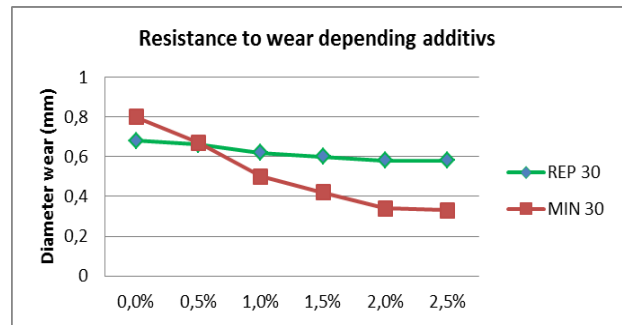
Figure 5. Resistance to wear

Table 5. Capability to resistance to extremely high pressures

Treat level of additives (%w/w)	REP 30 (N)	MIN 30 (N)
0,0	100	60
0,5	110	100
1,0	120	150
1,5	180	220
2,0	220	270
2,5	230	300
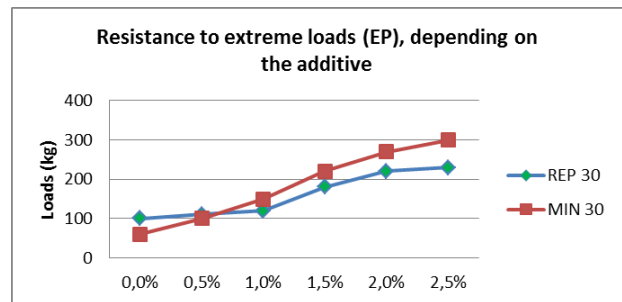
Figure 6. Resistance to load EP

3. RESULTS AND DISCUSSION

The research results showed the following observations:

- Vegetable oil has a better natural anti-wear characteristics and a better ability to resistance the extreme pressures and high loads compared to mineral base oils.
- By Adding of AW and EP additives improves the corresponding characteristics of the anti wear and the extreme pressures and high loads carrying capabilities of the tested vegetable and mineral oils.
- By Adding AW and EP additive has greater effect on the enhancement of mineral oil compared to vegetable oil. The same percentage of the additive effectively

improves wear characteristics of the mineral oil comparing to the vegetable oil, Figure 5. In the same way, the same percentage of the additive more effectively improves the mineral oil characteristic of high pressure carrying than comparing to the vegetable oil, as shown in Figure 6.

4. CONCLUSION

From the present research, it can be concluded that, although vegetable oils have better natural characteristics of the load carrying and anti-wear, they are less susceptible to additive compared to mineral oils. This could be explained by the different chemical structure of vegetable oils compared with mineral and because different mechanism of interaction with the additives that are designed to mineral base oils.

Vegetable oils can reach a much better performance by using additives that are intended for vegetable oils. The best known manufacturers have been developing additives and they already can offer efficient additives intended to improve the characteristics of vegetable oils that are increasingly in use.

REFERENCES

[1] S.Z. Erhan, S. Asadauskas: Lubricant basestocks from vegetable oils, Industrial Crops and Products, Vol.11, pp.277-282, 2000.

[2] B. Kržan, J. Vižintin: *Use and development of biodegradable oils* in *Tribology of mechanical systems; a guide to present and future*, ASME Press, New York, 2004.

[3] L. Bogatu, I. Petre, A. Marin, C. Amira: *Biodegradable hydraulic lubricants based on Modified vegetable oils*, Serbiatrib`07, 10th international conference on tribology, Kragujevac, 2007.

[4] A. Arnsek, J. Vizintin: Scuffing load capacity of rapeseed-based oils, Lubrication Engineering, Vol. 55, pp. 11-18, 1999.

[5] M. Stojilković: *Research application of ecological oils in the tribological systems*, Doctoral dissertation, 2014.

[6] M. Stojilković, D. Vukolov, M. Kolb: Tribology testing of biodegradable oils, *Stručno znanstveni skup Maziva*, 2013, Rovinj, Croatia

[7] M. Stojilković, D. Golubović, D. Ješić: Ecotribology Aspects in the Lubricants Application, *6th International Symposium on Exploitation of Renewable Energy Sources*, Mart 2014, Subotica, Serbia

[8] M. Stojilković, D. Golubović, D. Ješić: Tribological characteristics of biolubricants, *7th International Symposium on Exploitation of Renewable Energy Sources "EXPRES 2015"*, Mart 2015, Subotica, Serbia

[9] M. Stojilković, M. Kolb: Tribological properties of biodegradable universal tractor transmission oil, *14th International Conference on Tribology "SERBIATRIB '15"*, May 2015, Belgrade, Serbia

[10] M. Stojilković: Tribological properties of vegetable oils, *2nd International Scientific Conference "COMETA 15"*, December 2014, Jahorina, BIH

[11] M. Stojilković, Z. Davidović: The effect of certain additives on the foaming of vegetable oil, *Stručno znanstveni skup Maziva 2015*, Rovinj, Croatia

[12] Adhvaryu A., Erhan S.Z., Perez J.M., Tribological studies of thermally and chemically modified vegetable oils for use as environmentally friendly lubricants, Wear, Vol. 257, pp. 357 367, 2004.

[13] Babić M., Tribology in industry - Papers during twenty years, *Tribology in Industry*, Pages 5, Kragujevac, 1998.

[14] L. Bogatu, C. Tanasescu: Uleiuri lubrifiante biodegradabile, Buletinul Universitatii Petrol-Gaze din Ploiesti, Vol. 57, No. 2, pp.53, 2005.

[15] B. Kržan, B. Čeh, I. Košir, J. Vižintin: Tribološko ponašanje biljnih ulja, Goriva i maziva, Vol. 49, No. 4, pp.352-367, 2010.

Tribometry

15th International Conference on Tribology – SERBIATRIB '17

17 – 19 May 2017, Kragujevac, Serbia

COMPUTATIONAL DETERMINATION OF MANUFACTURE CONDITION RESULTING IN A PRE-SET WEAR RESISTANCE.

Vyacheslav F. BEZJAZYCHNY, A. SOLOVYOV

Rybinsk State Aviation Technical University, 152934, 53, Pushkin str., Yaroslavl region, Rybinsk, Russia

Abstract: It is known the wear resistance of the contact surfaces is mostly determined with quality parameters of surface layer, including roughness of surface, degree and depth of hardening of surface layer. These parameters depend on physical-mechanical properties of machined and instrumental materials, cutting modes, geometry of cutting part of instrument.
Authors defined relation between the above mentioned process parameters of cutting and cutting parameters that allowed to defined the dependence for calculating the wear rate of machined surface. It is established the minimal wear rate, and also minimal value of wear of machined surface are maintained in case of machining at optimal cutting speed when the minimum of wear of cutter is achieved.

Keywords: Wear resistance, wear rate, surface layer, cutting mode, optimal cutting speed

1. INTRODUCTION

It is known the wear resistance of the contact surfaces is mostly determined with quality parameters of surface layer. These parameters depend on physical-mechanical properties of machined and instrumental materials, cutting modes, geometry of cutting part of instrument and other conditions of machining [1-8].

Thus the wear rate is a function of physical-mechanical properties of machined and instrumental materials (plastic shear resistance of machined material, thermal conductance and thermal diffusivity of machined and instrumental materials) , cutting mode (cutting speed, depth of cut, feed), geometry of cutting part of instrument (angles cutter, the cutter radius at the apex in the plan, the rounding of cutting edges).

2. THE BODY OF RESEARCH

A functional relationship is established between the cutting conditions, the tool geometry on the one hand and the surface parameters and accuracy of machining on the other hand. The investigations were made taking into account the work and tool material properties (yield limit, modulus of elasticity, coefficients of heat and temperature conductivity of the work material, heat conductivity coefficient of the tool material, etc.), the rigidity of the machine-fixture-tool-workpiece complex, dimensions of the workpiece machined and size of the cutting tool [9, 10].

$$(t, S, v, \varphi, r) = f \begin{pmatrix} \sigma_{\text{ост}}, Rz, h_{\text{H}}, T_{\text{P}}, \tau_{\text{P}}, \sigma_{\text{T}}, E, \beta, \\ a, c\rho, \lambda, \lambda_{\text{P}}, \mu, \theta_{\text{пл}}, \alpha, \gamma, \varphi_1, \\ \rho_1, \delta, j_{\text{сист}}, H, B_1, H_1, L, \alpha_1 \end{pmatrix},$$

where *S* is the feed; *t* is the depth of cutting; *v* is the speed of cutting; φ is the plan angle of the cutting edge; *r* is the tool nose radius; $\sigma_{\text{ост}}$ is the residual stress in the surface layer; h_H is the depth of hardening of the surface machined; R_z is the height of asperities of the surface; T_p is the dimensional tolerance in machining; *E* and σ_T is the modulus of elasticity and the yield limit of the work material; τ_P is the work material resistance to plastic shear; β is the coefficient of the linear temperature expansion of the work material; *a* is the temperature conductivity of the work material; μ is the dynamic response factor of the machine-fixture-tool-workpiece complex; λ and λ_P are the coefficients of the heat conductivity of the work and tool material, respectively; $j_{\text{сист}}$ is the rigidity of the machine-fixture-tool-workpiece complex; $\theta_{\text{пл}}$ is the melting temperature of the work material; δ is the wear land (flank wear) of the tool; *H* is the size of the workpiece machined; $B_1 * H_1$ and L_P are the section and length of the tool holder; α_1 is the heat transfer coefficient of the tool holder; α and γ are rake and clearance angles, respectively; φ_1 is the plan trail angle of the tool; ρ_1 is the cutting edge radius; $c\rho$ are the specific volume heat of the work and tool material.

It thus follows that cutting conditions and the tool geometry are functions of the surface characteristics, machining accuracy, work and tool material properties, workpiece, and cutting tool dimesions and the rigidity of the machine-fixture-tool-workpiece complex.
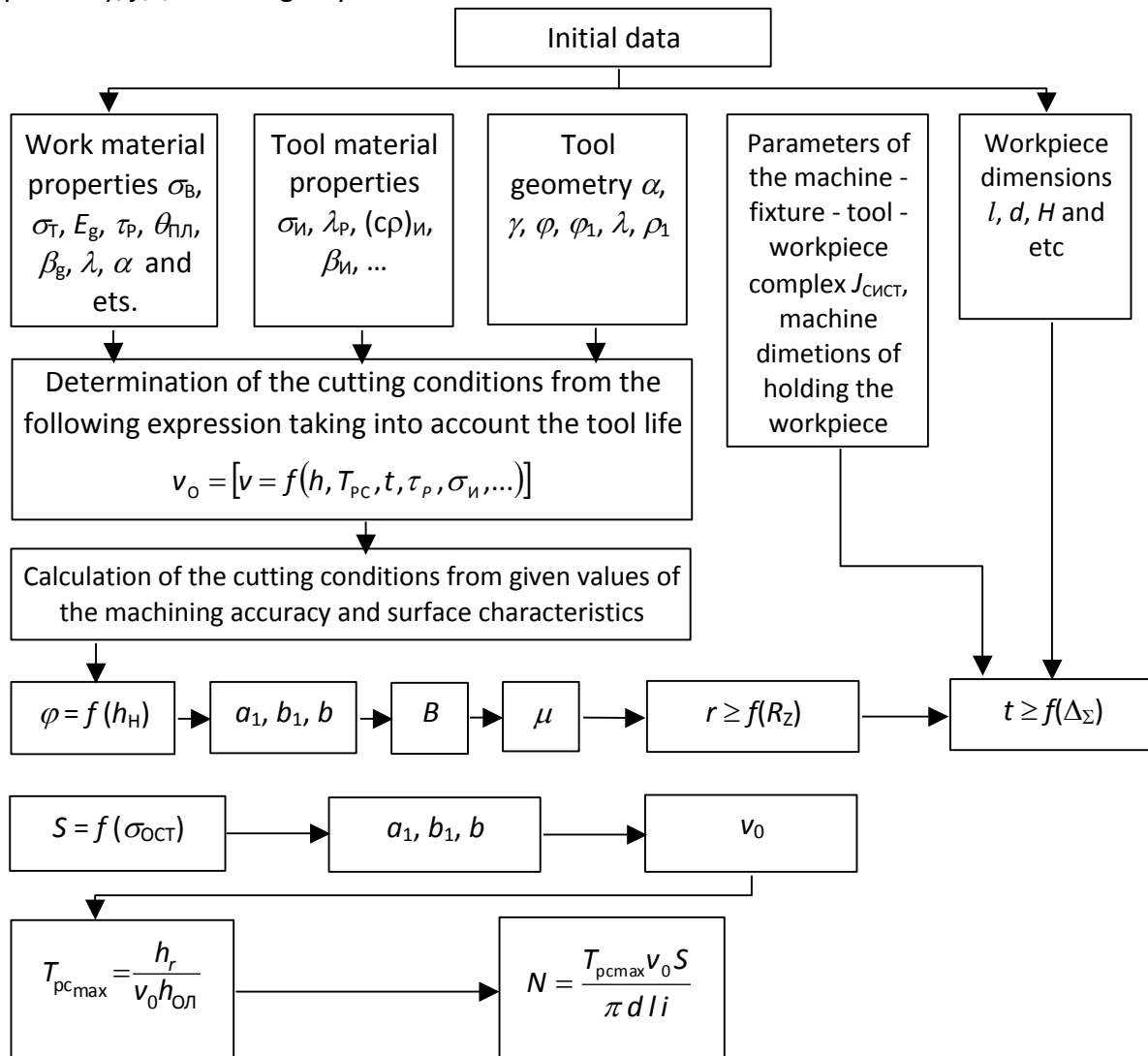

Figure 1. The sequence of the calculated determination of the optimum cutting speed V_0

When it is necessary to attain both the required accuracy of machining and combination of surface characteristics, machining coditions can be calculated from the data in the table given below. In this case the following sequence of steps may be proposed. First, cutting conditions are calculated from the initial data preseted in the table (work and cutting edge material properties, the tool geometry, parameters of the machine-fixture-tool-workpiece complex), taking into account tool life [11]. Then, machining conditions are specified, taking into account restrictions on the depth of hardening, the height of the asperities, the value residual stresses and the accuracy of machinig that are imposed by the required operating characteristics of the product.

On the figure 1: $\sigma_{\text{и}}$ is the compression ultimate strength of the tool material; l and d are the dimensions of the workpiece; h_r is the change in dimensional size of the tool; T_{PC} is the tool life period; a_1, b_1, b are the underformed chip thickness, the width of cut and the total length of the engaged cutting edge, respectively; $B=\frac{1}{\text{tg}}\beta_1$ is the inclination angle of the shear plane; Δ_Σ is the total machining error resulting from the cutting process; v_0 is the optimum speed of cutting; $h_{\text{ОЛ}}$ is the relative linear surface wear; i is the number of passes in cutting.

It is advisable to select cutting conditions which give optimum temperature providing minimum relative change in dimensional size and, therefore, maximum tool life. The speed of cutting, corresponding to the optimum temperature, is further termed optimum speed and can be calculated from the formula obtained by Dr. S. S. Silin on the basis of the analysis of the technological variables caused by cutting process [12]:

$$v_0 = \frac{K^2 \lambda_g c\rho\, a_1 b_1^2 \left(\dfrac{a_1}{\rho_1}\right)^{0,2}}{4\sin^{0,1}\alpha}\left(\frac{\theta_o}{P_Z}\right)^2\left[1+\sqrt{\frac{2{,}65\,\lambda_p\beta\varepsilon\left(\dfrac{a_1}{b_1}\right)^{0,3}P_Z}{K^2 a_1 b_1 \lambda_g c\rho\, \theta_o\left(\dfrac{a_1}{\rho_1}\right)^{0,065}\cdot\sin^{0,065}\alpha}}\right]^2$$

where β and ε are the wedge and tool nose angle, respectively; P_Z is the force of cutting; θ_0 is the temperature in the zone of cutting; K is the coefficient, dependent on the cutting speed and feed, as well as on the work material properties.

Operation at optimum speed of cutting provides the most favourable parameters of the quality of the surface layer. Thus, at optimum speed of cutting minimum asperity height of the surface machined and minimum approach of the contacting surfaces under load are observed (Figure 2).

Cutting at optimum speed gives minimum wear of the surface machined. The investigations were made at rolling friction and a load of 1470 N (Figure 3).

This is explained by the fact that the surface machined has the most uniform distribution of asperities at optimum speed of cutting (Figure 4).

When the optimum speed of cutting is known the wear rate value for the known machining conditions may be determined from the following theoretical formula:

$$J_h = \frac{10^3 a_2^{0,5}\varepsilon_1^{2,1}}{nr^{0,874}}\cdot\left\{\frac{0{,}6625a_1^{0,125}\left[4{,}3\sin^{0,115}\alpha v^{0,57}\alpha^{0,345}\lambda\left(\dfrac{t}{m}\right)^{0,3}+\lambda_p\beta\varepsilon a^{0,57}\rho_1^{0,075}\right]c\rho\theta_0}{\tau_p a^{-0,43}\sin^{0,025}\alpha v_0 t^{0,26} m^{0,74-n_0} c_0 b^{0,04}\rho_1^{n_0-0,1}(1-0{,}45\sin\gamma)}\right\}^{\frac{1,75}{1-n_0}}$$

where ε_1 is the optimum approach of the contacting surfaces, expressed in fractions of the maximum height of the profile asperities; α_2 is the coefficient dependent on the type of contact; n is the number of loading cycles to failure; t is the depth of cut; m is the ratio of the under formed chip thickness m the feed; c_0 and n_0 are values, dependent on the relation p_1/a_1.
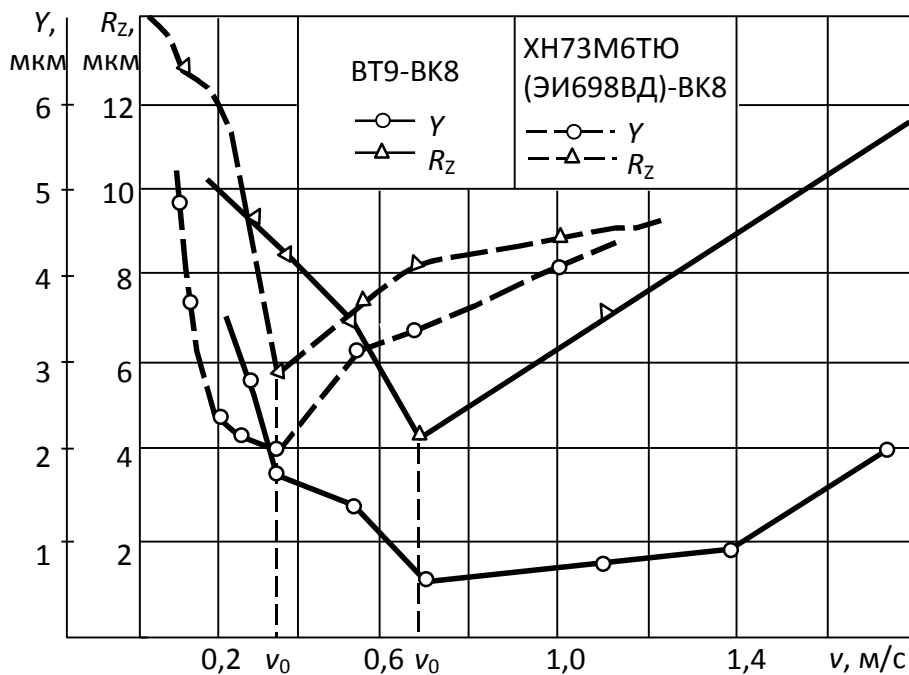
Figure 2. Relation between contacting area approach of the surfaces y and v cutting speed. Loading force $P = 1470N$. Work material alloy ВТ9; $\alpha = 10°$; $\gamma = 0°$; $\varphi = 45°$; $\varphi_1 = 15°$; $r = 1$ mm; $S = 0,2$ mm; work material alloy ХН73МБТЮ cutting conditions are similar, except $\gamma = 10°$
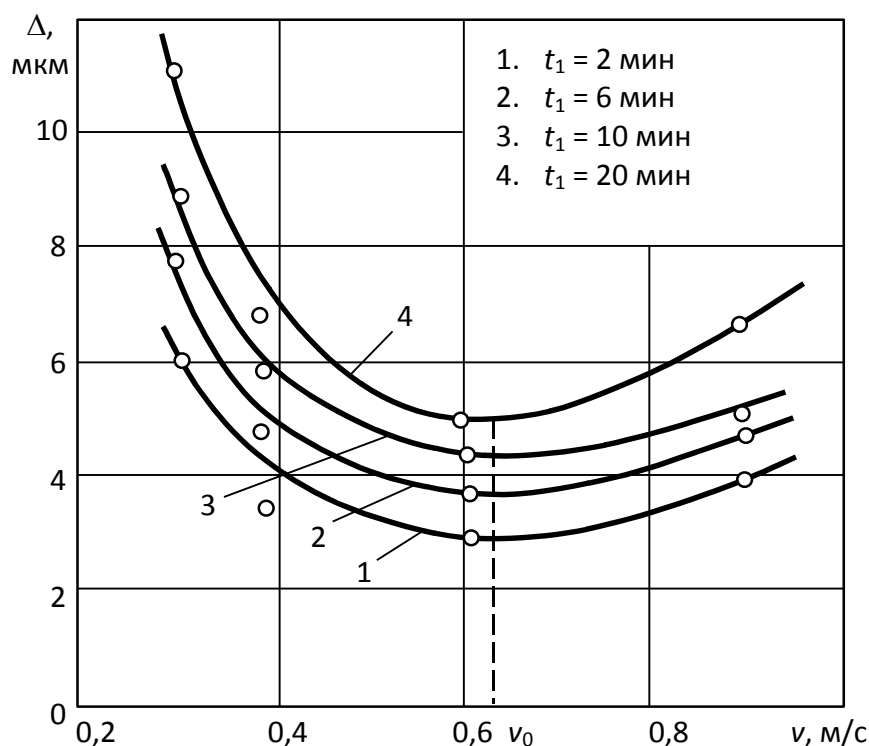
Figure 3. Relation of the wear rate value and the cutting speed. Work material alloy ВТ9; $S = 0,2$ mm; $t = 2$ mm; $r = 0,5$ mm; $\alpha = 10°$; $\gamma = 0°$; $\varphi = 45°$; $\varphi_1 = 15°$. Tool material ВК8. Δ – wear value of the surface machined; t_1 – time of friction.
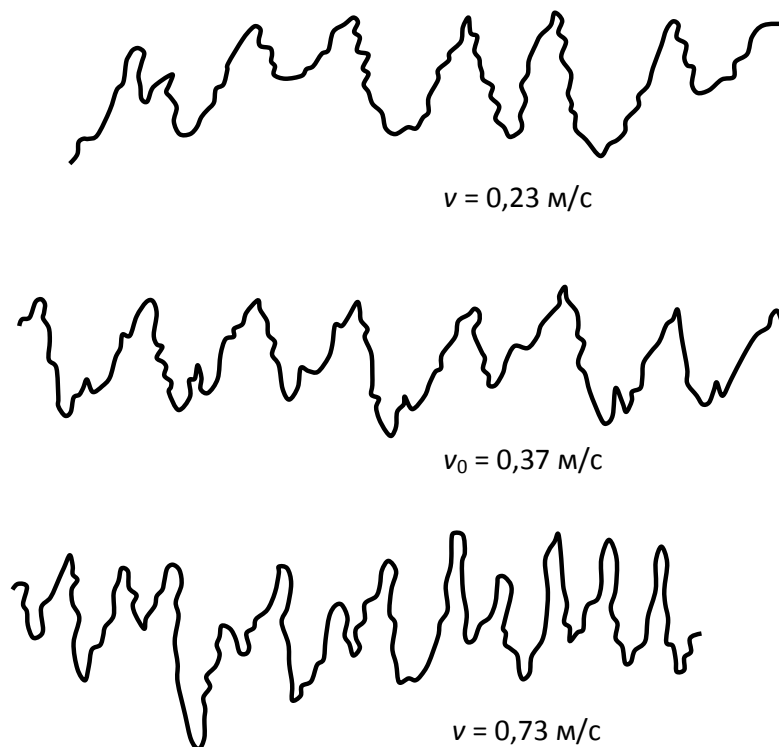
Figure 4. Profile graphs of the machined surface roughness. Work material ХН77ТЮР. Tool material ВК8; S = 0,2 mm; t = 2 mm; r = 0,5 mm; ρ_1 = 30 mkm; φ = 45°; φ_1 = 15°; $\gamma = \alpha$ = 10°. Vertical magnification 2000. Horizontal magnfication 80.
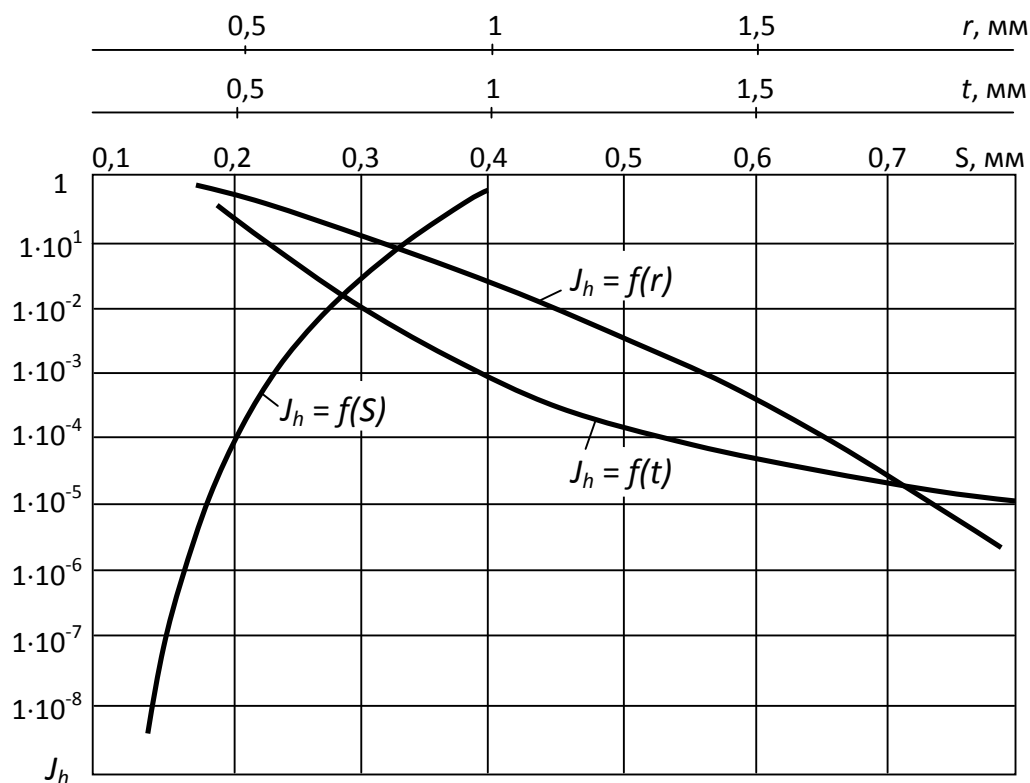
Figure 5. Relation of the wear rate to machining conditions of contacting surface.
Work material steel 40X. Tool material T15K6.

φ = 90°; φ_1 = 15°; α = 10°; γ = 15°;
at $J_h = f(S)$ - t = 1 mm, r = 0,5 mm;
at $J_h = f(t)$ - S = 0,27 mm, r = 0,5 mm;
at $J_h = f(r)$ - t = 1 mm, r = 0,5 mm

Thus, the wear rate is a function of the physical and mechanical properties of the work and tool material (resistance of the work material to plastic shear, heat and temperature coefficients of the work and tool material), of the cutting conditions (speed and feed of cutting, depth of cut), and of the geometrical parameters of tool cutting edge (tool angles and tool cutting edge radius).

The results of the wear rate calculations from the formula are given on Figure 5.

From the analysis of the results of calculations given in Figure 5, it may be assumed that the qualitative characteristic of the wear rate relating it to the machining conditions is correct. Increasing feed leads to increases both in the asperities height and spacing, and, as a result, to the subsequent increase of the wear rate of the surface machined. Increase of the cutting tool nose radius will reduce the asperities height and spacing, producing a reduction of the wear rate of the surface machined. Increasing the depth of cut will reduce the wear rate, if the ratio of depth of cut is more than naught point two. With further increases in the depth of cut the wear rate practically will not change because of analogous changes in surface roughness parameters when the depth of cutting is increased.

As a rule, quantative results of the calculations are found to be somewhat different from actual values of the wear rate obtained in the calculations.

3. CONCLUSION

Thus, it appears possible to calculate tribological charateristics of the surfaces machined and machining conditions providing specified operation characteristics (by theoretical methods).

4. REFERENCES

[1] Трение, износ и смазка (трибология и триботехника) / А. В. Чичинадзе, Э. М. Берлиндо, Э. Д. Браун и др.; Под общ. ред. А. В. Чичинадзе. – М. : Машино-строение, pp. 0 – 576, 2003.

[2] Трение и износ в экстремальных условиях: Справочник / Ю.Н. Дроздов, В. Г. Павлов, В. Н. Пучков. – Машино-строение, pp. 0 – 224, 1986.

[3] Мышкин Н. К., Петроковец М. И. Трибо-логия. Принципы и приложения. – Гомель: ИММС НАНБ, pp. 0 – 310, 2002.

[4] Thomas T. R. Rough surfaces, London: Imperial College Press, 1999.

[5] Stachowiak G. W., Batchelor A. W. Engineering Tribology. Butterworth – Heinemann – Woburn M. A. USA, 2001.

[6] Hebba M., Wachal A.: Tribologia, WNT, Warszawa, 1980.

[7] Nyman P.; Mäki R.; Gamemi B.; Influence of surface topography on friction characteristics in wet clutch application, Wear Vol. 261, No. 1, pp. 46-52, 2006,

[8] Nyman A.: Fretting w elementach maszyn Wyd. Pol., Gdanskiej, Gdansk, 2003.

[9] Безъязычный В. Ф. Метод подобия в технологии машиностроения. – М., Ма-шиностроние, pp. 0 – 320, 2012.

[10] Инженерия поверхности дета-лей / Колл. авт.; под ред. А. Г. Суслова. М., Машиностроение,pp 0 – 320, 2008.

[11] Макаров А. Д. Оптимизация процессов резания, М., Машгиз, pp. 0 – 278, 1976.

[12] Силин С. С. Метод подобия при резании материалов. – М., Машино-строение, pp. 0 – 152, 1979.

ANALYSIS OF SURFACE ROUGHNESS IN CO₂ LASER CUTTING USING DESIGN OF EXPERIMENTS

Miloš MADIĆ[*]**, Miroslav RADOVANOVIĆ, Predrag JANKOVIĆ**, **Dušan PETKOVIĆ**

Faculty of Mechanical Engineering in Niš, University of Niš, Serbia

*Corresponding author: madic@masfak.ni.ac.rs

Abstract: This paper is focused on the analysis of surface roughness obtained in CO₂ laser cutting of mild steel using oxygen as assist gas. To this aim a quazi-linear mathematical model for the prediction of surface roughness in terms of cutting speed, laser power and assist gas pressure was developed. The experimental data were collected upon realization of 2^3 factorial design with central points. The obtained results from additional validation trials indicated that the proposed model accurately relate surface roughness and laser cutting factors in the covered experimental hyper-space. It has been observed that between surface roughness and laser cutting process factors significant three-way interaction exists, which indicate the very complex nature of surface formation in laser cutting.

Keywords: CO₂ laser cutting, surface roughness, design of experiments, mathematical model, mild steel.

1. INTRODUCTION

Laser cutting is thermal based cutting method widely used in industry for contour cutting of different materials. The cutting process is achieved by concentrating high heat energy supplied by focused laser beam which results in melting and evaporation of workpiece material. Laser cutting is a complex process characterized by a number of input factors which determine efficiency of the entire process in terms of material removal rate, cut quality criteria and cost [1]. These factors are to be adequately set for each laser cutting system, laser cutting method, and workpiece material and thickness. As in many other machining processes, the determination of process regimes is done considering certain quality, productivity or cost criteria.

In recent years, researchers and practitioners worldwide are focused on mathematical modeling and optimization of laser cutting of different materials in terms of different criteria such as dross formation [1], surface roughness [2], material removal rate [3], kerf width [4], kerf taper [5], cost [6], heat affected zone [7], etc. Experimental comparison of the effects of process factors on process performances in the fiber and CO₂ laser cutting of low-carbon and stainless steel was also performed [8, 9]. In these, and many other practical and scientific studies the analysis, modeling and optimization of laser cutting process was performed by means of different methods, techniques, algorithms and approaches.

The present study deals with the analysis of surface roughness obtained in CO₂ laser cutting of mild steel using design of

experiments approach. The ultimate aim was to develop surface roughness prediction model in terms of main laser cutting factors such as cutting speed, laser power and assist gas pressure. To this aim 2^3 factorial plan with central points was adopted.

2. MATERIALS AND METHODS

2.1 Equipment and setup

The laser machine used in this study was the CO_2 laser ByVention 3015 manufactured by Bystronic (see Figure 20) delivering output power maximal output power of 2.2 kW at a wavelength of 10.6 μm. Maximum cutting area is 1152 x772 x 100 mm and positioning speed in X andY directions is 100 m/min.

The workpiece material used in the study was a 2 mm thick mild steel. From a mild steel plate the specimens with dimensions of 60 × 10 mm were cut using oxygen as assist gas with purity of $\geq$ 99.95 %. In experimentation the following process factors were kept constant: lens focal length of 127 mm, nozzle diameter of 1 mm, focus position (0 mm) and standoff distance of 0.7 mm. On the other hand, three main laser cutting factors were selected as main contributing factor leading to changes in surface roughness. Cutting speed (v), laser power (P) and assist gas pressure (p), were varied at two levels in experimentation.

Surface roughness of the edge was measured in terms of the average surface roughness (R_a) using Surftest SJ-301 (Mitutoyo) profilometer. Cut off length was 0.8 mm and evaluation length was 4 mm. The average value of three measurements taken along the cut at approximately in the middle of the workpiece thickness was recorded for each specimen. Surface roughness was selected as process response as its measurements are essential in characterization of the features of a machined surface [10].

2.2 Experimental design 2^3

Factorial designs are widely used in research and industry for assessing the effects of several factors on the observed process response (characteristic). Since these designs permit changing of factors only at two levels during experimentation, linear and quazi-linear relationship between factors and process response is assumed. Still, the general factorial designs are important because they form the basis for other designs which are used for further research on the considered process performance [11]. For example, by adding axial points to factorial designs one can obtain experimental designs of higher resolution (such as central composite deign) which can be used for development of second order mathematical models which assume nonlinear relationship between factors and process performance.

$$y = \beta_0 + \sum_{i=1}^{k} \beta_i x_i + \sum_{i<j} \sum_j \beta_{ij} x_i x_j + \\ + \sum_{i<j} \sum_{j<l} \sum_l \beta_{ijl} x_i x_j x_l + ... + \beta_{123...k} x_1 x_2 ... x_k$$. (1)

For the investigation of surface roughness in laser cutting this study applied 2^3 experimental design. This experimental design has three factors (x_1, x_2, x_3) which are varied in the experimentation at two levels (low and high) resulting in total of eight combinations of factors levels. If one assigns "-" and "+" for low and high factor levels, respectively, one obtains the general design matrix of the experiment (Table 1).

Using the general 2^3 design matrix one can estimate any main effect or interaction effect. If one joins, on the far right side of the table, a column of measured (calculated) process performance values for each trial (y_i), one can easily calculate contrast, i.e. a measure how average response is changing, by summing all y_i in trials where given factor or interaction is on low level (−) and subtracting it from the sum of all y_i in trials where given factor or interaction is on low level (+). For any 2^k experimental design with n replicates, the effect estimates can be calculated as [11]:

$$\text{Effect} = \frac{\text{Contrast}}{n2^{k-1}} .$$ (2)

Table 1. The general 2^3 design matrix

Trial	x_1	x_2	x_1x_2	x_3	x_1x_3	x_2x_3	$x_1x_2x_3$
1	–	–	+	–	+	+	–
2	+	–	–	–	–	+	+
3	–	+	–	–	+	–	+
4	+	+	+	–	–	–	–
5	–	–	+	+	–	–	+
6	+	–	–	+	+	–	–
7	–	+	–	+	–	+	–
8	+	+	+	+	+	+	+

In situations where continuous factors are used in experimentation, it is beneficial to observe response values for factor settings in between those realized in the experiment. This is particularly desirable when small changes in factor settings result in considerable increase or decrease in process performance. The method consisting of adding central points to the 2^k design is an approach to reveal whether assumption of linearity holds or there exists considerable nonlinearity in the covered experimental region. It has to be noted that addition of n_c replicates trials at central points $x_i=0$ ($i=1,...k$) do not affect the estimates of main and interaction effects [11].

The experimental design used for assessment of the effects of laser cutting factors and their interactions on surface roughness is given in Figure 1. In the experiment, two replicates in central point ($x_1=0$, $x_2=0$, $x_3=0$) were performed. The coded and real values of laser factors as well as surface roughness measurements are given in Table 2.
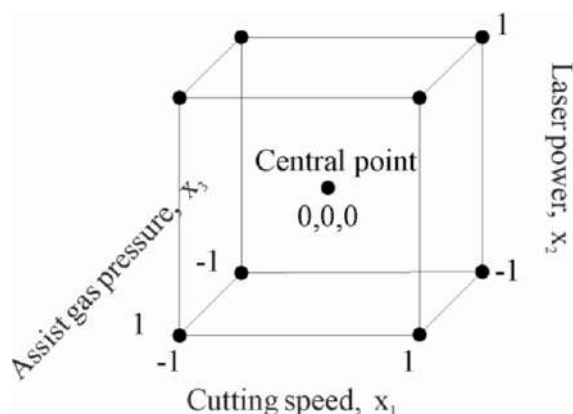
Figure 1. Applied experimenta design

Table 2. Experimental trials and results

Trial	x_1	x_2	x_3	v [m/min]	P [kw]	p [bar]	R_a [μm]
1	-1	-1	-1	3	0.9	3	1.26
2	1	-1	-1	7	0.9	3	0.83
3	-1	1	-1	3	1.3	3	1.53
4	1	1	-1	7	1.3	3	1.19
5	-1	-1	1	3	0.9	7	2.08
6	1	-1	1	7	0.9	7	1.61
7	-1	1	1	3	1.3	7	3.36
8	1	1	1	7	1.3	7	0.89
9	0	0	0	5	1.1	5	1.42
10	0	0	0	5	1.1	5	1.59

3. RESULTS AND DISCUSSION

Considering the previous discussion and with the use of Eq. 2 the main and interaction effects of laser cutting factors on surface roughness were calculated (Table 3). For example, the effect of factor x_1 (cutting speed) is obtained as: $((0.83+1.19+1.61+0.89)-(1.26+1.53+2.08+3.36))/2\cdot2^{3-1}=-0.93$

Table 3. Main and interaction effects

x_1	x_2	x_3	x_1x_2	x_1x_3	x_2x_3	$x_1x_2x_3$
-0.93	0.29	0.78	-0.48	-0.54	-0.02	-0.52

As could be observed from Table 3, the negative sign in front of the effect of cutting speed reveals that cutting speed and surface roughness are in opposite relationship. The main effects showing the difference in process performance at low and high levels are graphically represented in Figure 2.
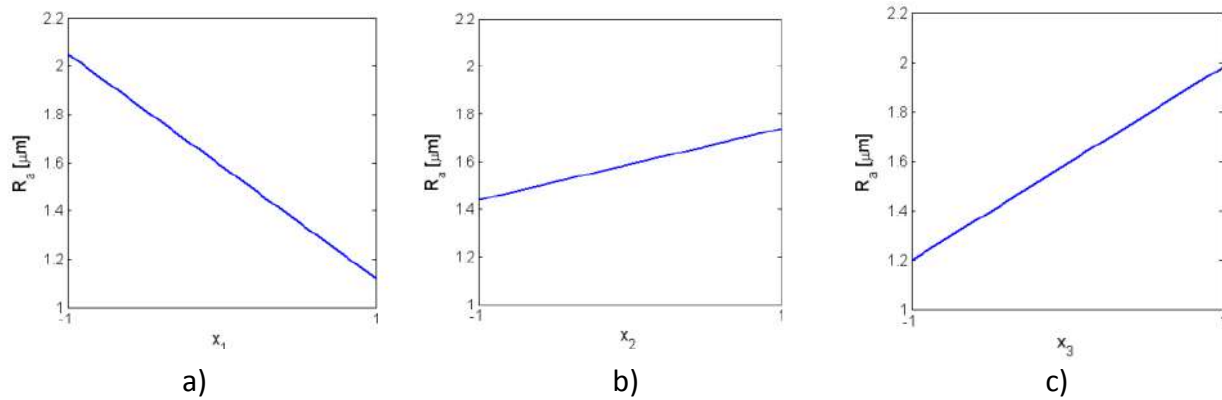
Figure 2. The main factor effects on surface roughness: a) cutting speed, b) laser power, c) assist gas pressure
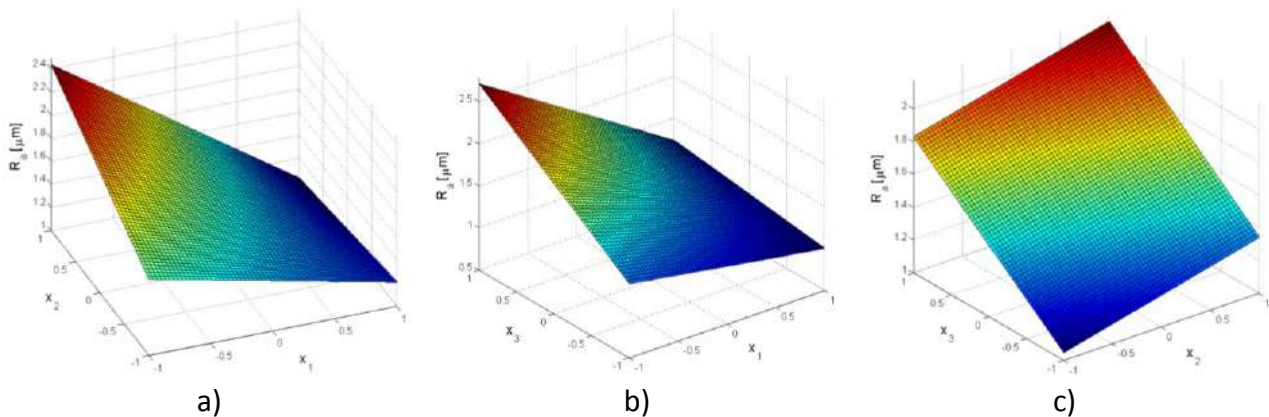
Figure 3. Change of surface roughness within covered experimental hyper-space a) interaction of cutting speed and laser power, b) interaction of cutting speed and assist gas pressure, c) interaction of laser power and assist gas pressure

As it is well known in 2^k factorial designs the regression coefficients of the linear or quazi-linear model are one half of the estimated effects so on the basis of calculated effects one can develop mathematical model for relating surface roughness and laser cutting factors in the following form:

$$R_a = 1.59 - 0.46x_1 + 0.15x_2 + 0.39x_3 \\ -0.24x_1x_2 - 0.27x_1x_3 - 0.26x_1x_2x_3 \quad . \quad (3)$$

Here it should be noted that the intercept, β_0=1.59, is estimated as the mean average of surface roughness obtained in all trials. As given in Eq. 3, the interaction term x_1x_2 was omitted in the model since the effect of this interaction is several times smaller and thus can be neglected.

The validity of the developed model was assessed by calculating coefficient of determination and mean absolute error. Coefficient of determination of R^2=0.99 and mean absolute error of 1.6 % prove that the

proposed quazi-linear model is adequate for describing the relationships between laser cutting factors and surface roughness in the covered experimental hyper-space. The 3D surfaces in Figure 3 visualize the change of surface roughness values with respect to change in laser cutting factors.

As could be observed from Figure 3 maximal surface roughness values corresponds to combination of low cutting speed and high values of laser power and assist gas pressure. Combination of the low cutting speed and high laser power produce higher heat input generating higher melt volume. Moreover, higher levels of assist gas (oxygen) pressure affect hydrodynamics of the molten metal flow and also result in increased exothermic-induced burning of the cut surface. These effects in sum deteriorate surface quality of the laser cut.

On the other hand minimal surface roughness values correspond to either low

---

levels of laser power and assist gas pressure and high level of cutting speed or high levels of all three cutting factors. Not only in the case of minimal roughness values, it can be observed that certain surface roughness values can be obtained with a drastically different combinations of laser cutting factor values and this is consequence that the third order interaction term is significant and is included in the model.

The obtained results clearly indicate a very complex nature of surface roughness formation in laser cutting and the need of development of mathematical models for its prediction for each workpiece material and thickness, given laser cutting method and selection laser cutting experimental hyper-space.

Finally, the developed model was used to estimate surface roughness values for laser cutting regimes which were not used in experimentation. Two combinations of laser cutting factor values were tested:

Combination 1: Cutting speed = 5 m/min, laser power = 1.1 kW and assist gas pressure = 7 bar, or in terms of coded factor values (x_1=0, x_2=0, x_3=1), produced surface roughness value of R_a=2.26 µm, and

Combination 2: Cutting speed = 3 m/min, laser power = 1.3 kW and assist gas pressure = 3 bar, or in terms of coded factor values (x_1=0, x_2=0, x_3=1), produced surface roughness value of R_a=1.44 µm

a)

b)
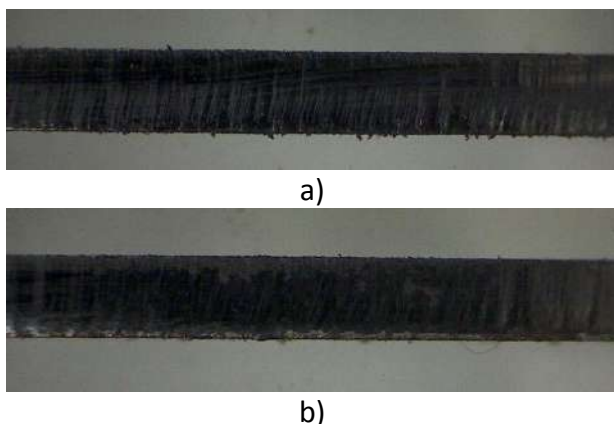
Figure 4. Cut surface patterns obtained in validation trials a) combination 1, b) combination 2

The prediction error between predicted and experimentally measured surface roughness value were obtained around 5% which further confirms the validity of the developed model.

The cut surface patterns obtained under these conditions are given in Fig. 4.

4. CONCLUSION

This study presented the design of experiments approach for analysis and modeling of surface roughness in CO_2 laser cutting of mild steel using oxygen as assist gas. Cutting speed, laser power and assist gas pressure were considered in the experiment that was planned according to the 2^3 factorial design with central points.

From the analysis of obtained results the following conclusions can be drawn:

- Cutting speed and assist gas pressure main effects predominantly affect surface roughness.
- Interaction effect of laser power and assist gas pressure is negligible, however, the three-way interaction of laser power, assist gas pressure and cutting speed has considerable effect on surface roughness.
- The developed quazi-linear model accurately relates surface roughness and laser cutting factors in the covered experimental hyper-space and can be used as a basis for further investigations of surface roughness.

Formulation and solving single and multi-objective laser cutting problems considering surface roughness as functional constraint is future research scope.

REFERENCES

[1] M. Madić, M. Radovanović, Ž. Ćojbašić, B. Nedić, M. Gostimirović: Fuzzy logic approach for the prediction of dross formation in CO_2 laser cutting of mild steel, Journal of

Engineering Science and Technology Review, Vol. 8, No. 3, pp. 143-150, 2015.

[2] R. Čep, Š. Maltová, M. Pagáč, M. Sadílek, J. Lichovník: Parameters influence of CO_2 laser on cutting quality of polymer materials, Transactions of the VŠB - Technical University of Ostrava, Mechanical Series, Vol. 50, No. 1, pp. 9-16, 2016.

[3] M. Madić, M. Radovanović, L. Slătineanu, O. Dodun: Optimization of laser cut quality characteristics considering material removal rate based on Pareto concept, Applied Mechanics and Materials, Vol. 657, pp. 216-220, 2014.

[4] A.F.M. Tahir, A.R. Rashid: Experimental evaluation of CO_2 laser cutting quality of UHSS using oxygen as an assisted gas, Jurnal Teknologi, Vol. 78, No. 7, pp. 69-73, 2016.

[5] S.K. Singh, S. Gangwar: Parametric optimization of cutting parameters of laser assisted cutting using Taguchi analysis and genetic algorithm, i-Manager's Journal on Future Engineering and Technology, Vol. 11, No. 3, pp. 36-42, 2016.

[6] H.A. Eltawahni, M. Hagino, K.Y. Benyounis, T. Inoue, A.G. Olabi: Effect of CO_2 laser cutting process parameters on edge quality and operating cost of AISI316L, Optics and Laser Technology, Vol. 44, No. 4, pp. 1068-1082, 2012.

[7] A. Cekic, D. Begic-Hajdarevic: Definition of mathematical models of high-alloyed steel 1.4828 in CO_2 laser cutting, Procedia Engineering, Vol. 100, pp. 435-444, 2015.

[8] A.M. Orishich, A.G. Malikov, V.B. Shulyatyev, A.A. Golyshev: Experimental comparison of laser cutting of steel with fiber and CO_2 lasers on the basis of minimal roughness, Physics Procedia, Vol. 56, pp. 875-884, 2014.

[9] E. Librera, G. Riva, H. Safarzadeh, B. Previtali: On the use of areal roughness parameters to assess surface quality in laser cutting of stainless steel with CO_2 and fiber sources, Procedia CIRP, Vol. 33, pp. 532-537, 2015.

[10] R. Horváth, A. Drégelyi-Kiss, G. Mátyási: Application of RSM method for the examination of diamond tools, Acta Polytechnica Hungarica, Vol. 11, No. 2, pp. 137-147, 2014.

[11] D.C. Montgomery: *Design and Analysis of Experiments*, John Wiley and Sons, New York, 2008.

THE TECHNIQUE OF DESIGNING AND CALCULATING TRIBOCONTACT OF THE MATING MACHINE PARTS IN THE EQUILIBRIUM STATE

Vyacheslav F. BEZJAZYCHNYJ, Alexey N. BOLOTEIN, Alexander N. SUTYAGIN

Federal State-Financed Educational Institution of High Education "P. A. Solovyov Rybinsk State Aviation Technical University", Rybinsk, Yaroslavl region, Russian Federation,
*Corresponding author: technology@rsatu.ru

Abstract: The article describes the features of contact interaction of the mating machine parts without lubricant considering power and thermal factors, allowing carrying out the design and calculation of tribocontact in step of design and technological preparation of production. The description of an approach for determining the value of the equilibrium parameters of the quality of the surface layer in order to reduce the duration of the break-in period of mating parts in units of new products is presented. The operation of the software implemented on the basis of the developed mathematical model of the visualization of topography of the machined surface, as well as its change as a result of the break-in period is shown.

Keywords: friction, wear rate, machining, quality parameters, equilibrium state.

1. INTRODUCTION

At present, in connection with the intensive development of means for measuring the geometrical parameters of the surfaces of parts, a growing number of methods and techniques for measuring, and, together with them, software products. There are new possibilities of measuring systems; therefore the number of parameters describing the surface of a part also increases. The task of measuring and visualizing the surface relief of micro objects is extremely relevant in various fields of science and industry. Methods for measuring and visualizing the surface relief using computerized optical complexes require large calculations and were implemented only at the current level of computer technology. The software requires an increase in the amount of hardware resources and is continuously complicated. To perform high-precision measurements, high-quality software products are required, so now special standards in the field of software quality are developed.

2. THE STUDIED MATHEMATICAL MODEL

According to ISO 25178-2 the set of measured data of the height of surface irregularities in the volume on the basis of the introduced standards is proposed to be analyzed and described by the autocorrelation function f_{ACF} (t_x, t_y) (Fig. 1). This function describes the correlation between the surface and a similar surface transformed by analysis of the set of points (t_x, t_y) (1):

$$f_{ACF}(t_x, t_y) = \frac{\iint\limits_A z(x,y)z(x-t_x, y-t_y)\,\mathrm{d}x\,\mathrm{d}y}{\iint\limits_A z(x,y)z(x,y)\,\mathrm{d}x\,\mathrm{d}y}, \quad (1)$$

where $z(x, y)$ is the height of the surface with a limited scale at the position x, y, and the coordinate system is based on the reference surface; A is the domain of definition, (t_x, t_y) is the set of measured points.
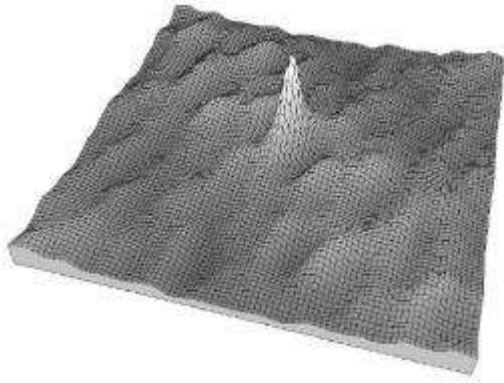

Figure 1. Function of autocorrelation

In addition, taking into account the Laplace transform, we can use the operator $F(p, q)$ which transforms a surface with a bounded scale into a Fourier space (2):

$$F(p,q) = \iint_A z(x,y)e^{-(ipx+ipy)}\,dxdy\,, \qquad (2)$$

where $z(x, y)$ is the height of the surface with a limited scale at the position x, y; p, q are complex numbers; A is the domain of definition.

Applying various kinds of data filters obtained from various equipment for scanning the surface of a part, it is possible to visualize the surface by means of both specialized software supplied with the measuring equipment and by using special software packages.

The classical process of modeling consists in the design of parts and products according to the nominal values of the geometric characteristics of length, width and height. In modern CAD/CAM/CAE systems, the surface roughness parameters are not taken into account in the form of generating surface coordinates, although in principle this possibility can be realized by constructing a surface by, for example, importing the coordinates of points from a file. In this case, there is a problem of positioning parts during the assembly of the product in the assembly file or in the file of the electronic model of the product.

Calculation of the coordinates of the points of surfaces cannot be carried out only on the basis of various models of the theory of probability, since the geometric parameters of the quality of the surface layer are directly dependent on the machining conditions, in particular, on the shaping motion during the processing of blanks.

The surface of a real machine part is largely different from the idealized geometric shape, which is depicted in the drawings. Surface roughness consists of deterministic irregularities due to the type of processing and random in size, shape and location of irregularities. The deterministic profile is characterized by a periodic combination of irregularities of a strictly defined shape, and can be described by a periodic function.

During machining there is influence on roughness from geometric characteristics of the cutting tool, value of feed, plastic deformation in chip formation zone, friction of the resulting surface against the surface of the cutting tool, elastic deformations arising during the machining, dynamic phenomena caused by vibrations during the machining, also the properties of machining coolant.

The process for the formation of the machined surface occurs as a result of successive passage of the cutting tool along the surface of the workpiece in the direction of the speed V, each successive pass being shifted from the previous one by the feed amount S. Thus, a transverse roughness is formed in the cross-section in the feeding direction.

The parameters of the transverse roughness are determined on the basis of the geometrical parameters of the cutting tool: the radius at the vertex r, the angles in the plan φ and φ_1, and the feed amount S.

Consider a square wave $f(x)$ of length $2L$. In the range $[0, 2L]$, this can be described by an expression of the form (3):

$$f(x) = 2[H(x/L) - H(x/L - 1)] - 1\,, \qquad (3)$$

where $H(x)$ is the Heaviside function, x is the argument, and taking into account that the formation of the transverse roughness depends on the radius at the vertex r of the cutting tool, the angles in the plan φ and φ_1, the feed S, the cutting depth t, the cutting forces P_x and P_y, the cutting zone temperature Θ_p, for the function of transverse roughness for turning (4):

$$f_1(x) = F(t, P_x, P_y, r, \varphi, \varphi_1, \theta_p, S, x). \quad (4)$$

In addition to the transverse roughness, there is a longitudinal roughness measured in the direction of the cutting speed due to the oscillations of the technological system, as a consequence of the rigidity of the technological system j, as well as the cutting speed v, the front γ and the posterior α angle of the cutting tool, cutting forces P_z and P_y, temperature in the cutting zone Θ_p. In addition, the longitudinal roughness can be influenced by errors associated with the wear and tear of equipment, for example, the spindle of the machine.

Longitudinal roughness can be represented by a pseudo-random number algorithm that is based on the Box-Muller transformation or described by the transition function to the general normal distribution after obtaining the standard normal random profile value, which allows the generation of a normal random variable to be completed.

In this case, for the longitudinal roughness function for turning (5):

$$f_2(y) = F(j, P_z, P_y, \gamma, \alpha, \theta_p, v, R, \sigma, z, y) \quad (5)$$

where z is the surface roughness value due to the action of random factors, σ is the intensity of the impact of random factors on the longitudinal roughness, or after the transformation, R is the radius of the workpiece.

On the basis of the functions (4) and (5), specialized software was developed that allows generating the coordinates of the points of the surface of a workpiece machined by turning (Fig. 2) and forming a spectrogram of a rough surface (Fig. 3). Visualization of the obtained set of points for surface construction

can be realized in any CAD system based on the import of the coordinates of points from the file (Fig. 4).

Figure 2. A fragment of the specialized software for generating the coordinates of the points of the surface of a workpiece
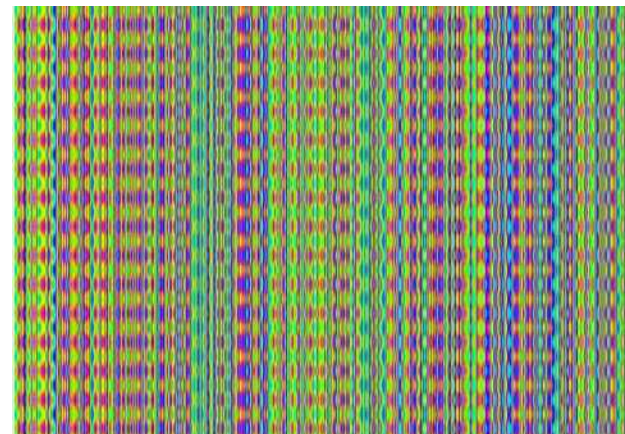
Figure 3. Forming a spectrogram of a rough surface by means of specialized software

The normalization of the parameters of the surface roughness of the workpiece is directly related to application conditions. Roughness determines not only such performance properties as fatigue strength, wear resistance, contact stiffness, but also is closely related to the mechanical properties of the surface layers. Surfaces contact of machine parts is discrete.
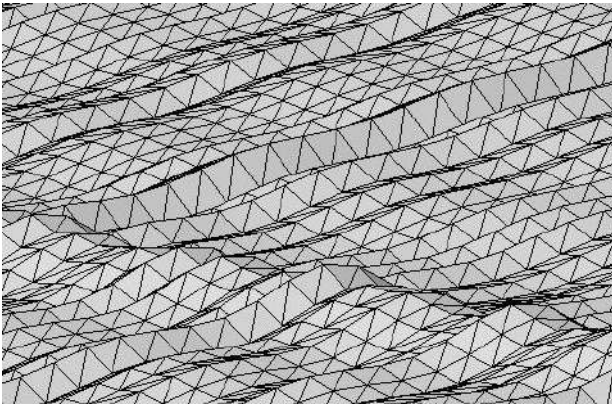
Figure 4. Visualization of the obtained set of points of a surface of a part, processed by turning, in CAD KOMPAS-3D

The ratio of the nominal area of contact to the actual depends on the load and often is about fraction of a percent. In the process of compression, various surface protrusions are being under the different stresses. The protrusions, originally located farther from the opposite surface, have lower stresses, and those located closer to the surface of the pressed counter body are larger. Specific pressures are obtained commensurate with the hardness of the material and can exceed the hardness of the harden material by up to 3-5 times.

Research the wear can provide a theoretical justification of the possibility of existence of stable reproducing geometric shapes of surfaces and their physical and mechanical properties in wear process in the given conditions of relative motion and loading. Thus, equilibrium parameters of the quality of the surface layer are formed, which conformal are reproduced during the period of normal operation of the unit.

For surfaces of parts machined by turning, the functions of the transverse and longitudinal roughness can be represented in the first approximation by equations (4) and (5); an algorithm can be offered to visualize changing of roughness of the contacting surfaces during operation. Such an algorithm can be implemented in the software of both static and dynamic representation of the contact of surfaces. Fragment of the work of the developed software for generating the coordinates of the points of the surface of the part after run-in is shown (Fig. 5).
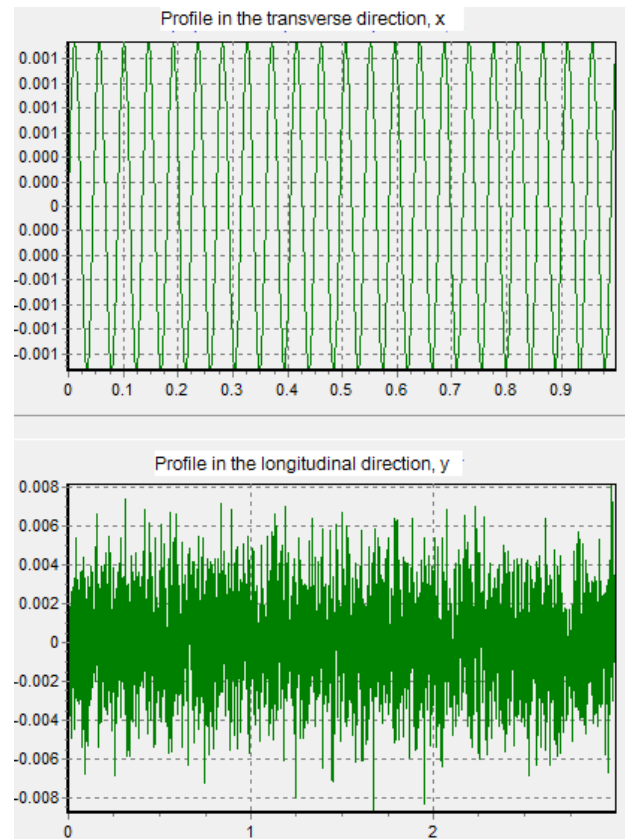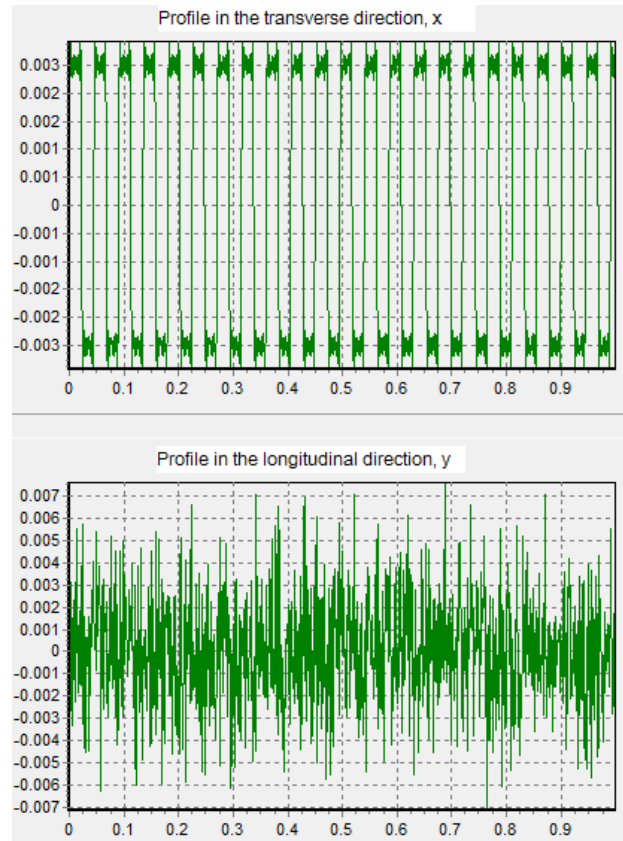

**Figure 5.** A fragment of the specialized software for generating coordinates of the points of the surface of the part after the run-in

Forming a spectrogram of a rough surface after the run-in by means of specialized software is shown on figure 6.
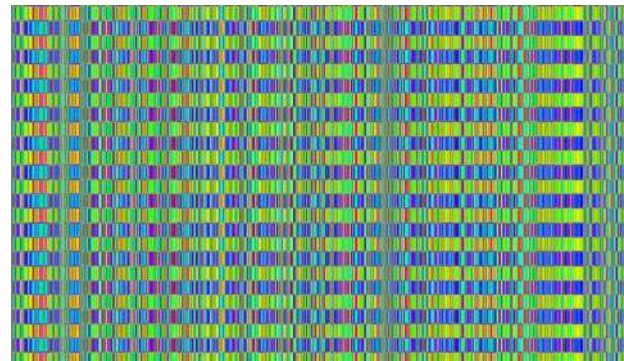
Figure 6. Forming a spectrogram of a rough surface after the run-in by means of specialized software

The view of the combs of irregularities in the contact zone according to the developed algorithm is satisfactory. To visualize the obtained set of points of the used surface of a part, CAD KOMPAS-3D was used based on the import of the coordinates of points from the file (Fig. 7). Profile of the surface has acquired brightly expressed contact areas similar to those shown in the photograph of the real

surface after the run-in, performed with an increase of 40.
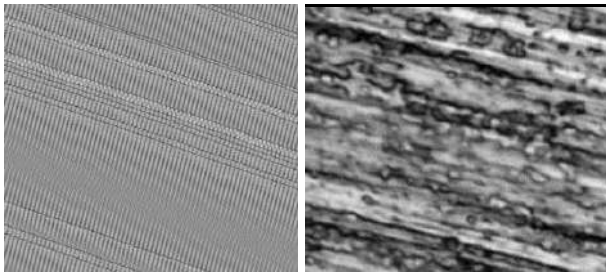
Figure 7. Visualization of the obtained set of points of the run-in surface of a part in CAD KOMPAS-3D and comparison with the photograph of the real surface of the part after running-in (increase 40)

Based on the foregoing, it is possible to present an algorithm for calculating the equilibrium 3D roughness in the following form (Fig. 8).
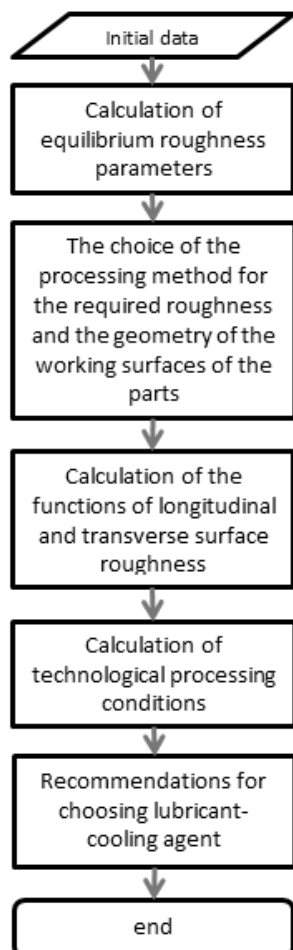
Figure 8. Algorithm for calculating the equilibrium 3D roughness

As initial data the conditions of operation of parts in the friction unit, the physical and mechanical properties of the materials of the mating parts are taken into account. The calculation of the parameters of the equilibrium roughness can be performed using the dimensionless Kragelsky-Kombalov criterion. Based on the calculated value of the parameter of the equilibrium roughness and the geometry of the working surfaces of the parts, a choice is made of the processing method: turning, milling, grinding etc. Next, the longitudinal and transverse surface roughness functions are calculated from equations (4) and (5). Calculation of technological processing conditions is performed on the basis of known design dependencies for selected methods of surface treatment of the workpiece. Depending on the method and processing modes, recommendations for choosing lubricant-cooling agent are offered.

3. CONCLUSION

The main factors influencing the formation of three-dimensional roughness are revealed, and the basic equations for calculating the longitudinal and transverse roughness's of the surfaces of parts obtained by turning are presented on the basis of ISO 25178-2.

The obtained mathematical models describing the roughness of the treated surface in the three-dimensional measurement are implemented algorithmically in the developed software, allowing visualizing the pattern of the formation of a rough surface obtained by machining.

REFERENCES

[1] V. F. Bezjazychnyj: *Metod podobija v tehnologii mashinostroenija* (Method of Similarity in mechanical engineering), Mashinostroenie, Moscow, 2012
[2] A. V. Chichinadze, E. D. Brown, N. A. Boucher,*Osnovy tribologii (trenie, iznos, smazka)* (Fundamentals of tribology (friction, wear and lubrication)), - Mashinostroenie, Moscow, 2001.

PREDICTION OF SURFACE ROUGHNESS IN PLASMA JET CUTTING PROCESS USING NEURAL NETWORK MODEL

Ivan PEKO[1], Bogdan NEDIĆ[2], Aleksandar ĐORĐEVIĆ[2], Stefan ĐURIĆ[2], Dragan DŽUNIĆ[2], Ivica VEŽA[1], Marko JANKOVIĆ[2]

[1]University of Split, Faculty of Electrical Engineering, Mechanical Engineering and Naval Architecture, Split, Croatia,
[2]University of Kragujevac, Faculty of Engineering, Kragujevac, Serbia
*Corresponding author: ipeko@fesb.hr

Abstract: Plasma Jet Cutting process is one of the most important nonconventional machining methods that uses a thermal energy of highly ionized gas to cut specified material. Its optimal combination of cut quality, productivity and costs in cutting various types of materials increase its demand in the market and usually position it in front of the other cutting processes. This process is controlled by technological parameters recommendations given by the manufacturers of the cutting equipment. These parameters recommendations usually do not lead to optimal cut quality but refer to manufacturers' business targets. Accordingly, various experimental researches have been done trying to describe process and define technological parameters levels that lead to optimal cut quality. In this paper, mathematical model for prediction of surface roughness in plasma jet cutting process was developed. Process parameters whose influence was analyzed are cutting speed and arc current. Experiments were conducted according to Taguchi L9 orthogonal array design on aluminium sheet thickness of 3 mm. Mathematical model was created using a single hidden layer artificial neural network trained with the Levenberg-Marquardt algorithm. Prediction accuracy of developed model was verified using statistical measures such as Mean Squared Error (MSE) and correlation coefficient (R) between experimental and predicted values. To analyze the main and interaction effects of the plasma cutting parameters on the surface roughness 2D and 3D diagrams were generated from which optimal cutting regions were identified.

Keywords: plasma jet cutting, experiments, surface roughness, neural networks, modeling

1. INTRODUCTION

Plasma jet cutting process is a nonconventional thermal process that uses an energy of highly ionized gas injected into an electric arc to cut various materials such as mild steel, stainless and aluminium at various thicknesses. Advantages that characterize this cutting process and position it in front of the other nonconventional processes are competitive investments, high productivity, long consumables life and lower costs per part. Working with plasma jet cutting systems is usually supported by machinery manufacturers recommendations. Because of process complexity it is not simple to obtain best cut results just by using these recommendations. It is necessary to conduct a comprehensive researches trying to analyze influences of process parameters on cut

surface quality and to find their values that lead to optimal results. In the last few years examinations about plasma jet cutting process and obtained cut surface quality have been occupation of many reserchers.

Kumar Das et al. [1] conducted experiments on EN31 steel and investigated influence of process parameters such as gas pressure, arc current and torch height on material removal rate and surface roughness characteristics. Their experimental results were analyzed through ANOVA and grey relational analysis. Bini et al. [2] analyzed influence of arc voltage, cutting speed, plasma gas flow rate, shield gas flow rate and shield gas composition on kerf position and shape in cutting of 15 mm thick mild steel plates. ANOVA and Response Surface Methodology (RSM) were used for data analysis and optimization. Gullu et al. [3] investigated variations of structural specifications in heat affected zone that occur after cutting of AISI 304 stainless steel and St52 carbon steel, considering to cutting speed. Gariboldi et al. [4] conducted experiments on titanium sheets using high tolerance plasma arc cutting process. They investigated temperature and microstructural variations in the regions near to the cutting edge and geometric and surface atributes that occur under different process conditions such as using different feed rates and adoption of oxygen and nitrogen as cutting and shielding gases. Salonitis et al. [5] monitored cut quality by measuring the kerf conicity, the edge roughness and the size of the heat affected zone. Experiments were conducted on 15 mm thick S235 mild steel sheets by varying process parameters: cutting speed, cutting current, cutting height and plasma gas pressure. They used Taguchi method and RSM for data analysis and optimization. Chamarthi et al. [6] conducted experiments on 12 mm thick Hardox 400 plate and investigated influence of arc voltage, cutting speed and plasma gas flow rate on unevenness of cut surface. ANOVA and Design Expert software were used for results analysis and optimization. Nedic et al. [7] analyzed the cut quality in plasma jet cutting process using standard EN ISO 9013. They investigated the influence of arc current and cutting speed on surface roughness, kerf width, dross width and height of molten metal on the bottom edge of the cut in cutting 15 mm thick S235 steel plate. Radovanovic et al. [8] used artificial neural network (ANN) modeling approach to describe the influence of cutting speed, cutting current and plate thickness on surface roughness (Rz). Developed ANN model was used for generating contour plots which show optimal process parameters area. Peko et al. [9] conducted experiments on 15 mm thick structural steel S235 plate. They investigated the influence of cutting current and cutting speed on surface roughness (Ra). Artificial neural networks were used for mathematical modeling and optimization.

In present research paper experiments were conducted on aluminium alloy 5083 plate thickness of 3 mm. It was analyzed the influence of cutting speed and arc current on the cut surface roughness (Ra). Mathematical modeling was carried out using artificial neural networks.

2. PRINCIPLE OF PLASMA JET CUTTING

Plasma jet cutting process was developed at the end of 1950s. Plasma is a state of substance which is obtained by supplying a tremendous amount of energy to any gas or when a gas is subjected to a high electric field. In this process an electric arc is generated between the electrode and the work piece, where the electrode acts as a anode and work piece is taken as cathode. The plasma gas expands with the high velocity through the nozzle at the same time an electric current passes through this gas with the help of a tungsten electrode due to which a high intensity plasma jet is generated. In a nozzle there is a space between the outer periphery of the electrode and an inner periphery of the nozzle where the plasma gas get heated and ionized which leads the jet to expand in volume and pressure greatly. This jet has a sufficient energy to melt or vaporize the surface being cut and move very fast to flow the molten metal away from the cut [10] (Figure 1).

The basic plasma cutting system consists of a power supply, an arc starting circuit and a torch. These system components provide the electrical energy, ionization capability and process control that is necessary to produce high quality, highly productive cuts on a variety of different materials. Plasma cutting can be used to cut plates to 180 mm thick [8].
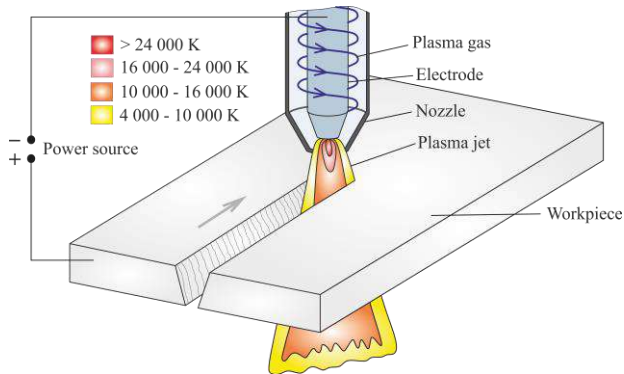

Figure 1. Plasma Jet Cutting process

3. EXPERIMENTAL PROCEDURE

Experimental work was conducted on a CNC FLAMECUT 2513 plasma jet cutting machine. Plasma jet cutting parameters considered in this paper are cutting speed (*v*) and arc current (*I*). These parameters were varied in the following ranges: cutting speed 2000-6000 mm/min, arc current 45-85 A on more levels (Table 1.). Parameters that were kept constant throughout the experimentation are: nozzle diameter of 1.2 mm, plasma gas pressure of 6 bar and cutting height of 1 mm. Specimens were cut on aluminium alloy 5083 plate thickness of 3 mm with the use of compressed air as plasma gas (Figure 2). In each experimental trial straight cut 80 mm in length was made and the cut quality was evaluated in terms of surface roughness (*Ra*) values. The *Ra* was measured using Talysurf Hobson 6 profilometer. Each measurement of surface roughness was taken in the middle of the cut surface height and in the middle of the cut length. The measurements were repeated three times to obtain average values. Experimental design matrix was constructed in accordance with the standard L_9 Taguchi orthogonal array (OA) (Table 2).
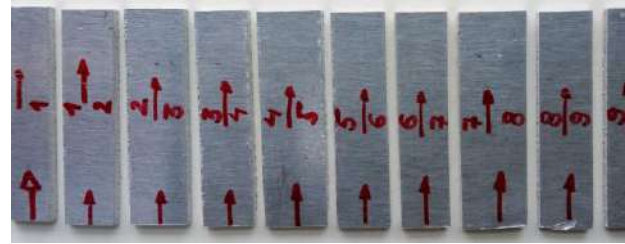
Figure 2. Plasma jet cut specimens prepared for surface roughness measurement

Table 1. Plasma jet cutting parameter values

Parameter	Unit	Level		
		1	2	3
Cutting speed, v	mm/min	2000	4000	6000
Arc current, I	A	45	65	85

Table 2. Experimental plan and results

Exp. trial	Process parameters		Experimental results
	Cutting speed, v [mm/min]	Arc current, I [A]	Surface roughness, Ra [µm]
1	2000	45	15.3
2	2000	65	17.7
3	2000	85	19.3
4	4000	45	13.2
5	4000	65	7.4
6	4000	85	13.0
7	6000	45	10.6
8	6000	65	8.9
9	6000	85	5.5

4. MATHEMATICAL MODELING

To analyze the effects of the plasma jet cutting process parameters on the surface roughness a mathematical modeling should be preformed. Mathematical model enables an estimation of surface roughness values obtained with any combination of cutting process parameters. Although the mathematical models obtained by regression analysis are very promising for various applications, it was shown that artificial neural

networks offer better data fitting capability than regression models for complex processes with many non-linearities and interactions such as plasma jet cutting process. Artificial neural networks are able to learn the key information patterns within multidimensional information domain and can be used in modeling of complex physical phenomena [11, 12]. Therefore, in this paper a mathematical model for prediction of surface roughness was developed using artificial neural netwoks.

To describe the relationship between surface roughness (*Ra*) and input process parameters: cutting speed (*v*) and arc current (*I*) a feed-forward backpropagation artificial neural network was selected. Two neurons in the input layer (for the each of input process parameters), one neuron in the output layer (for the surface roughness response) and one hidden layer were selected to define ANN architecture (Figure 3). Hidden layers have a function to map a complex relations between inputs and outputs of ANN model. In this case single hidden layer was chosen because it was concluded that such neural network architecture is appropriate to model each relationship between process parameters and performance measures in engineering problems [13, 14, 15, 16]. Aiming to find the simplest ANN model that has the total prediction error considerably low it was decided that number of hidden neurons will be three.
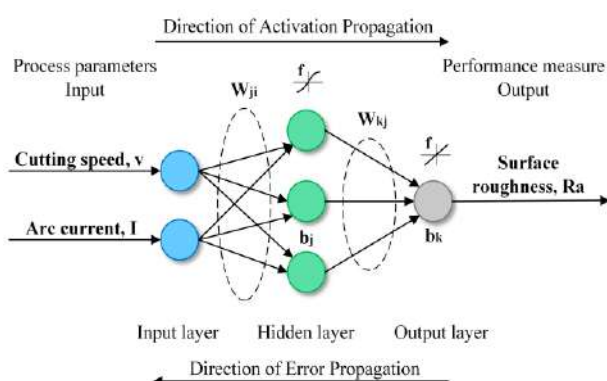
Figure 3. Selected feed-forward backpropagation ANN architecture

Before training the experimental data were normalized in the range [-1,1] and randomly divided into three subsets, for training (50%),

for validation (25%) and for testing (25%). Hyperbolic tangent sigmoid and linear transfer functions were used in the hidden and output layer, respectively. Prior to ANN training initial values of weights were set according to Nguyen-Widrow method. Training was performed using Levenberg-Marquardt backpropagation algorithm with momentum.

The mean squared error (MSE) was selected as the performance measure of the ANN training process. That is the average squared difference between predicted and experimental values. The goal is to get MSE as close as possible to zero. The training process was stopped when no further improvements in performance was achieved and by considering the well known bias-variance compromise in neural network model development [11]. Another measure of developed model accuracy is the correlation coefficient (R). It shows the strength of correlation between predicted values and actual data. Good ANN model should have R values ≥0.8 [17]. MSE and R values of developed ANN model were given in Table 3 and in Figure 4.

Table 3. MSE values for ANN model

Number of epochs: 5			
	Train	Validation	Test
MSE	0.067	0.015	0.100

R (Train) = 0.91, R (Validation) = 1, R (Test) = 1

Figure 4. Correlation between experimental and ANN predicted values

5. RESULTS AND DISCUSSION

According to MSE and R values it can be concluded that developed model has good prediction accuracy and it can be used further to analyze the effects of cutting process parameters on the surface roughness response. The effects of individual process parameters were show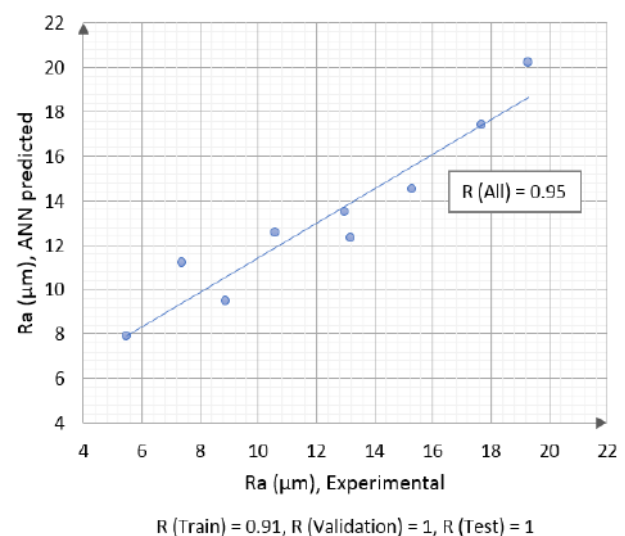n in Figure 5 and Figure 6 by changing one parameter while keeping other parameter constant at center level - level 2. Influence of parameters interaction was shown in Figure 7.

From next figures it can be observed that surface roughness is quite sensitive to selected process parameters. It is obvious that increase in the cutting speed results in a decrease of surface roughness. This decrease is more expressed at higher currents. On the other side the arc current has a different influence on surface roughness considering cutting speed values. At lower cutting speed values (<4000 mm/min) an increase of arc current leads to increase of surface roughness while at higher cutting speed values (>5000 mm/min) lower arc current results in a slight increase of surface roughness. From Figure 7 optimal cutting parameters region can be defined. That would be process under cutting speed values >5000 mm/min and arc current values >65 A. These ranges result in the minimal cut surface roughness.
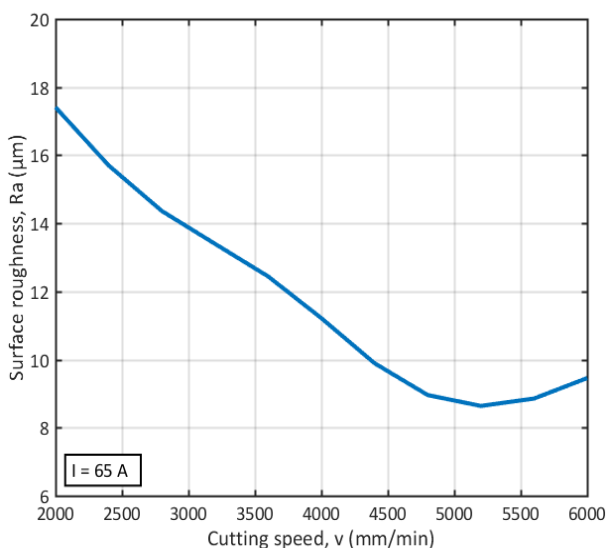
Figure 5. The effect of cutting speed (*v*) on surface roughness (*Ra*)
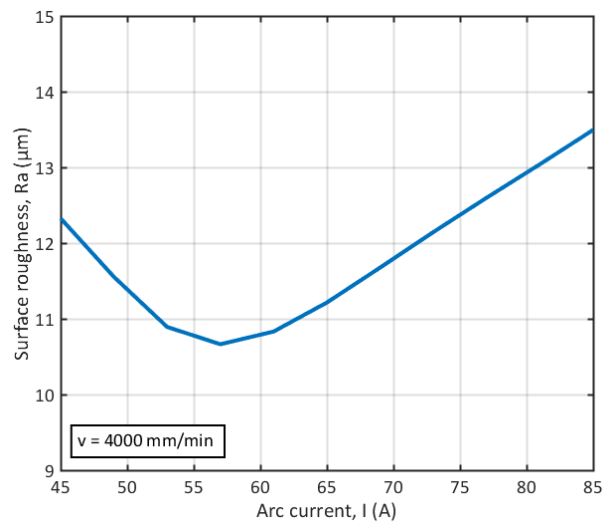
Figure 6. The effect of arc current (*I*) on surface roughness (*Ra*)
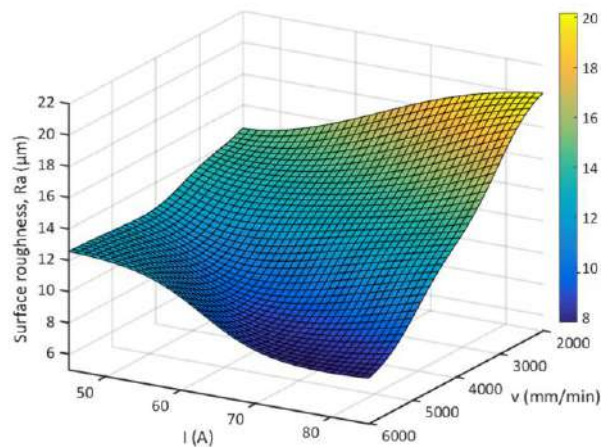
Figure 7. The effect of parameters interaction on surface roughness (*Ra*)

6. CONCLUSION

Plasma jet cutting process is a nonconventional thermal process that has wide industrial application and many competitive benefits. Identification of process parameters that lead to optimal cut surface quality has been in a research focus of many authors. In this paper prediction of surface roughness in cutting of aluminium plate using artificial neural network model was performed. Prediction accuracy of developed model was validated using statistical measures. According to these indicators the model has proven to be effective for further anaylsis of process parameters effects on surface roughness and to define optimal cutting region. This region

includes parameters values: cutting speed >5000 mm/min and arc current >65 A. Future research will be oriented towards improvement of the developed model incorporating more experimental data either as comparison of prediction capabilities different mathematical modeling approaches.

ACKNOWLEDGEMENT

REFERENCES

[1] M. Kumar Das, K. Kumar, T. K. Barman, P. Sahu: Procedia Materials Science: Optimization of process parameters in plasma arc cutting of EN31 steel based on MRR and multiple roughness characteristics using grey relational analysis, Vol. 5, pp. 1550-1559, 2014.

[2] R. Bini, B. M. Colosimo, A. E. Kutlu, M. Mono: Journal of Materials Processing Technology: Experimental study of the features of the kerf generated by a 200 A high tolerance plasma arc cutting system, Vol. 196, pp. 345-355, 2008.

[3] A. Gullu, U. Attici: Materials and Design: Investigation of the effects of plasma arc parameters on the structure variation of AISI 304 and St 52 steels, Vol. 27, pp. 1157-1162, 2006.

[4] E. Gariboldi, B. Previtali: Journal of Materials Processing Technology: High tolerance plasma arc cutting of commercially pure titanium, Vol. 160, pp. 77-89, 2005.

[5] K. Salonitis, S. Vatousianos: Procedia CIRP: Experimental investigation of the plasma arc cutting process, Vol. 3, pp. 287-292, 2012.

[6] S. Chamarthi, N. Reddy Sinivasa, M. Elipey Kumar, D. V. Reddy Ratmana: Procedia Engineering: Investigation analysis of plasma arc cutting parameters on the unevenness surface of Hardox 400 material, Vol. 64, pp. 854-861, 2013.

[7] B. Nedic, M. Jankovic, M. Radovanovic, G. Globocki Lakic: Quality of plasma cutting, in: Proceedings of the International Conference on Tribology, 15-17.5.2013, Kragujevac, Serbia, pp.314-319.

[8] M.Radovanovic, M. Madic: Modeling the plasma arc cutting process using ANN, Nonconventional Technologies Review, Vol. 4, pp. 43-48, 2011.

[9] I. Peko, B. Nedic, A. Djordjevic, D. Dzunic, M. Jankovic, I. Veza: Tribology in Industry: Modeling of surface roughness in plasma jet cutting process of thick structural steel, Vol. 38, No. 4, pp. 522-529, 2016.

[10] K. N. Prajapati, H. R. Sathavara, D. K. Soni: International Journal of Advance Research in Engineering, Science and Technology: A review on plasma arc cutting, Vol. 2, No. 6, pp. 52-54, 2015.

[11] M. Madic, M. Radovanovic: International Journal of Physical Sciences: Comparative modeling of CO_2 laser cutting using multiple regression analysis and artificial neural network, Vol. 7, pp. 2422-2430, 2012.

[12] S. A. Fazeli, H. Rezvantalab, F. Kowsary: Thermal Science: Thermodynamic Analysis and Simulation of a New Combined Power and Refrigeration Cycle using Artificial Neural Network, Vol. 15, No. 1, pp. 29-31, 2011.

[13] M. J. Madic, M. Radovanovic: Thermal Science: Analysis of the heat affected zone in CO_2 laser cutting of stainless steel, Vol. 16, pp. S363-S373, 2012.

[14] K. Hornik, M. Stinchcombe, H. White: Neural Networks: Multilayer feedforward networks are universal approximators, Vol. 2, No. 5, pp. 359-366, 1989.

[15] G. Cybenko: Mathematics of Control, Signals and Systems: Approximation by superpositions of a sigmoidal function, Vol. 2, No. 4, pp. 303-314, 1989.

[16] S. Karagiannis, P. Stavropoulos, J. Kechagias: An aaplication of neural networks for prediction of surface texture parameters in turning, in: Proceedings of the International Conference on Neural Networks-Fuzzy Systems, 15-17.3.2014, Venice, Italy, pp. 80-84.

[17] M. Madic, M. Radovanovic: IMK-14 Istraživanje i razvoj: Methodology of neural network based modeling of machining processes, Vol. 17, No. 1, pp. 11-16, 2011.

NANO-STRUCTURAL STANDARD OF WEAR

Sergey Vasiliy FEDOROV[1]

[1]Kaliningrad State Technical University, Kaliningrad, Russia
*Corresponding author: fedorov@klgtu.ru

Abstract: At most full evolution of tribocontact the unique nanostructure (subtribosystems) is formed and the basis of which is one mechanical (nano) quantum. Mechanical quantum represents the least structural form of solid material body in conditions of friction. It is dynamic oscillator of dissipative friction structure and can be examined as the elementary nanostructure of metal's solid. At friction in state of most complete evolution of elementary tribocontact all mechanical quantums with the exception of one elasticity and reversibly transform energy of outer impact (mechanic movement). In these terms only one mechanical quantums is the lost – standard of wear. Some practical examples with using of mechanical quantum idea as standard of wear are considered.

Keywords: Tribocontact, evolution, nanostructure, elementary structure, wear, wear standard

1. INTRODUCTION

When exploitation of friction pair a contact is deformed and its states and properties are changed too. From the structural-energy interpretation of friction process point of view a contact of friction has evolution regularities. It is determined by competition of two opposite interrelated and simultaneous trends: growth of latent energy density u_e of various defects and damages which are generated and accumulated in the material due to work done by the external forces ω_p and reduction (release) of the density as a result of relaxation processes in deformed body element. The first trend is concerned with strain hardening and damage of material, the second — with dynamic recovery and dissipation of the strain energy which govern the thermal effect q of plastic deformation. During evolution contact process the size of wear particles are changed. Minimum wear has the contact at term of most full evolution. It is maximum adaptation. Minimum wear particle size should be considered as the standard of wear.

2. TRIBOERGODYNAMICS METHOD

This paper in its basis is a logical completion of axiomatic analysis of sliding friction (rolling) within the framework of triboergodynamics, a scientific trend suggested by the author [1-3].

The general evolution regularities of states and properties of tribosystem in the frame of triboergodynamics are analysed. Triboergodynamics is based on our modern knowledge of friction: 1. friction is a phenomenon of resistance to relative motion between two bodies, originating at their surfaces contact area; 2. friction is the process of transformation and dissipation of energy of external movement into other kinds of energy; 3. friction is the process of elasto-plastic

deformation, localized in thin surface layers of rubbing materials.

Methodology of triboergodynamics [1-3] is based on the analysis method to plastic deformation of ergodynamics of deformed solids [4]. Ergodynamics is a synthesis to the problem of deformation most general laws of thermodynamics for non-reversable processes, molecular kinetics and dislocation theory in their mutual, dialectical tie on the basis of a most general law of nature – the law of energy conservation at its transformations.

Within the framework of triboergodynamics the model of elastic-plastic deformation of contact volumes is examined as a generalized mechanism of transformation and dissipation energy and determines essence of resistance to surfaces displacement.

Friction is regarded as a global (energy) phenomenon of relative movement transformation. It strongly obeys equation of energy balance and from thermodynamic point of view it is a competition of two simultaneous, interconnected and opposite tendencies of accumulating latent (potential) energy ΔU_e of various kinds of defects and damages of contact volumes structures and releasing (dissipation) energy Q due to various relaxation processes.

According to the energy balance scheme (Figure 1) for plastic deformation and fracture [2,4] presented below, equations for friction work W_f , frictional force F and friction coefficient μ (without lubrication) has view

$$W_f = \Delta U_e + Q =$$

$$= \Delta U_{e_1} + \Delta U_{e_2} + \Delta U_{T_1} + \Delta U_{T_2} + \vec{Q}_1 + \vec{Q}_2 , \quad (1)$$

$$\dot{W}_f = \dot{U}_e + \dot{Q} =$$

$$= \dot{U}_{e_1} + \dot{U}_{e_2} + \dot{U}_{T_1} + \dot{U}_{T_2} + \dot{\vec{Q}}_1 + \dot{\vec{Q}}_2 , \quad (2)$$

$$F_l = \frac{\Delta U_e}{l} + \frac{Q}{l} = \frac{\Delta U_{e_1} + \Delta U_{e_2}}{l} + \frac{Q_1 + Q_2}{l} , (3)$$

$$F_v = \frac{\dot{U}_{e_1} + \dot{U}_{e_2}}{v} + \frac{\dot{Q}_1 + \dot{Q}_2}{v} =$$

$$= F_{mechanical} + F_{molecular} , \quad (4)$$

$$\mu_l = \frac{\Delta U_{e_1} + \Delta U_{e_2}}{Nl} + \frac{Q_1 + Q_2}{Nl} =$$

$$= \mu_{adapt} + \mu_{dis} = \mu_{adapt} + \mu_{T(dis)} + \mu_{\bar{Q}(dis)} , \quad (5)$$

$$\mu_v = \frac{\dot{U}_{e_1} + \dot{U}_{e_2}}{Nv} + \frac{\dot{Q}_1 + \dot{Q}_2}{Nv} =$$

$$= \mu_{deformation} + \mu_{adhesion} , \quad (6)$$

where $\Delta U_e = V_f \Delta u_e$; $Q = V_f q$; $\vec{Q} = V_f \vec{q}$; $\dot{U}_e = V_f \dot{u}_e$; $\dot{u}_e = \mathrm{d}u_e / \mathrm{d}t$ - is the rate of latent energy density change in the contact volumes; V_f - is the deformable (friction) volume; μ - friction coefficient; μ_{adapt} - adaptive friction coefficient; $\mu_{T(dis)}$ and $\mu_{\bar{Q}(dis)}$ - static and dynamical components of dissipative friction coefficient; ΔU_T - thermal component of internal energy; N - normal load; l - distance of friction; v -sliding velocity. The latent energy density Δu_e is an integral parameter of tribostate and damageability (failure (Δu_e^*)).

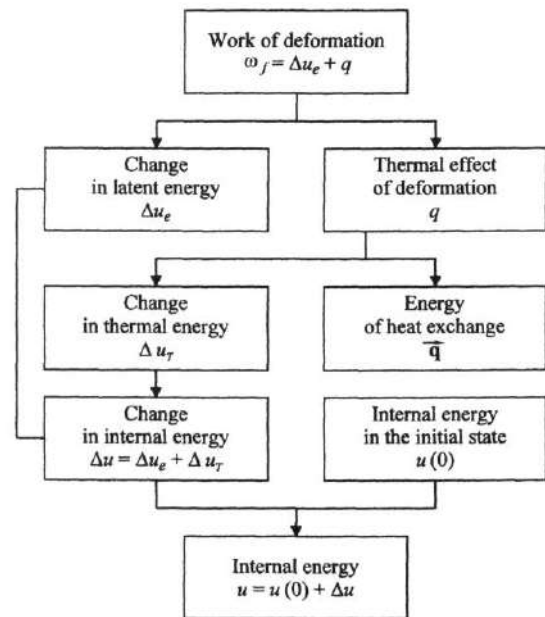**Figure 1.** Scheme of the energy balance for the plastic deformation of a solid body [1-4]

Thus, viewed thermodynamically [1-3], the work done by friction forces W_f (the friction power $\dot{W}_f$), the friction force F and the friction coefficient μ may be classified conventionally into two specific components with different kinetic behavior [4-6]. The first component is associated with microscopic

mechanisms of adaptive type and relates to the change of latent (potential) energy ($\Delta u_{e1}, \Delta u_{e2}$) of various elementary defects and damages that are generated and accumulate in the deformable volumes of materials friction pair (Figure 2). This energy is a unique and integral characteristic of the submicro- and microstructural transformations that occur in plastically strained materials [4-6]. This energy is a measure of strain hardening and damageability of materials. The second component is associated with microscopic mechanisms of dissipative type and relates to dynamic recovery processes in which latent energy is released and heat effect of friction (q_1, q_2) take place. This energy originates in the motion and destruction of various elementary defects of opposite signs, the egress of these defects to the surface, the healing of reversible submicroscopic discontinuities, etc. The ratios of the components Δu_{e1} and Δu_{e2} as well as q_1, q_2 of the balance vary over a wide range, depending on the physical, chemical, and structural properties of the materials that comprise the friction couple and the friction process conditions.
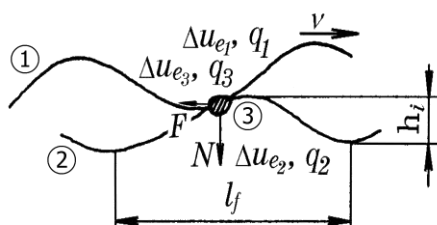

Figure 2. Schematic view of elementary friction's contact [1]

Thus, the thermodynamic analysis of friction (plastic deformation and fracture) has led to generalized (two-term) relations (1)-(6) for the force F and coefficient of friction μ, which agrees with current concepts of the nature of friction.

Relationships (1)-(6) which generalize the mechanism of energy dissipation at friction allow classify the tribosystem states. According to ergodynamics of deformed solids (relationships $\Delta u = \Delta u_e + \Delta u_T$ and

$q = \Delta u_T + \vec{q}$) and equations (1)-(6), all exhibitions of friction and wear may be reduced conventionally at least to two basically different states: the first state defines all types of damage and wear, the second — the so-called "wearless" condition. The state of damage and wear is characterized by the components of energy balance (1)-(6), which are responsible for accumulation of internal energy $\Delta u = \Delta u_{e1} + \Delta u_{e2} + \Delta u_{T1} + \Delta u_{T2}$ in deformed volumes, i.e. the process is irreversible. The "wearless" state is characterized by the components responsible for dynamic dissipation (reversibility) of strain energy into elastic and structural dissipated energy $\vec{q} = \vec{q}_1 + \vec{q}_2$ of friction contact.

In its turn, the first state may be classified depending on the relation between potential Δu_e and kinetic Δu_T components of internal energy. It is subdivided conventionally into mechanical damage and wear (due to so-called structure activation) and thermal damage and wear (due to thermal activation). For instance, let the thermal component of internal energy Δu_T be equal to zero ($\Delta u_T = 0$) and the internal energy variation at damage and wear be defined only by variation of the potential $\Delta u_e (\Delta u = \Delta u_e)$ component. Then, the mechanical damage and wear with brittle fracture of surfaces take place. On the contrary, if we have $\Delta u_e = 0 (\Delta u = \Delta u_T)$, then the thermal damage and wear with ductile fracture of surfaces take place. All the intermediate values of the components are associated with quasi-brittle or quasi-ductile fracture of solids.

In the most general case, the energy balance at dry friction (1) should be written as

$$W_f = \Delta U_{e1} + \Delta U_{e2} + \Delta U_{e3} + Q_1 + Q_2 + Q_3 \quad . \quad (7)$$

In the special case, where the friction is localized into volume of the "third body" equation (7) develops into

$$W_f = \Delta U_{e3} + \vec{Q}_3. \quad\quad (8)$$

According to thermodynamic theory of strength [4], the damageability parameter and

the fracture criterion are defined in terms of the internal energy density u accumulated within the strained element of a solid body. A solid body is assumed to suffer fracture if the internal energy density has reached a critical value u^* in at least a single macrovolume that is responsible for fracture.

3. ENERGY INTERPRETATION OF LEONARDO DA VINCI (AMONTON'S) FRICTION COEFFICIENT

According to thermodynamic theory of strength [4], the structure parameter should be related to the portion of the accumulated plastic deformation that is responsible for strain hardening. This portion is uniquely and integrally defined by the density of the potential component of internal energy (that is, the latent energy Δu_e density) of various defects and damages that accumulate in a plastically strained material. With this in mind, if we neglect the heat effect Q of friction, one will infer from the thermodynamic analysis of friction of equations (1)-(6) that the Amonton (Leonardo da Vinci) friction coefficient is

$$\mu = \frac{\Delta U_e}{\mu^* N l} = \frac{F}{N}; \; F = \frac{\Delta U_e}{l}; \; Q \cong 0, \; \mu^* = 1. \quad (9)$$

Consequently, the coefficient of friction has a very deep physical sense. On the one hand, it is the parameter which generally characterizes the resistance of relative displacement (movement) of surfaces, for it reflects the portion of energy, which «is done by friction away» as accumulated latent energy ΔU_e, by relation to parameter of external forces work $\mu^* N l$ (energy of external relative movement). On the other hand, it is the generalized characteristic of damage, for it is defined of the latent energy density Δu_e as integral characteristic of the structure defectiveness measure, because this energy is the generalized parameter of damage. Here too, coefficient of friction generally reflects the structural order (disorder) of deforming contact volume, since the parameter $\Delta U_e = \Delta u_e V_f$ is defined of the energy of

defects and damages of different types, that are accumulated into contact volumes V_f solids.

Therefore, coefficient of friction is a true and generalized parameter of tribosystem state. From this conclusion we can say that the analysis of the evolution of the states of a tribosystem is primarily an analysis of the latent deformation energy accumulated within the contact friction volumes.

4. ENERGY REGULARITIES OF RUBBING SURFACES EVOLUTION

An analysis of modern experimental data using equations (1)-(9) has shown that the experimental friction curves of type $\mu = \mu(N,v)$ are the generalized friction curves that reflect the evolution (the change in the friction coefficient) of tribosystem.

We propose an energetic interpretation of the experimental friction curves $\mu = \mu(N,v)$ (Figure 3).
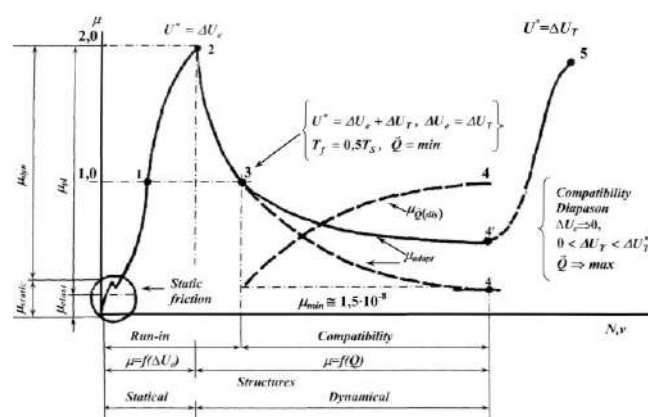
Figure 3. Structural-energy diagram for evolution of rubbing surfaces [1-3]. μ_{stat}; μ_{dyn}; μ_{elast}; μ_{plast} – static, dynamic, elastic, plastic friction coefficients correspondingly; T_f; T_s – ignition (flash) temperature in contact friction volume in point 3 and melting temperature.

According to our concept [1-3], the ascending portion of the friction coefficient curve μ is mainly controlled by processes associated with the accumulation of latent energy ΔU_e in various structural defects and damages. Here the increase in μ is due to the

increasing density of latent (potential) energy Δu_e and the increasing adaptive friction volume V_f. The descending portion of the friction curve is mainly controlled by processes associated with the release and dissipation of energy $Q = \Delta U_T + \vec{Q}$. Here the decrease in μ is due to the decrease in latent energy density within the friction volume V_f or (which is virtually the same) to the decrease of the adaptive friction volume V_{adapt} ($u_e = u_e^*$) and to the increase of the dissipative volume V_{dis} ($\vec{q}^* = u_e^*$).

Tribosystem evolution presented as a diagram (Figure 2), has adaptive-dissipative character (1) and reflects competitive (dialectical) nature of friction. Evolution curve has a set of principal points (1-5) of transitive states of tribosystem, which strongly obeys a balance principle of friction. The most characteristic areas between these points reflect general properties of its non-linear dynamics.

So, in Figure 2 it is possible to see the following conventionally designated points and stages: 0-1 – a stage of static friction and deformational strengthening; 1 – a point of limit for deformational strengthening; 1-2 – a stage of pumping of excess energy; 2 – a point of gripping (adhesion) and transition of outer friction into internal (critical non-stability): 2-3 – a stage of forming dissipation structures (formation of heat fluctuation in friction volume); 3 – a point of minimum compatibility (maximum frictionness); 1-2-3 - a stage of selforganization; 3-4 – a stage of compatibility; 4 – a point of wearlessness (anormal-low friction); 5 – a point of thermal adhesion.

An ideal evolution of tribosystem is symmetrical. The process starts and finishes within areas of elastic behavior. A plastic maximum (a superactivated condition) exists between them as a condition of selforganisation and adaptation.

In the most general case evolution (adaptation) regularities of tribosystems may be presented as a 2-stage (Figure 2). At the first stage (0-2) of adaptation the evolution of friction contact rushes to form some critical volume of friction V_f (point 2). It is elementary tribosystem that is the elementary and self-sufficient energy transformer. The first stage - latent energy density growth Δu_e to a limited magnitude Δu_e^* within critical friction volume V_f.

This friction volume V_f is constant at the second stage of evolution, but here it is evolutionary developed owing to structural transformation; by this one may realize wide spectrum of compatibility friction structures (Figure 3).

The second stage (2-4) – structural transformation of critical friction volume (elementary tribosystem) V_f into adaptive V_{adapt} and dissipative V_{dis} volumes. The limit (point 4) of this stage is characterized by a full transformation of adaptive critical volume V_{adapt}^* into V_{dis}^* dissipative.

The volumes mentioned above characterize different regularities of transforming energy of outer mechanical movement at friction. Adaptive volume V_{adapt} is connected with non-reversible absorption of deformation energy. It is in this volume where latent deformation energy Δu_e accumulates and where the centres of destruction initially emerge (birth). Dissipative volume V_{dis} is capable of reversible transformation (dissipate) of outer movement energy. It doesn't accumulate latent deformation energy owing to reversible elastic-viscous-plastic deformation.

Suggested theoretical and calculation assessments [1-3,7-9] showed that dissipative friction volume performs reversible elastic energy transformation of outer mechanical movement with density $\vec{q}^*$ equal to critical density of latent energy u_e^*.

Culmination of tribosystem evolution is its final and limited condition of point 4 – a state of anomalously low friction and wearlessness (maximum efficient).

Calculation show [1-3] that at an ideal tribosystem evolution an adaptive (Amontons) friction coefficient μ_{adapt} in a point 2 of a

diagram falls abruptly down, reaching in a point 4 the value of elastic friction coefficient μ_{elast}. For point 4 of compatibility area 3-4 an equation of energy balance (1) showed be put in the following way:

$$\mu_{adapt} = \mu^* - \mu_{dis} =$$

$$= 1 - \mu_{dis} = \mu_{plast} = 0 = \mu_{elast} ; \ \mu^* = 1,0 \quad (10)$$

Thus, point 4 stands for an ideal evolution of contact friction volume a condition of ideal elastic-viscous-plastic deformation. Equation (10) shows as a matter of fact exactly it, i.e. Amontons friction coefficient μ_{adapt} being in its essence plastic friction coefficient μ_{plast} has a minimum value equal to zero. It follows then, that plastic friction became elastic with friction coefficient μ_{elast}. It means that plastic deformation of contact volume friction is implemented with the maximum dynamic dissipation ($\vec{Q} = \max$) of accumulated latent energy. That is why the value of accumulated energy in point 4 is equal to zero ($\Delta U_e = 0$). This fact proves an ideal condition at full evolution of contact volume. From the physics point of view this condition may be explained by the full dissipation of accumulated energy ΔU_e^* in point 2 and by newly emerged structures of point 4 in the form of elastic energy of interaction between them (dynamic dissipation energy $\vec{Q}^*$). Here, $\mu_{dis} = 1,0$. The structural elements themselves are defectlessness - $\mu_{adapt} = 0$, and friction is elastic - $\mu = \mu_{elast}$.

It has been demonstrated [2,3,7-9] that value of minimum adaptive friction volume V_{adapt}^{min} corresponding to the zero meaning of plastic friction component μ_{adapt} is not equal to zero, but is equal to some minimum structural element of deformed solid body.

5. THE IDEA OF MECHANICAL (NANO) QUANTUM OF DISSIPATIVE FRICTION STRUCTURES

The result of ideal elementary tribosystem (contact) evolution is forming of unique nanostructure – a mechanical (nano) quantum. Strict notions about mechanical quantum have been obtained [2,7-9] considering equation of quasiideal solid body for point 4 of diagram of friction evolution

$$\vec{Q}^* = \vec{S}_Q T = \mu_{dis}^* N l_f = V_f^* u_e^* = V_f^* \vec{q}_* , \quad (11)$$

which is particular case of solving equation of energy friction balance (1) at $\mu_{adapt} = 0$ and $\mu_{dis} = 1 = \mu_{dis}^*$. Here $\vec{S}_Q$ – inertia entropy of compatible friction volume; T - characteristic temperature of contact friction volume; l_f - linear size of elementary contact.

Correspondingly, in conditions of maximum compatibility (point 4) when tribosystem implements full evolution cycle of adaptation with formation of most perfect dissipative structure, the behaviour of structure is subject to equation of quasiideal solid body condition. So, it is to be presumed that, interaction between elements of this structure, are minimized – a condition of ideal elasticity in dynamics. Equation (5) with taking into account Plank-Boltzmann formula $S = k \ln W$ and real number of atoms oscillators N_f in the volume of elementary tribosystem (contact) V_f^* is brought to the form explaining friction regularities from the point of view of system evolution:

$$\mu_{\text{diss}} = \frac{\vec{S}_Q T}{N l_f} = \frac{k T N_f \ln W}{N l_f} , \quad (12)$$

$$\mu_{adapt} = 1 - \mu_{diss} = 1 - \frac{k T N_f \ln W}{N l_f} =$$

$$= 1 - \frac{\vec{S}_Q T}{N l_f} = \frac{S_U T}{N l_f} . \quad (13)$$

Where k - Boltzmann constant; W - condition probability; S_U - configuration entropy of friction (contact) volume.

Tribosystem always tends to some optimal condition, characterized, i.e. to a most probable condition $W' = N_f \ln W$ for the given friction conditions.

Analysis and solution of these equations [2,7-9] allows to demonstrate the principle of constant probability value (parameter of tribosystem condition (order)) W for the whole range of compatible friction precisely $\ln W = 3$ and $W = e^3 = 20{,}08553696...$.

The value of thermodynamic probability W equal to $20{,}08553696...$ was interpreted [2,3,7-9] as a minimum value of linear, atomic oscillators in one of three directions of minimum adaptive friction volume V_{adapt}^{min} corresponding to condition of practically absolute elastic friction – anomalously-low friction (safe deformation threshold). Then the number of atomic oscillators in this volume equals

$$V_Q = \left(e^3\right)^3 = \left(20{,}08553695...\right)^3 = 8103{,}083969$$

atom's oscillators.

It is the universal size (volume) of mechanical quantum [2,3,7-9].

On the other hand, adopting the meaning of Boltzmann entropy S, a universal friction constant $R_f = k N_f$ [2,3,7-9] is obtained, which characterizes in physical meaning «energetical size» of elementary tribosystem (TS), containing in ideal conditions the same number of atomic oscillators N_f (mechanical quanta N_Q):

$$R_f = k \cdot N_f = k \cdot W^3 \cdot N_Q = R_{MQ} \cdot N_Q,$$

$$\left(\frac{J}{grade \cdot TS}\right);$$
(14)

$$R_{MQ} = k \cdot W^3, \quad \left(\frac{J}{grade \cdot MQ}\right), \qquad (15)$$

where R_{MQ} - universal constant of deformation at friction.

As it follows from calculations [2] the size of minimum adaptive friction volume V_{adapt}^{min} coincides in its value with the size of submicroscopic area in crevice mouth, which is equal for metals $(4...9) \cdot 10^{-6}$ mm, i.e. of critical volume size responsible to fracture. Thus the size of minimum adaptive friction volume $V_{adapt}^{min} = V_{elast}$, can be presented as the size of some mechanical quantum.

Table 1. Parameter W for Metals and Steels [3]

Metals and steels	$E \times 10^{-3}$, MPa	$\left(u_e^*\right) \Delta H_S \times 10^{-3}$, MJ/m^3	$E/3E_r$
Cr	235,4	8,5	27,69
Mg	44,4	1,9	23,37
Ag	79,0	3,7	21,35
Au	78,7	4,0	19,67
Co	200,1	10,6	18,88
Fe	211,4	9,9	21,35
Ta	184,4	10,6	17,39
Ti	105,9	6,7	15,8
Nb	104,0	9,2	11,3
Zr	95,6	5,7	16,77
Mo	316,9	12,0	26,4
W	392,4	14,4	27,25
Ni	201,1	9,4	21,39
Iron	210,9	10,1	20,88
20	200,1	9,5	21,06
1Kh13	206,0	8,9	23,14
3Kh13	218,8	9,2	23,78
Kh18N9T	199,1	9,4	21,19
Kh18M9	199,1	9,6	20,74
30Kh	214,1	10,2	20,99
30N3	207,5	10,3	20,11
40	209,4	9,7	21,58
30G2	207,2	10,0	20,72
30KhGN3	208,0	10,2	20,4
G13	204,0	10,0	20,4
50S2G	196,2	10,3	19,05
U8	198,0	10,3	19,22
U12	198,0	10,4	19,04

$$\Delta H_S = 3E_r, \quad E/3E_r = 20{,}77.$$

This mechanical quantum constitutes a minimum number of atoms capable to provide such a configurational distribution (structure) which obtains the property of reversibly taking and dissipating (recovering) energy of outer mechanical movement. It also constitutes minimum structure in conditions of plastic deformation and it is formed at tribosystem transition (deformed volume) through an ultimately activated (critical) condition (see Figure 2) due to development of selforganisational tribosystem adaptation processes. Mutual rotation-oscillation movement of these mechanical quanta in respect of each other within elementary tribosystem (contact) determines condition of most perfect dissipative friction structure.

Properly speaking, such condition is described by equation of quasiideal solid body condition (9), a condition when interaction between structural elements (mechanical quanta) is minimized – a condition of ideal elasticity of quasiviscous flow. Calculation friction coefficient between quanta equals about 10^{-8} [2,3,7-9].

A conclusion that mechanical quantum constitutes a minimum structural form at plastic deformation (friction) is supported by calculation. If values of elasticity modules E correspond to atomic (true) elastisities E_r then values equal to 60 are obtained, where $60 = 3W$ can be interpreted as a characteristic of volume elasticity of one mechanical quantum – minimum adaptive friction volume V_{adapt}^{min}. Calculation assessment of parameter $W \cong 20 = E/3E_r$, done for various metals and steels gives an average value 20,77 ((Table)); $\Delta H_S = 3E_r$ - entalpy of melting.

A conclusion is made [2] that the number of atoms (mechanical quantum (MQ)) within volume of one elementary tribosystem (TS) in conditions of ideal tribosystem evolution is a constant value. Thus, it is possible to speak about the quantity of substance equal by mass to one elementary tribosystems and to one mechanic quantum.

6. SYNERGISM OF TRIBOSYSTEM AND STATE OF OPTIMUM

Mechanical quantum is dynamic oscillator of dissipative friction structure. An ideal quasielastic contact condition at its full evolution constitutes effect of most fully dissipated energy of outer mechanical movement throughout newly formed (by mechanism of selforganization) structural elements – mechanical quantums (dynamic oscillators) which most fully realize their rotationary – oscillatory behavior in relation to each other within elementary tribosystem volume. Their resistance to relative interaction here is minimally elastic and corresponds to elasticity of ideal atomic (thermodynamically balanced) interactions at the level of electron orbits.

Universal constants of mechanical quantum and elementary tribosystem (material point) determine quantum model of surface damping:

$$\mu_{dis} = \frac{3R_{MQ}T_{n_i}}{NI_f} = \frac{U_{1Q^{n_i}}}{U_{1Q^{n_*}}} = \frac{n_i}{n_*} = 1 - \mu_{adapt},$$

$$\mu_{adapt} = 1 - \frac{n_i}{n_*} = \frac{n_{dest}}{n_*}, \qquad (16)$$

taking into account destruction quantums n_{dest} (non-reversible process component) and damping quanta n_i (reversible, elastic component – fatique number), and also probability evolution tribosystem model to a most ordered condition:

$$\mu_{adapt} = 1 - \mu_{dis} = 1 - \frac{R_f T \ln W_i}{NI_f} = 1 - \frac{\ln W_i}{\ln W_*} \quad (17)$$

where $3R_{MQ}T = U_{1Q}$ - energy of one mechanical quantum; W_i and W_* - current and ultimate probabilities of tribosystems compatibility conditions.

According to a model of quantum surface damping at friction in state of most complete evolution (adaptation) of elementary tribosystem all mechanical quanta with the exeption of one elasticity and reversibly transform energy of outer impact (mechanic movement). One mechanical quantum of radiation ($\cong 8103$ atoms) – is a minimum loss (essence of wearlessness or other wear primary standart).

Linear size of quantum is equal to diameter of spherical ideal crystal with atomic roughness :

$$D_{MQ} = 2 \cdot W \cdot \overline{d}_a \cdot (3/4 \cdot \pi)^{1/3} = 7,177 nm. \quad (18)$$

Here $\overline{d}_a$ - mean atomic diameter for metals; $W = e^3$ - parameter of state for mechanical quantum [2,3,7-9].

Mechanical quantum (Figure 4) can be examined as the elementary nanostructure of metal's solid body.

Calculations have shown [2,3,7-9] the number N_Q of such mechanical «quanta»

(subtribosystems) within the elementary tribosystem's volume $V_f^* = V_{dis}^*$ to be $0{,}63 \cdot 10^8$, which is close to the safe number n_* of fatigue cycles.

In these terms (point 4) only one mechanical quantum [2,3,7-9] is the lost – standard wear. The tribosystem (friction contact) has the ideal damping properties – «wearlessness».
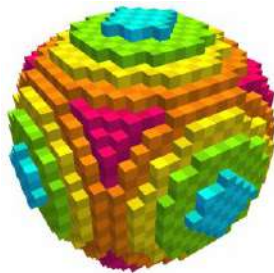

Figure 4. Model of elementary nanostructure of friction (8103 atomic cubical cells) [2,3,7-9]

The principle of mechanical quantum determines nanoquantum levels of all friction parameters of compatible tribosystems and other.

7. NANOQUANTUM MODELS OF TRIBOSYSTEM MAXIMUM CAPACITY FOR WORK

7.1 Gear wear calculation principle

The all parameters of compatibility (optimal) friction have to be in quanta levels - commensurable with the parameters of the one mechanical quantum – standard of wear.

So, all heavy-loaded tribosystems it is necessary to examine with position of tribosystem ideal evolution. This ideal state of tribocontact is true indicator of tribosystem state for practical examples of tribology. It is the standard of maximum tribosystems efficiency - anomalously low friction and wearlessness.

The state of friction contact under its most full evolution is the characteristic with exploitation of hard loaded Hertzian contact, for example, on the surfaces of gear wheels teeth and systems of wheel-rail and other. We can examine the active surface of gear wheel,

which consist of equilibrium spherical form asperities after run-in. During one revolution of gear wheel each asperity of gear wheel teeth is loaded one time too. Under it the loss of one friction contact is equal to one mechanical (nano) quantum. Therefore, the whole contact volume is fatigue failured during about 63 millions cycles. The linear wear h_* of gear wheel is equal to diameter size $Q_{TS} = 2{,}85 \cdot 10^{-6}$ m of an equilibrium friction volume V_f^* (Figure 9) [10]. It is the physical criterion of wear. One may understood that the constructive (limiting) criterion of gear teeth is equal to the limit bend strength between tooth surfaces. For example, it is about $0{,}3$ modulus of gear wheel tooth.

Thus, an elementary nano-structure of deformed solids may examine as the standard of wear and to apply with optimization the life time of real hard pressed Hertzian contact systems.
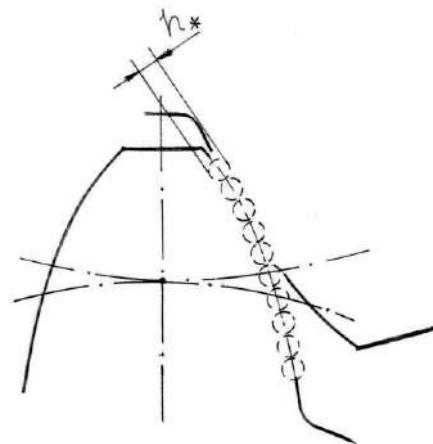

Figure.5. Model of an active surface of gear wheel with equilibrium spherical form asperities.

7.2 Estimation of bearing capacity for work of internal combustion engines

Take the engine with a frequency of $n = 1500 \, \text{min}^{-1}$ shaft rotation. Take the limit wear (linear) of bearing is equal to $h^* = 0{,}1 \, \text{mm}$. We know the line size [10] elementary tribosystem: $D_{TS} = 2{,}85 \, \text{mkm} = 2{,}85 \cdot 10^{-6} \, m$. For every revolution shaft one elementary tribosystem (equilibrium, run-in contact) loses one

mechanical quantum. The number of turns required to wear one elementary tribosystem equals the number of mechanical quantum in this tribosystem.

So, there are $n_{MQ} = 0.63 \cdot 10^8$ revolutions.

Now you can define the time of wear for one elementary tribosystem:

$$t_{TS} = \frac{n_{MQ}}{n} = \frac{0.63 \cdot 10^8}{1500} = 42000 \, \text{min} = \frac{42000}{60} =$$

$$700 \, \text{hour} = \frac{700}{24} = 29.166 \, \text{day} =$$

$$= \frac{29.166}{365} = 0.0799 \, \text{year}.$$

Now let's define the number of layers of elementary tribosystems into linear wear - 0,1mm:

$$a_{h^*} = \frac{h^*}{D_{TS}} = \frac{1 \cdot 10^{-4}}{2.85 \cdot 10^{-6}} = 0.35 \cdot 10^2 = 35.$$

Now, let's define the time of wear of shaft-bearing system with the ultimate linear given wear - $h^* = 0.1 \, \text{mm}$, namely:

$$t_{motor} = t_{TS} \cdot a_{h^*} = 0.0799 \cdot 35 = 2.7968 \, \text{year}.$$

Total we have 2,7968 years of continuous operation on limit load.

If you work 8 hour per day, then we get the following result:

$$2.7968 \cdot 3 = 8.39 \, \text{year}.$$

This is a very real result for modern cars. And if the ride is not 8 hours per day and less durability increases considerably-really to decades.

For this result we have the wear rate - $i = 4 \, nm/h$. It is good correspondence with the data for wear rate - $i = 5 \, nm/h$ by Prof. F. Franek [11].

7.3 The principle of critical velocity of rolling wheels

This speed limit is determined by the principle of filling the entire nominal friction sliding system area with elementary tribosystems, damping process. Above this speed happens full unloading tribosystem, detachment of wheels from the surface of the rail as distorts the principle of minimum resistance to movement (the principle of one elementary tribosystem or irreversibility). In this case, all mechanical quanta of elementary tribosystem will repel the wheel. There will be no quantum which activates a process to maintain the system in an excited state.

The calculation will be performed in the following order. Denote elementary nominal contact area. By definition [12], on elementary, nominal area of tribosystem can accommodate and work of $n_* = 0.63 \cdot 10^8$ elementary tribosystems. Each elementary tribosystem (for model of spherical roughness) has a size of $D_{1TS} = 2.85 \cdot 10^{-6} \, m$ and is able to implement rolling wheel path in the elementary act of rolling at length of this tribosystem.

Thus, if per unit of time all elementary tribosystems work on elementary nominal area of friction time, then the path passable wheel per unit of time, equal to

$$L_{\Sigma TS} = D_{1TS} \cdot n_{TS}^* = 2.85 \cdot 10^{-6} \cdot 0.63 \cdot 10^8 =$$
$$= 179.55 \, m$$

Consequently, the critical speed of wheel rolling is equal

$$v_* = L_{\Sigma TS} \cdot 3600 = 646.38 \, km/h.$$

This result is close to modern speed of 574,8 km/h (TGV, France).

8. CONCLUSIONS

8.1. Structural-energy analysis of the friction process allows us to examine the friction process as the evolution process;
8.2. From the energy balance equations of friction follows that the evolution of tribosystem (contact) has an adaptive-dissipative character.
8.3. Experimental friction curves of $\mu = \mu(N, v)$ type may be examined as generalized friction experimental curves;
8.4. The fuller evolution of tribosystem has symmetrical view - the friction process is started and finished within elastic area.

8.5. Under fuller evolution of friction contact (elementary tribosystem) the unique nanostructure is formed; the basis of this structure is the mechanical (nano) quantum and the contact (material point of mechanics) consists of about $0,63 \cdot 10^8$ such quanta.

8.6. We can examine the mechanical quantum as the least structural form of solid material body and the standard of wear.

8.7. Interaction between nanoquanta is nature the net elasticity. The value of the coefficient of friction between mechanical quanta has the order - $\mu_{MQ} = 1,587 \cdot 10^{-8}$.

8.8. Exploitation of gear wheels and other heavy-loaded tribosystems (Hertzian contact) are subjected to model of nanoquantum damping, when one mechanical quantum of contact is the standard of wear.

REFERENCES

[1] S.V. Fedorov: General Model of Friction. Journal of Friction and Wear, vol. 14, No. 3, pp. 20-28, 1993

[2] S.V.Fedorov: *The Foundations of Triboergodynamics and Physico-Chemical Prerequisits of Compatibility Theory* (in Russian), Kaliningrad State Technical University Press, Kaliningrad, 2003.

[3] S.V. Fedorov: Energy Model of Sliding Friction Coefficient and Generalized Regularities of Tribosystems Evolution, in: *Transactions of the 19th International Colloquium Tribology «Tribology-Industrial and Automotive Lubrication*, TAE, 21-23.01.2014, Esslingen, Germany.

[4] V.V. Fedorov: *Thermodynamic Aspects of Strength and Fracture of Solids* (in Russian), Science, Tashkent, 1979.

[5] V.V. Fedorov: *Kinetics of Damage and Fracture of Solids* (in Russian), Science, Tashkent. 1985.

[6] V.V. Fedorov: Ergodynamic concept of failure, Strength of Materials (Translated from Russian), Vol.23, No. 8, pp. 883-889, 1991.

[7] S.V. Fedorov: The Friction Coefficient and its Relation to the Contact Fatigue Characteristics of Materials. Industrial Laboratory. Translated From Zavodskaja Laboratorija. Vol. 61, No. 1, pp.41-49, 1995.

[8] S.V. Fedorov: The mechanical quantum of dissipative friction structures is the elementary tribonanostructure. In: *Transactions of IV World Tribology Congress 2009, 6-11.09.2009,* Kyoto, Japan, pp. 926.

[9] S.V. Fedorov: Generalized Energy Model of Sliding Friction Coefficient and Regularities of Tribosystem Evolution, In: *Transactions of V World Tribology Congress* 2013, 8-13.09.2013, Turino, Italy, pp. 1-9.

[10] S.V. Fedorov: Calculation of the true friction volume, Friction & Lubrication in Machines and Mechanisms. Vol. No.5 2010. pp. 3-7.

[11] F. Franek, T. Wopelka, M. Jech: On-Board Applicable High-Resolution Wear Measurement Technique For Internal Combustion Engines, in: *Transactions BALTTRIB'2011*, 11-19. 11. 2011. Kaunas, Lithuania, pp.196-201.

[12] S.V.Fedorov; *Energetical Nature of the Wheel Elastic Rolling* (in Russian), Kaliningrad State Technical University Press, Kaliningrad, 2004.

METHODS AND PRINCIPLES OF DETERMINING THE FOOTWEAR AND FLOOR TRIBOLOGICAL CHARACTERISTICS

Dušan STAMENKOVIĆ[1,*], Milan BANIĆ[1], Milan NIKOLIĆ[1], Miroslav MIJAJLOVIĆ[1], Miloš MILOŠEVIĆ[1]

[1]Faculty of Mechanical Engineering Niš, Serbia
* Corresponding author: stamendu@gmail.com

Abstract: *There are many standards relating to the anti-slip properties of footwear and flooring. These standards describe the different test methods and procedures for determining the footwear and floor slip resistance in different conditions. In this paper authors systematize the standards in this field applied in the EU and in Serbia and cite the Serbian institutes which are certified for this type of testing. In addition, the authors have carried out an analysis and comparison of the tests that are defined in these standards, indicating their advantages and disadvantages. Importance of the static and kinetic friction testing in determining the anti-slip properties of footwear and flooring is specifically indicated. Considering the current standards in area of slip resistance of the footwear and floor covering authors have determined the testing conditions for laboratory measuring the friction forces of different floor and footwear materials. The laboratory measurement has carried out at Faculty of Mechanical Engineering in Niš. The measuring results and their analysis are presented in the paper, as well.*

Keywords: *tribological characteristics, footwear, flooring, experimental methods, standards.*

1. INTRODUCTION

Numerous accidents occur due to the slipping during human walking. Selection of appropriate shoes and floor combination, considering the slip resistance properties, is the most important measure for slipping accidents prevention. Evaluation of floor and footwear slip resistance should be based on understanding of basic tribological characteristics. There are different principles and methods to assess the slip resistance of flooring coverings and footwear.

Wetzel et al. [1] describe the requirements concerning the slip resistance and the state of art in slip resistance measurement standards in the European Union. They note: ''Slip resistance is influenced by a numerous factors, such as: combination of shoe sole, floor covering, contaminants and their properties; surface structures of shoe soles and floor coverings and changes to them as a result of wear; motion speed and ambient parameters'' [1].

The comparison of the slip resistance of outdoor footwear and safety footwear according the performed experimental research is described in the paper [2].

In paper [3] author points out that there are many different standards and methods for assess the slip resistance, but there are no obligation to apply them for the producers of footwear and floors. He indicates that evaluation of slip resistance should be based on understanding of basic tribological characteristics between the shoes and floors.

A number of organizations have developed standard tests for measuring friction force ie. coefficient of friction. These tests have numerous similarities, but vary greatly in type and purpose. List of tests that have been standardized by ASTM is presented in [4]. Some are directed towards a particular application, while others are for general evaluation of materials.

Structural, operation and interaction parameters should be taken into account in friction experimental research of solid elements [5]. The contact between rubber and hard material is specific compared to pure metal-metal contact. In contact between rubber and hard surface, friction depends significantly on load and on geometry of the surfaces [6]. The author in the paper [7] claims that friction force between rubber and rough (hard) surface can be described by the adhesion and hysteretic components.

There are different European standards that have adopted various test methods and rating systems [11-15]. These standards include test methods that are based on different principles and are used under different conditions. Analysis of their advantages and disadvantages are presented in papers [8-9].

Basic factors influencing accidents and injuries in human walking can be divided in next groups: footwear, floor, human factors and environment (location) [10]. Footwear factors are: sole construction, sole material, sole elasticity, sole hardness, tread pattern, wear etc. Floor factors are: material type, roughness, hardness, maintenance, wear, etc. Human factors represent individual characteristics of human such as gait, age, weight, mobility, etc. Environment factors are lighting, humidity, obstacles, changes of surfaces, contaminants, etc.

Footwear and floor factors in friction testing are considered in this paper.

2. BASIC PRINCIPLES OF FRICTION TEST METHODS

The basic principle of determining the footwear and floor slip resistance is testing the real materials in real conditions considering the tribological characteristics.

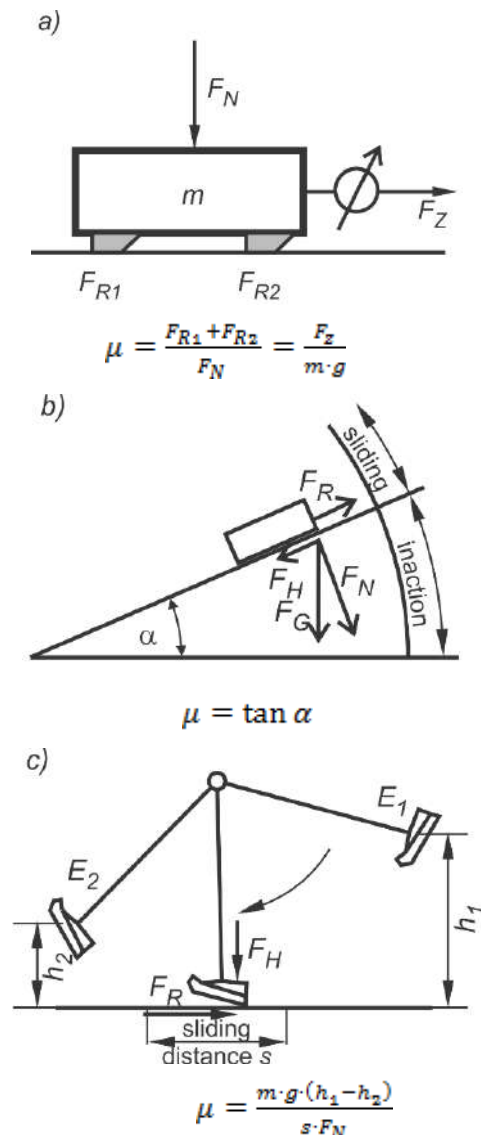The possibility of determination of friction coefficient is presented on Figure 1.

a)

$$\mu = \frac{F_{R_1} + F_{R_2}}{F_N} = \frac{F_Z}{m \cdot g}$$

b)

$$\mu = \tan \alpha$$

c)

$$\mu = \frac{m \cdot g \cdot (h_1 - h_2)}{s \cdot F_N}$$

Figure 1. Friction coefficient determination by pulling force (a), friction angle (b) and energy loss (c)

Main principles of friction coefficient determination are the tests with measuring of the pulling force (Fig. 1a), where friction coefficient is ratio of pulling force (F_Z) and pulled weight (mg); tests with measuring the friction angle (Fig. 1b), where friction coefficient is in function of friction angle (α); and tests with measuring of energy loss due to friction (Fig. 1c), where friction coefficient is a function of difference of potential energies (E_1 – potential energy at the start, E_2 – potential energy at the end of measurement).

2.1 Static and dynamic coefficient of friction

There are static and dynamic (kinematic) friction force and according to that static and dynamic coefficient of friction. There are opposing views about the importance of static and dynamic coefficient of friction in slip measurement. Some engineers claim that the dynamic coefficient of friction is more important than the static coefficient for an evaluation of slip resistance.

The static coefficient of friction is usually greater than the dynamic coefficient of friction and it is the initial barrier against slippage. If slippage has begun, a higher dynamic coefficient of friction may help one to recover from a slip, but it is better to prevent the slippage and static friction is relevant for that.

Static friction is friction between two bodies that are not moving relative to each other. The static friction force must be exceed by an applied force before an object can move. The static friction has an important role in transport means, especially in railway and road vehicles, but also in human walking. Regardless of the installed power of the drive units, motion of a vehicle is only possible if there is an adequate static friction between drive wheels and the ground. In the same way static friction between shoes sole and floor coverings is necessary for human motion.

2.2 Basic group of parameters in a friction test

In a friction test the resulting tribometric characteristics data must be understood as tribological systems characteristics associated with the following group of parameters [5]:

- **Structural parameters**, which characterize the components (materials, lubricant, and environment) involved in the friction process and their physical, chemical, and technological properties;
- **Operational parameters**, that is, the loading, kinematic, and temperature conditions and their functional duration;

- **Interaction parameters**, which characterize, in particular, the action of the operating parameters on the structural components of the tribological system and define its contact and lubrication modes.

Structural parameters include triboelements, interfacial element such as lubricant or dirt particles, and environmental medium such as air or moister. Structural parameters can be divided in:

- Geometric parameters (geometry dimensions, surface topography, etc);
- Microstructural parameters (grain size, dislocation density, etc);
- Mechanical parameters (elastic modulus, hardness of triboelements; viscosity and viscosity-pressure of interfacial elements and environmental medium, etc)
- Chemical parameters (volume composition and surface composition of triboelements; composition of interfacial elements and environmental medium such as acidity and humidity, etc)
- Physical parameters (density, thermal conductivity, etc).

The basic operational parameters in tribology [5] are:

- Type of motion (sliding, rolling, spin, and impact; the kinematics can be continuous, intermittent, reverse, or oscillating);
- Load, defined as the total force (including weight) that acts perpendicular to the contact area between triboelements;
- Velocity, to be specified with respect to the vector components and the absolute values of the individual motions of triboelements;
- Temperature of the structural components at stated location and time, that is, the initial (steady state) temperature and the friction-induced temperature rise;

- Time dependence of the set of operational parameters;
- Duration of operation or test.

2.3 Friction conditions in contact rubber-substrate

Rubber is the most often used material for shoe sole, so the contact between rubber and hard material should be studied. Rubber friction differs in many ways from frictional properties of most other solids due to very low elastic modulus of rubber and high internal friction.

In situation of contact between rubber and hard surface the friction depends markedly on load and on geometry of the surfaces [6]. Rubber is a truly elastic solid and if the sliding surfaces are flat (so that they touch over a large number of contact regions) the area of contact and friction force are more nearly directly proportional to the load.
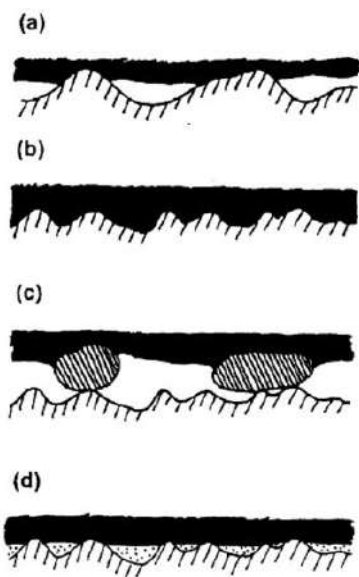

Figure 2. Rubber in contact with a hard substrate with a rough surface [7]

When a hard steel ball slides over a clean rubber surface the friction is dominated by the adhesion between the surfaces. When the surfaces are thoroughly lubricated the friction is dominated by the deformation of the rubber due to elastic hysteresis losses [6].

The friction force between rubber and rough (hard) surface can be described by the adhesion and hysteretic components [7].

Contact of rubber and hard substrate with a rough surface is presented in Figure 2 in different conditions [7]. Rubber on a hard substrate with long-wavelength surface roughness is shown in Figure 2a. Because of adhesion to the substrate, rubber in contact area deforms in to completely follow the short- wavelength surface roughness profile of the substrate (Figure 2b). Rubber surface dusted by small particles sliding on a hard substrate is presented in Fig. 2c and rubber sliding on a water covered surface is presented in Figure 2d.

3. FOOTWEAR AND FLOOR SLIP RESISTANCE STANDARDS

Testing and assessment of anti-slip characteristics of footwear and floor is of major importance for the prevention of slipping accidents. Numerous different methods and devices have been developed over the years to measure the slip resistance of floor and footwear. Different European countries have adopted various test methods and rating systems. Because these test methods are based on different principles and are used under different conditions there is no correlation between them. No single test currently in use is perfect. All have their advantages, but also their own particular disadvantages [8].

The most often used standard tests for floor testing are Ramp test according to the German norms DIN 51130 and DIN 51097, Pendulum test according to the British and EU norm BS EN 13036-4, and tribometer test according to the norms DIN 51131 and BS EN 13893. The operating principle of ramp test is measuring of the friction angle; the principle of pendulum test is measuring the energy loses due to the friction and the tribometer test is based on measuring the pulling force which is actually the friction force.

In the ramp test (DIN 51130), a test person (operator) is wearing standard footwear and walks backwards and forwards over a sample of a flooring material that has been evenly coated with oil (Figure 3). The angle of the

ramp is increased until the operator slips [11]. The acceptance angle obtained is used to express the degree of slip resistance. In the ramp test (DIN 51097) the operator walks barefoot.

Figure 3. Ramp test

According the angle of ramp there are five class of slip resistance that is shown in Table 1.

Table 1. Slip resistance classes of floorings according to the norm DIN 51130

Classification	R 9	R 10	R 11	R 12	R 13
Slip angle [o]	6÷10	10÷19	19÷27	27÷35	>35

The pendulum test measures the loss of energy due to friction as the standard rubber-coated slider assembly slides across the test surface [12]. Pendulum friction tester is presented in Figure 4. It provides a standardized value of slip resistance. This is the pendulum test value (PTV).

Figure 4. Pendulum friction tester

The pendulum is the preferred test method in the United Kingdom. Relative risk of slipping is determined with PTVs (Table 2).

Table 2. Slip potential due to PTV

Slip potential	PTV
HIGH	0÷24
MODERATE	25÷35
LOW	>36

Tribometer test method is based upon a friction force measurement. A body equipped with sliders is pulled at a constant speed over the flooring surface. The force required to pull the body is determined over the length of the measuring distance. An example of a tribometer tester according to the norms DIN 51131 is shown in Figure 5.

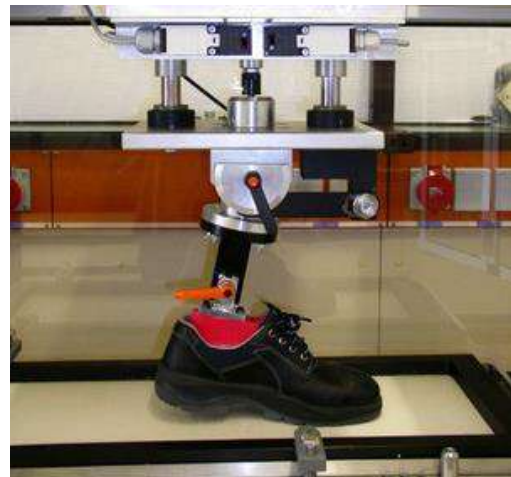**Figure 5.** An example of a tribometer tester

Figure 6. Test equipment for measurement the slip resistance of footwear

In order to determine the sliding friction coefficient, this force is divided by the vertically acting force. This test can be carried out in wet and in dry conditions both in a laboratory and on-site. This device is predominantly used in Germany, Poland and Austria [9].

The method for measurement of the slip resistance of shoes is described in EN 13287 [14]. The footwear to be tested is placed on the base of ceramic tile or steel floor, subjected to a given normal force (Figure 6). The base is moved horizontally and sliding of footwear occurs.

Dynamic coefficient of friction is calculated according the measured frictional force. Glycerin or sodium lauryl sulphate solution acts as contaminant on the surface.

Some EU standards related with measuring of slip resistance of footwear and floor coverings are adopted in Serbia. There are:

SRPS EN ISO 13287:2014 - Personal protective equipment - Footwear - Test method for slip resistance;

SRPS EN 13036-4:2012 - Road and airfield surface characteristics - Test methods - Part 4: Method for measurement of slip/skid resistance of a surface: The pendulum test;

SRPS EN 13893:2011 - Resilient, laminate and textile floor coverings - Measurement of dynamic coefficient of friction on dry floor surfaces.

Manufacturers and distributors of protective footwear in Serbia are usually required to test their products according to standard SRPS EN ISO 13287. But manufacturers and distributors of other types of footwear rarely present the slip resistance properties of their products. In rare cases they advertise the slip resistance of their shoes referring to standards EN ISO 13287 and DIN 51130.

Manufacturers and distributors of sports flooring in Serbia presenting their products usually refer to standard EN 13036-4 (Pendulum test). Manufacturers and distributors of laminate and textile floor coverings most often refer to standard EN 13893. Other manufacturers and distributors of floor coverings refer to standard DIN 51131, DIN 51130 and DIN 51097.

4. EXPERIMENTAL INVESTIGATION

Determination of floor and footwear slip resistance is often conducted by measuring the friction force and calculating the coefficient of friction. Dynamic (kinetic) coefficient of friction is the most often determined.

The requirements setting in the standard very often are not in compliance to the real conditions. For example in standard DIN 51130 specimens of floor material is the same material as the application, but footwear is special, and walking of test person is with low speed. Also, this way of walking on ramp isn't the same as walking on horizontal surface. In pendulum test sliders are made of materials with specific characteristics which are not similar to the shoe sole. The kinematic of pendulum isn't similar with kinematic of human walking/running, as well.

The contact pressure depends on the person's weight and surface texture and shoe soles, and the relief (texture) of substrate. Velocity of sliding corresponding to human stroke has a great range, from slow walking to running.

Importance of dynamic and static coefficient of friction should be considered as the equal.

Based on the above, in experimental determination of friction coefficient it is significant to provide the following:
- Experimental samples should be made of real shoes sole/floor materials with determined mechanical properties,
- Surface structure (macro and micro structure, roughness, etc.),
- Contact pressure,
- Sliding velocity,
- Contact condition (temperature of contact bodies, lubricant, contaminants, etc.),
- Environment (temperature, humidity, etc).

In order to estimate the laboratory test procedure and check the test conditions experimental research is performed at Faculty of Mechanical Engineering in Nis, Serbia.

Principle of determining the friction coefficient in performed experimental research is measuring the pulling force. Applied measuring method is based on settings in standards EN 13893 and DIN 51131. The measurement was carried out on dry and

wet surfaces. The test facility is equipped with sliders which are pulled parallel to the surface of the floor covering.

Materials of sliders were shoe sole made of rubber and leather (three pieces with dimensions 10x40 mm) cut from the real shoes. Experimental samples of flooring covers were three different materials: laminate, ceramic tiles and linoleum (vinyl). Contact pressure was 91 kPa.

Sliding distance was 500-800 mm. Sliding velocities were: 2, 10, 50 and 250 mm/s.

Friction force was measured and coefficient of friction was calculated in experimental research.

The test equipment is shown in Figure 7.

Figure 7. Test equipment in laboratory at Faculty of mechanical engineering in Nis

A typical example of measured friction force is presented in Figure 8.
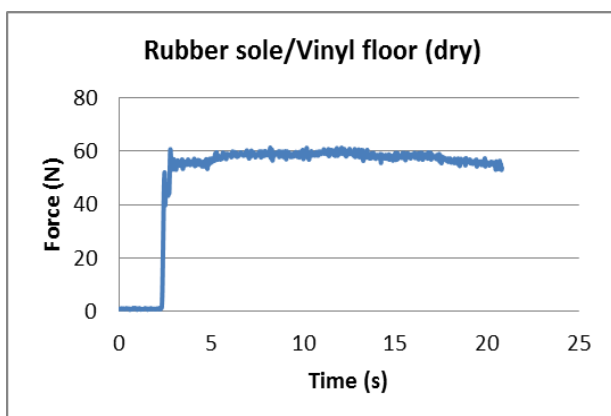
Figure 8. Measured friction force in sliding rubber sole sample on vinyl floor covering

Static and kinetic coefficients of friction were estimated during the experiment. There are significant differences between static and kinetic friction coefficient values in different type of contact and different conditions (Figure 9). Static and kinetic friction coefficient values presented in Figure 9 are average values of groups which consist of five measurements.
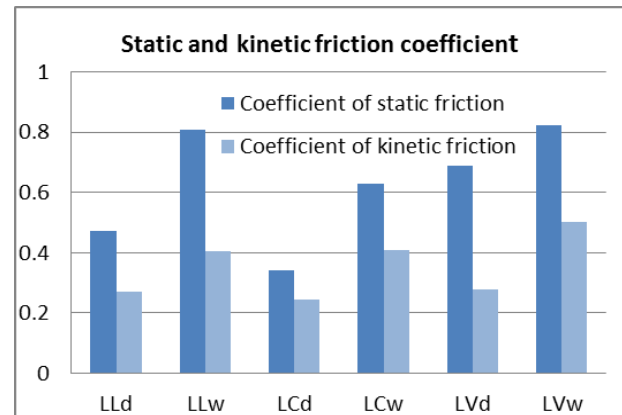

Figure 9. Static and kinetic friction coefficient values (LL-leather-laminate; LC- leather-ceramic tile; LV-leather-vinyl; d-dry contact; w-wet contact)

In most cases the values of static friction coefficient is higher than kinetic friction coefficient. But in some situations static friction coefficient is equal or smaller than kinetic friction coefficient.

Investigation of different contact conditions and different material samples required numerous tests (measurements). Each contact case was tested five times. Deviations of friction coefficient values within the group of measurement were not so big. Figure 10 presents the maximum and minimum values of friction coefficients in testing the leader sole samples on floor coverings within the twelve groups of five measurements.
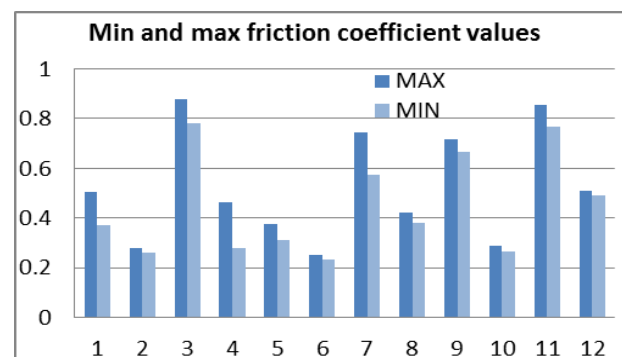

Figure 10. Minimal and maximal experimental friction coefficient values

Comparing the kinetic friction coefficient values in dry and wet condition it can be seen that values in wet condition are bigger in case

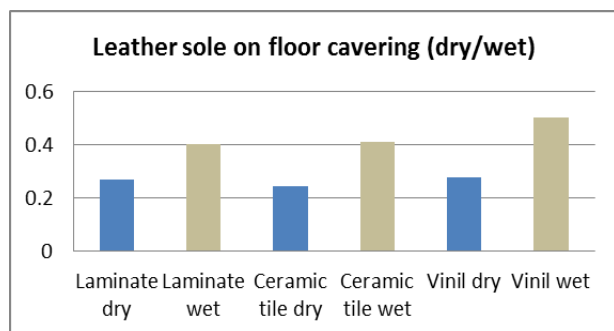of leader sole sliding on all types of flooring coverings (Figure 11).

Figure 11. Average values of kinetic friction coefficient values in case of leather sole samples
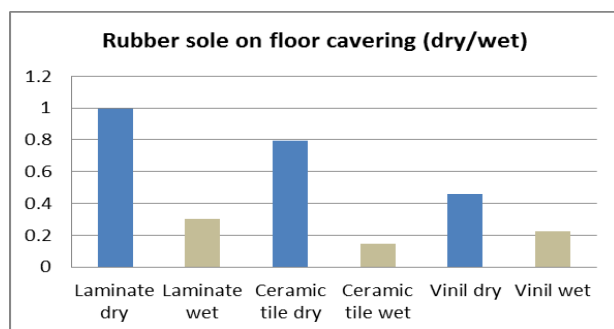

Figure 12. Average values of kinetic friction coefficient values in case of rubber sole samples

In contrast to the case of leather sole samples, kinetic coefficient of friction in case rubber sole sliding is two to three times lower in wet condition than for the dry condition (Figure 12).

5. CONCLUSION

There are numerous causes of slip accident in human walking and they are mostly stochastical. The key activity in slip accident prevention is systematic examination of influential parameters and implementation of the measures which are sufficient to prevent harm. But no one shoe sole design will be the best on all different types of surface and contaminants, and because of that it is necessary to investigate different combinations of materials and conditions.

Measuring (determining) of the friction coefficient should be conducted in conditions which are identical with real conditions. Measuring with different types of shoe sole (soft and hard; smooth and rough) should be conducted in cases where the substrate material is known. In order to provide environmental conditions that may occur in real conditions (sunny, very hot, cool, dry, wet-rain, wet-snow, etc.) on-site testing is preferably. If shoe material is known, flooring materials should vary with different properties of hardness, macro and micro texture, etc**.**

Evaluation of floor and footwear slip resistance should be based on recognition of the basic tribological parameters and their testing.

Assessment of the floor and shoe slip resistance should be based on the recognition of the basic tribological parameters for specific friction contact and their testing in application conditions.

REFERENCES

[1] C. Wetzel, U. Windhövel, D. Mewes, O. Ceylan: Slipping on pedestrian surfaces: methods for measuring and evaluating the slip resistance, International Journal of Occupational Safety and Ergonomics, Vol. 21, No. 3, pp. 256-267, 2015.

[2] C. Wetzel, T. Schotes, A. Kahl, U. Windhövel: Slip resistance of Footwear, A practical comparison between outdoor footwear and safety footwear, Health & Safety International, Vol. 33, pp. 29-37, 2010.

[3] D. Stamenković: Science in Safety the bearing tribology has on slips, trips and falls, Health & Safety International, Vol. 52, No. 1, pp. 59-65, 2014.

[4] K. Budinski: Laboratory Testing Methods for Solid Friction, in: D. Olson (Ed.) *Friction, Lubrication and Wear Technology*, ASM International Handbook Committee, Vol. 18, pp. 45-58, 1992.

[5] H. Czichos: Basic Tribological Parameters, in: D. Olson (Ed.) *Friction, Lubrication and Wear Technology*, ASM International Handbook Committee, Vol. 18, pp. 762-774, 1992.

[6] F. Bowden, D. Tabor: *Friction - An Introduction to Tribology,* Florida, USA 1982.

[7] B.N.J. Person: Sliding friction, Surface Science Reports, Vol. 33, No. 3, pp.83-119, 1999.

[8] Measuring the slip resistance of floorings and footwear, available at: https://oshwiki.eu/wiki/Measuring_the_slip_r esistance_of_floorings_and_footwear, accessed: 1.3.2016.

[9] P. Marchal, M. Jacques, A. Sigari: Comparison of measurement methods of the friction coefficient of floor coverings, INRS/CSTB joint publication, 2015.

[10] SATRA Slip Resistance Guide: Safety, protective and occupational footwear supplied into the European market, 2010.

[11] DIN 51130, *Testing of floor coverings – Determination of the anti-slip property – Workrooms and fields of activities of slip danger, walking method - Ramp test*, 2010.

[12] BS EN 13036-4, Road and airfield surface characteristics – Test methods; Part 4: Method for measurement of slip/skid resistance of a surface – The pendulum test, 2003.

[13] BS EN 13893 *Resilient, laminate and textile floor coverings – Measurement of dynamic coefficient of friction on dry floor surfaces*, 2007.

[14] DIN 51131, *Testing of floor coverings - Determination of the anti-slip property - Method for measurement of the sliding friction coefficient*, 2014.

[15] ISO 13287, *Personal protective equipment - Footwear - Test method for slip resistance*, 2012.

A GRAPHIC ANALYTICAL MODELING LINEAR CONTACT BETWEEN STEEL AND COMPOSITE MATERIALS REINFORCED WITH GLASS FIBERS AT HIGH PRESSURES AND TEMPERATURES

Dorin RUS[1], Virgil FLORESCU[1], Anca SASU[2], Robert URSACHE[2]
[1] Mechanical Department, University of Civil Engineering, Bucharest, Romania)
*Corresponding author: rusdorin@gmail.com

Abstract: *Issues of wear occur in the thermoplastic injection molds at high temperature and high speed injection so they can achieve a pressure of 100 MPa and temperatures of 210 ^{0} C Steels used have been C120 which is used to make steel screws injectors and Rp 3 is a tool steel. In this article we are showing a graphical analytical modeling linear contact, between steel and composite materials reinforced with glass fibers (SGF) at high pressures and high temperatures, based on experimental determinations of the worn surface depending on the metal friction coefficient and the evolution of the temperature. The purpose is the evaluation of the dependence of the sliding speed and the load loading of the specimen, the amount of wear evaluated and measured depth of wear. The thermoplastic composite material transfer processes due to metal abrasion and corrosion, adhesion to the contact determined with Archard relationship by measuring the length of all using three points were determined graphically. A wear volume and depth of wear depending on load and contact pressure for different composite materials reinforced with glass fiber.*

Keywords: *contact temperature, friction coefficient, plastic material transfer, hardness of steel, steel surface wear, plastics with glass fibers, dry friction, linear contact.*

1. INTRODUCTION

The process of injecting thermoplastic materials for injection molding machines with auger is highly complex, including numerous factors which influence the wear of metal surfaces in permanent contact with the material at melting temperature. In the technical literature, the following wear factors for injection molding machines are known: the processing conditions (auger geometry, working temperature, working pressure), the steels used for fabricating the cylinder and the auger, the geometrical conditions between the cylinder and the auger.

In the injection process two conditions must be observed: the composite materials have different lubrication properties in molten state which, if not strictly observed, lead to an interruption of material feed in the cylinder and therefore to the increase of adhesion wear. The second condition for the process of filling the cylinder is that there should be no ares with molten material present or areas with partially molten material, as they will lead directly to an increase in the wear of metal surfaces coming into contact with the injected material.

Composite materials containing corrosive, volatile elements are a special case. These

evaporate in the cylinder during the injection process and thus lead to an increase in corrosive wear. Composite materials reinforced with glass fiber have high mechanical properties within a wide range of values. The friction coefficient metal/plastic was presented with micro welds of the couples occuring via contact. Bilik [1] determined values for the friction coefficient, which is not constant, observing that the values depend on the temperature, the statue of the surface and the contact pressure. Dwyer-Joyce [2] has used elastic, hydraulic and dynamic contact tests. Using the spherical machine on disk for studying the removal of the material in partially sliding contact with the particles, Stachowiak, et al. [3] have studied the experimental testing pin-on-disk including abrasive particles and ball-on-plane in order to study three-body abrasion. He has found out that the best direct correlation between wear and particles is present in the sphere-on-plane case. Li, et al., [4] studied the tribological properties of nanocomposite materials and the mechanical properties by means of micro hardness tests. Using SEM (scanning electron microscope) scanning, Chang, et al., [5] studied the temperature behaviour of polyetheretherketone (PEEK) and polyetherimide (PEI), reinforced with short carbon fibers (CSA). By performing an analysis of the wear mechanism at microscopic level, Myshkin [6] studies the deformation of the material and the adhesion for composite materials and notices that the component of the friction force is much larger than the adhesive component. For adhesion, the well-known Johnson-Kendall-Roberts (JKR) model [7] and the Derjaguin-Muller-Toporov (DMT) were created [8] .Shen and Dumbleton [9] have studied the wear behaviour of ultra-high-molecular-weight polyethylene (UHMWPE) and of the Delrin polyoxymethylene, establishing a relationship between the sliding distance, normal pressure, wear factor and linear wear.

Chang and Friedrich [10] have shown that nanoparticles improve the performances of short fiber reinforced polymers (SFRP) under maximum sliding conditions. Vos, et al., [11] have studied the behaviour of polyetheretherketone composites reinforced with short glass fibers and have discovered that wear is influenced by the thermal treatment of SFRP. West [12] has shown that, for normal forces, the friction force and the friction coefficient are proportional to the friction factor. Jost [13] has shown that adhesion wear is a component encountered mainly in the polyamide/metal couple with lubricant or dry contact.

Bartenev, Lavrentiev et al [14] have demonstrated the increase of the friction force with the increase of the sliding speed.

The mechanisms for improving the physical and mechanical properties of composite materials reinforced with glass fibers are not entirely known. The advantage of SFRPs is the low price. However, during fabrication, respectively during the injection of the material, significant damage is caused to the components of the injection molding machine. Lancaster and Evans [15] have shown that for reinforced polymers a decrease in ruggedness can be seen for the plastic on metal disk contact. Kukureka, et al., [16] have studied wear in the PA66 polyamide in rolling-sliding contact, and the wear is ten times bigger for composite materials reinforced with carbon fibers than for composite materials without reinforcement. Clerico [17] has studied the polyamide/metal couple and establishes that the value of the friction coefficient is bigger for shorter periods of using the couple than for longer periods. Bely [18], Bartenev and Laventiev [19] have studied the orientation of the glass fibers in the polymer mass. They have come to the conclusion that if the glass fibers have a different orientation from the polymer, then the friction coefficient increases. Wang, et al., [20] have studied Nylon 1010 composite with MoS_2 filler and short carbon fibers and have found out that oxide particles increase the adherence between the sample and the contact surface. Guo, et al., [21] have studied the friction coefficient for hybrid composite materials with nano-SiO_2 filler and have noticed a significant

decrease in wear and in tribological properties. Lancaster [22] has established that for polymers reinforced with natural fibers, the friction coefficient depends on the state of the surface and the lubrication of the couple. Barlow [23] has established that the increase of the friction coefficient is proportional to the increase of the sliding speed. Cho and Bahadur [24] have studied polyphenylene sulfide composites (PPS) and CuO-filled nanosize polyphenylene under compression. They have found out that during the contact of the polymer on polymer couples similar phenomena as in the case of the metal on polymer contact occur, in other words, that a transfer film is formed. Jacobi [25] has discovered that glass fiber reinforced polyamides have a friction coefficient between 0.5 and 0.04.

P. Boey, W. Ho and S.J. Bull [26] have studied hybrid surfaces and the effect of high temperatures on the abrasive wear of glass fiber reinforced polymers for the ASTM G65/1994 test, modified standard and adjusting the scheme with rubber (ASTM G65) rotary wheel. W. Knappe and W.D. Mahler [27] have studied wear for different types of steels coated with different layers, for injection molding machines with auger. H. Ladwig and K.D. Sommer [28] have studied the construction of the injection molding screw for a large number of injection cycles, determining auger shapes with lower corrosion. W.W. McCandless et al [29] have performed an analysis of the corrosion and wear for injection molding machines with auger.

Dorin Rus et al [30,31] have shown the behaviour of composite materials reinforced with short glass fibers from the standpoint of the tribological behaviour of the polymer/metal couple.

In specialist literature there are numerous advanced studies concerning the wear of polymers and to a lesser extent studies concerning the wear of the metal part. So far, the results in the specialist literature correspond to the results of our research. However, studies do not show the correlation between wear and friction, in order to have a clear image of the highly complex friction and wear process.

In this article we have studied the process for the Timken type contact, linear dry contact under sliding friction conditions.

2. METHODS

2.1 Analytical method

The Timken friction couple with linear contact is the base for calculations. Wear imprints remain on the metal surface due to the contact between the plane and the cylinder (Fig. 1).
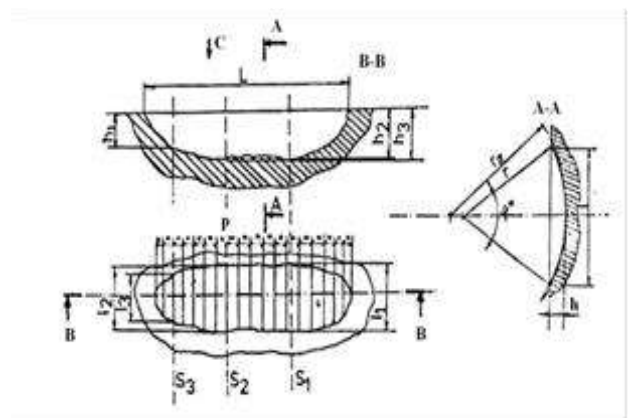

Figure 1. The imprint scheme for Timken friction couples

We have considered the wear imprint as formed from cylindrical sectors with the length q. Thus, we can write that the lateral surface is a cylindrical sector where: S_i (lateral surface of the crystal sector), φ_i (the angle), r (the circle radius) :

$$S_i = 0.5r^2 \left(\pi\varphi_i^0 / 180° - \sin\varphi_i \right) \tag{1}$$

However, due to deformations during the contact between thermoplastic material and metal, the elastic deformation of the bush under the action of the load, an increase in the radius of the cylindrical bush occurs, as seen in (Fig. 2)

We have used polymers reinforces with 20% or 30% glass fibers. The purpose is establishing a link between the sliding speed, normal load and the contact temperature
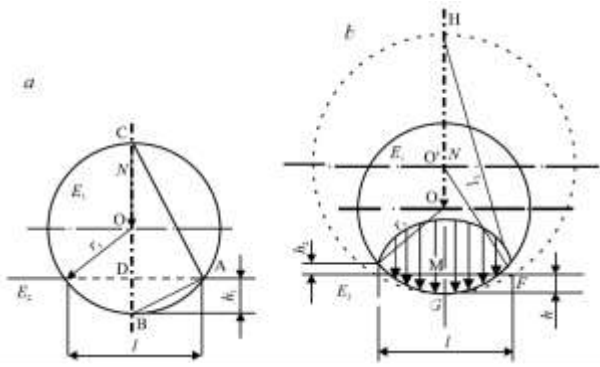
Figure 2. The elastic deformation of the cylindrical liner on the contact area (bottom) for Timken friction couples (a) – theoretical, and (b) – real

Taking into account the fact that r_1 is the non-deformed radius of the cylinder, and that r_2 is the radius of the deformed cylinder (Fig. 2b), then

$$r_2 > r_1 \tag{2}$$

However h_2 represents the decrease of the wear imprint from (a) to (b), considering the fact that the deformation of the cylinder is negligible:

$$h_2 = h_1 - h \tag{3}$$

But l is the length of the wear imprint, ΔABC :

$$(2r_1 - h_1)h_1 = l^2/4 \tag{4}$$

The value of the depth, h_1, is small and we can neglect it:

$$h_1 = l^2/8r_1 \tag{5}$$

Same happens for ΔFGH :

$$(2r_2 - h_2)h_2 = l^2/4$$

Same consideration for h_2:

$$h_2 = l^2/8r_2 \tag{6}$$

(4) and (5) are introduced into (2) :

$$h = l^2(1/r_1 - 1/r_2)/8 = l^2(r_2 - r_1)/8r_1r_2 = l^2/8r \tag{7}$$

r is a curvature radius equivalent for the deformed cylinder:

$$1/r = 1/r_1 - 1/r_2 = (r_2 - r_1)/r_1r_2 \tag{8}$$

From the relationship (4):

$$(r_2 - r_1)/r_1r_2 = l^2/8h_2 \tag{9}$$

But using Hertz's formula for the length of the wear imprint, where v (Poisson ratio), L (the length of the wear imprint), E (equivalent Young module), we can write a relationship starting from the hypothesis that the couple is loaded elastically, with an elliptical load distribution:

$$l^2/4 = 8Nr(1 - v^2)/\pi EL \tag{10}$$

Using the indexes 1 and 2 we can write :

$$1/E = 0.5\left[(1 - v_1^2)/E_1 + (1 - v_2^2)/E_2\right] \tag{11}$$

We introduce the equivalent elasticity module in (12):

$$E = 2E_1E_2/0.91(E_1 + E_2) \tag{12}$$

From the relationship (7) we will express the length of the wear imprint as:

$$l = 4\left[2Nr(1 - v^2)/\pi EL\right]^{1/2} \tag{13}$$

$$h_2 = 0.527N(E_1 + E_2)/LE_1E_2 \tag{14}$$

The depth for the wear imprint is obtained from relationships (5) and (14):

$$h = (l^2/8r_1) - 0.527N(E_1 + E_2)/LE_1E_2 \tag{15}$$

We obtain the lateral area of the wear sector, considering that the wear imprint consists of cylindrical sectors:

$$S_i = r^2\phi^3/12 \tag{16}$$

We replace ϕ with the ratio l/r (12):

$$S_i = l^3(r_2 - r_1)/12r_1r_2 = 2lh_2/3 \tag{17}$$

We can obtain the relationship for the transversal lateral area and replace h_2 in (16):

$$S_i = 0.35l(E_1 + E_2)Nl/E_1E_2L \tag{18}$$

Considering that l_m is the wear imprint, the wear volume has the value:

$$V_u = \sum_{i=1}^{n}(S_iq_i) = 0.351(E_1 + E_2)Nl_m/E_1E_2 \tag{19}$$

But:

$$V_u/A = kvtN/A \tag{20}$$

But h_u is the depth of the layer of removed material:

$$h_u = kpvt \qquad (21)$$

The equation (20) is an expression of the dependency of wear on the contact pressure, but

$L_f = vt$ so we can write:

$$k = h_u / pvt = h_u / pL_f \qquad (22)$$

$$k = V_u / Nvt = V_u / NL_f \qquad (23)$$

It is necessary to perform length measurements of the wear imprint in 3 different locations, thus analyzing the correct value. Using the value we obtained, we can obtain the wear depth h_{mu} and the volume of wear material that was removed V_u

2.2 GRAPHIC METHOD

Tests were performed using the following sliding speeds: a) 18.56; b) 27.85 ; c) 37.13; d) 46.41; e) 55.70: f) 111.4 cm /s. Volume wear and wear depth were calculated under different wear conditions, modifying the parameters normal load and sliding speed. The steels used were of the C120 and Rp3 types. All tests were performed for a period of one hour. Wear parameters were expressed in mm/h and cm^3/h. Tests were carried out using different polymers reinforced with 30% glass polymers. We have performed the graphic interpretation for each material and sliding speed, see figures from Fig 3 to Fig. 11.

Table 1 Regression functions between wear scar volume (V_u) and normal load (N)

Friction couple	v (cm/s)	Regression function wear scar volume (V_u)
Polyamide + 30% SGF/C120 steel	18.56	$V_u = 0.0005\ N^2 + 0.012\ N$
Polyamide + 30% SGF/C120 steel	27.85	$V_u = 0.0004\ N^2 + 0.0188\ N$
Polyamide + 30% SGF/C120 steel	37.13	$V_u = 0.0005\ N^2 + 0.0104\ N + 0.1423$
Polyamide + 30% SGF/C120 steel	55.70	$V_u = 0.0034\ N^2 - 0.0922\ N + 0.877$
Polyamide + 30% SGF/C120 steel	111.4	$V_u = 0.0006\ N^2 - 0.0205\ N + 0.272$
Polyamide + 30% SGF/C120 steel	153.57	$V_u = 0.0007\ N^2 + 0.1668\ N + 0.0675$
Polyamide + 30% SGF/ Rp3 steel	18.56	$V_u = 0.0003\ N^2 + 0.018\ N$
Polyamide + 30% SGF/Rp3 steel	37.13	$V_u = 0.0004\ N^2 + 0.0077\ N + 0.2291$
Polyamide + 30% SGF/Rp3 steel	46.41	$V_u = 0.0003\ N^2 + 0.0236\ N$
Polycarbonate + 20% SGF/C120 steel	27.85	$V_u = 0.0002\ N^2 + 0.0212\ N + 0.0138$

Using a special program the regression functions for (V_u) Table 1 and for (h_u) Table 2 were calculated. The parameters were expressed depending on the normal load.

Table 2. Regression functions between wear scar depth (h_u) and normal load (N)

Friction couple	v (cm/s)	Regression function wear scar depth (h_u)
Polyamide + 30% SGF/C120 steel	18.56	$h_u = 0.0007\ N^2 + 0.1099\ N$
Polyamide + 30% SGF/C120 steel	27.85	$h_u = 0.0017\ N^2 + 0.0223\ N + 2.5401$
Polyamide + 30% SGF/C120 steel	37.13	$h_u = 0.0027\ N^2 - 0.0345\ N + 3.7722$
Polyamide + 30% SGF/C120 steel	55.70	$h_u = 0.0038\ N^2 + 0.0017\ N + 4.0728$
Polyamide + 30% SGF/C120 steel	111.4	$h_u = 0.0005\ N^2 - 0.0607\ N + 5.0222$
Polyamide + 30% SGF/C120 steel	153.57	$h_u = 0.0062\ N^2 - 0.0569\ N + 5.1224$
Polyamide + 30% SGF/ Rp3	18.56	$h_u = 0.0008\ N^2 + 0.0106\ N + 2.2026$

steel		
Polyamide + 30% SGF/Rp3 steel	37.13	$h_u = 0.0032\,N^2 - 0.1452\,N + 5.7442$
Polyamide + 30% SGF/Rp3 steel	46.41	$h_u = 0.0022\,N^2 - 0.061\,N + 4.8439$
Polycarbonate + 20% SGF/C120 steel	27.85	$h_u = 0.002\,N^2 + 0.1141\,N + 2.6028$

We have opted for a graphic presentation of the experiments in order to have an overview on the Timken type couple for glass fiber reinforced polymers and metal under complex conditions of modifying normal loads, contact pressures and temperatures, with the variation of the sliding speeds.
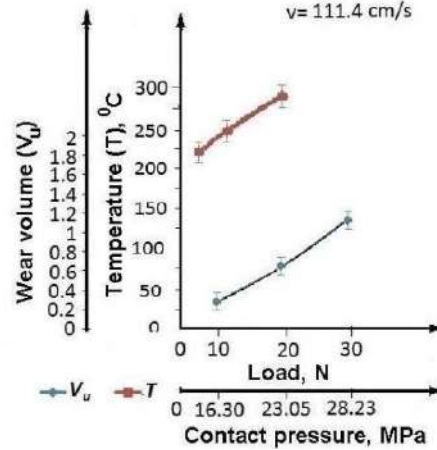

a)

b)
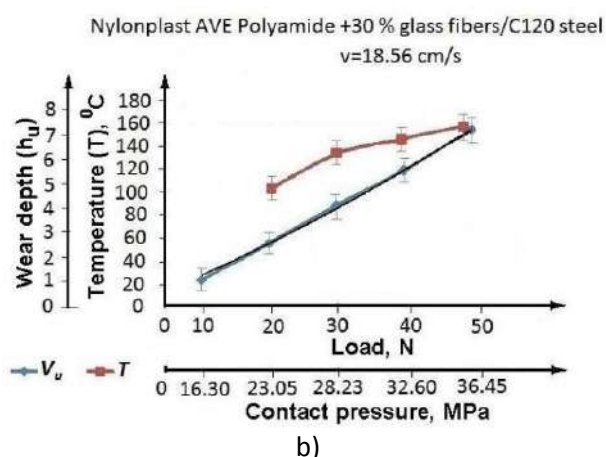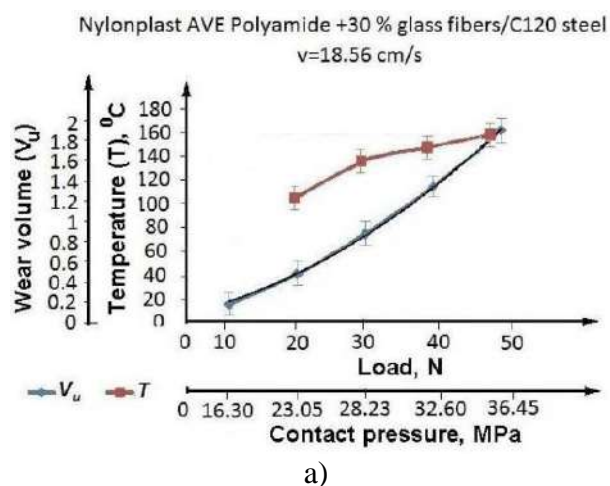
Figure 3. Wear evolution as scar wear volume (a) and depth (b) function of the normal load and contact temperature and variation of contact temperature Nylonplast AVE Polyamide + 30% SGF / C120 steel

a)

b)
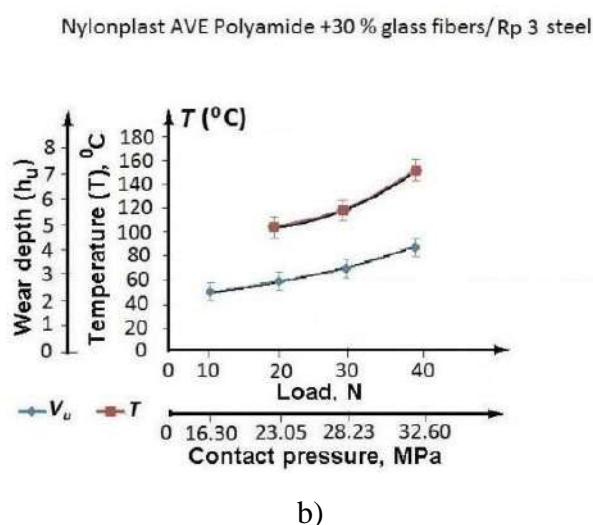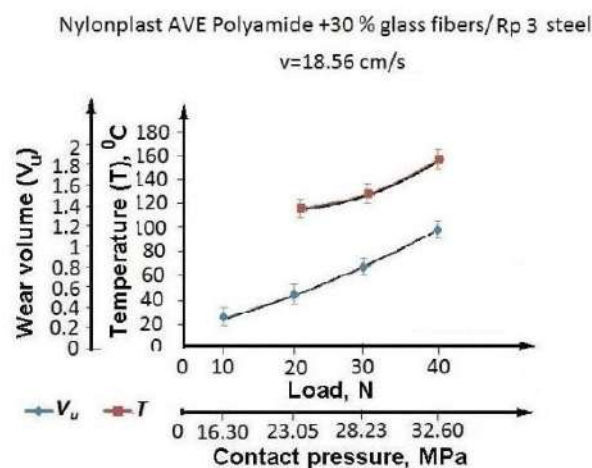
Figure 4. Wear evolution as scar wear volume (a) and depth (b) function of the normal load and contact temperature and variation of contact temperature Nylonplast AVE Polyamide + 30% SGF / Rp3 steel

a)
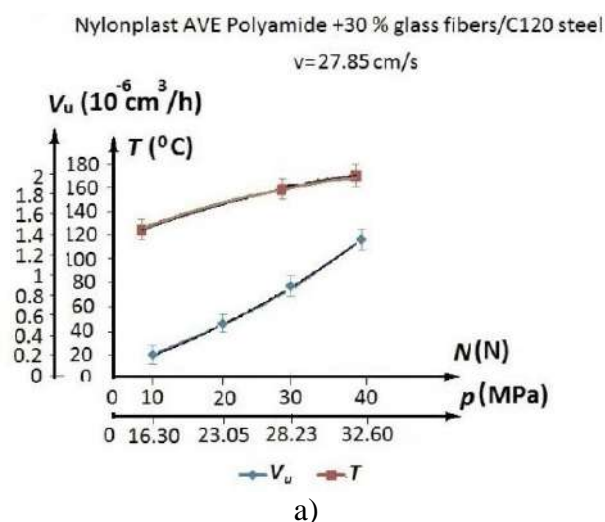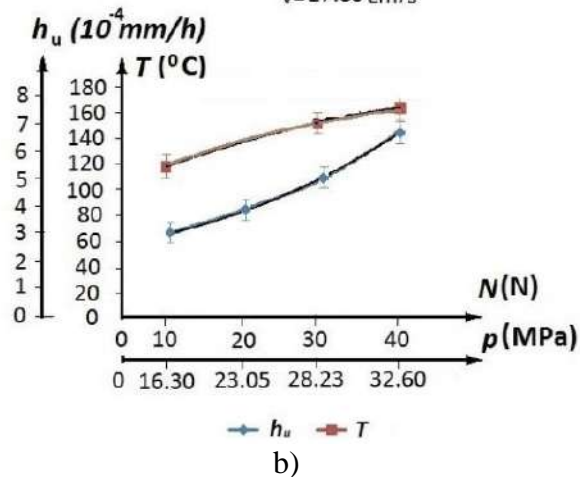
b)

Figure 5. Wear evolution as scar wear volume (a) and depth (b) function of the normal load and contact temperature and variation of contact temperature Nylonplast AVE Polyamide + 30% SGF / C120 steel
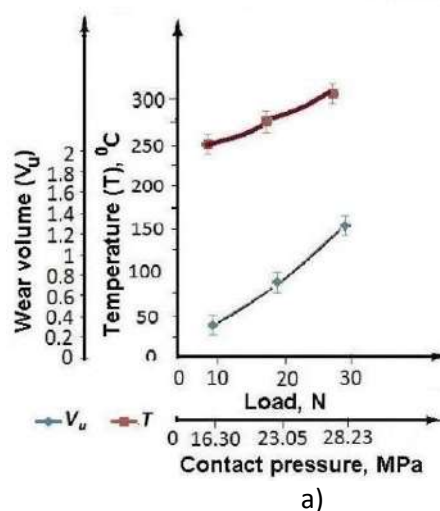

a)
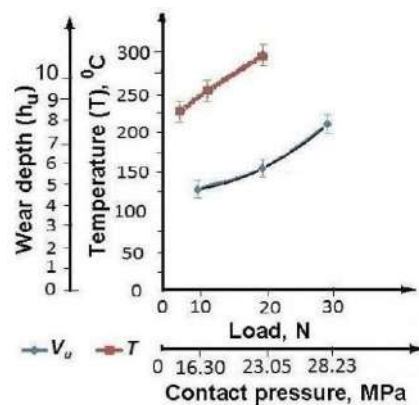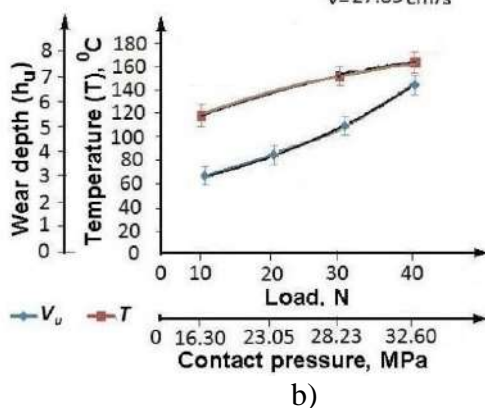
b)

Figure 6. Wear evolution as scar wear volume (a) and depth (b) function of the normal load and contact temperature and variation of contact temperature Nylonplast AVE Polyamide + 30% SGF / Rp3 steel

a)

b)

Figure 7. Wear evolution as scar wear volume (a) and depth (b) function of the normal load and contact temperature and variation of contact temperature Nylonplast AVE Polyamide + 30% SGF / C120 steel

a)

Figure 8. Wear evolution as scar wear volume (a) and depth (b) function of the normal load and contact temperature and variation of contact temperature Nylonplast AVE Polyamide + 30% SGF / C120 steel
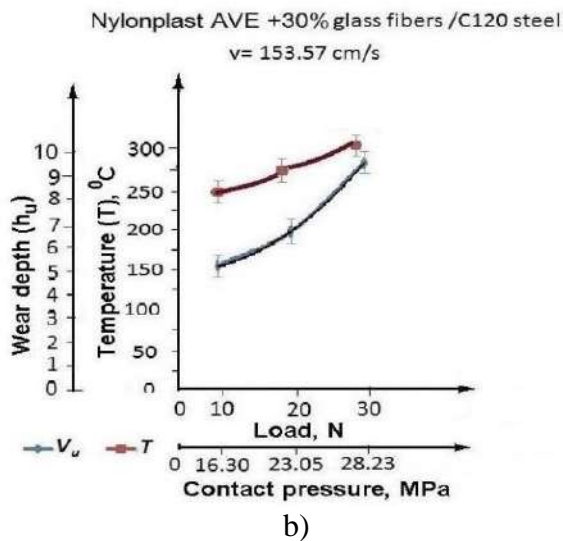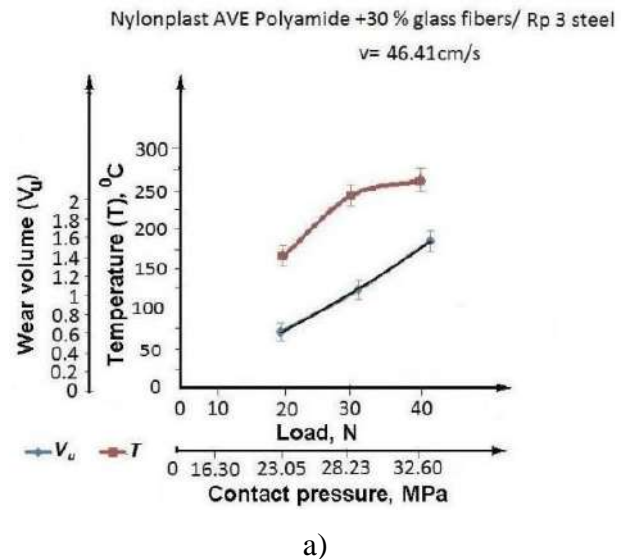

Figure 9. Wear evolution as scar wear volume (a) and depth (b) function of the normal load and contact temperature and variation of contact temperature Nylonplast AVE Polyamide + 30% SGF / Rp3 steel

Figure 10. Wear evolution as scar wear volume (a) and depth (b) function of the normal load and contact temperature and variation of contact temperature Nylonplast AVE Polyamide + 30% SGF / Rp3 steel
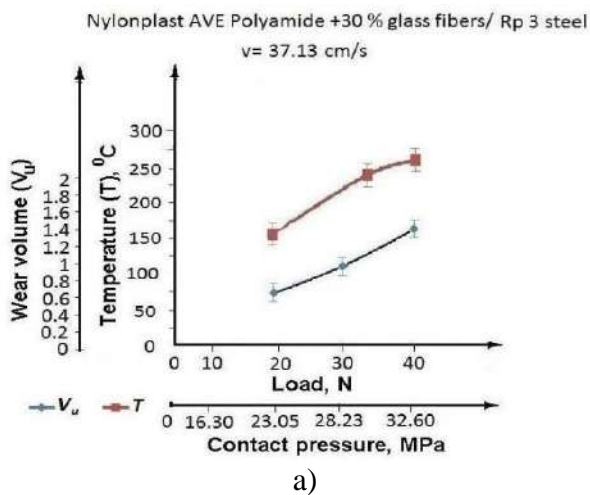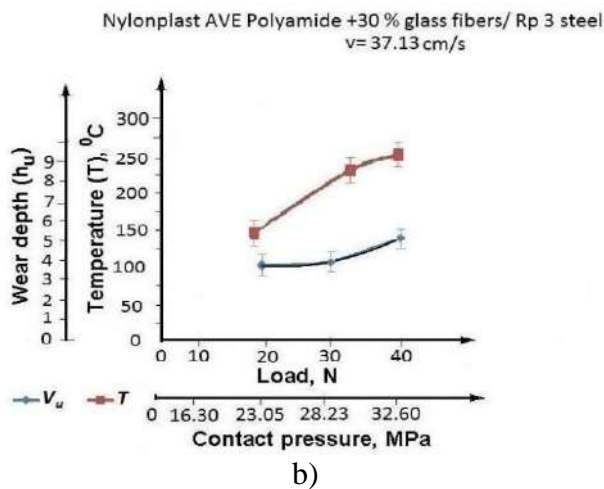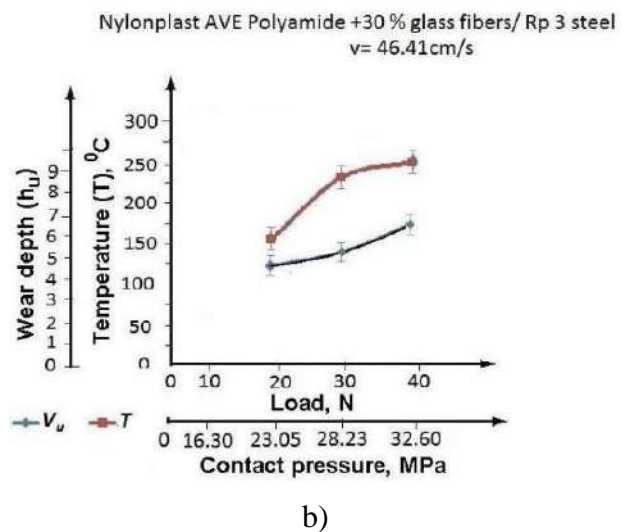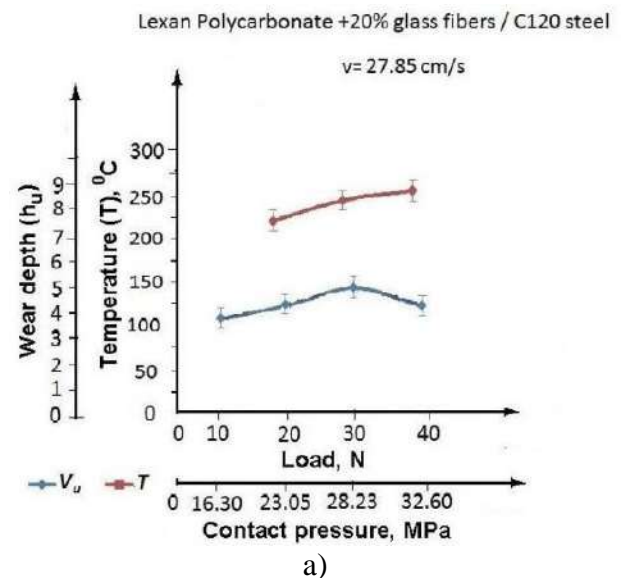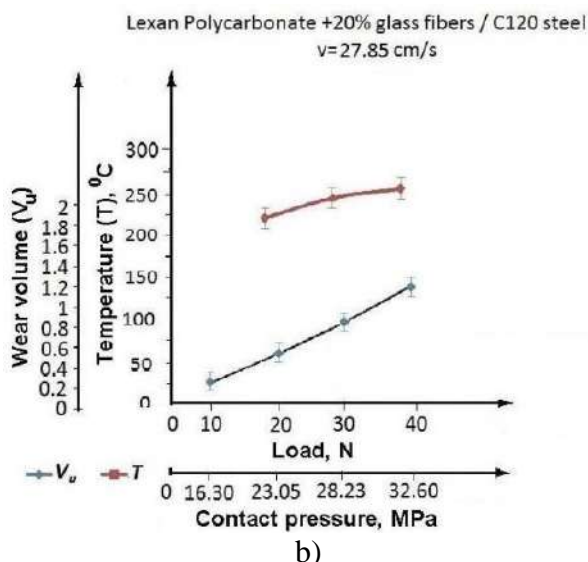
Figure 11. Wear evolution as scar wear volume (a) and depth (b) function of the normal load and contact temperature and variation of contact temperature PC Lexan 3412 + 20% SGF / C120

3. CONCLUSION

The injection process of thermoplastic composite polymers reinforced with glass fiber is a highly complex process, as can be seen in (Fig 12). Adhesion and corrosion phenomena occur during injection. The Timken couple polymer on metal simulates the conditions inside the auger very well, obtaining temperatures of 300 ^{0}C which leads to material flow.
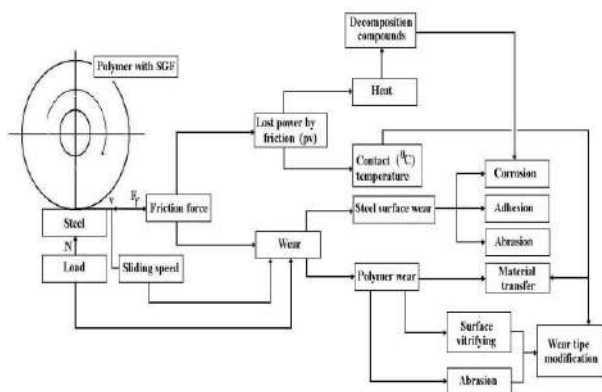

Figure 12. The complexity of the evolution process of friction-wear at a linear contact polymer with SGF / steel

For the Rp3 steel the equation (9) is confirmed, meaning that the friction coefficient has an absolute value that is smaller than the friction coefficient for the C120 steel. This also results from the wear volume *(Vu)* which is smaller for the Rp3 steel used for manufacturing tools.

We can notice once again that with the increase of the normal load, an increase in the wear volume also occurs. We can see that we have a parabolic increase in wear and not a linear increase. This means that if the load increases, the temperature and the wear volume also increase. This is a known fact and it can be demonstrated.

Another aspect is noticed – each polymer has a specific behaviour so that the determined regression functions are not common.

ACKNOWLEDGEMENTS

REFERENCES

[1] M. Bilik : *Parî trenia metal-plastmassa v maşinah i mechanizmah*, Maşinostroienie, Moskva 1965.

[2] R.S. Davyer-Joice, R.S. Sayles, E. Ioannides: An investigation into the mechanisms of closed three-body abrasive wear, Wear, Vol. 175, No. 1-2, pp. 133-142, 1994.

[3] G.B. Stachowiak, G.W. Stachowiak: The effects of particle characteristics on three-body abrasive wear, Wear, Vol. 249, No. 3-4, pp. 201-207, 2001.

[4] C. Li, Z. Zhong, Y. Lin, K. Frederich: Tribological properties of epoxy nanocomposites: III. Characteristics of transfer films, Wear, Vol. 262, No. 5-6, pp. 799-706, 2007.

[5] L. Chang, Z. Zhang, H. Zhang, A.K. Schlarb: On the Sliding wear of nanoparticles filled polyamide 66 composites, Composites Science and Technology, Vol. 66, No. 16, pp. 3188-3198, 2006.

[6] N.K. Myshkin, M.I. Petrokovets, A.V. Kovalev: Tribology of polymers: Adhesion, friction, wear, and mass-transfer, Tribology International, Vol. 38, No. 11-12, pp.910-921, 2005.

[7] Johnson K.L., Kendall K., Roberts A.D.: Surfac energy and the contact of elastic solids. Proc. Roy. Soc. A 324, 301(1971)

[8] B.V. Deryagin, V.M. Muller, Y.P. Toporov: Adhesive contact deformation of a single microelastic sphere. J. Colloid Interface Sci. 53 (1975) 314.

[9] C. Shen, J.H. Dumbleton: The Friction and Wear Behavior of Polyoximethylene in Convection with Joint Replacement, Wear, Vol. 38, No. 2, pp. 291-303, 1978.

[10] L. Chang, K. Friedrich: Enhancement effect of nanoparticles on the sliding wear of the sliding wear of short fiber-reinforced polymer composites: A critical discussion of wear mechanisms, Tribology International. Vol. 43, No. 12, pp. 2355-2364, 2010.

[11] H. Voss, K. Friedrich: On the wear behavior of short-fiber-reinforced PEEK composites, Wear, Vol. 116, No. 1, pp. 1-18, 1987.

[12] G.H. West, J.M. Senior: Frictional Properties of Polyethylene, Wear 19, No. 1, pp. 37-52, 1973.

[13] H.Jost: Zum Verschleissverhalten von Polyamid, Plaste und Kautschuk, Vol. 17, No. 4, pp. 266-270, 1970.

[14] G.M. Bartenev, V.V. Lavrentiev, N.A. Konstantinova: The actual Area and friction Properties of Elastomers under Frictional Contact with Solid Surfacesm, Wear, Vol. 18, No. 6, pp. 439-448, 1971.

[15] J.K. Lancaster, D.C. Evans: Wear of Polymers, in: D. Scott (Ed.) *Treatise on Mat. Sci. and Technology*, Academic Press, pp. 13-86, New York 1979.

[16] S.N. Kukureka, C.J. Hooke, M. Rao, P. Liao, Y.K. Chen: The effect of fibre reinforcement on the friction and wear of polyamide 66 under dry rolling-sliding contact, Tribology International, Vol. 32, No. 2, pp. 107-116, 1999.

[17] Clerico M. A.: Study of the Friction Wear of Nylon against Metal, Wear, Vol. 13, No. 3, pp. 183-197, 1969.

[18] V.A. Bely, A.I. Sviridenok, M. I. Petrokovets: *Friction and Wear in Polymer based Materials*, Pergamon Press, Oxford, 1982.

[19] G.M. Bartenev, V.V. Lavrentiev: *Trenie i iznos polimerov*, Himia, Leningrad, 1972.

[20] J. Wang, M. G. B. Songhao, G. Shirong: Investigation of the influence of MoS2 filler on the tribological properties of carbon fiber reinforced nylon 1010 composites, Wear, Vol. 255, No. 1-6, pp. 774-779, 2003.

[21] Q.B. Guo, M.Z. Rong, G.L. Jia, K.T. Lau, M.Q. Zang: Sliding wear performance of nano SiO2 / short carbon fibre / epoxy hybrid composites, Wear, Vol. 266, No. 7-8, pp. 658-665, 2009.

[22] J.K. Lancaster: Lubrication of Carbon Fibre reinforced Polymers, Wear, Vol. 28, No.3, pp. 315-352, 1972.

[23] D.A. Barlow: Some Observations of the Friction Properties of Vinyl, Wear, Vol. 20, No. 2, pp. 151-157, 1972.

[24] S. Bahadur: The development of transfer layers and their role in polymer tribology, Wear, Vol. 245, No. 1-2, pp. 92-99, 2000.

[25] H.R. Jacobi: Neue Erkenntnisse über Gleitschaften von Polyamiden, Kunststoffe, Vol. 47, No. 5, pp. 234-239, 1957.

[26] P. Boey, W. Ho, S.J. Bull: The effect of temperature on the abrasive wear of coatings and hybrid surface treatments for injection-moulding machines, Wear, Vol. 258, No. 1-4, pp. 149-156, 2005.

[27] W. Knappe, W. Mahler: Modellversuche zum Verschleiß in Kunststoffverarbeitungsmaschinen, Kunststoff Rundschau, Vol. 19, No. 2-3, pp. 45-51, 1972.

[28] H. Ladwig, K.D. Sommer: Verscuche zur Erhöhung der Verschleißfestigkeit von Zylindern und Schnecken bei der Verarbeitung von glassfaserverstärkten Polyamiden auf Spritzgießmaschinen, Plastverarbeiter, Vol. 21, (1970) 259-260.

[29] W.W. McCandless: Verschleißfeste und korrosionbeständige Zylinder und Schnecken für Kunststoffmaschinen, Industrie – Anzeiger, Vol. 91, No.25, pp. 25-29, 1969.

[30] D. Rus, L. Capitanu: Wear of Polished Steel Surfaces in Dry Friction Linear Contact on Polimer Composites with Glass Fibres, Tribology in Industry, Vol 35, No. 4, pp. 337-344, 2013.

[31] D. Rus: *Linearer Trockenkontakt KGF-Polymer/Stahl: Versuchsergebnisse und Kommentare aufgrund der Modellierung unter Bedingungen der Verarbeitung durch Spritzgießen*, Akademikerverlag, Germany, 2015.

A SIMPLIFIED TEST RIG AS A TOOL TO INVESTIGATE COMPLEX LUBRICATION PHENOMENA AT THE PISTON-RING CYLINDER LINER INTERFACE

Polychronis S. DELLIS[1]
[1]ASPETE, Department of Mechanical Engineering Educators, Athens, Greece
*Corresponding author: pasd@city.c.uk

Abstract: *The lubrication regime at the piston-liner assembly plays a significant role in engine friction and it is, therefore, a major concern in modern engine designs. Nowadays, the stringent emission regulations, require the characterization of the oil film in between and under the piston-rings of the piston-liner assembly so that, first to understand the complex tribological system and second, to achieve through experimental results minimal energy losses and at the same time meeting the strict emissions standards. In a simplified test rig, a steady piston-ring section of overall width 5 mm is placed under a flat surface used as a reciprocating liner. The advantage of this layout is that it can ignore the many uncertainties that follow the piston movement in an internal combustion engine, such as piston-ring and piston dynamics, starved lubrication, liner geometry deformation, lubricant and additive degradation and blow-by in order to generate reliable results. Moreover, a number of sensors, such as optical ones (laser induced fluorescence - LIF) and transducers that can measure the lubricant film thickness, the oil film pressure, friction between the surfaces and temperature, can be fitted more easily and provide measurements of the lubrication between the two surfaces. Visualisation results in the test rig provide a good understanding of the lubrication regime at the piston-cylinder assembly and thus, the onset and development of cavitation throughout the stroke is identified.*

This presentation is focused on previous experimental findings in the simplified test rig, how these can be applied on specially designed and modified engines with the respective sensors fitted and the issues concerning the engine experiments. An emphasis is given on the simplified test rig lubricant parametric study, as some very useful results can be drawn for further analysis and possible engine applications, so that further friction reduction can be achieved via design consideration and oil formulation.

Keywords: *piston-ring lubrication, single-ring test rig, engine experiments, oil film, friction and pressure measurements, visualisation, cavitation, laser induced fluorescence*

1. INTRODUCTION

The lubrication regime formed in the piston-ring cylinder liner interface which is one of the biggest contributor to mechanical losses, is critical to the amount of surface contact, friction, oil consumption and wear. The optimum lubrication of the piston-rings is necessary to reduce friction and also limit oil consumption.

The lubricant film formed between the piston-ring and cylinder liner is very thin and the measurement of this essential variable is difficult. All the proposed methods

(capacitance, resistance, Laser Induced Fluorescence – LIF, ultrasound, inductance) are combined with respective error sources. Therefore, it is of great importance to have tools available for evaluation of friction, oil film thickness and pressure, at the interface between the piston-ring and liner. The test rig can be used for investigation of effects of different components and running conditions and also for validation of numerical simulation models [1].

Of particular interest is the role of cavitation in the performance of the piston-ring pack. When considering lubricant flow, it is known that when the pressure becomes too low (drops below the lubricant vaporisation pressure or the saturation pressure of dissolved air), the continuous film will rupture and air bubbles are formed. Once the pressure drops to a critical value, the oil will cavitate, separating into liquid and vapor [2].

In the 2011 European Comission White Paper on transport a reduction of at least 60% of greenhouse gas emissions from transport by 2050, with respect to 1990 levels, was called for. Therefore, the efficiency and frictional losses in a vehicles powertrain are areas of great importance [3].

This manuscript presents the comparison between cavitation visualisation results from a simplified experimental single ring test rig and the extension of the same method applied to a motored single cylinder engine. Since in an engine the liner and piston–ring configuration are reversed relative to the examined test rig, any direct extrapolations of the conclusions should be treated with some extra caution [4]. The solid results derived from the simplified test rig are also presented and used for Laser Induced Fluorescence calibration that can be applied to the simplified test rig at first and the engine afterwards.

2. EXPERIMENTAL SET-UP

Both engine and simplified test rig measurements were accomplished. Data from the simplified single-ring test rig were going to be verified from the engine test rigs. At the same time, the many uncertainties that follow the engine experiments, that can introduce certain difficulties during data interpretation when studied, were going to be eliminated. The test rig, with its inherent and purposed simplicity can be used as a test bed for developing new advanced sensor fittings and signal output, prior to their installation in an engine test bed.

2.1 MAN-AVL Castrol lubrication engine

For the purpose of studying the oil film properties, a supercharged, 2-litre, single cylinder MAN AVL - Castrol engine was used as an experimental test bed. This specially modified engine is using lubricant draining points in different positions, so that oil could be drained out of the engine during its operation. After the initial engine installation [5], it was proposed that the method used for oil film visualization was going to be an issue that had to be solved first, and study after.

Figure 1. The MAN-AVL Castrol engine cylinder block (upper part, with liner and piston) [5]

Figure 2. The MAN-AVL Castrol lubrication engine without the cylinder block – upper part [5]

Cavitation which was evident at an idealized test rig [4, 6], was also going to be observed in engine experiments and conclusions were going to be drawn regarding the phenomenon of cavitation and how can it be characterized with the addition of oil film pressure measurements.
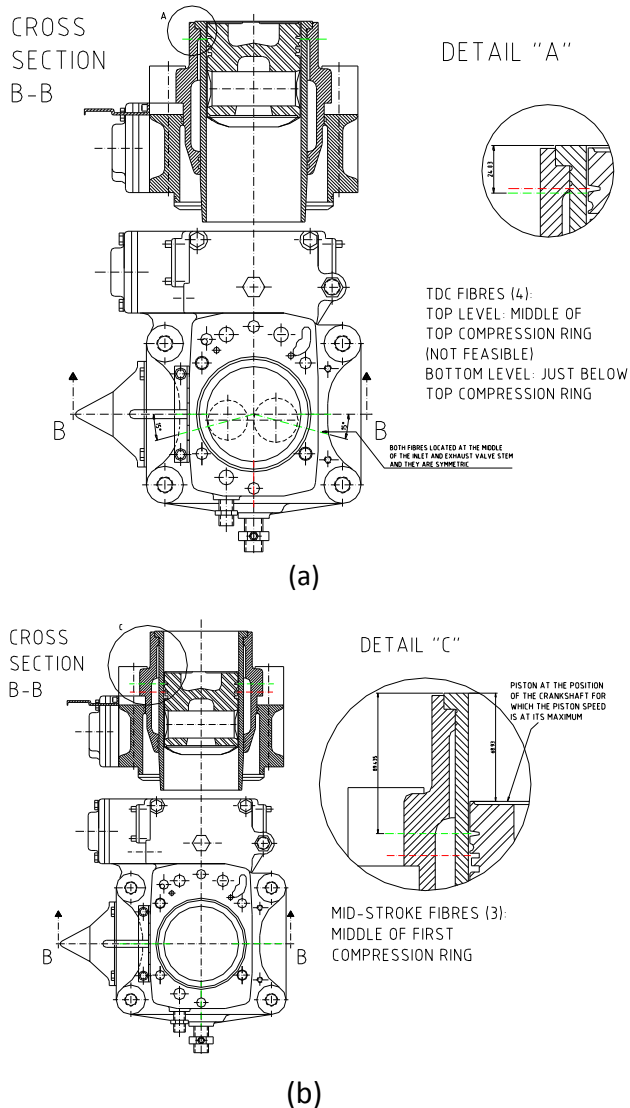

(a)

(b)

Figure 3. (a) Detailed drawings of the proposed TDC fibre probes installation.
(b) Detailed drawings of the proposed mid-stroke fibre probe installation [5]

2.2 Lister-Petter PHW1 diesel engine used for the LIF engine experiments

Engine visualisation experiments were carried out after the introduction of a direct-injected, single-cylinder water-cooled Lister-Petter PHW1 diesel engine used for the LIF engine experiments in previous research

projects [7], [8]. The PHW1 engine was coupled to a Plint TE/46 engine test bed. Table 1 shows the Lister-Petter engine specifications and Figure 4 the dynamometer – engine setup.

Table 1. Lister Petter engine specifications

Cylinder Bore	87.31/87.35
Stroke	110 mm
Stroke/Bore ratio	1.26:1
Swept volume	659 cm^3
Compression ratio	16.5:1
Connecting rod length	231.9 mm
Conrod/crank ratio	4.22:1
Oil capacity	2.8 l
Max engine torque	32.5 Nm@1700 rpm
Max Speed	2000 rpm
Tangential Ring Tension	
Top ring	14.36-19.21 N
2nd	14.54-19.43 N
3rd	13.16-17.57 N
4th	21.17-28.6 N

Figure 4. Plint dynamometer coupled to the Lister-Petter engine

For the purpose of visualisation, pockets had to be machined in the sides of the engine block enabling a large viewing area for the imaging process. The pockets were machined with spark erosion technique. The quartz windows were made to suit the spark eroded pockets. Above, between and below the window pockets, holes have been machined to accommodate a pressure transducer (novel

technique) and optical fibres, similar to an engine block fitted with LIF probes, that was used for oil film thickness engine data ([7], [8]).

Figure 5. 3-D views of Lister Petter engine block and piston [9].

Figure 6. Details of the pressure transducer fittings, the fibre probes and the viewing windows of the Lister Petter engine liner

Figure 7. Upper and lower window, (a) anti-thrust side window visualisation area (b) front side of the Lister-Petter block [9].

Figure 8. Lister-Petter engine experimental set-up [9].

During the Lister-Petter engine visualisation experiments, better images were taken from the lower windows, at both anti-thrust side and front side (Figures 7 (a) and (b)). The pressure transducer (Kulite XCQ-080 500 psi (absolute)) failed as the very small wiring of the Wheatstone bridge amplifier was snapped during fitting of the pressure measuring unit from the measuring stations. LIF measurement probes were not fitted prior to the acquisition of the pressure signal. From the six pressure monitoring points the four were saved; the necessary machining on the outer surface of the engine liner distorted the bore [9].

2.3 Simplified Single Ring Test rig

In Figure 9 below, the single-ring test rig configuration can be seen.
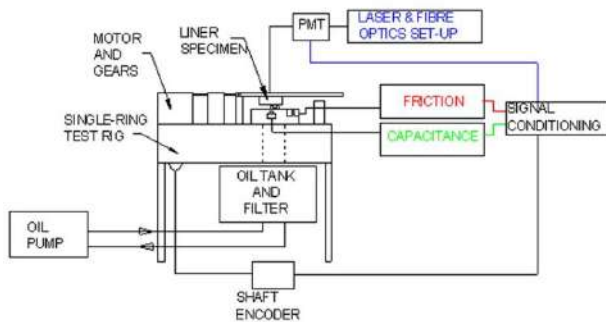

Figure 9. Single ring test rig schematic diagram [4]

This experimental set-up provided some solid results of LIF measurements, capacitance, pressure measurements, friction and visualization with the use of an optical liner (Figure 10). Results can be seen in Figures 11 and 12, where a sample of the parametric study results for visualization experiments, LIF and pressure is evident.
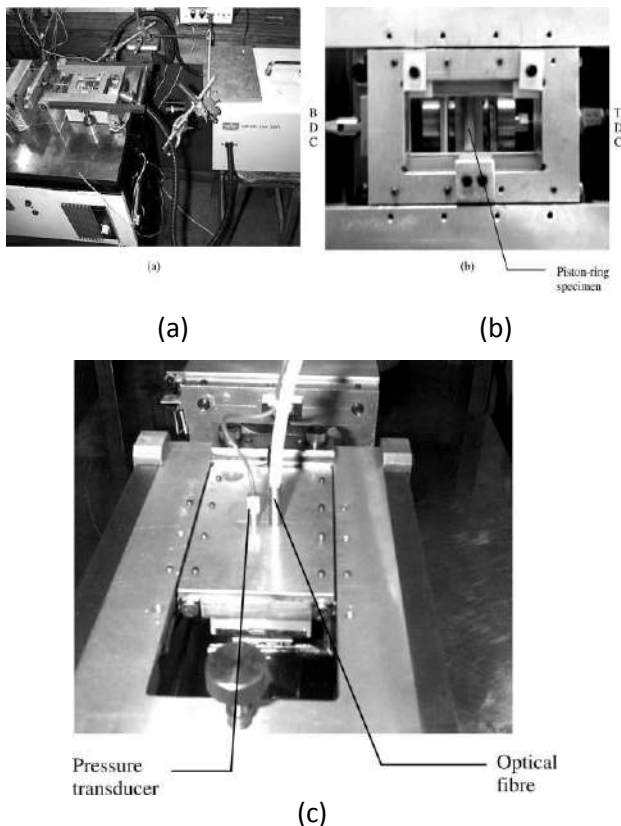

(a)   (b)

(c)

Figure 10. (a) Test rig with glass liner and flash lamp; (b) close-up of the glass liner and piston-ring specimen used for the visualization experiments (c) liner fitted with the pressure transducer and optical fibre (LIF sensor) [4]

3. RESULTS

3.1 Simplified Single Ring Test rig

In this section, visualization results from the single ring test rig can be seen in Figure 11 and friction results as well as oil film pressure combined with oil film visualization in Figure 12, respectively. The solid results from the single ring test rig, lead to similar applications to the engine test bed, so that direct comparisons could be made.
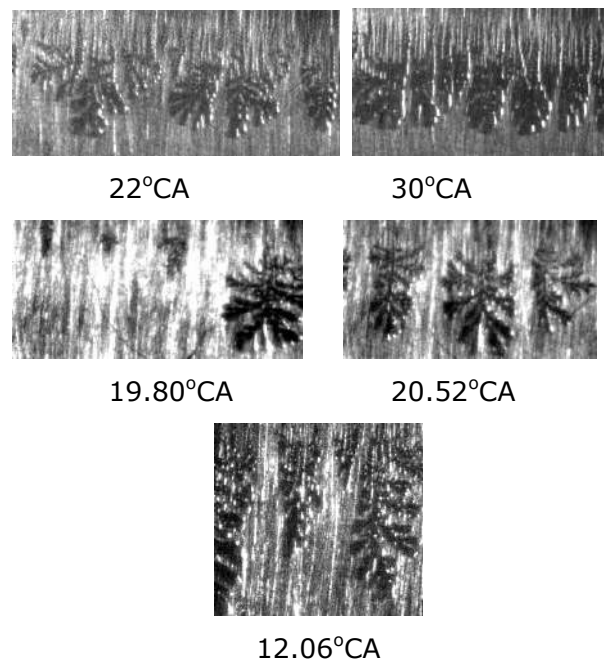

22°CA   30°CA

19.80°CA   20.52°CA

12.06°CA

Figure 11. (a) Fern growth captured using different magnification systems. (a) CF-3 magnification (65.3), 700 r/min, 22mm stroke, 1869 N/m. (b) CF-4 magnification (66.8), 700 r/min, 22mm stroke, 1869 N/m. (c) CF-4 magnification with extension lens (68.7), 700 r/min, 22mm stroke, 2843 N/m [4]

3.2 Engine visualization results – comparison with single ring test rig

Engine visualization experimental data were also acquired and a direct comparison of the visualization results from both test rigs is attempted. There is evidence of the string cavities that appear on the surface of the barrel-faced top compression ring of the Lister PHW1 engine. The research approach to understanding cavitation that was identified in Figure 13, has followed the outcome of the visualisation research study of the single-ring test rig.
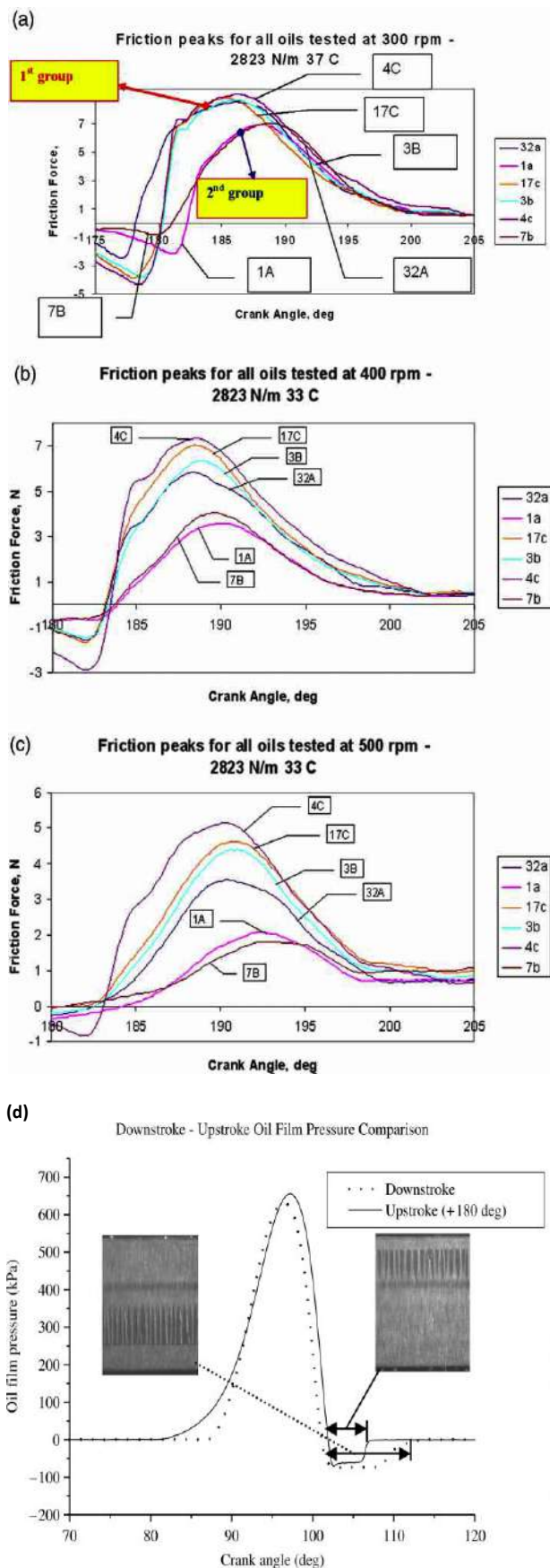
Figure 12. (a), (b), (c) friction parametric study for 6 different CASTROL oil blends, (d) combination of oil film pressure measurements and cavitation visualisation ([4], [10])

The idealised single-ring test rig is being used as a large scale model in contrast to the real sized engine test rig. In the case of the single-ring test rig, the ring was covered in the majority of the stroke with string cavities. During flow reversal, the cavitation is initiated by fern-shaped cavities which grow further, to form up bigger ferns and fissure type cavities. Later on in the stroke they develop to strings on the surface of the piston-ring and they grow so that they will be reaching its trailing edge. It is important to note, that LIF results (see Figure 14) show as well the point where the lubricant cavitates, under the piston-ring at mid-stroke.

In the case of the engine, however, the stages of cavitation inception and initial development are not clear because the size of visualisation window has hindered imaging of the oil flow at the reversal points close to the dead centres. As seen in figures 5, 6, 7 the quartz windows size is limited within the areas of the measuring stations (pressure transducer and fibre optic hole). On one hand, the quartz sectioned liner provided cavitation images similar to the ones recorded for the single - ring test rig, on another, the overall size and their span compared to the stroke length is not adequate to "scan" the whole of the engine stroke length.
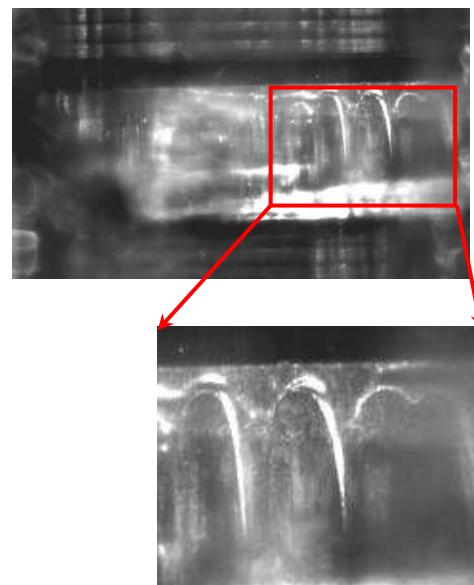

Figure 13. Lister Petter anti-thrust side lower window, top compression ring at 576° CA exhaust stroke, camera at 11.17 cm from top edge [10]

The following schematic (Figure 14) shows the most probable cavitation development in the engine during the stroke according to the images taken. The cavitation stages derived, are postulated from engine imaging and the simulation test rig results visualisation data.
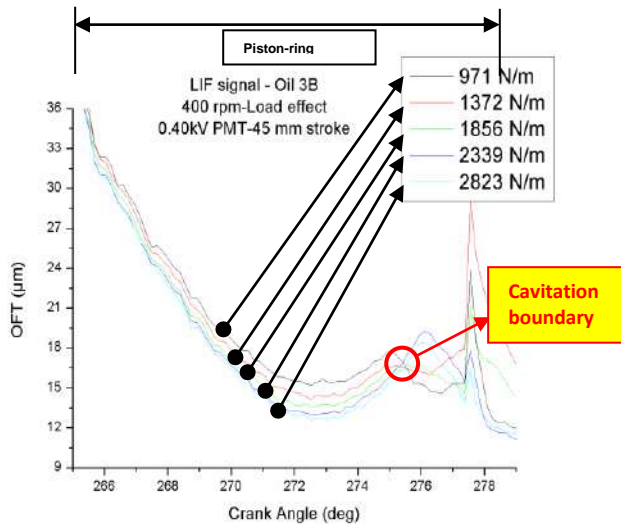

Figure 14. Load variation on LIF results (dynamic calibration) – upstroke
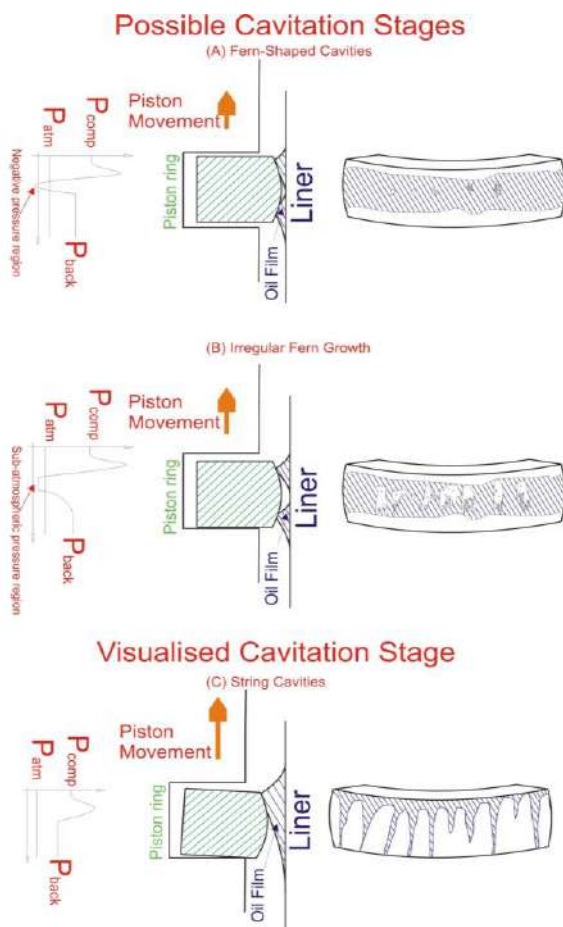

Figure 15. Possible Cavitation stages on the Lister-Petter engine [9]

Furthermore, it should be taken into account that the lubrication is distorted by the insertion of the quartz windows as shown in the liner surface profilometry results in Figure 16.
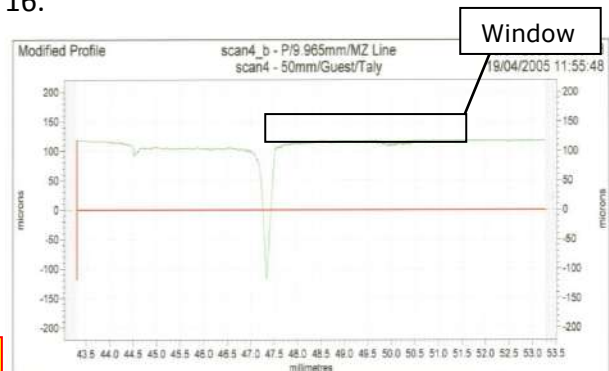

Figure 16. Surface profilometry of lower side of upper window [10]

An attempt was made to compare the imaging taken from both experimental test rigs, based on the testing parameters and the image properties.

Table 2. Comparison between Lister Petter and test rig test conditions

Test Conditions	Single Ring Test Rig	Lister – Petter Engine
Speed (rpm)	300	398
Load (N/m)	971	motoring
Stroke Length (mm)	50	110
Linear Velocity (m/sec)	1.728	2.016
Distance from (mm)	TDC: 25	top edge of top land at TDC: 111.99

The comparison between the two experimental test rigs necessitates a "cavitation factor" coefficient to be determined. This coefficient is the ratio of the width or the length of the string cavities divided to the piston ring width [10].

$$\text{Cavitation factor}_i = \frac{widthofstring}{widthofpistonring}$$

Following the measurement scale of the image, the string distances for every case (test rig and engine) are presented (Table 3), so that averaged string distances measured from the images can be taken for every case.

Table 3. Measured string distances for test rig and engine

Measured string distances (mm)		
Single-Ring Test Rig	Lister-Petter Engine	
0.292	0.531	
0.167	0.368	
0.250	0.344	
0.292	0.478	
0.333	0.514	
0.292	0.589	
0.167	0.414	
0.292		
0.292		
0.250		
0.292		
0.250		
0.333		
0.275		
0.333		
0.367		
0.267		
0.208		
0.200		
0.208		
0.292		
Average width	0.268	0.463
σ	0.056	0.090

Cavitation factors CF calculated for the engine CF_{engine} = 0.194 and respectively for the test rig $CF_{test\ rig}$ = 0.054. CF_{engine} is 72.16% greater than $CF_{test\ rig}$. In the case of the single ring test rig, the strings are covering approximately 50% of the piston ring length and have a very uniform shape, due to the limited factors affecting the lubrication of the single ring test rig [10].

3.3 LIF Calibration

The identification of cavitation, which was first evident during the LIF experiments and further on identified in the visualization experiments in both the simplified test rig and the engine, imposed the necessity of calibrating the LIF results in order to get a complete picture of the oil film thickness and the point where the oil film breaks. The process of calibrating the LIF signal, is described in [11], where the single-ring test rig is used again as a safe method to acquire the results from LIF and surface profilometry of a specially machined groove on the surface of the piston-ring specimen.

Groove data were acquired at the area where the fitted fiber on the liner specimen travels. Since the stylus of the profilometer was acquiring data for the groove every 10 μm of groove length, five (5) profiles in sequence have been averaged to get the averaged data that were going to be compared to the LIF signal (the diameter of the fiber core is 50 μm). Eventually the area of the groove over which the fiber travels was covered in the best way possible.

Figure 16 shows the fibre travelling over the groove of known depth used for the LIF calibration [11].
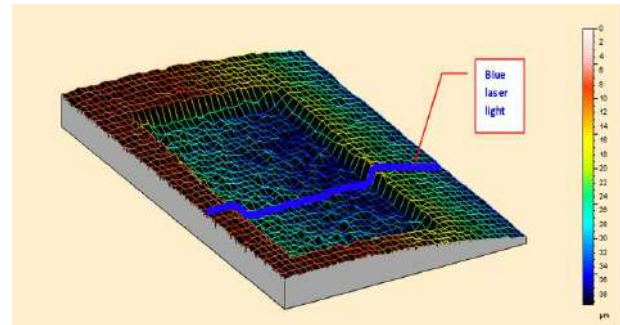
Figure 16. The groove with the blue - highlighted line shows the area over which the optical fiber travels [11]
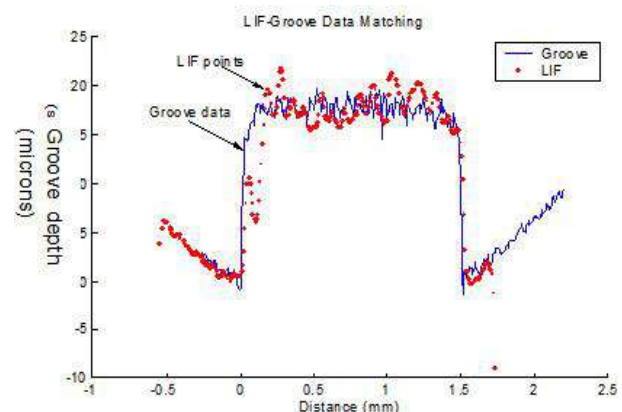

Figure 17. Matching of groove data and averaged LIF data [11]

It is evident, that this specially machined piston-ring can be used for LIF calibration of the engine experiments. As it was stated before, from the MAN-AVL engine lubricant stations, used lubricant can be extracted and when poured into the single-ring test rig, it can

be used for the calculation of a calibration coefficient as described above. This coefficient can calibrate the LIF data derived from the engine and this time a more accurate calibration coefficient can be derived because the oil used for the calculation of the coefficient and the oil used in the engine experiments is exactly the same (meaning that its chemical composition has been degraded to the same extent). This is very important because the chemistry of the lubricant is an important factor to its fluorescence properties and according to this procedure it is taken into account when calibration is attempted.

As already stated, LIF results from the single-ring test rig showed, at first, the point where the lubricant cavitated (oil film rupture shown in Figure 14).

In Table 4, calibration coefficients are derived, and data are given for a specific Castrol lubricant blend, at four different temperatures [11].

Table 4. Temperature results for the calibration coefficients [11]

Oil Temperature (°C)	38	50	60	70
Calibration Coefficient (μm/Volt)	295	364	353	389
Standard Deviation (μm/Volts)	14	26.9	21	55.37
Error (%)	5	7	6	14

4. CONCLUSIONS

The single-ring test rig is a tool that provides robust results in terms of lubricant film thickness, LIF, oil film pressure, friction measurements, and visualization – cavitation results. It is therefore, important to study and test whichever experimental method used, first at the test rig and afterwards in the engine test bed. The test rig results improve the researcher's confidence in experimental testing, thus minimizing the risk when applying the same method in engine experiments. Another supporting factor is that the

experimental results can be interpreted in a much safer and easier manner. The engine experiments are inherited with many uncertainties, which will be further enhanced from cycle to cycle inconsistencies.

Even without the engine application, the single ring test rig results can strongly support parametric study of different lubricants, different piston-ring curvature and its effect in oil film pressure and even so friction results throughout the stroke and study the different lubrication regimes (hydrodynamic, elastohydrodynamic, boundary and mixed) with the inclusion of the parametric study, that is mentioned above. It is therefore a necessity to simulate realistic engine speed and strokes, so that the results are as close as possible to a real engine. The usefulness of the single ring test rig is easily recognizable from:

- the identification of cavitation in the LIF results,
- the successful implementation of the optical liner to acquire lubricant cavitation images and the miniature pressure transducer for the oil film pressure results prior to applying the same method to an engine and
- the proximity of the LIF calibration testing (low rpm and no hydrodynamic film) and the recognition of the many parameters that affect the derivation of a solid lubricant calibration coefficient.

The author gratefully acknowledges these contributions.

REFERENCES

[1] M. Söderfjäll, A. Almqvist, R. Larsson: Component test for simulation of piston ring – Cylinder liner friction at realistic speeds, Tribology International, Vol. 104, pp. 57-63, 2016.

[2] A. Almqvist, P. Wall: Modelling cavitation in (elasto)hydrodynamic lubrication, in Pranav H. Darji (Ed.): *Advances in tribology* doi:10.5772/63533, INTECH, pp 197-213, 2016.

[3] A. Spencer: *A Simulation Tool for Optimising Combustion Engine Cylinder Liner Surface Texture*, PhD thesis, Department of Engineering Sciences and Mathematics, Lulea University of Technology, Lulea, 2013.

[4] P. Dellis, C. Arcoumanis: Cavitation development in the lubricant film of the piston-ring assembly, Proc. IMechE, Part J: J. Engineering Tribology, 218, pp. 157–171, DOI: 10.1243/1350650041323340, 2004.

[5] P. Dellis: *Piston ring lubrication and its link to exhaust particulates emissions in internal combustion engines,* MPhil to PhD transfer report, Department of Mechanical Engineering, Imperial College of Science, Technology and Medicine, London, 2000.

[6] C. Arcoumanis, M. Duszynski, H. Flora, P. Ostovar: Development of a piston-ring lubrication test-rig and investigation of boundary conditions for modelling lubricant film purposes, SAE paper 952468, 1995.

[7] M. Duszynski: *Measurement of Lubricant Film Thickness in Reciprocating Engine*s, PhD thesis, Imperial College of Science, Technology and Medicine, London, 1999.

[8] E.A. Pyke: *Investigation of Piston Ring Lubrication Using Laser Induced Fluorescence*, PhD thesis, Imperial College of Science, Technology and Medicine, London, 2000.

[9] P. Dellis, C. Arcoumanis: Measurements of lubricant film thickness in reciprocating piston cylinder assemblies and engines, Journal of Physics, Conference Series, Volume 45, pp 161-161, 2006.

[10] P. Dellis: *Aspects of lubrication in piston cylinder assemblies*, PhD thesis, Imperial College London, Department of Mechanical Engineering, London, 2005.

[11] P. Dellis: An Attempt to Calibrate the Laser Induced Fluorescence (LIF) Signal used for Oil Film Thickness (OFT) Measurements in Simulating Test Rigs, Tribology in industry, Vol. 38, No. 4, pp. 525-538, 2015.

INFLUENCE OF SURFACE QUALITY ON 3D DIGITIZATION RESULTS OBTAINED BY CLOSE-RANGE PHOTOGRAMMETRY

Željko SANTOŠI, Igor BUDAK*, Mario ŠOKAC, Đorđe VUKELIĆ

University of Novi Sad, Faculty of Technical Sciences, Novi Sad, Serbia
*Corresponding author: budaki@uns.ac.rs

Abstract: *3D digitizing of high quality machined metal surfaces is considered as highly uncertain in case of application of image based methods. This is due to their monotonous visual texture and a very high degree of reflection. The aim of this paper is the investigation of influence of surface quality on the 3D digitization results obtained by close-range photogrammetry based on structure from motion approach. As an object for 3D digitization RUGOTEST 1 (Roughness Comparison Specimens) was used. RUGOTEST 1 is etalon for tactile and visual comparison of the workpiece surface finish according to various machining processes. Image based 3D reconstruction can be time consuming and it depends on image resolution, number of images and computer processing performances. The experiment has been carried out with circular image acquisition strategy, highest resolution of images and controlled light conditions. After acquisition of the images, they were processed by the specialized software and analysis of obtained results was performed. Obtained results show poor 3D digitization quality for all surfaces i.e. machining processes. Future research will focus on investigation of the application of light textures in order to enhance photogrammetric 3D reconstruction performance.*

Keywords: *surface quality, 3D digitization, close-range photogrammetry, structure from motion, rugotest 1, 3D data analysis*

1. INTRODUCTION

Rough surfaces of the workpiece can not be avoided, as they are results of the application of different machining processes. They are defined by a qualitative data (by comparing the surface roughness with a standardized sample) and quantitative data (measuring the microgeometry with the adequate measurement devices, based on the contact and non-contact measurement methods).

The development of close-range photogrammetry based on SfM (Structure from Motion) approach has enabled a quick and simple way to get appropriate 3D models. 3D models can precisely provide both, qualitative and quantitative information of 3D digitized surface. This principle is based on capturing photos of the object from different angles with as much as possible overlaps within the photos. In practice, the most often used strategy for capturing photos is the circular strategy, in which photos cover the object in a full 360° circle. 3D model of the object are obtained, after photos processing, so that classifies this method as a passive 3D digitizing method. In order to obtain high-quality 3D models a high quality photographs are required, including the optimal lighting conditions for photographs acquisition, large depth of field and a high resolution photographs.

The difference between classic photogrammetry and photogrammetry based on SfM approach is that no calibrated camera is previously required. In SfM approach the camera parameters are calculated in the image processing step based on the detected key-points, and this process is also called autocalibration [1]. By determining and overlapping characteristic key-points from the set of photos it is possible to determine their relative position in 3D space.

Very good results have been shown in the field of cultural heritage due to the fact that a large number of objects can be digitized with this method that have different dimensions and geometrical complexity with reasonable accuracy [2,3]. This method also finds applications in other areas such as Mechanical Engineering [4], Biomedical Engineering [5], Geology [6], Construction and Architecture, [7], Video Game industry etc. The biggest advantage of this method is its availability, as from the system acquisition (camera) point of view, as well as from software support point of view [8].

The aim of this research is to investigate the influence of surface quality on the 3D digitizing results obtained by SfM. Surface quality of machined parts significantly affects their working capability, wear, load capacity, dynamic strength etc. In conventional methods of machined surfaces, quality depends on many factors such as the type of operation, workpiece material, tool, equipment, machine tools, cutting parameters etc. According to the degree of irregularities a surface quality of the machined part is determined, so that for a specific surface area, in relation to its function, an optimum surface quality is defined.

Light rays fall on the surface of an object and, depending on the optical characteristics of the object, some of light is partially absorbed, while some of light rays are reflected. Reflection is an undesirable phenomenon that affects the proper functioning of optical systems in a certain extent. During photographs' acquisition light rays that are reflected from the surface of the object, directly affect the part of the sensor creating a hotspots that manifests as a white region on photographs. Moving the camera to the next point of view, in relation to the object being photographed, a change of the angle occurs at which previous hotspot occurred. This is a reason why a loss of data has also occurred. Due to relative changes in position between the illumination and the camera, finding and matching of common points on the photos becomes very difficult.

2. MATERIALS AND METHODS

As an object for 3D digitization RUGOTEST 1 [9] is used which is the standard for comparison of a visual and tactile quality of the machined surfaces, depending on the type of machining process (Figure 1.). This object comprises of samples of surface roughness according to ISO 2632-1 and 2632-2 standard class from N10 to N2 treated with: side and face milling, grinding, lapping, planing/turning and honing-superfinish treatment. Object dimensions are 120x90 mm, while the dimensions of a single sample plate are 12x20 mm. The acquisition was carried out with DSLR full frame camera adjusted on maximal image resolution of 22 Mpix, equipped with a 50mm focal length lens.
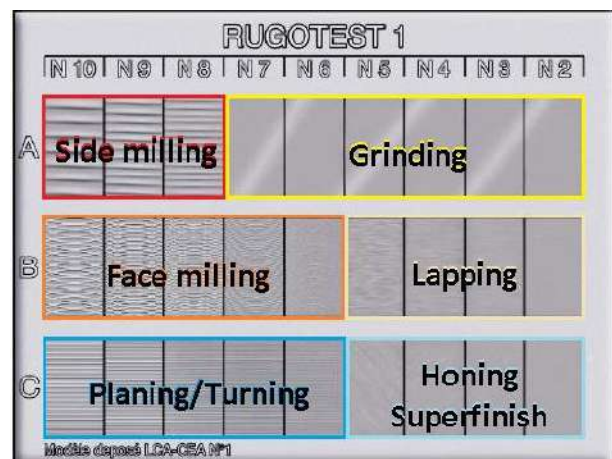

Figure 1. RUGOTEST 1 etalon for tactile and visual comparison of the workpiece surface finish according to various machining processes

Acquisition strategy is designed so that the minimum number of photos cover the entire workpiece. A total of 12 images was captured

and they are grouped into 6 stereopairs (Figure 2.) from a distance of approx. 50 cm.
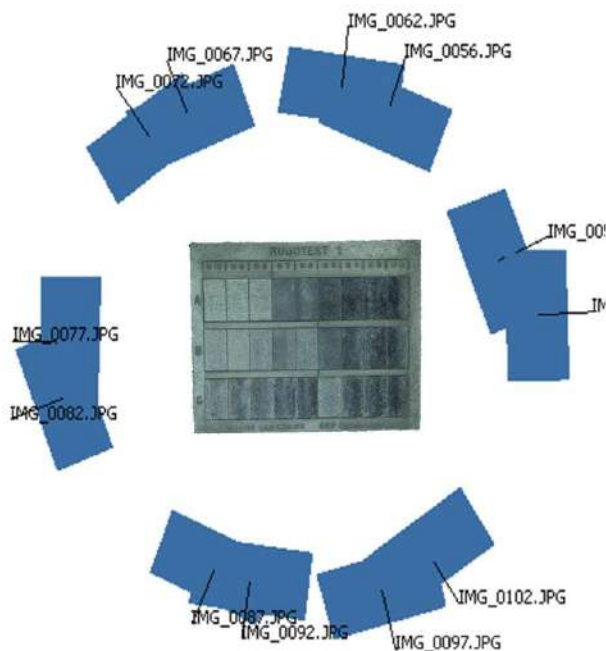

Figure 2. Acquisition of photos, circular pattern

The level of detail that has been achieved with this setting is expressed through Ground Sample Distance (GSD) (1) of 0.07mm.

$$GSD = D \cdot p_x / f \qquad (1)$$

D in formula (1) is the distance between the camera and a 3D object, p_x - size of one pixel on the sensor and f - the camera lens focal length. The theoretical value of the GSD should be taken with caution as it is extremely difficult to be achieved. It is being corrected with the most common coefficient of 1.5, so the real value of GSD in this case was around 0.105 mm. Since the photogrammetric measurements are dimensionless, and the results of 3D digitization does not correspond to the real situation, it is necessary to use reference markers with the known spacing between them for the purpose of scaling of the digitized 3D object.

As already stated, SfM is the passive 3D digitizing method, and photos that are taken are processed after the acquisition. Processing consisted of two phases:
1) detection and finding characteristic key-points on photographs (results in sparse point cloud) and
2) generating dense point cloud.

3. RESULTS AND DISCUSSION

Table 1 shows the results of processing in the context of 3D digitizing of the whole etalon for each phase. As it can be seen from Table 1 for the first phase the mean value of the key point size is 3.6 pixels, that when multiplied by the value of GSD results in the value of the real size of the average key point of 0.36x0.36mm. Based on the calculated average value of the key point a 3D digitizing of microgeometry is excluded, but it is possible to show its impact on overall results. The impact of microgeometry is reflected primarily in the ability of software to recognize those key points on at least two images with the lowest possible RMS reprojection error. Also in Table 1. is given the time needed for the each phase and the total processing time.

Table 1. General results of image processing

Sparse point cloud	
Number of photos	12
Points	2086 valid of 3769 found
RMS reprojection error	1.05966 (2.56126 pix)
Max reprojection error	6.96332 (16.7881 pix)
Mean key point size	3.61273 pix
Effective overlap	2.11064
Generation Time Mode: Higest quality	1 minute 33 seconds
Dense point cloud	
Points	2603740
Generation time Mode: High quality	6 minutes 55 seconds
Total processing time	8minutes 28 seconds

Out of the entire point cloud only points that make specimens are isolated and on them appropriate inspection (flatness or cylindricity) was carried out. The software measures the GD&T tolerance according to the ISO standards (1101, 5459 etc.) and according to the ASME Y 14.5 [10]. In order to perform these measurements, reference planes and cylinders were created by Gaussian best fit method [10] on Figure 3.
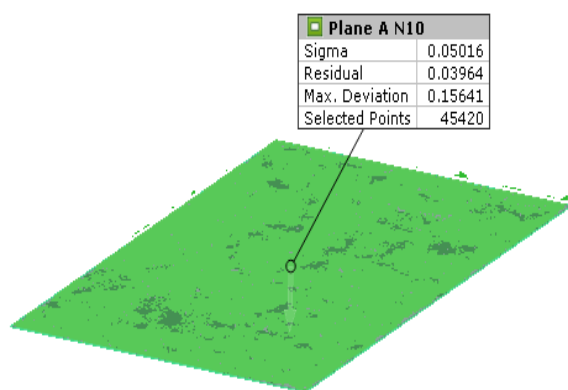
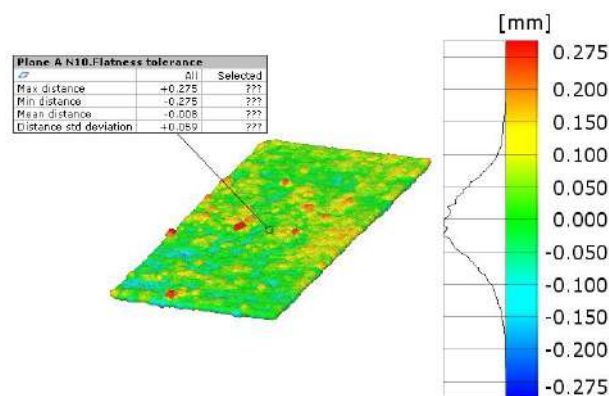**Figure 3.** Example of referent fitting plane creation

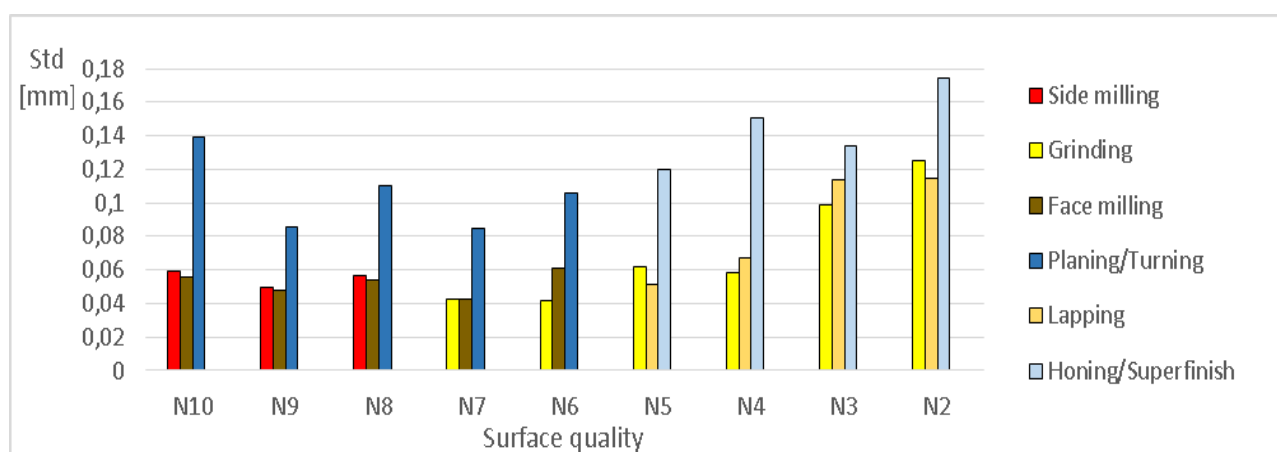**Figure 4.** Example of flatness tolerance of plane A N10

Figure 5. Standard deviation of flatness (Side milling, Grinding, Face milling, Lapping) and cylindricity (Planing/Turning, Honing/Superfinish) of measured specimens

Figure 4. graphically shows the flatness tolerance of a specimen A N10 which was treated with side milling, while Figure 5. graphically shows the standard deviation of the measured flatness and cylindricity tolerance of all specimens. On all cylindrical machined surfaces can be seen, from Figure 5, that they have a poorer 3D digitizing performance, and this can be explained by the fact that in every position when photo was captured, a high degree of reflection has been present.

4. CONCLUSION

On the basis of the presented results it can be concluded that the type and surface quality have a significant impact on the results of 3D digitizing by SfM. Generally, with an increase of the surface quality, followed by reduced surface roughness, obtained results are significantly worse. This is supported by a change in the visual characteristics of the machined surface - with a roughness reduction "mirror like" property is emphasized which influences greatly on the 3D digitizing results. The future research will be focused on reducing the influence of reflections and ensuring the improvement of the visual characteristics of the treated surface in order to improve the 3D digitizing results of machined surfaces.

ACKNOWLEDGEMENT

REFERENCES

[1] R. Hartley: *Multiple View Geometry in Computer Vision Second Edition*, A. Zisserman, Cambridge University Press, 2004.

[2] J. McCarthy: Multi-image photogrammetry as a practical tool for cultural heritage survey and community engagement, Journal of Archaeological Science, Vol. 43, pp. 175-185, 2014.

[3] A. Koutsoudis, B. Vidmar, G. Ioannakis, F. Arnaoutoglou, G. Pavlidis, C. Chamzas: Multi-image 3D reconstruction data evaluation, Journal of Cultural Heritage, Vol. 15, pp. 73-79, 2014.

[4] T. Luhmann: Close range photogrammetry for industrial applications, ISPRS Journal of Photogrammetry and Remote Sensing, Vol. 65, pp. 558–569, 2010.

[5] M. Eulitz, G. Reiss: 3D reconstruction of SEM images by use of optical photogrammetry software, Journal of Structural Biology, Vol. 191, pp. 190-196, 2015.

[6] L. Javernick, J. Brasington, B. Caruso: Modeling the topography of shallow braided rivers using Structure-from-Motion photogrammetry, Geomorphology, Vol. 213, pp. 166-182, 2014.

[7] V.Stojakovic: Terrestrial photogrammetry and application to modeling architectural objects, Vol. 6, pp. 113-125, 2008.

[8] Comparison of photogrammetry software, available at: https://en.wikipedia.org/wiki/Comparison_of_photogrammetry_software, accessed: 24.02.2017.

[9] RUGOTEST Roughness Comparison Specimens, available at: http://www.tesatechnology.com/en-gb/products/rugotest-roughness-comparison-specimens-p366.htm?redirect=1&c=fr#.WNDK-Wco-70 accessed: 25.02.2017.

[10] GOM Correlate Evaluation Software for 3D Testing, available at: http://www.gom-correlate.com

SERBIATRIB '17

15th International Conference on Tribology

Kragujevac, Serbia, 17 – 19 May 2017

MARKOV MODEL OF MECHANICAL INTERACTION FOR ROUGH SURFACES AND ITS APPLICATION FOR ESTIMATION OF SERVICE LIFE OF TRIBOLOGICAL SYSTEMS OF THE PISTON ENGINE

Yurii GORITSKIY[1], Ivan MIGAL[1], Konstantin GAVRILOV[2,]*, Muboriz IZZATULLOEV[2]
[1]National Research University "MPEI", Moscow, Russia
[2] South Ural State University, Chelyabinsk, Russia
*Corresponding author: gavrilovkv1@rambler.ru

Abstract: This article describes, develops and applies approach proposed earlier to build models of the interaction of rough surfaces for one of the tasks of simulation of tribological systems of the piston engine. In this paper we described the general approach to building a model of interaction between rough surfaces, leading to the analysis of the Markov process. This method we applied for friction process, and for fatigue failure mode in which the surface element is destroyed after repeated contacts. As an example, we considered the "main bearing-crankshaft" tribosystem of a diesel engine.

Keywords: surface asperities interaction, Markov process, tribological parameters, service life

1. INTRODUCTION

For the development of components machines and mechanisms, where friction determines the durability and dimensions, there is a need for methods that enable to estimate the friction characteristics in time: friction force, coefficient of friction, contact area, run-in time, wear and so on [1, 2].

Friction characteristics determined by such factors as surface microgeometry, physical characteristics of materials, velocity and the applied load. Most methods were based on the representation of the relief function for the random arguments [3, 4]. Such models can estimate the area of contact, the friction force, coefficient of friction, wear, etc. However, this approach ignores the surfaces change and, consequently, contact and friction characteristics over the time. In this paper

model of random change of surfaces heights over the time for "main bearing-crankshaft" tribosystem is supplemented by taking into account the presence of a lubricant in a mixed friction mode.

The "main bearing-crankshaft" tribosystem is mostly in the hydrodynamic lubrication regime, but at high loading levels, tribosystem is in the mixed or boundary lubrication regimes that is important for the determination of the service life.

2. THE HYDROMECHANICAL CHARACTERISTICS OF THE "MAIN BEARING-CRANKSHAFT" TRIBOSYSTEM

Reactions of a lubricant film were determined on the basis of results of numerical integration of modified equation Elrod for pressure in a lubricant film [5]. In this

paper used modification, written relative to function $\Omega(\varphi, \bar{z})$ in form

$$\frac{\partial}{\partial \varphi}\left[\frac{\bar{h}^3}{12\bar{\mu}_{eff}^*}\frac{\partial}{\partial \varphi}(g\Omega)\right]+$$

$$+\frac{1}{a^2}\frac{\partial}{\partial \bar{z}}\left[\frac{\bar{h}^3}{12\bar{\mu}_{eff}^*}\frac{\partial}{\partial \bar{z}}(g\Omega)\right]= \qquad (1)$$

$$=+\frac{\overline{w}}{2}\frac{\partial}{\partial \bar{z}}\left\{\bar{h}\left[1+(1-g)\Omega\right]\right\}+$$

$$+\frac{\partial}{\partial \tau}\left\{\bar{h}\left[1+(1-g)\Omega\right]\right\},$$

where $\bar{h}=h/h_0$; $\bar{\mu}_{eff}^*=\mu_{eff}^*/\mu_0$; $-a\leq \bar{z}\leq a$; $\bar{z}=z/R$; $\varphi=xR$; $a=B/2R$; $\tau=w_0 t$; $\overline{w}=(w_2-w_1)/w_0$; $\bar{h}$, $\bar{\mu}_{eff}$ - dimensionless film thickness and the effective viscosity of the lubricant; B,R − the width and radius of the bearing; μ_{eff}^* − effective viscosity of the lubricant, the corresponding temperature to T_{eff}^* ; μ_0 , h_0 , w_0 − respectively lubricant viscosity, typical film thickness at the center position of the shaft in the bearing and rotation speed of crankshaft; $\overline{w}$ − the dimensionless rotary shaft velocity; g − the switching function.

The main hydromechanical characteristics (HMC) of the tribosystem are: $h_{min}(\tau)$ − instantaneous values of the minimum oil film thickness; $p_{max}(\tau)$ − instantaneous values of the maximal hydrodynamic pressure; h_{min}^* − average value of $h_{min}(\tau)$; p_{max}^* − average value of $p_{max}(\tau)$; $N(\tau)$ and N^* − instantaneous and average power loss of friction; Q^* − the average flow rate of oil; T_{eff}^* − the average effective temperature of the lubricating layer; $\alpha_{h_{lim}}$,% − the areas, where minimal thickness of a lubricant film less than the permissible value h_{lim} equal 1.5 μm, which we determined from profilograms of samples of the "main bearing-crankshaft" tribosystem of diesel engine.

The function $\Omega(\varphi, \bar{z})$ is related to the degree of filling of the clearance $\theta(\varphi, \bar{z})$ and is characterized by a function that determines the mass content of the liquid phase (oil) in the volume of the clearance of the journal bearing using the relationship $\theta = 1+(1-g)\cdot \Omega$.

Given the initial data and the methodology for calculating the trajectory of shaft on the lubricating layer [6, 7], we calculated the HMC for all main bearings of diesel engine, but only two of them (2nd and 3rd main bearings) had nonzero values of $\alpha_{h_{lim}}$ (Table 1).

Table 1. HMC of the "main bearing-crankshaft" tribosystem of diesel engine

Num. bear.	h_{min}^*, μm	p_{max}^*, MPa	N^*, W	Q^*, kg/s	$\alpha_{h_{lim}}$, %
2	4.296	131.1	2056	0.067	7.8
3	4.697	131.6	1820	0.063	11.1

Table 1 shows that the h_{min} for the 2nd and 3rd main bearings reach the values less than the total value of the sum of the maximum heights of microasperities for the contact surfaces.

For only the period of tribosystem's working time, where h_{min} less h_{lim} (contact area), we analyzed characteristics of the "main bearing-crankshaft" tribosystem using Markov chains. Description of the used approach is below.

3. METHODS

To analyze the process of friction in the contact area we used the discontinuous model where surfaces are represented by asperities of random height [8]. Asperities in contact deform and destruct each other, that is why heights of contacting asperities may change. Total height change of all surface asperities leads to roughness transformations and variation of friction characteristics.

Let's consider K pairs of asperities positioned in one raw. Time is discontinuous and is measured in shift counts. After n shifts heights of asperities of one surface are represented by vector $\xi_k(n), (k=1,...,K)$, and heights of asperities of the other surface are represented by vector $\eta_k(n)$. The asperity

height change of the kth pair in one shift is described by general equations:

$$\xi_k(n+1) = \Psi(\xi_k(n), \eta_{k-1}(n)), \quad (2)$$

$$\eta_k(n+1) = \Phi(\xi_k(n), \eta_{k-1}(n)), \quad (3)$$

$$k = \overline{1,K}, \ \eta_0(n) = \eta_K(n),$$

where Φ and Ψ determine stochastic mechanism of asperity interaction as a sphere interaction [9], with random radiuses. Presented model of asperity interaction takes into account elastic-plastic deformation and wear.

It is proposed to describe the trajectory of height changes of single asperity by means of Markov series [10]. The height ξ of single asperity changes when it interacts with asperities of other surface, having heights $\eta(t)$ at the moment t. It is supposed, that asperity with the height ξ interacts with the series of asperities of the other surfaces with heights $\eta_1, \ldots \eta_n \ldots$, distributed with density $q_\eta(y)$. Thus series of heights $\xi_1, \ldots \xi_n \ldots$ is obtained, height value ξ_{n+1} depends on ξ_n and η_{n+1}:

$$\xi_{n+1} = \Psi(\xi_n, \eta_{n+1}), \quad (4)$$

where Ψ determines accepted mechanism of asperity contact interaction.

Series $\xi_1, \ldots \xi_n \ldots$ is Markov series. Moreover, heights $\xi_1, \ldots \xi_n \ldots$ are discontinuous, series $\xi_1, \ldots \xi_n \ldots$ becomes Markov chain. Similarly, ξ is distributed with density $p_\xi(x)$ and next equation is obtained:

$$\eta_{n+1} = \Psi(\eta_n, \xi_{n+1}). \quad (5)$$

Once two functions Ψ and Φ are elaborated the system of equations for stationary distributions p^* and q^* is obtained:

$$\begin{cases} p^* = p^* \cdot P_\xi(q^*, \Psi), \\ q^* = q^* \cdot P_\eta(p^*, \Phi), \end{cases} \quad (6)$$

where $P_\xi(q^*, \Psi)$ and $P_\eta(p^*, \Phi)$ are matrices of transition probabilities for series of ξ_n and η_n. Elements of matrices are determined by

distributions p^*, q^* and by two functions Ψ and Φ.

We can write the interaction function for the discrete model. If $\xi(t)$ - the height of the fixed element at the moment t, $\xi_n = \xi(t_n)$, $\xi_{n+1} = \xi(t_n+\tau)$ then for fixed element of the surface ξ:

$$\begin{aligned} \xi_{n+1} &= \Psi(\xi_n, \eta_n) = \\ &= \xi_n - D_\xi(\delta_n) - W_\xi(\delta_n) + (V_N/2)\Delta t' \end{aligned} \quad (7)$$

where $\delta_n = \xi_n - \eta_n$ - contact intersection at the moment t_n, $D_\xi(\delta_n)$ - the magnitude of the decrease of the height of the protrusion due to plastic deformation, $W_\xi(\delta_n)$ - change in height as a result of fatigue failure, $(V_N/2)\Delta t$ - the half value of convergence of surfaces under normal load during the time $\Delta t = \tau$. More detail in [11, 12].

4. RESULTS AND DISCUSSION

Initial data were determined on base of profilograms of specimens of the shaft and bearing: the surface ξ is the surface of the bearing, surface η - the surface of the shaft.

For period of time, where h_{min} less h_{lim} we estimated next parameters: the distribution of the heights of roughness of surfaces (p_ξ, q_η); dependence of the roughness of the surfaces (σ_ξ, σ_η) on the friction distance; the average contact area; the friction force F_{fr} and friction coefficient f; the linear wear l_h.

Fig. 1a, 1b present the height distribution of surfaces in function of the friction distance. Fig.1a shows the result of the surfaces change after running-in. It can be seen that after the run-in, the surface of the bearing was deformed. The process of run-in was observed until the pressure on the projections of the surface became less than twice true fracture stress for the bearing.

Then there is the process of fatigue failure. High protrusions are destroyed, the elastic force of mechanical contact increases due to convergence of the surfaces, increasing the proportion of mechanical contact and to reduce the proportion of liquid contact.
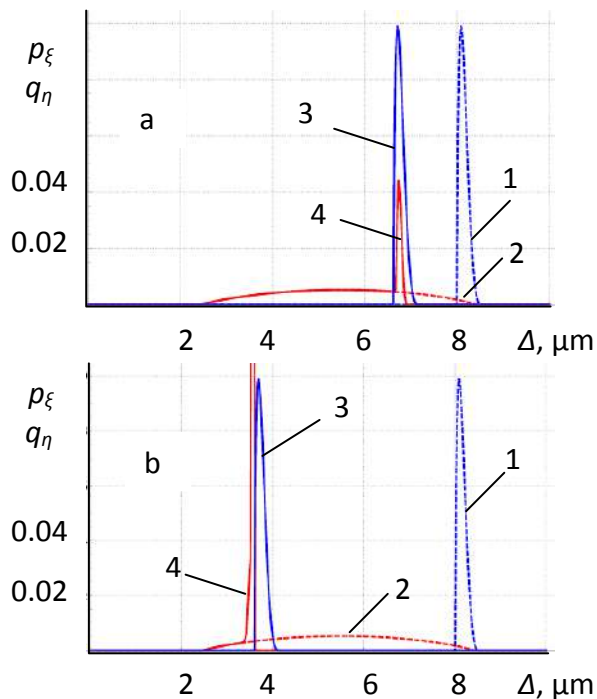
Figure 3. The dependence of wear (the convergence of surfaces) for the 2nd (curve 2) and 3rd (curve 1) main bearings on rev.

Figure 1. The distribution of the heights of roughness of contact surfaces: after run-in time (a) and after friction distance 1380 km (b): 1, 2 - initial curves for shaft and bearing respectively; 3,4 - curves after interaction.

Fig.2 depicts the dependence of the surface roughnesses on the friction distance (L). Here you can also see the transition between the mixed and hydrodynamic regimes: the curve break at 430 km of the friction distance.
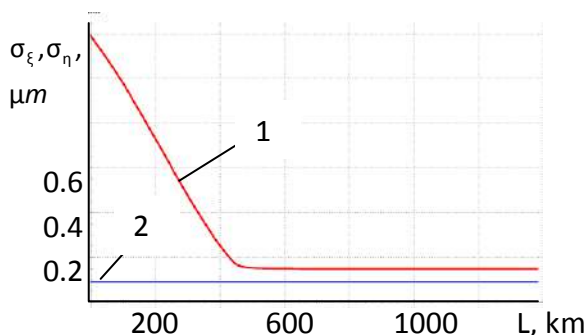

Figure 2. The heights of surface roughness of bearing (1) and shaft (2) in function of friction distance.

Fig.3 represents the dependence of wear (the convergence of surfaces) for the 2nd and 3rd main bearings on the number of revolutions of the crankshaft. As a result the mixed friction regime for one revolution for the 3rd main bearing is longer than for the 2nd main bearing (see Table 1), and the wear for the 3rd main bearing is more intensive.
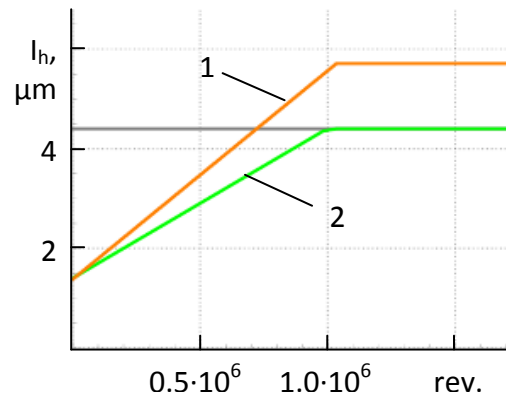
5. CONCLUSION

1. The HMC of the "main bearing-crankshaft" tribosystem were calculated for diesel engine, which allowed us to estimate the duration of the surfaces contact interaction for the 2nd and 3rd main bearings of diesel engine.
2. We proposed a Markov model of the interaction of rough surfaces, which was supplemented by taking into account the presence of a lubricant in a mixed friction mode. It allows us to estimate the friction characteristics over the time for contact area of tribosystem taking into account the transition between the mixed and hydrodynamic regimes.
3. The proposed model can be used to estimate the service life of different tribosystems operating under different friction modes.

ACKNOWLEDGEMENT

REFERENCES

[1] A. Vencl, A. Rac: Diesel engine crankshaft journal bearings failures: Case study // Engineering Failure Analysis 44 (2014), pp.217–228.

[2] V.E. Lazarev, K.V. Gavrilov A.A. Doikin, J. Sequrd-Base, G. Vorlaufer: Estimation of the tribotechnical parameters of the "piston skirt-cylinder liner" contact interface from IC-engine for decreasing the mechanical losses // 1st International Conference on Energy Production and Management in the 21st Century: The Quest for Sustainable Energy, 23–25 April 2014, Ekateringburg, Russian Federation // WIT Transactions on Ecology and the Environment. – 2014. – Volume 190. – VOLUME 1. – pp. 625-635.

[3] P.R. Nayak: Random Process Model of Rough Surfaces. Journal of Lubrication Technology, July. Elsevier. pp. 398 – 407, 1971.

[4] J.A. Greenwood, J.B.P. Williamson: Contact of Nominally Flat Surfaces, Proceedings of Royal Society, Series A, vol. 295. Elsevier. pp. 300 – 319, 1966.

[5] Y. Rozhdestvensky, K. Gavrilov: Numerical and experimental investigations of tribosystems of piston en-gines taking into account boundary lubrication regime, macro and microgeometry of contact interface // STLE Annual Meeting & Exhibition. May 18-22, 2014. Disney's Contemporary Resort Lake Buena Vista, Florida,USA.http://online.stle.org/STAFFLIVE/Shared_Content/Extended_Abstracts/EA_AM2014/Fluid_Film_Bearings/Numerical%20and%20Experimental%20Investigations%20of%20Tribosystems%20of%20Piston%20Engines.aspx.

[6] Y. Goritskiy, K. Gavrilov, Y. Rozhdestvensky, A. Doikin: Numerical model of mechanical interaction between rough surfaces of tribosystem of the high forced diesel engine // Procedia Engineering. 129. 2015. pp. 518-525.

[7] Y. Rozhdestvensky, K. Gavrilov, A. Doykin, I. Levanov: Numerical and Experimental Investigations of Piston - Cylinder Tribosystem of Diesel Engine, in: Proceeding of 5th World Tribology Congress, WTC. (2013), pp.1255-1258.

[8] Y. Goritskiy, Y. Ismailova, K. Gavrilov, Y. Rozhdestvensky, A. Doikin: A Numerical Model for Mechanical Interaction of Rough Surfaces of the "Piston-Cylinder Liner" Tribosystem // FME Transactions. 2015. 43. pp. 249-253.

[9] K.L. Johnson: Contact Mechanics, Cambridge University Press, 1987.

[10] J.L. Doob: Stohastic Processes. New York – Jonh Willey & Sons, 1953.

[11] D. Tigetov, Y. Goritskiy: Markov model of mechanical interaction of rough surfaces in the process of friction // Friction and lubrication in machines and mechanisms. 2010, №3. pp. 4-13. (in Russian)

[12] Y. Goritskiy, S. Glavatskih, Y. Brazhnikova: Markov model of interaction of rough surfaces // Friction and lubrication in machines and mechanisms, 2014, №2.– M.: Mechanical engineering. pp. 11-20. (in Russian)

STATIC COEFICIENT OF FRICTION AT LOW VALUES OF CONTACT PRESSURE IN CONDITIONS OF LUBRICATION

Ivan BIJELIĆ, Nemanja MOR, Tijana STOŽINIĆ*, Slobodan MILOŠEVIĆ, Vesna TUBIN
Technical College of Professional Studies, Novi Beograd, Serbia
* Corresponding author: tijana.stozinic@visokatehnicka.edu.rs

Abstract: This work considers the effect of normal contact pressure on the value of static coeficient of friction. Contact couples are formed by full steel cylinders of different mass and circumference that are sliding on a hollow, shell shaped cylinder. The contact couples are completely submerged in oil and possess the identical conditions of lubrication. The experiment was conducted on the specially designed tribometer of high reliabilty of measurement. The results of the research indicate a significant influence of the level of the normal load and the contact pressure on the value of the coeficient of friction.

Keywords: Contact pressure, rings, cylinders, static coeficient of friction, tribometer.

1. INTRODUCTION

As a science, tribology greatly enables the solution of various global problems connected to energy and material consumption, along with the cost reduction and increase of work efficiency of the complex technical systems [1]. Modern methods of experimental research, in addition to requirements of reliabilty of the measuring systems, place a number of additional, complex demands and limitations. All of this imposes a constant need for the development of new and improvement of existing measurement devices and machines. Tribological research of the experimental kind in the present day is not only the need of research institutions, but of a large number of manufacturing companies as well, since they realized that such research is necessary to survive in the market, and are developing new materials and coatings by using special load conditions, aggresive enviroments and similar conditions.

A large number of articles in international magazines concerns the issues of the coefficient of static friction. In this regard, it should be noted that research is moving in several directions, such as: a) Research connected to the design of the topography of the contact surfaces which provides the maximum value of the coeffiecient of static friction [2]; b) Research related to the development and the tribological tests of composite biomaterials [3]; c) Research related to the identification and quantification of the impact of various factors on the size of the static coefficient of friction in the systems of clamping accessories for metalworking [4]; d) Research related to the impact of vibration, humidity and other factors on the carrying capacity of the connection achieved by friction [5]; e) Development of devices for the measurement of the static coefficient of friction, detection of the start of movement and measurement of the adhesion force [6]. f)

Development of theoretical models for calculating the value of static coefficient of friction of certain materials [7]. From this partial literature review it can be concluded that the field of research related to the static coefficient of friction is very topical. Considering the topic of work it should be noted that research related to the measurement of the coefficient of friction on the principle of the inclined plane is also very relevant [8] especially in terms of comparing the obtained results with results obtained by measuring the static friction coefficient using other methods of measurement.

The surface roughness and the state of the contact surfaces is of great interest and significance in a number of applications including fluid flow. Numerous theories have been based on hypotheses and a number of considerations, stemming from the experimental data and explaining the influence of different contact surfaces on the coefficient of friction. In studies [9,10] the authors show that an increase in temperature of the bodies in contact has a significant effect on the increase of static friction coefficient. Static friction is generated at the moment of the macro tangential movement of the body in motion relative to a static body in contact [11,12]. The coefficient of static friction is dependent on several parameters, primarily on the contact surfaces, normal load, atmospheric pressure and temperature, the absorption properties, the state of the processed surfaces and materials in contact [13].

2. EXPERIMENTAL RESEARCH

Experimental research was carried out on the tribometer for the measurement of static friction coefficient of sliding and rolling. The scheme of the basic configuration of the tribometer is shown in Figure 1.

On the stand (position 1.) there are placed specially designed bolts (position 11.) which are used for leveling the tribometer stand. The leveling is performed via a specially designed circumferentor for leveling in two planes. The bearing plate (position 2.) slides on the groove built on top of the stand. On the support plate (position 2.) are attached tightly both a screw nut (position 12.) and a zero position indicator (position 19.) On the stand (position 1.) are fixed the carrier plates (position 6.) which hold the axial-radial bearings inside them (position 7.) Helical spindle (position 9.) on a 1 mm step is coupled with a screw nut (position 12.) and with a nonius caliper (position 8.) through which the reading of displacements is measured with an accuracy of one minute.
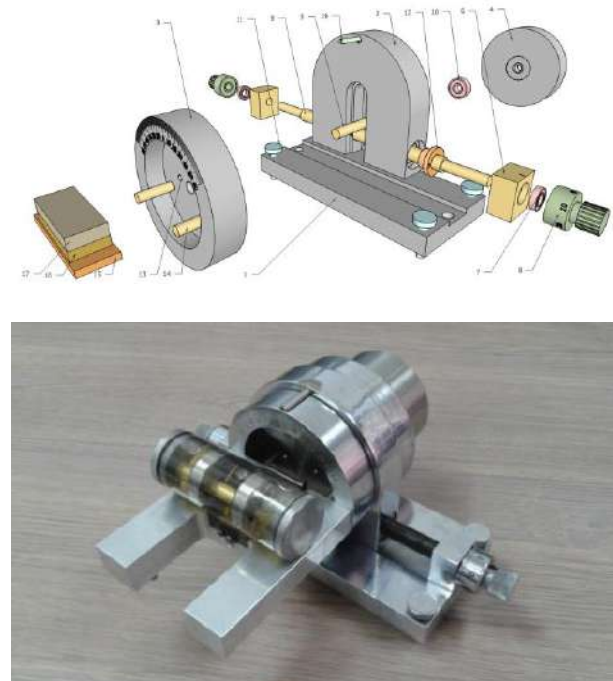

Figure 1. Schematic representation of a tribometer

On the bearing plate (position 2.) a groove has been dug, through which it is possible to move in vertical direction the bolt (position 5.), that has two ball bearing attached on each of its sides (position 10.) Ball bearings are pressed into discs (positions 3 and 4.) On the disc (position 3.) there is engraved an angular scale in degrees and two clamped pins (position 14). On the inner side of the disc (position 3.) are attached two limit beads (position 13). Contact pairs (positions 15. and 16.) with a weight (position 17) with a detachable fixing to the sample (position 16.) are placed on the pins (position 14). Turning the nonius (position 8.) linearly moves the support plate (position 2.) while the discs (positions 3. and 4.) roll on the stand (position 1.), and so rotate the plane of overlap of the contact pairs (positions 15. and 16.) for the

desired angle. An additional burden is added via removable weights (item 17).

For the implementation of programs of experimental research, the basic configuration of the tribometer (shown in Figure 1.) was supplemented by a module (Figure 2.) which is through the pins (Position 14 - Figure 1) attached to the disk with a scale (Position 3 - Figure 1).
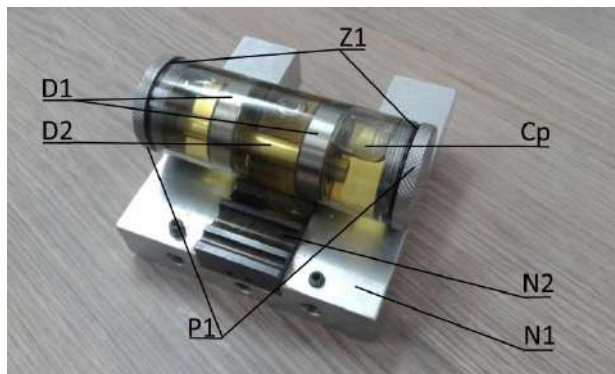

Figure 2. Photographic example of the auxiliary module.

The additional module consists of: sub-assembly supports (position N1) and the sub-assembly of the carrier contact pairs (position N2). The carrier of the contact pairs (position N2) is mechanically fastened to the sub-assembly carrier (position N1). The sample holder is a transparent plastic tube (Position CP) in which on a specified distance are fixed two shell shaped hollow cylinders (bearings) forming the first contact element (position D1.) A transparent plastic tube is filled with hydraulic oil HIDROL 46 for the lubrication of the contacts and, after insertion of the second contact element shaped like a full cylinder (pin or rod) (position D2), is hermetically sealed through gaskets (the position Z1) and lids (position P1).

The contact pairs, hollow cylinders and the full cylinder (rod) are made of stainless steel EN 1.4021. The inner diameter of hollow cylinders is Du = 28mm, and the width of the hollow cylinders is Bd = 11mm. Hollow cylinders are in the course of execution of two independent experiments in contact with the cylinders (pins or rods) of diameter: dv= 3 mm and 6 mm, and of length: b_1 = 75m.

Based on the given geometric values of the diameter and the width/length of the contact elements, the values of the theoretical Hertz pressure can be determined based on a pattern:

Based on the known value of the normal load F_n, as well as the known type of contacts (of the cylinder in the inner cylinder), the value of the contact pressure can be calculated using the expressions known from the theory of elasticity:

$$p = 0,798 * \sqrt{\frac{q}{v(k_1 + k_2)}} \; ; \; \text{where}$$

$$v = \frac{D_1 * D_2}{D_1 - D_2} \, , \; k_1 = \frac{1 - \mu_1^2}{E_1} \, , \text{ and } k_2 = \frac{1 - \mu_2^2}{E_2} \; (1)$$

Where p is the contact pressure, q is a load per length unit of the cylinder, D_1 is the diameter of the cylinder bearing, D_2 is the diameter of the rods (pins), μ_1 is the Poisson's ratio of the pin material, μ_2 is the Poisson's ratio of bearing material, E_1 is the modulus of elasticity of the material of the pin and E_2 is the modulus of elasticity of the material of the bearing. Since the pin and the bearings are made of the same material, $\mu_1 = \mu_2$ and $E_1 = E_2$.

The measured values of the angle of rotation of the inclined plane and the value of the friction coefficient calculated based on a pattern: $\mu = tg\alpha$ are given in Table 1. In order to increase the reliability of measurements and the determination of the middle values and the dispersion of the coefficient of friction, the measurements were repeated 30 times for both contact pairs.

The medium values of the coefficient of friction and the corresponding dispersion are:

For the cylinder contact with a diameter of dv=3 mm per cylinder:

$$\mu_{sr} = 0,317; \quad \sigma = 0,04276$$

For the cylinder contact with a diameter of dv=6 mm per cylinder:

$$\mu_{sr} = 0,2996; \quad \sigma = 0,02593$$

On the figure 3., a diagrammatic representation of the coefficient of friction is shown for all of the 30 measurements of the both contact pairs.
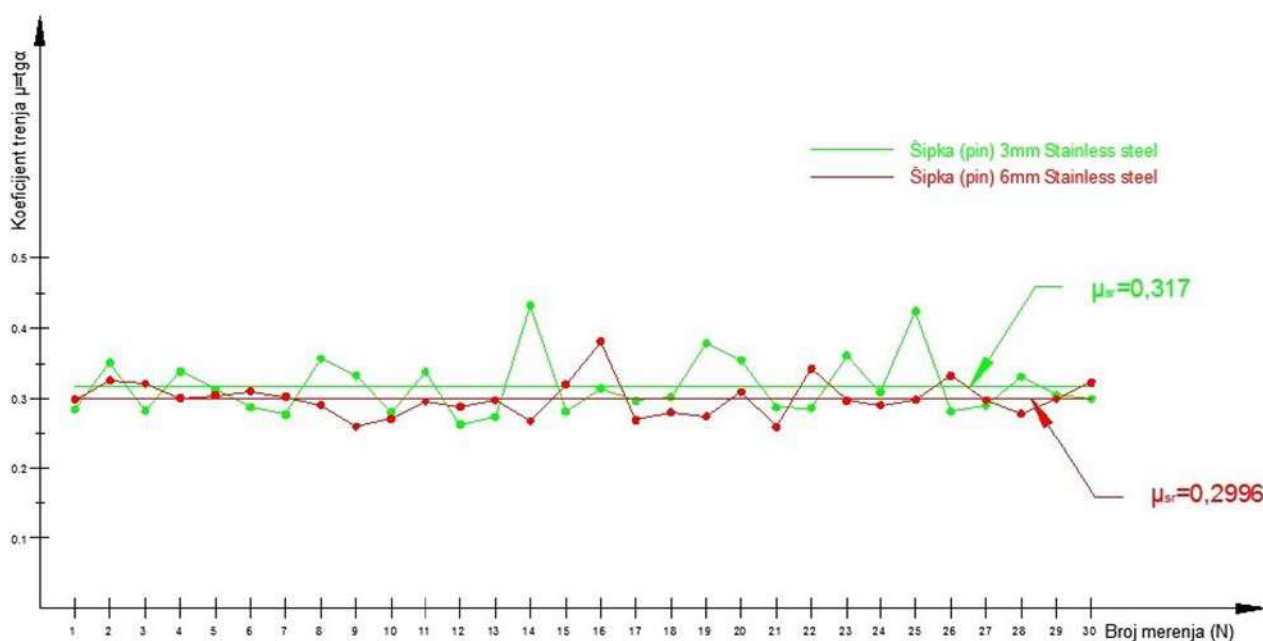
Figure 3. A diagrammatic representation of the value of the coefficient of friction

Table 1. The measured values of angles and coefficients of friction

Rod (pin) Ø 3mm Stainless steel			Rod (pin) Ø 6mm Stainless steel		
N	Angle α°	μ= tgα	N	Angle α°	μ= tgα
1	15,87	0,284	1	16,63	0,299
2	19,33	0,351	2	18,03	0,325
3	15,77	0,282	3	17,80	0,321
4	18,70	0,338	4	16,73	0,301
5	17,38	0,313	5	16,93	0,304
6	16,03	0,287	6	17,26	0,311
7	15,50	0,277	7	16,83	0,302
8	19,63	0,357	8	16,20	0,291
9	18,42	0,333	9	14,58	0,260
10	15,68	0,281	10	15,20	0,272
11	18,70	0,338	11	16,46	0,295
12	14,68	0,262	12	16,08	0,288
13	15,33	0,274	13	16,58	0,298
14	23,38	0,432	14	15,01	0,268
15	15,72	0,281	15	17,75	0,320
16	17,45	0,314	16	20,88	0,381
17	16,53	0,297	17	15,08	0,269
18	16,80	0,302	18	15,66	0,280
19	20,72	0,378	19	15,36	0,275
20	19,51	0,354	20	17,21	0,310
21	16,03	0,287	21	14,55	0,260
22	15,98	0,286	22	18,91	0,343
23	19,86	0,361	23	16,53	0,297
24	17,16	0,309	24	16,20	0,291
25	22,98	0,424	25	16,60	0,298
26	15,73	0,282	26	18,38	0,332
27	16,18	0,290	27	16,56	0,297
28	18,31	0,331	28	15,56	0,278
29	16,96	0,305	29	16,66	0,299
30	16,68	0,300	30	17,88	0,323

3. DISCUSSION

Based on the analysis of the literature sources it can be concluded that the research in the field of the coefficient of static friction is very relevant. The research presented in this paper were performed in order to determine the impact of the Hertz contact pressure on the value of the coefficient of static friction. In order to achieve the identical testing conditions, the contact pairs are made of the same material and using the grinding pre-treatment brought to approximately the same value of the surface roughness ($R_a = 0,62 - 0,73\ \mu m$). Creating identical test conditions can largely be contributed to achieving contact in the enviroment filled with fluid (oil). As from the aforementioned, it can be concluded (Figure 2),

that the contact pairs were fully submerged in oil. That was contributed by a specially designed module which was effectively upgraded to the basic configuration of the tribometer for measuring the coefficient of static friction and the coefficient of the rolling friction. The tests were carried out at a theoretical maximum value of the contact - Hertz pressure p = 29,8 MPa in the case of the contact rod with the diameter of Ø3mm and cylinder, and p = 56,3 MPa in the case of a contact rod of a diameter of Ø6mm and the cylinder.

Based on the experimental results it can be concluded that lower contact pressure values correspond to higher values of the coefficient of sliding friction. Also, the dispersions of the coefficient of friction are considerably higher at lower contact pressures. As it is written for the rod with the diameter of Ø3mm, the middle value of the coefficient of friction is as follows: μ_{sr} = 0,317 at σ = 0,04276 and for the rod of the diameter Ø6mm the middle value of the coefficient of friction is μ_{sr} = 0,2996 at σ = 0,02593, which is in accordance with the literature sources. At low contact pressures the contact is achieved mainly on the tops of bumps with great influence from the micro-geometry of the surface itself. In addition to that, the share of the adhesion effect of the presence of a lubricant at low values of load is much higher.

4. CONCLUSIONS

Research in the field of tribology as a science and tribology as a technology is well represented in the modern world. In particular, the current field of tribology is represented by tribometry. Tribometry specializes in finding new and improving the existing methods and devices for quantifying parameters of friction and wear. For the needs of the study from which the results were presented in this paper, a specially designed and implemented module was mounted on the basic configuration of the tribometer to measure both the coefficient of static friction and the coefficient of the rolling friction. The projected module allows for the measurement

of the friction coefficient to be carried out in a controlled environment to allow for complete lubrication of the contact pairs which are immersed in oil. This opens up the opportunity to explore not only the impact of the Hertz contact pressure on the value of the coefficient of friction, which was done in this paper, but also examine the effect of viscosity and the general quality of the lubricant. The results of the research described in this paper point to the significant impact of the level of normal load, or contact pressure, on the value of the coefficient of friction, which is consistent with the data in the literature.

Future research should be directed to upgrading the designed module by using the elements that allow testing of contact pairs in the controlled gas enviroment (vacuum, argon and other gases). The authors of this paper believe that from a technical point of view there is no problem in terms of upgrading the existing module, so this will most certainly be the subject of future research of the authors of this work in the field of tribometry.

5. LITERATURE

[1] Ivković, B, Tribologija u industriji na pragu dvadeset prvog veka, Tribologija u industriji, N1/4, Kragujevac, 1999.

[2] Lars Hammerstr, Staffan Jacobson, Designed high-friction surfaces—Influence of roughness and deformation of the counter surface, Wear, Vol. 264, pp. 807–814, 2008.

[3] S.H. Teoh, R. Thampuran, W.K.H. Seah, Coefficient of friction under dry and lubricated conditions of a fracture and wear resistant P/M titanium-graphite composite for biomedical applications, Wear, Vol. 214, No. 2, pp. 237-244, 1998.

[4] W. Xie, E.C. De Meter, M.W. Trethewey, An experimental evaluation of coefficients of static friction of common workpiece–fixture element pairs, International Journal of Machine Tools & Manufacture, Vol. 40, No. 4, pp. 467–488, 2000.

[5] Mohammad Asaduzzam Chowdhurya, Md. Maksud Helali, The effect of frequency of vibration and humidity on the coefficient of friction, Tribology International, Vol. 39, pp. 958–962, 2006.

[6] Habib S. Benabdallah, Static friction coefficient of some plastics against steel and aluminum under different contact conditions, Tribology International, Vol. 40 pp. 64–73, 2007.

[7] E.L. Deladi, M.B. de Rooij, D.J. Schipper, Modelling of static friction in rubber–metal contact, Tribology International, Vol. 40, pp. 588–594, 2007.

[8] Na Jin Seoa, Thomas J. Armstrongb, Philip Drinkaus, A comparison of two methods of measuring staticcoefficient of friction at low normal forces, Ergonomics, Vol. 52, No. 1, 121–135, 2009.

[9] B. Jeremic, D. Vukelic, P. Todorovic, I. Macizic, M. Pantic, D. Dzunic, B. Tadic, Static Friction at High Contact Temperatures and Low Contact Pressure, Journal of Friction and Wear, Vol. 34, No. 2, pp. 114–119, 2013.

[10] P. Todorovic, M. Blagojevic, Dj. Vukelic, I. Macuzic, M. Jeremic, A. Simic and B. Jeremic, Static rolling friction coefficient at high temperature, Journal of Friction and Wear, Vol. 34, No. 6, 2013.

[11] Elena Loredana Deladi, Static Friction in Rubber-Metal Contacts with Application to Rubber Pad Forming Processes, PhD thesis, University of Twente, Twente, 2006.

[12] N.K. Myshkin, C.K. Kim, M.I. Petrokovets: Introduction to tribology, CMG Publishers, Seoul, 1997.

[13] K.-H. Zum Gahr, K. Voelker: Friction and wear of SiC fiberreinforced borosilicate glass mated to steel, Wear, Vol. 225, No. 2, pp. 885–895, 1999.

SERBIATRIB '17

15th International Conference on

Serbian Tribology

Society

Tribology

Faculty of Engineering

University of Kragujevac

Kragujevac, Serbia, 17 – 19 May 2017

INFLUENCE OF GENERATED TEMPERATURE ON STATIC COEFFICIENT OF SLIDING FRICTION

Petar TODOROVIC[1], Nikola RADOVANOVIC[1], Nenad VRANIC[1], Milan RADENKOVIC[1*], Milutin ZIVKOVIC[2]

[1]Faculty of Engineering, Kragujevac, Serbia
[2]Higher Technical School of Mechanical Engineering, Trstenik, Serbia
*Corresponding author: radenkovic@kg.ac.rs

Abstract: *Experimental examination of static coefficient of sliding friction on the inclined plane is presented in this paper. Authors of this paper designed new equipment for measuring of static coefficient of sliding friction and results obtained using this equipment were used to analyze the influence of generated temperature on static coefficient of sliding friction. Experimental investigation was conducted on contact pair steel-rubber.*

Keywords: *static coefficient or friction, generated temperature, rubber.*

1. INTRODUCTION

Determining the value of sliding friction coefficient is very important for design engineers. However, there are large numbers of parameters which directly influence on determining the values of coefficient of friction [1, 2].

Based on relative velocity of bodies in contact, two types of friction can be recognized: friction of motionless bodies and friction of moving bodies [3, 4]. Friction which occurs at motionless bodies is static friction and it depends on many parameters such as: materials in contact, surface roughness, normal load, temperature of environment etc [2].

Deladi et al. [5] developed a static friction model for contact between rough rubber and metal surfaces. This model is based on the contact of a viscoelastic–rigid asperity couple. Single asperity contact is modelled in such a way that the asperities stick together in a central region and slip over an annulus at the edge of the contact. The slip area increases with increasing tangential load. Consequently, the static friction force is the force when the slip area is equal to the contact area. Andrade-Neto and Leyva-Cruz [6] have examined the motion of a body that rolls on an inclined plane, without the assumption of a rigid body. Under these conditions, the body may suffer small deformations. From the equations of motion they obtain an analytical expression for the acceleration of the center of mass and show that some cases reported in the literature can be obtained as special cases of our expression. Olsson et al. [7] reviews friction phenomena and friction models of interest

for automatic control. Particular emphasis is given to two recently developed dynamic friction models the Bliman-Sorine model and the LuGre model. Djurdjanovic et al. [8] presented the results of experimental estimation of the coefficient of static friction in a sliding bearing loaded with external force, simultaneously exposed to the influence of heat. L. Briançon, H. Girard and J.P. Gourc [9] proposed new procedure, called the "Force Procedure", which consists of measuring the force required to restrain a box on top of the interface beyond a limiting value of sliding displacement. With the "Force Procedure", the friction is determined from the curve of friction mobilization versus plane inclination. Fulleringer and F.Bloch [10] consider the paper-on-paper contact as an example of application. They first underline several drawbacks for the two main standard methods, namely the inclined and horizontal plane methods. In particular, the horizontal plane test method often involves stick-slip oscillations that make the measurement of the friction force impossible. They proposed a method for characterizing these oscillations and removing their influence on the friction force measurement. The comparison of the proposed method to standards suggests that proposed method delivers measurements that are much more accurate and repeatable. Hanaor et al. [11] by spline-assisted-discretization analyzed asperity interactions in pairs of contacting fractal surface-profiles. For elastically deforming asperities, force analysis reveals greater friction at surfaces exhibiting higher fractality, with increasing molecular-scale friction amplifying this trend. In systems where adhesive-type interactions play an important role, such as those where cold-welded junctions form, friction is minimizedat an intermediate value of surface profile fractality. Large number of investigations was performed using equipment of various design and contact geometry [12-14].

Authors of this paper presented new equipment for measuring of static coefficient of sliding friction and results obtained using this equipment were used to analyze the influence of generated temperature on static coefficient of sliding friction.

2. TEORETICAL BACKGROUND

Coefficient of friction is dimensionless value which is used for determining value of friction force. The friction force is force exerted by a surface when an object moves across it or makes an effort to move across it and it has values from 0 to F_{gr}.

$$F_{\mu max} = F_{gr} = \mu_0 \cdot N, \qquad (1)$$

Where F_{gr} is friction force with value when object starts to move, μ_0 coefficient of friction and N normal force. Friction force has tangential direction at the point of contact two objects and it is oppositional force to motion of two surfaces in contact.

The two of the most common types of friction are static and kinetic, or sliding and rolling friction. Force of sliding friction F_μ when object is not moving is equal to active force that tries to move that object and it is defined by Coulumb's law. Maximum value of frce of sliding friction is $F_\mu \leq F_{\mu max} = \mu_0 \cdot N$. If there is no sliding between the two contact surfaces, static friction can occur with value that is greater then the value of coefficient of kinetic friction. Coefficient of static friction cannot be determined by calculations but by experiment.
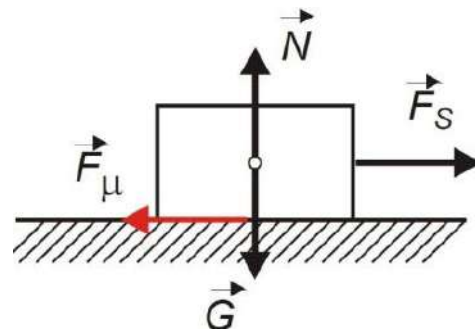

Figure 1. Acting forces between two objects in contact

Figure 1 represents two objects in contact as well as active forces in contact zone.
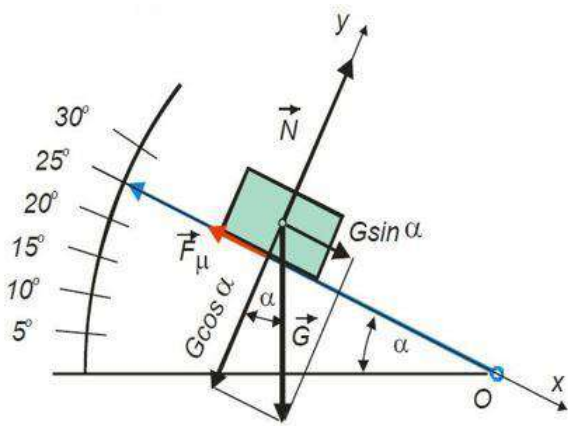

Figure2. Determining the static coefficient of static friction

Determining the static coefficient of friction is shown on figure 2. As it can be seen on figure 2, Force G has two components, one on x axis $(G \cdot sin\alpha)$and one on y axis $(-G \cdot cos\alpha)$. Next to Force G there is also a force of friction F_μ which has negative value since it acts oposite of direction of x axis. Normal force N has positive value and acts in direction of y axis.

$$\sum X_i = G \cdot sin\alpha - F_\mu = 0 \qquad (2)$$

$$\sum Y_i = N - G \cdot cos\alpha = 0 \qquad (3)$$

$$F_\mu = G \cdot sin\alpha \qquad (4)$$

$$N = G \cdot cos\alpha \qquad (5)$$

$$G = m \cdot g \qquad (6)$$

Since it is,$F_\mu \leq F_{gr} = \mu \cdot N \qquad (7)$

$$\mu \cdot G \cdot cos\alpha = G \cdot sin\alpha \qquad (8)$$

$$\mu = \frac{F_\mu}{N} = \frac{G \cdot sin\alpha}{G \cdot cos\alpha} \qquad (9)$$

thus, $\mu = tg\alpha \qquad (10)$

3. TRIBOMETER DESIGN

Design of presented tribometer uses method for measuring static coefficient of friction on an inclined plane. Base purpose of presented tribometer is determining of static coefficient of friction for metal and non-metal materials in different conditions (with and without lubrication in contact zone). Material used for construction of presented device was chromed construction steel which enables long lifetime cycle of device.

Presented tribometer enables experimental determination of sliding angle, angle when object starts to move, and coefficient of static friction. Relative measurement errorduring determination of static coefficient of friction is 0.02.Surface in contact of two contact element during measurement is 18 x 50 mm, and weights used are 1N. As mentioned, type of contact is surface-to-surface. Tribometer is constructed with several specimens for experimentation of static coefficient of friction. Specimens are made from material like chrome steal, brass, copper, bronze, thermal untreated steal, plastic, hard wood (beech), wood (poplar), leather, glass and rubber.

Before conducting experiments on the presented tribometer it is necessary to conduct leveling of the device. This is conducted with a specially designed level in two planes, figure 3. At the start of process of leveling it is necessary to position rolling disk into starting point. It is recommended to position rolling disk on the middle of movement path.

Figure3. Process of leveling in two planes

All impurities from the contact surface of specimens are necessary to be removed before conducting experiments. This can be done using alcohol and clean dry rag. If experiments are conducting in order to understand influence of some lubrication fluid on static coefficient of friction it is necessary to place thin layer of that lubrication fluid after specimen is removed from all impurities. When specimen is clean and ready for experiments it is necessary to place it on the device. After removing all impurities in order to start experiments it is necessary to place both contact elements, which we are analyzing on the device.

When the preparation is finished, process of measuring coefficient of static friction can start by rolling the disk with marked angle and coefficient of friction in small steps. Turning of the rolling disk should be done in steps of one minute with pauses in order to check movement of contact element. At the point when movement starts it is necessary to read the value of angle and coefficient of friction, figure 4. As it can be seen from figure 4, value of coefficient of static friction can be determined on the upper scale and value of the angle at the point when contact element started its movement can be seen on lower scale.

Figure 4. Determining the coefficient of static friction

4. EXPERIMENTAL RESULTS

Experimental investigation was done using contact pair steel-rubber with two types of measurements. First type contained 200 measurements with 20 second breaks between measurements. After measurement contact pair was separated for 20 seconds and then measurement was repeated. The measurement results of this type are shown in Table 2. Second type contained 200 measurements without breaks between measurements. The results of this type of measurement are shown in Table 2. Both types contained faze of preparation which included 10 measurements without taking results. Average value of measured values of static coefficient of sliding friction is shown in Table 1.

Figure 3 shows histogram of measured values of static coefficient of sliding friction. Blue color represents the first type of measurement which included 20 second breaks. Red color represents the second type of measurement without 20 second breaks. Histogram shown on figure 3 was created based on result analysis of tables 2 and 3.

5. DISCUSSION

Experimental investigation was conducted on a device for experimental determination of static coefficient of sliding friction, using Coulomb's law, $\mu = tg\varphi$. Experimental plan contained 400 measurements which were divided into two types. First type contained 200 measurements which had 20 second brakes between conducted experimental measurements. Average value of experimentally measured static coefficient of sliding friction for contact pair steel-rubber in type of measurements with 20 second breaks was 0.44285. Second type contained 200 measurements without braks. Average value of experimentally measured static coefficient of sliding friction for contact pair steel-rubber in type of measurements without 20 second breaks was 0.726. When results of these two types of measurements are compared it can be concluded that there is considerable difference betweenvalues of static coefficient of sliding friction. With statistical analysis was performed allocation of coefficient of sliding

friction by classes in both cases, in order to detect a characteristic phenomenon.

Diagram with blue colour on Figure 5 presents basicly ideal Gaussian distribution. Dispersion of experimental data is posible to lower with increasing number of measurements. Diagram with red colour on figure 5 does not represend idealy Gaussian distribution, which is result of generated temperature in contact zone. Generated temperature increases with every next conducted experiment.

Table 1. Average value and dispersion of measured values of static coefficient of siding friction

	First type, Measurements with 20 second breaks		Second type, Measurement without breaks	
Average value, μ	0.44285		0.726	
Dispersion	0.04179	9%	0.085029	12%

Table 2. Classes and the frequency in the measurement of the friction coefficient with breaks

Class values, μ	Mean of the class, x_i	Frequency, f_i	Relative frequency, f_{ri}	Cumulative relative frequency
0.36-0.37	0.365	9	0.045	0.045
0.38-0.39	0.385	14	0.070	0.115
0.40-0.41	0.405	28	0.140	0.255
0.42-0.43	0.425	35	0.175	0.430
0.44-0.45	0.445	42	0.210	0.640
0.46-0.47	0.465	28	0.140	0.780
0.48-0.49	0.485	16	0.080	0.860
0.50-0.51	0.505	14	0.070	0.930
0.52-0.53	0.525	9	0.045	0.975
0.54-0.55	0.545	5	0.025	1
Total	-	200	1	-

Table 3. Classes and the frequency in the measurement of the friction coefficient without breaks

Class values μ	Mean of the class x_i	Frequency f_i	Relative frequency f_{ri}	Cumulative relative frequency
0.54-0.57	0.555	1	0.005	0.005
0.58-0.61	0.595	15	0.075	0.080
0.62-0.65	0.635	25	0.125	0.205
0.66-0.69	0.675	26	0.130	0.335
0.70-0.73	0.715	54	0.270	0.605
0.74-0.77	0.755	21	0.105	0.710
0.78-0.81	0.795	18	0.090	0.800
0.82-0.85	0.835	17	0.085	0.885
0.86-0.89	0.875	14	0.070	0.955
0.90-0.93	0.915	7	0.035	1
Total	-	200	1	-

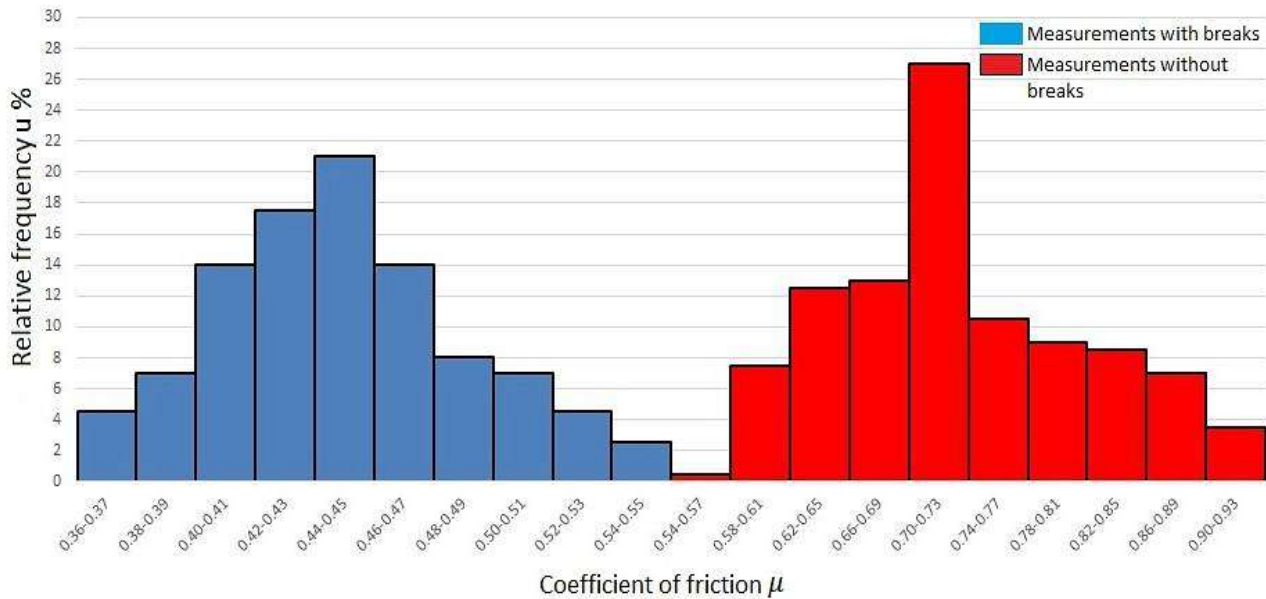## Histogram allocation of frequency

Figure5. Histogram of measured values

By comapring average values of measured static coefficient of sliding friction it can be concluded that experiment with 20 breaks have lower values o static coefficient then experiment without breaks between measurements.

6. CONCLUSION

Based on theoretical and experimental examinations it can be concluded:

Presented device can be used in order to experimentally determine static coefficient of sliding friction for different types of materials in different conditions.
Experimental process is very easy to conduct
Relative error is minimal. Error can be only in false reading of value of static coefficient of sliding friction on scale.
Experimental values gathered with this device are same as results in literal data.
This device is very useful as a tool for teaching, since it is very easy to use.
Conducted experiment shows an increase of value of static coefficient of sliding friction for the same pair of contact elements when there are no brakes between conducted experiments.

REFERENCE

[1] P.Bau: The significance and use of the friction coefficient, Tribol., Vol. 34, pp. 585-591, 2001.

[2] B. Ivkovic, M. Djurdjanovic, D. Stamenkovic:The influence of the contact surface roughness on the static friction coefficient, Tribology in Industry, Vol. 22, No. 3-4, pp. 41-44, 2000.

[3] V.V. Maksak: *Predvaritel'no esmeshenie I kontaktnaya zhestkost'* (Preliminary Displacement and Contact Hardness), Nauka, Moskow, 1975.

[4] N.K. Myshkin, M.I. Petrokovets: Treniesmazka, iznos (Friction, Lubrication, Wear), Fizmatlit, Moskow, 2007.

[5] E.L. Deladia, M.B. de Rooij, D.J. Schipper: Modelling of static friction in rubber–metal contact, Tribology International Vol. 40, No 4, pp. 588-594, 2007

[6] A.V. Andrade-Neto, J.A. Leyva-Cruz: Theoretical analysis and proposal for

experimental determination of the coefficient of rolling friction on an inclined plane, RevistaBrasileira de Ensino de Fisica, Vol. 37, No. 4, pp. 4303(1)- 4303(5), (2015)

[7] H.Olsson, K.J. Astrom, C. Canudas de Wit, M. Gafvert and P.Lischinsky: Friction models and friction compensation, European Journal of Control Vol. 4, No. 3, pp:176-195, 1998.

[8] Miroslav B. Đurđanović, Dragan S. Veličković, Slobodan V. Jovanović: Coefficient of the al/al static friction at small velocity and displacement both, Architecture and Civil Engineering Vol. 2, No 2, pp. 101 − 107, 2000.

[9] L. Briançon, H. Girard, J. P. Gourc: *A new procedure for measuring geosynthetic friction with an inclined plane*, Geotextiles and Geomembranes, Vol. 29, pp: 472-482, 2011.

[10] N. Fulleringer, J.-F.Bloch: Forced stick-slip oscillations allow the measurement of the friction force: Application to paper materials,Tribology International, Vol. 91,pp. 94–98, 2015.

[11] Dorian A.H. Hanaor, YixiangGan, ItaiEinav: Static friction at fractal interfaces, Tribology International, Vol. 93, pp. 229–238, 2016.

[12] SnežanaRadonjić, JelenaBaralić, NedeljkoDučić*: Determination of static friction factor by using tribometer,* in: 6 th International Symposium, Technical Faculty Čačak, 3–5th June 2011

[13] D.N. Olaru, C. Stamate, G. Prisacaru: Rolling friction in a micro tribosystem, Tribology Letters, Vol. 35, pp. 205-210, 2009.

[14] H.S. Benabdallah: Static friction coefficient of some plastics against steel and aluminium under different contact conditions, Tribology International, Vol.40, pp.64-73, 2007.

**Serbian Tribology
Society**

SERBIATRIB '17

**15th International Conference on
Tribology**

**Faculty of Engineering
University of Kragujevac**

Kragujevac, Serbia, 17 – 19 May 2017

POSSIBILITIES OF ARTIFICIAL NEURAL NETWORK APPLICATION IN BIOTRIBOLOGICAL RESEARCH

**Aleksandar ĐORĐEVIĆ[1],*, Milan ERIĆ[2], Marko PANTIĆ[2],
Dragan DŽUNIĆ[2], Miladin STEFANOVIĆ[2], Slobodan MITROVIĆ[2]**
[1]Higher technical school of processional studies Zvečan, Zvečan, Serbia
[2]University of Kragujevac, Faculty of Engineering, Kragujevac, Serbia
*Corresponding author: adjordjevic@kg.ac.rs

Abstract: *A tribological system is a complex non-linear system composed of the elements that are connected structurally and functionally. Tribomechanical system structure is made of elements, characteristics of elements and interaction of these elements. Function of tribomechanical system is the transformation of inputs into the technical output. The aim of this paper is to present an overview of artificial neural networks, its development and possible applications of neural networks in the analysis of the results values of certain parameters in tribological related research. The possibility of artificial neural networks application to solve complex nonlinear problems and to identify bio-tribological characteristics of ceramic materials in terms of abrasion resistance and coefficient of friction is presented.*

Keywords: *tribological characteristics, prediction, neural networks, mathematical modelling*

1. INTRODUCTION

Application of ANNs became wider in last few decades, especially in different areas of production engineering. Hence, in tribological experiments, application of ANNs models for prediction of tribological properties values become more present, i.e. for wear rate and friction coefficient, according to the defined terms of the contact, for materials that are tested. Neural networks have been used for prediction of short fibre composites tribological properties [1], for prediction of carbon fibber and TiO$_2$ composites properties [2], plasma nitrided 316L stainless steel tribological properties [3], for prediction of composite PEEK-CF30 tribological behavior [4], etc.

Particular attention of researchers in recent years was occupied by bio-tribology. Bio-tribology is one of the current and rapidly growing field of tribology. The diversity of research activities in bio-tribology is very large and includes many scientific fields. A large number of papers in various fields of bio-tribology from year to year are published in numerous prestigious scientific journals [5]. A very important area in recent years that is the focus of numerous studies is the field of research and development of new biomaterials. The term biomaterial, refers to materials with such unique characteristics which make them particularly suitable for close contact with the living tissue, and whose production process is often applied, or mimics a biological phenomenon [6]. New

nanomaterials such as nanotubes, carbon fibres, nanolegure, as well as various types of polymers, ceramics, or metal alloys and the nanocomposite and a number of other powerful new class of materials are promising extraordinary achievements in the medical materials and services. Materials, observed at a nano level may exhibit totally different characteristics in relation to those which are manifested on a macro level, thus allowing the unique application. In recent years a numerous areas of health services have progressed to the point that their new approaches to day-to-day raise the patients lifestyles.

Having in mind previously mentioned, ANNs method were identified as appropriate for prediction of bio-tribological parameters of non-metal ceramic material prepared with different finishing processes. Ceramic is an inorganic, non-metallic material that is solidified by the heating process and has about 30% of the crystal structure of [7]. In dentistry it was always pursued and will be strived to find new materials that have suitable characteristics to replace the natural tooth structure. With the development of science in general and the development of dentistry through various scientific and technical research, aesthetic materials for prosthetic purposes have evolved almost to the extent that their properties meet all necessary requirements in the form of aesthetics, function and biocompatibility. Excellent characteristics enabled the widespread use of ceramics as the restorative in the field of aesthetic dentistry [8].

In the present research paper experiments were conducted on lithium disilicate ($Li_x(SiO2)_y$) sample. The material is characterized by high values of bending strength and broad application in making restorations and teeth bridges. Based on the idea that the future of all-ceramic non-metal systems in to use PRESS (pressing technology) and CAD/CAM technology a new advanced system called IPS e.max (*Ivoclar Vivadent, Liechtenstein*) was developed. It embraces the most aesthetic and high-resistant materials intended for the

PRESS and CAD/CAM technology. Hence, commercial material IPS e.max CAD lithium disilicate glass ceramics for CAD/CAM systems and the pressing technology was designed. Blocks for CAD / CAM are blue in color, they are moulded in one piece and within the metasilicate phase (partially crystallized, Li_2SiO_3). As raw material, the value of their bending strength is smaller which allows their quick processing in the CAD/CAM system. A crystallization process is performed to obtain a final form of the crystal of lithium disilicate ($Li_2Si_2O_5$). Therefore, blocks are receiving a significantly higher bending strength with the values of 360 MPa [8,9].

In this paper, the influence of input nanotribometer parameters, i.e. parameters of the device used for testing tribological characteristics on to the lithium disilicate ($Li_x(SiO2)_y$) sample has been analysed. Artificial neural network approach was used for mathematical modelling and for identification of input tribometer parameters that lead to minimal degree of wear and coefficients of friction values.

2. THE TRIBOLOGICAL PROCEDURE

Within the tribological examination the characterization of tribological phenomena, friction and wear, according to the defined terms of the contact, for lithium disilicate ($Li_x(SiO2)_y$) are determined. Tribology tests whose parameters are shown in Table 1 are realized on the linear alternating nanotribometer CSM module, at normal load micro modes.

Table 1. Tribological input parameters [9]

Device characteristics
- Linear alternating module (linear mode of acquisition)
- Half of amplitude: 0.5 mm
- Frequency: 100 Hz
- The ambient temperature: 23±2 °C
Tested samples
Commercial metal ceramics (finishing: polished, glazed and brushed)
- lithium disilicate ($Li_2Si_2O_5$) (*IPS e.max CAD*)
The second body in contact

- Commercial pellet: alumina (Al$_2$O$_3$)	
- Pellet diameter: 1.5 mm	
The values of normal force	
- F_n: 250 mN; 500 mN; 750 mN; 1000 mN	
Maximall sliding velocity	
- v: 4 mm/s; 8 mm/s; 12 mm/s	
The test duration	
- 10.000 cycles (20 m)	
Environment contact zone	
- artificial saliva	

Based on this literature review, it was decided that the tribological examination should be carried out in the presence of artificial saliva in the contact zone, in order to more realistically simulate real conditions of the oral environment. The results of the in vitro wear test, which were conducted in [10], showed that the artificial saliva can also have the effect of cooling and lubrication during the wear process. Also, the risk of damage to the contact surfaces of the materials can be significantly reduced in the region of artificial saliva, compared with a dry state. Lubrication mechanism saliva is based on the complete separation of the sliding surfaces in contact with a thin layer of saliva [11].

The contact elements of tribomechanical system are samples made from commercial non-metal ceramics produced by *Ivoclar Vivadent* manufacturer and commercial alumina pellets (Al$_2$O$_3$) with the diameter of 1.5 mm. It is generally known that the alumina has an ultra-high hardness with the value 9, according to Mohs scale [12], immediately behind the diamond, and excellent wear resistance.

Tribological examinations were intended for tracking of wear and friction values, depending on the slip distance. During the examinations, the friction coefficient values were recorded in real time, by applying TRIBOX 2.9.0. software. After each test, the sample is removed from nanotribometer and the image of wear traces are recorded with optical microscopes. Abrasion of the surface material layer is measured by the average area of a track wear with software tools, based on

optical images wear trace. Trace wear volume and wear rate were calculated for each test, according to ASTM G133-05 Standard, after the total distance travelled by 20 m. Wear rate (W) was calculated according to the following equation [13]:

$$W = \frac{V}{s}, \text{ [mm3/m]} \qquad (1)$$

wherein the V − is the worn volume of material [mm^3], and s − is the travelled distance [m]. The value of wear rate (W) was expressed in the [mm^3/m], that is, as the volume being lost [mm^3] per unit of travelled distance [m]. A worn surface of the sample volume, is calculated by the average area of a track wear and the known geometric pattern, assuming that the volume corresponds to the flat worn segment of the pellets. Geometrical characteristics of the pellets are adopted as dimensions of alumina pellets with which the surface of the sample is in contact. As the alumina pellets wear can be described as "undetectable", it is presumed that only the surface wear of the sample is obtained and accordingly calculated according to the G133-05 standard.

3. ARTIFICIAL NEURAL NETWORK MODELLING OF WEAR RATES AND FRICTION COEFFICIENTS

More or less similar to real biological neural networks, ANNs are made up of interconnected, simple processing elements called artificial neurons. When they process information, the processing elements in the NN operate simultaneously and collectively, like biological neurons. ANNs have the required properties similar to those which possess the biological neural network, such as the ability to learn, to be self-organizing and support the robustness [14]. Similarly to biological neuron, each ANN neuron receives the inputs, processes them and delivers the outputs. The inputs can be a input set of data or the output from another neuron. The output can be the final result, or may be input to another neuron. In biological neurons and synapses, there are different strengths of

synaptic transmission, and intensities in the neurons, in the ANN these strengths are represented as the values of the weight coefficients. These neurons are grouped in layers. Each ANN contains only one input layer, zero or more hidden layers and one output layer. The most frequently applied structure of the ANN is a neural network consisting of three layers, all the layers except the input layer contain neurons. Number of inputs in ANN, corresponds to the number of defined independent parameters used for prediction, while the number of neurons in the output layer is equal to the number of dependent parameters whose values should be predicted. There is a direct ANN proportions between the number of hidden layers and the number of neurons in them and ANN capabilities to approximate complex functions. This does not mean that the networks with more complex structures work better. The reason for poor performance in these cases is linked to the fact that the complicated ANNs are more sensitive to noises that exist in the input data. It is necessary to make a compromise between the approximate ANNs capabilities and noises that are entered by the input data.

The power of neural network models lies in the fact that the weights *w* and biases *b* can be adjusted. Weights adjustment procedure is based on a specific data set and it is called ANN training with a certain data set (training set). The basic idea of training is to adapt the data network, i.e. to determine the relations that exist between the independent and dependent data in the training set. Using a custom network in future situations (for new data) is possible on the basis of previously established relationships and network capacity to generalize these relations to a broader group and thus reach possible conclusions.

ANN training is presented at the Figure 1. The present sample consists of two parts of the input and the target data portion (supervised learning). Initially, the network weight coefficients have assigned random values (usually in the range of -1 to 1). The input part of the first sample is put into the network. Network calculates the output on the basis of: the value of weight and biases, the number of layers that are in incorporated, and the type and quantity of neurons in each layer. The output value from the network is compared with the target value of the sample and the weights values of the network are adjusted, so that the metric, which describes the distance between the target value and outputs, is minimized.
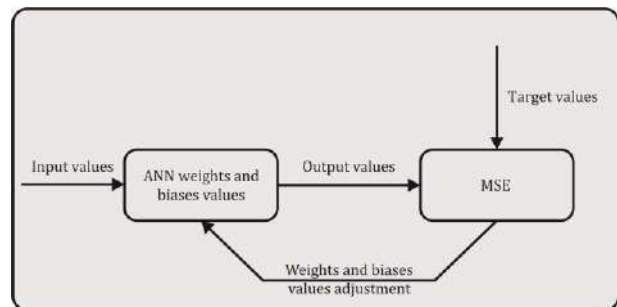

Figure 1. General framework of ANN training process

The parameters that are associated with training algorithms, that should be appointed, are: error function, learning rate and number of iterations. Error function is used to measure the difference between the target value and output values of the network. The values of ANN weights are updated in the direction that makes the error function to be minimized. Frequently used functions are Mean Square Error (MSE) and Mean Absolute Error (MAE). For training and testing of ANN commonly is applied MSE. MSE may be used as a target function to be minimized, in order to obtain optimal initial values of the ANN weight coefficients [15].

There are two basic types of ANN training, which are incremental and serial training. In the context of the incremental training weights and biases of the ANN are adjusted each time when one of the input samples is introduced to the ANN, while in the serial training, connection weights of ANN neurons are adjusted only when all the input samples are introduced into the network [16]. The cycle of bringing the entire training set in an ANN is called an epoch, a number of cyclical repetitions is the characteristic of the ANN, called the total number of epochs.

The updating mechanism of the ANN weights value is called a training algorithm. There are several training algorithms proposed in the literature [17, 18, 19]. The most commonly used training algorithm is related to the feed-forward ANN. ANN is characterized as a feed-forward network, if it is possible to connect the input layer to the hidden layers and the output layer, in a way that the each neuron is only associated with neurons from the preceding layers. All the algorithms use the MSE function to adjust the values of the weight coefficients and biases, so that the MSE function is minimized. The value of MSE function is determined by applying the back propagation techniques. Backpropagation is a mechanism of ANN learning, this is an iterative process in which the difference between the outputs of the network and the target values are given back into the ANN, so that the values of ANN weights coefficients and biases are gradually adapted to create output values that are closer to the target values [20].

In this paper, the three layered feed-forward backpropagation ANN architecture has been proposed for modelling. The input layer of the ANN model consists of two neurons corrsponding to the two bio-tibological parameters that were varied in the experiments, normal force (F) and sliding velocity (v) and the output layer has one neurons for prediction of wear rate (W) or friction coefficients (μ). Due to the different contact conditions (polished surface, glazed surfaces, and brushed surface) and number of parameters that have to be predicted (W and μ), six different ANN models were determined, one for each condition and parameter.

For all six ANN models, the entire experimental data set ($N_{tot}=12xnxm$) was divided into a six data subsets for different parameters prediction (n=2) and different conditions (m=3). After this data are further divided within each of six subsets into a data subset for training, a data subset for validation and a data subset for testing. 50 % randomly selected data have been employed for training, 25 % for validation and 25 % for testing, separately for each of the six subsets of experimental data.

Main problems that could occur in backpropagation are ANNs overfitting and overtraining. Overtraining means that ANN only memorizes the training data set and excellent learns these data but doesn't have an ability to generalize to new data and because of that performance of the validation set decreases [21]. Having this in mind, the objective is to determine the compatible ANN model that has the total MSE acceptably low [22, 23]. Selected ANN architecture had one hidden layer with ten neurons for prediction and bio-tribological process modelling. It has been presumed that this architecture could obtain minimal MSE value, between the output values and real experimental target data. Two different functions have been used as a transfer function, from the input to a hidden layer it was transigmoid function, and between hidden and output layer it was pure linear function. Prior to ANN training the training data were normalized within the range [-1 1] and the initial weights values were adopted according to Nguyen-Widrow method. The performance of the network was measured by the MSE of the predicted outputs with regards to the real experimental target data. The goal is to get MSE as close as possible to zero. The zero meaning that there is no error between outputs of the network and target values. In this case, ANN model trainings were initially set to terminate after a maximum number of epochs, but they was stopped after a certain number of epochs since no further improvement in the MSE was achieved. MSE values were obtained after trainings, validations and testing of ANN models and they are shown in Table 2.

Table 2. MSE values of ANN model

| Mod-el no.	ANN archite-cture	Mean Squared Error (MSE)			No. of epo-chs
		Training	Validation	Testing	
M 1	2-10-1	0.0014	0.011220	0.0213	4
M 2	2-10-1	0.0004	0.003248	0.001	3
M 3	2-10-1	0.0000	0.006359	0.0011	6
M 4	2-10-1	0.0012	0.000311	0.0021	4
M 5	2-10-1	0.0001	0.000070	0.0075	5
M 6	2-10-1	0.0028	0.003130	0.0059	5

Except MSE another performance measure for ANN model is correlation coefficient (R). This is a statistical measure of the strength of correlation between predicted and experimental values. A perfect correlation is obtained when R=1. A suitable ANN model should have the correlation coefficient greater than 0.8. Correlation coefficients of the developed wear rate prediction ANN models for all three diferently processed surfaces are shown in Fig. 2a,b,c.
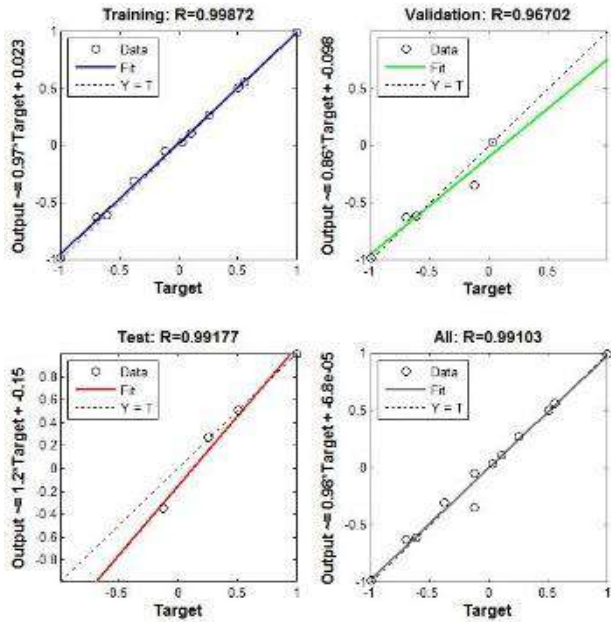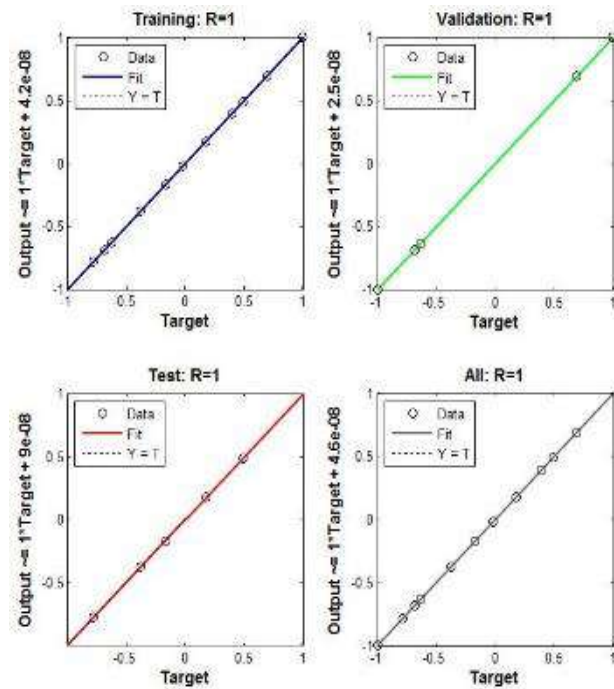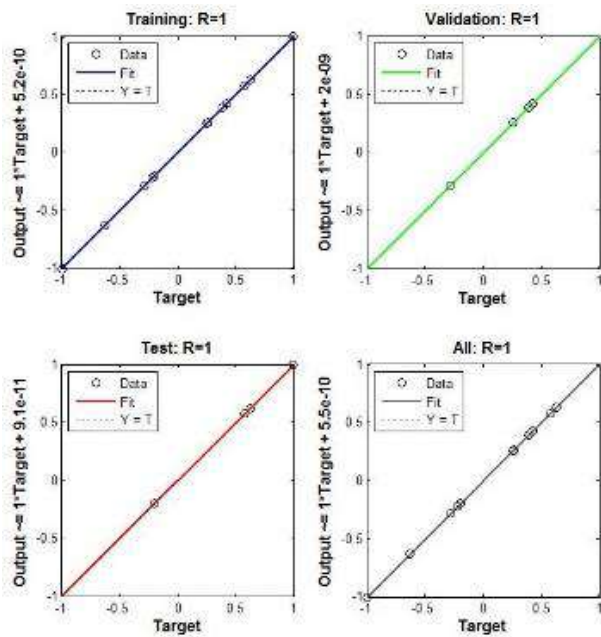

a) polished surface
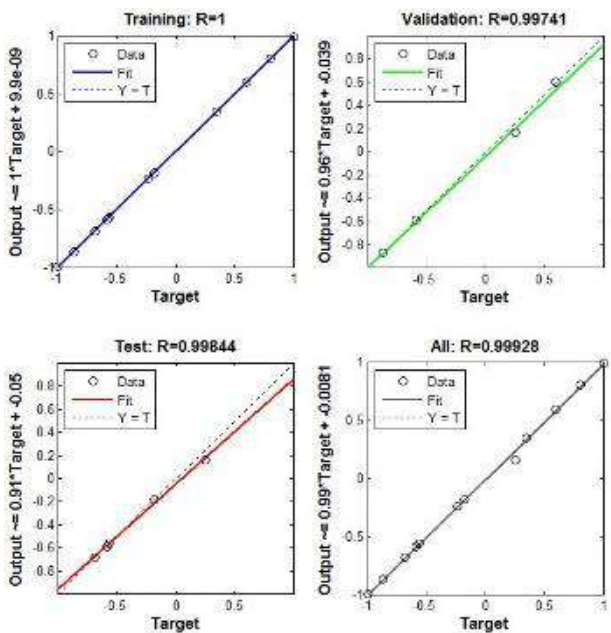
b) glazed surfaces
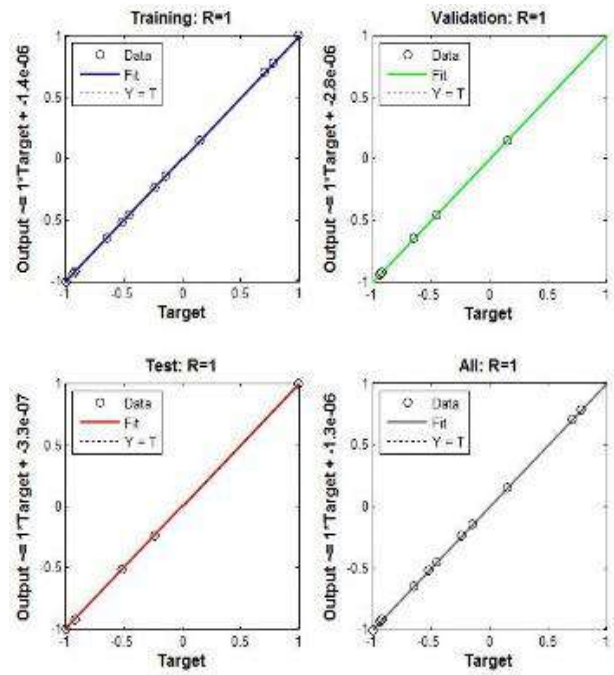
c) brushed surface

Figure 2. Correlation between predicted and experimental data during training, validation and testing of the developed ANN model for wear rate.

Similarly to the previous correlation coefficients of the developed friction coefficients prediction ANN models for all three differently processed surfaces are shown in Fig. -3a,b,c.

a) polished surface

b) glazed surfaces
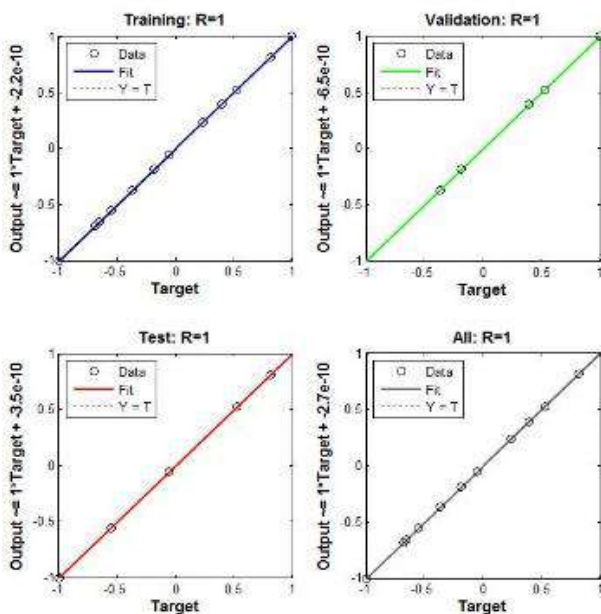
c) brushed surface

Figure 3. Correlation between predicted and experimental data during training, validation and testing of the developed ANN model for friction coefficients.

Table 3. The weights and biases of developed ANN model for polished surface wear rate prediction

Weights		Biases	
w_{ji}	w_{kj}	b_j	b_k
2.9459	-3.1857	0.21534	-4.5085	-0.21755
3.0566	3.1389	-0.0533	-3.5304	
-3.0417	2.9174	0.42509	2.8794	
4.3825	0.09847	0.52473	-1.559	
1.8201	4.0076	0.27768	-0.5393	
-2.9782	-3.2504	0.46395	-0.9972	
-4.1289	-1.5583	-0.3946	-1.4537	
0.50834	4.3896	0.10039	2.4669	
3.5561	1.9841	0.57493	3.8784	
3.2914	3.5083	-0.3414	3.9908	

The weights and biases of the wear rate ANN model with polished surface that were determined in training process are given in Table 3, for other models values are determined in a similar manner.

Using the weights and biases from Table 3-8 and in accordance with selected ANN architecture the exact mathematical relationship between bio-tribological response, Wear rate (*W*), friction coefficients (*μ*) and input bio-tribological parameters, normal force (F) and sliding velocity (v) in different contact conditions can be expressed by the following Equations 2 and 3. In these equation X is the column vector which contains normalized values of F and v and w_{norm} and μ_{norm} are the normalized value for the *W and μ* for each of the defined contact conditions. To obtain actual values of Wear rate and friction coefficients it is necessary to denormalize the obtained output values.

$$w_{norm} = \left[\frac{2}{1+e^{-2(X \cdot w_{ji}+b_j)}} - 1 \right] \cdot w_{kj} + b_k \quad (2)$$

$$\mu_{norm} = \left[\frac{2}{1+e^{-2(X \cdot w_{ji}+b_j)}} - 1 \right] \cdot w_{kj} + b_k \quad (3)$$

The next section provides an overview of measured and predicted values of the wear rate and friction coefficients, within the framework of materials bio-tribological examinations, according to the previously defined contact conditions.

4. RESULTS

Using Equation 2 and 3 and by varying values of both input parameters the effects of bio-tribological process on the wear rate and friction coefficient were analyzed. Hence, comparisons of actual target data and those predicted by developed ANN models were obtained. Results are shown in Tables 4-5.

Table 4. The real and predicted values of the wear rates of commercial ceramic lithium disilicate (*IPS e.max CAD*)

Wear rate, W, mm³/m			
Force	Velocity	Polished surface	
F_n, N	v, mm/s	Real values	ANN predicted values
0.25	4	1.893	1.97743
	8	3.512	3.89983
	12	3.983	3.97447

F_n, N	v, mm/s	Real values	ANN predicted values
0.5	4	5.244	5.60719
	8	6.617	5.40687
	12	7.446	7.4358
0.75	4	6.635	6.99912
	8	8.653	8.72522
	12	10.013	9.98442
1	4	7.846	7.85105
	8	10.279	10.302
	12	12.648	12.6478
Force	**Velocity**	**Glazed surfaces**	
F_n, N	v, mm/s	**Real values**	**ANN predicted values**
0.25	4	1.905	1.905
	8	3.240	3.23984
	12	3.744	3.74389
0.5	4	2.449	2.44915
	8	5.363	5.36283
	12	7.203	6.82267
0.75	4	3.647	3.64679
	8	7.592	7.59199
	12	9.553	9.55301
1	4	5.122	5.12221
	8	8.655	8.65501
	12	10.348	10.348
Force	**Velocity**	**Brushed surface**	
F_n, N	v, mm/s	**Real values**	**ANN predicted values**
0.25	4	0.028	0.028
	8	0.084	0.084001
	12	0.100	0.099999
0.5	4	0.352	0.351996
	8	0.469	0.469004
	12	0.524	0.523996
0.75	4	0.721	0.721001
	8	0.806	0.806005
	12	1.075	1.075001
1	4	1.582	1.581998
	8	1.651	1.650994
	12	1.848	1.848

Table 5. The real and predicted values of the friction coefficients of commercial ceramic lithium disilicate (*IPS e.max CAD*)

Friction coefficient, μ			
Force	**Velocity**	**Polished surface**	
F_n, N	v, mm/s	**Real values**	**ANN predicted values**
0.25	4	0.441	0.441
	8	0.406	0.406
	12	0.372	0.372
0.5	4	0.383	0.383
	8	0.347	0.347
	12	0.308	0.308
0.75	4	0.325	0.32501
	8	0.284	0.284
	12	0.255	0.255
1	4	0.249	0.249
	8	0.238	0.238
	12	0.213	0.213
Force	**Velocity**	**Glazed surfaces**	
F_n, N	v, mm/s	**Real values**	**ANN predicted values**
0.25	4	0.419	0.419
	8	0.359	0.359
	12	0.332	0.332
0.5	4	0.366	0.366
	8	0.337	0.337
	12	0.314	0.314
0.75	4	0.313	0.313
	8	0.248	0.248
	12	0.236	0.236
1	4	0.245	0.24499
	8	0.187	0.187
	12	0.134	0.134
Force	**Velocity**	**Brushed surface**	
F_n, N	v, mm/s	**Real values**	**ANN predicted values**
0.25	4	0.247	0.247
	8	0.240	0.24
	12	0.195	0.195
0.5	4	0.229	0.229
	8	0.218	0.218
	12	0.188	0.188
0.75	4	0.224	0.224
	8	0.207	0.207
	12	0.184	0.184
1	4	0.202	0.202
	8	0.183	0.183
	12	0.171	0.171

Analysing the experimental data the area of parameters combinations within certainly comes to sheet metal cutting was defined. This area was shown in Figs. 4a,b,c-5a,b,c.
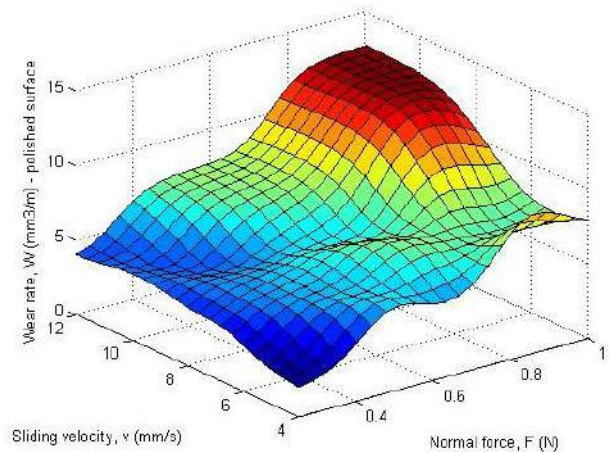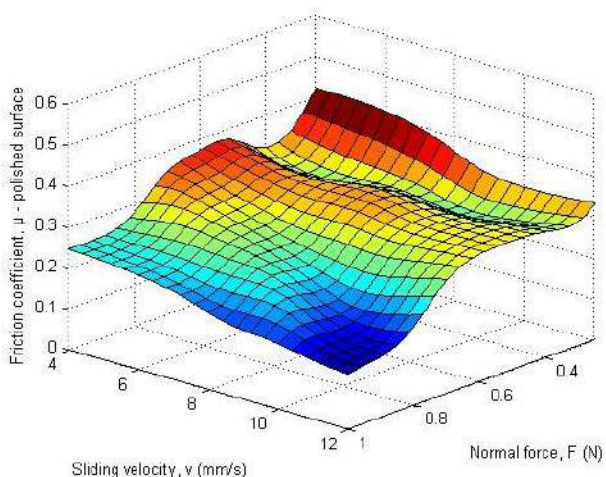

a) polished surface
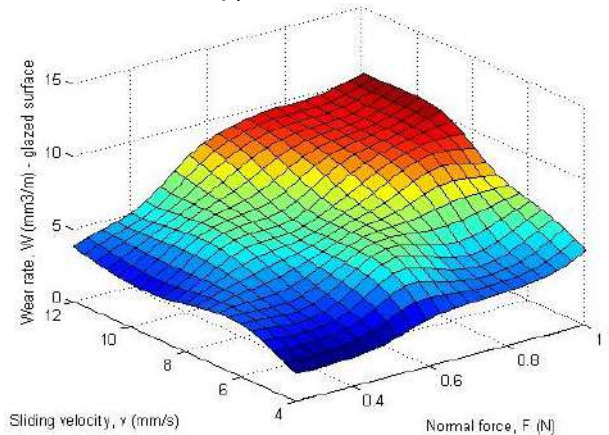
b) glazed surfaces
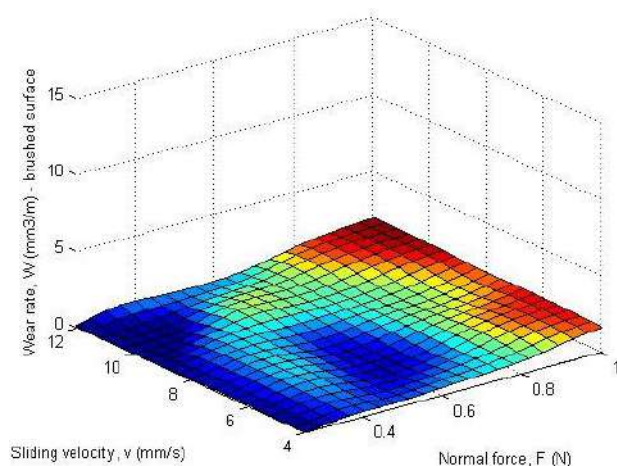
c) brushed surface

Figure 4. Influence of the F-v interaction on the wear rate (*W*)

c) brushed surface

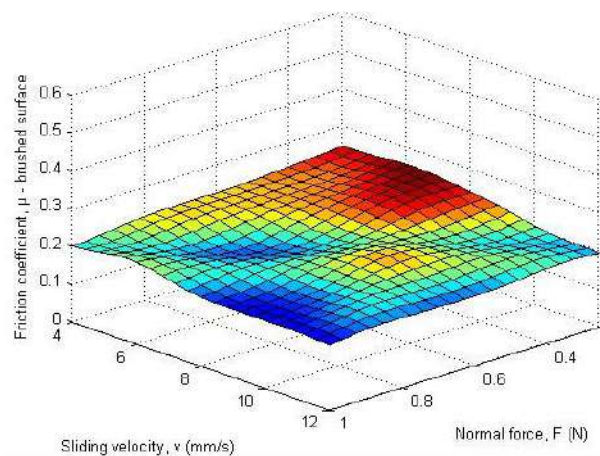**Figure 5.** Influence of the F-v interaction on the friction coefficient (*μ*)

From Figures. 4a,b,c-5a,b,c it can be concluded that higher values of normal force (>0.8 N) and sliding velocity (>8 mm/s) lead to higher values of wear rate (*W*), while the lower values of normal force (<0.4 N) and sliding velocity (<8 mm/s) lead to higher values of friction coefficient (*μ*). Having this in mind, it is necessary to further optimize the input values in order to obtain preferred outputs.

a) polished surface

b) glazed surfaces

5. CONCLUSION

In this paper a mathematical modelling of wear rate and friction coefficient in bio-tribological process was introduced. This was performed using ANN models for different surface conditions. ANNs have proven to be suitable due to their potential to learn nonlinear features of any system from incomplete experimental data regardless of external noise. Model was verified using bio-tribological experimental values obtained by means of nanotribometer. Beside that a comparison between experimental and predicted values was conducted. These indices showed that the models are quite acceptable for all defined conditions. Created model was used to describe the influence of input bio-tribological parameters such as normal force and sliding velocity on analysed material wear rate and friction coefficient. According to this the plots were created that can be used to identify bio-tribological conditions that may lead to minimal wear rate or friction coefficient.

Future research will take in consideration other materials and conditions, or the application of an optimization method used for optimal values achievement of wear rate or friction coefficient. Their values will be included in mathematical modelling procedure to obtain a complete view of output bio-tribological properties.

REFERENCES

[1] Z. Zhang, K. Friedrich and K. Velten, "Prediction on tribological properties of short fibre composites using artificial neural networks", Wear, vol. 252, no. 7-8, pp. 668-675, 2002.

[2] J. Zhu, Y. Shi, X. Feng, H. Wang and X. Lu, "Prediction on tribological properties of carbon fiber and TiO2 synergistic reinforced polytetrafluoroethylene composites with artificial neural networks", Materials & Design, vol. 30, no. 4, pp. 1042-1049, 2009.

[3] A. Yetim, M. Codur and M. Yazici, "Using of artificial neural network for the prediction of tribological properties of plasma nitrided 316L stainless steel", Materials Letters, vol. 158, pp. 170-173, 2015.

[4] X. LiuJie, J. Davim and R. Cardoso, "Prediction on tribological behaviour of composite PEEK-CF30 using artificial neural networks", Journal of Materials Processing Technology, vol. 189, no. 1-3, pp. 374-378, 2007.

[5] Z. Zhou, H. Yu, J. Zheng, L. Qian and Y. Yan, Dental Biotribology, 1st ed. New York, NY: Springer New York, 2013.

[6] T. Larsson, M. Martinez and J. Valles, "Biomaterials for Healthcare", A decade of EU-funded research, European Commission, Directorate – General for Research, Industrial technologies, Unit G3, Value – Added Materials, 2007.

[7] H. Hennicke, "Zum Begriff Keramik und zur Einteilung keramischer Werkstoffe", Berichte der Deutschen Keramischen Gesellschaft, vol. 44, pp. 209-211, 1967.

[8] M. Pantić, S. Mitrović, M. Babić, D. Jevremović, T. Kanjevac, D. Džunić and D. Adamović, "AFM Surface Roughness and Topography Analysis of Lithium Disilicate Glass Ceramic", Tribology in Industry, vol. 37, no. 4, pp. 391-399, 2015.

[9] M. Pantić, "Tribological characterization of advanced dental materials", PhD thesis, University of Kragujevac, Faculty of Engineering, 2017.

[10] Z. Zhou and J. Zheng, "Oral tribology", Proceedings of the Institution of Mechanical Engineers, Part J: Journal of Engineering Tribology, vol. 220, no. 8, pp. 739-754, 2006.

[11] I. Hahn Berg, M. Rutland and T. Arnebrant, "Lubricating Properties of the Initial Salivary Pellicle — an AFM Study", Biofouling, vol. 19, no. 6, pp. 365-369, 2003.

[12] S. Mukherjee, Applied mineralogy, 1st ed. Dordrecht: Springer, 2011.

[13] I. Hutchings, Tribology: Friction and Wear of Engineering Materials, 1st ed. Michigan, United States: Edward Arnold Publishers Ltd, University of Michigan, 1992.

[14] S. Li, D. Wunsch, E. O'Hair and M. Giesselmann, "Comparative Analysis of Regression and Artificial Neural Network Models for Wind Turbine Power Curve Estimation", Journal of Solar Energy Engineering, vol. 123, no. 4, pp. 19-41, 2001.

[15] Y. Chang, J. Lin, J. Shieh and M. Abbod, "Optimization the Initial Weights of Artificial Neural Networks via Genetic Algorithm Applied to Hip Bone Fracture Prediction", Advances in Fuzzy Systems, vol. 2012, pp. 1-9, 2012.

[16] S. Kumar, Neural networks: a classroom approach, 1st ed. New York City, NY: McGraw-Hill Education, 2004.

[17] A. Askarzadeh and A. Rezazadeh, "Artificial neural network training using a new efficient optimization algorithm", Applied Soft Computing, vol. 13, no. 2, pp. 1206-1213, 2013.

[18] S. Panda, A. Sarangi and S. Panigrahi, "A new training strategy for neural network using shuffled frog-leaping algorithm and application to channel equalization", AEU - International Journal Of Electronics And Communications, vol. 64, no. 11, pp. 1031-1036, 2014.

[19] V. Chandwani, V. Agrawal and R. Nagar, "Modeling slump of ready mix concrete using genetic algorithms assisted training of Artificial Neural Networks", Expert Systems with Applications, vol. 42, no. 2, pp. 885-893, 2015.

[20] Y. Chang, J. Lin, J. Shieh and M. Abbod, "Optimization the Initial Weights of Artificial Neural Networks via Genetic Algorithm Applied to Hip Bone Fracture Prediction", *Advances in Fuzzy Systems*, vol. 2012, pp. 1-9, 2012.

[21] I. Peko, B. Nedić, A. Đorđević, D. Džunić, M. Janković and I. Veža, "Modeling of Surface Roughness in Plasma Jet Cutting Process of Thick Structural Steel", Tribology in Industry, vol. 38, no. 4, p. 529, 2016.

[22] S. Tzafestas, P. Dalianis and G. Anthopoulos, "On the overtraining phenomenon of backpropagation neural networks", Mathematics and Computers in Simulation, vol. 40, no. 5-6, pp. 507-521, 1996.

[23] L. Prechelt, "Automatic early stopping using cross validation: quantifying the criteria", Neural Networks, vol. 11, no. 4, pp. 761-767, 1998.

COMPARISON OF PID AND FUZZY PID CONTROLLER FOR A LINEARISED MAGNETIC BEARING.

Theodoros K. PSONIS[1*], Epaminondas D. MITRONIKAS[2], Pantelis G. NIKOLAKOPOULOS[3]

[1] Phd student at the Department of Electrical and Computer Engineering in the University of Patras Rio, Patras, Greece

[2] Assistant Professor at the Department of Electrical and Computer Engineering in the University of Patras Rio, Patras, Greece

[2] Assistant Professor at the Department of Mechanical Engineering and Aeronautics in the University of Patras Rio, Patras, Greece

*Corresponding author: tpsonis@ece.upatras.gr

Abstract: *This paper is a presentation of a linear model of a magnetic bearing and a comparison of two controllers concerning their control performance. Initially, the benefits obtained by the use of magnetic bearings in the electromechanical systems are presented. Afterwards, the necessity for a suitable controller design is discussed in terms of the instability of the open loop system. Looking for a suitable control manner, a controller that behaves non-linearly, such as a fuzzy PID controller has been chosen in this paper. The use of such a non-linear controller improves both the results and the range of its use of the above system. The linear and the Fuzzy PID controller are compared using extensively simulation tests with the existence of white noise signal. The results of these comparisons, concerning the stability of these controllers are discussed and presented.*

Keywords: *Circuit stability, Fuzzy control, Fuzzy logic, linear model, Magnetic bearings, PID control*

1. INTRODUCTION

The use of magnetic levitation in motor bearings is a relative new idea which has been widely investigated through the last years. This idea seems to have many advantages over the conventional technology of existing bearings, like ball or oil bearings. The main advantage is that, due to levitation, the rotor and the bearing don't have any friction between them. This means that the motor has lower maintenance costs and longer life of the shaft. An additional factor contributing to the cost is the elimination of the lubrication seals. This elimination gives the potential for redefinition of rotor's dimensions and limits of strength. As lack of friction means absence of additional vibrations caused by it and the maximum rotation speed of the shaft can be also increased. In addition, the non-contact between the rotor and the bearing and the absence of lubrication make these new bearings ideally suitable for use in a variety of vacuum applications and sterile clean rooms. These advantages, have been the subject of research work in a wide range of studies of magnetic bearings [1-4]. The above studies have shown the need for the use of linear controllers, in order to control the behavior of the magnetic bearings [5]. The need for better

results in conjunction with the limited abilities of linear controllers, lead the studies to create more complex models. Farmakopoulos et.al [6] presented PID models regarding the linear Active Magnetic Bearing and a Hydromagnetic Bearing. They also presented the stability limits of the proposed controllers.

Furthermore, a non-linear controller for magnetic bearings control which was tested on a linearized system reportedly offers many advantages. In ref. [7] it is referred by the authors, that the use of Fuzzy as a controller, the system could have some advantages like shorter tuning time, accelerated response and reduced overshoot. All the above resulted to more robust systems and improved their dynamic and static performances. Other works studied exclusively the fuzzy controller and present classifications based by inputs of fuzzy [8], or compare the fuzzy controllers to a specific system [9]. In [9] the basic design principles of a fuzzy PID controller and the comparison with a regular PID is presented. These two controllers have been simultaneously tested using the same linearized active magnetic bearing (AMB) model which is excited by external disturbances. The system of an AMB and the classical PID controller has been analytically presented in [10].

2. METHODOLOGY

2.1 Models and Formulations

The system that is being studied here, represents a structure of an AMB which has one degree of freedom. It consists of a pair of electromagnets and a cylindrical mass of iron which corresponds to the rotor of the machine (figure 1). This mass has diameter 5cm and length 5cm. It is assumed that the mass density of the shaft is 7.9 g/cm3 for the sake of convenience calculations. The number of turns are 50 for each pole and the gap between the rotor and the inner wall of the bearing set is 0.5 mm [11-14].
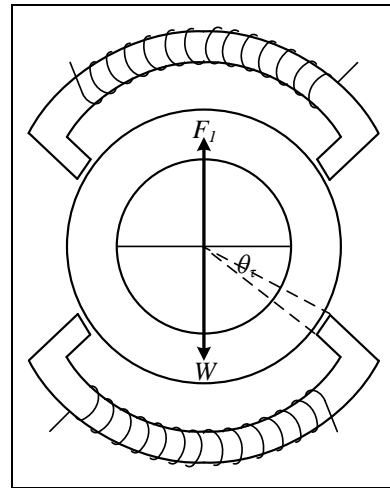
Figure 1. A 1D magnetic bearing.

The actual system of the magnetic bearing contains non-linearities due to the use of non-ideal coils, electromagnetic forces and due to the air gap. For linearizing the above system, the following assumptions have been made: the rotor is rigid and symmetric, gyroscopic effects is neglected, leakage of magnetic flux is neglected, the magnetic iron is operating below the saturation level, unbalance in the rotor is purely static, rotor motion in the axial direction is neglected and the flux leakage in the air gap is neglected [5,15]. At the equilibrium point of the rotor, the weight (W) and the force that comes from the electromagnet (F_1) are acted in the system , as described in the following equations (1-3):

$$F_1 - W = 0 \Rightarrow I_{bias} = \sqrt{\frac{(W \times 2 \times g)}{\left(\frac{N^2 \times \mu_0 \times S}{2 \times g}\right)}} \tag{1}$$

$$S = l \times \left(\pi \times D \times \frac{\theta_t}{360} \right) = 5.45 \times 10^{-4} \, m^2 \tag{2}$$

$$I_{bias} = 4.91779 A \tag{3}$$

The characteristic equation of the above magnetic bearing can be simply written as:

$$\frac{k_i}{m \times s^2 - k_x} \tag{4}$$

The above characteristic equation represents a system which has no zeros and two poles:

$$S_{1,2} = \pm \sqrt{\frac{k_x}{m}}.$$

The system is unstable as it has a positive pole. The stability of the system is achieved with the presence of an appropriate control of closed loop system.

At first, the system is designed to be controlled with a classic PID controller. The gains of the controller have been selected in our previous paper [10], where the stability of the system, the speed of the controller and the system response have been investigated. The gain values are as follows: Proportional Gain 1526.6269, Integral Gain 13330.5096 and Differential Gain 15.8724. The reference tracking of the PID controller is shown in fig. 2.
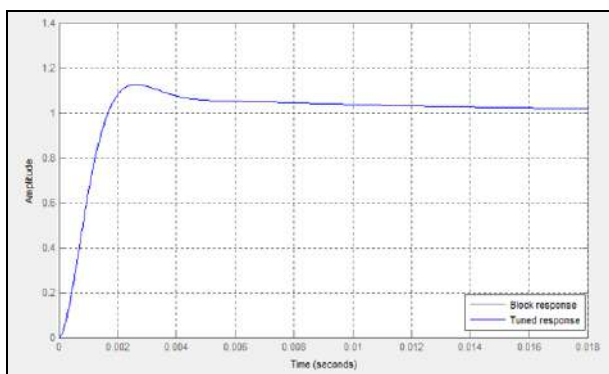
Figure 2. Reference tracking for PID controller.

In figure 3, the block diagram of the system and the noise existence is also presented. This noise signal, is white noise which has been added to the system in order to simulate the external disturbances which can adversely affect the system. The position where the noise has been added into the system is not accidental, and it is described by an individual block. Also, the transfer function of magnetic bearing is the transfer function of a linearized system in which the previous assumptions [5,15] are valid. Therefore, the linearized system which is described by the transfer function of figure 3 is a system which can be considered isolated from external disturbances.

The determination of the type and the value of the external disturbances was based on [6], which represents the operation of a magnetic bearing, which in its turn accepts external disturbances to the downforce of the machine's shaft. The white noise has been selected, as it is an ideal form of noise, which is independent of the frequency variations. The spectrum of the white noise has the same constant value for all the range of the frequencies [16]. This interference of noise causes disturbances in the system which the PID controller seeks to cancel. As the noise isn't a constant value, it would be desirable to redefine the controller gains based on noise values in each cycle of the closed-loop system. This ability is being provided to the system by the Fuzzy controller. This controller is based on a knowledge representation method and a fuzzy logic decision-making mechanism. This knowledge is introduced to the controller by the fuzzy rules. For the determination of the rules, it's necessary to understand the influence of the controller gains to the response of the system. The theoretical data regarding this influence are shown in Table 1. For obtaining quantitative knowledge some trials were made via simulations, and the results are shown in the Table 2.
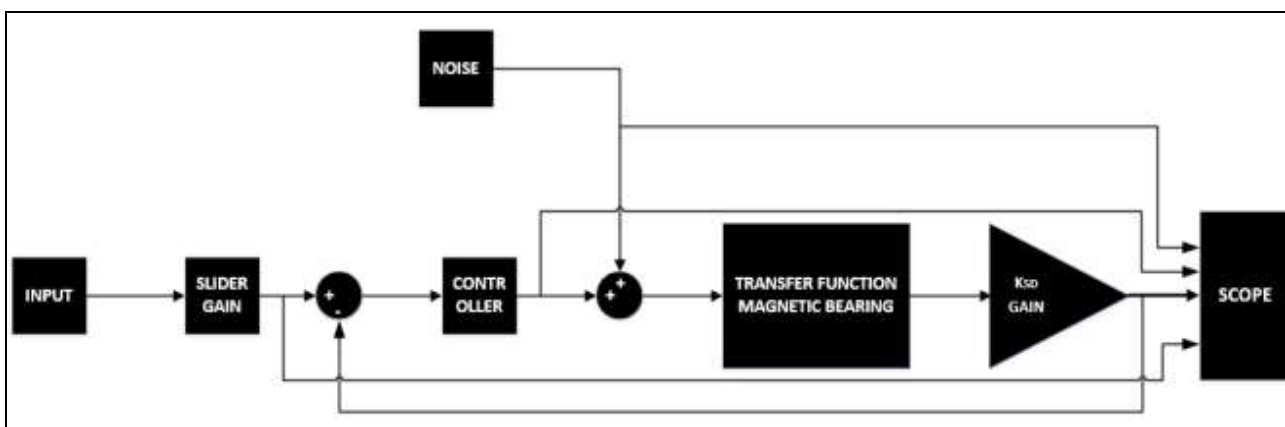
Figure 3. Block Diagram of the system with PID controller.

**Table 1.** Effect of controllers in the system

Controller	Raising time	Raising	Restoration time	Permanent error
Proportional	Reduction	Increase	Minor change	Reduction
Integral	Reduction	Increase	Increase	Elimination
Derivative	Minor change	Reduction	Reduction	Minor change

Table 2. Test data for the gains effect in the system

	Raising time	Raising	Restoration time	Permanent error
Kp (initial value 1526.6269)				
1200	Reduction	Reduction	Indifferent	Increase
1600	Reduction	Increase	Indifferent	Reduction
1800	Increase	Increase	Reduction	Reduction
2000	Increase	Increase	Reduction	Reduction
3000	Increase	Increase	Reduction	Reduction
Ki (initial value 13330.5096)				
10000	Indifferent	Reduction	Indifferent	Increase
15000	Indifferent	Increase	Indifferent	Reduction
18000	Indifferent	Increase	Indifferent	Reduction
23000	Indifferent	Increase	Indifferent	Reduction
32000	Indifferent	Increase	Indifferent	Reduction
Kd (initial value 15.8724)				
10	Increase	Increase	Increase	Indifferent
18	Reduction	Reduction	Reduction	Indifferent
22	Reduction	Reduction	Reduction	Indifferent
30	Reduction	Increase	Increase	Indifferent

The fuzzy PID controller (fig.4) has two inputs, the rotor position error and the derivative of it, and three outputs which are the three gains of it discriminate between temporary and permanent errors. The variation of the PID's gains, which are the outputs of fuzzy controller (fig 6-9), is determined by certain rules, which

are set after the evaluation of the above theoretical and experimental data on the influence of gains [16]. In figure 10 the block diagram of the system with the fuzzy PID controller is presented. the PID controller. The small range of the position error (fig.5) in combination with the derivative of it, makes the controller more sensitive even in small disturbances and helps
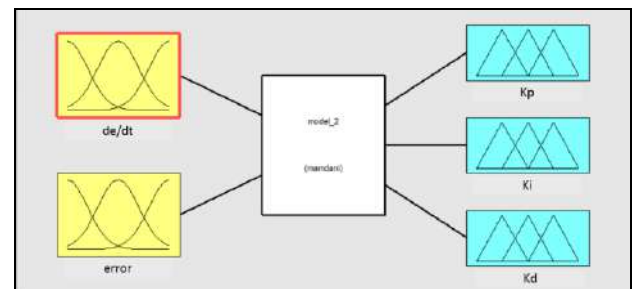
Figure 4. Structure of the fuzzy controller.
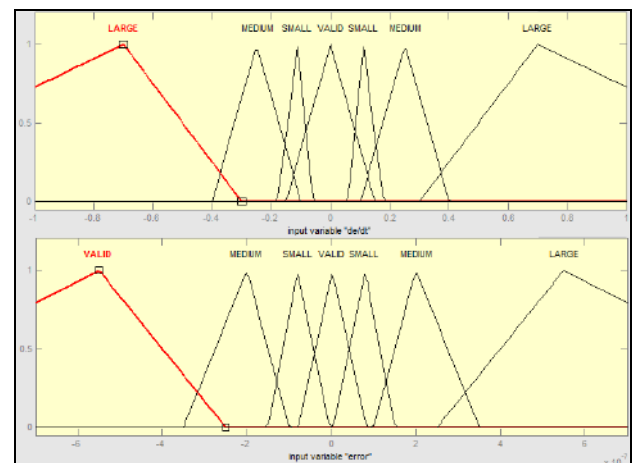
Figure 5. Input membership functions of the fuzzy controller.
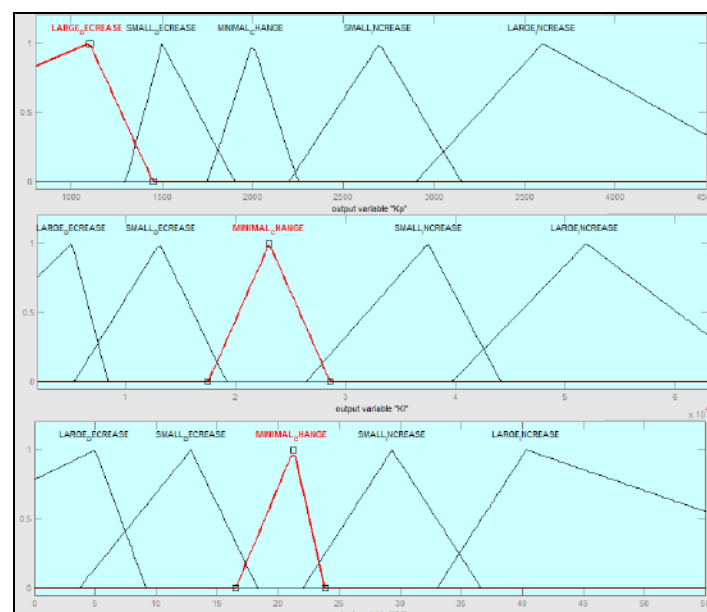
Figure 6. Output membership functions of the fuzzy controller.
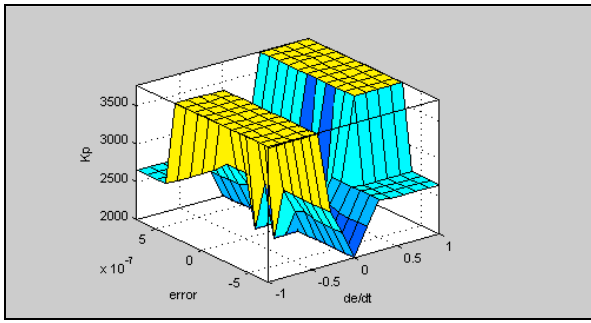
Figure 7. The output surface of Kp.

Figure 8. The output surface of Ki.

Figure 9. The output surface of Kd.

3. SIMULATION RESULTS WITH FUZZY AND A CLASSIC PID CONTROLLER.

The system with the simple PID controller (fig. 3) has the following time-unchanged transfer function as the controller's gains are fixed.
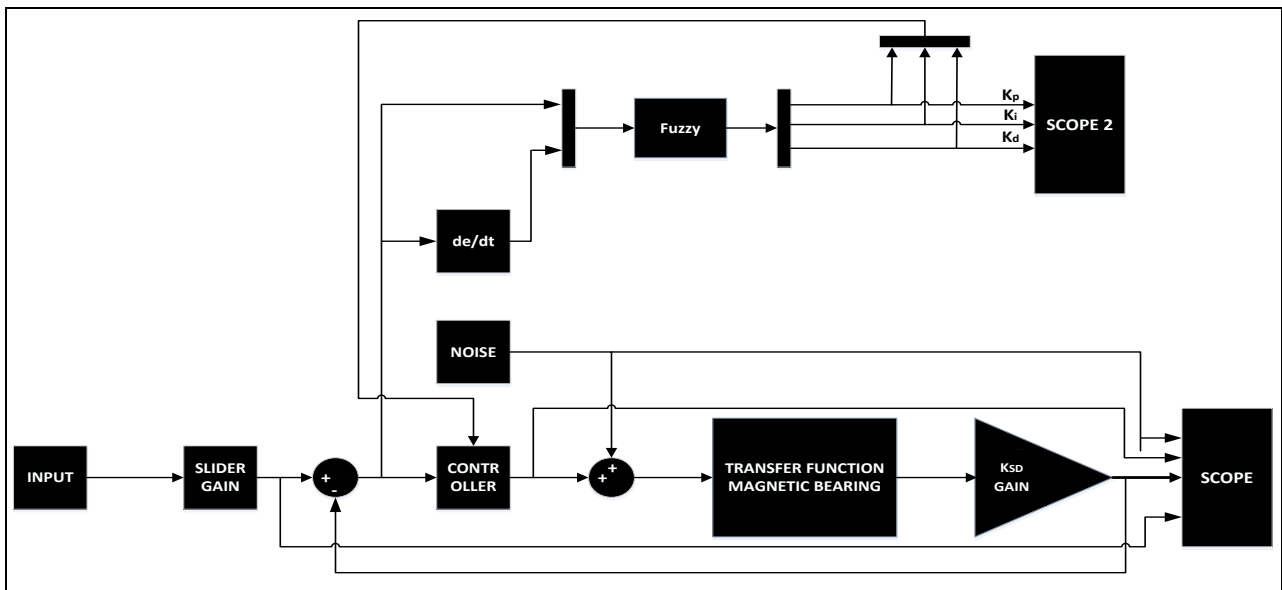

Figure 100. Block Diagram of the system with fuzzy PID controller.

$$\frac{X}{X'} = \frac{\left\lfloor s^2\left(K_p + N \times K_d\right) + s\left(K_p \times N + K_i\right) + K_i \times N\right\rfloor \times k_i \times k_{sn}}{m \times s^4 + N \times m \times s^3 + \left(\left(K_p + N \times K_d\right) \times k_i \times k_{sn} - k_x\right)s^2 + \left(\left(K_p \times N + K_i\right) \times k_i \times k_{sn} - k_x \times N\right) \times s + k_i \times K_i \times N \times k_{sn}}$$

(5)

The poles of the above function are:

P1=-9.71450, P2=-90.13387
P3= - 1128.92409 + 1177.08749*i,
P4= - 1128.92409 - 1177.08749*i

The stability of the system derives from the fact that all the poles have a negative real part, which means that they reside in the left half-plane.

The system with fuzzy PID controller has a time-changing transfer function as the gain of controller changes in each cycle of the system. The variation of the gains, (outputs of the fuzzy controller), is made through the fuzzy rules so that the system remains stable, having all poles in the left (negative), half-plane.
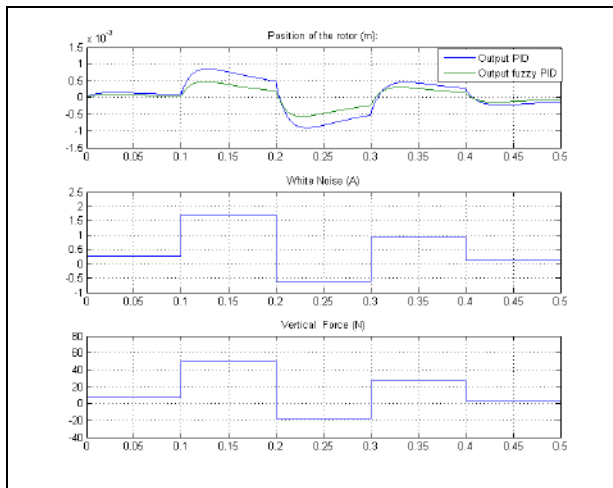
Figure 111. Plot of PID and fuzzy PID outputs for a noise power of 0.05.
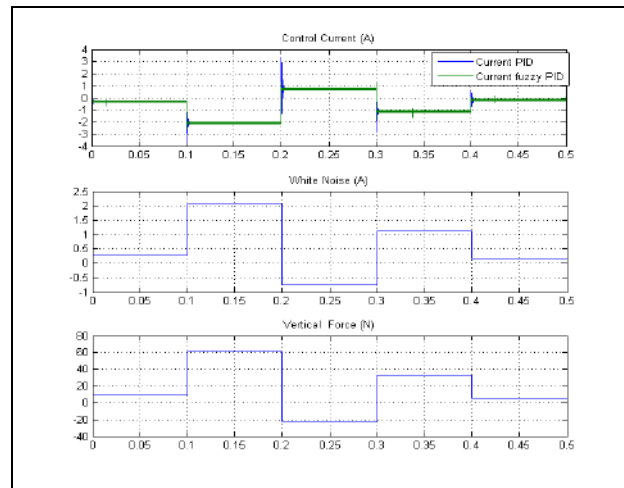
Figure 14. Plot of PID and fuzzy PID control currents for a noise power of 0.075.
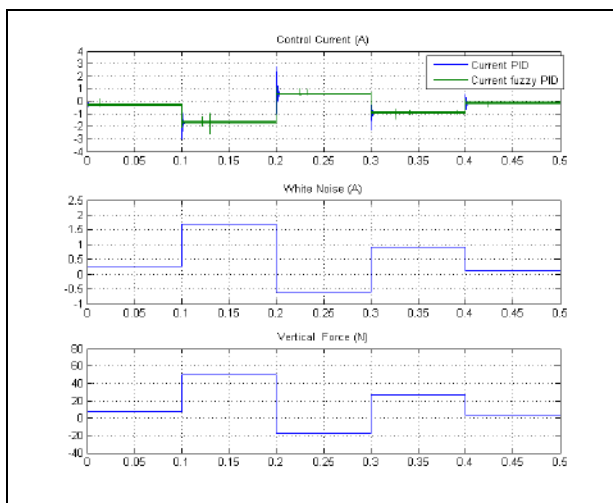
Figure 12. Plot of PID and fuzzy PID control currents for a noise power of 0.05.
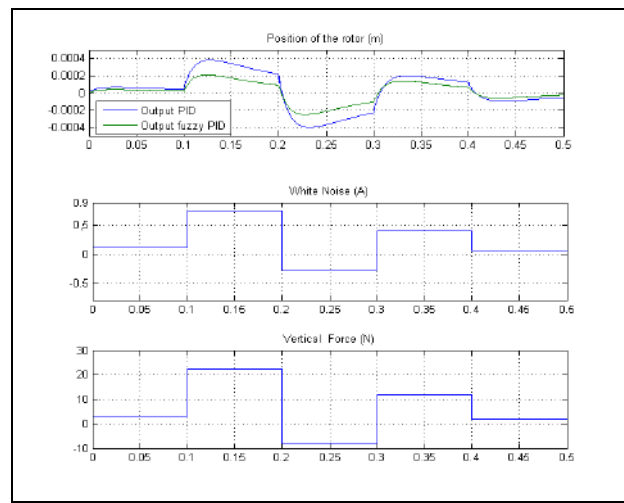
Figure 15. Plot of PID and fuzzy PID outputs for a noise power of 0.01.
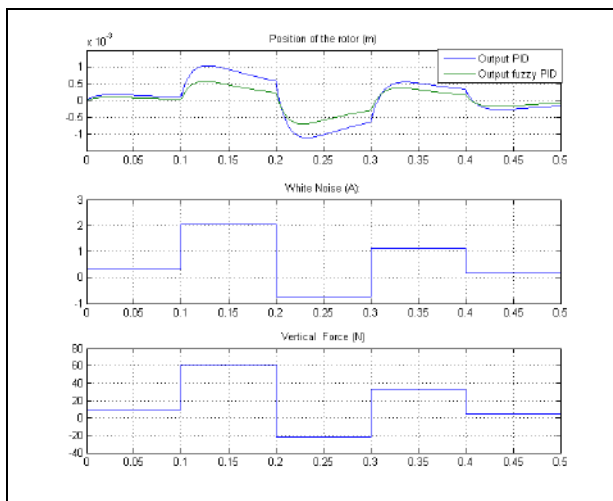
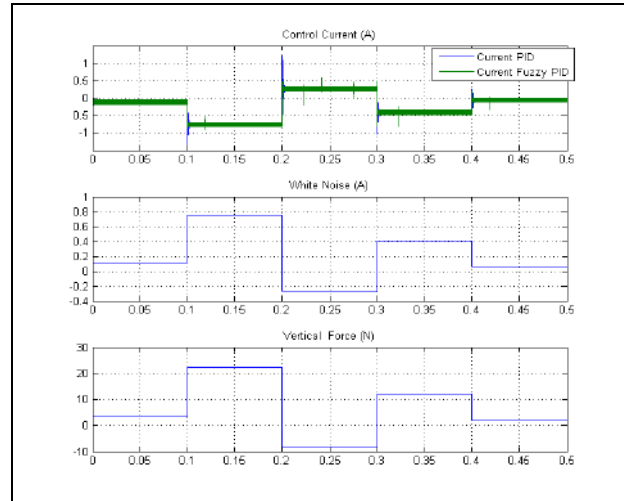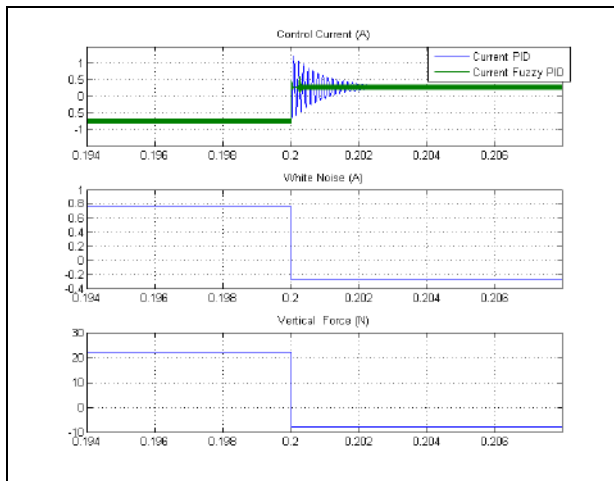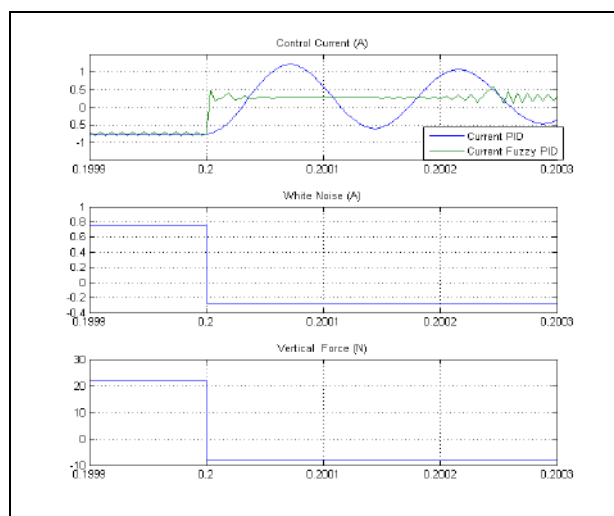**Figure 12**. Plot of PID and fuzzy PID outputs for a noise power of 0.075.

Figure 16. Plot of PID and fuzzy PID control currents for a noise power of 0.01.

Figure 17. Plot of PID and fuzzy PID control currents for a noise power of 0.01 (detail view).

Figure 18. Plot of PID and fuzzy PID control currents for a noise power of 0.01 (detail view).

The analysis of the above diagrams leads to important conclusions. First, the similarity of the controller's output is obvious. However the fuzzy controller leads to a more effective PID control. Furthermore, as the fuzzy leads to a better PID, it is evident that it has better response than the classic PID. The main conclusions derived by the diagrams are the following two: Firstly, the system with the fuzzy controller is stable as the position of the rotor and the current of the controller remains within the permissible limits. This had also been secured from the study and the determination of the fuzzy controller rules. Secondly, (figs. 16-18), the control current of fuzzy is less than the control current of PID controller. This means, that the overall electrical efficiency of the bearing can be maximized.

4. CONCLUSION

In this paper a comparison between two different controllers for an active magnetic bearing is presented. This comparison shows the advantages of fuzzy PID controller than the classic PID concerning both the response of the system and the energy needed to supply the control system. The fuzzy controller supplies in each cycle of the control new PID gains. This process results to a stable system with an optimum PID controller. Finally, the two controllers has been simulated in the same time with a white noise signal, which represents external disturbances. The long term objective is the creation of a fuzzy control system for the real motor. The investigation is still under process and the controller may be improved by adding new rules and use new forms of input and output fuzzy membership functions

NOMENCLATURE

F_1:   Force from electromagnet.
g: The gap between the rotor and the inner wall of the bearing
Ibias: Current bias.
K_D: Derivative Gain
K_I: Integral Gain
Ki: Force-Current factor
K_P: Proportional Gain
k_{sn}:   Sensor Gain
k_x: Force-Displacement factor (stiffness coefficients)
l: Stack length.
m: mass of shaft
N: Number of turns
PID: Proportional Integral Derivative
S: Cross-section area of flux path.
W: Weight of shaft
ϑ_t: Angle between shaft and electromagnet. ϑ_t = 25 deg
μ_0:   Permeability of free space.

REFERENCES

S.G., E. Maslen, *Magnetic Bearings Theory, Design and Application to Rotating Machinery*, Springer, Berlin, 2009.

[1] C. S., H. S., P. Wang, J. D., A feasibility Study of Bearingless Motor Based on Three-Pole Active Magnetic Bearing, International Journal of Automation and Smart Technology, Vol. 2, pp. 1-8, 2012.

[2] D. L., S. You, Adaptive control of an active magnetic bearing with external disturbance, ISA Transacion, Vol. 53, pp. 1410-1419, 2014.

[3] A. Chiba, T. Fukao, O. Ichikawa, *Magnetic Bearings and Bearingless Drives*, Elsevier, Amsterdam, 1, 2005.

[4] D. Polajžer, J. Ritonja, G. Ŝtumberger, D. Dolinar and J. Lecointe, Decentralized PI/PD position control for active magnetic bearings, Electrical Engineering (Archiv für Elektrotechnik) , Vol. 89, No. 1, pp. 53 – 59, 2006.

[5] M. G. Farmakopoulos, E. K. Loghis, P. G. Nikolakopoulos, N. I. Xiros, C. A. Papadopoulos. Modeling and Control of the Electrical Actuation System of an Active Hydromagnetic Journal Bearing (AHJB), Proceedings of the ASME 2014 International Mechanical Engineering Congress & Exposition, Montreal, Canada, 2014.

[6] S.-C. Chen, V.-S. Nguyen, D.-K. Le, T.-H.-N. Nguyen. Nonlinear Control of an Active Magnetic Bearing System Achieved Using a Fuzzy Control with Radial Function Neural Network, journal of Applied Mathematics,2014,18, DOI: 10.1155/2014/272391, 2014.

[7] B. Akbiyik, I. Eksin, M. Guzelkaya, E. Yesin. Evaluation of the Performance of Various Fuzzy PID Controller Structures on Benchmark Systems. ELECO,4rd International Conf. of Electrical and Electronics Engineering, 2005.

[8] E. Yeşil, M. Güzelkaya, İ. Eksin. Fuzzy PID controllers: An overview, The Third Triennial ETI International Conference on Applied Automatic Systems, 1, 105-112, 2003.

[9] T. Psonis, P. Nikolakopoulos, E. D. Mitronikas. Design of a PID controller for a linearised Magnetic Bearing. International Journal of Rotating Machinery Volume 2015, Article ID 656749, 12 pages, 2015.

[10] W. de Boer . Active Magnetic Bearings: modelling and control of a five degrees of freedom rotor. M.Sc. Thesis, Eindhoven University of Technology, NL, 3-5, 1998.

[11] G. Schweitzer. Active magnetic bearings-chances and Limitations, Proc. 6th Internat. IFToMM Conf. on Rotor Dynamics, Sydney, Sept. 30-Oct. 3, 2002.

[12] B. Polajžer, D. Dolinar, G. Štumberger, J. Ritonja, B. Grčar, K. Hameyer. Design of Horizontal Shaft Active Magnetic Bearing System,2nd International seminar on Vibrations and acoustic noise of electric machinery, 51-55, 2000.

[13] B. Polajžer, D. Dolinar, G. Štumberger, J. Ritonja, J-P. Lecointe. Decentralized PI/PD position control for active magnetic bearings. Electrical Engineering, 89, 53-59. DOI: 10.1007/s00202-005-0315-1, 2006.

[14] M.K. Habib, J. Inayat-Hussain. Fuzzy Logic Based Control of Rotor Motion in Active Magnetic Bearings. Cybernetics and Intelligent System, IEEE, 2, 1219-1225,2004.

[15] T. Psonis, E. D. Mitronikas, P. Nikolakopoulos. A fuzzy control model for bearingless motors. Proceeding of the ICEAF IV International Conference of Engineering, Skiathos,Greece, 2015.

INFLUENCE OF TIP WEAR ON THE RESULTS OF AFM MEASUREMENTS

Dragan KUKURUZOVIĆ [1*], Pal TEREK [1], Aleksandar MILETIĆ [1], Lazar KOVAČEVIĆ [1], Branko ŠKORIĆ[1]

[1] University of Novi Sad, Faculty of technical sciences, Trg Dositeja Obradovića 6, 21000, Novi Sad, Serbia,

*Corresponding author: kukuruzovic@uns.ac.rs

Abstract: Nanotechnology shapes our present and will shape our future. The age of nanotechnology begun with invention of tools, such as scanning probe microscopes (SPM) which enable imaging and manipulation of atoms and molecules, as well as surface mapping of different properties in nanometer range. A family of SPM techniques was born with the development of scanning tunnelling microscopy (STM) and atomic force microscopy (AFM). AFM is generally used for three-dimensional surface measurement on nanometer and micrometer scale. Three-dimensional image is formed by scanning sharp tip over the surface of a measured sample, and detecting probe movement in a vertical direction. During imaging, tip wears-off and becomes blunt. In this study, influence of tip wear on measured topography is investigated. For that purpose, AFM measurements were conducted on two hard coated samples. One sample was mirror polished, while the second was fine grinded. A set of low magnification (scan area of 100 x 100 μm^2) and a set of high magnification measurements (scan area of 5 x 5 μm^2) were made on each sample. One new, and two worn tips were used for the measurements. Before the AFM measurements, all the tips were examined by scanning electron microscopy. We found that the tip wear does not have significant influence on the results of low magnification measurements, neither qualitative, nor quantitative. On the other hand, the tip condition is of the fundamental importance for the high magnification measurements.

Keywords: AFM, tip wear, surface roughness, SEM

1. INTRODUCTION

Nanotechnology is a broad term that covers many areas of science, research and technology that involves understanding mater at the nanometer scale. In recent years it received increasing amount of attention and is being spoken as the driving force behind a new industrial revolution [1]. However, in order to research nanoscale object, one needs to see them. Scanning probe microscopy (SPM) allows topographic imaging of the atomic-scale features [2]. SPM techniques are used not only for imaging in nanometer realm, but also for nanofabrication [3].

A family of SPM techniques has been developed to date. Atomic force microscopy (AFM) is one of the most commonly utilized SPM techniques. Supplementary to 3D surface imaging, it allows measurements of magnetic, electrical or mechanical properties of the widest possible range of samples with nanometer resolution [4–6].

The AFM surface morphology imaging offers three different modes of usage: the contact (static) mode, tapping (intermittent

contact) mode and noncontact mode [6]. The employed mode is selected on the basis of sample material, environment, and desired reliability. Nevertheless, all modes imply atomic interaction between AFM tip and the sample, and tip geometry plays a vital role in the quality of the obtained surface measurements. AFM results are a convolution of the tip geometry and the shape of the features being imaged [7].

Constant interactions between AFM tip and sample atoms consequently lead to wear of the AFM tip geometry [8]. This wear increases the surface contact between two bodies, and consequently increases the minimum size of the features that can be detected [9]. Thus, tip wear significantly reduces the quality of AFM images, and is an extensively studied phenomenon.

In order to obtain high-quality surface topographies, researchers need to regularly change scanning probes. Sharp, high quality AFM probes are fairly expensive, and their replacement significantly increases the measurement costs. Therefore, there were numerous studies that have tried to correlate scan parameters to tip wear in order to minimize it [8]. By optimizing scan parameters, one can reduce wear of AFM tips and minimize measurement costs induced by the need for probe replacement. Another potential approach is to precisely define the maximum allowable wear that can still give adequate results for specific measurements, by keeping in mind dominant topological features. Therefore, for certain measurement one could use worn and discarded AFM probes without notable reduction in the quality of obtained results.

In this study, three contact mode AFM probes were subjected to various numbers of repeated measurements. Their worn geometry is correlated to the results of AFM measurements of samples with different morphology.

2. EXPERIMENTAL DETAILS

This study was performed for contact mode AFM measurements. This mode was selected because the wear and its influence on measurement results is more pronounced in comparison to the two other AFM operation modes.

Three new commercial contact mode AFM probes were selected for this investigation. The probes were made from antimony doped silicon. AFM probe nominal parameters are as follows: cantilever length 525 µm, cantilever width 35 µm, cantilever thickness 4 µm, spring constant 0.9 N/m, tip radius 8 nm, resonant frequency 20 kHz.

The AFM measurements were performed by using the VEECO diCP II atomic force microscope. Following measurement parameters were used: gain of 0.5, set point was set at 225, resolution of 256, frequency of 50 Hz and the scanning direction was orthogonal to the cantilever of the probe (X direction, from left to right). AFM probes were subjected to varying number of low magnification measurements, as stated in Table 1. These measurements were performed in order to obtain initial variance in AFM tip wear, and are hereinafter called initial measurements.

Table 1. Number of times the AFM probe was used.

AFM probe	Number of measurements
T1	> 20
T2	> 50
T3	> 250

After initial measurements, two sets of measurements were performed in order to analyze subsequent performance of AFM probes: a set of low magnification (scan area of 100 x 100 µm^2), and a set of high magnification measurements (scan area of 5 x 5 µm^2). These measurements will hereinafter be called final measurements.

Final measurements were performed on two types of substrates with different surface morphologies. The first substrate was duplex TiN PVD hard coating deposited on DIN 1.2344 (AISI H13) tool steel that was subjected to progressive grinding with 100 to 2,000 grit silicon carbide sandpapers. Hereinafter this

sample will be labeled rough substrate. The second substrate (labeled smooth) was duplex TiAlSiN PVD hard coating deposited on the same tool steel. Only additional difference in sample preparation was mirror polishing with diamond paste performed after progressive grinding.

The AFM tip geometry vas evaluated by Scanning electron microscopy (JOEL JSM 6460 LV Scanning electron microscope).

3. RESULTS AND DISCUSSION

To confirm starting geometry of the AFM tips, one of the AFM probes (T1) was imaged before the start of initial measurements, Figure 1.
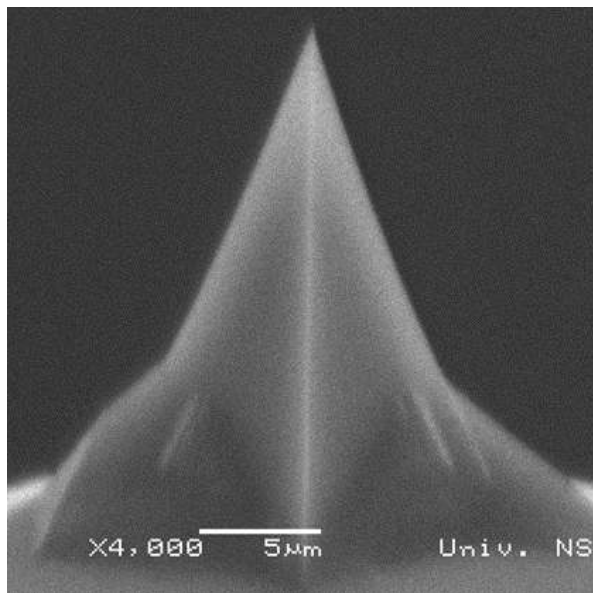
Figure 1. SEM image of an unused AFM tip

The unused tip has symmetric pyramidal geometry. The apex of the tip is very sharp and has the radius of a couple of nanometers. Therefore, tip apex should be able to reach into smaller grooves on the substrate surface, and is adequate for surface imaging of samples used in this study.

In order to correlate tip geometries to the surface topographies of final measurements, all AFM tips were analyzed under high magnifications. SEM images from this analysis are given in Figure 2.

AFM tip T2 has suffered the least amount of wear. The tip showed continuous gradual wear without signs of fracture. The tip apex

consequently has notably larger radius than the unused tip shown in Figure 2. However, its sharpness should still be sufficient to achieve measurements of adequate quality.
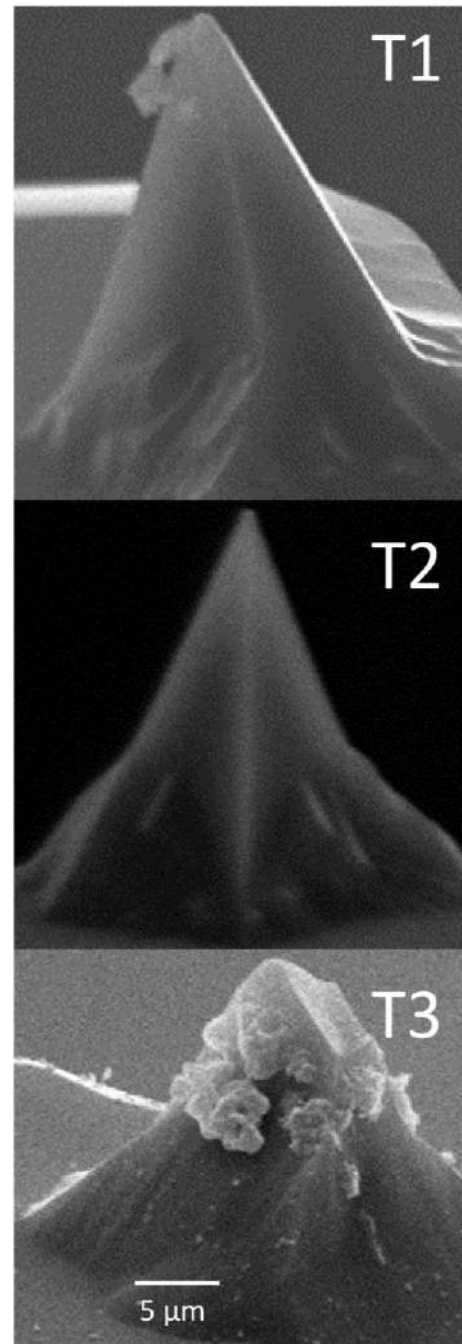
Figure 2. SEM images of AFM tips after final measurements

AFM tip T1 has suffered higher wear than the T2 tip. Some debris can be seen on the side of the tip and are loosely connected to its apex. EDS analysis of the debris and surrounding tip apex showed almost identical chemical compositions. Therefore, it could be postulated that the debris represent tip apex that has fractured during measurements. This

behavior is not uncommon since silicon AFM tips have a tendency of apex fracture [10]. Fracture of the apex made T1 tip relatively blunt. Thus, lower quality of measurements could be expected.

As expected, AFM tip T3 exhibited the highest worn volume. Wear debris encompass the tip and has made its apex completely blunt with a radius that is order of magnitude larger than at the start of the measurements.

High magnification analysis of worn AFM probes exhibits some deviations in correlation between number of measurements and worn volume. AFM tip T1 exhibited higher wear despite conducting half as many measurements. The explanation could be found in several phenomena. The T1 tip was studied in unused condition before conducting any measurements. In order to obtain valid SEM images, i.e. avoid charging effect, the tips were plated with thin coat of gold. This coating could have influenced subsequent tip operation and wear mechanisms. Additionally, SEM analysis lasted several hours. Electron bombardment during this process could have influenced the tip properties. Finally, tip impact during the approach process can lead to the apex fracture. This process is random and can occur after only few approaches [8].

Quantitative AFM results of the final measurements are given in Figure 3. As a quality indicator for the performed measurements, surface arithmetical mean height (Sa) is used.

Roughness of high and low magnification zones obtained by the same probes from the same samples vary significantly. The resolution of both high and low magnification measurements is the same and both images have 256 × 256 data points. Therefore, despite the fact that the AFM tip traces surface topology accurately even in low magnification measurements, the sampling rate prevents detection/recording of the small surface features. In the same manner, large features are out of the scope of high magnification measurements, and cannot be detected by these measurements. Therefore, direct comparison between low and high magnification measurements cannot be made.
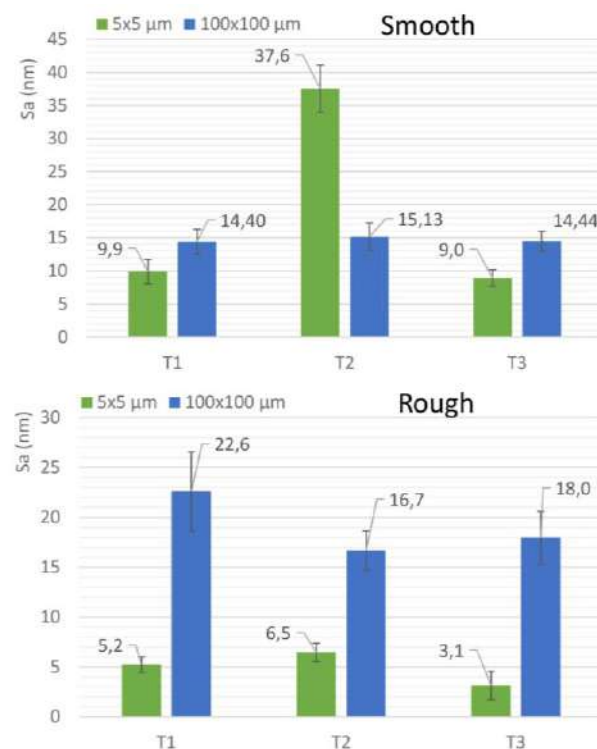

Figure 3. Average surface roughness of the examined samples. Error bars represent ± one standard deviation.

In order to analyze the effect of tip wear on obtained surface roughness measurements a one-way ANOVA was conducted at the $p < 0.05$ level. Analysis was made for every group of measurements conducted with the same magnifications on the same samples. In most of the measurements the tip geometry has statistically significant influence on obtained results. This is in accordance with the standard procedure to use unworn AFM probes, and discard them after only few measurements on hard samples. However, it was found that the tip geometry had no statistically significant effect on low magnification roughness measurement of rough samples ($F_{(2,15)} = 0.29$, $p = 0.75$).
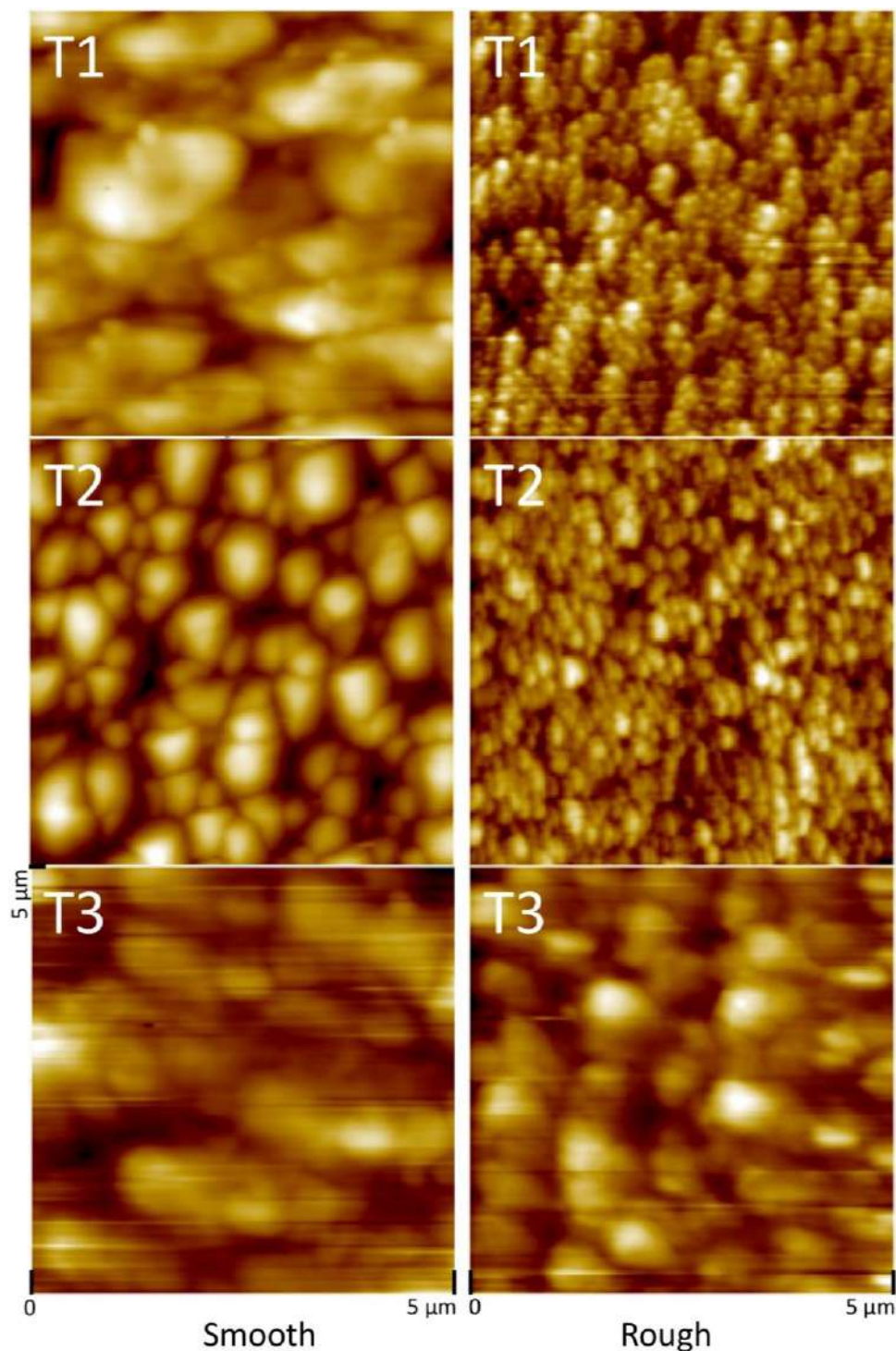
Figure 4. High magnification surface topography images

AFM surface topography images obtained with high magnification are presented in Figure 4. Tested samples, i.e. TiAlSiN and TiN PVD hard coatings, have columnar grain structure. Therefore, qualitative analysis of the effect of tip wear can be performed by tracking changes in the size and shape of the grains. As expected, highest resolution of these surface features is obtained when using AFM probe T2 that has preserved sharpest apex, Figure 2. Obtained image is clear, and size and shape of the grains can be easily observed on both samples. Contrary to these results, images obtained with AFM probe T3 are blurred and surface features cannot be distinguished. The tip of this probe has suffered significant wear and its large diameter apex was unable to penetrate into deep narrow grooves. Thus, only grain clusters can be clearly discerned on both samples. The

quality of AFM probe T1 images is inexplicit. Individual grains on smooth sample were somewhat blurred, but clearly recognizable. Their quality is similar to the one obtained by the T2 AFM probe. On the other hand, image quality of the rough sample was poor, and closely resembles those obtained by AFM probe T3. This qualitative analysis is in agreement with quantitative results presented in Figure 3. Roughness values for smooth samples by AFM tip T1 are only slightly smaller than the ones obtained by T2. However, for rough samples this difference is almost fourfold.

Images obtained by AFM tips T1 and T3 had notable, regularly repeating, horizontal bands, Figure 4. In most cases, these bands are attributed to ambient vibrations. However, all measurements were performed in similar conditions where AFM was isolated and mounted on anti vibration table. Since the bands are almost absent on all images obtained by utilizing tip T2, explanation should be sought in tip geometry. The main difference between these tips is the presence of the debris near the tip apex. They change geometry of the tip and create multiple apexes that start to copy certain features that were picked up while the surface was scanned [7].

4. CONCLUSIONS

In this paper, study of the effects of tip wear on the results of AFM measurements is presented.

In most cases, tip geometry has detectable impact on measurement quality. However, one-way ANOVA analysis has shown that tip wear has negligible influence on AFM measurements of rough samples made with low magnification. Therefore, for this purpose one can utilize previously worn and discarded AFM probes.

Horizontal bands on AFM images that are commonly dismissed as vibration related, can be caused by debris adhering near the tip apex and changing its geometry. If they start to appear on regular intervals, it can be used as a sign of necessity to replace AFM probe.

REFERENCES

[1] T.C. Yih, V.K. Moudgil: Nanotechnology comes of age to trigger the third industrial revolution, Nanomedicine: Nanotechnology, Biology and Medicine, Vol. 3, pp. 245, 2007.

[2] K. Bobrov, A.J. Mayne, G. Dujardin: Atomic-scale imaging of insulating diamond through resonant electron injection, Nature, Vol. 413, pp. 616–619, 2001.

[3] L.B. Zhang, J.X. Shi, J.L. Yuan, S.M. Ji, M. Chang: The Advancement of SPM-Based Nanolithography, Materials Science Forum, Vol. 471–472, pp. 353–357, 2004.

[4] Y. Han, S. Schmitt, K. Friedrich: Nanoscale Indentation and Scratch of Short Carbon Fiber Reinforced PEEK/PTFE Composite Blend by Atomic Force Microscope Lithography, Applied Composite Materials, Vol. 6, pp. 1–18, 1999.

[5] J. Moghal, H. Suttle, A.G. Cook, C.R.M. Grovenor, H.E. Assender: Investigation of the mechanical properties of aluminium oxide thin films on polymer substrates by a combination of fragmentation and scratch testing, Surface and Coatings Technology, Vol. 206, pp. 3309–3315, 2012.

[6] P. Eaton, P. West: *Atomic Force Microscopy*, Oxford University Press, 2010.

[7] P. West, N. Starostina: *A Guide to AFM Image Artifacts*, Santa Clara, CA, USA, n.d.

[8] B. Xue, Y. Yan, Z. Hu, X. Zhao: Study on Effects of Scan Parameters on the Image Quality and Tip Wear in AFM Tapping Mode, Scanning, Vol. 36, pp. 263–269, 2014.

[9] A. Yacoot, L. Koenders: Aspects of scanning force microscope probes and their effects on dimensional measurement, Journal of Physics D: Applied Physics, Vol. 41, pp. 103001, 2008.

[10] J. Liu, J.K. Notbohm, R.W. Carpick, K.T. Turner: Method for Characterizing Nanoscale Wear of Atomic Force Microscope Tips, ACS Nano, Vol. 4, pp. 3763–3772, 2010.

Biotribology

STABILITY LOSS OF THE CEMENTED STEM OF HIP PROSTHESIS DUE TO FRETTING CORROSION FATIGUE

Lucian CAPITANU[1], Liliana-Laura BADITA[2],*, Virgil FLORESCU[3]

[1]Institute of Solid Mechanics of the Romanian Academy, Bucharest, Romania

[2]National Institute of Research and Development for Mechatronics & Measurement Technique, Bucharest, Romania

[3]University of Civil Engineering, Bucharest, Romania

*Corresponding author: badita_l@yahoo.com

Abstract: Aim of this project was to study the fretting behaviour of the cemented femoral stem fixation of a total hip prosthesis, trying to capture the loss of contact between the femoral stem and polymetylmethacrilate cement fixation. To have a landmark, studies were performed compared with cementless fixation, where no fretting phenomenon occurs, on real prostheses, under biological 3D loading conditions. A fatigue test device, installed on a servo-hydraulic triaxial dynamic testing machine was used. It allowed monitoring the flexion-extension, abduction-adduction, inner-outer rotation movements, and the variation of the torsional torque, depending on normal loading. The test ends when the sample does not fail after 2000000 cycles, or when it has reached a predetermined number of cycles. Test fluid medium used was NaCl mixed with distilled water, a favourable environment for appearance of fretting corrosion. After the failure of stem fixation at 2450000 cycles, the mantle of bone cement remaining adherent on femoral stem was removed. Microscopic inspection of the femoral stem and of the inner part of the polymetylmethacrilate mantle demonstrated the existence of corrosion of the femoral stem surface beneath the cement mantle, and Fe_2O_3 deposits on the femoral stem surface and on the inner part of the mantle.

Keywords: Hip prosthesis, polymetylmethacrilate, Ti6Al4V, cemented stem, fretting fatigue corrosion

1. INTRODUCTION

Fretting refers to the process involving movements of low amplitude, more precisely movements with total amplitude smaller than the width of contact between two components. There are several application areas where this phenomenon occurs, such as aerospace industry, implants in the human body, automotive, etc. In the recent years, several studies have focused on the understanding of this phenomenon, and on finding solutions to prevent and/ or avoid it.

Fatigue design of certain components in these areas, without taking into account the effect of fretting, will certainly lead to premature and unexpected failure in many applications [1]. Fretting corrosion is a degradation phenomenon of contact in an aqueous medium. It is one of the most critical issues in designing total hip prostheses, since it occurs at the contact surface between femoral stem and bone cement [2]. Fretting in a total hip prosthesis is due to the destruction of the passive oxide on metal, leading to increased corrosion and to the generation of residues,

such as polymer and metal oxides particles [3]. This leads to serious dysfunctions of the prosthetic hip joint. Cyclic loading due to human gait and differences between the mechanical properties of the femoral stem and bone cement give rise to loss of contact between the two materials. This leads to secondary effects, such as damage and cracking of cement. Remains, including metal oxides and ions, penetrate the bone tissues through cracks and, finally, induce inflammation of bone tissues. Currently, the most used materials for manufacturing femoral stems are CoCr alloy, Ti alloys or austenitic stainless steels (SS 316L). Bone cement, such as polymetylmethacrilate (PMMA) is introduced into the spongy and the cortical bones. Damage by fretting corrosion between SS 316L femoral stem and PMMA bone cement was experimentally investigated under similar conditions to those found in a real prosthesis [4]. The interfacial energy dissipated and the wear volume, after 2000000 cycles were measured. It has been demonstrated that the wear volume can be expressed as a function of the dissipated interfacial energy. Fretting phenomena have been studied both in air and in aerated solutions. When exposed to air, it was not observed any significant wear on stainless steel, but mechanical wear was found when it came in contact with PMMA. It has been found that the wear volume of PMMA is linearly correlated with the cumulative energy dissipated [5]. Fretting – material's damage caused by small oscillating movements between the bodies in contact – can lead to surfaces deterioration and dimensional changes. A remarkable decrease of the useful life in the presence of bulk effort can also be seen. Surface's damage is defined as the fretting wear, while the development of the crack can be called fretting fatigue [6]. For the life estimation at fretting fatigue, the complete process problems are usually divided into two phases – crack's initiation and crack's propagation. There is still a debate on the proportion of life time taken by these two phases, most of the authors considering both

of them in the stage of estimating the total life. Therefore, it still continues the search for more appropriate selection criteria. Each criterion is appropriate in some selected combinations of materials, geometry, type of contact conditions, and loading.

The level of fretting damage is determined by the amplitude of the relative sliding between the femoral stem and bone cement [7]. If the sliding amplitude is so small that some contact parts remain adherent, and others slide over the other opposite surface, the cracks are predominantly generated in the vicinity of the contact edges (fretting fatigue). If the sliding amplitude is large enough to make all the parts of a surface to slide over the other surface, the wear takes place over the entire contact surface (fretting wear). It was identified by numerical modelling, in which the sliding amplitude between the femoral stem and bone cement is about 0.05 mm under the strains applied during normal human gait. It was observed that the sliding amplitude induces the fretting wear in total hip prosthesis. The concentration of chloride (ionic strength), the concentration of protein (albumin) and solution pH could affect the fretting corrosion of materials used in a total hip prosthesis. Influences of ionic strength, of albumin and of the potential applied were studied by fretting corrosion tests using SS 316L and PMMA bone cement. It was established that the ionic strength increases the wear volume on SS 316L at the open circuit potential. Albumin with concentration of 1 gL^{-1} does not play a significant role in determining the total wear volume of SS 316L, compared with albumin of 0 gL^{-1}. At a potential applied E = -0.4 V (SCE), there is a threshold concentration (NaCl solution) of 0.1 M over which the metal dissolution is improved. A concentration of 20 gL^{-1} albumin decreases the wear volume of SS 316L, but increases the wear volume of PMMA [7]. Similar findings were presented and for femoral stems made of Ti6Al4V alloy [8]. In the human body, Ti6Al4V alloy is immersed in a physiological solution having a high concentration of NaCl (~ 0.2 M) at a

temperature of 38 ^{0}C. Because of the significant difference in mechanical properties (especially Young's modulus, with a ratio of 90 between Ti6Al4V and PMMA) shielding stress occurs. This physical phenomenon can be explained as follows. Metallic materials and polymers do not present the same deformation under applied stress, leading to unsoldering between the metal and cement. Therefore, the adhesion between metal and polymer loses after a short period of human gait. This unsoldering involves fretting (friction under small displacements) and subsequent friction between materials in contact. Thereafter, Ti6Al4V and the bone cement are subjected to small displacements, friction loadings in a corrosive environment, resulting in fretting corrosion. Consequently, the wear between the bone cement and Ti6Al4V alloy occurs. It involves the generation of debris, which often cause inflammations or reactions, ending with aseptic loosening of implants fixation and the necessity of replacement.

Giannakopoulos et al. [9] stated that the fretting problem can be addressed as a matter of simple fatigue subjected to a localized stress concentration. They developed an analytical model for the fretting fatigue at a corner of a rounded mandrel in contact with a substrate and made an analogy with fatigue crack initiation at the notch of a tip. They analysed the similarities and differences between the stress concentration factors at the edge of the contact mandrel on flat rounded suddenly and the tip of a blunt crack. The methodology analogous to the notch provided a direct connection between the life of fretting fatigue crack initiation of a flat mandrel with rounded corners and the life of simple fatigue crack initiation of a smooth sample of the same material. Model predictions compared with fretting fatigue experiments on Ti6Al4V showed a good concordance.

Fretting fatigue is a type of multiaxial fatigue, having a non-proportional loading, thus introducing multiaxial stress fields and severe stress gradients. Therefore, in order to define the failure, multiaxial criteria are used. In the past, multiaxial criteria that use critical

damage parameters have been developed, together with various ways to define the estimated life. Generally, stress and strain components combined with material constants are fully assimilated to the limit of fatigue resistance in tension/ inverted torsion or by Manson-Coffin and Basquin relation [10]. Hence, it allows computing the estimated life time according with the fretting fatigue scenario. Some researchers have used the approach of continuum damage mediums (CDM) mechanics, which is based on thermodynamic potential function and on the fact that crack initiation life can be estimated using bulk materials properties. Based on the approach used to model the initiation of fretting fatigue crack, different criteria can be classified as: critical plane approach, invariant stress approach and CDM approach. The aim of this paper was to study the fretting behaviour of the cemented femoral stem fixation of a Ti6Al4V/ UHMWPE total hip prosthesis. To have a landmark, studies were performed compared with cementless fixation, where no fretting phenomenon occurs. The study was done on real prostheses, under biological 3D loading and motion conditions.

2. MATERIALS AND EXPERIMENTAL TECHNIQUES

2.1 Materials

Typically, the stems of hip prostheses are made of SS 316L, Ti6Al4V or CoCr alloys, because of their mechanical properties and good biocompatibility [1]. In this study, the contact of Ti6Al4V alloy with PMMA was studied, simulating the femoral stem/ fixation material contact. PMMA is a thermoplastic optically transparent material. At room temperature, it is a hard and brittle material. Its mechanical resistance is much smaller than that of Ti6Al4V alloy, so a prosthetic stem made of Ti6Al4V alloy, with chemical composition shown in Table 1, was used. Fixation was realized with PMMA bone cement (PMMA Perspex$^{®}$) whose mechanical properties are shown in Table 2.

Table 1. Chemical composition of the Ti6Al4V alloy (w/w)

Elements	Composition
Al	5.60-6.75
O (max)	0.020
N (max)	0.05
V	3.50-4.50
Fe (max)	0.40
St (max)	0.015
H (max)	0.10
Other (max)	0.40
Ti	Balance

Table 2. Mechanical properties of the tested materials

	Ti6Al4V	PMMA
Poisson Coefficient (υ)	0.29	0.39
Young modulus (E) [MPa]	119	2.5
Yield strength (σ_c) [MPa]	825	65
Tensile strength (σ_t) [MPa]	805	75

2.2 Experimental devices

Fretting tests were performed on a Instron® device for fatigue testing of the femoral stem cemented fixation of the total hip prosthesis – Figure 1, installed on a servo-hydraulic multiaxial dynamic testing machine MTS Bionix, equipped with testing system for hip implants – Figure 2.

Instron® device – Figure 1(a) simulates fatigue loading of a hip cemented stem during a gait cycle. Device consists of a support made of a composite femur model from Sawbones® transparent plastic with intramedullary channel, in which the prosthetic stem is cemented. It has a low friction loading head, incorporating a low friction bearing and an adapter for mounting to the system loading cell – Figure 1(b). This device is mounted in a sealed saline chamber, which contains a NaCl high concentration solution (~ 0.2 M) at a temperature of 38 ^{0}C. The ensemble has a temperature regulator and a circulation pump for in vivo testing. The flexible support for prosthetic stem allows a wide variety of hip

geometries, offset angles, materials and embedding depths to be used. The device applies compression, bending and torsion to meet the ISO 7206-4 requirements.

(a)
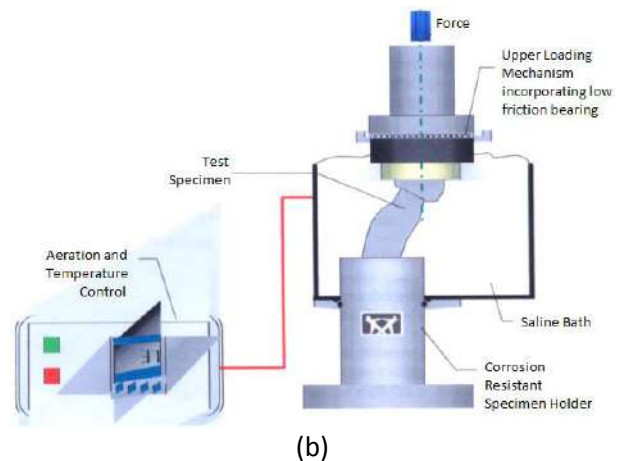
(b)

Figure 1. (a) Instron® fatigue test device for the femoral stem cemented fixation of the total hip prosthesis, and (b) Instron® testing system scheme for prosthetic stem fatigue fixture

Loading compression through the loading head makes the femoral stem specimen to be subjected to loads and frequencies as specified in ISO 7206-8. The test ends either when the sample does not fail after 2000000 cycles, or when it has reached a predetermined number of cycles. In the case of this research, the test was stopped at 2450000 cycles, when indices of fretting appeared. Test fluid medium used was NaCl mixed with distilled water and testing frequency was 10 Hz.

MTS Bionix servo-hydraulic multiaxial dynamic testing machine (Figure 2) allows triaxial testing of hip implants and in tribological terms [11].

Figure 2. MTS Bionix servo-hydraulic multiaxial dynamic testing machine, equipped with system for testing the hip implants

MTS Bionix system is equipped with three rotating motors for inner-outer rotation (IOR), flexion-extension (FE) and abduction-adduction (AA) movements and with three displacement transducers, one for each type of movement. In addition, it has a transducer for the moment of torsion, with two Wheatstone decks, one for measuring linear force and the other to measure the torsion moment. The moment transducer is of resistive type and it is coupled with a current converter type 662 20 h-04, to process received signals from each Wheatstone deck.

The test machine allowed setting number of cycles, the amount of the normal force on the joint implant (the force *F* that has a pulsating form), the lower and upper limits of the angular displacement of each rotation, as well as the law of motion for each type of rotation according to ISO 14242-3.

Appropriate fitting of the sample was verified before the time of the test. It has been adjusted at the pump pressure value of 210 bar, the controller and the application "Station Manager" were started, by which were made relations to the system calibration settings and adjusted. After that, zero settings had been done. After the command – response adjustments, the output values for each axis (axial, torsion, FE, AA, IOR) have zeroed.

3. EXPERIMENTAL RESULTS AND DISCUSSION

Through the "ELITE" software the vertical push force and the displacement angles were set: FE, AA, IOR, according to ISO 14242 upgraded in 2014, which sets the parameters for orthopaedic implants testing, of the limits 1 and 2.

Values in Table 3 show the force, its maximum amount being 3 kN. The sign is negative because it is a compression force (the negative sense of the *z* axis).

Values for abduction-adduction, inner-outer rotation and flexion-extension angles are presented in Tables 4, 5 and 6.

Table 3. Values for the axial force of pressing

(1) Channel: Axial; Force measurement (kN)				
Time (sec.)	Segment count	Wave	1 Limit (kN)	2 Limit (kN)
0.0005	10000	Sinus	-0.3000	-0.3000
0.1195	10000	Sinus	-3.0000	-1.5000
0.2000	10000	Sinus	-1.5000	-0.3000
0.1800	10000	Sinus	-3.0000	-0.3000
0.1200	10000	Sinus	-3.0000	-0.3000
0.3800	10000	Sinus	-0.3000	-0.3000

Table 4. Values for Abduction-Adduction angle, according to ISO 14242

(1) Channel: Axial; Force measurement (kN)				
Time (sec.)	Segment count	Wave	1 Limit (kN)	2 Limit (kN)
0.0005	1.0000	Sinus	-3.0000	7.0000
0.1195	1.0000	Sinus	7.0000	-4.0000
0.2000	1.0000	Sinus	-4.0000	3.0000
0.3800	1.0000	Sinus	3.0000	3.0000

Table 5. Values for Inner–Outer Rotation angle, according to ISO 14242

(1) Channel: Axial; Force measurement (kN)				
Time (sec.)	Segment count	Wave	1 Limit (kN)	2 Limit (kN)
0.0005	1.0000	Sinus	-10.0000	2.0000
0.5000	1.0000	Sinus	2.0000	-10.0000
0.4995	1.0000	Sinus	-10.0000	-10.0000

Table 6. Values for Flexion-Extension angle, according to ISO 14242

(1) Channel: Axial; Force measurement (kN)				
Time (sec.)	Segment count	Wave	1 Limit (kN)	2 Limit (kN)
0.0005	1.0000	Sinus	25.0000	-18.0000
0.5000	1.0000	Sinus	-18.0000	25.0000
0.4995	1.0000	Sinus	25.0000	25.0000

After entering values for force and angle of movement in FE, AA, IOR, it was set the number of test cycles to 2000000 cycles.

For MTS Bionix system calibration, the prosthesis was subjected to simultaneous requests of FE, AA and IOR during a cycle and was considered a time of 5 seconds, where human subject achieves 5 complete cycles. In Figure 3 are shown the graphs of vertical contact force: the answer come from the force transducer is represented by the red colour and blue is the command set.

(a)

(b)
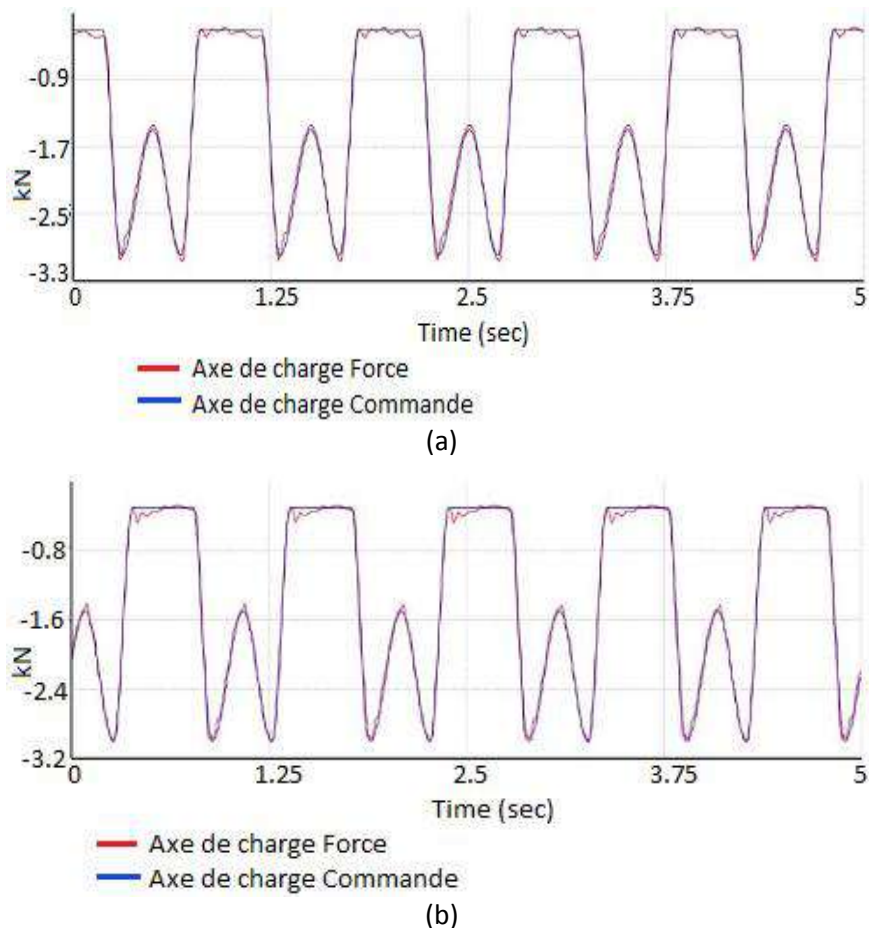
Figure 3. Time graph of the vertical contact force, command-response (blue-red) when testing the cemented prosthesis (a) and (b) a cementless prosthesis (press-fitted stem)

In time graph of the vertical contact force and angular displacement of the flexion-extension (Figure 4) is presented for a cemented prosthesis (a) and (b) a cementless prosthesis. At the same time, the graph of the vertical contact force and angular

displacement of the abduction-adduction (Figure 5) is presented when testing the cemented prosthesis (a) and (b) a cementless prosthesis.

In Figure 6 is presented the graph of normal force and angular displacement in inner-outer rotation (a) when testing the cemented prosthesis and (b) cementless prosthesis.

(a)

(b)
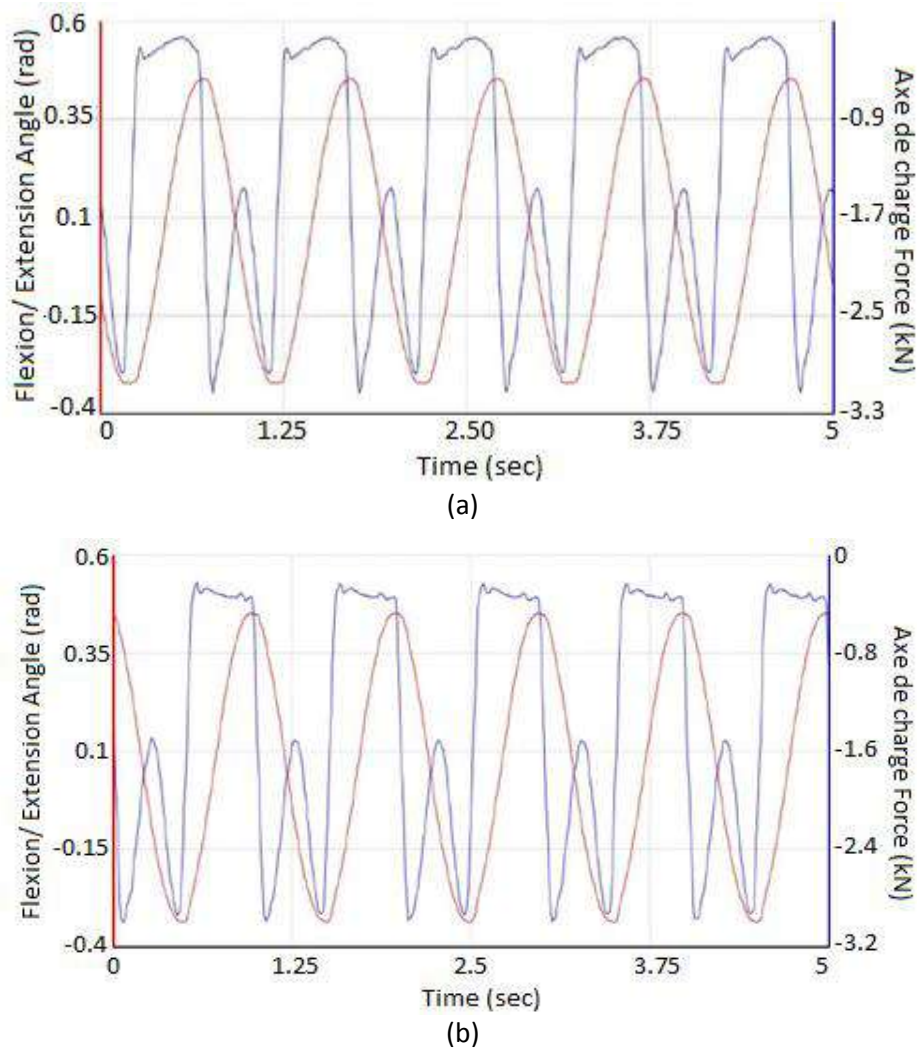
Figure 4. In time graph of the vertical contact force and angular displacement of the flexion-extension when testing the cemented prosthesis (a) and (b) a cementless prosthesis

(a)

(b)
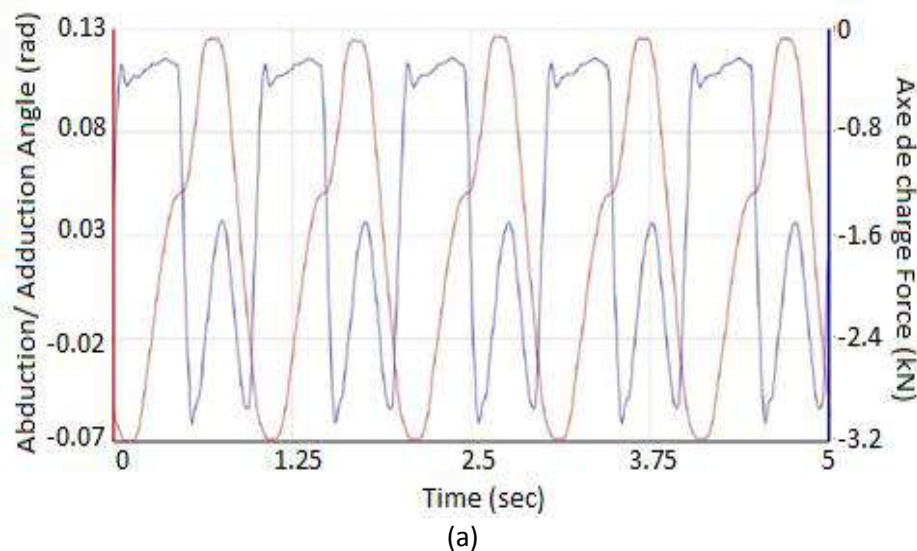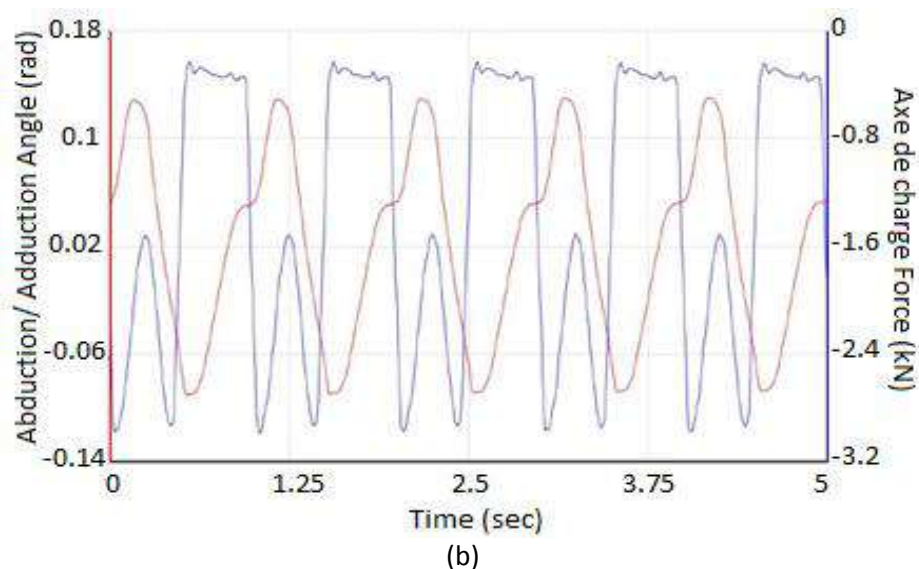
Figure 5. In time graph of the vertical contact force and angular displacement of abduction-adduction when testing (a) the cemented prosthesis and (b) a cementless prosthesis

(a)

(b)
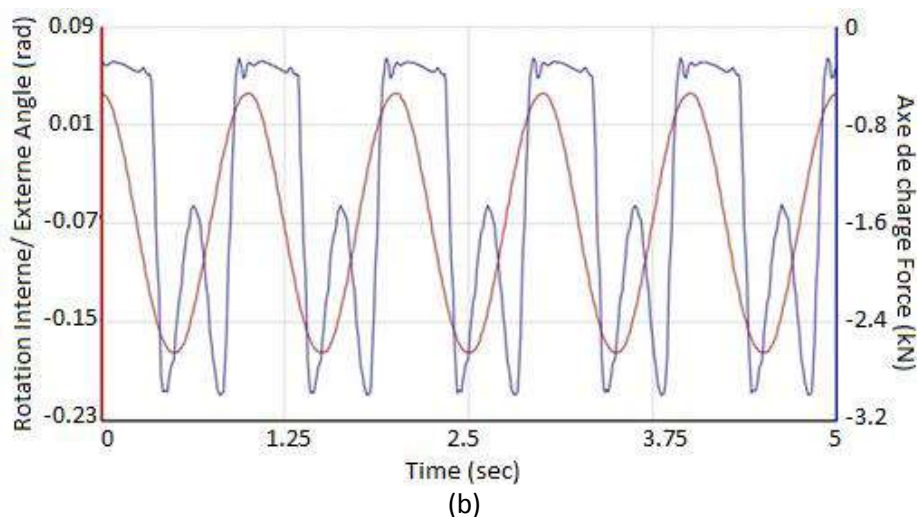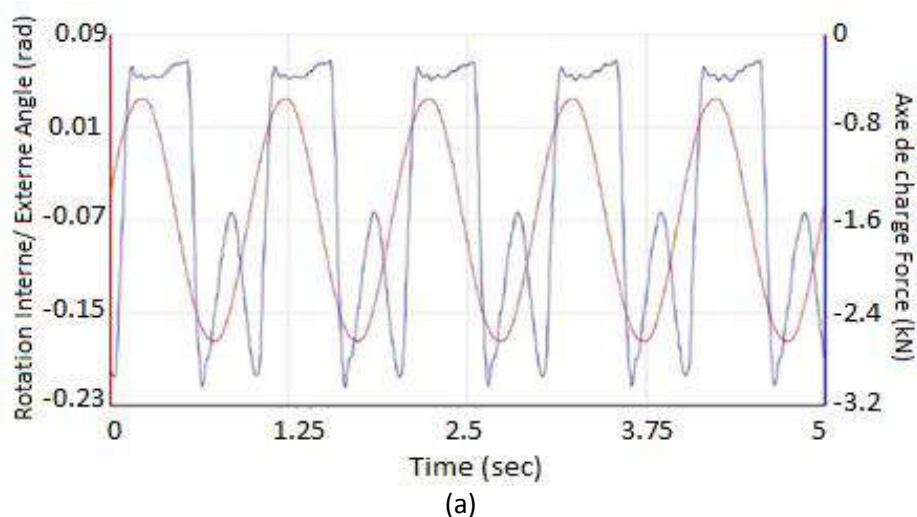
Figure 6. In time graph of the vertical contact force and angular displacement of inner-outer rotation when testing (a) the cemented prosthesis and (b) a cementless prosthesis

It can be seen as a function of time graph of the vertical contact force and angular displacement command-response when testing the cemented prosthesis and cementless prosthesis, is very similar for both AA, FE, IOR.

Representations of Figures 7 and 8 are very important because they show comparatively the in time variation graph of vertical contact force (blue) and in time variation graph of the friction torque (red) of cemented stem and cementless stem. These records were made at 2450000 cycles, when limits of the torque range became larger and more variable, showing that friction between the femoral head and the acetabular cup became bigger, obviously not due to wear, because the wear occurs after millions of cycles. To illustrate this, Figures 7 and 8 show three records for each stem.

Figure 7 presents the graph of the vertical contact force and the friction torque, for the cemented stem testing.

Figure 8 shows the graph of the vertical contact force and of the friction torque, at the cementless stem testing.
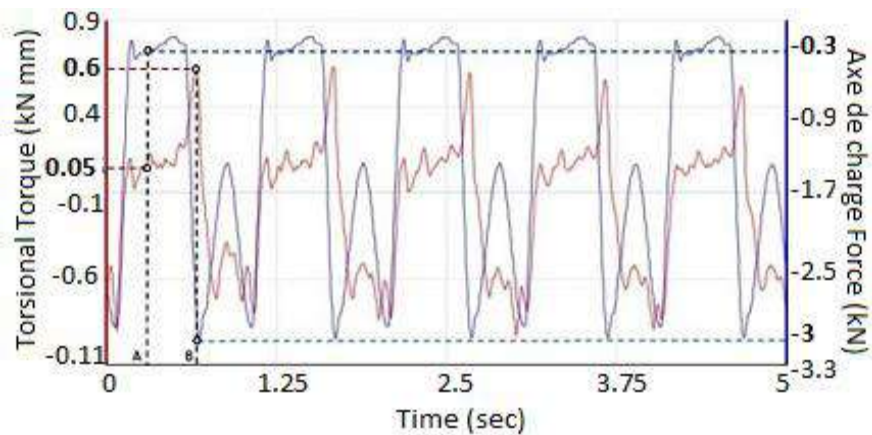
(a)
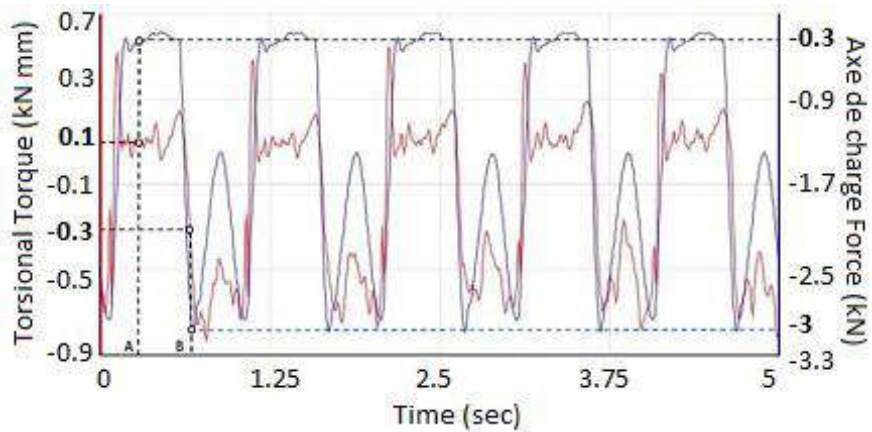
(b)
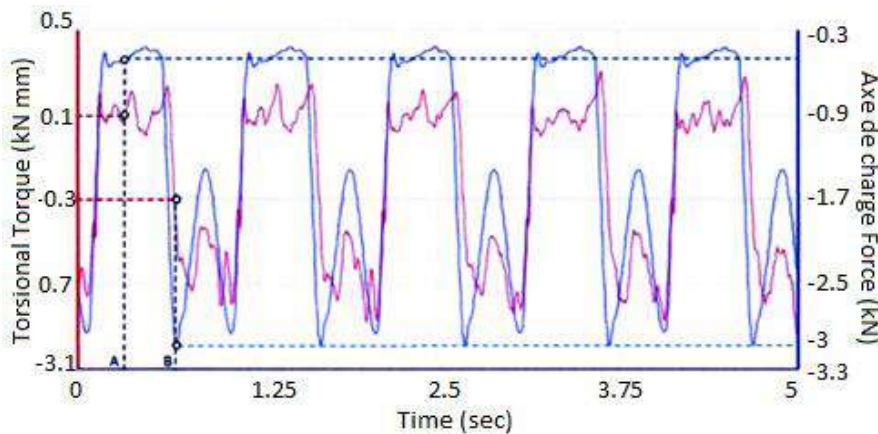
(c)

Figure 7. In time graph of vertical contact force (blue) and of the friction torque (red), at the cemented stem testing
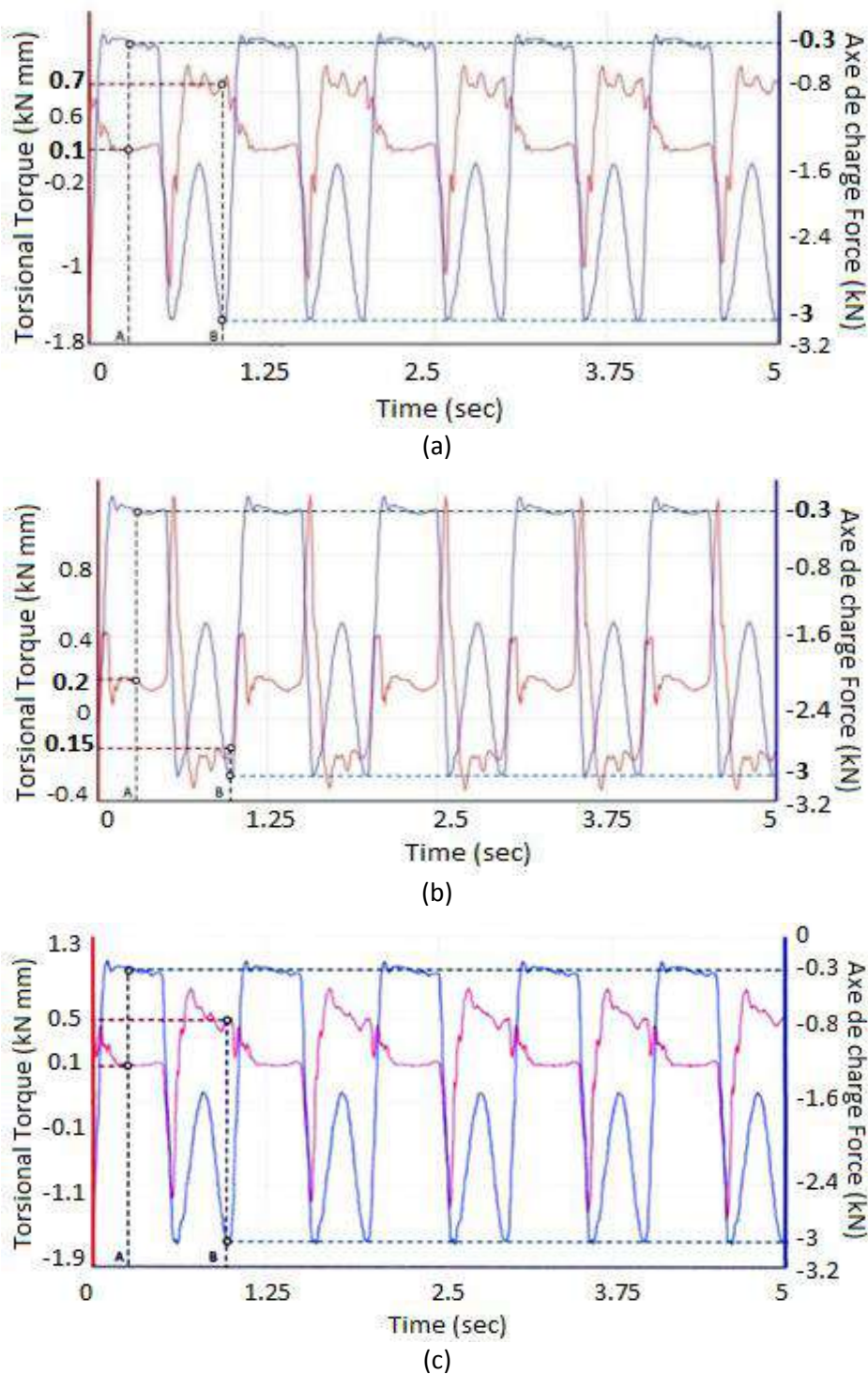
Figure 8. In time graph of vertical contact force (blue) and of the friction torque (red), at the cementless stem testing

In these graphs, the minimum and maximum values of the magnitudes variation represented can be observed. These values are marked on the x axis with A and B points.

The joint of the hip implant presented in Figure 1(b) is a spherical joint with 3 degrees of freedom, which represents the three rotations around the coordinate axes (ω_x, ω_y, ω_z) – Figure 9.

Translational constraints on the 3 coordinate axes are materializing by forces W_x, W_y, W_z. The friction moment in a spherical joint is given by the relationship:

$$M_f = \mu R W \qquad (1)$$

where: M_f is torsional moment of friction, μ is friction coefficient, R is the joint radius (in the case of the femoral head of 28 mm, R = 14 mm = 0.014 m), W is the resultant of forces W_x, W_y, W_z from joint (mean the normal contact force on the joint), whose values have been set to minimum 0.3 kN and maximum 3 kN.
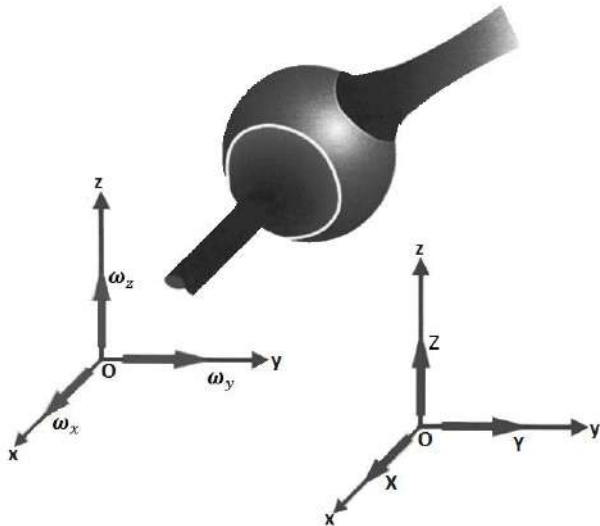
Figure 9. Degrees of freedom of rotation and translational movement restrictions imposed by the spherical joint in Figure 1(b)

On the basis of the presented graphs, Tables 7 and 8 summarize the values of friction torque recorded and of the calculated mean friction coefficient in testing of the cemented stem of the hip prosthesis, compared to cementless hip implant testing, at 2450000 cycles.

It appears that when testing the cemented stem the medium value of global friction coefficient (μ = 0.0147) is less than in the cementless implant (μ = 0.0253).

The relatively high difference between the maximum and minimum value of friction torque, and the visual observation of prosthesis functioning by transparent support fixing it, appeared to be a sign of the fretting wear manifestation. The testing was stopped when this difference occurred, at 2450000 cycles, and the prosthesis has been removed from Instron® device.

Stem prosthesis was easily extracted from the composite bone support, after some left-right movements, together with much of the PMMA cement mantle. Figure 10 shows images of both sides of the cemented stem prosthesis with a part of cement mantle, extracted after 2450000 cycles, from Instron® device.

Table 7. Values of friction torque and calculated friction coefficient for cemented stem

Graph	Point	W (kN)	M (kNmm)	μ
Fig. 7(a)	A	0.3	0.1	0.0238
	B	3	0.3	0.0072
Fig. 7(b)	A	0.3	0.05	0.0119
	B	3	0.6	0.0143
Fig. 7(c)	A	0.3	0.1	0.0238
	B	3	0.3	0.0072
Average value of the mean friction coefficient				0.0147

Table 8. Values of friction torque and calculated friction coefficient for cementless stem

Graph	Point	W (kN)	M (kNmm)	μ
Fig. 8(a)	A	0.3	0.1	0.0238
	B	3	0.7	0.0167
Fig. 8(b)	A	0.3	0.1	0.0238
	B	3	0.5	0.0119
Fig. 8(c)	A	0.3	0.1	0.0715
	B	3	0.5	0.036
Average value of the mean friction coefficient				0.0253

Figure 10. The sides of the cemented stem prosthesis together with a part of the cement mantle, extracted after 2450000 cycles of fatigue test, from Instron® device

PMMA cement mantle was carefully removed from the femoral stem to preserve as much as possible its integrity. The stem and PMMA mantle were separately optically inspected and photographed.

Obvious corrosion of the femoral stem surface beneath the cement mantle, and reddish Fe_2O_3 deposits on the femoral stem surface and, by transfer, on the inner part of the PMMA mantle were observed. These are due to fretting corrosion.

In Figure 11 are shown photographic images of contact sides of the Ti6Al4V femoral stem and of the PMMA mantle, after fretting experiment.

(a)   (b)
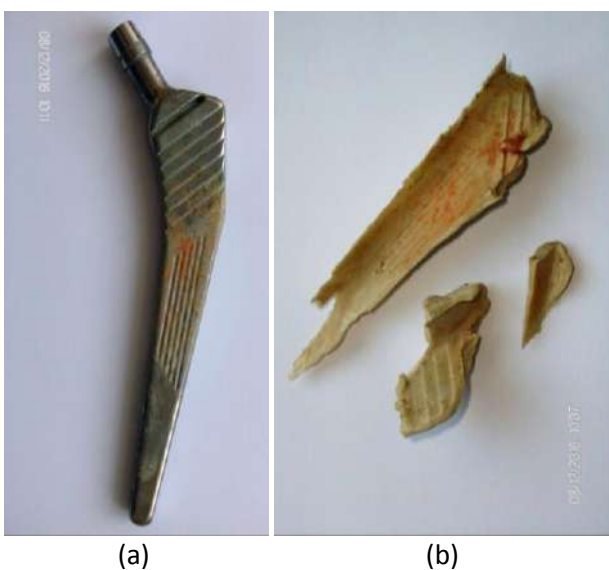
Figure 11. Contact sides appearance of cemented stem (a) and cement mantle (b), extracted after 2450000 cycles of fatigue test, from Instron® device

The recovered Ti6Al4V stem and interior cement mantle were further inspected by optical microscopy, hoping to identify specific cracks of fretting fatigue. The inspection proved to be very difficult due to the shape with grooves of the femoral stem and in replica, of the inner surface of the PMMA mantle. In this situation it could not be used only a Mini Handheld Digital Microscope CELESTON® #44302, with 15-30x magnification. Despite these difficult conditions, very interesting images (Figure 12) of the femoral stem surface after fretting experiment were recorded. They emphasize the existence of some obvious cracks on the stem surface – Figure 12(a) and of a PMMA thin interface on the stem surface – Figure 12(b).

(a)   (b)
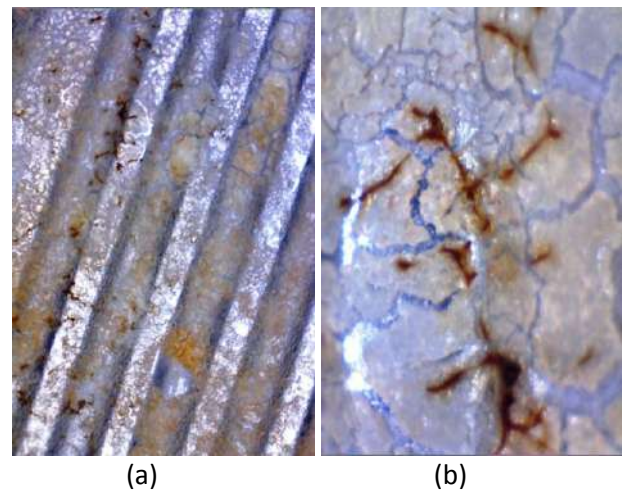
Figure 12. (a) Optical image of the femoral stem surface after fretting experiment and (b) an x30 image of a core of fretting corrosion cracks

(a)   (b)
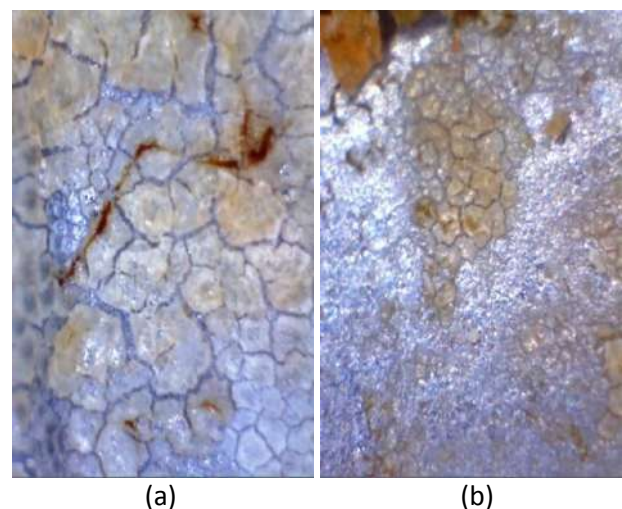
Figure 13. Microscopic images (x30) of the stem – cement mantle interface after the fretting fatigue test

The interface seems to have acted as a replica film, which shows the cracks that appear to be due to internal forces induced by fretting in the stem material. Fretting stress imposes to a localized volume under the surface, very complex and non-proportional triaxial fatigue stresses. Images in Figures 13 indicate that the prone gradient of the fretting effort allows the crack to propagate to the surface, slowing or stopping its spread in depth.

Also, Figure 12(b) and Figure 13 suggest that growth of fretting cracks seems to be trans-granular and this observation suggests that cracks growth can be influenced by the crystallographic structure of the stem's material. This observation is consistent with studies of D. B. Garcia and A. F. Grandt Jr. [12].

4. CONCLUSION

Fretting behaviour of the cemented femoral stem fixation of a Ti6Al4V/ UHMWPE total hip prosthesis was studied, trying to capture the loss of contact between the femoral stem made of Ti6Al4V alloy and PMMA cement fixation. To have a landmark, the studies were performed comparatively with cementless fixation, where no fretting phenomenon occurs. The study was done on real prostheses, under biological 3D loading and motion conditions.

It was used a Instron$^®$ device for fatigue testing of the femoral stem cemented fixation of the total hip prosthesis, installed on a MTS Bionix servo-hydraulic triaxial dynamic testing machine. It allowed both monitoring the flexion-extension, abduction-adduction and inner-outer rotation movements, and the variation of the torsional torque, depending on normal loading.

Ti6Al4V alloy was immersed in a solution having a high concentration of NaCl (~ 0.2 M) at a temperature of 38 ^{0}C.

Because of the significant difference in mechanical properties (Young's modulus, with a ratio of 90 between Ti6Al4V and PMMA) shielding stress occurs. This physical phenomenon can be explained by the fact that the metallic material and polymer do not present the same deformation under the applied stress, leading to unsoldering between the metal and cement. Therefore, the adhesion between metal and polymer loses after a short period. This unsoldering involves the fretting and subsequent friction between materials in contact. Thereafter, Ti6Al4V and the bone cement are subjected to small displacements, friction loadings in a corrosive environment, resulting in fretting corrosion. Consequently, the wear between the bone cement and Ti6Al4V alloy occurs, involving the generation of debris.

After the failure of stem fixation of cemented prosthesis at 2450000 cycles, it was visually inspected, photographic records were made, whereupon the mantle of bone cement remaining adherent on the femoral stem was removed. Visual and microscopic inspection of the femoral stem and of the inner part of the PMMA mantle demonstrated the existence of obvious corrosion of the femoral stem surface beneath the cement mantle, Fe_2O_3 deposits on the femoral stem surface and on the inner part of the PMMA mantle.

REFERENCES

[1] M. Buciumeanu, I. Crudu, L. Palaghian, A.S. Miranda, F.S. Silva, Influence of wear damage on the fretting fatigue life prediction of an Al7175 alloy, International Journal of Fatigue, Vol. 31, pp. 1278–1285, 2009.

[2] K. Kim, J. Geringer, J. Pellier, D.D. Macdonald, Fretting corrosion damage of total hip prosthesis, Friction coefficient and damage rate constant approach, Tribology International, Vol. 60, pp. 10-18, 2013.

[3] H. Gelb, H.R. Schumacher, J. Cuckler, P. Ducheyne, D.G. Baker, In vivo inflammatory response to polymethylmethacrylate particulate debris: effect of size, morphology, and surface area, Journal of Orthopaedic Research, Vol. 12, pp. 83-92, 1994.

[4] J. Geringer, B. Forest, P. Combrade, Fretting-corrosion of materials used as orthopaedic implants, Wear, Vol. 259, pp. 943-951, 2005.

[5] J. Geringer, D.D. Macdonald, Modelling fretting-corrosion wear of 316L SS against poly(methylmethacrylate) with the Point

Defect Model, Fundamental theory, assessment, and outlook, Electrochimica Acta, Vol. 79, pp. 17-30, 2012.

[6] N.A. Bhatti, M. Abdel Wahab, A review on fretting fatigue crack initiation criteria, International Journal of Fracture Fatigue and Wear, in: *Proceedings of the 5th International Conference on Fracture Fatigue and Wear*, 24-26.08.2016, Kitakyushu, Japan, pp. 78-85.

[7] J. Geringer, J. Pellier, M.L. Taylor, D.D. Macdonald, Fretting corrosion with proteins, The role of organic coating on the synergistic mechanisms, Thin Solid Films, Vol. 528, pp. 123-129, 2013.

[8] H.A. Fadag, S. Mall, V.K. Jain, A finite element analysis of fretting fatigue crack growth behavior in Ti–6Al–4V, Engineering Failure Analysis, Vol. 12, pp. 537-548, 2005.

[9] A.E. Giannakopoulos, T.C. Lindley, S. Suresh, C. Chenut: Similarities of stress concentrations in contact at round punches and fatigue at notches: implications to fretting fatigue crack initiation, Fatigue & Fracture of Engineering Materials & Structures, Vol. 23, pp. 561-571, 2000.

[10] M. Nesládek, M. Španiel, J. Jurenka, J. Růžička, J. Kuželka, Fretting fatigue experimental and numerical approaches, International Journal of Fatigue, Vol. 44, pp. 61-73, 2012.

[11] V. Florescu, L. Capitanu, L.L. Badita, V. Filip, A Novel Engineering Spherical Bearing, with Potential Application for a Hip Implant, Journal of Mechanics Engineering and Automation, Vol. 6, pp. 217-226, 2016.

[12] D.B. Garcia, A.F. Grandt Jr., Fractographic investigation of fretting fatigue cracks in Ti–6Al–4V, Engineering Failure Analysis, Vol. 12, pp. 537-548, 2005.

BIOMECHANIC AND TRIBOLOGY IN HUMAN WALKING

Milan NIKOLIĆ [1],*, Dušan STAMENKOVIĆ [1], Milan BANIĆ[1], Aleksandar MILTENOVIĆ [1]
[1]Faculty of Mechanical Engineering Niš ,Serbia
*Corresponding author: milan.nikolic.nis@gmail

Abstract: *Biomechanics of human walking has a lot of applications in science, sport, medicine and everyday life. It is very useful to know which forces exist and how they act between human body (foots, knees, hips, muscles) and ground (floors, walkways, sport terrains). Friction in contact between shoe sole and floor is necessarz for human walking. Friction force has variable influence on human body and it depends on floor surface, kinematics of human walking, shoes sole etc. Some floor conditions need the human walking with shorter steps, lower speed, shoes with special sole tread etc. According to floor surface, shoes sole materials and their conditions man should adapt step length and angle reaching between legs and ground for specific case. This paper presents some of the research in that manner.*

Keywords: *biomechanics, human walking, friction, footwear, floor, slip resistance.*

1. INTRODUCTION

Research on biomechanics of human locomotion have a wide range of applications in medicine, sports, ergonomics, science, etc. These studies are refered to forces acting between the earth and the human body. These forces can be recorded by measuring or can be determined using a simulation computer model. In this way, one can determine the joint reaction forces, torque in the joints (hips, knees, ankles) and friction forces.

2. THE LOAD OF THE HUMAN BODY IN WALKING CONDITION

In standing condition, on human body is subjected to force usually called normal force. It is ground reaction force and it acts in vertical direction.

When human starts to walk or run, more forces occur. One of them is an friction force which is necessary for walking/running.
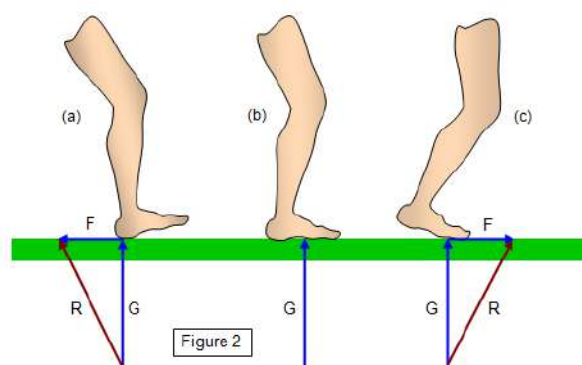
Figure 1. Ground reaction forces [1]

The vertical force is marked with *G* and friction force marked with F (Figure 1). Force shown with *G* is smaller then force while standing. Vertical force in standing condition is less than force G (while walking or running) because standing force has to balance only the human weight. In walking or running condition

force G is 1.5 up to 2.9 times greater than force in standing condition [1].

Friction force *F* acts opposite to the direction of movement, which means that foot is pushing forward in start of stance phase. At the end of step, that is in swing phase, foot pushing backwards and friction force acts in the direction of movement. In both cases, friction force prevents slipping.

In the human running, increase of speed, stride length and frequency of movement of the legs is greater than in walking. Both legs rotate as someone runs and the centre of gravity of the body also moves up and down for a few cm during the each step in both conditions, walking and running.

Shoes should provide better friction characteristics in contact with floor and absorb these forces.

3. HUMAN WALKING PHASES

In biomechanics one can notice the following division of moving: translation and rotation.

Also, moving can be divided to basic movement and combined movement. Another important movement types are cyclic and noncyclical movement. Typical cyclic movement are walking and running.
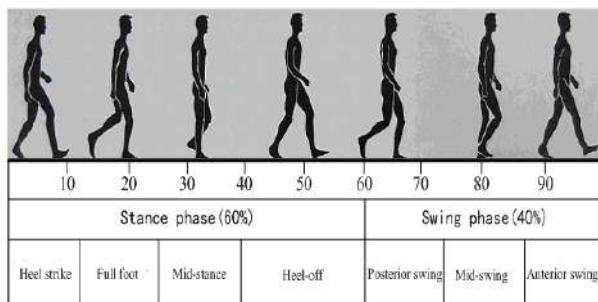
Figure 2. Human walking phases

If the walking of one leg is observed, the following phases are indentified: stance and swing. In the phase of stance, foot is on the ground and gives support to the body (Figure 2). In the swing phase foot is in the air.

Every phase has two periods: 1a period of front stance, 1b period of back stance, 2a period of back swing and 2b period of front swing. If the walk cycle is observed from the

top plane, one can see that walk have length and width (Figure 3)[2].
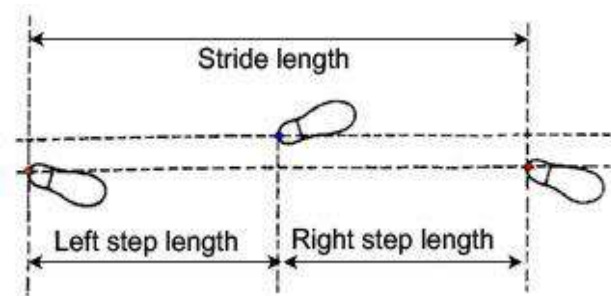
Figure 3. Length and width of step [2]

Tables 1 and 2 show average values of step parameters (time and space). These values are obtained with measuring in special laboratories for kinematic research of walking [2].

Table 1. Average values of step time parameters [2]

Time parameters	Average values
Cycle time (ms)	900
Stance phase (%cycle)	59
Swing phase (%cycle)	41
Frequency (steps/min)	134

Table 1. Average values of step space parameters[2]

Space parameters	Average values
Step length (mm)	530
Two step length (mm)	1060
Step width (mm)	110
Speed (m/s)	1.17
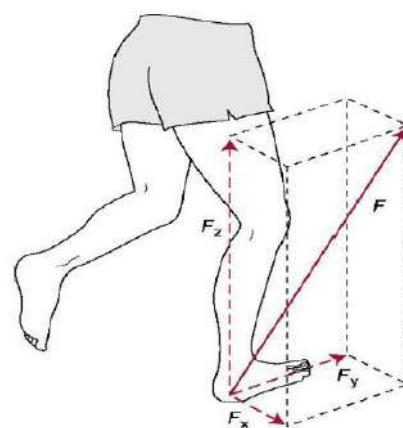
Figure 4. Reaction forces and components [2]

Beside kinematic analysis, for fundamental study of human walking the kinetic analysis is also necessary. Kinetic analysis gives the values of forces and moments which act on the human body and inverse (on the ground).

Reaction force acts with same intensity in opposite direction relative to the force which acts on the ground by human (Figure 4).

Vertical force component *Fz* rises rapidly when heel strike the ground (to 120% of body mass). When foot is on the ground with whole surface, the reaction force falls to 80% of body mass and raises again in phase of back stance. When foot leaves the ground the reaction force falls to zero because there is no contact between foot and ground. *Fy* force component acts backward during phase of front stance (opposite of movement direction) and this force decrease body speed. When whole foot is on the ground, force *Fz* decreases and raises again during start phase of back stance and then acts in the movement direction and increases body speed. In straight line walking force *Fx* can be eliminated because its value is only 10% of body mass [2].

4. SPEED INFLUENCE ON KINEMATIC AND KINETIC OF WALKING

In walking process, phase stance is longer than phase of swing and when one leg is on the ground other is in the air. In human running, speed increases and in one part of step both legs can be without contact with the ground. When speed increases in walking, there are changes in kinematic and kinetic characteristics. Phase of stance is shorter and when falls below 50% it means that running is started. Speed change in walking and in running is possible in two ways: frequency increase and step length increase. Measuring data shows that frequency and step length increase proportionally [2].

Figure 5 shows the changes of the step length depending on the speed.

This means that speed of walking is changing proportionally with changing of step frequency and length.

With speed increase there is a change in rotation angles in hips, knees, ankles and pelvis. Amplitudes of angles are greater and walking cycle is shorter. If movement is shorter, angle, speeds and accelerations in every joint is greater.
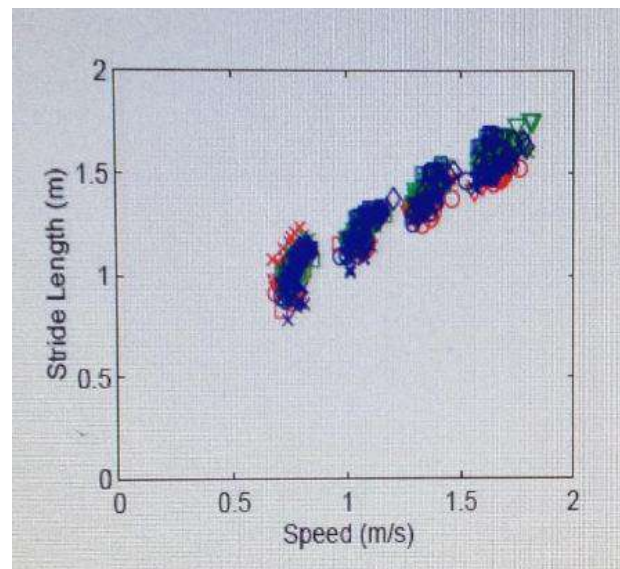
Figure 5. Step frequency depend on speed [2]

Speed change has influence not only on kinematic but also on kinetic, ie dynamic in walking. Ground reaction forces are greater, especially vertical *Fz.* With speed increasing, phase of stance is shorter, speed increase and forces are greater.
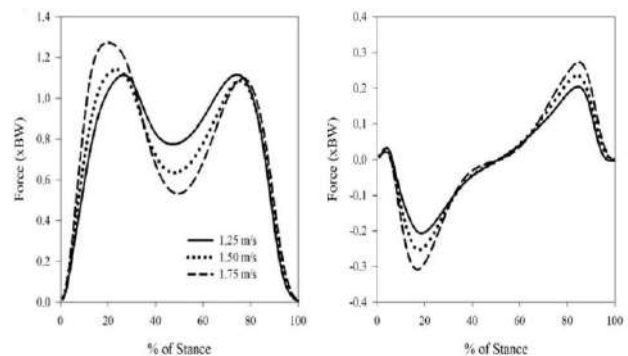

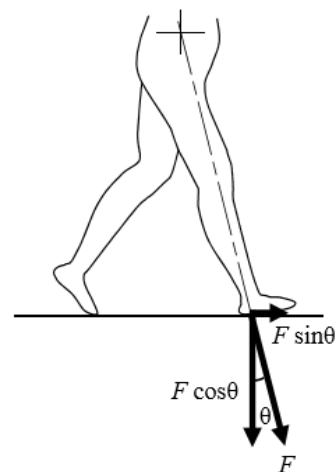**Figure 6.** Reaction forces *Fz* and *Fy* in stance phase [2]

Figure 7. Force components between leg and ground

Friction force has to be always greater than horizontal component **Fy** in order to prevent slips and falls. Relationship between friction coefficient and angle is expressed as **μ≥tan θ** (**θ** is angle between leg axis and vertical line as shown in Figure 7) [5]. With smaller friction coefficient θ angle have to be smaller, which means that human have to walk with shorter steps.

For example, if friction coefficient between shoes and ice is 0.18; safe angle of walking is less than 10 degrees. If human leg is one meter in length, than safe step length should be about 0,35 m . Angles of joint rotation are also smaller in that situation. That's explanation why some animals, like penguins or other, walk with very short steps on ice and slippery surfaces. If friction coefficient is 0,6 (shoes on wet concrete), safe angle of walking is bigger, about 30 degrees. In that case, steps can be longer (about 1.1 m).

5. EXPERIMENTAL RESEARCH OF FRICTION COEFFICIENT

The determination of the friction coefficient was performed on a test stand specially designed for that purpose. The asynchronous motor drives the screw shaft which rotation moves the ball screw nut along the shaft, together with plate which carries the force transducer. The plate is supported on the opposite end by a linear ball bearing which moves along the linear guide. The force transducer pulls the 11 kg slider which carries the sole samples and moves across the floor sample. The motor rpm is precisely controlled in a feedback loop by a frequency inverter connected to incremental encoder which measures the motor rpm. The HBM S2 (100 N) force transducer is connected to a 24-bit NI cDAQ acquisition device which samples the force data at 50 Hz rate. Scheme of measuring equipment is present on Figure 8.

The described setup enables the measurement of friction force which resists the slider motion across the floor sample at different sliding speeds, as well as determination of static friction force which can

be determined when the slider is pulled from a stand still position. The sole and floor samples are easily changeable and the setup enables the measurement of friction force in dry and lubricated conditions. 3 D model of test equipment is presented on Figure 9 and fhoto on Figure 10 .
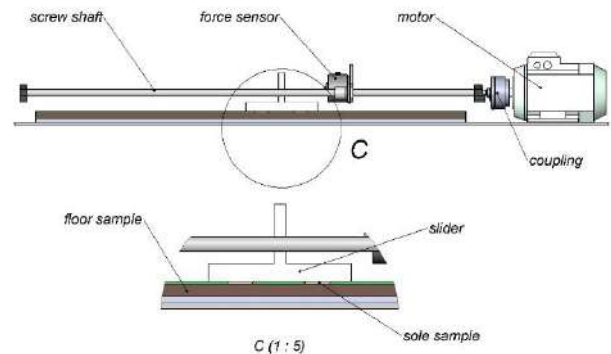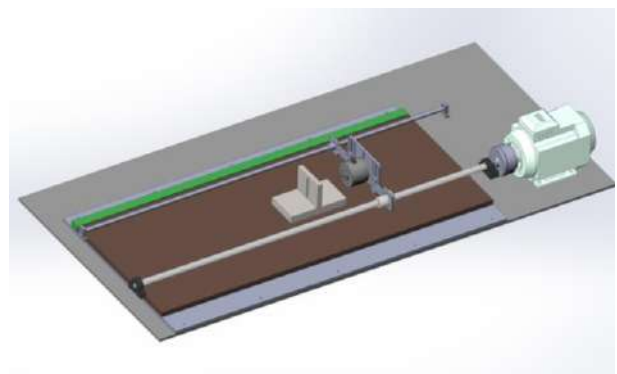

Figure 8. Scheme of measuring equipment

Figure 9. Measuring equipment 3d model

Figure 10. Measuring equipment

Dimensions of shoes rubber and leather testing samples were 10 x 40 mm with 6 mm height. Samples were cut from shoe soles. Floor samples were plates of laminate, ceramic tiles and vinyl. Sliding distance was 500-800 mm and velocities 2, 10, 50 and 250 mm/s were used in the experimental

investigation. Samples was prepared with sand paper and cleaned.

There was a lot of measuring data, different combination of soles and floors samples, condition (dry and wet) with repetitions. Figures 11 and 12 show recorded friction forces for two combinations (leather sole-laminate and rubber sole-ceramic tile). In both cases the measurements were performed in lubricated with water (wet conditions). In first case, static friction force raises over 100 N and than falls to kinetic force of 70 N.
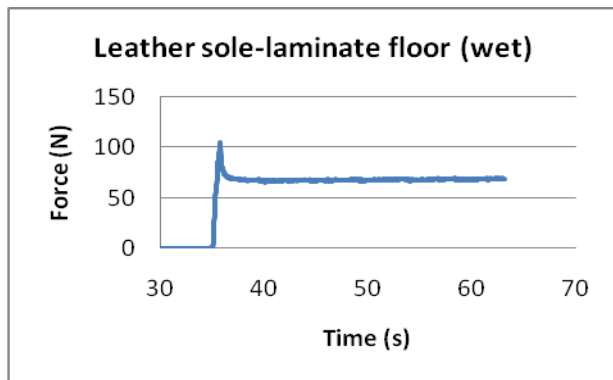

Figure 11. Friction force for leather sole and laminate floor (wet)
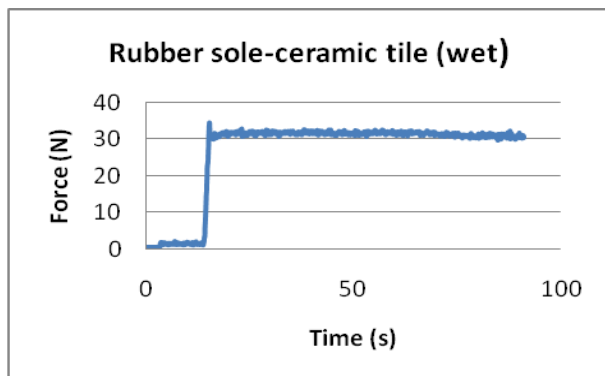
Figure 12. Friction force for rubber sole and ceramic tile (wet)
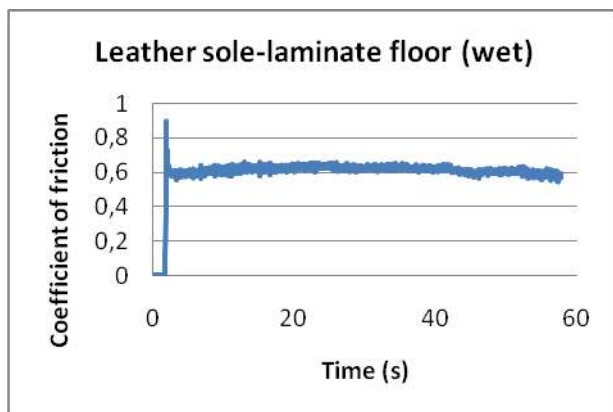
Figure 13. Static and kinetic friction coefficient for leather sole and laminate floor (wet)

For example with rubber sole and ceramic tile (wet conditions) static friction force raises up to 35 N and falls to kinetic friction force to 30-32N. One can see that difference between static and kinetic friction force is a lot higher in the first case.

Figure 13 shows friction coefficient in sliding between leather sole and laminate floor for wet conditions. Static friction coefficient raises up to 0,9 and than falls to kinetic coefficient of about 0,6.

Table 1. Average values of friction coefficient for leather and different floor coverings (dry and wet)

Leather sole-Laminate (dry)	μ_s	0,471914
Leather sole-Laminate (dry)	μ_k	0,268844
Leather sole-Laminate (wet)	μ_s	0,809646
Leather sole-Laminate (wet)	μ_k	0,43255
Leather sole - Ceramic tile (dry)	μ_s	0,340006
Leather sole- Ceramic tile (dry)	μ_k	0,244691
Leather sole- Ceramic tile (wet)	μ_s	0,63023
Leather sole- Ceramic tile (wet)	μ_k	0,408559
Leather sole-Vinyl (dry)	μ_s	0,687502
Leather sole-Vinyl (dry)	μ_k	0,277747
Leather sole-Vinyl (wet)	μ_s	0,823977
Leather sole-Vinyl (wet)	μ_k	0,502125

The Table 1 gives an overview of fricton coefficient values for leather sole samples in different experimental cases. One can see that there is a wide range of friction coefficient values for same sole material and different floors, as well as for dry/wet conditions. Lowest average static coefficient value is for ceramic tile on dry 0,34 and the biggest for vinyl on wet 0,82. The same case is for kinetic friction coefficient with values 0,24 and 0,50.

6. CONCLUSION

It is very important to know biomechanics of human walking for better understanding and research on friction between shoes and floors. With biomechanics one can understand how forces act on body (hips, knees, ankles) and reverse. There are a lot of parameters which have influence on friction force: speed of walking, leg angles, body mass, step length, frequency etc. With better knowing of this parameters, one can make better and more

precise model for investigation of friction between shoes and sole.

Measuring data show that for the same shoe sample there are a wide range of friction coefficients values for different floors and conditions. That means there are no unique materials of sole for all floor surfaces and all conditions. According presented research, one aspect for slip and fall prevention can be to warn humans to walk with shorter steps, less speed or lower frequency with different enviromental situations. Humans already do that unconsciously, but maybe it is good to make some warnings (not only wet floor, or slippery cautions) for walking on risky floors.

REFERENCES

[1] http://www.schoolphysics.co.uk/age16-19/Medical%20physics/text/Walking_/index.html

[2] V. Mrdaković: *Biomehanic analysis of walking*, Faculty of sport and physical education, Belgrade, Belgdare, 2013.

[3] M. Nikolić, D. Stamenković, M. Milošević, M.Banić: Tribology in human walking, in: *14th International Conference on Tribology – SERBIATRIB,*13-15.05.2015, Beograd, Serbia, p.p. 543-548.

[4] http://www.utdallas.edu/atec/midori/Handouts/walkingGraphs.htm

[5] K. Mabuchi, K. Tanaka, D. Uchijima, R. Sakai: Frictional Coefficient under Banana Skin, Tribology on line, Vol.7, No. 3, 2012, 147-151.

[6] DIN 51131 Testing of floor coverings - Determination of the anti-slip property - Method for measurement of the sliding friction coefficient, 2014.

ELECTROLESS NI–B COATING OF PURE TITANIUM SURFACE FOR ENHANCED TRIBOCORROSION PERFORMANCE IN ARTIFICIAL SALIVA AND ANTIBACTERIAL ACTIVITY

Ferda MINDIVAN[1,a], Cihan DARCAN[2,a], Harun MINDIVAN[3,a,*]

[1]Department of Technical Programs, Bozuyuk Vocational College, Bilecik Seyh Edebali University, Bilecik, Turkey

[2]Department of Molecular Biology and Genetics, Faculty of Arts and Science, Bilecik Seyh Edebali University, Bilecik, Turkey

[3]Department of Mechanical and Manufacturing Engineering, Engineering Faculty, Bilecik Seyh Edebali University, Bilecik, Turkey

[a]Biotechnology Application and Research Center, Bilecik Seyh Edebali University, Bilecik, Turkey

*Corresponding author: harun.mindivan@bilecik.edu.tr

Abstract: In the present study, the surface of commercial pure (Grade 2) titanium was coated with electroless Ni–B. The surface morphology, microstructure and phase identification were analysed by X-Ray Diffraction (XRD) and Field Emission Gun Scanning Electron Microscope (FEG-SEM) equipped with Energy Dispersive X-ray Spectroscopy (EDS). The tribocorrosion performance in a laboratory simulated artificial saliva was investigated using a reciprocating ball-on-plate tribometer coupled to an electrochemical cell. The antibacterial property of the electroless Ni–B film coated on pure titanium was basically investigated. From this study, it may be concluded that this electroless Ni–B coating process cannot only improve the hardness and tribocorrosion performance of the pure titanium, but can also provide antimicrobial activity.

Keywords: Antibacterial, electroless Ni-B coating, titanium alloy, triborocorrosion.

1. INTRODUCTION

Titanium (Ti) and its alloys have become one of the most attractive biomaterials thanks to their remarkable mechanical and corrosion resistance properties, as well as biocompatibility. However, the formation of a bacterial surface biofilm, compromised immunity at the implant/tissue interface and poor tribological performance may lead to persistent infections on and around corrosion resistant Ti biomaterials used in corrosive environments [1, 2]. Thus, numerous strategies focusing on the surface modification

of Ti alloys have been employed to render them protection from both wear, corrosion and even tribocorrosion [3 - 5]. The strategies include physical vapour deposition [6], thermal spray [6, 7], ion or laser nitriding [8 - 10], thermal oxidation [11, 12], micro-arc oxidation [13 - 15], diffusion [16] and anodic oxidation treatments [17]. On the other hand, the antibacterial properties are also necessary for Ti implant when exposed to the living tissue [18]. To add biofunction to Ti alloys, a process that changes a material's surface composition, structure, and morphology, leaving the bulk mechanical properties intact is necessary.

Antimicrobial, hard, wear and corrosion resistant surfaces reduce infection complications to prolong the useful life of dental and orthopedic implant materials. By doing so, surface engineered Ti implants could be able to withstand corrosive environment while simultaneously offering an improved wear protection and antibacterial activity. To achieve the desired results, electroless Ni-B coatings are good candidates to use in a variety of industrial applications for the following reasons: their unique properties, such as high hardness, low wear, lubricity, uniform thickness, good ductility, excellent solderability and antibacterial activity [19]. The aim of the present study is to investigate the effect of electroless Ni–B coating on the structural, tribocorrosion and antibacterial properties of commercial pure Ti (CP-Ti), which has not been reported yet.

2. EXPERIMENTAL METHODS

The CP-Ti (Grade 2) having a dimension of $20 \times 20 \times 1$ mm^3 was used as the substrate material. Before deposition, the surface of the CP-Ti samples was degreased with acetone, and rinsed with distilled water, and picked in 6 % HF for ~1 min at room temperature and then washed thoroughly with distilled water and dried in air. The chemical composition and operation conditions of the electroless Ni-B solution are reported in Table 1.

Table 1. Bath composition and operation conditions.

Composition	Ni-B
Nickel chloride	20 g L^{-1}
Sodium hydroxide	90 g L^{-1}
Sodium borohydride	1 g L^{-1}
Tallium nitrate	0.11 g L^{-1}
Ethylendiamine	100 ml L^{-1}
Bath temperature	90 °C
pH of solution	> 12

The surface and cross-section morphologies of the Ni-B coated CP-Ti were examined by Field Emission Gun Scanning Electron Microscope (FEG-SEM) equipped with Energy Dispersive X-ray Spectroscopy (EDS) and Nikon

Eclipse LV150 Light Optic Microscope (LOM), respectively. The phase constituents of the untreated CP-Ti and the Ni-B coated CP-Ti were determined by X-ray diffraction (XRD) using CuK$_\alpha$ radiation with a Panalytical Empyrean diffractometer. The cross-sectional hardness measurement was accomplished using Knoop diamond indentation under a 10 g load for a period of 15 seconds. The obtained results were the average of five measurements.

Tribocorrosion experiments were conducted in a triboelectrochemical cell containing 25 ml of simulated artificial saliva (SAS) installed on a linear reciprocating ball-on-flat tribometer with the working surface of the testing samples facing upwards against the counter material (10 mm diameter Al$_2$O$_3$ ball). Reciprocating sliding tests were carried out under Open Circuit Potential (OCP) conditions. OCP was monitored before, during and after reciprocation sliding contact with the Al$_2$O$_3$ ball. A potentiostat was used to record the potential between the testing sample and the reference electrode during tribocorrosion tests. The tribocorrosion tests consisted of the three steps: (1) stabilization of the system under the OCP for 600 s (in absence of sliding) to achieve a stable passive surface; (2) sliding under the OCP for 2700 s; (3) re-stabilization of the system under OCP (after sliding was stopped) for 600 s. The sliding started in a reciprocating system with total stroke length of 10 mm, sliding speed of 1.7 cm s^{-1}, normal load of 5 N and total sliding distance of 50 m. During the test, sample surface with an area of 1.5 cm^2 was exposed to the corrosive electrolyte. After tribocorrosion tests, the wear scars and Al$_2$O$_3$ balls were cleaned following the same cleaning procedure applied before testing and the contact surfaces of wear scars and Al$_2$O$_3$ balls were examined by SEM and LOM, respectively. Total material loss rates were determined by measuring the 2-D cross-sectional area profile of the wear scars (in three locations) by using a contact profilometer (Mitutoyo Surtest SJ-400) and converting this to a wear volume by taking account of the scar length. By the end of the OCP tribocorrosion tests, optical densities of SAS solution were measured using a UV-Spectrophotometer.

Freshly prepared SAS was analysed as the reference to evaluate the optical densities of solutions. After the spectrophotometric measurement of freshly prepared SAS solution by using fix visible light (wave length: 250 nm), the data obtained was automatically adjusted to zero in order to determine the optical densities of the SAS solutions utilized in the OCP tribocorrosion tests.

The antibacterial activity of electroless Ni–B coating on a CP-Ti substrate was determined using *Escherichia coli* O157:H7 (*E. coli*, Gram negative) by a disc diffusion method on nutrient agar medium. The untreated CP-Ti was used as a control. Bacterial suspensions (10^8 colony forming units/mL final cell concentrations) were poured into Petri dishes (9 cm) from flasks containing 25 mL sterile nutrient agar. Then the bacteria were evenly distributed over agar surface by a sterile bent. In this way, the large part of the bacteria was on the growth medium for cultivation. The inoculated plates were incubated aerobically at 37 °C for *E. coli* for 24 h, and then testing results were assessed. By measuring the diameter of the circular shape around the samples, which is inhibition halo (technically known as a ''plaque'', or zone of inhibition), provided information about the sensitivity or resistance of the cultivated microorganism to the biocide coating. All of the tests were done in triplicates.

3. RESULTS AND DISCUSSION

Figure 1 a, b displays the morphological and cross-sectional micrographs of the deposited electroless Ni–B coating on the CP-Ti substrate, respectively. The result of Fig. 1 a, b signs a columnar morphology without porosity and cracks, with a typical cauliflower-like surface texture. In fact this kind of surface morphology is responsible for the lubricious characteristics of the Ni-B coatings [19, 20]. It is evident that a deposit close to 15 µm is achieved at the CP-Ti substrate surface and the nickel agglomerates are distributed randomly in it. As is obvious in this figure, a desirable adhesion was established between the Ni-B coating and CP-Ti substrate.
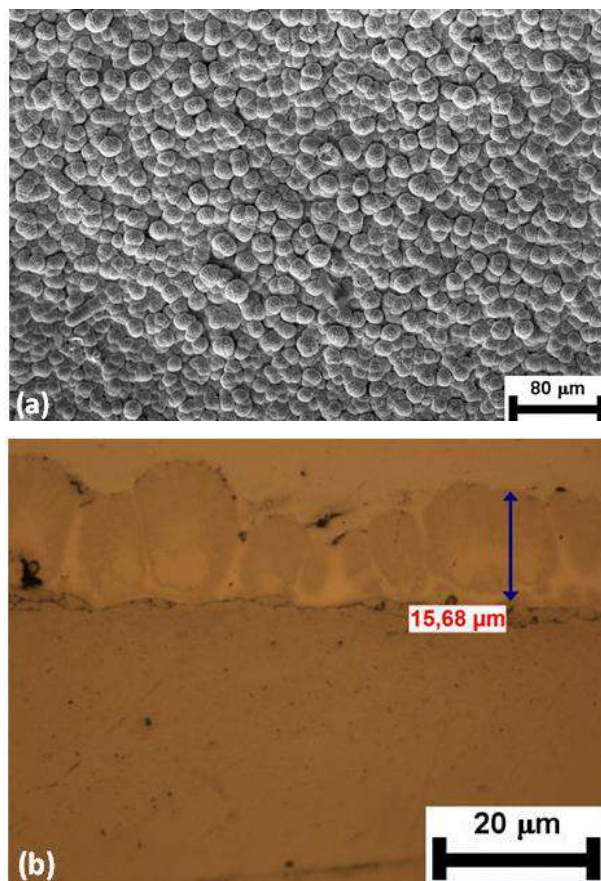
Figure 1. (a) Morphological and (b) cross-sectional micrographs of the electroless Ni–B coating.
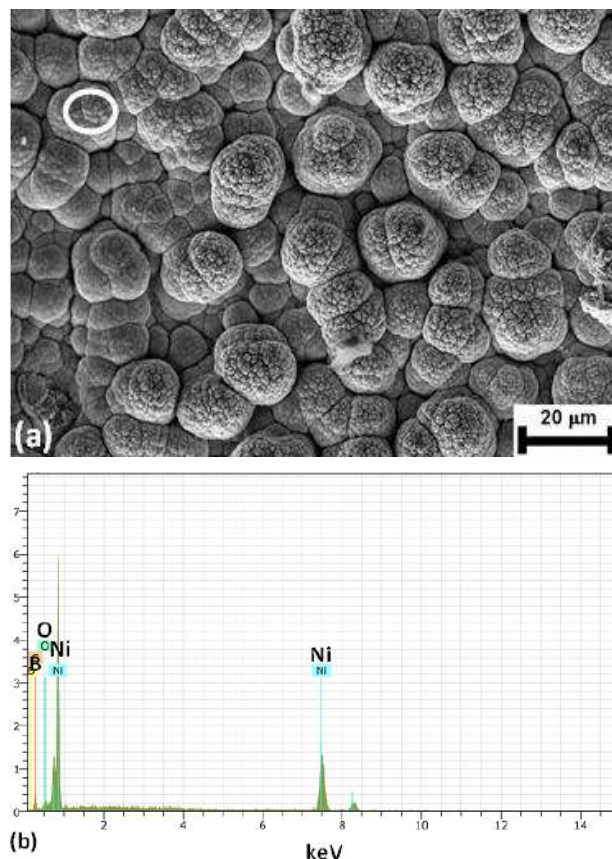
Figure 2. EDS spectra and analysis results.

Figure 2 shows the EDS spectra of the Ni-B coated CP-Ti. Quantitative elemental analysis of the coating indicates that the amount of boron is between 4 to 7 wt.%. Some researchers [21] have noted that boron content of electroless Ni–B coatings ranges almost from 1 to 10 wt. %, and the electroless Ni–B coating is amorphous for boron content higher than 5 wt. % [22, 23], as suggested by XRD data (Fig. 3).
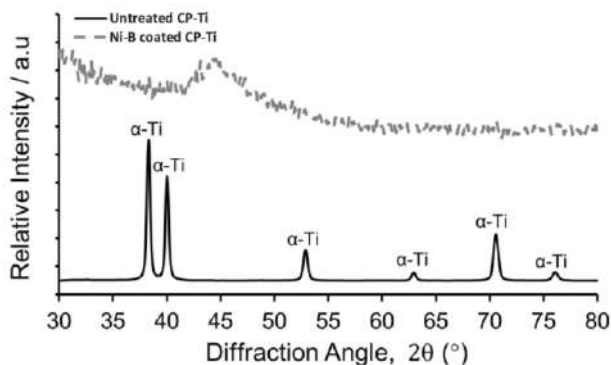

Figure 3. XRD patterns of the untreated CP-Ti and Ni-B coated CP-Ti.

The XRD patterns of the untreated CP-Ti and Ni-B coated CP-Ti are given in Fig. 3. As expected, the untreated CP-Ti is entirely composed of hexagonal α-phase (denoted as ''Ti'' in Fig. 3). On the other hand, the XRD pattern in Fig. 3 indicates the formation of Ni–B deposit in amorphous phase on the surface of CP-Ti, which is observed with the development of a single broad peak around 45° which corresponding to Ni (111). The predominance of peak pertaining to amorphous phase with a corresponding absence in the intensity of the peaks pertaining to α-Ti confirms the formation of a thick (~15 μm) and homogeneous Ni-B layer (Fig. 1 b), which would otherwise exhibit α-Ti as the predominant peak in the XRD pattern. In terms of Knoop microhardness, the formation of Ni-B film on the CP-Ti enables a significant improvement in cross-section hardness due to the presence of boron in the interstitial solid solution. Almost a three-fold increase in microhardness from 279 ± 11 to 818 ± 61 $HK_{0.01}$ is observed for CP-Ti after electroless Ni-B coating.

The tribocorrosion tests were performed at OCP conditions and the evolution of the potential as a function of time is shown in Fig. 4 along with their corresponding friction curves. The change in OCP of the untreated CP-Ti and Ni-B coated CP-Ti was measured before, during and after the sliding motion. Before sliding, the OCP of both untreated CP-Ti and Ni-B coated CP-Ti was about -320 mV. During the sliding, it can be clearly seen for the Ni-B coated CP-Ti that an initial drop in the OCP values at the beginning of the test was observed and then the Ni-B coated CP-Ti presented relatively stable OCP values. This indicates that the coating was not destroyed during sliding, hence no changes in the OCP until the end of the test. In fact, the cross-section scans performed across each wear showed that the wear scar depth for the Ni-B coated CP-Ti was 9 μm (Fig. 5). This clearly indicates that this coating was not fully penetrated. Therefore, the underlying CP-Ti substrate was neither exposed to the corrosive environment nor affected by plastic deformation. On the other hand, in case of the untreated CP-Ti, when sliding started, a sudden drop in the potential of ~630 mV can be observed. The voltage drop indicates the destruction of the passive layer at the contact region [24, 25] suggesting an increase in susceptibility of the CP-Ti surface for corrosion, and therefore a need for surface protection. In this case, the wear scar depth of the untreated CP-Ti was found to be approximately 15 μm (Fig. 5). It should be noted that the OCP stayed low during the sliding, constant at about -950 mV, together with high oscillations that are usually attributed to the repeated action of depassivation and repassivation of the untreated CP-Ti under sliding against an Al_2O_3 ball [24, 25]. Furthermore, the OCP during the wear test for the Ni-B coated CP-Ti was higher than the OCP of the untreated CP-Ti, indicating that the Ni-B coating was effective in protecting the untreated CP-Ti from corrosion during sliding. After the sliding motion was stopped, the untreated CP-Ti presented a shift in the noble direction with respect to the OCP, suggesting a progressive repassivation of the wear scar area, whereas the OCP values of the Ni-B coated CP-Ti became stable near the values recorded before the sliding started.
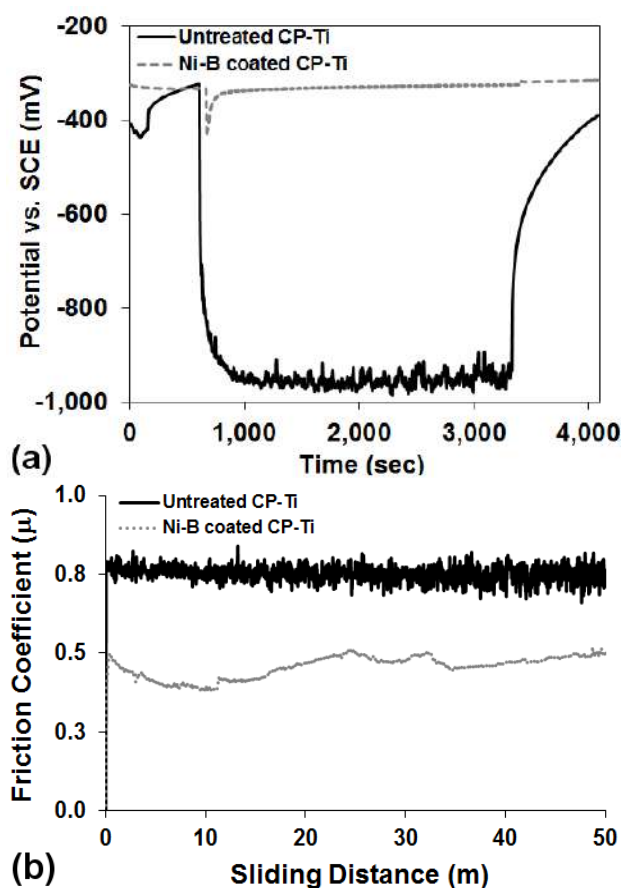
Figure 4. The evolution of the (a) OCP and (b) friction coefficients recorded in-situ before, during and after sliding in SAS solution.
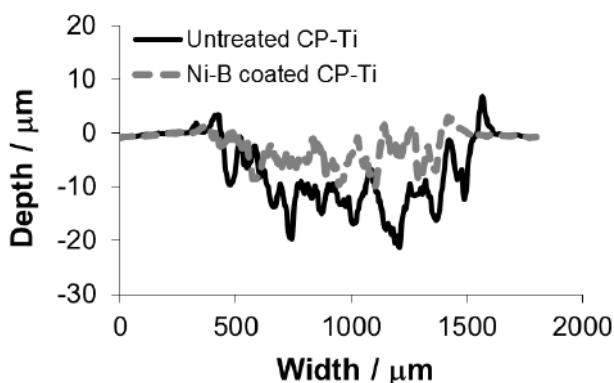

Figure 5. Surface profiles across the wear scars of the untreated CP-Ti and Ni-B coated CP-Ti tested in SAS solution.

The untreated CP-Ti exhibited the highest and most unstable friction coefficient (Fig. 4 b), confirming its already known poor tribological characteristic, and thus the need for surface protective treatment. On the other hand, it can be clearly seen that the Ni-B coated CP-Ti showed a lower and more stable friction coefficient in comparison to the untreated CP-Ti substrate (Fig. 4 b). This could be attributed to the function of lubricant of the particles

belonging to NiB coating with columnar structure under conditions of tribocorrosion (SAS solution). Accordingly, the Ni-B coated CP-Ti presented the low wear volume loss and the friction-reducing performance together with high amount of material transfer into the SAS solution (Table 2).

Table 2. Tribocorrosion test results of the untreated CP-Ti and the Ni-B coated CP-Ti.

Sample	Average friction coefficient	Wear volume loss (mm^3)	Optical density (a.u.)
Untreated CP-Ti	0.76	0.21	1.87
Ni-B coated CP-Ti	0.45	0.02	3.46

The low and high magnification views of the wear scars developed on the samples and their corresponding testing balls are shown in Fig. 6. As can be seen in Fig. 6, the worn surface of the untreated CP-Ti exhibited obviously micro-cutting, plowing grooves and plastic deformation, and the worn surface of Ni-B coated CP-Ti was narrow with a smooth and polished appearance. It can be found that the size of worn surfaces of the Al$_2$O$_3$ balls is also similar to the results in Table 2. Although the microhardness of the CP-Ti substrate was lower than that of Al$_2$O$_3$ ball, the CP-Ti had negative effects on the Al$_2$O$_3$ ball and the worn surface of the Al$_2$O$_3$ ball presented obvious plastic deformation, as shown in Fig. 6 a because the amount of soft untreated CP-Ti substrate transferred to the Al$_2$O$_3$ ball increased due to adhesion. Furthermore, the size of the worn surface of the Al$_2$O$_3$ ball in Fig. 6 b is significantly smaller than other, because of the existence of the self-lubricating Ni-B.

Antibacterial activity of the untreated CP-Ti and the Ni-B coated CP-Ti on agar plate was examined on the diameter of basic inhibition zone of *E. coli*, gram-negative bacteria, using disc diffusion technique. A zone of bacterial growth inhibition with a dimension of 30 mm was seen for the Ni–B coated CP-Ti, while growth inhibition was not observed for the untreated CP-Ti used as a control for comparative analysis (Fig. 7).
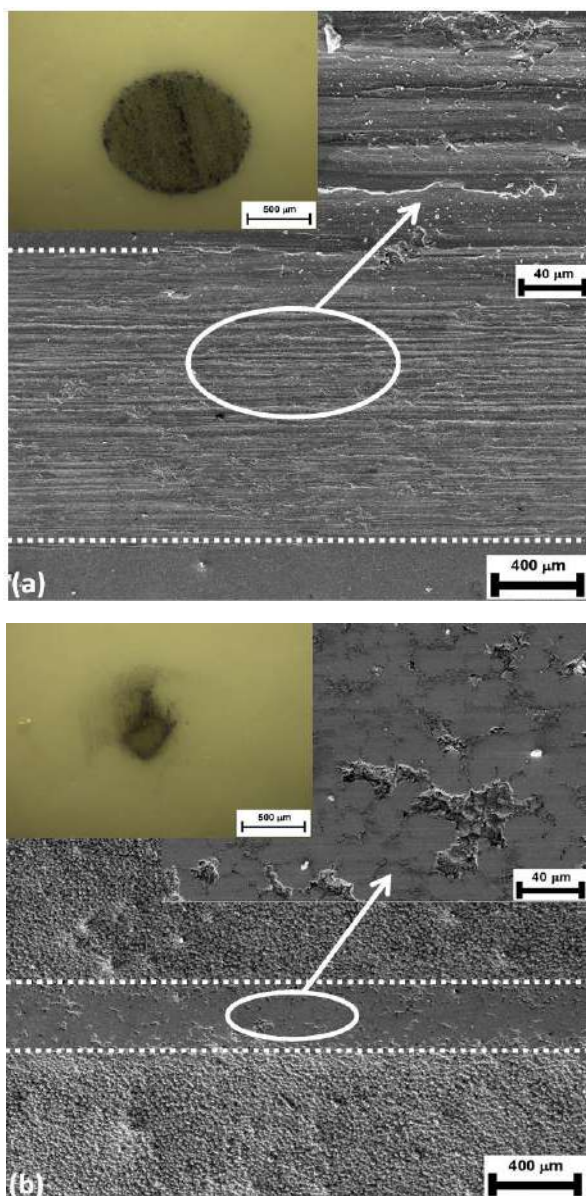
Figure 6. Low and high magnification SEM micrographs of wear scars generated on the (a) untreated CP-Ti, (b) Ni-B coated CP-Ti, and LOM images of their corresponding testing balls after tribocorrosion.
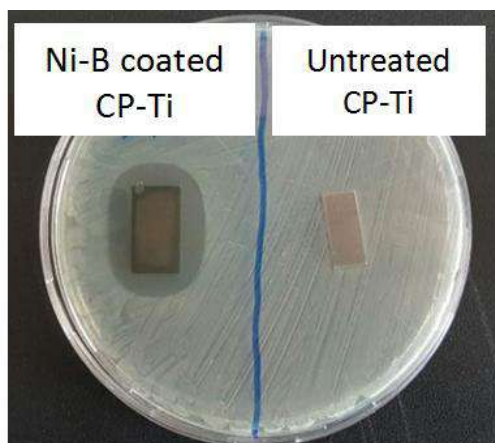

Figure 7. The photograph of bacteria growth on culture plates after 24 h: the untreated CP-Ti and Ni-B coated CP-Ti samples.

Thus, it appears that the Ni-B coated CP-Ti possess an excellent effectiveness in inhibition of bacterial growth comparing to the positive control. This could be attributed to the slight dissolving of Ni. It can be assumed that the release of Ni^{2+} from the Ni–B coating and its entry in bacterial cells can lead to a decrease of the bacterial growth. This mechanism has been proved for antibacterial activities of Ni–P coating [26].

4. CONCLUSIONS

A simple and cost-effective method was employed to modify the surface of commercial CP-Ti alloy. The results are summarized as follows:

- The surface modification on CP-Ti used as the substrate has been successfully carried out by electroless Ni–B deposition. XRD examination reveals that α-Ti phase for untreated CP-Ti and amorphous phase for Ni-B coated CP-Ti were obtained. The EDS analysis confirms the presence of Ni and B in the deposited layer. The LOM and SEM analyses show typical Ni–B coating structure with primary forms of a typical cauliflower-like morphology.
- Knoop microhardness of the modified surface reached 818 ± 61 $HK_{0.01}$, which was extremely higher as compared with the hardness of the original CP-Ti substrate of 279 ± 11 $HK_{0.01}$.
- Under OCP tribocorrosion conditions, the Ni-B coated CP-Ti exhibited better tribocorrosion performance when compared to the untreated CP-Ti. This was attributed to their improved frictional characteristics, and low wear scars depth that coincided with the absence of oscillations in the OCP.
- With an inhibition halo of 30 mm, the Ni–B coating exhibited a better biocidal effect on E. *coli* owing to less bacterial adhesion compared to the untreated CP-Ti control sample.

REFERENCES

[1] M. Kazemzadeh-Narbat, B. F.L. Lai, C. Ding, J.N. Kizhakkedathu, R. E.W. Hancock, R. Wang: Multilayered coating on titanium for controlled release of antimicrobial peptides for the prevention of implant-associated infections, Biomaterials, Vol. 34, No.24, pp. 5969-5977, 2013.

[2] R. Caroline: Innovative surface treatments of titanium alloys for biomedical applications, Materials Science Forum, Vol. 879, pp. 1570-1575, 2016.

[3] V.E. Annamalai, S. Kavitha, S. A. Ramji: Enhancing the properties of Ti6Al4V as a biomedical material: a review, The Open Materials Science Journal, Vol. 8, pp. 1-17, 2014.

[4] A. Revathi, S. Magesh, V.K.Balla, M. Das, G.Manivasagam: Current advances in enhancement of wear and corrosion resistance of titanium alloys –a review, Materials Technology: Advanced Performance Materials, Vol. 31, No.12 pp.1-9, 2016.

[5] I.S.V.Marques, M.F. Alfaro, M. T.Saito, M.T. Saito, C. Takoudis, R. Landers, M.F. Mesquita, F. H. N. Junior, M.T. Mathew, C. Sukotjo, V. A. R. Baraok: Biomimetic coatings enhance tribocorrosion behavior and cell responses of commercially pure titanium surfaces, Biointerphases, Vol. 11, No.3, pp. 1-14, 2016.

[6] V. Totolin, V. Pejaković, T. Csanyi, O. Hekele, M. Huber, M. R. Ripoll: Surface engineering of Ti6Al4V surfaces for enhanced tribocorrosion performance in artificial seawater, Materials and Design, Vol.104, pp.10-18, 2016.

[7] C. Richard, C. Kowandy, J. Landoulsi, M. Geetha, H. Ramasawmy: Corrosion and wear behavior of thermally sprayed nano ceramic coatings on commercially pure Titanium and Ti–13Nb–13Zr substrates, Int. Journal of Refractory Metals & Hard Materials, Vol. 28, No.1, pp.115–123, 2010.

[8] A. Zhecheva, W.Sha, S. Malinov, A. Long: Enhancing the microstructure and properties of titanium alloys through nitriding and other surface engineering methods, Surface & Coatings Technology, Vol. 200, No.7, pp. 2192– 2207, 2005.

[9] H. D. Vora, R.S.Rajamure, S. N. Dahotre, Y.H. Ho, R.Banerjee, N.B. Dahotre: Integrated experimental and theoretical approach for corrosion and wear evaluation of laser surface nitrided, Ti–6Al–4V biomaterial in physiological solution, Journal of The Mechanical Behavior of Biomedical Materials, Vol.37, 153-164, 2014.

[10] H.G. Jeong, Y.Lee, D.G.Lee: Effects of pre-heat conditions on diffusion hardening of pure titanium by vacuum rapid nitriding, Surface & Coatings Technology, In Press, 2017.

[11] P. Stratton, M. Graf: Thermochemical surface treatment of titanium, International Heat Treatment and Surface Engineering, Vol. 3, No.1-2, pp. 26-29, 2009.

[12] K. Aniołek,, M.Kupka, A.Barylski: Sliding wear resistance of oxide layers formed on a titanium surface during thermal oxidation, Wear, Vol. 356-357, pp. 23–29, 2016.

[13] T. Hanawa: Biofunctionalization of titanium for dental implant, Japanese Dental Science Review, Vol. 46, No.2, pp. 93—101, 2010.

[14] D. Teker, F. Muhaffel, M. Menekse, N. G. Karaguler, M. Baydogan, H. Cimenoglu: Characteristics of multi-layer coating formed on commercially pure titanium for biomedical applications, Materials Science and Engineering C, Vol. 48, pp. 579–585, 2015.

[15] H.Farnoush, F. Muhaffel, H. Cimenoglu: Fabrication and characterization of nano-HA–45S5 Bioglass composite coatings on calcium-phosphate containing micro-arc oxidized CP-Ti substrates, Applied Surface Science, Vol. 324, pp.765-774, 2015.

[16] M. Ipekci, F. Siyahjani, H. Cimenoglu: Thermochemical nitriding of commercial purity titanium, Defect and Diffusion Forum, Vol. 334-335, pp. 117-121, 2013.

[17] S. Kikuchi, J. Takebe: Characterization of the surface deposition on anodized-hydrothermally treated commercially pure titanium after immersion in simulated body fluid, Journal of Prosthodontic Research, Vol. 54, No.2, pp. 70–77, 2010.

[18] S. Ferraris, A. Venturello, M. Miola, A. Cochis, L. Rimondini, S. Spriano: Antibacterial and bioactive nanostructured titanium surfaces for bone integration, Applied Surface Science, Vol. 311, pp. 279-291, 2014.

[19] F. Bulbul: Antibacterial activity of electroless Ni–B coating, Materials Science and Technology, Vol.27, No.10, pp.1540-1546, 2011.

[20] F. Mindivan, H.Mindivan: The study of electroless Ni-P/Ni-B duplex coating on HVOF-sprayed martensitic stainless steel coating, Acta Physica Polonica A, Vol. 131, No.1, pp. 64-67, 2017.

[21] F. Delaunois, P. Lienard: Heat treatments for electroless nickel–boron plating on aluminium alloys, Surface and Coatings Technology, Vol. 160, No.2-3, pp. 239–248, 2002.

[22] T. Watanabe, Y. Tanabe: The lattice images of amorphous-like Ni–B alloy films prepared by electroless plating method, Transactions of the Japan Institute of Metals. Vol. 24, No. 6, pp. 396–404, 1983.

[23] V.Vitry, A.F.Kanta, F. Delaunois: Mechanical and wear characterization of electroless nickel-boron coatings, Surface & Coatings Technology, Vol. 206, No.7, pp. 1879–1885, 2011.

[24] H. Mindivan: Comparative study of tribocorrosion properties of some bio-based materials in simulated artificial saliva, Machines, Technologies, Materials, Vol. 12, pp. 58-60, 2016.

[25] F. Mindivan, H. Mindivan: Surface properties and tribocorrosion behaviour of a thermal sprayed martensitic stainless steel coating after pulsed plasma nitriding process, Journal Advances in Materials and Processing Technologies, Vol. 2, No. 4,pp. 514-526, 2016.

[26] Z. Sharifalhoseini, M. H. Entezari, R. Jalal: Evaluation of antibacterial activity of anticorrosive electroless Ni–P coating against *Escherichia coli* and its enhancement by deposition of sono-synthesized ZnO nanoparticles, Surface & Coatings Technology, Vol. 266, pp. 160–166, 2015.

SERBIATRIB '17

15th International Conference on Tribology

Kragujevac, Serbia, 17 – 19 May 2017

MICRO SCRATCH BEHAVIOUR OF LITHIUM DISILICATE GLASS CERAMIC AFTER GLAZING TREATMENT

Marko PANTIĆ[1], Slobodan MITROVIĆ[1], Miroslav BABIĆ[1], Danimir JEVREMOVIĆ[2], Tatjana V. KANJEVAC[3], D. DŽUNIĆ[1*], D. ADAMOVIĆ[1]
[1]University of Kragujevac, Faculty of Engineering, Kragujevac, Serbia
[2]University Business Academy, School of Dentistry, Pančevo, Serbia
[3]University of Kragujevac, Faculty of Medical Sciences, Department of Dentistry, Kragujevac, Serbia
*Corresponding author: dzuna@kg.ac.rs

Abstract: *The purpose of this in vitro study was to investigate micro scratch behaviour of lithium disilicate glass ceramics (LDGC) - IPS e.max CAD, after glazing treatment. LDGC is one of most used all-ceramic dental system which provides high aesthetic quality and all patient requirements: function, biocompatibility and aesthetic. Micro-scratch test was performed with a progressive load of 0.01 to 30 N, which meant that the values of the normal force increased with the change of time. Rockwell C diamond cone was used as the indenter, of radius tip 100 µm. The aim of this study is to test the wear resistance of glazed lithium disilicate, to determine the thickness of the glaze and quantify the tribo-mechanical characteristics of the glazed layer. The obtained results are presented in the form of values of the critical loads (L_c), the friction coefficient (µ), the penetration depth (P_d) and the residual depth (R_d).*

Keywords: *Micro Scratch Test, Lithium disilicate glass ceramic, Glazing tretments, Tribo-mechanical properties*

1. INTRODUCTION

In recent years, glass ceramics has become very important and one of the most commonly used materials in prosthetics, solely due to its excellent aesthetic characteristics, good mechanical strength and durability of restorations.

In 1991 the company Ivoclar Vivadent with IPS Empress System had the first breakthrough in the development of glass ceramics in aesthetic dentistry. Further development of glass ceramics was achieved in 1998 with the emergence of IPS Empress 2 system which was based on lithium disilicate [1]. The material is characterized by the high values of flexural strength and by the wide application in making restorations and bridges. A new advanced all-ceramic system called IPS e.max has been developed (Ivoclar Vivadent, Liechtenstein), based on the idea that the future of all-ceramic systems lies in the use of PRESS and CAD/CAM technology. It contains a superior aesthetic and high-resistant materials intended for the PRESS and CAD/CAM technology. IPS e.max system covers a wide range of indications of ceramic restorations in different zones of the load, combining a large flexural strength, aesthetics and ease of manufacture [2].

A large number of publications in the field of dentistry, and the fields that are close to it,

confirm the use of scratch test for a number of tribological testing of various biomaterials [3-10]. The ability of scratch test is to mechanically characterize the surface layer of the material that is being tested and to quantify the parameters such as the friction and the adhesion forces. It is widely used during the testing of all types of thin coatings and films (thickness of 0.1 - 30 μm), which forms nowadays the essential tool for the research, development and quality control of the surface layers of materials.

It is generally known that the scratch test is used to analyse all types of thin coatings and films. In aesthetic dentistry, the purpose of the glaze, as the form of the coating, is to reduce the porosity and surface roughness of the material itself and to improve the aesthetic appearance of restorations in the form of an aesthetic shine [11-15]. The important thing that must be emphasized is that the glaze with its presence on the surface layer of the ceramic does not improve the strength of the self-material [16].

The aim of this study is to test the wear resistance of glazed lithium disilicate, to determine the thickness of the glaze and quantify the tribo-mechanical characteristics of the glazed layer. The obtained results are presented in the form of values of the critical loads (L_c), the friction coefficient (μ), the penetration depth (P_d) and the residual depth (R_d).

2. EXPERIMENTAL PROCEDURE

MST Anton Paar micro-scratch tester, located at the Tribology center on the Faculty of Engineering in Kragujevac, was used to determine the tribo-mechanical characteristics of the glazed lithium disilicate (Figure 1).

The working principle of micro-scratch device is shown in Figure 2. The indenter tip (Rockwell C diamond cone, radius of the tip 100 μm) passes over the surface layer of the material with constant and progressive load, depending on the protocols defined in the software. The sample is fixed in the sample holder which is located on the anti-vibration table and moves at a constant speed on the X and Y axes. Normal force, penetration depth, acoustic emission and friction force are detected during the testing. Acoustic signal detector is placed above the diamond needle, and it registers the vibrations which appear when damage occurs. In addition to the acoustic sensor, the scratch test device has also encoders that register the friction force. The software may provide real-time results of the measurement. When the indenter moves on the sample, it comes to formation of various damages depending on the value of the applied force. The minimum value of the normal force (F_n) that causes damage is referred to as a critical load (L_c). Three values of critical load are most commonly detected (L_{c1}, L_{c2} and L_{c3}).

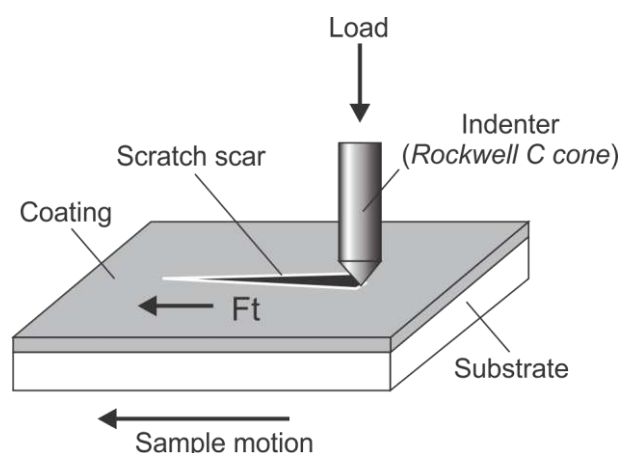
Figure 1. MST Anton Paar micro-scratch tester

Figure 2. The schematic view of scratch test and the working principle

Rockwell C diamond cone was used as the indenter, of radius tip 100 μm. The test was performed with a progressive load of 0.01 to

30 N, which meant that the values of the normal force increased with the change of time. The range was chosen as widely as possible in order to monitor the reaction of fully glazed surface on the change of load. Sliding speed of the sample, which was fixed in the sample holder on the work table, was constant 1 mm/min. The defined length of the scratch scar was 3 mm. The experiment was performed in the conditions without lubrication in ambient temperature of 23 ±2°C and the test was repeated three times. Before the testing, the glazed sample was ultrasonically cleaned well (30 minutes) and afterwards it was cleaned with 70 % alcohol in order to remove all the surface contaminants.

2.1 Material and samples preparation

IPS e.max CAD is the type of all-ceramics, which is characterised by a high aesthetic quality, so it can be said that its characteristics meet all prosthetic requirements in form of: aesthetics, function and biocompatibility of the material [15]. Table 2.4 presents the chemical composition of the commercial lithium disilicate IPS e.max CAD. SiO_2 and LiO_2 represent components which form $Li_2Si_2O_5$ crystals, while the P_2O_5 is added as a nucleating agent. Other Oxides with its characteristics further contribute to the material structure itself.

Table 2.4 Chemical composition of IPS e.max CAD [17]

Standard composition	(in % by weight)
SiO_2	57.0 – 80.0
Li_2O	11.0 – 19.0
K_2O	0.0 – 13.0
P_2O_5	0.0 – 11.0
ZrO_2	0.0 – 8.0
ZnO	0.0 – 8.0
Al_2O_3	0.0 – 5.0
MgO	0.0 – 5.0
Colouring oxides	0.0 – 8.0

The glazed sample is in the form of a block, the length of 18 mm, a width of 14 mm and a height of 12 mm. Before the glazing process, lithium disilicate is crystalized at the prescribed temperature according to instructions of the manufacturer Ivoclar Vivadent. After the crystallization, the surface of the sample is glazed as the form of the final treatment of the material, also according to the exact prescribed procedure of the manufacturer Ivoclar Vivadent. The glaze is applied by hand with a brush in a thin layer on a contact surface of the sample and represents the type of protective coating, wherein it is baked afterwards in an oven at the accurately prescribed temperature.

3. RESULTS AND DISCUSION

Tribo-mechanical tests were preceded by the AFM analysis in order to determine the roughness parameters Ra, 3D topography and surface roughness profile of the tested material (Figure 3).
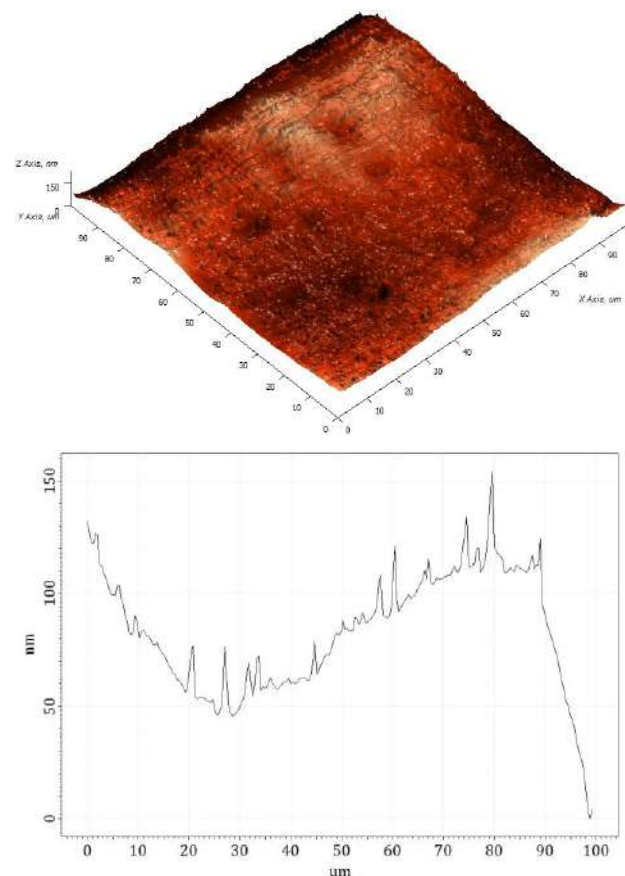
Figure 3. AFM analysis of IPS e.max CAD glazed surface - 3D topography and surface roughness profile

The measured value of the surface roughness (Ra) of the lithium disilicate glazed surface (IPS e.max CAD) is Ra = 19.817 nm. It is known that the process of glazing, due to

uneven application of the glaze layer, leads to surface irregularities in the form of wavy surfaces and gas bubbles, which can be clearly seen on the 3D image of the surface topography.

During the experimental testing, first the scanning (Pre-scan) of the contact surface was performed at the place of testing, due to the imperfections of the glazed surface (wavy surfaces), as well as different surface roughness, which oscillates at a micro/nano-level. Due to the penetration of the MST indenter in the surface layer of the glaze, at progressive load and movement of the sample at a sliding speed of 1 mm/min, there is a gradual formation of scratch scar of a certain depth. Due to the elastic relaxation of the material/coating itself, the new analysis of the surface was performed in the scratch scar itself after the end of scratch test (Post-scan) to determine the actual residual depth (R_d) in relation to the initial measured penetration depth (P_d). The obtained values of the different penetration depths, as well as the the friction coefficient, represent the mean values of 3 measurements and they entirely define the tribo-mechanical properties of the glazed surface of the material.

Figure 4 shows the scratch scar on the glazed surface of the material that comparatively follows the diagrams of the dependence of different penetration depths (P_d and R_d) depending on the friction coefficient and normal load. The loose particles of the surface layer of the glaze around the scratch scar, of different sizes, could be easily seen in the Figure 4, and they are made as a result of indentation and movement of Rockwell C diamond cone at the surface itself. The mechanisms that occur during the scratch test are usually micro-cutting and micro-ploughing. The panoramic view of the scratch scar was formed on the optical microscope which is an integral part of the device, with a magnification of 5×. Black spots that represent the surface imperfections of finial treatment in the form of wavy surfaces and gas bubbles, which are characteristic for the glazing treatment, can be seen in some optical panoramas of scratch scars. The Figure 4 clearly shows the trend of increase of friction coefficient values with a slight oscillation along the sliding distance, due to the increase of the normal load. The variation of the friction coefficient which appears in the form of distinct jumps and falls at the diagrams largely follows the trend of the oscillation of the value of the penetration depth (P_d) and residual depth (R_d), which clearly defines their mutual dependence.

The maximum value of the friction coefficient of lithium disilicate is ~0.22 and it penetration depth of the material of 34 mm, due to the effect of normal load of ~27 N. The residual depth (R_d) in relation to the measured penetration depth (P_d) is 15 mm. The value of the thickness of the glazed layer, read from the diagram R_d, is 20 μm.

Regarding the measured values of the critical loads, due to which there is an abrasive removal of the glazed layer at the progressive increase of normal load, Figure 5 shows their different critical stages in the scratch scar itself. Panoramic views of all scratch scars were photographed by OM with 5× magnification, while the individual images of the critical stage of the scratch scars, are presented with a magnification of 20×.

The abrasive wear, as a dominant type of wear, can be clearly seen in shown Figures 5 of the scratch scars. The reason is a drastic difference in the hardness of the two contact bodies during the relative motion. Rockwell diamond indenter has a significantly higher hardness in comparison to the hardness value of the tested sample.

Figure 5, characterised by different phase damages of the surface glazed layer of lithium disilicate, clearly show that the initial defects occur at normal load of the indenter of 4.5 N (L_{C1}). During the progressive increase of the normal load, the penetration of glazed surface occurs in the moment when the normal load reaches a value of ~18 N.
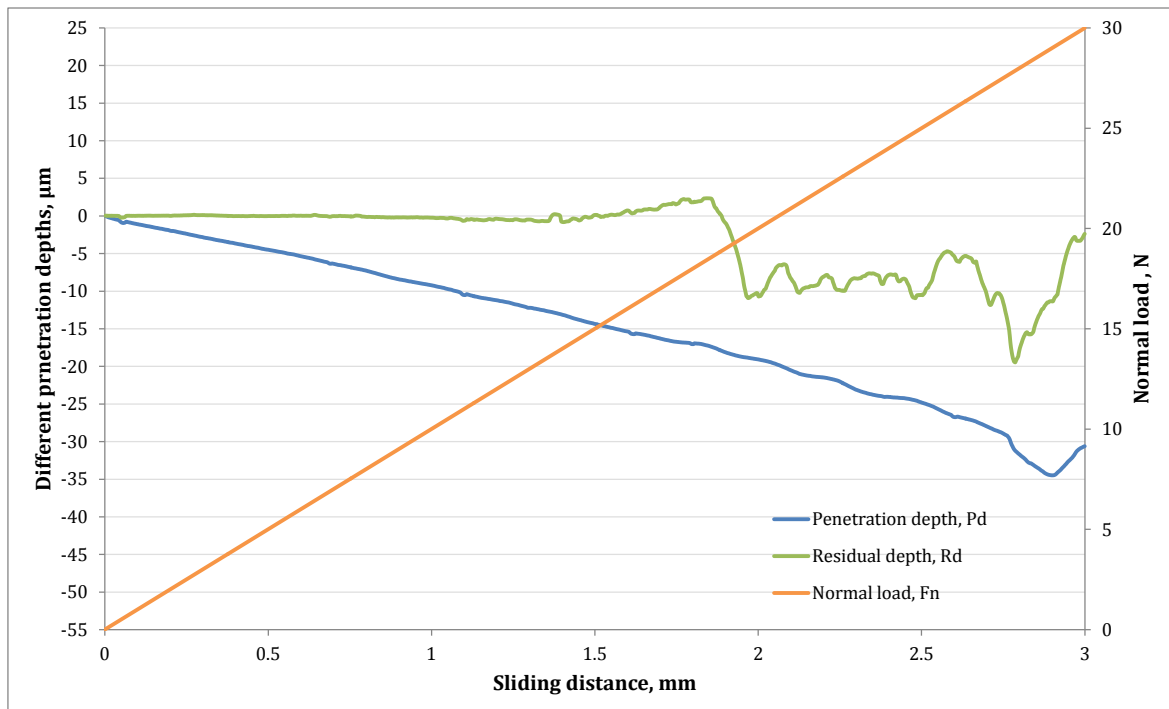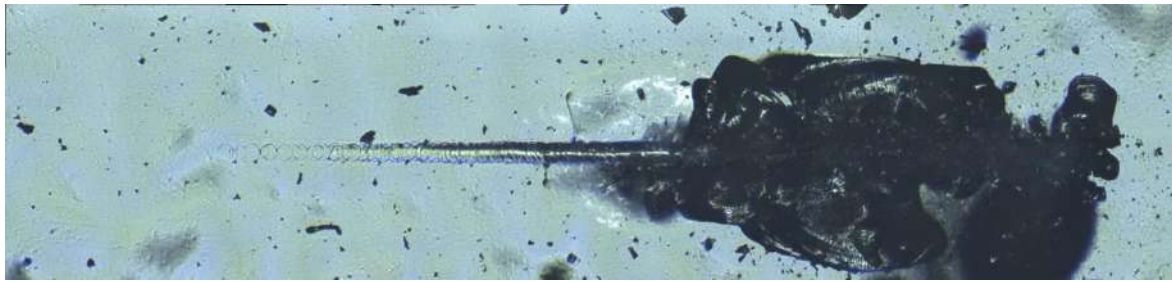
Figure 4. The scratch scar display of the glazed surface of lithium disilicate followed by the diagrams of different penetrating depths (P_d, R_d) depending on the friction coefficient and normal load
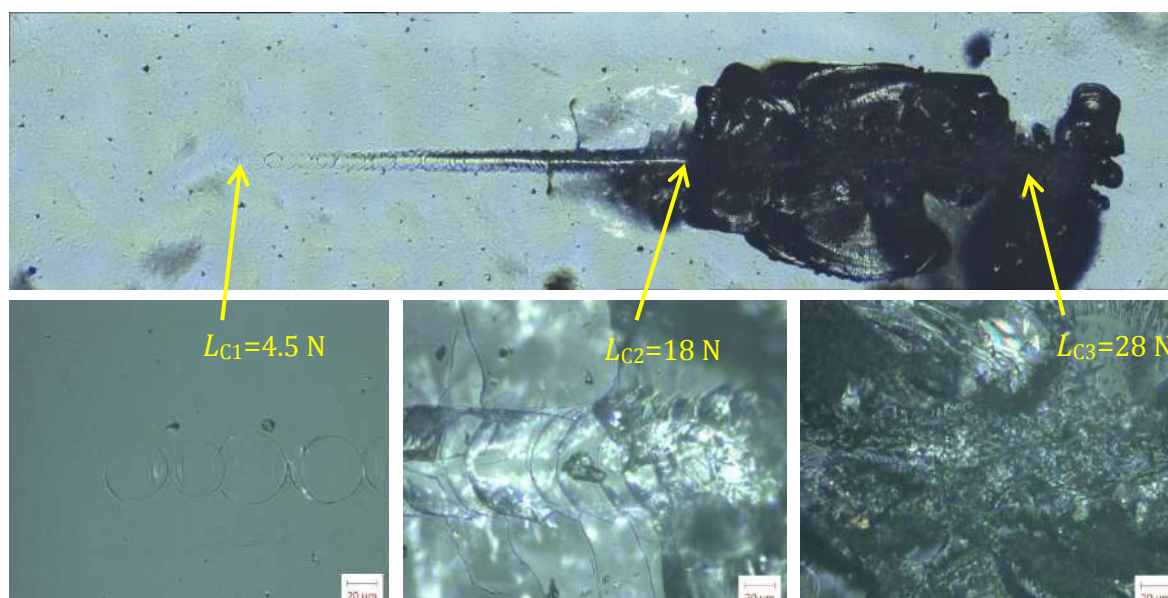
Figure 5. Defining critical loads due to which there is a different phase damages of the glazed lithium disilicate

This coating penetration can be clearly seen on the optical display L_{C2}, with magnification of 20×. After that moment, the indenter comes in contact with the surface of the base material. The further increase of the value of normal load, at the value of 28 N, shall cause the surface damages of lithium disilicate and encroachment of the indenter into the base material, which is clearly seen on the third image for L_{C3} value. All values of critical loads are obtained as mean values of three repeated measurements of the scratch test by statistical analysis in the software of MST. Also, all these changes of the critical loads are followed by the increase of the friction coefficient (μ) and the penetration depth (P_d and R_d), whose analysis are previously discussed.

The obtained results of this *in vitro* studies represent a very useful and unique information for the future comparison with clinical *in vivo* studies of the similar type, because at the time of literature review, there was no paper found with the similar subject and test plan relating to the tribo-mechanical tests of the glazed surfaces of the all-ceramic systems.

4. CONCLUSION

Scratch test was performed in order to determine the tribo-mechanical characteristics of glazed surfaces of commercial lithium disilicate ceramics. The optical display of the scratch scar shows that the glazed layer is very brittle. The AFM analysis has confirmed that the glaze surface is very wavy, which means that the glaze thickness itself may vary depending on the location of test. The experiment has confirmed that the thickness of the glazed layer based on the residual depth is about 20 μm.

Based on the obtained tribo-mechanical characteristics of glazed layer, their mutual dependence can be easily stated or that the changes of the friction coefficient values over time are in direct correlation with changes of the values of penetration depth (P_d) and residual depth (R_d).

A damage of the glazed layer occurs in the three characteristic phases during the progressive increase of the normal load. The effect of the force of 4.5 N causes the initial damage of glazed layer, and the moment of the glaze penetration during the abrasive effect of the indenter occurs at the indenter force of 18 N, while the total delamination of the glazed layer, in combination with the surface damages of the base material, occurs at the force value of 28 N.

Based on the all presented in the paper, the presented results of scratch analysis represent an excellent basis for all future tribo-mechanical tests of a similar type, as well as

the possibility of more detailed analysis of the present phenomena by using SEM microscopy.

ACKNOWLEDGEMENT

REFERENCES

[1] ASTM C1161 *Standard Test Methods for Flexural Strength of Advanced Ceramics at Ambient Temperature*, 2002.

[2] M. Pantić: *Tribological characterization of advanced dental materials*, PhD thesis, University of Kragujevac, Faculty of Engineering, Kragujevac, 2017.

[3] L.A. Flanders, J.B. Quinn, O.C. Jr Wilson, I.K. Lloyd: Scratch hardness and chipping of dental ceramics under different environments, Dent Mater, vol. 19, no. 8, pp. 716-724, 2003.

[4] S. Fouquet, M. Rollin, R. Pailler, X. Bourrat: Tribological behaviour of composites made of carbon fibres and ceramic matrix in the Si–C system, Wear, vol. 264, pp. 850–856, 2008.

[5] M.S. Al-Haik, S. Trinkle, D. Garcia, F. Yang, U. Martinez, H. Sumali, S. Miltenberger: Investigation of the nanomechanical and tribological properties of dental materials, Int. J. Theoretical and Applied Multiscale Mechanics, vol. 1, no. 1, pp. 1-15, 2009.

[6] A. Vencl, S. Arostegui, G. Favaro, F. Živić, M. Mrdak, S. Mitrović, V. Popović: Evaluation of adhesion/cohesion bond strenght of the thick plasma spray coatings by scratch testing on coatings cross-sections, Tribology International, vol. 44, no. 11, pp. 1281-1288, 2011.

[7] F. Živić, M. Babić, D. Adamović, S. Mitrović, P. Todorović, G. Favaro, M. Pantić: Influence of the surface roughness on adhesion of chrome coatings on alloy tool steel X165CrMoV12, Journal of the Balkan Tribological Association, vol. 18, no. 2, pp. 228–237, 2012.

[8] J. Zheng, Y. Li, M.Y. Shi, Y.F. Zhang, L.M. Qian, Z.R. Zhou: Micro tribological behaviour of human tooth enamel and artificial hydroxyapatite, Tribology International, vol. 63, pp. 177–185, 2013.

[9] S. Palaniappan, J.-P. Celis, B.V. Meerbeek, M. Peumanas, P. Lambrechts: Correlating in vitro scratch test with in vivo contact free occlusal area wear of contemporary dental composites, Dental Materials, vol. 29, pp. 259-268, 2013.

[10] O. Borrero-Lopez, A. Pajares, P.J. Constantino, B.R. Lawn: Mechanics of microwear traces in tooth enamel, Acta Biomaterialia, vol. 14, pp. 146-153, 2015.

[11] K.C. Cheung, B.W. Darvell: Sintering of dental porcelain: effect of time and temperature on appearance and porosity, Dent Mater J., vol. 18, pp. 163-173, 2002.

[12] G. Aksoy, H. Polat, M. Polat, G. Coskun: Effect of various treatment and glazing (coating) techniques on the roughness and wettability of ceramic dental restorative surfaces, Colloids Surf B Biointerfaces, vol. 53, no. 2, pp. 254-259, 2006.

[13] K. Mehulic, V. Svetlicic, S. Segota, D. Vojvodic, I. Kovacic, D. Katanec, N. Petricevic, D. Glavina, A. Celebic: A Study of the Surface Topography and Roughness of Glazed and Unglazed Feldspathic Ceramics, Coll. Antropol, vol. 34, pp. 235–238, 2010.

[14] S. Štefančić, L. Ćurković, G. Baršić, M. Majić-Renjo, K. Mehulić: Investigation of Glazed Y-TZP Dental Ceramics Corrosion by Surface Roughness Measurement, Acta stomatol Croat., vol. 47, no. 2, pp. 163-168, 2013.

[15] M. Pantić, S. Mitrović, M. Babić, D. Jevremović, T. Kanjevac, D. Džunić and D. Adamović: AFM Surface Roughness and Topography Analysis of Lithium Disilicate Glass Ceramic, Tribology in Industry, vol. 37, no. 4, pp. 391-399, 2015.

[16] T. Asai, R. Kazama, M. Fukushima, T. Okiji: Effect of overglazed and polished surface finishes on the compressive fracture strength of machinable ceramic materials, Dent Mater J., vol. 29, no. 6, pp. 661-667, 2010.

[17] K. Fischer, P. Bühler-Zemp, T. Völkel: *Scientific Documentation IPS e.max CAD*, Ivoclar-Vivadent AG, Schaan, 2011.

INVESTIGATION OF THE FAILURE BEHAVIOR OF TIN COATING ON BIOCOMPATIBLE STAINLESS STEEL APPLIED ON METAL-ON-METAL TOTAL HIP PROSTHESES WITH SELF DIRECTED BALLS

Virgil FLORESCU[1], Lucian CAPITANU[2], Dorin RUS[1], Anca SASU[1], Robert URSACHE[1]
[1]University of Civil Engineering Bucharest, Romania
[2] Institute of Solid Mechanics of the Romanian Academy, Romania
*Corresponding author: florescuvirgil@yahoo.com

Abstract: *The Total Hip Prosthesis (THP) is one of the biggest successes of the 20th century in the field of orthopaedic biomechanical engineering. The loss of stability THP are scheduled failure. TiN alloys or hard biocompatible materials coating is a solution of surface treatment for excellent abrasion resistance.*
The replacement of the sliding with the rolling movement is another solution for reliability improving of THP. Unfortunately, only rolling movement is a theoretical desideratum. The rolling movement is accompanied by balls slides into acetabular cup and cyclical inclined impact with sliding between balls and femoral head.
TiN alloys or hard biocompatible materials coating is solution of surface treatment for excellent abrasion resistance. The question is that this coating has a tribologicaly behaviour according with the stress and loading of orthopaedic endoprosthesis.
This paper reports about the investigation of the failure behavior of TiN coating on stainless steel medical grade (SS316L). From the above we believe that is a need for a tribological behavior study on cyclical impact and scratch tests of adherence with real geometrical parameter of THP.
The experimental techniques, stands and results and a conclusion on the reliability of these Conditions Stature submitted in THP are shown.

Keywords: TiN coating, cyclical inclined impact with sliding, scratch tests.

1. INTRODUCTION

Total hip prostheses with rolling motion is a constructive solution that is under analysis in terms of their reliability. The authors proposed a constructive solution for such a prosthesis which has the characteristic of self-directed movement of the balls [1]. Functional tests and behavioral studies have been conducted on this type of prosthesis.

Figure 1 shows the construction which consists of a number between 98 and 189 balls that roll between spherical femoral head and acetabular cup. This technical solution allows free self-directed migration of the balls, depending on the resistance opposed, with successive occupation of the "compensation space". For proper functioning of the prosthesis blanks are provided so that when a number of balls and tends to lock the ball in the end the string will release sideways movement appear as a continuous, self-directed, rolling bodies.

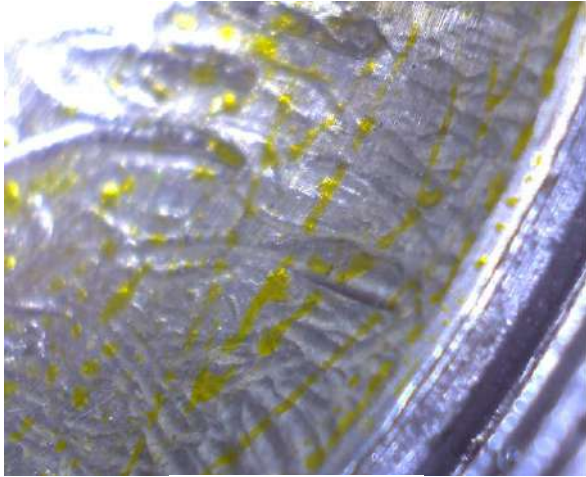**Figure 1.** Total hip prostheses with rolling bodies

Figure 2. Wear tracks

Figure 2 shows the tracks that appear in this area after 10 million cycles.

2. EXPERIMENTAL PROCEDURES

For tribological study was adopted ball on disk type of friction couple. Perhaps it seems surprising choice but it took into account the following considerations:

As the ball comes in contact with it collides acetabular cup and then there is sliding sideways, we thought to model the phenomenon with an inclined impact at an angle of 15 degrees followed by a distance of 10 mm sliding;

Given that the balls movement is random, we consider that during the first operating cycles, sliding is between clean (new) surfaces, without wear;

Over time, due to plastic deformation occurring, it is likely that another ball to follow the same way as the previous one. Therefore this study was performed 1, 3 and 10 cycles;

The materials of the balls is stainless steel medical grade (SS316L). Their radius are 2mm. We realized TiN deposition by laser pulse deposition process (PLD) on stainless steel

medical grade (SS316L) cylindrical samples with diameter of 22.5 mm. Deposits were made to 10000 pulses. The intensity of the diffraction of the analyzed layer is higher than that obtained with conventional techniques, such as reduced substrate influence. Relevant for analyze tension in the film is that the investigated depth interval remains relatively constant during the test. The average thickness of the deposited layer is 2.11 μm and was determined using AFM (Figure 3 and Figure 4).
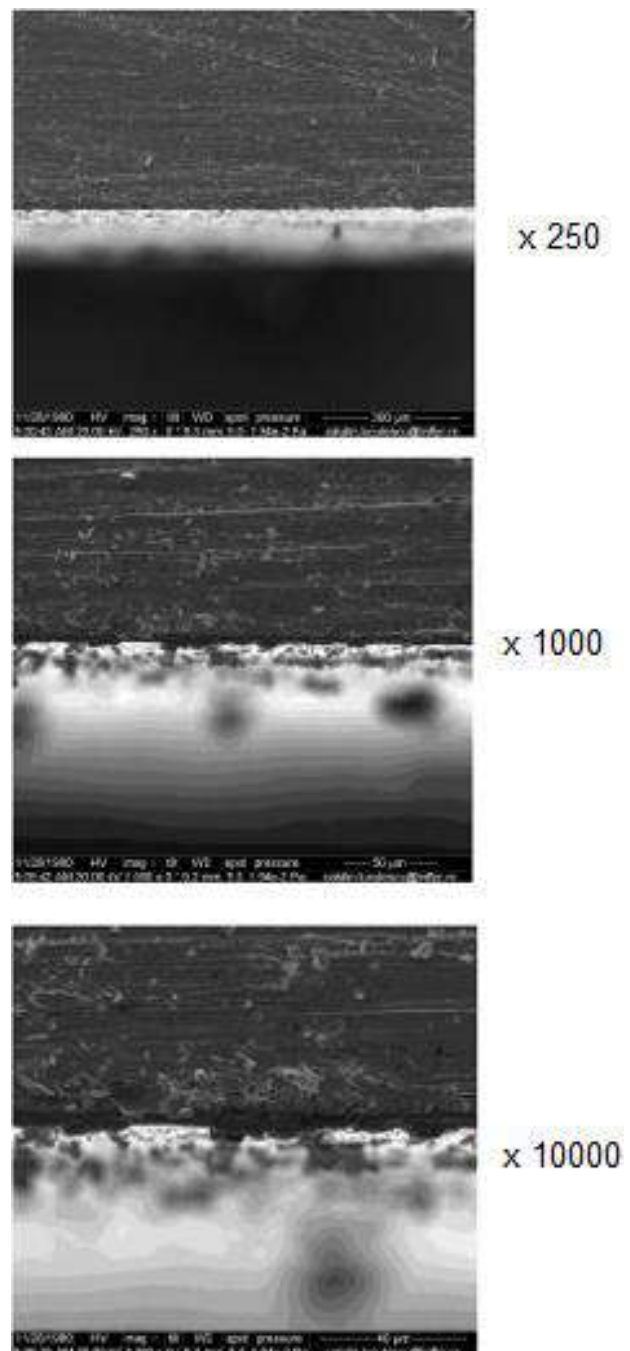
Figure 3. Thickness of the deposited layer determined using AFM

10000 pls → 2,2 μm

10000 pls 1 → 1,9 μm

10000 pls 10 → 2,4 μm
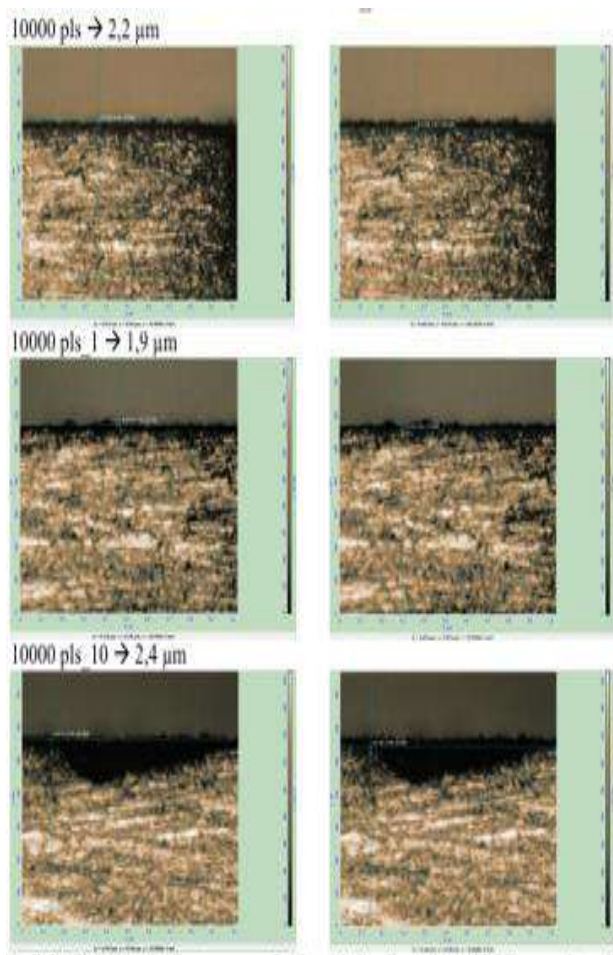
Figure 4. AFM cross section study TiN 10000 pulse deposition process (PLD)
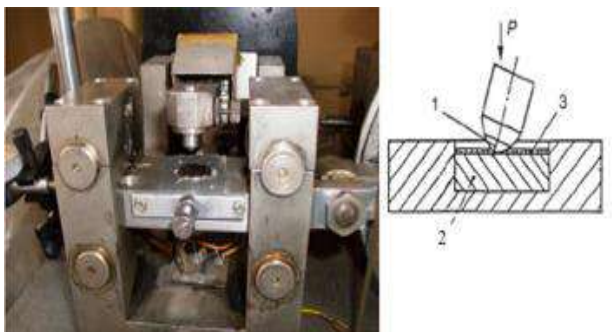
Figure 5. Stand and friction couple

S316L steel hardness values of samples prior to coating and TiN layers deposited microhardness were: Sample TIN / steel SS316L; 10000 pulses hardness substrate material 407; 429; 423 HV 5 kg; Average Hardness HV5 420; Microhardness layer 532; 545 HV 50 GRF; Average Hardness 539 HV0.5.

In previous studies it was determined that the maximum load on the ball can be reached in the most unfavorable case about 38 N [1, 2]. The stand is shown in Figure 5.

3. RESULTS

First of all was analyzed the trace obtained under a single pass.

A cycle is consisting in a loading through an inclined impact followed by a sliding with a load of 2.5, 5, 10, 20 si 40 N.

The sample disk is shown in Figure 6.
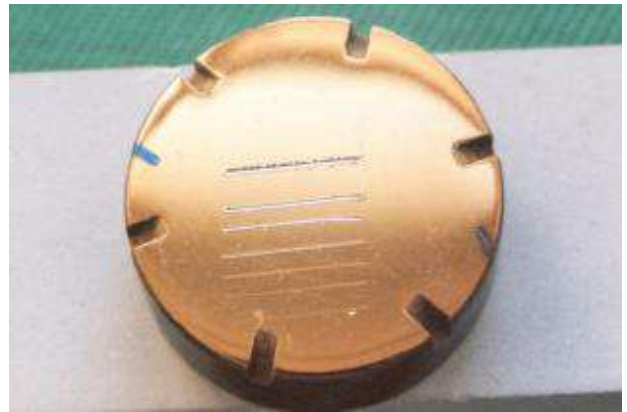
Figure 6. Sample disk

Figure 7 to Figure 8 present the traces mentioned above.
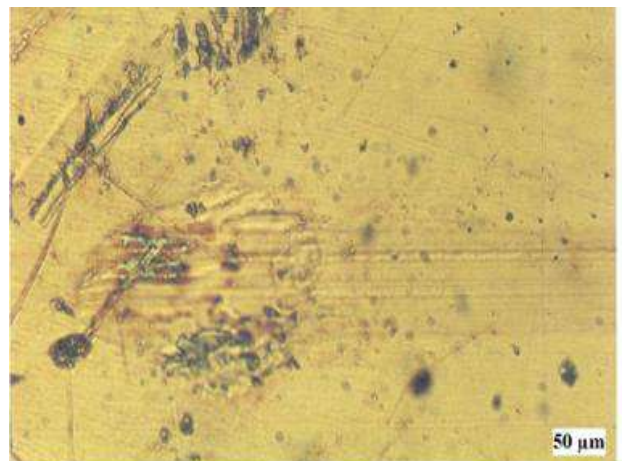
Figure 7. Impact indentation and plastic deformation F= 2.5 N

a)

b)

c)

d)
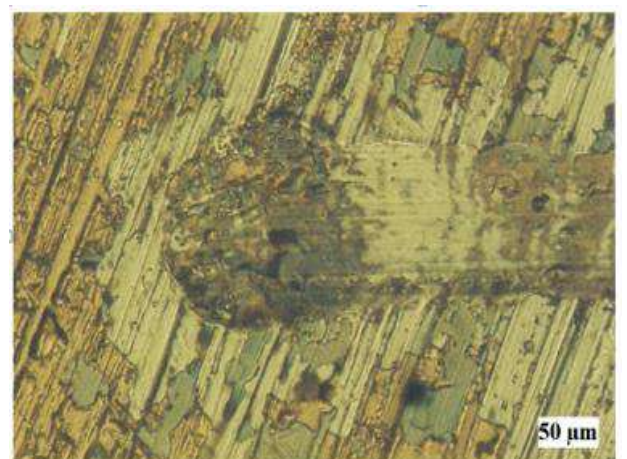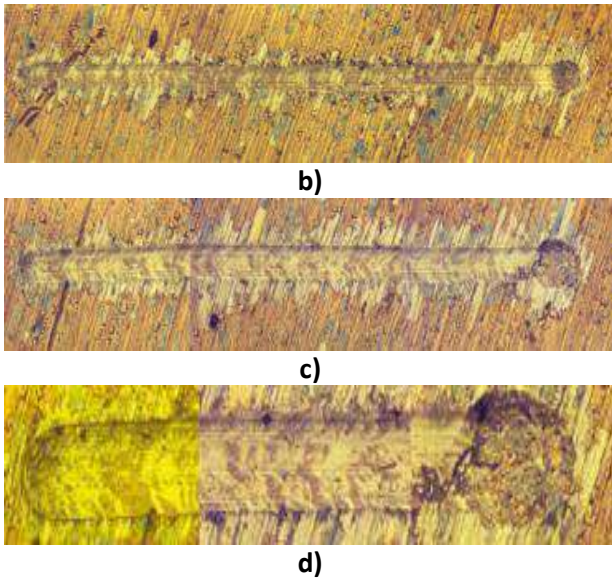
Figure 8. Impact indentation and plastic deformation a)F= 5N; b)F=10N; c)F= 20N; d)F=40N

The depth of the traces is presented in Table 1. These depths were measured by means of profilemeter recording of the type from Figure 9.
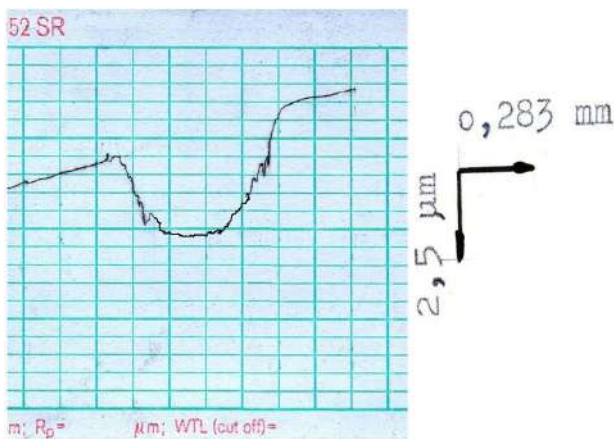
Figure 9. Central transversal profile

Table 1. Depth of traces

Load [N]	2.5	5	10	20	40
Depth [μm]	0.0216	0.0285	0.04	0.0625	0.0912

As regards 10 N loading, Figure 10 and Figure 11 are presenting the traces for 3 and 10 cycles.
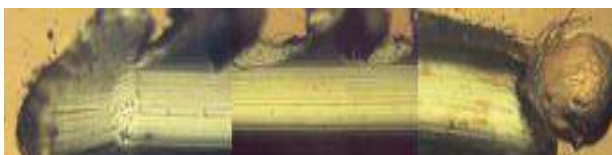
Figure 10. F=10 N, 3 cycles,200 x
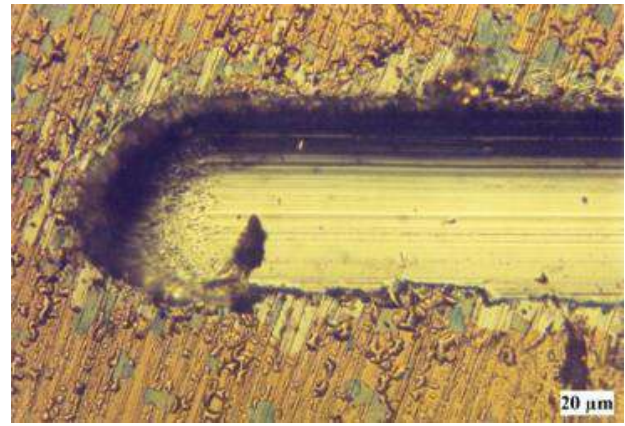
Figure 11. F= 10N, 10 cycles, Distorted material on the trace side
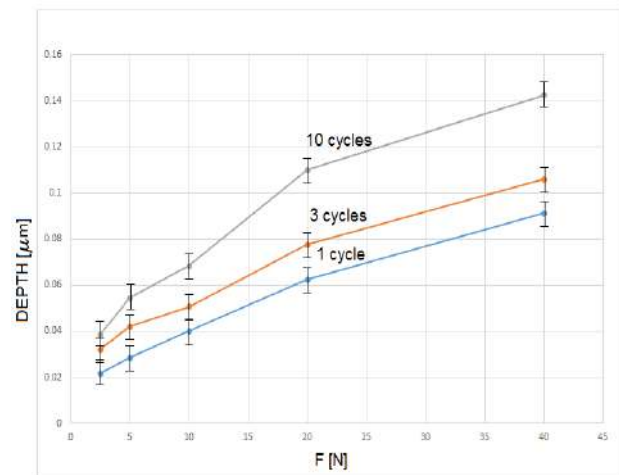
Figure 12. Depth evolution

The variation of the traces depths in relation to the loading and the number of cycles is presented in Figure 12. The reasults confirm the Bucaille and Felder [3].

4. CONCLUSION

The entry of a sliding at the end of the balls line is leading to a migration of the balls in compensation space through rolling lay outs.

It was marked out that the migration of the balls will be joined by an increased wear resistance of the deposited tin layer and of the subsurface work confirming the results obtained by Mezlini[4].

Plastic stress effect are joined by delamination materials, cutting, cracks, increased height of the material on the edges.

It may be observed that at a certain value of the loading delamination appears. This loading is leading to weariness and fretting phenomenon (these will be studied further).

The cracks and semicircular traces appeared at the base of the trace can be associated to a stick-slip phenomenon.

The indentation emerged as a result of the impact accounts to a guidance area towards an existent wear trace for a ball who is migrating and this is softening after multiple cycles.

REFERENCES

[1] V. Florescu, L. Capitanu: An overview on a daring technical ideas: Total Hip Prosthesis with Rolling Friction, LAMBERT Academic Publishing, Germany, ISNN 978-3-659-79776-7.

[2] G.Bergmann, G. Deuretzbracher, M. Heller, F. Graichen, A. Rohlmann, J. Strauss, G.N. Duda: Hip contact forces and gait patterns from routine activities, Journal of Biomechanics, Vol. 34, No. 7, pp. 859-71, 2001.

[3] J.L. Bucaille, E. Felder: L'essai de rayure sur polym`eres et m´etaux, Mat´eriaux et techniques, Vol. 89, No. 3–4, pp. 29–44, 2001.

[4] S. Mezlini, Ph. Kapsa, J.C. Abry, C. Henon, J. Guillemenet: Effect of indenter geometry and relationship between abrasive wear and hardness in early stage of repetitive sliding, 2005, Wear, Vol. 260, No. 2, pp. 412 – 421.

INVESTIGATION OF TRIBOLOGICAL PROPERTIES OF FRICTION PAIRS DURALUMIN – FLUOROPOLYMER USED FOR DESIGN OF PROSTHESES AND EXOSKELETONS

Pavel KOVALENKO[1,*], **Svetlana PEREPELKINA**[1], **Timur KORAKHANOV**[1]
[1]ITMO University, Saint Petersburg, Russian Federation
*Corresponding author: kovalenko_p.p@mail.ru

Abstract: *This paper deals with the processes occurring on the surfaces of materials during the interaction between metal and non-metal parts of prostheses, orthoses and exoskeletons. These mechatronic devices require careful selection of materials for design and manufacturing of their parts taking into consideration not only mechanical properties of the materials, but also their tribological characteristics. Friction pairs duralumin – fluoropolymer and steel 100CrMn6 – fluoropolymer were chosen for the research as the samples. Experimental research was carried out with the use of the universal friction machine MTU-1. For this research, the contact scheme "plane to plane" was used without lubricants. Friction coefficient and the temperature in the contact area versus the runtime were obtained as a result of the experiments. Furthermore, estimation of wear of contacting samples was performed. Analysis of the results allowed us to choose suitable materials for the design of orthoses, prostheses and exoskeletons.*

Keywords: *duralumin – fluoropolymer, friction coefficient, tribological properties, wear, temperature in the contact area, design of prostheses, orthoses, exoskeletons.*

1. INTRODUCTION

Recently, a wide range of various mechatronic devices has been developed for sufficient rehabilitation after injuries or diseases that cause dysfunctions of extremities. These devices, such as orthoses and exoskeletons, could be used for the recovery of lost functions of lower or upper limbs providing the opportunity of everyday training and relearning by reducing energy costs and muscular efforts [1-4]. In case of a lost extremity, a prosthesis could be used in order to improve the quality of life by replacing the missing limb [5]. Exoskeletons could be also used for industrial purposes where it is necessary to decrease the physical load or to enhance the muscular power of workers [6]. Most of these devices are wearable, which means that the weight of such systems plays a significant role and must be taken into consideration during the design. Another important issue related to the design of exoskeletons and orthoses is the choice of power supply. In order to increase the battery life batteries with high capacity might be used. However, this would increase the weight of the device, which makes it uncomfortable for the users and might increase the load on the parts of the system. This could increase friction in the joints of the device and, therefore, wear of the parts.

Requirements for the strength, weight, size and reliability of orthoses, exoskeletons and prostheses lead to the necessity of careful selection of materials for design and manufacturing of their parts. Not only the strength properties of the materials should be taken into consideration, but it is also necessary to consider the tribological properties of the friction pairs, which will increase the lifetime and energy efficiency of the device by reducing wear and friction losses in tribopairs.

2. MATERIALS FOR DESIGN OF ORTHOSES, PROSTHESES AND EXOSKELETONS

Various materials are used for design and manufacturing of mechatronic systems for robotic rehabilitation and assistance, such as stainless steel, alloys, polymers, rubber and fiber [7]. Some of these materials provide the structure with the required hardness, other materials are used for their elasticity and flexibility. All the materials have different tribological properties that have influence on wear and energy efficiency of the system.

Duralumin, stainless steel 100CrMn6 and fluoropolymer were chosen as the materials for this research. These materials could be used for the design of prostheses, orthoses and exoskeletons in order to reduce their weight, friction coefficient in tribopairs and wear of interacting parts.

Duralumin is widely used for design of friction pairs in prostheses, orthoses and exoskeletons due to its properties. First of all, the low weight of the structure reduces the load on the friction pairs, and secondly, duralumin is corrosion resistant, which reduces wear of the tribopair. Also, for duralumin parts it is easy to use a coating consisting, for example, of Al_2O_3 which does not require lubrication and is resistant to contamination.

Fluoropolymer could be used for design of various mechatronic devices because of its low friction coefficient. In addition, fluoropolymer is resistant to chemical influence, radiation and corrosion. Fluoropolymers are also flame-resistant or self-extinguishing when ignited. They are chemically inert to aggressive environment, which allows us to use different kinds of lubricants in friction pairs.

Stainless steel 100CrMn6 could be used for the design of parts of orthoses and exoskeletons that require high hardness and wear resistance.

Two sets of experiments were carried out in order to compare the friction processes in tribopairs fluoropolymer – steel 100CrMn6 and fluoropolymer – duralumin.

3. UNIVERSAL FRICTION MACHINE "MTU-1"

Recently, various measurement machines and methods have been developed for estimation of tribological properties [8, 9]. Another important issue is estimation of geometry and its deviation for the parts of complex shape, because the contact area and, therefore, friction in the tribopairs depend on these parameters [10].

In this paper, a universal friction machine MTU-1 was used for the experimental research of tribological properties of duralumin, steel 100CrMn6 and fluoropolymer (Fig. 1).
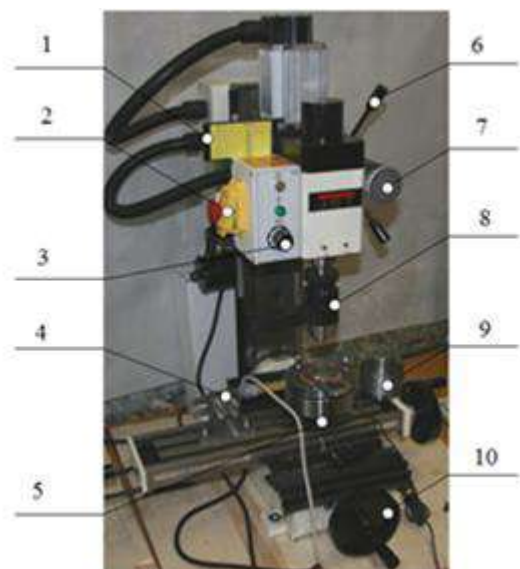

Figure 1. Universal friction machine "MTU-1"

In Figure 1, the following parts of the universal friction machine "MTU-1" are shown: 1 – table of rotation speed; 2 – power button; 3 – speed control button; 4 – friction torque measurement system with the elastic sensing

element; 5 – strain gauge for axial load measurement; 6 – handle for fast loading; 7 – handle for fine loading; 8 – chuck for the upper sample; 9 – lubricant reservoir; 10 – handle for displacement of the coordinate table.

The universal friction machine "MTU-1" is based on a vertical milling machine "JMD-X1" and contains the original friction assembly unit that allows us to save the parallelism of the contacted surfaces. Overall dimensions of the machine allow us to place it on the laboratory bench. The machine is resistant to vibration, electromagnetic interference, dust, humidity and temperature fluctuations.

The testing method for "MTU-1" is based on a relative rotational movement of the upper sample to the lower stationary sample with or without lubricants using different test schemes, such as disc to disk motion, sphere to ring motion, etc. The upper sample rotation speed without the load is adjustable from 0 to 2500 rpm, the pressing force on the samples can be varied from 50 to 1000 N [11].

4. EXPERIMENTAL RESULTS

The first set of experiments was carried out for the tribopairs fluoropolymer – steel 100CrMn6 with the following conditions: rotation speed was 300 rpm, starting load was 120 N. The forces and loads generated in orthoses were estimated by Silva et al. in [12].

In figure 2, the graph of the friction torque versus time for the tribopair fluoropolymer – steel 100CrMn6 is shown.
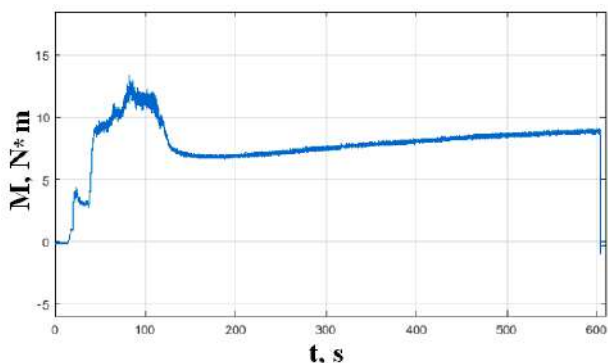
Figure 2. Graph of the friction torque versus time for the tribopair fluoropolymer – steel 100CrMn6

The analysis of the graph in Fig. 2 shows that at the beginning of the experiment the friction torque changed abruptly, which is caused by the beginning of the process of running-in in the tribopair. In Fig. 3 and 4, the graphs of the temperature in the contact area and friction coefficient versus time of the experiment for the tribopair fluoropolymer – steel 100CrMn6 are shown.
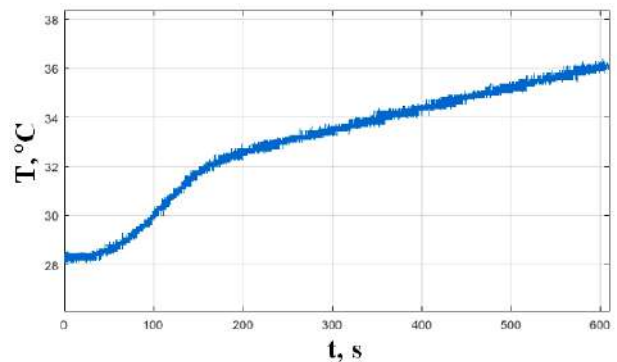

Figure 3. Graph of the temperature in the contact area versus time for the tribopair fluoropolymer – steel 100CrMn6

It could be observed from the graph in Fig. 3 that after approximately 100 seconds from the beginning of the experiment there is an inflection point. Apparently, the inflection point is due to the appearance of the partial reflow of the fluoropolymer surface at this point of time, which indicates the occurrence of a temperature flare at the contact point.
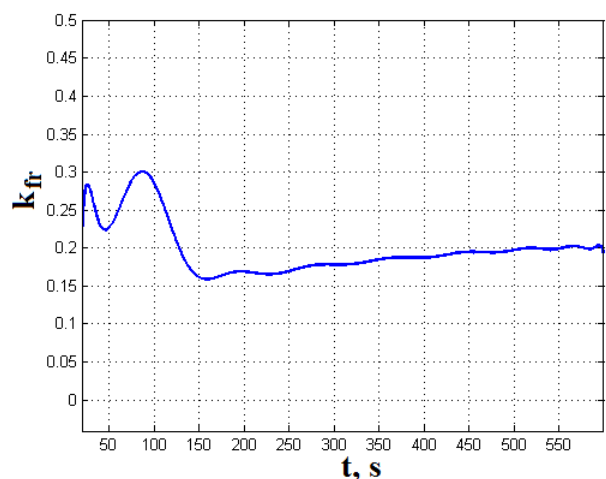

Figure 4. Graph of friction coefficient versus time for the tribopair fluoropolymer – steel 100CrMn6

The graph in Fig. 4 shows that the maximum friction coefficient is 0.3. It is observed during the running-in of the tribopair.

After the running-in, friction coefficient sharply decreases.

Figure 5 shows the photographs of fluoropolymer surface after the experiments. The pictures in Fig. 5 clearly show both the areas of reflow of fluoropolymer and the areas of selective transfer during friction.

It should be noted that the surface of the steel sample has virtually no changes, which is due to both the hardness and wear resistance of the steel.

Figure 5. Photographs of fluoropolymer surface after the experiment (the tribopair fluoropolymer – steel 100CrMn6, magnification is 88x)

The second set of experiments was devoted to the study of tribological properties of the tribopair duralumin – fluoropolymer. Experimental conditions were the following: rotation speed was 300 rpm, starting load was 150 N.

In Fig. 6, the graph of the friction torque versus time for the tribopair duralumin – fluoropolymer is presented. The graph shows that the friction torque remained approximately constant during the experiment, with small fluctuations. This is due to low friction coefficient of fluoropolymer and sufficient viscosity of duralumin.
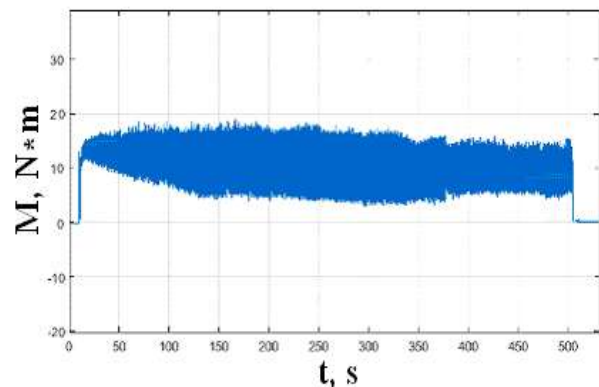
Figure 6. Graph of the friction torque versus time for the tribopair duralumin – fluoropolymer

In Fig. 7 and 8, the graphs of the temperature in the contact area and friction coefficient versus time for the tribopair duralumin – fluoropolymer are shown.
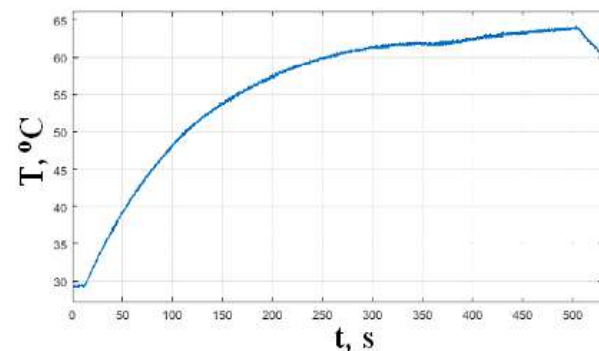

Figure 7. Graph of temperature in the contact area versus time for the trobopair duralumin – fluoropolymer
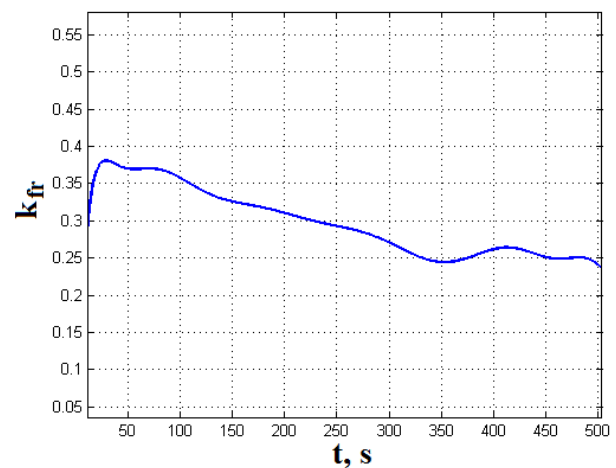

Figure 8. Graph of friction coefficient versus time for the tribopair duralumin – fluoropolymer

It could be observed from the graph in Fig. 7 that the temperature in the contact area gradually increases, which indicates the absence of scuffing in the tribopair.

It could be noticed from the graph in Fig. 8 that friction coefficient smoothly decreases during the experiment. This could be explained by the absence of significant wear on the surfaces of the samples. The maximum value of friction coefficient in this experiment is 0.38.

In Fig. 9, the photograph of the surface of fluoropolymer after the experiment is shown.

Figure 9. The surface of fluoropolymer after the experiment (the tribopair duralumin – fluoropolymer, magnification is 87x)

It could be seen from the photograph in Fig. 9 that there are areas of running-in on the surface, but their quantity and size are not significant.

5. CONCLUSION

The analysis of the results of the experiments shows that the tribopair duralumin – fluoropolymer has lower friction coefficient than the tribopair fluoropolymer – steel 100CrMn6. The friction process in the tribopair duralumin – fluoropolymer is more stable and does not cause abrupt changes of friction coefficient and friction torque. Friction coefficient in the tribopair duralumin - fluoropolymer smoothly decreases after running-in, which makes it possible to predict the behaviour of the tribopair with high accuracy. The results of the research allow us to make a conclusion that the use of the tribopair duralumin –fluoropolymer, especially with a coating on duralumin or with the use of a boundary lubrication, is more convenient and advantageous for design of friction pairs of prostheses, orthoses and exoskeletons.

In future work, it is necessary to define the optimal roughness parameters for contacting surfaces of the parts in order to reduce wear and friction in the tribopairs of exoskeletons, orthoses and prostheses and to increase their energy efficiency.

REFERENCES

[1] G.B. Prange, M.J. Jannink, C.G. Groothuis-Oudshoorn, H.J. Hermens, M.J. Ijzerman: Systematic review of the effect of robot-aided therapy on recovery of the hemiparetic arm after stroke, Journal of Rehabilitation Research and Development, Vol. 43, No. 2, pp. 171-184, 2006.

[2] A. Agrawal, S.K. Banala, S.K. Agrawal, S.A. Binder-Macleod: Design of a two degree-of-freedom ankle-foot orthosis for robotic rehabilitation, in: *Proceedings of IEEE international conference on rehabilitation robotics*, 2005, pp. 41-44.

[3] A. Dollar, H. Herr: Lower extremity exoskeletons and active orthoses: Challenges and state-of-the-art, IEEE Transactions on Robotics, Vol. 24, No. 1, pp. 144-158, 2008.

[4] S. Kim, Y. Son, S. Choi, S. Ham, C. Park: Design of a simple, lightweight, passive-elastic ankle exoskeleton supporting ankle joint stiffness, Review of Scientific Instruments, Vol. 86, No. 9, art. no. 095107, 2015.

[5] L. Resnik, M.R. Meucci, S. Lieberman-Klinger, C. Fantini, D.L. Kelty, R. Disla, N. Sasson: Advanced upper limb prosthetic devices: implications for upper limb prosthetic rehabilitation, Archives of Physical Medicine and Rehabilitation, Vol. 93, pp. 710–717, 2012.

[6] M.P. de Looze, T. Bosch, F. Krause, K.S. Stadler, L.W. O'Sullivan: Exoskeletons for industrial application and their potential effects on physical work load, Ergonomics, Vol. 59, No. 5, pp. 671-681, 2015.

[7] J.E. Sanders, J.M. Greve, S.B. Mitchell, S.G. Zachariah: Material properties of commonly-used interface materials and their static coefficients of friction with skin and socks, Journal of Rehabilitation Research and Development, Vol. 35, No. 2, pp. 161-176, 1998.

[8] V.P. Sel'kin, S.V. Kopylov: Friction machine for testing materials under boundary lubrication, Journal of Friction and Wear, Vol. 37, No. 2, pp. 184-186, 2016.

[9] A.Y. Grigoriev, D.M. Gutsev, A.P. Zozulya, I.N. Kovaliova, V.G. Kudritskii, N.K. Myshkin, M.S. Semenyuk: Reciprocating MTU-2K7 millitribometer, Journal of Friction and Wear, Vol. 35, No. 6, pp. 455-459, 2014.

[10] V.A. Pechenin, M.A. Bolotov, N.V. Ruzanov, M.V. Yanyukina: Optimization of measurements of the geometry of parts with complex surfaces, Measurement Techniques, Vol. 58, Issue 3, pp. 261-268, 2015.

[11] S. Perepelkina, P. Kovalenko, R. Pechenko: Investigation of Tribological Properties of Metallic Materials with the Use of the Universal Friction Machine "MTU-1", Procedia Engineering, Vol. 176, pp. 301-309, 2017.

[12] P.C. Silva, M.T Silva, J.M. Martins: Evaluation of the contact forces developed in the lower limb/orthosis interface for comfort design, Multibody System Dynamics, Vol. 24, No. 3, pp. 367-388, 2010.

BIOMIMETICS DESIGN FOR TRIBOLOGICAL APPLICATIONS

Lozica IVANOVIĆ[1],*, Aleksandar VENCL[2], Blaža STOJANOVIĆ[1], Biljana MARKOVIĆ[3]
[1]University of Kragujevac, Faculty of Engineering, Kragujevac, Serbia
[2]University of Belgrade, Faculty of Mechanical Engineering, Belgrade, Serbia
[3]University of East Sarajevo, Faculty of Mechanical Engineering, East Sarajevo, Bosnia and Herzegovina
*Corresponding author: lozica@kg.ac.rs

Abstract: *Biomimetics, biomimicry and bionics are synonyms for the scientific discipline of creating new structures inspired by nature. Biomimetics systematically analyses the evolutionary processes of living organisms, their structural relationships, the characteristics of natural materials and it studies how this knowledge can be used to create the optimal products and new sustainable materials. In the past decade, the biomimetics has received an incentive for the development by the technology modernization, and above all, by making it possible to study the micro- and nanolevels of biological structures. On the other hand, the miniaturization of technological devices has increased the need to understand the tribological phenomena on micro- and nanolevel, where is a huge potential for technological innovation. The integration of advanced research methods made it possible to discover new aspects in the structure and properties of biological materials and transfer that knowledge into new concepts or products. State-of-the-art of biomimetics progress is discussed, as well as, its goals and the potential to simultaneously achieve the financial and ecological contribution by realization of bio-inspired concepts. An overview of biomimetic researches is also provided, with special emphasis on the possibility of their tribological applications. The characteristic examples have been presented and those examples show how the structural and mechanical properties of the material were used as the basis for developing new creative solutions to solve the problem of friction in engineering applications.*

Keywords: *biomimetics, bionics, biomimicry, tribology, friction, nanotechnology.*

1. INTRODUCTION

Biomimetics is a science that is focused on solving technical problems through studying the imitation of nature's methods, mechanisms and processes [1,2]. It could be also defined as "biologically inspired design or adaptation or derivation from nature" [3]. The term biomimetics in the context of science was first introduced by Otto Schmitt in 1969 [4]. The term Biomimetics is derived from *bios*, meaning life, and *mimesis*, meaning to imitate [5]. The term biomimicry is also used in the literature, as a synonym for the term biomimetics. Janine Benyus in her book *Biomimicry: Innovation Inspired by Nature* defined biomimicry approach through three postulates, i.e. nature as a model, nature as a measure, and nature as a mentor. The nature as a model refers to the study and imitation of models from the nature. The nature as a measure means to apply ecological standards for evaluating the introduced innovations. The nature as a teacher means that we should not focus only on what

we can extract from the natural world, but on what we can learn from it [6].

The development of biomimetics has intensified in the past few decades, primarily due to increased interest of scientists in finding efficient and environmentally friendly technical solutions [7]. The basic principles of green or eco-tribology have been defined and the need for the integration of the specific areas and biomimetics has been emphasized, as well as, the need for their use in sustainable engineering [8].

Historically, the inspiration by models from the nature for solving human problems exists much longer. Man has always been fascinated by the beauty and harmony of the natural forms, as well as, numerous advantages of principles of nature's system functioning. By careful studying and researching the nature, he was revealing the laws of nature, trying to imitate and implement them [2]. Through evolution, nature's solutions are tested by many challenges, resulting either in their disappearance or improvement to the maximum efficiency. Although many of the capabilities of living organisms are still unknown, or are inaccessible in terms of technical performance, there are also those capabilities that have already been adapted or are in the concept stage. One of the first known examples of biomimetic product is the hook-and-loop fastener known under the trade mark Velcro®, patented in 1958 by Swiss engineer George de Mestral inspired by burdock (Arctium) [3,9]. Superhydrophobicity and self-cleaning effect of the lotus leaf surface were used for the development of facade paints under the commercial name Lotusan® [9-12]. The specific hierarchical structure of toe attachment pads of various insects, amphibian and reptiles, such as geckos, frogs or salamanders, have become the subject of the research, because of their biomimetic ability to attach to and move over vertical walls and the ceiling, and wet or even flooded environments without falling [3,13,14]. The adhesive made by Sandcastle worm (Fig. 1) was the inspiration for the development of surgical glue [15,16]. In addition to medical applications, this viscous waterproof material,

which is excreted by Sandcastle worm, can be a basis for the development of novel underwater paints and adhesives [17]. Scientific research of unique design of shark skin, which enables a very fast swim with minimum power consumption, led to the creation of a Riblet surface structure with reduced drag in the turbulent boundary layer [18,19]. Except the effect of drag reduction, shark skin has a feature of self-cleaning from the bacteria, i.e. inhibition of bacteria's attaching, colonizing and forming biofilms. This effect has been used in production of Sharklet™ surface textures [20,21].

Figure 1. Sandcastle worm and its tubular shell

In the past decade, biomimetics showed significant development due to the modernization of technology and above all the possibilities of studying the micro- and nanolevels of biological structures. On the other hand, the miniaturization of technological devices has increased the need for understanding of tribological phenomena at the micro- and nanolevel, which is the huge potential for technological innovation (Fig. 2) [22-25].
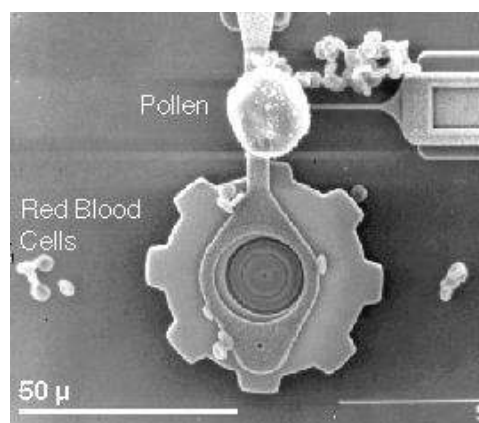

Figure 2. Drive gear chain and linkages [25]

Thanks to a better understanding of fundamental biological principles, biomimetic

research activity has been directed increasingly toward the development of bioinspired materials [26-28]. One idea, which is in the development stage, is to make the geometrical texture of the material with the ability to retain the lubricant in the microgrooves. [18,29].

One of the important goals of biomimetic research is to obtain properties of the material optimized for different functions by applying interdisciplinary and holistic approach. In order to achieve that in the best possible way, it is necessary to apply the methodology of biomimetic design.

2. BIOMIMETIC DESIGN METHODOLOGY

Biomimetic design implies the study of biological processes, their abstraction and implementation in order to optimize the product in the functional and ecological sense. Biomimetics as a scientific discipline should formulate a theory to explain the relationship between nature and technology, and to develop a methodology that will facilitate the design process. In accordance with various aspects of biomimetics, different biologically inspired design methods are defined and described in literature [30,31].

Table 1. Biomimicry design method (adapted from [31])

Phase	Description
Identification of need	Defining the problem, including in-depth analysis of unmet needs, in order to identify what is the problem that must be solved
Selection and sampling	Selection of the samples from nature that fit the problem and current needs
Observation of the sample	Observation and analysis of the components of morphological structures, functions and processes; Sample classification
Analogy of the natural system with the product	Analysis of possibility and validity of the analogy between the studied sample and product design
Design implementation	Implementation of functional, formal and structural analysis of the system

In general, the application of biomimetic design principles can be achieved in one of two ways: by finding solutions to the problem in the nature (Biomimicry design method, Table 1) or by inverse design method, searching for a problem for which a solution already exists in the nature (Bio-solution and the search method of a problem, Table 2).

Table 2. Bio-solution in search of a problem method (adapted from [31])

Phase	Description
Biological solution identification	Observation of the nature in search of potential solutions that could be applied to some existing problem
Defining the biological solution	Identification of components or systems involved in the observed phenomenon, in order to extract a biological solution
Principle extraction	Extraction of basic principle solution from the analysis of biological solution in the schematic notation
Reframing the solution	Reframing solutions in a way that users can see the benefit of biological functions
Problem search	Search may include some new problems, which is a key difference from the problem-driven processes method, i.e. biomimicry design method
Problem definition	Definition of analogy between the system and the components of biological solutions and problems in the schematic notation
Principle application	Realization of bio-inspired solutions in technological product or system

The first approach begins with the identification of problem and then the inspiration for solution of the problem is searched in the nature. The second approach is based on the observation of nature and its structures in order to collect useful information that could be an inspiration for engineering or design solutions.

Significant achievements have been realized in solving many engineering problems

by applying biomimetic design. Among others, many tribological problems have been solved but there are still many challenges and opportunities. So far, mainly surface texturing on the macro-, micro- and nanolevel have been used in solving the problems caused by tribological processes with the application of biomimetic design. The following examples show in more details the application of biomimetic design in solving some tribological problems. Most of the presented problems are associated with the increase/decrease of friction in tribological systems.

3. BIOMIMETIC DESIGN APPLIED IN SOLVING TRIBOLOGICAL PROBLEMS

3.1 Lotus effect

Sacred lotus plant in Asian religions is considered as a symbol for purity because its leaves cannot get wet and dirty, despite constant exposure to dust and rain [10]. After the rain, the drops of water roll-down picking-up all the dirt, and leaves remain dry and clean (Figs. 3a and 3b). A self-cleaning property of lotus leaves was discovered by Wilhelm Barthlott [10], who has extensively researched this complex biological phenomenon and has developed a colour facade StoLotusan® which has a surface microstructure similar to the lotus leaf. A high magnification image shows fine structure on the surface of lotus leaf (Fig. 3c). The area between the asperity peaks is too small for dust particles to reach it, and they stay at the asperity peaks. Similarly surface microstructure is obtained on the facade painted with StoLotusan® (Fig. 3d), providing the same self-cleaning effect (Fig. 3e).

3.2 Biomimetic tires

One of the aims of tire industry is to optimize the energy distribution between tires and road. Tires must fulfil several tasks simultaneously: during driving they should have a low rolling resistance to reduce fuel consumption; during braking they should have a high sliding resistance to shorten stopping

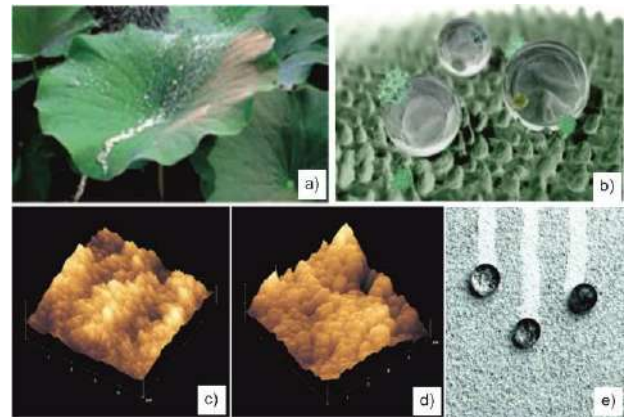distances; they should be durable and to ensure a silent drive.

Figure 3. Lotus effect: (a) lotus leaf, (b) computer graphic of lotus leaf surface, (c) microstructure of lotus leaf surface magnified 7000 times, (d) microstructure on the surface of StoLotusan® magnified 7000 times and (e) self-cleaning effect on paint that makes use of Lotus effect

The model for solving these tasks was found with cheetah, which slowly stalks prey and attains a high speed for a short period of time. During running, the flat paws of cheetah are narrow, so they produce low friction in contact with the ground. This facilitates low energy consumption. On the other hand, during slowing down and changing the running direction, their paws broaden and increase the contact surface with the ground. Therefore, the force is transmitted to the larger surface, which increases stability. Thus, cheetah's paws are optimized for the acceleration, efficient changing of the direction and high stability in curves (Fig. 4) [32].

Figure 4. Biomimetic tires inspired by cheetahs paw: Continental ContiPremiumContact™ summer tire

Applying this evolution strategy, the summer tire Continental ContiPremiumContact™ was obtained. This tyre has the same width as the conventional tire, but it widen during braking, thereby reducing the stopping distance of up to 10 %. This is achieved by appropriate choice of material and the profile of the tire (Fig. 4).

Biomimetic winter tire Continental ContiWinterContact™ TS 780 has a better performance on wet surfaces, the optimal grip and reduced stopping distance. These enhanced features enables the hexagonal tyre pattern (Fig. 5f), which is a replica of the surface structure of the toe pads of specific frog species (Figs. 5c, 5d and 5e): the tree frog (Fig. 5a), which lives on trees and is known for its climbing skills and the torrent frog (Fig. 5b), which is able to climb in wet conditions near waterfalls [33,34]. A V-shaped pattern of tire tread provides a quick evacuation of water from contact zone, thus reducing the risk of aquaplaning [35,36].

3.3 Riblet effect

Riblet effect is inspired by the unique structure of shark skin. Microscopic scales (dermal denticles) allow the water flow through the grooves without whirling and they effectively reduce the drag (Fig. 6a) [3,18]. Many materials applied in naval (Fig. 6b), aircraft and automotive industry are made by technical implementation of the shark skin structure [37].
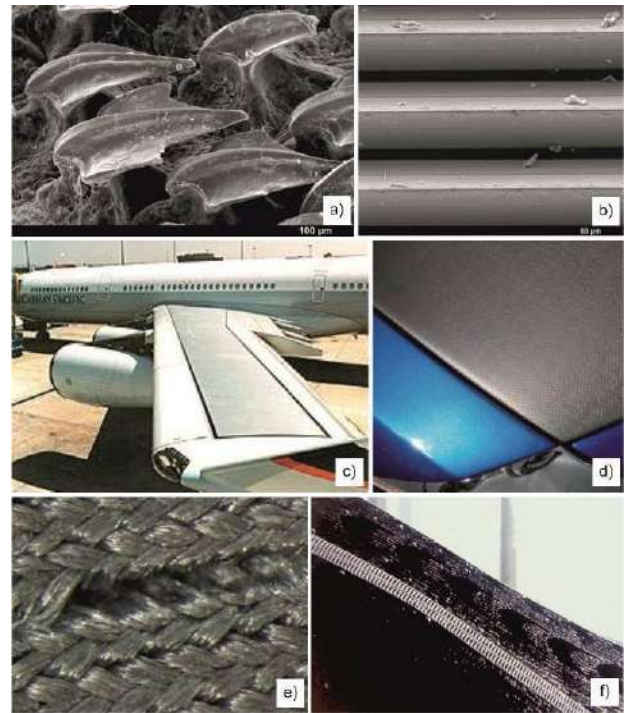
Figure 6. Riblet effect: (a) microscopic image of shark skin morphology, (b) application in naval industry, (c) application in aircraft industry, (d) application in automotive industry, (e) and (f) application in making swimwear
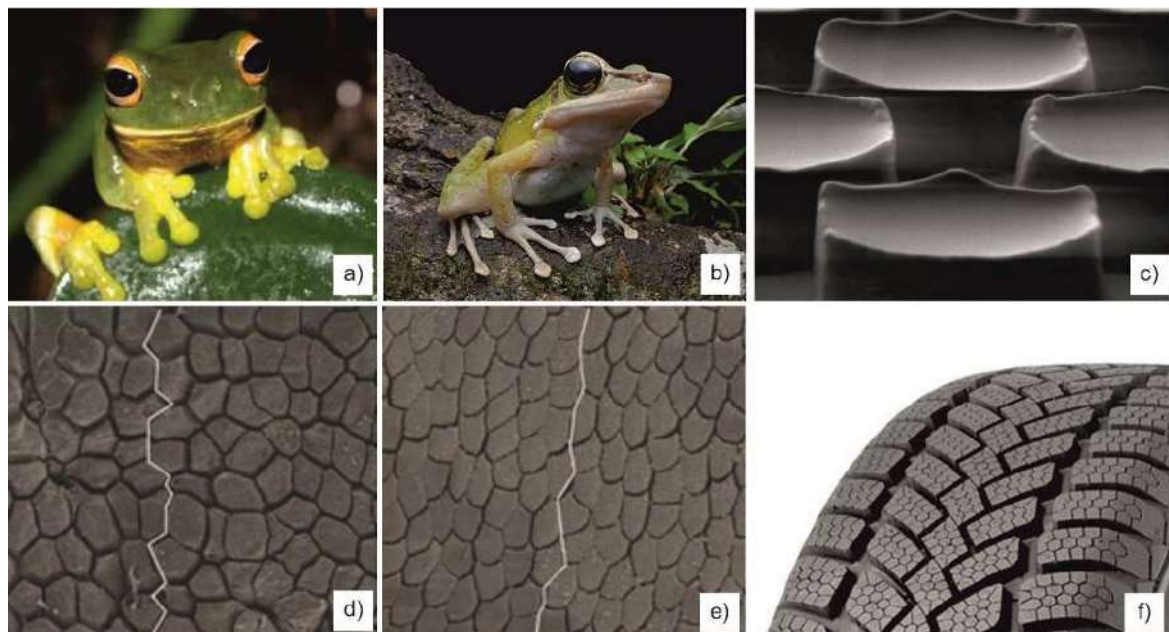
Figure 5. Biomimetic tires inspired by frogs toe pads: (a) tree frog, (b) torrent frog, (c) microscopic surface morphology of tree frogs toe pad, (d) and (e) micrographs of toe pad epithelia in different frog species (white solid lines illustrate shortest routes to the edge of pad) and (f) biomimetic product: Continental Continental ContiWinterContact™ TS 780 winter tire

Riblet effect is indirectly used for the development of the wing skin of Airbus aircrafts (Fig. 6c). The effect of 6 % less air drag was achieved, which leads to significant fuel savings. The new polyurethane composite is developed inspired by the properties of shark skin within the project *FRIMO Street Shark*. The body components, hood and roof of modified car model *BMW Z4* are made of this bionic material (Fig. 6d) [38].

Speedo® also made a bionic swimsuit from the fabric with Riblet effect (Fig. 6e) [3]. On the underwater photography of swimsuits, there are air bubbles "trapped" in the fabric, which allows the swimsuit to stay dry for a longer time (Fig. 6f) [39]. Thanks to the innovative design, the water drag is reduced by 3 % compared to similar products [32]. At the Olympic Games in Beijing in 2008, two-thirds of the swimmers wore Speedo swimsuits, and a large number of world records were broken [3].

3.4 Gecko effect

Geckos are lizards that can easily climb on smooth vertical surfaces and even move along smooth ceilings without falling. The skin on their feet is comprised of a complex hierarchical structure of lamellae, setae (microscale hairs), branches, and spatulae [40]. There are about 1.5 million setae on each toe, that branch off into 100 to 1000 nanoscale spatulae [41]. This provides a large real area of contact and high adhesion with a variety of surfaces (Figs. 7a, 7b and 7c).

Adhesive tape Geckskin™ is made by simulation and modelling of the structure of the gecko toes. This tape sticks due to intermolecular forces between the large number of synthetic fibres and surface (Figs. 7d and 7e). The biomimetic gecko robot *Stickybot* (sticky robot) was made at Stanford University in order to demonstrate the gecko adhesion (Fig. 7f). It has the toe pads of urethane material with tiny bristles whose tops have a thickness of 30 microns, which is enough to keep him on steep surfaces, although gecko foot spatulae is much thinner (approximately 100 to 200 nanometres).
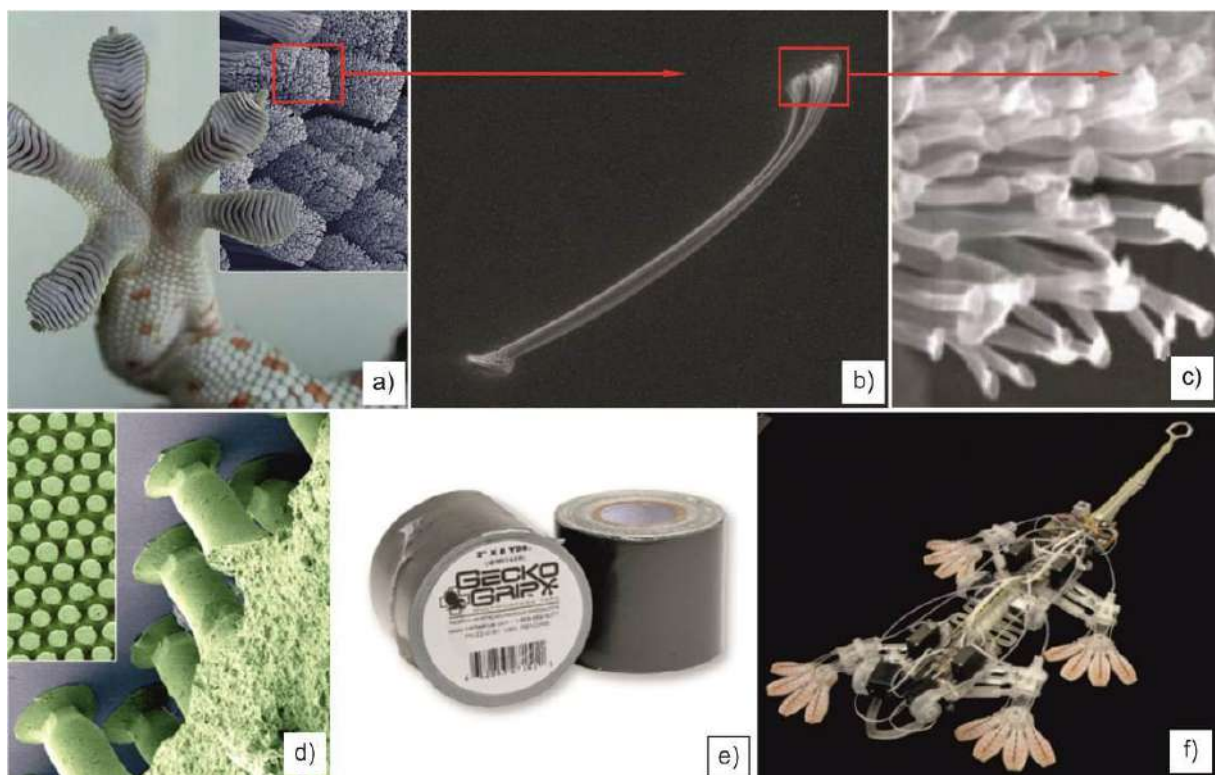

Figure 7. Gecko effect: (a) gecko feet structure with lamellae, (b) gecko foot setae, (c) gecko foot branches and spatulae, (d) millions of synthetic fibres in one square centimetre imitating gecko foot structure, (e) gecko adhesive tape and (f) biomimetic gecko robot *Stickybot*

3.5 Sandfish and snake scaled skin effect

More than 25 years professor Ingo Rechenberg from Berlin has studied the survival mechanisms of certain forms of life in the harsh desert conditions. One interesting example is a lizard *Scincus scincus* (Fig. 8). It is also known as a "sandfish", since it dives into the sand and moves below the surface in a swimming-like motion. It usually goes to the depth of several centimetres, and it can "swim" at a speed of 10 to 30 cm/s [42]. By analysing the scaled skin of this reptile, it was found that it had even smaller coefficient of friction than those of polished steel, flat and smoother glass, PTFE, and high-density nylon surfaces, and showed hardly any sign of wear after it suffered abrasion with sand [43,44].
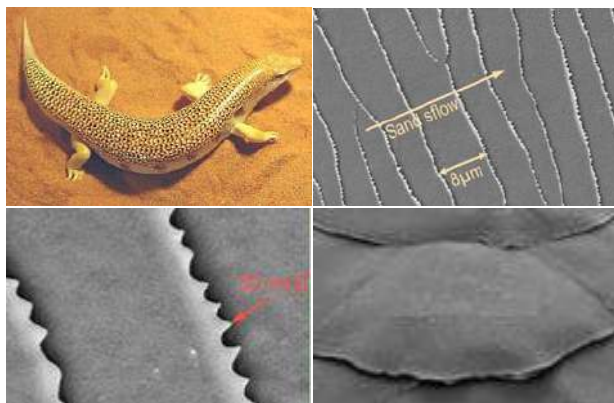
Figure 8. Sandfish (Scincus scincus) and microscopic images of its scaled skin

The shape and arrangement of scales of sand fish skin and certain types of snakes have inspired the scientists from Karlsruhe Institute of Technology to create a similar texture on bearing steel surfaces (Fig. 9), and test them in lubricated and unlubricated conditions [45].
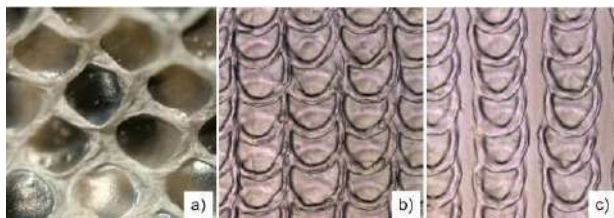
Figure 9. Surface texturing inspired by reptile scaled skin: (a) ball python (Python regius) scaled skin as inspiration, (b) artificial scales with vertically and horizontally overlapping scales and (c) artificial scale with horizontally overlapping scales; adapted from [45]

Two different surface textures were created in order to investigate the influence of scale distances on tribological properties. The first texture imitates scale skin arrangement on the stomach of one kind of a python (Fig. 9a). The artificial scales overlap in both directions, and they are very close to each other (Fig. 9b). The second texture consist of artificial scales arranged in vertical overlapping rows at a greater distance (Fig. 9c), similar to the structure of the sand fish skin (Fig. 8).

Tests in unlubricated sliding conditions have shown that the first texture (ball python) reduced friction by only 22 %, while the second texture (sandfish) reduced friction by more than 40 % in comparison to the untextured surface. On the other hand, for mineral oil lubricated sliding conditions scale-like textures seem not to be favourable, i.e. coefficients of friction were higher by 3 times with the first texture and by 1.6 times with the second texture [45].

The researchers' opinion is that this discovery may help to reduce friction in the nano- and micromechanical devices that can not be lubricated. Potential applications also include the reduction of friction in artificial hips, machines which operate in a vacuum environment, sensors used in anti-lock brake systems of cars, in the operating elements of computer hard drives, etc.

4. CONCLUSION

The development of biomimetics encourages creative product development in various industries. From the initial inspiration with nature, the biomimetics has evolved into a general methodology for innovation. Although the product development process is very complex, from the concept inspired by nature, then its implementation in innovation, to its commercialization, there is a growing interest in the application of biomimetic design methods. At this point, many new ideas and concepts inspired by nature are researched in the academic and industrial research and development centres. One of the reasons is that many of the technological innovations

could not be obtained by a traditional approach to the design. For a successful realization of the creative process, from inspiration by nature to engineering applications, it is first necessary to fully understand the behaviour of biological system, then establish an analogy with the technical problem, and finally realize the product by using modern technology.

This paper gives a broad overview of state-of-the-art of biomimetic research, while the examples developed for tribological applications are presented in more details. It is shown that the biomimetic design improves friction and generally properties of commercial products by applying the combination of unique characteristics of biomaterials, their excellent tribological properties and specific surface structures.

Many potential inspirations from nature for technological innovations is a good reason for more intensive development of biomimetic research.

ACKNOWLEDGEMENT

REFERENCES

[1] Y.H. Cohen, Y. Reich, S. Greenberg: Biomimetics: Structure-function patterns approach, Journal of Mechanical Design, Vol. 136, No. 11, pp. 111108-1-111108-11, 2014.

[2] Y. Bar-Cohen: Biomimetics – using nature to inspire human innovation, Bioinspiration & Biomimetics, Vol. 1, No. 1, pp. P1-P12, 2006.

[3] B. Bhushan: Biomimetics: Lessons from nature – an overview, Philosophical Transactions of the Royal Society A, Vol. 367, No. 1893, pp. 1445-1486, 2009.

[4] J.F.V. Vincent, O.A Bogatyreva, N.R. Bogatyrev, A. Bowyer, A.-K. Pahl: Biomimetics: Its practice and theory, Journal of the Royal Society Interface, Vol. 3, No. 9, pp. 471-482, 2006.

[5] A. Siddaiah, P.L. Menezes: Advances in bio-inspired tribology for engineering applications,

Journal of Bio- and Tribo-Corrosion, Vol. 2, No. 4, Paper 23, 2016.

[6] D.C. Wahl: Bionics vs. biomimicry: From control of nature to sustainable participation in nature, WIT Transactions on Ecology and the Environment, Vol. 87, pp. 289-298, 2006.

[7] I.C. Gebeshuber, P. Gruber, M. Drack: A gaze into the crystal ball: Biomimetics in the year 2059, Proceedings of the Institution of Mechanical Engineers, Part C: Journal of Mechanical Engineering Science, Vol. 223, No. 12, pp. 2899-2918, 2009.

[8] M. Nosonovsky, B. Bhushan: Green tribology: principles, research areas and challenges, Philosophical Transactions of the Royal Society A, Vol. 368, No. 1929, pp. 4677-4694, 2010.

[9] W. Barthlott, M. Mail, B. Bhushan, K. Koch, Plant surfaces: Structures and functions for biomimetic innovations, Nano-Micro Letters, Vol. 9, No. 2, Paper 23, 2017.

[10] W. Barthlott, C. Neinhuis: Purity of the sacred lotus, or escape from contamination in biological surfaces, Planta, Vol. 202, No. 1, pp. 1-8, 1997.

[11] Stolit® Lotusan®, available at: http://www.stocorp.com/sto_products/stolit-lotusan-finish, accessed: 30.03.2017.

[12] X. Wang, B. Ding, J. Yu, M. Wang: Engineering biomimetic superhydrophobic surfaces of electrospun nanomaterials, Nano Today, Vol. 6, No. 5, pp. 510-530, 2011.

[13] T. Liskiewicz, A. Morina, A. Neville: Friction in nature, WIT Transactions on Ecology and the Environment, Vol. 114, pp. 263-272, 2008.

[14] W. Huang, X. Wang: Biomimetic design of elastomer surface pattern for friction control under wet conditions, Bioinspiration & Biomimetics, Vol. 8, No. 4, Paper 046001, 2013.

[15] C.S. Wang, K.K. Svendsen, R.J. Stewart: Morphology of the adhesive system in the Sandcastle worm, *Phragmatopoma californica*, in: J. von Byern, I. Grunwald (Eds.): *Biological Adhesive Systems*, Springer, Wien, pp. 169-179, 2010.

[16] Sandcastle glue, available at: http://www.bioen.utah.edu/faculty/RJS/LabSite12/sandcastle%20glue.html, accessed: 10.02.2017.

[17] R.J. Stewart: Protein-based underwater adhesives and the prospects for their biotechnological production, Applied Microbiology and Biotechnology, Vol. 89, No. 1, pp. 27-33, 2011.

[18] H.A. Abdel-Aal: Functional surfaces for tribological applications: Inspiration and design, Surface Topography: Metrology and Properties, Vol. 4, No. 4, Paper 043001, 2016.

[19] Drag reduction with Riblet surfaces, available at: http://www.bionicsurface.com/en/riblet-surfaces, accessed: 10.02.2017.

[20] A. Sakamoto, Y. Terui, C. Horie, T. Fukui, T. Masuzawa, S. Sugawara, K. Shigeta, T. Shigeta, K. Igarashi, K. Kashiwagi: Antibacterial effects of protruding and recessed shark skin micropatterned surfaces of polyacrylate plate with a shallow groove, FEMS Microbiology Letters, Vol. 361, No. 1, pp. 10-16, 2014.

[21] The discovery of Sharklet, available at: http://sharklet.com/our-technology/sharklet-discovery, accessed: 10.04.2017.

[22] R.A. Singh, D.-C. Pham, J. Kim, S. Yang, E.-S. Yoon: Bio-inspired dual surface modification to improve tribological properties at small-scale, Applied Surface Science, Vol. 255, No. 9, pp. 4821-4828, 2009.

[23] I.C. Gebeshuber, H. Stachelberger, M. Drack: Diatom bionanotribology – biological surfaces in relative motion: Their design, friction, adhesion, lubrication and wear, Journal of Nanoscience and Nanotechnology, Vol. 5, No. 1, pp. 79-87, 2005.

[24] I.C. Gebeshuber, R. Gordon: Bioinspiration for tribological Systems on the micro- and n nanoscale: Dynamic, mechanic, surface and structure related functions, Micro and Nanosystems, Vol. 3, No. 4, pp. 271-276, 2011.

[25] MicroElectroMechanical Systems (MEMS), available at: http://www.sandia.gov/mstc/mems, accessed: 11.02.2017.

[26] F. Barthelat: Biomimetics for next generation materials, Philosophical Transactions of the Royal Society A, Vol. 365, No. 1861, pp. 2907-2919, 2007.

[27] I.C. Gebeshuber, B.Y. Majlis, H. Stachelberger: Tribology in biology: Biomimetic studies across dimensions and across fields, International Journal of Mechanical and Materials Engineering (IJMME), Vol. 4, No. 3, pp. 321-327, 2009.

[28] P. Fratzl: Biomimetic materials research: What can we really learn from nature's structural materials? Journal of the Royal Society Interface, Vol. 4, No. 15, pp. 637-642, 2007.

[29] A. Tsipenyuk, M. Varenberg: Use of biomimetic hexagonal surface texture in friction against lubricated skin, Journal of the Royal Society Interface, Vol. 11, No. 94, Paper 20140113, 2014.

[30] M. Helms, S.S. Vattam, A.K. Goel: Biologically inspired design: Process and products, Design Studies, Vol. 30, No. 5, pp. 606-622, 2009.

[31] C.A.M. Versos, D.A. Coelho: Biologically inspired design: Methods and validation, in: D.A. Coelho (Ed.): Industrial Design – New Frontiers, InTech, Rijeka, pp. 101-120, 2011.

[32] Autoreifen, available at: http://www.bionik-vitrine.de/autoreifen.html, accessed: 10.04.2017.

[33] M. Kappl, F. Kaveh, W.J.P. Barnes: Nanoscale friction and adhesion of tree frog toe pads, Bioinspiration & Biomimetics, Vol. 11, No. 3, Paper 035003, 2016.

[34] B.N.J. Persson: Wet adhesion with application to tree frog adhesive toe pads and tires, Journal of Physics: Condensed Matter, Vol. 19, No. 37, Paper 376110, 2007.

[35] J. Iturri, L. Xue, M. Kappl, L. García-Fernández, W.J.P. Barnes, H.-J. Butt, A. del Campo: Torrent frog-inspired adhesives: Attachment to flooded surfaces, Advanced Functional Materials, Vol. 25, No. 10, pp. 1499-1505, 2015.

[36] T. Endlein, W.J.P. Barnes, D.S. Samuel, N.A. Crawford, A.B. Biaw, U. Grafe: Sticking under wet conditions: The remarkable attachment abilities of the torrent frog, Staurois guttatus, PLoS ONE, Vol. 8, No. 9, Paper 73810, 2013.

[37] Haihaut-effekt, available at: http://www.bionik-vitrine.de/haihaut-effekt.html, accessed: 10.04.2017.

[38] Sharkskin surface, available at: http://www.street-shark.com/en, accessed: 20.02.2017.

[39] R. Sanders, B. Rushall, H. Toussaint, J. Stager, H. Takagi: Bodysuit yourself: But first think about it, American Swimming Magazine, Vol. 5, pp. 23-32, 2001.

[40] R. Ruibal, V. Ernst: The structure of the digital setae of lizards, Journal of Morphology, Vol. 117, No. 3, pp. 271-293, 1965.

[41] B. Bhushan: Gecko effect, in: B. Bhushan (Ed.): Encyclopedia of Nanotechnology, Springer, Dordrecht, pp. 943-951, 2012.

[42] W. Baumgartner, F. Fidler, A. Weth, M. Habbecke, P. Jakob, C. Butenweg, W. Böhme: Investigating the locomotion of the sandfish in desert sand using NMR-imaging, PLoS ONE, Vol. 3, No. 10, Paper 3309, 2008.

[43] W. Baumgartner, F. Saxe, A. Weth, D. Hajas, D. Sigumonrong, J. Emmerlich, M. Singheiser, W. Bohme, J.M. Schneider: The sandfish's skin: Morphology, chemistry and reconstruction, Journal of Bionic Engineering, Vol. 4, No. 1, pp. 1-9, 2007.

[44] M. Shimomura: The new trends in next generation biomimetics material technology: Learning from biodiversity, Science & Technology Trends Quarterly Review, No. 37, pp. 53-75, 2010.

[45] C. Greiner, M. Schäfer: Bio-inspired scale-like surface textures and their tribological properties, Bioinspiration & Biomimetics, Vol. 10, No. 4, Paper 044001, 2015.

TRIBOLOGICAL STUDIES IN CARTILAGINOUS TISSUE OF LAMB SYNOVIAL JOINTS LUBRICATED BY DISTILLED WATER AND INTERSTITIAL-FLUID-LIKE SOLUTION

Fausto MOREIRA-IZURIETA[1,*], Ahmad JABBARZADEH[1]

[1]School of Aerospace, Mechanical and Mechatronic Engineering, The University of Sydney, NSW, Australia

* Corresponding author: fmor7046@uni.sydney.edu.au

Abstract: *This research work, aims to expand the knowledge on how surfaces, as part of human joints, behave. The main factor to be analysed in the experiments embraced on this work is friction coefficient. Friction coefficient becomes vital as it changes along an individual's life; it is directly connected to tear and wear of cartilage tissue due to aging but severely affected by diseases. To get an insight on friction coefficient in human joints, experiments were performed in samples obtained from animal models. The experiment consisted in the measurement of the friction coefficient of the samples harvested from plateau and condyle portions of bones from synovial joints; controlled temperature was set to be 24ºC as the usual environmental temperature, and, 37ºC as the average body temperature. Setup used in the test was a ball-on-three-plates. Two lubrication configurations were set for the experiments: distilled water and a salty solution replicating human's body interstitial fluid. Total joint replacement is a field where tribology plays a vital role; surface interaction in natural motion in joints is characterised for being low-frictional and self-lubricated. The efforts in this study are essentially focused on the pursue of scientific information which leads to improvements for the current treatments, or cures, for diseased joints, before joint replacement to occur, and, moreover, for the cases in which joint replacement is inevitable, to design and construct better prosthetic devices for implants.*

Keywords: *Bio-tribology, synovial joints, friction coefficient, joint lubrication, articular cartilage.*

1. INTRODUCTION

Mechanics in the human body include a series of motion systems, and therefore, surface interactions between its components. Tribology in biological systems (or bio-tribology) embraces concepts in physics, chemistry, biology and material science [1]. Bio-tribology applications in biomedical engineering are from different nature; related examples are: total joint replacements, footwear tribology, skin tribology, ocular and oral tribology, among others [2].

Total joint replacements combine different materials in terms of surface interactions. Products combining metals, ceramics, UHMWPE, and other materials, have been proposed to recreate human joints; hence, surface interactions have a remarkable importance in the preservation of prosthetic devices.

From a biomechanical point of view, the best artificial replacement for any human

natural component is the one that recreates its characteristics as close as possible. The natural surface interactions in joints occur between layers of cartilage that cover the portion of bone structures which participate in motion. In addition, natural lubrication components, such as synovial fluid, are also a relevant part of these mentioned motion systems. Thus, total joint replacement prostheses should aim to replicate a cartilage-cartilage + synovial fluid systems.

1.1 Cartilaginous Tissue

Articular cartilage presents remarkable characteristics referring to fluid adhesion; this fluid adhesion helps lubrication in the joint. Lubrication in articular cartilage occur in two different ways: boundary and synovial lubrication [3]. Boundary lubrication can reach a low friction coefficient but lacks a fluid film of synovial fluid to improve its characteristics; this lubrication happens when slow and cyclic motion takes place [3]. In contrast, fluid film lubrication requires a film of synovial fluid between the moving surfaces which reduces even more the friction coefficient; it is common when cyclic and fast motion happens. Also, in this case, thickness of the lubricating fluid must be bigger than of the roughness of the opposing surfaces [3]. Nonetheless, some authors [4, 5], propose that combination of both mechanisms is the reason for low friction in synovial joints.
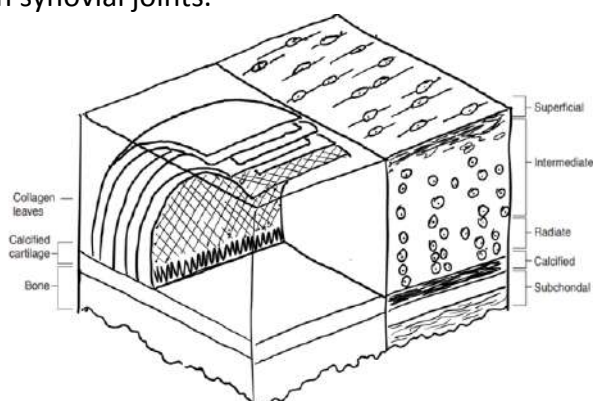
Figure 1. Cut section cut through the thickness of articular cartilage. Adopted from source: Carol A. Oati (2009) Kinesiology: The Mechanics and Pathomechanics of Human Movement, Lippincot Williams & Wilkins, Baltimore.

Unit cell of cartilage found in articulations are known as chondrocytes. They are present in small numbers and composed of several different materials such as proteoglycans, collagen, mainly type II, and others, but specially, 70-80% water [3]. Chondrocytes density, as well as water content and proteoglycan concentration varies along the tissue; closer to the surface, proteoglycan concentration is relatively low and water is high, while near subchondral bone, water is presence is low and proteoglycan is high [3, 6]. Collagen architecture also differs along the tissue [3].

1.2 Synovial Fluid

Synovial fluid is mainly composed of proteoglycan 4 (PRG4), hyaluronic acid (HA) and surface active phospholipids (SAPL); these lubricants are secreted by the chondrocytes in articular cartilage [7]. In a normal synovial joint, the friction coefficient is considered to be low, about 0.001 [8, 3]; to provide a comparison, Teflon has got a 0.04 friction coefficient. Synovial fluid behaviour differs depending on the external conditions, for instance, at high loads it provides poor friction coefficient, whilst, at low loads it has optimal properties [3]. Synovial fluid interaction with articular cartilage is what, specifically, gives joints such optimal motion with low friction coefficient. Studies by James, Fick and Baines, suggest that the hyaluronic acid chains in synovial fluid bind to articular cartilage because of the surface charges existing in the phospholipid layer on top of it [9].

1.3 Synovial Joints

Points where two bones connect are known as joints or articulations. Joints are meant to hold together parts of the body; some are moveable, or diarthroidal, and some are fixed [10]; diarthroidal joints are the ones that enable different sort of movements in the human body. Three main types of moveable joints have been defined for the human body: fibrous, cartilaginous and synovial.

Synovial joints allow full range of motion and several degrees of freedom in a single node. Synovial joints consist not only of interactive cartilaginous surfaces at the end of the bones, but also the presence of a natural lubricant known as synovial fluid [11, 10]. The best example for this type of joints is the knee; the knee is the joint created in the connection of the femur and the fibula. Its shape is conserved through the existence of different tendons and ligaments, among other structures. Specifically, the knee is formed between the condyles from the lower region of the femur and the upper plateau region of the fibula, with an intermediate structure known as the meniscus and protected by the patella, or knee cap [10].

Figure 2. Elements of the knee in motion. Adopted from: Subatra Pal (2014) Design of Artificial Human Joints & Organs, Springer US, New York.

The knee is the element responsible of providing stability and mobility to the whole body. It must be not only capable of supporting almost half of the body weight all the time (43% on each knee) [10].but also the most common and cyclic event of human daily activities, walking. The recommended number of steps per day for an adult is ten thousand [12]. These 10,000 steps also mean a minimum of the same number of cycles daily at each knee. The mechanical load existing when walking and standing is fundamental to stimulate osteoclasteogenesis as well as reducing risk of osteoporosis and other joint diseases [13].

2. METHODOLOGY

Methodology proposed for this research work has two main important components: the first one, involves the selection of an adequate animal model; the second one, refers to the study of the surface properties of cartilage, approached from the overview of the interaction of the participant surfaces during motion, thus, friction coefficient is analysed.

These experiments were performed in samples obtained from the selected animal models. These samples were subject to an adequate preservation protocol. The protocol consisted of collecting the models from a local distributor, immediately after slaughtering; this is, having passed less than 24 hours since the animal passed away. This, supported on the fact that cartilaginous samples last up to 72 hours in the appropriate preservation environment [6]. Also, samples were immediately reposed in a cold vacuum container, at approximately 4ºC, after harvesting; the vacuum container and the cold gel packs used are able to maintain the temperature for as long as two hours, time enough to carry the samples to the laboratory and perform the experiments.

Before the measurement of friction coefficient starts, the samples were reposed in their lubrication medium for. Lubrication mediums to be compared in this research are: distilled water, as a representation of purified water; and, a salty solution, representing interstitial or extracellular-like fluid, with a concentration of 154mM/L NaCl solved in distilled water [14, 15].

2.1 Models required for sample extraction

Animal models for these experiments had to be selected according to a series of factors. It was found that cartilaginous tissue from human beings is similar to most of bovine and equine models [6], however, two features differed widely: layer thickness and chondrocytes density. Firstly, the thickness layer of human cartilage in a healthy knee is of

about 2 mm in thickness, whilst from bovine models it is usually thinner than 1 mm; however, thickness is similar to the tissue found in equine models. Secondly, although cell concentration in cartilaginous tissue, as a non-vascularized tissue, is very low, cell population in human cartilage is broadly higher than what is found in both equine and bovine models. Having said this, results to be obtained from the experiments using samples from animal models for this research work, approximate to what it is expected to be more accurate in studies performed directly in human tissue. From this information, two different scenarios were analysed to select an adequate model for this work.

On one hand, human models' collection for research involve a large amount of ethical concerns and regulatory affairs. Furthermore, availability of these models is short; the type of model required for these experiments must come from a total knee replacement (TKR); when a TKR is performed, cartilaginous tissue is either unhealthy or has almost completely disappeared. Also, the quantity of samples desired to perform all the experiments is large and may involve more than one patient.

On the other hand, animal models for obtaining samples for these experiments, seem to be only partially adequate as they will show an approximate model. Considering that the analysis to be performed is related to surface characteristics, thickness of the tissue can be omitted. Moreover, as the constitution of the extracellular matrix (ECM) in animal models is largely similar the one found in human tissue, and bearing in mind that ECM is the one playing the most important role in friction coefficient, as it is the largest constituent of the tissue. Then, it is justified to utilize an animal model for the analysis of the matters concerning this investigation. Punctually, young adult lamb models (1-2 years old), acquired from a local butchery, were used to obtain the samples for these experiments. Figure 3. shows the whole forequarter shank of a young adult lamb and the two components fundamental for this

research: condyles and plateaus (also, menisci is seen at the bottom).

Cylindrical osteochondral samples were collected; dimensions required were: diameter 6mm, length 6mm (Figure 4). Three of these samples were required for each experiment. None of them was reused to guarantee the results of the experiments. The previously described dimensions were achieved by the construction of a specific tool for harvesting them in such dimensions. Samples were later incubated for 1 hour in the lubrication media to be tested, prior to the experiments.
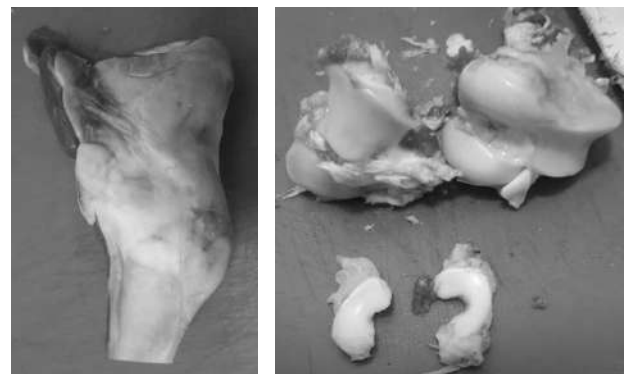

Figure 3. (left) Lamb forequarter shank; (right) forequarter shank divided in parts.

Figure 4. Samples extracted from condyle portion of bone.

2.2 Measurement of friction coefficient in cartilaginous tissue from synovial joints

To describe accurately the friction coefficient from cartilaginous tissue from the involved surfaces from synovial joints during motion, the analysis was focused in the two main cartilaginous surfaces from the participant components: plateaus and condyles. Surfaces in these two sections play an active role when movement takes place in a synovial joint.

Experiments consisted in the measurement of the friction coefficient of the samples harvested from plateau and condyle portions of bones from synovial joints. Measurement of the friction coefficient in the samples were carried on using a MCR302 Tribometer, from Anton Paar, equipped with a Peltier heated tribology cell T-PTD200 and a Peltier Hood H-PTD200 for precise temperature control; temperature was set to be 37ºC as the value for the average body temperature. Setup used in the test was a ball-on-three-plates, as shown in Figure 5. These experiments were partially reproduced with the techniques used and from experiments carried out in [14, 15].

Figure 5. Illustration: Tribological test setup.
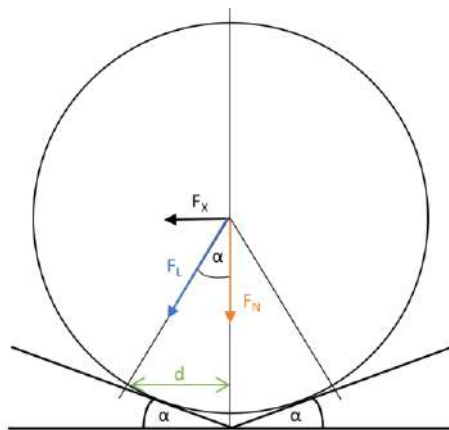
Figure 6. Ball-on-plate friction measurement function principle. Adopted from: Anton Paar (2011). Instruction Manual: Tribology Measuring Cell T-PTD200.

The functional principle of the ball-on-three-plates test involve the application of a normal force in a shaft with a spherical end which presses three faces of a same material. The measuring ball is rotating and the sliding speed of it is calculated. From the torque required to maintain the sliding speed, the frictional force is obtained. Finally, the friction

coefficient results from the relation between the normal load and the friction force [16].

The study of the friction coefficient on both, samples harvested from tibia plateaus and femoral condyles, was carried out under the application of two different normal loads: 10N and 5N; these representing a F_L on each of the three samples due to the force distribution explained below on Figure 6.

Normal force transmitted to the walls of the sample holder, considering it to be solid is:

$$F_L = \frac{F_N}{\cos(\alpha)} \qquad (1)$$

In this case, the force is distributed between three samples, which means:

$$F_L = \frac{F_N}{3 * \cos(\alpha)}$$

And, for the sample holder used, the angle α is equivalent to 45º.

Forces applied to each of the samples, F_L, for each of the main normal forces, F_N, are approximately 6.35 N for a normal force of 10N and 3.18N for a normal force of 5N.

According to the literature [48, 49], under physiological conditions contact pressures for knees vary between 1 − 5 MPa, with peaks that can reach up to four times these values. In the case of in-vitro frictional tests, a pressure of 0.1 − 1 MPa is suitable and are the values commonly used [14, 17, 18].
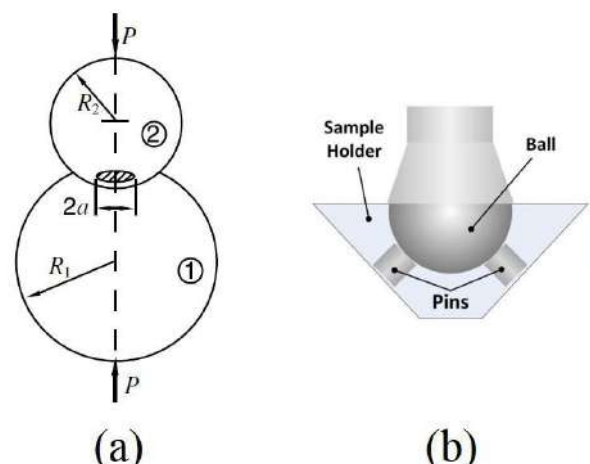

Figure 7. Contact area between two spheres. (a) standard case; (b) ball-on-plates case. Adopted from:
(a) Williams J. and Dwyer-Joyce (2001). Modern Tribology Handbook: Contact between solid surfaces (b) Anton Paar (2015). Application Report: Biotribological Investigation of Cartilage

A partial validation of this experiment can be affirmed by the fact that the normal forces applied achieve the pressure standardized for in-vitro frictional tests. However, this fact needs to be calculated accurately as the contact area in which the pressure exists, is the contact area between a spherical surface, the measurement device, and a flat surface, each of the samples extracted. Although each of the samples was extracted from a certain surface with a defined curvature (plateau or condyle), it can be considered flat, or, a portion of a sphere with infinite radius [19]. Figure 7 describes this accurately, comparing a general case in (a) and the specific case for this experiment in (b).

Contact area between two spheres of radius R_1 and R_2 which are pressed with a force F (P in figure 6), has a resultant contact area radius defined by as a, which results from:

$$a = \left(\frac{3*P*R}{4*E}\right)^{\frac{1}{3}} \qquad (2)$$

Where E is the contact Young's Modulus and is defined by the Young's modulus (E) and Poisson's ratio (v) of each material (glass and cartilage).

$$(3)$$

$$\frac{1}{E} = \frac{1 - v_1^2}{E_1} + \frac{1 - v_2^2}{E_2}$$

Young's modulus for glass is 50 – 90 GPa, while for cartilage it is 0.45 – 0.8 MPa. On the other hand, Poisson's ratio for glass is 0.2 and it is 0.4 for cartilage [3, 20].

$$(4)$$

$$\frac{1}{R} = \frac{1}{R_1} + \frac{1}{R_2}$$

Where the second sphere has an infinite radius R_2 equivalent to a flat surface. Then,

$$\frac{1}{R} = \frac{1}{R_1} \qquad and\ so, \qquad R = R_1$$

The maximum pressure occurs on the axis of symmetry and it is equivalent to 1.5 times the mean pressure P_m.

$$P_{max} = \frac{3}{2} P_m = \frac{3F}{2\pi a^2} \qquad (5)$$

Pressures calculated from forces, which generate a certain radius of contact between the glass ball and cartilage, are within the suggested margin of 0.1 – 1MPa for in-vitro testing of friction coefficient.

Table 1 describes the pressure generated by the different normal forces intended to be used in the friction coefficient experiments.

Table 1. Maximum pressure for different normal forces.

	Force [N]	a [mm]	P_{max} [MPa]
F_N	10	4.463338	0.240
	5	3.542554	0.190
F_L	6.35	3.836345	0.205
	3.18	3.046507	0.165

For each group of samples different experiments were performed, partially replicating the methodology from [45, 46]. Samples from [14, 15] were tested at incrementing speeds of 0.0001 rad/s to 0.1 rad/s with a salty solution (154mM/L NaCl in distilled water) acting as lubrication medium replicating extracellular fluid or interstitial fluid. Specific for this work, samples from each group, plateaus and condyles, were reposed for one hour in two different lubricants: distilled water and extracellular-like fluid.

3. RESULTS

The results obtained for the measurement of friction coefficient in cartilaginous tissue from two different surfaces, both in direct contact during motion, are highly dependent on the protocols followed not only to harvest the samples but also to preserve them.

Following the methodology proposed (for each experiment 600 points were collected), different points of view were emphasized in the results. These different approaches were defined to understand how friction coefficient behaves under different conditions. The lines trailed are: the sort of lubrication medium used; the normal load applied; the origin of the harvested sample; and, other combinations of these conditions that the authors considered relevant.

The first parameter to consider for future analysis of the results obtained is the normal force applied when comparing data obtained from experimentation with the two lubricants proposed.

Figure 8 shows the friction coefficient measured versus the sliding speeds. Compilation of the results from the interaction with the two lubricants are presented. It can be observed that the lubrication with distilled water as well as the salty solution are very close, however, a small statistical difference was found for these two means of lubrication ($p < 0.01$). Figure 9 below shows the same characteristics but when the applied force is equal to 10 [N]. In both cases, the behaviour is similar.
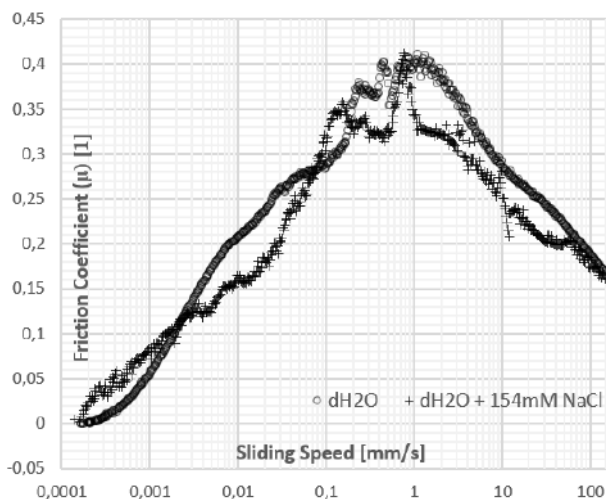
Figure 8. Compiled result for different lubricants interacting with Plateau samples with a 5 [N] normal force.
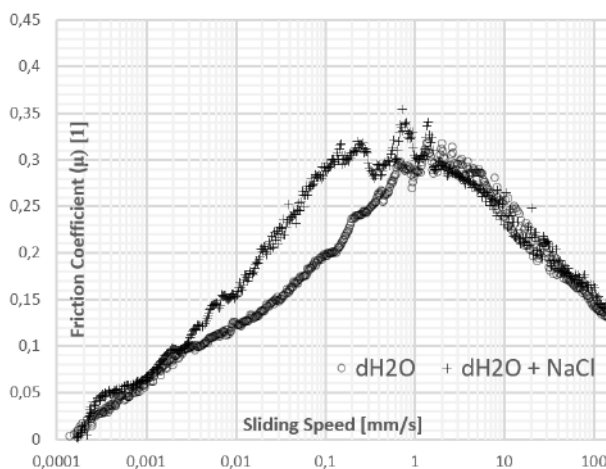
Figure 9. Compiled result for different lubricants interacting with Plateau samples with a 10 [N] normal force.

The next two figures (10 and 11) illustrates the data collected from the measurements for acting normal forces of 5 and 10 [N], respectively, for the two lubricants interacting with harvested samples from condyle sections. In this case first case, 5[N], no significant difference was found between distilled water and salty solution. On the other hand, for 10[N], statistical difference between distilled water and salty solution exists; even though it happens, it stays close to the limits (for $p<0.01$).
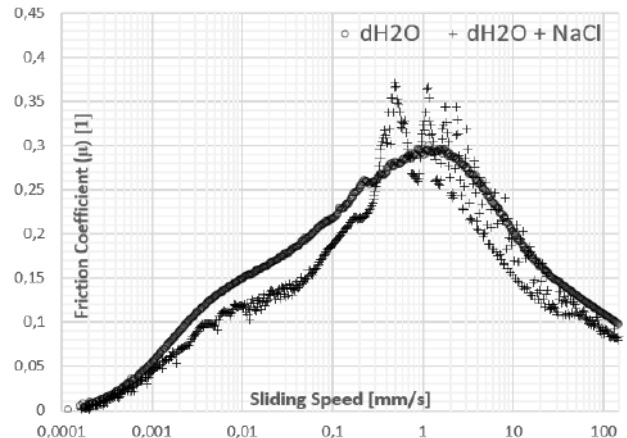
Figure 10. Compiled result for different lubricants interacting with Condyle samples with a 5 [N] normal force.
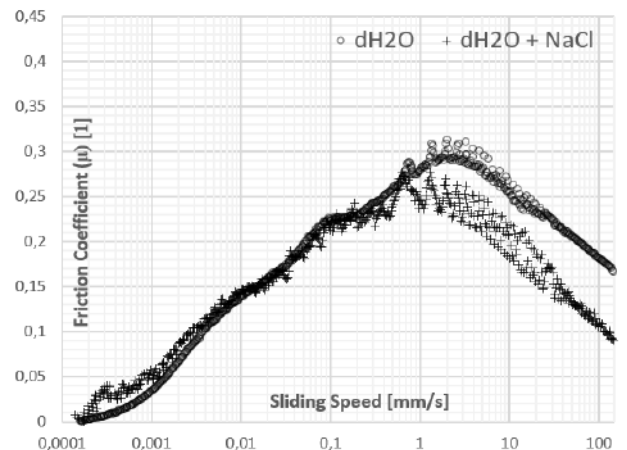
Figure 11. Compiled result for different lubricants interacting with Condyle samples with a 10 [N] normal force.

Average friction coefficient collected from the experiments for all the different cases is presented in table 2 below. Loading at 5 [N], as expected, generated lower friction coefficient. Friction coefficient from both, condyle and plateau samples, seem to be very close, however, results obtained from measurements in plateaus appear to be slightly smaller.

Table 2. Overall compilation of friction coefficient results.

μ - Friction Coefficient - 37ºC				
Normal Force [N]	Plateau		Condyle	
	dH2O	dH2O + NaCl	dH2O	dH2O + NaCl
5 [N]	0.2324	0.2113	0.1670	0.1500
10 [N]	0.1724	0.1983	0.1776	0.1578

To create a context, data collected from the measurements has been organized in ranges, according to the information available in work by Covert et. al. [57], where, sliding speeds in a healthy knee when performing common activities, were defined. Table 3 shows results from 5 [N] loading conditions and table 4 results for 10 [N] loading conditions.

Table 3. Sliding speeds and average friction coefficients associated to common activities. 5 [N] normal force.

μ - Friction Coefficient - 5 [N] - 37ºC				
Activity	Plateau		Condyle	
	dH2O	dH2O +NaCl	dH2O	dH2O +NaCl
Steady (0-1 [mm/s])	0.2014	0.1897	0.1498	0.1325
Walking (1-50 [mm/s])	0.3129	0.2677	0.2215	0.2054
Jogging (51-100 [mm/s])	0.2049	0.1923	0.1195	0.1014
Running (101-150 [mm/s])	0.1756	0.1683	0.1018	0.0844

Table 4. Sliding speeds and average friction coefficients associated to common activities. 10 [N] normal force.

μ - Friction Coefficient - 10 [N] - 37ºC				
Activity	Plateau		Condyle	
	dH2O	dH2O +NaCl	dH2O	dH2O +NaCl
Steady (0-1 [mm/s])	0.1386	0.1790	0.1381	0.1417
Walking (1-50 [mm/s])	0.2541	0.2525	0.2629	0.2072
Jogging (51-100 [mm/s])	0.1602	0.1698	0.1940	0.1206
Running (101-150 [mm/s])	0.1345	0.1461	0.1730	0.0982

4. DISCUSSION

Comprehension of the tribological behaviour of articular cartilage is important not only for those who suffer osteoarthritis, rheumatoid arthritis or have suffered severe traumatic injuries in joints, it is also important for those who are healthy and can been adequately advised, but, furthermore, it has also outstanding importance for those who have lost the battle to these illnesses and have had to undergo through a total joint replacement.

To obtain good quality results, the protocols established for collection and preservation of all the samples harvested are fundamental; even though cartilaginous tissue lacks vascularization, its preservation, in the adequate environment, would only guarantee the quality of the samples for 72 hours [6]. Another important factor to control the experiments results was having samples from young adult lamb (12 months old) to discard possible existent medical conditions that are not common to occur in young models.

Harvesting the samples has also a great importance in the protocol as, immediate damage could be induced if the selected tool touched the sample surface (surface of analysis); also, heating of the tool can induce dehydration of the sample, reducing its time of life, or even osteonecrosis, which may result in total damage and discard of the sample.

Sample required for the friction coefficient tests, needed to be cylindrical (6 mm in diameter and length), the extraction procedure followed was similar to the one used in osteochondral allograft transplantation, which mainly consists on the extraction of damaged cartilage portions for later replacement of them with the same patient's healthy cartilage extracted from a different location [10]. A tool for extraction of samples on the dimensions required was designed and constructed in stainless steel and samples were extracted by drilling through to areas of the bone: plateaus and condyles.

Different from similar experiments in the area [14], the current work studied samples

from two portions of the bone, plateaus and condyles. The reason for this is that they both participate actively in motion, but their geometry and function is different; tissue from cartilage involved in motion should not be considered to be the same in all areas. Similar to [14], lubrication means used to evaluate friction coefficient in the two mentioned bone sections: distilled water (dH2O), for a general friction coefficient approach, and, a salty solution (dH2O+154mM NaCl), mimicking the interstitial fluid found in human body.

Friction coefficient was also evaluated under the application of different normal loads; these loads in accordance to what the literature recommends for in vitro testing of friction coefficient which states that the normal load applied should generate a pressure of 0.1 – 1.5 [MPa] [14, 18, 17]. The frame of sliding speed at which the friction coefficient was done started at 0.0001 [mm/s], or 0.000350 rpm, and was increased up to 150 [mm/s], or 350 rpm, in a speed ramp of 1 second. Reasons for the selection of this speed is that, any lower sliding speed, cannot be controlled and would be considered static friction coefficient [14], and, speeds of between 1 and 150 [mm/s] represent common sliding speeds from walking to fast running [21, 22].

Results from friction coefficient measurements (table 2) indicated that in plateau portions in average for 5 [N] was of about 0.2 for distilled water and salty solution, similar to what is observed for 10 [N]. For condyle portions with a 5 [N] normal force, friction coefficient was, in average, 0.15 for distilled water and salty solution, similar results were obtained when a 10 [N] force was applied. No significant difference was found between friction coefficients measured at 5 [N] and 10 [N] for each lubrication medium. On the other hand, differences were significant when comparing the results obtained in plateau sections to the ones obtained in condyle sections; condyle sections tend to have a slightly smaller friction coefficient, this can be justified by the fact that condyle has got a thicker layer of cartilage [23].

It is important to remark some important differences in behaviour under diverse experiment conditions. It can be observed in all the figures that the friction coefficient increases up to a certain point and the immediately decreases. Reason for this to happen is that the cartilage starts swelling a certain amount of water in a certain time frame, after it is fully filled, the lubrication is improved; this behaviour varies depending on the load conditions, as well as, the lubricant.

When the lubrication media was simply distilled water, friction coefficient for a normal load of 5 [N] was smaller for condyle than for plateau. The reason for this to happen could be, firstly, that distilled water is nothing else than purified water which has a neutral electrostatic charge, and, secondly, that condyle cartilage layer is thicker than the one in plateau portions, and so, it is capable of swelling more water; supporting this fact, when the normal load is increased, the friction coefficient in plateau reduces almost down to the level of condyle, as there is more pressure, the water is forced into the ECM of plateau cartilage. Lubrication, then, occurs in a totally different way when the salty solution (ionized water), as the surface charges from the cartilaginous tissue, negatively charged [12], repel the charges from these lubricants, reducing the swelling ratio, but improving friction coefficient behaviour. Higher swelling ratio was observed in the experiments with distilled water, in some of them, the water applied on top of the sample holder was completely swelled by the tissue and, of course, increased heat and damaged surfaces were observed; when using salty solution swelling was evident but not as noticeable. In summary, surface charges may affect the interaction with different lubrication mediums.

Willing to place friction coefficient in context, tables 3 and 4, show the predicted friction coefficient for common activities like walking, running and jogging, all these having in consideration the sliding speeds previously described. From these results, it can be stated that, as the synovial fluid is a well-known non-Newtonian fluid [7], its behaviour varies under

the application of different loads. Connecting this last to the results from tables 3 and 4, synovial fluid, does not make a difference in friction coefficient when at low cyclic loads, thus, distilled water and interstitial-like fluid, widely present in the absence of synovial fluid when infection of inflammation occurs. In contrast, for high cyclic loads distilled water and the salty solution used in these experiments, do not prevent cartilage degradation as synovial fluid does. This happens in a similar way under different loads and in both, condyle and plateau, portions.

5. CONCLUSION AND FUTURE WORK

Reliable results from experimentation with biological samples depends on the protocols followed. A cartilage sample, for instance, can only be preserved for 72 hours. Protocols should aim to maintain the natural body environmental conditions to preserve samples. For sample harvesting, heat and stress from the tool should be controlled to avoid affections on the sample structures; heat on tools can lead to dehydration and osteonecrosis of the osteochondral samples.

Friction coefficient measured from different parts of the bone presented different results. Average friction coefficient for plateau portions is of 0.2 for distilled water and interstitial-like fluid. Average friction coefficient for condyle portions was of about 0.16 for both cases. Results did not vary significantly when different loads were applied. Friction coefficient tends to be lower in the condyle portions of bone, perhaps, because of the greater thickness of the cartilage layer, if compared to plateau portions.

Future work should aim to compare these two proposed lubricants with natural synovial fluid or an artificial substitution.

REFERENCES

[1] I. C. Gebeshuber: Biotribology inspires new technologies, Nano Today, Vol. 2, No. 5, pp. 30-37, 2007.

[2] D. Dowson: Bio-tribology, *The Royal Society of Chemistry,* Vol. 156, No. 1, pp. 9-30, 2012.

[3] J. M. Mansour: Biomechanics of Cartilage, in : *Kinesiology: The mechanic & pathomechanics of human movement*, Baltimore, Lippincott Williams & Wilkin, pp. 66-79, 2009.

[4] E. Radin, P. IL: A consolidated concept of joint lubrication, J Bone Joint Surg, Vol. 54-A, No. 1, pp. 607-616, 1972.

[5] E. Radin, I. Paul, D. Pollock: Animal joint behavior under excessive loading, Nature*,* Vol. 226, No. 1, pp. 554-555, 1970.

[6] C. Little, Interviewee, Personal discussion about cartilage characteristics. [Interview]. 7 October 2015.

[7] M. Blewis, G. Nugent-Derfus, T. Schmidt, B. Schumacher, R. Sah: A model of synovial fluid lubricant composition in normal and injured joints, Eur Cell Mater*,* Vol. 13, No. 1, pp. 26-39, 2007.

[8] S. Pal: *Design of Artificial Human Joints and Organs*, Springer, New York, 2014.

[9] D. James, G. Fick, W. Baines: A mechanism to explain physiological lubrication, *J Biomech Eng,* Vol. 132, No. 7, pp. 1-6, 2010.

[10] J. A. McGeough: Engineering of Human Joint Replacements, John Wiley & Sons New York, 2013.

[11] M. Kent: The Oxford Dictionary of Sports Science & Medicine, Oxford University Press, Oxford, 2007.

[12] 10,000 Steps Australia, Why 10000 steps a day, Walking with Attitude, Available: http://www.10000stepsaustralia.com/Walking-Articles/Why-10000-Steps-a-Day, accessed: 17.10. 2015.

[13] M. Yavropoulou and J. Yovos: Osteoclastogenesis--current knowledge and future perspectives, J Musculoskelet Neuronal Interact. *,* Vol. 8, No. 3, pp. 204-16, 2008.

[14] A. Paar: Application Report: Biotribological Investigation of Cartilage.," Anton Paar GmbH, Graz, AUSTRIA, 2015.

[15] Anton Paar: Application Report: Advanced Tribological Charactrerization of Limiting Friction of Greases, Anton Paar GmbH, Graz, AUSTRIA, 2015.

[16] A. Paar: The Tribology Measuring Cell - An Overview, in: *Antoon Paar Tribometry*, Anton

Paar GmbH, pp. 12-15, 2015.

[17] J. Katta, S. Pawaskar, Z. Jin, E. Ingham, J. Fisher: Effect of load variation on the friction properties of articular cartilage, in: *Proceedings of the Institution of Mechanical Engineers, Part J: Journal of Engineering Tribology,* 01.03.2017*.,* Sheffield University, UK, pp. 175-181, 2007.

[18] S. Chan, C. Neu, K. Komvopoulos y A. Reddi: The role of lubricant entrapment at biological interfaces: Reduction of friction and adhesion in articular cartilage, *Journal of Biomechanics,* Vol. 44, No. 11, pp. 2015-2020, 2011.

[19] J. A. Williams, R. S. Dwyer-Joyce: Contact Between Solid Surfaces, in: *Modern Tribology Handbook, Columbus*, CRC Press LLC, Ohio, pp. 121- 2001.

[20] T. E. ToolBox: The Engineering ToolBox, available: http://www.engineeringtoolbox.com/ , accessed 28.04.2016.

[21] J. Dumbleton: *Tribology on Natural and Artificial Joints*, New York: Elsevier, 1981.

[22] R. Covert, R. Ott y D. Ku: Friction characteristics of a potential articular cartilage biomaterial, Wear, Vol. 255, No. 1, pp. 1064-1068, 2003.

[23] D. Knudson: *Fundamental of Biomechanics*, Springer, New York, 2007.

Trenje, habanje i podmazivanje

15th International Conference on Tribology – SERBIATRIB '17

17 – 19 May 2017, Kragujevac, Serbia

UTICAJ FAKTORA PROCESA OBRADE NA TRIBOLOŠKE KARAKTERISTIKE PREVLAKA HROMA

Desimir JOVANOVIĆ[1], Bogdan NEDIĆ[2], Predrag JANKOVIĆ[3], Bratislav TRIFUNOVIĆ[1]

[1]Zastava oružje, Kragujevac, Srbija, tehnologija@zastava-arms.rs
[2]Fakultet inženjerskih nauka, Kragujevac, Srbija, nedic@kg.ac.rs
[3]Mašinski fakultet, Niš, Srbija, jape@masfak.ni.ac.rs

Abstract: Elektrolitčke prevlake hroma imaju široku i raznovrsnu primenu, što je uslovljeno karakterističnim osobinama ovih prevlaka. Nanose se da bi površina osnovnog materijala dobila odgovarajuća svojstva, kao što su: otpornost prema habanju, hemijska postojanost, potreban estetski utisak i dr. Ispitivanja galvanskih prevlaka hroma usmerena su najčešće na vezu prevlake sa osnovnim materijalom, dok je veoma malo podataka o uticaju faktora procesa obrade podloge za taloženje na karakteristike prevlaka. Prevlake hroma su taložene na čeličnu podlogu iz hromatno-sulfatnog elektrolita. Za ispitivanje galvanskih prevlaka hroma postavljen je model programiranog taloženja u sistemu planparalelnih ploča. Projektovan je program taloženja hroma jednosmernom strujom. Računarskom tehnikom praćen je i regulisan proces taloženja prevlake hroma, vrednost parametara na početku i tokom procesa. U radu su prikazani rezultati istraživanja uticaja faktora procesa obrade na tribološke karakteristike prevlake hroma taloženih u programiranom režimu jednosmerne struje.

Keywords: galvanske prevlake hroma, tribologija, hrapavost

1. UVOD

Stvaranje metalnih elektrolitičkih prevlaka na površini drugog metala ima dvostruku ulogu: zaštitu od korozije i promenu karakteristika površine metala, kao što su tvrdoća, električna provodljivost, dekoracija itd.

Tvrde prevlake hroma imaju primenu kod proizvodnje različitih alata, mašinskih delova, u industriji naoružanja i sl. U zavisnosti od karakteristika materijala, postojanja ili ne međusloja, funkcije elemenata i dr., debljina prevlaka hroma može biti od 0.5 do 500 μm [9].

Uticaj faktora procesa obrade i taloženja prevlaka, odnosno tehnološkog nasleđa, je veoma malo istraživan. Površinski slojevi obrađenih površina dobijenih različitim postupcima i režimima obrade mogu imati različitu struk-

turu, što se tek u periodu eksploatacije može ispoljiti. Osnovni parametri koji se nasleđuju kroz tehnološki proces izrade mogu se podeliti na dve grupe. S jedne strane to su parametri vezani za svojstva materijala: sastav, struktura, naponsko stanje i dr., dok su sa druge strane parametri vezani za makro i mikrogeometriju površina (geometrijski parametri), otpornost na koroziju i habanje i dr. [1, 2]. To ukazuje na kompleksnost problema i potrebu izučavanja.

U zavisnosti od odabranog režima taloženja (gustine struje i sastava i temperature elektrolita) pri taloženju hroma jednosmernom strujom menjaju se osobine prevlaka (sjaj, otpornost na habanje i koroziju, tvrdoća, unutrašnja naprezanja u prevlaci, defekti na površini prevlake). Isto tako pri taloženju hroma jednosmernom strujom javlja se problem kod prekida struje u procesu

taloženja, zbog pasivnosti površine hroma. Gotovo je nemoguće istaložiti drugi sloj hroma sa zadovoljavajućim prianjanjem za sloj istaložen pre prekida procesa [3, 8].

2. EKSPERIMENTALNA ISPITIVANJA

Kao podloga za nanošenje prevlaka odabran je čelik Č5730 (prema GOST-u 30HN2FA 1). Uzorci za ispitivanje su pločice dimenzija 6,3x15x10 mm (prema ASTM G 77). Posle izrade uzoraka glodanjem, izvršena je termička obrada poboljšanjem na odgovarajuću tvrdoću. Završna obrada uzoraka vršena je brušenjem sa više režima i poliranjem. Na ovaj način su dobijene različite karakteristike površinskog sloja i različite topografije površina uzoraka, tabela 1.

Tabela 1. Karakteristike uzoraka pre hromiranja

uzorak	vrsta obrade	Ra, μm	program taloženja
1	Brušenje, režim A4	0.970	1
2	Brušenje, režim A4	1.330	4
3	Brušenje, režim A3	1.230	2
4	Brušenje, režim A3	0.940	3
5	Brušenje, režim A2	0.990	4
6	Brušenje, režim A1	0.850	1
7	Poliranje	0.690	3
8	Poliranje	0.457	2

Prevlake hroma su taložene u programiranom režimu rada jednosmernom strujom, po zadatom planu eksperimenta (tabela 2).

Tabela 2. Parametri taloženja prevlaka

Parametri elektrolize	Programi taloženja			
	1	2	3	4
Gustina struje taloženja [A dm^{-2}]	30	30	60	60
Struja taloženja [A]	2	2	3.8	3.8
Vreme taloženja [h]	3	6	3	6
Radna temperatura taloženja je 55 ±1ºC				

U toku procesa taloženja, parametri jednosmerne struje su kontrolisani i regulisani u zadatim granicama. Korišćene anode su napravljene od olova sa 10 % antimona.

Na slikama 1 i 2, prikazani su izgledi uzoraka pre i posle nanošenja prevlaka. Ispitivanje prevlaka hroma vršena su na tribometru TR-95 sa kontaktom blok-on-disk u Laboratoriji za obradu metala rezanjem i tribologiju, Fakulteta inženjerskih nauka Univerziteta u Kragujevcu, slika 3. Tribometar TR-95 omogućava variranje uslova kontakta sa aspekta oblika, dimenzija i materijala kontaktnih elemenata, normalnog kontaktnog opterećenja i brzine klizanja. Ispitivanja se mogu vršiti u uslovima sa podmazivanjem i bez podmazivanja.

a - pre nanošenja prevlake

b- posle nanošenja prevlake

Slika 1. Uzorak broj 5, brušena podloga
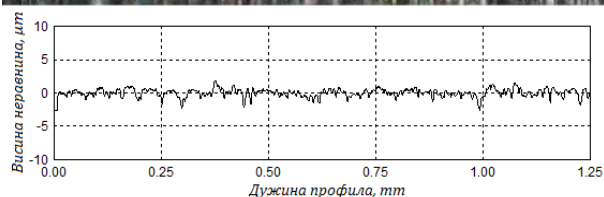
a - pre nanošenja prevlake

b- posle nanošenja prevlake

Slika 2. Uzorak broj 8, polirana podloga

Razvoj procesa habanja na bloku manifestuje se formiranjem i širenjem izraženog traga habanja. Početni nominalni linijski kontakt između diska i bloka usled razvoja procesa habanja postaje kontakt po određenoj površini, što kao posledicu ima razaranje materijala, najpre u površinskom sloju bloka. Promena širine traga habanja ima isti karakter za sve ispitivane uzorke samo je razlika u nivou njihove pohabanosti.

Parametri ispitivanja:

- Normalno opterećenje   10 N,
- brzine klizanja 0,25 m/s,
- Ukupan put klizanja 500 m.

Realizovana ispitivanja su bila sa graničnim podmazivanjem sa mineralnim uljem Hidrovisk HD 46 zbog velikog koeficijenta trenja u slučaju trenja bez podmazivanja i velikih vibracija u sistemu merenja sile trenja kod tribometra TR-95.
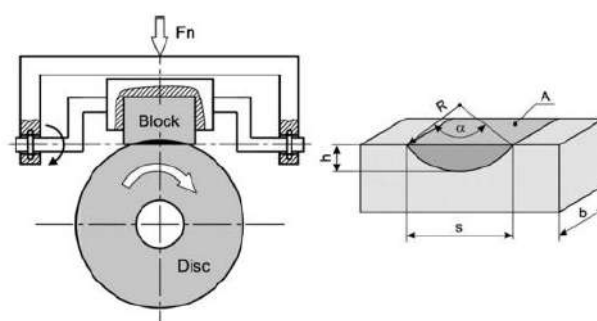
Slika 3. Trag habanja na bloku

U tabeli 3, prikazane su karakteristike ispitivanih prevlaka i ispitivanjem dobijene vrednosti koeficijenta trenja i širine traga habanja. Koeficijent trenja je srednja vrednost nakon uhodavanja posle 500 metara puta.

Tabela 3. Karakteristike prevlaka hroma

Uzorak	debljina δ, μm	Ra, μm	μ	trag habanja h, mm
1	22.48	1.242	0.76	1.395
2	88.90	1.880	0.86	1.260
3	34.00	1.600	0.80	1.323
4	39.70	1.390	0.82	1.260
5	88.90	1.368	0.86	1.240
6	24.76	0.870	0.73	1.360
7	39.10	0.870	0.84	1.275
8	33.86	0.600	0.78	1.350

Primeri signala koeficijenta trenja ispitivanih uzoraka sa prevlakama hroma taloženim na podlogama dobijenim različitom završnom obradom prikazani su na slici 4.

Paralelno sa praćenjem promene koeficijenta trenja praćen je i proces habanja bloka u uslovima trenja sa podmazivanjem. Kao para-

metar habanja korišćena je širina traga haba-nja na kontaktnoj površini ispitivanog bloka.
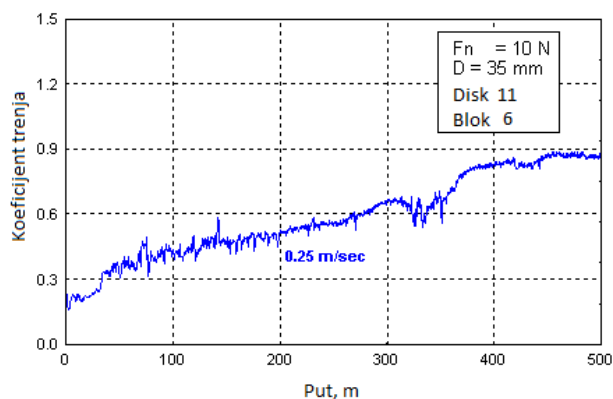
a) fino brušena površina
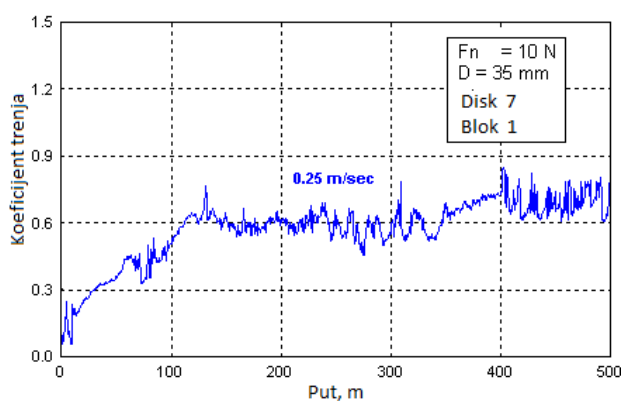
b) grubo brušena površina
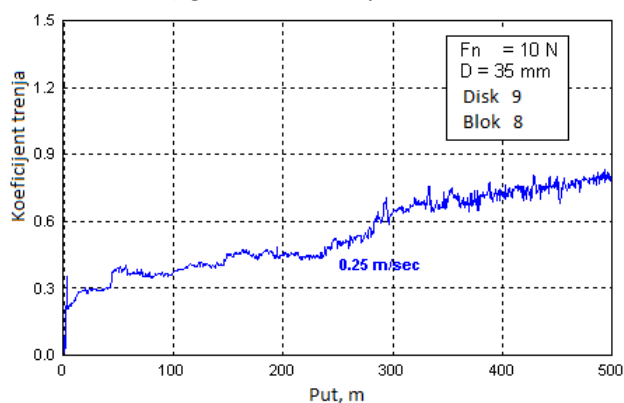
c) mehanički polirana površina

Slika 4. Promena koeficijenta trenja prevlaka hroma

3. ANALIZA REZULTATA

Na svim uzorcima prvo je izvršen pregled spoljašnjeg izgleda. Izgled prevlake praćen je vizuelno, na dnevnoj svetlosti, pod uglom od 45º. Površina prevlake kod svih uzoraka je sjajna i glatka. Nema dendrita, pregorelih i nepokrivenih mesta.

Koeficijent trenja se kreće u granicama od 0.73 do 0.86 što je u saglasnosti je sa rezultatima dobijenim u istraživanjima [4, 5, 7]. Vrednost koeficijenta trenja je viša kod prevlaka taloženih po programima 3 i 4, odnosno sa strujom gustine od 60 A/dm2. Ove prevlake imaju višu tvrdoću.

Promena širine traga habanja ima isti karakter za sve ispitivane uzorke samo je razlika u nivou njihove pohabanosti. Proces habanja karakteriše postizanje određenog nivoa, stabilizaciju i malu promenu širine traga habanja tokom vremena ispitivanja. Širina traga habanja je manja kod prevlaka dobijenih po programu 3 i 4, odnosno sa strujom gustine od 60 A/dm2.

Na slikama 5 i 6, dat je njihov grafički prikaz u zavisnosti od programa taloženja prevlaka.
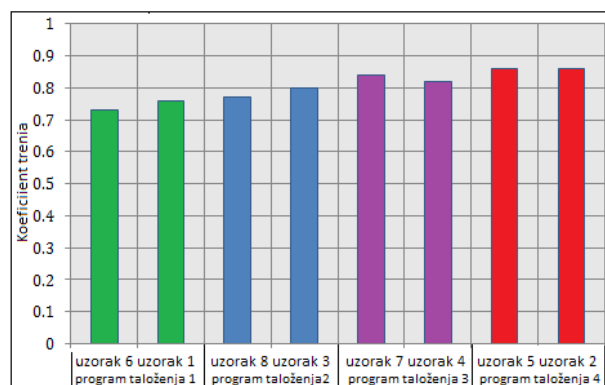
Slika 5. Promena koeficijenta trenja prevlaka hroma
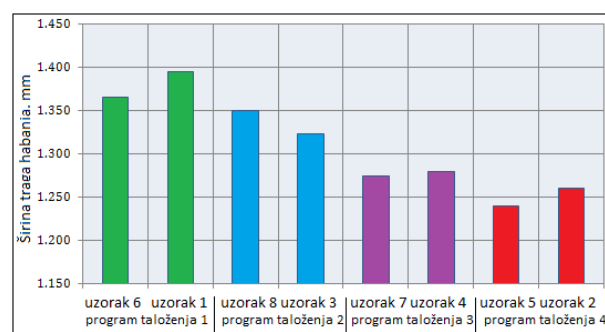
Slika 6. Promena širine traga habanja

Otpornost na habanje prevlaka hroma je određena na osnovu zapremine pohabanog materijala. Vrednosti zapremine pohabanog materijala za ispitivane prevlake hroma date su su u tabeli 4, a grafički prikaz na slici 7.

Tabela 4. Zapremina pohabanog materijala

Uzorak	program taloženja	Ra, μm	μ	Zapremina pohabanog materijala, mm³ x10⁻³
1	1	1.242	0.76	80.0671
2	4	1.880	0.86	58.9945
3	2	1.600	0.80	68.2957
4	3	1.390	0.82	61.8492
5	4	1.368	0.86	56.2290
6	1	0.870	0.73	74.1890
7	3	0.870	0.84	61.1271
8	2	0.600	0.78	72.5641
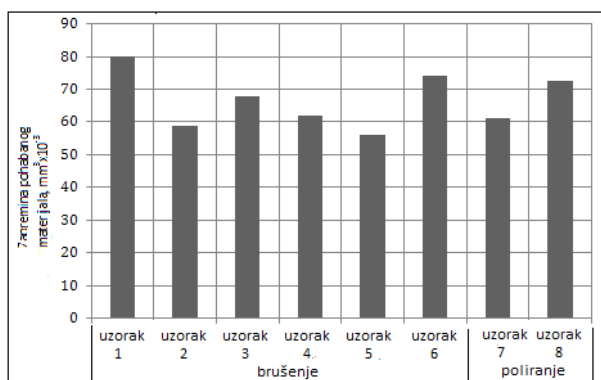
Slika 7. Zapremina pohabanog materijala

Ako se posmatra nivo pohabanosti ispitivanih uzoraka vidi se da uzorci 7, 4 i 2 imaju skoro isti nivo pohabanosti. Ovi uzorci imaju potpuno različite karakteristike podloge za taloženje prevlake, tvrdoća se kreće u rasponu od 39 da 42 HRC, hrapavost od 0.600 do 1.880 μm. Debljina prevlaka je takođe različita i kreće se u rasponu od 22.48 do 88.90 μm, tako da osnovni uticaj na nivo pohabanosti imaju faktori procesa taloženja.

Otpornost prema habanju prevlaka hroma povezana je sa njihovom tvrdoćom i plastičnošću po složenoj zavisnosti. Otpornost prema habanju prevlaka raste sa povećanjem mikrotvrdoće do oko 1000 $HV_{0.1}$. Dalje povećanje mikrotvrdoće uzrokuje smanjenje nivoa otpornosti na habanje. Ova pojava se dovodi u vezu sa tim da pri ovim vrednostima tvrdoća zrna prelazi čvrstoću njihove uzajamne veze. U tom slučaju habanje prevlaka nastaje uglavnom kao posledica drobljenja pojedinačnih zrna [3].

4. ZAKLJUČAK

Na osnovu dobijenih rezultata može da se zaključi da najveći uticaj na tribološke karakteristike prevlaka hroma imaju parametri taloženja. Uticaj stanje podloge na koju je istaložena prevlaka hroma je manji ali ne može da se zanemari.

Rezultati istraživanja promene topografije površine u zavisnosti od načina dobijanja prevlake hroma su pokazala da nanošenjem prevlake dolazi do značajne promene topografije. Uočljiv je primetan trend rasta hrapavosti površine sa produženjem vremena taloženja odnosno, sa porastom debljine prevlake, dolazi do porasta hrapavosti, a što je u skladu sa literaturnim navodima.

Vrednost koeficijenta trenja je viša kod prevlaka taloženih po programima 3 i 4, odnosno sa strujom gustine od 60 A/dm², i kreće u granicama od 0.73 do 0.86 što je u saglasnosti je sa rezultatima dobijenim u istraživanjima [4, 5, 7].

Kod prevlaka taloženih sa strujom gustine od 60 A/dm² su i vrednosti pohabanog materijala manje.

U zavisnosti od režima hromiranja i uslova eksploatacije, otpornost prema habanju delova sa prevlakama hroma povećava se tri do pet puta u odnosu na delove bez prevlaka.

Realizovana ispitivanja i dobijeni rezultati ukazuju na postojanje zavisnosti između tvrdoće podloge, debljine prevlake i širine traga habanja pri triboloških ispitivanjima, ali uspostavljanje korelativnih veza je moguće realizacijom znatno većeg broja eksperimenata.

5. LITERATURA

[1] Зинченко В. М.: Технологическая наследственность при изготовлении деталей, Технология металлов, 2007. № 5,

[2] Ящерицын П. И.: Технологическое наследование эксплуатационных параметров деталей машин. Справочник, Инженерный журнал № 9, 2004,

[3] Petrović B.: Elektrolitičko taloženje hroma iz samoregulišućih elektrolita, Zaštita materijala, vol.46, broj 1, 2005,

[4] Darbeida A., Stebut J., Barthol M., Belliar P., Lelait L., Zacharie G.: Comparative tribological study of chromium coatings with different specific hardness, Surface and Coatings Technology, 68/69, 1994,

[5] Martinkovič M, Kottfer D, Ferdinandy M, Maňková I.: The characterization of electro-plated Cr coating , Electrochimica Acta. 52, 2006,

[6] Nedić B**.**, Jovanović D**.**, Čupović M**.:** Characteristics of Chromium Coatings Programmed Current Regime, Proceedings: 35th International Conference On Production Engineering, Kraljevo-Kopaonik, 2013,

[7] **Jovanović D**., Nedic B.: Scratch Test Of Chromium Coatings, **J Balk Tribol. Assoc**, Vol. 22, No. 3, (2016).

[8] Sully A., Brandis E.: Chromium, Plenum Press, New York. 1987,

[9] Đorđević S., Maksimović M., Pavlović M., Popov K.: Galvanotehnika, Tehnička knjiga, Beograd, 1998,

INFLUENCE OF PROCESS FACTORS ON TRIBOLOGICAL PROPERTIES OF CHROMIUM COATINGS

Abstract: *Electrolytical chromium coatings have wide and various application, due to characteristics of these coatings. They are deposited with aim to give the surface of base material wanted characteristics such as: wear resistance, chemical stability, esthetic appearance etc. Investigations of galvanic chromium coatings are mostly directed to the connection of the coating with base material, while there is very few data of influence of base material to coating characteristics. Chromium is deposited on steel base from chromate-sulfate electrolyte. For investigation of galvanic chromium coatings model of programmed deposition is set in system of planparalel plates. Program of chromium deposition using direct current is projected. Process of coating deposition, values of parameters at the beginning and during the process, were followed and regulated computer. This paper presents the research results of tribological characteristics of chromium coatings deposited on the substrate obtained by different finishes with different hardness and topography.*

Keywords: *Tribology, galvanic chromium coating, hardness, topography*

REGENERACIJA SEGMENATA NA PAPUČAMA TRANSPORTA BAGERA U RB „KOLUBARA"

Dragoljub VELIČKOVIĆ [1], Svetislav Lj. MARKOVIĆ [2*], Milan VESIĆ[3], Nemanja JEREMIĆ[4]

[1] RB „Kolubara", Lazarevac, Srbija, e-mail: dragoljub.velickovic451@gmail.com
[2]Visoka škola tehničkih strukovnih studija, Svetog Save 65, Čačak, Srbija
[3]RB „Kolubara", Lazarevac, Srbija
[4]Jabučje bb, Lajkovac, Srbija
*Corresponding author: svetislav.markovic@vstss.com

Apstrakt: *U radu je objašnjen kompletan postupak regeneracije segmenata na papučama transporta većine bagerskih jedinica u RB „Kolubara". Do nedavno su, prema staroj praksi, pohabani segmenti transporta odstranjivani sa papuče, a umesto njih su postavljani novi. Međutim, sa novim zahtevima baziranim na ekonomskim principima gde se zahteva skraćenje vremena trajanja popravki, došlo se do osvajanja tehnologije regeneracije pohabanih segmenata. Tehnologija regeneracije pohabanih segmenata obuhvata navarivanje oštećenih otvora kako bi se izvršila njihova naknadna mašinska obrada razbušivanjem. Tehnologija takođe obuhvata i navarivanje gaznih površina segmenata. Ovom metodom otvara se mogućnost da se pohabani segmenti regenerišu i po nekoliko puta čime se postiže duži vek njihove eksploatacije. Primenom ove metode izbegava se ugradnja novih segmenata što dovodi do velike tehnoekonomske uštede, pogotovo imajući u vidu brojnost bagerskih jedinica na površinskim kopovima RB „Kolubara".*

Ključne reči: *bageri, regeneracija, segment transportera, navarivanje*

1. UVOD

Osnovni gazni element koji služi za kretanje svih bagerskih mašina na površinskom ugljenokopima „Kolubare" su papuče. Svaka papuča se sastoji iz tela papuče i segmenta.

Telo papuče se sastoji od tri osnovna lima od čelika Č0563, zatim nekoliko rebara, dva zatvarajuća lima, osovinice, četiri čaure i dva osigurača osovinica. Segment papuče je od čeličnog liva ČL.3134. Oblik papuče i oblik segmenta je isti za sve papuče, a razlikuju se po veličini gazne površine i veličini segmenta. Za vreme rada (kretanja) svih bagera dolazi do habanja papuče i segmenta. Na papuči dolazi

do deformacije – krivljenja i tanjenja limova od kojih su papuče izrađene, a na segmentima dolazi do habanja otvora i ravnih gaznih površina, koje su u međusobnom kontaktu sa vučnim segmentima pogonskih točkova bagera. Treba naglasiti da se segmenti papuče mnogo brže habaju od gaznih limova papuče, pa je regeneracija pohabanih segmenata postala neizbežna [1].

Ranije, dok nije osvojena tehnologija regeneracije segmenata papuča, rađena je zamena istih, pri čemu je pohaban segment, kao otpad, vraćan livnici na ponovno topljenje i livenje.

2. OPIS REGENERACIJE PAPUČA I TEHNOEKONOMSKA ANALIZA

Tehnologija regeneracije bagerskih papuča obuhvata [2]:

a) Regeneraciju gaznih površina papuče – limova, koja podrazumeva zamenu istanjenih limova, ispravljanje krivih limova, vađenje prslina – žljebljenje i ponovno zavarivanje.

b) Regeneraciju pohabanih segmenata, koja podrazumeva:
  - zamenu pohabanog segmenta novim,
  - delimičnu regeneraciju pohabanog segmenta,
  - potpunu regeneraciju pohabanog segmenta,

2.1 Zamena pohabanog segmenta papuče novim segmentom za bager glodar SRs 1200

Zamena starog pohabanog segmenta novim obuhvata sledeće operacije [2]:
  - gasno rezanje – vađenje pohabanog segmenta,
  - ručno brušenje bočnih strana novog segmenta, brušenje limova na papuči i ugradnju novog segmenta,
  - dogradnja novog lima oko segmenta (jer je stari oštećen),
  - zavarivanje novog segmenta,
  - ispravljanje deformisanih limova na papuči i zavarivanje uočenih prslina,
  - utiskivanje čaura u segment papuče.

Tabela 1. Pregled troškova rada

Vrsta radova	Norma sati	Cena sata	Ukupna cena
Bravarski radovi	15	614	9.210
Zavarivački radovi	40	684	27.360
Rendisanje	2,50	4.016	10.040
Borverk	6	8.551	51.306
		Σ	**97.916**

Tabela 2. Pregled utroška materijala

Materijal	Količina	Cena po jed. mere	Ukupna cena
Novi segment	1 kom	105.500	105.500
Elektroda INOX	10 kg	950	9.500

18/8/6 ø4 mm			
Elektroda PIVA 150 B ø4 mm	4 kg	180	720
Kiseonik	20 kg	60	1.200
Acetilen	10 kg	310	3.100
		Σ	**120.020**

Novi segment papuče košta oko 105.500 dinara. Na novom segmentu mora se pre ugradnje uraditi sledeće:
  - obrada otvora segmenata na borverku,
  - obrada ravne gazeće površine segmenta na dugohodnoj rendisaljci.

Ukupna cena za jednu papuču sa novim segmentom bi bila 217.936 dinara.

2.2 Delimična regeneracija pohabanog segmenta papuče

Pri ovom postupku regeneracije segmenta i papuče rade se sledeće operacije [2]:
  - pranje i čišćenje papuče,
  - ispravljanje krivih limova na papučama,
  - žljabljenje, brušenje i zavarivanje prslina na limovima papuča,
  - navarivanje pohabanih gaznih površina segmenata papuča,
  - utiskivanje čaura u segmente papuča.

Tabela 3. Pregled troškova rada

Vrsta radova	Norma sati	Cena sata	Ukupna cena
Bravarski radovi	12	614	7.368
Zavarivački radovi	56	725	40.600
		Σ	**47.968**

Tabela 4. Pregled utroška materijala

Materijal	Količina	Cena po jed. mere	Ukupna cena
Punjena žica Tube-Alloy 218-O McKay ø2.8 mm	15 kg	2.000	30.000
Elektroda INOX 18/8/6 ø4 mm	10 kg	950	9.500
Elektroda PIVA 150 B ø4 mm	4 kg	180	720
Lim ≠10 mm	6 kg	75	450
Kiseonik	8 kg	60	480
Acetilen	4 kg	310	1.240
		Σ	**42.390**

Ukupna cena za jednu papuču sa delimičnom regeneracijom papuče bi bila 90.358 dinara.

2.3 Postupak potpune regeneracije papuče i pohabanog segmenta

Pored postupka delimične regeneracije segmenata papuča transporta, može se primeniti i postupak potpune regeneracije istih.

Slika 1. Navarivanje otvora segmenta

Slika 2. Navarivanje pohabanog otvora

Postupak regeneracije obuhvata sledeće operacije [2]:
- pranje i čišćenje papuče,
- ispravljanje krivih limova na papuči,
- žljebljenje, brušenje i zavarivanje prslina na limovima papuča,
- navarivanje pohabanih gaznih površina na segmentu papuče,
- razbušivanje otvora na prvu čistu meru i navarivanje pohabanih otvora na segmentu,

- obradu (razbušivanje) navarenih otvora na segmentu,
- utiskivanje čaure u segment papuče.

Slika 3. Otvor u segmentu posle navarivanja

Slika 4. Obrada navarenih otvora na borverku

Tabela 5. Pregled troškova rada

Vrsta radova	Norma sati	Cena sata	Ukupna cena
Bravarski radovi	14	614	8.596
Zavarivački radovi	56	725	40.600
Borverk za razbuš.	4	2.500	10.000
Navarivanje otvora	12	2.500	30.000
		Σ	**89.196**

Tabela 6. Pregled utroška materijala

Materijal	Količina	Cena po jed. mere	Ukupna cena
Punjena žica Tube-Alloy 218-O McKay ø2.8 mm	15 kg	2.000	30.000
Elektroda INOX 18/8/6 ø4 mm	18 kg	950	17.100
Elektroda PIVA 150 B ø4 mm	5 kg	200	1.000
Lim ≠10 mm	6 kg	80	480

Materijal	Količina	Cena po jed. mere	Ukupna cena
Kiseonik	8 kg	60	480
Acetilen	4 kg	310	1.240
		Σ	**50.300**

Ukupna cena za jednu papuču sa potpunom regeneracijom papuče bi bila 139.496 dinara.

3. REZULTATI I DISKUSIJA

Tehnologija regeneracije pohabanog segmenta papuče podrazumeva postupke navarivanja određenom vrstom dodatnog materijala na oštećene površine i mašinsku obradu navrenih otvora segmenta. Navarivanje je proces nanošenja slojeva metala na radne površine nekih delova, radi povećanja njihove otpornosti na habanje. Navarivanje se vrši samo kod onih površina radnih delova koje su izložene najvećem habanju, pri čemu je ponekad moguće i višestruko navarivanje pre zamene delova novim. Dobra strana navara je ta što metal navara može biti različitog hemijskog sastava u odnosu na osnovni materijal. Navarivanje se zasniva na polaganju slojeva dodatnog materijala na podlogu, koja se obično razlikuje po hemijskom sastavu, kad je u pitanju regeneracija.

Navari otporni na habanje imaju različit hemijski sastav u odnosu na podlogu, pa je važno da dubina uvarivanja bude što manja, jer je u protivnom teško, ili čak nemoguće, dobiti navar traženog hemijskog sastava.

Tehnologija regeneracije pohabanih gaznih površina na segmentu obuhvata sledeće operacije:

1. Priprema pohabanih gaznih površina (dve vertikalne i jedne horizontalne) za navarivanje. Ona se sastoji od brušenja ručnom brusilicom nagnječenog materijala i čišćenja od korozije.
2. Sečenju – pripremi potrebnog broja pločica lima različite debljine (5, 10, 5 mm) od čelika Č0563.
3. Bravarsko zavarivački radovi pri postavljanju i zavarivanju isečenih pločica na dve vertikalne gazne površine.

Pločice se zavaruju REL postupkom uz korišćenje elektrode INOX 18/8/6, ø4 mm i obavezno predgrevanje površine segmenta gasno brenerom.

4. Navarivanju – popuni praznog prosotra između pločica i navarivanju jednog prolaza, sloja, preko pločica koji se takođe izvodi REL postupkom uz korišćenje elektrode INOX 18/8/6, ø4 mm. Ovom operacijom se u stvari vrši postavljanje – navarivanje takozvanog vezivnog sloja – pufer sloja između osnovnog materijala (ČL.3134 ili ČL.3160) i dodatnih navarenih slojeva od tvrde elektrode koji su obično debljina do 12 mm.
5. Navarivanje jednog sloja – pufer sloja na horizontalnoj gaznoj površini segmenta se isto radi REL postupkom i elektrodom INOX 18/8/6 ø4 mm.
6. Navarivanje po dva zadnja sloja na dve vertikalne i jednoj horizontalno gaznoj površini segmenta do postizanja konačnih mera po crtežu se izvodi REL postupkom uz korišćenje žice Tube-Alloy 218-O McKay ø2.8 mm.
7. Posle završenog navarivanja sa žicom Tube-Alloy 218-O McKay ø2.8 mm, vrši se brušenje – ravnanje gaznih površina ručnom brusilicom.

Tehnologija regeneracije pohabanih otovra na segmentu podrazumeva sledeće operacije:

1. Priprema oštećenih otvora na segmentu za navarivanje. Ona se sastoji u razbušivanju otvora na prvu čistu meru, a izvodi se na borverku uz korišćenje specijalno konstruisanog alata za ovu operaciju.
2. Navarivanje obrađenih otvora na segmentu se vrši MIG i MAG postupkom uz korišćenje žice INOX 18/8/6, ø1.2 mm, a izvodi se uz korišćenje zaštitnih gasova CO_2 i argona. Otvori se navaruju do konačne mere otvora na crtežu plus dodatak za obradu koji iznosi (5-6) mm po prečniku otvora.
3. Obrada navarenih otvora na segmentu papuče se vrši na borverku uz pomoć specijalno kostrukcionog alata.

Regeneracija jedne papuče sa zamenom pohabanog segmenta novim segmentom košta 217.936 dinara + PDV, a regeneracija jedne papuče sa potpunom regeneracijom pohabanog segmenta iznosi 139.496 dinara (rad+materijal) + PDV. Iz ovoga se vidi da razlika u ceni koštanja jedne regenerisane papuče i segmenta iznosi 217.936–139.496 = 78.440 dinara. Tako na primer, pri regeneraciji 116 komada papuča za bager Glodar SRs 1200, ušteda bi iznosila 78.440x116 = 9.099.040 dinara.

U jednom pogonu „Kolubare" prihvaćena je regeneracija papuče i segmenta i iskustvo pokazuje da je vek eksploatacije segmenta, kod kojeg su regenerisane gazne površine znatno duži nego kod novougrađenog segmenta. Ova razlika u dužini vremena eksploatacije je nastala iz razloga tog što je dodatni navareni sloj tvrde elektrode otporniji na habanje od osnovnog materijala (ČL.3134) novog segmenta.

Na globalnom nivou postoji velika ušteda u energiji i sirovini (regenerišu se pohabani segmenti, a smanjena je proizvodnja novih).

Opisani tehnološki proces regeneracije segmenata papuče i izvedena ekonomska računica se odnosi na segmente koji se izrađuju od čeličnog liva ČL.3134. U ponudi pojedinih proizvođača nalaze se segmenti papuča izliveni od čeličnog liva ČL.3160 (12% Mn). Za potrebe RB „Kolubara" osvojen je tehnološki postupak potpune regeneracije segmenata od tog materijala.

4. ZAKLJUČAK

Na osnovu velikog iskustva iz oblasti regeneracije navarivanjem i prethodno urađene analize, može se preporučiti (možda je bolje reći apelovati) svim privrednim subjektima koji u svom procesu rada–proizvodnje imaju povećane zahteve za zamenom habajućih radnih elemenata izrađenih od čelika i čeličnog liva da razmotre mogućnost regeneracije tih radnih elemenata tehnološkim postupkom navarivanja, umesto izrade novih i njihove zamene. Ovakav postupak je nužan, jer su uštede brojne, a pre svega znatno duži vek eksploatacije radnih elemenata, ušteda u osnovnoj sirovini (rude gvožđa), ušteda u energiji, radnim satima i čuvanju životne sredine.

LITERATURA

[1] Okvirno uputstvo za slučajeve reparatura kod rotornog bagera SRs 1200 × 22/2 (630 kW) + VR, „MAN TAKRAFF", prevod RB „Kolubara", 1990.

[2] Tehnologija regeneracije mašinske opreme, „Kolubara–metal", Lazarevac, 1985.

TRIBOLOŠKE KARAKTERISTIKE GALVANSKIH PREVLAKA I PREVLAKE VOLFRAM DISULFIDA

Stefan ĐURIĆ*[1], Bogdan NEDIĆ[1], Bratislav TRIFUNOVIĆ[2], Desimir JOVANOVIĆ[2], Aleksandra KOSTIĆ[3]

[1]Fakultet inženjerskih nauka Univerziteta u Kragujevcu, Srbija
[2]Zastava Oružje AD, Srbija; [3]Tehnički remontni zavod Kragujevac, Srbija
*Corresponding author: stefandjuric992@gmail.com

Abstract: Galvanske prevlake su najzastupljenije prevlake u oblasti površinske zaštite materijala. Kombinacijom više, ili kao samostalni metali uloga ovih prevlaka je da poboljša svojstva osnovnog materijala shodno eksploatacionim uslovima. U specifičnim uslovima gde se javljaju visoke radne temperature i pritisci, agresivne sredine u kojima su radni predmeti podložni koroziji potrebno je zaštiti material kako bi se produžio njegov radni vek. Primenom čvrstih maziva volfram disulfida na bazi nanočestica kao prevlake mogu se ostvariti dobra antihabajuća svojstva materijala. U skladu sa zahtevima iz industrije u radu su prikazani rezultati ispitivanja triboloških karakteristike galvanskih prevlaka cinka, kadmijuma, hroma i prevlake volfram disulfida.

Keywords: *galvanske prevlake, čvrsta maziva, tribološke karakteristike, koeficijent trenja, habanje*

Tribological characteristics of metal coatings and tungsten disulphide coating

Abstract: Galvanized coatings are the most common in the field of surface protection materials. The coating has the task to improve the properties of the base material under the conditions of exploitation. The specific conditions that experience elevated temperatures and pressures, and conditions of the aggressive environment in which the workpieces are exposed to corrosion it is necessary to protect certain materials. Besides, by using the solid lubricants of tungsten disulfide on the basis of the nano-particles as coating good anti-friction and anti-wear properties of the material can be achieved. In accordance with the requirements of the industry for replacing of cadmium coatings with other coatings in this paper are presented the results of tests of the tribological characteristics of the metal coatings from zinc, cadmium, chromium and tungsten disulfide coating.

Keywords: Galvanized coatings, solid lubricants, tribological characteristics, friction, wear

1. Uvod

Oštećenja koja se javljaju u kontaktu elemenata tehničkih sistema ili pri reakciji elemenata i atmosferske sredine su uglavnom skoncentrisana na male površine i tanke slojeve [1]. Procesi trenja i habanja izazivaju oštećenja materijala koja u velikoj meri utiču na životni vek i eksploatacijske karakteristike

materijala [2]. Ove karakteristike su definisane preko koeficijenta trenja, otpornosti na habanje, zamorne čvrstoće, otpornosti na koroziju i dr.

Za poboljšanje karakteristika površinskih slojeva i otpornosti na habanje, na osnovni materijal nanose se zaštitne i druge prevlake. Kvalitet modifikovanih površina definisan je fizičko-hemijskim karakteristikama koje se

određuju ispitivanjima. Ispitivanja se odnose na:
- karakterizaciju modifikovanih površina,
- određivanje fizičko-hemijskih osobina modifikovanih površina,
- određivanje triboloških karakteristika modifikovanih površina, itd. [1].

U radu su ispitane tribološke karakteristike galvanskih prevlaka cinka, kadmijuma, hroma i prevlake čvrstih maziva volfram disulfida. Za ispitivanja triboloških karakteristika korišćena je metoda BLOCK-ON-DISK. Metoda se zasniva na određivanju koeficijenta trenja klizanja merenjem normalne sile opterećenja i sile trenja. Ispitivani blok sa prevlakom je postavljen na specijalnu polugu, na koju su postavljene merne trake. Nomalna sila se preko poluge prenosi na blok koji ostvaruje kontakt po liniji sa diskom koji je postavljen na osovinu tribometra. Okretanju diska se suprotstavlja blok postavljen na mernu polugu pomoću koje se mere normalna sila opterećenja i sila trenja. Tokom procesa dolazi do habanja elemenata u kontaktu i odnošenja čestica sa površine [3], stim da se habanje bloka može meriti merenjem širine traga haba-nja. Ova tribološka ispitivanja se vrše prema standardu ASTM D2714-94 Standard Test Method for Calibration and Operation of the Falex Block-on-Ring Friction and Wear Testing Machine [4].

Zaštitne prevlake cinka, kadmijuma i hroma nanete su procesom galvanizacije. Ove prevlake imaju ulogu da zaštiti osnovni material od korozije i poboljšaju mehaničke karakteristike, u zavisnosti od primene [6].

Prevlaka volfram disulfida je naneta sprej postupkom i pripada grupi čvrstih maziva. Pretežno se koristi u oblasti vojne i vazduhoplovne industrije gde su specifični zahtevi rada na povišenim temperaturama i pritiscima kao i izlaganje agresivnim sredinama [1].

Naoružanje i vojna oprema posebno su važni sa aspekta zaštite materijala od štetnih uticaja. Naoružanje i vojna oprema su prilikom upotrebe izloženi kombinovanim naprezanjima u različitim uslovima primene, što dovodi do oštećenja površinskog sloja

materijala, kao i zamora materijala. Pored toga, veliki deo vojne opreme nije u stalnoj eksploataciji, pa se nalazi u skladištima i magacinima. To je posebno izraženo kod municije, koja se kao sredstvo samo jednom koristi i u tom trenutku mora da ispuni željeno dejstvo. S toga je zaštita sredstava naoružanja i ubojnih sredstava jedan od najvećih izazova odbrambene industrije [5,7].

2. GALVANSKE PREVLAKE I ČVRSTA MAZIVA

2.1 Galvanske prevlake

Elektrohemijsko nanošenje prevlaka ili galvanizacija predstavlja najzastupljeniji metod nanošenja metalnih prevlaka. Ove prevlake se nanose prvenstveno u cilju zaštite osnovnog materijala od mehaničkih oštećenja (habanja) i podizanja otpornosti na štetna dejstva atmosferskih uticaja (korozija). Takođe, primenom prevlaka se mogu poboljšati osobine električne i hemijske provodljivosti. Metalne prevlake se dele na:
- anodne metalne prevlake,
- katodne metalne prevlake.

U ovom radu ispitivane su tribološke karakteristike prevlaka cinka, kadmijuma i hroma. Prevlake cinka i kadmijuma pripadaju anodnim prevlakama.

To znači da je elektrodni potencijal sredine negativniji od elektrodnog potencijala metala, dok prevlake hroma pripadaju katodnim prevlakama i predstavljaju obrnuti proces [8].

Metoda se zasniva na principu obrade metalnih predmeta u elektrolitu uz dejstvo električne struje. Predmeti na koje se nanosi prevlaka se vezuju za nosač koji se nalazi na negativnom polu izvora jednosmerne struje i predstavlja katodu, dok se za pozitivan pol izvora jednosmerne struje spaja anoda. Elektrolit se sastoji od jedinjena metala koje formira zaštitnu prevlaku [5].

Prevlake cinka se pretežno koriste za zaštitu čelika od korozije, gde pokazuju najveću efikasnost. Cink ima negativniji elektrodni potencijal od vodonika, ali se zbog prenapetosti vodonika ipak taloži na katodi [8]. Debljina prevlake cinka zavisi od

eksploatacionih uslova dela na koji se cink nanosi [7].

Kadmijum je dvovalentan katjon i za razliku od cinka nema amfoteran karakter. Predstavlja dobru zaštitu za čelik i liveno gvožđe, prvenstveno od korozije ali i ima dobra električna svojstva, provodljivosti i lemljivosti [10, 11]. Zbog svojih štetnih uticaja na okolinu kao veoma toksičan element, teži se pronalaženju alternativnih prevlaka za kadmijum. Prevlake kadmijuma se uglavnom više ne koriste, izuzev u avio i vojne industrije gde se još uvek koristi, jer za sada nema dovoljno dobre i ekonomične zamene. Evropskim propisima i dokumentima je predviđeno potpuno izbacivanje iz upotrebe do 2020. godine [11, 12].

Hrom ima potencijal -0,56V i trebalo bi da se ponaša kao neplemenit metal ali se u praksi ponaša kao plemenit metal i odgovara mu elektrodni potencijal +1,36V [8]. Prevlake hroma su porozne, pa se za poboljšanu zaštitu od korozije nanose međuslojevi nikla ili bakra. Na ovaj način hrom štiti osnovni materijal od mehaničkih oštećenja i čuva dekorativni izgled, dok drugi metal štiti od korozije. Koristi se u industriji naoružanja, za zaštitu mašinskih delova i različitih delova alata [13].

2.2 Čvrsta maziva

Volfram disulfid pripada grupi čvrstih maziva i odlikuje ga mali koeficijent trenja, hemijskom stabilnošću na povišenim tempera-turama i dobra apsorpcija dinamičkih opterećenja u zoni kontakta [1]. Prevlake volfram disulfida pokazuju izuzetne tribološke karakteristike i odlična svojstva zaštite materijala nakon dugog skladištenja. Koriste se za zaštitu skoro svih metalnih površina, imaju izuzetna antifrikciona, antihabajuća i antikoroziona svojstva. Debljina prevlaka kreće se do 0,2 μm [14].

3. EKSPERIMENTALNA ISPITIVANJA

Eksperimentalna ispitivanja triboloških karakteristika zaštitnih prevlaka realizovana su metodom block-on-disc (slika 1). Prevlake se ispituju na tribometru TR-95 Centra za obradu metala rezanjem i tribologiju Fakulteta inženjerskih nauka Univerziteta u Kragujevcu.
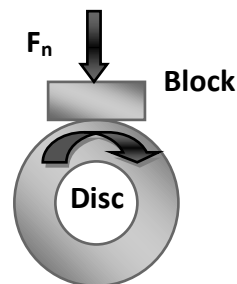
Slika 1. Kontakt **block-on-disc**

Kao osnovni materijal za kontaktne parove diska i bloka korišćen je se čelik 30HN2FA1 (po GOST-u, stara oznaka Č5730) na koji su nanete prevlake cinka, hroma, kadmijuma i volfram disulfida. Prevlake cinka nanete su u fabrici „Tehnički remontni zavod Kragujevac". Nakon nanošenja prevlake cinka vršeno je nanošenje fosfatnog sloja. Uzorci sa prevlakama hroma, kadmijuma i volfram disulfida su dobijeni iz fabrike „Zastava oružje". Prevlaka kadmijuma je naneta u preduzeću "Krušik" Valjevo. Ispitivani uzorci su bili dimenzija 15 x 10 x 6,3 mm (slika 2).
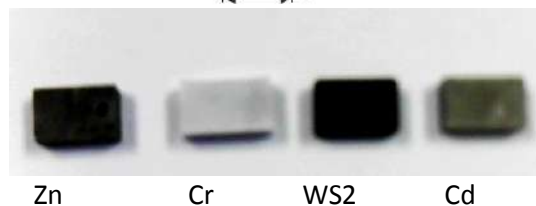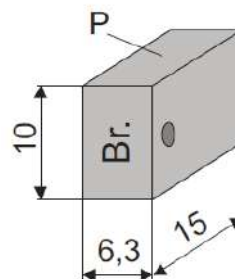
Slika 2. Sample for test on TR-95

Tokom ispitivanja varirane su vrednosti normalnih sila 3 N, 6 N i 9N pri različitim brzinama diska od 0.25 m/s, 0.50 m/s i 0.75 m/s za svako opterećenje posebno.

U tabeli 1 prikazane su vrednosti koefici-jenta trenja za tri različite vrednosti sila pri različitim brzinama kretanja.

Debljine prevlaka su bile:

- Cink 35 μm,

- Hrom 40 μm,
- Kadmijum 50 μm, i
- Volfram disulfid 200 μm.

Table 1. Koeficijent trenja

Prevlaka	Brzina klizanja m/s	Normalna sila		
		3N	6N	9N
Z_n	0.25	0.148	0.173	0.208
	0.5	0.179	0.196	0.237
	0.75	0.206	0.211	0.32
C_r	0.25	0.233	0.239	0.276
	0.5	0.209	0.218	0.251
	0.75	0.192	0.197	0.218
WS_2	0.25	0.136	0.155	0.165
	0.5	0.162	0.173	0.183
	0.75	0.192	0.192	0.216
C_d	0.25	0.228	0.241	0.267
	0.5	0.266	0.298	0.317
	0.75	0.311	0.319	0.322

Nakon realizovanih ispitivanja prevlaka na tribometru, analizom rezultata se može konstatovati da pri povećanju opterećenja raste koeficijent trenja kod svih prevlaka, dok sa povećanjem normalne sile opterećenja kod prevlaka cinka, kadmijuma i volfram disulfida raste korficijent trenja dok kod prevlake hroma opada.

Najmanji koeficijent trenja dobijen je pri ispitivanjima sa prevlakama cinka i volfram disulfida, stim da je pri opterećenju od 3 N najmanji koeficijent trenja kod prevlake cinka, a pod dejstvom normalne sile od 6 i 9 N najmanj koeficijent trenja je bio kod uzoraka sa prevlakom volfram disulfida.

Tokom ispitivanja metodom block-on-disc u kontaktu diska i bloka dolazi habanja materijala, u ovom slučaju do habanja zaštitne prevlake. Proces habanja karakteriše širina traga habanja (Figure 3). Na početku ispitivanja, disk ostvaruje kontakt sa blokom po liniji ali tokom ispitivanja dolazi do habanja i trag se širi u zoni kontakta dva materijala.
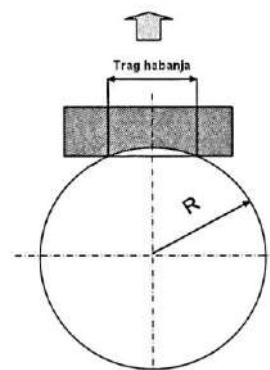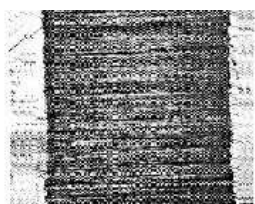
Slika 3. Trag habanja u kontaktu bloka i diska

U tabeli 2 prikazane su vrednosti širine traga habanja koje su izmerene nakon ispitivanja koeficijenta trenja.

Prevlaka volfram disulfida koja zajedno sa cinkom ima najmanji koeficijent trenja ima najširi trag habanja u svim slučajevima ispitivanja. Hrom ima najmanji trag habanja što je u skladu sa njegovom osnovnom primenom (zaštita od mehaničkih oštećenja), a takođe ima i najveću tvrdoću.

Table 2. Širina traga habanja

Prevlaka	Brzina klizanja m/s	Normalna sila		
		3N	6N	9N
Z_n	0.25	0.76	0.87	0.97
	0.5	0.84	0.9	0.98
	0.75	0.94	0.97	1.01
C_r	0.25	0.25	0.26	0.27
	0.5	0.27	0.28	0.3
	0.75	0.29	0.29	0.31
WS_2	0.25	1.22	1.24	1.35
	0.5	1.65	1.82	1.83
	0.75	1.77	2.03	2.21
C_d	0.25	0.5	0.74	0.83
	0.5	0.67	0.85	0.87
	0.75	0.68	1	1.04

Koristeći rezultate prikazane u prethodnim tabelama može se uspostaviti korelacija između promene brzine i opterećenja i širine traga habanja.

4. ANALIZA REZULTATA

Na osnovu dobijenih rezultata triboloških karakteristika prevlaka, najmanji koeficijent trenja imaju prevlake volfram disulfida i cinka.

Na slici 4 prikazane su vrednosti koeficijenata trenja za četiri različite vrste prevlaka pod istih uslova ispitivanja (brzina klizanja 0.5 m/s).
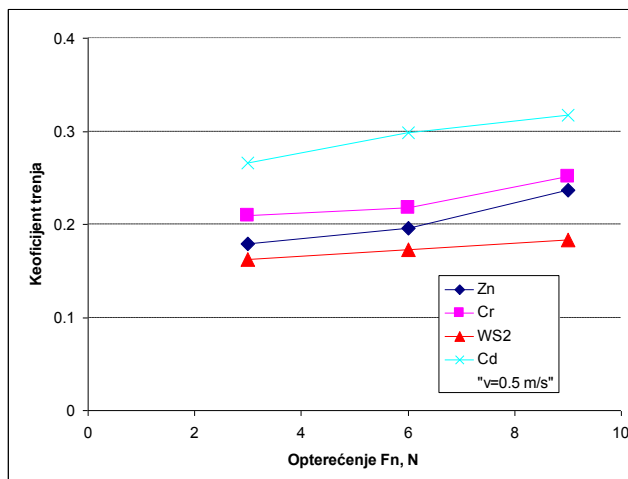
Slika 4. Koeficijent trenja za ispitivane prevlake (v=0.5 m/s)

Širine tragova habanja kod ispitivanih uzoraka sa prevlakama se razlikuju u zavisnosti od vrste prevlake i uslova ispitivanja (opterećenja i brzine klizanja). Za brzinu klizanja 0.5 m/s na slici 5 su prikazani vrednosti širina tragova habanja na bloku.
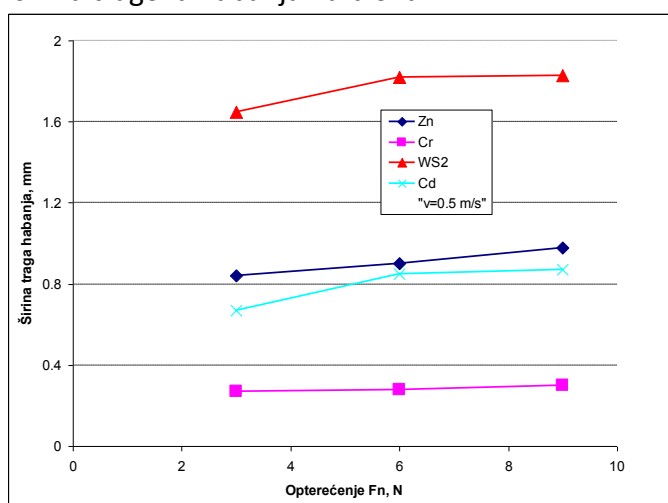
Slika 5. Širina traga habanja za ispitivane prevlake (v=0.5 m/s)

Najširi trag je kod prevlake volfram disulfida, koja je pokazala najmanji koeficijent trenja. Habanje koje se javlja pokazuje da je neophodno povećati tvrdoću prevlake volfram disulfida kako bi se umanjilo odnošenje prevlake, ali je suprotno tome potrebno zadržati nizak koeficijent trenja. Prevlaka hroma ima najmanji trag habanja i nema znatnih promena triboloških karakteristika sa promenom navedenih parametara.

5. ZAKLJUČAK

Ispitivanja triboloških karakteristika i uporedna analiza vrednosti koeficijenta trenja i širine traga habanja pokazuje postojanje međusobnih zavisnosti. Dalja ispitivanja potrebno je realizovati pri većim normalnim silama, većim brzinama klizanja i sa većim brojem uzoraka. Poseban akcenat će biti na ispitivanjima svojstava prevlaka volfram disulfida na bazi nano čestica, koje imaju izuzetna antrifrikciona i antihabajuća svojstva. Ovo je iz razloga pokušaja primene ovih prevlaka u specifičnim uslovima eksploatacije u kod opreme naoružanja i reznih i preserskih alata.

U daljim ispitivanjima, pored promene brzine i opterećenja, vršiće se ispitivanja sa većim broja ciklusa odnosno dužim pređenim putem kao i u uslovima podmazivanja i ispitivanja korozionih svojstava. Prevlake volfram disulfida su na bazi rastvora nano čestica što predstavlja mogućnost variranja velikog broja parametara prilikom nanošenja i tretiranja prevlaka tokom primene.

REFERENCES

1. B. Vasiljević, B. Nedić: *Modifikovanje površina*, Mašinski fakultet Univerzitet u Kragujevcu, Kragujevac, 2003.
2. B. Ivković, A. Rac: *Tribologija*, Jugoslo-vensko društvo za tribologiju, Kragujevac, 1995.
3. A. Zavos, P. Nikolakopoulos: Tribological characterization of smooth and artificially textured coated surfaces using block on ring tests, in: *Serbiatrib - 14th International*

Conference on Tribology, Kragujevac, Serbia, 2015.

4. ASTM D2714-94 *Standard Test Method for Calibration and Operation of the Falex Block-on-Ring Friction and Wear Testing Machine*, 2014.

5. V. Vujičić: *Korozija i tehnologija zaštite metala*, Vojna akademija, Beograd, 2002.

6. B. Nedić, D. Jovanović, G. Lakić Globočki: Influence of previous machining on characteristics of galvanic coatings, in: *Serbiatrib 2011*, Kragujevac, Serbia, 2011.

7. D. Jovanović: *Uticaj tehnologije izrade na karakteristike zaštitnih prevlaka*, PhD thesis, Fakultet inženjerskih nauka Univerziteta u Kragujevcu, Kragujevac, 2015.

8. M. Đurović: Protection equipment and construction of metal and metal coatings, in: Z. Gulušija, Č. Lanjevac (Ed.): Corrosion and protection material, ITNMS IDK, pp. 437-500, 2012.

9. K.R. Sriraman, H.W. Strauss, S. Brahimi, R.R. Chromik, J.A. Szpunar, J.H. Osborne, S. Yue: Tribological behavior of electrodeposited Zn, Zn–Ni, Cd and Cd–Ti coatings on low carbon steel substrates, Tribology International, Vol. 56, pp. 107-120, 2012.

10. I. Granić: *Galvanizacija Zaštita metala od korozije*, Tehnička knjiga nova, Beograd, 2013.

11. A. Agüero , J.C. del Hoyo, J. García de Blas, M. García, M. Gutiérrez, L. Madueño, S. Ulargui: Aluminum slurry coatings to replace cadmium for aeronautic applications, Surface & Coatings Technology, Vol. 213, pp. 229-238, 2012.

12. M. Stopić, B. Fridrih: Electrodeposition, characterization and corrosion investi-gations of galvanic tin-zinc layers from pyrophosphate baths, Vojnotehnički glasnik, Vol. 64, No. 3, pp. 649-669, 2016.

13. B. Nedić, D. Jovanović, M. Čupović: Characteristics of chromium coatings in programmed current regime, ICPE-35th International conference on production engineering, Kopaonik, Serbia, 2013.

14. L. Rapoport, V. Leshchinsky, M. Lvovskya, O. Nepomnyashchy, Yu Volovik , R. Tenne: Friction and wear of powdered composites impregnated with WS_2 inorganic fullerene-like nanoparticles, Wear, Vol. 252, pp. 518-527, 2002.

Authors Index

NANOVEA ®

A Better Measure.

Nanovea began designing and manufacturing instruments after years of experience in providing solutions for profilometry, mechanical and tribology applications. Firmly aligned with its vision, Nanovea aims to simplify advanced measurement technology to stimulate materials engineering for the common good. Ease of use, advanced automation and the dedication to superior accuracy are the driving forces behind Nanovea's full range of Profilometers, Mechanical Testers and Tribometers. Nanovea's instruments can be found internationally in distinguished educational and industrial organizations ranging from automotive to cosmetic, biotechnology to medical devices to microelectronics and space applications. Thousands of clients rely on Nanovea for accurate solutions, technically superior instruments, experienced assistance and comprehensive laboratory services.

N Today's Standard For Tomorrow's Materials.

nanovea.com

SERBIATRIB '17